

Green Energy and Technology

Frédérique Battin-Leclerc
John M. Simmie
Edward Blurock *Editors*

Cleaner Combustion

Developing Detailed Chemical
Kinetic Models

 Springer

Green Energy and Technology

For further volumes:
<http://www.springer.com/series/8059>

Frédérique Battin-Leclerc
John M. Simmie · Edward Blurock
Editors

Cleaner Combustion

Developing Detailed Chemical
Kinetic Models

 Springer

Editors

Frédérique Battin-Leclerc
Laboratoire Réactions et Génie des Procédés
CNRS, Université de Lorraine
Nancy
France

Edward Blurock
Reaction
Lund
Sweden

John M. Simmie
Combustion Chemistry Centre
National University of Ireland
Galway
Ireland

ISSN 1865-3529

ISSN 1865-3537 (electronic)

ISBN 978-1-4471-5306-1

ISBN 978-1-4471-5307-8 (eBook)

DOI 10.1007/978-1-4471-5307-8

Springer London Heidelberg New York Dordrecht

Library of Congress Control Number: 2013945290

© Springer-Verlag London 2013

This work is subject to copyright. All rights are reserved by the Publisher, whether the whole or part of the material is concerned, specifically the rights of translation, reprinting, reuse of illustrations, recitation, broadcasting, reproduction on microfilms or in any other physical way, and transmission or information storage and retrieval, electronic adaptation, computer software, or by similar or dissimilar methodology now known or hereafter developed. Exempted from this legal reservation are brief excerpts in connection with reviews or scholarly analysis or material supplied specifically for the purpose of being entered and executed on a computer system, for exclusive use by the purchaser of the work. Duplication of this publication or parts thereof is permitted only under the provisions of the Copyright Law of the Publisher's location, in its current version, and permission for use must always be obtained from Springer. Permissions for use may be obtained through RightsLink at the Copyright Clearance Center. Violations are liable to prosecution under the respective Copyright Law. The use of general descriptive names, registered names, trademarks, service marks, etc. in this publication does not imply, even in the absence of a specific statement, that such names are exempt from the relevant protective laws and regulations and therefore free for general use.

While the advice and information in this book are believed to be true and accurate at the date of publication, neither the authors nor the editors nor the publisher can accept any legal responsibility for any errors or omissions that may be made. The publisher makes no warranty, express or implied, with respect to the material contained herein.

Printed on acid-free paper

Springer is part of Springer Science+Business Media (www.springer.com)

Foreword

This book appears at a very interesting and important time, when many forces are converging almost simultaneously that will influence the next 100 years of science and technology. Rapid industrialization and economic growth, not only in developed countries but also in less-developed parts of the world, have placed great pressure on the availability of inexpensive energy. Combustion of fossil fuels is very cost-effective and has been the world's primary source of energy for many generations and will probably continue to be the dominant energy source worldwide for at least the next hundred years. The adverse environmental impacts of toxic emissions from combustion in automobiles and industrial operations have been evident for many years. Furthermore, in recent years the huge environmental impacts of combustion products, particularly in the form of carbon dioxide, have also become dramatically apparent, leading to global warming via greenhouse gas emissions.

Increasing concerns about global warming and the environment, and the realization that petroleum reserves are limited and declining today, are highlighting a growing need for new energy sources. While many new energy sources are likely to consist of renewable and nuclear energy, there is also a continuing and probably permanent need for the unique energy density provided by combustion of liquid hydrocarbon fuels. It is also likely to require a century for renewable and other new energy sources to make a significant impact on society, so we will continue to employ combustion of a wide variety of familiar and new fuels for a long time.

Many innovations will be required for us to continue using combustion as a primary energy source, particularly to improve the efficiency of combustion of current and future fuels. New types of engines are being developed, many of them based on ideas such as Homogeneous Charge Compression Ignition (HCCI) and its derivatives, engines that can operate on the wide range of fuels we expect to be used in the future. Chemical kinetics of fuel autoignition plays a particularly significant role in controlling the performance and emissions from these next-generation engines. New fuels include those derived from coal and oils found in shale formations, and from biomass, currently ethanol and other small alcohols, and biodiesel fuels produced largely from plant oils, and each of these new fuels presents great challenges to providing chemical kinetic models to describe their

combustion. Even if “perfect”, emission-free combustion were possible, it will still be essential to find ways to capture and sequester the CO_2 products of combustion in order to reduce emissions of this dominant greenhouse gas. Combustion science is being asked to develop capabilities to accomplish these goals, and kinetic modeling is a central tool to address the complex chemical properties of fuel oxidation and emissions. This book describes the work of prominent combustion chemistry researchers who build, test, and use chemical kinetic models to study combustion under idealized and practical operating conditions.

The science of chemical kinetic modeling of combustion of practical transportation fuels has matured dramatically in recent years. While kinetic models for relatively simple, small fuel molecules like hydrogen, methanol, propane, and natural gas represented the state of the art as recently as 10–15 years ago, today kinetic models are being developed and used to study more realistic and complex fuels such as gasoline, diesel fuel, and kerosene. These practical fuels each consist of many different types of hydrocarbon components, including paraffin, cyclic paraffin, olefin, aromatic, and oxygenated molecules, all of which present serious problems to solve in developing kinetic models for simulating their performance under combustion conditions.

The chemical complexity of modern fuels could not be described without the accompanying maturity of computing facilities, including computer size, processor speed, and development of sophisticated software to integrate the relevant chemical kinetics rate equations. In particular, the advent of massively parallel computing, with coordination of many hundreds or thousands of CPUs, with huge data storage facilities, and powerful visualization capabilities have all made it possible to carry out ambitious chemical kinetic simulations but also to imbed kinetics calculations into multi-dimensional computational fluid dynamics (CFD) models of real-life combustors. Such computer resources have become available only very recently and have made it possible to explore detailed chemistry features of proposed combustion systems so efficiently that novel engine designs can be imagined, designed, and tested in a fraction of the time that used to be required only a few years ago.

Dramatic growth in computing capabilities is having a large impact on combustion chemistry and chemical kinetics. Automatic generation of complicated chemical kinetic reaction mechanisms has become an entire sub-field of combustion, greatly reducing the amount of time needed to build a reaction mechanism for a large, complex fuel. For example, a reaction mechanism for a mixture of diesel primary reference fuels can include nearly 3000 different chemical species and more than 10,000 elementary chemical reactions, representing an immense bookkeeping task. Because practical fuels contain so many different components and their kinetic models can be so large, it is common for combustion modeling to simplify either the level of CFD detail or the level of chemical kinetics detail when simulating the behavior of practical combustion engines. One common solution is to examine idealized problems in simplified geometry while retaining the details of the chemical kinetics; this approach has been widely used to understand kinetics of fuel autoignition, often modeled by assuming homogeneous reaction conditions, or

by using simplified, one-dimensional geometry to study flame propagation, or flame quenching on cold engine walls. Another solution to the computational complexity and costs of simulating realistic combustion systems is to simplify or otherwise reduce the level of detail in the chemical kinetic model, and the processes and techniques for mechanism reductions and simplifications have also become important sub-fields in chemical kinetic modeling. Both automatic mechanism generation and mechanism reduction have their benefits and limitations and are discussed in chapters in this book.

In addition to computational science, many other different sciences are making important contributions to combustion chemistry in general and chemical kinetics of combustion in particular. Theoretical chemistry is now able to use computational tools such as electronic structure techniques to predict essential thermochemical properties of the many chemical species that are included in reaction mechanisms, as well as predict the rates of key reactions that are difficult or impossible to study individually in the laboratory. Important recent theoretical studies of the reaction pathways in Low Temperature Combustion (LTC) have clarified the roles of alkylperoxy radical isomerization pathways in controlling hydrocarbon ignition and the familiar fuel metrics of Octane and Cetane Numbers in evaluating fuel performance in Spark-Ignition and Diesel engines. Powerful analytical systems including large accelerators and advanced laser diagnostics have become very valuable in understanding elementary reaction processes in flames and even inside engines during practical operation. These diagnostics have had a great impact on the accuracy and usefulness of chemical kinetic models in engine and fuel optimization.

An ability to accelerate next-generation combustor design cycles is critical if modern civilization is to respond to the challenges presented by economic and environmental impacts of emissions of combustion. Carbon dioxide emissions are most prominent, although the importance of emissions of soot and oxides of nitrogen and sulfur is rapidly becoming evident. Prediction and understanding of all of these factors require in-depth descriptions of the details of combustion chemistry and the kinetics of the reactions that produce and consume each chemical species that participate in the combustion process.

Detailed chemical kinetic modeling can be used to screen proposed new fuels before significant efforts are expended to produce large amounts of those fuels, eliminating those that have adverse combustion properties. This is possible because a kinetic model can be built based primarily on a knowledge of the chemical structure of the fuel molecules. Some proposals have suggested genetic engineering processes to modify soy bean and other plant oils to produce a bio-diesel fuel with improved combustion and storage qualities. Others are pursuing physical and enzymatic processes that can produce usable fuels from cellulosic biomass from non-food crops. Large research collaborations, combining university, and industry researchers, are pursuing innovative processes that can convert lignocellulosic material from plants into a wide variety of alcohols, acids, furans, and many other possible fuels. Other ideas include bioengineering new types of algae that can produce combustible oils and be raised in huge chemical tanks. The

one common feature to all of these potential fuels is that once the fuel molecule structure from each process is established, chemical kinetic reaction mechanisms can be produced using the techniques reviewed in this book to describe their combustion, and such fuels can be examined computationally in advance of large-scale fuel production to evaluate their likely combustion properties.

Chemical kinetic modeling of combustion has become an essential tool in the understanding of current fuels and engine systems and an established science in its own right. As the sophistication and complexity of our energy world continue to grow in coming years, kinetic modeling will continue to make valuable contributions to world-wide energy production of energy while limiting its environmental impacts, and this book provides a fine survey of the important current trends in this field.

Livermore, California, February 2013

Charles K. Westbrook

Preface

This book arose out of the very successful *COST Action CM0901*¹ which was grant-aided in 2010 by the COST organization. COST is an intergovernmental framework for European Cooperation in Science and Technology² which encourages the coordination of nationally funded research on a European level.

Specifically our Action was contained within the “Chemistry and Molecular Sciences and Technologies” domain which is concerned with fostering expertise in discovering, understanding, producing, and manipulating molecular species.

Toward the conclusion of our Action it was decided to encapsulate the collaborative expertise, which had accrued, in the form of a book with the aim of summarizing the current state of the art. This is that book.

The contents of this book closely mirror the various themes and topics of the Action and the majority of the authors were active participants in the Action. All five working groups are represented in this text which is sub-divided into five Parts.

Part I, about the development of detailed kinetic mechanisms, is connected to working group I (Enlargement of the range of families of initial reactants for which well-validated detailed combustion models are available) headed by *Tiziano Faravelli* and includes contributions from Politecnico di Milano (Italy), Massachusetts Institute of Technology (USA), the National University of Ireland–Galway (Ireland), and the Centre National de la Recherche Scientifique (CNRS)—Nancy (France).

Part II, about techniques to obtain reliable experimental data, is linked to working group II (Writing of models for the formation and consumption of oxygenated pollutants) headed by *Henry Curran* and contains contributions from the National Defense Academy (Japan), Argonne National Laboratory (USA), the Département de Recherche en Ingénierie des Véhicules pour l’Environnement (France), CNRS—Nancy and Orléans (France), the University of Zaragoza (Spain), and the University of Lund (Sweden).

Part III, about soot and polycyclic aromatic hydrocarbons, is connected to working group III (Improvement of the models for formation of polyaromatic compounds and soot) headed by *Maria Alzueta* and includes contributions from

¹ <http://cost.ensic.univ-lorraine.fr/cost/>

² <http://www.cost.eu>

the University of Zaragoza (Spain), CNRS—Villeneuve d’Asq (France), Consiglio Nazionale delle Ricerche (Napoli), the Università degli Studi di Napoli Federico II (Italy), and the University of Cambridge (United Kingdom).

Part IV, about mechanism reduction and uncertainty analysis, is linked to working group IV (Improvement of the methods for mechanism reduction and uncertainty analysis) headed by *Alison Tomlin* and contains contributions from the University of Leeds (United Kingdom), Karlsruhe Institute of Technology (Germany), and Eötvös University of Budapest (Hungary).

Finally, Part V, about elementary reactions, is connected to working group V (Determination of thermochemical and kinetic parameters for elementary steps which are crucial for a successful simulation, but for which important uncertainties remain) headed by *Matthias Olzmann* and includes contributions from the Deutsches Zentrum für Luft-und Raumfahrt of Stuttgart (Germany), the Hungarian Academy of Sciences of Budapest (Hungary), Karlsruhe Institute of Technology (Germany), the Università degli Studi di Perugia (Italy), CNRS—Villeneuve d’Asq (France), Argonne National Laboratory (USA), and the University of Illinois at Chicago (USA).

Note that in addition to authors from eight European countries, this book also includes contributions from one author from Japan and three from the USA.

We, the editors, are deeply indebted to those numerous authors (too many to list here) who have contributed in a timely and competent fashion in spite of the many other demands on their time and energy.



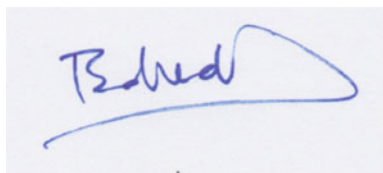
Nancy, France, 29 March 2013

Frédérique Battin-Leclerc



Galway, Ireland

John M. Simmie



Lund, Sweden

Edward Blurock

Contents

1	Introduction	1
	Frédérique Battin-Leclerc, Edward Blurock, John M. Simmie, María U. Alzueta, Alison S. Tomlin and Matthias Olzmann	
Part I Development of Detailed Kinetic Models: The Particular Case of Fuels Obtained from Biomass		
2	Modeling Combustion with Detailed Kinetic Mechanisms	17
	Edward S. Blurock and Frédérique Battin-Leclerc	
3	Automatic Generation of Detailed Mechanisms	59
	Edward S. Blurock, Frédérique Battin-Leclerc, Tiziano Faravelli and William H. Green	
4	Specificities Related to Detailed Kinetic Models for the Combustion of Oxygenated Fuels Components	93
	Frédérique Battin-Leclerc, Henry Curran, Tiziano Faravelli and Pierre A. Glaude	
5	Multistep Kinetic Model of Biomass Pyrolysis	111
	Tiziano Faravelli, Alessio Frassoldati, Emma Barker Hemings and Eliseo Ranzi	
Part II Obtaining Reliable Experimental Data to Validate Models Under a Wide Range of Experimental Conditions		
6	Speciation in Shock Tubes	143
	Kenji Yasunaga and Robert S. Tranter	
7	Rapid Compression Machines	163
	Alan Kéromnès	

8	Jet-Stirred Reactors	183
	Olivier Herbinet and Guillaume Dayma	
9	Tubular Flow Reactors	211
	Fabiola Monge, Veronica Aranda, Angela Millera, Rafael Bilbao and María U. Alzueta	
10	Flame Studies of Oxygenates	231
	Elna J. K. Nilsson and Alexander A. Konnov	
 Part III Experimental Studies and Modeling of PAH and Soot Formation		
11	Formation and Characterization of Polyaromatic Hydrocarbons	283
	Nazly E. Sánchez, Alicia Callejas, Jesús Salafranca, Ángela Millera, Rafael Bilbao and María U. Alzueta	
12	Laser Diagnostics for Selective and Quantitative Measurement of PAHs and Soot	303
	Xavier Mercier, Alessandro Faccinetto and Pascale Desgroux	
13	Characterization of Soot	333
	Cristina Arnal, Michela Alfè, Valentina Gargiulo, Anna Ciajolo, María U. Alzueta, Ángela Millera and Rafael Bilbao	
14	An Advanced Multi-Sectional Method for Particulate Matter Modeling in Flames	363
	Andrea D'Anna and Mariano Sirignano	
15	Modelling Soot Formation: Model of Particle Formation	389
	Edward K. Y. Yapp and Markus Kraft	
 Part IV Methods for Mechanism Reduction and Uncertainty Analysis		
16	Investigation and Improvement of Reaction Mechanisms Using Sensitivity Analysis and Optimization	411
	Alison S. Tomlin and Tamás Turányi	
17	Mechanism Reduction to Skeletal Form and Species Lumping . . .	447
	Alison S. Tomlin and Tamás Turányi	

18	Time-Scale Splitting-Based Mechanism Reduction	467
	Ulrich Maas and Alison S. Tomlin	
19	Storage of Chemical Kinetic Information	485
	Tamás Turányi and Alison S. Tomlin	
 Part V Thermodynamic and Kinetic Parameters for Elementary Chemical Steps		
20	Calculation of Molecular Thermochemical Data and Their Availability in Databases	515
	Elke Goos and György Lendvai	
21	Statistical Rate Theory in Combustion: An Operational Approach.	549
	Matthias Olzmann	
22	Primary Products and Branching Ratios for Combustion Multi-Channel Bimolecular Reactions from Crossed Molecular Beam Studies	577
	Nadia Balucani, Francesca Leonori and Piergiorgio Casavecchia	
23	Kinetic Studies of Elementary Chemical Steps with Relevance in Combustion and Environmental Chemistry	607
	Christa Fittschen	
24	Shock Tube Studies of Combustion Relevant Elementary Chemical Reactions and Submechanisms.	629
	Robert S. Tranter and Kenneth Brezinsky	
	Index	653

Chapter 1

Introduction

**Frédérique Battin-Leclerc, Edward Blurock, John M. Simmie,
Maria U. Alzueta, Alison S. Tomlin and Matthias Olzmann**

Abstract The purpose of this chapter is to describe the general context of this book and to present the five parts which compose it. The development of detailed chemical kinetic models for cleaner combustion is driven by the need to mitigate current environmental issues such as climate change and the potential impacts of gaseous and particulate pollutants on human health, particularly within highly populated urban regions. The first part presents the methods currently used to develop detailed kinetic models for combustion, especially in the case of fuels produced from biomass sources. The second part describes the experimental methods currently used to obtain reliable data in order to test the validity of models for the combustion of fossil and biofuels with a particular focus on the latter. The third part details the experiments and models more especially concerned with the formation of polyaromatic compounds and soot particles. The fourth part concerns the methods proposed for uncertainty analysis and model reduction and, finally,

F. Battin-Leclerc (✉)

Laboratoire Réactions et Génie des Procédés, CNRS, Université de Lorraine,
ENSIC, 1 rue Grandville 54000 Nancy, France
e-mail: frederique.battin-Leclerc@univ-lorraine.fr

E. Blurock

Reaction, Lund, Sweden
e-mail: edward.blurock@esblurock.info

J. M. Simmie

Combustion Chemistry Centre, NUI Galway, Galway, Ireland

M. U. Alzueta

Aragón Institute of Engineering Research (I3A), University of Zaragoza,
Río Ebro Campus. C/Mariano Esquillor s/n 50018 Zaragoza, Spain

A. S. Tomlin

Energy Research Institute, University of Leeds, Leeds LS2 9JT, UK

M. Olzmann

Institut für Physikalische Chemie, Karlsruher Institut für Technologie (KIT),
Kaiserstr. 12, 76131 Karlsruhe, Germany

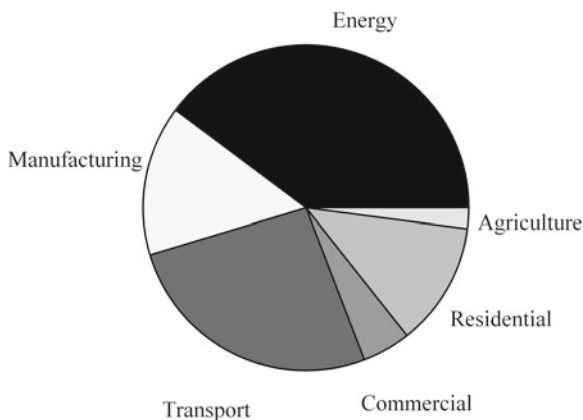
the fifth part describes the experimental and theoretical determination of thermochemical parameters and rate coefficients for the species and reactions included in the proposed models. This book is aimed at readers at an intermediate level between graduate students and junior scientists.

1.1 Context of the Book

Worldwide carbon dioxide (CO_2) emissions have increased from 21.0 Gt per year in 1990 up to 28.9 Gt in 2009 (International Energy Agency 2012). However, in Europe CO_2 emissions from all fuel combustion activities are generally decreasing and were 13 % lower in 2009 than in 1990—a by-product of the Kyoto Protocol. It should however be noted that the emissions from transport in Europe are 21 % higher for the same period (European Commission 2012a). Transport is responsible for around a quarter of European Union (EU 27) carbon dioxide (CO_2) emissions making it the second biggest CO_2 emitting sector after energy (see Fig. 1.1). Road transport accounts for more than two-thirds of EU transport-related greenhouse gas emissions (EEA 2011), with CO_2 being the main one.

An attractive solution to avoid CO_2 emission from transportation could lie in the development of electric or hybrid cars, notwithstanding that electricity is generated by hydropower, renewable energies, such as wind, sun or waves, or by nuclear power. Note that nuclear energy has its own environmental concerns in addition to safety ones. A main limitation in the development of electric cars lies still in the problem of energy storage. Thackeray et al. (2012) have reviewed the state-of-the-art of lithium-ion batteries which are revolutionizing electric energy storage. These authors have shown that, with a specific energy of around 150 W h kg^{-1} , the most advanced batteries do not yet have sufficient energy or life for use in electrified vehicles that would match the performance of internal combustion vehicles. This is illustrated by Fig. 1.2.

Fig. 1.1 EU27 CO_2 emissions by sector and mode of transport in 2009 adapted from European Commission (2012a)



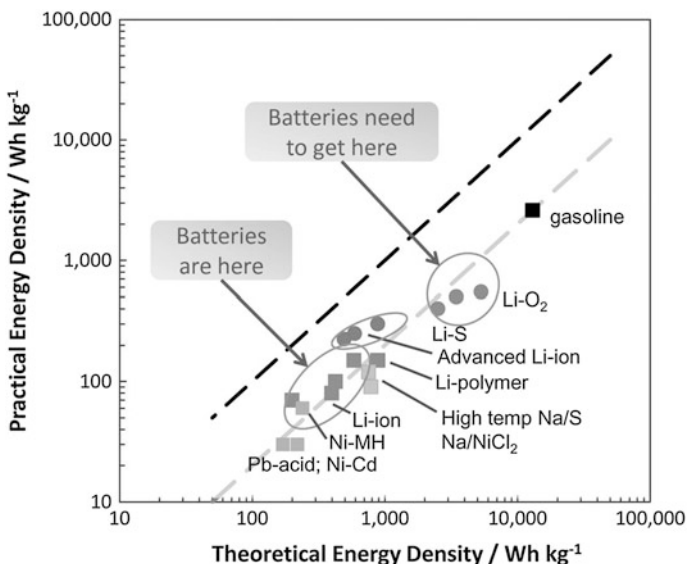


Fig. 1.2 A plot of theoretical specific energy of various rechargeable battery systems versus their practical specific energy compared to that of gasoline. Reprinted from Thackeray et al. (2012), copyright The Royal Society of Chemistry

Without waiting for new technologies such as electric cars to mature, the preservation of the environment urges us to improve as much as possible the engines currently used. It is vital to rapidly obtain a significant reduction of the emissions of greenhouse gases, but also of ozone precursors, primary particulates and particle precursors. Over many years, increasingly stringent directives for engine emission limits have been introduced worldwide for some regulated pollutants. Table 1.1 presents the Euro 6 limits which should be applicable in 2013 to new vehicles in Europe (European Commission 2012b).

In parallel with developments in post-treatment technologies (Wallington et al. 2006; Skalska et al. 2010; Giakoumis et al. 2012; Myung and Park 2012), industry worldwide is developing more efficient and cleaner internal combustion engines, such those based on Homogeneous Charge Compression Ignition (HCCI)

Table 1.1 Euro 6 emission limits for passenger cars (European Commission 2012b)

Mass of carbon monoxide (mg/km)	Mass of total hydrocarbons (mg/km)	Mass of non-methane hydrocarbons (mg/km)	Mass of nitrogen oxides (mg/km)	Mass of particulate matter (mg/km)	Number of particles (#/km)
<i>Spark ignition engines</i>					
1000	100	68	60	4.5	6.0×10^{11}
<i>Diesel engines</i>					
500	–	–	80	4.5	6.0×10^{11}

technologies. The HCCI engine combines the advantages of spark ignition engines with those of compression ignition or diesel ones. The homogeneous fuel/air mixture or charge guarantees low particulate emissions. High dilution leads to very low NO_x production, while still maintaining the high working efficiency of the diesel engine (Yao et al. 2009). However, the main challenge for the successful operation of HCCI combustion engines is the difficulty in controlling the moment of auto-ignition, which is directly governed by chemical kinetics (Flowers et al. 2002), requiring accurate detailed kinetic models. Note however that according to Reitz (2013), dual fuel injection (Lu et al. 2012) could be a solution to greatly improve combustion control in HCCI engines, using port fuel injection of a lower reactivity fuel (e.g. gasoline), coupled with optimised in-cylinder multiple injections of a more reactive fuel (e.g. diesel).

Another possible way to reduce CO₂ emissions, still using internal combustion engines, is to shift from hydrocarbon fossil fuels to biofuels (particularly bioethanol and biodiesel (Agarwal 2007)). The share of biofuels in fuels used for transport in Europe has increased from 0.1 % in 1996 upto 4.4 % in 2010 (European Commission 2012a).

Since the principal components of plant matter, cellulose and starch have a molecular formulae (C₆H₁₀O₅)_n, this means that these new fuels will contain substantial amounts of oxygen which will have both positive and negative impacts on exhaust emissions. Positive impacts may include reductions in particulate emissions (Westbrook et al. 2006), negative ones an increased propensity to form toxic by-products such as aldehydes (Jacobson 2007). Therefore, a deeper understanding of oxygenated bio-fuel combustion chemistry is also necessary to fully exploit both its positive aspects and to minimise the negative ones. Accordingly, a better understanding and modelling of biofuel combustion chemistry are high priority challenges which must be taken up before any further developments of innovative combustion processes are undertaken and before biofuel usage becomes widespread.

In the context of promoting the design of cleaner engines or gas turbines, the purpose of this book is to present the methods which are currently being used to develop detailed kinetic models for the combustion of oil based fuels, as well as of biofuels. The five parts which are included in this book are detailed hereafter.

1.2 Part I: Development of Detailed Kinetic Models: The Particular Case of Fuels Obtained from Biomass

Gasoline and diesel fuels have a “near-continuous spectrum” of hydrocarbon constituents. The constituents of gasoline contain from 4 to 10 atoms of carbon and can be divided into five main component families, as shown in Fig. 1.3a. The constituents of diesel fuel contain from 10 to 20 atoms of carbon with a typical distribution of the main component families shown in Fig. 1.3b.

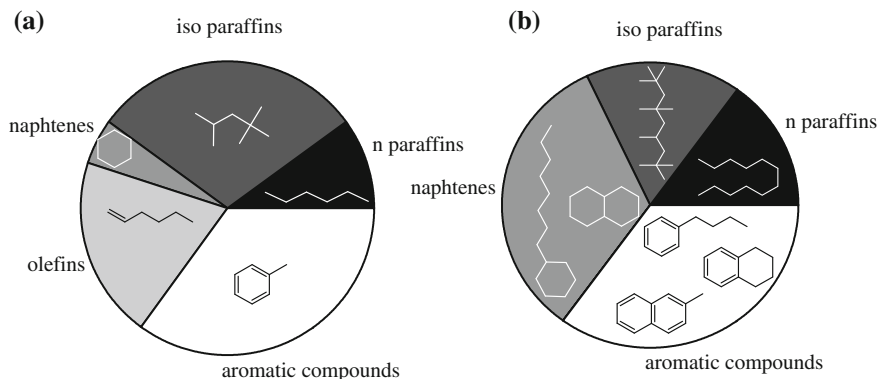


Fig. 1.3 Typical composition of (a) European gasoline (Guibet 1999) and of (b) a US diesel fuel (Pitz and Mueller 2011), and possible model compounds to represent the component families (for diesel fuel, models are not available for all presented model compounds)

The goal of designing cleaner internal combustion engines has prompted the recent growth of industrial projects targeting the development of detailed chemical kinetic models for the combustion of the above-mentioned constituents of fossil fuels and of mixtures of several of them, see reviews by Simmie (2003), by Battin-leclerc (2008), and by Pitz and Mueller (2011). The state of the art shows now the existence of detailed kinetic mechanisms which are built like a library of sub-models considering an increasing number of reactants with more and more details as illustrated by Fig. 1.4.

Concerning pure compounds, numerous models have been proposed for linear alkanes. This abundance of models diminishes considerably when other families of components are considered. Branched compounds and those containing more than

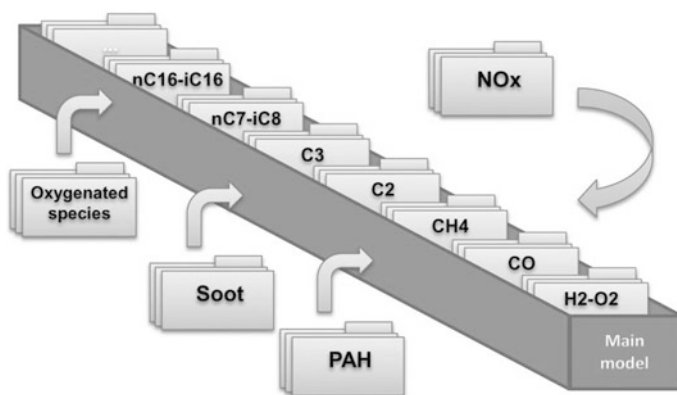


Fig. 1.4 Typical structure of a detailed kinetic model developed for fuel components (adapted from Frassoldati et al. 2010)

ten carbon atoms have been less thoroughly studied. Improvements are still needed in the kinetic modelling of the oxidation of alkenes, cyclic alkanes and aromatic compounds, especially those with a large alkylic chain (Battin-leclerc 2008; Pitz and Mueller 2011).

The ways to obtain transportation fuel from biomass have been reviewed by Huber et al. (2006). Models have started to appear for many types of oxygenated molecules that are considered as potential additives to gasoline or diesel fuel which can be obtained through a wide range of processes involving fermentation or catalytic reactions (Tran et al. 2012):

- *alcohols*, such as ethanol or butanol which can be added to gasoline,
- *fatty acid esters*, which are obtained through the trans-esterification of vegetable oils [the use of lipids produced from algae has been recently investigated (Rawat et al. 2013)] or animal fat with methanol or ethanol, respectively (Demirbas 2005) and can be easily mixed with diesel fuel (Giakoumis et al. 2012),
- acyclic ethers, such as dimethyl ether or ethyl tert-butyl ether,
- cyclic ethers, such as 2,5-dimethylfuran (Román-Leshkov et al. 2007).

Another method widely proposed is the gasification of biomass to produce a ‘syngas’ (a mixture of mainly carbon monoxide and hydrogen) which can thereafter feed a catalytic process (Fisher–Tropsch synthesis) to produce a liquid fuel (Xu et al. 2010). Fisher–Tropsch fuels, made of linear saturated hydrocarbons, can easily be used in diesel engines (Von Schaub et al. 2004).

In Part I of the book, the methods which are used to write detailed kinetic models for the combustion of hydrocarbons are introduced (Chap. 2), with a particular focus on automatic generation methods (Chap. 3). Then the specificities which need to be considered for modelling the two types of oxygenated molecules which are the most commonly considered in biofuels (alcohols and esters) are detailed (Chap. 4). Finally a multistep kinetic model of biomass pyrolysis, which is the first step of gasification and combustion processes, is presented (Chap. 5).

1.3 Part II: Obtaining Reliable Experimental Data to Validate Models Under a Wide Range of Experimental Conditions

Part II of the book deals with a number of experimental methods which give rise to an understanding of the complexities involved in the burning of a ‘fuel’ and allows testing the validity of models under a wide range of operating conditions. The predictions of such models can be used to rapidly estimate the main combustion parameters (such as auto-ignition delay times, laminar flame speed and heat release), which are required for the design of engines or turbines, to estimate fuel consumption and the formation of some of the main regulated pollutants (carbon monoxide, nitrogen oxides, unburned hydrocarbons and particles (see Table 1.1).

The models are also useful in their predictions of minor combustion products, such as alkenes, dienes, aromatics, polyaromatics, aldehydes, ketones, alcohols, acids, sulphur oxides, etc. which can be toxic as regards human health (Battin-Leclerc et al. 2011). Emissions of these intermediates are of great importance for air pollution studies (e.g. Legrand et al. 2003), as they are involved in the formation of urban smog and acid rain.

Some of the methods described in Part II provide a global measure of reactivity, such as Chap. 7 on rapid compression machines and Chap. 10 on flame speeds. Global measures of reactivity still have some part to play in the development of detailed chemical kinetic models (Simmie 2003) but are not perhaps as useful in teasing out the intricacies of the chemistry of combustion. A more effective methodology is presented in the other three chapters, on different types of flow reactors and on shock tubes, providing a detailed insight into the intermediates formed, ‘speciation’, during the combustion process.

The purpose of Chap. 8 is to discuss results obtained from jet-stirred (JSR) or continuously-stirred tank (CSTR) reactors whilst a review on tubular or plug-flow (PFR) reactors can be found in Chap. 9. The differing environments of perfect mixing and zero mixing as the reactants traverse the reactors give rise to different kinetic formulations but provide essentially the same type of information; that is, concentrations of reactants, intermediates and products as a function of temperature or residence time.

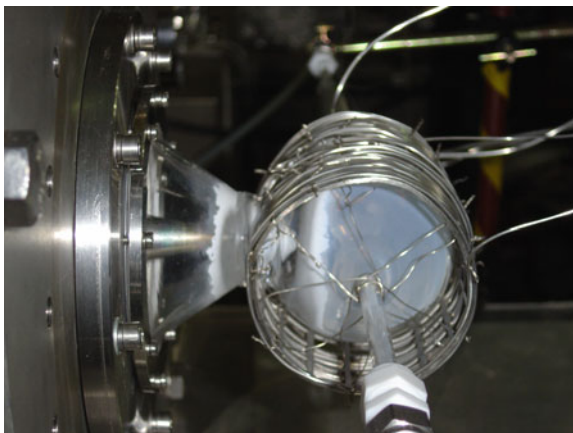
Chapter 6 discusses speciation behind reflected shock waves; the first section focuses on the use of a single-pulse shock tube and sampling the species present which have been formed during one heating and rapid cooling cycle, whereas the second section focusses on sampling during the course of the reaction.

Chapter 10 is somewhat different in tone; in addition to an exposition of the heat flux method for measuring flame speeds which is a significant advance on existing methods it also tabulates data obtained from flame experiments on oxygenates. It does this in a critical fashion assigning the reliability of existing experimental data and pointing out deficiencies in the validation and modelling. It also considers speciation by non-intrusive diagnostics and by probe sampling.

These methods are not in competition with each other but are truly complementary because they provide windows on different aspects of the combustion event. Thus for example, combustion in flames is largely mediated by reactions of hydrogen atoms whose high diffusivity allows them to travel from the hottest part of the flame to the coolest and initiate reactions there which would otherwise not be significant. The rapid compression machine and shock tube can obtain data under engine-relevant conditions of high temperatures and high pressures.

All of the above speciation experiments are heavily dependent upon chemical analytical techniques because combustion is a complex process invariably driven by free radicals whose transient and highly reactive nature does not permit the use of the more traditional methods. In addition, many of the neutral intermediates formed can be quite unstable and difficult to analyse for. Two examples spring to mind; in 2005, enols were detected in hydrocarbon flames (Taatjes et al. 2005) by photo-ionisation mass spectrometry (VUV-MBMS). In 2010, hydroperoxides were

Fig. 1.5 Photograph of a jet-stirred reactor connected to the chamber of a time of flight mass spectrometer



detected (Battin-Leclerc et al. 2010) in the effluent of a jet-stirred reactor (see Fig. 2.5) also by VUV-MBMS. So although both enols and hydroperoxides were long considered to be both present and important intermediates in the combustion of organic compounds, confirmation of their presence necessitated the use of expensive and difficult-of-access equipment (Fig. 1.5).

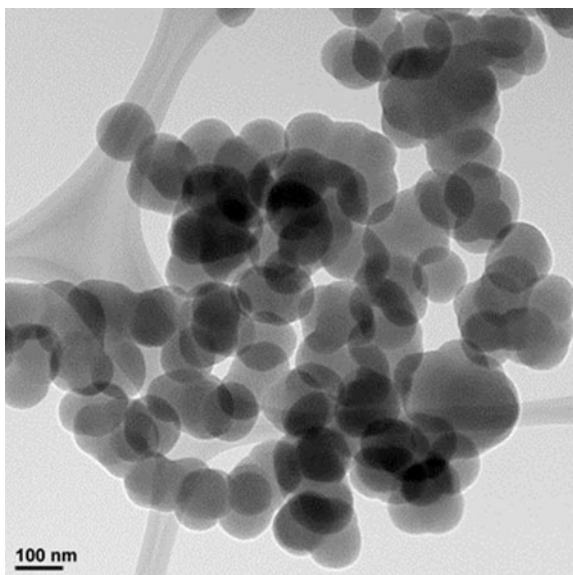
1.4 Part III: Experimental Studies and Modelling of PAH and Soot Formation

Soot and polyaromatic hydrocarbons (PAH) are unwanted products generated in high temperature fuel rich areas of a combustion chamber when burning a variety of fuels. Pyrolysis of the fuel and its derivatives leads to the formation of so-called soot precursors, i.e. small hydrocarbon molecules, such as acetylene and ethylene. These small molecules undergo progressive association reactions resulting in large molecules including a variable amount of aromatic rings, such as the PAH. Further growth of PAH may result in solid particles with a high carbon content, which are known as soot. Figure 1.6 presents the structure of a soot sample as observed by transmission electronic spectroscopy (TEM).

Both PAH and soot are a huge concern for human health, since their emissions, even in very low concentrations, entail serious risks. Additionally, these compounds, specially soot, exhibit important operational problems in combustion processes due to fouling effects and the increased inefficiency of combustion because of their presence. Even though research concerning PAH and soot has been an important topic in recent years, the difficulties associated to their study makes it a highly topical subject.

Progress in modelling PAH and soot formation requires both high quality experimental data and complex detailed models accounting for both the gas phase

Fig. 1.6 TEM image of soot sample is formed from ethylene pyrolysis in a flow reactor at 1475 K in the presence of nitrogen oxides (specifically N_2O); taken from Abián (2013)



and the solid phase chemistry converting small hydrocarbons into PAH and soot. To achieve this, specific methods for quantifying PAH and soot in combustion devices, such as flames and various types of reactors are needed. The complexity of the characterisation of PAH and soot makes it necessary to have available specific experimental setups and characterisation techniques allowing the determination of PAH and soot. Determination of PAH should include PAH speciation, either at the gas phase of effluents as well as those PAH adsorbed on soot surfaces, while soot evaluation must include both its quantification and characterisation, which additionally requires to be adapted to the specific concentration levels and characteristics of the experimental devices and specific operating conditions.

Part III of the book includes the description of the technologies used to quantify and characterise both PAH and soot obtained in thermo-chemical processes, such as combustion and others, in different laboratory experimental systems. In particular, in relation to PAH, details on different techniques for PAH determination with emphasis on chromatography-mass spectroscopy GC-MS (Chap. 11) and laser diagnostic techniques (Chap. 12), including PAH collection and sample treatment, when necessary, are given. Part III also includes an overview of the main techniques available to characterise carbon materials, and thus to soot, including: elemental analysis, physical adsorption with the determination of the specific surface area, electronic microscopy techniques, X-ray diffraction, Raman spectroscopy, infrared spectroscopy, thermo-gravimetric analysis, soot reactivity towards O_2 and NO , UV-visible spectroscopy, size exclusion chromatography and fluorescence spectroscopy (Chap. 13), as well as laser induced incandescence and absorption-based techniques (Chap. 12).

The modelling of soot formation in flames is also described (Chaps. 14 and 15), including the description of novel approaches for soot particle formation in flames. The models presented deal with the description of the two different strategies used to account for the gas phase chemistry, the molecular growth of aromatics into primary particle, together with the description of soot particles growth and oxidation. Additionally, examples of the comparison of modelling results with experimental determinations are given. The different approaches shown to describe soot formation are an example of the wealth of the research in this area.

1.5 Part IV: Methods for Mechanism Reduction and Uncertainty Analysis

The purpose of the mechanisms discussed in parts I-III is to accurately represent the complex kinetic phenomena that occur in practical combustion devices and which determine important combustion characteristics such as ignition behaviour within internal combustion engines for example. To be useful within the context of designing more efficient and cleaner combustion devices, kinetic mechanisms require two important features: (i) they should be represented in such a way that when coupled with models describing complex physical processes, solutions can be found using currently available computational resources; (ii) they should be robust enough to give reliable results under different modelled design scenarios which may include a broad range of temperatures and pressures. Both of these features present challenges. The purpose of *Part IV of this book* is to present the inherent uncertainties which are present within all kinetic mechanisms, as well as the recent developments in the field of chemical model reduction.

The sources of such uncertainty can include poor quantification of input parameters, errors in the measurement of key physical inputs (pressure, temperature etc.), or problems with the model structure. The latter may stem from a lack of understanding of the key processes leading for example to missing chemical pathways within the mechanism, or complex pressure and temperature dependencies of kinetic processes for which it is difficult to find accurate parameterisations over wide ranges of conditions. Despite ever improving methods for the estimation of rate coefficient and thermodynamic data it is not possible to quantify each parameter within a kinetic model perfectly. Within a complex model, the input parameters could be determined by measurement, theoretical calculation or estimation, and therefore will be uncertain to different extents. Where a number of experimental and/or theoretical estimates have been made which are in broad agreement, the uncertainty for example may be considerably lower than for one which has been estimated by expert opinion or by analogy to other parameters. The latter however may be a necessary step in developing new mechanisms for complex fuels such as large and/or oxygenated hydrocarbons. For the further improvement of such mechanisms it would be useful to know which parameters

have the biggest influence on the prediction of key combustion properties so that the types of methods discussed in Part V can be focused on such parameters.

Optimisation methods which combine information from a wide variety of sources may also be used to better constrain the input parameters to combustion models based on statistical approaches. In order to improve the robustness of a mechanism, ideally we would wish to focus kinetic studies or optimisation techniques on those parameters which affect the prediction of important combustion targets to the highest extent. It follows that determining parameter importance for key areas of model application should form an important part of strategies for model improvement and should be performed over wide ranges of temperatures and pressures. Methods for sensitivity/uncertainty analysis and optimisation will therefore be discussed within [Chap. 16](#).

We will see in Part I that comprehensive mechanisms describing fuel oxidation may contain many thousands of species and reactions. When incorporated into three-dimensional computational fluid dynamics (CFD) models, such detailed mechanisms may be beyond the scope of current computational capabilities. It follows therefore that finding reduced forms for chemical models, which are still able to accurately describe their chemical kinetic effects, is a critical research topic if we wish to utilise our improvements in understanding complex fuel oxidation within engineering design. Model reduction using different methods will be described, e.g. species lumping in [Chap. 17](#), time scale splitting based reduction in [Chap. 18](#) and tabulation and repro-modelling methods in [Chap. 19](#).

1.6 Part V: Thermodynamic and Kinetic Parameters for Elementary Chemical Steps

The basis of every detailed reaction mechanism in combustion and elsewhere is formed by a set of elementary chemical steps and its thermodynamic and kinetic parameters. The proper choice of this set and its adequate parameterisation is a necessary prerequisite for the scientific understanding and any successful modelling of a given chemical kinetic problem. A particular issue in combustion is the usually broad temperature and pressure range that can become relevant. It can easily cover several hundred K and one or two pressure decades. Accordingly, besides the absolute magnitude, the temperature and pressure dependences of the kinetic and thermodynamic parameters are of crucial importance.

Most kinetic experiments are condition-specific in a sense that completely different experimental setups have to be used for studying the same reaction in different temperature and pressure ranges. Consequently, experimental information on a rate coefficient is often limited to a rather small range of conditions. Here, well-founded theoretical models are most helpful to enable *adequate* extrapolations to other temperatures and pressures as well as to ensure consistency between kinetic and thermodynamic data. Note that many thermodynamic data, in

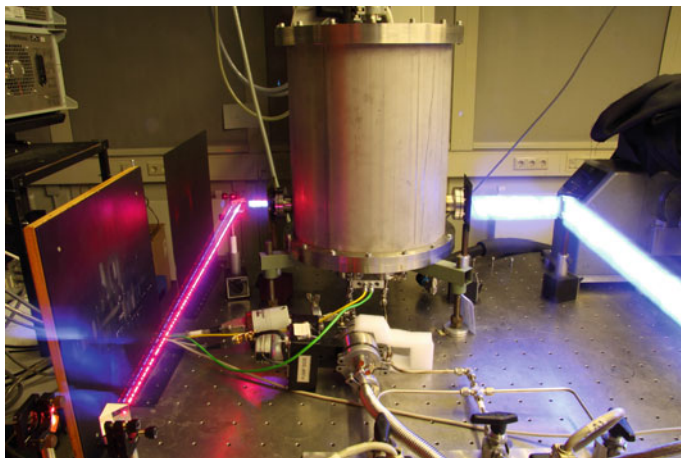


Fig. 1.7 Photograph of a laser photolysis reactor (photolysis laser on the *right*, detection laser on the *left*; long-time exposure)

particular at high temperatures, are indeed inferred from kinetic studies. Kinetic experiments usually require time-resolved species detection, and Fig. 1.7 shows a frequently used setup, a laser photolysis reactor. Time-resolved detection, however, can often be difficult or even impossible for a species of interest under the conditions of interest. To broaden the experimental database for combustion modelling, results from investigations, which are—at first sight—far away from combustion applications can be useful. Here again, reliable microscopic models help to extract the relevant data.

Finally, quantum chemistry in connection with statistical thermodynamics and statistical rate theory is more and more employed to calculate thermochemical and kinetic data from first principles that is, without making reference to experimental results. Nowadays, sufficient accuracy can often be reached, if the theoretical methods are chosen carefully. So all in all many and very diverse experimental and theoretical tools are available to obtain the information on elementary chemical steps necessary for combustion modelling. In Part V, [Chaps. 20–24](#), the currently most important methods are reviewed.

[Chapter 20](#) starts with an overview of methods for electronic structure calculations to determine properties of stationary points on the potential energy surface, which govern thermodynamic and kinetic quantities. Group additivity methods, which are particularly useful for quick estimates and the generation of large datasets are reviewed, and important databases available in the literature are described. [Chapter 21](#) deals with statistical rate theory and elucidates the calculation of rate coefficients for elementary chemical reactions over potential energy barriers and wells. Canonical and microcanonical transition state theories are outlined including the simplified statistical adiabatic channel model for barrierless reactions. Steady-state solutions of master equations for thermal and chemical

activation are elucidated. This approach is application-oriented with examples from the recent literature. In the subsequent [Chap. 22](#), molecular beam experiments are described that were used to determine branching ratios for reactions of oxygen atoms with closed-shell and open-shell hydrocarbon species. It is exemplified how methods of modern experimental and theoretical reaction dynamics can be used to obtain important information for combustion modelling including topics like electronically non-adiabatic effects that have so far only rarely found their way into practical calculations. [Chapter 23](#) outlines essential experimental techniques to study radical reactions in the gas phase. Different methods of radical production and detection are reviewed, and the determination of rate coefficients for the most common reactor types is elucidated. Finally, [Chap. 24](#) on shock tube studies of elementary chemical reactions and submechanisms closes Part V. Different shock tube techniques are briefly described, and recent applications to reactions of fuel molecules, bimolecular reaction steps of chain-carriers and reaction pathways towards soot formation are reviewed.

We note again that it is often only a combination of several techniques that provides the necessary data on elementary chemical steps over the complete range of conditions with sufficient accuracy. Part V compiles the currently most common experimental and theoretical methods.

Acknowledgments The authors thank M.M. Thackeray for providing the original of [Fig. 1.2](#) and T. Faravelli (see [Chaps. 3, 4, 5](#)) for providing [Fig. 1.4](#).

References

- Abián M, Pollutant reduction in combustion systems through flue gas recirculation (FGR), Ph. D. Thesis, University of Zaragoza, 2013
- Agarwal AK (2007) Biofuels (alcohols and biodiesel) applications as fuels for internal combustion engines. *Prog Energy Combust Sci* 33:233–271
- Battin-Leclerc F (2008) Detailed chemical kinetic models for the low-temperature combustion of hydrocarbons with application to gasoline and diesel fuel surrogates. *Prog Energy Combust Sci* 34:440–498
- Battin-Leclerc F, Herbinet O, Glaude P-A et al (2010) Experimental confirmation of the low-temperature Oxidation scheme of alkanes. *Angew Chem Int Ed* 49:3169–3172
- Battin-Leclerc F, Blurock E, Bounaceur R et al (2011) Towards cleaner combustion engines through groundbreaking detailed chemical kinetic models. *Chem Soc Rev* 40:4762
- Demirbas A (2005) Biodiesel production from vegetable oils via catalytic and non-catalytic supercritical methanol transesterification methods. *Prog Energy Combust Sci* 31:466–487
- EEA Report (2011) Greenhouse gas emissions in Europe: a retrospective trend analysis for the period 1990–2008 No 6/2011
- European Commission (2012a) EU energy in figures—Statistical pocketbook 2012. ISBN 978-92-79-22556-7
- European Commission (2012b) Commission regulation (EU) no 459/2012. Official J Eur Union
- Flowers DL, Aceves SM, Martinez-Frias J (2002) Prediction of carbon monoxide and hydrocarbon emissions in iso-octane HCCI engine simulation using multizone simulations. *Proc Combust Inst* 29:687–694

- Frassoldati A, Cuoci A, Faravelli T et al (2010) An experimental and kinetic modeling study of n-propanol and iso-propanol combustion. *Combust Flame* 175:2–16
- Giakoumis EG, Rakopoulos CD, Dimaratos AM et al (2012) Exhaust emissions of diesel engines operating under transient conditions with biodiesel fuel blends. *Prog Energy Combust* 38:691–715
- Guibet JC (1999) *Fuels and engines*. Paris, Publications de l'Institut Français du Pétrole, Editions Technip
- Huber GW, Iborra S, Corma A (2006) Synthesis of transportation fuels from biomass: chemistry, catalysts, and engineering. *Chem Rev* 106:4044–4098
- International Energy Agency (2012) IEA statistics. CO₂ emissions from fuel combustion. 2012 Edition
- Jacobson MZ (2007) Effect of ethanol (E85) versus gasoline vehicles on cancer mortality in the United States. *Environ Sci Technol* 41:4150–5157
- Legrand M, Preunkert S, Wagenbach D et al (2003) A historical record of formate and acetate from a high-elevation Alpine glacier: Implication for their natural versus anthropogenic budgets at the European scale. *J Geophys Res* 108:4788
- Lu X, Han D, Huang Z (2012) Fuel design and management for the control of advanced compression-ignition combustion modes. *Prog Energy Combust Sci* 37:741–783
- Myung CL, Park S (2012) Exhaust nanoparticle emissions from internal combustion engines: A review. *Int J Autom Technol* 13:9–22
- Pitz WJ, Mueller CJ (2011) Recent progress in the development of diesel surrogate fuels. *Prog Energy Combust Sci* 37:330–350
- Rawat I, Ranjith Kumar R, Mutanda T et al (2013) Biodiesel from microalgae: A critical evaluation from laboratory to large scale production. *Appl Energy* 103:444–467
- Reitz RD (2013) Directions in internal combustion research. *Combust Flame* 160:1–8
- Román-Leshkov Y, Barrett C, Liu Z et al (2007) Production of dimethylfuran for liquid fuels from biomass-derived carbohydrates. *Nature* 447:982–985
- Simmie JM (2003) Detailed chemical kinetic models for the combustion of hydrocarbon fuels. *Prog Energy Combust Sci* 29:599–634
- Skalska K, Miller JS, Ledakowicz S (2010) Trends in NO₂ abatement: A review. *Environ Sci Technol* 40:3976–3989
- Thackeray MM, Wolverton C, Isaacs E (2012) Electrical energy storage for transportation—approaching the limits of, and going beyond, lithium-ion batteries. *Energy Environ Sci* 5:7854–7863
- Taatjes CA, Hansen N, McIlroy A (2005) Enols are common intermediates in hydrocarbon oxidation. *Science* 308:1887–1889
- Tran LS, Sirjean B, Glaude P-A et al. (2012) Progress in detailed kinetic modeling of the combustion of oxygenated components of biofuels. *Energy* 43:4–18
- Von Schaub G, Unruh D, Rohde M (2004) Synfuels from biomass via fisher-Tropsch-synthesis - Basic process principles and perspectives. *Erdoel Erdgas Kohle* 120:327–331
- Wallington TJ, Kaiser EW, Farrell JT (2006) Automotive fuels and internal combustion engines: a chemical perspective. *Chem Soc Rev* 35:335–347
- Westbrook CK, Pitz WJ, Curran HJ (2006) Chemical kinetic modeling of the effects of oxygenate hydrocarbons on soot emissions from diesel engines. *J Phys Chem A* 110:6912–6922
- Xu C, Donald J, Byambajav E et al (2010) Recent advances in catalysts for hot-gas removal of tar and NH₃ from biomass gasification. *Fuel* 89:1784–1795
- Yao M, Zheng Z, Liu H (2009) Progress and recent trends in homogeneous charge compression ignition (HCCI) engines. *Prog Energy Combust Sci* 35:398–437

Part I
Development of Detailed Kinetic
Models: The Particular Case
of Fuels Obtained from Biomass

Chapter 2

Modeling Combustion with Detailed Kinetic Mechanisms

Edward Blurock and Frédérique Battin-Leclerc

Abstract Detailed chemical kinetic combustion models of real fuels (e.g., gasoline, diesel, and jet fuels) provide important chemical insight into the chemical phenomena behind the combustion process. The challenge is to find computationally feasible models that help explain the complex behavior observed during the combustion of complex mixtures of hydrocarbon species which make up real fuels. Detailed kinetic mechanisms, made up of a set of reactions and species, describing the chemical reactions between fuel, oxidizer, and intermediate species have proven to be useful in providing the link between the macroscopic phenomena and the microscopic behavior. The purpose of this chapter is to outline the structure, role and diversity of detailed mechanisms in combustion modeling. An important emphasis of this chapter is to describe the approximations and assumptions used. Within the set of chemical modeling methods in general, the interaction between detailed mechanism modeling and more complex chemical models, such as quantum chemical models, or much simpler models, such as skeletal, semi-detailed, and even global reaction mechanisms, is outlined.

2.1 Introduction

A model is an interpretation and an approximation of physical reality. A model is not only a representation of physical reality, but also a construction helping to understand the governing principles behind the physical reality and to make

E. Blurock
Reaction, Lund, Sweden
e-mail: edward.blurock@esblurock.info

F. Battin-Leclerc (✉)
Laboratoire Réactions et Génie des Procédés, CNRS, Université de Lorraine,
ENSIC, 1 rue grandville 54000 Nancy, France
e-mail: frederique.battin-leclerc@univ-lorraine.fr

predictions about physical behavior. In a sense, there is only one physical reality, but there can be a multitude of models representing it. A particular model represents a particular aspect the modeler focuses on. A model can serve multiple purposes. Two significant purposes of a model are understanding and prediction. Of course, these are not mutually exclusive. A “thorough” (the word is in quotes because the model is an approximation of reality) understanding implies that predictions are possible. The level of understanding described by the model is inherently coupled with the complexity and detail of the model. A detailed kinetic mechanism is one such model with its own set of assumptions which are detailed in this chapter for the field of combustion.

In early civilization, the power of the combustion phenomenon was ruled by gods with many mythological names such as Zhu Rong (Chinese), Kagu Tschuchi (Japanese), Hephaestus (Greek), and Vulcan (Roman). In the seventeenth century, Johann Joachim Becher explained the thermodynamics of fire with his phlogiston theory. In the eighteenth century, the role of oxygen and other molecules in combustion became apparent in Lavoisier’s and Priestley’s experiments and the chemical nature of the combustion process and matter itself began to be explored. The study of thermodynamics of combustion was spurred by the industrial revolution with the fundamental theories of Carnot (Carnot 1824) and Gauss (Dunnington et al. 2003; Gauss 1823) which are still in use. At the time of Faraday’s treatise and lecture, “The Chemical History of the Candle” (Faraday 1861), the interactions of the fundamental thermodynamics and chemical aspects of the flame were emerging. With Semenov’s theory of chain mechanisms and thermal explosions (Semenov 1935, 1958) the modern science of detailed combustion reactions began.

Studies of detailed kinetic mechanisms not only have the scientific importance of understanding nature around us, specifically the combustion process, but now they have environmental importance in trying to minimize man’s contribution to climate change, industrial economic importance in making the combustion process in flames, engines, and turbines in transportation and energy more efficient, and socio-political importance in helping to minimize the use of fuels. The goal of a comprehensive detailed mechanism is to extensively describe combustion phenomenon at a chemical level. Of course, without a first principle means of identifying all relevant species and reactions, we can only approximate this goal. Within a collisional dynamic framework, in order to explain the macroscopic nature of the combustion process, we would not only have to identify all the colliding species but also the frequency and energetics of all the collisions under the extensive range of temperatures, pressures, and reacting compositions found, for example, in engines.

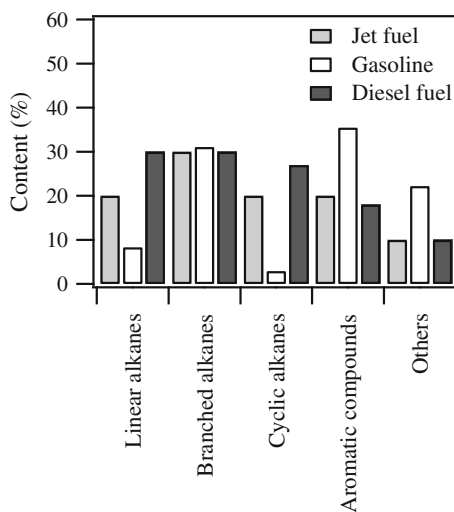
To describe ignition properties, whether in zero-dimensional homogeneous combustion or including also diffusion effects in multidimensional combustion, a model has to describe a whole range of temperature regimes. The models first have to reproduce macroscopic phenomena such as laminar flame velocities, ignition delay times, extinction strain rates, or turbulent or oscillatory behavior. They also have to explain the relative concentrations of the fuel and oxidizer and a range of

intermediate species including pollutants in premixed and non-premixed regimes. In addition, the models have to consider the wide range of combustion time scales found from simple one-dimensional to turbulent three-dimensional flames.

With the lack of a universal model of combustion, model design decisions have to be made. A major source of diversity in combustion models, even for the same fuel, stems from the modeler choosing the “important” properties and parameters needed to describe the chosen physical phenomenon as shown in the comparison of methane combustion models made by Rolland and Simmie (2004). Every model has its advantages and disadvantages. An important aspect of computer modeling is computational cost. Modeling detail in one aspect often comes at the price of neglecting another aspect. For example, with current computational resources, it is impossible to formulate an exact model of jet fuel, gasoline, or diesel fuel with their immense number, diversity, and size of fuel elements (see Fig. 2.1).

Not only does the modeler have to simplify a complex fuel composition with surrogates (see Sect. 2.6.5) but also to reduce the size of the map of operating conditions to be covered. Very few detailed models are valid for wide ranges of temperatures, pressures, or equivalence ratios. The key to the simplification of models, for example in the writing of reduced models or skeletal mechanisms (see Sect. 2.6.3 or for more details Chap. 17), is to limit the range of operating conditions to be considered. In zero-dimensional models, such as in the cases of homogeneous ignition in a rapid compression machine or oxidation in a perfectly stirred reactor, very detailed mechanisms (e.g. Sarathy et al. 2011; Westbrook et al. 2009) can be used. However, for computational fluid dynamic calculations, where there is extensive detail in the three-dimensional flow of the reacting species, only very simplified models, such as global or possibly skeletal mechanisms can be used. There is always a modeling trade-off between chemical detail and physical or flow detail in a model.

Fig. 2.1 Content in hydrocarbon classes found in usual transport fuels, jet fuels, gasolines, and diesel fuels (Guibet 1999; Westbrook 2005). Others consist mainly in alkenes and oxygenated compounds



Detailed combustion modeling plays an important role in elucidating reactive behavior under different conditions and in identifying the pathways leading to pollutant emissions in order to propose reduction methods. For example, Fig. 2.2 shows that at higher equivalence ratios, the amount of soot increases. But at lower equivalence ratios, as the temperature increases, the amount of NO_x emissions increase. At low temperature and equivalence ratio, both soot and NO_x emissions are low. It is under these conditions that the combustion in homogenous charge compression engine (HCCI) or in diesel low temperature combustion (LTC, an alternative approach to achieve HCCI-like combustion obtained by coupling closely autoignition to fuel injection (Dec 2009)) engines function (see Fig. 2.2). It is why it is expected to have lower emissions. Kinetic studies using detailed mechanisms play an integral part of the development HCCI or LTC diesel engines.

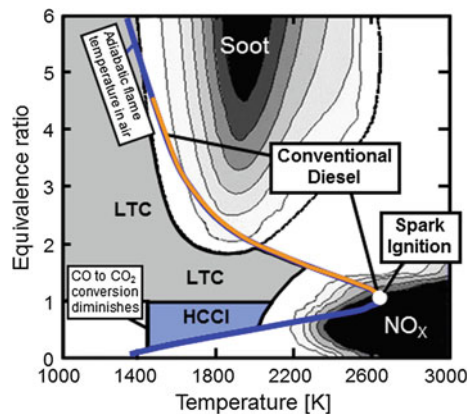
2.2 Chemical Combustion Models

There are a multitude of techniques to model a chemical process (e.g. Williams 1994; Tomlin et al. 1997; Griffiths and Barnard 1995; Warnatz et al. 2006). The focus of this chapter is one particular type of modeling, namely with *detailed combustion mechanisms*. But before presenting them some general features of chemical mechanisms are discussed.

2.2.1 Generalities About Chemical Mechanisms

At the simplest level, a chemical mechanism can be seen as just a list of reacting species and a list of their reactions. However, this and other chapters in this book will try to elaborate the considerable structure and detailed chemical and kinetic

Fig. 2.2 Temperature and equivalence ratio diagram plotting the ranges of NO_x and soot formation and showing the range of functioning of spark ignition, conventional diesel, low temperature combustion (LTC) diesel, and homogenous charge compression (HCCI) engines (Reprinted from Dec 2009, copyright Elsevier)



knowledge required behind these lists. To begin with, two sets of information are provided within the mechanism formulation. There is the thermodynamic information mainly represented by the thermochemical quantities associated with each species, and the kinetic information associated with the set of reactions detailing how the set of species react with each other.

Each reaction in a combustion mechanism is a description of how a set of reactant species are transformed into a set of product species. Ultimately, this description is transformed to numerical combustion models, which solve the mass and the energy conservation equations, according to the type of reactor with special software libraries dedicated to that, such as CHEMKIN (Kee et al. 1993).

An essential component of the numeric form describing chemistry is the *chemical source term*, i.e., the rate of change of concentration of the reacting species, which is extensively described in textbooks (Laidler 1987; Griffiths and Barnard 1995; Warnatz et al. 2006). For example, reaction i in the set of $m_{\text{reactions}}$ in a mechanism including n_{species} species can be generally written:

$$\sum_{k=1}^{n_{\text{species}}} v_{ki}^{\text{reactants}} X_k = \sum_{k=1}^{n_{\text{species}}} v_{ki}^{\text{products}} X_k \quad (2.1)$$

where v_{ki} is the stoichiometric coefficient related species X_k in reaction i . The *rate of progress*, q_i of reaction i can then be expressed:

$$q_i = k_i^{\text{reverse}} \prod_{k=1}^{n_{\text{species}}} [X_k]^{v_{ki}^{\text{products}}} - k_i^{\text{forward}} \prod_{k=1}^{n_{\text{species}}} [X_k]^{v_{ki}^{\text{reactants}}} \quad (2.2)$$

where $[X_k]$ is the molar concentration of species X_k and k_i^{forward} and k_i^{reverse} are the forward and reverse rate constants of reaction i . This, in turn, is used to compute the *rate of production* (ω_k) of species X_k :

$$\omega_k = \prod_{i=1}^{n_{\text{reactions}}} (v_{ki}^{\text{reverse}} - v_{ki}^{\text{forward}}) q_i \quad (2.3)$$

This is commonly known, especially in reactive flows associated with CFD (computational fluid dynamics) equations, as the chemical source term.

An important point is that even when writing down the initial chemical form, the species within the reactions are only labels, i.e., bookkeeping devices keeping track of their concentrations. The actual structural information is only implied by how the species react and the thermodynamic information associated with each species. As shown in the chemical source term, the numeric rate constants combined with the species concentrations form the heart of reactive chemistry.

Rate constants, k , are usually expressed using the classical Arrhenius (Arrhenius 1889) form of the rate expression, shown here with a temperature exponent:

$$k = AT^n e^{E_a/RT} \quad (2.4)$$

where A is the pre-exponential factor, n is the temperature coefficient, E_a is the activation energy, and R is the gas constant in $\text{J}\cdot\text{K}^{-1}$. More details about rate constant format are given in [Chap. 19](#).

Associated with each species is their temperature-dependent thermochemical data, specifically enthalpy, entropy, and heat capacities (see more details in [Chap. 20](#)). In combustion, this thermodynamic information is usually represented as two seven term “NASA polynomials,” first formulated by Zeleznik and Gordon ([1962](#)):

$$\begin{aligned}\frac{C_p}{R} &= a_1 + a_2T + a_3T^2 + a_4T^3 + a_5T^4 \\ \frac{H^\circ}{RT} &= a_1 + a_2\frac{T}{2} + a_3\frac{T^2}{3} + a_4\frac{T^3}{4} + a_5\frac{T^4}{5} + \frac{a_6}{T} \\ \frac{S^\circ}{R} &= a_1 \ln T + a_2T + a_3\frac{T^2}{2} + a_4\frac{T^3}{3} + a_5\frac{T^4}{4} + a_7\end{aligned}\quad (2.5)$$

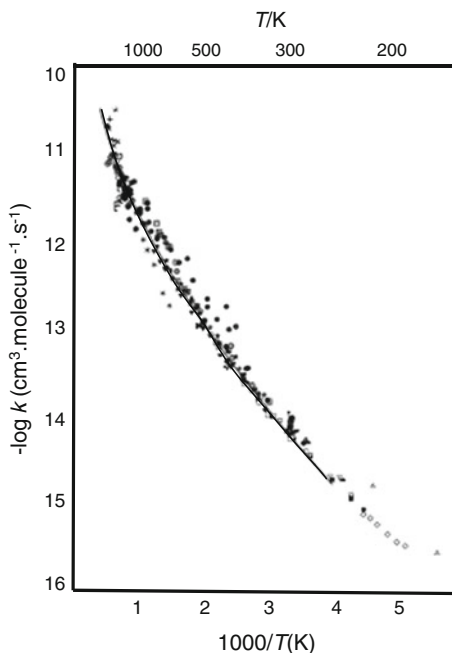
The temperature, T , dependent heat capacity, C_p , standard Enthalpy, H° , and standard Entropy, S° are represented with seven species dependent constants, a_i . Note that associated with each species are also their transport properties to be used for the evaluation of gas-phase multicomponent viscosities, thermal conductivities, diffusion coefficients, and thermal diffusion coefficients (see for instance, Wang and Frenklach ([1994](#))).

2.2.2 Detailed Chemical Mechanisms

A detailed chemical mechanism is usually considered to be composed of a particular type of reaction, namely, an *elementary reaction* (also called elementary step). An *elementary reaction* is a transition from a (set of) reactant molecular structure(s) to a (set of) product molecular structures. The transformation from the reactant molecular structures to the product molecular structures can be thought of the movement of the individual atoms making the reactants through intermediate structures until they reach the product molecular structures.

When the modeler writes down the reactants and products of an *elementary reaction*, he thinks about the complex molecular changes such as valence changes and the making and breaking of bonds that occur during the reactions (see [Sect. 2.4](#)). The rate constant associated with each elementary reaction is derived from the molecular structure and is not dependent on conditions under which it is measured, except temperature and in some cases pressure (for more detail, see [Chap. 21](#)). Many rate constants relevant to combustion can be obtained from databases (e.g., Baulch et al. [1992](#); Tsang and Hampson [1986](#)), evaluating experimental measurements and theoretical calculations; for more detail, see Part V about rate constant determinations. For more than 2 decades, data evaluations, as those shown in [Fig. 2.3](#), have been performed to assess the available kinetic data and then, based on these assessments, recommended rate constants with their uncertainties have been proposed.

Fig. 2.3 Standard rate constants compiled by Baulch et al. (1992) for the reaction $\text{CH}_4 + \text{OH} \cdot \rightarrow \text{CH}_3 \cdot + \text{H}_2\text{O}$. The points are experimental measurements from various sources and the line is the recommended rate constant in the Arrhenius form:
 $k = 2,27 \times 10^{-18} \text{ T}^{2.18} \exp(-1350/\text{T}) \text{ cm}^3 \text{ molecule}^{-1} \text{ s}^{-1}$ Baulch et al. (1992) also indicates uncertainties on rate constants, in this case ($\Delta \log k$) is $+0.1$ over the range 250–350 K, rising to $+0.2$ at 800 K and $+0.3$ at 2400 K



The reaction taken as an example for Fig. 2.3 also illustrates an important feature of combustion mechanisms: the involved molecular structures are not always stable molecules, but in many cases free radicals (or even atoms), e.g., uncharged species with an unpaired electron. Reactions involving free radicals can be divided in four types:

- *Initiation*: those creating radicals from fuel,
- *Termination*: those consuming radicals,
- *Propagation*: those transforming a radical into another one,
- *Branching*: those creating new radicals from a radical or an unstable product (degenerate branching steps).

Several types of elementary reactions have pressure-dependent rate constants, e.g., unimolecular fuel decomposition (see Sect. 2.4.2). In this case, many combustion models use the formalism proposed by Troe (1974), an extension of the Lindemann-Hinshelwood theory (Laidler 1987), to express the pressure-dependent rate constant, k , as a function of the rate constant at very low pressure k_0 , the rate constant at infinite pressure, k_∞ , and $[\text{M}]$ the total concentration of all the present species (third body). These expression for k with four reaction dependent constants, a , T^* , T^{**} , and T^{***} , can also be found in recommendation compilations such as (Baulch et al. 1992). Note that at very low pressure, k can be approximated by $k_0[\text{M}]$, and then increases until k_∞ which is obtained at very high pressure. In between the evolution of k versus $[\text{M}]$ followed a “fall off” curve which can be

approximated by Eq. (2.6). The low-pressure rate constant, k_0 , depends also on the nature of the third body gas. *Third-body efficiencies* are also specified in detailed models and can vary up to a factor of 18 between the least efficient gas, He, and the most efficient one, H₂O (Husson et al. 2013). While third-body efficiencies can have a significant influence, such as explaining *a priori* surprising acceleration of autoignition by addition of water (Anderlohr et al. 2010), important uncertainties exist in their values.

$$\frac{k}{k_\infty} = \frac{y}{1+y} F(y) \left(\text{with } y = \frac{k_0[M]}{k_\infty} \right)$$

$$\log F(y) \cong \frac{1}{1 + \left[\frac{\log(y)}{n} \right]^2} \log F_{\text{cent}} \left(\text{with } n = -0.75 - 1.27 \lg F_{\text{cent}} \right) \quad (2.6)$$

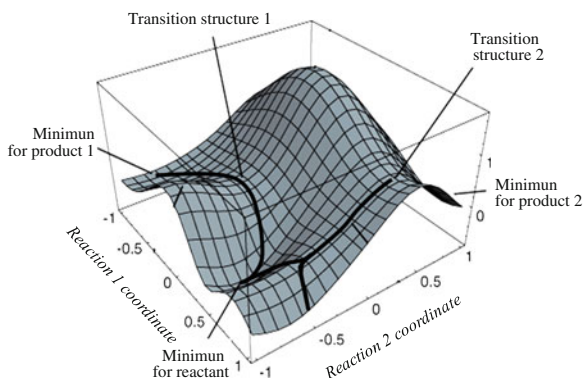
$$F_{\text{cent.}} = (1 - a) \exp\left(-\frac{T}{T^{***}}\right) + a \exp\left(-\frac{T}{T^*}\right) + \exp\left(-\frac{T^{**}}{T}\right)$$

The purpose of detailed mechanisms is not only to *a posteriori* reproduce given experimental results, but also to encompass *a priori* predictions of behaviors for which experimental investigation is difficult, even impossible, or too costly. Detailed mechanisms are also an invaluable tool that can give further chemical understanding of the chemical kinetic processes and species involved. Note that detailed mechanisms are used also for chemical modeling in other fields than combustion, such as atmospheric chemistry (Bloss et al. 2005) or astrochemistry (Venot et al. 2012).

Of increasing importance is computational chemistry based on electronic structure theory, quantum chemistry (Lewars 2011), and semi-empirical models for calculating the needed thermodynamic and kinetic constants. With the increased computational power of modern computers, more complex molecular systems can be calculated. These calculations can not only be used to substantiate experimental evidence, but often they can be used where experiments are very difficult or not even possible. In these models, an explicit three-dimensional structure of the combustion species is specified and its energy structure is derived.

Essentially, a single computational chemistry calculation starts with a three-dimensional configuration of atoms and is based on the resolution of the Schrödinger equation using different levels of assumptions (Harding et al. 2007; Pilling 2009). One of the fundamental assumptions is the *Born–Oppenheimer approximation* which separates the solution involving the nuclei and the electrons, i.e., the nuclei are assumed to be stationary. Given this atomic configuration, the orbital (and total) energy of the molecule is calculated. The Hartree–Fock approximation using a “Slater Determinant” representation of the electronic orbital wavefunctions (for further details see, for example, (Levine 2000)), enables the numerical calculation of this molecular energy. These orbital wavefunctions are represented in terms of basis sets (Hill 2013). The level, accuracy, and complexity of the computation largely depend on these basis sets. More details are given in Chap. 20.

Fig. 2.4 Potential energy surface of molecular configurations representing the reaction from reactants to products (1 and 2) along the reaction coordinates as detailed by Schlegel (1998)



Since the temperature-dependent thermodynamic constants used in combustion are dependent on the total and internal energy of a molecule, computational chemistry calculations are an ideal way to make systematic thermodynamic studies of classes of species. For example, studies have been made for *n*-alkanes (Vanssteenkiste et al. 2003) or a wide range oxygenated molecules or radicals (Sumathi and Green 2002; Sebbar et al. 2004, 2005; Da Silva and Bozzelli 2006; Simmie et al. 2008; Yu et al. 2006).

A single computation of an atomic configuration in three-dimensional space gives a single molecular energy. If “all” configurations of a set of atoms are calculated a *potential energy surface* (Lewars 2011) of these configurations can be calculated (see for example, Fig. 2.4). This potential energy surface can be used in molecular dynamics calculations to calculate rate constants (see Chap. 21). Uncertainties in these rate constant calculations are discussed by Goldsmith et al. (2013). Figure 2.4 displays the paths connecting reactants and products for two competing elementary steps in an energy diagram. The needed information in this complex energy surface is reduced to the “lowest energy” path between the reactant configuration and the product configuration. Each path has to overcome a thermodynamic barrier to form an activated complex called *transition state* or transition structure (Eyring 1935; Truhlar et al. 1996; Harding et al. 2007). As with individual species, each activated complex has its own thermochemical properties which can be calculated using computational methods (see Chap. 20). It can be shown that the energy to form this transition state from the reactants is the activation energy used in the Arrhenius form of the rate constant (Gilbert and Smith 1990).

2.2.3 Low and High Temperature Detailed Chemical Combustion Mechanisms

Advanced low temperature combustion concepts that rely on compression ignition have placed new technological demands on the modeling of the low temperature

reactions of O_2 with fuel (oxidation) in general and particularly on fuel effects in autoignition. Furthermore, the increased use of alternative and nontraditional fuels presents new challenges for combustion modeling and demands accurate rate coefficients and branching fractions for a wider range of reactants. Fuels, especially for transport industry, have long-chain hydrocarbon components.

This includes even the long-chain methyl esters of biodiesel. The study of the ignition of hydrocarbons is intimately related to several aspects of engine performance such as timing, efficiency, and emissions. Numerous books and reviews such as (Griffiths and Barnard 1995; Westbrook 2000; Battin-Leclerc et al. 2011; Zádor et al. 2011) have described the chemistry involved during ignition.

Figure 2.5 shows a simplified scheme of the main primary reactions, which are now usually included in models of the oxidation of an alkane (RH) according to the understanding previously gained (Pollard 1977; Kirsch and Quinn 1985; Walker and Morley 1997; Miller et al. 2005). Alkyl radicals ($R\cdot$) are produced from the reactant (RH) by hydrogen atom abstractions (H-abstractions), first during a short initiation period, by O_2 , and then primarily by $\cdot OH$ radicals. At low temperatures, i.e., below 900 K, $R\cdot$ radicals add to O_2 to yield peroxy ($ROO\cdot$) radicals.

Some consecutive steps then lead to the formation of hydroperoxides, which are degenerate branching agents, explaining the high reactivity of alkanes at low temperature. The $ROO\cdot$ radicals first isomerize to give hydroperoxyalkyl ($\cdot QOOH$) radicals. This isomerization, which occurs via an internal H-abstraction going through a cyclic transition state, has a very large influence on the low temperature oxidation chemistry (Kirsch and Quinn 1985). According to the size of the cyclic ring involved in the transition state, the formation of alkenes and $\cdot HO_2$ radicals can compete with isomerization, mainly at low temperature, by direct elimination from $ROO\cdot$ (Zádor et al. 2011)

$\cdot QOOH$ radicals can thereafter add on O_2 and yield $\cdot OOQOOH$ radicals. These react further by a second internal isomerization producing $\cdot U(OOH)_2$ radicals. The rapid unimolecular decomposition of $\cdot U(OOH)_2$ radicals leads to three radicals and is a branching step occurring at low temperatures. This global step occurs through the formation of alkylhydroperoxides including a carbonyl group, mainly ketohydroperoxides, which in turn can easily decompose giving two radicals. The proposed ketohydroperoxides have only been recently experimentally detected (Battin-Leclerc et al. 2010) under conditions observed close to autoignition. In this scheme, a $\cdot OH$ radical reacting by H-abstraction with the initial alkane leads to the formation of three free radicals, two $\cdot OH$, and a $XO\cdot$ radicals, in a chain reaction. This auto-acceleration process strongly promotes the oxidation of alkanes below 700 K.

When the temperature increases, the equilibrium $R\cdot + O_2 = ROO\cdot$ begins to shift back to the reactants and the formation of $ROO\cdot$ radicals is less favored compared to the strongly inhibiting formation of $\cdot HO_2$ radical and the conjugated alkene. This reaction is equivalent to a termination step since $\cdot HO_2$ radicals react mostly by a disproportionation reaction ($2 \cdot HO_2 = H_2O_2 + O_2$). Unimolecular decompositions of $\cdot QOOH$ radicals also compete with O_2 addition; $\cdot QOOH$ radicals can decompose into cyclic ethers, aldehydes or ketones and $\cdot OH$ radicals,

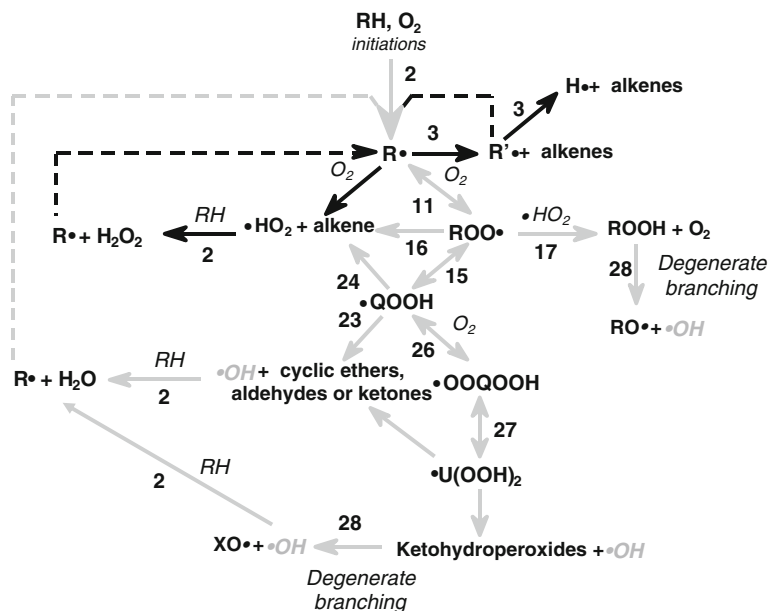


Fig. 2.5 Scheme of the chemistry involved during alkane oxidation. Reactions plotted in gray are important at low temperature (below 900 K), those in black at high temperature. The numbers close the arrows are those of the corresponding reaction classes proposed by Sarathy et al. (2011) as described further in this Chapter

or by β -scission into $\cdot HO_2$ radicals and conjugated alkenes or smaller species. Because of the decrease in the production of hydroperoxides, the reactivity decreases in the 700–800 K temperature range.

This temperature region exhibits a counterintuitive behavior and is called the region of *negative temperature coefficient* (NTC). As shown in Fig. 2.3 in the NTC region, the ignition delay times show the opposite of “normal” behavior, namely that the ignition delay time increases with increasing temperature. This phenomenon had been experimentally observed for many years but could not be satisfactorily explained until kinetic modeling was used to simulate the process. Extension of this type of kinetic analysis eventually led to a thorough description of the kinetics of engine knock, octane number, and HCCI ignition. Examples of experimental observations of NTC zones, as well as modeling using detailed kinetic mechanisms, are presented in Fig. 2.6. Note that in Fig. 2.6 models can fairly well reproduce the position of the NTC area and its variation with pressure, which shifts toward higher temperature when pressure increases. This shift is due to the influence of pressure on the equilibrium of the addition reactions of molecular oxygen to the alkyl and hydroperoxyalkyl radicals (Curran et al. 1998).

NTC is also an explanation for another specificity of the oxidation of alkane chemistry; the possible occurrence of *cool flame* phenomenon at temperatures several hundred degrees below the minimum autoignition temperature. During a

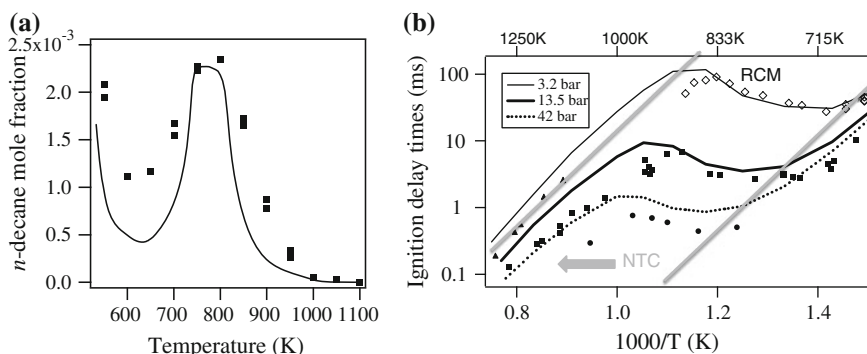


Fig. 2.6 Typical experimental and computed data showing the occurrence of negative temperature coefficient (NTC) behaviors: in a jet-stirred reactor for *n*-decane oxidation (see details in Biet et al. 2008), and b for ignition delay times of *n*-heptane in a rapid compression machine (data at 3.2 bar) and in a shock tube (see details in Buda et al. 2005). See Chaps. 7 and 8 for more details on jet-stirred reactors and rapid compression machine respectively

cool flame, or multiple cool flames, the temperature and the pressure increase strongly over a limited temperature range (typically up to 500 K), but the reaction stops before combustion is complete due to the decrease in reactivity in the NTC zone. The review paper of Townend (1937) shows when this phenomenon was beginning to be accepted and systematically explored.

At higher temperatures, the decomposition of H_2O_2 ($\text{H}_2\text{O}_2 (+\text{M}) = 2 \cdot\text{OH} (+\text{M})$) is a new branching step leading to an increase of the reactivity. This reaction becomes very fast above 900 K. Above about 900 K, the small alkyl radicals ($\text{R}'\cdot$) obtained by the decomposition of the initial alkyl radicals can in turn decompose to give alkenes and $\cdot\text{H}$ atoms. The reaction of $\cdot\text{H}$ atoms with oxygen leads to $\cdot\text{OH}$ radicals and $\cdot\text{O}\cdot$ atoms, which in turn regenerates $\cdot\text{OH}$ radicals by H-abstraction from the fuel. This reaction is the main branching step ensuring the full development of the ignition and the complete combustion.

The chemical behavior just discussed has lead to two different types of detailed mechanisms:

- A *low and intermediate temperature mechanism* which considers the addition to oxygen of alkyl radicals. This mechanism is of maximum complexity, and consequently usually of very large size, but it is absolutely needed to predict the chemistry occurring in or below the NTC zone.
- A *high temperature mechanism* which neglects the addition to oxygen of alkyl radicals. This mechanism is much less complex and of much limited size, but it can only be used to predict the chemistry occurring above the NTC zone, i.e., above 1000 K. The high temperature mechanism is well adapted for flame modeling for which diffusion effects have to be considered.

2.3 Species and Molecular Representation

A molecule (taken in a wide sense including both stable molecules and free-radicals) is a complex object with a multitude of model representations. Each model focuses on what physical reality should be modeled. For example, within physics, the forces and particles within the nucleus of the molecule are important to describe radioactive phenomenon. Within a computational chemistry model, the nucleus is essentially a point charge and the model is concerned with the “structure” and energy of the electron shells around the nucleus (Hehre 2003; Cramer 2004). In this model, each molecular configuration (positions of the nuclei within the molecule) has an energy and this information is used to deduce spectroscopic, thermodynamic, and reactive properties. But even within computational chemistry there is a wide range of possible representations (Davidson and Feller 1986), each with differing computational complexity and accuracy. In semi-empirical molecular models, quantum mechanical models are simplified using parameterization and the focus is on the valence electrons which are the key to chemical reactivity (Stewart 2007). In simpler organic chemistry models, such as Lewis structure (Lewis 1916; Gillespie and Robinson 2007), molecules are represented as atoms with bonds to other atoms and valence electronic properties (e.g., Balaban 1995).

2.3.1 Molecular Representations in Detailed Mechanisms

Within combustion, a multitude of modeling levels and representations of molecules are used. As outlined previously, the species representation within detailed mechanisms is actually just a label in a reaction and each label has some thermodynamic information associated with it. The actual complex structure of the individual species of the mechanism is encapsulated in the information in this representation. The thermochemical data is related to the molecular structure and bonding of the molecule with its functional groups and is a condensation of the complex molecular energies within a molecule. Aside from direct experimental data, another source of thermochemical data can indeed be computational chemistry computations. The rate constants are essentially a condensation of the change of molecular configuration over a complex potential energy surface as discussed in Sect. 2.2.2.

Determining which molecules and reactions to use in the detailed combustion mechanism can be said to be the result of analyzing and studying the reactivity of each species. Although kinetic and thermodynamic details emerge with experimental and computational analysis, initial guesses can be made by analyzing the “Lewis structure” of the species. This will be discussed in the next section.

2.3.2 Lewis Structures and Detailed Combustion Modeling

It is common in organic chemistry to use *Lewis structures* (Lewis 1916; Gillespie and Robinson 2007) to describe the fundamental properties of molecules and how they react. The Lewis structure description, basically, describes the molecule as one writes it down on a piece of paper; a set of atoms connected with a set of (multiple) bonds and possibly the existence of lone pairs and unpaired electrons (radicals) on the atoms. It is synonymous with the 2D graphical form (Balaban 1985), where the graphical nodes are the atoms with associated atomic information, such as atomic number, charge, and if it has a radical or lone pairs. The bonding information between these nodes tells which atoms are bonded together and how they are bonded, i.e., single, double, or triple bond and possibly if the bond has aromatic or resonant character. When the modeler writes molecules or reactions on a piece of paper, some of the implied three-dimensional character of the molecule is included. Figure 2.7 illustrates the cyclic structure of the six-membered ring and the tetrahedral nature of the 5 sp^3 -bonded carbon and oxygen atoms (for more complete explanation of bonding at this level consult any organic chemistry textbook, such as (Clayden et al. 2012)) that is needed to set up the intramolecular hydrogen abstraction during an isomerization of a peroxy radical obtained during the oxidation of *n*-decane.

The Lewis structure model is particularly useful in visualizing the radical behavior of species in combustion reactions. For example, Fig. 2.8 shows how “electron pushing” (see for example Levy (2008)) describes how an alkyl radical can decompose to form a radical and a double bond. The key to this analysis is that a bond is made up of two shared electrons. In the first (virtual) step, the shared electrons go to their respective carbon atoms. In the second step, the newly formed radical electron and the other radical become “shared” to form the second bond of

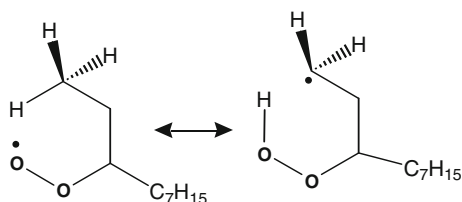


Fig. 2.7 Intramolecular hydrogen abstraction during the isomerization of decyl-3-peroxy radical (see reaction class 15 in Sect. 2.4.2)

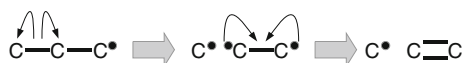


Fig. 2.8 Electron Pushing: this is an example radical decomposition forming a double bond. This example uses the property that a bond is made up of two shared electrons

the double bond. Using this level of analysis, a large portion of hydrocarbon combustion reactions can be explained and new reactions can be postulated. This technique is very common in organic chemistry.

2.3.3 Functional Groups

Lewis structures using electron pushing is a way to keep track and to analyze reactive behavior. However, the effect of different atoms, such as oxygen which plays a large role in hydrocarbon combustion, and different bonding, such as single, double, triple, resonant, and aromatic, is supplementary physical chemical information that has to be taken into account by the modeler. Every chemical environment, meaning an atom and its bonding, has an effect on the neighboring atoms and bonds. For example, a radical on a carbon atom is more energetically stable on a tertiary carbon atom than on a primary carbon atom which has the consequence that a tertiary hydrogen atom is more easily extracted from the carbon atom. These different types of hydrogen and carbon atoms are shown in Fig. 2.9.

Single-bonded oxygen atoms are more electronegative than, for example, carbon atoms and thus they draw electrons toward them thus weakening directly connected bonds. The concept used extensively in organic chemistry is that of the *functional group*, i.e., a (small) collection of atoms and bonds forming a chemical group which have distinct properties (for more information the reader can peruse almost any organic chemistry textbook or, for example (Trahanovsky 1971; Byrd and Hildreth 2001; Struyf 2009)). Functional groups are not only used to describe properties, but also to describe classes of molecules. For example in detailed combustion modeling, particularly those describing hydrocarbon oxidations, mechanisms can include *n*-alkanes, branched alkanes, alkyl radicals, olefins, allyl radicals, alcohols, aldehydes, ketones, aromatics, oxy radicals, peroxy radicals, hydroperoxyradicals, cyclic compounds, and furans. Without resorting to basic physical chemistry principles or even computational chemical principles, the modeler can refer to classes of reactions involving these functional groups. Those groups which are particularly important in combustion modeling are discussed in Sect. 2.4.1, “Concept of Reaction Classes.”

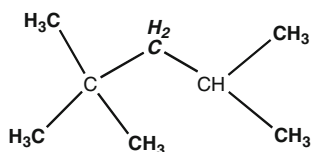


Fig. 2.9 Types of hydrogen and carbon atoms in an isooctane molecule. The primary H atoms and C-atoms are in bold, the secondary ones in bold and italics and the tertiary ones in normal font. The C-atom connected to no H-atom is a quaternary carbon atom

2.3.4 Molecular Representation and Reactivity

In order to understand chemical reactivity, how a molecule is represented and what information this representation contains is central. This applies for both modeling and for experiments. For example, for modelers trying to simulate experimental results, the representation of the molecule can be as simple as a number for the concentration of the species at a given time and/or place in the reactive system. Behind this representation lie other models and representations of the molecule. A spectroscopist measuring the concentration of a species identifies the species by its spectral features, often functional groups, which can involve the electronic or vibrational structure of the molecule; see for example Pretsch et al. (2009). The molecule is then represented by its spectrum. Of course, to describe the physical origin of the spectrum, even more detailed model representations, from statistical mechanical to quantum mechanical models are needed. Even within these models, there lie many levels of modeling and representations.

For the numerical simulation of combustion processes lay also many levels of models and representations. As discussed in Sect. 2.2.1, a common representation of a molecule in combustion is a species label with associated thermodynamics and reactivity. But once again, behind this representation can be a multitude of more detailed representations. For example, when a modeler creates a mechanistic step, the Lewis bonding representation could be used. What is important in this representation is keeping track of the valence electrons which could be involved in a bond, where each atom contributes an electron per bond—a paired electron in a lone pair occupying a valence orbital or a radical, a single electron without a pair in an orbital. For more complex structures, the modeler can draw the bonding on a piece of paper in the 2D graphical form. Here, the three-dimensional structure of the molecule is only implied.

For example, the intramolecular abstraction of a hydrogen atom by a peroxy group presented in Fig. 2.7 can be written in several ways, each showing a bit more information about the reactive step. The reaction could first be written as follows:



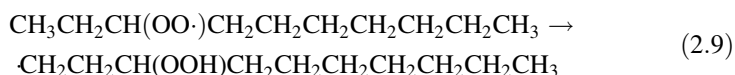
This emphasizes the hydrogen atom being extracted from an internal carbon atom creating a radical and the making of a hydroperoxy (OOH) bond. There is no indication whether the abstraction is from the primary or secondary carbon atom, how branched are the carbon atoms and other thermodynamic influences, such as the ring strain, needed to execute this transformation. This information however could be indirectly given in the associated rate constant. If this reaction is found in a reduced scheme (see Sect. 2.5.3), then the species labels could represent a lumped species and the reaction itself represents a set of lumped reactions.

To take into account the set of possibilities undergoing this intramolecular hydrogen abstraction, more information and more reactions would have to be written. To make the distinction as to where the intramolecular abstraction is

taking place, several more species labels are created and several more reactions are written. One such reaction could be written as:



where the ‘1’ refers to the carbon atom from which the hydrogen atom was extracted and the ‘3’ refers to the carbon atom where the peroxy group is. That this reaction is dealing with a linear alkane would be implicit from the reaction mechanism. It should be noted that one often sees this type of name due to the name length restrictions when converting the list of reactions for the numeric solver. Longer labels could be used to give a representation reflecting the long straight chain of the reacting species. For example, the same reaction could be written:



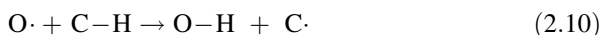
One important structural feature apparent in both the reactions 2.8 and 2.9 is that the hydrogen atom is abstracted from a primary carbon atom, i.e., one of the three hydrogen atoms at the terminal carbon atom in the hydrocarbon chain. The three-dimensional structure is more apparent if the same structures are drawn in 2D graphical form as in Fig. 2.10. Although the molecule is written on a flat 2D surface, the three-dimensional structure is implied through the zigzag drawing and the partial ring.

The position of the hydrogen atoms from the carbon atoms can be emphasized more by using a special notation used by organic chemists as shown in Fig. 2.7. The carbon atoms are drawn in a zigzag pattern in the plane of the paper. The dashed extended triangle denotes that the bond goes into the paper and the filled in extended triangle comes out of the paper. A simplistic bonding is implied with all bond lengths being about the same and that even the oxygen has a tetrahedral configuration. With the 2D graphical form, two important features which can affect the rate constant of this particular reaction are revealed. The bond and valence changes occurring at the atoms within the reactive species are described and the structure of transition state is implied. In the abstraction process of Fig. 2.7, a six-membered ring is formed. The rate constant should reflect further information about the abstraction being from a primary carbon atom and the ring strain due to the formation of a six-membered ring transition state.



Fig. 2.10 2D-graphical form of the intramolecular abstraction of a hydrogen atom by a peroxy group presented in Fig 2.7

For the current example (see Fig. 2.7), the reactive center, i.e., just those atoms involved in the reaction, consists of the carbon–hydrogen bond which is broken in the course of the reaction and the oxygen radical which abstracts the hydrogen:



However, the local molecular environment around the reactive center is what determines the first approximation to the rate constants. The local environment is the set of atoms and bonds, which are connected to the atoms carrying the reactive center. An example is a functional group. It is the job of the modeler to decide the extent of the local environment which has a significant effect on the rate constant. It should always be kept in mind that what is considered “significant” depends on the level of modeling being considered. In this particular example, a very significant feature is that the oxygen is in a peroxy functional group (as opposed to, for example, oxy radicals). An additional significant local feature is the type of carbon atom from which the hydrogen atom is abstracted, i.e., whether it is a primary, a secondary, or a tertiary carbon atom. This particular reaction has not only local “electronic” effects, but also a non-local steric effect and ring strain can affect the rate constant. In contrast to the “electronic” local features effecting the bond strength and radical stability, this is due to the structure of the transition state of the reaction. In this reaction, the transition state involves a ring structure determining which local effects should be considered is dependent on the level of modeling. This is a key assumption in determining reaction classes which will be discussed in the next section.

2.4 Reactions

As discussed previously, reactions in detailed mechanisms represent a transformation from one species to another. All the physical information associated with the reaction, whether it comes from experiments, simple physical chemistry arguments, or more complex calculations, is implied in the rate constants of the reaction and the thermodynamic data of the species. This gives considerable freedom in how the reaction is written.

There is no fundamental restriction as to the level of mechanistic detail a reaction class should represent. As discussed previously, a reaction in a detailed mechanism is a transformation from reactants to products. In essence, the only restriction is that the rate of this transformation can be represented in an Arrhenius form with possible pressure-dependent parameters (see Sect. 2.2.2). The following are some examples of types of reactions that can usually be considered:

- *Elementary reaction*: these are fundamental mechanistic steps, for example through one transition state.
- *Formally direct reaction*: these are reactive pathways that traverse more than one transition state in a single elementary step (Zádor et al. 2011).

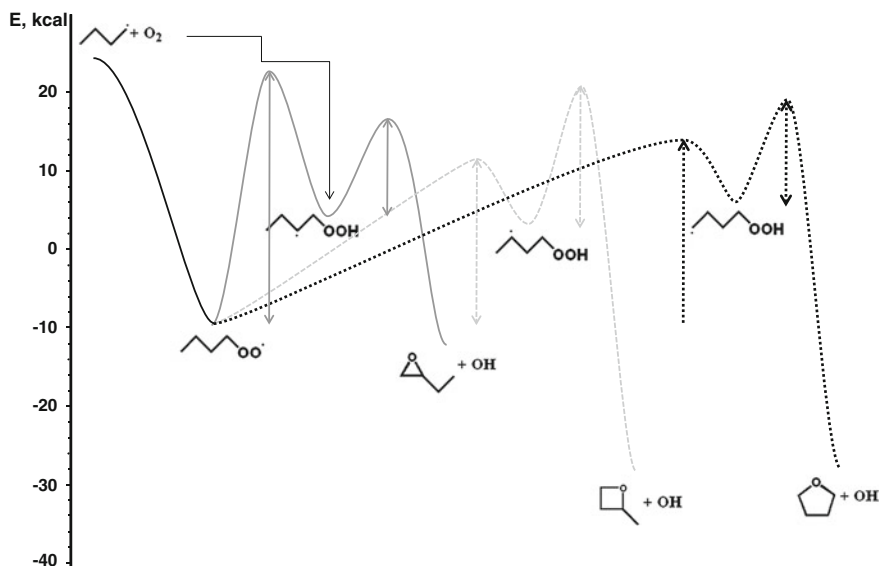
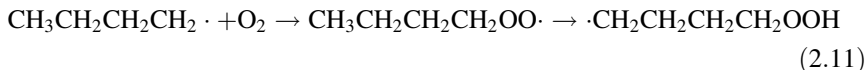


Fig. 2.11 Potential energy surface from the reaction of $R\cdot + O_2$ in the case 1-butyl radical as studied by Cord et al. (2012a). The straight arrows represent the energy variation from reactant to transition state for elementary reactions crossing a single transition state. The broken arrow represents an example of “formally direct” pathway as defined by Zádor et al. (2011)

- *Vertical lumped reaction*: the reaction formally goes through several transition states, but only the initial reactants and the final products are given in the reaction.
- *Lumped species reaction*: some or all of the species, reactants, and/or products, listed in the reaction are lumped (see Chap. 17).
- *(Semi-)global reactions*: a transition between a set of reactants to a set of products not necessarily representing any mechanistic structure.

Note that, to be considered a detailed mechanism, a mechanism should not consist mostly of lumped or (semi)-global reactions. In this case, it should be called *semi-detailed mechanism*.

For some elementary reactions, the full potential energy surface can be complex. Indeed in reactive systems where multiple reactive possibilities occur, the potential energy surface can have several minima, for the reactants and products, and transition states for the activated species. In understanding the system, however, the important information can be condensed to a diagram such as Fig. 2.11, where multiple minima and transition states (as maxima with a given activation energy) are shown. Figure 2.11 shows the path from butyl radical to hydroperoxybutyl radical can occur in two ways. The first is given as two consecutive “simply direct” elementary reactions, for example:

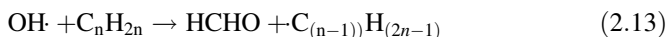


In addition, however, there is a “formally direct” (Zádor et al. 2011) pathway directly from the butyl radical to the hydroperoxybutyl radical, for example:



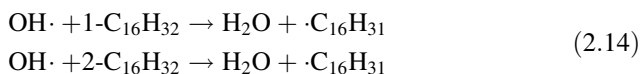
Formally direct pathways are single elementary steps, but they are mechanistically “indirect,” crossing sometimes multiple transition states. Their rate constants are more difficult to calculate than for “normal” elementary reactions. They can be derived from eigenvector-eigenvalue pairs in the solution to the master equation (see Chap. 21).

For practical purposes, reactions in most detailed mechanisms are not restricted to elementary steps. For example, in the secondary mechanism of hydrocarbon oxidation automatically generated by the EXGAS mechanism automatic generation software (more details can be found in Biet et al. (2008) or in Chap. 3), some reactions are vertically lumped so as to produce as products small species (including two or less carbon atoms) in only one reaction. For example, the addition of hydroxyl radicals to an alkene is written:

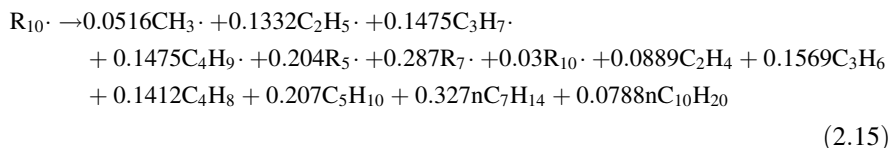


where n is the number of carbon atoms in the linear hydrocarbon.

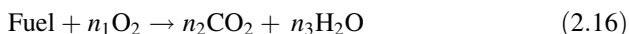
Reactions in detailed kinetic mechanisms can also sometimes be written using horizontal lumping, i.e., using lumped species. For example, in the n -hexadecane oxidation of Westbrook et al. (2009), the alkenyl species are lumped into one generic species, $\text{C}_{16}\text{H}_{31}$, which represents all combinations of positions of the double bond and the radical center so that for example:



More generally, outside the strict scope of detailed mechanisms, reactions can also have “global” or “semi-global” properties. Semi-global reactions can be found within “semi-detailed” mechanisms. For example, in the mechanism of the oxidation of n -decane of Ranzi et al. (2005), the decomposition of decyl radicals ($\text{R}_{10}\cdot$) is represented in a semi-global reaction:



One extreme example is the global combustion reaction proposed by Westbrook and Dryer (1981) which represents a whole mechanism of a hydrocarbon fuel:



2.4.1 Concept of Reaction Classes

Producing detailed combustion mechanisms for the oxidation of fuels with a large number of carbon atoms in its structure (larger than three) presents several shifts in mechanism production philosophy. First and foremost, it cannot be expected that the source of the rate constants be exclusively from experiments. The individual reactions that appear in mechanisms with larger hydrocarbons, due to their variety, complexity, and size, most likely do not have (and the majority never will have) isolated experiments giving direct rate constant information. For this reason, estimates of the reaction rate constants must come from general physical chemical principles. One way of encompassing and translating these general principles into specific reactive properties is to define reaction classes.

Reaction classes are kinetic generalizations that systematically embody the analogies and physical principles the modeler has to use to make educated guesses for the rate constants for reactions where no experimental evidence exists. The key assumption when using reaction classes is that only a local set of functional features around the reactive center (see Sect. 2.3.5) are significant when determining the numeric value of the rate constant. The concept of reaction classes is not restricted to automatic generation of detailed mechanisms. Even in the generation of large mechanisms by hand, reaction classes are used to produce detailed mechanisms. One example is the *n*-hexadecane mechanism of Westbrook et al. (2009).

A reaction class has essentially three sets of information:

1. A pattern or rule to recognize within the chemical reactants (can be more than one) when the reaction class should be applied,
2. A transformation of how the specific reactants are converted to products,
3. The rate constants associated with the transformation.

2.4.2 List of Reaction Classes Usually Used in Combustion Mechanisms

While reactions classes are slightly different depending on authors (see discussion by Battin-Leclerc 2008), there is some agreement for the main ones. In their

mechanisms of the oxidation of *n*-heptane (Curran et al. 1998), isooctane (Curran et al. 2002) and C₇–C₂₀ methylalkanes (Sarathy et al. 2011), the team of Livermore has defined reactions classes, which are certainly used in literature in detail. Those recently proposed by Sarathy et al. (2011) are listed below (reactions classes in italics are part of the secondary mechanisms, see Sect. 2.5.1):

- *High temperature reaction classes:*
 1. Unimolecular fuel decomposition
 2. H-atom abstraction from the fuel
 3. Alkyl radical decomposition
 4. Alkyl radical isomerization
 5. *H-atom abstraction reactions from alkenes*
 6. *Addition of radical species ·O· and ·OH to alkenes*
 7. *Reactions of alkenyl radicals with ·HO₂, ·CH₃O₂, and ·C₂H₅O₂*
 8. *Alkenyl radical decomposition*
 9. *Alkene decomposition*
 10. *Retroene decomposition reactions*
- *Low-temperature reaction classes:*
 11. Addition of O₂ to alkyl radicals ($\cdot R + O_2 = ROO\cdot$)
 12. $R\cdot + ROO\cdot = RO\cdot + RO\cdot$
 13. $R\cdot + HO_2\cdot = RO\cdot + OH\cdot$
 14. $R\cdot + CH_3OO\cdot = RO\cdot + CH_3O\cdot$
 15. Alkyl peroxy radical isomerization ($ROO\cdot = \cdot QOOH$)
 16. Concerted eliminations ($ROO\cdot = \text{alkene} + \cdot HO_2$)
 17. $ROO\cdot + HO_2\cdot = ROOH + O_2$
 18. $ROO\cdot + H_2O_2 = ROOH + HO_2$
 19. $ROO\cdot + CH_3O_2\cdot = RO\cdot + CH_3O\cdot + O_2$
 20. $ROO\cdot + ROO\cdot = RO\cdot + RO\cdot + O_2$
 21. $ROOH = RO\cdot + \cdot OH$
 22. *RO· decomposition.*
 23. $\cdot QOOH = \text{cyclic ether} + \cdot OH$ (cyclic ether formation)
 24. $\cdot QOOH = \text{alkene} + \cdot HO_2$ (radical site beta to OOH group)
 25. $\cdot QOOH = \text{alkene} + \text{carbonyl} + OH$ (radical site gamma to OOH group)
 26. Addition of O₂ to ·QOOH ($\cdot QOOH + O_2 = \cdot OOQOOH$)
 27. Isomerization of ·OOQOOH and formation of ketohydroperoxide and ·OH
 28. *Decomposition of ketohydroperoxide to form oxygenated radical species and ·OH*
 29. *Cyclic ether reactions with ·OH and HO₂.*
 30. *Decomposition of large carbonyl species and carbonyl radicals*

2.4.3 Kinetic Data of the Reaction Classes Used in Combustion Mechanisms

In this part, a few details are given about the kinetic data of the most important reaction classes usually considered in the primary mechanisms (see Sect. 2.5.1) of the oxidation of linear or branched alkanes. More details and data about other types of hydrocarbons can be found in review papers such as that of Battin-Leclerc (2008). Kinetic data needed in order to model the oxidation of alcohols and methyl esters are described in Chap. 4.

Except as in the case of the reverse of unimolecular fuel decompositions, described here after, the importance of reactions involving two large reacting radicals are usually of limited importance and are not detailed here. However, the reaction of $\text{RO}_2\cdot$ with $\cdot\text{HO}_2$ radicals can have some importance, especially in the case of small alkanes (e.g., propane (Cord et al. 2012b)) and are usually considered with a rate constant about $1 \times 10^{11} \text{ cm}^3 \text{ mol}^{-1} \text{ s}^{-1}$ (Curran et al. 1998).

- *Unimolecular fuel decomposition (class 1)*

These initiation steps can occur through the breaking of a C–C or a C–H bond. Their activation energy is taken equal to the standard enthalpy of reaction (ΔHr_0). Due to the high values of their activation energies (from 79 to 101 kcal/mol (see Luo (2003)), these reactions are only important above 1000 K. The pressure dependence of the rate constants of these reactions is usually taken into account using Troe’s formalism (see Sect. 2.2.2).

- *Hydrogen atom abstraction from the fuel (class 2)*

These reactions can occur by reactions with O_2 or with atoms and small radicals. Their rate constants depend on the type of alkylic hydrogen atoms which can be abstracted: primary, secondary, or tertiary, as shown in Fig. 2.9. Examples of proposed values are given in Table 2.1.

As described in Chap. 24, more accurate parameters have recently been proposed in the case of the abstractions by $\cdot\text{OH}$ radicals (Sivaramakrishnan and Michael 2009).

- *Radical decomposition (classes 3, 24, and 25)*

These reactions occur by breaking a (C–C), (C–H), or (C–O) bond in β -position of the carbon atom carrying the radical center. An usual method of estimating

Table 2.1 Rate constants for alkylic hydrogen atom abstractions, expressed in the form $k = A T^b \exp(-E/RT)$, with the units cm^3 , mol, s, kcal, by hydrogen atoms which can be abstracted (Buda et al. 2005)

H-abstraction	Primary H			Secondary H			Tertiary H		
	lg A	b	E	lg A	b	E	lg A	b	E
O_2	12.84	0	ΔHr	12.84	0	ΔHr	12.84	0	ΔHr
$\cdot\text{H}$	6.98	2	7700	6.65	2	5000	6.62	2	2400
$\cdot\text{OH}$	5.95	2	450	6.11	2	–770	6.06	2	–1870
$\cdot\text{CH}_3$	–1	4	8200	11.0	0	9600	11.00	0	7900
$\text{HO}_2\cdot$	11.30	0	17000	11.30	0	15500	12.00	0	14000

the rate constant is to write these reactions in the reverse direction (i.e., the addition of a radical to double bond). Values for the related additions have been proposed by Curran (2006). Typical activation energies for (C–C) bond breaking in alkyl radicals are around 27–31 kcal/mol (Buda et al. 2005).

- *Addition of O₂ (classes 11 and 26)*

The addition of O₂ to an alkyl radical is a barrierless reaction. As shown by DeSain et al. (2003), in the case of small alkyl radicals, such as ethyl or propyl radicals, the R· + O₂ reaction leads to a RO₂· adduct. The RO₂· adduct will either be stabilized or react via several “formally direct” pathways (Zádor et al. 2011). One of these is the concerted elimination of ·HO₂ to give the conjugated alkene (see class 16). Accurate computation of the related rate constants by statistical methods (Zádor et al. 2011) requires the implementation of variational methods (Truhlar et al. 1996). This makes the calculation of the related rate parameters difficult for large alkyl radicals. Estimated values from 1×10^{13} to 1×10^{12} cm³ mol⁻¹ s⁻¹ (Battin-Leclerc 2008) are usually considered for the rate constants of these reaction classes.

- *Radical isomerization (classes 4, 15 and 27)*

As shown in Fig. 2.12, this reaction occurs through the formation of a cyclic transition state which usually includes from four to eight atoms of carbon. The current models (e.g., Curran et al. 1998; Buda et al. 2005) use correlations to estimate the related rate constants which are based on previous work of Baldwin et al. (1982) and Hughes et al. (1992). In these correlations, as proposed by Benson (1976), the activation energy is considered to be equal to the sum of two contributions:

- (1) the activation energy for hydrogen atom abstraction from the molecule by analogous radicals,
- (2) the strain energy involved in the cyclic transition state.

Activation energies for isomerizations of alkyl peroxy radicals can then vary from 18 to 43 kcal/mol (Buda et al. (2005)). The rate constant proposed by Buda et al. (2005) for the reaction of Fig. 2.12 is $k_{15,\text{primary-H, 6-member ring}} = 5.7 \times 10^8 T \exp(-12,600/T) \text{ s}^{-1}$ (1413 s⁻¹ at 600 K). More accurate correlations have been recently proposed based on theoretical calculations (e.g. Sharma et al. (2010), Cord et al. (2012a)).

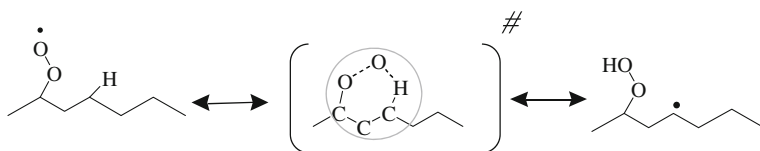


Fig. 2.12 Example of isomerization in the case of radical involved in *n*-heptane oxidation and structure of the cyclic transition state (#)

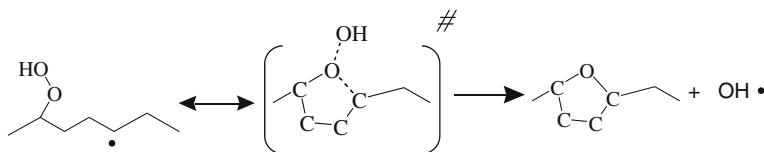


Fig. 2.13 Example of formation of cyclic ether in the case of radical involved in *n*-heptane oxidation

- *Formation of cyclic ethers (class 23)*

An example of this reaction class is shown in Fig. 2.13. The formation of oxirans, oxetanes, tetrahydrofurans, and tetrahydropyrans, containing 3, 4, 5, or 6 atoms, respectively, can be considered. In the current models (e.g. Curran et al. 1998, Ranzi et al. 2001, Buda et al. 2005), the rate constant for this type of reaction depends only on the size of the ring which is formed. However, recent work (Cord et al. 2012a) has shown the need to differentiate the type of carbon atom involved in the ring closure. The values proposed by Curran et al. (1998) for the formation of furans, the types of cyclic ethers which are formed in larger amounts as shown by experiments, is $k_{23,\text{furan}} = 9.4 \times 10^9 \exp(-3.5/T) \text{ s}^{-1}$.

- *Concerted eliminations ($ROO\cdot = \text{alkene} + \cdot HO_2$) (class 16))*

This reaction, which was first proposed by Quelch et al. (1992), occurs via a five-membered transition state. The rate constant used by Sarathy et al. (2011) for C_{7+} alkyl radicals is that proposed by DeSain et al. (2003) for propyl radicals, i.e., $k_{16,\text{secondary-H}} = 4.3 \times 10^{36} T^{-7.5} \exp(-17,900/T) \text{ s}^{-1}$ (377 s^{-1} at 650 K) when the C–H bond broken involves a secondary hydrogen atom. As shown by the values given in previous examples, with this estimated rate constant, this reaction class can, in some cases, compete with the isomerizations leading to the branching step and then have an inhibiting effect on the oxidation of alkanes.

2.5 Mechanisms and Submechanisms

A detailed mechanism is not just a simple list of reactions. There is a definite structure classifying sets of reactions within the total mechanism. These subsets of reactions are called submechanisms. A large detailed mechanism can be thought of as a collection of interacting submechanisms (see Fig. 1.4 in Chap. 1). The submechanisms interact in that the initial reacting species of one submechanism are the species produced from other submechanisms. Species that are not “consumed” within one submechanism should at least be “consumed” by another submechanism. Structuring a large mechanism as the sum of many submechanisms can help in building the mechanism itself.

In a large mechanism, a modeler can focus on the individual submechanisms and their role in the entire combustion process. Under differing reactive conditions, differing submechanisms contribute different aspects of reactivity in the entire

process. For example, in the combustion of large (more than four carbon atoms) hydrocarbons, a distinction is made between “high” temperature chemistry and “low” temperature chemistry producing the negative temperature coefficient behavior (see Sect. 2.3.3). For example, under high temperature conditions, species decompositions (to radicals) play a dominant role. In low temperature chemistry, additions (typically to oxygen) and recombinations can occur. In building a mechanism, if the mechanism is only to be used under high temperature conditions, only then the submechanisms which are significant under high temperatures need to be included. Those submechanisms having reactions which are significant only under low temperature conditions can be neglected. In the analysis of the mechanism (under all temperature conditions), for example, the modeler can analyze when each submechanism is significant.

The classification of submechanisms within a large mechanism can be based on several types of criteria:

- *Hierarchical submechanisms based on size of reactants*: within a given submechanism, only species of a given size are consumed. Smaller products (produced but not consumed within this submechanism) are consumed by submechanisms ‘lower’ in the hierarchy.
- *Primary, secondary, and base mechanisms*: it is a special case of the hierarchical structure. The *primary mechanism* is concerned by the reactions of the reactants and of the directly derived radicals. The *secondary mechanism* consumes the products of the primary mechanism. It would be possible to define iteratively tertiary and even n -ary mechanisms, but in practice in most combustion models, secondary mechanisms are designed to lead to intermediate species, which are finally consumed in a *base mechanism* (*seed mechanism*).
- *Pathways*: It is a chain of reactions or reaction classes. The remaining species at the end of this chain should be consumed by other submechanisms.
- *Reaction and molecule classes*: a submechanism can be classified by the reaction class it entails, for example hydrogen abstraction, or by reactant types, for example aldehydes.

2.5.1 Hierarchical Structure of Submechanisms

There are many ways to structure a large mechanism. One way, which is particularly useful in constructing a mechanism, is to divide the mechanism in a hierarchical structure with submechanisms including reactions for the large species build upon other submechanisms involving smaller species. In this view, a submechanism is designed with reactions to consume species of a given size (usually measured by the number of carbon atoms in the species) and to produce smaller species which, in turn, should be consumed by submechanisms lower in the hierarchy. For instance, a mechanism to model the oxidation of n -decane includes submechanisms describing the oxidation of n -nonane, n -octane, etc.

In the construction of a large mechanism, the modeler does not (or should not) construct the entire mechanism from scratch. Often, there are validated submechanisms (lower in the hierarchy) in the literature, which consume the products of the submechanisms that the modeler has designed. One example of this is in mechanism generation. Usually, the mechanisms for the larger hydrocarbons are produced automatically and the final products in these generated reactions are smaller hydrocarbons, typically with less than four carbon atoms. The submechanisms consuming these smaller hydrocarbons are not generated, but taken from the literature. This mechanism is called a base mechanism and is detailed in the next section.

2.5.2 Primary, Secondary, and Base Mechanisms

In one sense, this is classifying the hierarchical set of submechanisms in three levels. The emphasis of the primary mechanism is generally to provide more understanding of the combustion process of the fuel. The base mechanism is usually, a well-validated detailed mechanism of smaller species, which includes reactions taken from databases, which has already been validated under the conditions being considered. The secondary mechanism can be viewed as a necessary link between the primary mechanism and the reaction base mechanism.

2.5.3 Pathways

Within a mechanism (or submechanism), the products of a given reaction are the reactants of another reaction. This interaction can produce a chain of reactions called a reactive pathway. This is another feature of the mechanism construction which aids not only in the building of a mechanism, but also in the understanding of the reactive process. In building a mechanism, practically speaking, it is important that the products of a reaction are consumed as reactants in other reactions. The produced species could be consumed by a significant reverse reaction. If this is not the case, during a simulation there can be an artificial, i.e., not corresponding to reality, buildup of the species concentration, i.e., a “dead-end.”

For example, in low temperature chemistry, there is an accepted pathway for the combustion of large hydrocarbons (see [Fig. 2.5](#)). An alkyl radical is produced, there is an oxygen addition followed by an intramolecular H-atom abstraction which in turn is followed by another oxygen addition which eventually leads to branching agents. In designing the mechanism, this view can be seen as a book-keeping device, making sure that species are consumed and don't form dead-ends. In addition, this view could be important in terms of the reduction of a mechanism through the lumping of species and reactions. Several parallel paths could be lumped into one path.

2.6 Varying Complexity of Combustion Mechanisms

For the simulation of more complex physical experiments, where more than the combustion chemistry is being modeled, such as burners, turbines, and engines, the complexity of detailed modeling is too high. The computational effort in chemical modeling has to give way to modeling of the physical environment. With every physical dimension or spatial detail added to a model (for example, the number of cells in a CFD calculation), complex chemical models become computationally expensive. The chemical source terms are a sub-model within a larger more computationally expensive model.

At one extreme, there are zero-dimensional calculations where large detailed mechanisms can be studied. At the other extreme there are, for example, CFD simulations which only allow the simplest of chemical models, such as global reactions or tabulations (discussed in [Chap. 19](#)). In between, there are semi-detailed and skeletal mechanisms which are often derived from detailed calculations. As a modeler, an important computational decision that has to be made is how computational much effort can be put into exploring the detailed chemistry.

In the design of a detailed mechanism, there are many modeling decisions to be made. This leads to a great diversity of possible mechanisms to describe a combustion process. One of these is how much complexity is affordable as discussed above. In the next section, some of the other factors that lead to the diversity of detailed combustion mechanisms are discussed. In the remaining sections, mechanisms of differing complexity, from large detailed to semi-detailed, and global mechanisms are presented.

2.6.1 Validation and Nonuniqueness of Combustion Models

The diversity in detailed kinetic mechanisms comes from a variety of sources. First and foremost is the choice of fuels, the mechanism is trying to model. As the hydrocarbon fuel gets larger, such as including more carbon atoms, or more complex, such as branched, unsaturated, oxygenated or aromatic, and species, the mechanisms contain more reactions.

Another important aspect of a constructed model is its being able to predict unknown behavior and/or to mimic known experimental behavior. A model can be “validated” if it successfully predicts known behavior. Of course, it is important to note that validation itself is not a guarantee that the model is a correct representation of reality. Several models which can be fundamentally different can produce the same result. For example, a modeler can use either an optimized global mechanism (see [Sect. 2.6.4](#)) or a detailed mechanism to match the temperature dependence of ignition delay times. Of course, the detailed mechanism will also have the potential to reproduce further data about individual species.

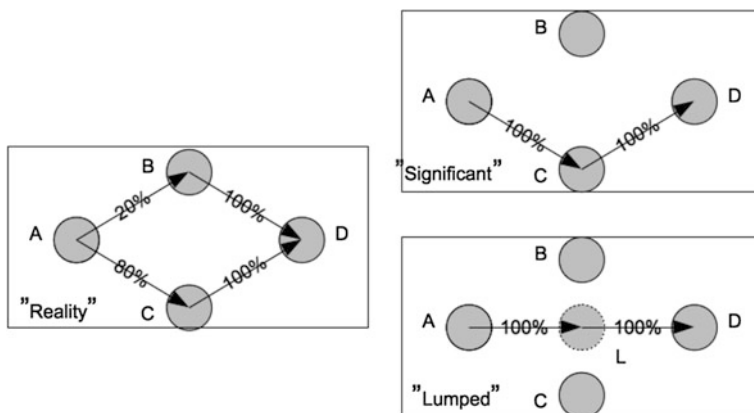


Fig. 2.14 Flow diagram from A through B and C to D. Three models are shown which are approximations of the flow from A to D

But if all that is needed to reproduce ignition delay time data, then the detailed model is too complex and not needed. This is a fundamental decision that a modeler has to make.

However, even two fundamentally different detailed mechanisms can match the same experimental data. How this can occur is illustrated in Fig. 2.14 which shows graphically a simple conversion path from species A through species B and C to species D. In this process (illustrated by the model labeled "Reality"), the reactions with species A as a reactant, 80 % of A is converted to A and 20 % of A is converted to B (by their respective sets of reactions). Furthermore, all of B and all of C are converted to D. In this simple model, one can conclude that all of A is converted to D. Suppose a modeler wanted to represent the conversion path from A to D with a fewer number of species. The model labeled "Significant" makes the assumption that since the majority of the conversion of A goes to C, the conversion to B can be neglected (is insignificant). This modeler assumes therefore all of A goes to C and all of C goes to D. In other words, instead of branching to both B and C, the model just neglects B and converts all to C (maybe increasing the rate to C to compensate). This model still says that all of A is converted to D, so from that viewpoint (for example, if there was no experimental evidence about species B and C), they are equivalent. The modeled labeled "Lumped" makes a different assumption, namely that the species B and C can be represented by a single "lumped" pseudo species, L. Once again from the viewpoint of A being all converted to D, this model matches the other two. If no validation data exists for species B and C, then all three models could be "correct," i.e., give the same conversion rates from A to D.

This example shows that the potential for a number of different models, even for a very simple system as that shown in Fig. 2.14 can be quite high. In a typical

combustion simulation, there can be hundreds of species, meaning that the number of conversion pathways through these species can be quite large.

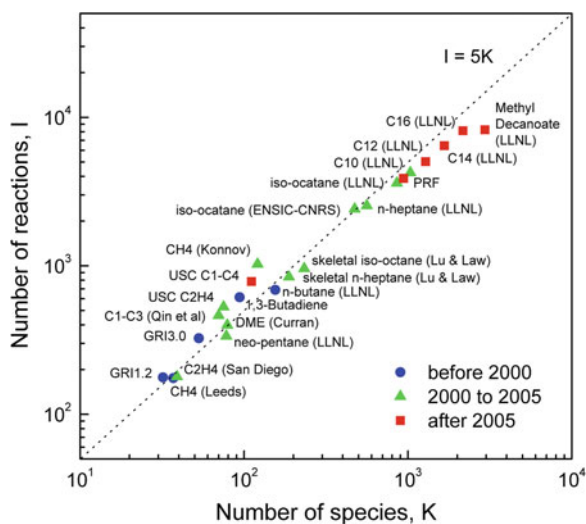
Rolland and Simmie (2004), for example, compared five detailed mechanisms for methane combustion and found considerable differences.

2.6.2 Highly Detailed Mechanisms

Two trends of detailed mechanisms from the literature are illustrated in Fig. 2.15. The first is that with the increasing computing power that has become available over the years, larger detailed mechanisms are computationally plausible. The second trend is that larger (in terms of number carbon atoms in the species) and more complex fuels (for example number of species in the surrogate fuel, see Sect. 2.6.5) are being modeled.

In building a detailed mechanism, the modeler tries to include all the reactions and species that are “necessary.” What is necessary can be governed by matching experimental results. However, it is not necessarily possible to know whether all necessary species have been included. A good example of this is low temperature chemistry. Cool flames were being systematically studied even in the 1920s. But before the role of alkylperoxy radicals were recognized, these species, which are now an integral part of modern low temperature chemistry mechanisms, were not included. Note that the most important aspect in a detailed mechanism is not to omit any significant species or reactions. As they involve a huge number of potential free parameters, the “optimization” of detailed mechanisms in order to mimic experimental results should be kept to a minimum. However, in practice, there is always a level in detailed mechanisms where the modeler has to make a

Fig. 2.15 The relationship between the number of species and the number of reactions (Reprinted from Lu and Law 2009, copyright Elsevier)



decision as to which reactions are significant and which are not, and also determine “reasonable” rate and thermodynamic constants. This often leads to a great diversity of mechanisms even for the same fuel.

2.6.3 Semi-Detailed and Skeletal Mechanisms

When highly detailed mechanisms are no longer computationally affordable, then the modeler has to rely on semi-detailed models or on skeletal mechanisms. While detailed mechanisms are based on fundamental reactions and try to model a wide range of conditions, skeletal mechanisms, derived from the detailed mechanisms, focus on a given chemical regime and are only valid in this regime. Skeletal reduction is typically the first step in mechanism reduction. It can be achieved through species reduction methods or by removing unimportant reactions from the detailed mechanisms. Much effort has been dedicated to the development of effective skeletal reduction techniques, as reviewed by Griffiths (1995); Tomlin et al. (1997); and Okino and Mavrovouniotis (1998); Nagy and Turanyi (2009). Chap. 17 of this book outlines these reduction techniques as follows:

- Skeletal Methods:
 1. Sensitivity based methods: for example (Turányi 1990)
 2. Graph based methods for example (Lu and Law 2006, 2005)
 3. The use of optimization in model reduction
 4. Adaptive and on-the-fly reduction.
- Lumping methods leading to semi-detailed mechanisms
- Chemistry-guided reduction

These methods have been used in the production of skeletal mechanisms such as those given in Table 2.2.

2.6.4 Global Mechanisms

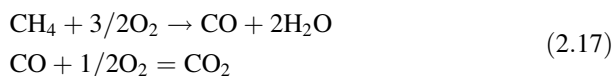
For many classes of CFD modeling, the reduction of the chemical source term has to go beyond skeletal and semi-detailed mechanisms. One class of mechanisms that accomplishes this is a “global mechanism,” a mechanism with a very limited number of species and reactions. A global mechanism is optimized either from reference detailed or semi-detailed mechanisms or directly from experimental data. Typically, they are optimized using temperature-dependent ignition delay times. There are a variety of global reaction mechanisms of different sizes (from 1 to about 20 reactions) representing a variety of reacting conditions. The size and complexity of the global mechanism a modeler chooses to use results, as with any

Table 2.2 A table of some skeletal mechanisms found in the literature

Number of species	Number of reactions	Fuel	Description	Reference
54	94	<i>n</i> -butane	Low temperature oxidation	Strelkova et al. (2010)
–	56	<i>n</i> -heptane	Two stage ignition	Peters et al. (2002)
29	52	<i>n</i> -heptane	Diesel HCCI engine	Patel et al. (2004)
68	283	<i>n</i> -heptane	Ignition and extinction phenomena	Lu and Law (2008)
131	651	<i>n</i> -heptane, but method also applied to <i>n</i> -alkanes from C ₈ to C ₁₅	Autoignition	Niemeyer and Sung (2011)
33	38	<i>n</i> -heptane, isooctane	0D HCCI combustion	Tsurushima (2009)
60	145	<i>n</i> -heptane, toluene	Ignition with soot formation	Chen et al. (2009)
49	62	<i>n</i> -heptane, isooctane, toluene	0D HCCI combustion	Machrafi et al. (2009)
42	62	<i>n</i> -heptane, isooctane, toluene	0D HCCI combustion	Huang et al. (2008)
88	363	Methyl ester bio-diesel fuel	Diesel engines combustion	Golovitchev and Yang (2009)

reduced mechanism, from a compromise between relative reactive accuracy needed for the calculation, the set of conditions and the computational complexity the modeler can afford.

One of the simplest global mechanisms consists of one global reaction representing complete combustion (see Eq.(2.16)) as proposed by Westbrook and Dryer (1981). Along the same line, the two-step model (with 3 species) proposed by Selle et al. (2004):



or the four-steps model published by Jones and Lindstedt (1998), which involves also the formation of H₂, are currently used to model turbulent methane flames.

The modeling of low temperature autoignition requires larger models. The “SHELL” mechanism originally developed by Halstead et al. (1975, 1977), given in Table 2.3, is another typical example. It has eight parameterized reactions and seven pseudo species. A global mechanism scheme can be optimized to represent different reacting systems. For example, the “Fuel” in the single global reaction or the “R” in the SHELL model can represent different fuels. The SHELL model has been applied by Sazhin et al. (1999) to model the ignition delay times on *n*-dodecane. A modified version of the shell model was developed by Hamosfakidis

and Reitz (2003) for *n*-heptane and tetradecane mixture and implemented into the KIVA-3 V CFD code. A series of engine simulations was then performed in order to assess its agreement with experimental data for engine applications.

2.6.5 Surrogates: Mechanisms of Complex Fuels

A real fuel is a complex mixture of not only a large number of different types of hydrocarbon species (such as linear alkanes, branched alkanes, cyclic alkanes, and different aromatics) as can be seen in Fig. 2.2, but also encompasses a whole range of species sizes (as shown by the number of carbon atoms in the species). To formulate and then numerically calculate with a detailed mechanism describing all the chemistry of all the species in a real fuel is not practical. For this reason, the kinetic models are simplified with the definition of a “surrogate” fuel, i.e., a mixture of a “small” number of species, on the order of 2–10 species (see Table 2.3, for example) representing the properties of the complex fuel.

The standard surrogate for gasoline, which is also used in the definition of the octane reference scale, is a mixture of *n*-heptane and isooctane (2,2,4-trimethylpentane). The octane number is defined as 0 for *n*-heptane and 100 for isooctane, and it is a measure of the antiknock characteristics of gasoline. A typical surrogate for diesel is the IDEA surrogate (Hentschel et al. 1994; Lemaire et al. 2009) which is a composition of 70 % *n*-decane, 30 % 1-methylnaphthalene (by volume). Table 2.4 lists some other examples of surrogate palette compounds making up different surrogates for different types of fuels in the literature. The table shows that the mixtures should not only contain representative molecules from all the types of molecules found in a real fuel (as shown in Fig. 1.3 of Chap. 1) but also in different ratios. With the development of detailed mechanisms with larger (more carbon atoms) and more complex (branched, cyclic, and aromatic) hydrocarbons, the surrogates can be more representative of the real fuels (Pitz and Mueller, 2011). An evaluation of gasoline surrogate components has been made by Pitz et al. (2007). A review of diesel surrogates can be found in the paper by Pitz and Mueller (2011)

Table 2.3 The basic SHELL model (Halstead et al. 1977). The reaction rates are parameterized against experimental data or a more detailed mechanism

Rxn	Type of step	Reaction	Rate
1	Initiation	$\text{RH} + \text{O}_2 \rightarrow 2\text{R}^*$	kq
2	Propagation	$\text{R}^* \rightarrow \text{R}^* + \text{P} + \text{Heat}$	kp
3	Propagation	$\text{R}^* \rightarrow \text{R}^* + \text{B}$	f1kp
4	Propagation	$\text{R}^* \rightarrow \text{R}^* + \text{Q}$	f4kp
5	Propagation	$\text{R}^* + \text{Q} \rightarrow \text{R}^* + \text{B}$	f2kp
6	Branching	$\text{B} \rightarrow 2\text{R}^*$	kb
7	Termination	$\text{R}^* \rightarrow \text{termination}$	f3kp
8	Termination	$2\text{R}^* \rightarrow \text{termination}$	k1

Table 2.4 Some surrogate compositions for diesel and jet fuels for which models have been developed. The quantities are given in mole percent (except * which are in mass percent). The references refer to the following: 1. (Lemaire et al. 2009), 2. (Kook and Pickett, 2011), 3. (Ramirez L. et al. 2010), 4. (Mathieu et al. 2009), 5. (Mati et al. 2007), 6. (Schultz, 1991), given in italics because it is only experiments, 7. (Violi et al. 2002), 8. (Dagaut and Cathonnet, 2006), 9. (Humer et al. 2007), 10. (Natelson et al. 2008), 11. (Steil et al. 2008), 12. (Honnet et al. 2009), 13. (Dooley et al. 2010), 14. (Wang et al. 2010), 15. (Malewicki et al. 2013)

Type of fuel	Diesel fuel					Jet fuel									
	1	2	3	4*	5	6	7	8	9	10	11	12	13	14	15
<i>n</i> -decane	70		70			16	67	60	60	50	70	80	43	70	
<i>n</i> -dodecane		77				21	74		60						40
tetradecane						6									
<i>n</i> -hexadecane					23	10									
isooctane					19	6	5						33	30	
heptamethylnonane				33											
cyclooctane						5									
methylcyclohexane						5	10	20	20	20					
<i>n</i> -propylcyclohexane				39	27										
<i>n</i> -butylcyclohexane										25					
tetralin						4									
benzene							1								
toluene							10	20	20				24		
<i>o</i> -xylene		23							20						
<i>m</i> -xylene						4									
<i>n</i> -propylbenzene					23			33		30					22
<i>n</i> -butylbenzene				29	5					25					
trimethylbenzene											20				8
<i>l</i> -methylnaphthalene	30		30		8	4									30

and a review of jet fuel surrogates can be found in the article of Dagaut and Cathonnet (2006).

To design an appropriate surrogate fuel, both chemical and physical comparisons have to be made between the surrogate and the real fuel. Farrell et al. (2007) in their program to develop “Fuels for Advanced Combustion Engines” (FACE) described the systematic steps toward developing a surrogate fuel:

- Select the palette compounds (Mueller et al. 2012) of the surrogate fuel based on specific physical and chemical principles. Outlined below are the design considerations that must be taken into account.
- Acquire the necessary elementary kinetic, thermochemical, and physical property data associated with the fuel and the surrogate.
- Develop accurate predictive chemical kinetic models using the selected surrogate and gather the necessary fundamental laboratory data to validate these mechanisms.
- Develop systematically reduced mechanisms based on the full detailed mechanisms, which are most likely too large to be practical in engine simulations.

To systematically accomplish the first step of deciding the candidate species for a surrogate fuel, Ranzi (2006) and Violi et al. (2002) outlined some general criteria:

- *Feasibility*. Candidates in the surrogate must have known detailed kinetic mechanisms.
- *Simplicity*. Mainly limited for computational capabilities to normal paraffins with <12 carbons, monocyclic paraffins with <8 carbons, and simple aromatics such as benzene, alkyl benzenes, and naphthalene.
- *Similarity*. The surrogate is required to match real fuels in both physical and chemical properties, including (i) volatility (boiling range and flash point), (ii) sooting tendency (smoking point and luminous number), and (iii) combustion property (heat of combustion, flammability limits, and laminar premixed flame mass burning rate).
- *Cost and availability*.

Farrell et al. (2007) and Mueller et al. (2012) outlined the “targets”; the modeler has to consider in designing a surrogate mixture which is “similar” to the real fuel. These targets are divided into three categories:

- *Property Targets*. Similarities in fundamental physical and chemical fuel properties:
 1. density
 2. matching the hydrogen and carbon amounts
 3. gross chemical composition
 4. phase behavior (e.g., vapor–liquid equilibrium and distillation characteristics)
 5. molecular transport properties.
- *Development Targets*. These are the kinetic and fluid dynamic processes that are important for validating surrogate mixture behavior, and that are typically evaluated in devices with better controlled conditions than those in real engines.
 1. kinetically-related phenomena (autoignition delay, burn rate, species evolution histories, emissions, etc.), with and without molecular-level transport coupling
 2. multicomponent spray vaporization
 3. droplet size distribution, and liquid penetration length
 4. experiments model validations in combustion bombs
 5. elementary kinetic studies to define specific reaction pathways.
- *Application Targets*. obtained from engine experiments,

1. combustion phasing and duration (timing and duration of cool flame and main heat release)
2. combustion efficiency
3. primary emissions (NO_x, soot, CO, and unburned hydrocarbons).

Farrell et al. (2007) noted further that because the physical and chemical complexity of a surrogate fuel will be reduced, compared to that of a commercial diesel fuel, it will in general not be possible (nor necessarily desirable) to match a wide range of properties such as viscosity, chemical composition (e.g., percent aromatics), and surface tension, with a single surrogate formulation.

2.7 Summary

In this chapter, we have presented the essential elements related to detailed kinetic mechanisms and their use to model combustion chemistry. A purpose of this chapter was also to be an introduction to the general concepts in modeling which will be used all over this book. The use of automatic generation software to produce these detailed kinetic mechanisms is given in detail in [Chap. 3](#). The specificities related to two particular types of biofuel, alcohols, and esters, are presented in [Chap. 4](#). As an example of the use of semi-global mechanisms to model complex reactions, the lumped reactions used to model biomass pyrolysis and devolatilization are described in [Chap. 5](#). Some methods to reduce the usually large size of detailed kinetic mechanisms are given in the Part IV of this book.

Acknowledgments This work was made in the frame of COST Action CM0901. F. Battin-Leclerc thanks the European Commission (“Clean ICE” ERC Advanced Research Grant) for financial support.

References

- Anderlohr JM, Pires Da Cruz A, Bounaceur R et al (2010) Thermal and kinetic impact of CO, CO₂, and H₂O on the postoxidation of IC-engine exhaust gases. *Combust Sci Technol* 182:39–59
- Arrhenius S (1889) On the reaction velocity of the inversion of cane sugar by acids. *Z Phys Chem* 4:226
- Balaban AT (1985) Applications of graph theory in chemistry. *J Chem Inf Comput Sci* 25:334–343
- Balaban AT (1995) Chemical graphs: looking back and glimpsing ahead. *J Chem Inf Com Sci* 35:339–350
- Baldwin RR, Hisham MW, Walker RW (1982) Arrhenius parameters of elementary reactions involved in the oxidation of neopentane. *J Chem Soc Faraday Trans I* 78:1615–1627
- Battin-Leclerc F (2008) Detailed chemical kinetic models for the low-temperature combustion of hydrocarbons with application to gasoline and diesel fuel surrogates. *Prog Energ Combust Sci* 34:440–498

- Battin-Leclerc F, Herbinet O, Glaude PA et al (2010) Experimental confirmation of the low-temperature oxidation scheme of alkanes. *Angew Chem Int Ed* 49:3169–3172
- Battin-Leclerc F, Blurock E, Bounaceur R et al (2011) Towards cleaner combustion engines through groundbreaking detailed chemical kinetic models. *Chem Soc Rev* 40:4762–4782
- Baulch DL, Cobos CJ, Cox RA et al (1992) CEC group on evaluation of kinetic data for combustion modeling. *J Phys Chem Ref Data* 21:411
- Benson SW (1976) *Thermochemical Kinetics*, 2nd edn. John Wiley, New York
- Biet J, Hakka MH, Warth V et al (2008) Experimental and modeling study of the low-temperature oxidation of large alkanes. *Energ Fuels* 22:2258–2269
- Bloss C, Wagner V, Jenkin ME et al (2005) Development of a detailed chemical mechanism (MCMv31) for the atmospheric oxidation of aromatic hydrocarbons *Atmos. Chem Phys* 5:641–664
- Buda F, Bounaceur R, Warth V et al (2005) Progress towards a unified detailed kinetic model for the autoignition of alkanes from C₄ to C₁₀ between 600 and 1200 K. *Combust Flame* 142:170–186
- Byrd S, Hildreth DP (2001) Learning the functional groups: keys to success. *J Chem Educ* 78:1355
- Carnot S (1824) *Réflexions sur la puissance motrice du feu, et sur les machines propres à développer cette puissance*. Paris, Librairie Bachelier
- Chen W, Shuai S, Wang J (2009) A soot formation embedded reduced reaction mechanism for diesel surrogate fuel. *Fuel* 88:1927–1936
- Clayden J, Greeves N, Warren S (2012) *Organic Chemistry*, 2nd edn. Oxford University Press, USA
- Cord M, Sirjean B, Fournet R et al (2012a) Improvement of the modeling of the low-temperature oxidation of *n*-butane: study of the primary reactions. *J Phys Chem A* 116:6142–6158
- Cord M, Sirjean B, Fournet R et al (2012b) Study of the low temperature oxidation of propane. *J Phys Chem A* 116:6142–6158
- Cramer CJ (2004) *Essentials of computational chemistry: theories and models*, 2nd edn. Wiley, West Sussex, England
- Curran HJ (2006) Rate constant estimation for C₁ to C₄ alkyl and alkoxy radical decomposition. *Int J Chem Kin* 28:250
- Curran HJ, Gaffuri P, Pitz WJ et al (1998) A comprehensive modeling study of *n*-heptane oxidation. *Combust Flame* 114:149–177
- Curran HJ, Gaffuri P, Pitz WJ et al (2002) A comprehensive study of iso-octane oxidation. *Combust Flame* 129:253–280
- Da Silva G, Bozzelli JW (2006) Enthalpies of formation, bond dissociation energies, and molecular structures of the *n*-aldehydes (acetaldehyde, propanal, butanal, pentanal, hexanal, and heptanal) and their radicals. *J Phys Chem A* 110:13058–13067
- Dagaut P, Cathonnet M (2006) The ignition, oxidation, and combustion of kerosene: a review of experimental and kinetic modeling. *Prog Energ Combust Sci* 32:48–92
- Davidson ER, Feller D (1986) Basis set selection for molecular calculations. *Chem Rev* 86:681–696
- Dec JE (2009) Advanced compression-ignition engines-understanding the in-cylinder processes. *Proc Combust Inst* 32:2727–2742
- DeSain JD, Klippenstein SJ, Miller JA et al (2003) Measurements, theory, and modeling of OH formation in ethyl + O₂ and propyl + O₂ reactions. *J Phys Chem A* 107:4415–4427
- Dooley S, Won SH, Chaos M et al (2010) A jet fuel surrogate formulated by real fuel properties. *Combust Flame* 157:2333–2339
- Dunnington GW, Gray J, Dohse F-E (2003) *Carl Friedrich Gauss: Titan of science*. The Mathematical Association of America, New York
- Eyring H (1935) The activated complex in chemical reactions. *J Chem Phys* 3:107–115
- Faraday M (1861) *A course of six lectures on the chemical history of a candle*. Griffin, Bohn & Co, London, UK

- Farrell JT, Cernansky NP, Dryer FL et al (2007) Development of an experimental database and kinetic models for surrogate diesel fuels. SAE International, Warrendale. No. 2007-01-0201
- Gauss CF (1823) *Theoria combinationis observationum erroribus minimis obnoxiae*. Gottingae, apud H Dieterich.
- Gilbert RG, and Smith SC (1990) *Theory of unimolecular and recombination reactions*. Blackwell Scientific Publication, Oxford
- Gillespie RJ, Robinson EA (2007) Gilbert N Lewis and the chemical bond: the electron pair and the octet rule from 1916 to the present day. *J Comp Chem* 28:87–97
- Goldsmith CF, Tomlin AS, Klippenstein SJ (2013) Uncertainty propagation in the derivation of phenomenological rate coefficients from theory: a case study of *n*-propyl radical oxidation. *Proc Combust Inst* 34:177–185
- Golovitchev VI, Yang J (2009) Construction of combustion models for rapeseed methyl ester bio-diesel fuel for internal combustion engine applications. *Biotechnol Adv* 27:641–655
- Griffiths JF (1995) Reduced kinetic models and their application to practical combustion systems. *Prog Energ Combust Sci* 21:25–107
- Griffiths JF, Barnard JA (1995) *Flame and Combustion*. 3rd ed, Chapman and Hall, London, UK
- Guibet JC (1999) *Fuels and engines*. Publications de l'Institut Français du Pétrole, Editions Technip, Paris
- Halstead MP, Kirsch LJ, Prothero A et al (1975) A mathematical model for hydrocarbon autoignition at high pressures. *Proc Roy Soc A Mat* 346:515–538
- Halstead MP, Kirsch LJ, Quinn CP (1977) The autoignition of hydrocarbon fuels at high temperatures and pressures-fitting of a mathematical model. *Combust Flame* 30:45–60
- Hamosfakidis V, Reitz RD (2003) Optimization of a hydrocarbon fuel ignition model for two single component surrogates of diesel fuel. *Combust Flame* 132:433–450
- Harding LB, Klippenstein SJ, Jasper AW (2007) Ab initio methods for reactive potential surfaces. *Phys Chem Chem Phys* 9:4055–4070
- Hehre WJ (2003) *A guide to molecular mechanics and quantum chemical calculations wavefunction*. Wavefunction, Inc. Irvine, 92612
- Hentschel W, Schindler KP, Haahtela O (1994) European diesel research IDEA-experimental results from DI diesel engine investigations. SAE International, Warrendale No. 941954
- Hill JG (2013) Gaussian basis sets for molecular applications. *Int J Quant Chem* 113:21–34
- Honnet S, Seshadri K, Niemann U et al (2009) A surrogate fuel for kerosene. *Proc Combust Inst* 32:485–492
- Huang C, Lu X, Huang Z (2008) New reduced chemical mechanism for homogeneous charge combustion ignition combustion investigation of primary reference fuels. *Energ Fuels* 22:935–944
- Hughes KJ, Halford-Maw PA, Lightfoot PD et al (1992) Direct measurements of the neo-pentyl peroxy-hydroperoxy radical isomerization over the temperature range 660–750 K. *Proc Combust Inst* 24:645–652
- Humer S, Frassoldati A, Granata S et al (2007) Experimental and kinetic modeling study of combustion of JP-8, its surrogates and reference components in laminar nonpremixed flows. *Proc Combust Inst* 31:393–400
- Husson B, Ferrari M, Herbinet O et al (2013) New experimental evidence and modeling study of the ethylbenzene oxidation. *Proc Combust Inst* 34:325–333
- Jones WP, Lindstedt RP (1988) Global reaction schemes for hydrocarbon combustion. *Combust Flame* 73:233–249
- Kee RJ, Rupley FM, Miller JA (1993) Chemkin II A fortran chemical kinetics package for the analysis of a gas-phase chemical kinetics Sandia Laboratories Report, SAND 89-8009B
- Kirsch L, Quinn C (1985) Progress towards a comprehensive model of hydrocarbon autoignition. *J Chim Phys-Chim Biol* 82:459–473
- Kook S, Pickett LM (2011) Soot volume fraction and morphology of conventional and surrogate jet fuel sprays at 1000-K and 67-MPa ambient conditions. *Proc Combust Inst* 33:2911–2918
- Laidler KJ (1987) *Chemical kinetics*, 3rd edn. Harper International, New York

- Lemaire R, Faccinetto A, Therssen E et al (2009) Experimental comparison of soot formation in turbulent flames of diesel and surrogate diesel fuels. *Proc Combust Inst* 32:737–744
- Levine IN (2000) *Quantum chemistry*. Prentice Hall, New Jersey, USA
- Levy DE (2008) *Arrow-pushing in organic chemistry: an easy approach to understanding reaction mechanisms*. John Wiley and Sons, Hoboken, New Jersey, USA
- Lewars EG (2011) *Computational chemistry: introduction to the theory of molecular and quantum mechanics*. 2nd edn. Springer
- Lewis GN (1916) The atom and the molecule. *J Am Chem Soc* 38:762–785
- Lu T, Law CK (2005) A directed relation graph method for mechanism reduction. *Proc Combust Inst* 30:1333–1341
- Lu T, Law CK (2006) Linear time reduction of large kinetic mechanisms with directed relation graph: *n*-heptane and iso-octane. *Combust Flame* 144:24–36
- Lu T, Law CK (2008) Strategies for mechanism reduction for large hydrocarbons: *n*-heptane. *Combust Flame* 154:153–163
- Lu T, Law CK (2009) Toward accommodating realistic fuel chemistry in large-scale computations. *Prog Energy Combust Sci* 35:192–215
- Luo YR (2003) *Handbook of bond dissociation energies in organic compounds*. CRC Press, Boca Raton
- Machrafi H, Cavadias S, Amouroux J (2009) The development and experimental validation of a reduced ternary kinetic mechanism for the auto-ignition at HCCI conditions, proposing a global reaction path for ternary gasoline surrogates. *Fuel Proc Technol* 90:247–263
- Malewicki T, Gudiyella S, Brezinsky K (2013) Experimental and modeling study on the oxidation of Jet A and the *n*-dodecane/iso-octane/*n*-propylbenzene/1,3,5-trimethylbenzene surrogate fuel. *Combust Flame* 160(17):30
- Mathieu O, Djebaïli-Chaumeix N, Paillard C-E et al (2009) Experimental study of soot formation from a diesel fuel surrogate in a shock tube. *Combust Flame* 156:1576–1586
- Mati K, Ristori A, Gaïl S et al (2007) The oxidation of a diesel fuel at 1–10 atm: experimental study in a JSR and detailed chemical kinetic modeling. *Proc Combust Inst* 31, 2939–2946
- Miller JA, Pilling MJ, Troe J (2005) Unravelling combustion mechanisms through a quantitative understanding of elementary reactions. *Proc Combust Inst* 30:43–88
- Mueller CJ, Cannella WJ, Bruno TJ et al (2012) Methodology for formulating diesel surrogate fuels with accurate compositional, ignition-quality, and volatility characteristics. *Energy Fuels* 26:3284–3303
- Nagy T, Turányi T (2009) Reduction of very large reaction mechanisms using methods based on simulation error minimization. *Combust Flame* 156:417–428
- Natelson RH, Kurman MS, Cernansky NP et al (2008) Experimental investigation of surrogates for jet and diesel fuels. *Fuel* 87:2339–2342
- Niemeyer KE, Sung C-J (2011) On the importance of graph search algorithms for DRGEP-based mechanism reduction methods. *Combust Flame* 158:1439–1443
- Okino MS, Mavrovouniotis ML (1998) Simplification of mathematical models of chemical reaction systems. *Chem Rev* 98:391–408
- Patel A, Kong S-C, Reitz RD (2004) Development and validation of a reduced reaction mechanism for HCCI engine simulations. SAE International, Warrendale. No. 2004-01-0558
- Peters N, Paczko G, Seiser R et al (2002) Temperature cross-over and non-thermal runaway at two-stage ignition of *n*-heptane. *Combust Flame* 128:38–59
- Pilling MJ (2009) From elementary reactions to evaluated chemical mechanisms for combustion models. *Proc Combust Inst* 32:27–44
- Pitz WJ, Mueller CJ (2011) Recent progress in the development of diesel surrogate fuels. *Prog Energy Combust Sci* 37:330–350
- Pitz WJ, Cernansky NP, Dryer FL et al (2007) Development of an experimental database and chemical kinetic models for surrogate gasoline fuels. SAE International, Warrendale. No. 2007-01-0175
- Pollard RT (1997) Hydrocarbons. In: Bamford CH, Tipper CFH (eds) *Comprehensive chemical kinetics: gas-phase combustion*, vol 17. Elsevier, Amsterdam

- Pretsch E, Bühlmann P, Badertscher M (2009) Structure determination of organic compounds: tables of spectral data, 4th edn. Springer, Berlin, Heidelberg
- Quelch GE, Gallo MM, Schaefer HF III (1992) Aspects of the reaction mechanism of ethane combustion. Conformations of the ethylperoxy radical. *J Am Chem Soc* 114:8239–8247
- Ramirez LHP, Hadj-Ali K, Diévert P et al (2010) Kinetics of oxidation of commercial and surrogate diesel fuels in a jet-stirred reactor: experimental and modeling studies. *Energy Fuels* 24:1668–1676
- Ranzi E (2006) A wide-range kinetic modeling study of oxidation and combustion of transportation fuels and surrogate mixtures. *Energy Fuels* 20:1024–1032
- Ranzi E, Dente M, Goldaniga A et al (2001) Lumping procedures in detailed kinetic modeling of gasification, pyrolysis, partial oxidation and combustion of hydrocarbon mixtures. *Prog Energy Combust Sci* 27:88–139
- Ranzi E, Frassoldati A, Granata S et al (2005) Wide-range kinetic modeling study of the pyrolysis, partial oxidation, and combustion of heavy *n*-alkanes. *Ind Eng Chem Res* 44:5170–5183
- Rolland S, Simmie JM (2004) The comparison of detailed chemical kinetic mechanisms: application to the combustion of methane. *Int J Chem Kinet* 36:467–471
- Sarathy SM, Westbrook CK, Mehl M et al (2011) Comprehensive chemical kinetic modeling of the oxidation of 2-methylalkanes from C7 to C20. *Combust Flame* 158:2338–2357
- Sazhin SS, Sazhina EM, Heikal MR et al (1999) The Shell autoignition model: a new mathematical formulation. *Combust Flame* 117:529–540
- Schlegel HB (1998) Geometry optimization, In: Schleyer PR, Allinger NL, Kollman PA et al (eds) *Encyclopedia of computational chemistry*, vol 2. Wiley, Chichester
- Schultz WD (1991) Oxidation products of a surrogate JP-8 fuel. *ACS Petrol Chem Div Preprints* 37:383
- Sebbar N, Bozzelli JW, Bockhorn H (2004) Thermochemical properties, rotation barriers, bond energies, and group additivity for vinyl, phenyl, ethynyl, and allyl peroxides. *J Phys Chem A* 108:8353–8366
- Sebbar N, Bockhorn H, Bozzelli JW (2005) Thermochemical properties, rotation barriers, and group additivity for unsaturated oxygenated hydrocarbons and radicals resulting from reaction of vinyl and phenyl radical systems with O₂. *J Phys Chem A* 109:2233–2253
- Selle L, Lartigue G, Poinot T et al (2004) Compressible large eddy simulation of turbulent combustion in complex geometry on unstructured meshes. *Combust Flame* 137:489–505
- Semenov NN (1935) *Chemical kinetics and chain reactions*. The Clarendon Press, Oxford
- Semenov NN (1958) *Some problems in chemical kinetics and reactivity*. Princeton University Press, Princeton
- Sharma S, Raman S, Green WH (2010) Intramolecular hydrogen migration in alkylperoxy and hydroperoxyalkylperoxy radicals: accurate treatment of hindered rotors. *J Phys Chem A* 114:5689–5701
- Simmie JM, Black G, Curran HJ et al (2008) Enthalpies of formation and bond dissociation energies of lower alkyl hydroperoxides and related hydroperoxy and alkoxy radicals. *J Phys Chem A* 112:5010–5016
- Sivaramakrishnan R, Michael JV (2009) Rate constants for OH with selected large alkanes: shock-tube measurements and an improved group scheme. *J Phys Chem A* 113:5047–5060
- Steil U, Braun-Unkloff M, Aigner M (2008) An experimental and modelling study on the autoignition of kerosene and surrogate fuel mixtures, 46th AIAA Aerospace Sciences Meeting and Exhibit, Aerospace Sciences Meetings American Institute of Aeronautics and Astronautics Reviews in computational chemistry, John Wiley & Sons, pp 45–81
- Stewart JJP (2007) *Semiempirical Molecular Orbital Methods*. In: Lipkowitz KB, Boyd DB (eds) *Reviews in Computational Chemistry, Vol1*. John Wiley & Sons, Inc., Hoboken, NJ, USA
- Struyf J (2009) Relating functional groups to the periodic table. *J Chem Educ* 86:190
- Strelkova MI, Safonov AA, Sukhanov LP et al (2010) Low temperature *n*-butane oxidation skeletal mechanism, based on multilevel approach. *Combust Flame* 157:641–652

- Sumathi R, Green WH (2002) Thermodynamic properties of ketenes: group additivity values from quantum chemical calculations. *J Phys Chem A* 106:7937–7949
- Tomlin AS, Turányi T, Pilling MJ (1997) Mathematical tools for the construction, investigation and reduction of combustion mechanisms. In: Pilling MJ (ed) *Comprehensive chemical kinetics: low-temperature combustion and autoignition*, vol 35. Elsevier, Amsterdam
- Townend DTA (1937) Ignition regions of hydrocarbons. *Chem Rev* 21:259–278
- Trahanovsky WS (1971) *Functional groups in organic compounds*. Prentice Hall, Englewood Cliffs, NJ
- Troe J (1974) Fall-off curves of unimolecular reaction. *Ber Buns Phys Chem* 78:478–488
- Truhlar DG, Garrett BC, Klippenstein SJ (1996) Current status of transition-state theory. *J Phys Chem* 100:12771–12800
- Tsang W, Hampson RF (1986) Chemical kinetic data base for combustion chemistry Part I Methane and related compounds. *J Phys Chem Ref Data* 15:1087–1279
- Tsurushima T (2009) A new skeletal PRF kinetic model for HCCI combustion. *Proc Combust Inst* 32:2835–2841
- Turányi T (1990) Sensitivity analysis of complex kinetic systems. Tools and applications. *J Math Chem* 5:203–248
- Vansteenkiste P, Van Speybroeck V, Marin GB et al (2003) Ab initio calculation of entropy and heat capacity of gas phase *n*-alkanes using internal rotations. *J Phys Chem A* 107:3139–3145
- Venot O, Hébrard E, Agúndez M et al (2012) A chemical model for the atmosphere of hot Jupiters. *A&A* 546:A43
- Violi A, Yan S, Eddings EG et al (2002) Experimental formulation and kinetic model for JP-8 surrogate mixtures. *Combust Sci Technol* 174:399–417
- Walker RW, Morley C (1997) Basic chemistry of combustion. In: Pilling MJ (ed) *Comprehensive chemical kinetics: low-temperature combustion and autoignition*, vol 35. Elsevier, Amsterdam
- Wang H, Frenklach M (1994) Transport properties of polycyclic aromatic hydrocarbons for flame modeling. *Combust Flame* 96:163–170
- Wang H, Warner SJ, Oehlschlaeger MA et al (2010) An experimental and kinetic modeling study of the autoignition of α -methyl-naphthalene/air and α -methyl-naphthalene/*n*-decane/air mixtures at elevated pressures. *Combust Flame* 157:1976–1988
- Warnatz J, Maas U, Dibble RW (2006) *Combustion: physical and chemical fundamentals, modeling and simulation, experiments, pollutant formation*. 4th ed, Springer, Berlin, Heidelberg
- Warth V, Stef N, Glaude PA et al (1998) Computed aided design of gas-phase oxidation mechanisms: Application to the modelling of normal-butane oxidation. *Combust Flame* 114:81–102
- Westbrook CK (2000) Chemical kinetics of hydrocarbon ignition in practical combustion systems. *Proc Combust Inst* 28:1563–1577
- Westbrook CK (2005) Challenges in combustion GCEP Research Symposium http://gcepstanfordedu/pdfs/uQx8GXJG882-3q6NMuyQOw/westbrook_symp05pdf
- Westbrook CK, Dryer FL (1981) Simplified reaction mechanisms for the oxidation of hydrocarbon fuels in flames. *Combust Sci Technol* 27:31–43
- Westbrook C, Pitz W, Herbinet O et al (2009) A comprehensive detailed chemical kinetic reaction mechanism for combustion of *n*-alkane hydrocarbons from *n*-octane to *n*-hexadecane. *Combust Flame* 156:181–199
- Williams FA (1994) *Combustion theory*. 2nd edn. Westview Press, Boulder
- Yu J, Sumathi R, Green WH (2006) Accurate and efficient method for predicting thermochemistry of furans and ortho-arynes: expansion of the bond-centered group additivity method. *J Phys Chem A* 110:6971–6977
- Zádor J, Taatjes CA, Fernandes RX (2011) Kinetics of elementary reactions in low-temperature autoignition chemistry. *Prog Energ Combust Sci* 37:371–421
- Zeleznik FJ, Gordon S (1962) A general IBM 704 or 7090 computer program for computation of chemical equilibrium compositions, rocket performance, and Chapman-Jouguet detonations. NASA-TN-D-1454

Chapter 3

Automatic Generation of Detailed Mechanisms

Edward Blurock, Frédérique Battin-Leclerc, Tiziano Faravelli
and William H. Green

Abstract The production of detailed mechanisms for the combustion of larger hydrocarbons is fundamentally different from the production of mechanisms for the reactions of smaller hydrocarbons. For the most part there are no direct experiments for the individual reactions. General physical principles, usually based on reaction classes, have to be employed. In addition, the production of larger mechanisms has to be careful and systematic to generate what could be mechanisms with thousands of species and reactions. The recurring and systematic use of physical principles to generate the mechanisms is facilitated by automated techniques in the form of automatic detailed mechanism generation systems. This chapter outlines the common principles, with some software technical details, of automatic generation systems. This is followed by a more detailed description of four individual systems, MAMOX, EXGAS, RMG and REACTION, each of which has unique aspects in their generation philosophy.

E. Blurock
Reaction, Lund, Sweden
e-mail: edward.blurock@esblurock.info

F. Battin-Leclerc (✉)
Laboratoire Réactions et Génie des Procédés, CNRS, Université de Lorraine, ENSIC, 1 rue grandville, Nancy 54000, France
e-mail: frederique.battin-leclerc@univ-lorraine.fr

T. Faravelli
Dipartimento di Chimica, Materiali e Ingegneria Chimica, Politecnico di Milano, Piazza L. da Vinci, 32, Milan 20133, Italy
e-mail: tiziano.faravelli@polimi.it

W. H. Green
Department of Chemical Engineering, Massachusetts Institute of Technology 66-350, 77
Massachusetts Avenue, Cambridge, USA
e-mail: whgreen@mit.edu

3.1 Common Principles of Automatic Generators

As detailed mechanisms of larger hydrocarbons grow larger, so does the complexity of their production. Although it is possible to produce large mechanisms of thousands of reactions by hand (see, for example, the work of (Westbrook et al. 2009; Sarathy et al. 2011)), having an automatic means of generation can be more efficient, more systematic and less error-prone. Automatic detailed mechanism generators can be viewed as expert systems using a database of chemical principles to systematically and efficiently produce large detailed mechanisms. One of the principle advantages of automatic generators is that the time-consuming and error-prone details of producing every single species and reaction in a large mechanism is taken over by the generation system. The modeler works at a higher conceptual level determining, for example, which submechanisms and which *reaction classes* should be generated. The generation procedure itself is more systematic which is important not only because of reduction of errors, but also in the consistency of the use of general kinetic principles, usually in the form of reaction classes, that are applied.

3.1.1 Core Structure of an Automatic Generator

Regardless of the particular implementation of an automatic generator, there are distinct commonalities in their structure. Within this common structure, there are several design and strategic decisions where each system can differentiate. Every generator has a set of core modules consisting of the *generator engine*, the *species pool*, the *molecule database* and the *reaction class database*:

- *Generator engine*. The central module, interacting with all the other modules, which steers the generation process.
- *Species pool*. These are the molecules that, under each iteration, serve as input to the generator engine to produce the reactions and molecules (taken in a wide sense including both stable molecules and free-radicals) of the current iteration.
- *Molecule database*. This is the set of predefined molecules that could be used within the generation process.
- *Reaction class database*. This database contains the information about each reaction class to be used in the generation process.

The iterative use of these modules by the reaction generation algorithm creates the reactions and species making up the generated mechanism. The input and output to the algorithm is:

- *Input*. The fuel molecule or set of fuel molecules.
- *Output*. The detailed mechanism associated with the fuel molecule(s).
The algorithm itself is iterative and has the following basic steps:
- *Initialization*. Fill the reaction pool with initial reactants.

- *Generate reactions.* Using the information in the reaction class database, create a new set of reactions and molecules using the species pool as input. Add the generated molecules and reactions to the mechanism.
- *Update the species pool.* Update the species pool with the newly generated species from step 2.
- *Check termination criteria.* If the algorithm is done, then exit, otherwise iterate to step 2.

The following sections elaborate these steps and outline the different strategies each step can have.

3.1.1.1 Initialization

The input to the algorithm is the fuel molecule or molecules. In the initialization step, these species are added to the species pool. The submechanism that is generated is considered as the *primary mechanism* or reaction¹ of those initial molecules. This generated submechanism is then used in conjunction with other submechanisms (which can be generated or produced by hand). The *Generate Reactions* step uses the species pool as input to generate the next set of reactions. It could be that in the initialization process, some “extra” reactants, such as small radicals used in some reactions have to be added to the species pool. These are taken from the molecule database.

3.1.1.2 Generate Reactions

In this step, the species pool is analyzed and those reaction classes from the reaction class database which are valid are applied. A reaction class is valid for a species (or set of species) if the *functional groups* required by the reaction class are present. The recognition of the necessary functional groups is done through some form of graph isomorphism (see [Sect. 3.1.3.4](#) and the general references (Balaban 1985, 1995)). The exact algorithm is highly dependent on the molecular representation (see [Sect. 3.1.3](#)). There could be some filtering done at this stage as to which reaction classes are available for application.

Each application of the reaction class produces a set of reactions and a set of molecules. This new set of reactions and molecules are collected. A crucial algorithm in this step is the determination of which molecules and reactions are equivalent (see [Sect. 3.1.3](#)). Only newly generated reactions and molecules are added to the new mechanism. During this generation step, there could be some filtering of applications and results. The filter could occur before or after the

¹ The *primary mechanism* includes the reactions of the reactants and of the directly derived radicals.

reaction class application. There could be other conditions, beside the availability of the functional groups which inhibit the application of the reaction class. For example, if the reaction class is known to generate a radical center and the reacting species is already a radical, the generation of a biradical could be inhibited. The filtering could also occur after the application of the reaction class. For example, the generated reaction and associated molecules may have some criteria they must fulfill. One class of such criteria could be based on “on-the-fly” kinetic or thermodynamic computations (this, for example, is crucial in the RMG system described in [Sect. 3.2.3](#)). The reactions are left in the final set only if they meet these criteria.

3.1.1.3 Update the Species Pool

The species pool is updated with the new set of generated species. There could be some filtering and even classification of the incoming species. There are essentially two algorithms to update the species pool:

- *Exhaustive*. The (filtered) set of generated molecules is added to the species pool, creating a larger pool.
- *Progressive*. The species pool is initialized and the (filtered) set of species is added at each step.

Under the exhaustive technique, the reactions are applied (in the Generate reaction step) until no new species are produced. This check is made after filtering. In the progressive technique, only selected species are used in the next step. For example, in the REACTION system (see [Sect. 3.2.4](#)) only the newly generated species are added at each step of the defined reaction pathway.

3.1.1.4 Termination Criteria Check

If no new species were added to the species pool then the process can terminate. This essentially means that all of the available or required reaction classes have been applied and no new reactions and molecules were created. This could result from the fact that new applications of the reaction classes give molecules and reactions already in the mechanism, or that there are no more reaction classes to apply.

3.1.2 *Convergence and Termination of the Generation Process*

As discussed in [Chap. 2](#), a typical combustion mechanism is a hierarchy of sub-mechanisms. The “top” mechanism, for example that of the original fuel, starts

with a large molecule and in the reactive process produces smaller, usually containing less carbon atoms, species. These smaller species are consumed in subsequent sub-mechanisms of the hierarchy. In general, when combustion mechanisms are designed and the individual reactions chosen, regardless of whether they are automatically generated or not, for the most part the species are reacted into smaller species. A particular submechanism is designed so that its products are consumed by other sub-mechanisms.

One of the challenges of *low temperature oxidation* of hydrocarbons (see [Chap. 2](#)) was that an addition, for example the addition of oxygen to an alkyl radical had to be modeled. However, this addition is allowed because subsequent reaction classes once again reduce or keep constant the size of the products, at least in terms of number of carbon atoms. Fortunately, the product species obtained, for example alkylperoxy radicals, have very specific structures (functional groups) so they can be targeted by very specific reaction classes which will eventually react them to smaller species. Recombinations also increase the size of the species in the generation process. If additions of hydrocarbon radicals or recombinations are allowed in the (automatic) generation process larger and larger molecules would be available to react further. The process would then only terminate if a maximum species size is specified, this is the case in EXGAS software (see [Sect. 3.2.2.4](#)). This problem would be even more severe for soot formation, where molecular growth is very important.

A terminating iterative process converges to the solution after a finite number of steps. One of the basic criteria can be that each step creates a “state” that is smaller than the original state. In mechanism generation the current state is the molecule to be reacted. One possible definition of the size of the state is the size of the species to react. After the application of a reaction class, smaller species are generated and the process is one step closer to convergence to the final mechanism. If a reaction class produces a species of the same size, then the generation process has to have some means of limiting the applications of that class to a finite number of times. Without this check, a reaction class such as isomerization would produce an infinite loop. One check to this process is to see whether the same molecule has already been produced. Since a given molecule can only have a finite number of isomers, a reaction class producing another isomer can only be applied a finite number of times (though the number of isomers can be very large for large molecules).

3.1.3 Molecular and Reaction Representations

As said in [Chap. 2](#), a combustion modeler uses many representations of molecule and subsequently reactions. These models help the human modeler understand the reactive process of combustion. To be useful in automatic generation these models have to be translated into machine readable data structures. These data structures go beyond the classical numerical representations that are normally associated with a computer aided computation. The evolutionary development of these

structures coincides with developments of modern computing techniques and languages (Chen 2006; Willett 2008). In addition, the representations, structures and many of the techniques used within automatic generation of combustion mechanisms stem from the extensive work in physical and organic chemistry in general, especially in the field of chemical information databases.

3.1.3.1 Molecule Names for Humans and Computers

A molecule is a complex object with many models and representations. A fundamental task in organic and subsequently combustion chemistry is to give each molecule a unique name. Two molecules with the same unique name can be said to be identical. In fact, assigning unique names or codes to a graph is one of the more computationally efficient ways to identify identical graphs. Unfortunately, the task of naming is still complex.

Naming a molecule, for the most part, uses the Lewis structure (see Chap. 2 and, for example (Gillespie and Robinson 2007; Lewis 1916)) and a usually used representation of the molecule is a two-dimensional (2D) graph (Balaban 1985, 1995). The atoms are graph nodes with additional information such as atomic number, charge, radical, etc. The graph bonds are essentially the full covalent bonds of the molecule. In general, finding a unique name, or more precisely a canonical form, for a graph is a complex task (Babai and Luks 1983) and is intimately connected to identifying if graphs are identical or not (graph isomorphism (Balaban 1985)). Within the field of chemistry these tasks are extremely important for molecular databases and data-mining chemical information. Fortunately, organic compounds, using the Lewis model, are usually not as complex as a general graph that has to be dealt with mathematically. For example, sp^3 atoms have at most four bonds which greatly simplifies the interconnectivity among graph nodes.

In organic chemistry standardization of names is an important task and the International Union of Pure and Applied Chemistry (IUPAC) has undertaken the standardizing of nomenclature. Having a standardized (canonical) name not only tells the organic chemist what the molecule looks like, but also simplifies searching. Two molecules are alike if the text string of their name is exactly the same. For example, the species *iso*-octane has the IUPAC name of 2,2,4-trimethylpentane. The IUPAC name is an example of linearizing the graphical structure of the molecule. Another, more compact linear name for molecules are the Wiswesser Line Notation (WLN) (Smith et al. 1968; Wiswesser 1982, 1985). Several variants such as the Simplified Molecular Input Line Entry System (*SMILES*) notation (Weininger 1988; Weininger et al. 1989), the SYBL line notation (Homer et al. 2008) and the *linear notation* (Côme et al. 1984; Warth et al. 2000 (see Sect. 3.2.2.1)) have also been proposed. These notations were mainly developed for simplified ASCII text entry of graphical molecular information into the computer. These notations represent the molecule as a “spanning tree” with the use of parenthesis to denote branching. Some notations rely on

molecular valence information to simplify the notation. For example, in the SMILES notation, hydrogen atoms are implicit.

Another human readable name for a molecule is the International Chemical Identifier (InChI) (Stein et al. 2003), “InChI” for short, which was developed by IUPAC and National Institute of Standards to facilitate molecular searches in databases and on the web. The current nomenclature has 6 layers of structural information about molecule. This is becoming a standard nomenclature for molecular searches on the internet.

3.1.3.2 Bonding Representations

The representation of molecular species for human–computer interfacing and for internal representation is not unique to combustion (Warr 2011) and is constantly evolving with the needs of the chemistry community in chemical database search, computer aided organic synthesis (Corey and Wipke 1969; Wipke and Howe 1977) and chemoinformatics (Engel 2006; Willett 2008). Of course, some of these needs have evolved hand in hand with developing software technologies (Engel and Gasteiger 2002; Chen 2006).

The naming of the chemical species, whether it be with the common name, IUPAC name or one of the linear notations, is an efficient way to get molecular data into the automatic generation system. The main purpose of these notations is that the name gives a direct correspondence to the molecular structure needed. However, within the computations needed for automatic generation these forms are not efficient. Though, for example, a canonical name is efficient for recognizing whether two species are equal. They are less efficient at recognizing, for example, whether a given substructure is within another species structure or the transformations of species creating a reaction.

As with the naming of species, the essential information in the main internal data structures for molecules consists of the Lewis model information, meaning a 2D graph representation. If additional molecular data is needed, it is usually added in a separate data structure. In computer science there has been essentially two ways to represent a graph both internally and for ASCII human–computer interfacing: a connection table (or matrix) or a graph as a set of atoms and a set of bonds between the atoms.

Historically, one can say one that the first computational representation of molecules was the atom connectivity matrix (sometimes also called the adjacency matrix) (Spialter 1963, 1964). This form was conducive to numerical programming languages such as FORTRAN. A species with n atoms would be represented as a matrix with n rows and n columns. A connection is signified by a non-zero value in the off-diagonal elements. Ugi applied this to molecules with the definition of the Bond-Electron (BE) matrix (Dugundji and Ugi 1973; Ugi and Wochner 1988). If a bond exists between atom i and atom j , then element m_{ij} of connectivity matrix \mathbf{m} has the order of the bond (1 for single, 2 for double, 3 for triple). In the era where computation was primarily numerical, an interesting

extension of the BE-matrix was the R-matrix, the difference between the product and reactant BE-matrix. The significance of the R-matrix is that it is an early representation of reactive changes that could be used directly to “calculate” product species from the reactant species which is an essential operation in automatic generation.

The connection table is a form which is close to the 2D graphical form and, for example, can be used as the internal representation and as ASCII input. The table usually consists of two parts, atom information and bonding. The exact syntax can vary, first due to historical developments and second due to individual needs of the software systems using it. Some of the more accepted variants have been developed by Molecular Design Limited (MDL) (Dalby et al. 1992). The description of the molecule has a fixed format (originally designed for FORTRAN-like formatting) and has at least two parts, the first being the atomic description and the second the bonding description. Additional parts can include additional information. This representation can basically be translated one-to-one to an internal 2D-graphical data structure.

A more general and modern relative to the MDL connection tables is the Chemical Markup Language (CML) (Murray-Rust and Rzepa 1999) which is a specialization for physical and organic chemistry of the Extensible Markup Language (XML). XML is a standard set up by the World Wide Web Consortium (W3C) for the transmission of data over the internet that is both human and machine readable. The advantage of a format based on XML is that a wide range of software in a wide range of languages has been independently developed. This includes a set of software (written in JAVA) that has been developed specifically for chemical applications, namely the Chemical Development Kit (CDK). There is a chemical data structure directly associated with the CML format. Some automatic generators are already using these standard softwares.

3.1.3.3 Canonicity and Molecular Equivalence

An important operation in automatic generation is to determine whether two molecules are the same or not. For example, in one of the recursive steps when a molecule is generated, it is important to recognize whether the molecule already exists in the species pool. During the generation process, molecular equivalence is used to determine whether two reactions are the same. Furthermore, since a generated mechanism is usually combined with other mechanisms, for example the base mechanism or another generated mechanism, it is important to identify equivalence.

A simple way to detect whether two molecules are equivalent is if they have equivalent names. However, looking at the complexity of the IUPAC nomenclature rules, determining the canonical (unique) name is non-trivial. For example, from the names 2,2,4-trimethylpentane and 4,2,2-trimethylpentane, a modeler could draw the same structure. However, only the first is the IUPAC name and one can not use the two names to textually see whether the two structures are the same. Even a simple molecule such as *n*-pentane can be written in four different ways in

the SMILES representation: CCCCC, C(C)CCC, C(CC)CC, C(CCC)C. Though if the extra computation is made to order the atoms for the SMILES notation (Morgan 1965), then the SMILES string can be used to identify equivalent molecules. A general algorithm for the identification of equivalent structures is the graph isomorphism algorithm (Balaban 1985). The full graph isomorphism algorithm yields an atom–atom correspondence between the graph molecules. If all the atoms in both molecules can be matched, then the molecules are equivalent (the algorithm can stop after the first pair is found).

Figure 3.1 shows an example with isooctane (2,2,4-trimethylpentane). Due to symmetry C_a , C_c and C_d atoms and, correspondingly, C_1 , C_3 and C_4 atoms are equivalent. In addition, C_g and C_h atoms and, correspondingly, C_7 and C_8 atoms are equivalent. This results in $((3 * 2 * 1) * (2 * 1))$ or 12 unique ways to pair atoms in the two molecules up.

3.1.3.4 Substructure Search

An essential part of recognizing whether a reaction class can be applied to a molecule is to recognize whether the essential functional group of the reaction class can be found in the molecule. This operation is highly dependent on representation of the reaction class and the molecule. If these representations are based on 2D-graphs, as with most automatic generators, then the general algorithm used is once again graph isomorphism (Ullmann 1976; Barnard 1993). Within some automatic generators the complexity of the graph isomorphism algorithm is reduced by making use of additional information and specialized graphs (such as dealing with a tree instead of a graph, as it is the case of EXGAS software, see Sect. 3.2.2.1) available during the search.

Suppose we wish to perform a hydrogen atom abstraction at a primary carbon on *n*-butane. Figure 3.2 shows the structures involved, the primary carbon atom, represented as a general methyl group, and *n*-butane molecule. The result of the

	Combinations											
	Set a1				Set a2				Set a3			
	c3		c4		c1		c4		c1		c3	
	g7	g7	g8	g8	g7	g7	g8	g8	g7	g7	g8	g8
a	1	1	1	1	3	3	3	3	4	4	4	4
b	2	2	2	2	2	2	2	2	2	2	2	2
c	3	3	4	4	1	1	4	4	1	1	3	3
d	4	4	3	3	4	4	4	4	3	3	1	1
e	5	5	5	5	5	5	5	5	5	5	5	5
f	6	6	6	6	6	6	6	6	6	6	6	6
g	7	7	7	7	7	7	8	8	7	7	8	8
h	8	8	8	8	8	8	7	7	8	8	7	7

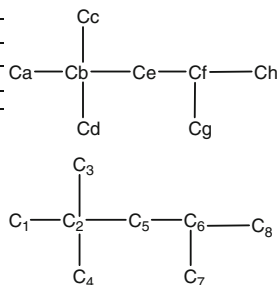


Fig. 3.1 Atom-to-atom correspondences between two *iso*-octane molecule graphs. There are twelve combinations due to symmetry. The sets are grouped according to how C_a , C_c and C_g atoms are matched

graph isomorphism, i.e. the atom-to-atom correspondence between the graphs, is shown in the table. Due to the symmetry of the methyl group, there are $(3 * 2 * 1)$ or 6 ways to match the methyl group at each of the two primary carbon atoms. Note first that only two sets of atoms are matched, those on carbon atom 1 and carbon atom 4. Each of the combinations involves the same atoms meaning there are two sets of three equivalent hydrogen atoms. Each of these sets has six combinations of atom-to-atom matches due to the combined symmetry of the methyl group and the primary group on the *n*-butane molecule. This redundancy, due graph symmetry, has to be taken into account to come up with the desired result of abstracting from a carbon atom from each end of the *n*-butane molecule.

To illustrate the role of reaction class structure symmetry, suppose the hydrogen abstraction is defined by removing H_b in Fig. 3.2 and the abstraction rate is defined per hydrogen atom. This means that six hydrogen atoms can be abstracted from butane. In the table these are the atom-to-atom combinations labeled: b5, b6, b7, b12, b13 and b14. Due to the symmetry of the methyl group, there are two combinations which would yield the same result. Each of these pairs would be combined to create one reaction. In total, six reactions would be generated. However, due to the symmetry of the methyl group and the symmetry of the *n*-butane molecule, all of these six reactions are equivalent. These would be recognized and then combined to one reaction with 6 times the rate of each one (the per hydrogen atom rate).

3.2 Systems Descriptions

The previous sections outlined the general principles and some algorithms of automatic mechanism generation. In this section several systems which have been applied to model combustion chemistry will be described. Each system has its own generation philosophy and database. On a software technical level, mainly due to their historical development parallel to the development of software systems in general within computer science, there are differences not only in the computer languages involved, but also the internal representations of the chemical and kinetic elements needed for generation. All systems described have fundamental

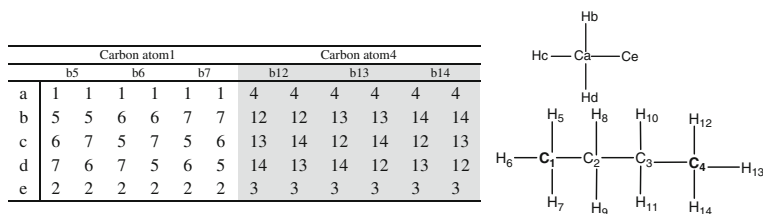


Fig. 3.2 Atom to atom correspondences for a primary methyl group in *n*-butane. There are 12 combinations

aspects which are in common. But all have particular aspects and strategies with particular advantages. In this section four automatic generation systems will be discussed:

- *MAMOX++* (Ranzi et al. 1995a). This system distinguishes itself by producing a hierarchy of (highly) lumped mechanisms derived numerically from automatically generated detailed mechanisms. The *MAMOX++* program is derived from the MAMA program in the SPYRO system (Dente et al. 1979, 1992) which was the first to automatically generate the pyrolysis mechanisms of large hydrocarbons, up to virgin naphthas and heavy gasoils. The same approach, applied to oxidation and combustion process, is based on the generation of a detailed primary mechanism and then on the optimization of the kinetic parameters within a highly generic mechanism (similar, for example, to the Shell model (see Chap. 2)).
- *EXGAS* (Côme et al. 1997). The main specificity of this publicly distributed system is the use of the most comprehensive reaction class database and the large choice given to the user for mechanism tailoring. EXGAS has already been used to generate detailed mechanisms for alkanes (from C₄ to C₁₆), alkenes, cycloalkanes, ethers (Glaude et al. 2000), alcohols (Moss et al. 2008) and methylesters up to C₁₉ (e.g. Hakka et al. 2010; Herbinet et al. 2011) which have been validated under a wide range of conditions. The mechanisms are composed of a comprehensive detailed primary mechanism, a lumped secondary mechanism and a C₀–C₂ (which can be supplemented with C₃–C₈ reactions) base mechanism.
- *RMG* (Green et al. 2001; Van Geem et al. 2006). This system distinguishes itself with a unique “generate and test” algorithm which generates a fundamental mechanistic step, estimates the rate constants and then, using a set of predefined physical conditions and cutoff criteria, determines “on-the-fly” whether the reaction should be included in the final mechanism (Susnow et al. 1997). The RMG system is also the only publicly distributed automatic generator of pressure-dependent reaction networks (Matheu et al. 2001; Allen et al. 2012).
- *REACTION* (Blurock 1995; Moreac et al. 2006). The main specificity of this last system is to use the concept of pathways instead of an exhaustive application of reaction classes. The result is the creation of mechanisms similar to those generated by hand. This system was also the first to represent the fundamental chemical information needed for generation solely in external databases independent of the generalized generation engine, so that the chemical information can be updated without modifying or recompiling the software.

3.2.1 MAMOX++

In the MAMOX++ and MAMA systems, detailed primary mechanisms are generated and then the parameters within a highly generic mechanism (similar, for example, to the Shell model) are optimized. For the further oxidation of the generated lumped products a hierarchical library of validated lumped mechanisms

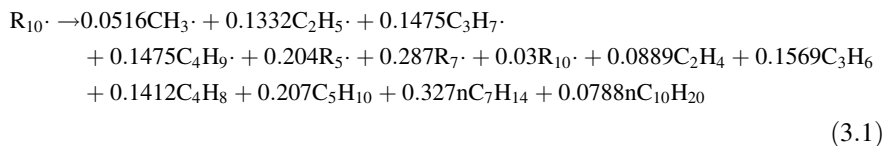
is searched and the corresponding lumped reactions used (Ranzi et al. 2005). The MAMA system in the SPYRO system (Dente et al. 1979) was the first to automatically generate mechanisms for the pyrolysis of hydrocarbons.

3.2.1.1 Lumping Procedure

The philosophy of the species lumping procedure is to produce a highly lumped primary mechanism derived from a comprehensive detailed primary mechanism. The generated lumped mechanism looks very similar to the Shell model of Halstead et al. (1975) and later derivations from Cox and Cole (1985), Hu and Keck (1987) and Cowart et al. (1991) in terms of the autoignition behavior of the fuel. They do however differ fundamentally in how the parameters are derived. Cowart et al. (1991) optimized the model for a particular fuel by adjusting the isomerization reaction of the alkyl peroxy radicals on the basis of engine data. The approach of MAMOX is to base the reduction on a detailed reaction mechanism. From the detailed mechanism, a set of (highly) lumped species and corresponding reactions are defined. The rate parameters are then optimized based on the generated detailed mechanism. The lumping rules are based on the primary product distributions predicted by the detailed model (Ranzi et al. 1995a, 2005).

3.2.1.2 Reduced Pyrolysis Mechanisms Using Steady State Approximation

The basic hypothesis for reduction under pyrolysis conditions is that the radicals larger than C_4 (μ -radicals) can only isomerize or decompose without significant interactions with the process mixture. In contrast, when generalizing this to oxidation reactions, it is necessary to take into account the fact that large intermediate radicals can interact with O_2 . The alkyl radicals obtained from the hydrocarbon fuel after a single hydrogen atom abstraction are lumped into one lumped species, R_n , where n is the number of carbon atoms. For example, in the n -decane mechanism the 5 n -decyl radicals of the detailed mechanism would be lumped into a single R_{10} species in the reduced mechanism. The sub-mechanism of all the isomerization and β -decomposition reactions is written explicitly in the detailed mechanism. Using this detailed mechanism, the (linear) system of continuity equations is solved under the steady state approximation at a given temperature to reduce the overall submechanism to one global reaction. For example, in the n -decane mechanism, the solution is (Ranzi et al. 2005):



There are three key assumptions in this approach:

1. Radicals larger than C_4 can only isomerize or decompose without significant interactions with the process mixture, but do react with oxygen to form peroxy radicals.
2. There is only marginal importance of large radical recombinations and hydrogen atom abstractions. These are bimolecular reactions competing with fast unimolecular reactions.
3. The overall decomposition and radical distribution is temperature independent. Default temperature is assumed to be 1000 K.

The lack of interaction means that this sub-mechanism can be treated independently of other sub-mechanisms within the total pyrolysis mechanism. Not including recombination reactions affects the solution in two ways. First, isomerization and β -decomposition in the forward direction are unimolecular reactions and thus their solution under the steady state approximation is linear. However, recombination reactions are bimolecular. This would bring in non-linear terms. In addition, not including recombination reactions further “decouples” the distribution dependence with smaller radicals. This means the solution for larger radicals does not involve the distribution of the smaller radicals. Using the steady state approximation is temperature dependent. However, empirical evidence states that the radicals mainly decompose at temperature close to 1000 K and derived distributions are relatively temperature independent.

The purpose of the steady state approximation (see [Chap. 18](#) for more details) is to reduce the complexity of the differential equations that must be numerically solved to determine the behavior of the fuel in a combustion process. In the simplest case, if one is interested in the time-dependent solution of the homogeneous adiabatic oxidation of a fuel, the system of reactions is translated into a system of differential equations. For example, the single β -decomposition reaction:



contributes to the following to the production and depletion of $1-C_{10}H_{21}\cdot$ radical:

$$\frac{d[1-C_{10}H_{21}\cdot]}{dt} = -k_f^D [1-C_{10}H_{21}] + k_r^D [C_2H_4][1-C_8H_{17}\cdot] \quad (3.3)$$

Note that in the forward direction there is a linear dependence on concentration. There is only one reactant, $1-C_{10}H_{21}\cdot$ radical. However, in the reverse direction, the radical addition, there is a non-linear dependence on concentration. There are two reactants, C_2H_4 and $1-C_8H_{17}\cdot$ radical. If the radical addition were considered insignificant relative to the β -decomposition, the second term could be neglected (equal to zero) and the dependence would be linear. In general, all β -decompositions (forward direction) contribute a linear term and all recombinations and radical addition contribute a non-linear term. If all recombination reactions were neglected (assumption number 2 above), then the system of equations describing all β -decompositions would be linear. Isomerizations are also represented by linear

equations. A single species isomerises to another and both the forward and reverse contributions to the differential equation are linear.

In general, the sum of all contributions from β -decomposition reaction D_j^i (the j th decomposition of species i), with rate constant $k_{i,j}^D$ and contribution from isomerisation reaction I_j^i (isomerization of species i to j), with rate constant $k_{i,j}^I$:

$$\frac{dX_i}{dt} = \sum_{D_j^i} k_{i,j}^D X_j + \sum_{I_j^i} k_{i,j}^I X_j \quad (3.4)$$

If a species i is in steady state, the concentration of that species does not change over time, i.e. $d[X_i]/dt = 0$. This transforms the set of linear differential equations to a set of linear algebraic equations. For a mechanism for a C_n alkane fuel, there are m alkyl radicals with n carbon atoms where $m = n/2$ (where n is even) or $m = n/2 + 1$ (where n is odd). This means there are m equations of the form of Eq. (3.4). These m algebraic equations can be used to represent the steady state concentrations of the radicals containing C_n carbon atoms. In the mechanism, this is represented as $R_n\cdot$. Successively solving the entire system allows the writing of the total β -decomposition of the $R_n\cdot$ radical in a form such as that shown in Eq. (3.1).

For the n -decane system, for example, there are five algebraic equations of the form of Eq. (3.4), one for each of the 5 C_{10} alkyl radicals. These can be used to derive their distribution in terms of the remaining alkyl radicals (those having less than 10 carbon atoms) and alkenes. The result is the distribution of the 5 alkyl radicals making up the lumped species, $R_{10}\cdot$. Table 3.1 empirically shows the relative temperature independence of the distribution for these 5 alkyl radicals. The distribution of species derived using the steady state procedure is actually temperature dependent.

One of the key assumptions MAMOX is that the temperature dependence of the reaction classes involved in lumping is minimal. The distribution derived at 1000 K is valid over a wide range of temperatures for the oxidation of hydrocarbons. The justification (Ranzi et al. 2005) is given in examining, for example, the product distribution of isomerization and β -decomposition of n -decyl radicals derived from hydrogen atom abstraction from n -decane (Table 3.1). The largest deviations stem from the primary $1-C_{10}H_{21}\cdot$ radical and its subsequent decomposition to ethylene and a radical. However, Ranzi et al. (2005) make the further justification that above 1200 K the life-times of these radicals are short (10^{-8} s).

3.2.1.3 Reduced Oxidation Mechanisms

Reduction of oxidation mechanisms, for example for the low-temperature oxidation chemistry of hydrocarbons, does not satisfy the conditions under which pyrolysis mechanisms were reduced. Under oxidative conditions the sub-mechanisms of the reactions with oxygen are a significant “external interaction” and

Table 3.1 This table illustrates the temperature effect on the *n*-decyl radicals and the product distributions

	800 K	Rate constant	1200 K	Ave	σ	σ/Ave (%)
<i>Relative concentrations (%)</i>						
1-C ₁₀ H ₂₁ ·	4.75	8.50	13.30	8.9	4.29	48
2-C ₁₀ H ₂₁ ·	24.17	24.81	26.09	25.0	0.98	4
3-C ₁₀ H ₂₁ ·	23.62	22.33	21.14	22.4	1.24	6
4-C ₁₀ H ₂₁ ·	23.41	18.55	18.55	21.0	2.43	12
5-C ₁₀ H ₂₁ ·	24.05	23.32	20.92	22.8	1.64	7
<i>Product distribution</i>						
C ₉ H ₁₈ + CH ₃ ·	0.042	0.052	0.059	0.05	0.008	16
C ₈ H ₁₆ + C ₂ H ₅ ·	0.148	0.133	0.119	0.13	0.014	11
C ₇ H ₁₄ + C ₃ H ₇ ·	0.152	0.148	0.135	0.14	0.009	6
C ₆ H ₁₂ + C ₄ H ₉ ·	0.152	0.148	0.135	0.14	0.009	6
C ₅ H ₁₀ + C ₅ H ₁₁ ·	0.148	0.133	0.119	0.13	0.014	11
C ₄ H ₈ + C ₆ H ₁₃ ·	0.149	0.141	0.136	0.14	0.007	5
C ₃ H ₆ + C ₇ H ₁₅ ·	0.153	0.157	0.168	0.16	0.008	5
C ₂ H ₄ + C ₈ H ₁₇ ·	0.056	0.089	0.130	0.09	0.037	40

The average (Ave) and standard deviation (σ) is over the three temperatures

cannot be neglected. In this case, another approach must be taken if the same degree of lumping is to be achieved. Instead of solving a set of linear equations as in the pyrolysis case, an optimization is used.

Analogous to the SHELL model, the major oxidation components are lumped (Ranzi et al. 1995a, b). In addition to R_n·, where n is the number of carbon atoms in the alkyl species, the oxygenated species of the low-temperature chemistry are lumped: alkylperoxy radicals (R_nOO·), hydroperoxyalkyl radicals (·Q_nOOH), hydroperoxyalkylperoxy radicals (·OOQ_nOOH), cyclic ethers (ETER_n) and keto-hydroperoxides (OOQ_nOOH). The branching agents and products of the side chains of the low-temperature chemistry are alkenes including n or less carbon atoms, as well as aldehydes, ketones and aldehyde radicals with 3 or less carbon atoms. The lumped primary mechanism for the oxidation of *n*-decane is shown in Table 3.2.

Once again, the parameters of this low-temperature primary mechanism are optimized relative to the generated full detailed mechanism. The key to the optimization is to analyze the initial “cumulative selectivity” of the lumped species using the detailed mechanism (see Fig. 3.3). The kinetic parameters of the lumped primary mechanism are optimized using non-linear regression analysis. The difference between the cumulative selectivity predictions at each temperature of the lumped mechanism and the detailed mechanism are analyzed. The parameters of the lumped species are optimized until the squares of the differences are minimized.

Table 3.2 Primary lumped mechanism for the oxidation of *n*-decane

Reactions	A	Ea/R
$n\text{-C}_{10}\text{H}_{22} \rightarrow 0.09\text{CH}_3\cdot + 0.26\text{C}_2\text{H}_5\cdot + 0.26\text{C}_3\text{H}_7\cdot + 0.26\text{C}_4\text{H}_9\cdot + 0.39\text{R}_5\cdot + 0.5933\text{R}_7\cdot + 0.1466\text{R}_{10}\cdot$	0.35×10^{18}	40750
$\text{R}\cdot + n\text{-C}_{10}\text{H}_{22} \rightarrow \text{RH} + \text{R}_{10}\cdot$	6 primary H-atoms and 16 secondary H atoms	
$\text{O}_2 \rightarrow \text{HO}_2\cdot$	0.23×10^{12}	22500
$\text{OH}\cdot \rightarrow \text{H}_2\text{O}$	0.53×10^{11}	850
$\text{H}\cdot \rightarrow \text{H}_2$	0.29×10^{12}	4000
... (see Ranzi et al. 2005)		
$\text{R}_{10}\cdot + \text{O}_2 \rightarrow n\text{-C}_{10}\text{H}_{20} + \text{HO}_2\cdot$	0.50×10^9	1750
$\text{R}_{10}\cdot \rightarrow 0.0516\text{CH}_3\cdot + 0.1332\text{C}_2\text{H}_5\cdot + 0.1475\text{C}_3\text{H}_7\cdot + 0.1475\text{C}_4\text{H}_9\cdot + 0.204\text{R}_5\cdot + 0.287\text{R}_7\cdot + 0.03\text{R}_{10}\cdot + 0.0889\text{C}_2\text{H}_4 + 0.1569\text{C}_3\text{H}_6 + 0.1412\text{C}_4\text{H}_8 + 0.207\text{C}_5\text{H}_{10} + 0.327n\text{C}_7\text{H}_{14} + 0.0788n\text{C}_{10}\text{H}_{20}$	0.35×10^{14}	15100
$\text{R}_{10}\cdot + \text{O}_2 \rightarrow \text{R}_{10}\text{OO}\cdot$	0.20×10^{10}	0
$\text{R}_{10}\text{OO}\cdot \rightarrow \text{O}_2 + \text{R}_{10}\cdot$	0.50×10^{14}	15600
$\text{R}_{10}\text{OO}\cdot \rightarrow \cdot\text{Q}_{10}\text{OOH}$	0.30×10^{13}	12100
$\cdot\text{Q}_{10}\text{OOH} \rightarrow \text{R}_{10}\text{OO}\cdot$	0.20×10^{11}	8100
$\cdot\text{Q}_{10}\text{OOH} \rightarrow \text{ETHER}_{10} + \text{OH}\cdot$	0.15×10^{11}	7100
$\cdot\text{Q}_{10}\text{OOH} \rightarrow n\text{-C}_{10}\text{H}_{20} + \text{HO}_2\cdot$	0.45×10^{13}	12100
$\cdot\text{Q}_{10}\text{OOH} \rightarrow 0.333\text{CH}_2\text{O} + 0.333\text{CH}_3\text{CHO} + 0.333\text{C}_2\text{H}_5\text{CHO} + 0.333n\text{-C}_7\text{H}_{14} + 0.333n\text{-C}_{10}\text{H}_{20} + \text{OH}\cdot$	0.20×10^{13}	11300
$\text{O}_2 + \cdot\text{Q}_{10}\text{OOH} \rightarrow \cdot\text{OOQ}_{10}\text{OOH}$	0.20×10^{10}	0
$\cdot\text{OOQ}_{10}\text{OOH} \rightarrow \text{O}_2 + \cdot\text{Q}_{10}\text{OOH}$	0.30×10^{15}	14600
$\cdot\text{OOQ}_{10}\text{OOH} \rightarrow \text{OQ}_{10}\text{OOH} + \text{OH}\cdot$	0.10×10^{13}	11600

Units are kmol, m, s, K. Lumped reactions for $n\text{-C}_{10}\text{H}_{20}$, ETHER_{10} and OQ_{10}OOH are part of the secondary mechanism (see Ranzi et al. 2005)

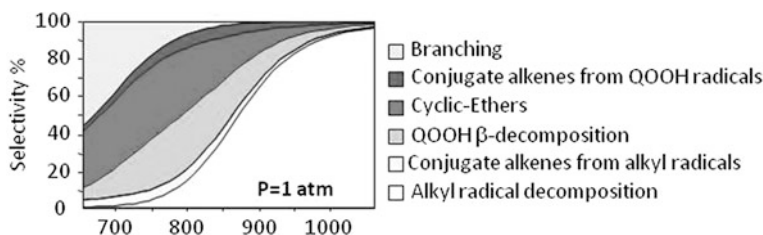


Fig. 3.3 The initial cumulative selectivities of the primary lumped species of *n*-decane oxidation at one atmosphere

3.2.2 EXGAS

Since the first attempts to model the oxidation of C_4 – C_8 alkanes (Côme et al. 1997; Warth et al. 1998), the EXGAS program, which is written in Pascal, has been extensively used to produce detailed kinetic models for the oxidation of a wide range of hydrocarbons:

- linear and branched alkanes up to C_{16} (Buda et al. 2005; Biet et al. 2008; Herbinet et al. 2012),
- linear alkenes from C_3 to C_7 (Heyberger et al. 2001; Touchard et al. 2005; Bounaceur et al. 2009),
- cycloalkanes (Buda et al. 2006; Sirjean et al. 2007; Pousse et al. 2010).

Recent developments on oxygenated reactants are presented in Chap. 4. Software EXGAS-ALKANES-ESTERS automatically generates detailed kinetic mechanisms for the oxidation of linear and branched alkanes, and linear methyl esters and is freely available for academic researchers (valerie.warth@ensic.inpl-nancy.fr). Note also that the development of an EXGAS version dedicated to alkylbenzenes is in progress.

3.2.2.1 Notation

The external notation used to transfer the chemical formulae of the reactants and of the primary species between the user and the computer is a one-dimensional notation (Côme et al. 1984). This “linear notation” is very close to the semi-developed notation in the case of non-cyclic compounds. For the ease of use by modelers, this notation is non-ambiguous, but also non-canonical as shown in Fig. 3.4 for *n*-dodecane. That means that a same species can be represented by different notations. In the internal notation, the two types of chemical acyclic species (molecules and free radicals), which are involved in this program, are represented by a tree-like structure (see example in Fig. 3.4) on which is applied an algorithm of canonicity. More details about these internal and external

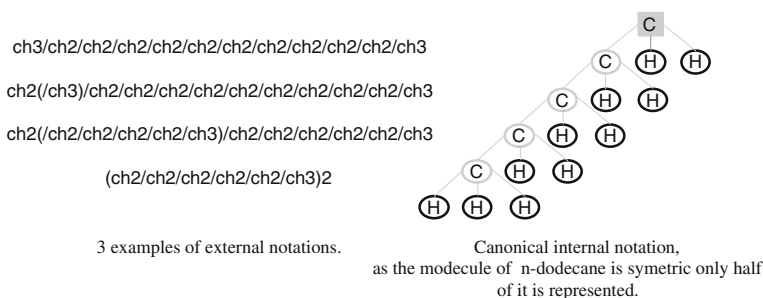


Fig. 3.4 External and internal notation in the case of *n*-dodecane

notations, and the notations used for cyclic molecules can be found in (Warth et al. 2000).

3.2.2.2 General Structure of an EXGAS Model

As presented in Fig. 3.5, a model generated by EXGAS is composed of three parts: a C_0 – C_2 base mechanism including all the reactions involving radicals or molecules containing less than three carbon atoms, a comprehensive primary mechanism, and a lumped secondary mechanism, containing reactions consuming the molecular products of the primary mechanism, which do not react in the reaction bases.

Thermochemical data for molecules or radicals are automatically calculated and stored as 14 polynomial coefficients, according to the CHEMKIN formalism (Kee

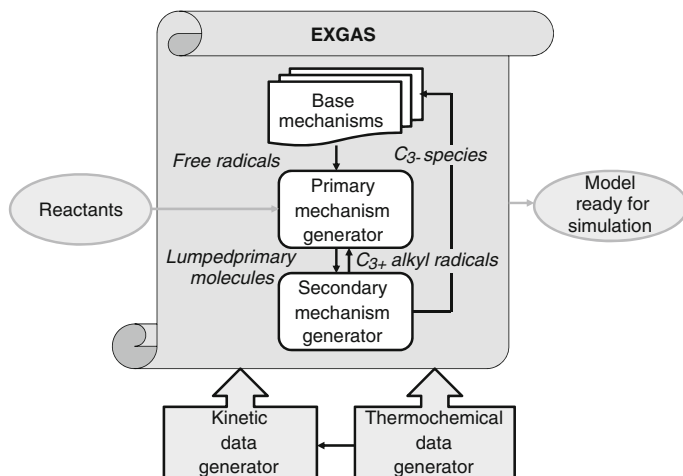


Fig. 3.5 General structure of the EXGAS system (adapted from Warth et al. 1998)

et al. 1993). These data are calculated using the software THERGAS (Muller et al. 1995) based on the group and bond additivity methods proposed by Benson (1976) (see Chap. 20).

The kinetic data of the reactions included in the primary or secondary mechanisms are also automatically provided: they are either calculated using thermochemical kinetic methods (Warth et al. 1998) or estimated using a wide range of correlations (Warth et al. 1998; Heyberger et al. 2001; Buda et al. 2005; Touchard et al. 2005; Biet et al. 2008; Glaude et al. 2010).

3.2.2.3 The Base Mechanisms

The C₀–C₂ base mechanism used by EXGAS was initially written by Barbé et al. (1995). Since then it has been continuously up-dated (see latest revision by Cord et al. (2012)). The pressure dependent rate constants follow the formalism proposed by Troe (1974) and efficiency coefficients have been included. This base mechanism can easily be completed to also consider the reactions of C₃–C₅ polyunsaturated hydrocarbons (Gueniche et al. 2009) and those of small aromatic compounds such as benzene, toluene or ethylbenzene (Husson et al. 2013).

3.2.2.4 The Primary Mechanism Generation

Figure 3.6 presents the structure of the algorithm (or generator engine) used for the generation of primary mechanism for alkanes and alkenes as well as the involved reaction classes. At the beginning, the species pool only contains the initial reacting hydrocarbons, which can be a single molecule or a mixtures, oxygen and the radicals present in the C₀–C₂ base mechanism. Then the first C₂₊ radicals are created by all the possible initiations from the molecular reactants and enter the species pool. In a second step, all radicals present in the species pool are submitted to the reactions present in the propagation loop; the radicals of the C₀–C₂ base mechanism react only by addition to the double bond or hydrogen atom abstraction with the reacting hydrocarbon. Each new created radical is to its turn included to the species pool and the algorithm is terminated when no new radical is created in the propagation loop. As the additions of carbon atom containing radicals is considered as a reaction class in the case of alkenes, the user needs then to specify a maximum species size to avoid the creation of an infinite propagation loop. In a final step, all the radicals created by initiations and propagations should be submitted to termination steps.

To avoid unnecessarily long reaction mechanisms, the following simplifying rules are generally used. Three different classes of radicals have been identified by the $\beta\mu$ rules of Goldfinger-Letort-Niclaude (Warth et al. 1998): β radicals which cannot decompose by unimolecular process (typical β free radicals are $\cdot\text{H}$, $\cdot\text{OH}$, or $\cdot\text{CH}_3$), μ radicals which can easily decompose by a unimolecular process involving the scission of a (C–C) or a (C–O) bond (typical μ free radicals are

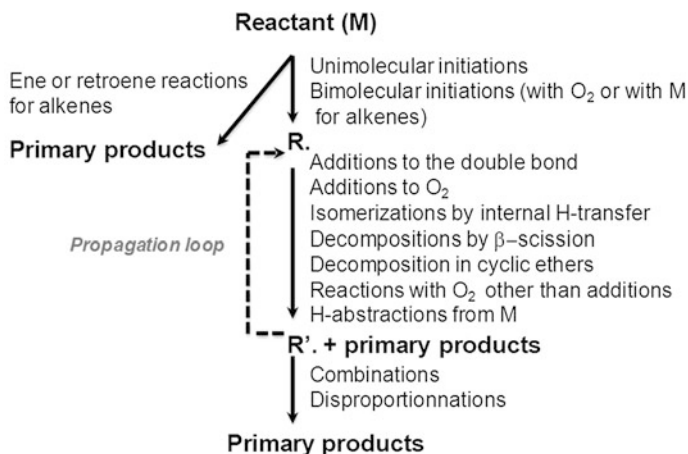


Fig. 3.6 Algorithm of generation used to generate the primary mechanisms of alkanes and alkenes in EXGAS

n-C₃H₇· and *s*-C₄H₉·), $\beta\mu$ radicals which have a β behaviour at low temperatures and a μ behaviour at high temperature (typical $\beta\mu$ radicals are ·OOH, ·CHO, ·OCH₃, or ·OOCH₃). Therefore according to these classes, the radicals involved in bimolecular reactions (e.g. H-abstractions or termination steps) are mostly of β and $\beta\mu$ types. More details can be found in Warth et al. (1998).

It is made possible for hydroperoxyalkyl radicals (·QOOH) to undergo a second addition to oxygen yielding ·OOQOOH radicals. Note that the possibility of a third addition to oxygen is not considered. The detailed isomerizations and subsequent decompositions of ·OOQOOH radicals can be considered, but in most cases, only the direct formation of ·OH radicals and a globalized ketohydroperoxide is written. The rate of this global step for a given ·OOQOOH radicals is the sum of the rates of all the possible isomerizations of this radical (Glaude et al. 2000).

Note also that the considered reaction classes and the level of simplification (e.g. types of radicals to be considered) can be chosen by the kineticist prior to the generation. For instance, for modelling a system above 1000 K, the generation of the addition to oxygen and the subsequent reactions could be discarded. Also breaking C–H bonds during β -scission decompositions can be omitted if these reactions can be neglected under the studied conditions (Glaude et al. 2000).

3.2.2.5 The Secondary Mechanism Generation

In most cases, the molecular products formed in the primary mechanism are lumped in order to reduce the size of the model. Lumping consists here in gathering the molecular products having the same global formulae and the same functional groups into one generic species: as an example, all isomers of linear

dodecene, which are primary products obtained during the oxidation of *n*-dodecane, are lumped as a single species: C₁₂H₂₄. This is very similar to what is used in MAMOX++. However when needed some important primary products (e.g. cyclic ethers) can be considered individually (Herbinet et al. 2012).

Secondary reactions are written for every type of molecular products: hydroperoxides, alkenes, cyclic ethers, aldehydes, alkanes, ketones, alcohols. However to avoid an explosion of the size of the mechanisms, these reactions are written in a global way in order to promote the formation of species which are already included in the primary mechanism and in the C₀–C₂ reaction base (Biet et al. 2008; Glaude et al. 2010). The kinetic data of the reactions of primary products generated by EXGAS are those of the first involved reaction: O–OH bond breaking for hydroperoxides, hydrogen atom abstractions for cyclic ethers, aldehydes, alkanes, ketones, and alcohols, and finally radical additions and retro-ene decompositions for alkenes.

Table 3.3 presents the lumped reactions automatically written by EXGAS for the consumption of lumped dodecene. Considering the formation of alkyl radicals, such as ·C₁₂H₂₅ or ·C₁₀H₂₁, the reactions of which are taken into account in details in the primary mechanism, allows a more accurate representation of the involved decomposition channels. Secondary molecules such as C₁₀H₂₁CHO or C₁₂H₂₄O-oxirane react again in the secondary mechanism, but with reactions of aldehydes and cyclic ethers, respectively (Biet et al. 2008).

Table 3.3 Lumped reactions written by EXGAS for the oxidation of dodecene

Other species involved	Products	Rate constant
<i>Additions</i>		
H-atoms	·C ₁₂ H ₂₅	1.32.10 ¹³ exp(−785/T) + 1.32.10 ¹³ exp(−1640/T)
·OH	HCHO + ·C ₁₁ H ₂₃ CH ₃ + C ₁₀ H ₂₁ CHO	1.4 × 10 ¹² exp(520/T) 1.4 × 10 ¹² exp(520/T)
O-atoms	CH ₂ CO + H + ·C ₁₀ H ₂₁	6.0 × 10 ⁴ T ^{2.56} exp(770/T)
·CH ₃	C ₄ H ₈ + ·C ₉ H ₁₉ C ₃ H ₆ + ·C ₁₀ H ₂₁	1.7 × 10 ¹¹ exp(3720/T) 9.6 × 10 ¹⁰ exp(4030/T)
·OOH	·OH + C ₁₂ H ₂₄ O-oxirane	1.0 × 10 ¹² exp(7150/T)
<i>H-abstractions</i>		
Small radicals (·X), such β or βμ radicals	XH + C ₄ H ₆ + ·C ₈ H ₁₇	As for the abstraction of 2 secondary allylic, 3 primary alkyl and 16 secondary alkyl hydrogen atoms from initial alkene as proposed by Buda et al. (2005), Heyberger et al. (2001))
<i>Retro-ene decompositions</i>		
–	C ₃ H ₆ + C ₉ H ₁₈	8.0 × 10 ¹² exp(−28400/T)

Rate constants are given in cm³, s^{−1}, mol units

3.2.3 RMG

The RMG open-source software package has its conceptual origins in the NetGen software developed by Broadbelt et al. (1994), which uses an exhaustive generation technique (see Sect. 3.1.2.3) of fundamental reaction steps (Green 2007). RMG is unusual in that it tests each generated species using a rate-based criterion “on-the-fly” (meaning during the generation process) to see whether it should be included in the final mechanism (Susnow et al. 1997). So while all reactions are considered, with the numerical rate-based tests only significant reactions filter through. This is a classic “generate and test” algorithm from classical artificial intelligence (Nilsson 1982). The success of this test is highly dependent on the accuracy of the derived thermodynamics and rate constants.

Another unusual feature of RMG is that it automatically identifies chemically-activated reaction sub-networks, using a similar strategy to that used for ordinary thermal reaction networks (Allen et al. 2012; Matheu et al. 2003). The pressure-dependent rate coefficients for all the reaction pathways inside each sub-network are computed using approximations to the master equation (master equation is described in Chap. 21). This special capability of RMG is particularly helpful for high-temperature low-pressure systems, where more than half of the important reactions may have significantly pressure dependent rate-coefficients. Most mechanisms generated in other ways omit many of these chemically-activated reaction pathways.

The reaction and species database and the methods used in the generation process also set this system apart from the others. The rate estimation rules are stored in an editable database, rather than being hard-coded into the software, conceptually similar to the approach of Blurock (1995) (see Sect. 3.2.4). This makes the software more maintainable, and it is easier to update rate estimates, or to add new ones. Similar to NetGen and related XMG software (Grenda et al. 2003; Matheu et al. 2003), some of the thermochemistry is computed on the fly during model generation by spawning quantum chemistry jobs (Magoon and Green 2013).

The RMG software was originally written by Song et al. (2004). The first published demonstration of its capabilities was (Van Geem et al. 2006). RMG currently includes free radical and concerted-reaction chemistry for molecules containing C, H, O, and S atoms. The current version does not consider ions or photochemistry, but optionally includes solvent effects on thermochemistry and on some rate coefficients (Jalan et al. 2013), so it can predict reactions in liquid phase. For a recent demonstration of its capability to predict complicated chemistry see (Harper et al. 2011). The latest version is available at <http://rmg.sourceforge.net>.

3.2.3.1 Rate Based Generation Algorithm: Network Expansion and Termination Criteria

At any given point in the algorithm, the species pool is divided into two sets, “reacted” and “unreacted” species (see Fig. 3.7). The species in the reacted set

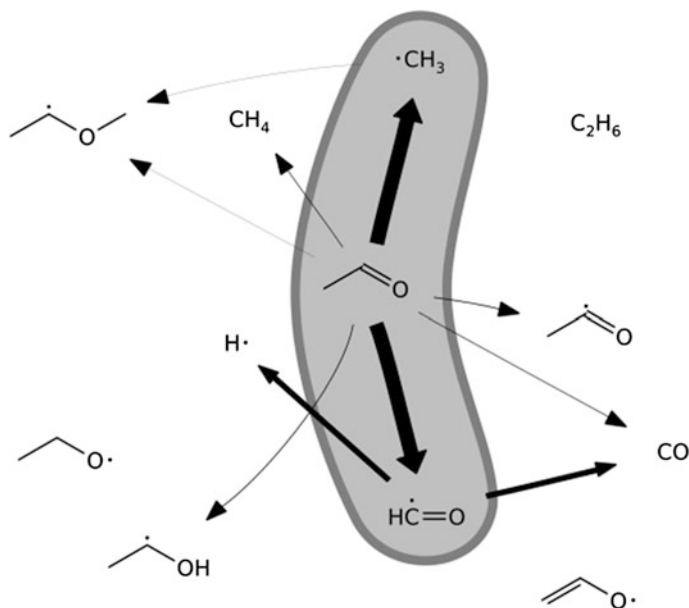


Fig. 3.7 Species pool connected by a reaction network in the case of the pyrolysis of acetaldehyde. The species pool is divided into two regions, reacted and unreacted

have been reacted with all possible allowed reaction classes. The unreacted species are products of the reactions of the reacted species. But the reaction classes have not yet been applied to the unreacted species.

The basis of the algorithm is to expand a network of reacted species one species at a time. The species chosen to be expanded is the unreacted species having the highest rate of formation. This is the species that is drawing out the most flux from the reacted network. The reaction network is deemed complete when this rate of formation is less than a given criteria. The reaction network is self-consistent and the perturbation of any additional reactions to outside this network is small, i.e. a minimum of flux leaves the network. In this philosophy of the generation the flow from a reacted species inside the network to a unreacted species outside the network is analyzed (Susnow et al. 1997). The unreacted species lie on the “edge” of the reaction network. The further reactions of the unreacted species could produce an expanded network involving “unknown” species. The network is only generated when the flux to the unreacted species at the edge of the reacted network is large enough.

During the analysis, the network is converted to a reactive system where each of the reactions is converted to a differential equation with respect to time as shown in Chap. 2. The system of equations is solved at regular time intervals until a particular reactant conversion, X_A , is achieved at time τ . At each time step the total rate of production (see Eq. (2.3) of Chap. 2) of each species, R_i , is determined. For

the reacted species, this is the sum of the rates of formation minus the rates of consumption. Since their consumption reactions have not been formed yet, only the rate of formation is computed for the unreacted species in the network. The maximum rate of formation for each species, $R_{i,\max}$, is determined for all time, t , intervals ($0 < t < \tau$). Note that R_i for all unreacted species is positive. The largest $R_{i,\max}$ of the unreacted species is the next species to be added to the reacted species network. The entire reaction network consisting of reacted and unreacted species is expanded with the given reaction classes applied to this new reacted species.

The expansion of the network is terminated when all the maximum rates of formation, $R_{i,\max}$, of the unreacted species is under a threshold, R_{\min} (Susnow et al. 1997). R_{\min} represents a combination of a characteristic rate (e.g. the disappearance rate of the reactant) R_{char} , indicating how fast the system is evolving, and the desired precision level, f_{\min} :

$$R_{\min} = f_{\min} R_{\text{char}} \quad (3.5)$$

One possible choice of R_{char} is the average conversion rate over time τ defined as:

$$R_{\text{char}} = [C_{A0} - C_A(\tau)]/\tau = X_A C_{A0}/\tau \quad (3.6)$$

where C_{A0} is the initial concentration of the reactant and C_A is the concentration of the reactant at the particular conversion X_A . If the formation of all unreacted species on the edge of the reacted network of species is less than the tolerance R_{\min} , then it is deemed that there is no significant flux outside the reacted network. Thus the network is deemed complete and the generation algorithm terminates. Upon termination, the sum total of the “leaks” to the unreacted species gives a measure of the overall error due to incompleteness of the reaction network.

Dividing up the species into reacted and unreacted species simplifies the solution to the differential equations resulting from the reaction network: the reverse reaction to that producing a unreacted species is ignored. This decouples the computation of the differential equations:

$$\frac{dC_j}{dt} = f(C_j) \quad (3.7)$$

$$R_i = \frac{dC_i}{dt} = g(C_j) \quad (3.8)$$

Where j is over all “reacted” species and i is over all unreacted species. Both functions f Eq. (3.7) and g Eq. 3.8) are (algebraic) polynomial functions in only reacted species. This means that the n differential equations Eq. (3.7), where n is the number of reacted species, is solved first for the set of reacted concentrations, C_j . This solution is then substituted into the algebraic expressions of the unreacted species Eq. (3.8) to determine each R_i .

The reacted network is solved independently of the unreacted network. This means the reacted network is considered a closed system and ignores the leaks into

the unreacted system. As the system nears completion, i.e. the leaks get smaller and smaller, the errors from this approximation become less significant. The independent calculation of each R_i is sufficient for the decision making process, i.e. to choose which species to expand next and whether the algorithm should terminate. The size of the set of reacted species is always considerably smaller than the size of the unreacted species set and hence represents a considerable computational savings.

As currently implemented in RMG this selection algorithm has been found to be very effective at automatically identifying the reaction pathways leading to major products and byproducts without including many unimportant species, but it sometimes omits low-flux sensitive reactions (e.g. degenerate branching steps important in ignition). Of course, the termination criteria is not unique. The formulation in NetGen (Broadbelt et al. 1994), from which RMG is conceptually derived, of the termination criteria was based on carbon atom count (Broadbelt et al. 1994) or “rank” of the reaction (Bhore et al. 1990; Broadbelt et al. 1994).

3.2.3.2 Pressure Dependent Networks: Activated Species Algorithm

The “Activated Species Algorithm” (ASA) treats chemically or thermally activated species as though they were distinct species to produce the connectivity of the pressure dependent channel networks (Matheu et al. 2001; Matheu 2002; Allen et al. 2012). The general flow of the algorithm is the same as with rate-based generation algorithm described previously.

If a reaction produces a single product (see example in Fig. 3.8), then it is a candidate for the pressure dependent network. The product, C^* , is added as an unreacted species. The reaction is added to the network with an initial rate constant corresponding to the high-pressure-limit, k^∞ . Using k^∞ gives the maximum possible flux through the reaction channel to any possible species in the pressure-dependent network. If its flux of formation satisfied the screening criteria, an activated network containing the reactions of C^* , such as isomerizations, collisional quenching or the production of exit products is explored (Grenda et al. 2003).

For the reactions currently in the reaction list (the 3 reactions in the right side of Fig. 3.8), temperature and pressure dependent rate constants are calculated, $k(T,P)$, using a modified version of CHEMDIS software (Bozzelli et al. 1997; Chang et al. 2000; Allen et al. 2012)). This code only gives an approximation (see discussion in Matheu et al. (2003) of the true pressure-dependent phenomenological rate coefficients (Miller and Klippenstein 2012) however CHEMDIS provides quick “on the fly” estimates of rate constants for complex, multiwell pressure dependent network using input quantities that are readily available in mechanism generation systems. In a post processing step, the computed rate coefficients, $k(T,P)$, are fitted to Chebyshev, logP, or Arrhenius form (see more details in Chap. 19). The Arrhenius values obtained from this sort of fitting have no simple physical meaning, and change with pressure.

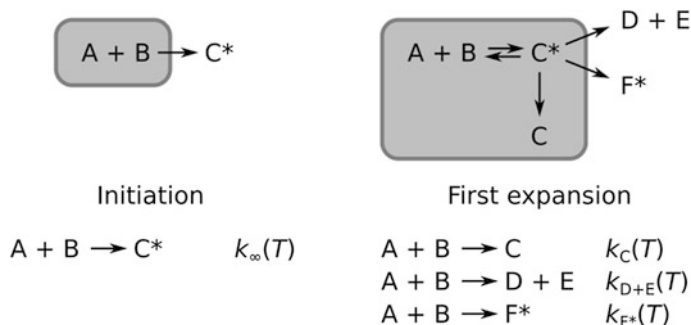


Fig. 3.8 Activated species algorithm: the reaction $A + B$ forms a single activated species, C^* . The activated species is then expanded to additional activated species, D , E and F^* . In addition the stabilized species, C , is added to the network

The reaction $A + B \rightarrow C^*$ is then replaced by the reaction $A + B \rightarrow C$ with $k_C(T, P)$ calculated by CHEMDIS and D , E and F^* are added as unreacted species. The criteria to determine whether the network is complete or not are similar to the general RMG criteria. It is dependent on how much flux “leaks” (R_{leak}), out of the network. In the case of pressure-dependent networks, this is the total flux to the activated species in the unreacted species list which is screened using temperature and pressure dependent rate constants. In the case of Fig. 3.8:

$$R_{\text{leak}} = (k_{D+E}(T) + k_{F^*}(T))[A][B] \quad (3.9)$$

For the pressure-dependent networks the characteristic rates in Eq. (3.5) have another form (for comparison see Eq. (3.6)) describing the total “input rate” to the pressure dependent network. For chemical activation (as in Fig. 3.8), the characteristic rate takes the form:

$$R_{\text{char}} = k_{\text{imp}}^{\infty} [A][B] \quad (3.10)$$

For dissociation reactions, the characteristic rate is the fraction of the collisions between the reactant, C and the bath gas which produce $[C^*(E)]$ at energies above the lowest barrier to dissociation (for a full explanation of terms see (Chang et al. 2000)):

$$R_{\text{char}} = \int_{E_0}^{E_{\text{max}}} k^s(T)[M] \frac{\rho_C(E) e^{-E/k_B T}}{Q_C(T)} dE [C] \quad (3.11)$$

Briefly, ρ_c is the density of states for C at energy E (calculated using thermodynamic estimates, see (Bozzelli et al. 1997), Q_C is the partition function for C).

If R_{leak} is above the threshold, the isomer corresponding to the largest element of the sum is selected as the next candidate for exploration. If it is F^* , the reaction

$A + B \rightarrow F$ (F being the stabilized species corresponding to F^*) is added to the reaction list with using $k_F(T)$ calculated by CHEMDIS, while the formation of $D + E$ is not included in the model, i.e. $D + E$ remains on the edge.

3.2.4 Reaction

The REACTION system (Blurock 1995; Moreac et al. 2006) is the first “data-driven” automatic generation system used in combustion. The primary design strategy is to have the hard-coded generation “engine” as small and as general as possible and let the external database guide the generation procedure. The standard reaction classes, for example from Curran et al. (1998), are in the form of an external database in 2D-graphical representations of the reactive center and important surrounding functional groups (Blurock 2004a, b). In addition, the generation strategy, i.e. how the reaction classes are applied, is not fixed as in other systems. This is accomplished through the concept of reaction pathways, i.e. a sequence of reaction classes, to generate mechanisms. This is in line with a main goal of REACTION which is to mimic how the combustion modeler thinks and generates a mechanism. The use of pathways instead of recursive use of a pool of reaction classes is closer to how a modeler would produce a mechanism.

REACTION stems from earlier work on the RETROSYN computer program (Blurock, 1990) for computer aided organic synthesis (CAOS). Both CAOS and automatic generators use reaction classes. The main difference is that in CAOS the modeler starts with the molecule to be synthesized and uses the reaction classes retro-synthetically (Corey and Wipke 1969; Wipke and Howe 1977), i.e. in reverse, to derive the starting reactants. The goal of RETROSYN was not to use “programmed” reaction classes, but to derive the reaction classes from an electronic database of synthetic organic reactions (Blurock 1990). The key to the process was to determine the maximal common subgraph (a special case of graph isomorphism) to determine the reactive center between the reactants and products. This derived database in the form of 2D-graphical structures was used to perform retro-synthetic analysis.

3.2.4.1 Reaction Patterns

Though, there is no strict definition of reaction class, a single reaction class describes a single type of reactivity. But all reactivity within a reaction class does not need to have the same rate constant. The reactive environment beyond, for example, the reactive center, could influence the rates. For example, a common distinction within a single reaction class is the effect of primary, secondary and tertiary carbon atoms. If a reaction class is to be described with 2D-graphical structures each of these different environments need be included. In REACTION this is done with reaction patterns (Blurock 1995; Ratkiewicz and Truong 2006)

where each individual distinguishing chemical environment leading to a different rate constant is represented as a set of reactant and product 2D graphical substructures.

For example, the hydrogen atom abstraction reaction class encompasses not only a wide range of abstractors, but also a range of types of hydrogen atoms. In the description of the reaction class by Curran et al. (1998), 11 radical abstractors are applied to hydrogen atoms on primary, secondary and tertiary carbon atoms. In order to describe these reactions with graphical substructures 33 reaction patterns are needed corresponding to the 11 abstractors and 3 types of carbon atom. The primary, secondary and tertiary carbon atoms are represented as generic carbon graphs. Matching is made through graphical isomorphism and atom-to-atom correspondence as described in Sect. 3.1.3. To apply this reaction pattern, the carbon structure is matched within the carbon and the hydroxyl radical is matched to the reactants in the species pool.

3.2.4.2 Pathways

As outlined in Chap. 2, a detailed mechanism is not just a collection of reactions, but has a distinct structure. One such structure is the reactive pathway. This is a linear sequence of reactions from an initial reactant to products. When creating a reaction mechanism, the modeler often starts with an initial species, possibly the fuel, and applies an initial reaction class. The products are then examined and the next reaction class is applied. One classic pathway that is built up in this way in combustion is the low temperature pathway (see Sect. 2.2.3) from fuel through to branching agents. This is an efficient means of building up a (sub)mechanism ensuring that the products of all reactions are consumed by other reactions.

REACTION differs from other automatic generators in that instead of applying recursively a pool of reaction classes, the reaction classes are arranged in pathways, i.e. a linear sequence of sets of reaction classes. The primary reasons for generating in this way are:

- A more controlled form a generation which inhibits the combinatorial explosion of possible reactions.
- It mimics more closely the way a modeler thinks and builds a complex detailed mechanisms.
- It provides a means of introducing a generation strategy without hard-coding the strategy in the generation engine.

The main difference in the generation procedure is that instead of continually adding newly generated species in the species pool, the species pool is initialized after every step with only newly generated species. This means that the reaction classes of the current step are only applied to the products of the last step. In designing a pathway, those products not consumed by one of the steps should be consumed by another submechanism.

A systematic comparison of the comprehensive *n*-hexadecane mechanism as generated by REACTION and that produced by Westbrook et al. (2009) yielded very similar mechanisms. Both mechanisms included all *n*-alkane mechanisms up until hexadecane. For the species with eight or more carbon atoms the two mechanisms were exactly the same for almost all the classes. They differed only when hand-generated mechanism did extensive lumping and in a few cases where the hand-generated did not include all combinations of reaction class applications.

In REACTION the reaction path is applied to a seed molecule and produces a submechanism. For the *n*-decane mechanism (Moreac et al. 2006), the *n*-pentane to *n*-decane seeds molecules were applied to 8 pathways to produce 48 generated submechanisms. For the *n*-tetradecane mechanism, *n*-pentane to *n*-hexadecane seed molecules were applied to 10 reaction pathways to produce 160 submechanisms. These included high and low temperature chemistry.

The important consideration in the design of pathways is that the products which are produced in the last step are the initial molecules of another submechanism. In general the REACTION pathways have been designed so that the final products have only one functional group: a simple radical, aldehyde, ketone and simple alkene or alkyne. There are pathways which involve these species or have them as initial molecules.

3.2.4.3 Generated Submechanisms and Base Submechanism

A generated mechanism from REACTION consists of all the generated submechanisms combined with a literature base mechanism. The “communication” between the mechanisms occurs between the product molecules of one mechanism and reacting molecules in another.

For the generated mechanisms the 2D graphical structure is known. Thus combining these mechanisms to one mechanism is straightforward, one needs only use graph isomorphism to decide if the molecules are the same or not. Consequently, one can determine whether the reactions are repeated also.

As outlined in Chap. 2, the species in a literature mechanism for numerical calculations are just labels. The 2D-graphical structure is not needed. However, to combine a literature mechanism with the generated mechanism a correspondence table with the species name in the literature mechanism and the 2D-graphical structure is needed. REACTION has a database of standard molecules with corresponding 2D graphical information. The correspondence table needs only give the literature species name that is associated with the REACTION database species name. If a generated reaction and literature reaction are the same, the literature reaction is chosen for the combined mechanism.

Given this correspondence table and the literature mechanism (in CHEMKIN format), a final combined mechanism can be created. A tool is provided by the REACTION system to facilitate the creation of the correspondence table. It essentially detects which molecules are not consumed in a forward reaction by the generated mechanisms. For the generated *n*-decane mechanism (Moreac et al.

2006), a literature mechanism based on Hoyermann et al. (2004) was used. This mechanism included essentially C_2 compounds (species with up to two carbon atoms) and was supplemented with additional reactions from the literature (see (Moreac et al. 2006)). The generated hexadecane mechanism was combined with the C_4 mechanism of Westbrook's *n*-hexadecane mechanism (Westbrook et al. 2009).

3.3 Concluding Summary

This chapter has drawn the main lines of automatic generation of combustion models, trying to enlighten some specificities of the four most advanced individual systems:

- MAMOX, with its particularly efficient extensive use of lumping,
- EXGAS, which is currently able to consider the widest range of reactive fuels and biofuels,
- RMG, with its unique rate-based “on-the-fly” screening of reaction and identification of chemically-activated reaction sub-networks,
- REACTION with its use of pathway.

Acknowledgments This work was made in the frame of COST Action CM0901. F. Battin-Leclerc thanks the European Commission (“Clean ICE” ERC Advanced Research Grant) for financial support.

References

- Allen JW, Goldsmith CF, Green WH (2012) Automatic estimation of pressure-dependent rate coefficients. *Phys Chem Chem Phys* 14:1131–1155
- Babai L, Luks EM (1983) Canonical labeling of graphs. In: Proceedings of the fifteenth annual ACM symposium on theory of computing. Presented at the STOC'83, Association of Computing Machines, New York, pp 171–183
- Balaban AT (1985) Applications of graph theory in chemistry. *J Chem Inf Comput Sci* 25:334–343
- Balaban AT (1995) Chemical graphs: looking back and glimpsing ahead. *J Chem Inf Comput Sci* 35:339–350
- Barbé P, Battin-Leclerc F, Côme GM (1995) Experimental and modelling study of methane and ethane oxidation between 773 and 1573 K. *J Chim Phys* 92:1666–1692
- Barnard JM (1993) Substructure searching methods: old and new. *J Chem Inf Comput Sci* 33:532–538
- Benson SW (1976) *Thermochemical kinetics*, 2nd edn. Wiley, New York
- Bhore N, Klein M, Bischoff K (1990) Species rank in reaction pathways—application of delplot analysis. *Chem Eng Sci* 45:2109–2116
- Biet J, Hakka MH, Warth V et al (2008) Experimental and modeling study of the low-temperature oxidation of large alkanes. *Energy Fuels* 22:2258–2269

- Blurock E (1990) Computer-aided synthesis design at Risc-Linz—automatic extraction and use of reaction classes. *J Chem Inf Comput Sci* 30:505–510
- Blurock E (1995) Reaction—system for modeling chemical-reactions. *J Chem Inf Comput Sci* 35:607–616
- Blurock ES (2004a) Detailed mechanism generation. 1. Generalized reactive properties as reaction class substructures. *J Chem Inf Comput Sci* 44:1336–1347
- Blurock ES (2004b) Detailed mechanism generation. 2. Aldehydes, ketones, and olefins. *J Chem Inf Comput Sci* 44:1348–1357
- Bounaceur R, Warth V, Sirjean B et al (2009) Influence of the position of the double bond on the autoignition of linear alkenes at low temperature. *Proc Combust Inst* 32:387–394
- Bozzelli JW, Chang AY, Dean AM (1997) Molecular density of states from estimated vapor phase heat capacities. *Int J Chem Kinet* 29:161–170
- Broadbelt LJ, Stark SM, Klein MT (1994) Computer generated pyrolysis modeling: on-the-fly generation of species, reactions, and rates. *Ind Eng Chem Res* 33:790–799
- Buda F, Bounaceur R, Warth V et al (2005) Progress towards an unified detailed kinetic model for the autoignition of alkanes from C₄ to C₁₀ between 600 and 1200 K. *Combust Flame* 142:170–186
- Buda F, Heyberger B, Fournet R et al (2006) Modeling of the gas-phase oxidation of cyclohexane. *Energ. Fuels* 20:1450–1459
- Chang AY, Bozzelli JW, Dean AM (2000) Kinetic analysis of complex chemical activation and unimolecular dissociation reactions using QRRK theory and the modified strong collision approximation. *Phys Chem Chem Phys* 2:1533–1568
- Chen WL (2006) Chemoinformatics: past, present, and future. *J Chem Inf Model* 46:2230–2255
- Côme GM, Muller C, Cunnin PY et al (1984) A linear chemical notation. *Comput Chem* 8:233–237
- Côme GM, Warth V, Glaude PA et al (1997) Computer-aided design of gas-phase oxidation mechanisms—application to the modeling of n-heptane and iso-octane oxidation. *Proc Combust Inst* 26:755–762
- Cord M, Sirjean B, Fournet R et al (2012) Improvement of the modeling of the low-temperature oxidation of n-butane: study of the primary reactions. *J Phys Chem A* 116:6142–6158
- Corey EJ, Wipke WT (1969) Computer-assisted design of complex organic syntheses. *Science* 166:178–192
- Cowart JS, Keck JC, Heywood JB et al (1991) Engine knock predictions using a fully-detailed and a reduced chemical kinetic mechanism. *Proc Combust Inst* 23:1055–1062
- Cox R, Cole J (1985) Chemical aspects of the autoignition of hydrocarbon-air mixtures. *Combust Flame* 60:109–123
- Curran HJ, Gaffuri P, Pitz WJ et al (1998) A comprehensive modeling study of n-heptane oxidation. *Combust Flame* 114:149–177
- Dalby A, Nourse JG, Hounshell WD et al (1992) Description of several chemical structure file formats used by computer programs developed at molecular design limited. *J Chem Inf Comput Sci* 32:244–255
- Dente M, Ranzi E, Goossens AG (1979) Detailed prediction of olefin yields from hydrocarbon pyrolysis through a fundamental simulation model (SPYRO). *Comput Chem Eng* 3:61–75
- Dente M, Pierucci S, Ranzi E et al (1992) New improvements in modeling kinetic schemes for hydrocarbons pyrolysis reactors. *Chem Eng Sci* 47:2629–2634
- Dugundji PDJ, Ugi PDI (1973) An algebraic model of constitutional chemistry as a basis for chemical computer programs. *Computers in Chemistry, Fortschritte Der Chemischen Forschung*. Springer, Berlin, pp 19–64
- Engel T (2006) Basic overview of chemoinformatics. *J Chem Inf Model* 46:2267–2277
- Engel T, Gasteiger J (2002) Chemical structure representation for information exchange. *Online Inf Rev* 26:139
- Gillespie RJ, Robinson EA (2007) Gilbert N. Lewis and the chemical bond: the electron pair and the octet rule from 1916 to the present day. *J Comput Chem* 28:87–97

- Glaude PA, Battin-Leclerc F, Fournet R et al (2000) Construction and simplification of a model of the oxidation of alkanes. *Combust Flame* 122:451–462
- Glaude PA, Herbinet O, Bax S et al (2010) Modeling of the oxidation of methyl esters-validation for methyl hexanoate, methyl heptanoate, and methyl decanoate in a jet-stirred reactor. *Combust Flame* 157:2035–2050
- Green WH (2007) Predictive kinetics: a new approach for the 21st century. In: Marin GB (ed) *Advances in chemical engineering*. Academic Press, Dordrecht, pp 1–313
- Green WH, Barton PI, Bhattacharjee B et al (2001) Computer construction of detailed chemical kinetic models for gas-phase reactors. *Ind Eng Chem Res* 40:5362–5370
- Grenda JM, Androulakis IP, Dean AM et al (2003) Application of computational kinetic mechanism generation to model the autocatalytic pyrolysis of methane. *Ind Eng Chem Res* 42:1000–1010
- Gueniche HA, Biet J, Glaude PA et al (2009) A comparative study of the formation of aromatics in rich methane flames doped by unsaturated compounds. *Fuel* 88:1388–1393
- Hakka MH, Bennadji H, Biet J et al (2010) Oxidation of methyl and ethyl butanoates. *Int J Chem Kinet* 42:226–252
- Halstead MP, Kirsch LJ, Prothero A et al (1975) A mathematical model for hydrocarbon autoignition at high pressures. *Proc Roy Soc A Math* 346:515–538
- Harper MR, Van Geem KM, Pyl SP et al (2011) Comprehensive reaction mechanism for n-butanol pyrolysis and combustion. *Combust Flame* 158:16–41
- Herbinet O, Biet J, Hakka MH et al (2011) Modeling study of the low-temperature oxidation of large methyl esters from C11 to C19. *Proc Combust Inst* 33:391–398
- Herbinet O, Husson B, Serinyel Z et al (2012) Experimental and modeling investigation of the low-temperature oxidation of n-heptane. *Combust Flame* 159:3455–3471
- Heyberger B, Battin-Leclerc F, Warth et al (2001) Comprehensive mechanism for the gas-phase oxidation of propene. *Combust Flame* 126:1780–1802
- Homer RW, Swanson J, Jilek RJ et al (2008) SYBYL line Notation (SLN): a single notation to represent chemical structures, queries, reactions, and virtual libraries. *J Chem Inf Model* 48:2294–2307
- Hoyermann K, Mauß F, Zeuch T (2004) A detailed chemical reaction mechanism for the oxidation of hydrocarbons and its application to the analysis of benzene formation in fuel-rich premixed laminar acetylene and propene. *Phys Chem Chem Phys* 6:3824
- Hu H, Keck J (1987) Autoignition of adiabatically compressed combustible gas mixtures. *SAE International*. n° 872110, Warrendale
- Husson B, Ferrari M, Herbinet O et al (2013) New experimental evidence and modeling study of the ethylbenzene oxidation. *Proc Combust Inst* 34:325–333
- Jalan A, West RH, Green WH (2013) An extensible framework for capturing solvent effects in computer generated kinetic models. *J Phys Chem B* 117:2955–2970
- Kee RJ, Rupley FM, Miller JA (1993) Chemkin II. A fortran chemical kinetics package for the analysis of a gas-phase chemical kinetics. Sandia Laboratories Report, SAND 89-8009B
- Lewis GN (1916) The atom and the molecule. *J Am Chem Soc* 38:762–785
- Magoon GR, Green WH (2013) Design and implementation of a next-generation software interface for on-the-fly quantum and force field calculations in automated reaction mechanism generation. *Comput Chem Eng* 52:35–45
- Matheu DM (2002) Integrated pressure-dependence in automated mechanism generation: a new tool for building gas-phase kinetic models. Ph.D. thesis, Massachusetts Institute of Technology. Department of Chemical Engineering
- Matheu DM, Lada TA, Green WH et al (2001) Rate-based screening of pressure-dependent reaction networks. *Comput Phys Commun* 138:237–249
- Matheu DM, Dean AM, Grenda JM et al (2003) Mechanism generation with integrated pressure dependence: a new model for methane pyrolysis. *J Phys Chem A* 107:8552–8565
- Miller JA, Klippenstein SJ (2012) Comment on automatic estimation of pressure-dependent rate coefficients (Allen JW, Goldsmith CF, Green WH *Phys Chem Chem Phys* 14:1131–1155 (2011)). *Phys Chem Chem Phys* 14:843–8433

- Moreac G, Blurock ES, Mauss F (2006) Automatic generation of a detailed mechanism for the oxidation of *n*-decane. *Combust Sci Technol* 178:2025–2038
- Morgan HL (1965) The generation of a unique machine description for chemical structures—a technique developed at chemical abstracts service. *J Chem Doc* 5:107–113
- Moss JT, Berkowitz AM, Oehlschlaeger MA et al (2008) An experimental and kinetic modeling study of the oxidation of the four isomers of butanol. *J Phys Chem A* 112:10843–10855
- Muller C, Michel V, Scacchi G et al (1995) A computer program for the evaluation of thermochemical data of molecules and free radicals in the gas phase. *J Chim Phys* 92:1154–1177
- Murray-Rust P, Rzepa HS (1999) Chemical Markup, XML, and the worldwide web. 1. Basic principles. *J Chem Inf Comput Sci* 39:928–942
- Nilsson NJ (1982) Principles of artificial intelligence. Birkhäuser, Basel
- Pousse E, Porter R, Warth V et al (2010) Lean methane premixed laminar flames doped by components of diesel fuel II: *n*-propylcyclohexane. *Combust Flame* 157:75–90
- Ranzi E, Faravelli T, Gaffuri P et al (1995a) Low-temperature combustion: automatic generation of primary oxidation reactions and lumping procedures. *Combust Flame* 102:179–192
- Ranzi E, Gaffuri P, Faravelli T et al (1995b) A wide-range modeling study of *n*-heptane oxidation. *Combust Flame* 103:91–106
- Ranzi E, Frassoldati A, Granata S et al (2005) Wide-range kinetic modeling study of the pyrolysis, partial oxidation, and combustion of heavy *n*-alkanes. *Ind Eng Chem Res* 44:5170–5183
- Ratkiewicz A, Truong TN (2006) Automated mechanism generation: from symbolic calculation to complex chemistry. *Int J Quantum Chem* 106:244–255
- Sarathy SM, Westbrook CK, Mehl M et al (2011) Comprehensive chemical kinetic modeling of the oxidation of 2-methylalkanes from C7 to C20. *Combust Flame* 158:2338–2357
- Sirjean B, Buda F, Hakka H et al (2007) The autoignition of cyclopentane and cyclohexane in a shock tube. *Proc Combust Inst* 31:277–284
- Smith EG, Wiswesser WJ, Addelston A (1968) The Wiswesser line-formula chemical notation. McGraw-Hill, New York
- Song J, Sumathi R, Yu J et al (2004) Next generation model construction software, and new approaches to estimating rates and thermochemistry for combustion. *Abstr Pap Am Chem Soc* 228:U233
- Spialter L (1963) The atom connectivity matrix (ACM) and its characteristic polynomial (ACMCP): a new computer-oriented chemical nomenclature. *J Am Chem Soc* 85:2012–2013
- Spialter L (1964) The atom connectivity matrix characteristic polynomial (ACMCP) and its physico-geometric (topological) significance. *J Chem Doc* 4:269–274
- Stein S, Heller S, Tchekhovski D (2003) An open standard for chemical structure representation—the IUPAC chemical identifier. In: Proceedings of the 9th international chemical information conference, pp 131–143
- Susnow RG, Dean AM, Green WH et al (1997) Rate-based construction of kinetic models for complex systems. *J Phys Chem A* 101:3731–3740
- Touchard S, Fournet R, Glaude PA et al (2005) Modeling of the oxidation of large alkenes at low temperature. *Proc Combust Inst* 30:1073–1081
- Troe J (1974) Fall-off curves of unimolecular reaction. *Ber Bunsenges Phys Chem* 78:478–488
- Ugi I, Wochner M (1988) Molecular logic and computer assistance in chemistry. *J Mol Struct THEOCHEM* 165:229–242
- Ullmann JR (1976) An algorithm for subgraph isomorphism. *J ACM* 23:31–42
- Van Geem KM, Reyniers MF, Marin GB et al (2006) Automatic reaction network generation using RMG for steam cracking of *n*-hexane. *AIChE J* 52:718–730
- Warr WA (2011) Representation of chemical structures. *Wiley Interdisc Rev Comput Mol Sci* 1:557–579
- Warth V, Stef N, Glaude PA et al (1998) Computed aided design of gas-phase oxidation mechanisms: application to the modelling of normal-butane oxidation. *Combust Flame* 114:81–102

- Warth V, Battin-Leclerc F, Fournet R et al (2000) Computer based generation of reaction mechanisms for gas-phase oxidation. *Comput Chem* 92:1666–1692
- Weininger D (1988) SMILES, a chemical language and information system. 1. Introduction to methodology and encoding rules. *J Chem Inf Comput Sci* 28:31–36
- Weininger D, Weininger A, Weininger JL (1989) SMILES. 2. Algorithm for generation of unique SMILES notation. *J Chem Inf Comput Sci* 29:97–101
- Westbrook C, Pitz W, Herbinet O et al (2009) A comprehensive detailed chemical kinetic reaction mechanism for combustion of n-alkane hydrocarbons from n-octane to n-hexadecane. *Combust Flame* 156:181–199
- Willett P (2008) From chemical documentation to chemoinformatics: 50 years of chemical information science. *J Inf Sci* 34:477–499
- Wipke WT, Howe WJ (eds) (1977) Computer assisted organic synthesis. ACS symposium series 61. American Chemical Society, Washington, DC
- Wiswesser WJ (1982) How the WLN began in 1949 and how it might be in 1999. *J Chem Inf Comput Sci* 22:88–93
- Wiswesser WJ (1985) Historic development of chemical notations. *J Chem Inf Mod* 25:258–263

Chapter 4

Specificities Related to Detailed Kinetic Models for the Combustion of Oxygenated Fuels Components

Frédérique Battin-Leclerc, Henry Curran, Tiziana Faravelli
and Pierre A. Glaude

Abstract This article presents the specific classes of reactions considered for modeling the oxidation of the two types of oxygenated molecules which are the most usually considered in biofuels: alcohols and esters. Using models for hydrocarbon oxidation as a reference, this paper also reports the major changes to be considered for the kinetic data of the main reaction classes which are the same as those taken into account for non-oxygenated reactants. Details are given in the case of hydrogen atom abstractions, radical decompositions by β -scission, RO_2 -radical chemistry, with especially intramolecular isomerizations, and reactions leading to unsaturated products and HO_2 radicals.

4.1 Introduction

Several reviews (Kohse-Höinghaus et al. 2010; Komninos and Rakopoulos 2012; Lai et al. 2011; Tran et al. 2012) have previously given an overview of the chemistry and the kinetic models related to the combustion of oxygenated

F. Battin-Leclerc (✉) · P. A. Glaude
Laboratoire Réactions et Génie des Procédés, CNRS, Université de Lorraine,
ENSIC, 1 rue grandville, 54000 Nancy, France
e-mail: frederique.battin-leclerc@univ-lorraine.fr

P. A. Glaude
e-mail: pierre-alexandre.glaude@univ-lorraine.fr

H. Curran
Combustion Chemistry Centre, National University of Ireland, Galway,
University Road, Galway, Ireland
e-mail: henry.curran@nuigalway.ie

T. Faravelli
Dipartimento di Chimica, Materiali e Ingegneria Chimica, Politecnico di Milano,
Piazza L. da Vinci, 32 20133 Milan, Italy
e-mail: tiziano.faravelli@polimi.it

molecules, which are considered as potential additives of fuels. This chapter does not present a comprehensive list of all of the studies performed on these compounds, but provides only a sample of the kinetic models of interest. As described in [Chap. 1](#) of this book, two main families of oxygenated reactant are considered as fuel additives: alcohols in gasoline and methyl esters in diesel fuels.

The family of molecules for which the largest number of models has been proposed is alcohols (see for example: Marinov [1999](#); Saxena and Williams [2007](#); Frassoldati et al. [2010](#); Cancino et al. [2010](#); Leplat et al. [2011](#); Togbé et al. [2011](#); Lee et al. [2012](#); Yeung and Thomson [2013](#)). Amongst these, many recent studies concern the high temperature reaction of isomers of butanol (e.g., Moss et al. [2008](#); Dagaut et al. [2009](#); Black et al. [2010](#); Grana et al. [2010](#); Harper et al. [2011](#); Karwat et al. [2011](#); Frassoldati et al. [2012](#); Sarathy et al. [2012](#); Yasunaga et al. [2012](#); Cai et al. [2012](#)). In the case of ethanol, the role of the peroxy chemistry can be neglected, as shown by the complete lack of a negative temperature coefficient behavior observed in a rapid compression machine even at the highest investigated pressures of 85 bar (Lee et al. [2012](#)). There have only been a few studies concerning the low temperature (the temperature zone corresponding to cool flame occurrence, see [Chap. 2](#)) oxidation of larger alcohols (e.g., Vranckx et al. [2011](#) for *n*-butanol, Sarathy et al. [2012](#) for isomers of butanol, Heufer et al. [2012](#) for *I*-pentanol, Tsujimura et al. [2012](#) for *iso*-pentanol, Togbé et al. [2010](#) for *I*-hexanol, Heufer et al. [2013](#) for *I*-pentanol and *I*-hexanol), with the papers of Sarathy et al. ([2012](#)) and Tsujimura et al. ([2012](#)) being very detailed about the reaction classes and the kinetic data specific to alcohols. Note also that experimental studies on the low-temperature reactions (550–700 K) of the hydroxyalkyl radicals derived from some C₂–C₅ alcohols have been performed using multiplexed time-resolved tunable synchrotron photoionization mass spectrometry after pulsed laser photolysis (Zádor et al. [2009](#); Welz et al. [2012](#), [2013a](#)).

A significant number of models have also been published describing the combustion of methyl esters, with many studies reporting on methyl butanoate (e.g., Fisher et al. [2000](#); Gail et al. [2008](#); Dooley et al. [2008](#); Walton et al. [2009](#); Hakka et al. [2010](#); Grana et al. [2012a](#); Farooq et al. [2012](#)), even if its small size prevents it from having a chemistry representative of the large molecules present in biodiesel. A fair number of models have also been written for methyl esters of intermediate size, from C₇ to C₁₀ (e.g., Dayma et al. [2009](#); Herbinet et al. [2008](#); Glaude et al. [2010](#); Herbinet et al. [2011a](#); Grana et al. [2012b](#); Diévert et al. [2012](#)). However, molecules produced from vegetable oils are methyl esters with a long carbon chain such as methyl palmitate (C₁₇H₃₄O₂) and methyl stearate (C₁₉H₃₈O₂) and models concerning these large compounds are still scarce (Herbinet et al. [2011b](#); Westbrook et al. [2011](#); Naik et al. [2011](#); Saggese et al. [2013](#)) with a lack of experimental data to validate them (Tran et al. [2012](#)). While mono-unsaturated and di-unsaturated esters, such as methyl oleate (C₁₉H₃₆O₂) and methyl linoleate (C₁₉H₃₆O₂), are the most abundant esters in biodiesel, very few studies are interested in their oxidation (Herbinet et al. [2010](#); Bennadji et al. [2011](#); Westbrook et al. [2011](#); Saggese et al. [2013](#); Yang et al. [2013](#)).

Note that the development of numerous models for oxygenated fuels (e.g., those for the butanol isomers by Sarathy et al. ([2012](#)), that for *iso*-pentanol by Tsujimura

et al. (2012) or that for methyl decanoate by Herbinet et al. (2008)) is based on the reaction classes proposed by Curran et al. (1998) for alkanes (see Chap. 2). In addition several models for alcohols (e.g., those proposed by Moss et al. 2008 and Harper et al. 2011) and methyl esters (e.g., those proposed by Glaude et al. 2010; Herbinet et al. 2011a, b; Grana et al. 2012b) have been written using the automatic generation software described in Chap. 3.

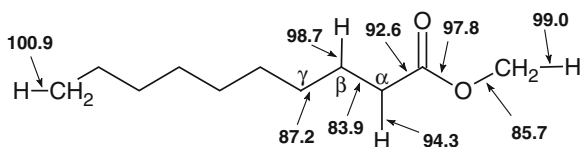
While they will not be the subject of this chapter, it should be mentioned that a large number of models have also been published concerning the combustion of acyclic saturated ethers, such as dimethyl ether (e.g., Curran et al. 2000; Zhao et al. 2008) and methyl-*tert*-butyl ether (e.g., Goldaniga et al. 1998; Glaude et al. 2000; Yasunaga et al. 2011). These models use kinetic data closely derived from those proposed for alkanes. Due to their possible use as biofuels (Román-Leshkov et al. 2007), a recent interest has arisen in modeling the oxidation of cyclic unsaturated ethers, such as furan (Tian et al. 2011), 2-methylfuran (Somers et al. 2013) and 2,5-dimethyl furan (Sirjean et al. 2013). The reactions of these unsaturated ethers are very specific to this type of molecule and cannot be described in a generic way.

The specificities due to the presence of a double bond in unsaturated esters are more related to the chemistry of alkenes (see e.g., Bounaceur et al. 2009 or Mehl et al. 2008) than to the chemistry of oxygenated molecules and will therefore not be described here. The aim of this chapter is to present the specific classes of reactions and kinetic parameters which are considered in the primary mechanism (as defined in Chap. 2) of the oxidation of saturated alcohols and methyl esters. These specificities will be mainly described in light of the knowledge gained in the modeling of reactions of the isomers of butanol and methyl decanoate, respectively.

The presence of the oxygen atoms in an alcohol or ester molecule involves a difference in the bond dissociation energies (BDEs) compared to those observed in hydrocarbon molecules. In the case of esters, the BDEs of the C–H, C–O, and C–C bonds close to the ester functional group were calculated by El-Nahas et al. (2007) for C₃–C₄ esters. Figure 4.1 presents the BDEs of methyl decanoate calculated using THERGAS (Muller et al. 1995) taking into account these newly published values (El-Nahas et al. 2007). Figure 4.1 shows that the C–C and C–H bonds which are the easiest to break are those connected to the C-atom in the α -position, i.e., the bonds closest to the ester functional group.

Only two specific reaction classes can be found in the primary mechanism of alcohols: molecular dehydrations and dehydrogenation reactions. Note that in the secondary mechanism of alcohols, the enol-keto isomerization reactions assisted by radicals and formic acid was found to be a new reaction class important in

Fig. 4.1 Bond dissociation energies (in kcal mol⁻¹) in methyl decanoate. Letters correspond to site identification



converting enols to aldehydes or ketones (Sarathy et al. 2012), but is not described here. For methyl esters, all of the reaction classes are the same as those used to model alkanes. However, while most of the reaction classes used to model oxygenated fuels can be directly derived from the models written for alkanes (H-atom abstractions, fuel radical β -scission decompositions, fuel radical reactions with O_2 , intra-molecular isomerization reactions, etc.), some changes in the kinetic parameters have to be taken into account and are discussed below. The changes in the rates constants of unimolecular initiation reactions mainly reflect changes in BDEs and are not detailed here.

4.2 Molecular Dehydrations and Dehydrogenations of Alcohols

Intra-molecular dehydration, leading to the formation of water and an alkene molecule via a kinetically favored four-centered cyclic transition state ring, is an important reaction class for alcohols. Note that if we consider isomers of butanol, there is one possible intra-molecular dehydration reaction for *1*-butanol, *iso*-butanol and *tert*-butanol, and two for 2-butanol (see Fig. 4.2).

Few kinetic parameters have been published concerning these reactions (e.g., Bui et al. 2002; Tsang 2004; Rosado-Reyes and Tsang 2012a (*1*-butanol); Rosado-Reyes and Tsang 2012b (2-butanol)), with activation energies in the range 62–69 kcal mol^{-1} . Disagreements can be observed between the proposed rate constants, which have been shown to be sensitive parameters in modeling shock tube ignitions delay times (Moss et al. 2008). Grana et al. (2010) have proposed a general rule for estimating the high-pressure limit rate constant for this class of reaction, using as a

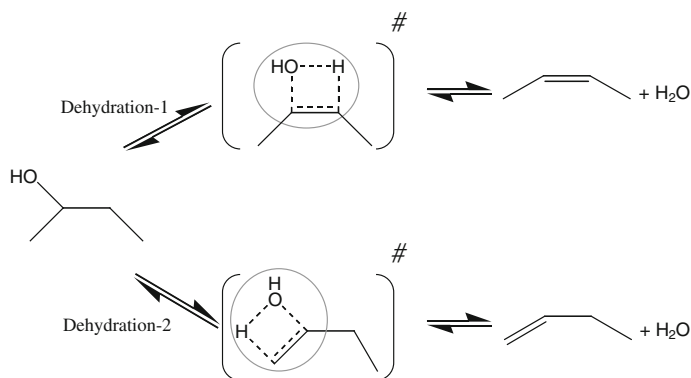


Fig. 4.2 Intramolecular dehydration reactions for 2-butanol

reference reaction the dehydration involving a primary OH group¹ and a single reference primary H-atom² with a rate constant of $k_{\text{Dehydration-ref}} = 5.0 \times 10^{13} \exp(-34,500/T) \text{ s}^{-1}$. The rate constants for the other reactions of the same class are obtained by taking the number of H-atoms which can be transferred for the A-factor into account and also considering a correction in the activation energy reflecting the type of H-atom and OH group involved in the transition state: a reduction of 1 and 3 kcal mol⁻¹ is considered for a secondary and tertiary H-atoms, respectively, and a reduction of 1.5 and 3.5 kcal mol⁻¹ is taken into account for secondary and tertiary OH group, respectively. Using this rule, $k_{\text{Dehydration-1}} = 1.0 \times 10^{14} \exp(-33,300/T) \text{ s}^{-1}$ and $k_{\text{Dehydration-2}} = 1.0 \times 10^{14} \exp(-33,800/T) \text{ s}^{-1}$. Note also that as for unimolecular initiations, Yasunaga et al. (2012) have proposed pressure-dependent rate constants fitted using the Troe formalism.

Grana et al. (2010) also considered dehydrogenation as another class of four-centered elimination reaction. Through this class of reaction, *I*-butanol yields *I*-butanal, 2-butanol produces methylethylketone, and *iso*-butanol gives *iso*-butanal. In the case of 2-butanol, $k_{\text{Dehydrogenation}} = 5.0 \times 10^{13} \exp(-35,000/T) \text{ s}^{-1}$ according to Grana et al. (2010).

Note that in the case of esters, theoretical studies of several types of molecular reactions have been performed (El-Nahas et al. 2007), but no easy decomposition appeared in the case of methyl esters. The only one having an impact on detailed kinetic modeling is the formation of ethylene and acid from ethyl esters via a favorable six-centered cyclic transition state.

4.3 Hydrogen Atom Abstractions

The hydrogen atom abstractions (H-abstractions) by atoms (i.e., ·H, ·O·) and small radicals (i.e., ·OH, ·CH₃, ·HO₂) are usually the most important channels for the fuel consumption. H-abstractions by O₂ are also possible. In the case of hydrocarbons, the rate constants of these reactions depend of the type of alkyl H-atoms which can be abstracted: primary, secondary, or tertiary. The abstraction of a primary H-atom is the most difficult, and that of a tertiary one is the easiest. In oxygenated reactants, more types of H-atoms have to be considered.

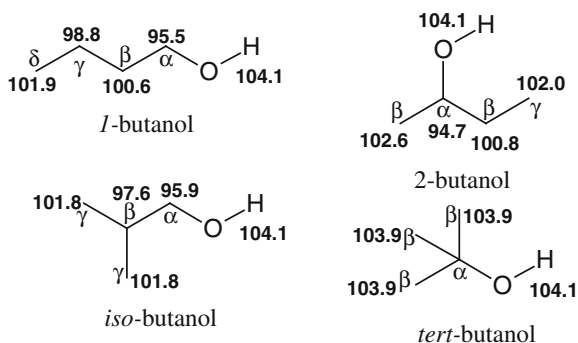
Figure 4.3 displays the C–H BDEs for the four isomers of butanol and shows that different values are obtained depending on the position of the C-atom in the molecule, with the lowest value being obtained for the αC–H bond.

These differences in BDEs result in differences in rate constants and consequently in differences in the selectivity of the primary radicals obtained by H-abstractions. To illustrate this, Fig. 4.4 presents the selectivity of C₄H₉O radicals obtained from *I*-butanol by H-abstraction with ·OH radicals as calculated by

¹ Primary OH group: –CH₂–OH, secondary: –CH–OH, tertiary: –C–OH.

² Primary H-atom: –CH₂–H, secondary: –CH–H, tertiary: –C–H.

Fig. 4.3 C–H bond dissociation energies (in kcal mol⁻¹) for the four isomers of butanol (the values are taken from Sarathy et al. 2012). Letters correspond to site identification



Frassoldati et al. (2012). The abstraction from the α C-atom is clearly the most favored. A similar result has been found for the abstraction by \cdot H atoms (Frassoldati et al. 2012).

Note that the BDE of the C–H bonds associated with the carbon atom in the α -position in an alcohol (from 94.7 to 95.9 kcal mol⁻¹ as shown in Fig. 4.3) or just neighboring an ester functional group (94.3 kcal mol⁻¹ (Fig. 4.1)) is close to that of a tertiary carbon atom (e.g., 95.7 kcal mol⁻¹) in isobutene (Luo 2003). Also, as shown in Fig. 4.3, the BDE of the O–H bond in alcohols is close to the BDE of the C–H bond in a primary carbon atom. This similarity has been used as a first approximation to derive rate constants for H-abstractions in oxygenated fuels by comparison to those used in alkanes (e.g., Grana et al. 2010 and Moss et al. 2008 for alcohols, Herbinet et al. 2008 for esters). In a second approximation, the changes induced in rate constants by the difference in C–H BDEs can be estimated using an Evans–Polanyi type correlation, such as that developed for the abstraction of H-atoms from hydrocarbons by Dean and Bozzelli (2000). This method has been implemented in automatic generation software such as EXGAS (Moss et al. 2008 for alcohols, Glaude et al. 2010 for esters) or used by Tsujimura et al. (2012) in their model of *iso*-pentanol. More details about automatic generation software

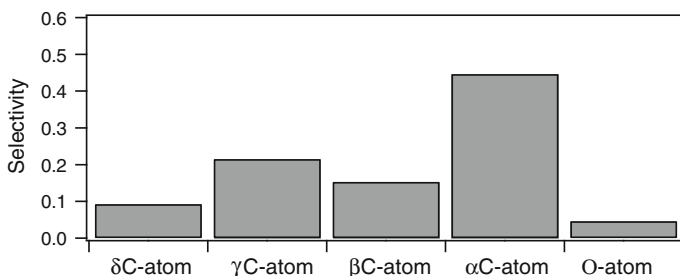


Fig. 4.4 Selectivity at 1000 K of the C₄H₉O radicals obtained from *1*-butanol by H-abstraction with \cdot OH radicals as calculated by Frassoldati et al. (2012)

are given in [Chap. 3](#). In the method of Dean and Bozzelli (2000), the rate constant for the H-abstraction is estimated as:

$$k = n_{\text{H}} A T^n \exp(-\{E_0 - f(\Delta H_0 - \Delta H)\}/RT) \quad (4.1)$$

where n_{H} is the number of abstractable H-atoms; A , n , and E_0 are the rate parameters for the case of a metathesis by the considered radical from ethane; ΔH_0 is the enthalpy of the metathesis by the considered radical from ethane; ΔH is the enthalpy of the metathesis by the considered radical from the reacting molecule; f is a correlation factor, the values of which are given by Dean and Bozzelli (2000) for each radical considered; and R is the gas constant.

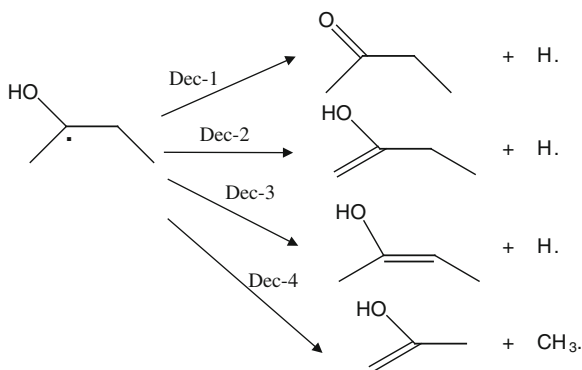
As discussed by Sarathy et al. (2012), in the case of the abstractions by $\cdot\text{OH}$ radicals, which in most cases is the dominant abstracting radical, more accurate rate constants can be derived from recent experimental measurements (e.g., Vasu et al. 2010 for *I*-butanol, Pang et al. 2012 for 2-butanol) and theoretical calculation (e.g., Zhou et al. 2011 for *I*-butanol). Zhou et al. (2011) have found that, in considering abstraction by oxygenated radicals such as $\cdot\text{OH}$ and $\text{HO}_2\cdot$ from oxygenated molecules, it is not accurate to assume similarity with abstraction from alkanes, as hydrogen bonding between the radical and the molecule in the transition state generally lowers the activation energy for abstraction but also ties up a rotor in the molecule. Thus rate constants for abstraction from alcohols by hydroxyl (Zhou et al. 2011) and hydroperoxyl radicals (Zhou et al. 2012) have been shown to be generally faster at lower temperature (due to the decrease in activation energy for abstraction) but slower at higher temperature (due to the decrease in entropy change) compared to alkanes.

4.4 Radical Decompositions by β -Scission

At temperature above 800 K, decomposition via β -scission reactions are the major consumption pathways for radicals produced from fuel molecules via H-atom abstraction. The presence of oxygen atoms in the radicals produced from alcohols and esters can have a significant impact on the values of the activation energies of this reaction class.

In the case of alcohols, radicals produced by H-atom abstractions are alkoxy and hydroxyalkyl radicals. The rate constants for the decompositions of alkoxy radicals have been studied by Rauk et al. (2003). The reactions of hydroxyalkyl radicals are not fully specific to alcohols as these radicals can also be formed from alkenes by the addition of $\cdot\text{OH}$ radicals to the double bond, with subsequent isomerizations allowing for the production of a number of possible isomers in large alkenes (Touchard et al. 2005). Figure 4.5 presents the possible decompositions via β -scission of the hydroxybutyl radical obtained from 2-butanol produced by H-abstraction from the carbon atom at the α -position. Figure 4.5 shows that decompositions by β -scission can be a source of enols, products first reported

Fig. 4.5 Decompositions by β -scission from the hydroxybutyl radical obtained from 2-butanol by H-abstraction from the carbon atom in α -position



by Taatjes et al. (2005) and most recently experimentally observed in a laminar premixed flame (Sarathy et al. 2012).

In the mechanism of Yasunaga et al. (2012), the rate constants for decompositions by β -scission are given for the reverse reactions: the value for the addition of a \cdot H atom to acetaldehyde is used for $k_{\text{Dec-1}}$, one close to that for the addition of a \cdot H atom to propene is assumed for $k_{\text{Dec-2}}$ and $k_{\text{Dec-3}}$, and that for the addition of a methyl radical to propene is considered for $k_{\text{Dec-4}}$. In the case of the hydroxybutyl radicals obtained by H-abstraction from a carbon atom in the β -position, breaking of C–O bonds is also possible with rate constants for the reverse reactions derived from those of the addition of an \cdot OH radical to butenes according to Yasunaga et al. (2012). This last channel is the main pathway for the formation of butenes at their peak locations in low-pressure laminar premixed flames of the four butanol isomers according to Sarathy et al. (2012). In the EXGAS software (Moss et al. 2008), the activation energies for these reactions were evaluated using Evans-Polanyi correlations not detailed here.

Decompositions by β -scission are also considered in the case of methyl esters and the breaking of C–C bonds is a source of unsaturated esters, products experimentally observed in a jet-stirred reactor (Herbinet et al. 2011a). Table 4.1 shows a summary of the activation energies, which are used in the EXGAS software for the decompositions by β -scission involving the breaking of a C–C, a C–O, or a C–H bond in radicals deriving from methyl esters.

4.5 RO₂· Radical Chemistry: Intramolecular Isomerizations

At temperature below 800 K, the radicals obtained from the fuel molecules by H-abstractions react mostly by addition to oxygen molecules to form peroxy radicals (RO₂·). The rate constants of these additions for alcohols and methyl esters are mostly derived from those used for alkyl radicals.

Table 4.1 Activation energies used for the decompositions by β -scission of oxygenated radicals involved in the oxidation of methyl esters (/ stands for a simple bond and // for a double bond)

Types of reaction	E_a (kcal mol ⁻¹)
$R/C(//O)/O^\bullet \rightarrow R^\bullet + CO_2^a$	5.1
$R/C(//O)/O/CH_2^\bullet \rightarrow R/C^\bullet//O + CH_2//O^a$	31.9
$R/CH^\bullet/C(//O)/O/CH_3 \rightarrow R/CH//C//O + CH_3O^\bullet{}^b$	49.0
$R/CH^\bullet/CH_2/C(//O)/O/CH_3 \rightarrow R/CH//CH_2 + CH_3O/C^\bullet//O^b$	30.7
$R/CH_2/C^\bullet//O \rightarrow R^\bullet + CH_2//C//O^c$	39.9
$R/CH^\bullet/CH_2/C(//O)/O/CH_3 \rightarrow H^\bullet + R/CH//CH/C(//O)/O/CH_3^b$	34.9

These values were calculated using quantum calculations performed at the CBS-QB3 level of theory (Glaude et al. 2010)

^a The calculation has been performed for $R^\bullet = CH_3^\bullet$

^b The calculation has been performed for $R^\bullet = H^\bullet$

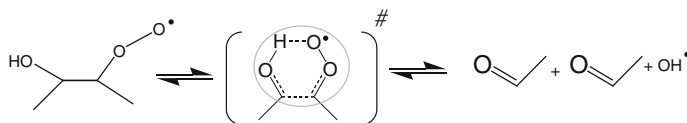
^c The calculation has been performed for $R^\bullet = C_2H_5^\bullet$

Intra-molecular isomerizations involving the transfer of a H-atom through a cyclic transition state are important reactions of alkyl and peroxy-alkyl radicals in the oxidation of hydrocarbons. The rate constants of the isomerizations of peroxy-alkyl radicals have been shown to be particularly sensitive parameters during the low-temperature oxidation of alkanes (Buda et al. 2005). These reactions also need to be considered in the case of oxygenated reactants.

As already reported in the case of alkenes (Stark and Waddington 1995) and as experimentally proven in the case of alcohols (e.g., Welz et al. 2013a), the isomerizations of hydroxyl-alkylperoxy radicals deriving from hydroxyl-alkyl radicals obtained by H-abstraction from a carbon atom in the β -position of an alcohol functional group can occur through the mechanism shown in Fig. 4.6 for 2-butanol.

This reaction, via the so-called “Waddington mechanism,” leads to the formation of aldehydes or ketones and $\cdot OH$ radicals, as shown in Fig. 4.6 for a peroxy radical obtained from 2-butanol. Note that Sarathy et al. (2012) considered that the formation of *l*-hydroperoxyacetone and a methyl radical can be a minor channel of the reaction via the Waddington mechanism for 2-butanol.

The rates constants of the isomerizations of radicals obtained from butanols involving a transition state with five or six members have been calculated by Zheng and Truhlar (2010) using quantum chemistry methods. These values were used by Sarathy et al. (2012) in their models written to describe the oxidation of the butanol isomers.

**Fig. 4.6** Isomerization of 2-hydroxy-3-butylperoxy radicals according to the mechanism of Waddington (Stark and Waddington 1995)

For heavier reactants for which theoretical calculations are difficult to perform, the activation energy for an isomerization can be estimated as the sum of two contributions as proposed by Benson (1976): (i) the activation energy for H-atom abstraction from the molecule by analogous radicals and (ii) the strain energy involved in the cyclic transition state.

The rate constants of the peroxy radicals deriving from alcohols are mostly directly derived from those used for alkanes (e.g., Curran et al. 1998), with just a correction in the activation energy when the abstracted H-atom is carried by the carbon atom in the α -position: e.g., the same value is used as that for a reaction involving a tertiary H-atom (Sarathy et al. 2012) or $-3.3 \text{ kcal mol}^{-1}$ (Tsujimura et al. 2012). The rate constants used by Sarathy et al. (2012) for the reaction via the Waddington mechanism are mainly derived from a study by Sun et al. (2007).

As shown by Glaude et al. (2010), in the case of esters, some values had to be changed to take into account the influence of the ester group. The activation energy for the internal H-abstraction in the α -position from the ester functional has been taken equal to that for the abstraction of a tertiary H-atom in the case of alkanes (i.e., 9 kcal mol^{-1} for a tertiary H-atom in an alkyl radical and 14 kcal mol^{-1} for a tertiary H-atom in peroxy-alkyl radicals (Buda et al. 2005)).

The ring strain energy involved in the transition state of some reactions of isomerization, transferring a H-atom above the ester function, had also to be re-estimated. These isomerizations concern ester alkyl radicals and ester alkyl-peroxy radicals. The ring strain energies of the transition states involved in the isomerization of ester alkyl radicals were deduced from the enthalpy of formation of the corresponding lactones measured by Wiberg and Waldron (1991). Ring strain energies are 9, 11, 11.2, and $12.5 \text{ kcal mol}^{-1}$ for five-, six-, seven-, and eight-membered ring lactones, respectively. These values can be compared to those used for alkyl radicals deriving from alkanes, i.e., 6.3, 1.0, 6.4, and $9.9 \text{ kcal mol}^{-1}$ for five-, six-, seven-, and eight-membered rings, respectively (Buda et al. 2005). The ring strain energies of the transition states involved in the isomerization of alkyl radicals obtained from esters are significantly higher than those obtained in the case of alkanes making the related isomerizations more difficult.

Some isomerizations of peroxy-alkyl radicals, shifting a H-atom above the ester function, involve cyclic transition states, which contain three oxygen atoms. This kind of isomerizations occurs via seven- and eight-membered rings as shown in Fig. 4.7. Two configurations are possible according to the position of the peroxy group: either the peroxy group is on the alkyl chain with the shifted H-atom on the methyl group of the ester function, or the peroxy group is on the methyl part of the ester function with the shifted H-atom on a carbon atom from the alkyl chain. Note that according to theoretical calculations (Glaude et al. 2010), the presence of the third oxygen atom in the ring together with the carbonyl group significantly increases the ring strain energy of the transition state involved: the calculated strain energies in Fig. 4.7 range from 7.7 to $13.6 \text{ kcal mol}^{-1}$, while the strain energy for two oxygen cyclic transition states are taken to be 5 kcal mol^{-1} for seven-membered rings and 4 kcal mol^{-1} for eight-membered rings. This dictates

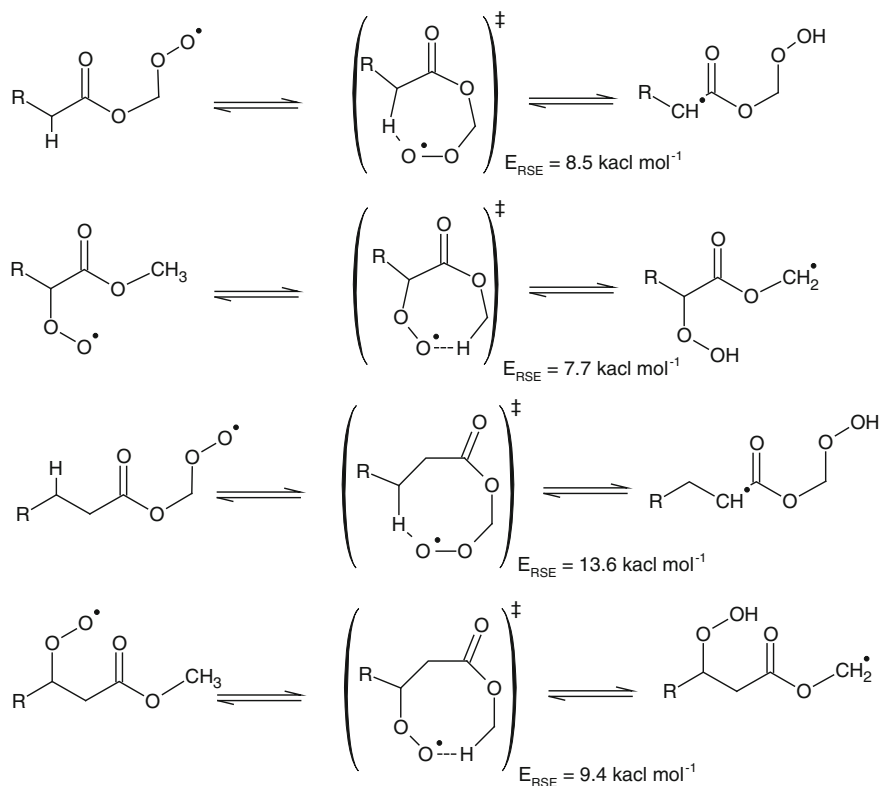
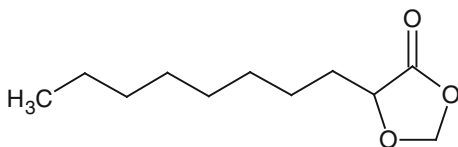


Fig. 4.7 Intramolecular isomerization involving transition states including seven and eight membered rings which contain three oxygen atoms, and related ring strain energies (E_{RSE}) of the involved transition states (adapted from Glaude et al. (2010)). These values were calculated using quantum calculations performed at the CBS-QB3 level of theory (Glaude et al. 2010)

that isomerizations of peroxyalkyl radicals in esters are more difficult compared to those for alkanes.

In the oxidation mechanism of alkanes, the hydroperoxy-alkyl radicals (QOOH \cdot) obtained by intra-molecular isomerization from RO $_2\cdot$ radicals react mainly via a second addition to molecular oxygen or by decomposition reactions yielding cyclic ethers and $\cdot\text{OH}$ radicals. While in the cases of alcohols, only the model of Tsujimura et al. (2012) for *iso*-pentanol considers the formation of an hydroxy cyclic ether, cyclic ethers with an ester function are common products in the oxidation of long-chained methyl esters. For instance, seven different C $_{11}$ H $_{20}$ O $_3$ methyl esters including a furan ring have been observed during the oxidation of methyl decanoate in a jet-stirred reactor (Glaude et al. 2010), amongst them a compound with the ester function included in the ring as shown in Fig. 4.8. The rate constant used for the formation of cyclic ethers from alcohols and ethers are directly derived from those used in the case of alkanes. This is also mostly the

Fig. 4.8 Cyclic ether with the ester function included in the ring (3-octyl,1,4-dioxola-2-one) as analyzed during the methyl decanoate oxidation in a jet-stirred reactor (Glaude et al. 2010)



case for the kinetic parameters used for the addition of QOOH· radicals to molecular oxygen.

Note that a new reaction class for the hydroperoxy-alkyl radicals (QOOH·) deriving from alcohols has recently been proposed by Cord et al. (2012) and experimentally and theoretically confirmed by Welz et al. (2013b). As shown in Fig. 4.9 in the case of a radicals deriving from 2-butanol, this reaction involved a water elimination producing an oxo-aldehyde which further decomposes by β -scission and is a source of ketones or aldehydes.

4.6 Reactions Leading to Unsaturated Products and HO₂· Radicals

The reaction of the fuel radicals with molecular oxygen via H-atom abstractions is also a source of unsaturated species, both in the case of alcohols and methyl esters. In the mechanisms of the low-temperature oxidation of alcohols (Sarathy et al. 2012; Tsujimura et al. 2012) written based on the reactions classes proposed by Curran et al. (1998) for alkanes, the concerted elimination of HO₂ radicals and enol or unsaturated alcohols from hydroxyalkyl-peroxy radicals has been considered as a new reaction class. The rate constant calculated by DeSain et al. (2003) for *n*-propyl radical has been used in the model of Sarathy et al. (2012). In the ester mechanisms written using the same philosophy, this new reaction class is not taken into account, and unsaturated esters are obtained from the QOOH· radicals by a C–C bond scission with the same rate constants used as those for alkanes. In the mechanisms generated by EXGAS, HO₂· radicals and unsaturated alcohols or esters are directly formed from the radicals obtained from the fuel molecules by H-atom abstractions with the same rate constants as those used for alkanes.

As illustrated in the case of 2-butanol in Fig. 4.10, another pathway for the generation of HO₂· radicals is from hydroxyl-alkyl radicals obtained by H-atom abstraction from a carbon atom in the α -position. This reaction leads to the formation of an aldehyde or a ketone of the same size as the reactant.

This reaction class was already considered in the case of the oxidation of large alkenes by Touchard et al. (2005) with rate constants derived from a study by Miyoshi et al. (1990). This reaction class was then automatically considered in the butanol mechanism of Moss et al. (2008). More recently, a theoretical study by Da

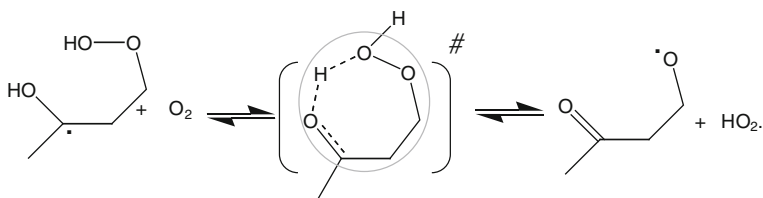


Fig. 4.9 H₂O elimination from a hydroperoxy-alkyl radicals (QOOH·) radical obtained from 2-butanol by H-abstraction from the carbon atom in β -position, addition to oxygen and isomerization

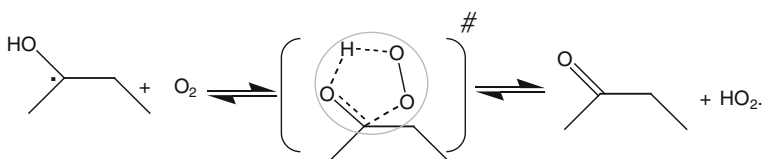


Fig. 4.10 HO₂ radical elimination from the hydroxybutyl radical obtained from 2-butanol by H-abstraction from the carbon atom in α -position

Silva et al. (2009) on ethanol has shown that this reaction proceeds with such a low barrier that the collision stabilization of the hydroxyl-peroxy radicals is unimportant. This would explain why ignition delay times for ethanol are longer than those for ethane as measured in a shock tube (Cooke et al. 1991). This reaction class has been taken into account in recent models for the oxidation of alcohols (Sarathy et al. 2012; Tsujimura et al. 2012) with the rate constant proposed by Da Silva et al. (2009), but still considering the formation of stabilized hydroxyl-peroxy radicals for radicals obtained by H-atom abstraction from a carbon atom in the α -position.

4.7 Conclusion

Two new reaction classes and the specificities in kinetic parameters associated to reaction classes in common with alkanes have been discussed for detailed kinetic oxidation models proposed in the cases of alcohols and methyl esters, two important types of oxygenated reactants considered as promising biofuels. This has been based on the important literature which has recently appeared on the modeling of the oxidation of these oxygenated molecules.

Acknowledgments This work was made in the frame of COST Action CM0901. F. Battin-Leclerc and P. A. Glaude thank the European Commission (“Clean ICE” ERC Advanced Research Grant) for financial support.

References

- Bennadji H, Coniglio L, Billaud F et al (2011) Oxidation of small unsaturated methyl and ethyl esters. *Int J Chem Kin* 43:204–218
- Benson SW (1976) *Thermochemical kinetics*, 2nd edn. Wiley, New York
- Black G, Curran HJ, Pichon S et al (2010) Bio-butanol: combustion properties and detailed chemical kinetic model. *Combust Flame* 157:363–373
- Bounaceur R, Warth V, Sirjean B et al (2009) Influence of the position of the double bond on the autoignition of linear alkenes at low temperature. *Proc Combust Inst* 32:387–394
- Buda F, Bounaceur R, Warth V et al (2005) Progress towards a unified detailed kinetic model for the autoignition of alkanes from C₄ to C₁₀ between 600 and 1200 K. *Combust Flame* 142:170–186
- Bui B, Zhu R, Lin M (2002) Thermal decomposition of iso-propanol: first-principles prediction of total and product-branching rate constants. *J Chem Phys* 117:11188–11195
- Cai J, Zhang L, Yang J et al (2012) Experimental and kinetic modeling study of tert-butanol combustion at low pressure. *Energy* 43:94–102
- Cancino LR, Fikri M, Oliveira AAMC et al (2010) Measurement and chemical kinetics modeling of shock-induced ignition of ethanol-air Mixtures. *Energ Fuels* 24:2830–2840
- Cooke DF, Dodson MG, Williams A (1991) A shock-tube study of the ignition of methanol and ethanol with oxygen. *Combust Flame* 13:233–236
- Cord M, Husson B, Lizardo Huerta JC et al (2012) Study of the low temperature oxidation of propane. *J Phys Chem A* 116:12214–12228
- Curran HJ, Gaffuri P, Pitz WJ et al (1998) A comprehensive modeling study of n-heptane oxidation. *Combust Flame* 114:149–177
- Curran HJ, Fischer SL, Dryer FL (2000) Reaction kinetics of dimethyl ether. II: low-temperature oxidation in flow reactors. *Int J Chem Kin* 32:741–759
- Da Silva G, Bozzelli JW, Liang L, Farrell JT (2009) Ethanol oxidation: kinetics of the α -hydroxyethyl radical + O₂ reaction. *J Phys Chem A* 113:8923–8933
- Dagaut P, Sarathy SM, Thomson MJ (2009) A chemical kinetic study of n-butanol oxidation at elevated pressure in a jet stirred reactor. *Proc Combust Inst* 32:229–237
- Dayma G, Togbé C, Dagaut P (2009) Detailed kinetic mechanism for the oxidation of vegetable oil methyl esters: new evidence from methyl heptanoate. *Energ Fuels* 23:4254–4268
- Dean AM, Bozzelli JW (2000) Combustion chemistry of nitrogen. In: Gardiner WC (ed) *Gas-phase combustion chemistry*. Springer, New York
- DeSain JD, Klippenstein SJ, Miller JA, Taatjes CA (2003) Measurements, theory, and modeling of OH formation in ethyl + O₂ and propyl + O₂ reactions. *J Phys Chem A* 107:4415–4427
- Diévarit P, Won SH, Dooley S et al (2012) A kinetic model for methyl decanoate combustion. *Combust Flame* 159:1793–1805
- Dooley S, Curran HJ, Simmie JM (2008) Autoignition measurements and a validated kinetic model for the biodiesel surrogate, methyl butanoate. *Combust Flame* 153:2–32
- El-Nahas AM, Navarro MV, Simmie JM et al (2007) Enthalpies of formation, bond dissociation energies and reaction paths for the decomposition of model biofuels: ethyl propanoate and methyl butanoate. *J Phys Chem A* 111:3727–3739
- Farooq A, Ren W, Lam KY et al (2012) Shock tube studies of methyl butanoate pyrolysis with relevance to biodiesel. *Combust Flame* 159:3235–3241
- Fisher EM, Pitz WJ, Curran HJ et al (2000) Detailed chemical kinetic mechanisms for combustion of oxygenated fuels. *Proc Combust Inst* 28:1579–1586
- Frassoldati A, Cuoci A, Faravelli T et al (2010) An experimental and kinetic modeling study of n-propanol and iso-propanol combustion. *Combust Flame* 175:2–16
- Frassoldati A, Grana R, Faravelli T et al (2012) Detailed kinetic modeling of the combustion of the four butanol isomers in premixed low-pressure flames. *Combust Flame* 159:2295–2311

- Gaïl S, Sarathy SM, Thomson MJ et al (2008) Experimental and chemical kinetic modeling study of small methyl esters oxidation: methyl (E)-2-butenate and methyl butanoate. *Combust Flame* 155:635–650
- Glaude PA, Battin-Leclerc F, Judenherc B et al (2000) Experimental and modeling study of the gas-phase oxidation of methyl and ethyl tertiary butyl ethers. *Combust Flame* 121:345–355
- Glaude PA, Herbinet O, Bax S et al (2010) Modeling of the oxidation of methyl esters-Validation for methyl hexanoate, methyl heptanoate, and methyl decanoate in a jet-stirred reactor. *Combust Flame* 157:2035–2050
- Goldaniga A, Faravelli T, Ranzi E et al (1998) Oxidation of oxygenated octane improvers: MTBE, ETBE, DIPE, and TAME. Twenty-seventh symposium (international) on combustion, The Combustion Institute, Pittsburgh, pp 353–360
- Grana R, Frassoldati A, Faravelli T et al (2010) An experimental and kinetic modeling study of combustion of isomers of butanol. *Combust Flame* 157:2137–2154
- Grana R, Frassoldati A, Cuoci A et al (2012a) A wide range kinetic modeling study of pyrolysis and oxidation of methyl butanoate and methyl decanoate. Note I: Lumped kinetic model of methyl butanoate and small methyl esters. *Energy* 43:124–139
- Grana R, Frassoldati A, Saggese C et al (2012b) A wide range kinetic modeling study of pyrolysis and oxidation of methyl butanoate and methyl decanoate–Note II: Lumped kinetic model of decomposition and combustion of methyl esters up to methyl decanoate. *Combust Flame* 159:2280–2294
- Hakka MH, Bennadji H, Biet J et al (2010) Oxidation of methyl and ethyl butanoates. *Int J Chem Kinet* 42:226–252
- Harper MR, Van Geem KM, Pyl SP et al (2011) Comprehensive reaction mechanism for *n*-butanol pyrolysis and combustion. *Combust Flame* 158:16–41
- Herbinet O, Pitz WJ, Westbrook CK (2008) Detailed chemical kinetic oxidation mechanism for a biodiesel surrogate. *Combust Flame* 154:507–528
- Herbinet O, Pitz WJ, Westbrook CK (2010) Detailed chemical kinetic mechanism for the oxidation of biodiesel fuels blend surrogate. *Combust Flame* 157:893–908
- Herbinet O, Glaude PA, Warth V et al (2011a) Experimental and modeling study of the thermal decomposition of methyl decanoate. *Combust Flame* 158:1288–1300
- Herbinet O, Biet J, Hakka MH et al (2011b) Modeling study of the low-temperature oxidation of large methyl esters from C11 to C19. *Proc Combust Inst* 33:391–398
- Heufer KA, Sarathy SM, Curran HJ et al (2012) A detailed chemical kinetic modeling study of *n*-pentanol oxidation. *Energy Fuels* 26:6678–6685
- Heufer KA, Bugler J, Curran HJ (2013) A comparison of longer alkane and alcohol ignition including new experimental results for *n*-pentanol and *n*-hexanol. *Proc Combust Inst* 34:511–518
- Karwat DMA, Wagnon SW, Teini PD, Wooldridge MS (2011) On the chemical kinetics of *n*-butanol: ignition and speciation studies. *J Phys Chem A* 115:4909–4921
- Kohse-Höinghaus K, Oßwald P, Cool TA et al (2010) Biofuel combustion chemistry: from ethanol to biodiesel. *Angew Chem Int Ed* 49:3572–3597
- Komninou NP, Rakopoulos CD (2012) Modeling HCCI combustion of biofuels: a review. *Renew Sust Energy Rev* 16:1588–1610
- Lai JYW, Lin KC, Violi A (2011) Biodiesel combustion: advances in chemical kinetic modeling. *Prog Energ Combust Sci* 37:1–14
- Lee C, Vranckx S, Heufer KA et al (2012) On the chemical kinetics of ethanol oxidation: shock tube, rapid compression machine and detailed modeling study. *Z Phys Chem* 226:1–28
- Leplat N, Dagaut P, Togbé C, Vandooren J (2011) Numerical and experimental study of ethanol combustion and oxidation in laminar premixed flames and in jet-stirred reactor. *Combust Flame* 158:705–725
- Luo YR (2003) Handbook of bond dissociation energies in organic compounds. CRC Press, Boca Raton
- Marinov NM (1999) A detailed chemical kinetic model for high temperature ethanol oxidation. *Int J Chem Kin* 31:183–220

- Mehl M, Vanhove G, Pitz WJ et al (2008) Oxidation and combustion of the n-hexene isomers: a wide range kinetic modeling study. *Combust Flame* 155:756–772
- Miyoshi A, Matsui H, Washida N (1990) Rate of reaction of hydroxyalkyl radicals with molecular oxygen. *J Phys Chem* 94:3016–3019
- Moss JT, Berkowitz AM, Oehlschlaeger MA et al (2008) An experimental and kinetic modeling study of the oxidation of the four Isomers of butanol. *J Phys Chem A* 112:10843–10855
- Muller C, Michel V, Scacchi G et al (1995) A computer program for the evaluation of thermochemical data of molecules and free radicals in the gas phase. *J Chim Phys* 92:1154–1177
- Naik CV, Westbrook CK, Herbinet O et al (2011) Detailed chemical kinetic reaction mechanism for biodiesel components methyl stearate and methyl oleate. *Proc Combust Inst* 33:383–389
- Pang GA, Hanson RK, Golden DM, Bowman CT (2012) Experimental determination of the high-temperature rate constant for the reaction of OH with *sec*-butanol. *J Phys Chem A* 116:9607–9613
- Rauk A, Boyd RJ, Boyd SL et al (2003) Alkoxy radicals in the gaseous phase: β -scission reactions and formation by radical addition to carbonyl compounds. *Can J Chem* 81:431–442
- Román-Leshkov Y, Barrett C, Liu Z et al (2007) Production of dimethylfuran for liquid fuels from biomass-derived carbohydrates. *Nature* 447:982–985
- Rosado-Reyes CM, Tsang W (2012a) Shock tube study on the thermal decomposition of *n*-butanol. *J Phys Chem A* 116:9825–9831
- Rosado-Reyes CM, Tsang W (2012b) Shock tube studies on the decomposition of 2-butanol. *J Phys Chem A* 116:9599–9606
- Saggese C, Frassoldati A, Cuoci A et al (2013) A lumped approach to the kinetic modeling of pyrolysis and combustion of biodiesel fuels. *Proc Combust Inst* 34:427–434
- Sarathy SM, Vranckx S, Yasunaga K et al (2012) A comprehensive chemical kinetic combustion model for the four butanol isomers. *Combust Flame* 159:2028–2055
- Saxena P, Williams FA (2007) Numerical and experimental studies of ethanol flames. *Proc Combust Inst* 31:1149–1156
- Sirjean B, Fournet R, Glaude PA et al (2013) A shock tube and chemical kinetic modeling study of the oxidation of 2,5-dimethylfuran. *J Phys Chem A* 117:1371–1392
- Somers KP, Simmie JM, Gillespie F et al (2013) A high temperature and atmospheric pressure experimental and detailed chemical kinetic modelling study of 2-methyl furan oxidation. *Proc Combust Inst* 34:225–232
- Stark MS, Waddington RW (1995) Oxidation of propene in the gas phase. *Int J Chem Kin* 27:123–151
- Sun H, Bozzelli JW, Law CK (2007) Thermochemical and kinetic analysis on the reactions of O₂ with products from OH addition to isobutene, 2-hydroxy-1,1-dimethylethyl, and 2-hydroxy-2-methylpropyl radicals: HO₂ formation from oxidation of neopentane, Part II. *J Phys Chem A* 111:4974–4986
- Taatjes CA, Hansen N, McIlroy A et al (2005) Enols are common intermediates in hydrocarbon oxidation. *Science* 308:1887
- Tian Z, Yuan T, Fournet R et al (2011) An experimental and kinetic investigation of premixed furan/oxygen/argon flames. *Combust Flame* 158:756–773
- Togbé C, Dagaut P, Mzé-Ahmed A (2010) Experimental P, Kinetic detailed modeling study of 1-hexanol oxidation in a pressurized jet-stirred reactor and a combustion bomb. *Energy Fuels* 24:5859–5875
- Togbé C, Halter F, Foucher F (2011) Experimental and detailed kinetic modeling study of 1-pentanol oxidation in a JSR and combustion in a bomb. *Proc Combust Inst* 33:367–374
- Touchard S, Fournet R, Glaude PA et al (2005) Modeling of the oxidation of large alkenes at low temperature. *Proc Combust Inst* 30:1073–1081
- Tran LS, Sirjean B, Glaude P-A et al. (2012) Progress in detailed kinetic modeling of the combustion of oxygenated components of biofuels. *Energy* 43:4–18
- Tsang W (2004) Energy transfer effects during the multichannel decomposition of ethanol. *Int J Chem Kin* 36:456–465

- Tsujimura T, Pitz WJ, Gillespie F et al (2012) Development of isopentanol reaction mechanism reproducing autoignition character at high and low temperatures. *Energy Fuels* 26:4871–4886
- Vasu SS, Davidson DF, Hanson RK et al (2010) Measurements of the reaction of OH with n-butanol at high-temperatures. *Chem Phys Lett* 497:26–29
- Vranckx S, Heufer KA, Lee C et al (2011) Role of peroxy chemistry in the high-pressure ignition of n-butanol—experiments and detailed kinetic modelling. *Combust Flame* 158:1444–1455
- Walton S, Wooldridge M, Westbrook C (2009) An experimental investigation of structural effects on the auto-ignition properties of two C5 esters. *Proc Combust Inst* 32:255–262
- Welz O, Zádor J, Savee JD et al (2012) Low-temperature combustion chemistry of biofuels: pathways in the initial low-temperature (550–750 K) oxidation chemistry of isopentanol. *Phys Chem Chem Phys* 14:3112
- Welz O, Savee JD, Eskola AJ, Sheps L, Osborn DL, Taatjes CA (2013a) Low-temperature combustion chemistry of biofuels: pathways in the low-temperature (550–700 K) oxidation chemistry of isobutanol and *tert*-butanol. *Proc Combust Inst* 34:493–500
- Welz O, Klippenstein S, Harding LB et al (2013b) Unconventional peroxy chemistry in alcohol oxidation: the water elimination pathway. *J Phys Chem Lett* 3:350–354
- Westbrook CK, Naik CV, Herbinet O et al (2011) Detailed chemical kinetic reaction mechanisms for soy and rapeseed biodiesel fuels. *Combust Flame* 158:742–755
- Wiberg K, Waldron R (1991) Lactones. 2. Enthalpies of hydrolysis, reduction, and formation of the C4–C13 monocyclic lactones. Strain energies and conformations. *J Am Chem Soc* 113:7697–7705
- Yang B, Westbrook CK, Cool TA et al (2013) Photoionization mass spectrometry and modeling study of premixed flames of three unsaturated C₅H₈O₂ esters. *Proc Combust Inst* 34:443–451
- Yasunaga K, Simmie JM, Curran HJ et al (2011) Detailed chemical kinetic mechanisms of ethyl methyl, methyl *tert*-butyl and ethyl *tert*-butyl ethers: the importance of uni-molecular elimination reactions. *Combust Flame* 158:1032–1036
- Yasunaga K, Mikajiri T, Sarathy SM et al (2012) A shock tube and chemical kinetic modeling study of the pyrolysis and oxidation of butanols. *Combust Flame* 159:2009–2027
- Yeung C, Thomson M (2013) Experimental and kinetic modeling study of 1-hexanol combustion in an opposed-flow diffusion flame. *Proc Combust Inst* 34:795–802
- Zádor J, Fernandes RX, Georgievskii Y et al (2009) The reaction of hydroxyethyl radicals with O₂: A theoretical analysis and experimental product study. *Proc Combust Inst* 32:271–277
- Zhao Z, Chaos M, Kazakov A et al (2008) Thermal decomposition reaction and a comprehensive kinetic model of dimethyl ether. *Int J Chem Kin* 40:1–18
- Zheng J, Truhlar DG (2010) Kinetics of hydrogen-transfer isomerizations of butoxyl radicals. *Phys Chem Chem Phys* 12:7782–7793
- Zhou CW, Simmie JM, Curran HJ (2011) Rate constants for hydrogen-abstraction by OH for n-butanol. *Combust Flame* 158:726–731
- Zhou CW, Simmie JM, Curran HJ (2012) Rate Constants for Hydrogen Abstraction by HO₂ from n-Butanol. *Int J Chem Kinet* 44:155–164

Chapter 5

Multistep Kinetic Model of Biomass Pyrolysis

Tiziano Faravelli, Alessio Frassoldati, Emma Barker Hemings
and Eliseo Ranzi

Abstract This chapter analyzes the main kinetic features of biomass pyrolysis and devolatilization. To this goal, the biomass is characterized first, and successively the release of the species and char formation is described. Biomass is considered as a mixture of reference constituents: cellulose, hemicellulose, and lignin. Devolatilization of biomasses is a complex process in which several chemical reactions take place in both the gas and the condensed phases alongside the mass and thermal resistances involved in the pyrolysis process. A novel computational characterization of the released species is applied in the proposed devolatilization models, which attempts to characterize pyrolysis reactions with a lumped stoichiometry using a limited number of equivalent components to describe not only gaseous products but also tar species. The proposed model is also adopted to analyze the optimal operating conditions for fast biomass pyrolysis. The operating conditions required to maximize the yield of liquid products are investigated and discussed. Crucial issues are the fast and complete heating of biomass particles to reduce char formation and the rapid cooling of released products to reduce the role of secondary gas-phase pyrolysis reactions.

T. Faravelli (✉) · A. Frassoldati · E. Barker Hemings · E. Ranzi
Department of Chemistry, Materials and Chemical Engineering, Politecnico di Milano,
piazza L. da Vinci, 32, 20133 Milan, Italy
e-mail: tiziano.faravelli@polimi.it

A. Frassoldati
e-mail: alessio.frassoldati@polimi.it

E. Barker Hemings
e-mail: emma.barkerh@gmail.com

E. Ranzi
e-mail: eliseo.ranzi@polimi.it

5.1 Introduction

When considering sources of new clean fuels, of course, biomass plays a significant role. Biomass can be used directly as a fuel for combustion or can be an indirect source of clean fuels. Biomass can be used as a starting raw material to produce valuable commercial products and oxygenated fuels by utilizing fermentation processes. Biomass gasification is a source of syngas, whilst the pyrolysis converts biomass into chemicals, but especially into (bio)fuel oils. For this reason, a chapter in this book is devoted to the modeling of the biomass volatilization, not only for the aforementioned importance in pyrolysis, but also because it is the first step of the gasification and combustion processes.

The world energy demand is currently in the range of 3×10^7 TeraJoule (TJ) and projections indicate a trend of growth up to $3.7\text{--}3.83 \times 10^7$ TJ by 2035 (World Energy Outlook 2010). Biofuels are also responsible for the growth in liquid fuel consumption. Their growing importance is particularly relevant with reference to the transportation sector.

Biomass is a promising alternative source of energy. With a potential enormous availability and no net CO_2 emissions, biomass is considered as the largest and most sustainable energy resource (Naik et al. 2010). Biomass includes a wide range of organic materials. Cellulose, hemicellulose and lignin are generally acknowledged as the major components of biomass material, which also contains inorganic constituents (ashes) and water.

Several issues have arisen contributing to the limited exploitation, up to date, of the potential of biomass. Major considerations concerning the economic sustainability of biomass processing have been repeatedly addressed. The sheer variety of biomass sources results in different products whose properties require characterization. Solid feedstock tends to agglomerate, and depending on its composition, can lead to corrosion, introducing further reactor design and configuration issues (Biagini et al. 2006). The need for standard specifications and procedures in the perspective of the development of bio-refineries, together with an analysis of the socioeconomic changes associated with the conversion from traditional to alternative energy resources, has been addressed. From the technical and technological point of view, several attempts to develop an effective process for biomass treatment have been carried out with varying amounts of success, and there is still considerable room for further improvement and optimization.

Although some major achievements have been made in the past decades, several issues remain open in the effective and convenient exploitation of biomass. From the scientific standpoint, a more fundamental understanding of the physical and chemical transformations occurring in biomass processing is necessary. This knowledge is of crucial importance for the development of large-scale processes for biomass, as well as innovative catalytic systems for the upgrading of bio-products. With respect to thermal treatments of biomass, the interplay of kinetics and transport phenomena is considered as determinant, and the definition of optimal operating conditions of reaction temperature and vapor residence time

needs further investigation (Bridgewater et al. 1999). Secondary gas-phase reactions represent a relevant field of interest as well. At present, there is only a limited understanding of these pathways and the development of a clear understanding of the elementary steps is proving to be challenging.

Chemical kinetics and transport phenomena are indeed strongly coupled to thermal processes and further insight in the modeling of the two is necessary. The aim of the modeling effort is to provide useful tools for predictions of the biomass products and reliable identification of optimal process parameters and operating conditions.

Several attempts in developing models for biomass treatments are reported in the literature. Di Blasi (2008) reviewed in detail the kinetic and transport models of biomass pyrolysis. With specific focus on kinetic models, a major distinction is made between one-component and multi-component reaction mechanisms. The former simplifies the overall process in a single, global reaction in which gases, tars, and char are formed from biomass. This results in an easy-to-use tool, but suffers from a very limited applicability. The high degree of simplification introduced allows only for qualitative predictions of the product yields, with very scarce, or no information on the product distribution. Multi-component models are more complex, as they include an attempt to characterize the feedstock composition. Decomposition rates and conversion time for most biomass samples are predicted with reasonable accuracy, but detailed product distribution and composition are not always available. Another extensive review of the state-of-the-art in pyrolysis modeling of lignocellulosic solid fuels is made by Moghtaderi (2006). A distinction between thermal and comprehensive models is introduced. Thermal models are based on energy balances, whereas comprehensive ones include a chemical kinetic scheme and a model for transport phenomena. The degree of detail, especially concerning the kinetic scheme, might vary and is generally limited. This leads to the conclusion that special attention is required to improve the knowledge and to develop more accurate, general, and robust chemical kinetic mechanisms to account for the product distribution deriving from pyrolysis processes.

White et al. (2011) recently reviewed the kinetic models for the pyrolysis of biomass available in the literature. The goal of their work was to assess kinetic models in relation to the feasibility, design, and scaling of industrial biomass conversion applications (Raveendran et al. 1996; Sensöz and Can 2002). White et al. (2011) also report that the decomposition of biomass is generally described by a single equation as the variable of conversion α , which is defined either as the mass fraction of biomass substrate that has decomposed or as the mass fraction of volatiles evolved:

$$\alpha = \frac{w_0 - w}{w_0 - w_f} = \frac{v}{v_f}$$

where w is the mass of substrate present at any time t , w_0 is the initial substrate mass, w_f is the final mass of solids remaining after the reaction, v is the mass of

volatiles present at any time t , and v_f is the total mass of volatiles evolved during the reaction. The reaction rate is exclusively a function of the degree of conversion α , and the temperature, T , whereas changes in other process parameters (e.g., heating rate, residence time, particle size, sample quantity, reaction interface, atmosphere, and pressure) theoretically should have no effect on the reaction rate.

Furthermore, in most devolatilization schemes, the overall kinetic scheme for biomass is obtained from the combination of the submodels for the three principal biomass pseudocomponents, hemicellulose, cellulose, and lignin, and, sometimes, moisture (Teng et al. 1997; Branca et al. 2005; Radmanesh et al. 2006; Várhegyi et al. 1997; Branca and Di Blasi 2003). The total devolatilization rate is given by the summation of the individual volatilization rates for each fraction, weighted according to the percentage of respective pseudocomponent initially present in the original biomass material.

In semi-global models, biomass pyrolysis products are differentiated into volatiles, tars, and char and are used for 'lumped' kinetic analysis (Branca et al. 2007; Radmanesh et al. 2006; Thurner and Mann 1981; Di Blasi 1996; Shafizadeh and Chin 1977; Di Blasi 1998). Multiple-step models are more complex and in principle more rigorous, as the formation rates of all the individual product species (Branca et al. 2005; Hajaligol et al. 1982), along with any potential heat and mass transfer limitations are included. Other types of kinetic models include the distributed activation energy model (DAEM), which has been successfully applied to both plant (Tsamba et al. 2007; Boroson et al. 1989; Várhegyi et al. 2002; Biagini et al. 2002; Ferdous et al. 2002; Becidan et al. 2007; Sonobe and Worasuwannarak 2008; Wang et al. 2008; Várhegyi et al. 2009a, b) and fossil (e.g. coal) (Anthony and Howard 1976; Biagini et al. 2002; Anthony et al. 1975; Howard 1981; Agarwal 1985; Braun and Burnham 1987; Agarwal et al. 1987; Pitt 1962) biomass pyrolysis.

More complex models describe the evolution of the lattice structures of the biomass. The bio-FLASHCHAIN (Niksa 2000) applies the flash distillation mechanism to a distributed-energy chain statistics to predict the monomer production. Bio-FG DVC (Chen et al. 1998) model combines the functional group (FG) model, used to describe the gas evolution, with the depolymerization-vaporization-cross-linking (DVC) algorithm. Chemical structural parameters are the starting point for chemical percolation and devolatilization (bio-CPD) models, where biomass is represented as a chain copolymer of cellulose, hemicellulose, and a lignin-like component (Fletcher et al. 1992).

White et al. (2011) also discussed the role of heat and mass transport limitations in biomass systems. Suuberg et al. (1996) discussed the importance of heat transfer in the case of high heating rates, which are also expected to lower char yields when compared with slower heating rates (Hajaligol et al. 1982; Zanzi et al. 2002). The poor thermal conductivity of biomass is responsible for thermal gradients within the solid particle, which increases as heating rates increase, and thus results in higher apparent reaction temperatures. Therefore, under certain process conditions the rate determining step is represented by heat transfer, which has to be correctly included in the description of the system (Simmons and Gentry 1986). The

influence of biomass particle size is not negligible when considering transport phenomena. The catalytic effect of inorganic ashes is also critically discussed, even though its understanding remains controversial in the literature.

In the light of the generally acknowledged existing opportunities in kinetic modeling of biomass thermal conversion, and the recognized importance of this domain of research, this chapter aims at the presentation of a modeling approach to biomass pyrolysis and oxidation, tested, and validated against experimental data found in the literature. An application to the production of bio-oil shows limits and possibilities of the model.

5.2 Biomass Characterization and Devolatilization Model

The comprehensive description of the thermal degradation of biomass materials is a very complex and challenging problem, as its complexity occurs at several levels:

- **Multicomponent problem:** Biomass is a complex mixture of organic and inorganic components and needs to be properly characterized;
- **Multiphase problem:** The solid biomass partly reacts in a condensed (metaplast) and gas phase (secondary reactions of released products), and results in the formation of a solid (char, or biochar), a liquid (bio-oil), and a gas phase;
- **Multiscale problem:** The transport phenomena in the gas and solid phases, and between the solid and gas phases need to be considered both at the particle scale and at the reactor scale in order to define local temperature and concentrations and consequent reactivity.

Figure 5.1 offers a schematic representation of the above-mentioned elements, whose complexity is enhanced by the fact that a coupled and comprehensive approach is needed.

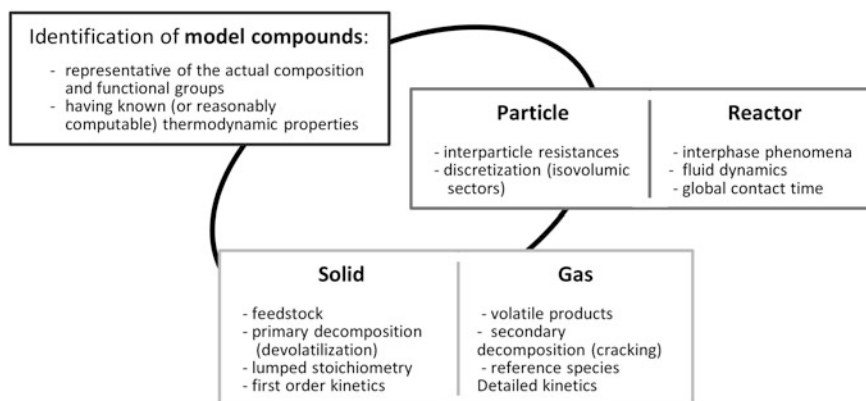


Fig. 5.1 Schematic representation of the thermal decomposition of biomass as a multicomponent, multiphase, and multiscale problem

The first challenge in dealing with biomass is related to the heterogeneous nature of the material. Elemental compositions of different biomass materials are largely varying, and determine its reactivity. The characterization of biomass can rely on elemental, proximate, and biochemical analysis, but they are often unavailable, incomplete, or uncertain. It is therefore a very useful modeling tool for the characterization of biomass materials starting from basic information, such as their elemental analysis. Thus, biomass composition is defined in terms of a limited number of selected model or reference compounds. The core of the present work on biomass processing resides in the kinetic modeling of the reactions in the solid and gas phases. With reference to biomass treatment, the heat and mass transfer limitations within the solid particle must be taken into consideration in order to define local conditions which are determinant for the overall reactivity. When the simulation of fixed or fluidized bed reactors is attempted, a model of the reactor is also required.

5.2.1 Biomass Characterization

Biomass materials are numerous and very different and are generally recognized as a combination of the three major reference components: cellulose, hemicellulose, and lignin. However, the description of these species is not unique as only cellulose is a regular polymer having a precise chemical formula. Hemicellulose is a polymer of different monomeric sugars. Lignin is a very irregular polymer, in which aromatic clusters are interconnected by several alkyl, and oxygenated substituents. Despite its complexity, a reasonable characterization of biomass is important in the definition of its reacting behavior, and therefore of the final products. An elemental analysis provides a first characterization of the C/H/O ratios, together with the indication of N and S, normally present in smaller extent. Other relevant data came from the proximate analysis of biomass, in which the humidity, the volatile, the fixed carbon, and the ash content are measured. Biochemical characterization of biomass provides the relative amount of cellulose, hemicellulose and lignin, but is not usually available. Extensive literature on the subject of biomass characterization exists, and we refer to for further details (Phyllis 2011; Database 2011).

Once the experimental analysis of biomass is available, the problem is shifted to the use of this information for the characterization of biomass in terms of a few reference species, included in the kinetic mechanism that is used to simulate biomass pyrolysis. The choice of the reference species to be included in the kinetic scheme is the first step in biomass characterization. As biomass is generally composed of a mixture of cellulose, hemicellulose and lignin, in the pioneering work of Ranzi et al. (2008) reference species representative of these polymers were chosen. Cellulose was characterized as its monomeric unit of glucose (CELL: $-C_6H_{10}O_5-$). Hemicellulose is more complex, as the polymer is irregular and contains monomeric units of sugars having both five- and six-membered rings.

A monomeric unit having the chemical structure and composition of xylan was selected as hemicellulose reference component (HCE: $-C_5H_8O_4-$). The lignin structure, constituted of clusters of aromatic compounds with methoxy and hydroxyl substituents and interconnected by propanoid chains, is more complex and irregular. In order to describe the large variety of hardwood and softwood structures, the lignins were represented by a combination of three reference species or monomeric units rich in carbon (LIGC: $C_{17}H_{17}O_5$), in hydrogen (LIGH: $C_{22}H_{29}O_9$), and in oxygen (LIGO: $C_{20}H_{23}O_{10}$), respectively (Faravelli et al. 2010). Figure 5.2 shows the chemical structure of the five reference species, also reported in the C/H diagram of Fig. 5.3. On the basis of the elemental C/H/O analysis of the biomass material, a suitable combination of the reference species can be derived. As only three atomic balances are available, the five reference species are combined in three new species (S1, S2 and S3), also shown in Fig. 5.3. The points S1, S2, and S3 are the edges of a triangle in the C/H diagram, and the triangle includes a great number of typical biomass materials. The three elemental balances allow deriving the relative amounts of S1, S2 and S3, as well as the corresponding values of the five reference biomass components. While the definition of the five reference species of CELL, HCE, LIGC, LIGH, and LIGO was made upon a consideration of the chemical nature of biomass, the selection of S1, S2, and S3 was aimed at representing the highest number of typical biomass materials in terms of the reference species. Figure 5.3 reports some biomass materials and shows that they are reasonably well represented by the above-mentioned definitions.

The proposed characterization is extremely useful and valuable in most cases, especially when dealing with woody biomass. The definition of new reference components, such as gallic acid for phenolics, caproic acid for fatty acids, and isoprenoid species for terpenes, offers the opportunity to enlarge the triangle in the C/H diagram, offering a more exact characterization of biomass. This is one possibility to extend the capability of the characterization model. Of course, this would also require the appropriate kinetics to describe the reactivity of the new reference species.

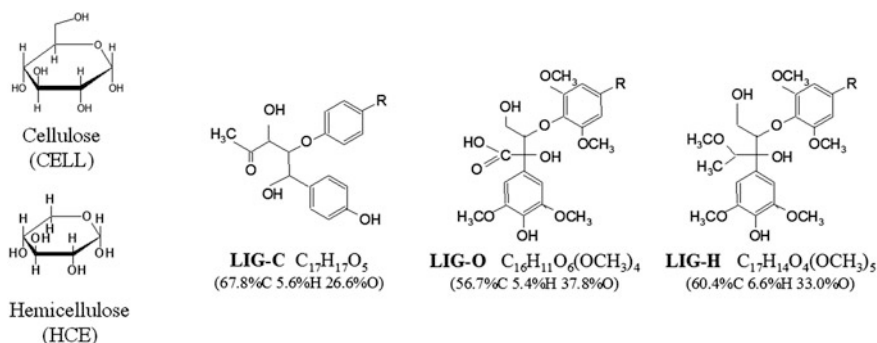
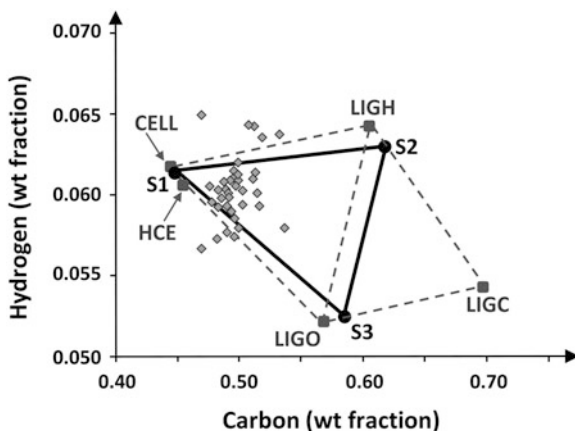


Fig. 5.2 Reference species for cellulose, hemicellulose and lignin in the kinetic model (Ranzi et al. 2008)

Fig. 5.3 Reference species for biomass characterization in the C/H diagram. Diamonds represent different biomasses taken from (Phyllis 2011)



Biomass materials are also characterized by a defined amount of humidity, N, S, and ash. The composition of reference species is, of course, considered on dry, ash free (daf) basis, and also normalized in respect of N and S content. Ashes can also act as catalysts and they can favor biomass decomposition.

5.2.2 *The Kinetic Model of the Devolatilization of Reference Species*

The main objective of the kinetic modeling of biomass pyrolysis is to define the reactivity of the system with an adequate characterization of the residual char and the released tar and gas species. This characterization is an important aspect for the design and optimization of the process units, in which the pyrolysis and partial oxidation and/or combustion reactions simultaneously occur with mass and heat transfer resistances.

The initial biomass composition is described with the five reference components. The intermediate and final products consist of a larger variety of constituents and therefore extensive use of lumping, with the definition of appropriate lumped species representing a variety of different isomers and structures, is necessary. Similar procedures have already been successfully applied to several processes of pyrolysis and combustion in the gas phase and liquid phase, for instance for hydrocarbons and plastics (Ranzi et al. 2001; Faravelli et al. 2001).

The kinetic model of biomass pyrolysis is thus composed of lumped stoichiometries, representing the reactivity of the reference species which are in principle just fictional, and in practice represent an extended group of actual species. The reactions of course satisfy the mass balance for the elemental species and are chosen in order to represent the major classes of intermediate products, such as acids, aldehydes, ketones, alcohols, phenols, etc. The resulting kinetic mechanism

involves a limited number of references or equivalent components able to describe the whole system. These species include:

- Actual species: Species reported directly with their formula (H_2O , CO_2 , CH_4 , CH_2O , CH_3OH , ...);
- Heavy species: These lumped components are larger molecules representative of the initial and intermediate compounds in the evolving structure of the biomass. As a result of subsequent pyrolysis reactions, monomer units are first processed into peripheral groups, so they can react further and be released from the metaplastic phase. Several lumped components are used to describe the evolution toward the residual char and lighter gases;
- Chemisorbed species in the solid matrix: These species, linked to the solid residue, describe the progressive decomposition and charification process with the final release of CO and H_2 .

In the following, a brief account of the major reactions of cellulose, hemicellulose, and lignin is provided. The details have been published in (Ranzi et al. 2008) and very recently revised (Hemings 2012). Reactions are listed with their kinetic constants expressed in Arrhenius form with the following units: l, mol, cal, s. The kinetic models have been built on the basis of experimental data and other kinetic information available in the literature. As a general rule, the kinetic model first involves de-polymerization processes with the formation of a metaplastic phase. A competition is then established among cracking reactions with char and permanent gas formation and vaporization of tar species with high molecular weight. Low temperatures (<500 K) enhance the cross-linking reaction, leading to the formation of light gases and a “secondary” char, which increases the total carbonaceous residue. Intermediate temperatures (500–800 K) favor the devolatilization reactions of volatile tar species from the metaplast. At higher temperatures, the decomposition reactions prevail, and the charification of the original solid matrix goes with the production of light gases. Secondary gas-phase reactions control the decomposition of tar species.

The devolatilization of each reference species of the biomass is not dependent on the kinetics of the others. Although there is some evidence that an interaction between the three constituents exists (Wang et al. 2011; Hosoya et al. 2009), this simplified assumption is generally accepted and used. The proposed kinetic model, far from being completely satisfactory, still represents a step forward with respect to most of the one-step, or basic multi-step global kinetic models available in the literature (Di Blasi 2008).

5.2.2.1 Cellulose

The pyrolysis of cellulose is a molecular process that involves free radicals and occurs in the metaplastic phase. At low temperatures, the species undergo progressive dehydration with the formation of intermolecular COC bonds involving

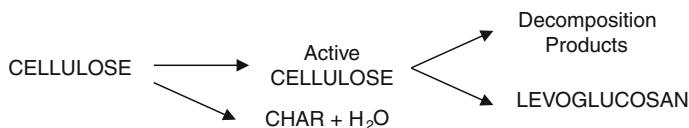


Fig. 5.4 Major reaction pathways in the decomposition of cellulose

branching and cross-linking, which promotes the formation of a char residue. The main reaction in the process of cellulose degradation is a depolymerization reaction chain that through the dimer cellobiosan ($C_{12}H_{20}O_{10}$) produces the monomer levoglucosan (LVG) ($C_6H_{10}O_5$), the main reference tar product from cellulose.

The kinetically limiting stage is the subsequent vaporization of cellulose tar, whose boiling point is in a range of 200–350 °C. The resistance to mass transport in the solid matrix and in the molten phase increases the relative importance of degradation and the subsequent formation of the char (Radlein et al. 1991). At temperatures above 230 °C, the pyrolysis of cellulose also follows a radical process, where the initiation reaction is the breaking of the C–OH bonds. Major products, such as hydroxyacetaldehyde (HAA: $C_2H_4O_2$), glyoxal ($C_2H_2O_2$), CH_3OH , CH_2O , the CO, and CO_2 are produced through β -scission reactions with rupture of C–C bonds within the polymer, and subsequent radical reactions and dehydrations.

A significant amount of 5-hydroxymethylfurfural (HMFU) is also observed in the degradation products. The macroradicals in the liquid phase also propagate the radical chain with the additions on unsaturated bonds, with cross-linking reactions and the progressive formation of char.

Figure 5.4 shows a schematic representation of cellulose devolatilization scheme, and the detailed reactions are listed in Table 5.1. Some validation tests for the kinetic mechanism of cellulose decomposition are proposed in Fig. 5.5. Details on the experimental data and the validation procedure are in Ranzi et al. (2008).

Several authors have suggested that an active intermediate is present in cellulose decomposition (the lumped species CELLA in Fig. 5.4 and Table 5.1) (Varhegyi et al. 1994). As for the major tar products coming from cellulose decomposition, LVG prevails at sufficiently low temperatures, while when the temperature is higher than 450 °C, HAA becomes more relevant. Part b of Fig. 5.5 well represents this evidence. HAA does not come from the subsequent reactions of LVG, but derives directly from the degradation of cellulose. The competition between depolymerization and decomposition of cellulose can then be suitably supported on the basis of these tests.

5.2.2.2 Hemicellulose

The behavior of hemicellulose pyrolysis is different from that of cellulose: its thermal degradation starts at lower temperatures and shows a greater tendency to

Table 5.1 Multistep kinetics of the decomposition of cellulose

Reaction	Rate constant (s^{-1})
CELL \rightarrow CELLA	$8 \times 10^{13} \exp(-45000/RT)$
CELLA \rightarrow 0.95HAA + 0.25Glyoxal + 0.2C ₂ H ₄ O + 0.25HMFU + 0.2C ₃ H ₆ O + 0.16CO ₂ + 0.23CO + 0.9H ₂ O + 0.1CH ₄ + 0.61Char	$1 \times 10^9 \exp(-30000/RT)$
CELLA \rightarrow LVG	$4 \times T \exp(-10000/RT)$
CELL \rightarrow 5H ₂ O + 6Char	$8 \times 10^7 \exp(-32000/RT)$

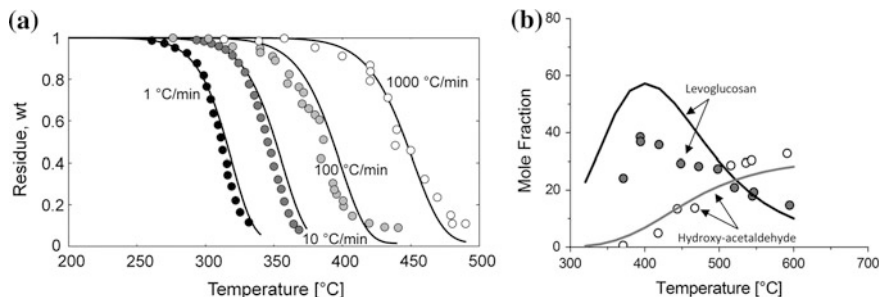


Fig. 5.5 Validation tests for the kinetic mechanism of cellulose decomposition: comparisons of model predictions (*lines*) and experimental data (*points*). Panel (a) thermogravimetric analyses at different heating rates. 1 and 10 °C/min experimental data are from Antal et al. (1998), 100 and 1000 °C/min from Milosavljevic and Suuberg (1995). Panel (b) product distribution: levoglucosan and hydroxy-acetaldehyde. Experimental data from Radlein et al. (1991)

form a char residue, as a result of a greater importance of cross-linking and dehydration reactions. Hemicellulose is a copolymer with pentose sugars, such as xylose ($C_5H_{10}O_5$), and mannose ($C_6H_{12}O_6$) as hexose.

The primary products released are different from those of cellulose and include the corresponding monomers of the starting material. In the kinetic model, hemicellulose is simply considered to be a regular polymer with xylose as a monomer ($C_5H_8O_4$).

The same assumption was made by Williams and Besler (1996) when they studied the influence of temperature and heating rate on slow pyrolysis of biomass. Their experimental data, obtained varying the heating rate between 5 and 80 °C/min, indicate that hemicellulose decomposes mainly in the range of temperature of 250–400 °C, with a slow subsequent loss of weight of the residue.

Table 5.2 and Fig. 5.6 give details about the kinetic mechanism. Hemicellulose depolymerizes to form the activated monomers HCE1 and HCE2, which represent the reaction intermediates in the solid matrix subjected to successive stages of vaporization and degradation. HCE1 undergoes vaporization, with the formation of the volatile tar (XYLAN).

It may also undergo high temperature decomposition to form char and light gases. HCE2 only undergoes high temperature decomposition. To account for the latter, high temperature weight loss, experimentally noticeable from TG measurements of hemicellulose decomposition, is described with the definition of a chemisorbed FG $G\{COH_2\}$ which reproduces the slow final release of H_2 and CO . Similarly, $G\{H_2\}$, $G\{CH_4\}$, $G\{CO\}$, and $G\{CO_2\}$ are species trapped in the metaplast and successively released to the gas phase. Figure 5.7 shows a sample of validation of the devolatilization model of hemicellulose.

Table 5.2 Multistep kinetics of the decomposition of hemicellulose

Reaction	Rate constant (s^{-1})
HCE \rightarrow 0.4HCE1 + 0.6HCE2	$1 \times 10^{10} \exp(-31000/RT)$
HCE1 \rightarrow 0.75G{H ₂ } + 0.8CO ₂ + 1.4CO + 0.5CH ₂ O + 0.25CH ₃ OH + 0.125H ₂ O + 0.125C ₂ H ₅ OH + 0.625CH ₄ + 0.25C ₂ H ₄ + 0.675Char	$3 \times 10^9 \exp(-32000/RT)$
HCE1 \rightarrow 0.25G{H ₂ } + 0.25H ₂ O + 0.8CO ₂ + 0.65G{CO} + 1.5G{COH ₂ } + 0.625CH ₄ + 0.375C ₂ H ₄ + 0.675Char	$0.15 \times T \exp(-8000/RT)$
HCE1 \rightarrow XYLAN	$3 \times T \exp(-11000/RT)$
HCE2 \rightarrow 0.2CO ₂ + 0.5CH ₄ + 0.25C ₂ H ₄ + 0.8CO ₂ S + 0.8G{COH ₂ } + 0.7CH ₂ O + 0.25CH ₃ OH + 0.125C ₂ H ₅ OH + 0.125H ₂ O + Char	$1 \times 10^{10} \exp(-33000/RT)$

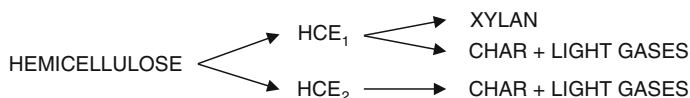
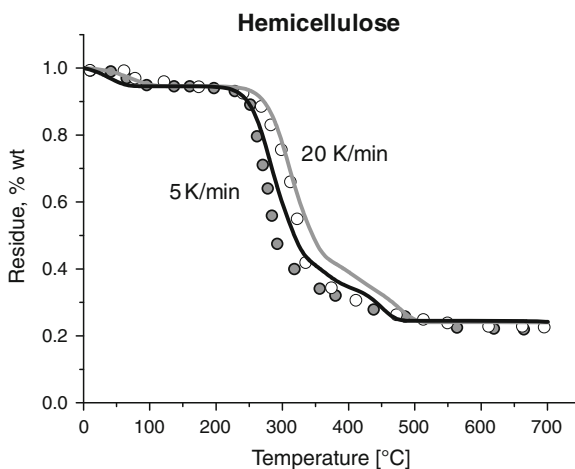


Fig. 5.6 Major reaction pathways in the decomposition of hemicellulose

Fig. 5.7 Validation tests for the kinetic mechanism of hemicellulose decomposition. Comparisons of model predictions (*lines*) and experimental data (*points*) (Williams and Besler 1996)



5.2.2.3 Lignin

The structure of lignin is of considerable complexity, thus making it more difficult to describe its pyrolysis. The presence of β -O-4 bond and the energy of the different bonds present in the original irregular polymer affect the degradation process. The reference species of lignin are reported in Fig. 5.2, with their chemical structure, composition, and the relative wt.% of the elements.

The decomposition of lignin is influenced by the presence of phenolic-type reaction intermediates. The presence of resonant stabilized phenoxy radicals is crucial to the definition of the reaction pathways leading to the formation of the char residue. Typical reactions include the addition of radicals, with consequent substitution. As these radicals often are heavy phenoxy radicals, this reduces the amount of releasable species in the tar phase and carbon residue increases accordingly. The release of volatiles is widespread over a large temperature range, and normally completes at around 400 °C. At higher temperature there is a final release of CO and H₂, with the consequent enrichment of carbon in the residual 'char'. The simplified kinetic scheme of the decomposition of lignin considers the evolution of the different components. LIGH and LIGO decompose releasing gases (rich in hydrogen and oxygen, respectively) and forming the same intermediate (LIGOH).

During the early stages of pyrolysis, LIGC gives rise to the pseudospecies LIGCC, with the consequent formation of gases and char. Both LIGOH and

LIGCC decompose to form a different pseudospecies (LIG), developing gas, tar, and other compounds forming the char. Finally, LIG always evolves to char, forming gas and tar. The detailed reactions are listed in Table 5.3. $C_9H_{10}O_2$ (paracoumaryl alcohol) and $C_{11}H_{12}O_4$ stand for the whole class of substituted phenol components, with differing methoxyl content.

Very detailed experimental analysis of the volatilization of lignin using a heating rate of 20 °C/min was reported by Jakab et al. (1995), who studied 16 isolated lignins from softwood and hardwood species. These data were used for the validation of lignin kinetic model and they are thoroughly discussed in (Faravelli et al. 2010), an example is reported in Fig. 5.8.

5.2.2.4 Release of the Chemisorbed Functional Groups

Some condensed groups are assembled in the kinetic model. These species can be considered as compounds trapped in the metaplast and successively released to the gas phase. The introduction of these species is necessary in order to account for the slow and persistent weight loss in TGA measurements observed at high temperatures, when the devolatilization itself should be completed. Table 5.4 shows these reactions. It can be easily inferred from the expression of the kinetic constant that the most refractory group is the $G\{COH_2\}$, which is released only at high temperature. The missing release of this component is also responsible for the presence of relatively high quantities of oxygen in biochar.

5.2.2.5 Biomass Volatilization

The simulation of the biomass pyrolysis results from the superimposition of the weighted models of the different volatilizations of the constituents, i.e. cellulose, hemicellulose, and lignin. For example, Fig. 5.9 shows the decomposition of different biomasses at different heating rates.

Almond shell mainly consists of cellulose (47 wt.%), with hemicellulose and lignin accounting for 26 and 23 wt.%, respectively. Lignin (37 wt.%) is the main constituent of pine, followed by cellulose (37 wt.%) and hemicellulose (20 wt.%). Lignin starts reacting first, whilst cellulose is the last, even though cellulose reacts faster. Lignin is also the main responsible of char formation, followed by hemicellulose, whilst the residue from cellulose is always less than 10 %.

5.3 Fast Biomass Pyrolysis

The production of bio-oil is a further example of application of the previous models. Fast biomass pyrolysis is a complex process where chemical kinetics, operating conditions, and transport phenomena play a significant role. The yield of

Table 5.3 Multistep kinetics of the decomposition of lignin

Reaction	Rate constant (s^{-1})
LIG-C \rightarrow 0.35LIGCC + 0.1pCoumaryl + 0.08Phenol + 0.41C ₂ H ₄ + H ₂ O + 0.495CH ₄ + 0.32CO + G{COH ₂ } + 5.735Char	$4 \times 10^{15} \exp(-48500/RT)$
LIG-H \rightarrow LIGOH + C ₃ H ₆ O	$2 \times 10^{13} \exp(-37500/RT)$
LIG-O \rightarrow LIGOH + CO ₂	$1 \times 10^9 \exp(-25500/RT)$
LIGCC \rightarrow 0.3Coumaryl + 0.2Fenol + 0.35C ₃ H ₄ O ₂ + 0.7H ₂ O + 0.65CH ₄ + 0.6C ₂ H ₄ + G{COH ₂ } + 0.8G{CO} + 6.4Char	$5 \times 10^6 \exp(-31500/RT)$
LIGOH \rightarrow 2 H ₂ O + 1.45CH ₄ + 0.7C ₂ H ₄ + 10.15Char + 0.5G{H ₂ } + 1.8G{CO} + 4.2G{COH ₂ }	$1 \times 10^2 \exp(-15000/RT)$
LIGOH \rightarrow LIG + H ₂ O + CH ₃ OH + 0.45CH ₄ + 0.2C ₂ H ₄ + 1.4G{CO} + 0.6G{COH ₂ } + 0.1G{H ₂ } + 4.15Char	$3 \times 10^8 \exp(-30000/RT)$
LIG \rightarrow C ₁₁ H ₁₂ O ₄	$12 \times T \exp(-12000/RT)$
LIG \rightarrow H ₂ O + 0.5CO + 0.2CH ₂ O + 0.4CH ₃ OH + 0.2C ₂ H ₄ O + 0.2C ₃ H ₆ O + 0.6CH ₄ + 0.65C ₂ H ₄ + G{CO} + 0.5G{COH ₂ } + 5.5Char	$1 \times 10^9 \exp(-30000/RT)$

Fig. 5.8 Validation tests for the kinetic mechanism of pyrolysis of lignins (heating rates 20 °C/min). Comparisons of model predictions (*lines*) and experimental data (*points*) (Jakab et al. 1995)

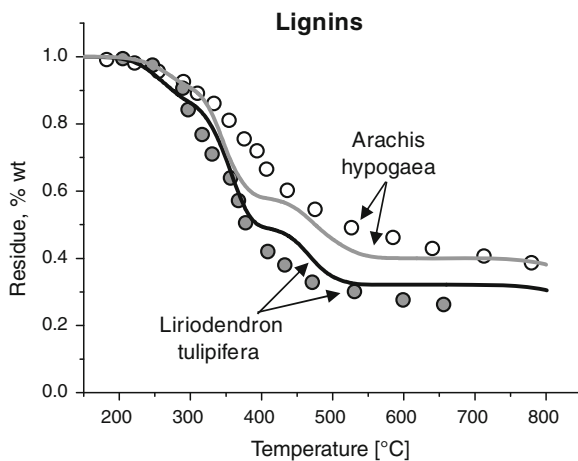


Table 5.4 Kinetics of the release of the chemisorbed species

Reaction	Rate constant (s^{-1})
$G\{CO_2\} \rightarrow CO_2$	$1 \times 10^5 \exp(-24000/RT)$
$G\{CO\} \rightarrow CO$	$1 \times 10^{13} \exp(-50000/RT)$
$G\{CH_4\} \rightarrow CH_4$	$5 \times 10^{13} \exp(-50000/RT)$
$G\{H_2\} \rightarrow H_2$	$5 \times 10^{11} \exp(-50000/RT)$
$G\{COH_2\} \rightarrow CO + H_2$	$5 \times 10^{11} \exp(-71000/RT)$

the liquid product is largely dependent on the temperature, heating rate, and residence time of the biomass in the reactor and of the time spent by the released species in the gas phase at high temperature. In general, yield of solid (char) decreases and the yield of gases increases at higher temperatures. A maximum yield of bio-oil is usually attained at approximately 750–800 K.

Fast pyrolysis can therefore maximize the liquid yields from small biomass particles. In fact, it is recognized that under pyrolysis conditions, low temperatures and long residence times of the gas and tar species released by the biomass favor char formation. Conversely, high temperatures and long residence times increase the role of the successive decomposition of the released primary tar products, thus favoring the conversion to light gases. As a result of the relative importance of these different mechanisms, higher heating rates, moderate temperatures, and short hot vapor residence times can be used to optimize the yield of liquid species. In this way, the intermediate products are recovered in the form of a liquid bio-oil.

Because of the low thermal conductivity of biomass, only particles with diameter below a few mm can reach fast pyrolysis regimes. For this reason, relatively small or thin particles in fluidized-bed reactors with short vapor residence times are examples of fast heating and large, thick or coarse particles (3–6 cm) or biomass briquettes in packed-bed reactors are involved in a slow heating process (Bridgwater 2003; Di Blasi 2009).

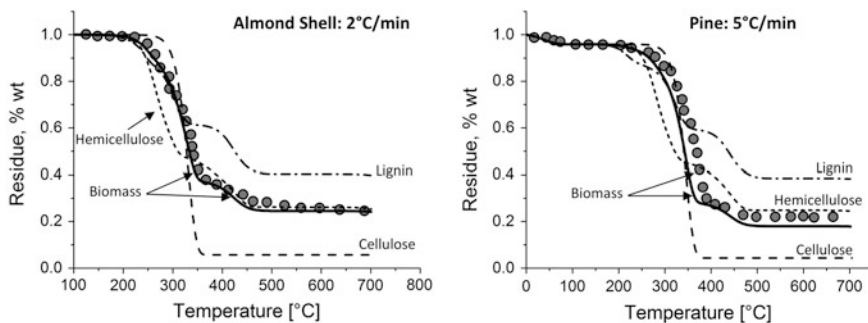
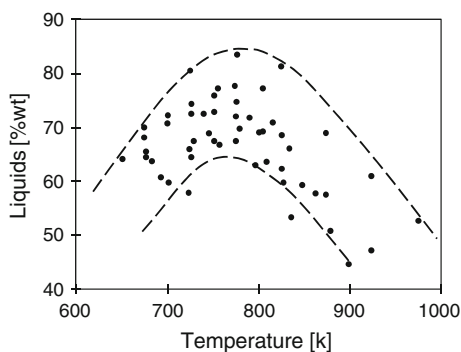


Fig. 5.9 Validation tests for the kinetic mechanism of pyrolysis of biomasses. Comparisons of model predictions (*lines*) and experimental data (*points*). Almond shell experimental data are from Caballero et al. (1997), pine ones from Williams and Besler (1996)

The experimental data of Fig. 5.10 show the important effect of temperature on the bio-oil yields from fast pyrolysis (Di Blasi 2009). The optimal operating conditions for temperature are around $\sim 750\text{--}800$ K. This is where the bio-oil yields span between 60 and 85 wt.%. The yields are sensitive to different reactor designs, operating conditions (volatile residence times, particle characteristics) and different biomass samples (softwood/hardwood). The low bio-oil yields at low temperatures can be explained as be the consequence of both incomplete devolatilization of the solid particles and by the favored char formation, due to cross-reticulation reactions of liquid and tar components. At high temperatures, the effect of the secondary gas-phase reactions of bio-oil components explain the decrease of the liquid oil yield. It is important to observe that under typical fast pyrolysis conditions both the chemistry and heat and mass transfer processes play a critical role in controlling the bio-oil yields. To maximize the bio-oil formation it is important to accurately control the heating rate and process temperatures. This ensures a rapid heating of the biomass particles (fast pyrolysis) and results in the minimization of the secondary gas-phase reactions of released products. Therefore, the modeling of fast pyrolysis processes requires the combined use of

Fig. 5.10 Bio-oil yields in fast pyrolysis (Calonaci et al. 2010)



comprehensive kinetic models, capable of describing biomass degradation, and the proper conservation equations accounting for the simultaneous heat and mass transfer resistances both at the particle scale and the reactor scale (Pierucci and Ranzi 2008).

One-component reaction models, which simplify the overall process in a single, global reaction, have a very limited applicability: The high degree of simplification allows for a mainly qualitative prediction of the product yields, without details about the composition and chemical nature of the bio-oil. Only multi-component models are able to predict the decomposition rates and conversion time for most biomass samples with good accuracy. However, a detailed prediction of released product composition is still lacking. Due to the important role of gas-phase reactions, the multi-step biomass degradation model has to be coupled with a gas-phase kinetic mechanism able to characterize the primary pyrolysis and oxidation reactions of the released species. The main characteristics of these are described in Chap. 4 for some of the oxygenated compounds. This is a first attempt to tackle a tough, multiscale and multiphase problem, because it is necessary to include and analyze, both at the particle scale and the reactor scale, the following steps of the fast pyrolysis process: (1) Heating and drying of solid particles, including heat and mass resistances; (2) Devolatilization of biomass; and (3) Secondary gas phase pyrolysis reactions.

5.3.1 Secondary Gas-Phase Reactions

Volatile components released by biomass can undergo successive gas-phase pyrolysis and/or oxidation reactions (Calonaci et al., 2010). The primary pyrolysis and oxidation reactions of the oxygenated species of Table 5.5 must be defined and new mechanisms are proposed to model and characterize the chemistry of those components.



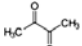
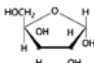
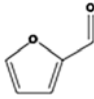
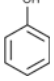
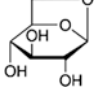
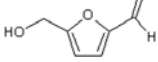
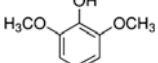
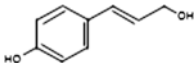
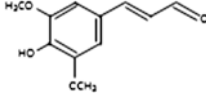
New and more detailed experimental information (Azeez et al. 2010) as well as more accurate kinetic studies will support the development of the kinetic mechanism for the successive gas-phase reactions of the species involved in the multi-step kinetic model of biomass devolatilization. In this way, these gas-phase reactions can be easily modified, improved and/or extended, thus improving the reliability of the model as a whole.

5.3.2 Model Predictions and Comparisons with Experimental Measurements

The first example of comparisons refers to the fast pyrolysis of pine spruce sawdust, characterized in terms of reference components in Fig. 5.11.

Aguado et al. (2000) studied the pyrolysis of this biomass in a conical spouted bed reactor, which guarantees the optimal operating conditions required by flash

Table 5.5 Main volatile species released from biomass devolatilization

Chemical name	Formula	
Methanol	CH ₄ O	
Ethanol	C ₂ H ₆ O	
Glyoxal	C ₂ H ₂ O ₂	
Acetic acid	C ₂ H ₄ O ₂	
Hydroxy-acetaldehyde	C ₂ H ₄ O ₂	
Ethylene glicol	C ₂ H ₆ O ₂	
<i>n</i> -propanol	1-C ₃ H ₇ OH	
<i>iso</i> -propanol	2-C ₃ H ₇ OH	
hydroxyl-oxo-propanal	C ₃ H ₄ O ₃	
propanal, 3-hydroxy-	C ₃ H ₆ O ₂	
propane-1,3-diol	C ₃ H ₈ O ₂	
propanedial	C ₃ H ₄ O ₂	
<i>n</i> -butanol	C ₄ H ₁₀ O	
<i>sec</i> -butanol	C ₄ H ₁₀ O	
<i>iso</i> -butanol	C ₄ H ₁₀ O	
<i>tert</i> -butanol	C ₄ H ₁₀ O	
Furan	C ₄ H ₄ O	
tetrahydro-furan	C ₄ H ₈ O	
butanedione	C ₄ H ₆ O ₂	
xylofuranose	C ₅ H ₈ O ₄	
furan-2-carboxaldehyde	C ₅ H ₄ O ₂	
Phenol	C ₆ H ₆ O	
levoglucosan (cellobiosan)	C ₆ H ₁₀ O ₅	
5-hydroxymethyl-furfural	C ₆ H ₆ O ₃	
2,6-dimethoxy-phenol	C ₈ H ₁₀ O ₃	
4-(3-hydroxy-1-propenyl)-phenol	C ₉ H ₁₀ O ₂	
3-(4-hydroxy-3,5-dimethoxy-phenyl)-acrylaldehyde	C ₁₁ H ₁₂ O ₄	

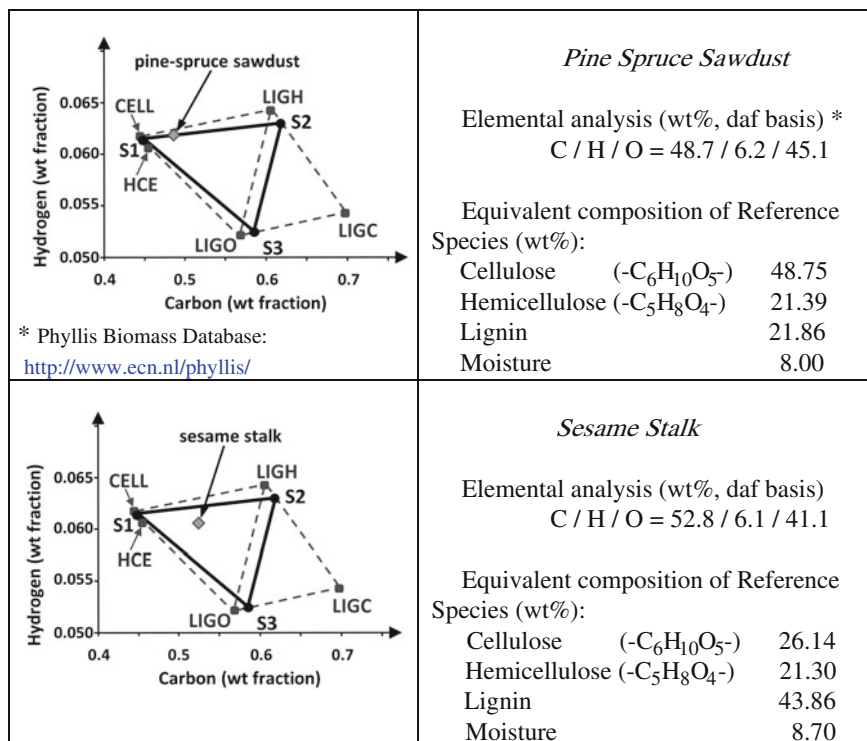


Fig. 5.11 Biomass characterization from elemental analysis to reference species (Aguado et al. 2000; Ates et al. 2004)

pyrolysis: short gas residence time, rapid heating of the feed, and good gas–solid heat and mass transfer.

Under these conditions, a maximum yield of liquid of ~ 70 wt.% is experimentally obtained at 723 K, in agreement with Fig. 5.10. A quite flat maximum of ~ 69 wt.% is predicted by the devolatilization model in the temperature range 690–740 K, well in line with experimental observations.

Moreover, Table 5.6 shows the comparisons between the measured and predicted product yields of char, gas, and liquid (including water). A similar comparison in the same table refers to the fast pyrolysis of sesame stalk in a fixed bed reactor (Ates et al. 2004). The biomass is characterized in terms of reference species from the elemental C/H/O analysis, as shown in Fig. 5.11. The model predicts a flat maximum liquid yield of ~ 55 wt.% in the temperature range 700–850 K while the experiments show the same maximum at 770–820 K. In line with the experimental data, the model predicts a water quantity of ~ 14 wt.%.

Table 5.6 also contains a comparison between model predictions and the experimental results of Westerhof et al. (2010) who analyzed the fast pyrolysis of pine wood in a fluidized bed reactor. They observed a maximum oil yield of ~ 55

Table 5.6 Experimental and predicted products from fast pyrolysis

Reference	Aguado et al. (2000)		Ates et al. (2004)		Westerhof et al. (2010)	
Biomass	Pine spruce sawdust		Sesame stalk		Pine wood	
Temperature (K)	Model	Exp.	Model	Exp.	Model	Exp.
	720		770		750	
<i>wt fractions</i>						
Solid residue	0.141	0.12	0.228	0.22	0.271	0.17
Gases	0.172	0.17	0.231	0.26	0.179	0.23
Total liquids	0.686	0.70	0.540	0.52	0.55	0.58
H ₂ O	0.116	0.09	0.142	0.16	0.126	0.12
Organic liquids	0.570	0.61	0.398	0.36	0.424	0.46

wt.% at 750 K. The model predicts a very similar value, which depends on the biochemical composition of the pine wood (cellulose 35 wt.%; hemicellulose 29 wt.%; lignin 28 wt.%). Also in this case, the model succeeded in predicting the water content. At 750–800 K, the maximum oil content ranges between 55 and 80 %, due to the different biomasses, as already shown in Table 5.6. A sensitivity analysis clearly indicates that the maximum oil yield is obtained from pure cellulose.

Figure 5.12 shows the influence of temperature on bio-oil and water yields from sesame stalk and pine wood pyrolysis (Ates et al. 2004; Westerhof et al. 2010). The good agreement between the experimental data and model predictions is confirmed. Not only the maximum yields are correctly predicted, but also the effect of temperature on those yields is reproduced by the model. According to the model, CO₂ and CO are the main gas species from primary devolatilization, while small quantities of CH₄ and C₂ hydrocarbons (C₂H₄ and C₂H₆) are also released. Primary H₂ yield is very limited and only occurs at high temperatures. At high temperatures, residual char becomes nearly constant, because further degradation reactions are negligible.

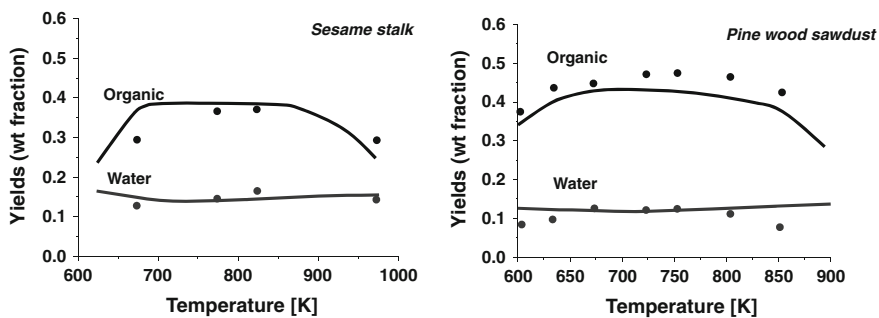


Fig. 5.12 Yields of bio-oil and water from fast pyrolysis (Ates et al. 2004; Westerhof et al. 2010). Comparison between experimental data (points) and model (lines)

In the case of small particles, the model, in general, predicts very flat bio-oil yields and gas formations at temperatures higher than 750–770 K, where the biomass devolatilization is completed. These predictions agree quite well with the experiments. The predicted chemical composition of liquid products also agrees fairly well with the experimental data reported in the literature (Aguado et al. 2000; Oasmaa et al. 2010). Bio-oil consists of over 40 % carbohydrates or sugars (mainly LVG and cellobiosan), while substituted phenol, guaiacol, and syringol species derived from lignins span between 10 and 20 %. Alcohols, aldehydes, furans, and small oxygenated species constitute up to 15–25 %, while water ranges between 10 and 20 % of the dry biomass.

As already observed, the bio-oil yield in Fig. 5.10 shows a maximum relative to temperature. This is a result of the competition between the primary biomass devolatilization, which forms tar, and the secondary gas-phase reactions of tar vapors, which deplete tar and are relevant mainly at high temperatures and longer residence times. Consequently, gas yield increases continuously with temperature. The pine spruce sawdust (Aguado et al. 2000) considered previously can be conveniently used to show the effect of secondary gas-phase reactions on bio-oil yield and composition and on the formation and gas species.

Gas and tar species released from the biomass during the devolatilization process are maintained at the reactor temperature for different residence times, ranging from 0.1 and for 3 s. These times, which are typical times for fast pyrolysis processes, allow the secondary gas-phase reactions to play a relevant role mainly at high temperatures. Figure 5.13 shows the effect of these reactions and these different hot vapor residence times on bio-oil yield. At temperatures higher than 900 K, significant decomposition of tar species is predicted even at very short residence times.

Figure 5.14 shows in more detail the effect of the residence times of the gas phase at 923 K on the conversion of LVG and HAA. A significant consumption of these oxygenated tar species can be observed with the corresponding large increase

Fig. 5.13 Effect of secondary pyrolysis reactions. Predicted bio-oil yield versus temperature at two vapor residence times

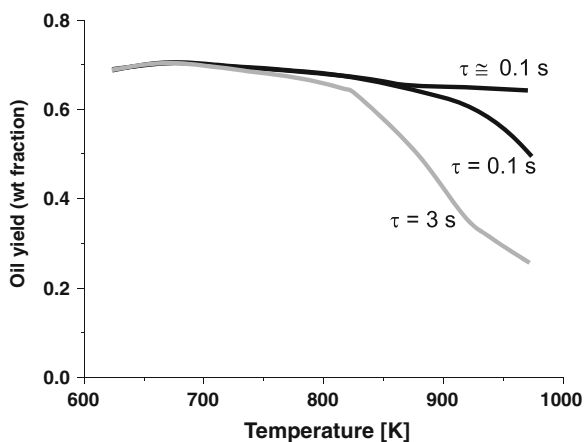
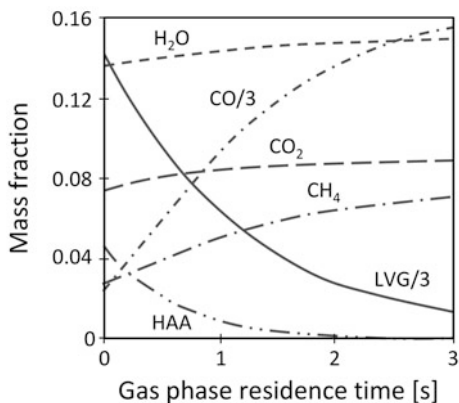


Fig. 5.14 Secondary pyrolysis reactions. Time evolution of major species at 923 K

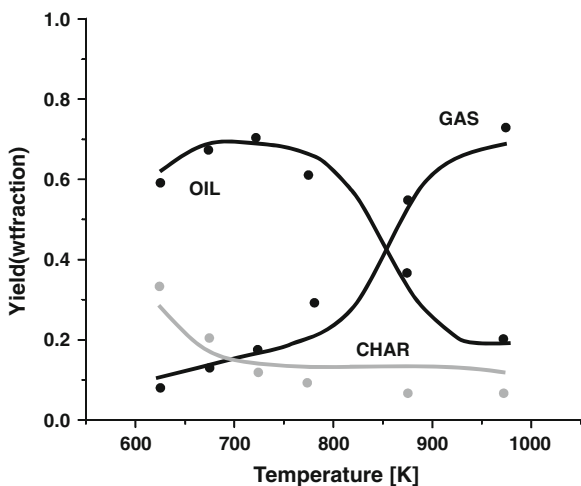


in CO and other light gas species. These predictions agree quite well with the experimental measurements and indicate that a higher process temperature enhances the effect of secondary pyrolysis, with the corresponding formation of light gases, and increases the CO/CO₂ ratio.

Figure 5.15 shows comparisons between the experimental and predicted yields of fast pyrolysis in the spouted bed of Aguado et al. (2000). At temperatures lower than 700 K, the devolatilization process is not completed. For large particles, the devolatilization times, as well as the heat transfer resistances, become the critical parameters. At high temperatures, the effect of secondary gas-phase pyrolysis reactions is evident and explains the consumption of bio-oil and the formation of gas species.

A comprehensive mathematical model of biomass devolatilization, both at the reactor scale and the particle scale, is required to properly describe oil yield

Fig. 5.15 Pine spruce sawdust pyrolysis. Oil, gas, and char yields versus temperature (Aguado et al. 2000). Comparison between experimental data (points) and model (lines)



behavior. Heat diffusivity inside the solid particle and heat transfer resistances helps to explain the partial volatilization of the biomass at low and intermediate temperatures.

At high temperatures, the secondary pyrolysis reactions of tar species need to be accounted with a proper vapor residence time. Note that the good agreement for liquid and gas yields shown in Fig. 5.15 was obtained with an effective vapor contact time of ~ 5 s, which is significantly higher than the nominal one indicated by Aguado et al. (2000). This deviation could be due to the difficulty in measuring the effective gas residence times in the spouted bed reactor, in which gas recirculation is critical.

Thermal diffusivity becomes a rate determining factor for the devolatilization of large particles. Figure 5.16 shows the effect of particle size on the biomass devolatilization. According to the model, large particles require significantly higher temperatures and/or longer residence times to reach complete conversion. For this reason, as a result of the partial devolatilization, bio-oil yields are limited at low temperatures especially for large particles. For the same reason, the oxygen content in the residual charcoal decreases when pyrolysis temperature increases.

By simply combining the average conditions reported in Figs. 5.13 and 5.16, it is possible to explain and reproduce the experimental results reported in Fig. 5.10 quite closely. Thus, Fig. 5.17 shows the yields of oil, char, and gas from a lignocellulosic biomass. The two limit curves combine the effect of incomplete devolatilization and/or large particles at low temperatures, with the role of secondary pyrolysis reactions, at high temperatures.

Fig. 5.16 Effect of heat transfer resistances. Predicted bio-oil yield versus temperature for different solid particle sizes (1 mm: *dashed lines*; 2 cm: *plain lines*) and residence times (1 min: *gray lines*; 10 min: *black lines*)

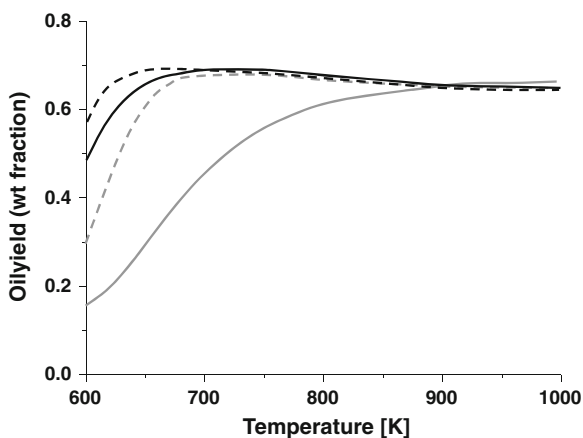
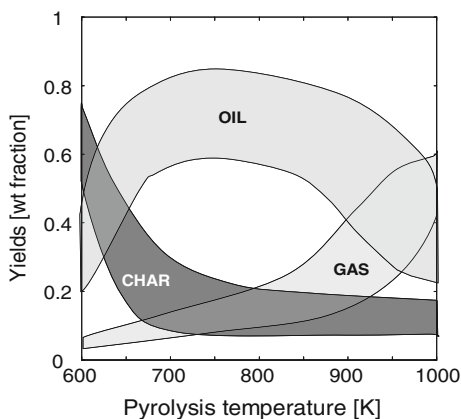


Fig. 5.17 Predicted typical yields of oil, char and gas from fast pyrolysis of biomass



5.4 Conclusion

To predict gas composition from biomass gasifiers, or the bio-oil yields in fast pyrolysis reactors, it is crucial to describe and properly combine the four different features of this complex process:

- Biomass characterization
- Solid fuel devolatilization
- Secondary reactions in the gas phase
- Char gasification.

Biomass characterization is considered a straightforward combination of three reference components: cellulose, hemicellulose, and lignins. First, multistep kinetic models of solid fuel volatilization were developed and validated. This mechanism was also coupled with specific secondary gas-phase reactions. Despite their simple expressions, these models allow the characterization of the degradation steps, their characteristic times, and the prediction of product distributions. These aspects make the proposed mechanisms a useful tool in the design and optimization of industrial gasifiers, where the presence of tars needs to be either enhanced or lowered. The focus on product and by-product formation is a further advantage when considering pollutant emissions from such devices.

The application to bio-oil production is a further example which proves the possibilities of these models. It shows and quantifies the critical role of secondary reactions and transport phenomena, heat transfer in particular.

Given the acknowledged complexity of biomass characterization and pyrolysis, it is clear that the discussed modeling approach is only a preliminary step and that further efforts and tailored experiments are required for improving the reliability of the overall kinetic model, which will necessarily undergo revisions, extension, and further validations in the future. The current biomass situation resembles the early days of the development of the carbo-chemistry and the petrochemical industry. A large amount of research and process development is still required.

Acknowledgments Part of this work was made in the frame of COST Action CM0901. The authors are in debt to Prof. Sauro Pierucci and to the many students who have contributed to model development: Gabriele Migliavacca, Tiziano Maffei and Samuele Sommariva are particularly acknowledged.

References

- Agarwal PK (1985) Distributed kinetic parameters for methane evolution during coal pyrolysis. *Fuel* 64:870–872
- Agarwal PK, Agnew JB, Ravindran N et al (1987) Distributed kinetic parameters for the evolution of gas species in the pyrolysis of coal. *Fuel* 66:1097–1106
- Aguado R, Olazar M, San José MJ et al (2000) Pyrolysis of sawdust in a conical spouted bed reactor. Yields and product composition. *Ind Eng Chem Res* 39:1925–1933
- Antal MJ, Varhegyi G, Jakab E (1998) Cellulose pyrolysis kinetics: revised. *Ind Eng Chem Res* 37:1267–1279
- Anthony DB, Howard JB (1976) Coal devolatilization and hydrogasification. *AIChE J* 22:625–656
- Anthony DB, Howard JB, Hottel HC et al (1975) Rapid devolatilization of coal. *Proc Combust Inst* 15:1303–1317
- Ates F, Pütün E, Pütün AE (2004) Fast pyrolysis of sesame stalk: yields and structural analysis of bio-oil. *J Anal Appl Pyrol* 71:779–790
- Azeez AM, Meier D, Odermatt J, Willner T (2010) Fast pyrolysis of African and European lignocellulosic biomasses using Py-GC/MS and fluidized bed reactor. *Energy Fuels* 24:2078–2085
- Becidan M, Várhegyi G, Hustad JE et al (2007) Thermal decomposition of biomass wastes. A kinetic study. *Ind Eng Chem Res* 46:2428–2437
- Biagini E, Lippi F, Petarca L et al (2002) Devolatilization rate of biomasses and coal-biomass blends: an experimental investigation. *Fuel* 81:1041–1050
- Biagini E, Barontini F, Tognotti L (2006) Devolatilization of biomass fuels and biomass components studied by TG-FTIR technique. *Ind Eng Chem Fundam* 45:4486–4493
- Boroson ML, Howard JB, Longwell JP et al (1989) Product yields and kinetics from the vapor phase cracking of wood pyrolysis tars. *AIChE J* 35:120–128
- Branca C, Di Blasi C (2003) Kinetics of the isothermal degradation of wood in the temperature range 528–708 K. *J Anal Appl Pyrol* 76:207–219
- Branca C, Albano A, Di Blasi C (2005) Critical evaluation of global mechanisms of wood devolatilization. *Thermochim Acta* 429:133–141
- Branca C, Iannace A, Di Blasi C (2007) Devolatilization and combustion kinetics of quercus cerris bark. *Energy Fuels* 21:1078–1084
- Braun RL, Burnham AK (1987) Analysis of chemical reaction kinetics using a distribution of activation energies and simpler models. *Energy Fuels* 1:153–161
- Bridgwater AV (2003) Renewable fuels and chemicals by thermal processing of biomass. *Chem Eng J* 91:87–102
- Bridgwater AV, Meier D, Radlein D (1999) An overview of fast pyrolysis of biomass. *Organ Geochem* 30:1479–1493
- Caballero JA, Conesa JA, Font R et al (1997) Pyrolysis kinetics of almond shells and olive stones considering their organic fractions. *J Anal Appl Pyrol* 42:159–175
- Calonaci M, Grana R, Hemings Barker et al (2010) Comprehensive kinetic modeling study of bio-oil formation from fast pyrolysis of biomass. *Energy Fuels* 24:5727–5734
- Chen Y, Charpenay S, Jensen A et al (1998) Modeling biomass pyrolysis kinetics. *Proc Combust Inst* 27:1327–1334
- Database (2011) http://www1.eere.energy.gov/biomass/feedstock_databases.html

- Di Blasi C (1996) Kinetic and heat transfer control in the slow and flash pyrolysis of solids. *Ind Eng Chem Res* 35:37–46
- Di Blasi C (1998) Comparison of semi-global mechanisms for primary pyrolysis of lignocellulosic fuels. *J Anal Appl Pyrol* 47:43–64
- Di Blasi C (2008) Modeling chemical and physical processes of wood and biomass pyrolysis. *Prog Energy Combust Sci* 34:47–90
- Di Blasi C (2009) Combustion and gasification rates of lignocellulosic chars. *Prog Energy Combust Sci* 35:121–140
- Faravelli T, Pincirolì M, Pisano F et al (2001) Thermal degradation of polystyrene. *J Anal Appl Pyrol* 60:103–121
- Faravelli T, Frassoldati A, Migliavacca G et al (2010) Detailed kinetic modeling of the thermal degradation of lignins. *Biomass Bioenergy* 34:290–301
- Ferdous D, Dalai AK, Bej SK et al (2002) Pyrolysis of lignins: experimental and kinetic studies. *Energy Fuels* 16:1405–1412
- Fletcher TH, Kerstein AR, Pugmire RJ et al (1992) A chemical model of coal devolatilization: 3. Direct use of ¹³C NMR data to predict effects of coal type. *Energy Fuels* 6:414–431
- Hajaligol MR, Howard JB, Longwell JP et al (1982) Product compositions and kinetics for rapid pyrolysis of cellulose. *Ind Eng Chem Proc Des Dev* 21:457–465
- Hemings BE (2012) Detailed kinetic models for the thermal conversion of biomass. Ph.D. thesis Politecnico di Milano, Italy
- Hosoya T, Kawamoto H, Saka S (2009) Solid/liquid—and vapor-phase interactions between cellulose—and lignin-derived pyrolysis products. *J Anal Appl Pyrol* 85:237–246
- Howard JB (1981) Fundamentals of coal pyrolysis and hydrolysis. In: Elliot MA (ed) *Chemistry of coal utilization: second supplementary volume*. Wiley Interscience, New York, pp 665–784
- Jakab E, Faix O, Till F, Székely T (1995) Thermogravimetry/mass spectrometry study of six lignins within the scope of an international round robin test. *J Anal Appl Pyrol* 35:167–179
- Milosavljevic I, Suuberg EM (1995) Cellulose thermal decomposition kinetics: global mass loss kinetics. *Ind Eng Chem Res* 34:1081–1091
- Moghtaderi B (2006) The state-of-the-art in pyrolysis modelling of lignocellulosic solid fuels. *Fire Mater* 30:1–34
- Naik S, Goud VV, Rout PK et al (2010) Characterization of Canadian biomass for alternative renewable biofuel. *Renewable Energy* 35:1624–1631
- Niksa S (2000) Predicting the rapid devolatilization of diverse forms of biomass with bio-FLASHCHAIN. *Proc Combust Inst* 28:2727–2733
- Oasmaa A, Solantausta Y, Arpiainen V et al (2010) Fast pyrolysis bio-oils from wood and agricultural residues. *Energy Fuels* 24:1380–1388
- Phyllis (2011) The composition of biomass and waste. <http://www.ecn.nl/phyllis/>
- Pierucci S, Ranzi E (2008) A general mathematical model for a moving bed gasifier. In: Bertrand B, Xavier J (eds) *18th European symposium on computer aided process engineering*. Elsevier, pp 901–906
- Pitt GJ (1962) The kinetics of the evolution of volatile products from coal. *Fuel* 41:267–274
- Radlein D, Piskorz J, Scott DS (1991) Fast pyrolysis of natural polysaccharides as a potential industrial process. *J Anal Appl Pyrol* 19:41–63
- Radmanesh R, Courbariaux Y, Chaouki J et al (2006) A unified lumped approach in kinetic modeling of biomass pyrolysis. *Fuel* 85:1211–1220
- Ranzi E, Dente M, Goldaniga A et al (2001) Lumping procedures in detailed kinetic modeling of gasification, pyrolysis, partial oxidation and combustion of hydrocarbon mixtures. *Prog Energy Combust Sci* 27:99–139
- Ranzi E, Cuoci A, Faravelli T et al (2008) Chemical kinetics of biomass pyrolysis. *Energy Fuels* 22:4292–4300
- Raveendran K, Ganesh A, Khilar KC (1996) Pyrolysis characteristics of biomass and biomass components. *Fuel* 75:987–998

- Sensöz S, Can M (2002) Pyrolysis of pine (*Pinus Brutia* Ten.) chips: 1. Effect of pyrolysis temperatures and heating rate on the product yields. *Energy Sources Part A: Recovery Utilization Environ Eff* 24:347–355
- Shafizadeh F, Chin PPS (1977) Thermal deterioration of wood. In: Goldstein IS (ed) *Wood technology: chemical aspects*, vol 43. American Chemical Society, Washington DC, pp 57–81
- Simmons GM, Gentry M (1986) Particle size limitations due to heat transfer in determining pyrolysis kinetics of biomass. *J Anal Appl Pyrol* 10:117–127
- Sonobe T, Worasuwanarak N (2008) Kinetic analyses of biomass pyrolysis using the distributed activation energy model. *Fuel* 87:414–421
- Suuberg EM, Milosavljevic I, Oja V (1996) Two-regime global kinetics of cellulose pyrolysis: the role of tar evaporation. *Proc Combust Inst* 26:1515–1521
- Teng H, Lin HC, Ho JA (1997) Thermogravimetric analysis on global mass loss kinetics of rice hull pyrolysis. *Ind Eng Chem Res* 36:3974–3977
- Thurner F, Mann U (1981) Kinetic investigation of wood pyrolysis. *Ind Eng Chem Proc Des Dev* 20:482–488
- Tsamba AJ, Yang W, Blasiak W et al (2007) Cashew nut shells pyrolysis: individual gas evolution rates and yields. *Energy Fuels* 21:2357–2362
- Várhegyi G, Jakab E, Antal MJ (1994) Is the Broido-Shafizadeh model for cellulose pyrolysis true? *Energy Fuels* 8:1345–1352
- Várhegyi G, Antal MJ Jr, Jakab E et al (1997) Kinetic modeling of biomass pyrolysis. *J Anal Appl Pyrol* 42:73–87
- Várhegyi G, Szabó P, Antal MJ Jr (2002) Kinetics of charcoal devolatilization. *Energy Fuels* 16:724–731
- Várhegyi G, Czégény Z, Jakab E et al (2009a) Tobacco pyrolysis. Kinetic evaluation of thermogravimetric-mass spectrometric experiments. *J Anal Appl Pyrol* 86:310–322
- Várhegyi G, Chen H, Godoy S (2009b) Thermal decomposition of wheat, oat, barley, and *Brassica carinata* straws. A kinetic study. *Energy Fuels* 23:646–652
- Wang G, Li W, Li B et al (2008) TG study on pyrolysis of biomass and its three components under syngas. *Fuel* 87:552–558
- Wang S, Guo X, Wang K et al (2011) Influence of the interaction of components on the pyrolysis behavior of biomass. *J Anal Appl Pyrol* 91:183–189
- Westerhof RJM, Brilman DWF, van Swaaij WPM et al (2010) Effect of temperature in fluidized bed fast pyrolysis of biomass: oil quality assessment in test units. *Ind Eng Chem Res* 49:1160–1168
- White JE, Catallo WJ, Legendre BL (2011) Biomass pyrolysis kinetics: a comparative critical review with relevant agricultural residue case studies. *J Anal Appl Pyrol* 91:1–33
- Williams PT, Besler S (1996) The influence of temperature and heating rate on the slow pyrolysis of biomass. *Renewable Energy* 7:233–250
- World Energy Outlook (2010) Edition, International Energy Agency
- Zanzi R, Sjöström K, Björnbom E (2002) Rapid pyrolysis of agricultural residues at high temperature. *Biomass Bioenergy* 23:357–366

Part II
Obtaining Reliable Experimental Data to
Validate Models Under a Wide Range of
Experimental Conditions

Chapter 6

Speciation in Shock Tubes

Kenji Yasunaga and Robert S. Tranter

Abstract A shock tube is a device in which a shock wave is normally formed by the rupture of a diaphragm, which divides a gas at high pressure from a test section containing the species of interest at a lower pressure. The shock wave brings the test gas virtually instantaneously to a known high temperature and pressure, maintains that condition for a time and then is supplanted by an expansion wave which cools the sample rapidly. During this time, the test gas can be studied by continuous sampling, for example to a time-of-flight mass spectrometer or alternatively sampled at the end of process by gas chromatography or other appropriate analytical techniques. Here, we discuss both methodologies and show with examples the benefits of both approaches.

6.1 Introduction

Complex phenomena such as ignition delay times and laminar flame speeds are useful measures of the reactivities of fossil or bio-fuels and are therefore widely used for the validation of detailed chemical kinetic models (Simmie 2003). However, measurements of the reactants, intermediates and products formed during a pyrolytic or combustion event are much more valuable since they provide direct evidence of the chemical changes taking place. Thus, ‘speciation’ is the subject of this chapter, and it will deal with two different approaches to this end.

K. Yasunaga (✉)

Department of Applied Chemistry, National Defense Academy, 1-10-20 Hashirimizu,
Yokosuka, Japan

e-mail: yasunaga@nda.ac.jp

R. S. Tranter (✉)

Chemical Sciences and Engineering, Argonne National Laboratory, 9700 S. Cass Ave.
Argonne, Argonne, IL 60439, USA

e-mail: Tranter@anl.gov

One can categorize shock tubes into two distinct classes; the first a single pulse shock tube can produce speciation data at the end of shock heating whilst the second, more conventional type, can produce time dependent speciation. Time-dependent speciation can be obtained by coupling the shock tube to a mass spectrometer, typically a time-of-flight, which can separate and quantify ions at a high repetition rate. Nonintrusive optical diagnostics are also employed but are not able to identify and quantify more than a few species at this moment of time and are not considered here. However, considerable progress is being made on multispecies optical diagnostics (Davidson et al. 2011).

6.2 Single Pulse Shock Tube

Single pulse shock tubes are designed to heat a gas mixture for a constant period, the dwell or residence time, at a high temperature, the reflected shock temperature, and then rapidly quench the hot gases back to room temperature preserving the high temperature composition. The resulting gases are then sampled and analyzed.

This combination of single pulse shock tubes and gas sampling has been used to investigate a large number of species some illustrative examples of which include halogen compounds (Simmie et al. 1969; Tsang and Lifshitz 1999; Rajakumar et al. 2002), oxygenates (Herzler et al. 1997; Lifshitz and Ben Hamou 1983; Hidaka et al. 1989) and aromatic hydrocarbons (Lifshitz et al. 2004; Sivaramakrishnan et al. 2006). In each experiment profiles of species concentrations with respect to temperature and pressure are obtained. Often kinetic data can be extracted and frequently the data are used to also develop and validate complex mechanisms. For instance, species profiles obtained for oxygenates (Yasunaga et al. 2010, 2012) are being utilized to validate detailed chemical kinetic mechanisms. Some of the species encountered have very low vapor pressures which renders sampling problematic because of condensation and subsequent loss of sample. So heating systems for the mixture preparation section, the manifold, the shock tube itself and the sampling system have been constructed to circumvent this problem for single pulse shock tubes (Lifshitz et al. 2009).

Single pulse shock tubes are currently operating that collectively span an enormous range of reaction pressures from subatmospheric to 1,000 bar. Typically, the shock tubes are operated with reaction temperatures $<2,500$ K with the upper limit being defined by rate of reaction and the residence time, typically 1–3 ms, which is a function of the shock tube geometry. The analytical techniques, primarily gas chromatography, used in single pulse shock tube work are generally very sensitive and the initial concentration of reagents introduced into the shock tube normally fall in the range 10 ppm to 1 % with concentrations in the 50–200 ppm range being the norm.

6.2.1 Principle of Single Pulse Shock Tube

The single pulse shock tube commonly used is a magic-hole-type shock tube (Hidaka et al. 1985; Lifshitz et al. 1963). These tubes are composed of high- and low-pressure sections and a dump tank. The function of the dump tank is to ‘swallow’ the reflected shock wave and prevent multiple re-heating of the test gases.

A schematic diagram of a single pulse shock tube is shown in Fig. 6.1. Operation of a single pulse shock tube involves filling the low pressure section and dump tank to the same pressure, pressurizing the high pressure section and bursting the diaphragm. Sample gas is collected through a sampling port after shock heating for analysis. Two methods are commonly used. In the first method, gases are simply withdrawn through an orifice located in the center of the end wall of the driven section. In the second method, a gas collection pipe is pushed through a port in the sidewall of the driven section near the endwall to the center of the shock tube before collection of a sample begins. This later design has been chosen to avoid collecting test gas from the side wall boundary layer that forms behind the shock wave because this has not experienced the full temperature behind the reflected shock and consequently has not undergone the same chemical change as the bulk gas mixture itself. A typical side wall sample port is shown in Fig. 6.2.

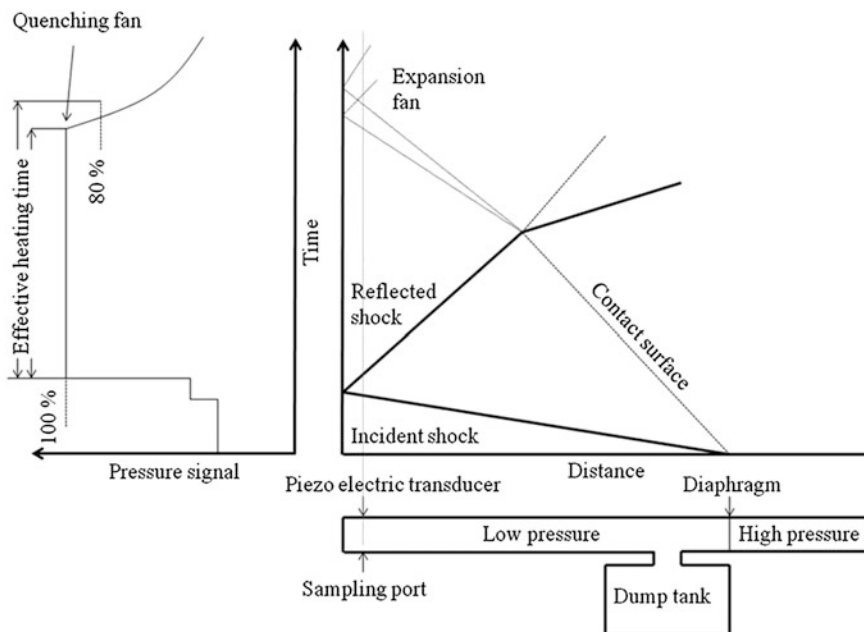
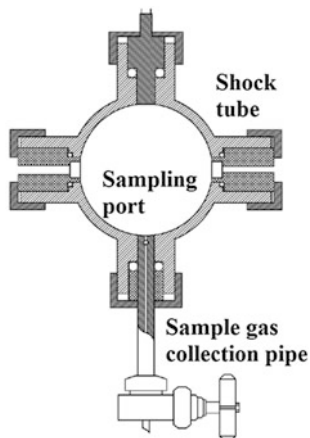


Fig. 6.1 Schematic diagram of single-pulse shock tube

Fig. 6.2 Schematic diagram of sample port

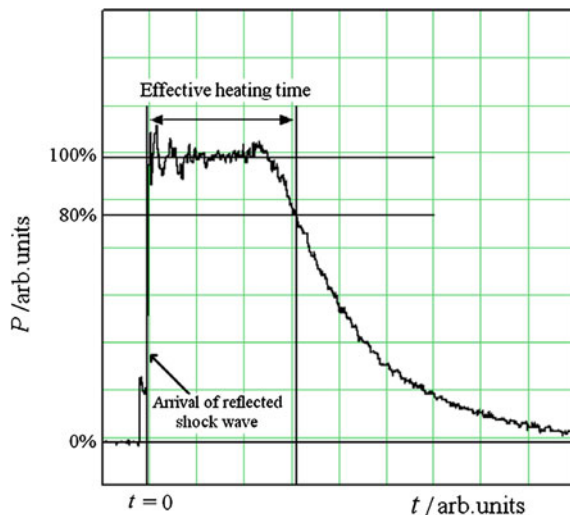


The temperature behind the incident shock wave is commonly very low, and the timescale is insufficient to activate the chemical reaction compared to that behind the reflected shock wave, so the sample gas is effectively heated just once. Pressure remains constant for a certain period after the arrival of the reflected shock wave, and then the pressure rapidly decreases due to the arrival of the quenching fan. A typical pressure trace is shown in Fig. 6.3.

From the equation of adiabatic expansion which relates the pressure, p , at time t and the reflected shock pressure p_5 to the reflected shock temperature T_5 and the temperature T during the cooling phase we have:

$$p/p_5 = (T/T_5)^{\{\gamma/(\gamma-1)\}}$$

Fig. 6.3 A typical pressure profile with the definition of effective heating time



And the rate of change of temperature is described by:

$$(dT/dt) = \{(\gamma - 1)/\gamma\}(T_5/p_5)(dp/dt)$$

where γ is ratio of specific heats after shock heating behind the reflected shock wave. The cooling rate can therefore be estimated from the slope of pressure versus time. Typical cooling rates of 10^5 – 10^6 K s⁻¹ reported (Lifshitz et al. 1963; Hidaka et al. 1985) are so large that the chemical reactions are frozen very quickly; however, some reactions do persist during this cooling phase. In order to account for this we define here an effective reaction time as the time interval between shock wave arrival at the end-plate and until such time as the reflected shock pressure has decreased to 80 % of its maximum value, Fig. 6.3.

6.2.2 Data Acquisition

Most single pulse shock tubes are coupled to one or more gas chromatographs to determine the concentrations of reactants and products as a result of shock heating. However, sometimes samples are withdrawn into sample vessels for later analysis or to utilize analytical instruments at a different facility. A variety of detectors such as thermal conductivity, flame ionization, electron capture, mass spectrometric, and others can be mounted on the gas chromatographs allowing most organic species to be detected.

The calibration methods to estimate the concentrations of reactant and products are introduced below. The sensitivities of the detector to each species is determined by developing calibration curves of the detector response, peak area (or height), to known concentrations of the species. These sensitivities are normalized against standard species which helps minimize error in calibration. Possible candidates for standard species include the diluent gases, usually argon or nitrogen. The merit of this method is that it does not require a perfect mass balance. However, this method is restricted to the case in which the diluent gases are capable of being detected. One of the authors commonly uses a gas chromatograph with a TCD, which can detect reactants, products and argon. Similar techniques can be employed with other detectors, which are not sensitive to inert gases by selecting appropriate standard molecules. The sensitivity, S , against argon as an internal standard is calculated for species X in a series of calibration experiments in which measured area ratios are related to known concentration ratios as:

$$S = (A_X/A_{Ar}) \times ([Ar]/[X])$$

where A is the peak area and the square brackets denote concentration. The concentrations of species, $[X]$, as a result of shock heating are estimated using the sensitivity together with measured area ratios and the known concentration of argon:

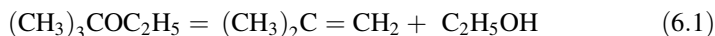
$$[X] = (1/S) \times (A_X/A_{Ar}) \times [Ar]$$

Typically, a 95–105 % mass balance of chemical species is obtained using this method provided that the sample is not adsorbed or condensed or polymerizes during the transfer process.

6.2.3 Validation of Single Pulse Shock Tube

The data produced by a single pulse shock tube experiment are a little unusual in that one obtains a distribution of species concentrations after some reaction time at a particular temperature and pressure. Due to a number of constraints, it is difficult to vary the reaction time. Thus, an experimental dataset consists of points spanning a wide range of temperature, a small range of reaction times and a small pressure range. For a simple unimolecular reaction, it is possible to recover accurate rate coefficients from these data by simulating each experiment. For more complex reactions, it is still possible to recover kinetic data although the datasets may be more useful as targets for model development. To validate the single pulse shock tube technique and show that reliable kinetic data can be obtained Tsang and Lifshitz (2001) compared the results of single pulse shock tube experiments with those from other reactors. For the validation, they selected a series of unimolecular decomposition reactions, which include direct formation of stable products to reduce the complexity of chemical reactions.

Ethyl *tert*-butyl ether (ETBE) is a good example of a suitable validation molecule because it decomposes mainly via a molecular elimination reaction under single pulse shock tube conditions:



producing stable species directly. The kinetics of this process was measured by Yasunaga et al. (2008) using both a single pulse shock tube coupled to a GC and a conventional shock tube with UV absorption spectroscopy. The results of single pulse shock tube experiments are shown in Fig. 6.4 together with a computer simulation. The rate constant of $1.7 \times 10^{14} \exp(-254,000 \text{ J mol}^{-1}/RT) \text{ s}^{-1}$ for reaction (6.1) was estimated to explain the decomposition of ETBE and production of isobutene and ethanol.

The rate of reaction (6.1) was also estimated by monitoring the time-dependent concentration of isobutene and ETBE at high dilution to reduce the influence of secondary reactions. A typical absorbance profile for ETBE decomposition with simulation lines at 195 nm is shown in Fig. 6.5. The main absorbers at 195 nm in the ETBE pyrolysis system are ETBE and isobutene. After the arrival of the reflected shock wave, the absorbance profile shows rapid increases due to the absorption by ETBE, then gradually grows because isobutene is produced through the reaction (6.1). The influence of secondary reactions is so small that absorbance profiles can be approximately reproduced using simple first order equations, as

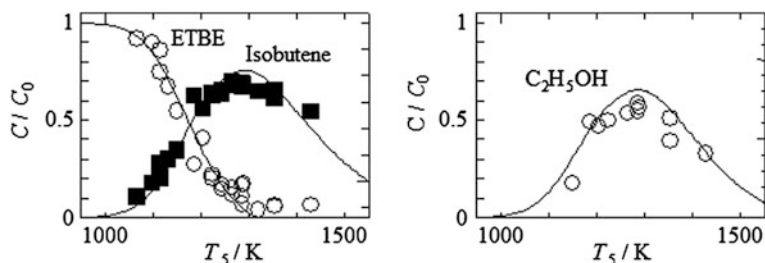


Fig. 6.4 Species concentration profiles for the pyrolysis of 3 % ETBE diluted in Ar at $P_5 = 1.9\text{--}3.4$ atm, effective heating time = 1.1–1.4 ms, lines simulation. C_0 denotes the initial concentration of ETBE, C those of ETBE and products as a result of shock heating

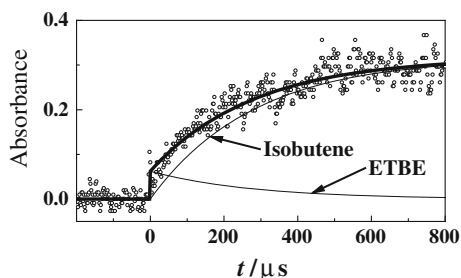


Fig. 6.5 A typical absorbance profile in ETBE pyrolysis at 195 nm; shock conditions, 0.0167 % ETBE diluted in Ar, $T_5 = 1,231$ K, $P_5 = 8.1$ atm

shown below, together with the Lambert–Beer law which relates concentrations and molar absorptivity:

$$[(\text{CH}_3)_3\text{COC}_2\text{H}_5] = [(\text{CH}_3)_3\text{COC}_2\text{H}_5]_0 \times \exp\{-(k_i + k_o)t\}$$

$$[(\text{CH}_3)_2\text{C} = \text{CH}_2] = k_i/(k_i + k_o) [(\text{CH}_3)_3\text{COC}_2\text{H}_5]_0 \times \exp[1 - \exp\{-(k_i + k_o)t\}],$$

where k_i and k_o signify the rate constants for the reaction producing isobutene and other products, respectively. The estimated rate constants (open circles), k_i , are shown in Fig. 6.6 together with the rate expression, $1.7 \times 10^{14} \exp(-254 \text{ kJ mol}^{-1}/RT) \text{ s}^{-1}$, adopted to explain species concentration profiles. The rate expression estimated from species concentration profiles agrees well with those estimated by UV absorption spectroscopy.

6.2.4 Reactions of Oxygenates and Aromatic Hydrocarbons

The principle, data acquisition, and validation of single pulse shock tube are described above. The concentration profiles are more useful to examine reaction

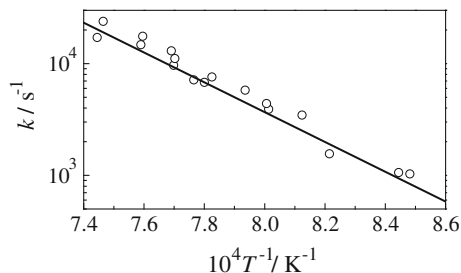
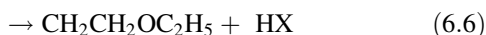
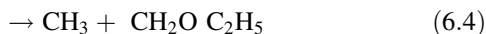
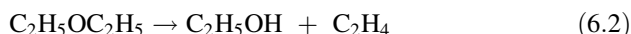


Fig. 6.6 Arrhenius plots for k_i ; symbols are the rates estimated from UV absorption at 195 nm over pressure range between 2.5 and 8.9 atm, *line* is rate expression, $1.7 \times 10^{14} \exp(-254.0 \text{ kJ mol}^{-1}/RT) \text{ s}^{-1}$ adopted to explain gas chromatographic results in single pulse shock tube

mechanisms because they reflect lots of information for reactions and their rate constants. Diethyl ether (DEE) (Yasunaga et al. 2010) mainly decomposes via unimolecular decomposition and hydrogen abstraction by radicals under shock tube conditions. Some of important reactions to explain the reactivity of DEE at high temperature are listed below:



where X indicates atoms and radicals like H, O, CH₃, and OH. Computer simulation can capture the observed concentration profile of C₂H₅OH when the rate constant of reaction (6.2) is described properly, because this is the sole reaction producing C₂H₅OH. Atoms and radicals abstract hydrogen atoms from DEE to produce CH₃CHOC₂H₅ and CH₂CH₂OC₂H₅. CH₃CHO and C₂H₅, C₂H₄ and C₂H₅O are produced from the uni-molecular decomposition of CH₃CHOC₂H₅ and CH₂CH₂OC₂H₅, respectively. The concentration of CH₃CHO includes the information about the rate of reaction (6.5), because CH₃CHOC₂H₅ is the principal producer of CH₃CHO. The concentration of DEE is sensitive to the total rate of DEE decomposition, which means that it has sensitivity to the five reactions listed above. As explained here, concentration profiles are so useful to examine the reaction mechanism that this method is applied to oxygenates and aromatic hydrocarbons whose reactivity are still unclear.

Polyaromatic hydrocarbons (PAH) are assumed as a soot precursor. Hydrogen abstraction/acetylene addition is a well-known (Bockhorn et al. 1983; Frenklach et al. 1985; Frenklach and Wang 1991; Wang and Frenklach 1997) mechanism of

the growth of PAH. The yields of acenaphthylene and naphthalene as a result of the reactions between naphthyl radicals and acetylene were measured in a single pulse shock tube (Lifshitz et al. 2009). The rate parameters estimated from ab-initio calculations explained these yields reasonably. Single pulse shock tube studies have also been conducted at high pressures, up to 50 bar, to investigate PAH formation and have revealed the importance of addition of cyclic radicals and molecules to molecular growth (Comandini and Brezinsky 2012).

The above examples demonstrate the use of single pulse shock tubes to investigate reactivity of oxygenates and mechanisms of PAH formation. However, they only scratch the surface of the detailed insights single pulse shock tube studies give to complex reaction mechanisms. With the very broad experimental range and ability to detect multiple species, single pulse shock tubes are a valuable tool to investigate fundamental chemical kinetic problems and provide comprehensive datasets for the development of complex mechanisms.

6.3 Time-of-Flight Mass Spectrometry and Shock Tubes

Time-of-flight mass spectrometry (TOF-MS) is a valuable although somewhat niche tool in shock tube research that leads to greater understanding of combustion mechanisms through ‘real-time’ measurement of gas composition and identification of products and intermediates. At the time of writing, there are three shock tube ST/TOF-MS apparatuses in routine use (Tranter et al. 2007; Dürrstein et al. 2011a, b) all of which are evolutions of the instrument of Bradley and Kistia-kowsky (1961) which was developed in the early 1960s. Until his retirement in 2000, Kern (see Kern et al 2001 and references therein) produced the majority of ST/TOF-MS data related to combustion research including the important observation that recombination of propargyl radicals leads to the formation of benzene (Wu and Kern 1987); now considered one of the primary steps to the production of PAH in flames.

All current ST/TOF-MS experiments are conducted behind reflected shock waves and gases continually elute from the reaction zone via a small orifice (typically <0.3 mm) in the end-wall of the driven section into a chamber maintained at low pressure. Conditions are selected so that the eluting gases form a supersonic jet and the fast expansion rapidly cools the gases and quenches reactions thereby preserving the composition as it was in the shock heated reaction zone. The jet is directed into the ionization zone of the TOF-MS, with or without first being formed into a molecular beam with a skimmer, and a pulsed ionization source generates packets of ions that are mass analyzed providing time/concentration data. An example ST-TOF-MS interface is shown in Fig. 6.7.

Most ST/TOF-MS experiments are conducted at reflected shock pressures less than a few bar with the primary limitation being the need to keep a sufficiently low pressure, $<3 \times 10^{-5}$ Torr, in the ion source of the mass spectrometer while maintaining adequate signal levels. The experiments typically have an observation

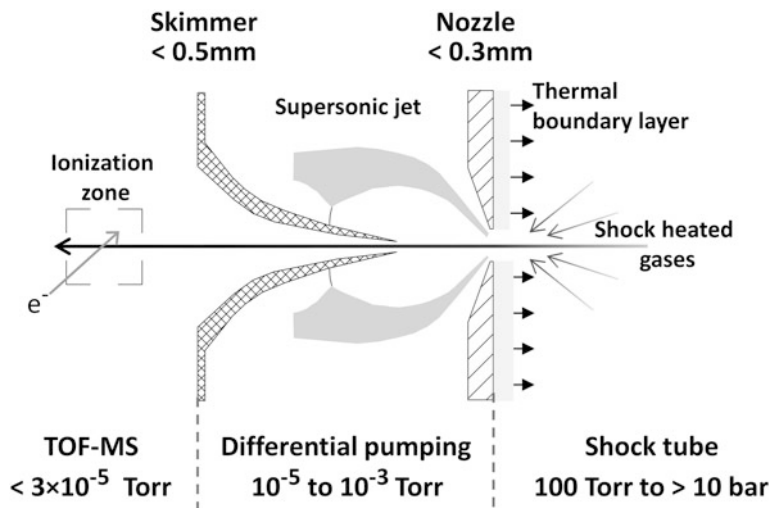


Fig. 6.7 Sketch of a differentially pumped interface between a shock tube and the ion source of a mass spectrometer. The mass spectrometer can be placed either on-axis with the shock tube or orthogonal to it. The skimmer may be removed and the nozzle moved to within 3 mm of the ionization zone

period of 1–2 ms during which mass spectra are acquired before the arrival of the shock wave and after reflection of the shock wave from the driven section end wall. To obtain adequate signal levels, the initial reagent concentrations are normally in the range 0.5–5 %.

All current ST/TOF-MS setups create ions with electron impact (EI) ionization sources which can be pulsed up to 150 kHz giving a mass spectrum every 6.67 μ s. These sources can generally be tuned over a wide range of ionization energies although for ST/TOF-MS experiments they are typically not used below 28 eV due to insufficient signal intensity at lower energies. However, even at quite low energies EI ionization is rather brutal and tends to fragment molecules extensively making assignment of mass spectra challenging when multiple species are ionized simultaneously; a normal occurrence in ST/TOF-MS experiments. The complexity of spectra obtained is illustrated by experiments on the pyrolysis of ethylene glycol vinyl ether (EGVE), Fig. 6.8, where the fragments of EGVE also correspond to parent and fragment ions of many products and several products also share fragments. However, even for such complex spectra key mechanistic clues can be obtained (Yang et al. 2011).

Coupling a shock tube to a TOF-MS and obtaining reliable high quality data is not a trivial task and the challenges of building and running an early ST/TOF-MS are charmingly described by Moulton (1964). An excellent discussion of the ST/TOFMS technique is given in Kern et al. (2001) including details of calibration methods. A discussion of modern instruments with particular emphasis on sampling is available in Tranter et al. (2007) and a compact, adjustable interface between the shock tube and mass spectrometer is presented in Dürrstein et al. (2011b).

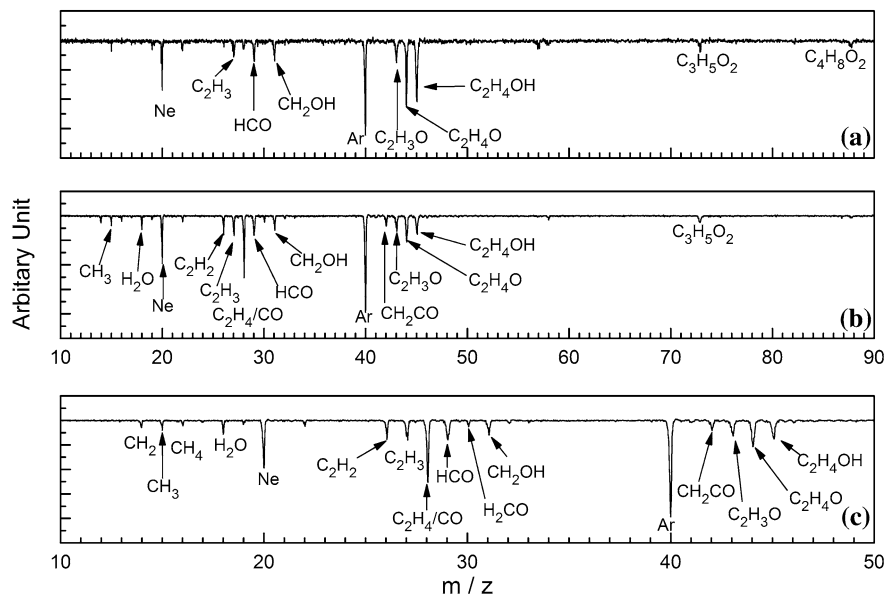


Fig. 6.8 Electron impact, 30 eV, mass spectra of the pyrolysis of ethylene glycol vinyl ether in a shock tube ($T_5 = 1,217$ K and $P_5 = 913$ Torr). Argon was added as an internal standard. **a** Pre-shock i.e. only EGVE, and the bath gas neon. **b** ~ 100 μ s after reflection of the shock wave. **c** Expansion of a portion of **b**. Note that many possible products share the same fragments, e.g., H_2CO fragments to HCO in the ion source and HCO is also formed from fragmentation of EGVE. Reproduced by permission of the PCCP owner societies from Yang et al. (2011)

The above text broadly outlines the main features of ST/TOF-MS experiments but what may not be apparent is that these apparatuses incorporate many conflicting demands and a functioning ST/TOF-MS is the result of many compromises. Some of the main challenges related to effects of pressure and sampling are briefly discussed below although they are covered in detail in the above references.

The most obvious challenge is that the pressures in the shock tube are orders of magnitude greater than the operating pressures of a TOF-MS. One method of addressing this is to use a differentially pumped molecular beam sampling (MBS) interface such as shown schematically in Fig. 6.7. With this arrangement, less demands are placed on the vacuum pumps and relatively large, flat (~ 0.3 mm orifice) nozzles can be used with reflected shock pressures up to ~ 3 – 4 bar. As shown schematically in Fig. 6.7 a cold thermal boundary layer, TBL, is established following reflection of the shock wave and grows back into the shock heated zone. Gases from the shock heated zone are withdrawn through this layer. Voldner and Trass (1980) have shown that gases from the TBL are confined to the outer portion of the jet, at short times, and that the time taken for the TBL to engulf the sampled gases scales with the 4th power of the nozzle diameter. Thus, large diameter nozzles can significantly increase the sample time, and they are less susceptible to

blockage, a problem in pyrolytic studies. However, the orifice diameter must be sufficiently small that gases escaping through it do not create significant flow within the shock tube (Tranter et al. 2007). An additional advantage of the flat nozzle shown in Fig. 6.7 is that it is simple to manufacture. The benefits of a differentially pumped MBS have to be weighed against the two principal drawbacks. Firstly, signals can be weak particularly if the separation between the nozzle and skimmer is more than a few nozzle orifice diameters. Secondly, the nozzle and skimmer must be precisely aligned to ensure that only gases from the reaction zone in the shock tube are sampled and that none of the cold gases from the TBL enter the TOF-MS.

If the flat nozzle is replaced with a small conical nozzle, ~ 1 mm high and 1 mm base diameter, then sampling from the TBL is avoided, at least for about 1 ms when the TBL becomes thick enough to engulf the nozzle. Such nozzles are relatively difficult to manufacture and spatial constraints make it difficult to obtain the optimum separation between nozzle and skimmer while maintaining good flow through the nozzle. A commonly used configuration with conical nozzles dispenses with the skimmer entirely. Here the advantage of differential pumping is lost and to prevent over pressurizing the TOF-MS the nozzle orifices are reduced, <0.1 mm. These smaller nozzles are more prone to blockage although judicious selection of reagents and concentrations can minimize this. If the nozzle is placed within 2–3 mm of the ionization source, then good signal levels can be obtained.

A further consideration is the orientation of the TOF-MS relative to the shock tube. In apparatuses that do not incorporate a skimmer they are normally co-axial which simplifies positioning the nozzle close to the ion source. However, both neutral species and ions will enter the TOF-MS requiring additional pumping capacity on the flight tube of the TOF-MS to maintain sufficiently low pressures in the vicinity of the detector ($<1 \times 10^{-6}$ Torr). If the TOF-MS is placed orthogonal to the flight tube then ions are extracted perpendicular to the path of the molecular beam and neutrals pass directly through the ion source and are evacuated from the chamber. With this arrangement maintaining good vacuum in the TOF-MS is simple but careful consideration has to be given to ion extraction to ensure efficient extraction. In the author's opinion, it is quite simple to build an apparatus that accommodates both arrangements and it is fairly easy to change the alignment of shock tube and TOF-MS to suit a particular experiment.

A final consideration of the effect of pressure in ST/TOF-MS experiments is that there is a large step change in pressure in the shock tube following reflection of the shock wave. Consequently, there is a corresponding increase in pressure in the ion source which results in the generation of more ions and stronger signals, Fig. 6.9. Thus, if one simply plots peak area, which is proportional to concentration, against reaction time meaningless kinetic data will be obtained. To compensate for the change in signal level with changing pressure a nonreactive standard, either the bath gas or often argon, is used to scale peak areas for each ionization/analysis cycle, see Kern et al. (2001) for details.

The following discussion focuses on the use of ST/TOF-MS experiments to investigate elementary reactions in the early stages of PAH formation. In

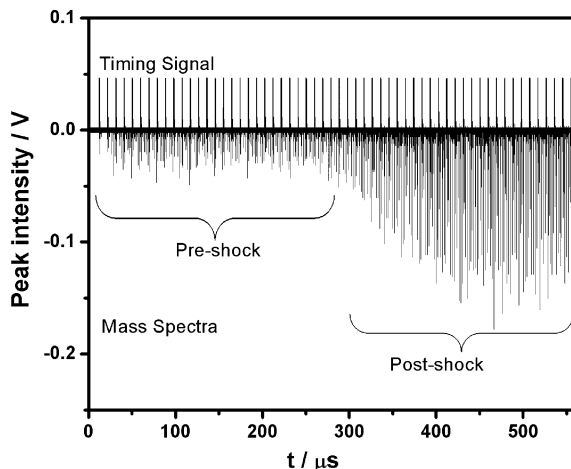


Fig. 6.9 ST/TOF-MS data obtained at an ionization cycle frequency of 105 kHz. $P_5 = 558$ Torr, $T_5 = 1,360$ K. The downward spikes, labeled as mass spectra, show the preshock as well as the postshock data. The upward spikes show the timing signals used to create ion packets in the molecular beam and extract them into the TOF-MS. Reprinted with permission from Tranter et al. (2007). Copyright 2007, American Institute of Physics

particular, the technique has proved most valuable in combination with other shock tube experiments such as laser schlieren densitometry and single pulse where complementary data are obtained. Often the experiments are also performed in conjunction with high level theoretical investigations to fully elucidate multi-channel reactions. Earlier in this chapter, the use of single pulse shock tubes to study PAH formation was briefly discussed. The following discussion illustrates the benefits of using multiple techniques to study complex problems such as PAH formation. For instance, the ST/TOFMS methods yield information about radical species and time histories that cannot be obtained by single pulse methods. But the single pulse methods provide more details about stable species and over a broader experimental range than the ST/TOFMS can.

6.3.1 Formation of Polyaromatic Hydrocarbons

Determining reaction mechanisms for the formation of the building blocks of soot from small molecules and radicals in the gas phase has been an active topic of experimentalists and theoreticians. Currently, one of the main accepted mechanisms for formation of the first aromatic ring in flames is the association of two propargyl radicals followed by isomerization of the linear C_6H_6 molecules. This key step was first proposed by Kern (Wu and Kern 1987) from ST/TOF-MS experiments on allene dissociation. Although, later detailed theoretical studies (see

Miller and Klippenstein 2003 and references therein) revealed the complex sequence of isomerization steps that convert the linear adducts to benzene. In a combustion environment, a hydrogen atom can easily be abstracted from benzene by a number of radicals to give the phenyl, C_6H_5 , radical, a key species in soot production. Phenyl radicals are quite stable and recombination could be competitive with other growth reactions such as addition of acetylene.

Earlier experimental studies considered biphenyl to be the sole product of phenyl self-reaction, (Heckmann et al. 1996). However, a mechanism based on this suggestion could not simulate shock tube/laser schlieren densitometry (ST/LS) experiments on phenyl self-reaction (Tranter et al. 2010). A weakness of the ST/LS technique is that it measures a global property, the density gradient, and one has to infer the chemistry through simulation of the data. ST/TOF-MS, however, directly identifies products and intermediates and complements the ST/LS experiments by providing key mechanistic information.

Results from ST/TOF-MS experiments on phenyl recombination with phenyl iodide as the precursor are shown in Fig. 6.10 and were a key part in understanding the complex nature of phenyl radical association. The upper panel shows a pre-shock mass spectrum of the reagent mixture containing phenyl iodide dilute in neon with a little argon as an internal standard, see Tranter et al. (2010) for details. The lower panel shows a mass spectrum from the reacting mixture. Clearly seen are m/z 154, biphenyl, and m/z 76 and 78, *o/m/p*-benzynes and benzene, respectively. The formation of *o/m/p*-benzynes simultaneously with benzene indicates that two phenyl radicals not only add to give biphenyl but also undergo

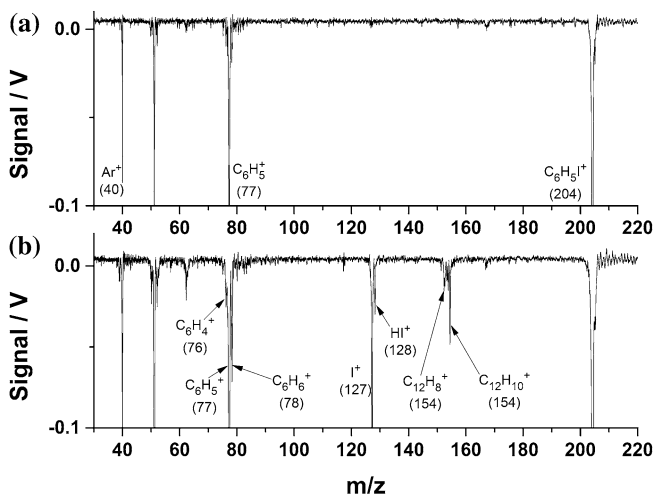


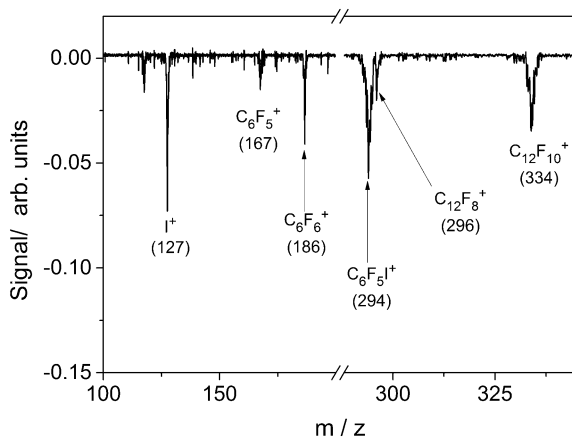
Fig. 6.10 TOF-MS from the dissociation of iodobenzene. Conditions: 2% C_6H_5I /3% Ar/95% Ne; $T_5 = 1,239$ K; $P_5 = 632$ Torr; ~ 250 μs after reflection of the shock wave. Reprinted (adapted) with permission from Tranter et al. (2010). Copyright 2010 American Chemical Society

disproportionation. While no attempt was made to extract kinetic data from the ST/TOFMS experiments, the mass spectra revealed new mechanistic paths which, when included in a model, provided good simulations of the ST/LS data. Furthermore, from the ST/LS results, rate coefficients and branching ratios for the recombination and dissociation reactions could be obtained, which were in excellent agreement with the theoretical predictions of Harding and Klippenstein (Tranter et al. 2010). It is particularly significant and surprising that at combustion temperatures the branching ratio ($k_{\text{dis}}/k_{\text{rec}}$) to *o/m*-benzynes is ~ 0.5 suggesting that the role of benzyne radicals in PAH growth is much more significant than previously thought. Later, ST/TOF-MS studies (Dürstein et al. 2011a) arrived at similar conclusions. Recently, single pulse shock tube experiments from Brezinsky's laboratory (Comandini et al. 2012) have confirmed the importance of *o*-benzyne in PAH growth.

Disproportionation/recombination should be quite general in association reactions of aromatic radicals and may also be a significant route for growth of halo-substituted aromatics. In Fig. 6.11 a mass spectrum from ST/TOF-MS experiments with perfluoriodobenzene, $\text{C}_6\text{F}_5\text{I}$, is shown (Tranter 2013). These experiments are analogous to those with $\text{C}_6\text{H}_5\text{I}$ and examine the self-reaction of perfluorinated phenyl radicals. The mass spectra in Figs. 6.10b and 6.11 are essentially identical apart from the increase in mass due to fluorine substitution. *o/m/p*- C_6F_4 radicals were not observed most likely because of low concentrations of these species. However, the peak at m/z 296, C_{12}F_8 , can only come from recombination of two perfluorobenzyne radicals, compare. m/z 152 in Fig. 6.10b (Tranter et al. 2010).

A natural extension of the above experiments is to study dissociation and recombination of *o*-benzyne, the dominant C_6H_4 radical, by the ST/LS and ST/TOF-MS techniques (Tranter et al. 2012). For $T > 2,000$ K fluorobenzene dissociates by HF elimination, Fig. 6.12, in ST/LS experiments to give *o*-benzyne. These temperatures are also sufficient to dissociate *o*-benzyne radicals which primarily yield C_2H_2 and C_4H_2 (Zhang et al. 2007; Xu et al. 2007).

Fig. 6.11 TOF-MS from the dissociation of perfluoriodobenzene. Conditions: 2% $\text{C}_6\text{F}_5\text{I}$ /2% Ar/95% Ne; $T_5 = 1,639$ K; $P_5 = 734$ Torr; ~ 200 μs after the reflection of the shock wave



slow dissociation of *o*-benzyne. Ultimately, it was concluded that *o*-benzyne is sufficiently stable that at lower temperature end of the ST/LS experiments it reacts preferentially with the parent molecule rather than decomposing, Fig. 6.12, providing an additional route to C₆H₂ molecules.

6.4 Conclusion

The methodology of using a single pulse shock tube with gas sampling is discussed. This simple method has been in use for more than a half century, and is still capable of producing useful speciation data for compounds undergoing pyrolysis and/or oxidation such as oxygenates and PAH.

This chapter also gives a brief overview of the benefit of ST/TOF-MS experiments and why they are worth pursuing despite the many challenges. It is the only technique that can measure all the hydrocarbon and oxygenate intermediates, products and radicals simultaneously in a shock tube experiment in real time. The current implementations of ST/TOF-MS with electron impact ionization are limited by fragmentation in the ion source although even when the fragmentation is severe useful mechanistic data can be obtained (Yang et al. 2011). Although kinetic data can be obtained from ST/TOF-MS experiments (Giri 2011; Giri et al. 2008), the real strength of the technique is identifying intermediates and their time evolution. Coupling a shock tube with selective photoionization by VUV radiation and MS is the next logical challenge for experimentalists.

Acknowledgments RST gratefully acknowledges support from the Office of Basic Energy Sciences, Division of Chemical Sciences, Geosciences, and Biosciences, U.S. Department of Energy, under contract number DE-AC02-06CH11357.

References

- Bockhorn H, Fetting F, Wenz HW (1983) Investigation of the formation of high molecular hydrocarbons and soot in premixed hydrocarbon-oxygen flames. *Ber Bunsen Ges Phys Chem* 87:1067–1073
- Bradley JN, Kistiakowsky GB (1961) Shock wave studies by mass spectrometry. I. Thermal decomposition of nitrous oxide. *J Chem Phys* 35:256–263
- Comandini A, Brezinsky K (2012) Radical/ π -bond addition between *o*-Benzyne and cyclic C-5 hydrocarbons. *J Phys Chem A* 116:1183–1190
- Davidson DF, Hong Z, Pilla GL et al (2011) Multi-species time-history measurements during *n*-dodecane oxidation behind reflected shock waves. *Proc Combust Inst* 33:151–157
- Dürstein SH, Olzmann M, Aguilera-Iparraguirre J et al (2011a) The phenyl+phenyl reaction as pathway to benzyne: an experimental and theoretical study. *Chem Phys Lett* 513:20–26
- Dürstein SH, Aghsaee M, Jerig L et al (2011b) A shock tube with a high-repetition-rate time-of-flight mass spectrometer for investigations of complex reaction systems. *Rev Sci Instrum* 82:084103
- Frenklach M, Wang H (1991) Detailed modeling of soot particle nucleation and growth. *Proc Combust Inst* 23:1559–1566

- Frenklach M, Clary DW, Gardiner WC et al (1985) Detailed kinetic modeling of soot formation in shock-tube pyrolysis of acetylene. *Proc Combust Inst* 20:887–901
- Giri BR, Tranter RS (2007) Dissociation of 1,1,1-trifluoroethane behind reflected shock waves: shock tube/time-of-flight mass spectrometry experiments. *J Phys Chem A* 111:1585–1592
- Giri BR, Kiefer JH, Xu H et al (2008) An experimental and theoretical high temperature kinetic study of the thermal unimolecular dissociation of fluoroethane. *Phys Chem Chem Phys* 10:6266–6273
- Heckmann E, Hippler H, Troe J (1996) High temperature reactions and thermodynamic properties of phenyl radicals. *Proc Combust Inst* 26:543–550
- Herzler J, Manion AJ, Tsang W (1997) Single-pulse shock tube studies of the decomposition of ethoxy compounds. *J Phys Chem A* 101:5494–5499
- Hidaka Y, Shiba S, Takuma H, Suga M (1985) Thermal decomposition of ethane in shock waves. *Int J Chem Kinet* 17:441–453
- Hidaka Y, Oki T, Kawano H, Higashihara T (1989) Thermal decomposition of methanol in shock waves. *J Phys Chem* 93:7134–7139
- Kern RD, Singh HJ, Jhang Q (2001) Mass spectrometric methods for chemical kinetics in shock tubes. In: Ben-Dor G, Igra O, Lifshitz A (eds) *Handbook of shock waves*, vol 3. Academic Press, New York
- Lifshitz A, Ben Hamou H (1983) Thermal reactions of cyclic ethers at high temperatures. I. Pyrolysis of ethylene oxide behind reflected shocks. *J Phys Chem* 87:1782–1787
- Lifshitz A, Bauer SH, Resler EL (1963) Studies with a single pulse shock tube. The thermal cis → trans isomerization of 2-butene. *J Chem Phys* 38:2056–2063
- Lifshitz A, Suslensky A, Tamburu C et al (2004) Thermal decomposition, isomerization and ring expansion in 2-methylindene. Single pulse shock tube and modeling study. *J Phys Chem A* 108:3430–3438
- Lifshitz A, Tamaburu C, Dubnikova F (2009) Reactions of 1-naphthyl radicals with acetylene. Single-pulse shock tube experiments and quantum chemical calculations. Differences and similarities in the reaction with ethylene. *J Phys Chem A* 113:10446–10451
- Miller JA, Klippenstein SJ (2003) The recombination of propargyl radicals and other reactions on a C₆H₆ potential. *J Chem Phys A* 39:7783–7799
- Moulton DM (1964) Shock wave studies by time of flight mass spectrometry. Ph.D. thesis, Harvard University, Cambridge
- Rajakumar B, Reddy KPJ, Arunan E (2002) Uni-molecular HCl elimination from 1,2-dichloroethane. *J Phys Chem A* 106:8366–8373
- Simmie JM (2003) Detailed chemical kinetic models for the combustion of hydrocarbon fuels. *Prog. Energy Combust Sci* 29:599–634
- Simmie JM, Quiring WJ, Tschuikow-Roux E (1969) The thermal decomposition of perfluorocyclobutane in a single-pulse shock tube. *J Phys Chem* 73:3830–3833
- Sivaramakrishnan R, Tranter RS, Brezinsky K (2006) High pressure pyrolysis of toluene. 1. Experiments and modeling of toluene decomposition. *J Phys Chem A* 110:9388–9399
- Tranter RS (2013) unpublished work
- Tranter RS, Giri BR, Kiefer JH (2007) Shock tube/time-of-flight mass spectrometer for high temperature kinetic studies. *Rev Sci Instrum* 78:034101
- Tranter RS, Klippenstein SJ, Harding LB et al (2010) Experimental and theoretical investigation of the self-reaction of phenyl radicals. *J Phys Chem A* 114:8240–8261
- Tranter RS, Lynch PT, Annesley CJ (2012) High temperature sources of phenyl and benzyne radicals. 22nd international symposium Gas Kinet. University of Colorado at Boulder, Boulder, CO, 18–22 June 2012
- Tsang W, Lifshitz A (1999) Kinetic stability of 1,1,1-trifluoroethane. *Int J Chem Kinet* 30:621–628
- Tsang W, Lifshitz A (2001) Single pulse shock tube. In: Ben-Dor G, Igra O, Lifshitz A (eds) *Handbook of shock waves*, vol 3. Academic Press, New York
- Voldner EC, Trass O (1980) Evaluation of thermal-boundary layer interaction in shock-tube sampling for kinetic-studies *J Chem Phys* 73:1601–1611

- Wang H, Frenklach M (1997) A detailed kinetic modeling study of aromatics formation in laminar premixed acetylene and ethylene flames. *Combust Flame* 110:173–221
- Wu CH, Kern RD (1987) Shock tube study of allene pyrolysis. *J Phys Chem* 91:6291–6296
- Xu C, Braun-Unkloff M, Naumann C et al (2007) A shock tube investigation of H atom production from the thermal dissociation of ortho-benzyne radicals. *Proc. Combust Inst* 31:231–239
- Yang X, Kiefer JH, Tranter RS (2011) Thermal dissociation of ethylene glycol vinyl ether. *Phys Chem Chem Phys* 13:21288–21300
- Yasunaga K, Kuraguchi Y, Hidaka Y et al (2008) Kinetic and modeling studies on ETBE pyrolysis behind reflected shock waves. *Chem Phys Lett* 451:192–197
- Yasunaga K, Gillespie F, Simmie JM et al (2010) A multiple shock tube and chemical kinetic modeling study of diethyl ether pyrolysis. *J Phys Chem A* 114:9098–9109
- Yasunaga K, Mikajiri T, Sarathy M et al (2012) A shock tube and chemical kinetic modeling study of the pyrolysis and oxidation of butanols. *Combust Flame* 159:2009–2027
- Zhang X, Maccarone AT, Nimlos MR et al (2007) Unimolecular thermal fragmentation of ortho-benzyne. *J. Chem Phys* 126:44312

Chapter 7

Rapid Compression Machines

Alan Kéromnès

Abstract A rapid compression machine is a type of ideal internal combustion reactor which is well suited for gas phase kinetics studies and physical processes of combustion. These studies consist in recording the evolution of the reactivity and of the composition of the reacting mixtures as a function of temperature, pressure, residence time and the composition of the compressed mixture. Pressure measurement is used to analyse the evolution of the combustion process, but more recent studies couple pressure measurement with optical diagnostics in order to assess the homogeneity of the combustion process. Speciation based on rapid sampling of the intermediates formed, during the oxidation of the fuel, is typically carried out by gas chromatography.

7.1 Overview of the Rapid Compression Machine

The study of the combustion process needs to be performed with experimental devices which can reproduce thermodynamic conditions closed to that of real combustors (internal combustion engines, gas turbines, etc...). Rapid compression machines (RCM), firstly used in 1906, are able to reproduce these thermodynamic conditions (pressure, temperature) by compressing an air/fuel mixture up to the studied conditions—temperatures of 600–1,100 K, pressures of 1–70 bar. Furthermore, the issues encountered in real engines (blow-by, temperature and mixture heterogeneities, varying volume, metallic swarf, etc.) can be avoided. They also present the advantage of allowing an easy access to the combustion chamber for optical measurements or sampling of the mixture. Therefore, RCMs are more and more being used to study the combustion process mainly auto-ignition

A. Kéromnès (✉)

Département de Recherche en Ingénierie des Véhicules pour l'Environnement (DRIVE),
EA 1859, 49 rue Mademoiselle Bourgeois, 58000 Nevers, France
e-mail: alan.keromnes@u-bourgogne.fr

phenomenon. RCM was firstly used in order to determine the auto-ignition temperature and is now used for extensive study of the combustion properties of fuels.

The compression process has to be as short as possible in order to assume an adiabatic compression process. Commonly rapid compression machines (RCM) are able to achieve this within a few dozen of milliseconds (10–70 ms). After the compression process, the volume of the combustion chamber has to be kept constant in order to maintain constant thermodynamic conditions and allow the study of the combustion process. Usually, the combustion process can be studied between 2 and 500 ms after the end of the compression stroke.

The rapid compression machine can be used to study the auto-ignition phenomenon and the development of combustion. Most studies consist in recording the evolution of pressure as a function of time and determine the ignition delay time. The evolution of the ignition delay time is then studied as a function of equivalence ratio, fuel mixture composition, and the thermodynamic conditions reached at the end of the compression process: End of compression temperature and pressure. To the author's knowledge, there are an increasing number of RCM (from 5 at the end of the 1980s to more than 20 in 2011) in operation all over the world.

This Chapter will present the different technologies currently used, the validation and the simulation of RCMs and the diagnostics which can be used to study the combustion process.

7.2 Design of the Rapid Compression Machine

The critical points while designing a rapid compression machine are the quickness of the compression process, thanks to the driver mechanism, and the ability of the machine, thanks to the braking mechanism, to keep constant the thermodynamics conditions at the end of compression process (pressure, temperature and volume) for the study of the combustion process.

The design of the machine must also take into account the thermodynamic conditions which have to be achieved at the end of the compression process in terms of temperature and pressure range. These conditions can be easily defined thanks to the analysis parameter evolution during the compression which can be assumed as adiabatic. Therefore, the end of the compression pressure, p_c , and temperature, T_c , will only depend on the initial pressure, p_i , and temperature, T_i , respectively, the geometry of the machine (volumetric compression ratio ε) and the thermodynamic properties of the mixture composition (ratio of heat capacities, $C_p/C_v = \gamma$) see Eqs. (7.1) and (7.2):

$$p_c = p_i \varepsilon^\gamma \quad (7.1)$$

$$T_c = T_i \varepsilon^{\gamma-1} \quad (7.2)$$

A typical pressure curve recorded during RCM experiments (Fig. 7.1 left) includes the compression phase (from A to B) and the constant volume phase (from B to E) during which the auto-ignition phenomenon occurs (from B to D). The pressure decrease which can be noticed during the constant volume phase is due to a cooling effect because of the heat losses. As the temperature decreases under constant volume and mass conditions, this results in a corresponding pressure decrease. The ignition delay time is measured between the end of the compression process (B) and the onset of the combustion (C). Then, the development of the combustion inside the combustion chamber occurs until the pressure reaches the maximum pressure (D). This pressure curve is typical for a single-stage ignition process. During a two-stage ignition process (Fig. 7.1 right), a first heat release, also called “cool flame” (see Chap. 2), is recorded (first stage) and is followed by the main heat release (second stage).

The following section will present the main designs developed in order to achieve these important characteristics. This part will mainly focus on the different strategies used in order to achieve a rapid compression and a constant volume combustion process.

7.2.1 Review of the Main RCMs Technologies

The first RCM built in 1906 (Falk 1906) was a vertical single piston apparatus whose piston was driven by the fall of a mass. However, there was no braking mechanism. Different technologies are currently used. They differ by the driver mechanism, the stopping mechanism, the number pistons and the size of the combustion chamber. However, three main categories can be defined:

- Single piston RCM
- Twin piston RCM
- Camshaft connection RCM.

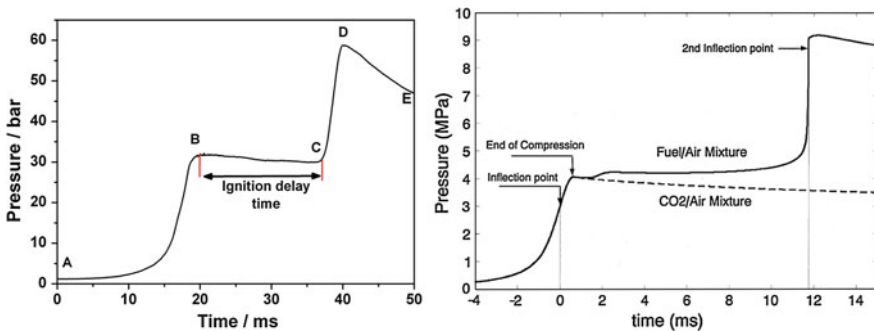


Fig. 7.1 Typical pressure curves measured in the rapid compression machine from NUI Galway (left) and in MIT (right) (Tanaka et al. 2003)

7.2.1.1 Single Piston

The first version of the RCM used in MIT was built in the 1940s. It is a vertical single piston apparatus (Fig. 7.2) fired by the expansion of compressed gas. The piston velocity is controlled by the flow of hydraulic oil. The hydraulic braking mechanism also held the piston at top dead centre (TDC) after the compression process. The stroke of the piston can be changed in order to achieve different end of compression pressure and temperature. This has an impact on the compression time which can vary from 10 to 30 ms.

The piston has the subject of a particular design in order to limit the temperature heterogeneities inside the combustion chamber. Lee and Hochgreb (1998) carried out a computational fluid dynamics (CFD) study of the aerodynamic and

Fig. 7.2 Cross section view of the MIT rapid compression machine (Lee and Hochgreb 1998; Copyright Elsevier)

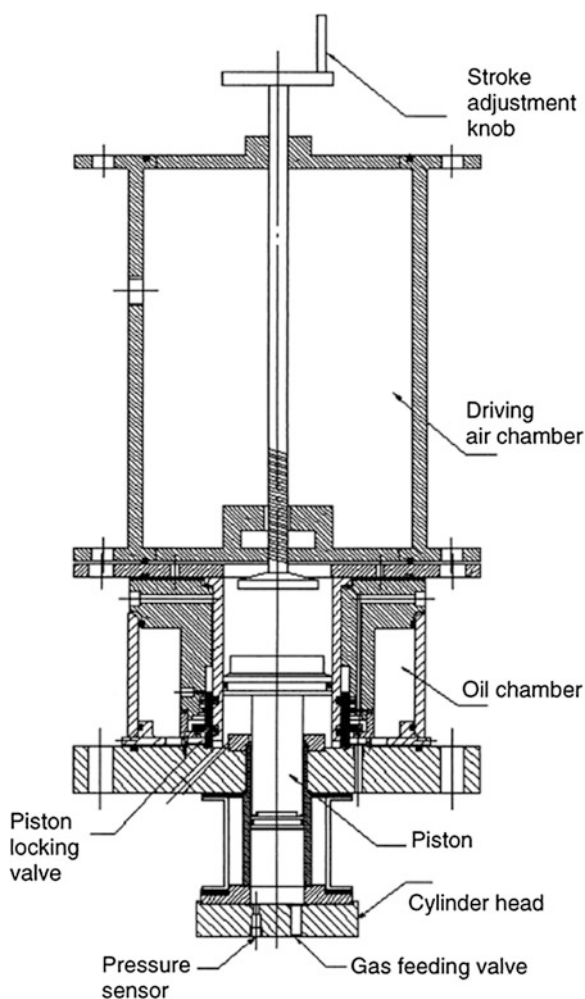
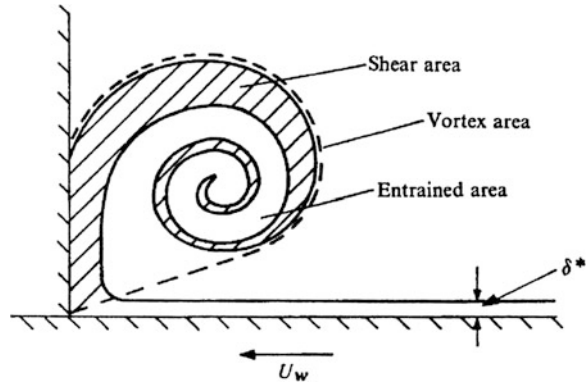


Fig. 7.3 Sketch of the piston corner vortex (Lee and Hochgreb 1998; Copyright Elsevier)



the boundary layer during the compression process. They found that the cold boundary layer is rolled up by the piston during the compression (Fig. 7.3) and results in a vortex which is released at the end of compression. This vortex can be trapped by a specially design crevice behind the piston head.

A similar design is used for horizontal machines in Leeds since the late 1970s (Beeley et al. 1979) and in Case Western Research University (CWRU) (Mittal and Sung 2006) since 2006. The machine in CWRU also uses a crevice piston in order to reduce the aerodynamic inside the combustion chamber.

Two RCMs in Japan—one in Tokyo University (Kono et al. 1983) and the other in Keio University (Lim et al. 2004) also use air as a driving force and hydraulic oil in order to control the velocity of the piston and maintain the volume constant after the compression process.

Two fully hydraulically controlled RCMs have also been built. The first one, firstly reported in 2003 (Bysveen and Almas 2003), is used in the Norwegian University of Science and Technology (NTNU); the second one, firstly reported in 2007 (Guibert et al. 2007), was built in University Pierre et Marie Curie (UPMC) in France. This second machine is fully heated thanks to three heating resistance inside the wall of the sleeve and the combustion chamber is wrapped with heating tapes. The aim of such machines is to fully control the piston velocity thanks to a hydraulic cylinder and a servo valve. Thus, the reproducibility of the compression process is guaranteed by the full control of the system.

The last type of single piston RCM was designed by TRW and relocated in the University of Michigan (Donovan et al. 2004). This machine uses a free piston or sabot which is launched by compressed gas. The dimension of this RCM is unusual since the length of the driven section is 2.74 m.

7.2.1.2 Twin Piston RCM

Two twin piston RCMs are used in the National University of Ireland Galway (NUIG). This machine was firstly designed by Shell-Thornton in 1968, used until



Fig. 7.4 Picture of one of the two twin-piston rapid compression machines located in the Combustion Chemistry Centre, NUI Galway

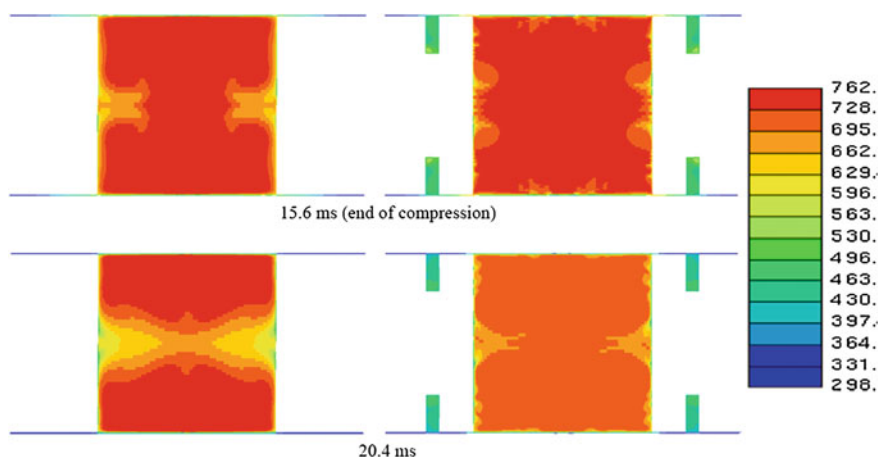


Fig. 7.5 Temperature distribution inside the combustion chamber at the end of the compression process (*top*) and during the constant volume phase (*bottom*) with (*right*) and without (*left*) the crevices in the piston head (Würmel and Simmie 2005; Copyright Elsevier)

the middle of the 1980s and then acquired, re-commissioned and modified by NUIG in the mid 1990s. This machine is composed of two similar systems which include compressed air as a driving force and hydraulic oil in order to control the piston velocity (Fig. 7.4).

This unique design allows reduction of the compression time (below 17 ms) and reducing the aerodynamic thanks to the symmetry of the system (Brett et al. 2001; Würmel et al. 2007a, b). Moreover, a CFD study (Würmel and Simmie 2005) of the combustion chamber was performed. It was shown that there is a stagnation plane in the middle of the combustion chamber. Crevices have also been added to the pistons in order to suppress the vortex created by during the

compression phase. This results (Fig. 7.5) in a more homogeneous temperature distribution when crevices are used. A similar RCM was also built in 2005 at Argonne National Laboratory (Gupta et al. 2005).

7.2.1.3 Camshaft Connection

Two RCMs have been designed with a particular right-angle shape in France. This design solves one of the main problems of RCMs which is to bring the piston to a dead stop at the end of the compression process. The first one, driven thanks to air expansion, was designed in Lille University (Ribaucour et al. 1992) at the end of the 1980s and is composed of two pistons which are perpendicular and are connected by a cam (Fig. 7.6). The second one was designed in the Laboratoire de Combustion et de Détonique in Poitiers (Strozzi et al. 2007). Its driven system is controlled by a hydraulic cylinder.

7.2.2 Improvements to RCMs

Much effort has gone into improved designs in order to reach steady and homogenous conditions at the end of compression not only to allow a high level of reproducibility but also to create well-defined conditions which can then be successfully simulated. Therefore, research teams often reached the same solutions

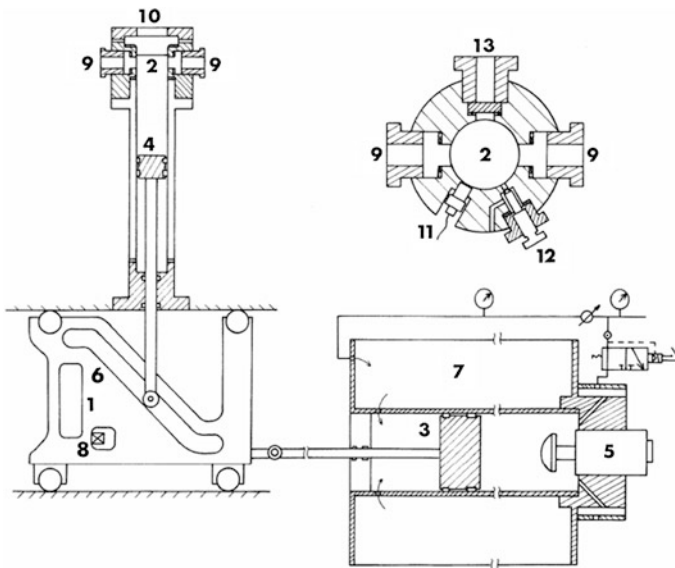


Fig. 7.6 Sketch of the perpendicular RCM from at Lille University (Carrier et al. 1990)

such as promoting the temperature homogeneity and the control of the velocity of the piston.

Many of the more recent studies have worked with very low vapour pressure (high molecular weight) fuels and this necessitates pre-heating the mixing tank(s), the gas-handling manifold and the RCM itself to high constant initial temperatures in excess of 373 K (see for example Husson et al. 2012). While this is an added complexity, it can reduce the requirement for using high heat capacity ratio, γ , gases to reach high compressed gas temperatures.

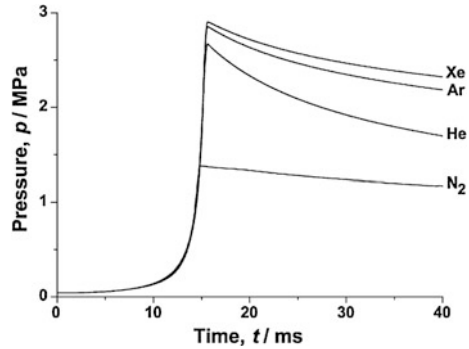
7.2.2.1 Temperature Homogeneity

Lee and Hochgreb (1998) investigated the homogeneity of the temperature inside the combustion chamber, at the end of the combustion chamber and at the combustion process thanks to a CFD study. They noticed that the cold boundary layer along the piston sleeve is rolled up during the compression process and released when the piston reached the TDC. This results in temperature heterogeneities before the combustion process (Fig. 7.5). Therefore, the auto-ignition phenomenon cannot be considered as homogeneous. In order to avoid the issue, they designed a crevice around the piston head in order to trap the cold boundary layer during the compression process. Thus, the temperature is more homogeneous inside the combustion chamber.

In order to improve the impact of the crevice and avoid any disturbance caused by the gases trapped in the crevice during the combustion phase, Mittal and Gupta (2012) computationally studied the impact of using crevice containment thanks to CFD simulations. They implemented a seal between the crevice and the stepped combustion chamber to prevent gas motion from the crevice to the combustion chamber. Results show that there are no negative influences on the flow field and that the roll-up vortex is largely suppressed.

The homogeneity of the temperature also depends on the physical properties of the compressed mixture. The tested mixture is usually composed with fuel, oxygen and a mixture of diluents (carbon dioxide, nitrogen, argon, helium, xenon) in various proportions. Würmel et al. (2007a) studied the impact of different diluent gases on ignition delay times. By using different nature of gases (monatomic and polyatomic), different temperature and pressure range can be achieved. Compared to nitrogen, and due to their higher specific heat capacity ratio, monatomics, such as argon, helium and xenon, will extend upward the temperature and pressure range, whereas polyatomics, such as carbon dioxide will reduce the compressed pressure and temperature. However, monatomics present a lower heat capacity and will result in greater heat losses at the end of the compression process (Fig. 7.7). Thus, during the design, a trade off has to be found between the pressure and temperature range achievable in the RCM and the heat loss issue.

Fig. 7.7 Impact of the diluent on pressure profile ($p_i = 0.04$ MPa, $T_i = 298$ K) (Würmel et al. 2007a; Copyright Elsevier)



7.2.2.2 Piston Positioning

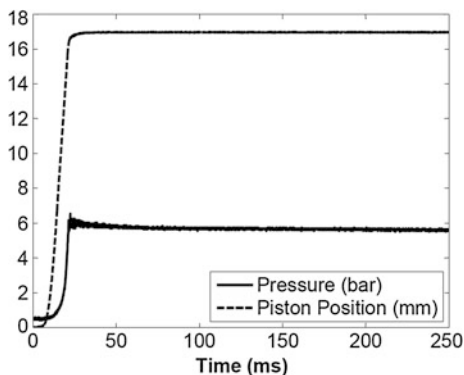
In the first RCMs, the control of the piston position and speed was only governed by fluid dynamics and mechanics. As the driving force was the expansion of a gas and the control of the velocity of the piston was achieved by hydraulic oil, a careful design of the hydraulic stopping mechanism was needed. After the compression process, both the residual driving pressure and the hydraulic pressure have to ensure that the piston does not move before or during the combustion process. Therefore, the piston displacement profile depends on the opposed pressure applied by the tested mixture on the piston head.

In order to avoid such issues, hydraulic controlled RCM have been developed. The latest one (Guibert et al. 2007) was developed in the Institut Jean Le Rond d'Alembert (UPMC, Paris). They use a hydraulic piston jack to move the piston. This piston jack is connected to a three-stage servovalve which controls the velocity and the position of the piston during and after the compression process. This design allows a closed-loop control of the piston motion and increase the reproducibility of the machine. This piston displacement profile is defined by the user before the experiment and reproduced accurately by the machine during the test.

7.3 Validation of the Rapid Compression Machine

As shown previously, the design of a rapid compression machine is difficult and the critical issues to overcome are to ensure the constant volume combustion process and the reproducibility of the machine. This following section deals with the assessment of these two key points of RCM.

Fig. 7.8 Evolution of the piston position and the chamber pressure during the compression of 500 mbar of perfluoropropane in NUIG-RCM



7.3.1 Constant Volume and Pressure Process

The validation of such a device has to go through a few steps. First of all, the main goal of a rapid compression machine is the ability to study the combustion process during a constant volume phase. Therefore, the RCM's ability to stop the piston dead after the compression process is crucial. In order to validate such a process, the position of the piston has to be measured precisely during both the compression phase and the constant volume phase. The constant volume process is usually checked by compressing perfluoropropane (C_3F_8). This particular gas has a very advantageous property, namely a specific heat ratio close to 1. Therefore, the temperature only increases slightly during the compression process Eq.(7.2). This phenomenon leads to a much reduced heat loss during the constant volume phase and the resulting pressure is almost constant (Fig. 7.8).

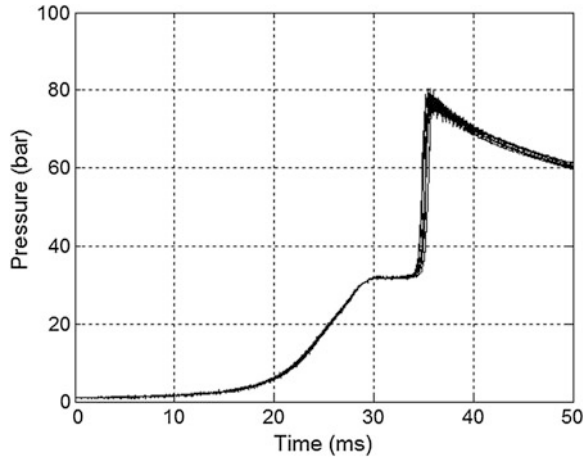
This type of tests is also used in order to control the airtightness of the combustion chamber after the combustion process. Since the piston stops dead, any pressure drop would be due to leaks from the combustion chamber. Therefore, a constant volume profile validates both the airtightness of the combustion chamber and the constant volume profile. Care must be taken not to *exceed* the saturated vapour pressure of perfluoropropane during the compression otherwise the test is invalid.

7.3.2 Reproducibility

The reproducibility of the experiments is always critical and it has to be as high as possible. One of the final results measured in RCM is ignition delay times. Their reproducibility is influenced by many factors so of which are not RCM dependent.

First of all, the reproducibility of the compression process with a non-reactive mixture is necessary preliminary for the reproducibility with reactive mixtures and ignition delay time measurements. The second step is the reproducibility of the

Fig. 7.9 Example of reproducibility over 10 compression and combustion runs for a mixture of 90 % iso-octane and 10 % n-heptane in air at an equivalence fuel air ratio of 0.6 ($p_i = 1$ bar, $T_i = 323$ K)



initial conditions thanks to a control of the initial pressure and temperature and the composition of the tested mixtures. Usually, the tested mixture is prepared manually in stainless steel tanks in order to test the same mixture. When all these necessary conditions are achieved, the reproducibility of the RCM for reactive mixtures can be assessed. Figure 7.9 presents a compilation of 10 experiments for a reactive mixture of iso-octane and air. The 10 pressure profiles present an excellent superposition both during the compression and the combustion processes. Due to the accuracy of the control of initial pressure and temperature, a variation of the ignition delay times within $\pm 5\%$ of the mean measured values is acceptable (Würmel et al. 2007a).

7.4 Modelling of the Rapid Compression Machine

Different types of model can be used in order to reproduce numerically the behaviour of a rapid compression machine, from the simplest one, only based on thermodynamics to three-dimensional model based on CFD advanced model using large eddy simulation (LES) and direct numerical simulation (DNS).

7.4.1 Thermodynamic Model

Thermodynamic models are based on the laws of thermodynamics and the ideal gas law. They are mainly used in order to compare the accuracy of chemical kinetics mechanisms with ignition delay times measured in the RCM thanks to chemical kinetics software.

In order to reproduce the behaviour of the rapid compression machine, the volume profile is needed. For each experiment with a reactive mixture (fuel + oxygen + diluents), an experiment with a non-reactive mixture is performed by replacing the oxygen by nitrogen in the test mixture. Because nitrogen and oxygen have similar thermodynamic properties, the recorded pressure profile presents the same pressure drop as the profile with the reactive mixture due to very similar heat loss properties. The reason for recording a pressure profile with a non-reactive mixture for each experiment is to characterise real heat losses in the kinetic simulations. A volume profile is calculated assuming adiabatic compression and expansion processes and frozen chemistry. This volume profile is used as an input in the model. This adiabatic volume expansion assumption is used in order to take into account the cooling effect due to heat losses. According to such assumption, the loss of energy due to heat losses to the wall is modelled via an expansion of the volume of the combustion chamber. Therefore, this approach takes into account a mean temperature inside the combustion chamber and does not account for potential temperature gradient, due to lower temperature zone close to the wall, higher temperature in the hot core region and mixing between these two regions.

Such an assumption is very useful and reduces computing time when detailed chemical kinetics mechanisms are used to model the auto-ignition of the fuel and compare measured ignition delay times with chemical kinetics mechanisms predictions. However, since the entire combustion chamber is modelled as a perfectly stirred reactor assuming a uniform heat release, this approach cannot reproduce non-uniform heat release due to temperature heterogeneities caused by the boundary layer.

7.4.2 Computational Fluid Dynamics

CFD models have been mainly used in order to study the aerodynamics and the temperature homogeneity inside the combustion chamber (Lee and Hochgreb 1998; Würmel and Simmie 2005; Mittal and Sung 2006) and the impact of the temperature on the combustion process (Mittal et al. 2008; Mittal and Gupta 2012; Lodier et al. 2012; Griffiths et al. 2012). Most of the studies used the Reynolds-Averaged Navier-Stokes (RANS) simulation but more advanced simulation such as DNS and LES have been used by Jakirlić et al. (2000) and Lodier et al. (2012).

Most of these studies aimed at reducing the effect of the aerodynamics inside the combustion chamber during and after the compression process (Lee and Hochgreb 1998; Würmel and Simmie 2005; Mittal and Sung 2006; Mittal and Gupta 2012) in order to create a homogeneous temperature field inside the combustion chamber. Therefore, these CFD studies were performed with a non-reactive mixture and aimed at designing appropriate piston crevices in order to trap the cold boundary layer.

The second type of CFD study includes aerodynamics and kinetics modelling thanks to detailed or reduced chemical kinetics mechanisms (Mittal et al. 2008; Mittal and Gupta 2012; Griffiths et al. 2012). They compared the results of zero-dimensional code with CFD codes and evaluated the assumption of uniform heat release throughout the combustion chamber. For the predictions of single stage ignition and in particular the ignition delay times, results show really good agreement between zero-dimensional model and CFD model. However, the auto-ignition phenomenon is not homogeneous and a disagreement appears for the prediction of the ignition delay time of the second-stage of the ignition process for hydrocarbons showing two-stage ignition (Mittal et al. 2010; Griffiths et al. 2012). For such cases, the impact of the cold boundary layer cannot be neglected since the gases which are colder than the core zone react before the core zone and accelerate the reaction which results in a shorter ignition delay time.

However, this type of simulation only models large-scale fluid motion and smaller scale motion needs to be modelled thanks to more detailed such as DNS and LES. This type of simulation includes the calculation of the turbulence inside the combustion chamber and its potential impact on the combustion process cannot be modelled. Jakirlić et al. (2000) studied the aerodynamics inside a rapid compression machine designed to create a swirling flow. The impact of turbulence on combustion inside a rapid compression machine has been studied numerically by Lodier et al. (2012) based on the design from Guibert et al. (2010). They reported different ignition behaviours from homogeneous ignition process to localised spot ignition.

7.5 Diagnostics and Typical RCM Results

Different diagnostics can be used in RCM in order to study the physics and kinetics prior to and during combustion process. The main diagnostic used in RCM is the measurement of instantaneous pressure inside the combustion chamber thanks to pressure transducer. More complex diagnostics are also used in order to study the development of the combustion process such as rapid sampling coupled with gas chromatography and optical diagnostics with or without on laser-based diagnostics.

7.5.1 Pressure Profile

Assuming an adiabatic compression process Eq.(7.3), the pressure profile is used to determine the temperature reached at the end of the compression process, T_c , based on the initial pressure, p_i , and temperature, T_i and the pressure at TDC, p_c .

$$\ln\left(\frac{p_c}{p_i}\right) = \int_{T_i}^{T_c} \frac{\gamma}{\gamma - 1} \frac{dT}{T} \quad (7.3)$$

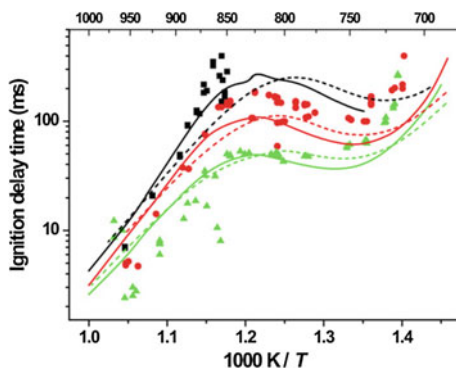


Fig. 7.10 Effect of equivalence ratio on ignition delay time for propane oxidation in “air,” $p_c \approx 30$ atm. (filled square) $\phi = 0.5$; (filled circle) $\phi = 1.0$; (filled triangle) $\phi = 2.0$. Solid lines HCT simulations, dashed lines RCMBL simulations (code for simulating RCM assuming adiabatic core region and thermal boundary layer) (Gallagher et al. 2008; Copyright Elsevier)

The ignition delay times are also measured thanks to the pressure profile. By varying the initial conditions (pressure, temperature, equivalence ratio, ...), it is possible to obtain the evolution of the ignition delay times as a function of temperature and/or equivalence ratio (Fig. 7.10) (Gallagher et al. 2008).

7.5.2 Optical Diagnostics

The second major area of interest in this field is the optical visualisation of combustion propagation during the combustion process, and is of relevance both to the chemical kineticists and also to fluid dynamicists and engineers. Optical visualisation utilises a wide variety of methods in order to assess different parameters including fuel mixture and temperature gradient and subsequent flame initiation homogeneity, spray visualisation for liquid fuels and the visualisation of the fluid dynamics. Thanks to the constant volume process, RCM can provide an important optical access to the whole combustion event. Different techniques can be used in order to study the initiation and the development of the combustion process.

7.5.2.1 Direct Visualisation

Simple diagnostics such as direct visualisation of the chemiluminescence and Schlieren imaging can be used to examine the combustion process and analyse its development (Walton et al. 2007; Guibert et al. 2010). In the Schlieren imaging process, a high-intensity point light source is refracted through a gathering lens

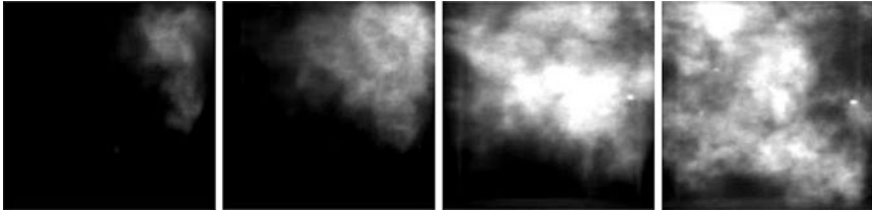


Fig. 7.11 Direct visualisation of the combustion process of 1-hexene/air mixture ($T_c = 840$ K, $p_c = 36.6$ bar, equivalence ratio: 0.4, Frame rate: 6,250 image/s) (Guibert et al. 2010; Copyright Elsevier)

and the parallel beams of light directed through the combustion chamber. At the exit port, the parallel beams are then re-focused onto the camera CCD array. The interference of light generated by the combustion event is recorded as grey scale images and shows the propagation of the ignition event over time. Since the time from full compression to initiation of ignition is measured in milliseconds, an ultra high speed camera is required. This technique also relies on two diametrically opposed optical access windows. This technique is well established and would provide a relatively simple first run analysis of chamber homogeneity. However, it does not provide a planar image or slice through the access of interest, providing instead a three-dimensional “shadow” of the event. It can be used to show if heterogeneity exists but does not exclusively prove homogeneity (Strozzi et al. 2008).

Guibert et al. (2010) used direct visualisation and noticed a development of the combustion through the combustion chamber (Fig. 7.11). Optical band-pass filter can be added to the camera in order to select particular wavelength corresponding to the emission of selected species (for example, excited OH^* : 308 nm).

7.5.2.2 Laser-Based Diagnostics

Laser-based diagnostics have been used in order to study the thermodynamics conditions (temperature, homogeneity) prior to the combustion event, the aerodynamics and the combustion process.

**Laser Induced Fluorescence (LIF)*

Laser-based diagnostics, such as LIF (for more details about LIF, see Chap. 12), increase the accuracy of the analysis, by exclusively viewing a perpendicular radial plane within the combustion chamber (Clarkson et al. 2001; Strozzi et al. 2009; Tran et al. 2011). This technique requires an optical window perpendicular to the viewing port. Laser light of a specific wavelength is focused to create a planar beam or sheet of light which bisects the volume of interest. The laser light excites specific species on this plane and they re-emit light at a selected wavelength during the relaxation through fluorescence, and it is therefore possible to scrutinise the behaviour of important intermediate species such as OH and CH. Optical filters are then used to

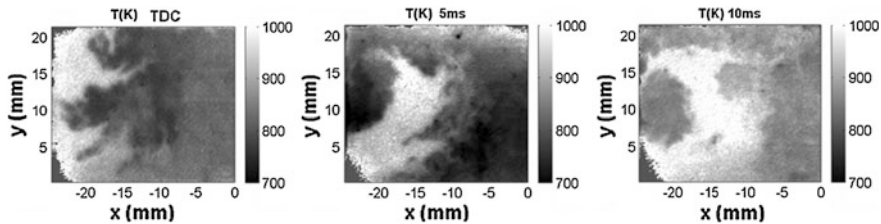


Fig. 7.12 Temperature field in the chamber of RCM measured by LIF (Strozzi et al. 2009; Copyright IOP Publishing)

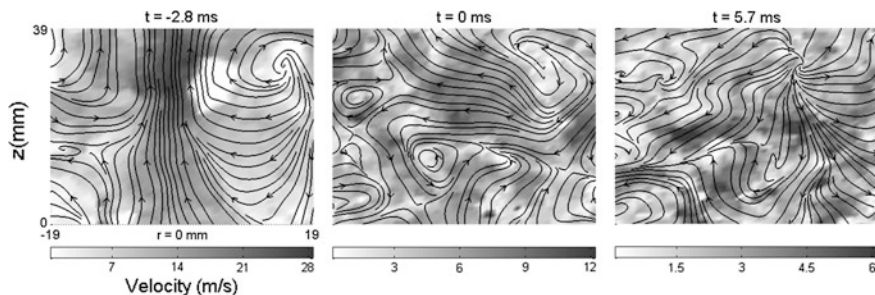


Fig. 7.13 Velocity magnitude fields and flow streamlines within the reference inert mixture at the compression end (Guibert et al. 2010; Copyright Elsevier)

isolate the specific wavelength and species concentrations can be recorded using a high-speed camera mentioned. Areas with higher concentrations of these species and/or higher temperature will emit light at a higher intensity, and therefore heterogeneity in terms of light-intensity gradients will indicate areas of thermal gradients. However, only a few studies have been reported in RCM. Figure 7.12 represents the temperature field measured thanks to LIF inside the combustion chamber of a RCM.

**Particle Image Velocimetry (PIV)*

PIV is widely used to characterise the velocity field inside internal combustion engines. However, there are a limited number of applications inside rapid compression machine. This technique requires two perpendicular optical accesses to the combustion chamber which are used in order to illuminate the flow field thanks to a laser sheet and record the Mie scattering images. The flow has to be seeded with particles. Under such high temperature and pressure conditions, solid particles, such as zirconium oxide, are needed. Guibert et al. (2010) and Strozzi et al. (2012) coupled visualisation of the combustion process with PIV measurement (Fig. 7.13) of non-reacting mixture and reported different regimes for the development of the combustion process.

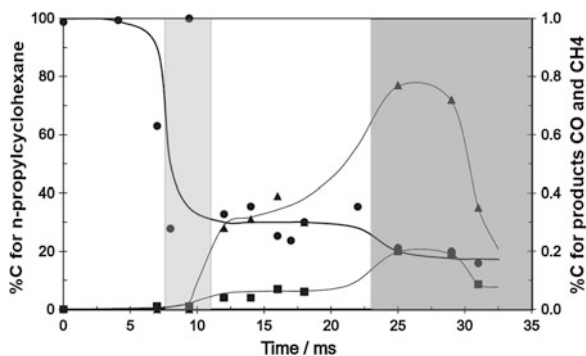


Fig. 7.14 Species concentration-time profiles expressed as the percentage of the carbon atoms initially present in PCH (%C) during the two-stage ignition of a propylcyclohexane/O₂/inert mixture. $\phi = 0.5$, $p_c = 0.7$ MPa, $T_c = 669 \pm 9$ K. The cool flame (*light grey*) (see Chap. 2) and ignition (*dark grey*) are shown as grey zones. (Crochet et al. 2010; Copyright Elsevier)

7.5.3 Rapid Sampling

In order to investigate the important intermediate species during the combustion process, a direct measurement of species concentration is needed. Rapid sampling inside the combustion can provide such information. Minetti et al. (1994) designed a rapid sampling apparatus in order to collect the reaction products. On triggering, the sampling apparatus connect the combustion chamber with an expansion chamber initially separated by a diaphragm. Due to the rapid adiabatic expansion, the sample undergoes a high rate of cooling which quenches the chemical reactions. The quenched sample is then analysed qualitatively and quantitatively. With successive experiments and sampling at different times, concentration profiles as a function of time can be obtained for initial, intermediate and final products, Fig. 7.14.

While *periodic* sampling and subsequent analyses of a reacting mixture provide useful information on stable species, the alternative approach of *continuous* sampling has not yet been attempted to my knowledge. Given that the timescales in RCM experiments are much slower than those encountered in shock tubes (see Chap. 6), coupling of a RCM to a time-of-flight mass spectrometer should be eminently possible. The additional refinement of tunable photo-ionisation, currently achieved via synchrotron radiation, would be desirable.

7.6 Conclusion

Quite apart from the technological improvements which have been mentioned above as being desirable, the single most important advance would be to couple CFD solutions with a detailed chemical kinetic mechanism. Only in this way can

gas motions, heat losses, etc. and realistic chemistries be properly allowed for as opposed to the ad hoc present-day approaches.

References

- Beeley P, Gray P, Griffiths JF (1979) Shock sensitivity of liquid propellants: the exothermic decomposition of isopropyl nitrate under rapid compression. *Proc Combust Inst* 17:1415–1423
- Brett L, MacNamara J, Musch P et al (2001) Simulation of methane autoignition in a rapid compression machine with creviced pistons. *Combust Flame* 124:326–329
- Bysveen M, Almas T (2003) Fuel quality evaluation by changing the compression ratio in a hydraulic dynamic combustion rig. SAE Technical Paper 2003-01-3081
- Carlier M, Corre C, Minetti R et al (1990) Autoignition of butane: a burner and a rapid compression machine study. *Proc Combust Inst* 23:1753–1758
- Clarkson J, Griffiths JF, MacNamara JP et al (2001) Temperature fields during the development of combustion in a rapid compression machine. *Combust Flame* 125:1162–1175
- Crochet M, Minetti R, Ribaucour M et al (2010) A detailed experimental study of *n*-propylcyclohexane autoignition in lean conditions. *Combust Flame* 157:2078–2085
- Donovan MT, He X, Zigler BT et al (2004) Demonstration of a free-piston rapid compression facility for the study of high temperature combustion phenomena. *Combust Flame* 137:351–365
- Falk KG (1906) The ignition temperatures of hydrogen-oxygen mixtures. *J Am Chem Soc* 28(11):1517–1534
- Gallagher SM, Curran HJ, Metcalfe WK et al (2008) A rapid compression machine study of the oxidation of propane in the negative temperature coefficient regime. *Combust Flame* 153:316–333
- Griffiths JF, Piazzesi R, Sazhina EM et al (2012) CFD modeling of cyclohexane auto-ignition in RCM. *Fuel* 96:192–203
- Guibert P, Kéromnès A, Legros G (2007) Development of a turbulence controlled rapid compression machine for HCCI combustion. SAE Technical Paper 2007-01-1869
- Guibert P, Kéromnès A, Legros G (2010) An experimental investigation of the turbulence effect on the combustion propagation in a rapid compression machine. *Flow Turbul Combust* 84(1):79–95
- Gupta S, Bihari B, Sekar R et al (2005) Ignition characteristics of methane-air mixtures at elevated temperatures and pressures. SAE Technical Paper 2005-01-2189
- Husson B, Bouneacur R, Tanaka K et al (2012) Experimental and modeling study of the oxidation of *n*-butylbenzene. *Combust Flame* 159:1399–1416
- Jakirlić S, Volkert J, Pascal H et al (2000) DNS, experimental and modelling study of axially compressed in-cylinder swirling flow. *Int J Heat Fluid Flow* 21:627–639
- Kono M, Shiga S, Kumagai S et al (1983) Thermodynamic and experimental determinations of knock intensity by using a spark-ignited rapid compression machine. *Combust Flame* 54:33–47
- Lee D, Hochgreb S (1998) Rapid compression machines: heat transfer and suppression of corner vortex. *Combust Flame* 114:531–545
- Lim OT, Sendoh N, Iida N (2004) Experimental study on HCCI combustion characteristics of *n*-heptane and iso-octane fuel/air mixture by the use of a rapid compression machine. SAE Technical Paper 2004-01-1968
- Lodier G, Merlin C, Domingo P et al (2012) Self-ignition scenarios after rapid compression of a turbulent mixture weakly-stratified in temperature. *Combust Flame* 159:3358–3371

- Minetti R, Ribaucour M, Carlier M et al (1994) Experimental and modelling study of oxidation and Autoignition of butane at high pressure. *Combust Flame* 96:201–211
- Mittal G, Gupta S (2012) Computational assessment of an approach for implementing crevice containment in rapid compression machines. *Fuel* 102:536–544
- Mittal G, Sung CJ (2006) Aerodynamics inside a rapid compression machine. *Combust Flame* 145:160–180
- Mittal G, Raju MP, Sung C (2008) Computational fluid dynamics modeling of hydrogen ignition in a rapid compression machine. *Combust Flame* 155:417–428
- Mittal G, Raju MP, Sung C (2010) CFD modeling of two-stage ignition in a rapid compression machine: Assessment of zero-dimensional approach. *Combust Flame* 157:1316–1324
- Ribaucour M, Minetti R, Carlier M et al (1992) Autoinflammation à haute pression. Conception, réalisation et test d'une machine à compression rapide. *J Chim Phys* 89:2127–2152
- Strozzi C, Sotton J, Bellenoue M et al (2007) Self-ignition of a lean methane-air mixture at high pressure in a Rapid Compression Machine. In: *Proceedings of the European Combustion Meeting, Chania, Greece, vol 3*
- Strozzi C, Sotton J, Mura A et al (2008) Experimental and numerical study of the influence of temperature heterogeneities on self-ignition process of methane-air mixtures in a rapid compression machine. *Combust Sci Technol* 180:1829–1857
- Strozzi C, Sotton J, Mura A et al (2009) Characterization of a two-dimensional temperature field within a rapid compression machine using a toluene planar laser-induced fluorescence imaging technique. *Meas Sci Technol* 20:125403
- Strozzi C, Mura A, Sotton J et al (2012) Experimental analysis of propagation regimes during the autoignition of a fully premixed methane-air mixture in the presence of temperature inhomogeneities. *Combust Flame* 159:3323–3341
- Tanaka S, Ayala F, Keck JC (2003) A reduced chemical kinetic model for HCCI combustion of primary reference fuels in a rapid compression machine. *Combust Flame* 133:467–481
- Tran K, Morin C, Guibert P (2011) Anisole laser induced fluorescence (LIF) for imaging local heterogeneities in temperature in a rapid combustion machine. In: *Proceedings of the European Combustion Meeting, Cardiff, Wales, vol 4*
- Walton SM, He X, Zigler BT et al (2007) An experimental investigation of iso-octane ignition phenomena. *Combust Flame* 150:246–262
- Würmel J, Simmie JM (2005) CFD studies of a twin-piston rapid compression machine. *Combust Flame* 141:417–430
- Würmel J, Silke EJ, Curran HJ et al (2007a) The effect of diluent gases on ignition delay times in the shock tube and in the rapid compression machine. *Combust Flame* 151:289–302
- Würmel J, Simmie JM, Curran HJ (2007b) Studying the chemistry of HCCI in rapid compression machines *Int J Vehicle Design* 44:84–106

Chapter 8

Jet-Stirred Reactors

Olivier Herbinet and Guillaume Dayma

Abstract The jet-stirred reactor is a type of ideal continuously stirred-tank reactor which is well suited for gas-phase kinetic studies. It is mainly used to study the oxidation and the pyrolysis of hydrocarbon and oxygenated fuels. These studies consist in recording the evolution of the conversion of the reactants and of the mole fractions of reaction products as a function of different parameters such as reaction temperature, residence time, pressure, and composition of the inlet gas. Gas chromatography is classically used for the analysis of the species in the gas phase, but recent studies aimed at coupling new types of analytical devices to a jet-stirred reactor to observe new types of species and to gain accuracy in the identification and the quantification of species.

Nomenclature

Latin Symbols

A	Adimensional constant which is equal to 0.3 in the case of air at 20 °C and at atmospheric pressure
c_{sound}	Speed of sound
C_A^o	Concentration of a species A at the outlet of the JSR
C_A^i	Concentration of a species A at the inlet of the JSR
d	Diameter of a nozzle in the JSR
F_j^o	Mole flow rate of the species j at the outlet of the JSR
F_j^i	Mole flow rate of the species j at the inlet of the JSR
h_j^o	Mole enthalpy of formation of the species j at the outlet of the JSR

O. Herbinet (✉)

Laboratoire Réactions et Génie des Procédés, CNRS, 1 rue Grandville 54000 Nancy, France
e-mail: olivier.herbinet@univ-lorraine.fr

G. Dayma

Institut de Combustion Aérothermique Réactivité et Environnement, CNRS, 1C Avenue de la Recherche Scientifique 45071 Orléans, France
e-mail: guillaume.dayma@cnrs-orleans.fr

h_j^i	Mole enthalpy of formation of the species j at the inlet of the JSR
i	Index for reaction
j	Index for species
P	Pressure of the gas in the JSR
Q	Volume flow rate in the JSR
$Q_S(x)$	Volume flow rate of the gas at the distance x from the outlet of a nozzle in the JSR
Q_0	Volume flow rate of the gas at the outlet of a nozzle in the JSR
r	Radial distance from the axe of a jet from a nozzle in the JSR
r_i	Rate of the reaction i
R	Radius of the JSR
Re	Reynolds number
R_r	Recycling rate in the JSR
t	Time needed to carry the whole volume of gas in the JSR from one nozzle to the following one
T	Temperature of the gas in the JSR
u_a	Axial velocity of a jet from a nozzle in the JSR
u_0	Velocity of the gas at the outlet of a nozzle in the JSR
u_r	Radial velocity of a jet from a nozzle in the JSR
V	Volume of the JSR
W	JSR heat loss
x	Axial distance from a nozzle in the JSR
x_{fuel}	Mole fraction of a fuel

Greek Symbols

α	Dimensional constant in the expression of the radial velocity of a jet from a nozzle in the JSR
β	Angle at the top of the cone formed by a jet from a nozzle in the JSR
η	Dynamic viscosity of the gas
Φ	Equivalence ratio
$v_{i,j}$	Algebraic stoichiometric coefficient
ρ	Specific weight of the gas
τ	Residence time of the gas in the JSR

8.1 Overview of the Jet-Stirred Reactor

Gas-phase kinetic studies are mostly performed using closed vessels, burners, and continuous stirred-tank reactors. Among continuous stirred-tank reactors is the jet-stirred reactor. One of its major advantages relies on the efficient mixing of the gas phase which provides identical and homogeneous compositions of the outlet gas

and of the gas inside the reactor. When operated at steady state and at constant residence time, temperature and pressure, this type of reactor is easily modeled by a very simple system of mass balances. Another advantage of this reactor is the possibility of being coupled with analytical techniques such as gas chromatography and mass spectrometry for the identification and the quantification of the species in the gas phase.

One of the best ways to achieve the mixing of the gas phase is to use turbulent jets obtained from nozzles. Despite the strong pressure drop in the nozzles, this technique provides very intense internal recycle streams. The material used for the manufacturing of the reactor is of great importance. The use of metal is not recommended because of possible large wall effects and the use of Pyrex glass or fused silica is preferred.

The jet-stirred reactor has often been used to study the gas-phase oxidation and the thermal decomposition of fuels. These studies consist in measuring the evolution of the mole fractions of species at the outlet of the reactor as a function of different parameters such as reaction temperature, residence time, pressure, and composition of the inlet gas (the fuel concentration and the equivalence ratio in combustion experiments). The reactivity of the fuel and the selectivity of the reaction products can be deduced from these data.

The residence time of the gas in the reactor (Eq. 8.1) is actually a mean residence time (or space time) which is defined as the ratio of the volume of the reactor, V , and of the volume flow rate of the gas flowing through the reactor, Q , which is also the volume flow rate at the outlet of the reactor, Q^o (Fig. 8.1).

To verify that the reactor can be considered as a continuous stirred-tank reactor, one can measure the residence time distribution by doing a short injection of a very small amount of tracer at the inlet and by recording the evolution of the concentration of the tracer at the outlet. The reactor is an ideal continuous stirred-tank reactor if the residence time distribution $E(t)$ can be represented by the expression given by Eq. 8.2.

$$\tau = V/Q \quad (8.1)$$

$$E(t) = \frac{1}{\tau} \exp\left(-\frac{t}{\tau}\right) \quad (8.2)$$

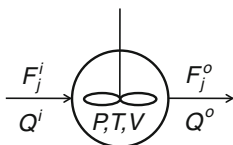


Fig. 8.1 Simplified scheme of a jet-stirred reactor of volume V working at constant temperature T and pressure P . F_j^i and F_j^o are the mole flow rates of the species j at the inlet and at the outlet of the reactor. Q^i and Q^o are the volume flow rates of the gas at the inlet and at the outlet of the reactor (Q^o is defined under the conditions of pressure and temperature inside the reactor)

To our knowledge, glass or fused silica jet-stirred reactors have been used for gas-phase kinetic studies by three research teams. It is largely used in Nancy (France) at the Laboratoire Réactions et Génie des Procédés for the study of the oxidation and of the pyrolysis of hydrocarbons and oxygenated fuels at atmospheric pressure (e.g., Marquaire and Côme 1978; Herbinet et al. 2007, 2011c; Hakka et al. 2009; Battin-Leclerc et al. 2010). A high pressure jet-stirred reactor is used in Orléans (France) at the Institut de Combustion Aérothermique Réactivité et Environnement for the study of the oxidation of various type of fuels (e.g., Dagaut et al. 1994; Mzé-Ahmed et al. 2010) and for the study of the kinetics of nitrous oxides formation and destruction (e.g., Dayma and Dagaut 2006). It was also used in Leeds (United Kingdom) at the Department of Physical Chemistry and Center for Combustion and Energy to study stationary-state and oscillatory ignition phenomena in fuel oxidation (e.g., Baulch et al. 1988; Griffiths and Inomata 1992). Metallic jet-stirred reactors have been used for the study of the low temperature oxidation of hydrocarbons (e.g., Cavaliere et al. 1993; Ciajolo and D'Anna 1998) and for the study of the cracking kinetics of biomass pyrolysis vapors (Baumlin et al. 2005).

8.2 Jet-Stirred Reactor Construction Rules

The basis for the design of spherical jet-stirred reactors was proposed by the team of Villermaux in Nancy (France) in the 1970s (Matras and Villermaux 1973; David and Matras 1975). A little earlier Bush (1969) proposed rules for the construction for cylindrical jet-stirred reactors. Although both designs can be used for gas-phase kinetic studies, spherical jet-stirred reactors are preferred to minimize dead volumes. In this chapter, we focus on the design of spherical jet-stirred reactors.

The jet-stirred reactor designed by the team of Villermaux is composed of a sphere in which the reaction takes place. The fresh gases enter the reactor through an injection cross located at the center of the sphere and composed of four nozzles

Fig. 8.2 Picture of the jet-stirred reactor used in Nancy (France) and which was developed from the rules of construction proposed by the group of Villermaux



providing the jets ensuring the mixing of the gas phase. Figure 8.2 displays a picture of the jet-stirred reactor which is still in use at the Laboratoire Réactions et Génie des Procédés (Nancy, France) and which was developed from the rules of construction proposed by the team of professor Villermaux.

The rules of construction of a jet-stirred reactor rely on the theory of the free jet: the jet from a nozzle leads to the motion of the gas phase in which it flows and this motion results in the distribution of the initial kinetic energy in small turbulent pieces of gas phase. It is assumed that a jet provided by a nozzle in the reactor widens in form of a cone which bends along a circumference between two nozzles (Bush 1969) as shown in Fig. 8.3.

8.2.1 The Theory of the Free Jet

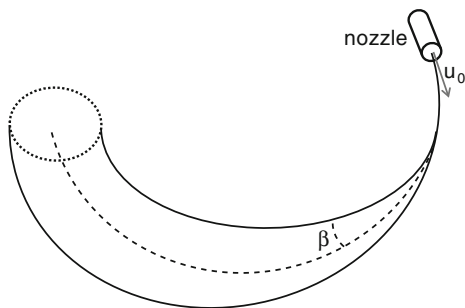
A jet is assumed to be free if the condition of Liepmann and Laufer (David and Matras 1975) is satisfied (Eq. 8.3). In Eq. 8.3, u_0 is the velocity of the gas at the outlet of a nozzle, R is the radius of the spherical reactor, ρ is the specific weight of the gas, and η is the dynamic viscosity of the gas. The velocity of the gas u_0 (Eq. 8.4) can be expressed as a function of the radius of the reactor R , of the diameter of the nozzle d and of the residence time τ which is given in Eq. 8.1. Replacing u_0 in Eq. 8.3 we obtain the condition given by Eq. 8.5.

$$\frac{u_0 \pi R \rho}{2 \eta} \geq 7.10^4 \quad (8.3)$$

$$u_0 = \frac{4Q}{\pi d^2} = \frac{4R^3}{3\tau d^2} \quad (8.4)$$

$$\frac{2\pi \rho R^4}{3 \tau d^2 \eta} \geq 7.10^4 \quad (8.5)$$

Fig. 8.3 Scheme of the cone of gas from a nozzle in the jet-stirred reactor. u_0 is the velocity of the gas at the outlet of a nozzle. β is the angle at the top of the cone formed by the jet



This condition is always satisfied for reactors with a radius R greater than 1 cm and given the other conditions on the residence time τ and the internal diameter of the nozzles d which are described in the following paragraphs.

Hinze and Hegge Zijnen (1949) experimentally established the expression of the velocity in a free jet with axial symmetry (Eqs. 8.6 and 8.7). $u_a(x)$ is the velocity on the axe of the jet at the distance x from the nozzle and $u_r(x, r)$ is the velocity at the distance r from the axe of the jet and at the distance x from the nozzle (see Fig. 8.4). The parameter α in Eq. 8.7 is a dimensionless constant which depends on the nature of the gas and of the thermodynamic conditions ($\alpha^{-1} = 0.016$ for air at 293.15 K).

$$u_a(x) = 6.39 u_0 \frac{d}{x + 0.6d} \quad \frac{x}{d} > 10 \quad (8.6)$$

$$u_r(x, r) = \frac{u_a}{(1 + \alpha \frac{r^2}{x^2})^2} \quad (8.7)$$

Hinze and Hegge Zijnen (1949) experimentally measured u_a and u_r for different values of β which is the angle at the top of the cone as shown in Figs. 8.3 and 8.4. It was observed that the velocity u_r is almost zero when β is greater than 11° . The volume flow rate $Q_S(x)$ through the section of the cone at the distance x of the nozzle is obtained from the integration of $u_r(x, r)$ on this section considering $\beta = 11^\circ$ as limit value for the upper bound of the integration interval. The expression of $Q_S(x)$ is given by Eq. 8.8. Q_0 is the volume flow rate of the gas at the outlet of the nozzle. The parameter A is an adimensional constant which is equal to 0.3 in the case of air at 293.15 K and at atmospheric pressure. Matras and Villermaux (1973) showed that the value of the parameter A increases with the temperature, leading to a better mixing of the gas phase ($A = \pi/4$ at 723.15 K and at atmospheric pressure).

$$Q_S(x) = A Q_0 \frac{x}{d} \quad (8.8)$$

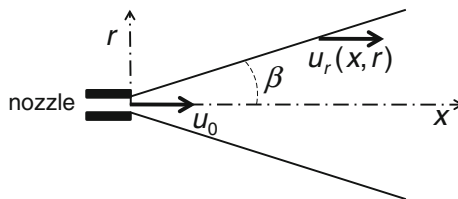


Fig. 8.4 Simplified scheme of the cone of gas from a nozzle in the jet-stirred reactor with the representation of the velocities in the jet. x and r are the axial and the radial positions, respectively. u_0 is the velocity of the gas at the outlet of a nozzle. $u_r(x, r)$ is the velocity at the distance x from the nozzle and at the distance r from the axe of the jet. β is the angle at the top of the cone formed by the jet

8.2.2 Criteria of Construction

The homogeneity of the composition of the gas phase in the jet-stirred reactor relies on the three following criteria:

- The jets from the four nozzles must be turbulent; in other words the internal mixing in each of the four jets must be turbulent.
- The four jets must be able to provide a good mixing of the whole gas phase in the reactor; the jets must provide very intense internal recycle streams.
- The velocity of the jets at the outlet of the nozzles must not exceed the speed of sound.

The first and the third criteria fix the range of accessible residence times and the second criterion fixes the geometrical ratio between the internal diameters of the reactor and of the nozzles.

8.2.2.1 Turbulent Jets

The Reynolds number R_e of the jets from the nozzles must be turbulent. The expression of the Reynolds number is given by Eq. 8.9.

$$R_e = \frac{\rho(2r)}{\eta} \frac{Q_S(x)}{\pi r^2} = \frac{\rho(4Q_S(x))}{2\eta\pi x \tan(\beta)} \quad (8.9)$$

Using Eq. 8.10, we obtained a new expression of the Reynolds number which does not depend on the distance x (Eq. 8.11).

$$4Q_S(x) = 4Q_0 A \frac{x}{d} = A \frac{x}{d} \frac{4\pi R^3}{3\tau} \quad (8.10)$$

$$R_e = \frac{4\rho AR^3}{6\eta d \tau \tan(\beta)} \quad (8.11)$$

Experimentally, it is observed that the mixing is not good enough for Reynolds number R_e less than 800. The upper limit for the residence time τ is obtained from Eq. 8.12.

$$\tau \leq \frac{\rho AR^3}{230\eta d} \quad (8.12)$$

8.2.2.2 Recycling

The recycling rate R_r is defined as the ratio between the residence time τ and the time t which is needed to carry the whole volume of gas in the reactor from one

nozzle to the following one. It is also the ratio between the volume flow rate $Q_S(x)$ at $x = \frac{\pi R}{2}$ (distance from one nozzle to the following one) and the volume flow rate Q_0 of the gas at the outlet of a nozzle (Eq. 8.13).

$$R_r = \frac{\tau}{t} = \frac{Q_S\left(\frac{\pi R}{2}\right)}{Q_0} \quad (8.13)$$

Using the geometrical relationship between the two volume flow rates with $x = \frac{\pi R}{2}$ (Eq. 8.14), we obtained for R_r the expression given by Eq. 8.15.

$$Q_S\left(\frac{\pi R}{2}\right) = Q_0 \cdot \frac{\pi AR}{2d} \quad (8.14)$$

$$R_r = \frac{\pi AR}{2d} \quad (8.15)$$

Experimentally, it was observed that the recycling rate R_r must be larger than 30 to have a good mixing of the gas phase. This leads to the condition given by Eq. 8.16 that fixes the required ratio between the radius of the reactor and the internal diameter of the nozzles.

$$\frac{R}{d} > 64 \quad (8.16)$$

8.2.2.3 Sonic Limit

The velocity u_0 of the gas at the outlet of a nozzle must be lower than the speed of sound $c_{\text{sound}}(T, P)$ at the temperature and the pressure of the reaction (Eq. 8.17). The velocity u_0 can be expressed as a function of the radius of the reactor R , the diameter of the nozzle d and the residence time τ (Eq. 8.18), which leads to the lower conditions on the residence time (Eq. 8.19).

$$u_0 \leq c_{\text{sound}}(T, P) \quad (8.17)$$

$$u_0 = \frac{4Q_0}{\pi d^2} = \frac{4R^3}{3d^2\tau} \quad (8.18)$$

$$\tau \geq \frac{4R^3}{3d^2 c_{\text{sound}}(T, P)} \quad (8.19)$$

8.2.2.4 Verification of the Criteria for Nancy JSR

For the verification of the criteria, it was considered that the gas flowing through the reactor was argon. Calculations were performed at a temperature of 723 K and

a pressure of 10^5 Pa. The radius of the reactor, R , and the internal diameter of the nozzle, d , were taken equal to $3 \cdot 10^{-2}$ and $3 \cdot 10^{-4}$ m, respectively.

The upper limit for the residence time is given by Eq. 8.12. At 723 K, the specific weight and the dynamic viscosity of argon are equal to $0.71 \text{ kg} \cdot \text{m}^{-3}$ and $4.23 \cdot 10^{-5} \text{ Pa} \cdot \text{s}$, respectively. The value of the parameter A is not known but it is assumed that it does not change significantly from one gas to another. For the calculation, the value of A for air at 723 K was used ($A = \pi/4$). The calculation leads to a maximum residence time of 5.2 s.

The lower limit is given by Eq. 8.19. The speed of sound can be calculated from the equation for an ideal gas (Eq. 8.20).

$$c_{\text{sound}} = \sqrt{\gamma RT/M} \quad (8.20)$$

In Eq. 8.20, γ is the adiabatic index, R is the molar gas constant and M the molecular weight of the gas. For argon, at 723 K, c_{sound} is equal to $500 \text{ m} \cdot \text{s}^{-1}$. The calculation leads to a minimum residence time of 0.8 s.

The recycling rate is given by Eq. 8.15. The calculation leads to a recycling rate of 123 which is more than the minimum required value of 30.

8.3 Improvements to Jet-Stirred Reactor

The jet-stirred reactor developed by the team of Villermaux was later improved for the study of the oxidation and thermal decomposition of hydrocarbons and oxygenated molecules. One of the major improvements was to preheat the incoming mixture to obtain a more homogeneous temperature in the reactor. New versions of this type of reactor were then developed for studies at high pressure (up to 40 bars) and for studies of hetero-homogenous reactions.

8.3.1 Temperature Homogeneity

The homogeneity of the temperature in the reactor is of importance in gas phase kinetic studies as reaction rates are very sensitive to this parameter. The jet-stirred reactor, the rules of construction of which are presented in the previous part of this chapter, was designed to have a homogeneous composition of the gas phase but little attention was paid to the homogeneity of the temperature.

Azay and Côme (1979) studied the influence of gas preheating on the thermal gradient in a jet-stirred reactor designed according to the rules of David and Matras (1975). Temperature gradients up to 80 K were recorded in the gas phase inside the reactor with no preheating and a significant difference in the mole fractions of methane was observed in the oxidation of *neo*-pentane with and without preheating of the fresh gases.

Following the observations of Azay and Côme (1979), preheating was added to avoid the formation of temperature gradients due to cold fresh gases entering the reactor (Fig. 8.5). The design of the preheater was based on the work of Houzelot and Villermaux (1977). They showed that annular geometries with high surface-volume ratio perform very well for heat transfer as heating rates of $10 \text{ K}\cdot\text{s}^{-1}$ can be achieved.

The dilution in an inert gas also helps to reduce the formation of temperature gradients in the gas phase due to the strong exothermicity of the reaction in combustion experiments (or due to the endothermicity in pyrolysis studies). Gas-phase kinetic studies are usually performed under high dilution conditions using an inert gas such as nitrogen, helium, or argon. Fuel inlet mole fractions are typically in the range $10^{-4} - 10^{-2}$.

The heating can be performed using either an oven or heating wires. The advantages of using heating wires are that there is very little thermal inertia and that it is possible to coil them directly around the different parts of the reactor and to heat the zones at different temperatures (Azay et al. 1981). Thus, the preheating can be divided into several zones (typically two) to obtain progressive heating of the fresh gases before they enter the reactor. The measure of the reaction temperature is performed thanks a thermocouple which is slipped in the intra-annular part of the preheater with the extremity of the thermocouple located in the center of the sphere as shown in Fig. 8.5.

8.3.2 High-Pressure Gas-Phase Kinetic Studies

In order to investigate the pressure effect on the reactivity and the homogeneity of the mixture, some other improvements were made at the Institut de Combustion Aérothermique Réactivité et Environnement (Orléans, France). To extend the experimental investigation range to pressures above atmospheric, the quartz

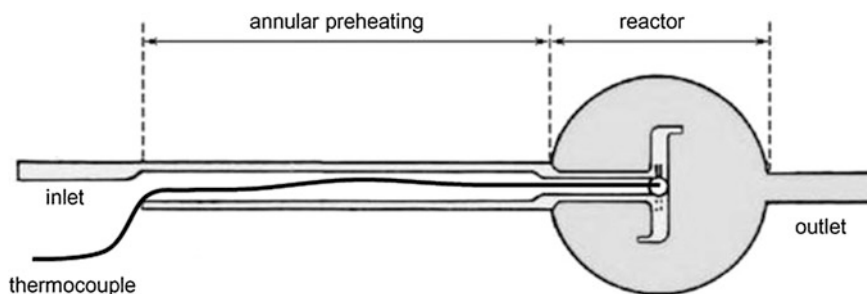


Fig. 8.5 Scheme of the jet-stirred reactor and of the annular preheating used in Nancy for oxidation and thermal decomposition gas-phase studies

reactor is located inside a stainless-steel pressure-resistant jacket (Dagaut et al. 1986). Working under high pressure is made possible by means of pressure balancing inside and outside the reactor. This was achieved by drilling four holes at the bottom of the propagation tube as shown in Fig. 8.6. The pressure is kept constant in time in the apparatus by means of a pressure regulator on the exhaust line. A safety valve prevents any accidental pressure rise in the system.

Although built following the guidelines established by the team of Professor Villermaux, the design of the reactor was revisited. The reactor is still a sphere made of fused silica to prevent wall catalytic reactions, but the injectors were shifted toward the upper part of this sphere instead of being located in the equatorial plane. Nevertheless, the four nozzle outlets are still located in the equatorial plane of the spherical reactor, so that the shape of the streams recommended by Matras et al. to ensure a perfect mixing is respected. This new design of the injectors allows a physical investigation of the whole volume of the reactor. By means of a system probe position adjuster, a thermocouple probe and a sampling sonic quartz probe can be moved along the vertical axis of the reactor. The thermocouple wires are enclosed in a thin-wall fused silica tube which is fixed against the sample probe. A residence-time distribution study was performed at 10 atm (~ 1 MPa) by pulsed injection of argon at the inlet of this reactor at room temperature: this led to the same conclusions as Matras et al. with their own design. Thus, this reactor is perfectly stirred for mean residence times varying from 0.01 to several seconds in the pressure range of 1–10 atm. Moreover, the reactor's homogeneity can be checked during experiments by measuring the temperature of the gases by means of a chromel–alumel thermocouple probe and by analyzing by gas chromatography the gases sampled with the sonic probe at different locations inside the reactor.

Fig. 8.6 Detail of the reactor developed in Orléans. The holes at the bottom of the prolongation tube are for pressure balancing

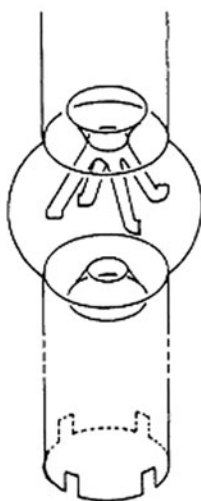
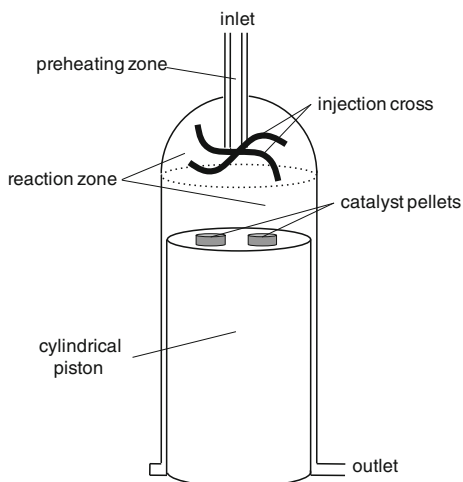


Fig. 8.7 Scheme of the special version of the jet-stirred reactor developed in Nancy for the study of the coupling of hetero-homogeneous reactions



8.3.3 Study of Hetero-Homogeneous Reactions

A special version of the jet-stirred reactor was developed at the Laboratoire Réactions et Génie des Procédés (Nancy, France) in the 1990s for the study of the coupling of hetero-homogeneous reactions (Côme et al. 1996). The spherical jet-stirred reactor was modified to make it possible to add pellets of catalyst or matrix (for the study of the fabrication of composite materials) inside the reactor (Fig. 8.7): the upper part of the reacting zone is hemispherical (as in the original jet-stirred reactor), whereas the lower part is cylindrical with a removable piston. The catalyst is deposited on the surface of the piston.

This type of reactor was mainly used for the study of the catalytic partial oxidation of methane (Côme et al. 1996; Fleys et al. 2006) and for the study of surface reactions in chemical vapor infiltration of pyrocarbon (Ziegler et al. 2005).

8.4 Sampling Methods

The sampling of the species in the gas phase is of importance for the accuracy of the analysis. One major difficulty is to avoid any change in the composition of the gas between the outlet of the reactor and the analysis. Two types of methods can be used for the sampling: online and offline sampling.

The offline sampling consists in collecting the species in a vessel connected to the outlet of the reactor and to inject the content of the vessel in a gas chromatograph. The species can be kept in the gas phase with collection and storage in a low pressure (50 mbar) Pyrex bulb to avoid condensation of water and species with low vapor pressure (Dagaut et al. 1986) or can be condensed in the solid

phase at liquid nitrogen temperature and afterward reheated with addition of a solvent such as acetone (Herbinet et al. 2007; Hakka et al. 2009). This second option (use of a solvent) can be problematic as there is a risk of reaction between unstable species (e.g., species with hydroperoxide functions) and the solvent.

The online sampling consists in sending the gas exiting from the reactor directly through the loop of the injection valve of a gas chromatograph. The tube used for connecting the outlet of the reactor to the injection system must be heated to avoid condensation of the species and it is better to use a tube the wall of which has been rendered inert to avoid adsorption phenomena and reactions at the wall (Herbinet et al. 2011a).

The sampling with species remaining in the gas phase is definitely the best manners to limit changes in the composition of the gas exiting from the reactor. Nevertheless, it was observed that unstable species such as hydroperoxides still decompose before the analysis as they are very reactive and that there is still a risk that some species with low vapor pressures, such as polycyclic aromatic hydrocarbons, condense in the transfer line. For these heavy species, it is better to use offline sampling for a more accurate quantification (Hakka et al. 2009; Bax et al. 2010).

The online sampling can be performed in the gas flowing in the outlet of the reactor or in the gas phase inside the reactor using a sonic probe. The second method is used when the reactor and the analytical apparatuses are working at different pressures (for example in the high-pressure oxidation studies or when the analytical device works at very low pressure). The use of a sonic probe, with a very small orifice, helps to maintain the difference of pressure between the reactor and the analytical device. The pressure drop through the orifice also leads to the freezing of the reaction thanks the concomitant decrease of temperature and of the

Fig. 8.8 Picture of a sonic probe (*in the left*) and of a glass finger with a thermocouple inside (*in the right*) used to sample species and measure the reaction temperature in the high pressure jet-stirred reactor used in Orléans (Dagaut et al. 1986)



partial pressures. Figure 8.8 displays a picture of a sonic probe and of a glass finger with a thermocouple inside used to sample species and measure the reaction temperature in the high pressure jet-stirred reactor used in Orléans (Dagaut et al. 1986).

8.5 Analytical Devices

One of the advantages of the jet-stirred reactor is the possibility of easy coupling with several types of analytical devices. Gas chromatography is the most used technique for the quantification and the identification of species. This technique is well adapted to the analysis of most stable molecules such as hydrocarbons or permanent gases. However, it is not well adapted to the quantification of some species (e.g., water and formaldehyde for which Fourier transform infrared spectroscopy is more suitable), of unstable molecules (such as hydroperoxides which are common intermediates in the low temperature oxidation of hydrocarbons), and of radicals. Thus, tentatives of coupling of the jet-stirred reactor with new analytical techniques (e.g., mass spectrometry with direct sampling in the reactor and spectroscopic techniques) have been carried out to quantify an enlarged range of types of species.

8.5.1 Gas Chromatographic Analyses

Gas chromatography is a very common analytical technique that is widely used for the identification and the quantification of species in gas-phase kinetic studies. This technique is mainly coupled to the following detectors: flame ionization detectors (FID) for the quantification of species containing carbon atoms, thermal conductivity detector (TCD) for the quantification of permanent gases and mass spectrometer which can be used for both the identification and the quantification of species. Figure 8.9 displays mole fraction profiles obtained in the experimental study of the oxidation of methyl decanoate using gas chromatographic analysis (Glaude et al. 2010).

The identification of the reaction products is most of the time performed using a gas chromatograph coupled to a mass spectrometer with electron impact ionization at 70 eV. The identification work becomes sometimes difficult in gas-phase studies as the mass spectra of the species are not always in the databases and as the mass spectra of isomers are very similar. The deciphering of experimental mass spectra can be carried out when they are not available in the databases. For example, this is often the case for cyclic ethers which are very common and important intermediates formed by the propagation steps involved in the low temperature oxidation of hydrocarbons (Herbinet et al. 2011b).

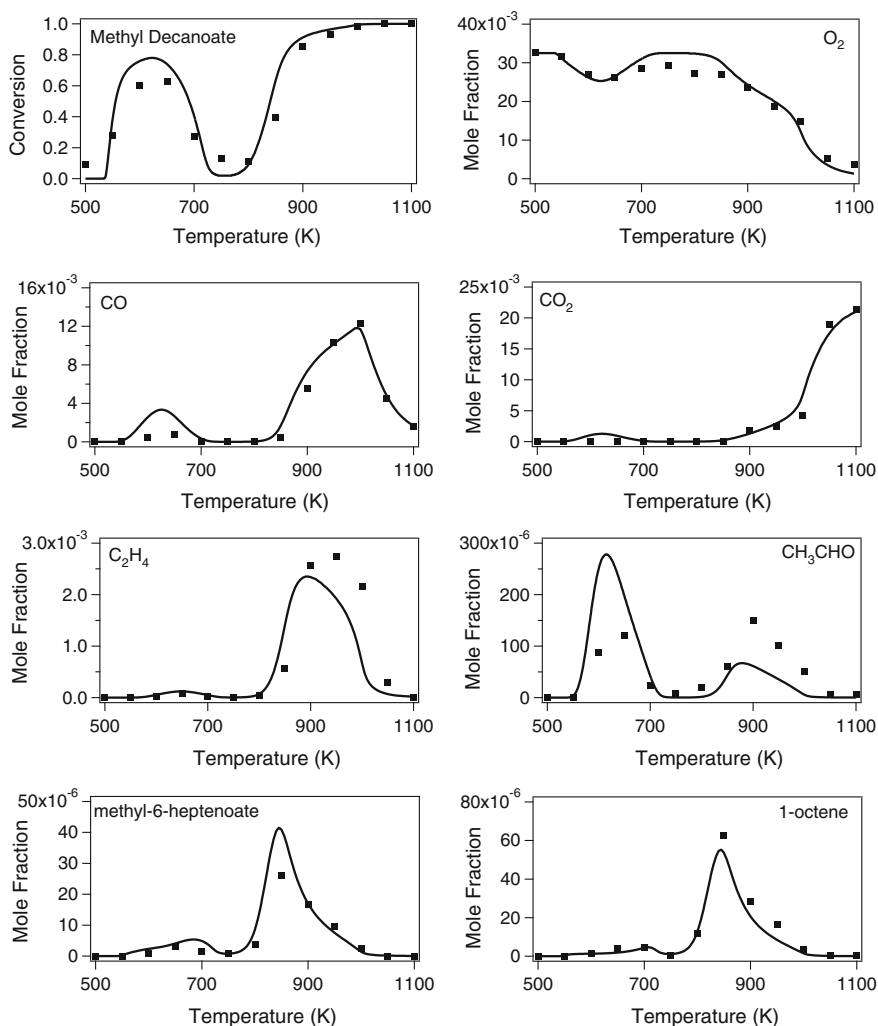


Fig. 8.9 Mole fraction profiles of reactants and of some reaction products obtained using gas chromatography during the experimental study of the oxidation of methyl decanoate in a jet-stirred reactor. Symbols are experimental data and lines are data computed with a model (Glaude et al. 2010)

8.5.2 Infrared Spectroscopy

Fourier transform infrared spectroscopy is a technique used to obtain the infrared spectrum (IR) of a molecule and since, in principle, each IR spectrum is unique it therefore aids identification. In addition, the technique can be used quantitatively provided that standards are available whose spectrum can be obtained under the

same set of conditions as the analytes themselves. This is because the structure of the spectra is sensitive to concentration, as well as pressure and temperature. Hence, the pressure and the temperature of the analysis cell are controlled and the cell is connected to the sampling probe of the reactor by means of heated line to avoid condensation. The cell is filled of the reacting mixture at the pressure and the temperature at which the standards of species targeted were performed. Finally, a software is able to deconvolute each experimental spectrum and recover the individual spectra and to quantify.

Figure 8.10 displays mole fraction profiles of CO, CO₂, H₂O, NO, NO₂, and CH₂O obtained in the experimental study of the oxidation of a blend of *n*-heptane and toluene (80–20 mol%) in a jet-stirred reactor using Fourier transform infrared spectroscopy (Dubreuil et al. 2007).

8.5.3 SVUV Photo-Ionization Mass Spectrometry

A coupling of a jet-stirred reactor and a reflectron time-of-flight mass spectrometer (RTOF-MS) with tunable synchrotron vacuum ultra violet (SVUV) photo-ionization was achieved using a molecular beam sampling system (Battin-Leclerc et al. 2010; Herbinet et al. 2011a). The coupling was made through a cone-like nozzle which was pierced with a very small orifice (the diameter of which was about 50 μm) and which was inserted in the lateral wall of a spherical jet-stirred reactor (Fig 8.11). Figure 8.12 is a picture of the jet-stirred reactor connected to the mass spectrometer at the National Synchrotron Radiation Laboratory (Hefei, China).

This arrangement alleviates the problem of changes in the composition of the gas between the outlet of the reactor and the analytical apparatus. SVUV photo-ionization mass spectrometry is a very powerful method for the identification of

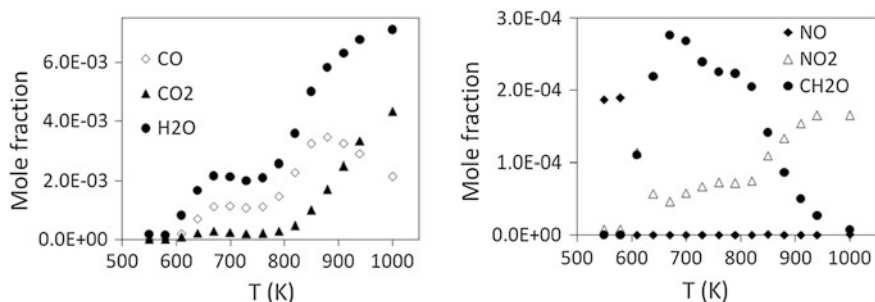


Fig. 8.10 Mole fraction profiles of CO, CO₂, H₂O, NO, NO₂ and CH₂O using Fourier transformed infrared spectroscopy during the experimental study of the oxidation of a blend of *n*-heptane and toluene in a jet-stirred reactor (Dubreuil et al. 2007). Experiments were performed in a jet-stirred reactor at a pressure of 10 atm, a residence time of 0.5 s, fuel and NO inlet concentrations of 800 and 50 ppmv, respectively, and equivalence ratio of 2

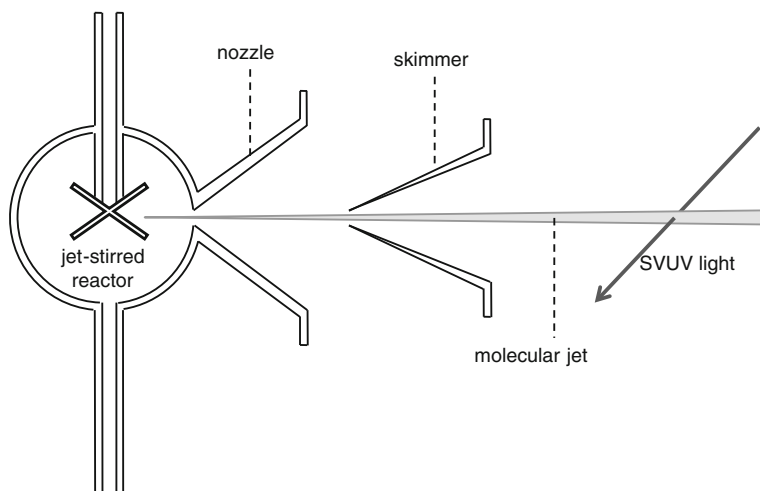
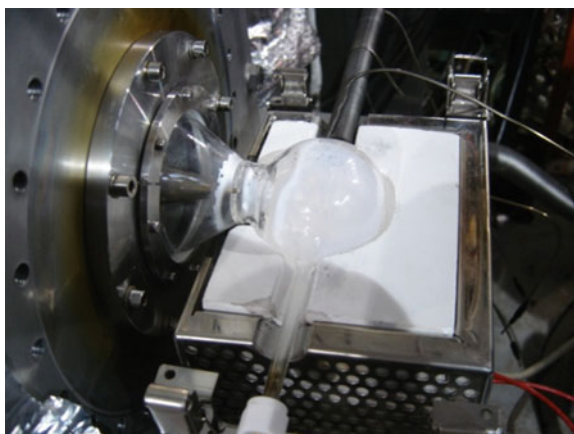


Fig. 8.11 Simplified scheme of the coupling of a jet-stirred reactor and a reflectron time-of-flight mass spectrometer with tunable synchrotron vacuum ultra violet photo-ionization using a molecular beam sampling system

Fig. 8.12 Photograph of the jet-stirred reactor coupled to the reflectron time-of-flight mass spectrometer at the National Synchrotron Radiation Laboratory (Hefei, China)



molecules (especially unstable molecular intermediates) and radicals in gas-phase kinetic studies (Hansen et al. 2009; Li and Qi 2010; Qi 2013). This analytical technique was already used to study the oxidation of hydrocarbons and allowed the identification of enols in flame experiments (Taatjes et al. 2005). Two major difficulties in this technique are the separation of isomers which are identified using their photo-ionization energies (which are sometimes very close) and the quantification of species which requires the knowledge of the cross-sections of the species as a function of the photon energy.

The study of the low-temperature oxidation of *n*-butane was performed using a jet-stirred reactor coupled to the RTOF-MS (Herbinet et al. 2011a). No radical

species were observed during this study due to the very low concentration of this type of species in a jet-stirred reactor (as an example, orders of magnitude of the concentrations of hydroperoxyl and hydroxyl radicals are 1 and 0.01 ppm, respectively). But this technique allowed the identification of an important class of molecules involved in the low temperature oxidation chemistry of hydrocarbons: hydroperoxides and ketohydroperoxides. Figure 8.13 displays the mole fraction profiles of hydroperoxides and ketohydroperoxides detected in the study of the low-temperature oxidation of *n*-butane (experiments performed at 106 kPa, a residence time of 6 s, fuel and oxygen inlet mole fractions of 0.04 and 0.26, respectively).

8.5.4 Cavity Ringdown Spectroscopy

A jet-stirred reactor has been coupled to a cavity where continuous wave cavity ring-down spectroscopy (cw-CRDS) can be performed at the Laboratoire Réactions et Génie des Procédés (Nancy, France) in collaboration with the laboratory PhysicoChimie des Processus de Combustion et de l'Atmosphère (Lille, France). cw-CRDS is a technique which has already been used to measure the concentrations of OH and HO₂ radicals in the photolysis of hydrogen peroxide (Parker et al. 2011). The coupling of the jet-stirred reactor and of the spectroscopic cell was achieved using a sonic probe as in flame experiments (Fig. 8.14). The use of a

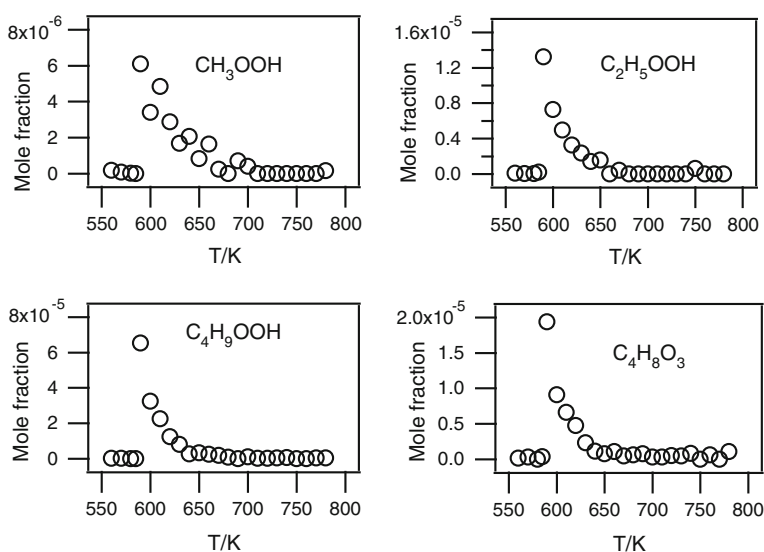


Fig. 8.13 Experimental mole fractions of hydroperoxides and ketohydroperoxides formed in the low temperature oxidation of *n*-butane. Experiments were performed in a jet-stirred reactor and using SVUV photo-ionization mass spectrometry (Herbinet et al. 2011a)

sonic probe instead of a molecular beam allowed the sampling of species in the gas phase in the reactor and the maintenance of a high enough pressure in the spectroscopic cell.

Studies of the oxidation of methane and *n*-butane were recently performed using this apparatus (Bahrini et al. 2012a, b). The high sensitivity of this absorption technique allowed the quantification of some stable species in the oxidation of methane: water, methane, and formaldehyde (Fig. 8.15), whose IR spectra around 1,506 nm are well structured and well-known, particularly for methane and formaldehyde. Hydrogen peroxide, which was not detected in the methane oxidation study because its concentration was too low, could be quantified in the *n*-butane study. The corresponding mole fraction profile is displayed in Fig. 8.16.

8.6 Effect of Wall Reactions

It has long been known that the coating of the wall of a reactor can have an influence on the kinetics of combustion phenomena (Pollard 1977; Griffiths and Scott 1987). As an example, wall reactions can affect the reactivity of a fuel and can change the boundaries between the different oxidation phenomena (slow oxidation, cool flames, and auto-ignition) that can occur in a batch reactor (Konnov et al. 2005). Brocard and Baronnet (1983), who studied the oxidation of methyl tert-butyl ether in different closed vessels (packed and unpacked, coated and uncoated), also observed large difference of reactivities that were attributed to wall effects. A catalytic effect was also observed in the oxidation of methyl and ethyl tert-butyl ethers in a jet-stirred reactor (Glaude et al. 2000).

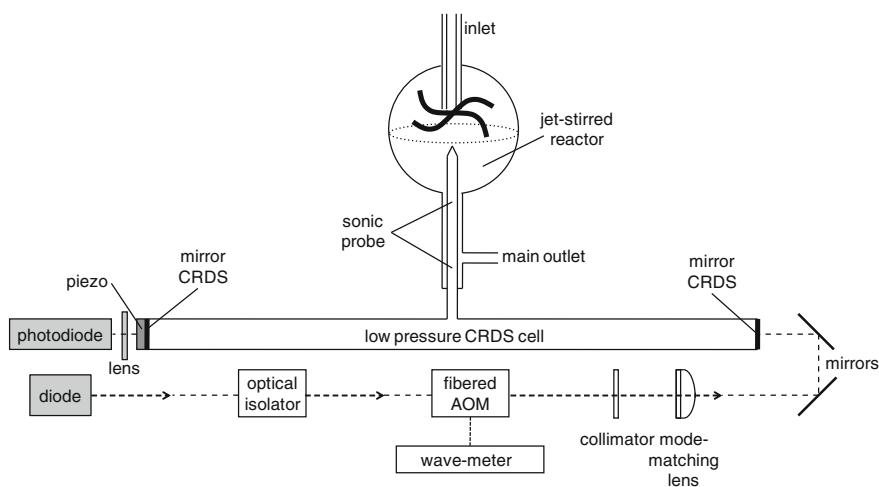


Fig. 8.14 Scheme of a jet-stirred reactor coupled to a cavity cw-CRDS (Bahrini et al. 2012a,b)

Fig. 8.15 Mole fraction profiles of methane, water and formaldehyde obtained in the study of the oxidation of methane in a jet-stirred reactor using cw-CRDS and gas chromatography (GC) analyses (Bahrini et al. 2012a). Experiments were performed in a jet-stirred reactor at a pressure of 106 kPa, a residence time of 2 s, fuel and oxygen inlet mole fractions of 0.0625

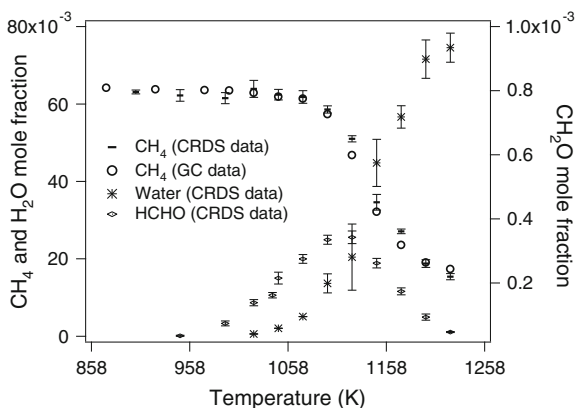
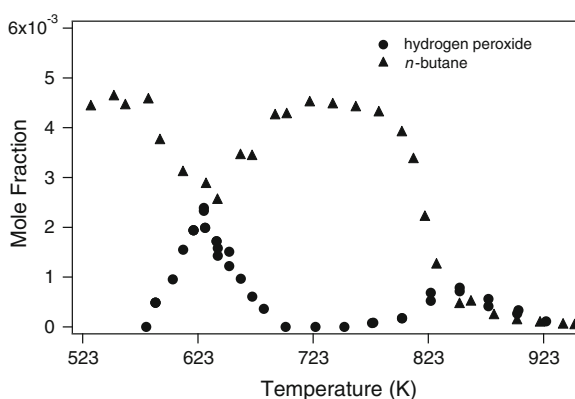


Fig. 8.16 Mole fraction profiles of hydrogen peroxide (cw-CRDS analyses) and *n*-butane (gas chromatography; mole fraction/5) obtained in the study of the oxidation of *n*-butane in a jet-stirred reactor (Bahrini et al. 2012b). Experiments were performed in a jet-stirred reactor at a pressure of 106 kPa, a residence time of 6 s, fuel and oxygen inlet mole fractions of 0.023 and 0.149, respectively



The effect of wall reactions in a jet-stirred reactor was numerically investigated by adding wall reactions involving the HO₂ radical in a detailed kinetic model for the oxidation of methane (Fig. 8.17). These wall reactions were taken from the work of Porter et al. (2008). The first reaction is the adsorption of the HO₂ radical at the wall and the second reaction is the reaction of adsorbed HO₂ radicals yielding water and oxygen. It can be seen in Fig. 8.17 that these wall reactions have a slight inhibiting effect on the reactivity.

8.7 Modeling and Simulation

One advantage of the jet-stirred reactor relies on the relatively easy modeling which simplifies a lot the simulations with detailed kinetic models (Scacchi et al. 1996). This type of reactor is modeled by two types of equations: the mass equation and the conservation of energy (Villermaux 1995).

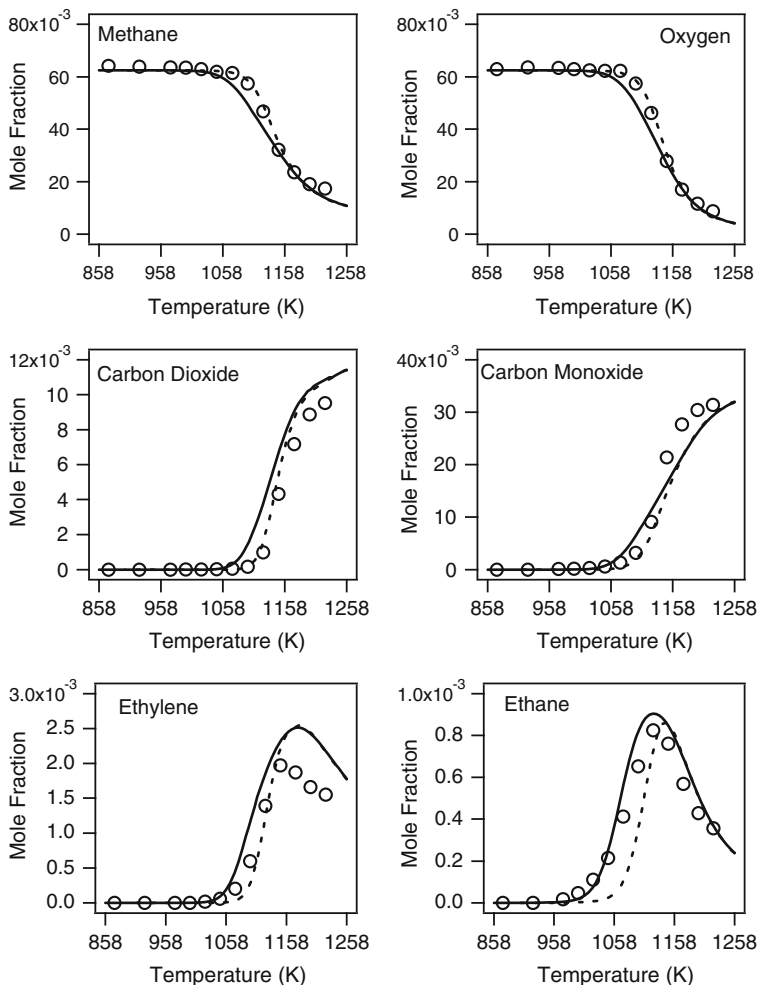


Fig. 8.17 Influence of the addition of wall reactions in a detailed kinetic model of the oxidation of methane. Symbols: experimental data obtained using gas chromatography; Full line: model without wall reactions; Dashed line: model with wall reactions. Experiments were performed in a jet-stirred reactor at a pressure of 106 kPa, a residence time of 2 s, fuel and oxygen inlet mole fractions of 0.0625

The mass equation is given by Eq. 8.21. In this equation, F_j^i and F_j^o are the mole flow rates of the species j at the inlet and at the outlet of the reactor, respectively, V is the volume of the reactor, r_i is the rate of the reaction i , and $v_{i,j}$ is the stoichiometric coefficient of the species j in the reaction i ($v_{i,j}$ is positive if the species j is formed in the reaction i , and negative if it is consumed).

$$F_j^o = F_j^i + \sum_i v_{i,j} r_i V \quad (8.21)$$

For the special case of a unimolecular reaction $A \rightarrow P$, the expression of the concentration C_A^o of the species A at the outlet of the reactor (Eq. 8.22) can be easily deduced from the mass equation given by Eq. 8.21. In Eq. 8.22, C_A^i is the concentration of the species A at the inlet of the reactor, k is the kinetic constant of the reaction $A \rightarrow P$, and τ is the residence time.

$$C_A^o = C_A^i / (1 + k\tau) \quad (8.22)$$

The conservation of energy is given by Eq. 8.23. In this equation, h_j^i and h_j^o are the mole enthalpies of formation of the species j at the inlet and at the outlet of the reactor, and W is the reactor heat loss. Note that jet-stirred reactors are most of the time operated at constant temperature. In this case the heat loss term W in Eq. 8.23 disappears.

$$\sum_j F_j^o h_j^o + W = \sum_j F_j^i h_j^i \quad (8.23)$$

A system composed of $j + 1$ algebraic equations is obtained. This system can be solved using a Newton algorithm. PSR program included in Chemkin II (Glarborg et al. 1986) is largely used to performed jet-stirred reactor simulations. This program solves the system of algebraic equations using the damped modified Newton algorithm. This algorithm needs a starting estimate of the solution to begin the iteration. A difficulty is to provide a reasonable starting estimate. If no good starting estimate is available, the software uses the equilibrium composition at an estimated temperature as starting estimates. For very difficult problems, it is recommended to start the calculation with a long residence time and a high temperature and then to use the continuation feature to shorten the residence time and decrease the temperature progressively. Sometimes, the Newton method does not converge and a transient computation with integration of a system of ordinary differential equations using the backward-Euler method is performed before returning to the Newton algorithm.

8.8 Experimental Studies of Oxygenated Fuels

Jet-stirred reactors have been used for the studies of the oxidation and pyrolysis of numerous hydrocarbons and oxygenated compounds (Tran et al. 2012). Experimental studies of the oxidation and the pyrolysis of oxygenated compounds in a jet-stirred reactor are displayed in Table 8.1. It can be seen that many studies of the oxidation of alcohols and esters have been carried out. There is much less studies on ethers and particularly on cyclic ethers which can be derived from

Table 8.1 Experimental studies of the oxidation and the pyrolysis of oxygenated compounds performed in a jet-stirred reactor

Species	Experimental conditions					References
	T (K)	P (kPa)	Φ	τ (s)	x_{fuel}	
<i>Alcohols</i>						
Ethanol	1000–1200	101	0.2–2	0.04–0.24	0.003	Aboussi 1991
	890–1250	101	0.25–2	0.07–0.7	0.002	Leplat et al. 2011
<i>n</i> -butanol	800–1250	101–1010	0.25–2	0.07–0.7	0.001–0.012	Dagaut et al. 2009; Sarathy et al. 2009
2-butanol	770–1250	1013	0.275–4	0.7	0.001–0.0015	Togbé et al. 2010a
iso-butanol	770–1250	1013	0.275–4	0.7	0.001–0.0015	Togbé et al. 2010a
<i>n</i> -pentanol	770–1220	1013	0.35–4	0.7	0.001–0.0015	Togbé et al. 2011
iso-pentanol	530–1220	1013	0.35–4	0.7	0.001–0.0015	Dayma et al. 2011
<i>n</i> -hexanol	560–1220	1013	0.5–3.5	0.7	0.001–0.0015	Togbé et al. 2010b
<i>Ethers</i>						
Dimethyl ether	550–1275	101–1013	0.2–2.5	1	0.001–0.002	Dagaut et al. 1996, 1998a
Methyl tert-butyl ether; ethyl tert-butyl ether; tert-amyl methyl ester; dipropyl ether	800–1150	1013	0.5–2.0	0.5	0.001	Goldaniga et al. 1998
Dimethoxymethane	800–1200	507	0.444–1.778	0.25	0.0015	Daly et al. 2001
Tetrahydrofuran	800–1100	101–1013	0.5–1.0	0.1–0.5	0.001	Dagaut et al. 1998b
<i>Aldehydes</i>						
Propanal	800–1100	1013	0.3–2.0	0.7	0.0015	Veloo et al. 2013
<i>Esters</i>						
Methyl-butanoate	850–1400	101	0.375, 0.75 and 1.13	0.07	0.00075	Gaïl et al. 2008
Methyl-2-butenoate	530–1220	1013	0.5, 1 and 2	0.7	0.001	Karsenty et al. 2012
Methyl pentanoate	500–1000	1013	0.5–1.5	1.5	0.001	Dayma et al. 2008
Methyl hexanoate	550–1150	1013	0.6–2	0.7	0.001	Dayma et al. 2009

(continued)

Table 8.1 (continued)

Species	Experimental conditions					References
	T (K)	P (kPa)	Φ	τ (s)	x_{fuel}	
Methyl decanoate	500–1100	106	1	1.5	0.0021	Glaude et al. 2010
Methyl palmitate/ <i>n</i> -decane	773–1123	106	1–4	Pyrolysis	0.0218	Herbinet et al. 2011c
	550–1100	106	1.0	1.5	0.00052/ 0.00148	Hakka et al. 2009
Methyl oleate/ <i>n</i> -decane	550–1100	106	1.0	1.5	0.00052/ 0.00148	Bax et al. 2010
Rapeseed oil methyl esters	800–1400	101–1013	0.25–1.5	0.07–1	0.0005	Dagaut et al. 2007

ligno-cellulosic biomass. Note that almost no jet-stirred experimental data study about the oxidation of aldehydes and ketones was reported while these species are important intermediates formed in the combustion of hydrocarbons and oxygenated species (Piperel et al. 2009).

As shown in Table 8.1 there is a lack of JSR data for some types of molecules. Future studies could focus on large methyl esters that are present in biodiesel fuels (methyl palmitate, methyl stearate, methyl oleate, methyl linoleate, and methyl linolenate) in order to study the influence of double bonds in the oxidation chemistry. Another interesting field of investigation is the study of the oxidation of the numerous molecules derived from the decomposition of ligno-cellulosic biomass (C_2 – C_3 hydroxy-carbonyl species such as hydroxyl-acetone, anhydrosugars such as levoglucosan, furans such as furfural and aromatics such as guaiacol). In addition, the study of aldehydes, ketones, and cyclic ethers will be valuable for the understanding of the oxidation chemistry of petrol-based fuels.

References

- Aboussi B (1991) PhD dissertation, University of Orleans, France
- Azay P, Côme GM (1979) Temperature gradients in a continuous flow stirred tank reactor. *Ind Eng Chem Process Des Dev* 18:754–756
- Azay P, Marquaire PM, Pommier P et al (1981) A versatile oven with very little thermal inertia. *J Chem Educ* 58:441
- Bahrini C, Herbinet O, Glaude PA et al (2012a) Detection of some stable species during the oxidation of methane by coupling a jet-stirred reactor (JSR) to cw-CRDS. *Chem Phys Lett* 534:1–7
- Bahrini C, Herbinet O, Glaude PA et al (2012b) Quantification of hydrogen peroxide during the low-temperature oxidation of alkanes. *J Am Chem Soc* 134:11944–11947
- Battin-Leclerc F, Herbinet O, Glaude PA et al (2010) Experimental confirmation of the low-temperature oxidation scheme of alkanes. *Angew Chem* 122:3237–3240
- Baulch DL, Griffiths JF, Pappin AJ et al (1988) Stationary-state and oscillatory combustion of hydrogen in a well-stirred flow reactor. *Combust Flame* 73:163–185
- Baumlin S, Broust F, Ferrer M et al (2005) The continuous self stirred tank reactor: measurement of the cracking kinetics of biomass pyrolysis vapours. *Chem Eng Sci* 60:41–55
- Bax S, Hakka MH, Glaude PA et al (2010) Experimental study of the oxidation of methyl oleate in a jet-stirred reactor. *Combust Flame* 157:1220–1229
- Brocard JC, Baronnet F (1983) Chemical kinetics of the oxidation of methyl tert-butyl ether (MTBE). *Combust Flame* 52:25–35
- Bush SF (1969) The design and operation of single-phase jet-stirred reactors for chemical kinetic studies. *Trans Inst Chem Eng* 47:59–72
- Cavaliere A, Ciajolo A, D'Anna A et al (1993) Autoignition of n-heptane and n-tetradecane in engine-like conditions. *Combust Flame* 93:279–286
- Ciajolo A, D'Anna A (1998) Controlling steps in the low-temperature oxidation of n-heptane and iso-octane. *Combust Flame* 112:617–622
- Côme GM, Li Y, Barbé P, Gueritey N et al (1996) Competition between the gas and surface reactions for the oxidative coupling of methane: 2. Isothermal experiments in a catalytic jet-stirred gas phase reactor. *Catal Today* 30:215–222
- Dagaut P, Reuillon M, Boettner JC et al (1994) Kerosene combustion at pressures up to 40 atm: Experimental study and detailed chemical kinetic modeling. *Symp (Int) Combust* 25:919–926

- Dagaut P, Cathonnet M, Rouan JP et al (1986) A jet-stirred reactor for kinetic studies of homogeneous gas-phase reactions at pressures up to ten atmospheres (~ 1 MPa). *J Phys E: Sci Instrum* 19:207–209
- Dagaut P, Boettner JC, Cathonnet M (1996) Chemical kinetic study of dimethylether oxidation in a jet stirred reactor from 1 to 10 ATM: experiments and kinetic modeling. Twenty-sixth symposium (International) on combustion, vol 26. The Combustion Institute, Pittsburgh, pp 627–32
- Dagaut P, Daly C, Simmie JM et al (1998a) Oxidation and ignition of dimethylether from low to high temperature (500–1600 K): Experiments and kinetic modeling. Twenty-seventh symposium (International) on combustion, vol 27. The Combustion Institute, Pittsburgh, PA, pp 361–69
- Dagaut P, McGuinness M, Simmie JM et al (1998b) The ignition and oxidation of tetrahydrofuran: experiments and kinetic modeling. *Combust Sci Tech* 135:3–29
- Dagaut P, Gail S, Sahasrabudhe M (2007) Rapeseed oil methyl ester oxidation over extended ranges of pressure, temperature, and equivalence ratio: experimental and modeling kinetic study. *Proc Combust Inst* 31:2955–2961
- Dagaut P, Sarathy SM, Thomson MJ (2009) A chemical kinetic study of n-butanol oxidation at elevated pressure in a jet stirred reactor. *Proc Combust Inst* 32:229–237
- Daly CA, Simmie JM, Dagaut P et al (2001) Oxidation of dimethoxymethane in a jet-stirred reactor. *Combust Flame* 125:1106–1117
- David R, Matras D (1975) Rules for the construction and extrapolation of reactors self-stirred by gas jets. *Can J Chem Eng* 53:297–300
- Dayma G, Dagaut P (2006) Effects of air contamination on the combustion of hydrogen-effect of NO and NO₂ addition on hydrogen ignition and oxidation kinetics. *Combust Sci Tech* 178:1999–2024
- Dayma G, Gail S, Dagaut P (2008) Experimental and kinetic modeling study of the oxidation of methyl hexanoate. *Energ Fuel* 22:1469–1479
- Dayma G, Togbé C, Dagaut P (2009) Detailed kinetic mechanism for the oxidation of vegetable oil methyl esters: new evidence from methyl heptanoate. *Energ Fuel* 23:4254–4268
- Dayma G, Togbé C, Dagaut P (2011) Experimental and detailed kinetic modeling study of isoamyl alcohol (isopentanol) oxidation in a jet-stirred reactor at elevated pressure. *Energ Fuel* 25:4986–4998
- Dubreuil A, Foucher F, Mounaïm-Rousselle C et al (2007) HCCI combustion: effect of NO in EGR. *Proc Combust Inst* 31(2):2879–2886
- Fleys M, Simon Y, Swierczynski D et al (2006) Investigation of the reaction of partial oxidation of methane over Ni/La₂O₃. *Energ Fuels* 20:2321–2329
- Gail S, Sarathy SM, Thomson MJ et al (2008) Experimental and chemical kinetic modeling study of small methyl esters oxidation: methyl (E)-2-butenate and methyl butanoate. *Combust Flame* 155:635–650
- Glarborg P, Kee RJ, Grcar JF et al (1986) PSR: a Fortran program for modeling well-stirred reactor. Sandia report 86-8209
- Glaude PA, Battin-Leclerc F, Judenherc B et al (2000) Experimental and modeling study of the gas-phase oxidation of methyl and ethyl tertiary butyl ethers. *Combust Flame* 121:345–355
- Glaude PA, Herbinet O, Bax S et al (2010) Modeling of the oxidation of methyl esters—validation for methyl hexanoate, methyl heptanoate, and methyl decanoate in a jet-stirred reactor. *Combust Flame* 157:2035–2050
- Goldaniga A, Faravelli T, Ranzi E et al (1998) Oxidation of oxygenated octane improvers: MTBE, ETBE, DIPE, and TAME. Twenty-seventh symposium (International) on combustion, vol 26. The Combustion Institute, Pittsburgh, pp 353–60
- Griffiths JF, Scott S (1987) Thermokinetic interactions: fundamentals of spontaneous ignition and cool flames. *Prog Energ Combust Sci* 13:161–197
- Griffiths JF, Inomata T (1992) Oscillatory cool flames in the combustion of diethyl ether. *J Chem Soc Faraday T* 88:3153–3158

- Hakka MH, Glaude PA, Herbinet O et al (2009) Experimental study of the oxidation of large surrogates for diesel and biodiesel fuels. *Combust Flame* 156:2129–2144
- Hansen N, Cool TA, Westmoreland PR et al (2009) Recent contributions of flame-sampling molecular-beam mass spectrometry to a fundamental understanding of combustion chemistry. *Prog Energy Combust Sci* 35:168–191
- Herbinet O, Marquaire PM, Battin-Leclerc F et al (2007) Thermal decomposition of n-dodecane: experiments and kinetic modeling. *J Anal Appl Pyrol* 78:419–429
- Herbinet O, Battin-Leclerc F, Bax S et al (2011a) Detailed product analysis during the low temperature oxidation of n-butane. *Phys Chem Chem Phys* 13:296–308
- Herbinet O, Bax S, Glaude PA et al (2011b) Mass spectra of cyclic ethers formed in the low-temperature oxidation of a series of n-alkanes. *Fuel* 90:528–535
- Herbinet O, Glaude PA, Warth V et al (2011c) Experimental and modeling study of the thermal decomposition of methyl decanoate. *Combust Flame* 158:1288–1300
- Hinze JO, Hegge Zijnen BG (1949) Transfer of heat and matter in the turbulent mixing zone of an axially symmetrical jet. *Appl Sci Res* 1:435–461
- Houzelot JL, Villermaux J (1977) Mass transfer in annular cylindrical reactors in laminar flow. *Chem Eng Sci* 32:1465–1470
- Karsenty F, Sarathy SM, Togbé C et al (2012) Experimental and kinetic modeling study of 3-methylheptane in a jet-stirred reactor. *Energ Fuel* 26:4680–4689
- Konnov AA, Zhu JN, Bromley JH et al (2005) The effect of NO and NO₂ on the partial oxidation of methane: experiments and modeling. *Proc Combust Inst* 30:1093–1100
- Leplat N, Dagaut P, Togbé C et al (2011) Numerical and experimental study of ethanol combustion and oxidation in laminar premixed flames and in jet-stirred reactor. *Combust Flame* 158:705–725
- Li Y, Qi F (2010) Recent applications of synchrotron VUV photoionization mass spectrometry: insight into combustion chemistry. *Acc Chem Rev* 43:68–78
- Matras D, Villermaux J (1973) Un réacteur continu parfaitement agité par jets gazeux pour l'étude cinétique de réactions chimiques rapides. *Chem Eng Sci* 28:129–137
- Marquaire PM, Côme GM (1978) Non quasi-stationary state pyrolysis. Induction period of *neo*-pentane pyrolysis. *React Kinet Catal Lett* 9:165–169
- Parker AE, Jain C, Schoemaeker C et al (2011) Simultaneous, time-resolved measurements of OH and HO₂ radicals by coupling of high repetition rate LIF and cw-CRDS techniques to a laser photolysis reactor and its application to the photolysis of H₂O₂. *Appl Phys B* 103(3):725–733
- Piperel A, Dagaut P, Montagne X (2009) Impact of acetaldehyde and NO addition on the 1-octene oxidation under simulated HCCI conditions 32:2861–2868
- Pollard RT (1977) Gas phase combustion. In: Bamford CH, Tipper CFH (eds) *Comprehensive chemical kinetic*, vol 17. Elsevier Amsterdam, pp 249–368
- Porter R, Glaude PA, Buda F et al (2008) A tentative modeling study of the effect of wall reactions on oxidation phenomena. *Energ Fuel* 22:3736–3743
- Qi F (2013) Combustion chemistry probed by synchrotron VUV photoionization mass spectrometry. *Proc Combust Inst* 34:33–63
- Mzé-Ahmed A, Hadj-Ali K, Diévert P et al (2010) Kinetics of oxidation of a synthetic jet fuel in a jet-stirred reactor: experimental and modeling study. *Energ Fuel* 24:4904–4911
- Sarathy SM, Thomson MJ, Togbé C et al (2009) An experimental and kinetic modeling study of n-butanol combustion. *Combust Flame* 156:852–864
- Scacchi G, Bouchy M, Foucaut JF et al (1996) Cinétique et catalyse. Tec & Doc Lavoisier, Paris
- Taatjes CA, Hansen N, McIlroy A et al (2005) Chemistry: enols are common intermediates in hydrocarbon oxidation. *Science* 308:1887–1889
- Togbé C, Mzé-Ahmed A, Dagaut P (2010a) Kinetics of oxidation of 2-butanol and Isobutanol in a jet-stirred reactor: experimental study and modeling investigation. *Energ Fuel* 24:5244–5256
- Togbé C, Dagaut P, Mzé-Ahmed A et al (2010b) Experimental and detailed kinetic modeling study of 1-hexanol oxidation in a pressurized jet-stirred reactor and a combustion bomb. *Energy Fuels* 24:5859–5875

- Togbé C, Halter F, Foucher F, Mounaim-Rousselle C et al (2011) Experimental and detailed kinetic modeling study of 1-pentanol oxidation in a JSR and combustion in a bomb. *Proc Combust Inst* 33:367–374
- Tran LS, Sirjean B, Glaude PA et al (2012) Progress in detailed kinetic modeling of the combustion of oxygenated components of biofuels. *Energy* 43:4–18
- Veloo PS, Dagaut P, Togbé C et al (2013) Jet-stirred reactor and flame studies of propanal oxidation. *Proc Combust Inst* 34:599–606
- Villermaux J (1995) *Génie de la réaction chimique: Conception et fonctionnement des réacteurs*. Tec & Doc Lavoisier, Paris
- Ziegler I, Fournet R, Marquaire PM (2005) Influence of surface on chemical kinetic of pyrocarbon deposition obtained by propane pyrolysis. *J Anal Applied Pyrol* 73:107–115

Chapter 9

Tubular Flow Reactors

Fabiola Monge, Veronica Aranda, Angela Millera, Rafael Bilbao
and María U. Alzueta

Abstract Tubular flow reactors for studying combustion chemistry are extensively used due to their operational flexibility. In these reactors, conditions of temperature, pressure, and gas fluid residence time can be carefully controlled. The different real reactors (turbulent and laminar regimes, with and without temperature profiles) can attain almost ideal behavior (plug flow), diminishing the mathematical difficulties in the simulation of such environments. Nevertheless, the advantages and disadvantages, as well as the deviations of real reactors from ideality, must be considered in order to choose the most suitable reaction system in each case. Tubular flow reactors are proposed as one of the possible facilities to investigate the oxidation of oxygenated compounds, which have been suggested as additives to diesel fuel in order to reduce the formation of soot. Among oxygenates, this chapter focuses on the study of some alcohols (methanol, ethanol, propanol, and butanol) and ethers (dimethylether and dimethoxymethane), aiming to show the results that can be obtained by using a tubular flow reactor.

List of Important Symbols and Abbreviations

A	Reactant
C	Concentration
d_r	Tube diameter
D	Dispersion coefficient
\mathcal{D}	Diffusion coefficient
$E(t)$	Residence time distribution
F	Molar flow rate
k	Reaction rate constant
L	Length of the reactor
p	Pressure
Q	Volumetric flow rate

F. Monge · V. Aranda · A. Millera · R. Bilbao · M. U. Alzueta (✉)
Aragón Institute of Engineering Research (I3A), University of Zaragoza, Río Ebro Campus,
C/Mariano Esquillor s/n 50018 Zaragoza, Spain
e-mail: uxue@unizar.es

r	Radius
$(-r_A)$	Rate of reaction
R	Radius
t	Time
T	Temperature
u	Velocity of fluid
V	Volume
X_A	Fraction of A converted

Greek Symbols

μ	Viscosity of fluid
ρ	Density of fluid

Dimensionless Groups

Bo	Bodenstein number
Re	Reynolds number
Sc	Schmidt number

Abbreviations

DME	Dimethylether
DMM	Dimethoxymethane
PFR	Plug flow reactor
RTD	Residence time distribution

9.1 Introduction

A bench scale tubular flow reactor consists of a cylindrical tube with a constant diameter, where the reactant mixture flows continuously along the tube. This type of reactor is easy to construct and operational problems as leaks, repairs, etc. are reduced. These reactors can be used to study photochemistry, high temperature chemistry (Cutler et al. 1988), and to obtain experimental results that allow us to carry out kinetic studies and mainly to validate detailed kinetic models.

Some of the chemical processes that can be studied in tubular flow reactors (Lee et al. 2000) are coupled reaction systems, gas phase elementary reaction rates, and isolated elementary reactions by means of the consumption of specific reactive radicals.

Tubular flow reactors are suitable, in particular, for the study of the hydrocarbon oxidation processes. This kind of process is characterized by radical

reactions that require high temperature and short reaction times because of their high reaction rate. The tubular flow reactors enable operational flexibility and are suitable to work with low residence times and high temperature and pressure conditions (Santamaría et al. 2002). They can easily be used with gas chromatography and Fourier transform infrared spectroscopy (FTIR) analyses.

Various questions have been raised concerning the qualities of data derived from tubular flow reactors. The questions deal mainly with the fluid flow pattern in the reactor and the existence of temperature gradients. These important questions are further analyzed in the following sections.

One of the processes, that is being extensively studied, is the gas phase oxidation of oxygenated compounds, mainly because of their relevance as diesel additives. Some studies of oxidation of oxygenated compounds in tubular flow reactors will be described later within this Chapter.

9.2 Fluid Flow Pattern in Tubular Flow Reactors

Three factors configure the contacting or fluid flow pattern.

(a) *State of aggregation of the flowing stream*

It is its tendency to clump and for a group of molecules move about together. The state of aggregation of the flowing material depends on its nature. In the extremes, these states are microfluid and macrofluid. In the microfluid state, individual molecules are not attached to their neighbors and each one moves independently. Some examples are gases and not very viscous liquids. In the macrofluid state, molecules move about in clumps and each clump is uniform in composition. Some examples are noncoalescing disperse set droplets, very viscous liquids, and solid particles.

(b) *Earliness of mixing*

The fluid elements of a single flowing stream can mix with each other early or late in their flow through the vessel. Usually, this factor has little effect on the overall behavior for a single flowing fluid. However, it can be important for a system with several entering reactant streams if the mixing occurs with no sufficient time for reaction.

(c) *The residence time distribution (RTD) of the material that is flowing through the vessel.* Individual molecules can stay different times in the reactor. The RTD or exit age distribution function $E(t)$ fulfills that:

$$\int_0^{\infty} E(t)dt = 1 \quad (9.1)$$

9.3 Ideal Plug Flow Reactor Model

Models are useful for representing material flow in real vessels. The results obtained with two ideal flow patterns, plug flow, and mixed flow, are simple to treat. A tubular flow reactor can be a source of high quality rate data when the flow pattern can be idealized as a plug flow.

Steady state plug flow reactors consider that the fluid is perfectly mixed in the radial direction and, consequently, each “plug” or cross-section of the reactor has uniform fluid properties (velocity, composition, temperature and pressure) (Levenspiel 1999). If the radial flow velocity is uniform, all the elements will have the same residence time in the reactor.

It is supposed that fluid flows along the axial direction with negligible diffusive transport in that direction and there is no mixing between the thin “plugs” (differential volume of a fluid element, dV), Fig. 9.1. It is assumed that fluid composition changes progressively through the reactor.

Since the fluid composition changes progressively along the length in a plug flow reactor, the material balance, Eq. (9.2), is made for a fluid element (dV) and applied for the reactant A:

$$\text{In} - \text{Out} = \text{Accumulation} + \text{Consumption} \quad (9.2)$$

Considering the steady state (the accumulation term is zero) and the nomenclature shown in Fig. 9.1, it results:

$$F_A - (F_A + dF_A) = (-r_A)dV \quad (9.3)$$

Taking into account that:

$$dF_A = d[F_{A0}(1 - X_A)] = -F_{A0}dX_A \quad (9.4)$$

It results:

$$F_{A0}dX_A = (-r_A)dV \quad (9.5)$$

Therefore:

$$\int_0^V dV/F_{A0} = \int_0^{X_{Af}} dX_A/(-r_A) \quad (9.6)$$

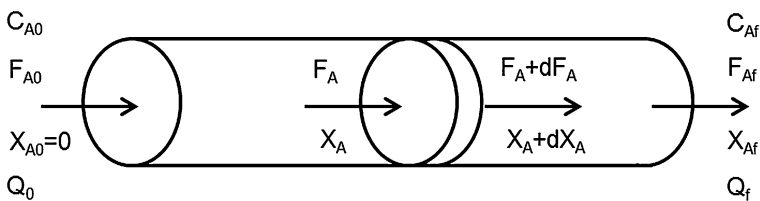


Fig. 9.1 Sketch of a plug flow reactor

Where the reaction rate per unit volume ($-r_A$) depends on the temperature and the reactant concentration. F_A is the molar flow rate of the reactant, F_{A0} the inlet molar flow rate of the reactant and X_A the fraction of A converted.

9.4 Flow Regimes in the Vessel

The radial velocity profile depends on the flow regime on the vessel. Figure 9.2 shows the radial velocity profiles corresponding to turbulent and laminar flows compared with the plug flow.

Turbulent flow appears at high velocity gas flows. It is the flow regime that best approaches plug flow, because the high gas velocity results in an almost flat velocity profile on the cross section. Dryer (1972) found wall effects to be unimportant and that radial concentration and temperature variations were small. Turbulent flow also offers advantages relatives to the isothermal assumption, since mixing favors the heat transfer and the radial temperature uniformity. However, turbulent flow also has some disadvantages. For example, one disadvantage is that related to the high flow velocities needed to obtain turbulent flow. Sometimes, these high flow rates may not be achievable in laboratory reactors, or involve high cost of reactants. In addition, in some cases and in order to have a significant fluid residence time, the installation results in very long reactors. Additionally, the formation of eddies in the turbulent regime can produce mixing in longitudinal direction, moving away from an assumption of a plug flow reactor, and the theoretical differential volume of a fluid element, dV , would become thicker.

Another disadvantage of turbulent flow reactors is the unknown position of the reaction start within the mixing region. Thus, the reaction zone is not totally defined. Usually, the mixing time is determined by fitting experimental data.

Laminar regime assumes that the flow of every element fluid is orderly and parallel to the walls of the reactor, without any perpendicular flow to that direction. This leads to a parabolic velocity (u) profile, Fig. 9.2, given by the equations:

$$u = u_{\max} \left[1 - (r/R)^2 \right] \quad (9.7)$$

$$u_{\max} = u(r = 0) = (P_1 - P_2/4\mu L)R^2 = 2u_m \quad (9.8)$$

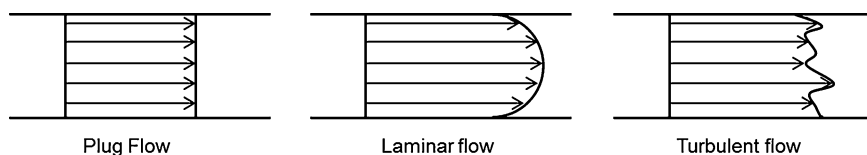


Fig. 9.2 Radial velocity profiles in tubular reactor

where u_m is the average velocity, R the total reactor radius, r the radius where the measure is taken, L the total length, μ the viscosity of the fluid, and $P_1 - P_2$ the fluid pressure drop.

For laminar flow in tubes, different regimes can be obtained.

- (a) If the tube is long enough, the molecular diffusion in the lateral direction will have enough time to disturb the parabolic velocity profile and plug flow or dispersion model can be applied. In the dispersion model, a diffusion-like process superposed on plug flow is assumed. To distinguish this process from molecular diffusion, it is called dispersion or longitudinal dispersion. To characterize the dispersion model the dimensionless group (D/uL) is used, where D is the dispersion coefficient (m^2/s). When $D/uL = 0$, ideal plug flow is obtained. When D/uL value increases, larger deviations from plug flow are obtained.
- (b) If the tube is short enough or the material is very viscous, the molecular diffusion has not enough time to act and pure convection regime is obtained. The pure convection model assumes that each element of fluid slides past its neighbor with no interaction by molecular diffusion. Thus, a spread in the fluid residence according to the radial parabolic velocity profile must be considered.

In this case, the fluid residence time distribution, $E(t)$, is used to calculate the reactant concentrations, C_A , according to the equation:

$$\bar{C}_A/C_{A0} = \int_0^{\infty} (C_A/C_{A0})E(t)dt \quad (9.9)$$

For the radial parabolic velocity profile, the residence time distribution is:

$$E(t) = \bar{r}^2/2t^3 \quad \text{for } t > \bar{t}/2 \quad (9.10)$$

Some examples for different kinetic order of a Newtonian fluid in a pipe are:

- Zero order

$$\bar{C}_A/C_{A0} = (1 - k\bar{t}/2C_{A0})^2 \quad (9.11)$$

- First order

$$\bar{C}_A/C_{A0} = (\bar{t}^2/2) \int_{\bar{t}/2}^{\infty} e^{(-kt/\bar{t}^3)} dt \quad (9.12)$$

- Second order

$$\bar{C}_A/C_{A0} = 1 - kC_{A0}\bar{t}[1 - ((kC_{A0}\bar{t}/2) \ln(1 + (2/kC_{A0}\bar{t})))] \quad (9.13)$$

where k is the reaction rate constant, \bar{t} the mean residence time of fluid in the pipe, C_{A0} the inlet reactant concentration and \bar{C}_A the mean concentration of the reactant.

(c) If the flow velocity is so slow, then the main movement of the fluid is by molecular diffusion, not by bulk flow, pure diffusion regime is obtained.

Usually, gases are likely to be in the dispersion regime approaching to plug flow, liquids in dispersion regime or pure convection regime, and the very viscous liquids (such as polymers) in the pure convection regime. The pure diffusion regime is rarely met outside of reservoir engineering.

To characterize the different regimes in laminar flow, the Bodenstein number (ud_t/D) can be used. D is the diffusion coefficient of the fluid and it is not the axial dispersion coefficient except in the pure diffusion regime. It measures the flow contribution made by molecular diffusion.

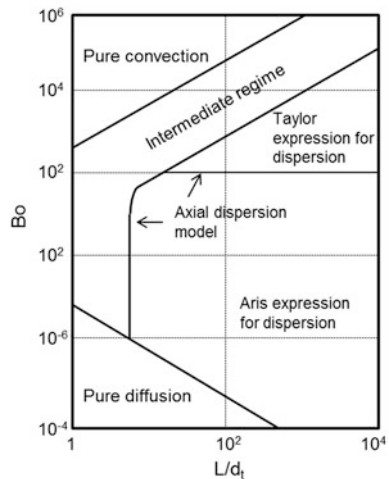
$$Bo = Re \cdot Sc = d_t u \rho / \mu \cdot \mu / \rho D \tag{9.14}$$

Figure 9.3 shows the different regimes as a function of Bo and L/d_t , where L is the vessel length and d_t the vessel diameter. The point on the chart corresponds to the fluid being used (Schmidt number, Sc), the flow conditions (Reynolds number, Re) and vessel geometry (L/d_t). ρ is the density of the fluid. This chart only has meaning if laminar flow is obtained. It does not apply for turbulent flow.

9.5 Temperature Gradients in the Reactor

The existence of temperature profiles can also complicate the analysis of the experimental data obtained. Usually, the reactor is heated by an electrical oven and

Fig. 9.3 Map showing which flow models should be used in any situation



longitudinal and radial temperature gradients can exist in the reactor. Longitudinal temperature gradients depend on the way that the fluid is heated or cooled and on the influence of the endothermicity or exothermicity of the reaction.

It is important to achieve fast heating of the fluid at the inlet of the reactor and conversely, fast cooling that at the outlet to prevent further reaction. These facts can allow us to obtain an important zone with a constant temperature. An example of a longitudinal temperature profile is shown in Fig. 9.4.

The influence of the endothermicity or exothermicity on the longitudinal temperature gradient can be minimized if the reactant is highly diluted and therefore low heat is released during the reaction.

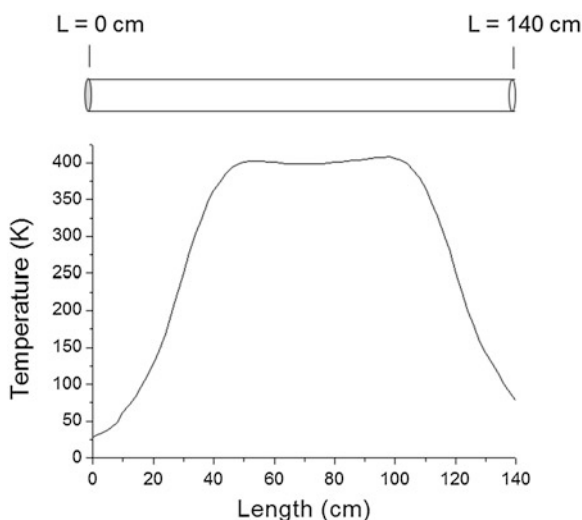
The radial temperature profile is not significant if the fluid flow is in turbulent regime, since mixing favors heat transfer and the radial temperature uniformity. If the fluid flow is in a laminar regime, a radial temperature gradient can be created. These gradients can be minimized by decreasing the tube diameter.

9.6 An Example of a Laboratory Scale Tubular Flow Reactor

Figure 9.5 shows an example of a laboratory scale tubular flow reactor developed by Kristensen (1997), and that is used by the Combustion and Harmful Emission Control group of the Technical University of Denmark and by the Thermo-Chemical Processes Group in the University of Zaragoza, Spain.

It is reasonable to approximate the laminar flow field to plug flow if the gas is premixed and the radial velocity gradients are sufficiently small to allow fluid

Fig. 9.4 Temperature profile for 400 K along the reactor length measured on a tubular flow reactor with temperature gradient



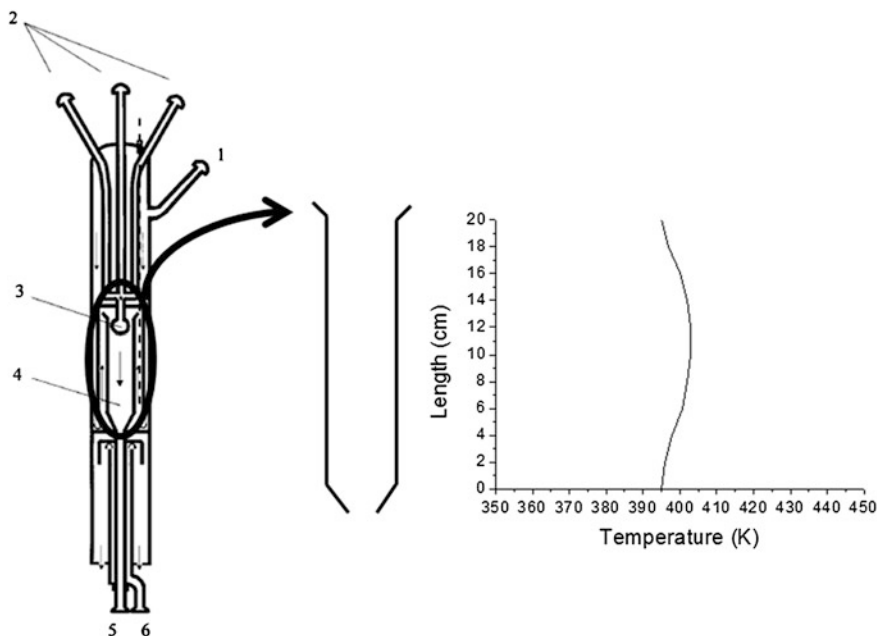


Fig. 9.5 Temperature profile for 400 K along the reactor length on a laminar flow reactor with a flat temperature gradient within ± 5 K

elements to exhibit similar residence times. Based on correlations shown in Fig. 9.3, in the present reactor, low axial dispersion conditions are obtained at volumetric flow rates of 1–3 standard liter per minute (Rasmussen et al. 2008a). Thermal gradients along the reactor can be minimized if the reaction zone is located far enough from the ends of the oven. Moreover, reactants must be pre-heated before being mixed.

The reactor shown in Fig. 9.5 has one main reactor inlet (1) and three injector inlets (2). The main gas and the three inlet gases are heated separately and mixed in point number 3. The gases react along the reaction zone (4). The reaction is frozen at the reactor outlet using an external addition of air, which is fed through the point number 6. The product gases go out of the reactor through the exit numbered as 5.

As it can be observed in Fig. 9.5, the reaction zone does not show any significant temperature profile, as it was intended.

9.7 Oxygenated Compounds

Typical additives for diesel fuel are compounds that contain oxygen in their molecular constitution which alters the electronic structure and the C/H ratio. The

influence of oxygen as a component of the fuel in the formation of soot has been studied in numerous works and, the results show that generally an increase of the oxygen content in the fuel composition results in a diminution of particulate matter (Choi and Reitz 1998; Pepiot-Desjardins et al. 2008; Demirbas 2009). Although oxygenated compounds can lead to the formation of soot due to their carbon content, the oxygen that is present in the molecule structure can participate in reactions forming new intermediate compounds or in the oxidation of soot precursors and soot which have been already formed (Sison et al. 2007).

Oxygenates that are usually blended with diesel fuel are alcohols, ethers and esters because of their physical and chemical properties. In the present study a literature review of the studies of the oxidation of methanol (CH_3OH), ethanol ($\text{C}_2\text{H}_5\text{OH}$), propanol ($\text{C}_3\text{H}_7\text{OH}$), butanol ($\text{C}_4\text{H}_9\text{OH}$), dimethylether ($\text{C}_2\text{H}_6\text{O}$, DME), and dimethoxymethane ($\text{C}_3\text{H}_8\text{O}_2$, DMM) under flow reactor conditions is presented. The use of oxygenated additives affects directly some important properties of the fuel such as density, viscosity, volatility, behavior at low temperatures, and cetane number (Ribeiro et al. 2007). For that reason and, since the engine performance and emissions produced can be altered, it is important to optimize the amount of additive to be blended.

Some important advantages of the use of alcohols as fuel additives or substitutes come from their low viscosity that favors the injection and atomization; the reduction of pollutant emissions due to high oxygen content, low C/H ratio, and low sulfur content; high evaporative cooling that reduces the temperature in the system; and a high laminar propagation speed that improves the engine thermal efficiency (Sayin 2010).

DME and DMM also present good effects on the ignition and combustion when mixed with diesel fuel because of the high oxygen content, low C/H ratio, and the absence of C–C bonds. Regarding DME, it has a higher cetane number than diesel fuel, what is seen as an advantage from the point of view of the ignition timing delay. However, DME presents some disadvantages which are related to its low lubricity, low calorific value, and high vapor pressure (Park 2009). To solve the latter problem, DME should be pressurized to liquefy for being blended with diesel fuel, what makes it difficult to be readily used in current engines. For this reason, DMM is an interesting fuel additive because it is a liquid miscible with diesel fuel (Maricq et al. 1998). Nevertheless, DMM presents a low cetane number if it is compared to DME, leading to an increase of the ignition timing delay and the burn rate (Lu et al. 2007).

On the other hand, the selected oxygenated compounds in this study have an additional interest because all of them can be obtained from biorefinery processes. This fact provides an attractive use of these compounds, since governments are promoting the use of biofuels in order to decrease the dependency of the transport sector on fossil fuels (Wiesenthal et al. 2009).

9.8 Alcohols: Methanol, Ethanol, Propanol, Butanol

9.8.1 Methanol

Several studies have been focused on the study of the oxidation of methanol under flow reactor conditions aiming to describe the reaction pathways of such process and identify and obtain important kinetic data. In this chapter, some of the most relevant research works related to this issue are presented.

The first study including a systematic study of the oxidation of methanol under flow reactor conditions was that carried out by Westbrook and Dryer (1979). The authors developed a detailed chemical kinetic model that can describe the oxidation of methanol under flow reactor and shock tube conditions (see Chap. 6), between 1000 and 2180 K. The data obtained in the reactors were used to estimate the values of several reaction kinetic constants, such as the thermal decomposition of methanol or the CH_2OH radical, which are key reactions in the oxidation of methanol. On the other hand, the contribution of the interactions of radical CH_3O was neglected since they were considered as insignificant.

In Fig. 9.6, some of the experimental methanol pyrolysis results (Aronowitz et al. 1977) obtained in a turbulent flow reactor, used to develop the mechanism above, are shown. Figure 9.6 shows the reaction product distribution, as well as the temperature profile, along the turbulent flow reactor.

Later works (e.g., Cathonnet et al. 1982; Norton and Dryer 1989, 1990) contributed to progress in the understanding of the reactions involved in the methanol oxidation process. Among them, the work of Held and Dryer (1998) includes an updated and optimized model previously released (Westbrook and Dryer 1979) and a detailed chemical kinetic mechanism which was validated through experimental data at different pressure and temperature conditions. This mechanism has been successfully used in a later research work focused on the study of the pyrolysis and oxidation of methanol in a laminar flow reactor (Jazbec and Haynes 2005).

The work of Alzueta et al. (2001) on the oxidation of methanol was carried out in a flow reactor and between 700 and 1500 K for different oxidation regimes, finding the carbon oxides as the main reaction products. The gas phase chemical kinetic mechanism developed in this study reproduces satisfactorily the experimental results, matching the main reaction pathways found with some of the published previously studies (Westbrook and Dryer 1979; Norton and Dryer 1989; Held and Dryer 1998).

More recently, Rasmussen et al. (2008b) studied the oxidation of methanol under different oxidation regimes in the 650–1350 K temperature interval, aiming to identify the branching ratio of the reaction of methanol with OH and H to decompose into CH_3O and CH_2OH given the existing discrepancy. This work reasserts the findings that establish that methanol mainly decomposes through CH_2OH radical.

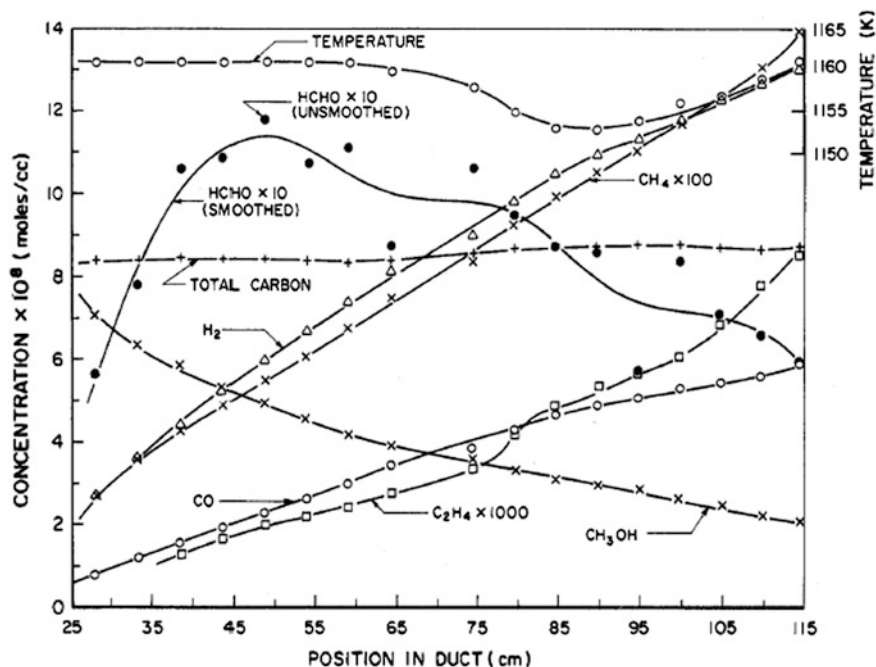


Fig. 9.6 CH_3OH , CO , CH_4 , C_2H_4 , HCHO and H_2 concentration profiles and temperature profile along the turbulent flow reactor for the methanol pyrolysis at 1158 K. Reprinted from Aronowitz et al. (1977), Copyright 1997, with permission from American Chemical Society

The oxidation of methanol mixed with other hydrocarbons has not been exhaustively studied, and most of the research works found were carried out in flames and shock tubes (e.g., Nakamura et al. 1982; Böhm and Braun-Unkoff 2008). A recent research work of Esarte et al. (2012) presented an experimental and modeling study of the interaction of methanol mixed with acetylene, one of the main soot precursors, focusing on the gas phase interactions and soot formation from the reacting mixtures.

9.8.2 Ethanol

Given that ethanol has been considered as a fuel substitute and additive for a long time, there are a number of studies focused on the investigation of ethanol oxidation processes, including studies under flow reactor conditions.

The first detailed work on the oxidation of ethanol (Dagaut et al. 1992) presented a chemical kinetic mechanism able to describe the pyrolysis of ethanol. In the same year, and based on the previously described study of the oxidation of methanol (Norton and Dryer 1990, 1991), a kinetic model was proposed for the oxidation of

ethanol under flow reactor conditions at 1100 K (Norton and Dryer 1992). Authors identified that most of ethanol reacts with OH radicals and demonstrated the importance of considering the three isomeric forms of C_2H_5O radical and the branching ratio in the mechanism, which was identified as is shown in Fig. 9.7:

Given the limitations of the mechanism developed by Norton and Dryer (1992), some years later, Marinov (1999) presented a detailed chemical kinetic mechanism, which is still nowadays one of the most accepted for describing ethanol oxidation in different reaction systems, including flow reactors.

The conversion reactions for ethanol oxidation from the mechanism of Marinov (1999), together with the mechanism of Glarborg et al. (1998), updated by Alzueta et al. (2001), were used to develop a new chemical kinetic mechanism able to describe the oxidation of ethanol and its interaction with NO in a flow reactor (Alzueta and Hernández 2002). This mechanism reproduces satisfactorily the experimental data for the conversion of ethanol and the formation of CO and CO_2 as the major products of the reaction. As an example, Fig. 9.8 shows the good agreement between experimental and simulation results for the concentration of ethanol, CO and CO_2 as function of temperature, for almost stoichiometric conditions.

The mechanism by Alzueta and Hernández (2002), and updated by Abián et al. (2008) was validated in a recent work on the pyrolysis of ethanol under flow reactor conditions (Esarte et al. 2011a). In this work, the capability of ethanol to decompose into soot precursors and its tendency to form soot was demonstrated and evaluated.

The role of ethanol as fuel substitute and additive has led to the development of some research works on the oxidation of ethanol mixed with hydrocarbons in reaction systems such as flames, jet-stirred reactors, or shock wave reactors (e.g., Alexiou and Williams 1996; Song et al. 2003). However, not many works regarding the oxidation of hydrocarbon/ethanol mixtures under flow reactor conditions are available in the literature (Abián et al. 2008; Esarte et al. 2009, 2011b). In those works, the effect of ethanol as fuel substitute and additive was evaluated. As an example of the results obtained in the work of Esarte et al. (2009), Fig. 9.9, shows the amount of soot collected for different percentages of ethanol in the fuel blend. The results indicate that low concentrations of ethanol in the initial blend have a strong influence in the decrease of the amount of soot collected, while the diminution is less sharp when the ethanol concentration increases above 5000 ppm.

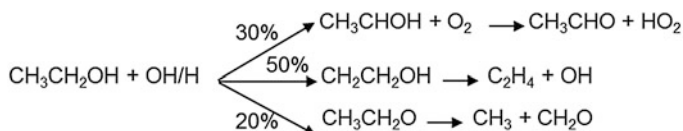


Fig. 9.7 Reaction pathways involved in the formation of the three isomeric forms of C_2H_5O radical

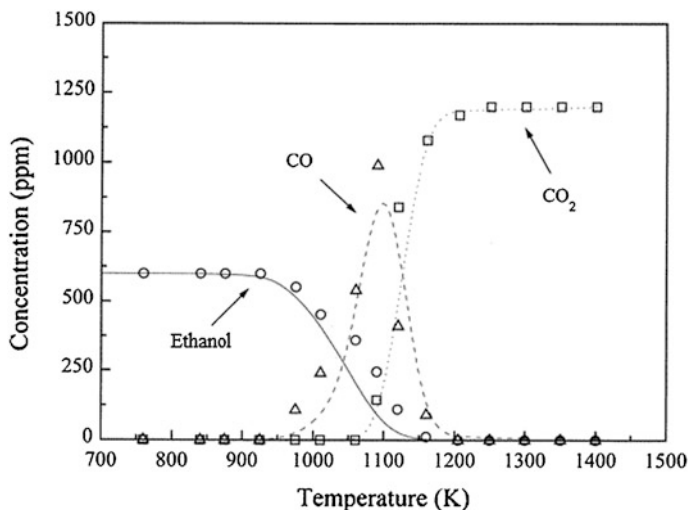
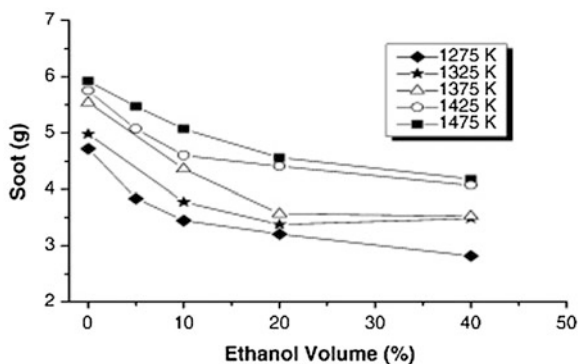


Fig. 9.8 Concentration of C_2H_5OH , CO and CO_2 as a function of temperature under almost stoichiometric conditions. Symbols represent experimental data and lines correspond to simulated results. Reprinted with permission from Alzueta and Hernández (2002), Copyright 2002, with permission from American Chemical Society

Fig. 9.9 Amount of soot collected as a function of the percentage of ethanol volume. Reprinted from Esarte et al. (2009), Copyright (2009), with permission from Elsevier



9.8.3 Propanol

There exist some old studies on the thermal decomposition of the isomers of propanol mainly in discontinuous reaction systems from the 1950 s (e.g., Smith and Gordon 1956; Trenwith 1975) and some recent works on the oxidation of propanol isomers in flames and shock tubes (e.g., Sinha and Thomson 2004; Frassoldati et al. 2010) given that the oxidation of the isomers of propanol as oxygenated fuels has recently attracted attention. However, very little research work on the oxidation of propanol isomers under flow reactor conditions has been found in the literature.

A study found on the oxidation of *n*-propanol and *iso*-propanol was carried out under flow reactor conditions in the 1020–1200 K temperature interval (Norton and Dryer 1991). In this work the authors established that *n*-propanol presents a higher tendency to dehydrogenation instead of dehydration due to the presence of α C-H bonds forming alkenes. Meanwhile, *iso*-propanol goes through dehydration processes leading to the formation of alkenes and dehydrogenation leading to ketones. The proposed mechanism is used successfully in a later work on the oxidation of *n*-propanol and *iso*-propanol flames (Sinha and Thomson 2004).

A recent research work (Esarte et al. 2012) included experimental and modeling data on the oxidation of acetylene mixed with *iso*-propanol under flow reactor conditions under sooting and nonsooting conditions. From this work, it was concluded that the presence of *iso*-propanol affects the combustion of acetylene, enhancing oxidation reactions that lead to the diminution of the formation of soot precursors, but they also promote its formation by the decomposition into small intermediate hydrocarbons.

Much work remains to be done regarding the pyrolysis and oxidation of propanol isomers and mixtures of these compounds with different hydrocarbons since the combustion mechanism and their contribution to pollutants formation is still not clear.

9.8.4 Butanol

Although the interest in the oxidation of butanol is very recent, mainly because of its potential use as an oxygenated fuel, there was some work done in the 1950 s (Barnard 1957). More recently, some research works on the oxidation of the different isomers of butanol have been carried in different combustion systems, mainly in shock tubes and flames (e.g., Moss et al. 2008; Sarathy et al. 2009, Frassoldati et al. 2012). The outcome of these studies highlighted the importance of studying the differences in the oxidation processes of the different isomers of butanol.

Only a few research works on the oxidation of butanol under flow reactor conditions have been found in the literature. The work of Norton and Dryer (1991) was focused on the oxidation of *tert*-butanol between 1020 and 1120 K and it was concluded that the oxidation process comes mainly through dehydration and the major products are alkenes and small amounts of ketones that are formed secondarily by means of dehydrogenation. Recently, Lefkowitz et al. (2012) studied the oxidation of *tert*-butanol in a variable pressure flow reactor at 12.5 atm and temperatures of 675–950 K. In these conditions, the *tert*-butanol oxidation comes through hydrogen abstraction and methane and acetone are observed as reaction products.

The aforementioned work of Esarte et al. (2012) also includes an analysis of the effect of *n*-butanol on the oxidation of acetylene. The observations of this study indicated that the presence of *n*-butanol in the reacting mixture alters the

combustion of acetylene, enhancing oxidation reactions that disfavor the formation of soot precursors. However, the presence of this alcohol also promotes the formation of small hydrocarbons that favor the growth of larger hydrocarbons and PAH that could finally lead to the formation of soot.

As an example of the results obtained in Esarte et al. (2012), Fig. 9.10 shows soot and gas yields obtained for different temperatures in the pyrolysis experiments of acetylene, acetylene-methanol, acetylene-ethanol, acetylene-isopropanol, and acetylene-*n*-butanol mixtures from 1275 K. The soot yield increases (Fig. 9.10a) and gas yield decreases (Fig. 9.10b) as temperature does for a given fuel mixture. Moreover, substituting in the reacting mixture part of acetylene by alcohols leads to a diminution of soot yield, being methanol the most effective alcohol.

9.9 Ethers: Dimethylether and Dimethoxymethane

9.9.1 Dimethylether

As has been already mentioned, apart from alcohols, ethers are also proposed as substitutes or additives to conventional fuels, being dimethylether (DME) the simplest ether.

First results of DME in flow reactors are those related to DME pyrolysis under different experimental conditions (e.g., Benson and Jain 1959; Pacey 1975; Held et al. 1977). These experimental data were used to obtain kinetic information about DME oxidation. Nevertheless, one of the most important detailed chemical kinetic models for the oxidation of DME is the mechanism developed by Curran et al. (1998). This mechanism was able to predict the correct distribution and concentrations of intermediate and final products formed in the oxidation of DME, both in a jet-stirred reactor and in a shock tube. Although in this study the mechanism was

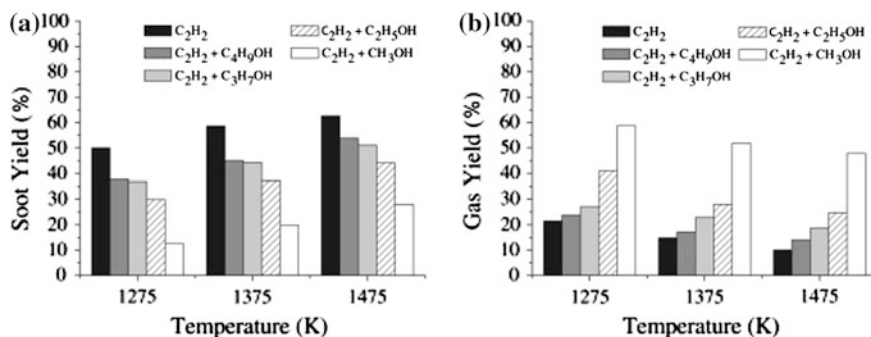


Fig. 9.10 a Soot yield and b Gas yield obtained in the pyrolysis of pure acetylene and the pyrolysis of acetylene-alcohol mixtures at 1275, 1375 and 1425 K. Reprinted from Esarte et al. (2012) Copyright (2012), with permission from Elsevier

not tested for flow reactor, the developed model has been used in later works including flow reactors.

For instance, Alzueta et al. (1999) developed a new mechanism using the reaction subset of DME oxidation presented by Curran et al. (1998) and combined it with the mechanism of Glarborg et al. (1998), which describes the interactions between C_1/C_2 hydrocarbons and NO. In this study, experiments of the oxidation of DME in a flow reactor at atmospheric pressure in the 600–1500 K temperature interval, for different air/fuel ratios and in the presence of nitrogen oxides were carried out. As an example of some other information provided by a chemical kinetic mechanism, Fig. 9.11 shows a complete reaction diagram for the DME oxidation under the conditions of this study.

Since DME has been proposed as a substitute or an additive of fuel, different investigations about mixtures DME/hydrocarbons have been found in the literature. Usually, the hydrocarbons studied are those that show a significant tendency to form soot and its precursors. Most of these studies have been performed in flames (e.g., Song et al. 2003; Park 2006), and only some investigations have been carried out under flow conditions (Amano and Dryer 1998; Tamm et al. 2009; Esarte et al. 2010; Brumfield et al. 2013).

9.9.2 Dimethoxymethane

Despite having been concluded that dimethoxymethane (DMM) can be used as an additive in reformulated fuels (Sirman et al. 2000), it has not been studied as extensively as DME. DMM oxidation studies have been performed in static reactors (Molera et al. 1974a), jet-stirred reactor (Daly et al. 2001) and flames (Molera et al. 1974b). However, to our knowledge, there is not any study in the literature about DMM oxidation under flow reactor conditions, except for the study carried out by Monge et al. (2012). This research has been performed at atmospheric pressure, in the temperature interval of 373–1473 K, different air excess ratios, and in the absence and the presence of nitric oxide. The experimental results

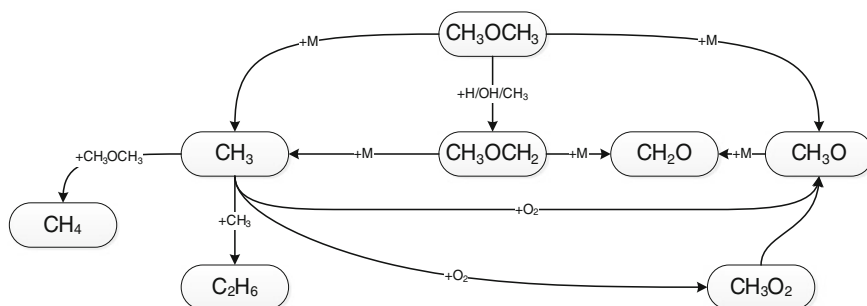


Fig. 9.11 Reaction pathways for the DME oxidation

show a low influence of the stoichiometry on the DMM oxidation, being shifted to lower temperatures under oxidizing conditions and NO presence. The main products found are methane, methanol, methyl formate, ethane, ethylene, acetylene, carbon monoxide, and carbon dioxide.

References

- Abián M, Esarte C, Millera Á et al (2008) Oxidation of acetylene-ethanol mixtures and their interaction with NO. *Energy Fuel* 22:3814–3823
- Alexiou A, Williams A (1996) Soot formation in shock-tube pyrolysis of toluene, toluene-methanol, toluene-ethanol, and toluene-oxygen mixtures. *Combust Flame* 104:51–65
- Alzueta MU, Hernández JM (2002) Ethanol oxidation and its interaction with nitric oxide. *Energy Fuel* 16(1):166–171
- Alzueta MU, Muro J, Bilbao R et al (1999) Oxidation of dimethyl ether and its interaction with nitrogen oxides. *Isr J Chem* 39:73–86
- Alzueta MU, Bilbao R, Finestra M (2001) Methanol oxidation and its interaction with nitric oxide. *Energy Fuel* 15:724–729
- Amano T, Dryer FL (1998) Effect of dimethyl ether, NO_x, and ethane on CH₄ oxidation: high pressure, intermediate-temperature experiments and modeling. *Proc Combust Inst* 27:397–404
- Aronowitz D, Naegeli DW, Glassman I (1977) Kinetics of pyrolysis of methanol. *J Phys Chem* 81:2555–2559
- Barnard JA (1957) The pyrolysis of n-butanol. *Trans Faraday Soc* 53:1423–1430
- Benson SW, Jain DVS (1959) Further studies of pyrolysis of dimethyl ether. *J Chem Phys* 31:1008–1017
- Böhm H, Braun-Unkhoff M (2008) Numerical study of the effect of oxygenated blending compounds on soot formation in shock tubes. *Combust Flame* 153:84–96
- Brumfield B, Sun W, Ju Y et al (2013) Direct in situ quantification of HO₂ from a flow reactor. *J Phys Chem Lett* 4:872–876
- Cathonnet M, Boettner JC, James H (1982) Study of methanol oxidation and self ignition in the temperature range 500–600 °C. *J Chim Phys PCB* 79:475–478
- Choi CY, Reitz RD (1998) An experimental study on the effects of oxygenated fuel blends and multiple injection strategies on DI diesel engine emissions. *Fuel* 78:1303–1317
- Curran HJ, Pitz WJ, Westbrook CK et al (1998) A wide range modeling study of dimethyl ether oxidation. *Int J Chem Kinet* 30:229–241
- Cutler AH, Antal MJ, Jones M (1988) A critical-evaluation of the plug-flow idealization of tubular-flow reactor data. *Ind Eng Chem Res* 27:691–697
- Dagaut P, Boettner JC, Cathonnet M (1992) Kinetic modeling of ethanol pyrolysis and combustion. *J Chim Phys PCB* 89:867–884
- Daly CA, Simmie JM, Dagaut P et al (2001) Oxidation of dimethoxymethane in a jet-stirred reactor. *Combust Flame* 125:1106–1117
- Demirbas A (2009) Biofuels securing the planet's future energy needs. *Energy Convers Manage* 50:2239–2249
- Dryer F (1972) High temperature oxidation of carbon monoxide and methane in a turbulent flow reactor. Ph.D. thesis, Princeton University, Princeton, New Jersey
- Esarte C, Millera Á, Bilbao R et al (2009) Gas and soot products formed in the pyrolysis of acetylene-ethanol blends under flow reactor conditions. *Fuel Process Technol* 90:496–503
- Esarte C, Millera Á, Bilbao R et al (2010) Effect of ethanol, dimethylether, and oxygen, when mixed with acetylene, on the formation of soot and gas products. *Ind Eng Chem Res* 49:6772–6779

- Esarte C, Peg MA, Ruiz MP et al (2011a) Pyrolysis of ethanol: gas and soot products formed. *Ind Eng Chem Res* 50:4412–4419
- Esarte C, Callejas A, Millera Á et al (2011b) Influence of the concentration of ethanol and the interaction of compounds in the pyrolysis of acetylene and ethanol mixtures. *Fuel* 90:844–849
- Esarte C, Abián M, Millera Á et al (2012) Gas and soot products formed in the pyrolysis of acetylene mixed with methanol, ethanol, isopropanol or n-butanol. *Energy* 43:37–46
- Frassoldati A, Cuoci A, Faravelli T et al (2010) An experimental and kinetic modeling study of n-propanol and iso-propanol combustion. *Combust Flame* 157:2–16
- Frassoldati A, Grana R, Faravelli T et al (2012) Detailed kinetic modeling of the combustion of the four butanol isomers in premixed low-pressure flames. *Combust Flame* 159:2295–2311
- Glarborg P, Alzueta MU, Dam-Johansen K et al (1998) Kinetic modeling of hydrocarbon/nitric oxide interactions in a flow reactor. *Combust Flame* 115:1–27
- Held AM, Manthorne KC, Pacey PD et al (1977) Individual rate constants of methyl radical reactions in pyrolysis of dimethyl ether. *Can J Chem* 55:4128–4134
- Held TJ, Dryer FL (1998) A comprehensive mechanism for methanol oxidation. *Int J Chem Kinet* 30:805–830
- Jazbec M, Haynes BS (2005) Kinetic study of methanol oxidation and the effect of NO_x at low oxygen concentration. In: 5th Asia-Pacific conference on combustion. The University of Adelaide, Adelaide, Australia
- Kristensen PG (1997) Nitrogen burnout chemistry. Ph.D. thesis, Technical University of Denmark, Denmark
- Lee JC, Yetter RA, Dryer FL et al (2000) Simulation and analysis of laminar flow reactors. *Combust Sci Technol* 159:199–212
- Lefkowitz JK, Heyne JS, Won SH, Dooley S, Kim HH, Haas FM, Jahangirian S, Dryer FL, Ju Y (2012) A chemical kinetic study of tertiary-butanol in a flow reactor and a counterflow diffusion flame. *Combust Flame* 159:968–978
- Levenspiel O (1999) *Chemical reaction Engineering*, 3rd edn. Wiley, New York
- Lu X, Ma J, Ji L et al (2007) Experimental study on the combustion characteristics and emissions of biodiesel fueled compression ignition engines with premixed dimethoxymethane. *Energy Fuel* 21:3144–3150
- Maricq MM, Chase RE, Podsiadlik DH et al (1998) The effect of dimethoxy methane additive on diesel vehicle particulate emissions. SAE Technical papers n° 982572
- Marinov NM (1999) A detailed chemical kinetic model for high temperature ethanol oxidation. *Int J Chem Kinet* 31:183–220
- Molera MJ, García-Domínguez JA, Santiuste JM (1974a) Slow gas-phase oxidation of methylal. *An Quím* 70:579–586
- Molera MJ, García-Domínguez JA, Santiuste JM (1974b) Cool flames and explosions in methylal oxidation. *An Quím* 70:764–767
- Monge F, Millera A, Bilbao R, Alzueta MU (2012) Oxidation of dimethoxymethane in a flow reactor. WIP Poster. In: 34th international symposium on combustion
- Moss JT, Berkowitz AM, Oehlschlaeger MA et al (2008) An experimental and kinetic modeling study of the oxidation of the four isomers of butanol. *J Phys Chem A* 112:10843–10855
- Nakamura M, Koda S, Akita K (1982) Sooting behavior and radiation in methanol/benzene/air diffusion flames. *Proc Combust Inst* 19:1395–1401
- Norton TS, Dryer FL (1989) Some new observations on methanol oxidation chemistry. *Combust Sci Technol* 63:107–129
- Norton TS, Dryer FL (1990) Toward a comprehensive mechanism for methanol pyrolysis. *Int J Chem Kinet* 22:219–241
- Norton TS, Dryer FL (1991) The flow reactor oxidation of C1–C4 alcohols and MTBE. *Proc Combust Inst* 23:179–185
- Norton TS, Dryer FL (1992) An experimental and modeling study of ethanol oxidation kinetics in an atmospheric pressure flow reactor. *Int J Chem Kinet* 24:319–344
- Pacey PD (1975) Initial-stages of pyrolysis of dimethyl ether. *Can J Chem* 53:2742–2747

- Park JK (2006) Modelling study of the effect of chemical additives on soot precursors reduction. *Int J Automot Technol* 7:501–508
- Park SW (2009) Numerical study on optimal operating conditions of homogeneous charge compression ignition engines fueled with dimethyl ether and n-heptane. *Energy Fuel* 23:3909–3918
- Pepiot-Desjardins P, Pitsch H, Malhotra R et al (2008) Structural group analysis for soot reduction tendency of oxygenated fuels. *Combust Flame* 154:191–205
- Rasmussen CL, Rasmussen AE, Glarborg P (2008a) Sensitizing effects of NO_x on CH₄ oxidation at high temperature. *Combust Flame* 154:529–545
- Rasmussen CL, Wassard KH, Dam-Johansen K et al (2008b) Methanol oxidation in a flow reactor: Implications for the branching ratio of the CH₃OH+OH reaction. *Int J Chem Kinet* 40:423–441
- Ribeiro NM, Pinto AC, Quintella CM et al (2007) The role of additives for diesel and diesel blended (ethanol or biodiesel) fuels: a review. *Energy Fuel* 21:2433–2445
- Santamaría JM, Herguido J, Menéndez MA, Monzón A (2002) *Ingeniería de reactores*. Síntesis, Madrid
- Sarathy SM, Thomson MJ, Togbé C et al (2009) An experimental and kinetic modeling study of n-butanol combustion. *Combust Flame* 156:852–864
- Sayin C (2010) Engine performance and exhaust gas emissions of methanol and ethanol-diesel blends. *Fuel* 89:3410–3415
- Sinha A, Thomson MJ (2004) The chemical structures of opposed flow diffusion flames of C3 oxygenated hydrocarbons (isopropanol, dimethoxy methane, and dimethyl carbonate) and their mixtures. *Combust Flame* 136:548–556
- Sirman MB, Owens EC, Whitney KA (2000) Emissions comparison of alternative fuels in an advanced automotive diesel engine. SAE Technical papers n° 2000-01-2048
- Sison K, Ladommatos N, Song HW et al (2007) Soot generation of diesel fuels with substantial amounts of oxygen-bearing compounds added. *Fuel* 86:345–352
- Smith SR, Gordon AS (1956) Studies of diffusion flames. II. Diffusion flames of some simple alcohols. *J Phys Chem* 60:1059–1062
- Song KH, Nag P, Litzinger TA et al (2003) Effects of oxygenated additives on aromatic species in fuel-rich, premixed ethane combustion: a modeling study. *Combust Flame* 135:341–349
- Tamm S, Ingelsten HH, Skoglundh M et al (2009) The influence of gas phase reactions on the design criteria for catalysts for lean NO_x reduction with dimethyl ether. *Appl Catal B-Environ* 91:234–241
- Trenwith AB (1975) Thermal decomposition of isopropanol. *J Chem Soc, Faraday Trans 1* 71:2405–2412
- Westbrook CK, Dryer FL (1979) Comprehensive mechanism for methanol oxidation. *Combust Sci Technol* 20:125–140
- Wiesenthal T, Leduc G, Christidis P et al (2009) Biofuel support policies in Europe: Lessons learnt for the long way ahead. *Renew Sustain Energy Rev* 13:789–800

Chapter 10

Flame Studies of Oxygenates

Elna J. K. Nilsson and Alexander A. Konnov

Abstract This chapter presents a comprehensive review of flame studies performed on oxygenated hydrocarbons or *oxygenates* of general formula $C_xH_yO_z$. In particular those studies in which the authors have measured laminar flame speeds or have concentrated on speciation in flames. It is the first time that such tabulation is performed and summarizes the work carried out since the 1950s. In addition, the methods employed in determining flame speeds are outlined and their strengths and weaknesses highlighted. In a similar fashion the various diagnostic methods for measuring species concentrations in situ are reviewed.

10.1 Introduction

In most practical situations combustion is accompanied by flames, with a few exceptions like detonations or explosions, flames of different natures and appearances propagate in engines, in domestic appliances, in gas turbine combustion chambers, etc. It is therefore natural that laboratory studies of flames provide valuable information on combustion characteristics important both for solution of engineering problems and for development and validation of combustion models.

Fuel diversification is nowadays an economical and strategic necessity. Renewable nonfossil fuels could be produced in many different ways, yet almost all alternative fuels (except hydrogen and syngas) possess a common feature; they all are oxygenated hydrocarbons. An important advantage of oxygenated fuels is that under equivalent conditions they produce less soot as compared to hydrocarbons. On the other hand, the incomplete combustion of alternative fuels may

E. J. K. Nilsson · A. A. Konnov (✉)
Division of Combustion Physics, Lund University, Lund, Sweden
e-mail: alexander.konnov@forbrf.lth.se

lead to emission of small amounts of the oxygenates themselves or their intermediates. For instance, alcohols or alcohol/gasoline blends emit more aldehydes than gasoline itself (Wei et al. 2012b). The emission of oxygenated compounds can also occur from the combustion of fossil fuels; the presence of noticeable amounts of monocarboxylic acids in the exhaust of diesel and gasoline engines has been reported. However, there are very few studies showing their origin during combustion or kinetic models proposed to explain their formation and consumption pathways (Battin-Leclerc et al. 2008). With the rapidly growing number of newly proposed alternative fuels and blends, all classes of oxygenated hydrocarbons could be considered as either potential components or intermediates or undesirable products of incomplete combustion. It is important therefore to investigate combustion of a complete range of oxygenated fuels and formation and consumption of their intermediates in flames.

The present chapter focuses on laboratory flames, particularly on premixed laminar flames. In general applications, from domestic appliances to engines and gas turbines, the flames are often non-premixed and/or turbulent. For these cases fluid dynamics complications largely hamper investigations of the chemistry behind flame structure and propagation. Moreover, contemporary computer codes are capable in modeling one-dimensional flames with complex detailed kinetic schemes, while the modeling of 3D reactive flows is still computationally expensive and challenging. An extensive understanding of the premixed laminar flames is, thus, an important research field since it enables development and validation of accurate chemical kinetics schemes. These can then be used as a solid foundation when developing models for more complex combustion applications.

Several applications or computer codes suitable for the modeling of 1D flame have been developed mostly with the same functionality. These codes interpret detailed reaction mechanisms, related thermodynamic and transport properties of all species involved, and calculate flame structure and burning velocity of a given mixture at required conditions. Most popular commercial software packages such as Chemkin and Cosilab, have user-friendly interfaces and provide many easy-to-learn modeling examples. Open source code, such as Cantera or in-house code, such as Chem1D, require some programming skills; yet they are becoming more and more widespread with an increasing number of user-support groups.

In the following, emphasis is given to the measurements of laminar burning velocity and flame structure; different experimental approaches are outlined with their advantages and disadvantages. Then, for each class of oxygenates, a short overview and summary tables of available experiments and indication of the quality of validation are given with letter codes described in Table 10.1.

Experimental measurements are compared with simulations to determine whether detailed reaction mechanisms are performing well or to indicate remaining deficiencies in our understanding of the flame chemistry. The quality of the comparison is characterized as “good” if the difference between model predictions and measured parameter is within experimental uncertainty. It is considered “satisfactory” if experimental trends or dependence is reproduced only qualitatively.

Table 10.1 Letter codes used in summarizing tables

	A	B	C	D	E
Relevance to practical systems	Fuel or major part of existing fuel mixtures	Currently considered as potential/prospective fuel	Fuel tracer or important intermediate of a fuel	Pollutant	No direct relevance
Laminar burning velocity	Consistent measurements from different labs and methods	Consistent or reliable data for limited range of conditions	Limited number of reliable data	Data are not reliable	No data
Flame structure	Consistent measurements from different labs and methods	Consistent or reliable data for limited range of conditions	Limited number of reliable data	Data are not reliable	No data
Model validation	Good agreement with a model, which was also validated for other systems (shock tube, etc.)	Good agreement with flame data achieved by model adjustments	Satisfactory or qualitative agreement	Model exist for this species, yet not validated for flame data	No model developed so far

10.2 Laminar Burning Velocities

The adiabatic laminar burning velocity is a fundamental parameter of the combustible mixture, which depends on the equivalence ratio, pressure, and temperature. By definition, the laminar burning velocity is the velocity of a steady one-dimensional adiabatic free flame propagating in the doubly infinite domain. The laminar burning velocity at standard conditions, that is, atmospheric pressure and initial temperature of 298 K is invaluable for characterization of combustion properties of the given fuel, for understanding of the underlying chemistry and for validation of models.

Although comparison of the laminar burning velocities with 1D modeling is often used for validation of detailed reaction mechanisms, one should remember that the majority of the measurements performed prior to the 1980s possess significant spread and could deviate from the “real” values by as much as a factor of 2 (Brown and Smith 1994). A greater part of the methods for measuring laminar burning velocities involves curved (Bunsen type), stretched (counterflow), or spherical time-varying flames. Wu and Law (1984) demonstrated experimentally that flame stretch due to flame front curvature and/or flow divergence must be taken into account in the data processing. The effects of stretch on apparent laminar burning velocity are now well established (Law and Sung 2010).

10.2.1 Bunsen Flames

A flame stabilized on a Bunsen burner (Fig. 10.1) is the simplest laboratory flame, which provides a clue to the concept of laminar burning velocity. Assuming that combustible mixture is completely burnt in the flame front, one can easily derive that the burning velocity, S_L , relates to the velocity of the fresh mixture, v , as $S_L = v \sin \alpha$, where α is the half-angle of the flame cone. Advantages of the Bunsen burner method are obvious: (a) it is simple in realization, only a stable flow of a combustible mixture is required; (b) cone shape/angle measurements could be easily made photographically, since all hydrocarbon flames are visible; (c) the burner could be preheated to study temperature dependence or set in a high-pressure chamber to measure burning velocities at industry-relevant conditions; and (d) a wide range of burning velocities could be measured using appropriate burner diameter.

The limitations and disadvantages of this method were realized long ago. They are: (a) the definition of the flame surface is not unambiguous: the cone is never perfect and different methods of determination of the flame surface like direct photography, schlieren, or shadowgraphy give different results; (b) flame modification close to the burner rim occurs due to heat losses; (c) ambient air may entrain into the bottom part of the flame and thus modify stoichiometry. These disadvantages are documented and discussed in classical textbooks, for example, by

Fig. 10.1 Rim-stabilized conical flame (Bunsen flame)



Fristrom and Westenberg (1965). Nowadays, it is clearly realized that variable curvature and thus stretch along the flame affects local burning velocity, moreover on burners having different diameters the stretch is different. Still, the Bunsen burner method can be used when all other methods fail for some reasons. Recently, the accuracy of a similar experimental method (slot burner) was revisited and corrections based on 2D direct numerical simulations have been proposed by Selle et al. (2011). The authors concluded that this method is not well adapted to mixtures with a Lewis number far from unity, such as hydrogen/air flames.

10.2.2 Spherically Expanding Flames

A single ignition point of a still combustible mixture will lead to the propagation of a spherical expanding flame. First installations of this type (often called “bombs”) were equipped with pressure gauges. From the pressure records burning velocity could be deduced using an approach developed and described by Lewis and Von Elbe (1961). Nowadays, most of the bombs also provide optical access to visualize flame propagation, see Fig. 10.2. This method for measuring burning velocities is currently the most popular one due to many important advantages: (a) possibility to operate at high pressures and different initial temperatures handling

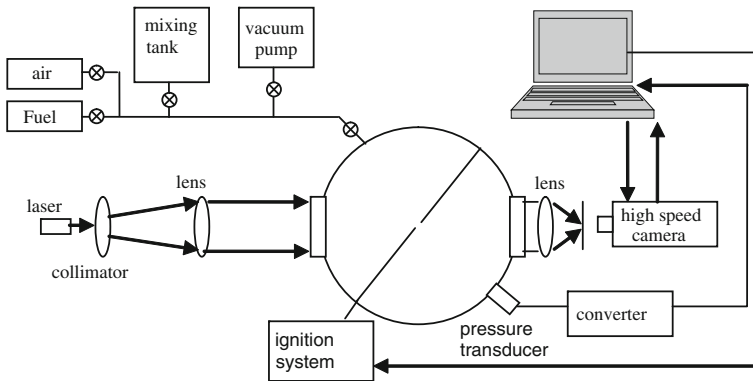


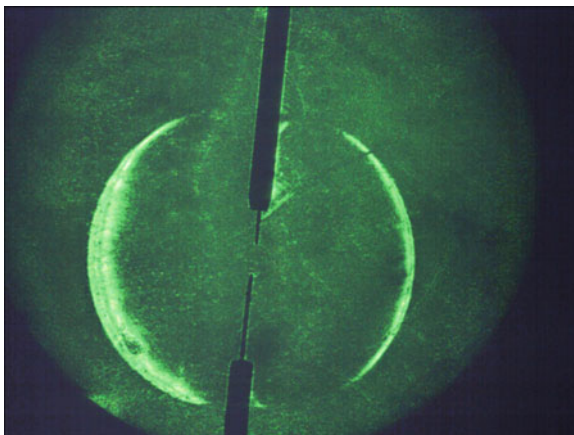
Fig. 10.2 Schematic of experimental rig for spherical expanding flame study

small amount of combustible mixture at each experiment; (b) wide range of velocities can be measured; (c) direct measurement of the pressure variation to choose nearly-constant pressure range; and (d) optical measurements of the flame front development allowing accurate data processing.

Through the years of the bomb method development, its limitations and disadvantages were in most cases successfully addressed. First, the influence of the spark energy on initial stage of the flame propagation could be revealed and the minimal energy needed to ignite the mixture should be used. Electrodes affect the shape of the flame front as seen in Fig. 10.3; laser ignition could be used in a bomb with optical access. Slowly burning flames are affected by buoyancy, which drastically modifies the flame shape; if required, measurements could be conducted under microgravity, like in a drop tower or in parabolic flight. Formation of cellular instability at high pressures is often suppressed by replacing nitrogen by helium. Pressure rise due to flame development depends on the bomb size; to extend nearly-constant range of pressures a double confinement could be used (Burke et al. 2009).

While determination of the flame front speed is relatively simple, either linear or nonlinear extrapolation to zero stretch is required to derive the laminar burning velocity. Different methods for data processing have been proposed by, e.g., Saeed and Stone (2004), by Tahtouh et al. (2009), by Varea et al. (2012). Nonlinear extrapolation to zero stretch is nowadays considered as the most reliable approach, yet it can be complicated by the improper choice of the data used for extrapolation (Ranzi et al. 2012). The last issue, which was often overlooked in the derivation of the burning velocity from spherical flame experiments, is normalization of the velocity using densities before and after the flame front. Usually, the ratio of these densities is calculated on the assumption of ideal adiabatic flame propagation; however, the validity of this assumption has never been checked. Further analysis is therefore needed to reconcile inconsistent results obtained using spherical flames.

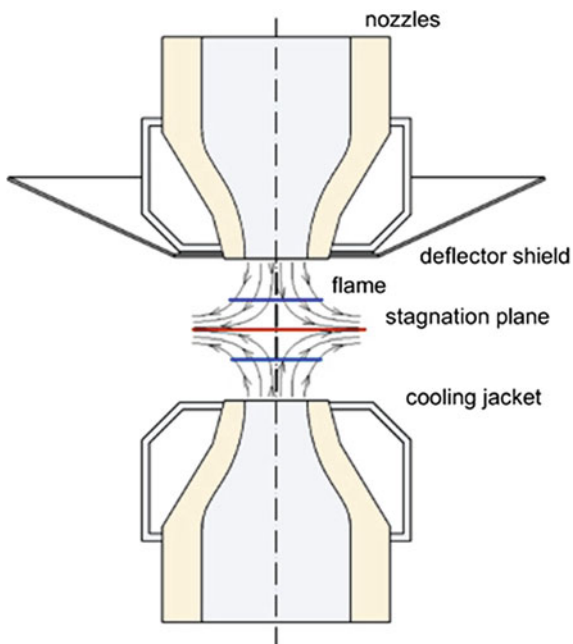
Fig. 10.3 Typical shadowgraph of a developing spherical flame



10.2.3 Counterflow Flames

The counterflow flame method was first introduced by Wu and Law (1984). It was developed in parallel with the theory of stretch effects on laminar burning velocity. By impinging two identical premixed flows onto each other, diverging jets with stagnation plane in the middle are formed. Twin flames are then stabilized in between by the stretch, as seen in Fig. 10.4. Using laser Doppler or particle

Fig. 10.4 Scheme of counterflow flames



imaging velocimetry, local flow velocities are measured and the corresponding stretch is evaluated. Then, choosing a reference velocity, usually just before the flame front, a correlation between this velocity and stretch can be established. Extrapolation of this correlation toward zero stretch gives the unstretched burning velocity.

Advantages of the counterflow method made it increasingly popular: (a) aerodynamically stabilized flames are nearly adiabatic and stable in laboratory coordinates, which facilitates implementation of additional laser diagnostics; (b) aerodynamic strain helps stabilizing flat flame and avoid cellularity in mixtures otherwise unstable; and (c) fresh gases could be preheated and the installation could be placed into a high-pressure vessel to measure burning velocities at industry-relevant conditions.

The counterflow method, however, possesses some technical difficulties: (a) steady source of seeding particles is needed; (b) flow uniformity is essential to approach 1D conditions of stretch. Major disadvantages are related to the extrapolation to zero stretch: similar to expanding spherical flames, either linear or nonlinear extrapolation is required. Specific theoretical problem of this method is a definition of the reference plane, which is still not unambiguous.

10.2.4 Premixed Planar Flames

Premixed planar flames stabilized on flat burners are intuitively attractive for the experimental study of the flame structure and flame burning velocity, since they resemble steady 1D adiabatic free flames propagating in the doubly infinite domain. In the laboratory, however, the planar flame is stabilized through heat loss to the surface of the burner from which the fresh mixture is introduced. Then the flame becomes adiabatic only in the limiting case of zero heat loss to the burner when the flame turns unstable. The method proposed by Botha and Spalding (1954) for the determination of the laminar burning velocity by linear extrapolation of the burning velocities with various heat losses to the zero heat loss was based on this consideration. A new method of adiabatic flame stabilization on flat burners was introduced by de Goey et al. (1993). This method is based on balancing the heat loss required for the flame stabilization by the convective heat flux from the burner surface to the flame front.

The scheme of the burner is shown in Fig. 10.5. It consists of the burner head mounted on a plenum chamber. The burner plate made of brass, is perforated with small holes and is attached to the burner outlet. The burner head has a heating jacket fed with circulating water or oil to keep the temperature of the burner plate constant. The plenum chamber has a separate cooling system supplied with water at a temperature of 298 K. Thus, the heating jacket keeps the burner plate edges at a certain temperature higher than the initial gas temperature, thus warming up the unburned gases flowing through. If the flame is stabilized under sub-adiabatic conditions, the gas velocity is lower than the adiabatic flame burning velocity and

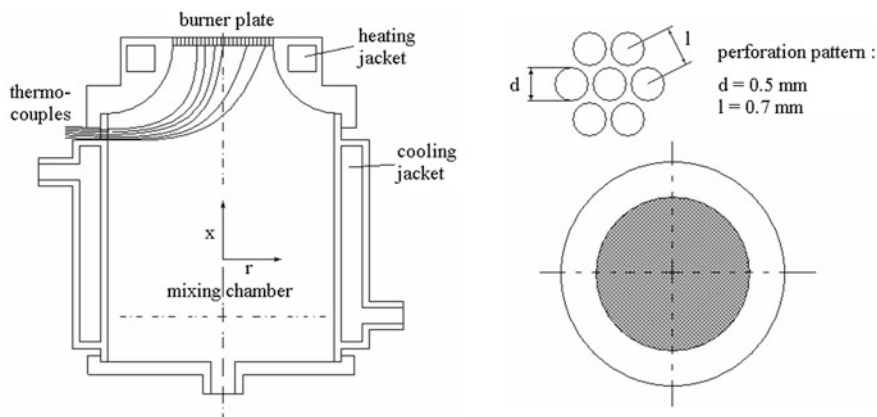


Fig. 10.5 Schematic of the heat flux burner (*left*), and perforated burner plate (*right*)

the sum of the heat loss and heat gain is higher than zero. Then the center of the burner plate is hotter than the heating jacket. If the unburned gas velocity is higher than the adiabatic burning velocity (super-adiabatic conditions) the net heat flux is lower than zero and the center of the burner plate is cooler than the heating jacket. By changing the flow rate of the gas mixture, an appropriate value of the gas velocity can be found to nullify the net heat flux. In this case, the radial temperature distribution in the burner plate is uniform and equal to the temperature of the heating jacket. Experimentally, the series of thermocouples attached to the burner plate allows measuring the temperature distribution in it. The flow rate at which the net heat flux is zero is shown to be the adiabatic flame burning velocity (van Maaren et al. 1994).

It has been shown that the heat flux method is suitable for the determination of the adiabatic flame temperature and flame burning velocity, for example, (van Maaren et al. 1994; van Maaren and de Goey 1994; Dyakov et al. 2001; Bosschaart and de Goey 2003, 2004a, b). It was also implemented for nonintrusive measurements of radicals in the flame front (Evertsen et al. 2003). The majority of measurements using the heat flux method have been performed at atmospheric pressure. Bosschaart and de Goey (2004b) and Konnov et al. (2010) extended this method to sub-atmospheric pressures. Goswami et al. (2013) reported first measurements at pressures up to 5 bar.

An obvious advantage of the heat flux method is nearly zero stretch of the flames, and thus no stretch extrapolation is required. The flames are adiabatic with respect to the burner and that facilitates comparison with 1D modeling. A major disadvantage is that the flame can be too close to the burner surface at atmospheric pressure; hence possible impact of radical sink should be further investigated. Difficulty in flame stabilization at high pressures due to cellularity has been reported (Goswami et al. 2013); this is due to a lack of stretch that in turn helps

stabilize spherical and counterflow flames. Moreover, most of the published measurements using the heat flux method have been performed on burners of 30 mm in diameter; possible edge effects have therefore not been investigated.

10.2.5 Summary

Quite often measurements of the laminar burning velocities are reported with a stated accuracy of 1–2 %. These evaluations are usually based on the accuracy of equipment used. In practice, however, scattering of available data at the same conditions of temperature, pressure, and equivalence ratio often exceeds 5 and even 10 %. There are several reasons for this inconsistency. First, technical details important in data processing are most often not reported in archival publications. Thus, each attempt of measurements in a new laboratory and even revisiting the same experiment after some time has passed at the same place is unique since operating experiment and data processing involves the effect of operator. Second, both equipment and theory behind each of the methods described above are in a constant development. Moreover, there are no protocols in place to renounce older data even if the author himself or herself realized that the published results were incorrect or highly uncertain. This leads to an accumulation of results hardly suitable for model validation due to large degree of scatter.

10.3 Flame Structure

Many experimental methods have been developed to study spatial profiles of species concentrations in laminar flames. Intrusive techniques based on the analysis of local gas composition withdrawn by a probe and nonintrusive spectroscopic techniques are often complementary since they possess different advantages and disadvantages. Temperature profiles also need to be measured in flames for quantitative comparison with simulations.

10.3.1 Nonintrusive Laser Diagnostics

Exciting capabilities of laser diagnostics were recently reviewed by, e.g., Kohse-Hoinghaus et al. (2005), Cheskis and Goldman (2009), Kohse-Hoinghaus and Brockhinke (2009). Earlier reviews (Kohse-Hoinghaus 1994; Daily 1997; Wolf- rum 1998; Cheskis 1999) were focused on extension of the list of detectible species and on the achievements in quantitative measurements. In most cases, spectroscopic techniques were tested in flames of methane and other conventional fuels, yet flames of oxygenated species were also visited (Desgroux et al. 1994).

The major advantage of the laser techniques is their non-intrusiveness: it is often assumed that laser radiation does not change the flame structure. Sometimes this is not the case, as for example in photo-fragmentation laser-induced fluorescence studies (Johansson et al. 2011), yet these effects could be revealed and analyzed experimentally.

Different types of species (small radicals, molecules, and soot) require different spectroscopic methods to be applied. It is only absorption spectroscopy and Raman scattering that allow for simultaneous measurements of several (major) components of the mixture. Therefore, quantitative simultaneous registration of several important species in flames is quite challenging (Kohse-Hoinghaus et al. 2005; Sjöholm et al. 2013). This is in contrast to probe sampling methods discussed below. The list of species accessible by nonintrusive spectroscopic techniques, although impressive, mostly includes small radicals and molecules, which are usually not fuel-specific. Therefore, even though laser diagnostics provides extremely valuable information from flames including those of oxygenates, major progress in understanding of the combustion chemistry of new and renewable fuels has been achieved recently, mostly thanks to probe techniques.

For the purpose of the analysis of combustion chemistry in flames via comparison with detailed kinetic modeling, one should remember some limitations of spectroscopic techniques, which are summarized below. The accuracy of the concentration measurements by nonintrusive methods is mostly defined by the accuracy of spectroscopic parameters used. Laser absorption of OH radical, for example, is a mature technique, which provides an accuracy of 2–4 % or better (Herbon et al. 2002). Typical accuracy of NO concentration measurements in flames using laser-induced fluorescence is about 5–10 % (Kohse-Hoinghaus et al. 2005), while in the much more complicated case of NCN radicals it is still not better than a factor of 2–3 (Sutton et al. 2008).

10.3.2 Probe Sampling Methods

Probe sampling methods have one thing in common: local gas composition withdrawn from the flame by a probe is investigated externally after transporting it to an analyzer. The analyzers could be commercial, for example, paramagnetic for O₂, chemiluminescence for NO_x, or gas-chromatography for many stable species, or unique homemade mass spectrometers, or sometimes combination of these (Dias et al. 2004). Recent contributions by flame-sampling molecular-beam mass spectrometry to a fundamental understanding of combustion chemistry have been summarized by Hansen et al. (2009), Kohse-Hoinghaus and Brockhinke (2009), Vovelle et al. (2009). This technique allows for simultaneous measurements of a much wider range of species than spectroscopic methods, and, with recent development of photoionization sources, allows in some cases identification of isomers (Hansen et al. 2006a, b; Yang et al. 2007a, b).

The disadvantages reside in the intrusive nature of the probe sampling. Sampling probes cause modification to the temperature and concentration profiles, making a 1D flame essentially 2D. These effects are rarely considered in full detail in comparing measurements and flame modeling (Hartlieb et al. 2000; Doute et al. 1997; Cattolica et al. 1982; Desgroux et al. 1995). Modifications of the temperature profiles due to the presence of a sampling cone are often of the order of 100–400 K. To take this into account, Hartlieb et al. (2000) proposed an accurate, yet laborious procedure to perform temperature profile measurements at various distances of the sampling cone from the burner and to repeat also modeling of the flame structure using specific temperature profiles for each sampling position. This approach yields calculated concentrations of intermediate species sometimes more than a factor of 10 higher or lower than those calculated using a single unperturbed temperature profile.

Sampling probes not only modify the flame structure, they may affect the sampling gas composition due to surface reactions on their walls. It was realized long ago, for example by Kramlich and Malte (1978), Hori (1980), and Schoenung and Hanson (1981) that CO and NO are oxidized in the sampling probes into CO₂ and NO₂, respectively. Recently Bahrini et al. (2012) observed that HO₂ radicals are lost completely on a quartz probe surface during sampling from a well-stirred reactor.

While calibration of stable species can be straightforward and reliable, the quantification of radical concentrations is often not very accurate. All these aspects, thoroughly addressed in dedicated studies and relevant reviews, show that absolute concentrations of stable species are typically accurate to within 10–20 %, while for radicals the accuracy is usually not better than 20–50 % (Biordi 1977; Hansen et al. 2009). Further conservative analysis revealed that typical errors are less than 30 % for direct calibration, less than a factor of 2 for radicals and up to a factor of 4 for isomers (Osswald et al. 2011). This implies that disagreement of the probe sampling data with the modeling which does not exceed these typical experimental uncertainties should not be considered as a motivation for the model modification or adjustment.

10.3.3 Temperature Measurements

Temperature profiles are often used as a model input to predict the flame structure. The accuracy of the temperature measurements should be very good, preferably not less than a few Kelvins, due to exponential dependence of rate constants of many key reactions on the temperature. Contemporary spectroscopic methods, however, demonstrate typical accuracy of 2–3 %, that is, 30–50 K (Daily 1997; Cheskis 1999; Kohse-Hoinghaus et al. 2005; Cheskis and Goldman 2009). Temperature profiles measured using thermocouples and spectroscopic techniques could also diverge significantly (Kasper et al. 2009a, b). Moreover, thermocouples induce perturbation of the flame structure showing incorrect readings, especially in

the region of high temperature gradient that is in the flame front (Skovorodko et al. 2012).

The importance of accurate temperature profiles should not be underestimated. For example, detailed species profiles of rich and lean premixed acetone flames were reported by Li et al. (2008). The results have been modeled by Pichon et al. (2009) and Chong and Hochgreb (2011a, b). Both groups report a divergence between experiment and modeling, in particular when the temperature profile by Li et al. (2008) was used. Results were improved by a drastically altered temperature profile. One may conclude that the temperature profile was inconsistent with the concentration profiles obtained in the same study.

10.4 Alcohols

Unless otherwise stated the flames mentioned in Sects. 10.4–10.10 are premixed and laminar. In the tables, the experimental techniques used in each publication are listed, insofar as possible the methods are named as in the publications, which mean that in some cases essentially the same methods are named differently in the tables. For example, the spherical flame method described in Sect. 10.2.2 may have different names (constant volume bomb, spherical vessel, etc.).

For some methods there are commonly accepted abbreviations, used in a consistent manner in the reviewed publications. These abbreviations are used in the tables, and their full meaning is given here:

CARS	Coherent Anti-Stokes Raman Spectroscopy
EI	Electron Ionization
FID	Flame Ionization Detection
FTIR	Fourier Transform Infrared
GC	Gas Chromatography
HPLC	High Pressure Liquid Chromatography
LIF	Laser-Induced Fluorescence
MBMS	Molecular Beam Mass Spectrometry
NDIR	Non Dispersive Infrared
PI	Photon Ionization
PIV	Particle Imaging Velocimetry
REMPI	Resonance Enhanced Multi-Photon Ionization
RTOF	Reflectron Time Of Flight
TCD	Thermal Conductivity Detector
VUV	Vacuum Ultraviolet

Alcohols are the most widely used oxygenated fuels. Their usefulness as fuels has been known since the invention of the engine. Ethanol is by far the most common biofuel, methanol is also used to some extent, and other alcohols such as butanol and propanol have been proposed as future vehicle fuels.

Table 10.2 Experimental data for laminar burning velocities of methanol

T/K	p/atm	φ	Method/comment	References
298	0.85	0.7–1.4	Horizontal tube	Wiser and Hill (1955)
298	1	0.8–1.4	Bunsen burner	Gibbs and Calcote (1959)
470–600	0.4–18	1	Closed vessel, pressure derived	Ryan and Lestz (1980)
298–700	0.4–40	0.8–1.5	Closed vessel, pressure derived	Metghalchi and Keck (1982)
298–800	1–8	0.7–1.4	Closed vessel, flame ionization	Gulder (1983a)
318–368	1	0.5–2	Counter-flow	Egolfopoulos et al. (1992a)
295–650	0.5–13.5	0.7–1.5	Closed vessel, pressure derived	Saeed and Stone (2004)
385–480	1	0.7–1.4	Closed vessel, Schlieren	Liao et al. (2007a)
373–473	1–7.5	0.7–1.8	Closed vessel, Schlieren	Zhang et al. (2008)
343	1	0.7–1.5	Counterflow, PIV	Veloo et al. (2010)
298–353	1	0.7–1.5	Heat flux	Vancoillie et al. (2012)

The simplest alcohols are the most well-studied oxygenates considering all types of combustion characteristics. Laminar burning velocities as well as flame structure data are rather well reproduced by chemical kinetics models. Since flames of the pure compounds have been extensively studied, recent research focuses on mixtures of the alcohols with other fuels and on effects of different additives and diluents (Table 10.2).

10.4.1 Methanol

Laminar burning velocities of methanol flames have been extensively studied over a range of temperatures (295–800 K), pressures (up to 40 atm), and equivalence ratios (0.5–2.0). The two earliest studies (Wiser and Hill 1955; Gibbs and Calcote 1959) were using methods not considered reliable today, and the first three studies using closed vessel methods (Ryan and Lestz 1980; Metghalchi and Keck 1982; Gulder 1983a) did not take stretch effects or the possibility of cellular flame structure into account and can therefore not be expected to give reliable results. In the later studies, different methods have been used to deal with stretch effects and flame structure, the scatter in the results under similar conditions is likely a result of variation in the success of the applied corrections. The agreement between different studies is generally best at the lean side. The most recent study used the heat flux method that does not require any stretch corrections (Vancoillie et al. 2012). The agreement with other recent experiments and modeling is good at lean to stoichiometric conditions. At the rich side, Vancoillie et al. (2012) report higher burning velocities than other experiments, in good agreement with the modeling. No flame structure data are available in the literature, such data would be of value for validation of kinetic mechanisms.

Table 10.3 Experimental data for laminar burning velocities of ethanol

T/K	p/atm	φ	Method/comment	References
300–500	1–8	0.7–1.4	Constant volume bomb	Gulder (1983b)
363–453	1	0.6–1.8	Counterflow flat flame	Egolfopoulos et al. (1992b)
323–413	1	0.75–1.6	Stagnation plane flat flame	Wang et al. (1997)
450	3	0.55–1.3	Constant volume bomb	Farrell et al. (2004)
358–480	1	0.7–1.4	Constant volume bomb, Schlieren	Liao et al. (2007b)
300–393	1–14	0.7–1.5	Constant volume, spherical bomb	Bradley et al. (2009)
343	1	0.7–1.5	Counter-flow, PIV	Veloo et al. (2010)
300–650	1–5	0.8–1.1	Spherical/cylindrical vessel, shadowgraphy	Eisazadeh-Far et al. (2011)
400	1	0.8–1.4	Spherical flame, shadowgraphy	Broustail et al. (2011)
298–358	1	0.65–1.55	Heat flux	Konnov et al. (2011)
310, 380, 450	0.5–4	0.7–1.4	Spherical flame, pressure and Schlieren	Marshall et al. (2011)
373	1–50	0.7–1.5	Spherical flame, laser tomography	Varea et al. (2013)
298–338	1	0.56–1.01	Heat flux	Nauc�ler et al. (2012)

10.4.2 Ethanol

Ethanol is by far the liquid fuel that has been most extensively studied. A wide range of methods has been used to determine the laminar burning velocity: spherical flames, counterflow flames, stagnation flow flames, and the heat flux method using burner stabilized flat flames. In all cases, except the heat flux method, flame stretch necessitates correction to zero stretch rates to obtain the stretch free laminar burning velocity. A number of different approaches to stretch correction have been used, and it is likely that the rather large scatter in experimental results is due to differences in these corrections, as discussed by Varea et al. (2013). In general the agreement is good at the lean side, while the scatter is significant at the rich side, possibly as a result of the use of stretch correction methods that are not applicable at the rich side. The heat flux method applied to a non-stretched flame support the lower values for rich mixtures obtained in constant volume bombs (Konnov et al. 2011) (Table 10.4).

Recent studies focus on mixtures of ethanol with other relevant fuels. An example of this is a study of iso-octane/ethanol/air mixtures by Varea et al. (2013). Another interesting aspect is to study the effect of different diluents. The laminar

Table 10.4 Experimental data for flame structure of ethanol

T/K	p/atm	φ	Method/comment	References
298	0.05	1.0–2.57	MBMS/EI/REMPI, NO-LIF	Kasper et al. (2007)
Ambient	0.05	1.0	Burner stabilized flame, MBMS	Leplat et al. (2008)
Ambient	0.05	0.75, 1, 1.25	Flat premixed flames, MBMS/EI	Leplat et al. (2011)

burning velocity of ethanol flames under oxyfuel conditions was investigated by Nauclér et al. (2012).

Three studies of flame structures of flat burner stabilized ethanol flames have been performed under similar conditions (Kasper et al. 2007; Leplat et al. 2008; 2011). Molecular beam mass spectrometry was used to determine concentration profiles of stable species. Based on these measurements, Leplat et al. (2011) propose a mechanism of the main consumption pathways for ethanol under flame conditions (Table 10.4).

A wide selection of chemical kinetic schemes for ethanol combustion exists, from detailed to reduced versions. The one that is likely most commonly used is the mechanism by Marinov (1999) which has shown to give good predictions of experimental results over a wide range of conditions. In later years, models relying on more recent chemical kinetic data have been published, for example by Leplat et al. (2011) and Saxena and Williams (2007).

10.4.3 Propanol

Veloo and Egolfopoulos (2011) report that laminar burning velocities of n-propanol/air flames are close to those of propane/air flames investigated in the same study, while isopropanol gives 3–5 cm/s lower results. Chemical kinetic modeling shows that this lower reactivity of isopropanol is the result of high concentrations of the relatively unreactive allyl radical, produced from the intermediate species propene, much more common in the isopropanol flame compared to those of n-propanol or propane (Tables 10.5, 10.6).

Table 10.5 Experimental data for laminar burning velocity of propanol

Isomer	T/K	p/atm	φ	Method/comment	Reference
iso	423	1–10	0.7–1.5	Spherical flame, shadowgraphy	Togbe et al. (2011a, b)
<i>n</i>	423	1–10	0.7–1.5	Spherical flame, shadowgraphy	Galmiche et al. (2011)
<i>n</i> , iso	343	1	0.8–1.5	Counterflow	Veloo and Egolfopoulos (2011)

Table 10.6 Experimental data for flame structure of propanol

Isomer	T/K	p/atm	φ	Method/comment	References
iso	318	1		Opposed flow diffusion flame, quartz microprobe, GC	Sinha and Thomson (2004)
<i>n</i> , iso	Ambient	0.02, 0.04	0.75, 1.80	Synchrotron PI, MBMS	Li et al. (2008)
<i>n</i> , iso	Ambient	0.034, 0.046	1.0–1.94	MBMS, EI and VUV-PI	Kasper et al. (2009a, b)

Li et al. (2008) studied the *n* and iso isomers and conclude that they possess significant differences in intermediate composition and pollutant formation. Compared to the alkane analogs, the propanol flames show a pollutant formation with a comparably larger fraction being oxygenated pollutants. Kasper et al. (2009a, b) report that product mole fractions from the two isomers are largely identical in their flat premixed laminar flames. Some differences were identified, mainly concerning oxygenated intermediates which were mostly of the CH_xO type for *n*-propanol and $\text{C}_2\text{H}_x\text{O}$ type for iso-propanol.

10.4.4 Butanol

Laminar burning velocities of different isomers of butanol have been determined using spherical flame techniques in recent years. No results at ambient conditions are reported. Gu et al. (2010) studied the four isomers and concluded that the reactivity depends structure; the more branching the lower the laminar burning velocity: *n*-butanol > sec-butanol > iso-butanol > tert-butanol. Veloo et al. (2010) showed that *n*-butanol has a laminar burning velocity essentially identical to that of its alkane analogue, which is consistent with results on propanol reported by the same group (Veloo and Egolfopoulos 2011), see Sect. 10.4.3. For butanol the maximum in laminar burning velocity is found at an equivalence ratio of 1.1 for all isomers. Gu et al. (2009) reported on a maximum at 1.3 for *n*-butanol, but in a later study from the same group a value of 1.1 is presented (Table 10.7, 10.8).

Species profiles of butanol flames of all four isomers were reported by Osswald et al. (2011). A large number of stable species and intermediates were identified. It was shown that the isomers give different intermediates and products, for example tert-butanol, is most prone to hydrocarbon formation while *n*-butanol produces high levels of toxic oxygenated products.

Chung et al. (2012) focused on the NO_x formation capacity of two butanol isomers in comparison to butane, and it is concluded that the alcohols produce less NO_x than alkanes.

Mechanistic considerations and chemical kinetic models for combustion of butanol isomers have been published in conjunction with several of the

Table 10.7 Experimental data for laminar burning velocities of butanol

Isomer	T/K	p/atm	φ	Method/comment	References
<i>n</i>	413–473	1–2.5	0.8–1.7	Spherical flame, schlieren	Gu et al. (2009)
<i>n</i> , iso, sec, tert	428	1–7.5	0.7–1.5	Spherical flame, schlieren	Gu et al. (2010)
<i>n</i>	343	1	0.7–1.5	Counterflow, PIV	Veloo et al. (2010)
iso, sec, tert	343	1	0.8–1.5	Counterflow	Veloo et al. (2010)
<i>n</i> , iso	353	1–3	0.7–1.6	Spherical flame	Liu et al. (2011)
tert	428–488	1–5	0.8–1.4	Spherical flame	Gu et al. (2011a)
<i>n</i>	428	1	0.7–1.5	SF, dilution N_2 0–15 %	Gu et al. (2011b)

Table 10.8 Experimental data for flame structure of butanol

Isomer	T/K	p/atm	ϕ	Method/comment	Reference
<i>n</i> , iso, tert, sec	300	0.04	1.71	Burner stabilized flame, MBMS/EI, VUV/PI	Yang et al. (2007a, b)
<i>n</i> , iso	Ambient			Counterflow diffusion	Grana et al. (2010)
<i>n</i> , iso, tert, sec	Ambient	0.04	1.7	Burner stabilized flame, MBMS/EI, VUV/PI	Osswald et al. (2011)
tert	Ambient	1		Counter flow, probe sampling, GC	Lefkowitz et al. (2012)
<i>n</i> , iso	Ambient	1		Stagnation flame, PIV	Chung et al. (2012)

experimental datasets (Grana et al. 2010; Lefkowitz et al. 2012). Two recent publications focusing on modeling of all four butanol isomers are by Frassoldati et al. (2012) and Sarathy et al. (2012).

10.4.5 *n*-Pentanol

A study on *n*-pentanol (Togbe et al. 2011) reported laminar burning velocities in good agreement with modeling using a model previously developed for smaller alcohols. The experiments were performed using the spherical flame method with shadowgraphy, at conditions of 1 atm and 423 K over a range of equivalence ratios from 0.7 to 1.4.

10.4.6 *n*-Hexanol

Togbe et al. (2010) measured laminar burning velocities using a spherical flame method with Schlieren imaging at 423 K and at 1–10 bar. They report pressure dependence in the laminar burning velocity in good agreement with the trend for other alcohols and reproduce the experimental data well using a reaction mechanism for C1–C6 alcohols.

Yeung and Thomson (2012) measured species profiles at atmospheric pressure in an opposed flow diffusion flame of *n*-hexanol + air. The model by Togbe et al. (2010) gives species profiles in reasonable agreement with the experiments.

10.4.7 Summary

A summary of the work performed on alcohols is given in Table 10.9.

Table 10.9 Classification of work performed to date

Alcohol	Practical relevances	S_L	Flame structure	Model validation	Selected experiments	Selected models
Methanol	A	A	E	A	Vancoillie et al. (2012)	Li et al. (2007)
Ethanol	A	A	B	A	Konnov et al. (2011), Leplat et al. (2011)	Leplat et al. (2011)
Propanol	B	C	B	B	Veloo and egolfopoulos (2011)	Veloo and egolfopoulos (2011)
Butanol	B	B	B	A	Veloo and egolfopoulos (2010)	Frassoldati et al. (2012), Sarathy et al. (2012)
<i>n</i> -Pentanol	B	C	E	C	Togbe et al. (2011a, b)	Togbe et al. (2011a, b)
<i>n</i> -Hexanol	B	C	C	C	Togbe et al. (2010); Yeung and Thomson (2012)	Togbe et al. (2010)

10.5 Ketones

Ketones are present as reaction intermediates in flames of oxygenates and it is therefore necessary to understand their combustion characteristics for development of accurate detailed mechanisms. Apart from acetone, few ketones have been studied under flame conditions. The reason for the interest in acetone is that it is used as a fuel tracer to facilitate LIF imaging, it is therefore present in research flames.

10.5.1 Acetone

In recent years, experimental determinations of laminar burning velocity of acetone in air has been performed using several methods, with highly variable results. As an example the differences are close to 10 cm/s around unit stoichiometry. The studies reported by Black et al. (2007) and Pichon et al. (2009) are from the same research group, the later study was performed because the model indicated that the first set of experimental results were not correct. The group recommends the use of the later dataset, which is also in reasonable agreement with the results by Burluka et al. (2010) at the lean side and around unit stoichiometry. On the rich side Burluka et al. give significantly higher results (by 5–10 cm/s). Chong and Hochgreb (2011a, b) report results significantly higher over the whole range of equivalence ratios. The most recent study, by Nilsson et al. (2013) was done using the heat flux method where the laminar burning velocity is determined from temperature measurements in an adiabatic flat laminar flame. This mean no stretch correction was needed, which gives confidence in the results. Nilsson et al. (2013) also report modeling results in good agreement with the experiments; previous modeling efforts by Pichon et al. (2009) and Burluka et al. (2010) have not shown agreement with experimental results (Table 10.10).

Detailed species profiles of rich ($\phi = 1.83$) and lean ($\phi = 0.76$) premixed low pressure (0.02 and 0.04 atm) acetone flames obtained using tunable synchrotron photoionization and MBMS were reported by Li et al. (2008). In the lean flame they identified 26 intermediate species, 5 radicals, and in the rich flame 39 intermediates and 9 radicals. The results have been modeled by Pichon et al. (2009) and Chong and Hochgreb (2011a, b). Both groups report a divergence

Table 10.10 Experimental data for laminar burning velocities of acetone

T/K	p/atm	ϕ	Method/comment	References
298	1	0.9–1.6	Spherical bomb	Black et al. (2007)
298	1	0.8–1.5	Spherical bomb	Pichon et al. (2009)
298	1	0.7–1.7	Constant volume bomb	Burluka et al. (2010)
298	1	0.6–1.4	Jet wall stagnation flame	Chong and Hochgreb (2011a, b)
298–358	1	0.6–1.4	Heat flux	Nilsson et al. (2013)

between experiments and modeling, in particular when the temperature profile by Li et al. (2008) is used, results were improved by a drastically altered temperature profile.

10.5.2 Methyl-Ethyl and Diethyl Ketones

The only available study on experimental and modeled laminar burning velocities of these two ketones was presented by Serinyel et al. (2010). The compounds have about the same flame speeds at lean conditions, while around stoichiometry the larger molecule (diethyl ketone) burns about 5 cm/s faster. The laminar burning velocities were measured at equivalence ratios in the range 0.8–1.5 at 1 atm and 305 K. The results can be compared to the results for acetone, determined by the same research group using the same experimental setup, which is in the range 5–10 cm/s lower (Pichon et al. 2009). It should be noted that later studies of acetone have given higher results than those reported by Pichon et al. (2009) based on this the accuracy of the results for methyl-ethyl ketone and diethyl ketone can be questioned and further studies using other methods are needed.

Decottignies et al. (2002) studied how seeding of 1–3 % of MEK affects a low pressure methane flame, and developed a model in which methyl- and ethyl radicals are considered important.

10.5.3 Summary

A summary of the work performed on ketones is given in Table 10.11.

10.6 Aldehydes

Like ketones, aldehydes are important as reaction intermediates, with formaldehyde playing a particularly important role. All detailed hydrocarbon oxidation

Table 10.11 Classification of work performed to date

Ketone	Relevance to practical systems	S_L	Flame structure	Model validation	Selected experiments	Selected models
Acetone	C	B	C	C	Nilsson et al. (2013)	Nilsson et al. (2013)
Methyl-ethyl ketone	C	C	E	D	Serinyel et al. (2010)	Serinyel et al. (2010)
Diethyl ketone	C	C	E	D	Serinyel et al. (2010)	Serinyel et al. (2010)

mechanisms contain a subset of formaldehyde reactions. For some of the smaller fuels essentially every carbon atom passes through formaldehyde as the final organic intermediate.

10.6.1 Formaldehyde

The limited data on formaldehyde flames is likely due to the experimental challenges associated with keeping formaldehyde in a stable concentration in the gas phase. This complication also reduces the reliability of the existing results. Oldenhove de Guertechin et al. (1983) and Dias et al. (2012) present species profiles of stable and radical species under similar conditions in all respects except equivalence ratio. Based on an extensive evaluation of the reaction kinetics and the result from Oldenhove de Guertechin et al. (1983), Vandooren et al. (1986) conclude that under the conditions of their study the rate of formaldehyde disappearance is mainly controlled by the total radical concentration. Branch et al. (1991) report stable and radical species profiles for a laminar premixed flame with the composition $\text{CH}_2\text{O}/\text{NO}_2/\text{O}_2$. It is concluded that NO_2 is a poor oxidizer compared to O_2 (Table 10.12).

The results by Oldenhove de Guertechin et al. (1983) have been used by several later publications, as a basis for mechanism discussion and model validation (Olsson et al. 1989; Li et al. 2007; Dias et al. 2012). The well-established mechanism for methanol combustion, by Li et al. (2007), uses the Vandooren et al. (1986) data as the only validation of their formaldehyde sub-mechanism under flame conditions. The model is in satisfactory agreement with the experiment, considering the relatively large uncertainties in the experimental species profiles.

10.6.2 Acetaldehyde

Just like formaldehyde, acetaldehyde is an important reaction intermediate in many hydrocarbon flames, and its presence is widely reported in determination of species profiles in for example alcohol and ester flames. Acetaldehyde is not

Table 10.12 Experimental data for flame structure of formaldehyde

T/K	p/atm	ϕ	Method/comment	Reference
Ambient	0.03–0.053	0.15–1.0	Sampling cone/MBMS	Oldenhove De Guertechin et al. (1983)
Ambient	0.072	0.56	Burner stabilized flat flame, LIF, quartz microprobe, GC	Branch et al. (1991)
Ambient	0.03	0.22, 1.09	Burner stabilized flat flame, MB MS	Dias et al. (2012)

Table 10.13 Experimental data for flame structure of acetaldehyde

T/K	$p/$ atm	ϕ	Method/comment	Reference
Ambient	1		Stabilized flames, GC/MS	Bradley and Jones (1966)
Ambient	0.05	0.75, 1.0, 1.25	Laminar premixed flame, MBMS and electron impact ionization.	Leplat and Vandooren (2010)

considered a fuel, and this is probably the reason why the combustion characteristics of the pure compound are not well studied. In their pioneering study in 1959, Gibbs and Calcote measured the laminar burning velocity of acetaldehyde at standard conditions and at equivalence ratios in the range 0.8–1.3, but the validity of their results are questionable.

Bradley and Jones (1966) investigated profiles of temperature and a few stable species in low temperature acetaldehyde flames, only relative concentrations were obtained (Table 10.13). A recent determination of flame structure of a laminar premixed flame is by Leplat and Vandooren (2010), they measured profiles of the main stable species, and CH_3 radical. The experimental results were compared to modeling using the ethanol mechanism of Marinov (1999) with a few modifications concerning the acetaldehyde chemistry, and a model by Yasunaga et al. (2008), previously validated against shock tube experiments. None of the models manage to reproduce the profiles of intermediate species satisfactory (Yasunaga et al. 2008).

10.6.3 Propionaldehyde

Burluka et al. (2010) present an experimental and modeling study where the laminar burning velocity for propionaldehyde is determined. The results by Burluka et al. (2010) are shifted to higher equivalence ratios compared to those of Gibbs and Calcote (1959), which is a common result when comparing recent data with those of Gibbs and Calcote. Modeling performed with the Konnov 0.5 mechanism underpredicts the laminar burning velocities by a few cm/s at lean and stoichiometric conditions, while at the rich side the discrepancy is far more significant. The latest study, by Veloo et al. (2012), also presents both experimental and modeling results, in good agreement (Tables 10.14, 10.15).

Table 10.14 Experimental data for laminar burning velocities of propionaldehyde

T/K	p/atm	ϕ	Method/comment	Reference
298	1	0.8–1.4	Bunsen burner flame	Gibbs and Calcote (1959)
298	1	0.9–2.1	Constant volume bomb	Burluka et al. (2010)
343	1	0.75–1.6	Counterflow	Veloo et al. (2012)

Table 10.15 Experimental data for flame structure velocities of propionaldehyde

T/K	p/atm	ϕ	Method/comment	Reference
Ambient	1		Stabilized flames, GC/MS	Bradley and Jones (1966)
Ambient	0.05	1.0	Premixed flat flame. MBMS/EI	Kasper et al. (2009a, b)

The study of flame structure by Kasper et al. (2009a, b) reveals that higher molecular weight oxygenated fractions are formed, likely by addition of an alkyl radical to the fuel. Many of these species have the composition $C_xH_{2x}O$ ($x = 3-6$), but the experiments does not give information about the isomeric structure.

10.6.4 Summary

A summary of the work performed on aldehydes is given in Table 10.16.

10.7 Carboxylic Acids

Carboxylic acids are combustion intermediates detected in flames of oxygenates. In a study by Zervas (2005) organic acid formation from propane, isooctane, and toluene/isooctane premixed burner stabilized flat flames was investigated. Organic acid profiles at equivalence ratios from 0.83 to 1.25 were probe sampled from different heights of the flames, and investigated using GC/FID technique. The acids detected were formic, acetic, propionic, and isovaleric acid, and it was shown that the acid concentrations were strongly dependent on the fuel/air ratio.

Despite the obvious importance of carboxylic acids in flames, the experimental data are scarce and the mechanisms of their consumption in flames are not completely understood. Battin-Leclerc et al. (2008) developed a mechanism for C1–C3 carboxylic acids and conclude that they mainly originate from aldehydes of the

Table 10.16 Classification of work performed to date

Substance	Relevance to practical systems	S_L	Flame structure	Model validation	Selected experiments	Selected models
Formaldehyde	C	E	C	C	Dias et al. (2012)	Li et al. (2007)
Acetaldehyde	C	D	C	D	Leplat and Vandooren (2010)	
Propionaldehyde	C	C	C	C	Veloo et al. (2012), Kasper et al. (2009a, b)	Veloo et al. (2012)

Table 10.17 Classification of work performed to date

Substance	Relevance to practical systems	S_L	Flame structure	Model validation	Selected experiments	Selected models
Acetic acid	C	E	C	C	Leplat and Vandooren (2012)	Leplat and Vandooren (2012)

same structure. The only published flame study of a carboxylic acid is by Leplat and Vandooren (2012). They measured species profiles of acetic acid flat premixed flames at 0.05 atm and equivalence ratios 0.77, 0.9, and 1.05. Stable, radical, and intermediate species were detected using MBMS/EI technique. The model does a fairly good job in predicting species mole fractions, but for some species the position of the maximum mole fraction, i.e., the distance from the burner, is shifted to shorter distances in the modeling results compared to the experiments (Table 10.17).

10.8 Ethers

Ethers, in particular dimethyl ether, have been extensively studied since they were considered promising as replacements for fossil fuel diesel. They have been considered to be used as pure fuels and have come to practical use as octane-improving gasoline additives. Being renewable fuels the ethers have an advantage for the global environment compared to fossil fuels since they result in no net emission of CO_2 . Considering the local environmental impact extensive research has revealed that some of the products formed during ether combustion are affecting air quality and health (Franklin et al. 2001). Due to this the use of ethers as fuels need to be reconsidered, or the combustion process need to be optimized to achieve a more favorable emission composition.

10.8.1 Dimethyl Ether

Dimethyl ether is the simplest ether, containing no carbon–carbon bond, and the one that has been most extensively studied under flame conditions. During the last decade a range of scientific papers has been published reporting laminar burning velocities of dimethyl ether, different methods have been used and the effect of pressure investigated, but no systematic study considering temperature dependence has been published this far. Regarding pressure dependence, it has been shown that the laminar burning velocity decreases to about half when the pressure is changed an order of magnitude. At standard conditions there is satisfactory agreement (Daly et al. 2001; Qin and Ju 2005; Wang et al. 2009a, b; de Vries et al. 2011),

Table 10.18 Experimental data for laminar burning velocities of dimethyl ether

T/K	p/atm	φ	Method/comment	References
295	1	0.7–1.7	Spherical bomb	Daly et al. (2001)
298	1	0.7–1.5	Stagnation flame, PIV	Zhao et al. (2004)
298	1–10	0.7–1.7	Spherical bomb, schlieren	Qin and Ju (2005)
285	0.8–1.5	0.6–1.8	Constant volume bomb, schlieren	Huang et al. (2007)
293	0.8–1.5	0.8–1.2	Constant volume bomb, schlieren	Huang et al. (2008)
Ambient	1	0.7–1.8	Spherical flame, schlieren	Chen et al. (2009)
Ambient	1	0.6–1.6	Counter-flow, LDV	Wang et al. (2009a, b)
Ambient	1–10	0.7–1.5	CPSB, Schlieren	Lowry et al. (2011)
295	1–10	0.7–1.6	Constant volume bomb	de Vries et al. (2011)
298	1	1.0	Constant volume bomb	Chen et al. (2012)

Table 10.19 Experimental data for flame structure of dimethyl ether

T/K	p/atm	φ	Method/comment	References
Ambient	1	0.6–3.1	Laminar premixed, co-flow, probe, FTIR	Frye et al. (1999)
Ambient	0.04	0.98, 1.2	Premixed flame, MBMS, LIF (OH)	McIlroy et al. (2000)
300	1	0.67, 0.49	Premixed flat flame, GC and FTIR	Kaiser et al. (2000)
Ambient	1		Laminar diffusion flame, Counterflow, LIF, CARS	Brackmann et al. (2006)
300	0.026–0.04	1.2, 1.68	Premixed flat flame, MB PIMS	Cool et al. (2007)
300	0.04	2.0	MBMS/EI, PI VUV	Wang et al. (2008a, b)
300	0.033	0.93–1.86	Premixed, MB PIMS	Wang et al. (2009)
298	1		Non-premixed, counterflow	Hwang et al. (2009)
Ambient	0.04	1.5	Laminar premixed, TUV, MB MS	Chen et al. (2010)
473	0.04	1.0	RTOF-MS	Xu et al. (2011)
740	0.95	0.85, 1.0,	MBMS/EI	Zhang et al.
293		1.2		(2012a, b)

($\phi = 1.0$)

especially at the lean side. The maximum in laminar burning velocity is about 45 cm/s between equivalence ratios 1.1–1.2 (Tables 10.18, 10.19).

The early results by Zhao et al. (2004) are significantly higher than other results. As the laminar burning velocities of dimethyl ether + air mixtures are now rather well determined, more recent studies focus on mixtures of dimethyl ether with other fuels, for example, Lowry et al. (2011) present data on mixtures of dimethyl ether with methane, and compare these with results for pure dimethyl ether published by de Vries et al. (2011). Another aspect is the effect of dilution by Ar, N₂ or CO₂, investigated by Chen et al. (2012).

Species and temperature profiles have been determined in different flames over an extensive range of equivalence ratios and at low and atmospheric pressures, see Table 10.19. Conclusions that have been made from these flame studies are that dimethyl ether has lower CO emission than comparable alkanes (Frye et al. 1999) and that the decomposition of CH_3OCH_2 into CH_3 and CH_2O is important (Kaiser et al. 2000; Wang et al. 2009a, b).

Chen et al. (2010) present a study where 0–80 % of H_2 was mixed into a rich dimethyl ether flame. They found that as the amount of H_2 increases the flame temperature decreases, the normalized mole fractions of C1 intermediates increase, and the ratio of CO to CO_2 decreases. The conclusion they draw is that H_2 promotes complete combustion of dimethyl ether.

Several of the publications include modeling efforts. The earlier attempts gave modeling predictions significantly higher than the majority of the experimental results (Daly et al. 2001; Zhao et al. 2004; Qin and Ju 2005), while later on the agreement between modeling and experiments has improved significantly (Wang et al. 2009a, b; de Vries et al. 2011; Lowry et al. 2011; Xu et al. 2011).

10.8.2 Diethyl Ether

Two studies concerning laminar burning velocities of diethyl ether using spherical flame and Schlieren technique have been published by the same group (Di et al. 2009; Zhang et al. 2009). The first work investigated the influence of temperature and pressure on the laminar burning velocity of diethyl ether, and the second work focused on the effects of diluting the gas mixture with N_2 . As expected the trend is that the laminar burning velocity increases as initial gas mixture temperature increases, and decreases as pressure increases. The results of Di et al. (2009) and Gillespie et al. (2012) agree on the position of the maximum burning velocity at an equivalence ratio of about 1.1. But in general the data by Di et al. show larger scatter, at the lean side the burning velocities are 5–10 cm/s higher than the results by Gillespie et al. (2012), while at the rich side they are generally lower. Due to the considerable scatter in the results by Di et al. (2009), and the fact that this study possibly can suffer from stretch effects, the results by Gillespie et al. (2012) are considered to be more reliable (Table 10.20).

The only flame structure study of diethyl ether was published in 1965 by Agnew and Agnew (1965) using quartz probe sampling and GCMS; they identified

Table 10.20 Experimental data for laminar burning velocities of diethyl ether

T/K	p/atm	ϕ	Method/comment	References
323–363	1–10	0.7–1.6	Spherical flame, Schlieren	Di et al. (2009)
323–363	1	0.8–1.2	Spherical flame, Schlieren	Zhang et al. (2009)
298 - 398	1	0.55–1.60	Heat flux	Gillespie et al. (2012)

acetaldehyde as the main oxygenated intermediate in burner stabilized cool flames of equivalence ratio 3.9.

10.8.3 Ethyl Tert-Butyl Ether

The only available determination of laminar burning velocity of pure ethyl tert-butyl ether (Yahyaoui et al. 2008) reports a maximum value of 33 cm/s at equivalence ratio 1.1 at standard conditions. Measurements were performed using a spherical flame and shadowgraphy in the range of equivalence ratios of 0.5–1.5. The results were modeled using a reaction kinetics mechanism published previously by the same authors (Yahyaoui et al. 2007), overpredicting the laminar burning velocities by about 5 cm/s around stoichiometry, but providing a good agreement at rich and lean conditions. Laminar burning velocities of a high octane fuel consisting of ethyl tert-butyl ether (22.8 %), tert-butyl alcohol (11.9 %), and ethanol (65.3 %) were determined using the spherical flame method with high-speed Schlieren at 373–473 K and 1.0–7.5 atm (Gong et al. 2010).

10.8.4 Dimethoxy Methane

Sinha and Thomson (2004) investigated species concentrations in an opposed flow diffusion flame of dimethoxy methane ($\text{CH}_3\text{-O-CH}_2\text{-O-CH}_3$) using probe sampling and GC. It was concluded that large quantities of formaldehyde and methyl formate were present in the flame.

10.8.5 1,2-Dimethoxy Ethane

Lin et al. (2009b) have used synchrotron photoionization mass spectrometry to determine species profiles in a premixed laminar dimethoxy ethane ($\text{CH}_3\text{-O-CH}_2\text{-CH}_2\text{-O-CH}_3$) flame at an equivalence ratio of 1.97. The measured composition shows that the formation of intermediates is closely linked to the structure of the fuel.

10.8.6 Summary

A summary of the work performed on ethers is given in Table 10.21.

Table 10.21 Classification of work performed to date

Substance	Relevance to practical systems	S_L	Flame structure	Model validation	Selected experiments	Selected models
Dimethyl ether	B	A	B	A	De Vries et al. (2011)	Lowry et al. (2011)
Diethyl ether	B	B	C	C	Gillespie et al. (2012)	Gillespie et al. (2012)
Ethyl tert-butyl ether	B	C	E	C	Yahyaoui et al. (2008)	
Dimethoxy methane	B	E	C	E	Sinha and Thomson (2004)	
1,2-dimethoxy ethane	B	E	C	E	Lin et al. (2009b)	

10.9 Esters

Fuel mixtures comprising mono-alkyl esters of long chain fatty acids derived from vegetable oils are often referred to as biodiesel fuels. Biodiesels are used worldwide as blends with normal diesel, but also as a pure fuel. For this reason, there is a large interest in understanding the combustion characteristics of esters, and to construct chemical kinetics models to enable simulation of engines and flames. A typical biodiesel ester has a chain length of 16–18 carbons; a detailed kinetics model describing their oxidation is not feasible due to limitations in kinetic data for the compounds and also due to limited computer capacity for the simulations. Due to these limitations research on esters started out with the shorter chained ones, especially methyl butanoate. In recent years flame studies have been performed on esters ranging from the simplest one, methyl formate, up to methyl decanoate with the formula $C_{11}H_{22}O_2$. Although the shorter chained esters are not major constituents of biodiesel, studying them can be invaluable as a step toward understanding how the ester functionality affects the reactivity and combustion properties.

Progress in research concerning biodiesel has been subject to a few reviews in recent years (Battin-Leclerc 2008; Lai et al. 2011; Pitz and Mueller 2011). Lai et al. (2011) focus their review on mechanistic features of the methyl ester combustion and model development for many esters. Pitz and Mueller (2011) reviewed, among others, kinetic models developed for esters and concluded that “Given the rate of progress in mechanism development for ever-more representative biodiesel compounds, it is expected that full mechanisms for the methyl esters found in most common biodiesel fuels will be available soon.”

10.9.1 Methyl Formate

The laminar burning velocity of methyl formate has been determined from an outwardly propagating spherical flame, by Dooley et al. (2010). Laminar burning velocities were measured at standard conditions at $\phi = 0.8–1.6$. The most recent chemical kinetics mechanism for methyl formate flames was published by Dooley et al. (2010), building on the work by Westbrook et al. (2009). The experimental laminar burning velocities are well reproduced by the model (Table 10.22).

Major products reported in the flame study by Dooley et al. (2011) were CO and methanol, but also methane and formaldehyde were abundant. It was concluded that hydrogen abstraction dominates fuel consumption, and that abstraction from the methyl position gives higher reactivity than abstraction at the carbonyl position (Dooley et al. 2010). Radical–radical recombination reactions are considered important in the production of a number of trace species in low pressure flames. An example of this is the CH_3 radical reacting with HCO to give acetaldehyde.

10.9.2 Methyl Acetate

Profiles for major and intermediate species in a low pressure (0.02 atm), rich ($\phi = 1.82$) premixed laminar flat flame of methyl acetate was reported by Osswald et al. (2007). Measurements were done using synchrotron VUV ionization MBMS. Compared to simple hydrocarbon fuels the production of C_3H_3 was low, resulting in benzene concentrations of an order of magnitude lower than for the HCs. The reaction mechanism by Westbrook et al. (2009) includes methyl acetate. When the rate of the H abstraction reactions on the fuel radical where a hydrogen has been abstracted from the carbon next to the carbonyl group were decreased with almost an order of magnitude, the model showed good agreement with experiment by Osswald et al. (2007).

Table 10.22 Experimental data for flame structure of methyl formate

T/K	p/atm	ϕ	Method/comment	Reference
300	0.04	1.8	Burner stabilized flat flames, synchrotron VUV ionization MS	Westbrook et al. (2009)
300	0.029–0.04	1.0–1.8	Burner stabilized laminar flame, synchrotron VUV ionization MS	Dooley et al. (2011)

10.9.3 Methyl Butanoate

Two groups have very recently determined the laminar burning velocities for methyl butanoate (Wang et al. 2011; Liu et al. 2011). Liu et al. (2011) used a nonlinear correction method to account for stretch effects. Wang et al. (2011) also measured on the similar compound methyl crotonate, that contain a double bond, and conclude that the saturated compound methyl butanoate is less reactive and has a lower peak flame speed (59 cm/s of methyl butanoate compared to 62 cm/s of methyl crotonate). Wang et al. (2011) also measured extinction strain rates and when comparing different fuels observed trends similar to those for laminar burning velocities. Wang et al. (2011) modeled their results using several different chemical kinetics schemes, and conclude that in the case of methyl butanoate a model using a methyl butanoate sub-mechanism by Huynh et al. (2008) was the one that produced best agreement. Both Wang et al. and Liu et al. also tried the kinetic mechanisms by Dooley et al. (2008) and Gail et al. (2008) and found that they overpredicted the experimental results (Tables 10.23, 10.24).

Gail et al. (2007) and Sarathy et al. (2007) both studied diffusion flames in opposed flow burners, determining species profiles of stable products and intermediates. Based on their results, Sarathy et al. (2007) present reaction pathways for the combustion of methyl butanoate. Gail et al. (2007) model their experiments using a chemical kinetics scheme by Fisher et al. (2000), with minor modifications. The modeling does not accurately reproduce the consumption of methyl butanoate shown experimentally, but does better in predicting the concentrations of CO, CO₂, and other products.

Table 10.23 Experimental data for laminar burning velocities of methyl butanoate

<i>T</i> /K	<i>p</i> /atm	ϕ	Method/comment	Reference
403	1	0.7–1.5	Counterflow	Wang et al. (2011)
353	1, 2	0.7–1.7	Spherical flame, constant pressure bomb	Liu et al. (2011)

Table 10.24 Experimental data for flame structure of methyl butanoate

<i>T</i> /K	<i>p</i> /atm	ϕ	Method/comment	Reference
355, 413	1		Opposed flow diffusion flame, quartz microprobe, GC/FID, HPLC, NDIR (CO, CO ₂)	Sarathy et al. (2007)
Ambient	1.01		Opposite flow diffusion flame, quartz micro-probe, GC/FID, HPLC, NDIR	Gail et al. (2007)
Ambient	1		Stagnation flow, quartz microprobe, chemiluminescence NO–NO ₂ –NO _x analyzer	Feng et al. (2010)
300	0.04	1.56	Burner stabilized flat flames, synchrotron VUV ionization MS	Yang et al. (2011)
Ambient	0.04	1.54, 1.67	Burner stabilized flat flames, synchrotron VUV ionization MS	Yu et al. (2012)

Feng et al. (2010) used a stagnation flow configuration to study the emission characteristics of methyl butanoate and methyl crotonate premixed and nonpremixed flames. The experimental results are modeled using a combination of the USC Mech II and the kinetics scheme by Huynh et al. (2008). It is concluded that methyl butanoate forms significantly less NO_x compared to similar alkanes (Feng et al. 2010).

Recently, Yang et al. (2011) measured the composition of reaction intermediates in premixed flat flames of three $\text{C}_5\text{H}_{10}\text{O}_2$ isomers, methyl butanoate, methyl isobutanoate, and ethyl propanoate, to enable further model development. The results for temperature profile and species profiles of fuel, CO, CO_2 , H_2 , H_2O , and O_2 were similar for the three isomers. As a starting point for modeling of methyl butanoate the mechanism of Dooley et al. (2008) was used. An important general conclusion by Yang et al. (2011) is that the rates of H-abstraction reactions for alkoxy and alkyl groups are essentially identical in a wide range of ester fuels with the same functionality.

Yu et al. (2012) present species profiles for flames similar to the one studied by Yang et al. (2011), and a kinetic model based on the mechanism of Dooley et al. (2008). In addition, Yu et al. compare the pure methyl butanoate flames with methanol/methyl butanoate flames under the same conditions. They conclude that production of soot precursors, aldehydes, and ketones increase as the equivalence ratio increases, and that an addition of methanol decreases the production of those species. The paper also presents an analysis of CO_2 production in flames and its dependence on equivalence ratio and C/O ratio.

10.9.4 Methyl Isobutanoate

As mentioned in the previous section Yang et al. (2011) measured the composition of reaction intermediates in premixed flat flames of three $\text{C}_5\text{H}_{10}\text{O}_2$ isomers. Compared to methyl butanoate the flames of methyl isobutanoate produced higher concentrations of propene and other C3 species; this is explained by the fact that in methyl isobutanoate abstraction of any of the six primary H-atoms will eventually lead to production of propene, while the same is true for only two primary H-atoms in methyl butanoate.

10.9.5 Methyl Octanoate

Dayma et al. (2011) report profiles of stable species in a diffusion flame at a pressure of 1 atm and a temperature of 400 K, investigated using experiments (GC/FID, CO, and CO_2 NDIR) and modeling. The kinetics mechanism builds on the mechanism from the group of Dagaut (Dagaut and Cathonnet 2006; Dagaut and Togbe 2008; Dayma et al. 2008) with some updates and additions.

10.9.6 Methyl Decanoate

Wang et al. (2011) used a counter flow burner to investigate premixed and non-premixed flames of methyl decanoate at 1 atm and 403 K. Equivalence ratios of the premixed flames were in the range 0.7–1.5. The authors conclude that the ester group has a retarding effect on overall mixture reactivity. Methyl decanoate is found to have a peak burning velocity only slightly higher (62 cm/s compared to 59 cm/s) than that of methyl butanoate, which indicate that the overall effect of the ester group decreases as chain length increases. Wang et al. (2011) also performed experiments on extinction stretch rate and observed that they are similar to those of *n*-decane/air flames, this indicates that the effect of the ester group on overall reactivity diminishes as the carbon chain length increases. The flames were modeled using a skeletal methyl decanoate mechanism by Seshadri et al. (2009), reduced from the detailed kinetics mechanism by Herbinet et al. (2008), and the agreement is excellent. Seshadri et al. (2009) investigated extinction and ignition of methyl decanoate in counterflow flames and compared these with their reduced model, with good agreement. From their model reduction they can conclude that low temperature chemistry is of minor importance under the counterflow conditions, while high temperature reactions of fuel decomposition, radical abstraction, isomerization, and radical decomposition are of importance.

Sarathy et al. (2011) determined the profiles of stable species in a diffusion flame, and developed a skeletal mechanism extending the mechanisms by Herbinet et al. (2008) and Seshadri et al. (2009). Using modeling results they conclude that methyl decanoate is largely consumed by H abstraction. The agreement between experiments and modeling is fairly good, major discrepancies are reported for unsaturated methyl ester species.

Dievert et al. (2012) have used the above-mentioned experimental results in development and validation of a kinetic model for methyl decanoate combustion. A lumped kinetic model of methyl butanoate and methyl decanoate combustion (Grana et al. 2012a, b) builds on kinetics mechanisms of smaller esters.

10.9.7 Ethyl Formate

Species profiles in rich ($\phi = 1.82$), low pressure (0.04 atm) premixed laminar flat flames were determined by Osswald et al. (2007) using synchrotron VUV ionization MS. H abstraction from the ethoxy group was found to be important, and resulted in large production of acetaldehyde, to be compared to the isomer methyl acetate where H abstraction from methoxy group dominated and gave formaldehyde (Westbrook et al. 2009). The kinetic mechanism developed by Westbrook et al. (2009) is based on rate expressions for H atom abstraction on similar compounds; this approach gave good agreement with experiments after changing several rates by a factor of two or more. The need for these changes in

order to get good agreement with experimental results, indicates that the reactivities of C–H bonds in ethyl formate are different from the model compounds used.

10.9.8 Ethyl Acetate

Dayma et al. (2012b) obtained laminar burning velocities from spherical flame experiments and shadowgraphy at 423 K, 1–10 bar and $\phi = 0.7$ –1.5. They present a maximum laminar burning velocity of 54.1 cm/s at 1 bar, which is only a few cm/s lower compared to larger esters investigated in the same study (Table 10.25).

Ethyl acetate was one of the first esters studied under flame conditions; Gasnot et al. (2004) determined molecular species concentration profiles in laminar premixed methane flames seeded with up to 3 % ethyl acetate. Compared to the pure methane flames the seeded flames showed an increase in C2 and C3 hydrocarbon and oxygenated intermediates. Concentration of H₂ was much lower in the seeded flames.

Westbrook et al. (2009) derive a model for combustion of ethyl acetate, building on the reactivity of the corresponding functional groups on methyl acetate and ethyl acetate. The model is used to simulate a burner stabilized flame where both stable products and intermediates are detected. Production of C2 species is significant since they are produced directly from the ethyl group. Overall agreement between the model and experiment is satisfactory.

10.9.9 Ethyl Propanoate, Ethyl Butanoate, Ethyl Pentanoate

Laminar burning velocities for the three compounds were measured under the same conditions (423 K, 1–10 atm, and $\phi = 0.7$ –1.5) using spherical flame experiments and shadowgraphy. Dayma et al. (2012a, b) note that the pressure dependence of the laminar burning velocity of ethyl pentanoate is similar to that of alcohols. A chemical kinetics model that gives good agreement with experimental

Table 10.25 Experimental data for flame structure of ethyl acetate

<i>T</i> /K	<i>p</i> /atm	ϕ	Method/comment	Reference
350	0.05		Burner stabilized flame, microprobe sampling, GC/TCD/FID, GC/MS	Gasnot et al. (2004)
300	0.04	1.56	Burner stabilized flat flames, synchrotron VUV ionization MS	Westbrook et al. (2009)

results is presented, the model is built on previously developed mechanism for smaller alcohols (Dagaut and Togbe 2008).

Ethyl propanoate was the third $C_5H_{10}O_2$ isomer studied by Yang et al. (2011) in a rich ($\phi = 1.56$), low pressure (0.04 atm) premixed flat flame using synchrotron VUV MS. As a starting point for model development, mainly the mechanisms by Metcalfe et al. (2009) was used. Extension of the model was necessary to adjust to the premixed flame conditions; significant changes included increase of some H-abstraction rates on the fuel and additional radical decomposition reactions.

10.9.10 Methyl Crotonate

Both laminar burning velocities and species profiles of methyl crotonate ($CH_3-CH=CH-C(O)-O-CH_3$) have been published together with, and compared to, results for the saturated analog methyl butanoate. It was concluded that the unsaturated methyl crotonate is more reactive than its saturated analog. Wang et al. (2011) performed modeling using the USC Mech II with methylbutanoate sub-mechanism from Huynh et al. (2008) and methyl crotonate reactions from Gail et al. (2008), giving excellent agreement with experimental laminar burning velocities. From their comparison of species profiles in methyl crotonate and methyl butanoate flames Sarathy et al. (2007) conclude that methyl crotonate produce more benzene and other larger fragments that can act as soot precursors (Table 10.26).

Yang et al. (2011) investigated how the double bond in unsaturated esters (methyl crotonate, methyl metacrylate, and ethyl propenoate) affects the combustion chemistry. They conclude that the formation of oxygenated intermediates is enhanced in esters containing a double bond compared to saturated esters.

Table 10.26 Experimental data for flame structure of methyl crotonate

T/K	$p/$ atm	ϕ	Method/comment	Reference
355, 413	1		Opposed flow diffusion flame, quartz microprobe, GC/FID, HPLC, NDIR (CO, CO ₂)	Sarathy et al. (2007)
Ambient	1	0.7-1.5	Stagnation flow, quartz microprobe, chemiluminescence NO-NO ₂ -NO _x analyzer	Feng et al. (2010)
Ambient	0.026	1.56	Tunable synchrotron VUV	Yang et al. (2011)

10.9.11 Methyl Methacrylate and Ethyl Propenoate

Yang et al. (2011) present species profiles of rich ($\phi = 1.56$) low pressure pre-mixed flat ethyl propenoate and methyl methacrylate ($\text{CH}_3\text{-C}(\text{CH}_2)\text{-C}(\text{O})\text{-O-CH}_3$) flames determined using tunable synchrotron VUV/MBMS. A similar study for methyl methacrylate at lean conditions ($\phi = 0.75$) was published by Wang et al. (2008a, b).

10.9.12 Dimethyl Carbonate

The group of Thomson reports an experimental (Sinha and Thomson 2004) and there was one modeling study (Glaude et al. 2005) of dimethyl carbonate ($\text{CH}_3\text{-O-C}(\text{O})\text{-O-CH}_3$) in opposed-flow diffusion flames. Species profiles and flame temperature were determined at atmospheric pressure conditions and 318 K using probe sampling and GC, HPLC techniques. Addition of dimethyl carbonate to a propane flame indicated synergistic effects between the two fuels (Sinha and Thomson 2004). The chemical kinetics mechanism is based on reaction rates estimated from rate constants of similar compounds. Thermodynamic parameters and key branching ratios were obtained from quantum chemistry calculations (Glaude et al. 2005).

10.9.13 Palm Methyl Esters

Palm methyl esters with approximate formula $\text{C}_{19}\text{H}_{36}\text{O}_2$ have been studied by Chong and Hochgreb (2011a, b) using stagnation flame configuration and PIV technique. The investigated mixture compositions were in the range of equivalence ratios from 0.7 to 1.5, at atmospheric pressure and with an initial mixture temperature of 470 K. The maximum flame speed was determined to be 86.5 cm/s at an equivalence ratio of 1.14, which is comparable to diesel fuel measured in the same study.

Models have also been developed for larger esters, but have not yet been tested for flames due to the lack of experimental data. The model for large methyl esters from C11 to C19 has been developed by Herbinet et al. (2011). Catalanotti et al. (2011) developed a model for C14 methyl ester, while Westbrook et al. (2011) demonstrated a model for methyl esters palmitate, stearate, oleate, linoleate, and linoleate.

10.9.14 Summary

A summary of the work performed on esters is given in Table 10.27.

10.10 Cyclic Compounds

Cyclic ethers are a group of compounds that have recently been considered as potential fuels. It has been known for some time that 2,5-dimethylfuran has properties that make it useful as a fuel but only very recently was a method for production of the compound from biomass developed. Since about 2009 research on the combustion of cyclic ethers, in particular the five membered unsaturated structures named furans, has been initiated in many labs. Some compounds are considered to be of interest as fuels, others need to be studied since they are combustion intermediates or products. It is likely that during the coming few years experimental data as well as kinetics models of cyclic ethers will be significantly extended.

10.10.1 Furan

Tian et al. (2011) measured temperature and species profiles for low pressure (0.046 atm), rich (1.4, 1.8, and 2.2) furan flames using tunable synchrotron VUV and MBMS, and developed a chemical kinetic mechanism to model the results. Agreement between experiment and modeling is reasonable for many of the 40 experimentally detected species, but uncertainties in rate constants for some key reactions limit the capacity of the model.

10.10.2 2-Methylfuran

Laminar burning velocities were determined at standard conditions and at temperatures up to 398 K for equivalence ratios in the range of 0.55–1.65 (Somers et al. 2013). In the same publication a chemical kinetic mechanism was developed, showing excellent agreement with experimental results.

Wei et al. (2012b) present experimental species identification for lean (0.8) and rich (1.5) 2-methylfuran flames at low pressure (0.045 atm) determined using synchrotron VUV and MBMS technique.

A reaction pathway is presented by Wei et al. (2012b), based on identification of flame species. Somers et al. (2013) rely on ab initio calculations and chemical kinetics modeling of laminar burning velocities and ignition delays in development

Table 10.27 Classification of work performed to date

Substance	Relevance to practical systems		Flame structure	Model validation	Selected experiments	Selected models
	D	C				
Methyl formate	D	C B	B		Dooley et al. (2010), Westbrook et al. (2009)	Fisher et al. (2000), Westbrook et al. (2009)
Methyl acetate	D	E C	B		Osswald et al. (2007)	Westbrook et al. (2009)
Methyl butanoate	B	C C	B		Wang et al. (2011), Yang et al. (2011)	Fisher et al. (2000), Huynh et al. (2008), Wang et al. (2011)
Methyl isobutanoate	B	E C	D		Yang et al. (2011)	
Methyl pentanoate	C	E E	E			Hayes and Burgess (2009)
Methyl octanoate	B	E C	B		Dayma et al. (2011)	Dayma et al. (2011)
Methyl decanoate	B	C C	B		Wang et al. (2011)	Seshadri et al. (2009) Dievart et al. (2012)
Ethyl formate	D	E C	B		Osswald et al. (2007)	Westbrook et al. (2009)
Ethyl acetate	D	E C	B		Westbrook et al. (2009)	Dayma et al. (2012b)
Ethyl propanoate	C	C C	C		Dayma et al. (2012b)	Yang et al. (2011)
Ethyl butanoate	C	E E	E		Dayma et al. (2012b)	Hakka et al. (2010)
Ethyl pentanoate	C	C E	C		Dayma et al. (2012a, b)	Dayma et al. (2012a, b)
Methyl crotonate	D	C C	B			Gail et al. (2008), Huynh et al. (2008), Wang et al. (2011)
Methyl methacrylate	C	E C	E		Yang et al. (2012)	
Ethyl propenoate	C	E C	E		Yang et al. (2012)	
Dimethyl carbonate	D	E C	B		Sinha and Thomson (2004)	Glaude et al. (2005)
Palm methyl esters	A	C E	E		Chong and Hochgreb (2011a, b)	

of a mechanism for atmospheric pressure flames. The main difference between the mechanisms presented in the two studies is that at the lower pressures studied by Wei et al. (2012a, b) the cyclic structure is maintained to a larger extent than what is proposed in the model by Somers et al. (2013).

10.10.3 2,5-Dimethylfuran

A large part of the available data for this compound is by Wu et al., who have conducted studies on diluents effects (Wu et al. 2009a, b), temperature dependence (2011a), and pressure dependence (2011b) of the laminar burning velocity. The temperature exponent, a , is derived from the experiment of Wu et al. (2011a). A similar study by Tian et al. (2010) in a lower temperature range, leads to the conclusion that the laminar burning velocity of 2,5-dimethylfuran is similar to that of gasoline. The temperature ranges of Tian et al. (2010) and Wu et al. (2011a) do not overlap, but comparison of the result at 373 and 393 K shows reasonable consistency considering the maximum burning velocities were determined as 49 and 55 cm/s (Table 10.28).

Wu et al. (2009b) have also identified flame species for rich (2.0), low pressure (0.04 atm) premixed laminar flames using tunable synchrotron PI. 70 species were detected, including important radicals, and the result were used to elucidate possible reaction pathways.

Two recent studies have presented laminar burning velocities of 2,5-dimethylfuran blended with isooctane (Li et al. 2011; Wu et al. 2012).

10.10.4 Tetrahydrofuran

Kasper et al. (2011) present profiles of 88 species determined using synchrotron VUV, PI-MBMS for equivalence ratios 1.0 and 1.75, and fewer for three intermediate equivalence ratios. The reaction mechanism for oxidation of tetrahydrofuran in the flame is thoroughly discussed.

Table 10.28 Experimental data for laminar burning velocities of 2,5-dimethyl furan

T/K	p/atm	ϕ	Method/comment	References
393	1		Spherical flame, Schlieren	Wu et al. (2009a, b)
323–373	1	0.7–1.8	Constant volume bomb	Tian et al. (2010)
393–473	1	0.9–1.5	Constant volume bomb	Wu et al. (2011a)
393	1–7.5	0.8–1.5	Constant volume bomb	Wu et al. (2011b)

10.10.5 Tetrahydropyran

Labbe et al. (2013) present species profiles for rich (1.75), low pressure (0.026 atm) flames determined using synchrotron VUV PI-MBMS, and chemical kinetic modeling. Under the studied conditions tetrahydropyran destruction is dominated by H abstraction. Tetrahydropyran is a saturated six-membered ring containing CH_2 and one oxygen atom, and thus has many hydrogen atoms available for abstraction processes.

10.10.6 1,4-Dioxane

Lin et al. (2009a, b) present species profiles for rich (1.80), low pressure (0.02 atm) flames determined using synchrotron VUV MBMS. In contrast to noncyclic oxygenates the dioxane flame produced no aromatic intermediates. This is ascribed to the fact that there are two oxygen atoms in every molecule, available for reaction with hydrocarbon intermediates that would otherwise produce soot precursors of higher molecular weight.

10.11 Summary

A summary of the work performed on cyclic compounds is given in Table 10.29.

Table 10.29 Classification of work performed to date

Substance	Relevance to practical systems	S_L	Flame structure	Model validation	Selected experiments	Selected models
Furan	C	E	C	C	Tian et al. (2011)	Tian et al. (2011)
2-Methylfuran	C	C	C	C	Somers et al. (2013)	Somers et al. (2013)
2,5-Dimethylfuran	B	C	C	E	Wu et al. (2011a, b)	
Tetrahydrofuran	C	E	C	E	Kasper et al. (2011)	
Tetrahydropyran	C	E	C	C	Labbe et al. (2013)	
1,4-Dioxane	B	E	C	E	Lin et al. (2009a, b)	

10.12 Overview and Conclusions

This chapter covers measurements of laminar burning velocities and investigations of the flame structure of oxygenated species including most recent papers presented at the 34th International Symposium on Combustion, 2012. More details on the models validation using these and other types of experiments can be found in the reviews of Ranzi et al. (2012) and of Tran et al. (2012).

The present review shows that the most extensively studied oxygenated compounds are the alcohols; much research on ethanol and methanol was performed some 20 years ago, while propanol and butanol have received interest only during the past few years.

The least studied compounds are the ones that are not fuels themselves, but act as intermediates in many hydrocarbon flames; small aldehydes, ketones, and carboxylic acids. Further studies on the combustion characteristics of these compounds are invaluable in development and validation of detailed chemical kinetics models.

During about 10 years, the ethers have received a significant amount of attention due to their potential as a diesel substitute, the interest in these fuels has decreased since they have shown to emit unwanted pollutants. The focus of the research effort has instead been directed toward esters and cyclic ethers. The large interest in these two groups of compounds is apparent from the fact that the majority of the data concerning these compounds have been published during the last two years.

The esters are a large group and to increase the understanding of their combustion characteristics, systematic studies investigating the effect of structure like chain length, branching, and degree of saturation would be of high value.

Regarding laminar burning velocities in general, there is often a scatter in results from studies where different experimental methods have been used; this calls for further research on the applicability of the methods. In this context, we can also highlight the importance of determining the laminar burning velocities using several different methods, to reveal possible errors in experiments using one or more models.

References

- Agnew WG, Agnew JT (1965) Composition of the diethyl ether—air two-stage reaction stabilized in a flat-flame burner. In: Tenth symposium (international) on combustion, pp 123–138
- Bahrini C, Herbinet O, Glaude PA et al (2012) Detection of some stable species during the oxidation of methane by coupling a jet-stirred reactor (JSR) to cw-CRDS. *Chem Phys Lett* 534:1–7
- Battin-Leclerc F (2008) Detailed chemical kinetic models for the low-temperature combustion of hydrocarbons with application to gasoline and diesel fuel surrogates. *Prog Energy Combust Sci* 34(4):440–498

- Battin-Leclerc F, Konnov AA, Jaffrezzo JL et al (2008) To better understand the formation of short-chain acids in combustion systems. *Combust Sci Technol* 180(2):343–370
- Biordi JC (1977) Molecular beam mass spectrometry for studying the fundamental chemistry of flames. *Prog Energy Combust Sci* 3:151–173
- Black G, Pichon S et al (2007) An experimental and modelling study of the combustion of acetone. In: Third European combustion meeting
- Bosschaart KJ, de Goey LPH (2003) Detailed analysis of the heat flux method for measuring burning velocities. *Combust Flame* 132:170–180
- Bosschaart KJ, de Goey LPH (2004a) The laminar burning velocity of flames propagating in mixtures of hydrocarbons and air measured with the heat flux method. *Combust Flame* 136:261–269
- Bosschaart KJ, de Goey LPH (2004b) Extension of the heat flux method to subatmospheric pressures. *Combust Sci Technol* 176:1537–1564
- Botha JP, Spalding DB (1954) The laminar flame speed of propane/air mixtures with heat extraction from the flame. *Proc Royal Soc Lond Ser. A* 225:71–96
- Brackmann C, Bood J, Alden M et al (2006) Quantitative measurements of species and temperature in a DME-air counterflow diffusion flame using laser diagnostic methods. *Combust Sci Technol* 178(6):1165–1184
- Bradley JN, Jones GA (1966) Stabilized low temperature flames of acetaldehyde and propionaldehyde—a mass spectrometric study. *Combust Flame* 10(3):259–266
- Bradley D, Lawes M, Mansour MS (2009) Explosion bomb measurements of ethanol-air laminar gaseous flame characteristics at pressures up to 1.4 mpa. *Combust Flame* 156(7):1462–1470
- Branch MC, Sadeqi ME, Alfarayedhi AA et al (1991) Measurements of the structure of laminar, premixed flames of $\text{CH}_4/\text{NO}_2/\text{O}_2$ and $\text{CH}_2\text{O}/\text{NO}_2/\text{O}_2$ mixtures. *Combust Flame* 83(3–4):228–239
- Broustail G, Seers P, Halter F et al (2011) Experimental determination of laminar burning velocity for butanol and ethanol iso-octane blends. *Fuel* 90(1):1–6
- Brown MJ, Smith DB (1994) Aspects of nitrogen flame chemistry revealed by burning velocity modeling. *Proc Combust Inst* 25:1011–1018
- Burke MP, Chen Z, Ju Y, Dryer FL (2009) Effect of cylindrical confinement on the determination of laminar flame speeds using outwardly propagating flames. *Combust Flame* 156:771–779
- Burluka AA, Harker M, Osman H et al (2010) Laminar burning velocities of three $\text{C}_3\text{H}_6\text{O}$ isomers at atmospheric pressure. *Fuel* 89(10):2864–2872
- Catalanotti E, Hughes KJ, Pourkashanian M, Wilson CW (2011) Development of a chemical reaction mechanism for alternative aviation fuels. *Energy Fuels* 25:1465–1473
- Cattolica RJ, Yoon S, Knuth EL (1982) OH concentration in an atmospheric-pressure methane-air flame from molecular-beam mass spectrometry and laser-absorption spectroscopy. *Combust Sci Technol* 28:225–239
- Chen Z, Wei L, Huang Z et al (2009) Measurement of laminar burning velocities of dimethyl ether-air premixed mixtures with N_2 and CO_2 dilution. *Energy Fuels* 23(1):735–739
- Chen Z, Wei L, Gu X et al (2010) Study of low-pressure premixed dimethyl ether/hydrogen/oxygen/argon laminar flames with photoionization mass spectrometry. *Energy Fuels* 24:1628–1635
- Chen Z, Tang C, Fu J et al (2012) Experimental and numerical investigation on diluted DME flames: thermal and chemical kinetic effects on laminar flame speeds. *Fuel* 102:567–573
- Cheskis S (1999) Quantitative measurements of absolute concentrations of intermediate species in flames. *Prog Energy Combust Sci* 25:233–252
- Cheskis S, Goldman A (2009) Laser diagnostics of trace species in low-pressure flat flame. *Prog Energy Combust Sci* 35:365–382
- Chong CT, Hochgreb S (2011) Measurements of laminar flame speeds of acetone/methane/air mixtures. *Combust Flame* 158(3):490–500
- Chong CT, Hochgreb S (2011b) Measurements of laminar flame speeds of liquid fuels: Jet-a-1, diesel, palm methyl esters and blends using particle imaging velocimetry (piv). *Proc Combust Inst* 33:979–986

- Chung GA, Akih-Kumgeh B et al (2012) NO_x formation and flame velocity profiles of iso- and *n*-isomers of butane and butanol. *Proc Combust Inst* 34:831–838
- Cool TA, Wang J, Hansen N et al (2007) Photoionization mass spectrometry and modeling studies of the chemistry of fuel-rich dimethyl ether flames. *Proc Combust Inst* 31:285–293
- Dagaut P, Cathonnet M (2006) The ignition, oxidation, and combustion of kerosene: a review of experimental and kinetic modeling. *Prog Energy Combust Sci* 32(1):48–92
- Dagaut P, Togbe C (2008) Experimental and modeling study of the kinetics of oxidation of ethanol-gasoline surrogate mixtures (E85 surrogate) in a jet-stirred reactor. *Energy Fuels* 22(5):3499–3505
- Daily JW (1997) Laser induced fluorescence in flames. *Prog Energy Combust Sci* 23:133–199
- Daly CA, Simmie JM, Wurmel J et al (2001) Burning velocities of dimethyl ether and air. *Combust Flame* 125(4):1329–1340
- Dayma G, Gail S, Dagaut P (2008) Experimental and kinetic modeling study of the oxidation of methyl hexanoate. *Energy Fuels* 22(3):1469–1479
- Dayma G, Sarathy SM, Togbe C et al (2011) Experimental and kinetic modeling of methyl octanoate oxidation in an opposed-flow diffusion flame and a jet-stirred reactor. *Proc Combust Inst* 33:1037–1043
- Dayma G, Halter F, Foucher F et al (2012a) Experimental and detailed kinetic modeling study of ethyl pentanoate (ethyl valerate) oxidation in a jet stirred reactor and laminar burning velocities in a spherical combustion chamber. *Energy Fuels* 26(8):4735–4748
- Dayma G, Halter F, Foucher F et al (2012b) Laminar burning velocities of C₄–C₇ ethyl esters in a spherical combustion chamber: Experimental and detailed kinetic modeling. *Energy Fuels* 26:6669–6677
- de Goeij LPH, van Maaren A, Quax RM (1993) Stabilization of adiabatic premixed laminar flames on a flat burner. *Combust Sci Technol* 92:201–207
- De Vries J, Lowry WB, Serinyel Z et al (2011) Laminar flame speed measurements of dimethyl ether in air at pressures up to 10 atm. *Fuel* 90(1):331–338
- Decottignies V, Gasnot L, Pauwels JF (2002) A comprehensive chemical mechanism for the oxidation of methylethylketone in flame conditions. *Combust Flame* 130(3):225–240
- Desgroux P, Gasnot L, Pauwels JF et al (1994) A comparison of ESR and LIF hydroxyl radical measurements in flame. *Combust Sci Technol* 100:379–384
- Desgroux P, Gasnot L, Pauwels JF et al (1995) Correction of LIF temperature measurements for laser absorption and fluorescence trapping in a flame. Application to the thermal perturbation study induced by a sampling probe. *Appl Phys B* 61:401–407
- Di YG, Huang ZH, Zhang N et al (2009) Measurement of laminar burning velocities and Markstein lengths for diethyl ether-air mixtures at different initial pressure and temperature. *Energy Fuels* 23:2490–2497
- Dias V, Renard C, Van Tiggelen PJ et al (2004) Mass spectrometry, gas chromatography, and coupling GC/MS as complementary technics for flame structure analysis. *Combust Sci Technol* 176:1419–1435
- Dias V, Duynslaegher C, Contino F et al (2012) Experimental and modeling study of formaldehyde combustion in flames. *Combust Flame* 159(5)
- Dievart P, Won SH, Dooley S et al (2012) A kinetic model for methyl decanoate combustion. *Combust Flame* 159(5):1793–1805
- Dooley S, Curran HJ, Simmie JM (2008) Autoignition measurements and a validated kinetic model for the biodiesel surrogate, methyl butanoate. *Combust Flame* 153(1–2):2–32
- Dooley S, Burke MP, Chaos M et al (2010) Methyl formate oxidation: Speciation data, laminar burning velocities, ignition delay times, and a validated chemical kinetic model. *Int J Chem Kinet* 42(9):527–549
- Dooley S, Dryer FL, Yang B et al (2011) An experimental and kinetic modeling study of methyl formate low-pressure flames. *Combust Flame* 158(4):732–741
- Doute C, Delfau JL, Akkrich R et al (1997) Experimental study of the chemical structure of low-pressure premixed *n*-heptane-O₂-Ar and iso-octane-O₂-Ar flames. *Combust Sci Technol* 124:249–276

- Dyakov IV, Konnov AA, De Ruyck J et al (2001) Measurement of adiabatic burning velocity in methane-oxygen-nitrogen mixtures. *Combust Sci Technol* 172:81–96
- Egolfopoulos FN, Du DX, Law CK (1992a) A comprehensive study of methanol kinetics in freely-propagating and burner-stabilized flames, flow and static reactors, and shock-tubes. *Combust Sci Technol* 83(1–3):33–75
- Egolfopoulos FN, Du DX, Law CK (1992b) A study on ethanol oxidation kinetics in laminar premixed flames, flow reactors, and shock tubes. *Proc Combust Inst* 24:833–841
- Eisazadeh-Far K, Moghaddas A, et al. (2011) Laminar burning speeds of ethanol/air/diluent mixtures. *Proc Combust Inst* 33:1021–1027
- Evertsen R, van Oijen JA, Hermanns RTE et al (2003) Measurements of the absolute concentrations of HCO and CH₂ in a premixed atmospheric flat flame by cavity ring-down spectroscopy. *Combust Flame* 135:57–64
- Farrell RJ, Johnston RJ, Androulakis IP (2004) Molecular structure effects on laminar burning velocities at elevated temperature and pressure, SAE Paper 2004-01-2936
- Feng Q, Wang YL et al (2010) Fundamental study of the oxidation characteristics and pollutant emissions of model biodiesel fuels. *Ind Eng Chem Res* 49(21):10392–10398
- Fisher EM, Pitz WJ, Curran HJ et al (2000) Detailed chemical kinetic mechanisms for combustion of oxygenated fuels. *Proc Combust Inst* 28:1579–1586
- Franklin PM, Koshland CP, Lucas D, Sawyer RF (2001) Evaluation of combustion by-products of MTBE as a component of reformulated gasoline. *Chemosphere* 42:861–872
- Frassoldati A, Grana R, Faravelli T et al (2012) Detailed kinetic modeling of the combustion of the four butanol isomers in premixed low-pressure flames. *Combust Flame* 159(7):2295–2311
- Fristrom RM, Westenberg AA (1965) *Flame structure*. McGraw-Hill, New York
- Frye CA, Boehman AL, Tijm PJA (1999) Comparison of CO and NO emissions from propane, n-butane, and dimethyl ether premixed flames. *Energy Fuels* 13(3):650–654
- Gail S, Thomson MJ, Sarathy SM et al (2007) A wide-ranging kinetic modeling study of methyl butanoate combustion. *Proc Combust Inst* 31:305–311
- Gail S, Sarathy SM, Thomson MJ et al (2008) Experimental and chemical kinetic modeling study of small methyl esters oxidation: methyl (e)-2-butenate and methyl butanoate. *Combust Flame* 155(4):635–650
- Galmiche B, Togbe C, Dagaut P et al (2011) Experimental and detailed kinetic modeling study of the oxidation of 1-propanol in a pressurized jet-stirred reactor (JSR) and a combustion bomb. *Energy Fuels* 25(5):2013–2021
- Gasnot L, Decottignies V, Pauwels JF (2004) Ethyl acetate oxidation in flame condition: an experimental study. *Fuel* 83(4–5):463–470
- Gibbs GJ, Calcote HF (1959) Effect of molecular structure on burning velocity. *J Chem Eng Data* 4:226–237
- Gillespie F, Metcalfe WK, Dirrenberger P et al (2012) Measurements of flat-flame velocities of diethyl ether in air. *Energy* 43(1):140–145
- Glaude PA, Pitz WJ et al (2005) Chemical kinetic modeling of dimethyl carbonate in an opposed-flow diffusion flame. *Proc Combust Inst* 30:1111–1118
- Gong J, Jin C, Huang ZH et al (2010) Study on laminar burning characteristics of premixed high-octane fuel-air mixtures at elevated pressures and temperatures. *Energy Fuels* 24:965–972
- Goswami M, Derks S, Coumans K, et al (2013) The Effect of elevated pressures on the laminar burning velocity of methane + air mixtures. *Combust Flame* (submitted)
- Grana R, Frassoldati A, Faravelli T et al (2010) An experimental and kinetic modeling study of combustion of isomers of butanol. *Combust Flame* 157(11):2137–2154
- Grana R, Frassoldati A, Cuoci A et al (2012a) A wide range kinetic modeling study of pyrolysis and oxidation of methyl butanoate and methyl decanoate. Note i: Lumped kinetic model of methyl butanoate and small methyl esters. *Energy* 43(1):124–139
- Grana R, Frassoldati A, Saggese C et al (2012) A wide range kinetic modeling study of pyrolysis and oxidation of methyl butanoate and methyl decanoate—note ii: lumped kinetic model of decomposition and combustion of methyl esters up to methyl decanoate. *Combust Flame* 159(7):2280–2294

- Gu X, Huang Z, Li Q et al (2009) Measurements of laminar burning velocities and Markstein lengths of *n*-butanol-air premixed mixtures at elevated temperatures and pressures. *Energy Fuels* 23:4900–4907
- Gu X, Huang Z, Wu S et al (2010) Laminar burning velocities and flame instabilities of butanol isomers-air mixtures. *Combust Flame* 157(12):2318–2325
- Gu X, Li Q, Huang Z (2011a) Laminar burning characteristics of diluted *n*-butanol/air mixtures. *Combust Sci Technol* 183(12):1360–1375
- Gu X, Li Q, Huang Z et al (2011b) Measurement of laminar flame speeds and flame stability analysis of tert-butanol-air mixtures at elevated pressures. *Energy Conv Manage* 52(10):3137–3146
- Gulder OL (1983a) Laminar burning velocities of methanol, isooctane and isooctane/methanol blends. *Combust Sci Technol* 33(1–4):179–192
- Gulder OL (1983b) Laminar burning velocities of methanol, ethanol, and isooctane-air mixtures. *Proc Combust Inst* 19:275–281
- Hakka MH, Bennadji H, Biet J et al (2010) Oxidation of methyl and ethyl butanoates. *Int J Chem Kinet* 42(4):226–252
- Hansen N, Klippenstein SJ, Miller JA et al (2006a) Identification and chemistry of C₄H₃ and C₄H₅ isomers in fuel-rich flames. *J Phys Chem A* 110:3670–3678
- Hansen N, Klippenstein SJ, Taatjes CA et al (2006b) Identification of C₅H_x isomers in fuel-rich flames by photoionization mass spectrometry and electronic structure calculations. *J Phys Chem* 110:4376–4388
- Hansen N, Cool TA, Westmoreland PR et al (2009) Recent contributions of flame-sampling molecular-beam mass spectrometry to a fundamental understanding of combustion chemistry. *Prog Energy Combust Sci* 35(2):168–191
- Hartlieb AT, Atakan B, Kohse-Hoinghaus K (2000) Effects of a sampling quartz nozzle on the flame structure of a fuel-rich low-pressure propene flame. *Combust Flame* 121:610–624
- Hayes CJ, Burgess DR Jr (2009) Exploring the oxidative decompositions of methyl esters: Methyl butanoate and methyl pentanoate as model compounds for biodiesel. *Proc Combust Inst* 32:263–270
- Herbinet O, Pitz WJ et al (2008) Detailed chemical kinetic oxidation mechanism for a biodiesel surrogate. *Combust Flame* 154(3):507–528
- Herbinet O, Biet J et al (2011) Modeling study of the low-temperature oxidation of large methyl esters from C(11) to C(19). *Proc Combust Inst* 33:391–398
- Herbon JT, Hanson RK, Golden DM, Bowman CT (2002) A shock tube study of the enthalpy of formation of OH. *Proc Combust Inst* 29:1201–1208
- Hori M (1980) Effects of probing conditions on NO/NO_x ratios. *Combust Sci Technol* 23:131–135
- Huang Z, Wang Q, Yu J et al (2007) Measurement of laminar burning velocity of dimethyl ether-air premixed mixtures. *Fuel* 86(15):2360–2366
- Huang Z, Chen G, Chen C et al (2008) Experimental study on premixed combustion of dimethyl ether-hydrogen-air mixtures. *Energy Fuels* 22(2):967–971
- Huynh LK, Lin KC, Viola A (2008) Kinetic modeling of methyl butanoate in shock tube. *J Phys Chem A* 112(51):13470–13480
- Hwang C-H, Lee C-E, Lee K-M (2009) Fundamental studies of NO(x) emission characteristics in dimethyl ether (DME)/air non-premixed flames. *Energy Fuels* 23(1):754–761
- Johansson O, Bood J, Li B et al (2011) Photofragmentation laser-induced fluorescence imaging in premixed flames. *Combust Flame* 158:1908–1919
- Kaiser EW, Wailington TJ, Hurley MD et al (2000) Experimental and modeling study of premixed atmospheric-pressure dimethyl ether-air flames. *J Phys Chem A* 104(35):8194–8206
- Kasper TS, Osswald P, Kamphus M et al (2007) Ethanol flame structure investigated by molecular beam mass spectrometry. *Combust Flame* 150(3):220–231
- Kasper T, Osswald P, Struckmeier U et al (2009) Combustion chemistry of the propanol isomers—investigated by electron ionization and VUV-photoionization molecular-beam mass spectrometry. *Combust Flame* 156(6):1181–1201

- Kasper T, Struckmeier U, Osswald P et al (2009b) Structure of a stoichiometric propanal flame at low pressure. *Proc Combust Inst* 32:1285–1292
- Kasper T, Lucassen A, Jasper AW et al. (2011) Identification of tetrahydrofuran reaction pathways in premixed flames. *Z Phys Chemie-Int J Res Phys Chem Chem Phys* 225(11-12):1237–1270
- Kohse-Hoinghaus K (1994) Laser techniques for the quantitative detection of reactive intermediates in combustion systems. *Prog Energy Combust Sci* 20:203–279
- Kohse-Hoinghaus K, Brockhinke A (2009) *Combust Exp Shock Waves* 45:349–364
- Kohse-Hoinghaus K, Barlow RS, Alden M, Wolfrum J (2005) Combustion at the focus: laser diagnostics and control. *Proc Combust Inst* 30:89–123
- Konnov AA, Riemeijer R, de Goey LPH (2010) Adiabatic laminar burning velocities of $\text{CH}_4 + \text{H}_2 + \text{air}$ flames at low pressures. *Fuel* 89:1392–1396
- Konnov AA, Meuwissen RJ, De Goey LPH (2011) The temperature dependence of the laminar burning velocity of ethanol flames. *Proc Combust Inst* 33:1011–1019
- Kramlich JC, Malte PC (1978) Modeling and measurements of sample probe effects on pollutant gasses drawn from flame zone. *Combust Sci Technol* 18:91–104
- Labbe NJ, Seshadri V, Kasper T et al (2013) Flame chemistry of tetrahydropyran as a model heteroatomic biofuel. *Proc Combust Inst* 34:259–267
- Lai JYW, Lin KC, Violi A (2011) Biodiesel combustion: advances in chemical kinetic modeling. *Prog Energy Combust Sci* 37(1):1–14
- Law CK, Sung CJ (2010) Structure, aerodynamics and geometry of premixed flammlets. *Prog Energy Combust Sci* 26:459–505
- Lefkowitz JK, Heyne JS, Won SH et al (2012) A chemical kinetic study of tertiary-butanol in a flow reactor and a counterflow diffusion flame. *Combust Flame* 159(3):968–978
- Leplat N, Vandooren J (2010) Experimental investigation and numerical simulation of the structure of $\text{CH}_3\text{CHO}/\text{O}_2/\text{Ar}$ flames at different equivalence ratios. *Combust Sci Technol* 182(4–6):436–448
- Leplat N, Vandooren J (2012) Numerical and experimental study of the combustion of acetic acid in laminar premixed flames. *Combust Flame* 159(2):493–499
- Leplat N, Seydi A, Vandooren J (2008) An experimental study of the structure of a stoichiometric ethanol/oxygen/argon flame. *Combust Sci Technol* 180(3):519–532
- Leplat N, Dagaut P, Togbe C et al (2011) Numerical and experimental study of ethanol combustion and oxidation in laminar premixed flames and in jet-stirred reactor. *Combust Flame* 158(4):705–725
- Lewis B, Von Elbe G (1961) *Combustion, flames and explosions of gasses*. Cambridge University Press, New York
- Li J, Zhao ZW, Kazakov A et al (2007) A comprehensive kinetic mechanism for CO, CH_2O , and CH_3OH combustion. *Int J Chem Kinet* 39(3):109–136
- Li YY, Wei LX, Tian ZY et al (2008) A comprehensive experimental study of low-pressure premixed c-3-oxygenated hydrocarbon flames with tunable synchrotron photoionization. *Combust Flame* 152 (3):336–359
- Li Q, Fu J, Wu X et al (2011) Laminar flame speeds of DMF/iso-octane-air- N_2/CO_2 mixtures. *Energy Fuels* 26(2):917–925
- Liao SY, Jiang DM, Huang ZH et al (2007a) Laminar burning velocities for mixtures of methanol and air at elevated temperatures. *Energy Conv Manage* 48(3):857–863
- Liao SY, Jiang DM, Huang ZH et al (2007b) Determination of the laminar burning velocities for mixtures of ethanol and air at elevated temperatures. *Appl Therm Eng* 27(2–3):374–380
- Lin Z, Han D, Li S et al (2009a) Combustion intermediates in fuel-rich 1,4-dioxane flame studied by tunable synchrotron vacuum ultraviolet photoionization. *J Phys Chem A* 113(9):1800–1806
- Lin ZK, Han DL, Li SF et al (2009b) Synchrotron photoionization mass spectrometry study of intermediates in fuel-rich 1,2-dimethoxyethane flame. *J Chem Phys* 130(15)

- Liu W, Kelley AP, Law CK (2011) Non-premixed ignition, laminar flame propagation, and mechanism reduction of *n*-butanol, iso-butanol, and methyl butanoate. *Proc Combust Inst* 33:995–1002
- Lowry WB, Serinyel Z, Krejci MC et al (2011) Effect of methane-dimethyl ether fuel blends on flame stability, laminar flame speed, and Markstein length. *Proc Combust Inst* 33:929–937
- Marinov NM (1999) A detailed chemical kinetic model for high temperature ethanol oxidation. *Int J Chem Kinet* 31:183–220
- Marshall SP, Taylor S, Stone CR et al. (2011) Laminar burning velocity measurements of liquid fuels at elevated pressures and temperatures with combustion residuals. *Combust Flame* 158(10):1920–1932
- McIlroy A, Hain TD, Michelsen HA et al (2000) A laser and molecular beam mass spectrometer study of low-pressure dimethyl ether flames. *Proc Combust Inst* 28:1647–1653
- Metcalfe WK, Togbe C, Dagaut P et al. (2009) A jet-stirred reactor and kinetic modeling study of ethyl propanoate oxidation. *Combust Flame* 156(1):250–260
- Metghalchi M, Keck JC (1982) Burning velocities of mixtures of air with methanol, isooctane, and indolene at high-pressure and temperature. *Combust Flame* 48(2):191–210
- Naucler JD, Christensen M, Nilsson EJK et al (2012) Oxy-fuel combustion of ethanol in premixed flames. *Energy Fuels* 26(7):0
- Nilsson EJK, De Goey LPH, Konnov AA (2013) Laminar burning velocities of acetone in air at room and elevated temperatures. *Fuel* 105:496–502
- Oldenhove de Guertechin L, Vandooren J et al (1983) Mass-spectrometric analysis of onedimensional CH₂O/O₂ flames stabilized at low-pressures. *J Chimie Phys Physico-Chimie Biol* 80(7–8):583–594
- Olsson JO, Olsson IBM, Smooke MD (1989) Computer modeling of a premixed laminar formaldehyde flame. *J Phys Chem* 93(8):3107–3112
- Osswald P, Struckmeier U, Kasper T et al (2007) Isomer-specific fuel destruction pathways in rich flames of methyl acetate and ethyl formate and consequences for the combustion chemistry of esters. *J Phys Chem A* 111(19):4093–4101
- Osswald P, Gueldenberg H, Kohse-Hoeinghaus K et al (2011) Combustion of butanol isomers—a detailed molecular beam mass spectrometry investigation of their flame chemistry. *Combust Flame* 158(1):2–15
- Pichon S, Black G, Chaumeix N et al (2009) The combustion chemistry of a fuel tracer: measured flame speeds and ignition delays and a detailed chemical kinetic model for the oxidation of acetone. *Combust Flame* 156(2):494–504
- Pitz WJ, Mueller CJ (2011) Recent progress in the development of diesel surrogate fuels. *Prog Energy Combust Sci* 37(3):330–350
- Qin X, Ju YG (2005) Measurements of burning velocities of dimethyl ether and air premixed flames at elevated pressures. *Proc Combust Inst* 30:233–240
- Ranzi E, Frassoldati A, Grana R et al (2012) Hierarchical and comparative kinetic modeling of laminar flame speeds of hydrocarbon and oxygenated fuels. *Prog Energy Combust Sci* 38(4):468–501
- Ryan TWI, Lestz SS (1980) The laminar burning velocity of isooctane, *n*-heptane, methanol, methane, and propane at elevated temperature and pressures in the presence of a diluent, SAE paper no. 800103
- Saeed K, Stone CR (2004) Measurements of the laminar burning velocity for mixtures of methanol and air from a constant-volume vessel using a multizone model. *Combust Flame* 139(1–2):152–166
- Sarathy SM, Gail S, Syed SA et al (2007) A comparison of saturated and unsaturated *c*-4 fatty acid methyl esters in an opposed flow diffusion flame and a jet stirred reactor. *Proc Combust Inst* 31:1015–1022
- Sarathy SM, Thomson MJ, Pitz WJ et al (2011) An experimental and kinetic modeling study of methyl decanoate combustion. *Proc Combust Inst* 33:399–405
- Sarathy SM, Vranckx S, Yasunaga K et al (2012) A comprehensive chemical kinetic combustion model for the four butanol isomers. *Combust Flame* 159(6):2028–2055

- Saxena P, Williams FA (2007) Numerical and experimental studies of ethanol flames. *Proc Combust Inst* 31:1149–1156
- Schoenung SM, Hanson RK (1981) CO and temperature measurements in a flat flame by laser absorption techniques. *Combust Sci Technol* 24:227–237
- Selle L, Poinot T, Ferrer B (2011) Experimental and numerical study of the accuracy of flame-speed measurements for methane/air combustion in a slot burner. *Combust Flame* 158:146–154
- Serinyel Z, Chaumeix N, Black G et al (2010) Experimental and chemical kinetic modeling study of 3-pentanone oxidation. *J Phys Chem A* 114(46):12176–12186
- Seshadri K, Lu TF, Herbinet O et al (2009) Experimental and kinetic modeling study of extinction and ignition of methyl decanoate in laminar non-premixed flows. *Proc Combust Inst* 32:1067–1074
- Sinha A, Thomson MJ (2004) The chemical structures of opposed flow diffusion flames of C3 oxygenated hydrocarbons (isopropanol, dimethoxy methane, and dimethyl carbonate) and their mixtures. *Combust Flame* 136 (4):548–556
- Sjöholm J, Rosell J, Li B et al (2013) Simultaneous visualization of OH, CH, CH₂O and toluene PLIF in a methane jet flame with varying degrees of turbulence. *Proc Combust Inst* 34:1475–1482
- Skovorodko PA, Tereshchenko AG, Knyazkov DA et al (2012) Experimental and numerical study of thermocouple-induced perturbations of the methane flame structure. *Combust Flame* 159:1009–1015
- Somers KP, Simmie JM, Gillespie F et al (2013) A high temperature and atmospheric pressure experimental and detailed chemical kinetic modelling study of 2-methyl furan oxidation. *Proc Combust Inst* 34:225–232
- Sutton JA, Williams BA, Fleming JW (2008) *Combust Flame* 153:465–478
- Tahtouh T, Halter F, Mounaim-Rousselle C (2009) Measurement of laminar burning speeds and Markstein lengths using a novel methodology. *Combust Flame* 156:1735–1743
- Tian G, Daniel R, Li H et al (2010) Laminar burning velocities of 2,5-dimethylfuran compared with ethanol and gasoline. *Energy Fuels* 24:3898–3905
- Tian ZY, Yuan T, Fournet R et al (2011) An experimental and kinetic investigation of premixed furan/oxygen/argon flames. *Combust Flame* 158(4):756–773
- Togbe C, Dagaut P, Mze-Ahmed A et al (2010) Experimental and detailed kinetic modeling study of 1-hexanol oxidation in a pressurized jet-stirred reactor and a combustion bomb. *Energy Fuels* 24:5859–5875
- Togbe C, Dagaut P, Halter F et al (2011a) 2-propanol oxidation in a pressurized jet-stirred reactor (JSR) and combustion bomb: experimental and detailed kinetic modeling study. *Energy Fuels* 25:676–683
- Togbe C, Halter F, Foucher F et al (2011b) Experimental and detailed kinetic modeling study of 1-pentanol oxidation in a JSR and combustion in a bomb. *Proc Combust Inst* 33:367–374
- Tran LS, Sirjean B, Glaude PA et al (2012) Progress in detailed kinetic modelling of the combustion of oxygenated components of biofuels. *Energy* 43:4–18
- van Maaren A, de Goey LPH (1994) Stretch and the adiabatic burning velocity of methane- and propane-air flames. *Combust Sci Technol* 102:309–314
- van Maaren A, Thung DS, de Goey LPH (1994) Measurement of flame temperature and adiabatic burning velocity of methane/air mixtures. *Combust Sci Technol* 96:327–344
- Vancoillie J, Christensen M, Nilsson EJK et al (2012) Temperature dependence of the laminar burning velocity of methanol flames. *Energy Fuels* 26(3):1557–1564
- Vandoreen J, Deguertechin LO, Vantiggelen PJ (1986) Kinetics in a lean formaldehyde flame. *Combust Flame* 64:127–139
- Varea E, Modica V, Vandel A et al (2012) Measurement of laminar burning velocity and Markstein length relative to fresh gases using a new postprocessing procedure: application to laminar spherical flames for methane, ethanol and isooctane/air mixtures. *Combust Flame* 159(2):577–590

- Varea E, Modica V, Renou B et al (2013) Pressure effects on laminar burning velocities and Markstein lengths for isooctane–ethanol–air mixtures. *Proc Combust Inst* 34:735–744
- Veloo PS, Egolfopoulos FN (2011a) Flame propagation of butanol isomers/air mixtures. *Proc Combust Inst* 33:987–993
- Veloo PS, Egolfopoulos FN (2011) Studies of *n*-propanol, iso-propanol, and propane flames. *Combust Flame* 158(3):501–510
- Veloo PS, Wang YL, Egolfopoulos FN et al (2010) A comparative experimental and computational study of methanol, ethanol, and *n*-butanol flames. *Combust Flame* 157(10):1989–2004
- Veloo PS, Dagaut P, Togbe C et al (2012) Jet-stirred reactor and flame studies of propanal oxidation. *Proc Combust Inst* 34:599–606
- Vovelle Ch, Delfau J-L, Pillier L (2009) *Combust Exp Shock Waves* 45:365–382
- Wang CH, Ueng GJ, Jehng JJ (1997) The extinction limits and near-limits behaviors of premixed ethanol/air flame. *Int Commun Heat Mass Transf* 24(5):695–708
- Wang J, Struckmeier U, Yang B et al (2008a) Isomer-specific influences on the composition of reaction intermediates in dimethyl ether/propene and ethanol/propene flame. *J Phys Chem A* 112(39):9255–9265
- Wang T, Li S, Lin Z et al (2008b) Experimental study of laminar lean premixed methylmethacrylate/oxygen/argon flame at low pressure. *J Phys Chem A* 112(6):1219–1227
- Wang J, Chaos M, Yang B et al (2009a) Composition of reaction intermediates for stoichiometric and fuel-rich dimethyl ether flames: flame-sampling mass spectrometry and modeling studies. *Phys Chem Chem Phys* 11(9):1328–1339
- Wang YL, Holley AT, Ji C et al (2009b) Propagation and extinction of premixed dimethyl-ether/air flames. *Proc Combust Inst* 32:1035–1042
- Wang YL, Feng Q, Egolfopoulos FN et al (2011) Studies of *c*(4) and *c*(10) methyl ester flames. *Combust Flame* 158(8):1507–1519
- Wei LJ, Tang CL, Man XJ et al (2012a) High-temperature ignition delay times and kinetic study of furan. *Energy Fuels* 26(4):2075–2081
- Wei L, Li Z, Tong L et al (2012b) Primary combustion intermediates in lean and rich low-pressure premixed laminar 2-methylfuran/oxygen/argon flames. *Energy Fuels* 26:6651–6660
- Westbrook CK, Pitz WJ, Westmoreland PR et al (2009) A detailed chemical kinetic reaction mechanism for oxidation of four small alkyl esters in laminar premixed flames. *Proc Combust Inst* 32:221–228
- Westbrook CK, Naik CV, Herbinet O et al (2011) Detailed chemical kinetic reaction mechanisms for soy and rapeseed biodiesel fuels. *Combust Flame* 158(4):742–755
- Wiser W, Hill G (1955) A kinetic comparison of the combustion of methyl alcohol and methane. In: 5th symposium (international) on combustion, vol 5, pp 553–558
- Wolfrum J (1998) Lasers in combustion: from basic theory to practical devices. *Proc Combust Inst* 27:1–41
- Wu CK, Law CK (1984) On the determination of laminar flame speeds from stretched flames. *Proc Combust Inst* 20:1941–1949
- Wu X, Huang Z, Jin C et al (2009a) Measurements of laminar burning velocities and Markstein lengths of 2,5-dimethylfuran–air–diluent premixed flames. *Energy Fuels* 23:4355–4362
- Wu X, Huang Z, Yuan T et al (2009) Identification of combustion intermediates in a low-pressure premixed laminar 2,5-dimethylfuran/oxygen/argon flame with tunable synchrotron photoionization. *Combust Flame* 156(7):1365–1376
- Wu X, Huang Z, Jin C et al (2011a) Laminar burning velocities and Markstein lengths of 2,5-dimethylfuran–air premixed flames at elevated temperatures. *Combust Sci Technol* 183(3):220–237
- Wu X, Huang Z, Wang X et al (2011) Laminar burning velocities and flame instabilities of 2,5-dimethylfuran–air mixtures at elevated pressures. *Combust Flame* 158(3):539–546
- Wu X, Li Q, Fu J et al (2012) Laminar burning characteristics of 2,5-dimethylfuran and isooctane blend at elevated temperatures and pressures. *Fuel* 95(1):234–240

- Xu H, Yao C, Yuan T et al (2011) Measurements and modeling study of intermediates in ethanol and dimethyl ether low-pressure premixed flames using synchrotron photoionization. *Combust Flame* 158(9):1673–1681
- Yahaoui M, Djebaili-Chaumeix N, Dagaut P et al (2007) Experimental and modelling study of gasoline surrogate mixtures oxidation in jet stirred reactor and shock tube. *Proc Combust Inst* 31:385–391
- Yahaoui A, Djebaili-Chaumeix N, Dagaut P et al (2008) Ethyl tertiary butyl ether ignition and combustion using a shock tube and spherical bomb. *Energy Fuels* 22(6):3701–3708
- Yang B, Li Y, Wei L et al (2007a) An experimental study of the premixed benzene/oxygen/argon flame with tunable synchrotron photoionization. *Proc Combust Inst* 31:555–563
- Yang B, Osswald P, Li Y et al (2007) Identification of combustion intermediates in isomeric fuel-rich premixed butanol-oxygen flames at low pressure. *Combust Flame* 148(4):198–209
- Yang B, Westbrook CK, Cool TA et al (2011) Fuel-specific influences on the composition of reaction intermediates in premixed flames of three C₅H₁₀O₂ ester isomers. *Phys Chem Chem Phys* 13(15):6901–6913
- Yang B, Westbrook CK, Cool TA et al. (2011) The effect of carbon-carbon double bonds on the combustion chemistry of small fatty acid esters. *Z Phys Chemie-Int J Res Phys Chem Chem Phys* 225(11–12):1293–1314
- Yasunaga K, Kubo S, Hoshikawa H et al (2008) Shock-tube and modeling study of acetaldehyde pyrolysis and oxidation. *Int J Chem Kinet* 40(2):73–102
- Yeung C, Thomson MJ (2012) Experimental and kinetic modeling study of 1-hexanol combustion in an opposed-flow diffusion flame. *Proc Combust Inst* 34:795–802
- Yu W, Chen G, Huang Z et al (2012) Experimental and kinetic modeling study of methyl butanoate and methyl butanoate/methanol flames at different equivalence ratios and c/o ratios. *Combust Flame* 159(1):44–54
- Zervas E (2005) Formation of organic acids from propane, isooctane and toluene/isooctane flames. *Fuel* 84(6):0
- Zhang Z, Huang Z, Wang X et al (2008) Measurements of laminar burning velocities and Markstein lengths for methanol-air-nitrogen mixtures at elevated pressures and temperatures. *Combust Flame* 155(3):358–368
- Zhang N, Di YG, Huang ZH et al (2009) Experimental study on combustion characteristics of *n*(2)-diluted diethyl ether-air mixtures. *Energy Fuels* 23:5798–5805
- Zhang J, Wei L, Man X et al (2012a) Experimental and modeling study of *n*-butanol oxidation at high temperature. *Energy Fuels* 26(6):3368–3380
- Zhang K, Moshhammer K, Oßwald P et al (2012b) Experimental investigation of partially premixed, highly-diluted dimethyl ether flames at low temperatures. *Proc Combust Inst* 34:763–770
- Zhao Z, Kazakov A, Dryer FL (2004) Measurements of dimethyl ether/air mixture burning velocities by using particle image velocimetry. *Combust Flame* 139(1–2):52–60

Part III
Experimental Studies and Modeling of
PAH and Soot Formation

Chapter 11

Formation and Characterization of Polyaromatic Hydrocarbons

Nazly E. Sánchez, Alicia Callejas, Jesús Salafranca, Ángela Millera, Rafael Bilbao and María U. Alzueta

Abstract Issues concerning polycyclic aromatic hydrocarbons (PAH) carcinogenicity, and their important role in formation of dangerous pollutants, such as soot, have motivated their study under a wide range of laboratory conditions and for several kinds of thermochemical processes. Every experimental system, depending on the operating conditions, demands a specific protocol for PAH determination. This chapter aims to contribute to the knowledge of different procedures for PAH quantification both at the gas phase and when they are associated with soot particles. Different kinds of experimental set-ups for PAH formation together with the collection systems to capture them are explained here. Besides, some sample extraction techniques are reviewed, mainly focused on Soxhlet extraction because of its inexpensive equipment and overall simplicity to be applied by staff with limited analytical experience. Chromatographic techniques are also considered, paying special attention to gas chromatography coupled to mass spectrometry (GC–MS), popular in PAH analysis.

Abbreviations

PAH	Polycyclic aromatic hydrocarbons
GC–MS	Gas chromatography coupled to mass spectrometry
HACA	H-abstraction/C ₂ H ₂ addition route
EPA	Environmental Protection Agency
EPA–PAH	Polycyclic aromatic hydrocarbons classified by EPA as priority pollutants
PUF	Polyurethane foam
PTFE	Polytetrafluoroethylene
DCM	Dichloromethane
ASE	Accelerated solvent extraction

N. E. Sánchez · A. Callejas · J. Salafranca · Á. Millera · R. Bilbao · M. U. Alzueta (✉)
Aragón Institute of Engineering Research, University of Zaragoza,
Mariano Esquillor 50018 Zaragoza, Spain
e-mail: uxue@unizar.es

SFE	Supercritical fluid extraction
GPT	Thermochemical Processes Group
I3A	Aragón Institute of Engineering Research
HPLC–UV	Reversed-phase high performance liquid chromatograph with ultra-violet detection
FID	Flame ionization detection
SIM	Selected ion monitoring
SRM	Standard reference material

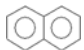
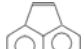

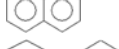
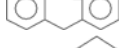
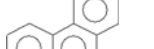







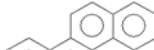
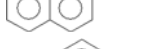

11.1 Introduction

Polycyclic aromatic hydrocarbons (PAH) are members of a class of air pollutants relevant to many scientific issues from a variety of aspects: chemical, toxicological, engineering, technological, public health, economic and regulatory (Finlayson-Pitts and Pitts 2000). They are a large number of compounds that consist of fused aromatic rings (Sander and Wise 1997). PAH are mainly formed in the combustion of fossil fuels and organic matter, and are ubiquitous in the atmosphere. Anthropogenic activities are the major sources of emission of PAH (WHO 2000; Lee 2001; Tang et al. 2005). It is well established that these aromatic compounds greatly contribute to the formation of primary soot particles, e.g. as explained by the H-abstraction/C₂H₂ addition (HACA) route (Frenklach 2002; Indarto et al. 2010), or they can appear adsorbed on the surface of soot. Thus, determination of PAH is, with no doubt, a necessary step for achieving a better understanding on the chemical details regarding the formation of nascent soot particles, which is still poorly understood (Faccineto et al. 2011).

Different studies have shown that PAH can cause harmful effects on the human health and the environment (ATSDR 1996; Schneider et al. 2002; De Kok et al. 2006). This risk is increased because PAH exist as more or less pure particles, associated with particulate matter and dust, the latter capable of penetrating into the lower respiratory tract (Luch 2005). The Environmental Protection Agency of the USA (EPA) has given priority to 16 PAH (EPA–PAH) (EPA 1998a) detailed in Table 11.1, which are commonly called as “priority aromatic hydrocarbon pollutants”, because of their widespread presence and the fact that some of them are considered as probable human carcinogens. Unquestionably, some PAH from this list are important intermediates in the soot formation process, and they have been studied in different modelling and experimental investigations (Appel et al. 2000; Li et al. 2009; Norinaga et al. 2009).

In this context, the characterization and quantification of PAH appearing in combustion processes is needed for determining the possible toxicological effect of the emission sources, or when a deeper understanding of soot formation is

Table 11.1 Structures, common names, used abbreviations, molecular formulas and molecular weights (MW) for the 16 EPA-PAH

Structure	Common name	Abbreviations for PAH	Molecular formula	MW (g mol ⁻¹)
	Naphthalene	NAP	C ₁₀ H ₈	128.18
	Acenaphthylene	ACY	C ₁₂ H ₈	152.20
	Acenaphthene	ACE	C ₁₂ H ₁₀	154.20
	Fluorene	FLO	C ₁₃ H ₁₀	166.23
	Phenanthrene	PHE	C ₁₄ H ₁₀	178.23
	Anthracene	ANT	C ₁₄ H ₁₀	178.23
	Fluoranthene	FLA	C ₁₆ H ₁₀	202.26
	Pyrene	PYR	C ₁₆ H ₁₀	202.25
	Benzo(a)anthracene	BaA	C ₁₈ H ₁₂	228.28
	Chrysene	CHR	C ₁₈ H ₁₂	228.28
	Benzo(b)fluoranthene	BbF	C ₂₀ H ₁₂	252.32
	Benzo(k)fluoranthene	BkF	C ₂₀ H ₁₂	252.32
	Benzo(a)pyrene	BaP	C ₂₀ H ₁₂	252.31
	Indeno(1,2,3-cd)pyrene	IcdP	C ₂₂ H ₁₂	276.34
	Dibenzo(a,h)anthracene	DahA	C ₂₂ H ₁₄	278.35
	Benzo(g,h,i)perylene	BghiP	C ₂₂ H ₁₂	276.34

required. This knowledge would allow the relevant authorities to develop strategies to reduce, if not eliminate, PAH emissions into our surrounding (Lee 2001).

Depending on the properties exhibited by PAH, mainly the vapour pressure, they exist in the gas phase or as solid particles. PAH at the outlet gas stream of combustion processes usually consist of compounds with few aromatic rings such as naphthalene (Finlayson-Pitts and Pitts 2000). The processes, where both PAH and particulate matter, such as soot, can be formed, require a specific method for collection and especially for PAH analysis, since their nature and the variety of organic matter need a particular technique capable to handle the complex mixture of products at the outlet (Lee 2001).

The aim of this chapter is to present a number of devices used to study the PAH formation in thermochemical processes. Different techniques for PAH determination/quantification are also considered, including PAH collection (taking into account the different places where PAH are found), sample treatment by solvent extraction techniques, and PAH analysis by chromatographic methodologies. An example on formation, collection and quantification of the 16 EPA-PAH in a specific tubular flow reactor in the pyrolysis of acetylene and ethylene will be also shown.

11.2 Characterization and Formation of Polycyclic Aromatic Hydrocarbons

Frequently for different processes, the concentration of PAH, such as the 16 EPA-PAH (Table 11.1), needs to be monitored in different places: the atmosphere (e.g. Mastral et al. 2003), soil (e.g. Ortiz et al. 2012), food (e.g. Viegas et al. 2012), water (e.g. Ardag et al. 2011) and exhaust gases (e.g. Ballesteros et al. 2010). In this latter case, PAH formation is evaluated for both pollution assessment and to achieve a better understanding of the effect of different variables on their formation and/or their role in soot formation. Several investigations on PAH and soot formation in flames have been carried out by using different devices: commercial burners, such as a McKenna burner (Apicella et al. 2003; Wu et al. 2006; Faccinetto et al. 2011), spray flames using spray burners (Allouis et al. 2003; Lemaire et al. 2010), or open diffusion flames by an stainless steel conical container and premixed flames by a flat-flame burner (Andrade-Eiroa et al. 2010a). Under pyrolysis conditions in shock tubes (Wang and Cadman 1998; Mathieu et al. 2007) (as it can be seen in Chaps. 6 and 24), tubular reactors (Mendiara et al. 2005; Norinaga et al. 2007; Ruiz et al. 2007a; Thomas and Wornat 2008; Sánchez et al. 2012a) and a well stirred reactor coupled to a plug flow reactor (Macadam et al. 1996; Manzello et al. 2007).

As an example, Fig. 11.1 shows the EPA-PAH formed from ethylene pyrolysis at 1,273 K at laboratory scale in a tubular reactor (Sánchez et al. 2012b). As it can be observed, under these specific conditions a higher concentration of lighter PAH (NAP and ACY, almost 60 % of the total) is formed. From Fig. 11.1, it is also

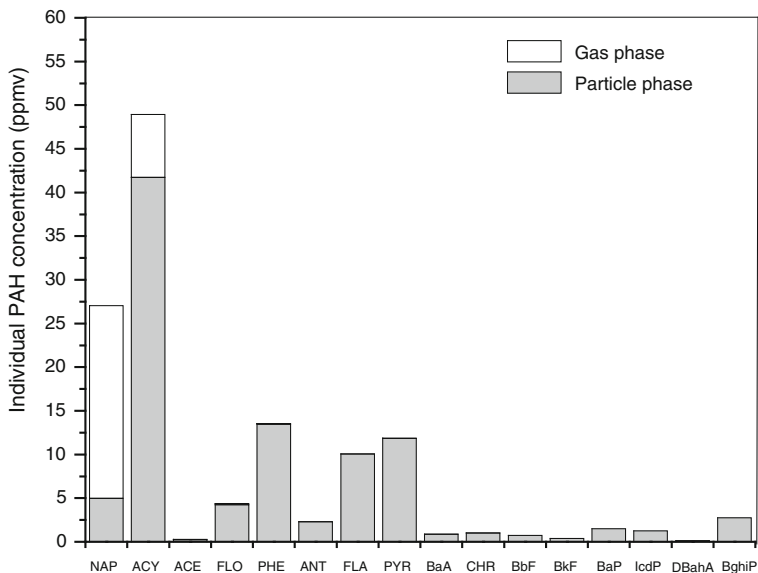


Fig. 11.1 PAH generated from ethylene pyrolysis at 1,273 K, with a fixed concentration of 30,000 ppmv in a tubular reactor (adapted with permission from Sánchez et al. 2012b. Copyright 2012 American Chemical Society)

deduced that the particle-gas phase PAH partitioning is an important issue to be considered in this kind of experiments, especially for lighter PAH preferably present at the gas phase, whereas the heavier ones are mainly found adsorbed on the particle.

11.3 PAH Collection

The collection technique should consider that PAH can appear on different surfaces (soot and reactor walls) as well as at the outlet gas stream. This distribution depends on their molecular weights, environment temperature, PAH concentration and soot characteristics (Christensen 2003; Sánchez et al. 2012a). It must also be taken into account that PAH cover a wide range of vapour pressures, e.g. approximately 10.6 Pa for naphthalene versus 2.0×10^{-10} Pa for coronene, at 298 K in both cases (Finlayson-Pitts and Pitts 2000). Figure 11.2 shows the PAH found in the particle phase and gas phase from biomass combustion in a cooking stove (Shen et al. 2011). In agreement with the data of Fig. 11.1, in both cases the lighter PAH remain preferentially at the gas phase, whereas the heavier ones show almost complete association with particles.

Several works (e.g. Shen et al. 2011; Kim et al. 2012) on PAH distribution in different conditions reveal the importance of considering their partitioning (particle-gas phase), especially when compounds involving only a few aromatic rings

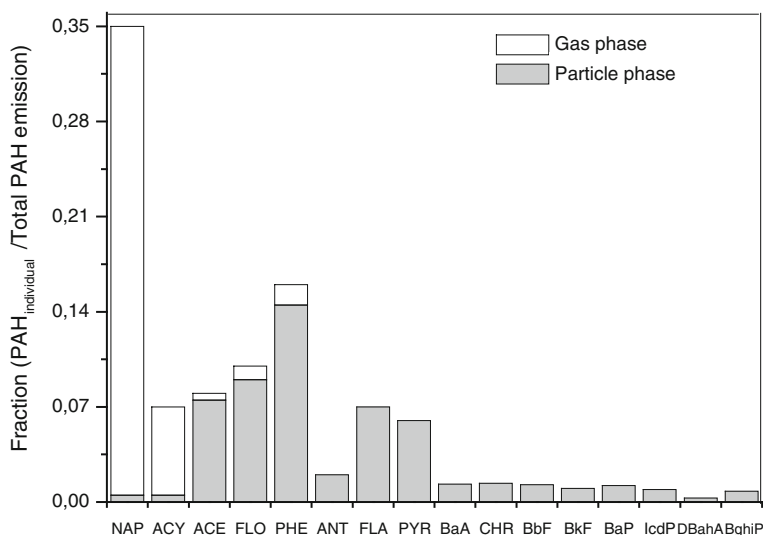


Fig. 11.2 Stacked bars show the PAH emission from crop residues burned in the cooking stove (combustion process) during a whole burning cycle (adapted with permission from Shen et al. 2011. Copyright 2012 American Chemical Society)

are evaluated, e.g. NAP and ACY. For airborne PAH both in gas and particle phases, large volumes of air must be sampled to achieve a high enough concentration factor. This is because their concentration in air at most locations is relatively low (of order ng m^{-3}) (Pandey et al. 2011), whereas in the laboratory, this depends on the specific operating conditions.

11.3.1 PAH in the Gas Phase

The method for PAH sampling can vary depending on their partitioning in the different phases. Beginning with the gas phase, NAP, ACY, methylnaphthalenes, and other abundant and highly volatile PAH are frequently trapped with sorbent materials. Polyurethane foam (PUF) and XAD resins are two of the adsorbents most commonly used for PAH sampling in gas phase (e.g. Lee et al. 2004). Different studies have proved that the XAD-2 resin exhibits a higher efficiency for PAH adsorption and retention than PUF. Additionally, the XAD-2 resin shows higher recovery of compounds with two and three aromatic rings, like NAP, which is abundant in the combustion processes outlet gases (Chuang et al. 1987). Other sorbent materials (e.g. XAD-4 and Tenax) have also been employed occasionally in air sampling or under controlled laboratory conditions (e.g. Liu et al. 2001; Font et al. 2003). Aromatic compounds can also be captured by other techniques, as those used by Wornat's group in their experiments (e.g. Somers et al. 2007).

Devices, like stainless steel probes or collectors equipped with a filter, for sampling combustion products along the flame axis are used in flame studies (e.g. Cijajolo et al. 2001; Bouvier et al. 2007; Andrade-Eiroa et al. 2010a). In conclusion, the collection of PAH depends on the kind of specific experimental set-up used.

11.3.2 PAH in the Particle Phase

Semivolatile compounds, like PAH associated to particles, can be collected on filters made of cellulose acetate, nylon or polytetrafluoroethylene (PTFE) (Mastral et al. 1996, 2003), quartz and glass fibre (Ballesteros et al. 2010; Sánchez et al. 2012a). Frequently, in thermochemical experiments, when the temperature of the outlet gas stream is high, glass or quartz fibre filters must be used. Therefore, it must be emphasized, the best filter to be chosen is that viable for the specific conditions used in the experiments (e.g. temperature, corrosion, high gas flow, size of solid particle generated).

11.3.3 Example of an Experimental Set-up for Formation and Collection of PAH

An experimental set-up used in the pyrolysis and oxidation of light hydrocarbons (e.g. C_2H_2 , C_2H_4 , CH_4), under well-controlled conditions, is shown in Fig. 11.3. It has been successfully used in several works (e.g. Ruiz et al. 2007a, b; Esarte et al. 2009; Sánchez et al. 2012a, b) and consists of different systems, namely: (1) gas feeding system, with mass flow meters and the gases to be fed; (2) reaction system, in which the reaction takes place in a quartz tube reactor of 45 mm internal diameter and 800 mm in length, since the reactor inlet and outlet are cooled by air flow; (3) soot and PAH collection system; (4) gas analysis system for volatile compounds. In the PAH-soot collection system of Fig. 11.3, the soot and their PAH associated are captured on a filter with fixed dimensions (30 mm external diameter, 100 mm length, and pore diameter lower than 1 mm). The PAH present at the gas phase are trapped when they pass through a tube packed with XAD-2 resin. The results showed in Fig. 11.1 were obtained by using this experimental system.

11.4 Sample Preparation and Extraction

Due to the high volatility of the lower molecular weight PAH, samples containing PAH must be preserved carefully (Li-bin et al. 2007). Filters with the particulate matter and their PAH adsorbed should be folded on the inner side, stored in glass bottles under refrigeration and analysed as quickly as possible.

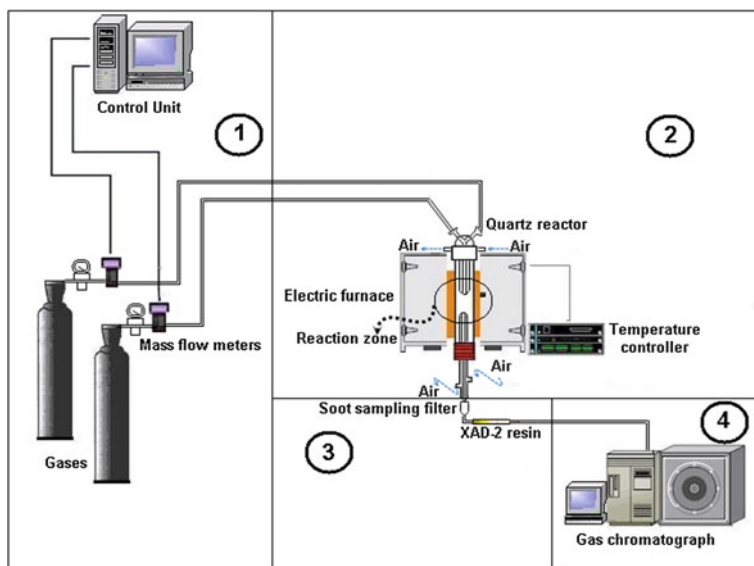


Fig. 11.3 Experimental set-up used for the light C₂ hydrocarbon pyrolysis and oxidation

The analysis of PAH commonly requires their trapping on a solid surface. This section will focus on the preparation of solid samples, which are to undergo elution with solvent. However, it is also worth mentioning that there are other solvent-free extraction techniques (not less important), such as the thermal extraction together with solid-phase micro-extraction (e.g. Ballesteros et al. 2009).

Sample preparation and extraction appear to be the most time-consuming stages in the analytical procedures (Luque de Castro and Luque de García 2002). The risk for analyte loss is also highest during this step. Hence, it is usually considered the bottleneck of PAH analytical methodologies. This represents one of the major problems associated with analysis of PAH in different samples. Other problems include: (1) most of PAH in environment samples are normally present in trace amounts (Lee 2001). On the contrary, some samples formed under laboratory controlled conditions contain high PAH amount, which can also become a serious problem due to saturation of the material used to collect them; (2) many organic compounds can be coextracted with PAH, which could interfere with their subsequent separation, identification and quantification; and (3) most of PAH are similar structurally and present isomeric forms, which makes difficult their separation and identification (Chen et al. 1996; Lee 2001). Hence, it is very important to choose an appropriate methodology for PAH determination, taking into account all these problems in any particular case.

Solvent-based extraction techniques for PAH determination are an active area of research and many novel techniques have been developed, some of them described below.

Ultrasonic extraction of PAH is a popular method because of both time and solvent-saving (Li-bin et al. 2007). Nevertheless, due to the limited contact time between the solvent and the sample, ultrasonic extraction may not be as rigorous as other extraction methods (EPA 2000), especially when the target sample contains a high PAH concentration. However, this technique has been used with success in several works (Kado et al. 2000; Mastral et al. 2001; Christensen et al. 2005).

PAH extraction is also possible by means of microwaves, which are high frequency (usually 2.45 GHz) electromagnetic waves that can be strongly absorbed by polar molecules, whereas weak interaction occurs with non-polar solvents. This results in accelerated extraction (through elevated temperatures) of polar compounds from various matrices into non- or weak polar solvents. The efficiency of extraction with microwaves lies in the ability of the bulk material to transform electromagnetic radiation into heat, without the disadvantage of convection and conduction, thus preventing loss of analyte (Lee 2001). The solvents commonly used for PAH extraction with microwaves are hexane, acetone and dichloromethane (DCM), among others (Lee 2001). Some results on microwaves applied for PAH determination are reported by Portet-Koltalo et al. (2008), who have used this technique for extracting a complex mixture containing PAH, nitrated PAH and heavy n-alkanes from a particularly refractory carbonaceous material resulting from combustion in a diesel engine.

Accelerated solvent extraction (ASE) is a kind of pressurized-fluid extraction method. Its advantage over classical techniques is to provide faster extraction (5–15 min), and a relatively low consumption of organic solvents (Lee 2001). However, ASE equipment is very expensive and this factor has limited its use.

Supercritical fluid extraction (SFE) is another technique commonly used in PAH characterization, mainly in environment samples with low PAH concentration (e.g. Becnel and Dooley 1998; Librando et al. 2004). SFE uses supercritical fluids (used as solvent) to seep through the pores of the sample, thus extracting the analytes. CO_2 , NH_3 , C_2H_4 , C_2H_6 , N_2O , C_3H_8 , C_3H_6 and H_2O are the most common substances used in SFE (Li-bin et al. 2007). The use of SFE avoids the necessity of a further extensive concentration and clean-up previous to analysis (Lee 2001). EPA 3561 is a method recommended for PAH extraction from different sources by using SFE (EPA 1996a). It suggests that the method performance demonstration should be based on the extraction of a certified sample and, alternatively, a comparison of SFE and Soxhlet extraction data using an environmentally contaminated PAH sample may be performed.

In this context, Soxhlet extraction is a reference extraction method for analysing the correct behaviour of emerging methods such as those above mentioned. Filtration of the extract from Soxhlet extraction is not required and several simultaneous extractions can be carried out by this inexpensive equipment (Luque de Castro and Priego-Capote 2010). Moreover, it is not necessary to employ highly qualified personnel for optimizing and carrying out extractions. In this way, the Soxhlet method is a good option for laboratories with limited experience on analytical chemistry or for researches not specifically devoted to the analytical

procedures, or non-analytical research in general. Hence, the next section will be focused mainly on this technique.

11.4.1 Soxhlet Extraction

Soxhlet extraction is a classical method because of its high extraction efficiency (Li-bin et al. 2007). Nowadays, it represents the main method of reference to compare the recovery obtained with other extraction techniques (e.g. Song et al. 2002; Gfrerer et al. 2004). Soxhlet extraction has some attractive advantages, since the sample is repeatedly soaked in fresh portions of solvent, facilitating the displacement of the transfer equilibrium.

Due to amount of PAH generated in combustion experiments, mainly when light hydrocarbons (e.g. soot precursors such as C_2H_2 , C_2H_4) are burned in fuel rich conditions, the Soxhlet extraction is a good option. Indeed, the high solvent volume used avoids the saturation of the extract, which may cause wrong results. The solvent from the Soxhlet extraction can be recovered by rota-evaporation and, after a distillation process, it could be used again.

The thermochemical processes group (GPT) of the Aragón Institute of Engineering Research (I3A) of the University of Zaragoza has developed and optimized an analytical method for PAH determination (Sánchez et al. 2013), which is shown as an example of an extraction procedure applied to samples obtained from pyrolysis processes. This method (GPT-I3A) includes the collection of PAH as explained in Sect. 11.3, followed by sample treatment using the Soxhlet extraction and subsequent extract analysis using gas chromatography coupled to mass spectrometry (GC-MS).

Prior to Soxhlet extraction, each sample is placed in a cellulose cartridge, whose packaging consists of quartz wool at the bottom, followed by 3 g of sodium sulphate anhydrous to absorb sample moisture. The target sample with 10 μ L of a solution of the five deuterated internal standards is added after the drying compound. Then, the cartridge is covered with quartz wool to prevent sample loss during extraction cycles. Finally, the cartridge, as a whole, is situated inside the thimble of the Soxhlet extractor.

Internal standards are used for correcting the possible losses of analytes during sample preparation, since the chromatographic signal of both the target compound and its internal standard have a similar response. Thus, if target compounds are lost during sample treatment, a proportional amount of their internal standard is lost as well. This ratio of signals, which is independent on the sampling history, is used to obtain the calibration curves and subsequently, the analyte concentration (Ferreira 2007).

Once the cartridge with the sample is placed within the thimble of the Soxhlet extractor, it is gradually filled with solvent from a distillation flask. The assembly extractor is operated as a batch system, since vapours of solvent move up to a condenser and flood over the thimble. When the liquid reaches the overflow level,

a siphon aspirates the solvent from the thimble-holder and unloads it back into the distillation flask (Luque de Castro and Priego-Capote 2010). This process is repeated until complete extraction is achieved. The extraction time for the optimized method is fixed at 24 h using a total amount of 200 mL of dichloromethane (DCM) and 4 extraction cycles per hour, in accordance with the EPA method 3540C (EPA 1996b). Other solvents can also be used, such as acetone, ethanol and hexane. Similar conditions have been used by other authors (Levendis et al. 2001; Moltó et al. 2005, 2011). Xue et al. (2007) showed that using Soxhlet extraction 24 h is suitable for PAH extraction from different coal samples, with DCM more effective than hexane.

Sometimes, PAH are present at low concentration, and thus further concentration of the extract is needed because of the large amount of solvent present. The most common solvent concentration process is done by rota-evaporation followed by a micro-concentration under gentle nitrogen stream. This is especially valid for relatively clean samples, since an additional careful concentration is required to achieve the detection limits. The aromatic compounds may be lost during the evaporation process of the solvent. For this reason, the sample concentration is another critical step during the sample treatment. In this way, compounds such as DCM offer an advantage due to their low boiling point, far below of those at which target compounds are evaporated, thus avoiding significant losses of analytes.

11.5 Identification and Quantification of PAH

The complex characterization of the PAH extract requires that analytical procedures must be able to detect relevant substances in a mixture of compounds with a wide range of volatilities, sizes and polarities. In case very little amount of material is available, PAH can be advantageously desorbed from material (soot) and then identified by using laser desorption/laser ionisation/mass spectrometry technique as detailed in Chap. 12. Additional studies using laser diagnostic techniques for determining the PAH-soot distribution and for their characterization are reported in Wartel et al. (2010) and Furuhashi et al. (2012).

Others use chromatographic methods such as reversed-phase high performance liquid chromatograph with ultraviolet detection (HPLC-UV) or GC-MS, combined with extraction processes (Poster et al. 2006; Borrás and Tortajada-Genaro 2007; Andrade-Eiroa et al. 2010a, b). Nevertheless, other techniques have been used (e.g. supercritical fluid chromatography and capillary electrophoresis) but are not generally acceptable (Lee 2001).

The capillary column technique in GC, used to separate PAH, has progressed since the sixties and has now become the standard method for the determination of these compounds. The main advantage of using GC for PAH analysis is that a slight modification of an existing GC protocol is usually enough to meet the requirements of a particular application. Further, by adjusting the carrier gas flow rate, temperature programming, and switching to a similar stationary phase,

different types of matrices can be effectively analysed using GC with detectors such as flame ionisation detection (FID). However, GC–MS coupling is nowadays preferred for the analysis of complex matrices. Mainly, the application of selected ion monitoring (SIM) represents an integrated tool for separation, identification, and quantification of PAH, because generally it affords greater selectivity, resolution and sensitivity than other techniques (Lee 1995; Poster et al. 2006).

Determinations of PAH from combustion in flow reactors by using GC–MS have been carried out over the past twenty years. Howard et al. (1995) studied the concentration ratios of the isomer pairs of some PAH in ethylene combustion with naphthalene injection using a plug flow reactor. The main objective of this work was to evaluate the mutagenic effect of the combustion products. Durlak et al. (1998) used GC–MS for determining PAH from polystyrene combustion in order to evaluate the feasibility of incineration for this material. Another point of view was considered by Wornat's group (Ledesma et al. 2002) who analysed PAH by means of GC–MS to obtain kinetic parameters on PAH formation relevant to the combustion of solid fuels. Other works (Thomas et al. 2007; Thomas and Wornat 2008, 2009) using GC–MS have been developed throughout this decade with different purposes, such as those developed by connecting a laminar flow muffle furnace to a laminar flow reactor for the combustion of different polymers, and using GC–MS to determine PAH (Wang et al. 2002, 2003).

HPLC has also been applied for several years ago in PAH separation. This technique is the method of choice for analysing moderate to high molecular weight PAH (Furton and Pentzke 1998; Ledesma et al. 2002). It also offers advantages, such as selectivity and use of sensitive detectors, as well as the possibility to be used as a PAH fractionation to other chromatography techniques, even though, it also provides high efficiency and short analysis time (Ferreira 2007).

The analytical method optimised by the GPT-I3A of the University of Zaragoza allows the determination and quantification of PAH by means of GC–MS, and it is presented here as an example of technique for determination of PAH in thermo-chemical processes. Chromatographic conditions used are shown in Table 11.2. The different parameters were chosen following the EPA recommendations (EPA 1998b, 1999). All analyses are performed in the SIM mode of the MS in order to enhance the selectivity and sensitivity of the method. Table 11.3 shows the SIM profile programmed in the MS for PAH quantification; values in bold refer to the ion used for quantification and the MS window time in which each ion is monitored. The GC-MS system consisted of a 7890A gas chromatograph with a 7683B autosampler coupled to a MSD 5975C mass selective detector from Agilent Technologies. The capillary column was a DB-17 ms 60 m × 0.25 mm ID × 0.25 µm film thickness also supplied by Agilent.

It is important to highlight that prior to the application of any method, an appropriated calibration of every compound together with validation of the method must be carried out in order to ensure the quality of results. It is common to use standard reference materials (SRM) with similar matrices to those which will be analysed to ensure that the method provides good agreement with the values of certified materials. The GPT-I3A method was validated using SRM 1650b, a fully

Table 11.2 GC-MS operating conditions

Parameter	Value
Carrier gas	Helium at 1 mL min ⁻¹
Injection mode	Splitless
Injection volume	1 μL
Injector temperature	300 °C
Temperature program	
Initial temperature	80 °C
Initial hold time	15 min
Ramp rate 1	5 °C min ⁻¹
Final temperature 1	110 °C
Hold time 1	5 min
Ramp rate 2	5 °C min ⁻¹
Final temperature 2	290 °C
Hold time 2	35 min
Ramp rate 3	1.5 °C min ⁻¹
Final temperature 3	320 °C
Final hold time 3	5 min
Transfer line temperature	280 °C

Table 11.3 Monitoring ion profile (SIM)

Compounds	Monitored ions	MS window time (min)
Naphthalene	128 –129	31.00–36.00
Naphthalene-d ₈	136 –108	
Acenaphthylene	152 –153	43.00–47.00
Acenaphthene	154 –153	
Acenaphthene-d ₁₀	164 –162	
Fluorene	166 –165	47.01–56.00
Phenanthrene	178 –179	
Anthracene	178 –179	
Phenanthrene-d ₁₀	188 –189	
Fluoranthene	202 –203	58.00–63.00
Pyrene	202 –203	
Benzo(a)anthracene	228 –226	67.00–72.00
Chrysene	228 –226	
Chrysene-d ₁₂	240 –236	
Benzo(b)fluoranthene	252 –253	81.00–84.00
Benzo(k)fluoranthene	252 –253	
Benzo(a)pyrene	252 –253	88.00–93.00
Perylene-d ₁₂	264 –260	
Indeno(1,2,3-cd)pyrene	276 –277	110.00–114.00
Dibenz(a,h)anthracene	278 –279	
Benzo(g,h,i)perylene	276 –277	116.00–120.00

characterized soot from a diesel engine (NIST 2006), and a commercial soot used as diesel soot surrogate called Printex-U. The recoveries of the EPA-PAH for SRM 1650b were higher than 80 % in most of the cases and the PAH analysis using the Printex-U showed good method repeatability with a standard deviation for individual PAH as low as 0.5 ppmv (Sánchez et al. 2013). This fact proves its effectiveness to be applied in samples containing PAH formed in pyrolysis processes.

Figure 11.4 shows some results of individual PAH concentration obtained by using the analytical method developed by the GPT-I3A. These outcomes were obtained from ethylene and acetylene pyrolysis operating under different reaction temperatures ranging between 1,073 and 1,323 K. Extended details can be found elsewhere (Sánchez et al. 2010, 2012a, b).

11.6 Summary

The aim of this chapter is to provide practical information about different procedures to be used in the determination and quantification of PAH, mainly coming from thermochemical processes.

The methodology for quantifying the PAH usually consists of: (a) an efficient sample collection, (b) the sample treatment, and (c) the quantification of target compounds. During step (a), the different surfaces where the PAH can be adsorbed should be taken into consideration. PAH associated with particulate matter or/and at the gas phase are typically found in thermochemical processes. Frequently, this latter fraction is collected by sorbent materials (e.g. XAD resins and/or polyurethane foam, PUF). At the gas phase in flames, PAH can be collected by using apparatus like stainless steel probes or collectors, equipped with a filter for sampling combustion products along the flame axis. Thus, in general, the suitable collection depends on the facility where PAH are formed. PAH adsorbed on soot are often collected on filters. In the second stage, (b), the collection of samples is normally followed by an extraction process. Finally, in the (c) stage, the obtained extract is usually characterized by chromatographic techniques. Other approaches for PAH characterization, not requiring the extraction step, include laser diagnostic techniques which are commonly used in flames.

Despite of the fact that solvent-free techniques such as solid-phase microextraction (SPME) can be successfully used for PAH analysis, those based on solvents are normally preferred for extraction of samples from thermochemical processes. Some examples of solvent-based techniques include: ultrasonic extraction, extraction by microwaves, supercritical fluid extraction (SFE), accelerated solvent extraction (ASE) and Soxhlet extraction.

The high performance liquid chromatography with ultraviolet detection (HPLC-UV) and the gas chromatography-mass spectrometry (GC-MS) are the techniques mainly used for the identification and quantification of PAH.

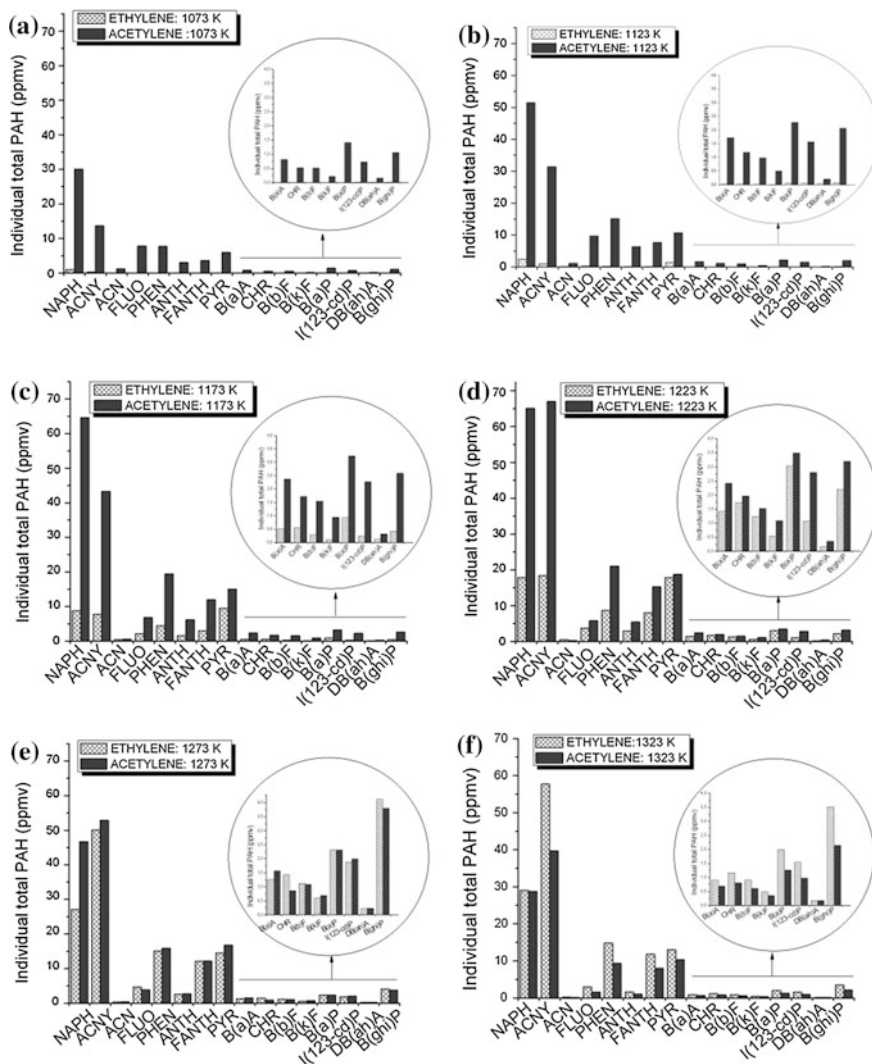


Fig. 11.4 Experimental results of PAH concentration obtained by GPT-I3A method, in the pyrolysis of acetylene and ethylene at different reaction temperatures: **a** 1073 K, **b** 1123 K, **c** 1173 K, **d** 1223 K, **e** 1273 K and **f** 1323 K (reprinted with permission from Sánchez et al. 2012b. Copyright 2012 American Chemical Society)

Nowadays, successful combinations of these techniques have been used for attaining the best results during the PAH speciation from thermochemical processes. Our experience suggests that the mentioned method (GPT-I3A), including the collection of PAH by using XAD-2 resin and quartz filters, followed by Soxhlet extraction of the samples and PAH quantification by means of GC-MS,

would be a good procedure for application to thermochemical processes. The main reasons include its proved effectiveness, as well as the fact that it does not require expensive equipment and its simplicity to be applied by limited analytical experience staff.

Acknowledgments This work has been performed at the Aragón Institute of Engineering Research (I3A) of the University of Zaragoza in the frame of the Thermochemical Processes Group (GPT). The authors express their gratitude to the MICINN, FEDER (Project CTQ2009-12205), Aragón Government and European Social Fund (ESF), for financial support. Ms N.E. Sánchez acknowledges the Banco Santander Central Hispano, University of Zaragoza and the Colombian Institute for the Development of Science and Technology (COLCIENCIAS) for the predoctoral grant awarded.

References

- ATSDR, Agency for Toxic Substances and Disease Registry (1996) Polycyclic aromatic hydrocarbons (PAHs), Atlanta. http://www.atsdr.cdc.gov/es/toxfaqs/es_tfacts69.html
- Allouis C, Apicella B, Barbella R et al (2003) Monitoring of fuel consumption and aromatics formation in a kerosene spray flame as characterized by fluorescence spectroscopy. *Chemosphere* 51:1097–1102
- Andrade-Eiroa A, Leroy V, Dagaut P et al (2010a) Determination of polycyclic aromatic hydrocarbons in kerosene and bio-kerosene soot. *Chemosphere* 78:1342–1349
- Andrade-Eiroa A, Diévert P, Dagaut P (2010b) Improved optimization of polycyclic aromatic hydrocarbons (PAH) mixtures resolution in reversed-phase-high-performance liquid chromatography by using factorial design and response methodology. *Talanta* 81:265–274
- Apicella B, Ciajolo A, Barbella R et al (2003) Size exclusion chromatography of particulate produced in fuel-rich combustion of different fuels. *Energy Fuels* 217:565–570
- Appel J, Bockhorn H, Frenklach M (2000) Kinetic modeling of soot formation with detailed chemistry and physics: laminar premixed flames of C2 hydrocarbons. *Combust Flame* 121:122–136
- Ardag H, Ozel MZ, Sen A (2011) Polycyclic aromatic hydrocarbons in water from the Menderes river. *Turkey Bull Environ Contam Toxicol* 86:221–225
- Ballesteros R, Hernández JJ, Lyons LL (2009) Determination of PAHs in diesel gas matter using thermal extraction and solid phase micro-extraction. *Atmos Environ* 43:655–662
- Ballesteros R, Hernández JJ, Lyons LL (2010) An experimental study of the influence of biofuel origin on particle-associated. *Atmos Environ* 44:930–938
- Becnel JM, Dooley KM (1998) Supercritical fluid extraction of polycyclic aromatic hydrocarbon mixtures from contaminated soils. *Ind Eng Chem Res* 37:584–594
- Borrás E, Tortajada-Genaro LA (2007) Characterization of polycyclic aromatic hydrocarbons in atmospheric aerosols by gas chromatography-mass spectrometry. *Anal Chim Acta* 583:266–276
- Bouvier Y, Mihesan C, Ziskind M et al (2007) Molecular species adsorbed on soot particles issued from low sooting methane and acetylene laminar flames: A laser-based experiment. *Proc Combust Inst* 31:841–849
- Chen BH, Wang CY, Chiu CP (1996) Evaluation of analysis of polycyclic aromatic hydrocarbons in meat products by liquid chromatography. *J Agric Food Chem* 44:2244–2251
- Christensen A (2003) Polycyclic aromatic hydrocarbon in exhaust emission from mobile sources-sampling and determination. Ph.D. thesis, University of Stockholm, Stockholm
- Christensen A, Ostman C, Westerholm R (2005) Ultrasound-assisted extraction and on-line LC–GC–MS for determination of polycyclic aromatic hydrocarbons (PAH) in urban dust and diesel particulate matter. *Anal Bioanal Chem* 381:1206–1216

- Chuang JC, Hannan SW, Wilson NK (1987) Field comparison of polyurethane foam and XAD-2 resin for air sampling for polynuclear aromatic hydrocarbons. *Environ Sci Technol* 21:798–804
- Ciajolo A, Ragucci R, Apicella B et al (2001) Fluorescence spectroscopy of aromatic species produced in rich premixed ethylene flames. *Chemosphere* 42:835–841
- De Kok TCM, Driee HAL, Hogervorst JGF, Briedé JJ (2006) Toxicological assessment of ambient and traffic-related particulate matter: A review of recent studies. *Mutat Res* 613:103–112
- Durlak SK, Biswas P, Shi J et al (1998) Characterization of polycyclic aromatic hydrocarbon particulate and gaseous emissions from polystyrene combustion. *Environ Sci Technol* 32:2301–2307
- EPA, Environmental Protection Agency (1996a) EPA-Method 3561: supercritical fluid extraction of polynuclear aromatic hydrocarbons, Ohio. <http://www.caslab.com/EPA-Methods/PDF/EPA-Method-3561.pdf>
- EPA, Environmental Protection Agency (1996b) EPA-Method 3540C: Soxhlet extraction, Ohio. <http://www.epa.gov/osw/hazard/testmethods/sw846/pdfs/3540c.pdf>
- EPA, Environmental Protection Agency (1998a) Locating and estimating air emissions from sources of polycyclic organic matter, Ohio. <http://www.epa.gov/ttn/chief>
- EPA, Environmental Protection Agency (1998b) EPA-Method 8270D: determination of semivolatiles organic compounds by gas chromatography/mass spectrometry (CG/MS), Ohio. <http://www.epa.gov/osw/hazard/testmethods/sw846/pdfs/8270d.pdf>
- EPA, Environmental Protection Agency (1999) EPA-Method TO-13A: Compendium of methods for the determination of toxic organic compounds in ambient air, Ohio. <http://www.epa.gov/ttnamti1/files/ambient/airtox/to-13arr.pdf>
- EPA, Environmental Protection Agency (2000) EPA-Method 3550C: ultrasonic extraction, Ohio. <http://www.caslab.com/EPA-Methods/PDF/EPA-Method-3550C.pdf>
- Esarte C, Millera A, Bilbao R et al (2009) Gas and soot products formed in the pyrolysis of acetylene–ethanol blends under flow reactor conditions. *Fuel Process Technol* 90:496–503
- Faccinetto A, Desgroux P, Ziskind M et al (2011) High-sensitivity detection of polycyclic aromatic hydrocarbons adsorbed onto soot particles using laser desorption/laser ionization/time-of-flight mass spectrometry: an approach to studying the soot inception process in low-pressure flames. *Combust Flame* 158:227–239
- Ferreira V (2007) *Cromatografía: fundamentos y práctica*, 2nd edn. Publication Service of the University of Zaragoza, Zaragoza
- Finlayson-Pitts BJ, Pitts JN (2000) *Chemistry of the upper and lower atmosphere*. Academic Press, California
- Font R, Esperanza M, García AN (2003) Toxic by-products from the combustion of kraft lignin. *Chemosphere* 52:1047–1058
- Frenklach M (2002) Reaction mechanism of soot formation in flames. *Phys Chem Chem Phys* 4:2028–2037
- Furton KG, Pentzke G (1998) Polycyclic aromatic hydrocarbons. In: Shibamoto T (ed) *Chromatographic analysis of environmental and food toxicants*, 1st edn. Marcel Dekker, New York
- Furuhata T, Kobayashi Y, Hayashida K et al (2012) Behavior of PAHs and PM in a diffusion flame of paraffin fuels. *Fuel* 91:16–25
- Gfrerer M, Gawlik BM, Lankmayr E (2004) Validation of a fluidized-bed extraction method for solid materials for the determination of PAHs and PCBs using certified reference materials. *Anal Chim Acta* 527:53–60
- Howard JB, Longwell JP, Marr JA et al (1995) Effects of PAH isomerizations on mutagenicity of combustion products. *Combust Flame* 101:262–270
- Indarto A, Giordana A, Ghigo G et al (2010) Polycyclic aromatic hydrocarbon formation mechanism in the particle phase. *Phys Chem Chem Phys* 12:9429–9440

- Kado NY, Okamoto RA, Karim J et al (2000) Airborne particle emissions from 2-and 4-stroke outboard marine engines: polycyclic aromatic hydrocarbon and bioassay analyses. *Environ Sci Technol* 34:2714–2720
- Kim JY, Lee JY, Choi S-D et al (2012) Gaseous and particulate polycyclic aromatic hydrocarbons at the Gosan background site in East Asia. *Atmos Environ* 49:311–319
- Ledesma EB, Marsh ND, Sandrowitz AK et al (2002) Global kinetic rate parameters for the formation of polycyclic aromatic hydrocarbons from the pyrolysis of catechol, a model compound representative of solid fuel moieties. *Energy Fuels* 16:1331–1336
- Lee HK (1995) Recent applications of gas and high-performance liquid chromatographic techniques to the analysis of polycyclic aromatic hydrocarbons in airborne particulates. *J Chromatogr A* 710:79–92
- Lee HK (2001) Modern techniques for the analysis of polycyclic aromatic hydrocarbons. In: Kleiböhmer W (ed) *Handbook of analytical separations*, 1st edn. Elsevier, Amsterdam
- Lee JJ, Huang K-L, Yu YY et al (2004) Laboratory retention of vapor-phase PAHs using XAD adsorbents. *Atmos Environ* 38:6185–6193
- Lemaire R, Therssen E, Desgroux P (2010) Effect of ethanol addition in gasoline and gasoline–surrogate on soot formation in turbulent spray flames. *Fuel* 89:3952–3959
- Levendis YA, Atal A, Carlson JB et al (2001) PAH and soot emissions from burning components of medical waste: examination/surgical gloves and cotton pads. *Chemosphere* 42:775–783
- Li Y, Tian Z, Zhang L et al (2009) An experimental study of the rich premixed ethylbenzene flame at low pressure. *Proc Combust Inst* 32:647–655
- Li-bin L, Yan L, Jin-ming L et al (2007) Development of analytical methods for polycyclic aromatic hydrocarbons (PAHs) in airborne particulates: a review. *J Environ Sci* 19:1–11
- Librando V, Hutzinger O, Tringali G et al (2004) Supercritical fluid extraction of polycyclic aromatic hydrocarbons from marine sediments and soil samples. *Chemosphere* 54:1189–1197
- Liu K, Han W, Pan W-P et al (2001) Polycyclic aromatic hydrocarbon (PAH) emissions from a coal-fired pilot FBC system. *J Hazard Mater* B84:175–188
- Luch A (2005) Polycyclic aromatic hydrocarbon-induced carcinogenesis—an introduction. In: Luch A (ed) *The carcinogenic effects of polycyclic aromatic hydrocarbons*, 1st edn. Imperial College Press, London
- Luque de Castro MD, Luque de García JL (2002) *Acceleration and automation of solid sample treatment*. Elsevier Science, Amsterdam
- Luque de Castro MD, Priego-Capote F (2010) Soxhlet extraction: past and present panacea. *J Chromatogr A* 1217:2383–2389
- Macadam S, Beér JM, Safofim AF (1996) Soot surface growth by polycyclic aromatic hydrocarbon and acetylene addition. *Proc Combust Inst* 26:2295–2302
- Manzello SL, Lenhart DB, Yozgatligil A et al (2007) Soot particle size distributions in a well-stirred reactor/plug flow reactor. *Proc Combust Inst* 31:675–683
- Mastral AM, Callén M, Murillo R (1996) Assessment of PAH emissions as a function of coal combustion variables. *Fuel* 75:1533–1536
- Mastral AM, Callén MS, García T et al (2001) Benzo(a)pyrene, benzo(a)anthracene, and dibenzo(a, h)anthracene emissions from coal and waste tire energy generation at atmospheric fluidized bed combustion (AFBC). *Environ Sci Technol* 35:2645–2649
- Mastral AM, López JM, Callén MS et al (2003) Spatial and temporal PAH concentrations in Zaragoza. *Spain Sci Total Environ* 307:111–124
- Mathieu O, Franche G, Djebaili-Chaumeix N et al (2007) Characterization of adsorbed species on soot formed behind reflected shock waves. *Proc Combust Inst* 31:511–519
- Mendiara T, Domene MP, Millera A et al (2005) An experimental study of the soot formed in the pyrolysis of acetylene. *J Anal Appl Pyrolysis* 74:486–493
- Moltó J, Conesa JA, Font R et al (2005) Organic compounds produced during the thermal decomposition of cotton fabrics. *Environ Sci Technol* 39:5141–5147
- Moltó J, Egea S, Conesa JA et al (2011) Thermal decomposition of electronic wastes: mobile phone case and other parts. *Waste Manage* 31:2546–2552

- NIST, National Institute of Standards and Technology (2006) Certified of analysis for standard reference material 1650b, diesel particulate matter, Gaithersburg. https://www-s.nist.gov/srmors/certificates/view_certGIF.cfm?certificate=1650B
- Norinaga K, Janardhanan VM, Deuschamann O (2007) Detailed chemical kinetic modeling of pyrolysis of ethylene, acetylene, and propylene at 1073–1373 K with a plug-flow reactor model. *Int J Chem Kinet* 40:199–208
- Norinaga K, Deuschmann O, Saegusa N et al (2009) Analysis of pyrolysis products from light hydrocarbons and kinetic modeling for growth of polycyclic aromatic hydrocarbons with detailed chemistry. *J Anal Appl Pyrolysis* 86:148–160
- Ortiz R, Vega S, Gutiérrez R et al (2012) Presence of polycyclic aromatic hydrocarbons (PAHs) in top soils from rural terrains in Mexico City. *Bull Environ Contam Toxicol* 88:428–432
- Pandey SK, Kim K-H, Brown RJC (2011) A review of techniques for the determination of polycyclic aromatic hydrocarbons in air. *Trends Anal Chem* 30:1716–1739
- Portet-Koltalo F, Oukebdane K, Dionnet F et al (2008) Optimisation of the extraction of polycyclic aromatic hydrocarbons and their nitrated derivatives from diesel particulate matter using microwave-assisted extraction. *Anal Bioanal Chem* 390:389–398
- Poster DL, Schantz MM, Sander LC et al (2006) Analysis of polycyclic aromatic hydrocarbons (PAHs) in environmental samples: a critical review of gas chromatographic (GC) methods. *Anal Bioanal Chem* 386:859–881
- Ruiz MP, Guzmán R, Millera A et al (2007a) Influence of different operation conditions on soot formation from C_2H_2 pyrolysis. *Ind Eng Chem Res* 46:7550–7560
- Ruiz MP, Callejas A, Millera A et al (2007b) Soot formation from C_2H_2 and C_2H_4 pyrolysis at different temperatures. *J Anal Appl Pyrolysis* 79:244–251
- Sánchez NE, Callejas A, Millera A et al (2010) Determination of polycyclic aromatic hydrocarbons (PAH) adsorbed on soot formed in pyrolysis of acetylene at different temperatures. *Chem Eng Trans* 22:131–136
- Sánchez NE, Callejas A, Millera A et al (2012a) Formation of PAH and soot during acetylene pyrolysis at different gas residence times and reaction temperatures. *Energy* 43:30–36
- Sánchez NE, Callejas A, Millera A et al (2012b) Polycyclic aromatic hydrocarbons (PAH) and soot formation in the pyrolysis of acetylene and ethylene: Effect of the Reaction Temperature. *Energy Fuels* 26:4823–4829
- Sánchez NE, Salafranca J, Callejas A et al (2013) Quantification of polycyclic aromatic hydrocarbons (PAH) found in gas and particle phases from pyrolytic processes using gas chromatography-mass spectrometry (GC-MS). *Fuel* 107:246–253
- Sander LC, Wise SA (1997) Polycyclic aromatic hydrocarbon structure index. NIST special publication 922. <http://www.nist.gov/mml/analytical/organic/upload/SP-922-Polycyclic-Aromatic-Hydrocarbon-Structure-Index-2.pdf>
- Schneider K, Roller M, Kalberlah F et al (2002) Cancer risk assessment for oral exposure to PAH mixtures. *J Appl Toxicol* 22:73–83
- Shen G, Wang W, Yang Y et al (2011) Emissions of PAHs from indoor crop residue burning in a typical rural stove: emission factors, size distributions, and gas-particle partitioning. *Environ Sci Technol* 45:1206–1212
- Somers ML, McClaine JW, Wornat MJ (2007) The formation of polycyclic aromatic hydrocarbons from the supercritical pyrolysis of 1-methylnaphthalene. *Proc Combust Inst* 31:501–509
- Song YF, Jing X, Fleischmann S et al (2002) Comparative study of extraction methods for determination of PAHs from contaminated soils and sediments. *Chemosphere* 48:993–1001
- Tang L, Tang X-Y, Zhu Y-G, Zheng M-H, Miao Q-L (2005) Contamination of polycyclic aromatic hydrocarbons (PAHs) in urban soils in Beijing, China. *Environ Int* 31:822–828
- Thomas S, Wornat MJ (2008) Effect of acetylene addition on yields of C1–C10 hydrocarbon products of catechol pyrolysis. *Energy Fuels* 22:976–986
- Thomas S, Wornat MJ (2009) Polycyclic aromatic hydrocarbons from the co-pyrolysis of catechol and 1,3-butadiene. *Proc Combust Inst* 32:615–622

- Thomas S, Ledesma EB, Wornat MJ (2007) The effects of oxygen on the yields of the thermal decomposition products of catechol under pyrolysis and fuel-rich oxidation conditions. *Fuel* 86:2581–2595
- Viegas O, Novo P, Pinho O et al (2012) A comparison of the extraction procedures and quantification methods for the chromatographic determination of polycyclic aromatic hydrocarbons in charcoal grilled meat and fish. *Talanta* 88:677–683
- Wang J, Richter H, Howard JB et al (2002) Polynuclear aromatic hydrocarbon and particulate emissions from two-stage combustion of polystyrene: The effects of the secondary furnace (afterburner) temperature and soot filtration. *Environ Sci Technol* 36:797–808
- Wang R, Cadman P (1998) Soot and PAH production from spray combustion of different hydrocarbons behind reflected shock waves. *Combust Flame* 112:359–370
- Wang Z, Wang J, Richter H et al (2003) Comparative study on polycyclic aromatic hydrocarbons, light hydrocarbons, carbon monoxide, and particulate emissions from the combustion of polyethylene, polystyrene, and poly(vinyl chloride). *Energy Fuels* 17:999–1013
- Wartel M, Pauwels J-F, Desgroux P et al (2010) Quantitative measurement of naphthalene in low-pressure flames by jet-cooled laser-induced fluorescence. *Appl Phys B* 100:933–943
- WHO, World Health organization, regional office for Europe (2000) Polycyclic aromatic hydrocarbons (PAHs). In: Air quality guidelines, 2nd edn. (CD-ROM version), Denmark. http://www.euro.who.int/__data/assets/pdf_file/0015/123063/AQG2ndEd_5_9PAH.pdf
- Wu J, Song KH, Litzinger T et al (2006) Reduction of PAH and soot in premixed ethylene–air flames by addition of ethanol. *Combust Flame* 144:675–687
- Xue J, Liu G, Niu Z et al (2007) Factors that influence the extraction of polycyclic aromatic hydrocarbons from coal. *Energy Fuels* 21:881–890

Chapter 12

Laser Diagnostics for Selective and Quantitative Measurement of PAHs and Soot

Xavier Mercier, Alessandro Faccinetto and Pascale Desgroux

Abstract Optical diagnostics are complementary techniques to conventional analytical methods of polycyclic aromatic hydrocarbons (PAH) and soot. They allow the selective and quantitative measurements of PAH concentrations and the determination of the soot volume fraction (f_v) in combustion processes. Due to their complex spectroscopy, selective detection of PAH requires a priori molecular cooling obtained by molecular beam generation strategies. The associated techniques are single or multiphoton ionisation coupled with time-of-flight mass spectrometry (PI/TOF-MS) and jet-cooled laser induced fluorescence (jet-cooled LIF). PI/TOF-MS also allows identifying PAH species adsorbed on soot surface. Laser induced incandescence (LII) and absorption-based techniques are currently used to measure f_v . This chapter details the main principles of these relevant spectroscopic techniques: jet-cooled LIF single and multiphoton ionisation coupled with time-of-flight mass spectrometry, laser induced incandescence and soot desorption methods.

12.1 Introduction

Optical diagnostics allow the detection of species from their spectroscopic properties. These properties are a “fingerprint” of the electronic structure of atoms and molecules, and can be exploited to give information on the composition and physical–chemical properties of environments like flames. Information is carried by the radiation naturally produced in a flame, like spontaneous emission, or otherwise induced by an external light source such as a lamp or a laser, as is the

X. Mercier · A. Faccinetto · P. Desgroux (✉)
Physicochimie des Processus de Combustion et de l’Atmosphère (PC2A), UMR Université/
CNRS 8522, Université Lille 1 — Sciences et Technologies, 59655 Villeneuve
d’Ascq Cedex, France
e-mail: pascale.desgroux@univ-lille1.fr

case in induced incandescence. In addition, other processes like absorption of light can give useful complementary information.

The potential of optical diagnostics has long been demonstrated, and it leads for example to the *in situ* and instantaneous determination of concentration fields of several chemical species in flames (Kohse-Höinghaus et al. 2005). However, large molecules such as polycyclic aromatic hydrocarbons (PAH) are characterised by unstructured and broadband spectra making *in situ* PAH identification impossible in practice (Desgroux et al. 2013). In order to counteract this difficulty, strategies have been developed that rely on preventive molecular cooling of the PAHs sampled in the flame via molecular beam generation or free jet expansion. The associated techniques for PAHs detection are photoionisation/time-of-flight mass spectrometry (PI/TOF-MS) and jet-cooled laser induced fluorescence (jet-cooled LIF).

Soot particles in flames can be detected from their thermal radiation that is well approximated by the Planck law. Particularly, controlled laser heating of the particles is achievable by radiation absorption. The subsequent thermal radiation measurement is the basis of the laser-induced incandescence (LII) technique and leads to the measurement of the soot volume fraction f_V . 2D imaging LII technique allows *in situ* measurements of f_V fields in flames. Calibration of LII measurements is often performed using absorption-based techniques applied to soot particles. The potential of these last techniques is also very important for studying steady combustion processes. Finally, the species adsorbed on soot surface the analysis of which allows to better understand the chemical soot growth process can be also detected after laser desorption coupled to PI/TOF-MS.

This chapter describes the state-of-the-art spectroscopic techniques above mentioned and currently used to measure selectively and quantitatively gaseous PAH sampled in flames or laser-desorbed PAH from soot particles. Then the principles of *in situ* optical diagnostics for soot monitoring are presented.

12.2 PAHs in the Gas Phase

12.2.1 Spectroscopy and Photophysics of PAHs

The photophysics of PAHs at room temperature has been discussed in detail in several books and reviews (Berlman 1971; Birks 1970). The different photophysical processes taking place after absorption of light (by laser excitation for instance) are usually described by the Jablonski diagram which is shown in Fig. 12.1. At room temperature, molecules occupy the lowest rovibrational levels of the ground electronic state S_0 according to a statistical repartition dependent on the temperature known as the Boltzmann law. The probability of occupation of a rovibronic level i characterised by an energy E_i , degeneracy g_i (the number of levels having the same energy) at temperature T is defined by the Boltzmann fraction:

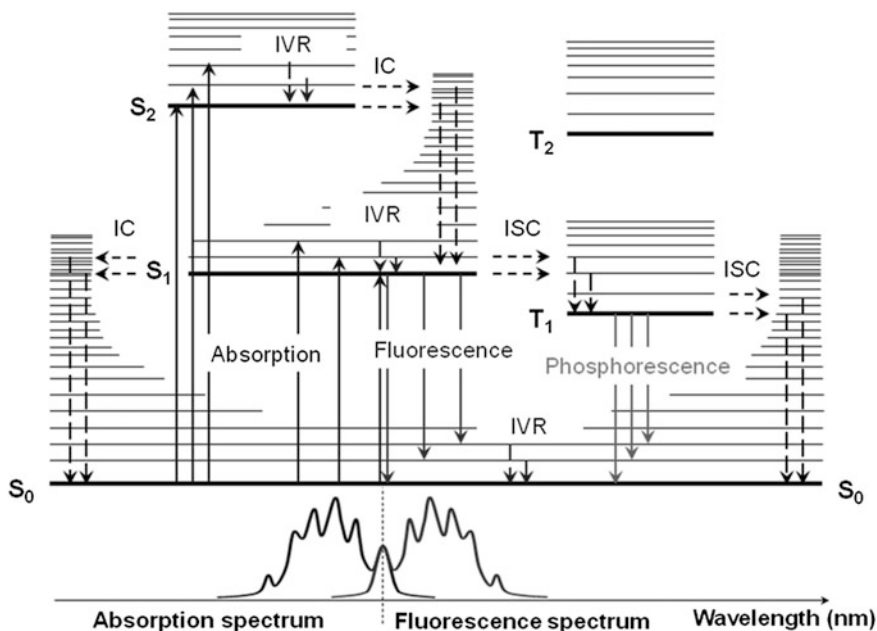


Fig. 12.1 Jablonski Diagram (room temperature approximation)

$$f_B = g_i \exp(-E_i/(k_B T)) / \sum_i g_i \exp(-E_i/(k_B T))$$

where k_B is the Boltzmann constant. Upon absorption of photons, molecules can be excited into one of the singlet excited states S_1 , S_2 or higher. Excitation can result from any transition reaching one of the vibrational sub-levels of one of the excited electronic states. As the energy of the vibrational levels is quantised, this should normally lead to a discrete spectrum of distinct absorption lines.

However, the number of rotational levels (which is represented in Fig. 12.1) associated to each vibrational level makes the number of possible transitions so large that it is impossible to get resolved spectra of PAHs at room temperature conditions. This is why excitation spectra of PAHs are generally characterised by unresolved and broadband structures. The only possibility to experimentally access a resolved structure (discussed later in Sect. 12.3) is to drastically cool the species in order to severely limit the number of populated rovibrational levels in the lowest electronic state and therefore the number of possible transitions from S_0 to any higher rovibronic levels.

The photophysics of PAHs is governed by the competition between radiative like fluorescence and phosphorescence, non-radiative processes like inter vibrational redistribution (IVR), internal conversion (IC) and intersystem crossing (ISC), which take place after the excitation of the molecules initially in the ground state.

Considering first a $S_1 \leftarrow S_0$ excitation, the molecules quickly lose their excess of energy by collisions with the neighbouring species by IVR (10^{-15} to 10^{-12} s) and fall to the lowest vibrational level of the S_1 state before to fluoresce. For higher transition as $S_n \leftarrow S_0$ ($n \geq 2$), molecules first relax by IVR down to the lowest vibrational level of S_n . From there, they pass to a high vibrational level of S_1 by IC (10^{-12} to 10^{-10} s). Then molecules lose energy by IVR until the lowest vibrational level of S_1 . From this level, they can relax to any of the vibrational levels of S_0 by IVR or by emitting photons which corresponds to the fluorescence emission spectrum, the intensity of which being proportional to the overlap integral of the vibrational wavefunctions of the original and final states as a consequence of the Franck—Condon factors (Herzberg 1991). Finally, relaxation from S_1 may also occur by ISC (10^{-11} to 10^{-8} s) from S_1 to T_1 (triplet state), potentially leading to phosphorescence emission (10^{-6} to 1 s).

Hence, the fluorescence emission is far from being the only possibility of relaxation of a species after absorption of a photon. The intensity of the fluorescence emission is governed by the fluorescence quantum yield which corresponds to the ratio between the fluorescence decay rate and the sum of all the radiative and non-radiative decay rates, which varies from 0 to 1 according to the species and the experimental conditions (T , p). It is to be noted that the shape of the fluorescence emission spectrum for a given PAH is always the same and does not depend on the excitation wavelength, since the emission of the fluorescence always takes place from the lowest vibrational level of S_1 .

PAHs are characterised by high absorption coefficients and quantum yield. Therefore, they are well suited for spectroscopic detection. At room temperature, the processes described above explain the specific intensity patterns of emission and absorption spectra which are said to possess mirror symmetry, with a spectral overlap corresponding to the vibronic transition $S_0(v'' = 0) \leftrightarrow S_1(v' = 0)$ in the absorption and emission spectra. The fluorescence emission spectrum is therefore always shifted at room temperature to higher wavelengths compared to the excitation one whereas it is not necessarily the case at high temperature where anti-Stokes (or blue-shifted) emission can be observed upon visible excitation as discussed in different papers (Bengtsson and Aldén 1995; Coe et al. 1981).

Another specificity of the PAH photophysics is that large PAHs have broader and red shifted absorption bands (Berlman 1971; Birks 1970) in comparison with smaller PAHs. Although PAH excitation spectra show broad band structure, a limited selectivity is provided by this last property which has been widely used to detect classes of PAHs (by number of aromatic rings) in flame experiments (Lee et al. 2004; Vander Wal et al. 1997; Wu et al. 2006; Xiao et al. 2005). However, the lack of spectroscopic data at high temperature (absorption cross-sections, quenching contribution, Boltzmann fraction, PAHs composition in flames...) makes quantitative *in situ* experiments almost impossible. Therefore, the only way to make selective measurements of PAHs is to reduce the rovibrational temperature of the species after probing from the flame in order to simplify their spectra as described in the following section.

12.3 PAHs Cooling Using a Supersonic Expansion

Two different setups, both using a supersonic expansion, can be implemented to reduce the temperature of PAHs before their analysis. The first one is generally used in combination with mass spectrometry analysis (molecular beam mass spectrometry MBMS) and consists of probing the flame with a cone-shaped probe to generate a free jet expansion. A skimmer, positioned a few millimetres after the cone, allows the generation of a molecular beam in which the ionisation of the species can be done as represented in Fig. 12.2a. The second option, which is used for the jet cooled LIF methods, relies on the sampling of species by a microprobe connected to the analysis chamber via a heated and low pressure line after which the free jet expansion is generated. LIF experiments in this case are directly done inside the free jet (Fig. 12.2b). The main difference between the probing methods concerns the range of the detectable species. Microprobe extraction only allows the detection of stable species whereas setups based on molecular beam generation (cone and skimmer) extends the detection to radicals. Indeed, when generating the free jet expansion directly from the flame, the chemical reactions inside the molecular beam are almost stopped as a consequence of the sudden reduction in temperature and a dramatic increase in the mean free pathway (about 1 m at 10^{-6} mbar) almost preventing any collision. Another important difference is the rotational temperature characterising the species cooled down with the two setups, which is only around 300–400 K in the molecular beam (Kamphus et al. 2002) whereas temperature as low as 90 K can be obtained in the supersonic expansion following microprobe sampling (Mercier et al. 2008; Wartel et al. 2010). As discussed below, this difference is essentially due to the higher initial temperature of the species before the expansion (around 1,500/1,800 K, i.e. the temperature of the flame, for the molecular beam method in comparison with a few hundreds of Kelvin for the free jet expansion setup) as illustrated in Fig. 12.2.

A free jet expansion is a rapid expansion of a gas through an orifice separating two chambers characterised by a pressure ratio at least equal to or greater than two. This sudden expansion has the effect of extracting the molecules from the initial gas mixture (first chamber defined by a pressure p_0 and a temperature T_0) and of accelerating them above the speed of sound (*supersonic* expansion). The physical properties of the gas expansion in a supersonic jet depend on many factors including the characteristics of the initial gas mixture (nature of molecules, molecular density, pressure, temperature, ...) as well as the experimental conditions in which the expansion is performed (orifice diameter and shape). A schematic drawing of the structure of a supersonic expansion is reported in Fig. 12.3a.

The cooling efficiency essentially depends on the pressure ratio between the two chambers and on the number of collisions at the entrance of the orifice that reduces the velocity distribution in a direction orthogonal to the expansion. At the outlet of the orifice, the gas expansion causes a gradual acceleration of the molecules at speeds greater than the speed of sound as well as it lowers the temperature (because of the conversion of thermal energy into directed kinetic energy by

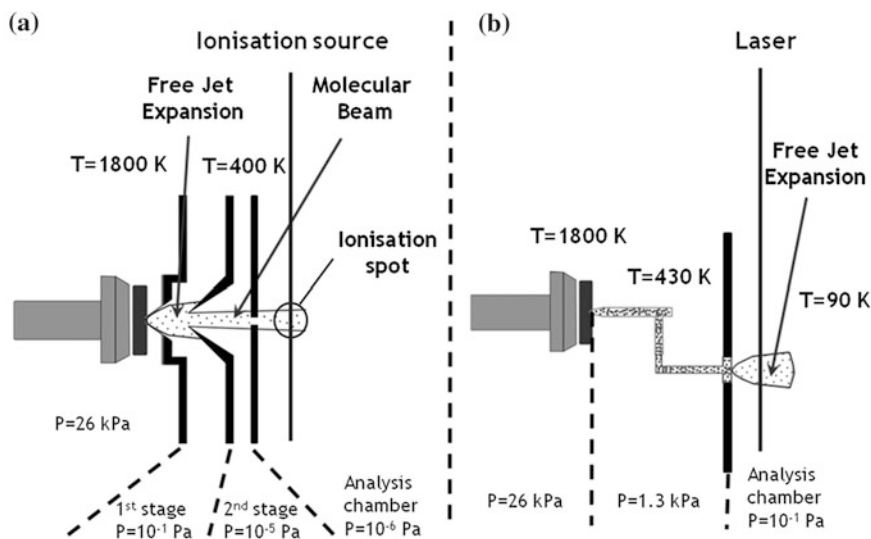


Fig. 12.2 a Molecular beam setup provided by a cone sampling. b Free jet expansion setup using a microprobe

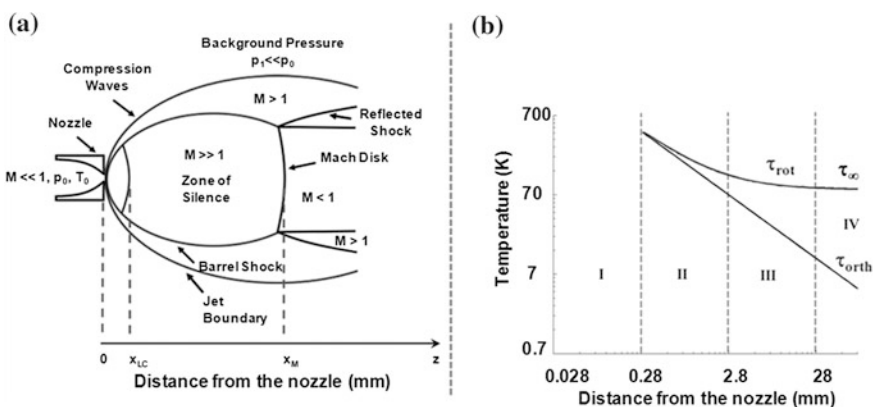


Fig. 12.3 a Free jet expansion. b Evolution of the orthogonal and rotational temperature in a free jet expansion of N_2 generated after a 1 mm nozzle aperture ($P_0 = 1.33 \text{ kPa}/T_0 = 430 \text{ K}$)

collisions) and the molecular density of the gas. The *zone of silence* corresponds to an area without any collisions between the molecules of the jet, which are accelerated unidirectionally and parallel to the jet axis. Finally, the molecules of the jet collide with the residual molecules in the chamber, which leads to a sharp deceleration of the molecules of the jet, resulting in a rapid increase of pressure and temperature. It is therefore a shock wave that terminates the zone of silence. The end of the zone of silence is characterised by the so-called Mach disk. The

position of the Mach disk along the jet axis, x_M , can be evaluated from the initial and final conditions of pressure (p_0 and p_1) and the diameter of the orifice d_0 (in case of a circular aperture) by the relation: $x_M = (2/3) d_0 (p_0/p_1)^{1/2}$ (Ashkenas and Sherman 1966).

The jet dynamic has been demonstrated to follow a gradual transition from the hydrodynamic regime to the molecular regime (Beijerinck and Verster 1981; Mazely and Smith 1988). Based on the work of these authors, the jet may be broken into the four distinct zones reported in Fig. 12.3b. The first one (zone I) is the isentropic region where the properties of the jet are characterised by the following hydrodynamic equations defined by (Ashkenas and Sherman 1966; Levy 1980; Shapiro 1953):

$$T = T_0 \frac{2}{(\gamma - 1)A^2} \left(\frac{d_0}{x - x_0} \right)^{2(\gamma-1)} \quad (12.1)$$

$$p = p_0 \left(\frac{2}{(\gamma - 1)A^2} \right)^{\frac{\gamma}{\gamma-1}} \left(\frac{d_0}{x - x_0} \right)^{2\gamma} \quad (12.2)$$

$$\rho = \rho_0 \left(\frac{2}{(\gamma - 1)A^2} \right)^{\frac{1}{\gamma-1}} \left(\frac{d_0}{x - x_0} \right)^2 \quad (12.3)$$

where $\gamma = C_p/C_v$ is the heat capacity ratio ($\gamma = 7/5$ for a diatomic gas) and A is a constant that depends on γ ($A = 3.65$ for a diatomic gas).

After a certain distance from the nozzle, the properties of the jet begin to deviate from these equations because of the rapid decrease of the molecular density inside the free jet expansion and the fact that the number of collisions becomes too small to ensure the thermalisation of the jet. Therefore, the gas can no longer be regarded as a continuous stream in this zone (zone II) which was defined by Mazely and Smith (1988) as the perturbed isentropic region. Zone III characterises a region in which a few collisions still occur but a severe drift to the isentropic behaviour is observed. This region is called the perturbed molecular region. Finally, at a distance x_{LC} from the nozzle (last collision distance), the properties of the jet do not evolve anymore and the rotational temperature of the species reaches its minimum value. The properties of the jet are said to be frozen and this zone, defined as the molecular zone (zone IV), characterises the zone of silence of the jet.

In order to illustrate this theory, we show in Fig. 12.3b the calculated evolution of the orthogonal (T_{orth}) and rotational (T_{rot}) temperatures during the generation of a supersonic jet of a flow of gas mixture assimilated to its major compounds N_2 , initially at 430 K and 1.33 kPa, and expanded through an orifice diameter of 1 mm.

In these conditions, we have calculated that the lowest reachable rotational temperature is about 85 K at a distance of 28 mm. This temperature is consistent with the one measured for benzene and naphthalene species probed from low pressure methane flames ($CH_4/O_2/N_2$) (Mercier et al. 2008; Wartel et al. 2010). It

is to be noted that the supersonic jet is not a system in thermodynamic equilibrium, which means that the study of this type of expansion requires the distinction between orthogonal, vibrational and rotational temperatures. The interested reader can refer to the work of Klots (1981) for more details.

12.4 Laser Induced Fluorescence

12.4.1 Principle of LIF

As discussed in the first section, the laser induced fluorescence (LIF) process can be described according to the Jablonski diagram by considering the competition between radiative and non-radiative processes which takes place after photon absorption by the molecules $N + h\nu \rightarrow N^*$. The variation of the population of the rovibronic excited level can be described by the first order differential equation:

$$dN^*/dt = Nk_{\text{abs}}U_v - (k_r + k_{\text{nr}} + k_{\text{coll}})N^* \quad (12.4)$$

where N and N^* are respectively the density number of the ground and excited rovibronic level ($\text{molec}\cdot\text{m}^{-3}$), k_{abs} is the absorption Einstein coefficient ($\text{m}^3\cdot\text{J}^{-1}\cdot\text{s}^{-2}$), U_v is the laser spectral density ($\text{J}\cdot\text{m}^{-3}\cdot\text{s}$), k_r is the relaxation rate by radiative processes (s^{-1}), k_{nr} is the relaxation rate by non-radiative processes (s^{-1}) and k_{coll} is the relaxation rate by collision (s^{-1}).

Note that $k_{\text{coll}} = \sum_i^n \tilde{k}_{\text{coll},i}N_{\text{coll},i}$ where $\tilde{k}_{\text{coll},i}$ corresponds to the collisional rate ($\text{m}^3\cdot\text{molec}^{-1}\cdot\text{s}^{-1}$) of each species i and $N_{\text{coll},i}$ are their concentrations.

The rate of the radiative processes consists of the sum of the fluorescence and the phosphorescence rates (s^{-1}), $k_r = k_{\text{LIF}} + k_{\text{Phos}}$ whereas the rate of the non-radiative processes (s^{-1}) includes all the non-radiative contributions, $k_{\text{nr}} = k_{\text{VR}} + k_{\text{IC}} + k_{\text{ISC}} + k_I + k_P$, where k_{VR} is the vibrational relaxation rate, k_{IC} is the IC rate, k_{ISC} is the ISC rate, k_I is the ionisation rate and k_P is the predissociation rate. In order to simplify the expressions, k_I and k_P will be considered equal to zero in the following.

After a short pulse excitation, in the hypothesis that a stationary state is rapidly reached (i.e. $dN^*/dt = 0$) and considering that $N + N^* = N_0$, Eq. 12.4 can be solved and $N^*(t)$ defined in the case of the linear excitation regime by the following expression:

$$N^*(t) = N_0 \frac{k_{\text{abs}}}{k_r + k_{\text{nr}} + k_{\text{coll}}} U_v \exp\left(-\frac{t}{\tau_{\text{eff}}}\right) \quad (12.5)$$

where $\tau_{\text{eff}} = \frac{1}{k_r + k_{\text{nr}} + k_{\text{coll}}}$ corresponds to the effective fluorescence lifetime (s).

The measured fluorescence signal corresponds to the flux of emitted photons from the probe volume V (cm^{-3}) and collected with a collection angle $\Omega/4\pi$ and an optical collection efficiency η , and can be defined by:

$$\varphi_{\text{LIF}}(t) = k_{\text{LIF}} N^*(t) \eta \frac{\Omega}{4\pi} V \quad (12.6)$$

which yields:

$$\varphi_{\text{LIF}}(t) = k_{\text{LIF}} N_0 \frac{k_{\text{abs}}}{k_r + k_{\text{nr}} + k_{\text{coll}}} U_v \eta \frac{\Omega}{4\pi} V \exp\left(-\frac{t}{\tau_{\text{eff}}}\right), \quad (12.7)$$

Equation 12.7 can be rewritten by considering $U_v = \frac{E}{A c \tau_L} g(\nu) = \frac{I_0}{c} g(\nu)$ where E is the laser energy per pulse (J), c is the speed of light ($\text{m}\cdot\text{s}^{-1}$), τ_L is the laser-pulse temporal length (s), A is the laser beam cross sectional area (m^2), $g(\nu)$ is a function characterising the spectral overlap between the laser and absorbant lines (Hz^{-1}). I_0 is defined as the laser spectral irradiance on line centre ($\text{W}\cdot\text{m}^{-2}$). This leads to:

$$\varphi_{\text{LIF}}(t) = \frac{I_0}{h\nu} \phi(p, T) \sigma(\nu, T) N_{\text{Total}} \eta \frac{\Omega}{4\pi} V \exp\left(-\frac{t}{\tau_{\text{eff}}}\right) \quad (12.8)$$

where $\phi(p, T) = k_{\text{LIF}}/k_{\text{Tot}}$ corresponds to the fluorescence quantum yield and $\sigma(\nu, T) = (h\nu/c) k_{\text{abs}} f_B(T) g(\nu)$ is the absorption cross section of the species where h is the Planck constant, c the speed of light and ν the excitation frequency (Hz).

Therefore, the measurement of fluorescence signal $\varphi_{\text{LIF}}(t)$ can lead to the determination of the total population N_{Total} of the probed species from the flame.

12.4.2 PAHs Measurement by Jet-Cooled LIF

This recent method is based on the extraction of species from laminar flames via an axially oriented microprobe which is a thin quartz tube (6 mm diameter) ended by a 20° conical aperture with a diameter of 300 μm . A schematic representation of the setup is shown in Fig. 12.4.

After extraction from the flame, the species are sent directly into a high vacuum chamber (0.1 Pa) where they are cooled down to about a constant temperature of 90 K within a free jet expansion. Under jet conditions, the PAH spectra become structured (only the very first energetic levels of the lowest vibrational states of S_0 remain sufficiently populated to lead to electronic transitions), allowing the selective detection of PAHs by LIF. However, as described in Sect. 12.3, the density of molecules along the central axis of the jet decreases extremely rapidly with the distance from the nozzle. Therefore, an experimental compromise has to be found between selectivity (low temperature to simplify the structure of the excitation spectra) and sensitivity (enough molecules to be excited inside the jet to get a measurable signal), meaning an excitation of the species somewhere in the zone III (Fig. 12.3). The simplification of the spectrum can be clearly seen in Fig. 12.5 where an excitation spectrum of naphthalene measured in an expanded

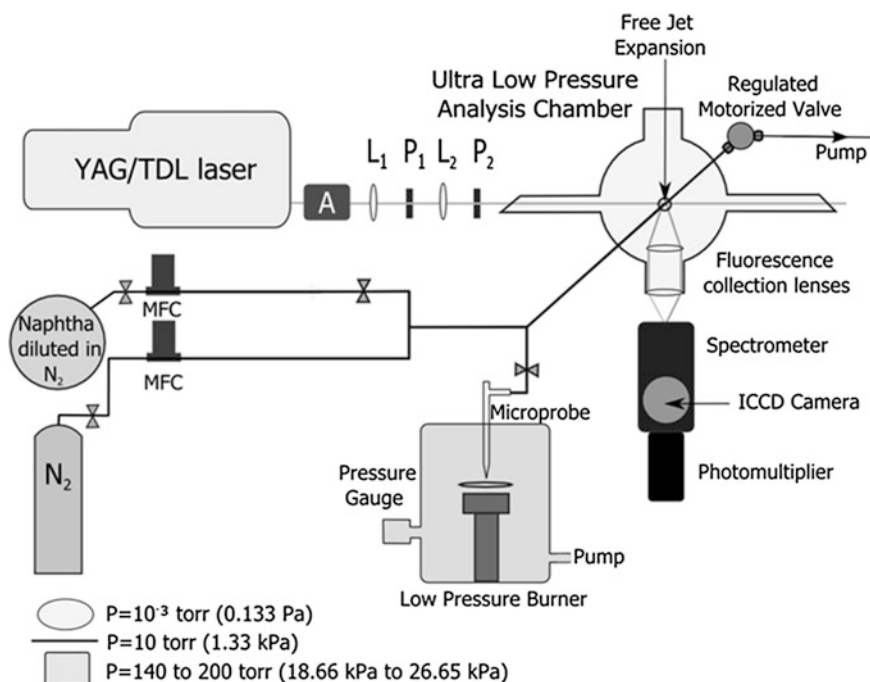


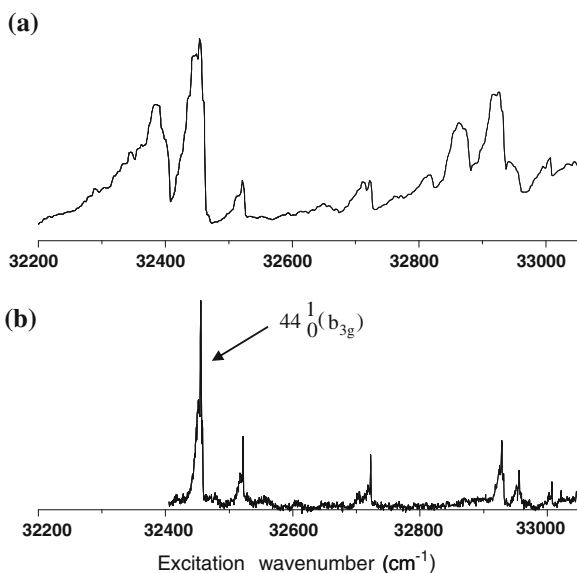
Fig. 12.4 Experimental jet cooled LIF setup for naphthalene concentration measurements in a low pressure flame

free jet has been reported in comparison with another one recorded under very low pressure conditions. Therefore, to carry out the measurement of the concentration profile of naphthalene in a flame, the method consists to tune the laser wavelength on the resonance of the intense spectral feature around 32455 cm^{-1} (30812 nm) and to follow the intensity of this line according to the height above the burner.

Due to the jet conditions (no collision), LIF signals can be considered as independent from quenching variations. As temperature is also constant at the position of the laser axis in the jet, the intensities of the LIF signals are therefore directly proportional to the concentration of the species (see Eq. 12.8). This way, a relative concentration profile of the naphthalene concentration above the burner is obtained. As it can be seen in Fig. 12.4, the analysis chamber can be independently connected either to the low pressure burner (via the microprobe) or to a reservoir filled with a known concentration of naphthalene. This last line is coupled with a nitrogen line which enables the generation of a flow of naphthalene diluted in nitrogen at different concentrations. The calibration of the relative concentration profile into absolute concentration can be done either by the standard addition method (addition of known amounts of the species to be calibrated in the sampling

Fig. 12.5 Excitation spectra of naphthalene. **a** Room temperature naphthalene vapour at 6.66×10^{-3} Pa (Behlen et al. 1981).

b Naphthalene extracted from the flame cooled down in the supersonic jet (Wartel et al. 2010, Copyright Springer)



line during the probing of the species from the flame—see Wartel et al. (2011) for more details) or by building a calibration curve of the LIF signal versus the concentration of the species. This relatively simple experimental setup provides real time and quantitative measurements of PAHs in flames. Moreover, it allows measurements of PAHs in sooting flames with the same accuracy as in non-sooting ones. So far, mole fraction profiles of benzene, naphthalene and pyrene have been recorded with this setup in different sooting and non-sooting flames of methane at various pressures and equivalence ratio (Mercier et al. 2008; Wartel et al. 2010, 2011). A sensitivity of a few parts per billion has been determined in sooting flames for the pyrene measurements with an uncertainty estimated at around $\pm 10\%$.

12.5 Detection by Photoionisation

Single and multiphoton ionisation (SPI or MPI) coupled to mass spectrometry is a convenient method of detection that offers high sensitivity and low detection limit if compared to the traditional electron ionisation. This technique can provide stable and radical PAH concentration profiles in flames (Kamphus et al. 2008; Li et al. 2009) and offers the possibility of identifying the large variety of PAH adsorbed on soot surfaces (Faccinetto et al. 2011; Öktem et al. 2005).

12.5.1 Resonance Enhanced Multiphoton Ionisation (REMPI)

Multiphoton absorption of light is a nonlinear phenomenon consisting of the simultaneous absorption of more than one photon by an atomic or molecular system. When the energy of the final state exceeds the ionisation energy, one electron is permanently removed and the overall process is referred to as MPI. Multiphoton absorption is a valuable spectroscopic and analytical tool since the selection rules are different than for single photon absorption, and therefore levels not connected to the molecular ground state by single photon transitions become readily accessible.

A simplified scheme of two photon ionisation of PAH in the nanosecond regime is shown in Fig. 12.6. ω is the frequency of the optical field, while S_0 , S_m , S_n are the real states of the molecular system: ground S_0 , one of the intermediates S_m , and final S_n . The energy difference between S_0 and S_n (transition frequency ω_{n0}) is not perfectly well defined, but rather spread into a continuous distribution by various line-broadening mechanisms. Therefore, the final state S_n is often described by a density of final states function $\rho_f(\omega_{n0})$.

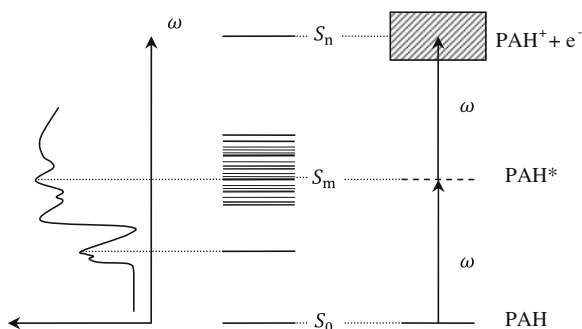
The number density of molecules initially in S_0 and reaching per unit time S_n by absorbing two photons is $\frac{\sigma_{n0}^{(2)}(\omega)I^2}{\hbar\omega}N_0(t)$, where $N_0(t)$ is the population in the ground state, I is the irradiance of the excitation laser beam and \hbar is the reduced Planck constant.

The two photon absorption cross section $\sigma_{n0}^{(2)}$ ($\text{m}^4 \cdot \text{W}^{-1}$) can be calculated by higher order perturbation theory (Boyd 2003):

$$\sigma_{n0}^{(2)} \propto \left| \sum_m \frac{\mu_{nm}\mu_{m0}}{\hbar(\omega_{m0} - \omega)} \right|^2 \rho_f(\omega_{n0} = 2\omega) \quad (12.9)$$

$\sigma_{n0}^{(2)}$ depends on molecular properties like the electric dipole transition moments μ_{nm} and the transition frequencies ω_{m0} . The sum in Eq. 12.9 spans all the intermediate states m accessible by the one photon transition. When ω is spectrally far

Fig. 12.6 PI of PAH in the nanosecond regime using UV-Vis excitation wavelength. Absorption spectrum (left), level structure (middle) and one-colour, two-photon REMPI scheme (right) are reported (Zimmermann et al. 2001, Copyright American Chemical Society)



from ω_{m0} , the first photon transition only involves virtual states (*highly non-resonant*) and $\sigma_{n0}^{(2)}$ can ultimately be treated as a constant. However, when ω is spectrally close to ω_{m0} then the denominator $\hbar(\omega_{m0} - \omega)$ becomes small and a single term dominates the sum (*resonant enhancement*). If the overall process leads to ionisation, it is referred to as resonance enhanced multiphoton ionisation (REMPI). Since in REMPI the absorption of the first photon is a real spectroscopic transition and does not only involve virtual states, selective excitation may take place from the intermediate level, leading to the overall highest ionisation efficiency.

Since an intermediate *real* state S_m is involved in the transition, the absorption of the two photons is not necessarily simultaneous, and therefore the properties of S_m play an important role on the efficiency of the REMPI transition. Particularly, large Franck–Condon factors, i.e. a sufficient overlap between the wavefunctions of the intermediate state and the ground and arrival state are required in order to obtain a high transition rate. Furthermore, the lifetime of the intermediate state has to be long enough to allow the absorption of the second photon, and the intermediate state must not relax too quickly, leading for instance to ISC or dissociation. If all these conditions are fulfilled, the overall REMPI efficiency is the largest (Boesl 2000).

As detailed elsewhere (Mercier et al. 2008), at room temperature several rovibrational levels of the lowest electronic state are occupied. The consequent broadening of the absorption bands makes REMPI possible for most low-mass PAH when exciting in the near UV. The most favourable case of one-colour, two-photon REMPI is illustrated on the right side of Fig. 12.6.

12.5.2 Time of Flight Mass Spectrometry (TOF-MS)

REMPI is a powerful analytical tool when coupled with other experimental techniques which allow fast ion detection, like TOF-MS.

In TOF-MS the mass separation is achieved by creating ions all with the same initial potential energy, and allowing them to travel in a field-free region. The ion velocity is then a function of the mass-to-charge ratio m/z , i.e. after a sufficiently long flight time species with different m/z can be detected sequentially in time. A TOF-MS is a device ruled by fundamentally simple physical principles. In the limit of non-relativistic energy, all the TOF-MS equations are well described by the Newtonian mechanics describing the potential–kinetic energy conversion and the force experienced by a charge in a static electric field (Guilhaus 1995; Guilhaus et al. 1997; Mamyryn 2001): $zeV = mv^2$ and $zeE = ma$ where z and m are the ion charge number and mass, e is the elementary charge, V and E are the electric potential and field, and v and a the velocity acquired and the acceleration experienced by the ion. Ions packets are generated in a dedicated region of the mass spectrometer (*ion source*), then accelerated towards a field-free region at the

end of which an ion mirror reflects and refocuses them on a microchannel plate detector where they are finally detected. The mass separation is achieved by the different flight times required to ions having different m/z to cover the distance between the ion source and the detector. Once all the experimental parameters are set, this time only depends on m/z by a simple quadratic relation $t^2 \propto m/z$, where t is called the *time-of-flight*.

TOF-MS offers two essential benefits over other mass spectrometry. First, it provides a virtually unlimited mass range. One advantage of TOF-MS is that it is inherently not limited in the higher mass range. It only requires longer travel times to extend the mass range. This feature represents the key to get knowledge about the chemistry of heavy species like high-mass PAH. Secondly, TOF-MS allows the simultaneous detection of multiple species, since the ion detection is sequential in time.

The coupling of REMPI and TOF-MS takes place in the ion source of the mass spectrometer, where the sample is introduced either in gas/aerosol form (i.e. molecular beam-based techniques), or alternatively its transition to the gas phase is obtained *in situ* (laser desorption). In most experimental setups the ionisation laser beam is directly focused between the mass spectrometer acceleration plates.

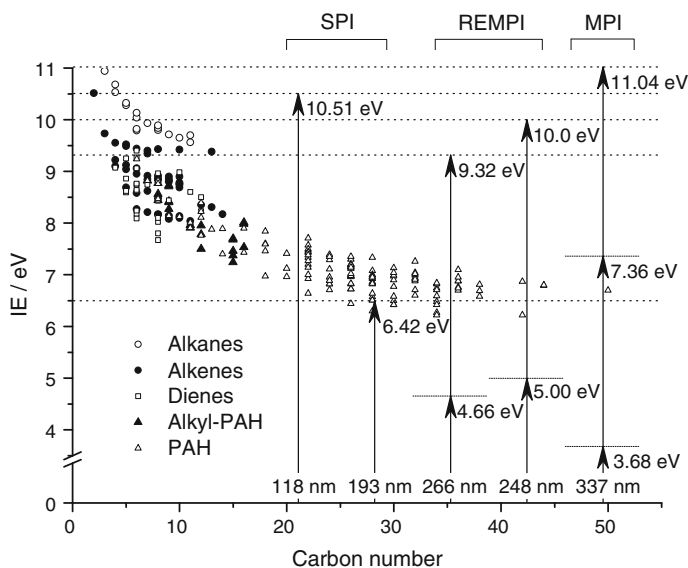


Fig. 12.7 Ionisation energies of selected classes of hydrocarbons (Lias 2012). SPI: single photon ionisation, REMPI: resonance enhanced multiphoton ionisation, and MPI: off-resonance multiphoton ionisation

12.5.3 PAH Measurements by REMPI/TOF-MS

Figure 12.7 shows the ionisation energy versus the number of carbon atoms of several *benzenoid* PAH and compares them to other classes of hydrocarbons (Lias 2012). The ionisation of fully saturated hydrocarbons (e.g. alkanes) requires up to 11 eV, and up to 8 eV are required for extended aromatic systems (e.g. PAH). SPI is very difficult to achieve experimentally since it requires laser excitation in the vacuum UV (VUV), and therefore MPI is often preferred in practical experiments. Near and mid-UV are usually good choices for the ionisation wavelength, since most PAH have large absorption cross sections in this spectral region (Cignoli et al. 1992), and the presence of intermediate levels makes REMPI possible in the wavelength range 238–310 nm (Haefliger and Zenobi 1998). Common choices for the ionisation wavelength include REMPI at 248 or 266 nm since these wavelengths can be easily generated by excimer lasers or by harmonic generation from Nd:YAG lasers. SPI at 118 and 193 nm has been used as well. Alternatively, a promising ionisation method has recently become feasible due to the availability of synchrotron facilities. Modern synchrotron-based VUV sources can provide relatively intense radiation with high spectral resolution in the range of interest 110–200 nm and have been used to identify a large number of species in flames including PAHs (Qi and McIlroy 2005; Qi 2013). This allows SPI with even higher ionisation efficiency with respect to REMPI experiments (Qi 2013). However, the complex and costly equipment required for this experiment still represents a critical limitation.

In REMPI TOF-MS standard experiments, the sample is directly introduced in the ion source using *in-line* molecular beam sampling (see Sect. 12.3) which can be analyzed by mass spectrometry (MBMS) or even deposited on substrates for further *ex situ* analyses (electron microscopy). Information on the gas phase composition can be obtained even on transient species. Although the molecular cooling obtained from a beam generated directly from a flame ($T_{\text{rot}} \sim 300$ K) is not as effective as microprobe sampling followed by molecular beam generation ($T_{\text{rot}} \sim 90$ K), the extra information provided by TOF-MS allows an easy identification of most unknown species, efficiently compensating the lower spectral resolution.

REMPI mass spectra of PAHs show intense signals corresponding to the molecular ions. PAHs are characterised by extended electronic resonance, and the loss of one π electron leaves the molecular backbone relatively undisturbed. As a result, the molecular ions have a long lifetime and can be detected as such. The smooth, resonant energy transfer in REMPI avoids the hard ion dissociation that is typical of electron impact ionisation. This allows the recording of fragment free mass spectra, which greatly enhances detection limits and sensitivities than the more traditional ion sources.

The ability of REMPI of efficiently identifying different isomers is an important yet still open topic, since mass spectrometry alone cannot distinguish molecules having the same exact mass, and detailed knowledge of the contribution of each

isomer to an observed mass peak is a critical step to validate PAH and soot growth models. The number of isomers quickly increases as a function of the number of atoms in the molecule. For instance, while the elemental formula $C_{10}H_8$ only allows one *benzenoid* structure, $C_{26}H_{16}$ allows 37 and more than 1489 have been theoretically predicted for $C_{38}H_{22}$ (Dias 1987). In REMPI, conformational isomers can be identified crossing the accurate mass and the ionisation efficiency data. However, the physical–chemical properties of a few low mass isomers only are known, and even a smaller number has been synthesised and can be used as analytical standard. In practice, the identification of PAHs is limited to some low-mass species, for which the number of isomers is still small.

Quantification protocols by REMPI TOF-MS have been defined for non-sooting flames (Kamphus et al. 2008; Kasper et al. 2007), while sooting flames still remain a challenge. The PAH concentrations can be calculated once the ionisation cross sections are known, but more often they are determined by internal calibration. Uncertainties mainly arise from the difficulties of keeping a stable and known concentration of the standard in the ion source, and additional difficulties arises since high mass PAH have very low vapour pressure (Kamphus et al. 2008).

A typical sensitivity threshold of 1 ppm (40 % uncertainty) for the measurements of PAHs with well known ionisation cross sections is reported, while an uncertainty factor of 2–4 is generally given for species with unknown (estimated) PI cross sections (Hansen et al. 2007; Kamphus et al. 2008).

12.6 PAHs Desorbed from Soot

This section provides a brief overview of the *ex situ* techniques used to sample soot in flames and shock tubes before the PAHs content be desorbed and analysed by REMPI TOF-MS. *Ex situ* methods are relatively easy to set in place and for this reason they are widespread although the range of detectable species is limited to the stable ones.

Historically, the first sampling protocols aimed to investigate a narrow inset in the ensemble of PAH formation conditions. To this purpose, thermophoresis on metal substrates like microscopy grids (Dobbins et al. 1998) and probe extraction with extremely high dilution ratios with an inert gas to avoid post sampling gas condensation (Öktem et al. 2005) were largely employed. The amount of recovered soot was typically in the μg range. Alternatively, a more important amount of flame materials can be extracted with low to no dilution during sampling (Facinnetto et al. 2011). At the cost of having gases condensing on the soot deposit and partially or completely losing the sampling spatial resolution, up to hundredths of mg of soot can be recovered. Such samples are suited to be solvent extracted for chromatography or directly analysed by thermal or laser desorption. In shock tubes, sampling relies on the deposition of soot particles on a target plate fixed on the end wall behind the reflected shockwave (Mathieu et al. 2009).

Sampled soot can be deposited on an inert substrate for further *ex-situ* analyses (desorption, solvent extraction, and electron microscopy) (see Chaps. 11 and 13). Solvent extraction of sampled soot followed by PI TOF-MS has been widely used (Alfè et al. 2008; Apicella et al. 2007). This configuration offers the additional advantage that the same sample can be analysed by gas chromatography/mass spectrometry (GC-MS). Despite GC-MS being limited to $m/z < 450$, this is so far the only combination of experimental techniques providing at the same time isomer selection and quantitative information of several low mass PAH.

Often, the sampled soot is deposited and destined for surface analyses. During soot surface analyses, the transition of the adsorbed and condensed PAHs to the gas phase is obtained by directly heating the sample (thermal desorption) or by energy transfer with an optical field (laser desorption). Once in the gas phase, REMPI TOF-MS is used to detect the PAHs as discussed in Sect. 12.5.3. Particularly, laser desorption is capable of being integrated into REMPI TOF-MS as the desorption can be easily performed in the TOF-MS ion source at the same time as the PI (Apicella et al. 2007; Dobbins et al. 1998; Mathieu et al. 2009), or in two different steps (Faccinnetto et al. 2011; Öktem et al. 2005). The advantages of this method include high sensitivity and a detection limit below 1 nmol g^{-1} , and therefore very little material is required in comparison to other techniques like GC-MS. For instance, a laser desorption REMPI TOFMS mass spectrum is shown in Fig. 12.8 (top). Following the carbon hydrogen diagram interpretation (Keller et al. 2000), at every peak attributed to PAH is assigned an elemental formula

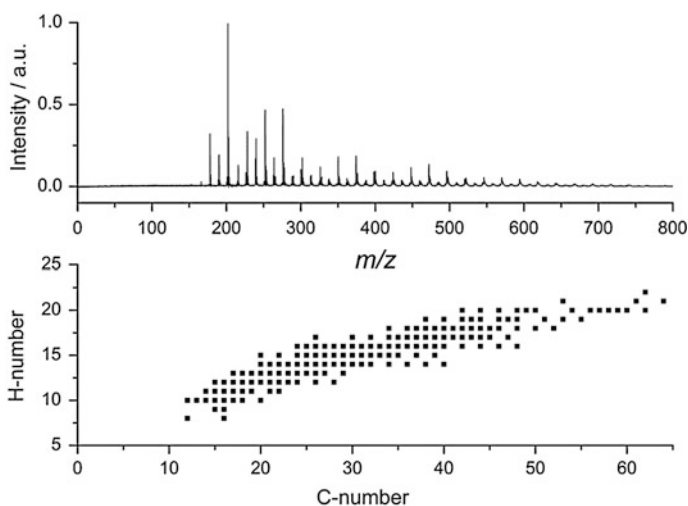


Fig. 12.8 Desorption REMPI TOF-MS mass spectrum of soot extracted from an ethylene flame (*top*) and corresponding carbon-hydrogen diagram (*bottom*), from which a mass growth rate H:C = 1:4 can be inferred. The m/z range in the top figure corresponds to the number of carbon atoms in the bottom figure

C_nH_m , which is then plotted as one point in the space (n, m) . The totality of points represents the ensemble of PAHs Fig. 12.8 (bottom).

Carbon–hydrogen diagrams provide useful information on the mass growth ratio of PAHs and make easy to compare data gathered in different experiments regardless the peak intensity, which is strongly affected by the ensemble of the selected experimental conditions.

The most important limitation of all *ex situ* techniques is the sample extraction itself. Ultimately, the reliability of the extraction procedure is determined by the control over the partitioning of PAHs between adsorbed, gas and condensed phase. The distribution of PAHs between the three phases depends on the physical and chemical properties of both PAHs (saturation vapour pressure) and the substrate on which they are adsorbed (specific area and composition). Due to the lack of knowledge on the surface properties of nascent soot, the adsorption mechanisms of PAHs on soot is not yet fully understood, and therefore detailed models on the PAHs partitioning between phases are not available.

12.7 Soot

Soot consists of nearly spherical primary particles that aggregate into complex fractal structures. The number of primary particles N_p in an aggregate can be expressed as (Sorensen 2001):

$$N_p = k_f \left(\frac{R_g}{d_p/2} \right)^{D_f} \quad (12.10)$$

where d_p is the diameter of the primary particles, R_g is the radius of gyration and D_f and k_f are the aggregate fractal dimension and prefactor, respectively. These two last parameters are sufficient to represent different shape and size clusters.

Their morphology and size distribution functions (PSDF) can be known respectively from transmission electron microscopy (TEM) investigations (see Chap. 13) and inline scanning mobility particle sizing (SMPS) (Abid et al. 2008; Zhao et al. 2003). A full morphological description of soot aggregates requires the determination of the above-mentioned parameters and the distribution width of N_p and d_p respectively (Reimann et al. 2009). Concerning the determination of soot quantity produced by a combustion process, the most accessible experimental quantity is the *soot volume fraction* f_v , which is the ratio of the volume of soot particles to the volume of gas in which the particles are contained. For a mono-disperse size distribution of spherical particles of radius r_p , $f_v = \frac{4}{3} \pi r_p^3 n_p$, n_p being the density of primary particles. This quantity can be determined by light extinction measurements or by laser-induced incandescence (LII). Soot morphology can also be determined partly by LII and elastic light scattering (ELS) (De Iuliis et al. 1998; Reimann et al. 2009).

This section focuses on LII, which has become a technique commonly applied for fundamental and practical applications in combustion. LII allows instantaneous measurements of spatial distribution of f_V in flames (Köhler et al. 2012), engines (Pickett and Siebers 2004) or at the exhaust of aeroengines (Delhay et al. 2009), and using this technique, important data for kinetic modelling of soot formation in flames (Desgroux et al. 2008; Köhler et al. 2012; Liu et al. 2011), determination of threshold sooting index (TSI) of various practical fuels (Desgroux et al. 2013; Lemaire et al. 2010; McEnally and Pfefferle 2009) are obtained. Light extinction technique is also described here, since it can be easily combined with LII for calibration and it is well suited to get f_V in steady diffusion and premixed flames.

12.7.1 Basic Knowledge of Soot–Light Interaction and Optical Properties

Interpretation of optical measurements such as LII, emission, and extinction is dependent on knowledge of the optical properties of soot material, i.e. how it absorbs and scatters light of wavelength λ . The corresponding scattering and absorption coefficients (or cross sections) depend on the *complex refractive index* of soot $m(\lambda) = n(\lambda) - ik(\lambda)$, with $n(\lambda)$ and $k(\lambda)$ representing, respectively, the real part and the imaginary part of the complex index at λ . Individual particles that form aggregates are generally small compared to the wavelength of light, so that they satisfy the Rayleigh limit of the Mie scattering theory ($\pi d_p/\lambda \ll 1$). In the Rayleigh limit, primary soot particles absorb light volumetrically and their absorption cross section σ_{abs} is given by (Sorensen 2001):

$$\sigma_{\text{abs}} = \pi^2 d_p^3 \frac{E(m(\lambda))}{\lambda} \quad (12.11)$$

$$\text{with } E(m(\lambda)) = -\text{Im} \left(\frac{m(\lambda)^2 - 1}{m(\lambda)^2 + 2} \right).$$

However, optical cross sections of aggregates cannot be adequately treated by simple electromagnetic theories for spheres because of the large dimension of the aggregate and its complex morphology. Fractal representation of soot aggregates has led to the generalisation of the classical Rayleigh–Debye–Gans scattering theory for fractal aggregates (RDG-FA). The RDG-FA formulation yields analytical expressions, directly relating optical cross sections to aggregate particle size and morphology (Sorensen 2001). Therefore, this scattering theory is very useful, especially with respect to the interpretation of *in situ* laser diagnostic techniques in combustion. Studies about validity and limits of this theory can be found in Farias et al. (1996), Liu et al. (2008), Merchiers et al. (2010), Yon et al. (2008).

The values of $m(\lambda)$ and $E(m)$ remain difficult to establish accurately because of the complex structure of soot (Bond and Bergstrom 2006; Dalzell and Sarofim

1969; Smyth and Shaddix 1996). Particularly, the dependence of $E(m)$ on the fuel, the kind of combustion and the degree of growth of the soot particle (nascent, young or mature soot) is not resolved, though recent works do observe an increase of $E(m)$ with the reaction time in premixed flames (Bladh et al. 2011; Maffi et al. 2011). The spectral dependence seems to be weak above 500 nm and a somewhat stable value from the literature for soot emitted from combustion sources is $E(m) = 0.39 \pm 0.06$ at 550 nm (Bond and Bergstrom 2006).

12.7.2 LII Technique

LII allows the measurement of f_V in flames or exhaust gases with high accuracy and sensitivity. It is based on the detection of increased thermal radiation emitted from soot particles heated to very high temperatures (~ 4000 K, i.e. around the sublimation temperature of carbon) by a short laser pulse. The principles of LII have been described in details (Santoro and Shaddix 2002; Schulz et al. 2006).

The heat and mass transfer processes of LII of soot aggregates, heated by a laser pulse of intensity $q(t)$, can be modelled by considering a single particle following the approaches detailed in (Eckbreth 1977; Michelsen et al. 2007; Melton 1984; Snelling et al. 2000). The energy balance equation is:

$$\frac{dU_{\text{internal}}}{dt} = \dot{q}_{\text{abs}} - \dot{q}_{\text{conduction}} - \dot{q}_{\text{sublimation}} - \dot{q}_{\text{radiation}} \quad (12.12)$$

where each of the terms represents a rate of energy loss or gain for the following processes (in order): internal energy, laser absorption, conduction to the surrounding gases, soot sublimation and thermal radiation. Equation 12.12 becomes:

$$\frac{4}{3}\pi r_p^3 \rho_s c_p \frac{dT_p}{dt} = \sigma_{\text{abs}} q(t) - 4\pi r_p^2 (T_p - T_g) K_T(t) + \frac{\Delta_v H}{M_C} \frac{dm}{dt} - \dot{q}_{\text{radiation}} \quad (12.13)$$

where ρ_s is the soot density, c_p the soot specific heat capacity, T_g is the surrounding gases temperature, K_T is the heat transfer coefficient, $\Delta_v H$ the heat of vapourisation of soot, M_C the molecular weight of soot vapour and dm/dt is the mass loss rate. The radiation heat loss term $\dot{q}_{\text{radiation}}$, which produces incandescence, is orders of magnitude smaller than other terms and is generally neglected.

The temperature $T_p(t)$ (see Eq. 12.13) and diameter $d_p(t)$ of the particle are derived by numerically solving the differential equations including the mass equation conservation. Detailed development on heat transfer modelling can be found in (Michelsen et al. 2007). The behaviour of $T_p(t)$ and $d_p(t)$ subsequently to a short laser pulse heating is highly dependent on the absorbed energy, i.e. on the incident laser fluence F as illustrated in Fig. 12.9. At high F , the soot temperature reaches the sublimation temperature leading to mass loss and particle diameter decrease. The particle cooling rate is also affected by F and it is obviously dependent on the particle size.

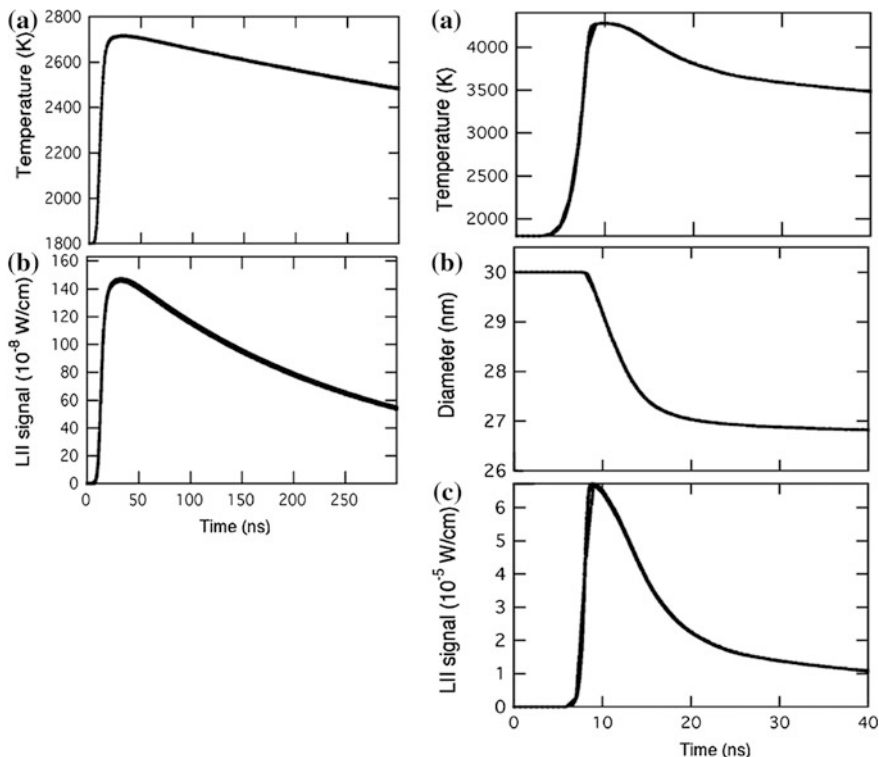


Fig. 12.9 Left side **a** Modelled temperature and **b** LII signal as function of time, $F = 0.05 \text{ J/cm}^2$. Right side **a** Modelled temperature, **b** Diameter and **c** LII signal as function of time, $F = 0.7 \text{ J/cm}^2$ (Michelsen et al. 2007, Copyright Springer)

The soot particle radiates isotropically according to the Planck equation, modified by the emissivity ϵ to correct for deviation from perfect blackbody emission. Thus, the power radiated by a single spherical particle (P_{LII}), of radius $r_p(t)$, at $\lambda = \lambda_{\text{em}}$ centred to the spectral interval $\Delta\lambda = \lambda_2 - \lambda_1$ can be expressed at any time during the laser pulse and during the cooling process as follows (Melton 1984)

$$P_{\text{LII}}(t, \lambda_{\text{em}}) = \int_{\lambda_1}^{\lambda_2} \frac{2\pi hc^2}{\lambda^5} \left[\exp\left(\frac{hc}{\lambda k_B T_p(t)} - 1\right) \right]^{-1} 4\pi r_p^2(t) \epsilon(\lambda) d\lambda \quad (12.14)$$

where the *emissivity* ϵ of soot particles is related to the *absorption efficiency* Q_{abs} at λ by:

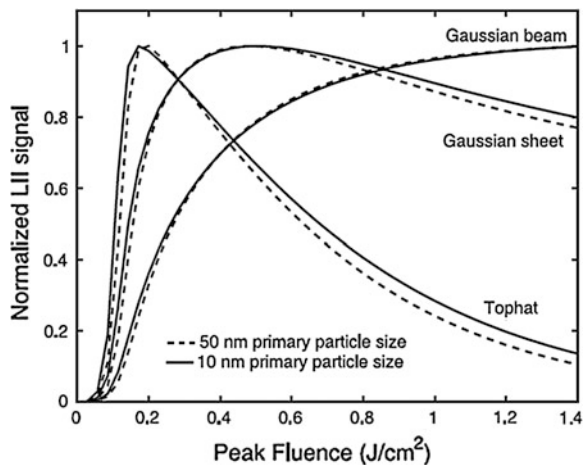
$$\epsilon(\lambda) = Q_{\text{abs}}(\lambda) = \frac{\sigma_{\text{abs}}}{\pi r_p^2} = 8\pi r_p \frac{E(m, \lambda)}{\lambda} \quad (12.15)$$

Thus, the LII signal (S_{LII}), which corresponds to the flux of incandescence photons emitted in all directions, issued from soot particles with volume fraction f_V , becomes:

$$S_{\text{LII}}(\lambda_{\text{em}}, T_p(t)) = \int_{\lambda_1}^{\lambda_2} 48E(m, \lambda) \frac{\pi^2 hc^2}{\lambda^6} \left[\exp\left(\frac{hc}{\lambda k_B T_p(t)} - 1\right) \right]^{-1} f_V d\lambda \quad (12.16)$$

Experimentally and theoretically, the prompt LII signal (i.e. the LII signal measured at the peak temperature $dT_p/dt = 0$) has been shown to be nearly proportional to f_V (Bladh et al. 2008; Melton 1984). However, its amplitude strongly depends on the temperature T_p reached by the particle during the laser process via Planck's equation (see Fig. 12.9). Therefore, the strategy for measuring f_V by LII generally consists to heat soot sufficiently that it just reaches sublimation temperature (Schulz et al. 2006), supposed to be nearly the same for any soot particle. Hence, f_V in the measurement field is quasilinearly related to the intensity registered on the detector. The adequate laser fluence can be easily adjusted from laser fluence curves, which represent the plot of the LII signal with the laser fluence. Fluence dependence of the LII signal has been shown to be very dependent on the choice of the detection sampling time (Witze et al. 2001) and on the spatial profile of laser irradiance. Figure 12.10 shows calculated fluence curves obtained with different spatial profiles of the laser irradiance (Bladh et al. 2006). In case of Gaussian profiles, the LII signal shows a rapid rise with laser energy until the particle sublimation begins and then levels off as the temperature remains relatively constant. The constancy is caused by a cancelling of signal loss due to soot sublimation and signal gain as the wings of the laser beam begin to heat a wider region of soot (Bladh et al. 2006; Delhay et al. 2005; Schulz et al. 2006). For tophat laser profiles, LII signal decrease is generally observed at high fluence due to soot mass loss. It is noted that the shape of the fluence curves may change along

Fig. 12.10 Fluence curves from 18-ns gate starting 20 ns after the start of the laser pulse for different optical configurations (Bladh and Bengtsson 2004, Copyright Springer)



the height above the burner in several flames (Cléon et al. 2011; Desgroux et al. 2008; Oh and Shin 2006), due to variability of optical physical properties of soot along the flame, thus the fluence needed for plateau behaviour must be confirmed.

Experimentally, the use of 1064 nm excitation laser is highly recommended to avoid possible interferences from laser-induced fluorescence of PAH (PAH-LIF) (Schoemaeker Moreau et al. 2004). The incandescence radiation at flame temperatures spans from the near UV to the infrared. Different strategies of spectral filtering are selected in order to limit possible spectral interferences from PAH-LIF and flame emission (Lee et al. 2004; Xiao et al. 2005). Detected with an intensified CCD camera, LII signal is temporally integrated over a gate width which may be delayed relative to the laser pulse to prevent interference from laser scattering or PAH fluorescence (Schulz et al. 2006). Temporally resolved LII decays are preferentially obtained with a fast photomultiplier.

From the analysis of the LII temporal decays, particle sizing can be achieved through comparison of modelled and measured particle cooling rates (Schulz et al. 2006; Michelsen et al. 2007; Lehre et al. 2003). The principal cooling mechanisms are conductive cooling and sublimation. Additional heat transfer mechanisms are summarised by Michelsen (Michelsen 2003). Hofmann et al. have developed a website, where LII signals can be simulated and experimental LII time decays compared to modelled signals to determine particle size (Hofmann et al. 2007). Impact of aggregation and polydispersity on particle cooling rates was discussed (Desgroux et al. 2013).

12.7.3 Extinction and Calibration Methods

Light extinction, or line-of-sight attenuation, allows the determination of f_V (Dasch 1992; Thomson et al. 2005). It is well suited to steady diffusion and premixed flames and can also be applied to unsteady flames to obtain time-averaged f_V maps. Light extinction uses the Beer–Lambert law to relate light transmittance $T(\lambda) = I(\lambda)/I_0(\lambda)$ to the line-integrated extinction coefficient, or optical thickness, as $\ln[T(\lambda)] = -\int K_{\text{ext}}(\lambda, x)dx$. In these expressions, $I_0(\lambda)$ is the incident light intensity, $I(\lambda)$ the transmitted light intensity across the medium, K_{ext} is the extinction coefficient: $K_{\text{ext}} = K_{\text{abs}} + K_{\text{sca}}$ where K_{abs} and K_{sca} are the absorption and scattering coefficients, respectively. $K_{\text{abs}} = n_p \sigma_{\text{abs}}$. If $K_{\text{sca}} \ll K_{\text{abs}}$, an approximation which works for particle diameter in the Rayleigh regime, f_V is directly deduced from the transmittance measurement:

$$f_V = \frac{K_{\text{abs}} \lambda}{6\pi E(m)} \quad (12.17)$$

Discussion about the validity of this assumption can be found in (Desgroux et al. 2013). For axisymmetric flames, the Abel inversion of multiple measurements chords is frequently used (Dasch 1992), later improved using Tikhonov

regularisation of the *onion peel* inversion algorithm (Daun et al. 2006). Light extinction is often implemented as a zero dimensional (0D), single line extinction. Various two-dimensional implementation of light extinction have been reported where expanded lasers or arc lamps are used as light sources (Arana et al. 2004; Snelling et al. 1999). Due to increasing evidence that large PAH or nanoparticles can attenuate light well into the visible, it is preferable to carry out measurements in the near-IR at $\lambda > 700$ nm (Migliorini et al. 2011; Zerbs et al. 2009).

Combination of LII and extinction techniques is very appropriate to get temporally and spatially-resolved f_V distribution in flame with high sensitivity. Calibration is achieved with single-pass light extinction or multi-pass cavity ring down spectroscopy (Desgroux et al. 2008; Schoemaeker Moreau et al. 2004; Vander Wal and Jensen 1998) in an appropriate zone of the flame (i.e. a zone with low f_V gradient for example).

The absolute value of f_V can also be obtained through an *auto-compensating* procedure based on the determination of each parameter of Eq. 12.16 (Snelling et al. 2005). The method employs colour pyrometry to resolve the heated particle temperature. Through detection of the LII emission at two or more wavelength bands using absolute intensity calibrated detectors, referred to here as auto-compensating LII, the temperature of the heated and subsequently cooling particles can be measured then f_V can be determined from the absolute emission intensity. The accuracy of all these techniques relies on accurate knowledge of the spectral variation of $E(m)$.

12.8 Concluding Remarks

This chapter has described laser diagnostics used to measure concentration of PAHs and soot particles in combustion processes. While laser diagnostics can inherently provide non-perturbing *in situ* measurements, such as LIF for small radicals or LII for soot particles, it has been shown that selective characterisation of PAHs requires a prior cooling of these species using supersonic expansion. Therefore, in the current state of the diagnostics abilities, both *in situ* and *ex situ* diagnostics (also presented in Chaps. 11 and 13) are required to provide as large as possible experimental database to validate kinetics model describing PAH and soot formation in combustion processes.

The technological progresses of the last two decades allowed access to cutting-edge techniques like synchrotron sources coupled to TOF-MS, which turned out to be a powerful tool to measure important gas-phase species in flames or jet-stirred reactors. Large radical species (including PAH radicals) can also be detected by PI/TOF-MS techniques at the condition that gaseous species be properly supersonic expanded after sampling. More generally, PI/TOF-MS-based techniques allow obtaining mass spectra both in the complex reactive mixture or after gaseous species desorption from a substrate. Jet-cooled LIF and LII techniques need less expensive and simpler set-ups and provide respectively the concentration of

selected PAHs and the soot volume fraction with considerable accuracy and precision.

The important challenge for the future concerns the identification of species involved in the soot nucleation step, i.e. accompanying the transition from the gas phase to the solid phase.

References

- Abid AD, Heinz N, Tolmachoff ED et al (2008) On evolution of particle size distribution functions of incipient soot in premixed ethylene-oxygen-argon flames. *Combust Flame* 154(4):775–788
- Alfè M, Apicella B, Tregrossi A et al (2008) Identification of large polycyclic aromatic hydrocarbons in carbon particulates formed in a fuel-rich premixed ethylene flame. *Carbon* 46(15):2059–2066
- Apicella B, Carpentieri A, Alfè M et al (2007) Mass spectrometric analysis of large PAH in a fuel-rich ethylene flame. *Proc Combust Inst* 31(1):547–553
- Arana CP, Pontoni M, Sen S et al (2004) Field measurements of soot volume fractions in laminar partially premixed coflow ethylene/air flames. *Combust Flame* 138(4):362–372
- Ashkenas H, Sherman FS (1966) In: JH de Leeuw (ed) 4th International symposium on rarefied gas dynamics, vol 2. New York
- Behlen FM, McDonald DB, Sethuraman V et al (1981) Fluorescence spectroscopy of cold and warm naphthalene molecules: Some new vibrational assignments. *J Chem Phys* 75(12):5685–5693
- Beijerinck HCW, Verster NF (1981) Absolute intensities and perpendicular temperatures of supersonic beams of polyatomic gases. *Physica* 111:327–352
- Bengtsson P-E, Aldén M (1995) Soot-visualization strategies using laser techniques. *Appl Phys B* 60(1):51–59
- Berlman IB (1971) *Handbook of fluorescence spectra of aromatic molecules*, 2nd edn. Academic Press, New York
- Birks JB (1970) *Photophysics of aromatic molecules*, 1st edn. Wiley, London
- Bladh H, Bengtsson P-E, Delhay J et al (2006) Experimental and theoretical comparison of spatially resolved laser-induced incandescence (LII) signals of soot in backward and right-angle configuration. *Appl Phys B* 83:423–433
- Bladh H, Bengtsson PE (2004) Characteristics of laser-induced incandescence from soot in studies of a time-dependent heat- and mass-transfer model. *Appl Phys B* 78(2):241–248
- Bladh H, Johnsson J, Bengtsson PE (2008) On the dependence of the laser-induced incandescence (LII) signal on soot volume fraction for variations in particle size. *Appl Phys B* 90(1):109–125
- Bladh H, Johnsson J, Olofsson NE et al (2011) Optical soot characterization using two-color laser-induced incandescence (2C-LII) in the soot growth region of a premixed flat flame. *Proc Combust Inst* 33(1):641–648
- Boesl U (2000) Laser mass spectrometry for environmental and industrial chemical trace analysis. *J Mass Spectrom* 35(3):289–304
- Bond T, Bergstrom R (2006) Light absorption by carbonaceous particles: an investigative review. *Aerosol Sci Technol* 40:27–67
- Boyd R (2003) *Nonlinear optics*. 2nd edn., Academic Press, New York
- Cignoli F, Zizak G, Benecchi S et al. (1992) *Atlas of fluorescence of spectra of aromatic hydrocarbons*, Editorial group and Graphic design: S. De Iulii, D. Ferretti
- Cléon G, Amodeo T, Faccinetto A et al (2011) Laser induced incandescence determination of the ratio of the soot absorption functions at 532 nm and 1064 nm in the nucleation zone of a low pressure premixed sooting flame. *Appl Phys B* 104(2):297–305

- Coe DS, Haynes BS, Steinfeld JI (1981) Identification of a source of argon-ion-laser excited fluorescence in sooting flames. *Combust Flame* 43:211–214
- Dalzell WH, Sarofim AF (1969) Optical constants of soot and their application to heat-flux calculations. *J Heat Transfer* 91(1):100–104
- Dasch CJ (1992) One-dimensional tomography: a comparison of Abel, onion-peeling, and filtered backprojection methods. *Appl Opt* 31:1146–1152
- Daun KJ, Thomson KA, Liu F et al (2006) Deconvolution of axisymmetric flame properties using Tikhonov regularization. *Appl Opt* 45:4638–4646
- De Iuliis S, Barbini M, Benecchi S et al (1998) Determination of the soot volume fraction in an ethylene diffusion flame by multiwavelength analysis of soot radiation. *Combust Flame* 115(1–2):253–261
- Delhay J, Bouvier Y, Therissen E et al (2005) 2D imaging of laser wing effects and of soot sublimation in laser-induced incandescence measurements. *Appl Phys B* 81:181–186
- Delhay J, Desgroux P, Therissen E et al (2009) Soot volume fraction measurements in aero-engine exhausts using extinction-calibrated backward laser-induced incandescence. *Appl Phys B* 95(4):825–838
- Desgroux P, Mercier X, Lefort B et al (2008) Soot volume fraction measurement in low-pressure methane flames by combining laser-induced incandescence and cavity ring-down spectroscopy: Effect of pressure on soot formation. *Combust Flame* 155(1–2):289–301
- Desgroux P, Mercier X, Thomson KA (2013) Study of the formation of soot and its precursors in flames using optical diagnostics. *Proc Combust Inst* 34(1):1713–1738
- Dias R (1987) *Handbook of Polycyclic Hydrocarbons*. Elsevier, Amsterdam, data available on NIST online database at www.nist.gov
- Dobbins RA, Fletcher RA, Chang HC (1998) The evolution of soot precursor particles in a diffusion flame. *Combust Flame* 115(3):285–298
- Eckbreth AC (1977) Effects of laser-modulated particulate incandescence on Raman scattering diagnostics. *J Appl Phys* 48(11):4473–4479
- Faccineto A, Desgroux P, Ziskind M et al (2011) High-sensitivity detection of polycyclic aromatic hydrocarbons adsorbed onto soot particles using laser desorption/laser ionization/time-of-flight mass spectrometry: An approach to studying the soot inception process in low-pressure flames. *Combust Flame* 158(2):227–239
- Farias TL, Köylü ÜÖ, Carvalho MG (1996) Range of validity of the Rayleigh-Debye-Gans theory for optics of fractal aggregates. *Appl Opt* 35(33):6560–6567
- Guilhaus M (1995) Special feature: Tutorial. Principles and instrumentation in time-of-flight mass spectrometry. Physical and instrumental concepts. *J Mass Spectrom* 30(11):1519–1532
- Guilhaus M, Mlynski V, Selby D (1997) Perfect timing: time-of-flight mass spectrometry. *Rapid Commun Mass Spectrom* 11(9):951–962
- Haefliger OP, Zenobi R (1998) Laser mass spectrometric analysis of polycyclic aromatic hydrocarbons with wide wavelength range laser multiphoton ionization spectroscopy. *Anal Chem* 70(13):2660–2665
- Hansen N, Kasper T, Klippenstein SJ et al (2007) Initial Steps of Aromatic Ring Formation in a Laminar Premixed Fuel-Rich Cyclopentene Flame. *J Phys Chem A* 111(19):4081–4092
- Herzberg G (1991) *Molecular Spectra and Molecular Structure (Electronic Spectra and Electronic Structure of Polyatomic Molecules)*. Vol. III, Krieger Publishing Company, Malabar
- Hofmann MB, Kock BF, Schulz C (2007) A web-based interface for modeling laser-induced incandescence (LIISim). In: 3rd European combustion meeting, Chania, Kreta. Available at <http://www.liisim.com>
- Kamphus M, Braun-Unkhoff M, Kohse-Höinghaus K (2008) Formation of small PAHs in laminar premixed low-pressure propene and cyclopentene flames: experiment and modeling. *Combust Flame* 152(1–2):28–59
- Kamphus M, Liu NN, Atakan B et al (2002) REMPI temperature measurement in molecular beam sampled low-pressure flames. *Proc Combust Inst* 29(2):2627–2633
- Kasper TS, Oßwald P, Kamphus M et al (2007) Ethanol flame structure investigated by molecular beam mass spectrometry. *Combust Flame* 150(3):220–231

- Keller A, Kovacs R, Homann KH (2000) Large molecules, ions, radicals and small soot particles in fuel-rich hydrocarbon flames. Part IV. Large polycyclic aromatic hydrocarbons and their radicals in a fuel-rich benzene-oxygen flame. *Phys Chem Chem Phys* 2(8):1667–1675
- Klots CE (1981) Rotational relaxation in sonic nozzle expansions. *J Chem Phys* 72:192–197
- Köhler M, Geigle KP, Blacha T et al (2012) Experimental characterization and numerical simulation of a sooting lifted turbulent jet diffusion flame. *Combust Flame* 159(8):2620–2635
- Kohse-Höinghaus K, Barlow RS, Aldèn M et al (2005) Combustion at the focus: laser diagnostics and control. *Proc Combust Inst* 30(1):89–123
- Lee SM, Yoon SS, Chung SH (2004) Synergistic effect on soot formation in counterflow diffusion flames of ethylene/propane mixtures with benzene addition. *Combust Flame* 136:493–500
- Lehre T, Bockhorn H, Jungfleisch B et al (2003) Development of a measuring technique for simultaneous in situ detection of nanoscaled particle size distributions and gas temperatures. *Chemosphere* 51(10):1055–1061
- Lemaire R, Therssen E, Desgroux P (2010) Effect of ethanol addition in gasoline and gasoline-surrogate on soot formation in turbulent spray flames. *Fuel* 89(12):3952–3959
- Levy DH (1980) Laser spectroscopy of cold gas-phase molecules. *Annu Rev Phys Chem* 31:197–225
- Li Y, Tian Z, Zhang L et al (2009) An experimental study of the rich premixed ethylbenzene flame at low pressure. *Proc Combust Inst* 32(1):647–655
- Lias SG (2012) Ionization energy evaluation. In: Linstrom PJ, Mallard WG (eds) (National Institute of Standards and Technology, Gaithersburg, MD) NIST Chemistry WebBook, NIST Standard Reference Database Number 69, 20899. <http://webbook.nist.gov/chemistry/>. Accessed 26 Nov 2012
- Liu F, He X, Ma X et al (2011) An experimental and numerical study of the effects of dimethyl ether addition to fuel on polycyclic aromatic hydrocarbon and soot formation in laminar coflow ethylene/air diffusion flames. *Combust Flame* 158:547–563
- Liu F, Thomson KA, Smallwood GJ (2008) Effects of soot absorption and scattering on LII intensities in laminar coflow diffusion flames. *J Quant Spectrosc Radiat Transf* 109(2):337–348
- Maffi S, De Iuliis S, Cignoli F et al (2011) Investigation on thermal accommodation coefficient and soot absorption function with two-color TIRE-LII technique in rich premixed flames. *Appl Phys B* 104(2):357–366
- Mamyryn BA (2001) Time-of-flight mass spectrometry (concepts, achievements, and prospects). *Int J Mass Spectrom* 206(3):251–266
- Mathieu O, Frache G, Djebaili-Chaumeix N et al (2009) Laser desorption-ionization time-of-flight mass spectrometry for analyses of heavy hydrocarbons adsorbed on soot formed behind reflected shock waves. *Proc Combust Inst* 32(1):971–978
- Mazely TL, Smith MA (1988) Kinetic analysis in thermally anisotropic systems: Application to supersonic free jet expansions. *J Chem Phys* 89:2048–2062
- McEnally CS, Pfeifferle LD (2009) Sooting tendencies of nonvolatile aromatic hydrocarbons. *Proc Combust Inst* 32(1):673–679
- Melton LA (1984) Soot diagnostics based on laser heating. *Appl Opt* 23(13):2201–2208
- Merchiers O, Eyraud C, Geffrin J-M et al (2010) Microwave measurements of the full amplitude scattering matrix of a complex aggregate: a database for the assessment of light scattering codes. *Opt Express* 18(3):2056–2075
- Mercier X, Wartel M, Pauwels JF et al (2008) Implementation of a new spectroscopic method to quantify aromatic species involved in the formation of soot particles in flames. *Appl Phys B* 91(2):387–395
- Michelsen HA (2003) Understanding and predicting the temporal response of laser-induced incandescence from carbonaceous particles. *J Chem Phys* 118(15):7012–7045
- Michelsen HA, Liu F, Kock BF et al (2007) Modeling laser-induced incandescence of soot: a summary and comparison of LII models. *Appl Phys B* 87(3):503–521
- Migliorini F, Thomson KA, Smallwood GJ (2011) Investigation of optical properties of aging soot. *Appl Phys B* 104:273–283

- Oh KC, Shin HD (2006) The effect of oxygen and carbon dioxide concentration on soot formation in non-premixed flames. *Fuel* 85(5–6):615–624
- Öktem B, Tolocka MP, Zhao B et al (2005) Chemical species associated with the early stage of soot growth in a laminar premixed ethylene-oxygen-argon flame. *Combust Flame* 142(4):364–373
- Pickett LM, Siebers DL (2004) Soot in diesel fuel jets: effects of ambient temperature, ambient density, and injection pressure. *Combust Flame* 138(1–2):114–135
- Qi F (2013) Combustion chemistry probed by synchrotron VUV photo-ionization mass spectrometry. *Proc Combust Inst* 34(1):33–63
- Qi F, McIlroy A (2005) Identifying combustion intermediates via tunable vacuum ultraviolet photoionisation mass spectrometry. *Combust Sci Technol* 177:2021–2037
- Reimann J, Kuhlmann S-A, Will S (2009) 2D aggregate sizing by combining laser-induced incandescence (LII) and elastic light scattering (ELS). *Appl Phys B* 96(4):583–592
- Santoro RJ, Shaddix CR (2002) Laser-Induced Incandescence. In: Kohse-Hoinghaus K, Jeffries J (eds) *Applied combustion diagnostics*. Taylor and Francis, New York
- Schoemaeker Moreau C, Therssen E, Mercier X et al (2004) Two-color laser-induced incandescence and cavity ring-down spectroscopy for sensitive and quantitative imaging of soot and PAHs in flames. *Appl Phys B* 78(3):485–492
- Schulz C, Kock BF, Hofmann M et al (2006) Laser-induced incandescence: recent trends and current questions. *Appl Phys B* 83(3):333–354
- Shapiro AH (1953) *The dynamics and thermodynamics of compressible fluid flow*, 2nd edn. Wiley, New York
- Smyth KC, Shaddix CR (1996) The elusive history of $m = 1.57\text{--}0.56i$ for the refractive index of soot. *Combust Flame* 107(3):314–320
- Snelling DR, Liu F, Smallwood GJ et al. (2000) Evaluation of the nanoscale heat and mass transfer model of LII: Prediction of the excitation intensity. In: *Proceedings of the 34th national heat transfer conference*, Pittsburgh, Pennsylvania
- Snelling DR, Smallwood GJ, Liu F et al (2005) A calibration-independent laser-induced incandescence technique for soot measurement by detecting absolute light intensity. *Appl Opt* 44(31):6773–6785
- Snelling DR, Thomson KA, Smallwood GJ et al (1999) Two-dimensional imaging of soot volume fraction in laminar diffusion flames. *Appl Opt* 38(12):2478–2485
- Sorensen CM (2001) Light scattering by fractal aggregates: a review. *Aerosol Sci Technol* 35(2):648–687
- Thomson KA, Gülder ÖL, Weckman EJ et al (2005) Soot concentration and temperature measurements in co-annular, nonpremixed CH₄/air laminar flames at pressures up to 4 MPa. *Combust Flame* 140(3):222–232
- Vander Wal RL, Jensen KA (1998) Laser-induced incandescence: excitation intensity. *Appl Opt* 37(9):1607–1616
- Vander Wal RL, Jensen KA, Choi MY (1997) Simultaneous laser-induced emission of soot and polycyclic aromatic hydrocarbons within a gas-jet diffusion flame. *Combust Flame* 109(3):399–414
- Wartel M, Pauwels JF, Desgroux P et al (2010) Quantitative measurement of naphthalene in low-pressure flames by jet-cooled laser-induced fluorescence. *Appl Phys B* 100(4):933–943
- Wartel M, Pauwels JF, Desgroux P et al (2011) Pyrene measurements in sooting low pressure methane flames by jet-cooled laser-induced fluorescence. *J Phys Chem A* 115(49):14153–14162
- Witze PO, Hochgreb S, Kayes D et al (2001) Time-resolved laser-induced incandescence and laser elastic-scattering measurements in a propane diffusion flame. *Appl Opt* 40(15):2443–2452
- Wu J, Song KH, Litzinger T et al (2006) Reduction of PAH and soot in premixed ethylene/air flames by addition of ethanol. *Combust Flame* 144(4):675–687
- Xiao J, Austin E, Roberts WL (2005) Relative polycyclic aromatic hydrocarbon concentrations in unsteady counterflow diffusion flames. *Combust Sci Technol* 177(4):691–713

- Yon J, Rozé C, Girasole T et al (2008) Extension of RDG-FA for scattering prediction of aggregates of soot taking into account interactions of large monomers. *Part Part Syst Char* 25:54–67
- Zerbs J, Geigle K, Lammel O et al (2009) The influence of wavelength in extinction measurements and beam steering in laser-induced incandescence measurements in sooting flames. *Appl Phys B* 96(4):683–694
- Zhao B, Yang Z, Wang J et al (2003) Analysis of soot nanoparticles in a laminar premixed ethylene flame by scanning mobility particle sizer. *Aerosol Sci Technol* 37(8):611–620
- Zimmermann R, Blumenstock M, Heger HJ et al (2001) Emission of nonchlorinated and chlorinated aromatics in the flue gas of incineration plants during and after transient disturbances of combustion conditions: delayed emission effects. *Environ Sci Technol* 35(6):1019–1030

Chapter 13

Characterization of Soot

Cristina Arnal, Michela Alfè, Valentina Gargiulo, Anna Ciajolo,
María U. Alzueta, Ángela Millera and Rafael Bilbao

Abstract The characterization of physical and chemical properties of the carbon particulate matter commonly named soot is relevant in the research on pollutants emitted in the atmosphere from combustion and industrial plants. The selection and the standardization of advanced analytical methods are necessary to provide reliable and reproducible results on the characteristics of carbon material. This chapter reports an overview of the main off-line techniques available to characterize carbon materials as: elemental analysis, physical adsorption with the determination of the specific surface area, electronic microscopy techniques, X-ray diffraction, Raman spectroscopy, thermogravimetric analysis, infrared spectroscopy, soot reactivity toward O₂ and NO, UV–Visible spectroscopy, size exclusion chromatography and fluorescence spectroscopy. The results of the implementation of these techniques on a commercial standard carbon material (Printex-U carbon black), considered as analog of soot, are reported as case study.

13.1 Introduction

Soot effects on environment and human health have become of great concern over the last years (Ahlström and Odenbrand 1989; Armas et al. 2010; Atribak et al. 2010; D’Anna 2009; Giechaskiel et al. 2009; Higgins et al. 2003; Nejar et al. 2007; Song et al. 2011; Xi and Zhong 2006) and the reduction of its emission has turned out to be a public priority. Natural particles emissions come from volcanic

C. Arnal (✉) · M. U. Alzueta · Á. Millera · R. Bilbao
ThermoChemical Processes Group (GPT), Aragón Institute of Engineering Research (I3A),
University of Zaragoza. Río Ebro Campus, C/Mariano Esquillor s/n, Zaragoza 50018, Spain
e-mail: cristina.arnal@unizar.es

M. Alfè · V. Gargiulo · A. Ciajolo
Istituto di Ricerche sulla Combustione—C.N.R, P.le V. Tecchio 80, 80125 Naples, Italy
e-mail: alfe@irc.cnr.it

eruptions, forest fires, and simple erosion, while the main anthropogenic sources of atmospheric fine and ultrafine particles of soot in urban areas are mobile sources, especially diesel engines (Buzea et al. 2007), as well as stationary sources as power plants. For the latter case, the control of the combustion conditions is relatively easy and, as the problem is focused on one point (stationary source), the employment of scrubbers can help to remove the soot emission problem (Hansen and Nazarenko 2004).

Soot particles are constituted of primary spherules of ca. 15–30 nm in diameter (Xi and Zhong 2006), often coated with organic chemicals as polycyclic aromatic hydrocarbons (PAH) which are well-known to be harmful to human health. The emission of these undesired products of combustion is related to high-temperature fuel-rich pyrolysis conditions. Even in combustion systems working in fuel-lean conditions, the occurrence of pyrolysis conditions inside the combustion chamber and/or during some phases of the combustion cycle may produce soot formation due to the fact that some fuel constituents can not find enough oxygen to react. Consequently, the final emission of soot from the combustion chamber is the result of concurrent pyrolysis and oxidation reactions affected by gas concentrations, mixing effects and different operating conditions (Sánchez et al. 2012).

Therefore, the composition and characteristics of soot are influenced by burning conditions and, at the same time, determine their effect on the environment. Moreover, soot can interact within the combustion systems with other gases present in the combustion chamber like oxygen, water vapor, NO_x , etc. (Arnal et al. 2012a; Mendiara et al. 2008). NO_x is another important pollutant produced from combustion chambers. Soot and NO_x may react in-situ with each other, thus reducing their emissions at the same time (Aarna and Suuberg 1997; Arnal et al. 2012b; Illán-Gómez et al. 1993; Mendiara et al. 2008). This reaction could be considered as a strategy of elimination of these air pollutants. Hence, the characterization of soot formed in combustion processes is of great interest since it has been reported that soot chemical–physical properties have a direct influence on its reactivity toward the combustion gases (Arnal et al. 2010; Ruiz et al. 2007). Therefore, the combination of different characterization analyses and interpretation of all the soot chemical–physical features is essential to correctly interpret and to predict its behavior within the combustion chamber when it comes into contact with the combustion gases.

On the other hand, the characterization of carbon materials is relevant for the development of new carbon materials that has been one of the main factors contributing to improve the quality of our life (Peña 2011). Due to their high accessible surface area, these carbon materials have industrial and technical applications such as catalyst supports and as model adsorbents for adsorption of inorganic compounds (González-Martín et al. 1994). Therefore, particle characterization has become an important tool in many industrial processes since it is indispensable to determine the chemical–physical properties of the material employed in terms of surface functionalization, C, H and N assessment, specific surface area, porosity, structure, thermal resistance, etc.

Overall, the choice of a proper analytical methodology for particle characterization is of great importance for both pollutant control and in the industrial manufacture and quality control. Therefore, in this context, this chapter reports an overview of the main off-line techniques available to characterize carbon materials. It has to be emphasized that off-line techniques involve sampling and handling of the carbonaceous material that could modify soot structure, leaving the validity of the method open to question. Nevertheless, the off-line approach offers the possibility to infer important information about the chemistry of the investigated materials, not easily available by on-line and in-situ techniques.

Specifically, the chapter describes techniques as elemental analysis, physical adsorption with the determination of the specific surface area, electronic microscopy techniques, X-ray diffraction, Raman spectroscopy, thermogravimetric analysis, infrared spectroscopy, soot reactivity toward O₂ and NO, UV-Visible spectroscopy, size exclusion chromatography, and fluorescence spectroscopy. The typical outputs of these techniques applied on a commercial carbon black, Printex-U, are also reported as case study. Printex-U was considered in different literature studies (Jung et al. 2008; Neeft et al. 1997; Setiabudi et al. 2004) to be a representative model material for diesel soot. The thermal-oxidative decomposition process, called Degussa Gas Black, of a mineral oil is the source of carbon black Printex-U. The oil is heated in a vaporizer and the resultant vapors are carried into a gas tube fitted with a multiplicity of burners, and the individual flames so produced impinge on the surface of a water-cooled drum. A portion of the carbon black generated is deposited on a roller while the rest enters into a filter system. A slight oxidative post-treatment also takes place (Arnal et al. 2012b).

13.2 Characterization Techniques

The most useful techniques employed in solid carbonaceous particles characterization as well as the information that these techniques provide are reported below.

13.2.1 *Elemental Analysis*

Elemental analysis is a technique based on sample combustion for the determination of the total content of carbon, hydrogen, nitrogen, sulfur, or oxygen in solid, liquid, volatile, and viscous samples (Brown 2001). The samples, encapsulated in tin or aluminum vials, are inserted into the analyzer and completely burned in the presence of excess oxygen. After the combustion, the volatile gases are further converted into CO₂, H₂O, N₂ (reduction from NO_x to N₂), and SO₂. Gases are captured, chromatographically separated, and detected by a thermal conductivity detector.

Elemental analyses of carbonaceous samples are mainly used to evaluate the H/C atomic ratio which is important, for instance, to define the number of active C–H sites available for oxidation attack.

The low molar H/C value for the Printex-U sample, lower than 0.1 (Arnal et al. 2012b), reflects its relatively highly graphitic nature similar to other carbon materials such as combustion-derived soot, having H/C ratios ranging from 0.4 to 0.1 (Alfè et al. 2009; Russo et al. 2012).

13.2.2 Physical Adsorption and Determination of the Specific Surface Area

The measurement of the specific surface area is based on the physical adsorption (physisorption) of gases or vapors. Physical adsorption of gases is mainly a thermodynamic phenomenon caused by attractive and repulsive forces responsible for the vapor condensation and for the deviations of the real gases with respect to the ideal ones. In the adsorption process at constant temperature (T), the decrease in the gas pressure or the increment in the adsorbent weight can be measured (Martín-Martínez 1990). The amount of adsorbed gas depends on the pressure, temperature, specific surface and porosity of the adsorbent, and the nature of the gas–solid system. For an adsorbed gas in a given solid, at a fixed temperature, the adsorbed quantity (x) is a function of the relative pressure of the adsorbate, P/P_0 , as follows (Martín-Martínez 1990):

$$x = \left(\frac{P}{P_0} \right)_T \quad (13.1)$$

where P is the partial pressure of the adsorbate in the gas phase, P_0 is the saturation pressure of the adsorbate at the adsorption temperature. By representing x versus P/P_0 , the adsorption isotherm can be obtained.

Besides temperature and pressure, the quantity of the adsorbed gas depends on the nature of the gas and the solid (Martín-Martínez 1990). The most accepted classification of the different isotherms is that one presented by Brunauer, Deming, Deming, and Teller (BDDT) which distinguishes five types of isotherms (Brunauer et al. 1940). Later on, a new type of isotherm (type VI) was identified by the IUPAC (Sing et al. 1985).

As function of the resulting type of isotherm, the pore size of the sample can be determined. With this aim, it is worth distinguishing among the different kinds of pores classified on the basis of their pore size. According to IUPAC (Sing et al. 1985), three types of pore sizes can be found:

- Macropores: pores with widths exceeding about 50 nm.
- Mesopores: pores of widths between 2 and 50 nm.
- Micropores: pores with widths not exceeding about 2 nm.

For porous solids having a high pore volume (the pore volume is related to the adsorbed gas), the adsorption and desorption processes are not reversible, i.e., they present the effect of hysteresis. The classical model of adsorption hysteresis is based on considering a pore of some shape, while the geometry of the interface is assumed to be different during desorption (Donohue and Aranovich 1998). A more detailed description on the interpretation of the different types of isotherms (Brunauer et al. 1940; Martín-Martínez 1990; Sing et al. 1985) and hysteresis (Donohue and Aranovich 1998; Jakubov 2008; Sing et al. 1985) is beyond the aim of this work and will not be discussed here, but can be found in the cited references.

The most widely used standard procedure for the determination of the specific surface area is the Brunauer-Emmett-Teller (BET) gas adsorption method (Brunauer et al. 1938) with N_2 at 77 K. The BET method performs the derivation of the isotherm equation for multimolecular adsorption by a method that is a generalization of Langmuir's treatment of the unimolecular layer (Brunauer et al. 1938).

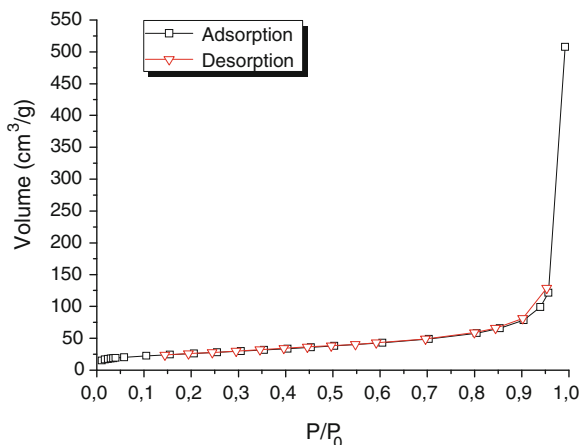
According to Sing (2008), the carbon blacks with surface areas up to $100 \text{ m}^2/\text{g}$ can be considered as, a nonporous material. Overall, the classification of a sample as nonporous material does not necessarily imply that the material does not have pores, but that the specific surface area obtained is not high enough to be considered as a "porous material".

For microporous materials, the most widely used standard procedure for the determination of the apparent surface area and the micropore volume is the Dubinin-Radushkevich (DR) method (Carrasco-Marín et al. 1993) with CO_2 at 273 or 298 K (Carrasco-Marín et al. 1993; Guerrero et al. 2008; Kapoor et al. 1989). Other methods have also been proposed in order to evaluate the surface area and pore size distribution, like Barrett-Joyner-Halenda (BJH) method, Horvath-Kawazoe (HK) method, t plot, α -S plot and density functional theory (DFT) method together with theoretical calculations based on the Grand Canonical Monte-Carlo (GCMC) method.

As previously mentioned, representing x versus P/P_0 , the adsorption isotherm can be obtained, as shown in Fig. 13.1, reporting the case of the carbon black Printex-U in nitrogen at 77 K.

The adsorption isotherm of Printex-U sample (Fig. 13.1) is similar to the isotherm III (Sing et al. 1985), which is representative of nonporous or macroporous materials (Martín-Martínez 1990) and where the adsorbate-adsorbent interactions are relatively weak (Sing et al. 1985). By using the BET equation, the specific surface area obtained for Printex-U was $92 \text{ m}^2/\text{g}$ (Arnal et al. 2012b), indicating that the material can be considered as nonporous.

Fig. 13.1 Adsorption and desorption isotherm of Printex-U with N_2 at 77 K



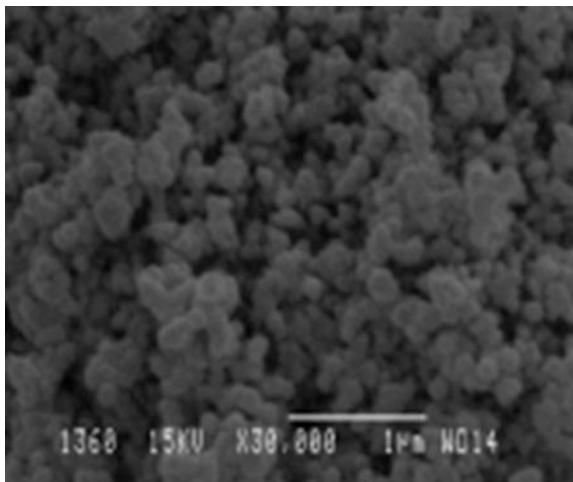
13.2.3 Electron Microscopy Techniques

The electron microscopy allows obtaining information about microstructure and nanostructure of the samples. Microscopy techniques can be used to analyze the structure and morphology of soot samples such as shape, size, distribution of the particles, and graphene layer orientation. The use of electrons in microscopy is very advantageous since they have very acceptable interaction with matter (Williams and Carter 2009). Scanning Electron Microscopy (SEM) and Transmission Electron Microscopy (TEM) use a beam of electrons to image the sample structure, although the way in which the images are produced and magnified is completely different (Goodhew et al. 2001a). From a general point of view, SEM provides images of external morphology (Goodhew et al. 2001b), whereas TEM looks into the internal structure of solids and analyzes the microstructural details.

13.2.3.1 Scanning Electron Microscopy

In SEM, the electron beam employed to light the sample scans the specimen for each spot, obtaining a proportional brightness. By controlling the beam position on the specimen, the brightness is modulated and transformed into an image which is displayed on a computer screen (Goodhew et al. 2001a). When the electron beam comes into contact with the surface of the solid, a wide range of signals are produced such as secondary electrons, backscattered electrons, etc. SEM images, in general, correspond to the secondary electrons emitted by the specimen when the electrons (from the electron beam) are accelerated with an energy between 1 and 30 keV, that is considerably lower than the typical TEM energies (100–300 keV). Those secondary electrons are produced when the incident electron excites the electrons of the specimen which move up to the surface of the

Fig. 13.2 SEM micrograph of Printex-U



sample, losing most of their energy during the process, and the ones that may finally escape from the specimen are measured (Goodhew et al. 2001a; Williams and Carter 2009). The production of secondary electrons is closely related to the topography of the specimen since, due to its low energy, only the electrons that are placed near to the surface (<10 nm) are able to leave the sample and can be counted (Goodhew et al. 2001a). That is the reason why SEM is a technique that provides morphological and topographic information of the solid surface. Hence, it is a helpful tool to evaluate the structural and texture changes produced, for instance, when the material has undergone different thermal treatments which affect its reactivity (Biagini et al. 2005; Cetin et al. 2004; Guerrero et al. 2008; Lu et al. 2002; Shim et al. 2004) or when the carbon material has been formed within different space times (Mendiara et al. 2005).

In Fig. 13.2, SEM image reveals the spherical morphology of Printex-U particles joined together to create particle aggregates of different sizes.

13.2.3.2 Transmission Electron Microscopy

In TEM, a thin specimen is radiated by an electron beam with an energy between 100 and 300 keV. The term “thin” is relative, but, in this context, it means electron transparent, i.e., that electrons are able to go through the sample. Therefore, in TEM, for a suitable study, the specimens should be as thick as <100 nm (Goodhew et al. 2001a; Williams and Carter 2009), wherever possible, so that it is feasible to transmit sufficient electrons in order to obtain enough electrons that, after passing through the sample, come into contact with the camera Charge-Coupled Device (CCD) detector and it is possible to obtain interpretable image.

The electrons that have passed through the sample can be divided into two types: those that scattered with a significant angle and those that present no

important angular deviation. The latter, use to be called “direct beam” (although in many texts can be described as “transmitted beam” regardless the fact that all the electrons going through the sample have been transmitted) (Williams and Carter 2009), and these electrons are the ones that are measured.

Therefore, TEM technique has significantly contributed to the detailed characterization of the structure of the carbon materials since it allows visualizing their nanotexture. Carbon materials usually present a multiscale organization (structure, microtexture, and texture). The microstructure is described by nanosized deformed polyaromatic layers which spatial organization may end up in different lamellar, porous, concentric, and fibrous microtextures. These microtextures form the skeleton of the carbon materials and are responsible for their properties (optical parameters, reactivity, etc.) (Ishiguro et al. 1997; Oberlin 1989; Rouzaud and Clinard 2002).

The morphology of airborne soot coming from combustion and carbon black produced by pyrolysis processes is very similar and depends on their sources and formation conditions (temperature, pressure, and time). The morphology of soot and carbon black consists of chain-like aggregates of almost spherical primary particles whose dimensions are strictly dependent upon precursor’s identity and general synthesis conditions. Soot with large primary particles (~ 100 nm) is obtained from inefficient combustion processes at low temperature (wood and coal burning, especially in traditional furnaces and stoves). Soot with smaller primary particles (20–40 nm), such as flame-formed soot or diesel soot, is obtained from practical combustion systems as modern domestic heating installation, fuel oil burners, diesel engines, etc. (Kuhner and Voll 1993).

The complex geometry of these aggregates can be characterized as mass fractals. The number of primary particles per aggregate, N_p , scales with the radius of gyration, R_g , as follows:

$$N_p = k_g \left(R_g/a \right)^{D_f} \quad (13.2)$$

where k_g is the fractal pre-factor (also known as the structural coefficient), a is the primary particle radius and D_f is the fractal dimension.

It is noteworthy to mention that the description of aggregates of fine particles as fractals is a simplification, since their self-similarity is only observed over extended, but finite, range of length scales. According to the definition of Mandelbrot, they can be called natural fractals (Mandelbrot 1975). The term has been widely accepted and adopted in different literature studies following the suggestion of several authors (Megaridis and Dobbins 1990; Cai et al. 1995; Köylü et al. 1995a, b).

A number of off-line and in-situ techniques for the evaluation of fractal dimension have been used in the literature. The most commonly used techniques are scattering (light, X-ray, or neutron), image analysis and settling (Bushell et al. 2002).

Starting from geometrical properties (primary particle mean diameter, maximum projected length, projected area, and overlap coefficient) that are directly measured from the projected aggregate image obtained by TEM, the number of

primary particles in an aggregate, radius of gyration, aggregate surface, and fractal dimensions, can be inferred.

As a general consideration, more open structures are associated with lower D_f while more compact structures are associated with higher D_f . Typical values for carbon blacks are $D_f = 1.8\text{--}2.0$ (Printex 25, Printex 60, and Printex 90 from Evonik Degussa) and $D_f = 1.87$ for diesel soot. Only carbon blacks with very high specific surface area ($>500\text{ m}^2/\text{g}$) are characterized by lower values mass fractal dimension ($D_f = 1.7\text{--}1.8$; FW200, Color Black XE2B). Flame-formed soot ranges from $D_f = 2.02\text{--}2.07$ (soot at the early stages of maturation process) and $D_f = 1.86\text{--}1.92$ (mature soot).

Vander Wal and Tomasek (2003) analyzed the structure of different kinds of soot by High Resolution-TEM (HR-TEM), relating the differences in nanostructure of the different types of soot to their reactivity.

One of the main concepts arisen from the structural characterization of the carbonaceous solids by TEM is the elemental basic structural unit (BSU). Firstly, BSU was defined as 2-3 polyaromatic (coronene-like) stacked layers considered as the elemental bricks of the carbon materials (Jäger et al. 1999; Oberlin 1989). Later on, Rouzaud and Clinard (2002) on the basis of HR-TEM fringe analysis, redefined this classical structural model since it resulted to be much more complex than the stacked coronene-like structures.

The HRTEM, by imaging directly the profile of the polyaromatic layers as fringes, has been used as a semi-quantitative technique to obtain information about the soot organization parameters as the length of the graphitic layers and the size of the coherent domains (Alfè et al. 2009, 2010; Rouzaud and Clinard 2002; Shim et al. 2000; Vander Wal and Tomasek 2003). To obtain these parameters, skeletonization techniques and post-processing of the data are needed (Sharma et al. 1999). This image analysis technique consists of different steps: (1) noise reduction through the filtration of TEM micrographs, (2) mathematical separation and reconnection of fringe layers, and (3) development of an image analysis algorithm to evaluate the quantifiable structural parameters (Sharma et al. 1999).

The structure of carbonaceous materials can vary from amorphous to crystalline structures (like graphite and diamond). Amorphous structures consist of a random organization of the carbon atoms (with nonstacked fringes) while the graphite structure consists of perfect straight and parallel fringes spaced by 0.3354 nm (Oberlin 1989; Rouzaud and Clinard 2002). Combustion-formed soot is considered as an intermediate case and it can be defined as a disordered carbon. It has been found that the soot nanoscale organization is dependent on the fuel nature (aliphatic, aromatic) and flame temperature (Alfè et al. 2009, 2010; Russo et al. 2012).

TEM micrograph of Printex-U, shown in Fig. 13.3, exhibits the typical chain-like structure formed by aggregates of random spherical primary particles with diameters ranging from 30 to 45 nm (Arnal et al. 2012b). At a higher magnification (Fig. 13.3b), a concentric graphitic layer organization may be observed inside each primary particle testifying the relatively high order degree of the Printex-U particles.

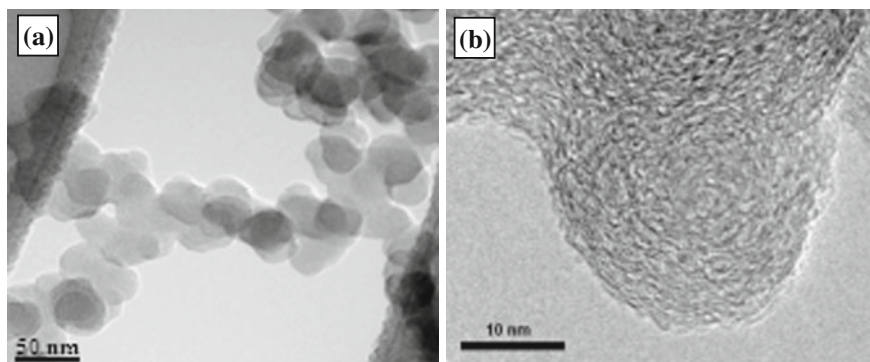


Fig. 13.3 TEM micrographs of Printex-U: (a) 50-nm scale and (b) 10-nm scale

13.2.4 X-Ray Diffraction

The X-Ray Diffraction (XRD) technique provides information about the crystalline structure of the investigated sample and has been widely employed for the structural characterization of carbon materials.

The fundamentals of this technique are based on the dispersion of one part of the incident X-ray radiation. This fraction is deviated from its original direction with the same energy due to its interaction with the radiated material. When an X-ray beam strikes one atom, the surrounding electrons of the atom start to oscillate with the period of the X-ray beam. If this incident beam comes into contact with a crystal (i.e., a group of atoms periodically ordered in the space), due to the order of the crystal, a diffracted beam (identical in wavelength and phase to the incident X-ray) will be emitted and measured (Birkholz 2006) meeting Bragg's Law. In a crystal, there are different plane families with different spacing, thus, different diffraction directions will exist. As the groups of spacings in a crystal are characteristic for each crystalline species, it may be considered that will not exist two crystalline substances with the same diffractogram diagram.

In a diffractogram, the radiation intensity after interacting with the sample (counts per second, Cps) is represented as function of the incident angle (θ). The crystallite height, L_c , and width, L_a , of the BSU, which are represented in Fig. 13.4a (Ciajolo et al. 2009) can be obtained from (002) and (10) diffraction peaks of the XRD pattern, respectively, by using the Scherrer equation (Cuesta et al. 1998; Darmstadt et al. 2000; Hussain et al. 2000; Iwashita et al. 2004; Seong and Boheman 2010), Eqs. (13.3) and (13.4). Whereas the graphitic interlayer spacing, d_{002} (Park and Seo 2007), may be obtained from (002) peak of the XRD pattern applying Bragg's law, Eq. (13.5). Figure 13.4a is a picture obtained by HRTEM, which have been skeletonized to graphically show these parameters. The percent of crystallinity can be also calculated (Hussain et al. 2000).

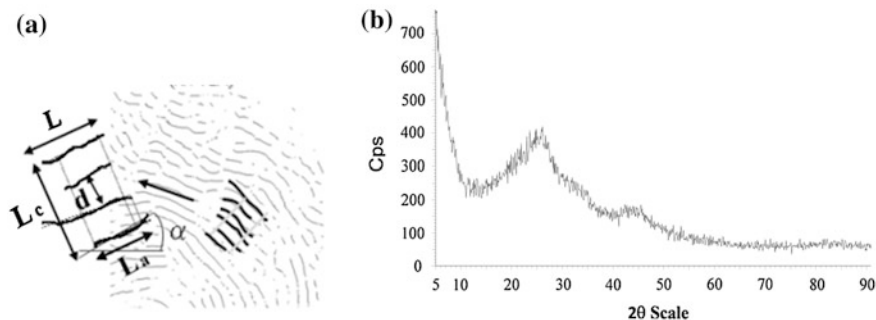


Fig. 13.4 (a) Schematization of the BSU in a skeletonized HRTEM soot image. L_a , L_c , and d_{002} are the diameter, height and interlayer spacing of the stacked layers (Reprinted with permission from Ciajolo et al. (2009)); (b) X-ray diffraction pattern of Printex-U sample (adapted from Arnal et al. 2012b)

$$L_c = \frac{K_{002}\lambda}{B_{002} \cos \theta_{002}} \quad (13.3)$$

$$L_a = \frac{K_{10}\lambda}{B_{10} \cos \theta_{10}} \quad (13.4)$$

$$d_{002} = \frac{\lambda}{\sin \theta_{002}} \quad (13.5)$$

where λ is the wavelength of the incident X-ray (1,54 Å for CuK α radiation), θ is the angle in degrees of the incident beam for (002) peak and (10) peak, K is a constant depending on the reflection plane: 0.89 for (002) peak and 1.84 for (10) peak, and B is the Full Width at Half-Maximum (FWHM) in radians of each respective peak (Cuesta et al. 1998; Lu et al. 2001).

Figure 13.4b shows the XRD pattern of Printex-U sample. The peak around $2\theta = 25\text{--}26^\circ$ corresponds to (002) reflection of carbon due to the stacking structure of graphitic basal planes (Arnal et al. 2012b). This angle, $2\theta = 25\text{--}26^\circ$, shifts to lower values and gets wider when increasing the degree of disorder, as observed for biomass chars (Guerrero et al. 2008). The background intensity is caused by the amorphous carbon concentration and the apparent asymmetry of the (002) band is due to the existence of the γ band on its left-hand side, at around 20° , which is associated with the packing of saturated structures such as the aliphatic side chains grafted on the edges of soot crystallites.

On the other hand, in Fig. 13.4b, the two-dimensional band (10), at $2\theta = 44^\circ$ can be noticed which is attributed to graphite-like atomic order, within a single plane. In comparison to the diffraction patterns observed for chars obtained from rice husk and eucalyptus (Guerrero et al. 2008), it can be concluded that the Printex-U sample has less amorphous structures and less aliphatic side chains, as reflected by the lower background intensity and (002) band asymmetry. These

results indicate that the structure of Printex-U particles is more ordered in comparison to biomass chars (Arnal et al. 2012b).

13.2.5 Raman Spectroscopy

Since the early 1970s, Raman spectroscopy has been employed to study the structural variations of carbon materials (Beyssac et al. 2003). Raman presents several advantages since it usually does not require any sample preparation and it is a nondestructive technique (although if the laser beam is focused on a small point or the power of the laser is too high, the sample could burn out). The structural defects in the basal plane of individual graphene layers may be obtained by Raman analysis (Lapuerta et al. 2012) giving an idea about the structural order/disorder of the carbonaceous samples. It is worth noting that Raman spectroscopy analyzes all kind of carbon structures present in the sample (from crystalline to amorphous), while in XRD only the crystalline phases are evidenced.

Raman spectroscopy is a technique based on the inelastic scattering of a monochromatic light, normally from a laser beam. The laser beam photons are absorbed by the sample and then reemitted. The frequency of the reemitted photons shifts to higher or lower values regarding the original monochromatic frequency. This shift is named Raman effect. The Raman effect is based on the molecular deformation in an electric field established by the molecular polarizability. Due to the periodic deformation, molecules start to vibrate with a characteristic frequency, emitting light of three different frequencies: Rayleigh, Stokes and Anti-Stokes scattering (Stokes and Anti-Stokes are symmetrically placed to Rayleigh band, left and right, respectively). Rayleigh scattering is produced when the excited molecule returns to the original vibrational state emitting with the same source's frequency. Although this signal represents the great majority, it is not useful at all for molecular characterization. Therefore, only a small fraction of the signal obtained corresponds to the useful scattering. Stokes scattering is hundreds of times greater than Anti-Stokes scattering (Atalla et al. 1992; Ferraro et al. 2003). For that reason, the usual way of working is employing the Stokes effect that, for convenience, it is placed in the positive part of the axis. In this way, Raman spectrum represents the intensity of the light scattered as function of the wavenumber shift, which is defined as the difference of the wavenumbers (cm^{-1}) between the observed radiation and the source radiation.

The most valuable data obtained from a Raman spectrum for carbon materials is found in a part of this Raman spectrum called first order region, corresponding to, approximately, a range between 1,000 and 1,800 cm^{-1} (Beyssac et al. 2003; Jawhari et al. 1995), whereas less work has been devoted to the second order region, attributed to overtone or combination scattering, in the 2,200–3,400 cm^{-1} range (Beyssac et al. 2003). In the first order region, the typical Raman spectrum of disordered carbon materials presents two prominent bands at ca. 1,350 cm^{-1} and at ca. 1,580 cm^{-1} (Ferrari and Robertson 2000). In order to obtain

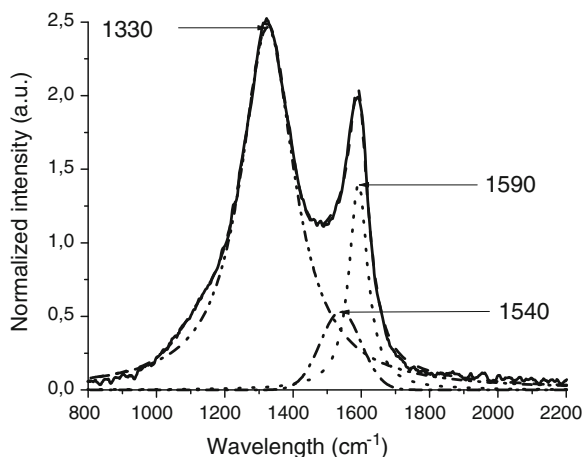
spectroscopic parameters, described later on, that accurately characterize different properties of some carbon blacks (Kameya and Hanamura 2011), a mathematic fit (deconvolution) consisting of Gaussian and/or Lorentzian lines use to be performed on the Raman spectrum. The two prominent bands just mentioned are generally named D (at ca. $1,350\text{ cm}^{-1}$) and G (at ca. $1,580\text{ cm}^{-1}$) peaks (Jawhari et al. 1995; Vollebregt et al. 2012). These peaks are the dominant in Raman spectra, even when carbon materials do not present a particular graphitic ordering (Robertson 2002). It is noteworthy to mention that G does not mean graphite. The G mode is due to the in-plane stretching vibration of any pair of sp^2 sites (C=C, both in chains and aromatic rings). The D mode represents the sp^2 sites due to 6-fold rings and not chains (Robertson 2002) becoming only active in presence of disorder, such as in-plane defects and heteroatoms (Beysac et al. 2003; Guerrero et al. 2008). Other bands could appear such as the so-called D' peak at about 1620 (which is found as a shoulder of the G peak), and $2,450$ and $3,250\text{ cm}^{-1}$ assigned to the non-zero-center phonons (Jawhari et al. 1995). Another band around $1,500\text{--}1,550\text{ cm}^{-1}$ can be noticed. This peak is ascribed to amorphous sp^2 bonded forms of carbon (Jawhari et al. 1995) and/or to defects outside the plane of aromatic layers like in tetrahedral carbons (Beysac et al. 2003). This band, depending on authors, may be either called A peak (Kameya and Hanamura 2011) or G2 peak (Guerrero et al. 2008; Shimodaira et al. 2001) or D3 peak (Beysac et al. 2003; Lapuerta et al. 2012).

It is noteworthy to mention the need of being very careful when treating the Raman spectra since depending on each author, the names of the peaks may vary, as just proved with the A, G2 or D2 band, which correspond to the same wavelength peak. It is important to keep in mind that the results of each researcher present in literature can only be compared to each other only if the laser is the same for all of them. The usual laser used in most of the works is an argon ion (Ar+) at 514.5 nm (Beysac et al. 2003; Guerrero et al. 2008; Lapuerta et al. 2012; Rodil et al. 2001; Shimodaira et al. 2001; Vollebregt et al. 2012) and for that reason, all the values given before for the bands correspond to this green laser (Ar+). However, other kinds of lasers like, e.g., frequency-doubled Nd:YVO₄ (Kameya and Hanamura 2011), or He-Ne at 633 nm (Haghseresht et al. 1999; Vollebregt et al. 2012) can be used. For the latter, differences between the D and G bands with He-Ne are more significant than with an Ar ion laser. With the use of another laser different from Ar+, the D band may present a dispersive behavior and its position can shift (Vollebregt et al. 2012).

The spectroscopic parameters, obtained from the deconvolution of Raman spectrum and which are helpful to evaluate the organization degree of the carbon materials (Beysac et al. 2003), are: peak position, bandwidth (Full Width at Half Maximum, FWHM) and different band intensity ratios.

Figure 13.5 shows the Raman spectrum of Printex-U in which the deconvolution with the fitting curves (one Gaussian line, at $1,540\text{ cm}^{-1}$, and two Lorentzian lines, at $1,330$ and $1,590\text{ cm}^{-1}$) may be observed (corresponding to the dotted and/or broken lines in Fig. 13.5). Haghseresht et al. (1999) report in their work that the increase of the I_{1330}/I_{1590} ratio (D to the G band ratio) testifies the increase of the

Fig. 13.5 Raman spectrum deconvolution for He–Ne laser at 633 nm with fitting curves of Printex-U



disordered carbon. In the case of Printex-U, a higher value of this ratio is obtained in comparison to carbon-based materials. This would imply that Printex-U is more disordered than those other carbon materials. Furthermore, the G band is sited around $1,590\text{ cm}^{-1}$ while this band was expected to appear at $1,582\text{ cm}^{-1}$. The strong influence of D' on G band could be the reason for this apparent shift (Vollebregt et al. 2012), confirming the disordered structure of Printex-U.

13.2.6 Thermogravimetry Analysis

Thermogravimetry Analysis (TGA) allows the determination of purity and thermal stability of a sample, the study of solid state reactions, the study of decomposition of inorganic and organic compounds, the determination of moisture, volatile and ash contents, the determination of kinetic parameters, the study of vaporizations, sorption, desorption and chemisorption of molecules on a sample, etc. (Brown 2001).

TGA evaluates the mass loss when a substance is heated at a given heating rate (dynamic TGA) or kept at constant temperature (static TGA). A plot of mass loss versus temperature (T) or heating time is defined thermogravimetric curve (TG plot). The sample mass losses are influenced by the set up parameters (heating rate, furnace atmosphere, geometry of sample holder and furnace, sample holder material, thermocouple location...), and by the material's chemical-physical features (particle size, sample packing, sample thermal conductivity, heat capacity of the sample material, occurrence of trapped gases or volatile species in the sample, sample stability, etc.).

TGA in oxidative environment is commonly used to study the oxidation behavior of carbon materials and the determination of kinetic parameters (Stratakis and Stamatelos 2003). TGA analyses performed in inert atmosphere are useful to evaluate the amount of volatile species (unburned fuel, PAH, etc.) adsorbed on the

sample and/or the presence on the surface of labile functional groups. TGA measurements are also used to analyze the chemical-physical modification occurring during the heating (volatilization, polymerization, polycondensation, cracking of side chains from aromatic rings and isomerization) (Luis 1987).

The TG plot of carbon materials typically exhibits different weight losses as function of temperature. The weight loss up to about 423 K is attributable to the water evaporation-desorption, a weight loss between 473 and 673 K is related to hydrocarbon desorption or decomposition of labile functional groups (hydroxyl, carboxylic, carbonylic, etc.). Between 673 and 1173 K, the weight loss is related to the oxidation of the carbonaceous core in the case of TG performed in oxidative environment (Paredes et al. 2009).

A correlation between nanostructure and reactivity toward oxidation of carbon-based materials was proposed (Vander Wal and Tomasek 2003). It was found that the oxidation reactivity is dependent on the accessibility of carbon in edge sites that are much more reactive than the basal plane carbon atoms, on the weakening of C–C bonds for effect of curvature due to five-membered rings (driving to an increase of sp^3 character, like in fulleroid structures) (Dresselhaus et al. 1996) and on the hydrogen content at the edge sites (Alfè et al. 2009). It was pointed out that (Alfè et al. 2009; Vander Wal and Tomasek 2003), provided that the lengths of the graphitic layers are the same (i.e., the accessibility of the carbon edge sites), the more the curvature of the soot (i.e., the surface area), the faster the reactivity toward oxidation.

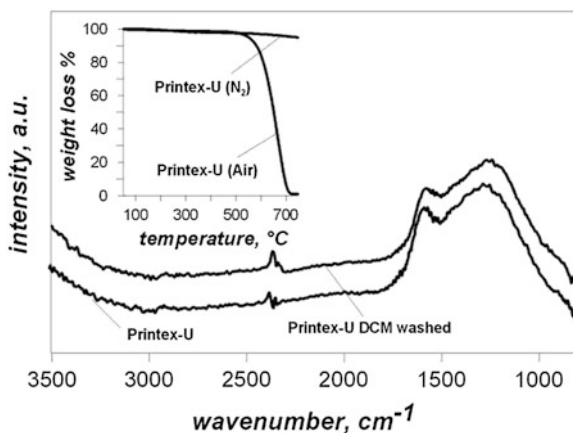
Printex-U sample exhibits a higher oxidation temperature at about 963 K (Fig. 13.6-inset) with respect to the combustion-formed carbon materials, 893–953 K (Alfè et al. 2009), indicating a higher graphitization degree, what is in agreement with the very low H content (with an H/C molar ratio <0.1). Moreover, the TG plot of Printex-U carried out in inert atmosphere (Fig. 13.6-inset) does not present any significant weight loss over the whole investigated temperature range, indicating a negligible surface functionalization and a negligible presence of species adsorbed on the sample surface.

13.2.7 Fourier Transform Infrared Spectroscopy

The Fourier Transform Infrared (FTIR) spectroscopy is a fundamental tool to investigate the local chemistry of the carbon materials. FTIR spectroscopy furnishes information about the occurrence of chemical functionality on the sample surface, and it is useful to obtain qualitative and semi-quantitative evaluation of the aromatic and aliphatic hydrogen content (Santamaria et al. 2010). FTIR spectroscopy is also useful to explore the occurrence of adsorbed species on soot surface.

FTIR spectra of black and strongly absorbent soot samples are commonly acquired in transmittance mode or by using the Attenuated Total Reflectance (ATR) method. In the case of transmittance spectra, soot is typically dried at 393 K for 3 h, mixed with dry KBr and used to prepare a 0.5–1 % KBr pellet of

Fig. 13.6 Inset: TG plots of Printex-U in oxidative (air) and in inert (nitrogen) environment; and ATR-FTIR spectra of Printex-U and Printex-U washed with DCM in the 800–3,500 cm^{-1} region



about 1 mm of path length whereas the ATR method allows the analysis of solid samples without further preparation. The infrared light penetration depth into the sample is typically between 0.5 and 2 μm , depending on the light wavelength, the angle of incidence and the indices of refraction of the ATR crystal (typically composed of germanium, zinc selenide and diamond) and the sample. One advantage of ATR-IR over transmission-IR is the limited path length into the sample. This avoids the problem of strong attenuation of the IR signal in highly absorbing media, such as black carbon materials.

ATR spectra of Printex-U and Printex-U extracted with dichloromethane (DCM), acquired in the 600–4,000 cm^{-1} spectral range by using a germanium crystal, are shown in Fig. 13.6. Spectra have been baseline corrected and shifted on the vertical axis for clarity.

The broad shape of the spectra is typical of a complex carbon network. The most characteristic feature of Printex-U is the 1,500–1,600 cm^{-1} band attributed to the C=C stretching vibrations of the sp^2 graphitic domains (Silverstein et al. 2005). The broadening of the region from 1,000 to 1,300 cm^{-1} due to the overlapping of the C–C and C–H plane deformation signals is consistent with a complex carbon aromatic network (Santamaria et al. 2010).

It is also noteworthy that bands below 950 cm^{-1} , characteristic of out-of-plane aromatic C–H bending vibrations and the signals at 3,030 cm^{-1} , corresponding to C–H aromatic stretching (Centrone et al. 2005) usually observed in combustion-formed soot, are not detected. Probably, this is due to the low percentage of C–H at the edge of the graphitic planes, as confirmed by the low hydrogen content detected by elemental analysis. Printex-U does not present detectable oxygenated functionalities, as demonstrated by the absence of the absorption bands attributable to oxygenated functionalities like: O–H stretching vibrations at 3,000–3,700 cm^{-1} , C=O stretching vibrations at 1,650–1,750 cm^{-1} , broadband due to the overlapping of C–OH and C–O stretching vibrations in the 1,300–1,100 cm^{-1} region (Acik et al. 2010).

It is also important to mention that Printex-U and Printex-U DCM-washed spectra (Fig. 13.6) exhibit quite similar features confirming the negligible presence of extractable species adsorbed on soot surface previously noticed by TGA.

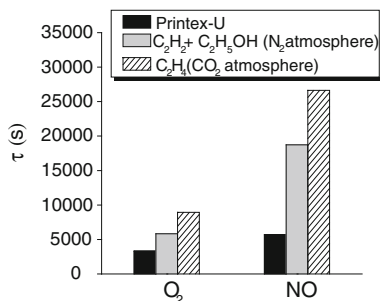
13.2.8 Soot Reactivity with O_2 and NO

Soot and NO_x are unwelcome products in many combustion systems where oxygen is also present. The reactions soot- O_2 and soot- NO within the combustion chamber may be used as a technique of minimization of the emissions (soot and NO) since they can react in-situ with each other, thus, reducing their emissions at the same time (Aarna and Suuberg 1997; Arnal et al. 2012b; Illán-Gómez et al. 1993; Mendiara et al. 2008). The reactions involved in the combustion of carbon materials are influenced by the reactivity of such materials. The reactivity of soot with different reactant gases may be considered itself as a characterization technique, since it provides information about the capability of the carbon material to interact with the gases. This reactivity would provide, as an overview, all the information given by some of the characterization techniques described above, e.g., the elemental analysis, the specific surface area, the distribution of the particles and graphene layer orientation, the crystalline and amorphous structure of the sample, TG analyses, FTIR spectra, etc. While results from these techniques may allow inferring how solid samples could interact with reactant gases, the specific reactivity measurement permit the quantification of reaction, providing thus the assessment of sample reactivity.

Nejar et al. (2007) and Wang et al. (1996) employed the temperature required to achieve the 50 % of the carbon conversion ($T_{50\%}$) to measure and to compare the reactivity of different carbon materials like charcoal, diesel soot and the commercial carbon black Printex-U, with Printex-U presenting the lowest reactivity. Aarna and Suuberg (1997) observed how the specific surface area affected the reactivity. They conclude that the reactivity measurement should be performed relatively to truly active surface area rather than total surface area. However, this measurement at present is not feasible to carry out since active surface areas have not been reliably characterized yet. According to Arnal et al. (2012b), Mendiara et al. (2008) and Ruiz et al. (2007), another way of measuring and comparing the reactivity of soot is to determine the time needed for the complete carbon conversion, τ . They calculate this parameter, τ , for interactions soot-reactant gases by using the Shrinking Core Model (SCM) with decreasing size particle and kinetic equations corresponding to chemical reaction control (Levenspiel 1999; Szekely et al. 1976), which is applicable for nonporous materials.

Following the latter method, the reactivity of Printex-U was measured and compared to two other kinds of soot, formed under well-controlled lab-scale conditions by hydrocarbon pyrolysis, determining the parameter τ for two reactant gases (O_2 and NO) at specific conditions. The application of the SCM with decreasing size particle and chemical reaction control implies the fitting of the

Fig. 13.7 Comparison of the complete carbon conversion times, τ , obtained in the reactivity experiments toward O_2 and NO for the different soot samples at 1,273 K (Reprinted with permission from Arnal et al. (2010))



experimental data to the following Eq. (13.6), connecting time, t , and carbon conversion, X_C :

$$\frac{t}{\tau} = 1 - (1 - X_C)^{1/3} \quad (13.6)$$

where τ is the time needed for the complete carbon conversion. The X_C value is calculated from Eq. (13.7) as the carbon weight reacted related to the initial amount of carbon in the reactor, W_{C0} :

$$X_C = \frac{W_{C0} - W_C}{W_{C0}} \quad (13.7)$$

The carbon weight remaining within the reactor at any time (W_C) is calculated from the measured time variation of CO and CO₂ concentrations (C_{CO} and C_{CO_2} , respectively) of the outlet gas, as well as the initial amount of carbon in the reactor (Arnal et al. 2012b).

The calculation of the τ value was obtained from the experiments performed for the three samples with 500 ppm of oxygen at 1,273 K and with 2,000 ppm of NO at 1,273 K (Arnal et al. 2010), Fig. 13.7.

In Fig. 13.7, it can be observed that the reactivity toward O_2 was higher than toward NO, since all soot samples presented lower complete carbon conversion times in the interaction with O_2 than in the interaction with NO. Among these three carbonaceous samples, Printex-U presented the lowest values of τ regarding its interaction with O_2 and NO, concluding that it was the most reactive sample toward both reactant gases at 1,273 K (Arnal et al. 2010).

13.2.9 UV-Visible Spectroscopy

The UV-Visible (UV-Vis) spectroscopy measures the absorption of radiation in the ultraviolet and visible region. UV-Vis spectroscopy is a suitable tool to achieve information on aromatic moieties of carbonaceous materials even if the interpretation of the spectra is generally complicated by the overlapping of bands from

different chromophores. The extended conjugation among unsaturated groups, typical of carbonaceous materials, causes a remarkable intensification of the absorption bands with a progressive shift of the maximum absorption toward higher wavelength.

UV and visible spectroscopy is commonly used for quantitative analysis. According to the Lambert–Beer law, the concentration of a substance in solution is directly proportional to the absorbance (A) of the solution:

$$A = \log_{10} \left(\frac{I_0}{I_t} \right) = \varepsilon c L \quad (13.8)$$

where I_0 is the intensity of the incident radiation, I_t is the intensity of the transmitted radiation, L is the length of the radiation path through the sample, c is the concentration of absorbing molecules, and ε is the extinction coefficient, a constant dependent only on the nature of the molecule and the wavelength of the radiation (Silverstein et al. 2005).

Instruments used for UV-Visible spectroscopy usually are single-beam instruments and double-beam instruments. The UV-Visible radiation sources are tungsten (visible region of the spectrum, 350–800 nm) and deuterium lamps (ultraviolet region of the spectrum, 160–350 nm).

UV-Visible absorption spectroscopy is suitable to obtain information on aromatic moieties of carbon materials. The UV-Visible spectra of PAH are characterized by a typical fine structure and high ε (Clar 1964; Silverstein et al. 2005). The increase of the conjugation and/or aromatisation degree causes a steep increase of the absorption coefficients that can vary by as much as a factor of two, three orders of magnitudes going from benzene to PAH (Clar 1964). Light PAH ($C < 24$) exhibit an UV-Visible spectrum with a fine structure with many peaks in the 250–350 nm range, whereas the UV-Visible spectrum of large PAH (L-PAH, $C > 24$) is shifted toward visible (Fetzer 2000) as a consequence of the higher conjugation of the π electron system. The location of rings, the chemical substitution and heteroatom content can significantly affect the transition energies (Silverstein et al. 2005). For example, alkyl substitution and the substitution with saturated rings shift the PAH absorption bands to higher wavelengths. PAH isomers with slightly differences in the arrangement of the aromatic units also exhibit very different UV-Visible spectra (Fetzer 2000).

Complex carbon-based materials present a variety of spectral response in terms of extinction coefficients (ε) as a consequence of the different extension of the aromatic domains. A typical broad shape extending in the visible region is generally ascribable to a large condensation degree of the aromatic moieties (Apicella et al. 2004).

In order to perform the UV-Visible investigation on Printex-U, the solid was extracted with DCM to remove species (mostly PAH) adsorbed on the particle surface. The extracted material was suspended in N-methyl-pyrrolidinone (NMP) by ultrasonic agitation obtaining a stable suspension. NMP (Shui 2005) is often used for the optical analysis of complex carbon-based materials even though its

strong absorption in the UV region limits the visualization of the spectra down to 260 nm. In Fig. 13.8, the height of normalized UV-Visible spectrum of DCM-washed Printex-U is reported together with the DCM-extract. The raw Printex-U is also reported for comparison. It is noteworthy that the spectra of raw Printex-U and DCM-washed Printex-U are indistinguishable, confirming the very low presence of species adsorbed on soot surface.

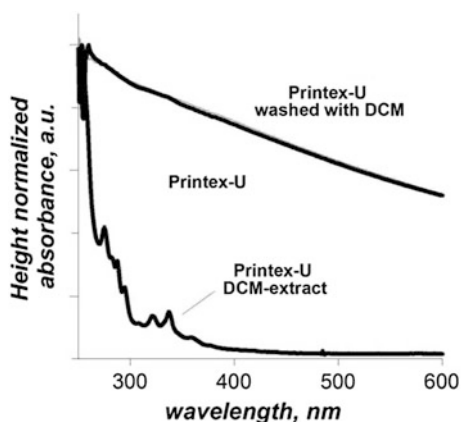
The spectrum of Printex-U and Printex-U extracted with DCM present the typical broad shape indicating the presence of highly conjugated systems as reported for complex carbon-based materials obtained through combustion processes (Apicella et al. 2004; Tregrossi et al. 2007). The spectrum of the DCM-extract exhibits the fine structure typical of light PAH with sharp peaks distributed in the UV region up to 250 nm indicative of PAH with 2–4 rings (Clar 1964; Silverstein et al. 2005). A deeper characterization of the DCM-extract will be proposed in the section dedicated to the Size Exclusion Chromatography.

In Fig. 13.9 the specific absorption coefficients of Printex-U are reported in comparison with soot formed in fuel-rich laminar premixed flames (Tregrossi et al. 2007) and reference carbon-based materials (Apicella et al. 2004).

Since soot suspensions are complex mixtures of unknown molecular weight, the absorption coefficients in the visible (500 nm) and in the UV (300 nm) have been evaluated on a mass basis (m^2/g). A detailed description of the spectroscopic properties and chemical-physical characteristics of the reference carbon-based materials is reported in Apicella et al. (2004). The absorption coefficients of the soot formed in fuel-rich flames are reported at different stages of soot formation, starting from the inception (I) up to end of flame (EOF) passing through a region where soot reaches its maximum formation rate (MFR).

The specific absorption of Printex-U is comparable, both in the UV and in the visible region, to the specific absorption of furnace carbon blacks (carbon black N110 and N330). The very high specific absorption in the visible region ($5 \text{ m}^2/\text{g}$) is comparable also to a benzene soot sampled at the end of the flame where the

Fig. 13.8 Height normalized absorption of Printex-U, DCM-washed Printex-U and DCM-extract



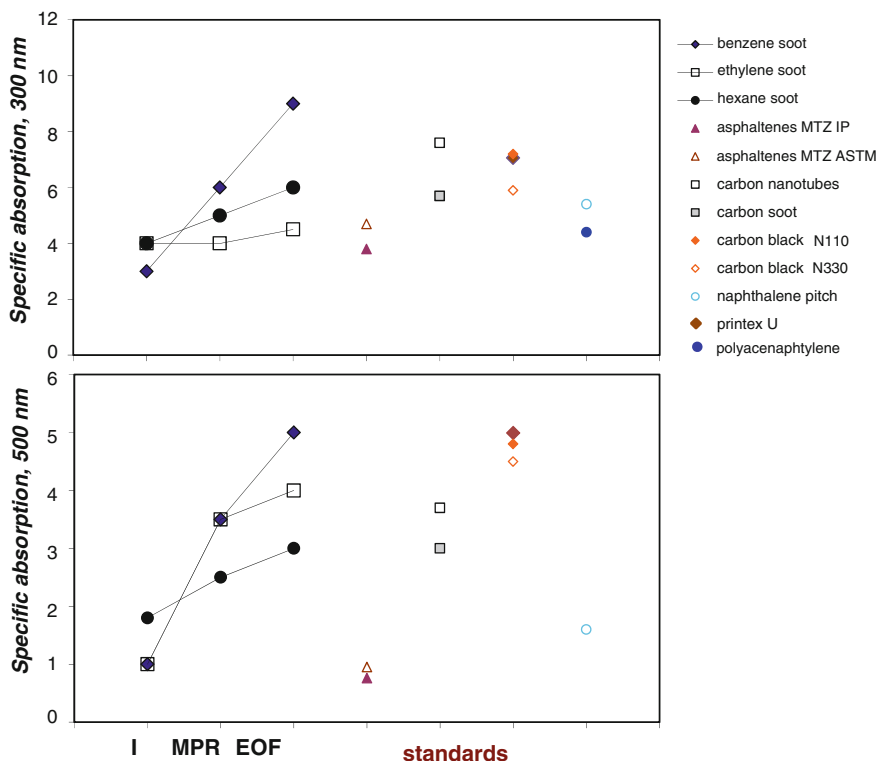


Fig. 13.9 Specific absorption (m^2/g) of carbon-based standard materials and flame-formed soot sampled in laminar flames at the soot inception (I), in the maximum soot formation rate (MFR) and at the end of flame (EOF) regions

aromatic moieties are well developed and soot reaches a good degree of structuration (Alfè et al. 2009; Russo et al. 2012).

13.2.10 Size Exclusion Chromatography

Size Exclusion Chromatography (SEC) is a separation technique based on the differing degrees of penetration of the sample molecules into the pores of a stationary phase. Each stationary phase has a separation range expressed in terms of a higher mass and a lower mass, below and above them it is possible to obtain a separation. Molecules/species with diameters greater than that of the pores flow through the column without being retained and they appear as a single peak in the chromatogram at the position corresponding to the interstitial volume (void volume of the column). Smaller molecules enter the pores and appear at different retention times in dependence of their penetration degree into the pores.

The most common stationary phases are reticulated organic polymers (polystyrene, divinylbenzene, polyvinylalchols...) or silica packed in beads with diameters of 2–10 μm . The bead pore diameters range between 4 and 500 nm. Stationary phases made up by polyvinylalchols or copolymerized with polyglyceromethacrylates or vinyl-polyacetates are commonly used for the separation of biological macromolecules (proteins, polysaccharides) in aqueous phases while polystyrene-divinylbenzene gels are used for the separation of macromolecules/particles dissolved/suspended in organic solvents (tetrahydrofuran, chloroform, dichloromethane). SEC allows the separation of masses ranging between 200 and 10^{10} u, so it offers a large domain of application in the separation of molecules. Each SEC column is characterized by a calibration curve built up through the analysis of standards with known masses. The calibration has to be performed with standard molecules as similar as possible to the sample under analysis.

The low solubility/suspensibility of carbon materials (PAH, tar, coal, soot, pitches, carbon black...) in organic solvents and the occurrence of interactions with the stationary phase (that is one of the common errors leading to an over- or underestimation of the molecular weight) often limit the application field of the SEC. The use of NMP as eluent allows the application of the SEC analysis to complex carbon-based samples offering a good stability of the suspensions and a limitation of the interactions with the stationary phase (Alfè et al. 2007, 2008; Apicella et al. 2003; Herod et al. 2000). Carbon-based samples are commonly analysed on polystyrene/divinylbenzene or pure divinylbenzene columns. Polystyrene (PS) standards are used to obtain the calibration curve because it was found that their retention times closely correlate with those of carbon materials (Alfè et al. 2007; Herod et al. 2000). A convenient detector for this kind of samples is a UV-Visible Diode Array.

SEC analyses of Printex-U and Printex-U DCM-extract have been performed on a PL-gel highly cross-linked individual-pore polystyrene/divinyl benzene column using NMP as eluent at a temperature of 353 K. SEC chromatogram of Printex-U presents a predominant single peak located beyond the exclusion limit of the SEC column (located at 10^5 u, not shown). Printex-U DCM-extract molecular weight (MW) distribution is more complex and it is reported in Fig. 13.10 together with the UV-Visible spectra acquired on-line for each chromatographic peak. The SEC chromatogram, usually reported as function of the sample elution time, is reported as function of the MW by transforming the elution time into MW on the basis of the MW calibration curve.

Printex-U DCM-extract is characterized by the predominance of a sharp peak in the 300–500 u range (peak “a”) and a smaller peak in the range from 500 to 800 u (peak “b”). A broad MW distribution in the 1,000–2,000 MW range is visible (peak “c”). A minor peak is also detected at $\text{MW} > 10^5$ u (peak “d”). The UV-Visible spectrum associated to the peak “a” presents the typical PAH fine structure which dominates the Printex-U DCM-extract total UV-Visible spectrum (Fig. 13.10). Peak “b” presents a broad absorption in the 300–350 nm region, suggesting the presence of oxygenated compounds (Silverstein et al. 2005). It has to be underlined that the presence of oxygenated groups could shift the elution

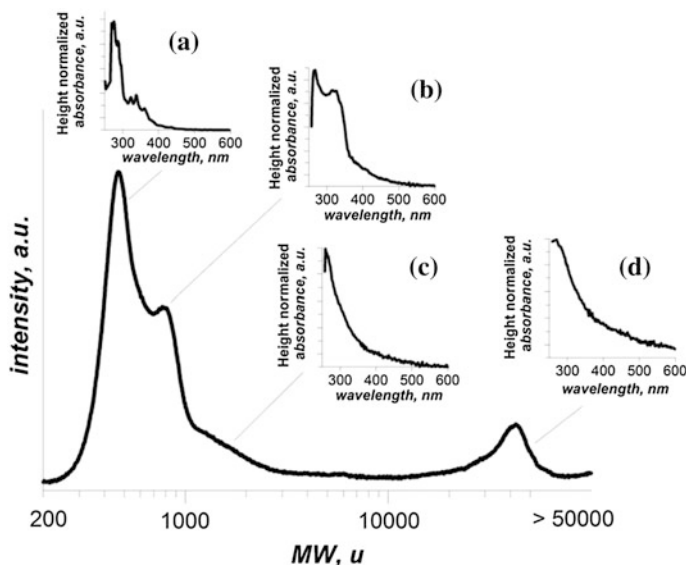


Fig. 13.10 SEC chromatogram ($\lambda = 350$ nm) of Printex-U DCM-extract. The insets (a–d) represent the normalized UV–Visible spectra acquired on-line for each chromatographic peak

time downstream because of a mechanism of nonpure exclusion with the column stationary phase. Peak “c” and peak “d” present the broad featureless structure typical of high MW aromatic species.

13.2.11 Fluorescence Spectroscopy

This section deals with the UV-Visible fluorescence spectroscopy of carbonaceous materials in liquid phase. This approach is complementary to in-situ and on-line diagnostics for soot and PAH described in [Chap. 12](#).

UV-Visible fluorescence spectroscopy is more specific and more selective than absorption spectroscopy, but the spectra deconvolution of complex mixture is difficult to be achieved because of the occurrence of self-quenching, self-absorption and energy transfer processes that can depress and strongly modify the fluorescence signal.

Absorption of an ultraviolet or visible photon promotes a valence electron from its ground state to an excited state with conservation of the electron’s spin. A molecule in the excited state will spontaneously return to the ground state releasing the energy absorbed during the excitation process. Fluorescence is the phenomenon associated with the release, in the form of a photon, of the absorbed energy between two energy levels with the same spin. Fluorescence is only

observed if the photon emission is more efficient in the relaxation mechanism than the combination of internal conversion and vibrational relaxation (Berlman 1971).

The fraction of excited molecules returning to the ground state by fluorescence is the fluorescent quantum yield, Φ_f , ranging from 1 (all the molecules in an excited state undergoes fluorescence) to 0 (fluorescence does not occur). The intensity of fluorescence, I_f , is proportional to the fluorescence quantum yield and to the amount of absorbed radiation $N\sigma I_0$:

$$I_f = k\phi_f N\sigma I_0 \quad (13.9)$$

where k is a constant accounting for the efficiency of collecting and detecting the fluorescent emission, σ the absorption cross-section, N the concentration and I_0 the intensity of the incident light (at the absorption wavelength).

The intensity of fluorescence increases with the increase of quantum yield, incident power of the excitation source, molar absorptivity and concentration of the fluorescing species. Fluorescence is high for aromatic systems and for aromatic molecules with rigid planar structures. The unsubstituted, nonheterocyclic aromatic compounds show high fluorescence quantum yield. Fluorescence is enhanced by the presence of electron-donating groups and decreased by electron-withdrawing groups. The fluorescence quantum yield is also influenced by temperature, solvent and pH. The analyte concentration is a key parameter which is able to influence the shape and the intensity of the fluorescence spectrum. In concentrated solution, quenching effects can take place causing a decrease of the fluorescence emission. Despite the necessity of working with dilute solutions, fluorimetry is a very sensitive technique and the detection limit of a fluorescent compound is often 1,000 times lower than the detection limit of the UV-Visible spectroscopy.

Fluorescence spectra are recorded by measuring the intensity of emitted radiation as function of either the excitation wavelength or the emission wavelength. In the emission spectrum, a fixed wavelength is used to excite the molecules, and the intensity of the emitted radiation is monitored as function of wavelength. The excitation spectrum provides a convenient means for selecting the best excitation wavelength for a quantitative or qualitative analysis. The synchronous fluorescence technique also furnishes useful information about fluorescent molecules. The synchronous spectrum is acquired by scanning simultaneously the excitation and emission wavelengths keeping constant the difference between the wavelengths ($\Delta\lambda$). The synchronous fluorescence technique provides spectra with more sharp peaks than the conventional emission spectra and it is particularly useful when it is applied to complex fluorescent mixtures. In a mixture of fluorescent components, each peak in a synchronous spectrum can be roughly associated to single component or to a class of components of the mixture, allowing the possibility of a multicomponent analysis (Vo-Dinh 1978).

In contrast to instruments of absorption spectroscopy, the optical paths for the source and detector are usually positioned at an angle of 90° . The excitation source is usually a high-pressure Xe arc lamp, which has a continuous emission spectrum

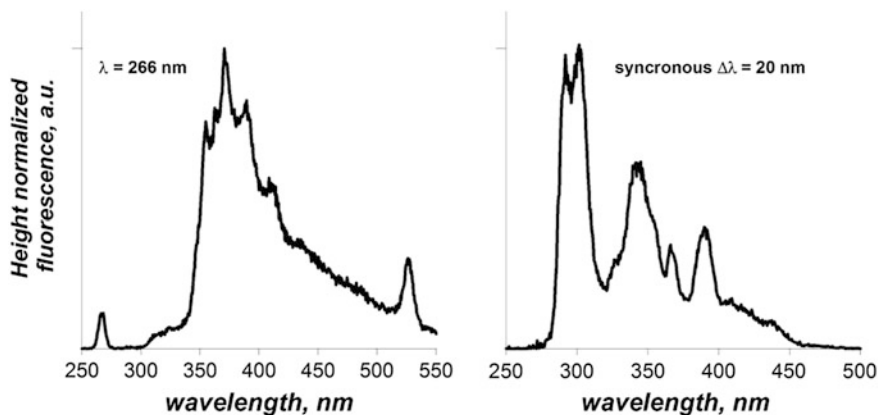


Fig. 13.11 Fluorescence emission spectra ($\lambda_{\text{exc}} = 266$ nm and synchronous) of Printex-U DCM-extract

that provides intense emission lines distributed throughout the ultraviolet and visible regions.

Optical methods based on fluorescence spectroscopy techniques are largely used for the analysis of PAH extracted by solvents (DCM, CS_2 , and NMP are the commonly used solvents) from carbonaceous materials. The fluorescence spectra of light PAH ($C < 24$) exhibit a fine structure with very intense peaks (quantum efficiency ~ 0.1). The emission in the UV region (300–350 nm) is typically of two and three rings PAH while the emission moves between 350 and 500 nm for four and five rings PAH (Berlman 1971). Polymer-like aromatic species with high molecular weights (tar-like, pitch, asphaltenes, char...) generate broad fluorescence spectra shifted toward the visible region (350–700 nm) and without the fine structure (Berlman 1971). These aromatic materials are characterized by lower quantum fluorescence efficiencies because of their nonrigid and nonplanar structure (Alfè et al. 2008; Bruno et al. 2008).

In the case of Printex-U only the DCM-extract component is fluorescent. In Fig. 13.11, the emission spectrum acquired by using excitation at 266 nm and the synchronous spectrum are reported. The fluorescence emission spectrum presents a fine structure with a higher intensity in the 250–400 nm indicating the presence of light PAH (2–4 rings) as confirmed by the UV-Visible analysis. The synchronous spectrum is more structured and presents four peaks, so roughly four classes of PAH can be counted as components of the mixture.

Acknowledgments This work was made with the support and in the frame of COST Action CM0901. Evonik Degussa GmbH is acknowledged for the Printex-U supplied. C. Arnal, M.U. Alzueta, A. Millera and R. Bilbao express their gratitude to the European Social Fund (ESF), MINECO and FEDER (Project CTQ2012-34423) for financial support. C. Arnal acknowledges the Ministerio de Educación for the predoctoral grant awarded (AP2008-03449), COST Action CM0901 and Obra social CAI through Programa Europa for the grants awarded. M. Alfè, V. Gargiulo and A. Ciajolo gratefully acknowledge the Ministero dello Sviluppo Economico within

the “Accordo di Programma CNR-MSE, Gruppo Tematico Carbone Pulito- Fondo per il Finanziamento Attività di Ricerca e Sviluppo di Interesse Generale per il Sistema Elettrico Nazionale and NIPS (Nanoparticle Impact on Pulmonary Surfactant Interfacial Properties)-Seed Project 2009-IIT for the financial support.

References

- Aarna I, Suuberg EM (1997) A review of the kinetics of the nitric oxide carbon reaction. *Fuel* 76:475–491
- Acik M, Mattevi C, Gong C et al (2010) The role of intercalated water in multilayered graphene oxide. *ACS Nano* 4:5861–5868
- Ahlström AF, Odenbrand CUI (1989) Combustion characteristics of soot deposits from diesel engines. *Carbon* 27:475–483
- Alfè M, Apicella B, Barbella R et al (2007) Distribution of soot molecular weight/size along premixed flames as inferred by size exclusion chromatography. *Energy Fuels* 21:136–140
- Alfè M, Apicella B, Tregrossi A et al (2008) Identification of large polycyclic aromatic hydrocarbons in carbon particulates formed in a fuel-rich premixed ethylene flame. *Carbon* 46:2059–2066
- Alfè M, Apicella B, Barbella R et al (2009) Structure-property relationship in nanostructures of young and mature soot in premixed flames. *Proc Combust Inst* 32:697–704
- Alfè M, Apicella B, Rouzaud JN et al (2010) The effect of temperature on soot properties in premixed methane flames. *Combust Flame* 157:1959–1965
- Apicella B, Barbella R, Ciajolo A et al (2003) Comparative analysis of the structure of carbon materials relevant in combustion. *Chemosphere* 51:1063–1069
- Apicella B, Alfè M, Barbella R et al (2004) Aromatic structures of carbonaceous materials and soot inferred by spectroscopic analysis. *Carbon* 42:1583–1589
- Armas O, Yehliu K, Boehman AL (2010) Effect of alternative fuels on exhaust emissions during diesel engine operation with matched combustion phasing. *Fuel* 89:438–456
- Arnal C, Esarte C, Abián M et al (2010) Characterization and reactivity of soots obtained under different combustion conditions. *Chem Eng Trans* 22:251–256
- Arnal C, Alzueta MU, Millera A et al (2012a) Influence of water vapor addition on soot oxidation at high temperature. *Energy* 43:55–63
- Arnal C, Alzueta MU, Millera A et al (2012b) Experimental and kinetic study of the interaction of a commercial soot with NO at high temperature. *Combust Sci Technol* 184:1191–1206
- Atalla RH, Agarwal UP, Bond JS (1992) Raman spectroscopy. In: Lin SY, Dence CW (eds) *Methods in lignin Chemistry*. Springer-Verlag, Berlin
- Atribak I, Bueno-López A, García-García A (2010) Uncatalysed and catalysed soot combustion under NO_x + O₂: Real diesel versus model soots. *Combust Flame* 157:2086–2094
- Berlman IB (1971) *Handbook of fluorescence spectra of aromatic molecules*, 2nd edn. Academic Press, New York
- Beysac O, Goffé B, Petit JP et al (2003) On the characterization of disordered and heterogeneous carbonaceous materials by Raman spectroscopy. *Spectrochim Acta A* 59:2267–2276
- Biagini E, Pintus S, Tognotti L (2005) Characterization of high heating-rate chars from alternative fuels using an electrodynamic balance. *Proc Combust Inst* 30:2205–2212
- Birkholz M (2006) *Thin film analysis by X-ray scattering*. Wiley-VC H, Weinheim
- Brown ME (2001) *Introduction to thermal analysis*, 2nd edn. Kluwer Academic Publisher, London
- Brunauer S, Emmett PH, Teller E (1938) Adsorption of gases in multimolecular layers. *J Am Chem Soc* 60:309–319

- Brunauer S, Deming LS, Deming WE et al (1940) On a theory of the van der Waals adsorption of gases. *J Am Chem Soc* 62:1723–1732
- Bruno A, Alfè M, Ciało A et al (2008) Time-resolved fluorescence polarization anisotropy of multimodal samples: the asphaltene case. *Appl Phys B: Lasers Opt* 90:61–67
- Bushell GC, Yan YD, Woodfield D, Raper J, Amal R (2002) On techniques for the measurement of the mass fractal dimension of aggregates. *Adv Colloid Interface Sci* 95:1–50
- Buzea C, Pacheco Blandino II, Robbie K (2007) Nanomaterials and nanoparticles: sources and toxicity. *Biointerphases* 2:MR17-MR172
- Cai J, Lu N, Sorensen CM (1995) Analysis of fractal cluster morphology parameters: structural coefficient and density autocorrelation function cutoff. *J Colloid Int Sci* 171:470–473
- Carrasco-Marín F, López-Ramón MV, Moreno-Castilla C (1993) Applicability of the Dubinin-Radushkevich equation to carbon dioxide adsorption on activated carbons. *Langmuir* 9:2758–2760
- Centrone A, Brambilla L, Renouard T et al (2005) Structure of new carbonaceous materials: the role of vibrational spectroscopy. *Carbon* 43:1593–1609
- Cetin E, Moghtaderi B, Gupta R et al (2004) Influence of pyrolysis conditions on the structure and gasification reactivity of biomass chars. *Fuel* 83:2139–2150
- Ciało A, Alfè M, Apicella B et al (2009) Characterization of carbon particulate matter relevant in combustion. *Chem Eng Trans* 17:99–104
- Clar E (1964) Polycyclic hydrocarbons. Academic Press, New York
- Cuesta A, Dhamelinourt P, Laureyns J et al (1998) Comparative performance of X-ray diffraction and Raman microprobe techniques for the study of carbon materials. *J Mater Chem* 8:2875–2879
- D’Anna A (2009) Combustion-formed nanoparticles. *Proc Combust Inst* 32:593–613
- Darmstadt H, Roy C, Kaliaguine S et al (2000) Solid state ¹³C-NMR spectroscopy and XRD studies of commercial and pyrolytic carbon blacks. *Carbon* 38:1279–1287
- Donohue MD, Aranovich GL (1998) Adsorption hysteresis in porous solids. *J Colloid Interf Sci* 205:121–130
- Dresselhaus MS, Dresselhaus G, Eklund PC (1996) Science of fullerenes and carbon nanotubes. Elsevier Science, Academic Press, USA
- Ferrari AC, Robertson J (2000) Interpretation of Raman spectra of disordered and amorphous carbon. *Phys Rev B: Condens Matter* 61:14095–14107
- Ferraro JR, Nakamoto K, Brown CW (2003) Introductory Raman spectroscopy, 2nd edn. Elsevier, San Diego
- Fetzer JC (2000) Large ($C \geq 24$) Polycyclic aromatic hydrocarbons: Chemistry and analysis. Wiley-Interscience, New York
- Giechaskiel B, Alföldy B, Drossinos Y (2009) A metric for health effects studies of diesel exhaust particles. *J Aerosol Sci* 40:639–651
- González-Martín ML, Valenzuela-Calahorra C, Gómez-Serrano V (1994) Characterization study of carbonaceous materials. Calorimetric heat of adsorption of p-nitrophenol. *Langmuir* 10:844–854
- Goodhew PJ, Humphreys J, Beanland R (2001a) The scanning electron microscope. In: *Electron Microscopy and Analysis*, 3rd edn. (electronic copy) Taylor and Francis Books UK. Available via Core Materials. <http://es.scribd.com/doc/27762962/The-Scanning-Electron-Microscope>. Accessed 26 Feb 2012
- Goodhew PJ, Humphreys J, Beanland R (2001b) Microscopy with light and electrons. In: *Electron Microscopy and Analysis*, 3rd edn. (electronic copy) Taylor and Francis Books UK. Available via Core Materials. <http://es.scribd.com/doc/27761327/Microscopy-With-Light-and-Electrons>. Accessed 26 Feb 2012
- Guerrero M, Ruiz MP, Millera A et al (2008) Characterization of biomass chars formed under different devolatilization conditions: differences between rice husk and eucalyptus. *Energy Fuels* 22:1275–1284
- Hansen J, Nazarenko L (2004) Soot climate forcing via snow and ice albedos. *P Natl Acad Sci USA* 101:423–428

- Haghseresh F, Lu GQ, Whittaker AK (1999) Carbon structure and porosity of carbonaceous adsorbents in relation to their adsorption properties. *Carbon* 37:1491–1497
- Herod AA, Lazaro MJ, Suelves I et al (2000) Size exclusion chromatography of soots and coal-derived materials with 1-methyl-2-pyrrolidinone as eluent: Observations on high molecular mass material. *Energy Fuels* 14:1009–1020
- Higgins KJ, Jung H, Kittelson DB et al (2003) Kinetics of diesel nanoparticle oxidation. *Environ Sci Technol* 37:1949–1954
- Hussain R, Qadeer R, Ahmad M et al (2000) X-ray diffraction study of heat-treated graphitized and ungraphitized carbon. *Turk J Chem* 24:177–183
- Illán-Gómez MJ, Linares-Solano A, Salinas-Martínez de Lecea C et al (1993) NO reduction by activated carbons. I. The role of carbon porosity and surface-area. *Energy Fuels* 7:146–154
- Ishiguro T, Takatori Y, Akihama K (1997) Microstructure of diesel soot particles probed by Electron-Microscopy- first observation of inner-core and outer shell. *Combust Flame* 108:231–234
- Iwashita N, Park CR, Fujimoto H et al (2004) Specification for a standard procedure of X-ray diffraction measurements on carbon materials. *Carbon* 42:701–714
- Jäger C, Henning T, Schlögl R et al (1999) Spectral Properties of Carbon Black. *J Non-Cryst Solids* 258:161–179
- Jakubov TS (2008) The reasons behind adsorption hysteresis In: Bottani EJ and Tascón JMD (eds) *Adsorption by carbons*, Elsevier Ltd., UK
- Jawhari T, Roid A, Casado J (1995) Raman-spectroscopic characterization of some commercially available carbon-black materials. *Carbon* 33:1561–1565
- Jung J, Lee JH, Song S et al (2008) Measurement of soot oxidation with $\text{NO}_2\text{-O}_2\text{-H}_2\text{O}$ in a flow reactor simulating diesel engine DPF. *Int J Automot Technol* 9:423–428
- Kameya Y, Hanamura K (2011) Kinetic and Raman spectroscopic study on catalytic characteristics of carbon blacks in methane decomposition. *Chem Eng J* 173:627–635
- Kapoor A, Ritter JA, Yang RT (1989) On the Dubinin-Radushkevich equation for adsorption in microporous solids in the Henry's law region. *Langmuir* 5:1118–1121
- Köylü ÜÖ, Faeth GM, Farias TL, Carvalho MG (1995a) Fractal and projected structure properties of soot aggregates. *Combust Flame* 100:621–633
- Köylü ÜÖ, Xing Y, Rosner DE (1995b) Fractal morphology analysis of combustion-generated aggregates using angular light scattering and electron microscope images. *Langmuir* 11:4848–4854
- Kühner G, Voll M (1993) Manufacture of carbon black. In: Donnet JB, Bansal RC, Wang MJ (eds) *Carbon black*, 2nd edn. Marcel Dekker Inc., New York
- Lapuerta M, Oliva F, Agudelo JR et al (2012) Effect of fuel on the soot nanostructure and consequences on loading and regeneration of diesel particulate filters. *Combust Flame* 159:844–853
- Levenspiel O (1999) *Chemical reaction engineering*, 3rd edn. John Wiley & Sons Inc., New York
- Lu L, Sahajwalla V, Kong C et al (2001) Quantitative X-ray diffraction analysis and its application to various coals. *Carbon* 39:1821–1833
- Lu L, Kong C, Sahajwalla V et al (2002) Char structural ordering during pyrolysis and combustion and its influence on char reactivity. *Fuel* 81:1215–1225
- Luis IC (1987) Chemistry of pitch carbonization. *Fuel* 66:1527–1532
- Mandelbrot BB (1975) *Les objets fractals: forme, hasard et dimension*. Flammarion, Paris
- Martín-Martínez JM (1990) Generalidades sobre adsorción física de gases y vapores en carbones. In: *Secretariado de Publicaciones de la Universidad de Alicante* (ed) *Adsorción física de gases y vapores por carbones*, Espagrafic (electronic copy). Available via Universidad de Alicante: http://rua.ua.es/dspace/bitstream/10045/4291/4/adsorcion_fisica_2.pdf. Accessed 12 Feb 2012
- Megaridis CM, Dobbins RA (1990) Morphological description of flame-generated materials. *Combust Sci Technol* 71:95–109
- Mendiara T, Domene MP, Millera A et al (2005) An experimental study of the soot formed in the pyrolysis of acetylene. *J Anal Appl Pyrol* 74:486–493

- Mendiara T, Alzueta MU, Millera A et al (2008) Influence of the NO concentration and the presence of oxygen in the acetylene soot reaction with NO. *Energy Fuels* 22:284–290
- Neeft JPA, Nijhuis TX, Smakman E et al (1997) Kinetics of the oxidation of diesel soot. *Fuel* 76:1129–1136
- Nejar N, Makkee M, Illán-Gómez MJ (2007) Catalytic removal of NO_x and soot from diesel exhaust: Oxidation behaviour of carbon materials used as model soot. *Appl Catal B* 75:11–16
- Oberlin A (1989) TEM studies of carbonization and graphitization. In: Throrer PA (ed) *Chemistry and physics of carbon*, vol 22. Marcel Dekker Inc., New York, pp 1–143
- Paredes JI, Villar-Rodil S, Solis-Fernandez P et al (2009) Atomic force and scanning tunneling microscopy imaging of graphene nanosheets derived from graphite oxide. *Langmuir* 25:5957–5968
- Park HY, Seo SI (2007) Characteristics of residual carbon derived from the combustion of vacuum residue in a test furnace. *Environ Eng Res* 12:109–117
- Peña MA (2011) Introducción. In: Faraldos M, Goberna C (eds) *Técnicas de análisis y caracterización de materiales*, 2nd edn. Consejo Superior de Investigaciones Científicas, Madrid
- Rodil SE, Ferrari AC, Robertson J et al (2001) Raman and infrared modes of hydrogenated amorphous carbon nitride. *J Appl Phys* 89:5425–5430
- Robertson J (2002) Diamond-like amorphous carbon. *Mater Sci Eng R* 37:129–281
- Rouzaud JN, Clinard C (2002) Quantitative high-resolution transmission electron microscopy: a promising tool for carbon materials characterization. *Fuel Process Technol* 77–78:229–235
- Ruiz MP, Callejas A, Millera A et al (2007) Reactivity towards O₂ and NO of the soot formed from ethylene pyrolysis at different temperatures. *Int J Chem Reactor Eng* 5:A50
- Russo C, Stanzione F, Tregrossi A et al (2012) The effect of temperature on the condensed phases formed in fuel-rich premixed benzene flames. *Combust Flame* 159:2233–2242
- Sánchez NE, Callejas A, Millera A et al (2012) Formation of PAH and soot during acetylene pyrolysis at different gas residence times and reaction temperatures. *Energy* 43:30–36
- Santamaria A, Yang N, Eddings E et al (2010) Chemical and morphological characterization of soot and soot precursors generated in an inverse diffusion flame with aromatic and aliphatic fuels. *Combust Flame* 157:33–42
- Seong HJ, Boehman AL (2010) Impact of intake oxygen enrichment on oxidative reactivity and properties of diesel soot. *Energy Fuels* 25:602–616
- Setiabudi A, Makkee M, Moulijn JA (2004) The role of NO₂ and O₂ in the accelerated combustion of soot in diesel exhaust gases. *Appl Catal B* 50:185–194
- Sharma A, Kyotani T, Tomita A (1999) A new quantitative approach for microstructural analysis of coal char using HRTEM images. *Fuel* 78:1203–1212
- Shim H-S, Hajaligol MR, Baliga VL (2004) Oxidation behavior of biomass chars: pectin and *Populus deltoides*. *Fuel* 83:1495–1503
- Shim H-S, Hurt RH, Yang NYC (2000) A methodology for analysis of 002 lattice fringe images and its application to combustion-derived carbons. *Carbon* 38:29–45
- Shimodaira N, Masui A, Takada A et al (2001) Structural information from the Raman spectra of activated carbon materials. American Carbon Society, 25th Biennial Conference on Carbon, Hyatt Regency Lexington, Lexington, 14–19 July 2001
- Shui HF (2005) Effect of coal extracted with NMP on its aggregation. *Fuel* 84:939–941
- Silverstein M, Webster FX, Kiemle D (2005) *Spectrometric identification of organic compounds*, 7th edn. Wiley, New York
- Sing KSW (2008) Overview of physical adsorption by carbons. In: Bottani EJ and Tascón JMD (eds) *Adsorption by carbons*, Elsevier Ltd., UK
- Sing KSW, Everett DH, Haul RAW et al (1985) Reporting physisorption data for gas/solid systems with special reference to the determination of surface area porosity. *Pure Appl Chem* 57:603–619
- Song J, Song C, Tao Y et al (2011) Diesel soot oxidation during the late combustion phase. *Combust Flame* 158:446–451

- Stratakis GA, Stamatelos AM (2003) Thermogravimetric analysis of soot emitted by a modern diesel engine run on catalyst-doped fuel. *Combust Flame* 132:157–169
- Szekely J, Evans JW, Sohn HY (1976) *Gas-solid reactions*. Academic Press Inc., New York
- Tregrossi A, Barbella R, Ciajolo A et al (2007) Spectral properties of soot in the UV-Visible range. *Combust Sci Technol* 179:371–385
- Vander Wal RL, Tomasek AJ (2003) Soot oxidation: dependence upon initial nanostructure. *Combust Flame* 134:1–9
- Vo-Dinh T (1978) Multicomponent analysis by synchronous luminescence spectrometry. *Anal Chem* 50:396–401
- Vollebregt S, Ishihara R, Tichelaar FD et al (2012) Influence of the growth temperature on the first and second-order Raman band ratios and widths of carbon nanotubes and fibers. *Carbon* 50:3542–3554
- Wang WX, Thomas KM, Cai HY et al (1996) NO release and reactivity of chars during combustion: The effect of devolatilization temperature and heating rate. *Energy Fuels* 10:409–416
- Williams DB, Carter CB (2009) *Transmission Electron Microscopy*, 2nd edn. Springer, New York
- Xi J, Zhong BJ (2006) Soot in diesel combustion systems. *Chem Eng Technol* 29:665–673

Chapter 14

An Advanced Multi-Sectional Method for Particulate Matter Modeling in Flames

Andrea D'Anna and Mariano Sirignano

Abstract An advanced multi-sectional approach for modeling the gas-to-particle process in flames is presented. It follows the chemical evolution and the internal structure of particles formed in flames, fully coupled with the main pyrolysis and oxidation of the fuel. The multi-sectional method is included in a detailed mechanism of hydrocarbon pyrolysis and oxidation which considers the detailed formation of important gaseous species such as acetylene, benzene, and polycyclic aromatic hydrocarbons (PAHs); the lumped molecular growth of aromatics and particle inception; and the lumped particle growth and oxidation. The complete model is tested without any adjustments to the scheme on premixed and non-premixed flames of various hydrocarbons at atmospheric pressure. Predictions are compared with experimental data on gas-phase species concentrations, particle volume fractions, H/C and sizes in laminar premixed and in co-flowing non-premixed flames.

14.1 From Experimental Evidence to Model Development

Our understanding of soot formation has evolved from a phenomenological description to almost quantitative modeling in the last 10 years due to the progress of diagnostic tools, which today allow analysis on an almost atomic level of the particles, either offline or in situ (see [Chaps. 12](#) and [13](#)). Their use has improved our knowledge about the physical and chemical properties of combustion-formed particles and also about the kinetics of particle formation in combustion environments.

A. D'Anna (✉) · M. Sirignano
Dipartimento di Ingegneria Chimica, dei Materiali e della Produzione Industriale,
Università degli Studi di Napoli Federico II, Piazzale Tecchio 80 80125 Naples, Italy
e-mail: anddanna@unina.it

A broad range of particles with dimensions ranging from molecular size to some hundreds of nanometers are formed in combustion. The “molecular” particles behave spectroscopically as polycyclic aromatic hydrocarbons (PAH) absorbing UV light and showing an intense broadband fluorescence when excited with lasers in the UV. At the same time, they interfere with the laser light giving rise to more scattering than gas-phase compounds, thus indicating that they have a cross-section larger than gases and are thus typical of condensed phases. This class of particles is often referred to as nanoparticle of organic carbon (NOC) or visible-transparent nanoparticles (D'Anna 2009a).

As the size increases a solid-state character clearly appears. Larger particles emit thermal radiation once heated-up by an intense laser pulse and absorb light from UV to the visible range. A continuous transformation of the smaller particles through coagulation, dehydrogenation, and surface addition of gas-phase molecules—acetylene and PAHs—into larger particles leads to the formation of primary soot particles, with sizes from 10 to 40 nm, and soot aggregates whose size can reach values as high as 1 μm .

Chemical and spectroscopic characterization of the particles coupled with morphological studies revealed that ordered and disordered structures coexist in the soot particles (see Chap. 13). The order arises due to stacking of planar polycyclic aromatic hydrocarbons (PAHs) to form parallel atomic layers; the disordered part is due to the presence of randomly oriented and/or nonplanar PAHs. The combustion environment in which the particles are formed determines the final concentration of the particles as well as their organization on an atomic scale. Low temperatures, short residence times, and relatively low concentration of PAHs in the flame favor the formation of particles with disordered structures. Higher temperatures, longer residence times, and relatively high concentration of PAHs favor the formation of ordered structures with wide regions containing parallel stacks of PAHs (Alfè et al. 2009; Russo et al. 2013).

A number of detailed chemical mechanisms of PAH formation have been proposed to study PAH growth in flame environments. Kinetic mechanisms are based on the reactions of the abundant gaseous species such as C_2H_2 and small aromatic compounds activated by H and OH radicals. Along with the chemical growth reactions, the simultaneous physical process of coagulation of PAHs to form particle nuclei is considered. The presence of PAH stacks in experimental images of soot particles obtained by high-resolution transmission electron microscopy (HR-TEM) is proof of the coagulation of PAHs.

Particle nuclei can continue to add molecules to increase their sizes or they can coagulate with other particles maintaining an invariant total mass. Two different kinds of coagulation can be considered: coalescence and agglomeration. Coalescence occurs when a molecule from the gas-phase or a small particle collides with a particle and the formed entity tends to reduce free surface to minimize free energy. It results in the inclusion of the colliding molecules or small particles into the larger ones. In larger particles, the timescale of particle inclusion into the particle is larger than the timescale of the agglomeration process. In that case the

colliding entities maintain their own structure and they aggregate to form an agglomerate of particles.

Although the coagulation process (as sum of coalescence and agglomeration) has been widely observed for large PAH molecules and for small particles, their rates and the exact pathways in which they occur are still debated. The ability of PAHs to coagulate depends on dispersion forces. Planar pericondensed aromatic molecules have a high tendency to coagulate; the higher the molecular mass, that is, the number of aromatic cycles in the molecule, the higher the binding energy. Nonplanar aromatic molecules show a different behavior. They exhibit lower binding energies also at high-molecular mass because of the steric conformation of the molecules, which hinders the molecules from reaching an interaction distance. Therefore, the chemical structure of the PAHs and their sizes are controlling factors in determining the rate of particle inception and the internal structure of the incipient particles. The coagulation of planar pericondensed PAH might be responsible for the formation of ordered stacks of aromatics, whereas the coagulation of nonplanar aromatics results in less ordered clusters. PAH coagulation and addition of gas-phase compounds on the particle surface lead to particulate loading.

Parallel to the mechanisms which determine the increase of the particle size, that is, growth and agglomeration mechanisms, reaction of the particles with O_2 and OH may occur through two parallel processes: oxidation and fragmentation. Oxidation is the removal of mass from particles due to chemical reactions by hydroxyl radical and oxygen molecule. Fragmentation is the break-up of single particles and large aggregates into smaller particles and aggregates. Recent results by Sarofim's group (Echavarria et al. 2011) have confirmed the importance of oxidation-induced fragmentation in correctly determining the burn-out rate of particles. The reactions of the fragmentation process have been recently included by Pitsch's group in their model to predict particle size distribution in premixed flames (Mueller et al. 2011). However, in that model only the fragmentation of aggregates has been considered.

Fragmentation can involve large aggregates containing a large number of primary particles. Stepwise splitting up of large aggregates for effect of oxidation-induced fragmentation can lead to smaller aggregates formed by just two primary particles. In this case a subsequent fragmentation forms isolated primary particles. Fragmentation can also involve primary particles. In this case internal burning fragments single particles into smaller clusters. This process can continue producing very small cluster fragments.

Aggregate fragmentation and single-particle fragmentation are conceptually different. The fragmentation of aggregates into smaller aggregates of primary particles is mainly linked with the presence of material condensed from the gas-phase or added to the particle by surface reactions which fill the space between the particle contact points. The fragmentation of particles into smaller particles deals with the internal structure of the single particles.

Based on the above considerations, a detailed mechanism of particle evolution is proposed to delve into the physical structure and chemistry of combustion-

formed particles. A multi-sectional method is used with a triple discretization of the particle phase in terms of C and H atom number, and morphology. This allows following not only the mass of particles, but also the hydrogen content and internal structure. This description of the particles improves the treatment of the inception and growth pathways by coupling their kinetics to features such as H/C ratio or morphology, following the hints suggested by the experimental evidences. In particular, modeling of the detailed structures of the particles allows the inclusion of oxidation pathways by OH and O₂, surface reactions, and O₂ induced fragmentation.

The model follows the chemical and internal structure evolution of particles formed in flames. Other sophisticated approaches are currently used to simulate internal structures of the particles (see [Chap. 15](#)). The model presented here is fully coupled with the main pyrolysis and oxidation reactions of the fuel. The coupling between gas and particle phase is important because of the role of abundant gaseous species such as C₂H₂, aromatic compounds and small radicals such as H and OH in the nucleation, growth, and oxidation processes.

The model is tested, without any adjustments to the scheme, on premixed and non-premixed flames of ethylene at atmospheric pressure. Predictions are compared with experimental data on gas-phase species concentrations, particle volume fractions, H/C and size in laminar, premixed, and in co-flowing non-premixed flames.

Hereafter the model will be presented in detail. First of all, the gas-phase reactions will be briefly described. Successively, the sectional method will be introduced and details on the multi-sectional approach and discretizations adopted will be given. Finally, the different processes for particle evolution and the reaction used for modeling them, molecular growth, gas-to-particle transition, oxidation, and oxidation-induced fragmentation, will be described.

14.2 Gas-Phase Chemistry and PAH Formation

The mechanism of oxidation and pyrolysis of small aliphatic hydrocarbons is built onto the GRI-Mech 3.0 for C1 and C2 species (Smith et al. [2013](#)) and the Miller and Melius mechanism for C3 and C4 species (Miller and Melius [1992](#)). It has been used to model several flame conditions at atmospheric pressure showing reasonable ability to predict the structures of aliphatic and aromatic hydrocarbon flames (D'Anna [2009b](#)).

Briefly, fuel-rich conditions promote molecular growth and hydrogen loss and also oxidation of the hydrocarbon molecules. In aliphatic fuel flames, acetylene and methane are the most abundant, gaseous, unburned hydrocarbons and benzene is the first aromatic product of the molecular growth process. Benzene formation is considered to occur by the addition of *n*-C4 radicals to C₂H₂ and the self-combination of propargyl radicals (C3-route). The sequential addition of C₂H₂ to phenyl radical (hydrogen abstraction acetylene addition—or HACA—mechanism,

Frenklach and Wang (1991, 1994) and the combination of resonantly stabilized radicals, that is, the combination of two cyclopentadienyl radicals and the combination of benzyl and propargyl radicals (Marinov et al. 1996), are the pathways considered for the growth of aromatic cycles up to pyrene. Since the combustion conditions can be quite different in terms of gas-phase species concentration and temperature history, very often some extreme conditions have been analyzed drawing generally valid conclusions. As for other steps in particle formation, it is very likely that these mechanisms march together and just in some case one is completely prevalent with respect to the other.

Pyrene is considered to be the largest possible gas-phase compound. All species with larger molecular weight are treated as lumped species and thus divided into classes. The gas-phase kinetic mechanism consists of 460 reactions involving 120 species.

14.3 Advanced Multi-Sectional Approach

Compounds with molecular weight larger than pyrene become very difficult to model due to their large number of isomers. Many approaches have been proposed through years.

Some methods have risen as the most efficient for soot prediction. Sectional approach, that is, discretization of the molecular mass of the species leading to soot, is one of the possible solutions to the particle population balance problem. In fact, to solve the population balance problem when an analytical solution is not possible, probably the first approach is to discretize the domain and try to get an approximate solution. The limit of this approach would be the use of an infinite number of sections to get the continuous solution. It uses lumped species in order to incorporate particle dynamics. Particles are divided into classes, but each one is treated as a gas-phase so that elemental reaction steps can then be written. This allows to account for a lot of chemical details of reaction steps which would otherwise be lost.

This method allowed in the beginning to have information on total amount of soot and particle size distribution, since the first discretization was made on the carbon atoms contained in each lumped species, that is, the mass of the particle. This first version has been developed by several groups and tested in many flame configurations for different fuels (Smooke et al. 1999; Richter et al. 2005; D'Anna and Kent 2008; Mauss et al. 2009; Dworkin et al. 2011). The advanced multi-sectional method (AMS) for particle description in flames presented here is the latest development in the discrete sectional approach (Sirignano et al. 2010; D'Anna et al. 2010).

The use of lumped species treats, numerically, all the particles as gas-phase species. This means that it is possible to evaluate a collision frequency and to assign an activation energy for each process in which particles are involved. The kinetic expression can be written in principle for each lumped species. Particles

react in a similar way, depending on some parameters, such as size, chemical composition, and morphology. Kinetic expressions will be tailored on particle features, assuming specific dependence on these parameters. If these dependences are chosen on the basis of physical meanings their validity can be wider. This approach tries to get more general expressions for particle reaction avoiding the tuning of kinetic rates for matching experimental data.

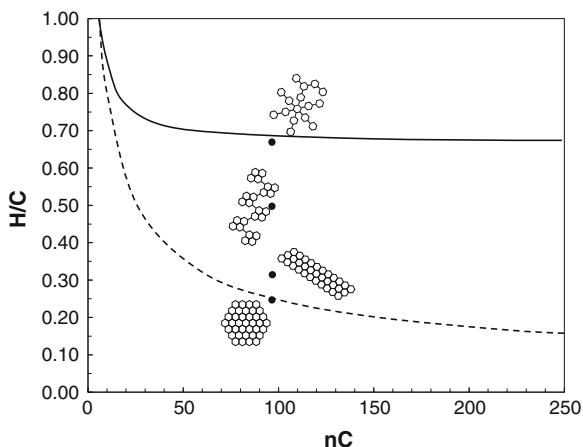
The molecular mass distribution is defined by a range of sections, each containing a nominal hydrocarbon species in order of increasing atomic mass. Carbon number ranges from 24 to 2×10^{10} and H/C for each carbon number ranges from 0 to 1. Thirty-one sections are used in a geometric series of carbon number with a ratio of two between sections. Five sections are used for H/C variation. The model introduces another discretization which accounts for the level of agglomeration of the compounds. Three entities are defined: molecules (ARM1i), clusters of molecules (ARM2i), and agglomerates of clusters (ARM3i). The index *i* represents the discrete sections in which the C-atom domain has been divided (31 sections), whereas the H atom content is taken into account by considering five different lumped species having the same number of C-atoms and different numbers of H atoms. Overall, 465 lumped species for the stable form and 465 for radicals are modeled. It is assumed that only one radical species is representative of each stable species. The equivalent size range of 1–800 nm is obtained with this discretization considering a density varying from 1 g/cm³ for the smallest species with the highest hydrogen content to 1.8 g/cm³ for species above 10 nm with the lowest hydrogen content.

14.3.1 Particle Phase Reaction: Gas-to-Particle Transition

The discretization operated for the lumped species furnishes a rough estimation of their molecular structure. Experimental evidence indicates that high molecular mass species generated in flames are essentially aromatic compounds (Homann 1998). So, for a given C-atom number, molecules with large H/C ratios must be aromatics having both σ - and π -bonds between C-atoms consisting of incompletely condensed oligomers of aromatics, whereas lower H/C molecules belong to the class of the maximally condensed aromatics hydrocarbons, that is, pericondensed aromatic compounds (PCAHs), in which only π -bonds among C exist. Figure 14.1 shows the H/C as a function of the number of C-atoms up to 250 for the oligomers of benzene (high H/C values—full line) and that of maximally condensed aromatics (low H/C values—dashed line). In the figure, an example of an aromatic molecule having 96 C-atoms and different H atom numbers is also shown.

Starting from pyrene, the molecular growth of aromatics is initiated by an H atom loss (R1, R2, and R3) from aromatic molecules ARM1i forming an aromatic radical ARM1i* (Table 14.1). For the H-abstraction reaction by H (R1) or OH (R2), the collision frequency evaluated by kinetic theory indicates a dependence

Fig. 14.1 H/C as a function of the number of C-atoms up to 250 for the oligomers of benzene (high H/C values—*full line*) and that of maximally condensed aromatics (low H/C values—*dashed line*). An example of the aromatic molecules having 96 C-atoms and different H atom numbers is also shown



on carbon atoms raised to the $2/3$ power. The effective possibility that the contact of H and OH radical produces an H-abstraction depends on H availability. Consequently, the reaction rate is scaled by the H/C of the particles. The reverse reaction rates are based on the similarity with PAHs of increasing mass; they depend on mass and H/C. Activation energies are made equal to those of H-abstraction from a benzenic ring in gas-phase PAHs (Frenklach and Wang 1994).

The spontaneous formation of radicals (R3) is built on the similarity with the naphthalene reaction. It is a unimolecular reaction. The reaction rate increases with an increase in the number of hydrogen atoms in the molecules (Richter et al. 2005).

Termination reactions of aromatic radicals with other aromatic radicals (R4) ending the growth sequence have rate constants evaluated from the collision frequencies of the reacting species. A collision between two molecules with differing number of carbon atoms scales with mean number to the $1/6$ power; it is considered to have zero activation energy (Frenklach and Wang 1994).

The formation of PCAHs is modeled by addition of acetylene (R5) (Frenklach and Wang 1994). The rate constant for acetylene addition to aromatic radicals (R5) is based on the reaction rate of naphthyl + acetylene scaled by increasing collision frequencies (Richter et al. 2005). PCAHs with a fixed number of C-atoms exist in a large number of isomers having different H atoms. The PCAHs having the lowest amount of H atoms are maximally condensed six-member ring structures. Their H/C ratio decreases to very low values as the molecular size increases; the largest of these compounds is a graphene sheet.

The formation of incompletely condensed aromatics is modeled both by H atom substitutions by a pericondensed structure, e.g., the formation of phenyl-pyrene or naphthyl-pyrene, and by aromatic radical addition to non-aromatic double bonds, such as those of pentagons condensed peripherally with hexagons (acenaphthylene type), and those of compounds like phenanthrene (R6). On the basis of structural

Table 14.1 Lumped species mechanism. Units are cal, mole, cm, s

Reactions	$k = AT^n \exp[-E/RT](nC)^p (H/C)^q$
<i>Molecules</i>	
R1	$ARM1i + H \leftrightarrow ARM1i^* + H_2$ $8.85E13 T^{0.5} \exp(-16,000/RT) nC^{2/3} H/C$
R2	$ARM1i + OH \leftrightarrow ARM1i^* + H_2O$ $8.85E13 T^{0.5} \exp(-4,650/RT) nC^{2/3} H/C$
R3	$ARM1i \rightarrow ARM1i^* + H$ $6.00E14 T^{0.5} \exp(-113,100/RT) nC H/C$
R4	$ARM1i^* + ARM1i^* \rightarrow ARM1i$ $8.00E12 T^{0.5} nC^{1/6}$
R5	$ARM1i^* + C_2H_2 \rightarrow ARM1i$ $3.00E6 T^{1.787} \exp(-3,262/RT) nC^{0.616}$
R6	$ARM1i^* + ARM1i \rightarrow ARM1i + H$ $2.00E13 T^{0.5} \exp(-15,000/RT) nC^{1/6}$
R7	$ARM1i + H \rightarrow ARM1i + H + H_2$ $6.00E14 T^{0.5} \exp(-25,000/RT) nC H/C$
R8	$ARM1i + OH \rightarrow ARM1i + HCO$ $3.00E12 T^{0.5} \exp(-10,600/RT) nC^{0.623}$
R9	$ARM1i^* + O_2 \rightarrow ARM1i + 2CO$ $4.30E11 T^{0.5} \exp(-8,000/RT) nC^{2/3}$
R10	$ARM1i + ARM1i \rightarrow ARM2i$ $\gamma 8.00E12 T^{0.5} nC^{1/6}$
<i>Clusters</i>	
R11	$ARM2i + H \leftrightarrow ARM2i^* + H_2$ $8.85E13 T^{0.5} \exp(-16,000/RT) nC^{2/3} H/C$
R12	$ARM2i + OH \leftrightarrow ARM2i^* + H_2O$ $8.85E13 T^{0.5} \exp(-4,650/RT) nC^{2/3} H/C$
R13	$ARM2i \rightarrow ARM2i^* + H$ $6.00E14 T^{0.5} \exp(-113,100/RT) nC H/C$
R14	$ARM2i^* + ARM1i^* \rightarrow ARM2i$ $8.00E12 T^{0.5} nC^{1/6}$
R14	$ARM2i^* + ARM2i^* \rightarrow ARM2i$ $8.00E12 T^{0.5} nC^{1/6}$
R15	$ARM2i^* + C_2H_2 \rightarrow ARM2i$ $3.00E6 T^{1.787} \exp(-3,262/RT) nC^{0.616}$
R16	$ARM2i^* + ARM2i \rightarrow ARM2i + H$ $2.00E13 T^{0.5} \exp(-15,000/RT) nC^{1/6}$
R16	$ARM2i^* + ARM1i \rightarrow ARM2i + H$ $2.00E13 T^{0.5} \exp(-15,000/RT) nC^{1/6}$
R16	$ARM1i^* + ARM2i \rightarrow ARM2i + H$ $2.00E13 T^{0.5} \exp(-15,000/RT) nC^{1/6}$
R17	$ARM2i + H \rightarrow ARM2i + H + H_2$ $6.00E14 T^{0.5} \exp(-25,000/RT) nC H/C$
R18	$ARM2i + OH \rightarrow ARM2i + HCO$ $3.00E12 T^{0.5} \exp(-10,600/RT) nC^{0.623}$
R19	$ARM2i^* + O_2 \rightarrow ARM2i + 2CO$ $4.30E11 T^{0.5} \exp(-8,000/RT) nC^{2/3}$
R20	$ARM1i + ARM2i \rightarrow ARM2i$ $\gamma 8.00E12 T^{0.5} nC^{1/6}$
R20	$ARM2i + ARM2i \rightarrow ARM2i$ $\gamma 8.00E12 T^{0.5} nC^{1/6}$
R21	$ARM2i + ARM2i \rightarrow ARM3i$ $\gamma 8.00E12 T^{0.5} nC^{1/6}$
R22	$ARM2i^* + O_2 \rightarrow ARM2i + ARM2i + 2CO$ $\beta 1.72E9 T^{0.5} \exp(-8,000/RT) nC^{5/3}$
<i>Agglomerates</i>	
R23	$ARM3i + H \leftrightarrow ARM3i^* + H_2$ $8.85E13 T^{0.5} \exp(-16,000/RT) nC^{2/3} H/C$
R24	$ARM3i + OH \leftrightarrow ARM3i^* + H_2O$ $8.85E13 T^{0.5} \exp(-4,650/RT) nC^{2/3} H/C$

(continued)

Table 14.1 (continued)

Reactions	$k = AT^n \exp[-E/RT](nC)^p (H/C)^q$
R25 ARM3i → ARM3i* + H	$6.00E14 T^{0.5} \exp(-113,100/RT) nC$ H/C
R26 ARM3i* + ARM1i* → ARM3i	$8.00E12 T^{0.5} nC^{1/6}$
R26 ARM3i* + ARM2i* → ARM3i	$8.00E12 T^{0.5} nC^{1/6}$
R26 ARM3i* + ARM3i* → ARM3i	$8.00E12 T^{0.5} nC^{1/6}$
R27 ARM3i* + C ₂ H ₂ → ARM3i	$3.00E6 T^{1.787} \exp(-3,262/RT)$ $nC^{0.616}$
R28 ARM3i* + ARM1i → ARM3i + H	$2.00E13 T^{0.5} \exp(-15,000/RT) nC^{1/6}$
R28 ARM3i* + ARM2i → ARM3i + H	$2.00E13 T^{0.5} \exp(-15,000/RT) nC^{1/6}$
R28 ARM3i* + ARM3i → ARM3i + H	$2.00E13 T^{0.5} \exp(-15,000/RT) nC^{1/6}$
R28 ARM3i + ARM1i* → ARM3i + H	$2.00E13 T^{0.5} \exp(-15,000/RT) nC^{1/6}$
R28 ARM3i + ARM2i* → ARM3i + H	$2.00E13 T^{0.5} \exp(-15,000/RT) nC^{1/6}$
R29 ARM3i + H → ARM3i + H + H ₂	$6.00E14 T^{0.5} \exp(-25,000/RT) nC$ H/ C
R30 ARM3i + OH → ARM3i + HCO	$3.00E12 T^{0.5} \exp(-10,600/RT) nC^{0.623}$
R31 ARM3i* + O ₂ → ARM3i + 2CO	$4.30E11 T^{0.5} \exp(-8,000/RT) nC^{2/3}$
R32 ARM3i + ARM3i → ARM3i	$\gamma 8.00E12 T^{0.5} nC^{1/6}$
R32 ARM1i + ARM3i → ARM3i	$\gamma 8.00E12 T^{0.5} nC^{1/6}$
R32 ARM2i + ARM3i → ARM3i	$\gamma 8.00E12 T^{0.5} nC^{1/6}$
R33 ARM3i* + O ₂ → ARM3i + ARM3i + 2CO	$\alpha 4.30E0 T^{0.5} \exp(-8,000/RT) nC^{5/3}$
R33 ARM3i* + O ₂ → ARM2i + ARM2i + 2CO	$\alpha 4.30E0 T^{0.5} \exp(-8,000/RT) nC^{5/3}$

nC is carbon number of the reactants except in reactions in which two lumped species are involved, where it represents average carbon number of the two reactants; H/C is the H-to-C ratio in the species; T is the flame temperature; R is the universal gas constant

similarity, the rate constant for phenyl + benzene is used as the reference for the corresponding aromatic radical + aromatic molecule reaction (R6) which is scaled for variation in collision frequencies (Richter et al. 2005).

The H/C ratio of the oligomers remains comparable to those of the aromatic molecules involved in the reactions and it remains quite unchanged as the molecular weight of the oligomers increases. Aromatic oligomers usually assume a nonplanar structure due to the less rigid structure of the σ -bond connecting the aromatic molecules.

Both pericondensed and incompletely condensed aromatics can grow indefinitely forming extremely large molecules. PCAHs can only add acetylene (R5) or other gaseous hydrocarbons (if an aromatic molecule is added an incompletely condensed aromatic is formed—R6). Incompletely condensed aromatics can also undergo dehydrogenation reactions migrating to pericondensed molecules (R7). The dehydrogenation has been considered occurring only on the stable species and not on radicals. The dehydrogenation process considers that, due to the complexity of the structures with increasing number of C-atoms, the radicals formed through the attack of an H atom cyclize forming a closed aromatic ring. The limiting stage is the rearranging of the structure to expel an H atom and form a new stable species with a lower H/C ratio, and consequently higher aromaticity. An activation energy

of 25,000 cal/mol has been estimated to better reproduce the experimental data (Sirignano et al. 2010). The dependence of the reaction rate on the number of H present in the structure is also considered.

The molecular growth process competes with molecule oxidation by OH and O₂ (R8 and R9). OH is used to oxidize the stable molecule, whereas O₂ oxidizes the radicals. The activation energy of the oxidation by OH (R8) is estimated from similar reactions for benzene and PAHs and the collision frequency accounts for the size of the particles involved (Neoh et al. 1985). Oxidation by O₂ (R9) uses the rate constant of naphthyl + O₂ accounting for the increase of collision frequencies of Xu et al. (2003).

Together with chemical growth, the physical process of PAH coagulation, that is, long-range interaction between colliding entities, occurs to form particle nuclei (R10). The current model introduces a further discretization which accounts for the formation of clusters of molecules (particle nuclei) here defined as ARM2i.

Clusters of molecules are stacks of PAHs held together by van der Waals interactions. Binding energies which form these clusters depend on the dimensions of the interacting aromatic molecules and on the capability of the aromatic molecules to reach an interaction distance. PCAHs which have an intrinsic planar structure due to the absence of σ -bonds can easily reach an interaction distance and arrange in parallel stacks. Structures which contain σ -bonds tend to assume a nonplanar structure so that the steric conformation of these molecules hinders π -electrons of the molecules reaching an interaction distance. This conformation is responsible for lower binding energies. Dehydrogenation of molecules leads to a more pericondensed structure, inducing planarity in the molecules and increasing the capability of the molecules to reach an interaction distance. As a consequence, coagulation of PAHs depends on molecule sizes, and on the number of π -bonds with respect to σ -bonds. Molecule size is accounted for through the number of C atoms, whereas the H/C accounts for the number of π - and σ -bonds. For the same C atom number, high H/C means σ -bond interactions in the molecule, nonplanar structure, and hence lower coagulation rate. On the other hand, low H/C means mainly π -bond interactions in the molecule, intrinsic planar structure, and hence higher coagulation rate.

Molecule coagulation (R10) is considered irreversible at this stage and its reaction rate is modeled by considering a coagulation efficiency with respect to the collision frequency. Collision frequency increases with the increase of molecular mass of the molecules, whereas the coagulation efficiency, γ , depends on both the temperature and chemistry of the colliding molecules. The chemistry of the particles is considered by evaluating the Hamaker constant (Hamaker 1937) for the species involved in the coagulation process. The Hamaker constant accounts for van der Waals body-body interactions. From benzenic ring to graphite the Hamaker constant ranges from 3×10^{-20} to 5×10^{-19} J.

A value of 5×10^{-20} J has been assigned to a compound with an H/C ratio of 0.5. The values of the Hamaker constant for the other compounds have been linearly scaled on the H/C ratio. The coagulation efficiency is evaluated by following D'Alessio et al. (2005): $\gamma = 1 - (1 + \Phi_0/T) \exp[-\Phi_0/T]$ evaluated as a

function of the flame temperature T , and the interaction potential Φ_0 between coagulating entities. The latter is a linear function of the Hamaker constant (Sirignano et al. 2010).

The computed coagulation efficiency is of the order of 10^{-4} for small colliding entities and increases to values of about 1 when the C number is about 10^6 . These values are in agreement with experimental coagulation rates (D'Alessio et al. 2005). The modeled results show that high H/C molecules, that is, mostly comprising incompletely condensed aromatics and hence nonplanar compounds, have much lower coagulation efficiencies than low H/C molecules, that is, planar pericondensed aromatic compounds, for the same number of C-atoms.

14.3.2 Particle Phase Reaction: Particle Growth Mechanism

Clusters of molecules, that is, particle nuclei, (ARM2i) can continue to react in the same way as the molecules (ARM1i). Table 14.1 reports the list of reactions involving ARM2i compounds. They can add molecules to increase their size (R11–R16), or remove H atoms by dehydrogenation (R17) or C atoms by OH and O₂ oxidation (R18 and R19), or they can coagulate with other molecules or other clusters (R20). If two clusters merge into one reducing free surface area so as to minimize their free energy a coalescence event occurs (R20). The formed cluster assumes a spherical shape and can be seen as a cluster of molecules larger than the previous two (Fig. 14.2).

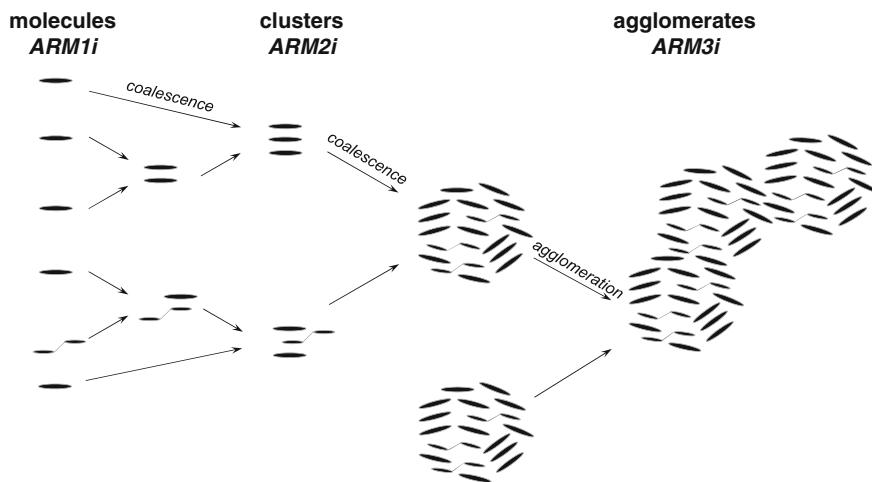
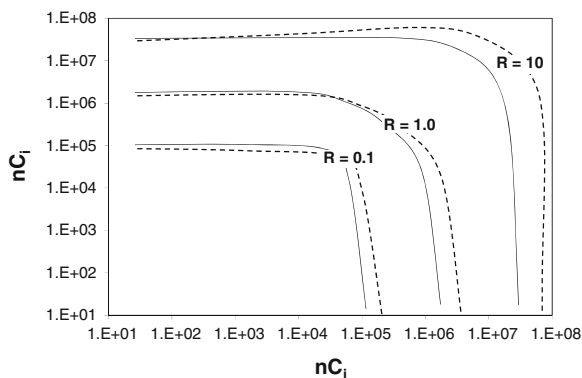


Fig. 14.2 Schematic of particle formation, particle coalescence and agglomeration processes. Incompletely condensed oligomers of aromatics $\text{—}\text{—}\text{—}$; pericondensed aromatic compounds $\text{—}\text{—}\text{—}$

Fig. 14.3 Ratio (R) of agglomeration/coalescence rates at 1800 K for low ($H/C < 0.25$ —full lines) and high ($H/C > 0.25$ —dashed lines) species



As the cluster size increases, the timescale of molecular coalescence becomes larger than the timescale of the agglomeration process, and consequently the coagulation events lead to the formation of agglomerates (R21). Figure 14.3 shows contours of the ratio of the agglomeration to coalescence regimes at 1800 K for low (lower than 0.25—full lines) and high (larger than 0.25—dashed lines) H/C species.

It appears that particles with an nC of 1×10^5 (equivalent size of about 10 nm) have a rate of coalescence higher than that of agglomeration. This behavior is reversed for structures with nC larger than 1×10^6 (equivalent size of about 20 nm). For particles of 10–20 nm, coalescence and agglomeration rates are similar which means that these particles can coalesce or agglomerate with the same probability. Sensitivity analyses have been conducted by changing the size and H/C ratio dependence of the coalescence rate. The coalescence–agglomeration ratio does not drastically affect the final concentration of the particles but it does determine the size of the primary particles which constitutes particle agglomerates.

Particle agglomerates (ARM3i) can undergo the same reactions as the clusters of molecules (ARM2i) and the single molecules (ARM1i) (R23–R32).

14.3.3 Particle Phase Reaction: Oxidation-Induced Fragmentation

Particles oxidation is generally considered a surface process through which carbon atoms are subtracted from the particles. If the oxidizing species are able to remove C-atoms near a contact point between two particles constituting an aggregate or even penetrate the pores internally oxidizing the particle, the break-up of the large aggregates and particles into smaller aggregates and particles can occur. These processes can be referred to as oxidation-induced fragmentation and can be seen as particular events of oxidation. Aggregate fragmentation (R33) and single particle fragmentation (R22) are both considered in the model.

The aggregates are fragmented when oxidation occurs at the contact points of the primary particles after the removal of a fraction δ of C atoms from the particles. This consideration is linked to the consideration that there is more than one pair of carbon atoms holding together the aggregate. The points of weakness are the contact points between the particles and the number of contact points in the aggregates is given by $(n_p - 1)$, where n_p is the number of primary particles in the aggregate that can be calculated as $n_p = n_{C_A}/n_{C_P}$, being n_{C_A} and n_{C_P} the number of C atoms in the aggregate and in the primary particle, respectively.

The probability that the oxidation occurs in a weakness point between two particles is equal to the inverse of the number of active sites on the particle surface for O_2 oxidation:

$$n_{\text{active sites}} = \chi \times \pi \times d_p^2$$

where χ is the number of sites per unit area ($\chi = 1.7 \times 10^{19} \cdot \text{m}^{-2}$ was estimated by Kazakov and Frenklach 1998), d_p is the particle size, and πd_p^2 is the primary particle surface area. Each oxidation event removes two carbon atoms (R31). To have an oxidation event which is able to activate fragmentation, a fraction δC of atoms has to be removed. The number of C atoms that must be removed to cause fragmentation can be expressed as follows:

$$\delta C = \alpha \times n_{C_P}$$

where α is a fraction of the C atoms constituting the primary particles.

The fragmentation rate of aggregates (R32) is then given by:

$$k_f = k_{O_2} \times (n_p - 1) / ((\chi \times \pi d_p^2) \times \delta C)$$

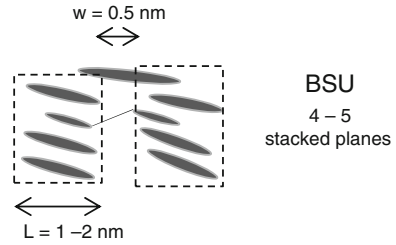
where k_{O_2} is the rate constant of the oxidation reaction.

The fragmentation of agglomerates with n_C lower than 1×10^6 is considered to form clusters of molecules (primary particles) (R33).

A similar approach is used to model fragmentation of particles into smaller particles (R22). Experimental data obtained by HR-TEM on incipient particles (Alfè et al. 2009) show that particles appear to be composed of clusters of aromatic compounds. Generally, the average molecular mass of the aromatic compounds included in a cluster is such that its length in the HR-TEM images is of the order of 1 nm which corresponds to compounds having about 20–25 C atoms. The number of aromatics in well-organized structures is always of the order of 4–5 stacked planes at a distance of about 0.35 nm. As a consequence, organized structures in an incipient particle, often referred to as basic structure units (BSUs), can be schematized as cylindrical units having equal base diameter and length of about 1 nm. These BSUs are randomly organized in the particles and are separated from each other by “pores” having a length of the same order of magnitude of the BSU and size of about 0.5 nm. Figure 14.4 shows a schematic representation of the BSUs inside the particle.

Molecular oxygen oxidizes a particle on its surface but it can also penetrate the pores internally oxidizing the particle. The calculated effective diffusivity time of

Fig. 14.4 Schematic representation of two BSUs



O_2 molecule inside the pores separating the BSUs is lower than the characteristic time of surface oxidation leading to the hypothesis that diffusivity of O_2 is not the controlling step in the internal oxidation of particles. On the other hand, because of the fast reactivity of OH oxidation, the OH radical does not penetrate the pores but oxidizes the particle on its surface.

When oxidation by O_2 occurs in the depth of the pores, the particle can fragment into two parts by the removal of δC -atoms. The number of C atoms in the BSU, $n_{C_{BSU}}$, is estimated by considering the BSU made up of 4 aromatic molecules each of 25 C atoms, on the basis of HR-TEM images. The number of BSUs constituting a particle, n_{BSU} , is obtained by dividing the number of C atoms in the particle by the number of C atoms constituting the BSU, $n_{BSU} = n_{C_p}/n_{C_{BSU}}$. The number of pores, n_{pores} , can be evaluated from the volume of a single pore relative to the particle volume. For cylindrical pores with a depth L , of the same order of magnitude of the BSU (1 nm) and diameter, w , of about 0.5 nm, the internal surface of the pores is $(\pi w L + \pi w^2/4)$. However, the point of weakness in the pore is considered to be at the bottom and so only this fraction of pore area is used $(\pi w^2/4)/(\pi w L + \pi w^2/4)$.

The particle fragmentation rate (R22) is related to the O_2 oxidation rate— k_{O_2} —by evaluating the probability that the oxidation occurs at the bottom of the pores after removal δC -atoms as discussed above. This number of carbon atoms is given here by

$$\delta C_{pores} = \beta \times n_{C_p}$$

where β represents the fraction of C atoms in the particle that must be removed to cause fragmentation.

The fragmentation rate for the particles (R22) is then:

$$k_f = k_{O_2} \times (\pi w^2/4 / (\pi w L + \pi w^2/4)) \times n_{pores} / (\delta C_{pores})$$

Values of $\alpha = 0.01$ and $\beta = 0.05$ give the best agreement of the modeled results with the experimental data of Echavarria et al. in premixed flames (Echavarria et al. 2011). The impact of these processes on the final soot burn-out and size distribution will be shown below.

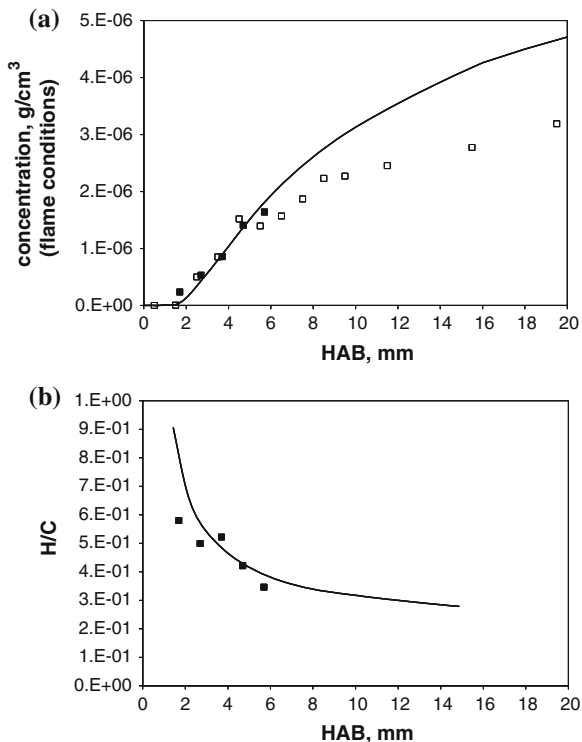
14.4 Use of the Advanced Multi-Sectional Method in Combustion Systems

14.4.1 Laminar Premixed Flames: Test Cases

The model is applied to sooting premixed flames of ethylene at atmospheric pressure (Ciajolo et al. 1996, 1998; Sgro et al. 2009). Different diagnostics have been used for their characterization. They furnish details of flame structures, particle concentrations, their size distribution functions, and the chemical structure and molecular mass of the condensed phases.

Figure 14.5 shows the comparison of the model to the experimentally determined concentration of total particulates and H/C ratio in the rich ethylene/oxygen premixed flames with equivalence ratio $\phi = 2.4$. The measured flame temperature profile is needed as an input to the model for a correct simulation of the flame structure. Modeled total particulate is here defined in agreement with experiment, as the mass of all compounds with a number of C-atoms higher than 10 (molecular mass equal or larger than naphthalene). Particulate concentration increases just downstream of the maximum flame temperature—located at about 2 mm height

Fig. 14.5 Comparison of the model (*lines*) to the experimentally determined concentrations (*points*) of (a) total particulate—the species with molecular mass equal or larger than naphthalene—and (b) its H/C ratio in the $\phi = 2.4$ ethylene/oxygen premixed flames at atmospheric pressure. Experimental data from Ciajolo et al. 1996 (\square) and 1998 (\blacksquare) (D’Anna et al. 2010, Copyright Elsevier)



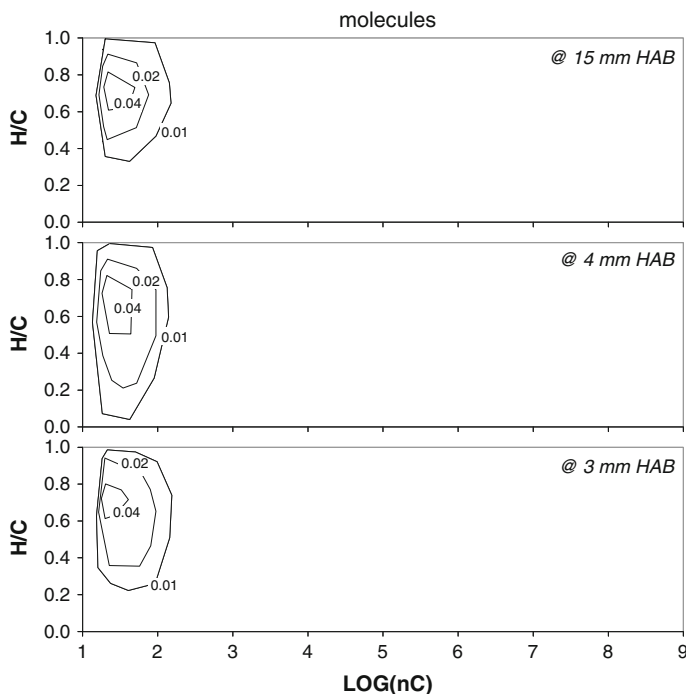


Fig. 14.6 Modeled H/C ratio distribution of molecules as a function of the C-atom numbers (nC) at three heights in the $\phi = 2.4$ flame. From *bottom* to *top*: 3, 4, and 15 mm. Lines are iso-concentrations in part per million (D'Anna et al. 2010, Copyright Elsevier)

above burner, HAB—at a fast rate and thereafter it levels off. By contrast, the H/C ratio decreases monotonically with increasing flame height. The model predicts the experimental data reasonably well and particularly it captures the increase in concentration of total particulates and the decrease in hydrogen content.

Figures 14.6, 14.7, and 14.8 show modeled H/C ratio distribution of the high-mass compounds against number of C-atoms at three heights in the $\phi = 2.4$ flame, namely at particle inception (3 mm), at the location where particle formation rate is maximum (4 mm), and in the post-flame region (15 mm). The predictions are for molecules (Fig. 14.6), clusters (Fig. 14.7), and agglomerates (Fig. 14.8).

The model indicates that molecules of aromatic hydrocarbons are formed at particle inception which occurs just downstream of the flame front. Their H/C ratio extends over a wide range of values, whereas their C-atom numbers do not exceed 100. The species with the largest concentrations have about 20–40 carbon atoms and H/C ranging from 0.6 to 0.8. The H/C of these compounds suggests that they comprise pericondensed and incompletely condensed PAHs.

Moving downstream into the main flame region the mass of single molecules remains quite unchanged and their H/C is reduced. These changes indicate a larger presence of pericondensed PAHs in the molecule pool. It occurs at the height

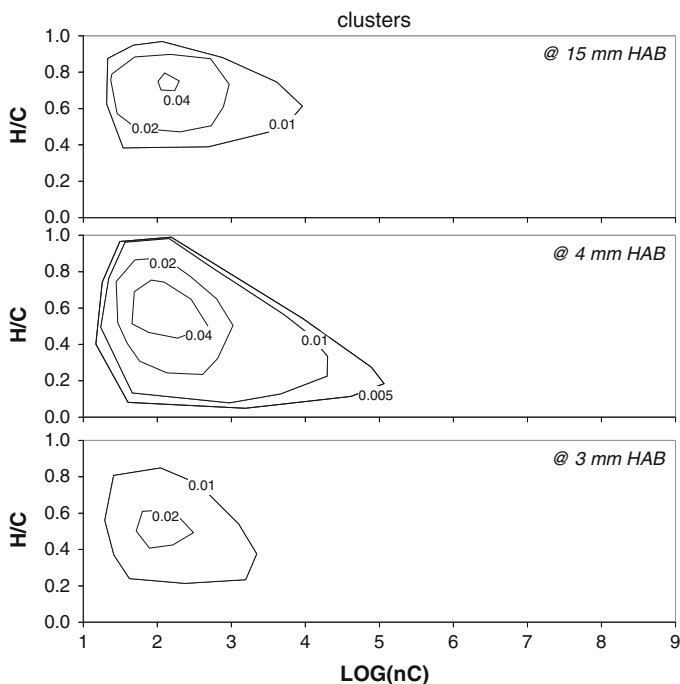


Fig. 14.7 Modeled H/C ratio distribution of clusters as a function of the C-atom numbers (nC) at three heights in the $\phi = 2.4$ flame. From *bottom to top*: 3, 4, and 15 mm. *Lines* are iso-concentrations in part per million (D'Anna et al. 2010, Copyright Elsevier)

where particulate concentration starts to increase quickly (at about 4 mm in Fig. 14.6). Thereafter, the molecular weight and the H/C of molecules remain unchanged with only slight variation toward smaller mass and larger H/C ratio moving into the post-flame region. The number of C-atoms in the molecules does not change dramatically in the various flame regions. Just a slight increase is found moving from the flame front to the post-flame region. This result is consistent with experimental findings which have shown hardly any appreciable increase of the molecular weight of aromatics along the flame axis.

Clusters show a different behavior along the flame axis as shown in Fig. 14.7. They are mainly formed by the molecules with the lowest H/C ratio since these molecules have larger aromatic character and exhibit larger binding energies resulting in increased coagulation efficiency. Figure 14.7 clearly shows that clusters reach masses generally larger than molecules. They start at the flame front with about 50 C-atoms, which correspond to a molecular mass of the order of 1,000 amu and a size of 1.5–2 nm (for unit density and a spherical form). The H/C ratios of these clusters reach values as low as 0.25. At the height where cluster concentration starts to increase quickly (at about 4 mm), larger masses and lower H/C ratio particles are formed. Here the C-atom numbers reach values as large as

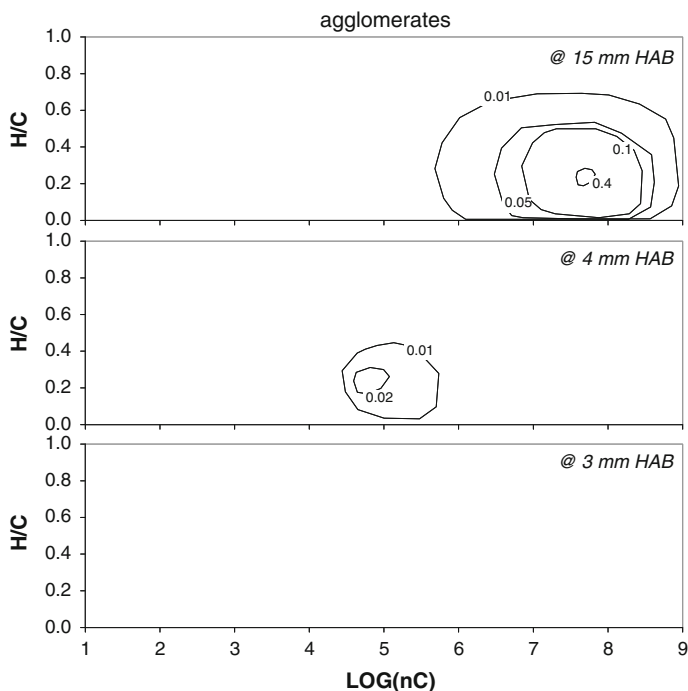


Fig. 14.8 Modeled H/C ratio distribution of agglomerates as a function of the C-atom numbers (nC) at three heights in the $\phi = 2.4$ flame. From *bottom* to *top*: 3, 4, and 15 mm. Lines are iso-concentrations in part per million (D'Anna et al. 2010, Copyright Elsevier)

1×10^5 and H/C as low as 0.1. These clusters can be considered to be the first soot particles. Thereafter, isolated particles show a reduction in mass and an increase in H/C ratios.

The formation of agglomerates is observed with the increase in C-atom number and the decrease in H/C ratio of the particles, as shown in Fig. 14.8. Agglomerates of particles represent the passage from the coalescence to the agglomeration process. The first entities belonging to this class of compounds are detected at the height where particulate concentration starts to increase quickly and they have about 5×10^4 C-atoms and an H/C of 0.25. Moving downstream from the flame front the number of C-atoms of the agglomerates increases to between 1×10^6 and 1×10^9 (equivalent spherical sizes of 30–300 nm) and H/C ratio decreases to 0.05.

The picture of mass grow described by the model is consistent with the C-atom distributions of particulates obtained by Ciajolo and coworkers sampling in flames and analyzing by size exclusion chromatography (SEC) (as shown in Chap. 13), the sampled material (Apicella et al. 2003). Figure 14.9 shows a comparison of the model to the experimentally determined mass distributions of total particulate at inception and in the post-flame region.

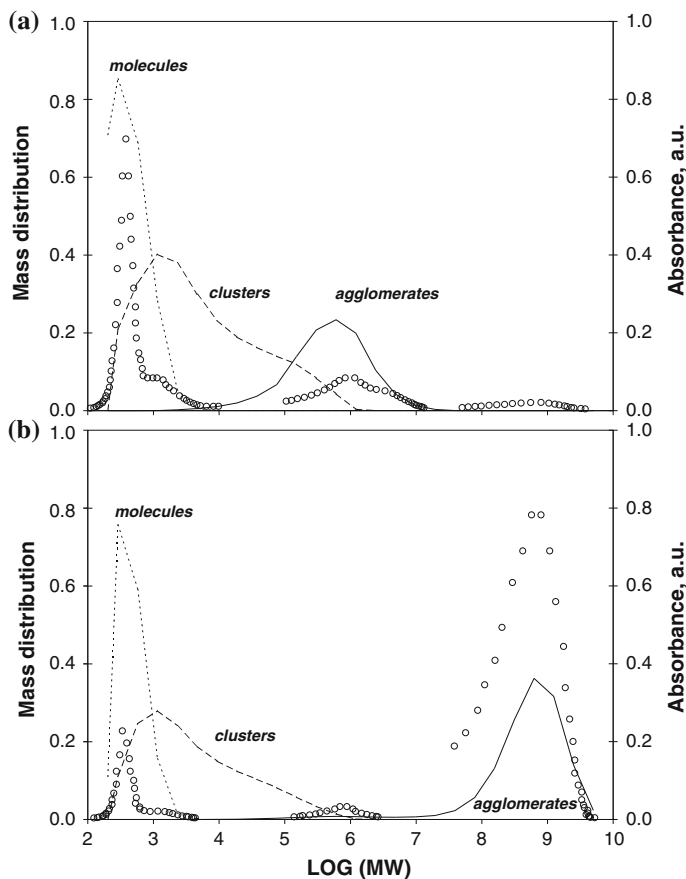


Fig. 14.9 Comparison of the model (lines—Sirignano et al. 2011) with the experimentally determined (points—Apicella et al. 2003) mass distributions of total particulate at (a) inception and (b) in the post-flame region. Mass distributions of total particulate are measured by size exclusion chromatography with absorption detection at 350 nm and normalized for accounting the relative contributions of soot and condensed hydrocarbon species (D’Anna et al. 2010, Copyright Elsevier)

Mass distributions of total particulate are measured by SEC with absorption at 350 nm and are normalized for the relative contributions of soot and condensed hydrocarbon species. Modeled results, instead, represent the concentrations of the different classes of compounds. Although a quantitative comparison cannot be made, the qualitative comparison gives a better understanding of the role of the different classes of compounds in the particulate formation process.

SEC mass distributions in Fig. 14.9 show four mass peaks: species with masses in the range 128–800, 800–5,000, 10^5 – 10^7 and 10^8 – 10^{10} amu. The model shows that the first peak is due to molecules of aromatic compounds having masses up to

2,000 amu. The second peak is due to particles with masses extending up to about 1×10^5 amu. The third peak is due to both particles with masses extending up to about 1×10^6 amu and agglomerates of particles. The fourth peak is due only to agglomerates of particles.

The abundance of the four mass species changes along the flame. At particle inception the first three mass peaks are observed, that is, the molecules of aromatic hydrocarbons, the isolated particles of 2 and 8 nm, and agglomerates of small particles. In the post-flame region the peaks due to the nascent particles are less evident being obscured by the presence of agglomerates of large particles. The model predictions are in agreement with experimental data and help the understanding of the chemical and physical nature of the detected substances.

The model is also applied to explore the effect of equivalence ratio on the formation of particulates. Figure 14.10 shows the comparison of the model to the experimentally determined volume fraction of total particulates at 12 mm height in several premixed flames of ethylene/air with equivalence ratios ranging from 1.5 to 2.5. Total particulate concentrations are determined by absorption measurements in the UV. The particulates comprise all of the carbonaceous species which have an appreciable absorption in the ultraviolet region (D'Alessio et al. 1998). Experimental volume fractions of nanoparticles with sizes larger than 1.5 nm and soot particles are also shown. Nanoparticles were detected by differential mobility analysis or DMA, whereas soot particles were detected by laser-induced incandescence (LII) as described in Chap. 12 and visible absorption (Sgro et al. 2009).

The concentration of total particulate determined by UV absorption increases at increasing equivalence ratios by about two orders of magnitude; the simulation predicts the trend well. It fails to reproduce the concentration of particulate at equivalence ratios close to the stoichiometric value, that is, below 1.6. However, here the error in the UV absorption can become very large due to the interference by gaseous stable species such as H_2O and CO_2 (Joutsenoja et al. 2001).

Model results (Fig. 14.10) show that different equivalence ratio thresholds exist for the types of compounds formed in flames. The onset of molecular compounds occurs at an equivalence ratio of 1.6 in reasonable agreement with the threshold of total particulate determined by UV absorption. Clusters are instead formed at equivalence ratios larger than 1.7. The concentration of the modeled clusters at different equivalence ratios agrees quite well with the concentration of particles detected by DMA which is very sensitive to nanoparticles but not to molecules. Modeled agglomerates of particles start to form at about 2.15. This is in excellent agreement with the threshold of soot particles determined by light absorption in the visible and by LII.

14.4.2 Laminar Diffusion Flames: Test Cases

The non-premixed, co-flowing nonsmoking ethylene/air flame of Santoro and co-workers (Santoro et al. 1983; Santoro and Semerjian 1984; Smyth et al. 1985;

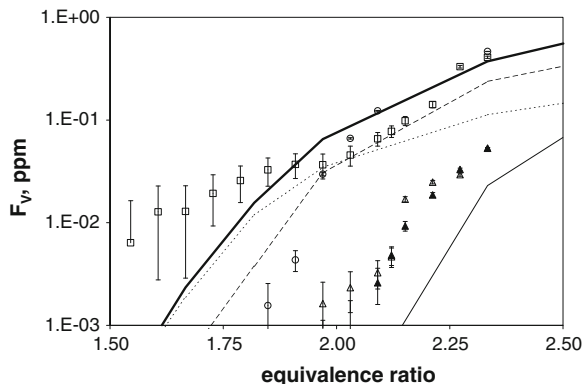


Fig. 14.10 Comparison of the model with the experimentally determined concentrations of total particulate and the different species structures at 12 mm height on the flame axis of several premixed flames of ethylene/air with equivalence ratios ranging from 1.5 to 2.5. Model results: molecules (*point line*), clusters (*dashed line*), agglomerates (*thin continuous line*), and total particulate (*thick continuous line*). Experimental data: total particulate from UV-Vis absorption (\square), nanoparticles from DMA (\circ), soot aggregates from LII (\blacktriangle), and from visible absorption (\triangle). Experimental data from Ciajolo et al. (1996) and Sgro et al. (2009) (D’Anna et al. 2010, Copyright Elsevier)

Santoro et al. 1987) has also been modeled. Figure 14.11 shows the comparison between predicted and measured temperature and species for this flame. Temperature, ethylene, acetylene, and benzene profiles are shown at 20 and 30 mm above the nozzle. The temperatures and the fuel concentration are well represented by the model at all heights. Benzene and acetylene predictions are somewhat high in the lower part of the flame and do not show the measured decay of these species at 30 mm height.

Radial profiles of particulate volume fractions are shown on the left side of Fig. 14.12 at measurement heights, 20, 30, 60, and 70 mm above the nozzle. The model gives good predictions of soot volume fractions and in particular reproduces the observed burnout of particles at 70 mm.

Particle size D63 is shown on the right side of Fig. 14.12 at the same heights. The model responds well to the heavily sooting fuel by generally representing the measured sizes of the particles.

Figure 14.12 reports as dashed lines the model predictions without particle fragmentation by oxidation. Oxidation-induced fragmentation, which is in parallel with surface oxidation, reduces particle size thereby increasing number concentration and also the rate of oxidation. The inclusion of oxidation-induced fragmentation pathways has improved model accuracy relative to our previous work (D’Anna and Kent 2008) to predict particle size and complete particle burn-out. Complete soot burn-out is now evident with the oxidation-induced fragmentation.

The model correctly reproduces soot concentrations in the wings; mean particle sizes are also well reproduced: maximum particle size is of the order of 100–150 nm compared with about 500–600 nm without fragmentation. D63

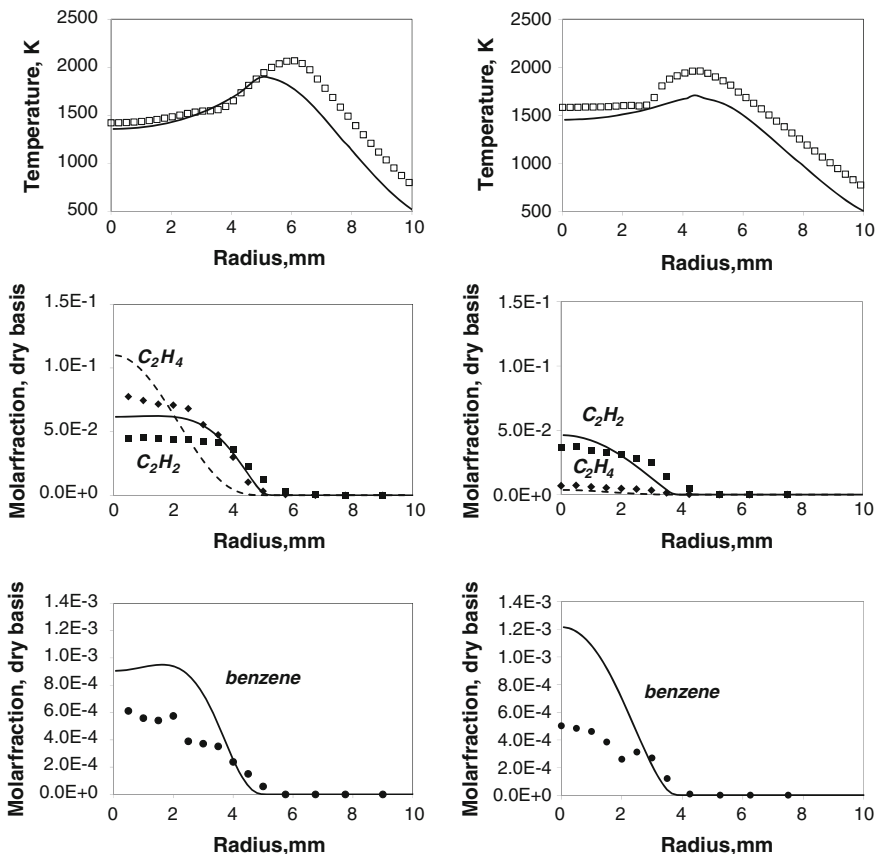


Fig. 14.11 Predicted (lines) and measured (points) temperature and species radial profiles in non-premixed ethylene co-flowing flame. *Left* 20 mm height, *right* 30 mm height. Experimental data from Santoro group (Santoro et al 1983, 1987). Temperature (\square , ___); ethylene (\blacklozenge , - - -); acetylene (\blacksquare , ___); benzene (\bullet , ___)

modeled data without the oxidation-induced fragmentation are divided by 3 in the figure.

The H-to-C ratio of the particulate collected along the flame axis was measured by Dobbins et al. (1998). The discrimination between C and H in the model allows us to calculate the H/C in the diffusion flame.

Figure 14.13 shows the comparison between measured and calculated H/C along the axis of the nonsmoking ethylene flame. Particles have been extracted from selected heights of the non-premixed coflowing ethylene flame using thermophoretic sampling and chemically analyzed by laser microprobe mass spectroscopy. Model follows the trend of the H/C ratio; it shows values of the order of 0.6, typical of PAHs, close to the burner mouth. Thereafter at about 20 mm, it sharply decreases to values of the order of 0.2 when soot formation starts also on

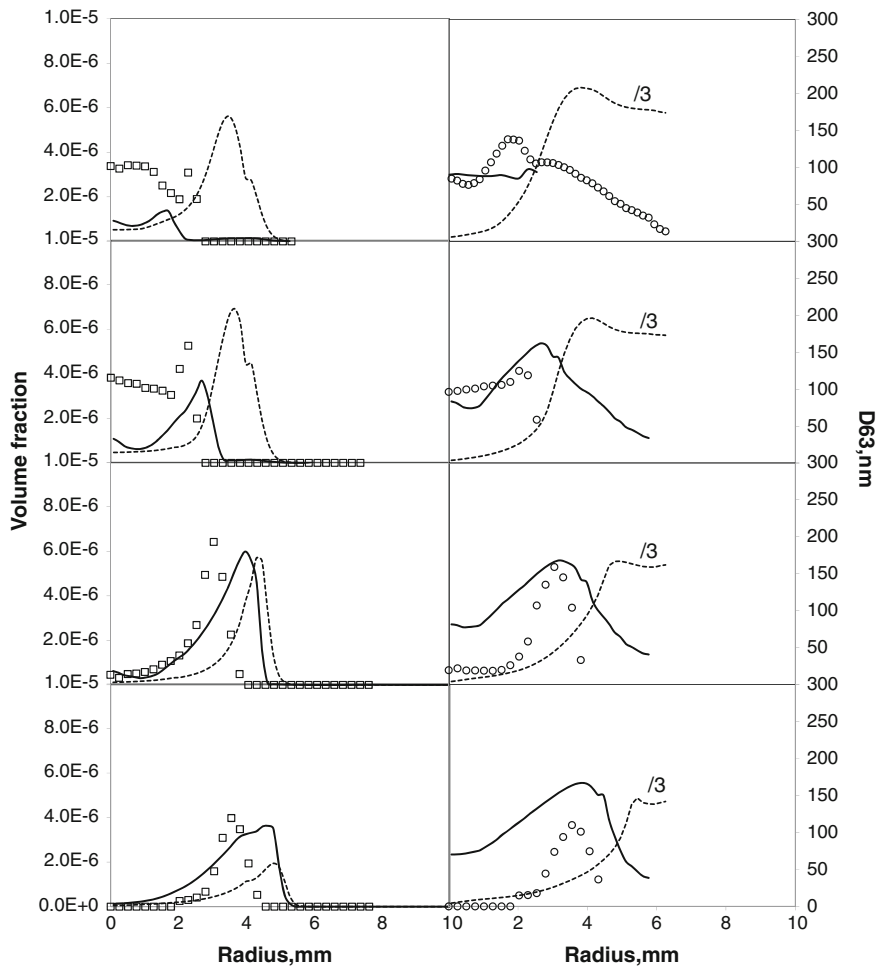
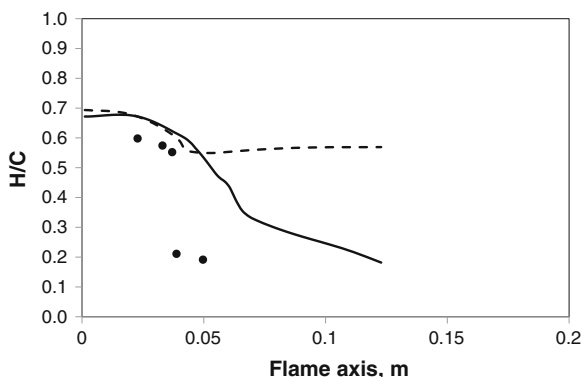


Fig. 14.12 Total particulate volume fraction (*left*) and mean particle size (*right*) profiles in non-premixed ethylene co-flowing flame. From *bottom* to *top* radial profiles at 20, 30, 60, and 70 mm height. Volume fraction data by laser-induced incandescence (Santoro et al. 1983, 1987). D63 data by scattering and extinction (Santoro et al. 1983, 1987). Modeled data: *continuous lines* represents results of the complete mechanism, *dashed lines* represents results of the mechanism without particle fragmentation induced by oxidation

the flame axis. The model does not predict the correct height where H-to-C ratio decreases, whereas the overall prediction of the aromatization process is matched. Figure 14.12 also shows the H/C profile obtained without taking into account the dehydrogenation pathway showing the importance of this mechanism in correctly reproducing the behaviors of particulate matter in flames.

Fig. 14.13 Comparison of predicted H/C along the flame axis of non-premixed ethylene flame (*lines*) with experimental data (*points*) from Dobbins et al. (1998)



14.5 Final Remarks

The latest version of a multi-sectional kinetic mechanism of aromatic growth and particulate formation is presented and it is tested over a range of different operating conditions in rich premixed and non-premixed flames of ethylene. The kinetic model has been built-up and refined by comparing model predictions with experimental data on the formation of high-molecular mass species and particles. Good predictions are obtained of major oxidation and pyrolysis products, as well as of trace species and particle concentrations and size distributions. The model is able to predict premixed and non-premixed flames of ethylene at atmospheric pressure without any adjustments to the scheme.

The model predicts a wide range of particle sizes. Particles with sizes below 10 nm having a modal diameter of about 2 nm are formed in premixed flames below the soot formation threshold and in the fuel side of non-premixed flames, in good agreement with the concentration of condensed hydrocarbon species and nanoparticle of organic carbon (NOC) experimentally detected by various techniques. The model predicts also the H/C ratios of these nanoparticles well in both premixed and non-premixed conditions.

Sensitivity of the predictions to the particulate-phase reaction rates has been performed showing the importance of the modeling of soot particle oxidation for the correct prediction of particle concentrations and sizes. In particular, the mechanism of oxidation-induced fragmentation allows the predictions of the right sizes of the particles and the complete burn-out in non-premixed conditions.

References

- Alfè M, Apicella B, Barbella R et al (2009) Structure–property relationship in nanostructures of young and mature soot in premixed flames. *Proc Combust Inst* 32:697–704
- Apicella B, Ciajolo A, Barella R et al (2003) Size exclusion chromatography of particulate produced in fuel-rich combustion of different fuels. *Energy Fuels* 17:565–570

- Ciajolo A, D'Anna A, Barbella R et al (1996) The effect of temperature on soot inception in premixed ethylene flames. *Symp (Int) Combust* 26:2327–2333
- Ciajolo A, Barbella R, Tregrossi A et al (1998) Spectroscopic and compositional signatures of PAH-loaded mixtures in the soot inception region of a premixed ethylene flame. *Symp (Int) Combust* 27:1481–1487
- D'Alessio A, D'Anna A, Gambi G et al (1998) The spectroscopic characterization of UV absorbing nanoparticles in fuel rich soot forming flames. *J Aerosol Sci* 29:397–409
- D'Alessio A, Barone AC, Cau R et al (2005) Surface deposition and coagulation efficiency of combustion generated nanoparticles in the size range from 1 nm to 10 nm. *Proc Combust Inst* 30:2595–2603
- D'Anna A (2009a) Combustion-formed nanoparticles. *Proc Combust Inst* 32:593–613
- D'Anna A (2009b) Particle inception and growth: experimental evidences and a modelling attempt. In: Bockhorn H, D'Anna A, Sarofim AF, Wang H (eds) *Combustion generated fine carbonaceous particles*. Karlsruhe University Press, Karlsruhe, pp 289–320
- D'Anna A, Kent JH (2008) A model of particulate and species formation applied to laminar, nonpremixed flames for three aliphatic-hydrocarbon fuels. *Combust Flame* 152:573–587
- D'Anna A, Sirignano M, Kent JH (2010) A model of particle nucleation in premixed ethylene flames. *Combust Flame* 157:2106–2115
- Dobbins RA, Fletcher RA, Chang H-C (1998) The evolution of soot precursor particles in a diffusion flame. *Combust Flame* 115:285–298
- Dworkin SB, Zhang Q, Thomson MJ et al (2011) Application of an enhanced PAH growth model to soot formation in a laminar coflow ethylene/air diffusion flame. *Combust Flame* 158:1682–1695
- Echavarria CA, Jaramillo IC, Sarofim AF et al (2011) Studies of soot oxidation and fragmentation in a two-stage burner under fuel-lean and fuel-rich conditions. *Proc Combust Inst* 33:659–666
- Frenklach M, Wang H (1991) Detailed modeling of soot particle nucleation and growth. *Symp (Int) Combust* 23:1559–1566
- Frenklach M, Wang H (1994) Detailed mechanism and modeling of soot particle formation. In: Bockhorn H (ed) *Soot formation in combustion: mechanisms and models*, Springer series in chemical physics 59. Springer-Verlag, Heidelberg, pp 165–192
- Hamaker HC (1937) The London–van der Waals attraction between spherical particles. *Physica* 4:1058–1072
- Homann K-H (1998) Fullerenes and soot formation new pathways to large particles in flames. *Angew Chem Int Ed* 37:2434–2451
- Joutsenoja T, D'Anna A, D'Alessio A et al (2001) Ultraviolet absorption spectra of carbon dioxide and oxygen at elevated temperatures. *Appl Spect* 55:130–135
- Kazakov A, Frenklach M (1998) Dynamic modeling of soot particle coagulation and aggregation: implementation with the method of moments and application to high-pressure laminar premixed flames. *Combust Flame* 114:484–510
- Marinov NM, Pitz WJ, Westbrook CK, Castaldi MJ, Senkan SM (1996) Modeling of aromatic and polycyclic aromatic hydrocarbon formation in premixed methane and ethane flames. *Combust Sci Technol* 116–117:211–287
- Mauss F, Netzell K, Marchal C et al (2009) Modeling the soot particle size distribution functions using a detailed kinetic soot model and a sectional method. In: Bockhorn H, D'Anna A, Sarofim AF, Wang H (eds) *Combustion generated fine carbonaceous particles*. Karlsruhe University Press, Karlsruhe, pp 465–482
- Miller JA, Melius CF (1992) Kinetic and thermodynamic issues in the formation of aromatic compounds in flames of aliphatic fuels. *Combust Flame* 91:21–39
- Mueller ME, Blanquart G, Pitsch H (2011) Modeling the oxidation-induced fragmentation of soot aggregates in laminar flames. *Proc Combust Inst* 33:667–674
- Neoh KG, Howard JB, Sarofim AF (1985) Effect of oxidation on the of soot. *Symp (Int) Combust* 20:951–957

- Richter H, Granata S, Green WH et al (2005) Detailed modeling of PAH and soot formation in a laminar premixed benzene/oxygen/argon low-pressure flame. *Proc Combust Inst* 30:1397–1405
- Russo C, Alfè M, Rouzaud J-N et al (2013) Probing structures of soot formed in premixed flames of methane, ethylene and benzene. *Proc Combust Inst* 34:1885–1892
- Santoro RJ, Semerjian HG, Dobbins RA (1983) Soot particle measurements in diffusion flames. *Combust Flame* 51:203–218
- Santoro RJ, Semerjian HG (1984) Soot formation in diffusion flames: flow rate, fuel species, and temperature effects. *Symp (Int) Combust* 20:997–1006
- Santoro RJ, Yeh TT, Horvath JJ et al (1987) The transport and growth of soot particles in laminar diffusion flames. *Combust Sci Technol* 53:89–115
- Sgro LA, Barone AC, Commodo M et al (2009) Measurement of nanoparticles of organic carbon in non-sooting flame conditions. *Proc Combust Inst* 32:689–696
- Sirignano M, Kent JH, D'Anna A (2010) Detailed modeling of size distribution functions and hydrogen content in combustion-formed particles. *Combust Flame* 157:1211–1219
- Sirignano M, Alfè M, Tregrossi A et al (2011) Experimental and modeling study on the molecular weight distribution and properties of carbon particles in premixed sooting flames. *Proc Combust Inst* 33:633–640
- Smith GP, Golden DM, Frenklach M et al (2013). http://www.me.berkeley.edu/gri_mech/
- Smooke MD, McEnally CS, Pfefferle LD (1999) Computational and experimental study of soot formation in a coflow, laminar diffusion flame. *Combust Flame* 117:117–139
- Smyth KC, Miller JH, Dorfman RC et al (1985) Soot inception in a methane/air diffusion flame as characterized by detailed species profiles. *Combust Flame* 62:157–181
- Xu F, El-Leathy AM, Kim CH et al (2003) Soot surface oxidation in hydrocarbon/air diffusion flames at atmospheric pressure. *Combust Flame* 132:43–57

Chapter 15

Modelling Soot Formation: Model of Particle Formation

Edward K. Y. Yapp and Markus Kraft

Abstract This article reports on detailed models of soot particle formation in combustion. First, we present the polycyclic aromatic hydrocarbon-primary particle (PAH-PP) model where soot particles are described by primary particles which are made up of PAHs. The model describes the formation, growth and oxidation of soot in laminar premixed ethylene flames. The connectivity between primary particles is stored to calculate the rounding of soot particles due to surface growth and condensation. We then show that a model intermolecular potential based on the simple Lennard-Jones potential supports the physical binding of PAHs as a viable mechanism for soot formation. We subsequently present the kinetic Monte Carlo-aromatic site (KMC-ARS) model which describes the structure and growth of planar PAHs. The PAH processes are represented as jump processes, and the energetics and kinetics were determined by quantum chemistry calculations. Lastly, we use molecular dynamics with a new potential specifically developed for PAH interaction and the combined PAH-PP/KMC-ARS model to show that pyrene dimerisation is unlikely to be the critical soot formation step at flame temperatures of about 1500–2000 K.

Abbreviations

C	Carbon
DFT	Density functional theory
DSA	Direct simulation algorithm
DSMC	Direct simulation Monte Carlo
H	Hydrogen
KMC	Kinetic Monte-Carlo

E. K. Y. Yapp · M. Kraft (✉)

Department of Chemical Engineering and Biotechnology, University of Cambridge,
Cambridge CB2 3RA, UK
e-mail: mk306@cam.ac.uk

E. K. Y. Yapp

e-mail: ekyy2@cam.ac.uk

KMC-ARS	Kinetic Monte-Carlo-aromatic site
LJ	Lennard-Jones
MD	Molecular dynamics
PAH	Polycyclic aromatic hydrocarbon
PAHAP	Polycyclic aromatic hydrocarbon anisotropic potential
PAH-PP	Polycyclic aromatic hydrocarbon-primary particle
PES	Potential energy surface
PSD	Particle size distribution
SAPT	Symmetry adapted perturbation theory
TEM	Transmission electron microscope
TST	Transition state theory

15.1 Introduction

This article presents some recent results relevant to the modelling of the formation of soot particles in flames.

A detailed population balance model is introduced to bridge the gap between particle population dynamics and gas-phase reactions. A basin-hopping optimisation technique is used to provide insight into the structure of nascent soot particles. Quantum chemistry and kinetic Monte Carlo (KMC) simulations are employed to describe growth and oxidation rates of polycyclic aromatic hydrocarbons (PAHs) in flames. Finally, using all model components described above, the critical size of PAHs which can form a soot particle is investigated (a) by using molecular dynamics (MD) simulations and (b) by fitting the detailed population balance model to mass spectrometry data.

15.2 Model of the Formation, Growth and Oxidation of Soot Particles in Laminar Premixed Ethylene Flames¹

In this section, the formation, growth and oxidation of soot in a laminar premixed flame is described in terms of a detailed population balance model named polycyclic aromatic hydrocarbon-primary particle (PAH-PP) and the laminar flame solver PREMIX.

The PAH-PP model is a detailed soot particle model where soot particles are represented by primary particles made up of PAHs. As each individual PAH in a soot particle is tracked, a detailed chemical model describing the interactions of

¹ All material has been drawn from Sander (2011) unless otherwise indicated.

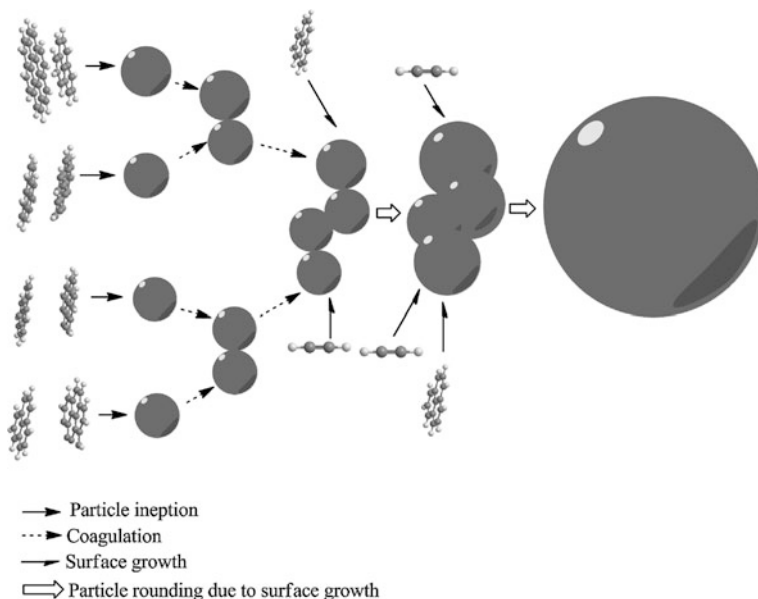


Fig. 15.1 Transformation processes in the PAH-PP model (Sander et al. 2011; Copyright Elsevier)

the soot particle with the gas-phase can be incorporated. The chemical model used here is the kinetic Monte-Carlo-aromatic site (KMC-ARS) model, which is described in Sect. 15.4. It is assumed that the first soot particles are formed from gas-phase species. In the case of a premixed laminar flame, the concentration of pyrene ($C_{16}H_{10}$) is precalculated using PREMIX (Kee et al. 1985) and read in as an input to the model. PREMIX is a one-dimensional laminar flame solver, which solves for the gas-phase chemical species and the first six moments of the soot particle size distribution (PSD) based on a spherical particle model (Appel et al. 2000). Further growth of these molecules is calculated using the KMC-ARS model. This growth happens either in the gas phase or, if the PAH is part of a soot particle, in the particle itself.

Figure 15.1 shows the different transformation processes in the model. These processes are summarised below:

Formation. A soot particle forms when two PAH molecules stick after collision. In the model, a size and mass-dependent collision efficiency determines the probability of sticking (see Sect. 15.5.2). The sticking of two PAHs incept a soot particle consisting of one primary particle which is made up of the two PAHs.

Coagulation. Two particles P_i and P_j collide creating a new particle P_k . It is assumed that one primary particle p_a of P_i and one primary particle p_b of P_j are in point contact in the new particle P_k .

Condensation. PAHs from the gas-phase condense onto the particles increasing the mass and sphericity (rounding) of the particle. It is implemented in the model by adding the gas-phase PAH to primary particle p_a within particle P_i .

Surface growth. PAHs in the soot particle react with the gas-phase. However, possibly due to steric hindrance, PAHs within the soot particle do not grow as quickly as PAHs in the gas-phase. To account for this the growth rate of PAHs within soot particles is multiplied by a growth factor g .

Soot particles increase in sphericity due to surface growth and condensation. Because the connectivity between primary particles is stored using a binary tree structure, the neighbours of each particle is known and a rounding factor r can be applied to any two neighbouring primary particles.

The particle population dynamics and the evolution of PAHs were recently coupled in the work by Chen et al. (2013). In the previous implementation, PAH growth is precalculated using the KMC-ARS model and the evolution of PAHs is stored in databases for various heights along the flame. The particle population dynamics is approximated by moving a sample volume containing stochastic particles through the flame at a gas velocity specified in PREMIX. Every pyrene molecule “transferred” into the particle model is assigned an evolution history from the database. In the current implementation, the evolution of PAHs is calculated during the simulation. A further process to be added is fragmentation where large aggregates break down into smaller aggregates which can be important in premixed flames (Mueller et al. 2011).

The population balance describing the inception, coagulation, condensation and surface growth processes is solved using the direct simulation Monte-Carlo (DSMC) method; also called the direct simulation algorithm (DSA). The numerical solution of the population balance when using the PAH-PP model includes the following steps:

- (1) Set start time $t \leftarrow t_0$ and initial position along the flame $x \leftarrow x_0$.
- (2) Calculate the rates R_i of formation, condensation and coagulation (described below).
- (3) Calculate an exponentially distributed waiting time dt with parameter:

$$R_{\text{tot}} = \sum R_i, \quad (15.1)$$

where R_i are the rates of the individual processes.

- (4) Increase time by the waiting time $t \leftarrow t + dt$ and update the position x .
- (5) Update the evolution of all the PAHs in the particles or in the gas-phase through the KMC-ARS model.
- (6) If $t \geq t_{\text{stop}}$ then end.
- (7) A process i is selected based on the probability:

$$P = \frac{R_i}{R_{\text{tot}}}. \quad (15.2)$$

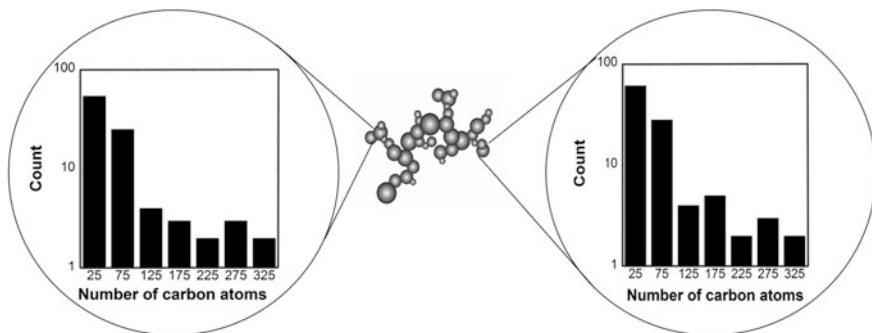


Fig. 15.2 A soot particle generated using the PAH-PP model and the detailed information stored for each primary particle (Sander et al. 2011; Copyright Elsevier)

- (8) Perform the process.
 (9) Go to step 2.

The rates of formation, condensation and coagulation are calculated from the transition-regime kernel K^{tr} and are multiplied by a sticking efficiency. K^{tr} is calculated as the harmonic mean of kernels K^{sf} and K^{fm} :

$$K^{\text{tr}}(A, B) = \frac{K^{\text{sf}}(A, B)K^{\text{fm}}(A, B)}{K^{\text{sf}}(A, B) + K^{\text{fm}}(A, B)}. \quad (15.3)$$

For a formation process, A and B represent PAHs; for a condensation process, A is a particle and B is a PAH, or vice versa; for a coagulation process, A and B are particles. The slip-free kernel K^{sf} and the free-molecular kernel K^{fm} are calculated as follows:

$$K^{\text{sf}}(A, B) = \frac{2k_B T}{3\mu} \left(\frac{1 + 1.257Kn_A}{d_c(A)} + \frac{1 + 1.257Kn_B}{d_c(B)} \right) (d_c(A) + d_c(B)), \quad (15.4)$$

$$K^{\text{fm}}(A, B) = 2.2 \sqrt{\frac{\pi k_B T}{2}} \left(\frac{1}{M(A)} + \frac{1}{M(B)} \right)^{\frac{1}{2}} (d_c(A) + d_c(B))^2, \quad (15.5)$$

where k_B is the Boltzmann constant; T is temperature; μ is the dynamic viscosity of the gas-phase; Kn_x is the Knudsen number of a PAH or particle x ; and $M(x)$ and $d_c(x)$ is the mass and collision diameter, respectively, of a particle or PAH, x . The Knudsen number can be easily calculated from the diameter of the particle. Correlations for the collision diameters have been determined by Sander et al. (2011).

Figure 15.2 shows an example of a soot particle generated using the PAH-PP model. The connectivity between primary particles is clearly shown and a count of a selection of PAHs (sorted by the number of carbon (C) atoms it contains) for two particular primary particles is shown as well.

Three parameters in the PAH-PP model (Sander et al. 2011): soot density ρ , growth factor g and rounding factor r were determined empirically by fitting the median of the logarithmic part of the PSD to a number of laminar premixed ethylene flames (Zhao et al. 2005). A low discrepancy series method was applied followed by a quadratic response surface optimisation. The shape of the PSD of large particles was well-matched but the number density of smaller particles was underpredicted. The results of the fitting procedure suggest that almost all the chemical growth takes place in the gas-phase and not inside the particle. Further, it indicates that the value of the soot density is around 1.5 g/cm^3 , which is slightly below the commonly assumed value of 1.8 g/cm^3 .

15.3 Model Intermolecular Potential Describing the Physical Binding of PAHs²

The purpose of this section is to find possible PAH configurations which minimise their potential energy surface and investigate the density of such a PAH structure.

The PAH-PP model describes the population dynamics of soot particles, i.e. their formation, growth, shape evolution and oxidation. However, the mechanism of how PAHs stick together is not quite understood and there is a need to refine the sub-models for particle formation and the models for which intra- and inter-particle molecular mobility plays a role. The forces that drive the interactions of molecules are determined by intermolecular potentials.

Intermolecular interactions describe the sum of attractive and repulsive forces between molecules. For large systems of molecules, the only computationally feasible approach to describe these interactions is to use model potentials. The total interaction energy of a molecular cluster can be approximated as the sum over all pairwise atom–atom interactions between atom a of molecule A and atom b of molecule B :

$$U = \sum_A \sum_{A < B} \sum_{a \in A} \sum_{b \in B} U_{ab}(R_{ab}, \Omega_{ab}), \quad (15.6)$$

where $U_{ab}(R_{ab}, \Omega_{ab})$ is the atom–atom interaction potential as some function of the atom–atom separation R_{ab} and their relative molecular orientation Ω_{ab} . Each molecule is treated as a rigid body, thereby ignoring intramolecular degrees of freedom.

A popular form for U_{ab} is the isotropic Lennard-Jones (LJ) potential plus point-charge electrostatic model:

² All material has been drawn from Totton et al. (2010) unless otherwise indicated.

$$U_{ab} = U_{LJ} + U_{elec} = 4\varepsilon_{ab} \left[\left(\frac{\sigma_{ab}}{R_{ab}} \right)^{12} - \left(\frac{\sigma_{ab}}{R_{ab}} \right)^6 \right] + \frac{q_a q_b}{R_{ab}}, \quad (15.7)$$

where ε_{ab} and σ_{ab} are the potential well-depth and size parameters, respectively, describing interactions between atoms a and b . These parameters have been empirically determined for hydrocarbons (van de Waal 1983): CC, CH and HH atom–atom interactions. The R^{-12} term represents repulsion while the R^{-6} term represents dispersion. q_a and q_b are partial charges on atoms a and b .

To calculate the optimal arrangement of several PAH molecules the LJ potential plus point-charge electrostatic model is used to generate a potential energy surface (PES) for a molecular cluster of PAHs. The PES is then transformed into a discrete set of energy levels by applying a global optimisation technique using a “basin-hopping” scheme (Wales and Doye 1997). The technique involves perturbing the geometry of the cluster and carrying out a minimisation on the resulting geometry. A step is accepted if the energy of the new geometry is less than at the previous step. If the energy of the new geometry is greater than before, an accept–reject scheme such as the Metropolis criterion is used (Li and Scheraga 1987) which helps the basin-hopping scheme to move through successive local minima.

Figure 15.3 shows the low energy cluster arrangement of pyrene and coronene. These two types of soot precursors are typically found in flame environments. Clusters of only 50 PAHs were considered because simulating larger systems would be computationally expensive. In reality, soot particles contain hundreds, if not, thousands of PAHs. In the simulations, the PAHs were initially randomly scattered whilst ensuring no molecular overlap. Note the formation of multiple stacks (PAHs aligned parallel to each other) made up of 2–4 PAHs. This approach was used to study homomolecular clusters but can be easily extended to the study of mixtures of PAHs.

Figure 15.4 shows a computationally generated transmission electron microscope (TEM) image of 50 coronene molecules compared against two experimental HR-TEM images of soot aggregates sampled from a diesel engine (Mosbach et al. 2009). While the experimental images suggest the presence of larger PAH structures, on the length scale of 2.5–3.0 nm, they show the formation of stacks and there is a qualitative agreement in the number of PAHs in each stack and the separation between the molecular planes.

These images clearly show the sticking of PAHs inside a soot particle and there is strong support for the physical binding of two PAHs as a viable mechanism for soot formation. Soot density is an important parameter in the PAH-PP model and a value of around 1.8 g/cm³ is commonly used. By defining a critical scaling factor such that all intermolecular space within a cluster is occupied, an improved estimate of soot density can be calculated. The density of a 50 coronene cluster, taken to be representative of a nascent soot particle, was calculated to be 1.12 g/m³.

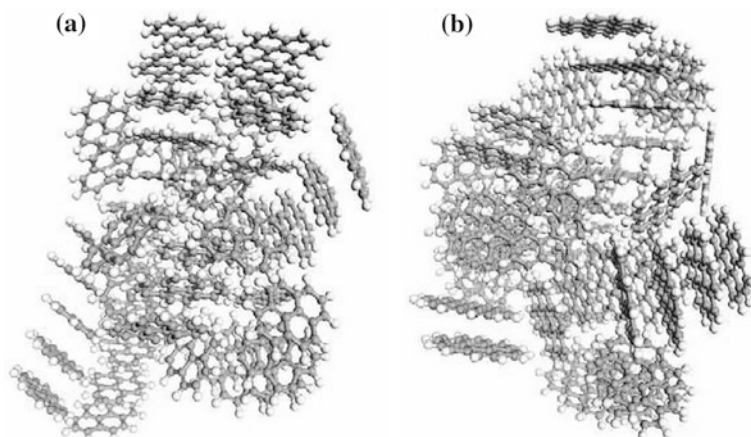


Fig. 15.3 Low energy cluster arrangement of **a** 50 pyrene molecules ($C_{16}H_{10}$) and **b** 50 coronene ($C_{24}H_{12}$) molecules, found using model intermolecular potential (Totton et al. 2010; Copyright Elsevier)

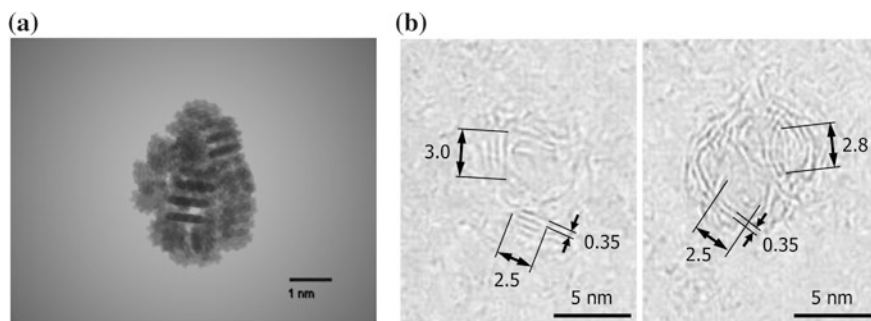


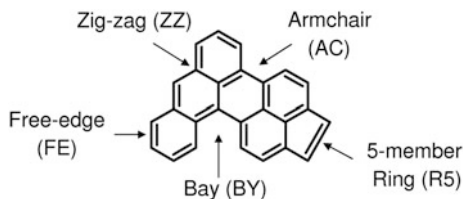
Fig. 15.4 **a** TEM-style projection of a cluster of 50 coronene molecules using model intermolecular potential (Totton et al. 2010; Copyright Elsevier) and **b** experimental TEM images of soot aggregates sampled from a diesel engine (Mosbach et al. 2009; Copyright Elsevier)

15.4 Model of the Gas-Phase Interactions of PAHs³

The chemical growth of PAHs is represented by the KMC-ARS model. The KMC-ARS model describes the structure and growth of planar PAH structures (Raj et al. 2009). A PAH is assumed to be fully represented by the number of C and hydrogen (H) atoms it contains, and the number and types of elementary sites on its edge. Figure 15.5 shows the four elementary sites (Celnik et al. 2008): free-edge,

³ All material has been drawn from Raj et al. (2009) unless otherwise indicated.

Fig. 15.5 PAH showing the different types of elementary sites on which different reactions and jump processes can take place in the KMC-ARS model (Raj et al. 2009; Copyright Elsevier)



zig-zag, armchair and bay sites. A five-member ring is to be distinguished from the other sites because it may occupy a zig-zag site (Frenklach et al. 2005). Each site has exactly two surface C atoms (bonded to a H atom) and is distinguished by the number of bulk C atoms (not bonded to a H atom). For example, a free-edge site has zero bulk C atoms, while a zig-zag site has one bulk atom; both sites have two surface C atoms.

This model simulates the growth of a PAH through a detailed set of PAH surface reactions and jump processes which are solved using the KMC algorithm. The surface reactions are assumed to take the modified Arrhenius form and the rate constant of each reaction is calculated as:

$$k(T) = AT^n \exp\left(\frac{-E}{RT}\right), \quad (15.8)$$

where A is the temperature-independent constant, T is the temperature, n is a constant, E is the activation energy and R is the universal gas constant.

A PAH may undergo different processes such as five-member and six-member ring addition, removal and oxidation at different reactive sites. Each of these processes is made up of a number of reversible and/or irreversible surface reactions. Including all the intermediate species in the reaction mechanism would be computationally unfeasible. Therefore, the intermediate species are assumed to be at steady-state, and ring addition and removal steps are assumed to be irreversible; hence, the name *jump* process. The jump processes are defined such that they take place only on certain sites or parent sites. A parent site is defined as a site on which a reaction takes place and is replaced in the reaction. The rate of a jump process at a parent site is calculated as:

$$R_i = k_i \times f_i \times C \times N_{\text{site}}(e), \quad (15.9)$$

where k_i is the rate constant from Eq. (15.8) and f_i is the fraction of radical sites of the parent type found using the steady-state assumption (Celnik et al. 2008). f_i is calculated as some function of the concentrations of the intermediate species and rate constants; C is the concentration of the gas-phase species involved in the reaction. $N_{\text{site}}(e)$ is the number of parent sites on the PAH as some function of the data structure e , which will be explained below.

The KMC algorithm allows the structure of a PAH to be tracked explicitly but is limited to single planar PAHs. The model is formulated mathematically by first defining a data structure, then defining the jump processes and each corresponding rate on the basis of this structure. However to derive a suitable data structure, the concept of a state space is first introduced.

The state space refers to all possible states in the system and each state corresponds to a unique point. The simplest state space is made up of the following state variables: positions of the C atoms and the bonds between them. Each C atom is assumed to be sp^2 hybridised which means that each bulk C atom is bonded to three other C atoms; while a C atom on the surface of the PAH is bonded to two other C atoms (and a H atom depending on whether a radical site is created.) The state space for a 2D representation of planar or near-planar PAHs can be represented as (Gómez-Lor et al. 2002):

$$E = (i, j, i_1, j_1, i_2, j_2, i_3, j_3), \quad (15.10)$$

where i and j are the x and y coordinates, respectively, of a C atom, and i_n and j_n are the coordinates of the n th C atom bonded to the C atom with coordinates (i, j) . Note that information about the bonds between C atoms is implied by the relative positions of the C atoms. For a surface C atom coordinates (i_3, j_3) are set to some pre-defined value.

For PAHs with a 3D geometry, such as a five-membered ring surrounded by five six-membered rings, additional coordinates can be added to the state space. However, the KMC algorithm may not be applicable and MD may be required to determine the resulting structure (Raj et al. 2010b). This state space provides sufficient information for the jump processes to be defined but it is difficult to do so; therefore, a higher-order data structure is required.

A 2D grid is generated and a single PAH is placed on this grid. Each C atom in the PAH is assigned a grid point and its structure is fully described by the data structure:

$$e = (c, s). \quad (15.11)$$

It is made up of a C atom vector:

$$c = (S_1, S_2, S_{in_1}, S_{in_2}, C_{type}, i, j), \quad (15.12)$$

where each surface C atom is part of two elementary sites S_1 and S_2 , and S_{in_1} and S_{in_2} are the indices of each site. C_{type} is used to differentiate between a surface and a bulk C atom, and (i, j) are its coordinates.

And a site vector:

$$s = (S_{type}, S_{in}, i_1, j_1, i_2, j_2), \quad (15.13)$$

where S_{type} and S_{in} have been defined above, and each site has two surface C atoms which have coordinates (i_1, j_1) and (i_2, j_2) .

The KMC algorithm is similar to the algorithm used in the PAH-PP model (Sect. 15.2) but the key differences are: (1) instead of initialising at some position along the flame in the PAH-PP model, a planar PAH is used to initialise e ; (2) the rate of each jump process is calculated and based on a probability calculated using this rate a process is selected; (3) vector c is updated when a jump process results in C addition or removal; and (4) vector s is updated when a parent site is replaced and neighbouring sites change.

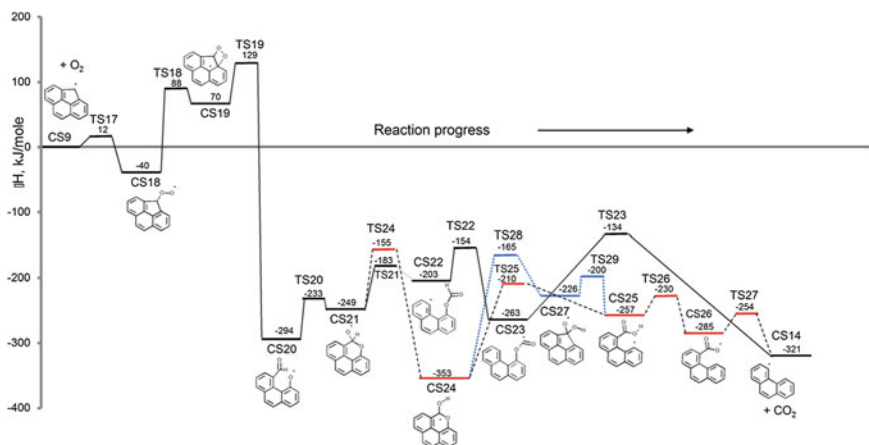


Fig. 15.6 Potential energy diagram of a suggested pathway for soot oxidation (Raj et al. 2012; Copyright Elsevier)

In the development of a reaction mechanism both the energetics and kinetics of the reactions are required. Quantum chemistry calculations, employing density functional theory (DFT), are performed to predict the geometry and energy of stable molecular species. The potential energy surfaces from these calculations are used to evaluate the rate constants of the surface reactions that take place on a PAH using transition state theory (TST).

Figure 15.6 is a potential energy diagram constructed from the energies of the reactants, transition states and products. It shows the oxidation of a five-membered ring in chemical species 9 (CS9) by O_2 to form 4-phenanthryl (CS14). This is part of one of the suggested pathways for the assumed model reaction for soot oxidation (Raj et al. 2012): 4-pyrenyl + $O_2 \rightarrow$ 4-phenanthryl + $2CO$. In their work, molecular structures were optimised using the B3LYP functional and the 6-311 ++G(d,p) basis set. The stable chemical species were optimised with different spin multiplicities to determine the multiplicity with the minimum energy and reasonable geometry. The same approach was used in the development of additional dehydrogenation jump processes to improve model predictions (Raj et al. 2010a). Future work involves constructing jump processes from oxidation reactions, such as the one above, and incorporating them into the KMC-ARS model.

15.5 Critical Soot Formation Size

It is often assumed that pyrene dimerisation is the critical soot particle formation step. However, more recently, there are a number of studies which challenge this view. In the next two sections we lay out two approaches which show that pyrene dimerisation may not be the critical step in the formation of soot at flame temperatures.

15.5.1 Polycyclic Aromatic Hydrocarbon Anisotropic Potential⁴

The computationally efficient and popular LJ potential may have been acceptable in Sect. 15.3, but a more accurate potential which considers the intermolecular forces between PAHs is required for the study of the critical soot formation size.

The LJ potential has a tendency to overestimate the well depths of interactions or binding energy between PAH molecules. This would lead to an underestimation of the critical soot formation size at typical flame temperatures of approximately 1500–2000 K (Wang 2011). A highly accurate quantum chemistry technique such as symmetry adapted perturbation theory (SAPT(DFT)) would have been ideal but is not feasible for large systems. The next best alternative is a simple potential parameterised using high-accuracy interaction energies of smaller PAHs calculated using SAPT(DFT). Totton et al. (2012) used this method to develop the general PAHAP potential which is based on the same three types of interactions (CC, CH and HH atom–atom pairs) as the LJ potential:

$$U_{ab} = G \exp[-\alpha_{ab}(R_{ab} - \rho_{ab}(\Omega_{ab}))] - f_6(R_{ab}) \frac{C_{6,\text{iso}}}{R_{ab}^6} + \frac{q_a q_b}{R_{ab}}. \quad (15.14)$$

The first term on the right-hand side is the short-range exchange-repulsion term and is modelled using an anisotropic Born–Mayer term. G is a constant energy unit and is set to 0.001 Ha. α_{ab} describes the hardness of the interaction between atoms a and b . The second term is the long-range dispersion term and is modelled using the isotropic coefficient $C_{6,\text{iso}}$ and the damping function $f_6(R_{ab})$ proposed by (Tang and Toennies 1984). The third term is the point-charge electrostatic model as in Eq. (15.7).

The PAHAP potential describes atomic shape anisotropy using angular expansions, but this feature is not currently supported by standard MD codes. Hence, an isotropic PAHAP potential is developed by neglecting the orientation dependence of the shape function ρ_{ab} . The isotropic potential parameters are fitted by calculating the interaction energies for coronene dimers in a variety of conformations. The resulting parameterisation is shown to accurately account for the interactions of other PAHs. Therefore, the isotropic PAHAP potential is transferable to PAHs other than coronene.

The thermodynamics of the homomolecular dimerisation of five representative PAHs was studied across a temperature range of 0–2500 K. Pyrene ($\text{C}_{16}\text{H}_{10}$), coronene ($\text{C}_{24}\text{H}_{12}$), ovalene ($\text{C}_{32}\text{H}_{14}$), hexabenzocoronene ($\text{C}_{42}\text{H}_{18}$) and circumcoronene ($\text{C}_{54}\text{H}_{18}$) were selected because they span a large mass range and for their thermal stability at temperatures as high as 3000 K (Stein and Fahr 1985). It

⁴ All material has been drawn from Totton et al. (2012) unless otherwise indicated.

was found that with an increase in PAH size, there was an increase in dimer stability (or equilibrium constant K_p). As temperature increases, K_p decreases which means that the PAH monomer is more stable than the dimer. The temperature for this crossover ($K_p = 1$ or Gibb's free energy of 0) was calculated to be 332 K for pyrene and 1387 K for circumcoronene. Both temperatures lie well below typical flame temperatures and this shows that PAHs as large as circumcoronene may not undergo a significant amount of dimerisation.

In addition MD simulations of the homomolecular clustering of the five PAHs were performed at five different temperatures (500, 750, 1000, 1250 and 1500 K) using the canonical NVT (moles-volume-temperature) ensemble with cubical periodic boundary conditions. The Nosé–Hoover thermostatting method (Hoover 1985; Nosé 1984) was used to maintain a constant temperature with a time constant of 0.05 ps. Each simulation contained 1,000 PAHs and was run for 1000 ps at a concentration of 2×10^{18} PAHs/cm³ which corresponds to 4 ms and 1×10^{15} PAHs/cm³, respectively, in actual flames. Inflated concentrations had to be used to account for the differing timescales between actual flames and that which is possible in MD simulations. To specify what constitutes a cluster and to control the stability of the cluster, two parameters have to be specified: a critical cut-off separation between two PAHs r_{crit} and a critical time length the two PAHs remain bound t_{crit} . The choice of $r_{\text{crit}} = 12 \text{ \AA}$ and $t_{\text{crit}} = 20 \text{ ps}$ was somewhat arbitrary but these values were chosen so as to suppress the number of clusters detected.

Figure 15.7 shows the trajectories of each of the five systems at the lowest system temperature of 500 K. Five runs were carried out for each of the systems and averaged to show the average proportion of PAHs that are part of a cluster and the maximum number of PAHs in any one cluster. This figure clearly shows that pyrene dimerisation cannot play a significant role in soot particle formation even at low temperatures; at 1500 K only circumcoronene was found to dimerize (not shown). To conclude, for the physical binding of PAHs based on van der Waals interactions large PAH molecules of the order of 50 carbon atoms are required.

15.5.2 Combined PAH-PP/KMC-ARS Model⁵

The PAH-PP model, which is a population balance model, and the KMC-ARS model, which is a PAH surface growth model, are combined to study the coagulation of PAHs and their clusters in laminar premixed ethylene flames.

The following assumptions are made: (1) the rate of surface growth of a PAH in a stack is independent of the number of PAHs in the stack. This implies that the PAH surface growth processes are independent of the transformation processes that occur on a particle; (2) all reactive sites on a cluster or stack, regardless of

⁵ All material has been drawn from Raj et al. (2010b) unless otherwise indicated.

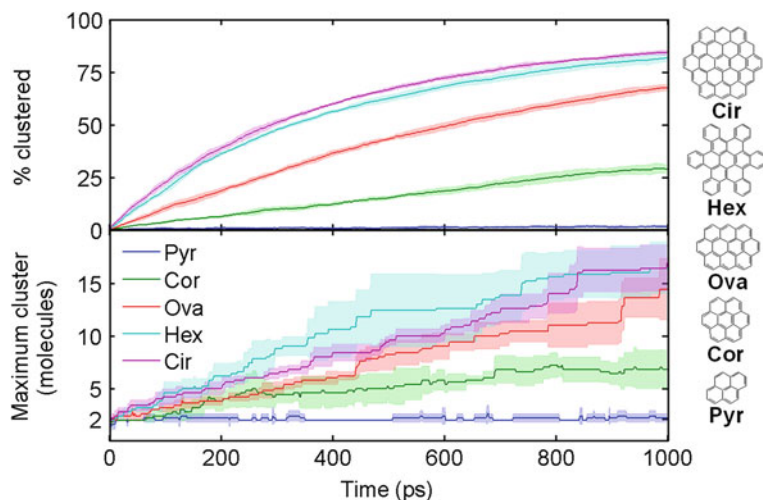


Fig. 15.7 Molecular dynamics results at 500 K for pyrene (*Pyr*), coronene (*Cor*), ovalene (*Ova*), hexabenzocoronene (*Hex*) and circumcoronene (*Cir*) where intermolecular interactions were modelled using the PAHAP potential as performed by Totton et al. (2012)

position or orientation, are equally accessible to gas-phase species. Note that the term cluster refers to randomly orientated PAHs while stacks are PAHs aligned parallel to each other.

The rate of coagulation between two colliding PAHs a and b is calculated as:

$$R_{C_{a,b}} = C_E \times E_F \times \beta_{a,b} \times C_a \times C_b, \quad (15.15)$$

where C_E is the collision efficiency, $E_F = 2.2$ is the van der Waals enhancement factor (Harris and Kennedy 1988), $\beta_{a,b}$ is the coagulation kernel, and C_a and C_b are the concentrations of PAHs a and b . An expression for $\beta_{a,b}$ in the free-molecular regime was found by Frenklach and Wang (1994), while the concentrations of PAHs are easily obtained from the simulation.

In order to calculate the rate of coagulation C_E is required. A correlation for C_E was found through qualitative comparisons between computed and observed mass spectra. The laminar premixed ethylene flames studied by Happold (2008) were chosen because of the availability of mass spectra. However, in these spectra, the concentrations of PAHs were measured in terms of varying intensities of ion signals for different PAH masses (monomers and dimers) which offered no direct comparison with computed number densities. Comparisons were made on the basis of three key features:

- (1) Position of the maxima of PAH dimers;
- (2) Position where there is a sharp decay in monomers;
- (3) Spread of the dimer mass spectra on either side of the maxima: position where dimer spectra starts and ends.

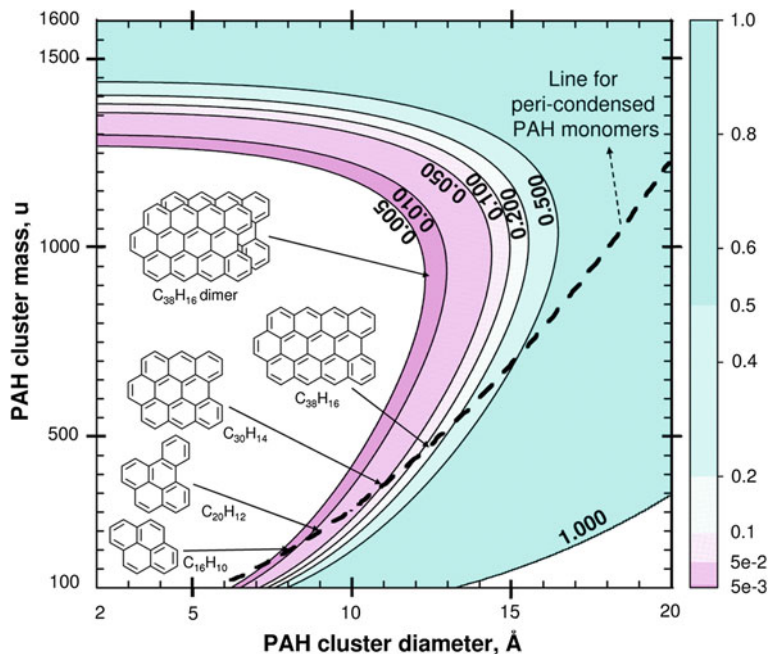


Fig. 15.8 Contour plot of collision efficiency used to calculate coagulation rates in the combined PAH-PP/KMC-ARS model (Raj et al. 2010b; Copyright Elsevier)

C_E was found to depend on the diameter and mass of the smaller of the two colliding PAH clusters: D_{\min} and M_{\min} respectively. The following functional form was suggested:

$$C_E = \frac{1}{1 + \exp\left(-\left(A \times \frac{D_{\min}^3}{M_{\min}} + \left(\frac{M_{\min}}{B}\right)^6 - C\right)\right)}, \quad (15.16)$$

where $A = 2 \text{ g}/(\text{mol} \cdot \text{\AA}^3)$, $B = 980 \text{ g/mol}$ and $C = 10$ (dimensionless) are fitting parameters which give a good agreement between the computed and observed mass spectra on the basis of the above three features.

Figure 15.8 is a contour plot of C_E against D_{\min} and M_{\min} . The line for peri-condensed PAH monomers separates clusters made up of two or more PAHs, such as the $C_{38}H_{16}$ dimer shown, from the monomers below the line. It is observed that increasing D_{\min} and M_{\min} increases C_E . A reasonable amount of coagulation can be expected for $C_E \geq 4\%$ which corresponds to $D_{\min} = 360 \text{ amu}$ and $M_{\min} = 10 \text{ \AA}$. Pyrene has a mass of about 200 amu and a diameter of about 7 Å, which means that collisions involving pyrene is highly unlikely to be successful. Note that C_E does not account for changes in pressure and was fitted to high-temperature flames of about 1800 K.

15.6 Conclusion

Several aspects of soot modelling have been discussed. The PAH-PP model combined with the KMC-ARS model describes soot particles in terms of its composition and shape. It also couples the particle to the surrounding gas-phase by tracking the gas-phase interactions of PAHs inside each primary particle. In addition two different potentials were used, which describe the forces between PAHs, to investigate the structure of nascent particles using basin hopping and MD. Both the combined PAH-PP/KMC-ARS model and MD were used to investigate the critical PAH size for successful dimerisation.

15.7 Final remarks

In this section, the similarities and differences between two approaches to soot modelling are discussed, namely the advanced multi-sectional method ([Chap. 14](#)) and the PAH-PP/KMC-ARS model ([Sects. 15.2](#) and [15.4](#); referred to as the stochastic model from hereon). In the sectional model particles are numerically treated as gas-phase species and by using lumped species, the numbers of carbon and hydrogen atoms are tracked. Also three different morphologies are considered: large molecules, cluster of molecules (i.e. single particles) and agglomerates of particles. The stochastic model contains the most detailed particle description that is currently available, with thousands of internal coordinates tracked, including not just chemical composition but morphology. From this detailed description, TEM images and mass spectra have been computationally generated.

In the sectional model, the largest gas-phase species is determined by the chemical mechanism used. In this case it is pyrene which has 16 carbon atoms. All species with a larger molecular weight are conceptually treated as particles but numerically are treated as in the gas-phase. The mass range of these particles is defined by a range of sections and each section is assigned an average molecular weight and H/C ratio ranging from 0 to 1. The number of carbon atoms ranges from 24 in the first section to 2×10^{10} in the last section. In each section, the three different morphologies are considered. In the stochastic model each PAH is represented by the number of carbon and hydrogen atoms it contains, and the number and types of elementary sites on its edge. Primary particles are made up of PAH clusters and the connectivity between primary particles is stored using a binary tree structure. In both models, the orientation of the PAHs or PAH stacks which makes up a primary particle is not known.

Both models allow for the inception, coagulation, condensation, and surface growth and oxidation of particles but it is in the treatment of some of these processes where the models differ. The sectional model accounts for the inception process, i.e. the formation of the first particles or particle nuclei, both through the

sticking of gas-phase PAHs and through the formation of large, polymer-like molecules that can coagulate forming the first particle. The coagulation efficiency used is size-dependent, approaching unity as the size of colliding particles increases. The model is also a function of the temperature and the interaction potential between coagulation entities. It has been confirmed by comparison with experimental data obtained at flame temperatures. Finally two different coagulation efficiencies are used for the coalescence and agglomeration times, allowing both single particles, up to a certain size, and agglomerates of particles, for larger compounds, to be considered. In the stochastic model, inception is the successful sticking of any two PAHs as determined by the collision efficiency model. An empirical correlation is used with a dependence on the diameter and mass of the smaller of the two colliding PAH clusters. The parameters of the model were obtained by fitting to various features of experimental mass spectra. Characteristic coalescence and agglomeration times are calculated in a similar fashion.

In the sectional model condensation and surface growth events increase the total mass of the particles. It accounts for the dehydrogenation process which allows for the lowering of the hydrogen content in particles typical of gas-phase PAHs to very low values typical of large soot aggregates. The gas-phase chemistry and particle phase are fully coupled and the chemical evolution of PAHs and particles is tracked. The stochastic model accounts for the increase in sphericity between any two primary particles in addition to accounting for the increase in mass. The exact structure and growth of each individual PAH is known. Although the particle dynamics and the chemical evolution of PAHs are fully coupled, it is not coupled to the gas-phase. Gas-phase species profiles computed using the PREMIX code with a method-of-moments soot model are fed as an input to the model.

Both models are able to account for the depletion of particles through surface oxidation. A novel aspect of the sectional model is the ability to take into account oxidation-induced fragmentation of soot aggregates and particles. The process is triggered after a critical fraction of carbon atoms is removed from the aggregate/particle. The fragmentation process has yet to be added to the stochastic model.

References

- Appel J, Bockhorn H, Frenklach M (2000) Kinetic modeling of soot formation with detailed chemistry and physics: laminar premixed flames of C2 hydrocarbons. *Combust Flame* 121:122–136
- Celnik M, Raj A, West R, Patterson R, Kraft M (2008) Aromatic site description of soot particles. *Combust Flame* 155:161–180
- Chen D, Zainuddin Z, Yapp E, Akroyd J, Mosbach S, Kraft M (2013) A fully coupled simulation of PAH and soot growth with a population balance model. *Proc Combust Inst* 34:1827–1835
- Frenklach M, Wang H (1994) Detailed mechanism and modelling of soot particle formation. In: Bockhorn H (ed) *Soot formation in combustion—mechanism and models*. Springer, Berlin

- Frenklach M, Schuetz CA, Ping J (2005) Migration mechanism of aromatic-edge growth. *Proc Combust Inst* 30:1389–1396
- Gómez-Lor B, Koper C, Fokkens RH, Vlietstra EJ, Cleij TJ, Jenneskens LW, Nibbering NMM, Echavarren AM (2002) Zipping up ‘the crushed fullerene’ $C_{60}H_{30}$: C_{60} by fifteen-fold, consecutive intramolecular H_2 losses. *Chem Commun* 59:370–371
- Happold J (2008) Geschichtete Polyzyklische aromatische Kohlenwasserstoffe alsbausteine der rußbildung. PhD thesis. Universität Stuttgart
- Harris SJ, Kennedy IM (1988) The coagulation of soot particles with van der Waals forces. *Comb Sci Tech* 59:443–454
- Hoover W (1985) Canonical dynamics: equilibrium phase-space distributions. *Phys Rev A* 31:1695–1697
- Kee RJ, Grcar JF, Smooke MD, Miller JA, Meeks E (1985) PREMIX: a FORTRAN program for modeling steady laminar one-dimensional flames. SANDIA National Laboratories technical report
- Li Z, Scheraga HA (1987) Monte Carlo minimization approach to the multiple-minima problem in protein folding. *Proc Nat Acad Sci USA* 84:6611–6615
- Mosbach S, Celnik MS, Raj A, Kraft M, Zhang HR, Kubo S, Kim K-O (2009) Towards a detailed soot model for internal combustion engines. *Combust Flame* 156:1156–1165
- Mueller ME, Blanquart G, Pitsch H (2011) Modeling the oxidation-induced fragmentation of soot aggregates in laminar flames. *Proc Combust Inst* 33:667–674
- Nosé S (1984) A molecular dynamics method for simulations in the canonical ensemble. *Mol Phys* 52:255–268
- Raj A, Celnik M, Shirley R, Sander M, Patterson R, West R, Kraft M (2009) A statistical approach to develop a detailed soot growth model using PAH characteristics. *Combust Flame* 156:896–913
- Raj A, Man PLW, Totton TS, Sander M, Shirley RA, Kraft M (2010a) New polycyclic aromatic hydrocarbon (PAH) surface processes to improve the model prediction of the composition of combustion-generated PAHs and soot. *Carbon* 48:319–332
- Raj A, Sander M, Janardhanan V, Kraft M (2010b) A study on the coagulation of polycyclic aromatic hydrocarbon clusters to determine their collision efficiency. *Combust Flame* 157:523–534
- Raj A, da Silva G, Chung SH (2012) Reaction mechanism for the free-edge oxidation of soot by O_2 . *Combust Flame* 159:3423–3436
- Sander M (2011) Mathematical modelling of nanoparticles from the gas-phase. PhD thesis. University of Cambridge
- Sander M, Patterson RIA, Braumann A, Raj A, Kraft M (2011) Developing the PAH-PP soot particle model using process informatics and uncertainty propagation. *Proc Combust Inst* 33:675–683
- Stein SE, Fahr A (1985) High-temperature stabilities of hydrocarbons. *J Chem Phys* 89:3714–3725
- Tang KT, Toennies JP (1984) An improved simple model for the van der Waals potential based on universal damping functions for the dispersion coefficients. *J Chem Phys* 80:3726–3741
- Totton TS, Chakrabarti D, Misquitta AJ, Sander M, Wales DJ, Kraft M (2010) Modelling the internal structure of nascent soot particles. *Combust Flame* 157:909–914
- Totton TS, Misquitta AJ, Kraft M (2012) A quantitative study of the clustering of polycyclic aromatic hydrocarbons at high temperatures. *Phys Chem Chem Phys* 14:4081–4094
- van de Waal BW (1983) Calculated ground-state structures of 13-molecule clusters of carbon dioxide, methane, benzene, cyclohexane, and naphthalene. *J Chem Phys* 79:3948–3961
- Wales DJ, Doye JPK (1997) Global Optimization by Basin-Hopping and the Lowest Energy Structures of Lennard-Jones Clusters Containing up to 110 Atoms. *J Phys Chem A* 101:5111–5116

- Wang H (2011) Formation of nascent soot and other condensed-phase materials in flames. *Proc Combust Inst* 33:41–67
- Zhao B, Yang Z, Li Z, Johnston MV, Wang H (2005) Particle size distribution function of incipient soot in laminar premixed ethylene flames: effect of flame temperature. *Proc Combust Inst* 30:1441–1448

Part IV
Methods for Mechanism Reduction and
Uncertainty Analysis

Chapter 16

Investigation and Improvement of Reaction Mechanisms Using Sensitivity Analysis and Optimization

Alison S. Tomlin and Tamás Turányi

Abstract The Chapter will describe a range of mathematical tools for model sensitivity and uncertainty analysis which may assist in the evaluation of large combustion mechanisms. The aim of such methods is to determine key model input parameters that drive the uncertainty in predicted model outputs. Approaches based on linear sensitivity, linear uncertainty and global uncertainty analysis will be described as well as examples of their application to chemical kinetic modelling in combustion. Improving the robustness of model predictions depends on reducing the extent of uncertainty within the input parameters. This can be achieved via a variety of methods including measurements and theoretical calculations. Optimization techniques which bring together wide sources of data can assist in further constraining the input parameters of a model and therefore reducing the overall model uncertainty. Such methods and their recent application to several combustion mechanisms will be described here.

16.1 Introduction

An important aspect of model validation and investigation is the determination of key model parameters which most strongly affect the prediction of important output targets. This is often approached by performing some kind of model sensitivity analysis which explores the relationships between the values of the input parameters of a mathematical or numerical model, and its predictions. In the

A. S. Tomlin (✉)

Energy Research Institute, University of Leeds, Leeds LS29JT, UK
e-mail: A.S.Tomlin@leeds.ac.uk

T. Turányi

Institute of Chemistry, Eötvös University (ELTE), Budapest, Hungary
e-mail: turanyi@chem.elte.hu

context of combustion, one example might be to explore the influence of changes to rate parameters or thermodynamic data on the prediction of key target outputs such as ignition delay times, flame speeds, or species concentration profiles over a wide range of temperatures and pressures. We may also wish to evaluate model robustness i.e. to determine how large the possible uncertainties in our predictions may be. Uncertainty analysis explores how our lack of knowledge of model inputs propagates to the predictive uncertainty of key model outputs. In this way it may be possible to compare the extent of overall model prediction errors with experimental errors for key targets. According to formal definitions (Saltelli et al. 2000) sensitivity coefficients should represent the contribution of the uncertainty in each input parameter to the overall predictive uncertainty of the model predictions. If we use this definition, then in order to determine sensitivity coefficients we require the uncertainty range of each input parameter to be specified. The calculated sensitivity coefficients can then be ordered so that the importance of parameters in terms of the contributions to the overall output uncertainty can be ranked. In this way we could determine for example, which rate coefficients within a mechanism have the biggest influence on predicted ignition delays across a range of temperatures and pressures of importance to practical combustion devices. This would provide a focus for methods for model improvement based on for example ab initio calculations or kinetic experiments, which would aim to reduce uncertainties in input data. This chapter will first of all describe the main approaches available for the sensitivity and uncertainty analysis of reaction mechanisms that are used to determine the main causes of predictive uncertainty. Model optimization will then be discussed which aims to combine data from wide ranges of sources in order to constrain the model parameters as tightly as possible.

16.2 Local Sensitivity Analysis

For a spatially homogeneous, dynamical system the change of the concentrations of variables \mathbf{Y} in time can be calculated by solving the following initial value problem:

$$\frac{d\mathbf{Y}}{dt} = \mathbf{f}(\mathbf{Y}, \mathbf{x}), \quad \mathbf{Y}(t_0) = \mathbf{Y}_0 \quad (16.1)$$

where \mathbf{Y}_0 is the initial concentration vector, and the parameter vector \mathbf{x} having m elements, may include Arrhenius parameters, 3rd body collision efficiencies, parameters of pressure dependence, thermodynamic data etc.

The effect of changes in parameter set \mathbf{x} on the concentrations at a given time can be characterized by a Taylor expansion:

$$Y_i(t, x + \Delta x) = Y_i(t, x) + \sum_{j=1}^m \frac{\partial Y_i}{\partial x_j} \Delta x_j + \frac{1}{2} \sum_{k=1}^m \sum_{j=1}^m \frac{\partial^2 Y_i}{\partial x_k \partial x_j} \Delta x_k \Delta x_j + \dots \quad (16.2)$$

where $\partial Y_i/\partial x_j$ is the first-order local sensitivity coefficient and $\partial^2 Y_i/\partial x_k \partial x_j$ is the second-order local sensitivity coefficient which represents an interactive effect between two parameters. Typically, only the first-order linear sensitivity coefficients $\partial Y_i/\partial x_j$ are used for mechanism analysis although we will see later that second-order effects can be present in combustion systems. The local sensitivity coefficient shows how the model output Y_i changes as a consequence of a change in the value of parameter x_j by a small amount, assuming that all other parameters are fixed at their nominal value. The elements of the local sensitivity matrix $\mathbf{S} = \{\partial Y_i/\partial x_j\}$ are the local sensitivity coefficients. The matrix \mathbf{S} therefore represents the linear approximation of the effects of parameter changes on model outputs. Since the units of model inputs and outputs can vary, and their values may differ by orders of magnitude, normalised sensitivity coefficients are generally used $(x_j/Y_i)(\partial Y_i/\partial x_j)$ which are dimensionless and therefore comparable to each other.

If we differentiate both sides of Eq. (16.1) with respect to x_j and use the chain rule, we obtain:

$$\frac{d}{dt} \frac{\partial \mathbf{Y}}{\partial x_j} = \mathbf{J} \frac{\partial \mathbf{Y}}{\partial x_j} + \frac{\partial \mathbf{f}}{\partial x_j}, \quad \frac{\partial \mathbf{Y}}{\partial x_j}(t_0) = 0 \quad (j = 1, 2, \dots, N) \quad (16.3)$$

or in matrix form:

$$\dot{\mathbf{S}} = \mathbf{J}\mathbf{S} + \mathbf{F}, \quad \mathbf{S}(0) = \mathbf{0}, \quad (16.4)$$

where $\mathbf{J} = \partial \mathbf{f}/\partial \mathbf{Y}$ is the Jacobian and $\mathbf{F} = \partial \mathbf{f}/\partial \mathbf{x}$. We denote $\mathbf{s}_i = \partial Y_i/\partial \mathbf{x}$ as the i -th column vector of the sensitivity matrix \mathbf{S} . Equation (16.4) shows that if a parameter is changed, it both directly influences the concentrations of those species that are present in the corresponding chemical reaction step (the second term on the right hand side of Eq. (16.4)) and indirectly affects other species through coupled chemical reaction steps (the first term on the right hand side of Eq. (16.4)). The concentration sensitivity indices are therefore time-dependent and the matrix \mathbf{S} belongs to a time interval (t_1, t_2) , where t_1 is the time of perturbation (initial time of the sensitivity calculation) and t_2 is the time of the observation of the effect of the perturbation (end time of the sensitivity calculation).

Several methods exist for the calculation of such indices with the decoupled direct method (DDM) perhaps being the most commonly applied (Dunker 1981, 1984). This approach is adopted in the Senkin software package which uses a finite difference method to approximate the matrices in Eq. (16.4) and utilises the fact that the Jacobian matrix in Eq. (16.4) is the same as that required for the solution of the original kinetic system of equations. More accurate solutions could be found by providing accurate analytical expressions for the terms in Eq. (16.4), or through the use of automatic differentiation (AD) techniques. Such methods exploit the fact that any computational function calculation is merely a sequence of simple operations such as additions, multiplications, etc. Therefore by applying the chain rule repeatedly, the derivatives of a function f can automatically be calculated to

machine precision. Given a function subroutine in a particular programming language, AD produces a subroutine describing the derivatives required to calculate the Jacobian matrix or various sensitivity measures up to machine precision (Bischof et al. 1996, 1997; Faure 2005). Whilst originally developed for atmospheric chemistry applications, more recently AD approaches have been applied within combustion for the investigation of the relative sensitivities of transport properties and reaction rates in premixed laminar flames (Brown and Revzan 2005) and the analysis of the sensitivity to turbulence model parameters within the FLUENT software environment (Bischof et al. 2004).

The brute force method is perhaps conceptually the simplest method for approximating linear sensitivity coefficients. In this method a single run of the original version of the model is first performed and the predicted target outputs are stored. Each parameter under investigation is then varied by a fixed percentage and the new prediction is compared with that of the original model. For a system with m parameters under investigation, a total of $(m + 1)$ model runs have to be performed in order to calculate sensitivity indices. For large systems with a high number of parameters it is clear that the brute force method carries a significant computational cost. One of its advantages however, is that any predicted model output can be selected for analysis, making the method flexible. Figure 16.1 shows an example of normalised linear sensitivity coefficients calculated using the brute force method for a model describing the oxidation of *n*-butane in a Jet Stirred

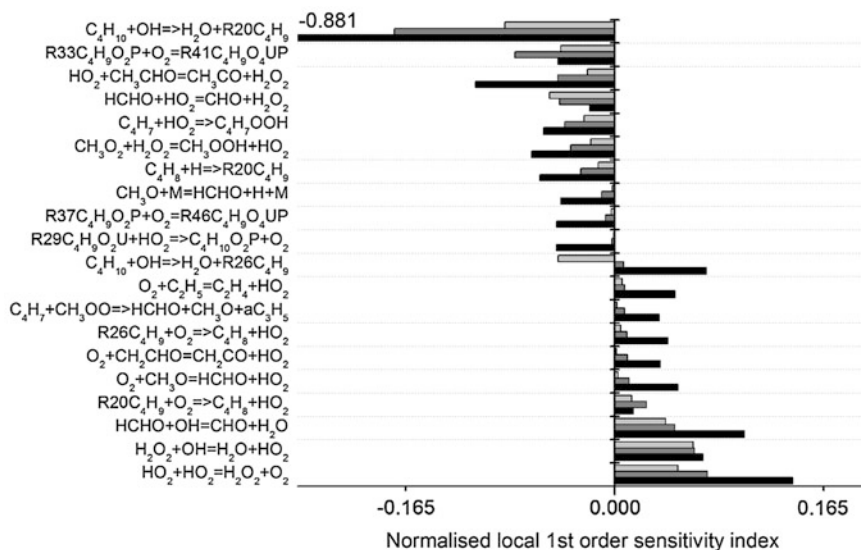


Fig. 16.1 Normalised linear sensitivity coefficients for the most important reactions at 675 K (black), 750 K (dark grey) and 775 K (light grey) derived from a model describing the oxidation of *n*-butane in a jet-stirred reactor (residence time of 6 s, atmospheric pressure, stoichiometric mixtures containing 4 % (mol) *n*-butane diluted in helium). EXGAS notation is used. Adapted with permission from (Cord et al. 2012). Copyright (2012) American Chemical Society

Reactor (JSR) at three reactor temperatures based on 25 % modifications to the A -factor for each reaction (Cord et al. 2012). The horizontal bar chart representation is commonly used to present local sensitivity coefficients and allows the user to see quickly how the importance of parameters/reactions changes for different simulation conditions or experimental set-ups. It is important however, to be clear when presenting such bar charts whether normalised coefficients have been used since otherwise direct comparison between different parameters or simulation conditions cannot easily be made.

In this case, when considering only the normalized sensitivity coefficients, the most sensitive reaction at all temperatures is $C_4H_{10} + OH \rightarrow H_2O + R2OC_4H_9$ ($R2OC_4H_9$ being the 1-butyl radical). However, this analysis does not take into account the level of uncertainty in the input A -factors. This reaction has been subject to a number of experimental and theoretical studies and therefore is fairly well known. The influence of its uncertainty on predicted butane concentrations may not be as high as these simple sensitivity coefficients suggest. This point will be discussed in the next section where the contribution of the uncertainty of parameters to output uncertainty is investigated.

16.3 Local Uncertainty Analysis

In order to properly account for the level of accuracy to which model inputs are known, we need to incorporate a quantified description of input uncertainties into our sensitivity/uncertainty analysis. For rate parameters of gas phase elementary reactions several data collections exist which have attempted to quantify uncertainties in rate coefficients over a range of temperatures of relevance to combustion applications (e.g. up to 2500 K) based on the evaluation of experimental and theoretical studies in the literature (e.g. Tsang and Hampson 1986; Baulch et al. 1992, 1994, 2005; Tsang 1992). The uncertainty parameter f is usually defined as:

$$f = \log_{10} \left(\frac{k^0}{k^{\min}} \right) = \log_{10} \left(\frac{k^{\max}}{k^0} \right) \quad (16.5)$$

where k^0 is the recommended (most probable or nominal) value of the rate coefficient based on an assessment of available experimental and theoretical studies, and k^{\max} and k^{\min} are the extreme upper and lower, but still possible values. Rearranging this equation yields:

$$\frac{k^{\max}}{k^0} = 10^f \quad (16.6)$$

Equation (16.6) means that the rate coefficient k^0 is uncertain according to a multiplication factor 10^f and on a logarithmic scale the upper and lower values are positioned symmetrically around the recommended value. Typical values of f are 0.3, 0.5 and 0.7, which means that the extreme values differ from k^0 by

multiplication factors of 2, 3.16 and 5 respectively. This uncertainty parameter f has been defined for a range of gas phase systems in a series of studies (Warnatz 1984; Tsang and Hampson 1986; Baulch et al. 1992, 1994, 2005; Tsang 1992; Konnov 2008). Low f values are usually estimated for reactions, which have been subject to several studies with results which are in reasonably good agreement. Higher values are suggested when only a limited number of studies exist for a parameter (e.g. over a limited range of temperatures and pressures) or there are significant differences among the results of various studies. Historically, the assessment of such data has been carried out according to expert judgement. More recently statistical approaches have been developed which attempt to determine uncertainty factors according to a common framework. These will be discussed later in Sect. 16.6.

For rate coefficients where f has been estimated, uncertainty ranges can be determined which may be used within the context of both local and global sensitivity analysis. If we wish to determine probability distributions of predicted model outputs, we also need to define probabilistic information about the input parameter. A typical approach for rate coefficients would be to assume that $\ln \{k\}$ is a random variable with a normal probability density function (*pdf*) and with an expected value of (k^0) i.e. its most likely value. Assuming that the minimum and maximum values of the rate coefficients correspond to 3σ deviations (Brown et al. 1999; Turányi et al. 2002; Zádor et al. 2005, 2006; Zsély et al. 2005, 2008) or 2σ deviations (Sheen et al. 2009; Sheen and Wang 2011) from the recommended value on a logarithmic scale, the uncertainty parameter f can be converted (Turányi et al. 2002) at a given temperature T to the variance of the logarithm of the rate coefficient:

$$m\sigma(\ln \{k\}) = f \ln 10 \quad (16.7)$$

$$\sigma^2(\ln \{k\}) = ((f \ln 10)/m)^2 \quad (16.8)$$

where $m = 3$ or 2 . If a normal distribution is assumed then the *pdf* of the rate coefficient can be easily described using this approach, with the width of the distribution depending on the value of f .

Uncertainties in thermochemical data are also of importance in assessing reversible reactions since enthalpies of formation are used in determining reverse rate coefficients. Several collections of thermochemical data with combustion relevance are listed in articles (Turányi et al. 2002; Zádor et al. 2005; Zsély et al. 2008). Most of these collections contain information about the uncertainty of enthalpies of formation. New methods for assessing such uncertainties have also been developed by Ruscic and co-workers using a global multi-dataset optimization approach including experimental measurements and state-of-the art theoretical data, through the generation of Active Thermochemical Tables or ATTs (Ruscic et al. 2004).

Where data evaluations have been performed and therefore f can be obtained, the uncertainty distributions described above can be propagated to give predictive

uncertainties in model outputs. If a group of input parameters are uncorrelated then:

$$\sigma^2(\mathbf{Y}) = \sum_j \left(\frac{\partial \mathbf{Y}}{\partial x_j} \right)^2 \sigma^2(x_j) \quad (16.9)$$

where $\frac{\partial \mathbf{Y}}{\partial x_j}$ are the local sensitivity coefficients defined in Eq. (16.2). Possible correlations between the parameters will be discussed later. If the input parameters are rate coefficients then the variance of the model solution Y_i can be calculated from the variance $\sigma^2(\ln k_j)$ of uncorrelated parameters $\ln k_j$ (Turányi et al. 2002; Zádor et al. 2005):

$$\sigma_{k_j}^2(Y_i) = \left(\frac{\partial Y_i}{\partial \ln k_j} \right)^2 \sigma^2(\ln k_j) \quad (16.10)$$

$$\sigma_K^2(Y_i) = \sum_j \sigma_{k_j}^2(Y_i) \quad (16.11)$$

$$S_{K\%ij} = \frac{\sigma_{k_j}^2(Y_i)}{\sigma_K^2(Y_i)} \times 100 \quad (16.12)$$

where $\sigma_{k_j}^2(Y_i)$ is the contribution of the uncertainty of reaction step j to model output Y_i , $\sigma_K^2(Y_i)$ is the contribution of all kinetic uncertainties, while $S_{K\%ij}$ shows the percentage contribution of $\sigma_{k_j}^2(Y_i)$ to $\sigma_K^2(Y_i)$. A similar series of expressions can be deduced for the effect of the uncertainty of the enthalpies of formation on model result Y_i (Turányi et al. 2002).

The measure $S_{K\%ij}$ is somewhat different from the normalised sensitivity coefficients discussed in the previous section and now takes into account the “state of knowledge” or uncertainty of the input parameters. The ranked uncertainty coefficients therefore give a better indication of the contribution of our lack of knowledge of each rate parameter to the overall uncertainty in model predictions. This allows the focus of future kinetic studies to be placed on those parameters which will give the most significant improvements in the robustness of the simulations. However, these indices are still based on the assumption that the linear sensitivity coefficients are valid across the whole of the input parameter distribution. Within nonlinear models, this may not always be the case and hence global methods for sensitivity analysis are emerging as useful tools in the analysis of combustion mechanisms.

16.4 Global Sensitivity and Uncertainty Analysis

In order to apply global uncertainty and sensitivity analysis, we should allow the parameters of our model to vary throughout the whole domain of parameter space rather than in a small region close to the nominal values. For highly non-linear

models containing significant uncertainties, global approaches can give a better indication of the overall contribution of each parameter uncertainty to uncertainties in output predictions since sensitivities may vary significantly within wide parameter ranges. Global methods are usually based on some kind of sampling approach where a large number of model runs are performed with the inputs sampled from their whole domain of feasibility, which may be a high dimensional space for large systems. The output is then described by a distribution rather than a single value. At the simplest level a range of possible values (x_j^{\min}, x_j^{\max}) is assigned to each parameter which is independent of the values of the other parameters. A uniform distribution is then assumed between (x_j^{\min}, x_j^{\max}) and a suitable sampling strategy adopted (Helton et al. 2006). A single model run is performed for each sample and the output distribution and the relationship between inputs and outputs is investigated in some way. We might also perform probabilistic sampling, based on assumed distributions for the input parameters (e.g. normal) as discussed in Sect. 16.3. The choice of input distributions often depends on the level of information available about parameter uncertainty. For data evaluated on the basis of many experiments we may be able to use a probabilistic approach, but for estimated parameters where perhaps only feasible ranges for the parameter can be suggested, we may have to use a uniform distribution. In either case, propagating uncertainties via a sampling approach will provide information on the range of possible predicted values, and in some cases the probability distributions for the outputs.

Many methods for global sensitivity analysis exist in the literature and excellent reviews of the topic are presented in (Saltelli et al. 2000, 2004, 2006, 2008; Tomlin 2013). We focus here on surface response methods (SRMs) which have been most commonly applied in combustion. The approach taken in SRMs is to develop a response surface approximation which describes the relationship between the parameters in the original model and selected target outputs. Using a sample of full model simulations based on assumed distributions for the inputs, a model approximation or meta-model is constructed, which can then be used as a surrogate for the full model in order to perform uncertainty and sensitivity analysis. The accuracy of the meta-model will determine the accuracy of the calculated sensitivity indices and will depend on various factors such as the sample size used, the fitting approach taken to develop the meta-model and the complexity of the response surface. High dimensionality of the model input parameter space does not always imply a complex functional relationship between the more influential model inputs and target outputs. SRMs can therefore often achieve accurate fits with an affordable number of model runs and therefore offer a promising approach for large parameter systems, or systems with high computational costs associated with the full model simulations, both of which may be the case for combustion applications. Several sensitivity analysis approaches based on SRMs have been developed including those based on polynomial chaos expansions (Balakrishnan et al. 2002; Reagan et al. 2004; Cheng and Sandu 2009; Najm et al. 2009; Blatman

and Sudret 2010), Gaussian process emulators (Oakley and O'Hagan 2002), orthonormal polynomials (Tomlin 2006), splines (Storlie and Helton 2008) and high dimensional model representations (Rabitz et al. 1999; Wang et al. 2001; Ziehn and Tomlin 2008; Ziehn et al. 2009; Tomlin and Ziehn 2011). We focus here on methods based on polynomial chaos expansion and high dimensional model representation (HDMR) methods which have been more commonly applied in combustion modelling.

HDMR methods are based on a hierarchical expansion of the functional relationship between the inputs and outputs of a model (Rabitz et al. 1999; Li et al. 2001). The HDMR is expressed as the hierarchical sum of component functions of increasing order and is usually restricted to up to 2nd order terms:

$$f(\mathbf{x}) = f_0 + \sum_{i=1}^m f_i(x_i) + \sum_{1 \leq i < j \leq m} f_{ij}(x_i, x_j) + \dots + f_{12\dots m}(x_1, x_2, \dots, x_n) \quad (16.13)$$

Here the zero'th order component f_0 denotes the mean value of the model response across the adopted sample. The first order component functions $f_i(x_i)$ give the effect of variable x_i acting independently (although generally nonlinearly) upon the output $Y(\mathbf{x})$, and the function $f_{ij}(x_i, x_j)$ is a second-order term describing the cooperative effects of the variables x_i and x_j upon the output $Y(\mathbf{x})$. Equation (16.13) provides the ANOVA (Analysis Of Variances) decomposition of $Y(\mathbf{x})$ as first discussed by Sobol', and therefore each term represents the relative influence of single parameters or pairs of parameters on the overall output variance. The ANOVA decomposition has several important properties (Sobol 2001). The mean of all non-constant component functions in Eq. (16.13) is zero and the terms are orthogonal. Furthermore the HDMR expansion is always of finite order (Rabitz and Alis 2000) making it computationally efficient if higher-order input variable interactions are weak and can be neglected.

The HDMR approach most commonly applied in combustion uses a random sample of inputs (RS-HDMR) based on a uniform distribution in order to generate the input–output mappings from which the meta-model is fitted (Ziehn and Tomlin 2008; Ziehn et al. 2009; Tomlin and Ziehn 2011; Wang et al. 2001). Quasi-random sampling such as using a Sobol' quasi-random sequence is often used to improve convergence when compared to standard random sampling approaches (Sobol' 1967). An efficient methodology was demonstrated in (Ziehn and Tomlin 2009) which also outlined the freely available Matlab based software GUI-HDMR for global sensitivity analysis. The approach was also extended to non-uniform distributions of input variables in (Wang et al. 2003).

Using the RS-HDMR method, the zeroth-order term f_0 is approximated by the average value of $Y(\mathbf{x})$ for all $\mathbf{x}^{(s)} = (x_1^{(s)}, x_2^{(s)}, \dots, x_n^{(s)})$, $s = 1, 2, \dots, N$

$$f_0 \approx \frac{1}{N} \sum_{s=1}^N Y(\mathbf{x}^{(s)}) \quad (16.14)$$

where N is the number of sampled model runs. The higher-order component functions are approximated using expansions in terms of suitable basis functions such as orthonormal polynomials:

$$\begin{aligned} f_i(x_i) &\approx \sum_{r=1}^k \alpha_r^i \varphi_r(x_i) \\ f_{ij}(x_i, x_j) &\approx \sum_{p=1}^l \sum_{q=1}^{l'} \beta_{pq}^{ij} \varphi_p(x_i) \varphi_q(x_j) \end{aligned} \quad (16.15)$$

where k, l, l' represent the order of the polynomial expansion, α_r^i and β_{pq}^{ij} are constant coefficients to be determined, and $\varphi_r(x_i)$, $\varphi_p(x_i)$ and $\varphi_q(x_j)$ are the orthonormal basis functions (Li et al. 2002a). The coefficients are determined using Monte Carlo integration over the chosen input sample (Li et al. 2002b). A single set of quasi-random samples N is required to determine all RS-HDMR component functions which can subsequently be used to calculate global sensitivity indices. The component functions themselves can also be plotted in order to investigate the influence of each parameter or pair of parameters on the model response.

The accuracy of the fitted meta-models can be tested in a variety of ways including testing the relative error (RE) between the response of the real model and the meta-model or a comparison of the predicted output *pdfs* (Ziehn 2008; Davis et al. 2011). Figure 16.2 shows a comparison of *pdfs* from the full model runs and from both the 1st and 2nd order HDMR meta-models. The investigated system is the same n-butane example used in Fig. 16.1. The poor representation of the tails in the output *pdf* using the first-order model in Fig. 16.2a suggests that higher-order effects, i.e. interactions between parameters, are important. The important features of the output *pdf* are however well captured by the second-order model and hence the HDMR expansion should give an accurate estimate of first- and second-order sensitivity indices. The penalty is that more than 4000 model runs were necessary in order to accurately fit the HDMR expansion up to second-order which increases the burden of the global method when compared to the linear brute force method where only 1300 runs were necessary in this case. However, far more information on nonlinear and interactive effects can be obtained.

Once an accurate meta-model has been created, it can be used to calculate sensitivity indices in the following way. Based on Eq. (16.15), the partial variances D_i and D_{ij} can be calculated (Li et al. 2002a; Feng et al. 2004):

$$D_i = \sum_{r=1}^{k_i} (\alpha_r^i)^2 \quad (16.16)$$

$$D_{ij} = \sum_{r=1}^{l_i} \sum_{q=1}^{l'_j} (\beta_{rq}^{ij})^2 \quad (16.17)$$

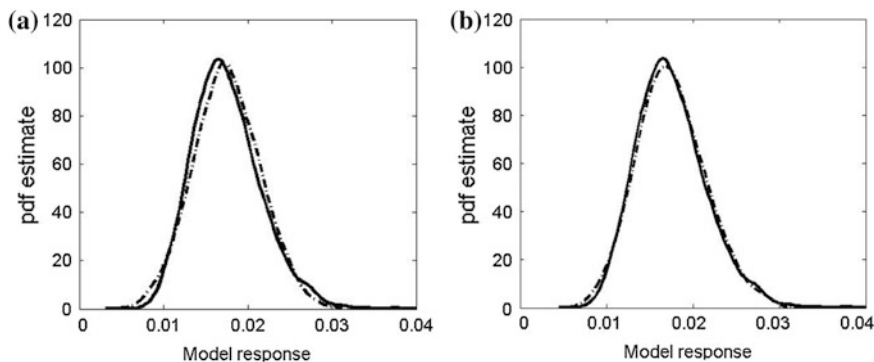


Fig. 16.2 Example *pdf* estimate using a (a) first and (b) second-order HDMR meta-model, where the meta-model (*dashed lines*) overlays the *pdf* of the full model runs (*solid lines*). The model describes the oxidation of *n*-butane in a jet stirred reactor (residence time of 6 s, atmospheric pressure, stoichiometric mixtures containing 4 % (mol) *n*-butane diluted in helium, $T = 750$ K)

Dividing these partial variances by the total variance of the model output, we obtain sensitivity indices:

$$S_{i_1, \dots, i_s} = \frac{D_{i_1, \dots, i_s}}{D}, 1 \leq i_1 < \dots < i_s \leq m \quad (16.18)$$

The first-order sensitivity index S_i shows the exclusive effect of parameter x_i on the model result. The second-order sensitivity index S_{ij} shows the interactive effect of parameters x_i and x_j . The sensitivity indices can then be ranked in order to determine the order of importance of the parameters, highlighting those which drive output uncertainty and therefore could be the focus of more detailed studies.

A related method is that of polynomial chaos expansions which is based on the spectral uncertainty (i.e. based on the stochastic spectral expansion of random quantities) methods introduced for combustion models in (Reagan et al. 2003, 2004; Najm et al. 2009) which was later extended to an SRM (Sheen et al. 2009). As discussed in the previous section, an uncertainty factor f is first assigned to each input variable e.g. rate coefficients k_i . These factors are then normalised into factorial variables \mathbf{x} in the following way for the case of rate coefficients:

$$x_i = \frac{\ln k_i / k^0}{\ln f_i} \quad (16.19)$$

where k^0 is the nominal value of the rate coefficient as above (Sheen et al. 2009). Hence $x_i = 0$ gives the nominal value, and -1 and $+1$ represent the lower and upper bounds, respectively, based on evaluated data (see e.g. Baulch et al. 1992, 1994, 2005). As discussed above, $\ln f_i$ is usually taken to represent either 2σ or 3σ for $\ln k_i$. A response surface of the predicted combustion properties is then generated with respect to \mathbf{x} . Whilst this can be a general expansion, it is often

restricted to a 2nd order polynomial expansion. Hence the r th model response $\eta_r(\mathbf{x})$ is written as:

$$\eta_r(\mathbf{x}) = \eta_{r,0} + \sum_{i=1}^m a_{r,i}x_i + \sum_{i=1}^m \sum_{j \geq i}^m b_{r,ij}x_ix_j \quad (16.20)$$

The uncertainty in \mathbf{x} may be expressed as a polynomial expansion of basis random variables ξ ,

$$\mathbf{x} = \mathbf{x}^{(0)} + \sum_{i=1}^m \boldsymbol{\alpha}_i \xi_i + \sum_{i=1}^m \sum_{j \geq 1}^m \boldsymbol{\beta}_{ij} \xi_i \xi_j + \dots, \quad (16.21)$$

where $\boldsymbol{\alpha}$ and $\boldsymbol{\beta}$ are column vectors of expansion coefficients, m is the number of rate coefficients under consideration and $\mathbf{x}^{(0)}$ is a column vector of normalised rate coefficients which are zero for the nominal reaction model. If the x 's are independent of each other and normally distributed, then a common choice for the form of ξ is a set of unit-normal random variables. If $\ln f_i$ represents a 2σ deviation of $\ln k_i$ then $\boldsymbol{\alpha}$ is $1/2 \mathbf{I}_M$, where \mathbf{I}_M is the M -dimensional identity matrix and $\boldsymbol{\beta}$ and all higher order terms are zero (Sheen et al. 2009). In the general case, combining the above two equations and truncating the higher order terms gives:

$$\eta_r(\xi) = \eta_r(\mathbf{x}^{(0)}) + \sum_{i=1}^m \hat{\boldsymbol{\alpha}}_{r,i} \xi_i + \sum_{i=1}^m \sum_{j \geq i}^m \hat{\boldsymbol{\beta}}_{r,ij} \xi_i \xi_j + \dots, \quad (16.22)$$

with coefficients of $\hat{\boldsymbol{\alpha}}_r = 1/2 \mathbf{I}_M \mathbf{a}_r$ and $\hat{\boldsymbol{\beta}}_r = 1/4 \mathbf{I}_M^T \mathbf{b}_r \mathbf{I}_M$. From Eq. (16.22) we can see that the distribution of the overall model prediction is given by its nominal value plus uncertainty contributions from each rate coefficient. The overall output variance may then be represented as the sum over terms involving the coefficients of the equivalent expansion. In this case:

$$\sigma_r(\xi)^2 = \sum_{i=1}^m \hat{\boldsymbol{\alpha}}_{r,i}^2 + 2 \sum_{i=1}^m \hat{\boldsymbol{\beta}}_{r,ij}^2 + \sum_{i=1}^m \sum_{j > i}^m \hat{\boldsymbol{\beta}}_{r,ij}^2 \quad (16.23)$$

The fractional contribution to the overall model uncertainty due to each input can therefore be estimated from the terms in the above equation and used to calculate global sensitivity coefficients. The HDMR and polynomial chaos methods can in principle both be used for ANOVA analysis and differ mainly in the form of the expansion used. In fact if the expansion was restricted to second-order polynomials in both cases then one would expect both methods to provide similar sensitivity indices. The polynomial chaos methodology has also been coupled with approaches for the optimization of rate coefficients (Sheen and Wang 2011), as will be discussed in Sect. 16.6.

16.5 Examples of Applications of Uncertainty Analysis in Combustion

An early application of local uncertainty analysis was demonstrated by Brown et al. (1999) who explored the predictive uncertainties in burning velocities of hydrogen-air flames due to uncertainties in reaction A -factors across a range of stoichiometries. In their study the local sensitivities were calculated using the standard Chemkin package (Kee et al. 1989) and uncertainty distributions for the input A -factors were based on evaluations such as (Baulch et al. 1992, 1994). The study demonstrated that the importance ranking of the reactions differed, depending on whether the normalised first-order sensitivities Eq. (16.3) or their normalised fractional contribution to the output variance Eq. (16.10) were used. This suggests that having some estimation of input uncertainties is an important part of identifying key reactions requiring better categorisation in order to improve model robustness. The resulting uncertainties in predicted burning velocities were estimated to be up to 14 %, although local sensitivities were used in this study and hence any nonlinearities across the input ranges were ignored.

The local uncertainty analysis approach was extended by Turányi and co-workers to include enthalpies of formation in uncertainty studies of predictions of laminar flame velocity v_L , maximum adiabatic flame temperature T_{\max} , maximum radical concentrations (Turányi et al. 2002; Zádor et al. 2005) and NO formation during methane combustion (Zsély et al. 2008). These studies performed a comparison between local and global methods based on a various sampling approaches. For these particular cases, local uncertainty analysis was found to give a good estimation of the uncertainty of the model results determined using sampling based approaches and at a lower computational cost. However, this is not always the case as discussed below. In the case studied by Zsély et al. (2008), the uncertainty in predicted NO concentrations caused by the uncertainties in enthalpies of formation was found to be smaller than that caused by uncertainties in the rate coefficients. Enthalpies of formation were however found to be important for several key species in the prediction of multiple stage ignition characteristics for a propane oxidation study in (Hughes et al. 2006). In particular, the simulation of ignition characteristics of propane was found to be highly sensitive to the thermochemistry of three hydroperoxyalkyl radicals and their derivatives. Enthalpies of formation should form an important part of any sensitivity analysis study for a combustion mechanism where reversible reactions are used.

RS-HDMR was applied in (Ziehn and Tomlin 2008) for the global sensitivity analysis of a one-dimensional low-pressure premixed methane flame model used to investigate the influence of fuel sulphur and nitrogen compounds on NO concentrations ([NO]) within the burnt gas region. PREMIX simulations were performed for a study of 176 input parameters (153 rate coefficients and 23 enthalpies of formation (ΔH_f°)) in order to determine their relative importance in driving the output uncertainty in predicted [NO] for a fuel-rich scenario with nitrogen and sulphur doping. For 176 inputs the full second-order HDMR expansion based on

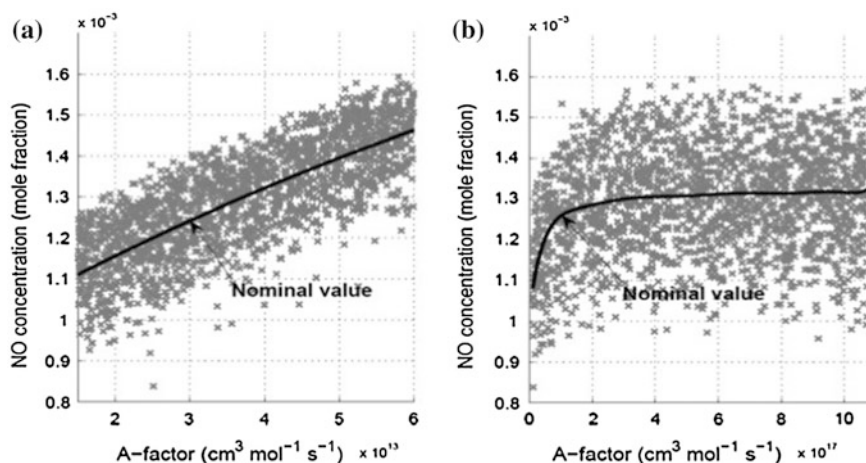


Fig. 16.3 First-order component functions and scatter plots for (a) $\text{SO} + \text{NH} = \text{NO} + \text{SH}$, (b) $\text{SO} + \text{OH} = \text{SO}_2 + \text{H}$. The mean f_0 is added to f_i for comparison with the scatter plot (reprinted from (Tomlin 2013) with permission from Elsevier)

Eq. (16.13) consists of 15,577 component functions (1 zeroth-order + 176 first-order + 15,400 s-order). However, an error threshold can be used, where only those component functions that improve the accuracy of the fitted meta-model are added into the expansion. Using an accuracy threshold of 1 % led to only five first-order component functions and no second-order component functions, yet despite this the resulting first-order HDMR meta-model model gave 99.05 % of the tested samples for predicted [NO] within the 5 % relative error range. This suggests that despite the high dimensionality of the input space, predictions were driven by only a small number of parameters, which is quite common for chemical kinetic systems. This means that efforts to improve model robustness can often be focussed on a low number of parameters.

This study also highlighted that the response to the change of the key parameters is not always linear. Figure 16.3 shows the first-order component functions overlaid by the scatter plots for the A-factors for reactions $\text{SO} + \text{NH} = \text{NO} + \text{SH}$ and $\text{SO} + \text{OH} = \text{SO}_2 + \text{H}$. For the reaction $\text{SO} + \text{NH} = \text{NO} + \text{SH}$, the component function shows a linear response across the whole range, indicating that a local sensitivity coefficient at the nominal parameter value would give an accurate picture of the overall response in this case. The A-factor for reaction $\text{SO} + \text{OH} = \text{SO}_2 + \text{H}$ however, shows a strong sensitivity at the lower end of its range that begins to saturate at higher values. A local estimate at the nominal value would not therefore give an accurate picture of the response to this parameter across its whole uncertainty range. On the other hand, the HDMR component functions are able to show the response to parameter changes across their whole range of feasible values.

HDMR was also applied for the global sensitivity analysis of the n-butane oxidation scheme described above for the same conditions shown in Fig. 16.1. Figure 16.4 shows the different sensitivity indices that are obtained when using normalised local sensitivities compared to the calculation of global sensitivities. In this case the local sensitivities have been scaled according to the relevant input uncertainties and normalised. This causes substantial differences compared to the coefficients shown in Fig. 16.1, since some reaction rates have much lower uncertainties than others. Although Fig. 16.4 shows that there is a broad agreement between the two methods in terms of the parameter importance ranking, there are also some notable differences. The addition of hydroperoxyalkyl radicals to oxygen $R33C_4H_9O_2P + O_2 = R41C_4H_9O_4UP$ has a higher global sensitivity index than local, which indicates that the response of the predicted n-butane mole fraction to changes in the A-factor for this reaction is non-linear. It also shows a second order interaction with the A-factor for the reaction $C_4H_{10} + HO_2 \Rightarrow H_2O_2 + R20C_4H_9$ which is illustrated in Fig. 16.5. The figure shows that when the A-factors for both reactions are at the lower end of their adopted ranges, the predicted butane mole fraction increases. It illustrates the possible importance of second-order effects in predicting overall uncertainties. These second-order effects were the reason why the first-order meta-model gave a poor representation of the model output *pdf* as shown in Fig. 16.2.

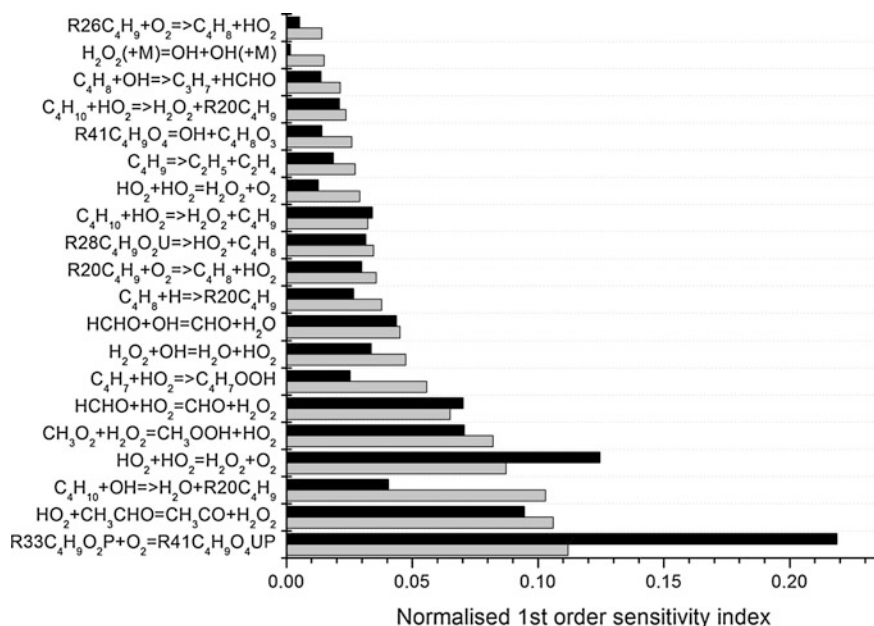
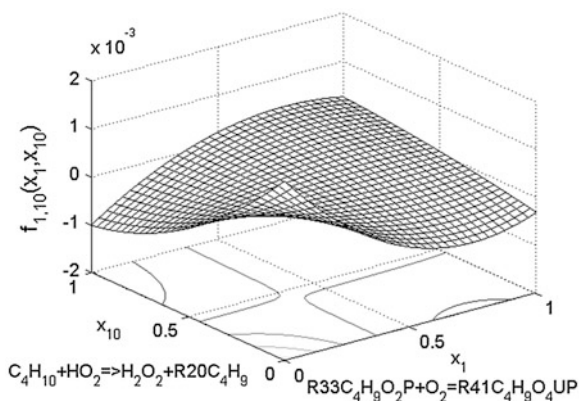


Fig. 16.4 Normalised estimates of first order contributions to the overall variance of predicted butane mole fraction at 750 K calculated using first order local sensitivities (*grey*) and the global HDMR method (*black*) under the conditions of Fig. 16.1. Adapted with permission from (Cord et al. 2012). Copyright (2012) American Chemical Society

Fig. 16.5 Second order component function showing the interaction between the A -factors for reactions $R33C_4H_9O_2P + O_2=R41C_4H_9O_4UP$ and $C_4H_{10} + HO_2 \Rightarrow H_2O_2 + R20C_4H_9$ for predicted butane mole fraction at 750 K under the conditions of Fig. 16.1



A response surface approach was also used to perform an iterative global sensitivity analysis for the case of methanol oxidation in order to determine the chemical reaction steps that most strongly influence predicted ignition delay times over a range of temperatures and pressures (Skodje et al. 2010; Klippenstein et al. 2011). Following the initial determination of reaction importance, the highest ranked rate coefficients were re-estimated using high-level quantum chemistry and transition-state-theory calculations. The mechanism was then updated with the new values which were deemed to have smaller uncertainty ranges than those in the initial mechanism. Further sensitivity analysis was performed and the updating process was iterated as new reactions emerged as the most important steps. For this case reactions $CH_3OH + HO_2$ and $CH_3OH + O_2$ were found to be the most important steps in determining the ignition delay time. The scatter plot and the first-order component function of the predicted ignition delay τ versus the normalised A -factor for the reaction $CH_3OH + HO_2$ at the first stage is shown in Fig. 16.6a. The low amount of scatter around the component function indicates a high sensitivity to this A -factor when compared to the other parameters considered. Its first order coefficient S_i is in fact around 0.9 for a wide range of temperatures and pressures. In the Skodje et al. (2010) study, the rate coefficient for this reaction was then updated to form the stage two mechanism. Since the A -factor for reaction $CH_3OH + O_2$ was the highest ranked reaction at the next stage, this was then updated. Figure 16.6b shows the simulated normalised *pdfs* for each update which is seen to become narrower as the model becomes better constrained. These estimates of predicted model uncertainty however, were based on the assumption that the transition-state-theory calculations were accurate to a factor of two. A full assessment of the uncertainties inherent within such approaches would form a useful development in the field and recently such studies are starting to emerge as discussed below.

Another point worth raising here is that sensitivity studies such as this provide information about which parameters might be constrained by a given experiment. If a single parameter dominates the variance in target predictions i.e. the S_i for this

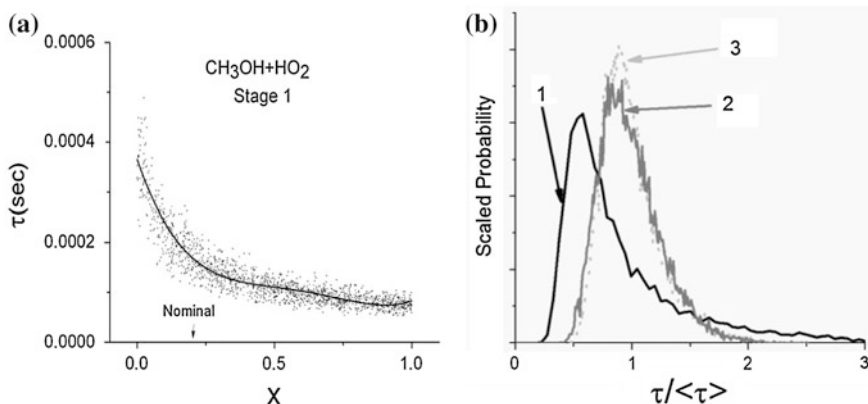


Fig. 16.6 **a** Scatter plot and first-order component function of the predicted ignition delay τ versus the normalised A -factor for the reaction $\text{CH}_3\text{OH} + \text{HO}_2$ based on the original mechanism of Li et al. (2007). **b** Distribution of normalised ignition delay times $\tau/\langle\tau\rangle$ obtained from random sampling at $(T, P, \phi) = (1150 \text{ K}, 5 \text{ bar}, 1)$. Stage 1—Initial mechanism (Li et al. 2007); stage 2—improvement in rate coefficient for $\text{CH}_3\text{OH} + \text{HO}_2$; stage 3—improvement in rate coefficient for $\text{CH}_3\text{OH} + \text{O}_2$ (adapted with permission from (Skodje et al. 2010), copyright (2010) American Chemical Society)

parameter is close to one, then accurate experimental values for the targets could be used to better constrain the parameter. Figure 16.6a indicates that ignition delay experiments should provide a very useful constraint on the rate coefficient for $\text{CH}_3\text{OH} + \text{HO}_2$ in the case studied here, since the scatter in the predicted response is low i.e. the response is mainly isolated to the effect of a single parameter which is the reaction rate for $\text{CH}_3\text{OH} + \text{HO}_2$. Within kinetics studies, experiments are designed to isolate parameters as far as possible in this way so that outputs such as concentration time-curves can be used to determine individual rate coefficients. Complete isolation however, is not always possible and sometimes a model comprising several reactions has to be used in order to develop parameterisations for the rate coefficient of interest. In addition, indirect experiments such as flame speed, ignition delay, or jet stirred reactor measurements, are not expected to isolate single reaction steps to the same extent and predictions of such properties are likely to be influenced by a number of parameters. Global sensitivity analysis can help to determine which parameters will be constrained by a given experiment. Measurements can then be coupled with knowledge of the response surface between inputs and predicted outputs in order to constrain the feasible region of the inputs (Frenklach 2007). If a number of experiments provide constraints on a given parameter then combining information from different studies may help to reduce the uncertainty in the estimated parameters. These issues will be discussed further in the following section dealing with optimization techniques.

Methods based on polynomial chaos expansions have also been applied to several combustion systems. In Sheen and Wang (2011) this approach was applied

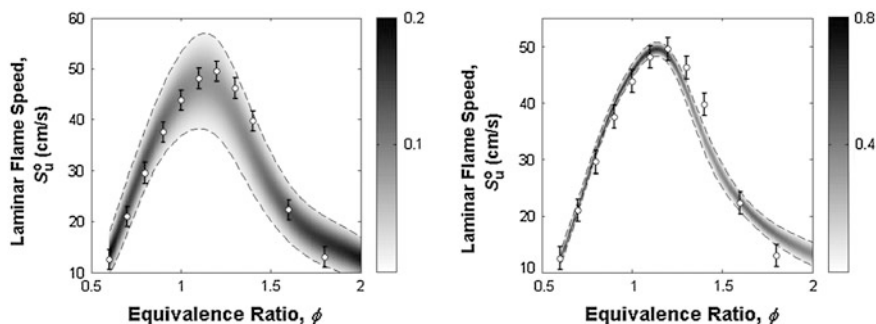


Fig. 16.7 Variation of laminar flame speed with equivalence ratio for ethylene–air flames, $P = 5$ atm. *Left panel* prior model. *Right panel* posterior model. *The shaded bands* indicate the 2σ standard deviation on the model prediction uncertainty; *shading intensity* indicates the probability density, and the actual $\pm 2\sigma$ limits are indicated by *the dashed lines*. Reprinted from (Sheen and Wang 2011) with permission from Elsevier

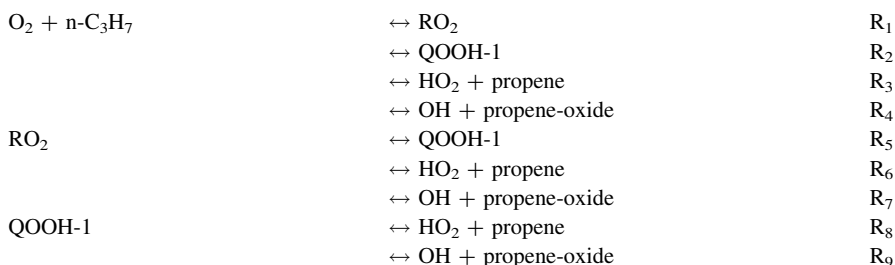
to a detailed $\text{H}_2/\text{CO}/\text{C1-C4}$ kinetic model using a set of experimental data for ethylene combustion to help to constrain the model input parameters. Uncertainty factors for each rate coefficient in the USC Mech (Wang et al. 2007) were adopted from literature evaluations, and then propagated through models for flame speed, flow reactor and ignition delay predictions. The approach was also coupled with optimization of the input rate parameter coefficients based on a wide range of target experiments and their uncertainties.

An example of the propagated uncertainties for the non-optimized (prior) model, represented by 2σ bands is shown in the left panel of Fig. 16.7 for predicted laminar flame speeds, with the shaded regions showing the predicted *pdf*. The figure demonstrates a larger scatter in the predictive uncertainties compared to the scatter in experimental measurements. This may be surprising when the study was based on state-of-the-art knowledge for the rate coefficients using evaluated data. It demonstrates the need for further methods to reduce uncertainties in predictive models, either by better quantification of rate coefficients through fundamental kinetic experiments or theoretical calculations, or alternatively through model optimization. The right hand panel of Fig. 16.7 shows the 2σ bands when experimental measurements are used to further constrain the feasible region of the sensitive input parameters. The 2σ bands are narrower in this case indicating that incorporating constraints imposed by indirect experimental measurements led to reductions in the overall uncertainty of the optimized model.

It is worth stressing that such 2σ error bands will be extremely sensitive to the selected input uncertainty factors f chosen for the study. For larger and more complex combustion mechanisms containing high numbers of estimated parameters, or parameters derived from theoretical methods, obtaining accurate values for f could be difficult. This raises questions about our ability to suggest predictive error bars for simulations involving highly complex fuel mechanisms unless we are able to better specify input uncertainties. Since theoretical methods are

becoming increasingly used to estimate chemical kinetic parameters (Miller et al. 2005; Pilling 2009), it is important to develop an understanding of the uncertainties inherent in such approaches. For this reason a number of recent studies have attempted to assess the uncertainty in rate constants derived from theory calculations.

For example, Goldsmith et al. investigated the potential uncertainties in the derivation of phenomenological rate constants using transition-state-theory for an example reaction system of n-propyl + O₂ which is a reaction of importance in the low temperature combustion of propane (Goldsmith et al. 2013). The potential energy surface for the system is shown in Fig. 16.8 indicating multiple transition states and also well skipping reaction channels. Nine individual rate constants were computed:



and uncertainties in barrier heights, well depths, vibrational frequencies, collision frequency, and energy transfer parameters were propagated through to the predicted rate constants over a range of temperatures and pressures using a quasi-random sampling approach. Sensitivities to inputs were explored using HDMR analysis with up to second-order terms. The resulting distributions in the predicted log of rate constants are demonstrated in Fig. 16.9, where the values have been normalised by the nominal value of the predicted rate where the best estimates of each of the inputs are used (i.e. the midpoint of the input ranges). The study demonstrated that even when energies relative to n-propyl + O₂ are known to within 1 kcal/mol, 3σ values in the predicted rate constants could be as large as a factor of 10. Larger uncertainties were found for predictions of the rate constants for the OH producing channels as shown by the wider distributions for these channels in Fig. 16.9. These reactions involve a competition between TS3 and other channels, thus increasing the overall sensitivity to parameter variation. Uncertainties in the rates for the well skipping channels were found to increase with increasing pressure. The large variability in predicted rates found in this study indicates the need to further constrain such predictions, potentially by incorporating information from experimental measurements as will be discussed in the following section on optimization. The predictive uncertainties were found to be both pressure and temperature dependent suggesting that experimental constraints over wide ranges of reaction conditions would be useful.

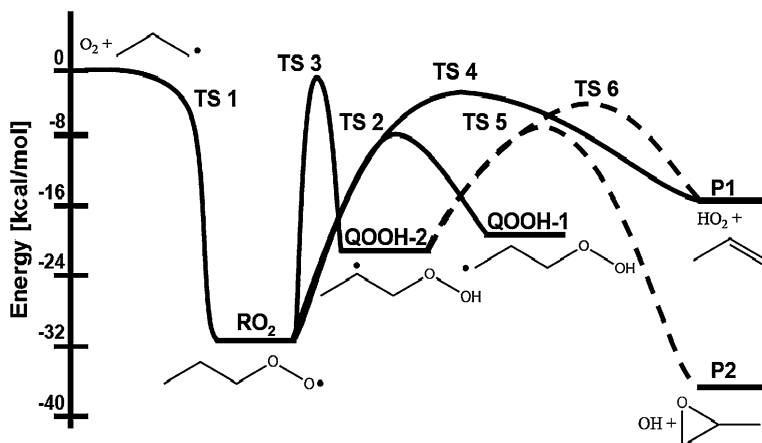
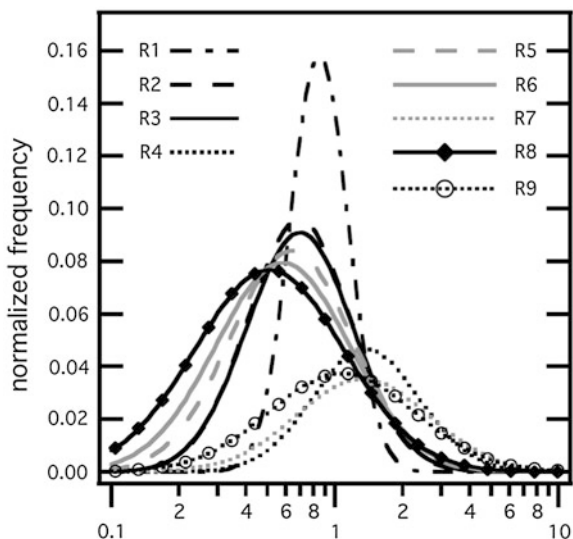


Fig. 16.8 Potential energy surface for $O_2 + n\text{-propyl}$, where the dotted lines were not included in the master equation calculations, and QOOH-2 was treated as an irreversible product. Reprinted from (Goldsmith et al. 2013) with permission from Elsevier

Fig. 16.9 Normalized frequency distribution $\log_{10}(k/k_{\text{nominal}})$ for the predicted rate constants for the $O_2 + n\text{-propyl}$ system at 600 K and 1 atm. Reprinted from (Goldsmith et al. 2013) with permission from Elsevier



16.6 Optimization

Spatially homogeneous (0D) combustion systems can be investigated experimentally by measuring the ignition delay times or temporal concentration profiles in shock tubes (see Chap. 6) or rapid compression machines (RCMs, see Chap. 7), the exit concentrations in perfectly stirred reactors (PSRs, see Chap. 8), and the

spatial concentration profiles in tubular reactors (see [Chap. 9](#)). The chemistry of combustion systems can also be explored by studying the laminar flame velocity or measuring the concentration-distance profiles in flat (1D) flames (see [Chap. 10](#)). All these types of measurements may be called indirect measurements, because the experimental results can be interpreted only via simulations using a detailed reaction mechanism and the simulation results depend on the rate parameters of several elementary reactions in the mechanism.

In the early days of combustion modelling, little information was known about the elementary reactions of combustion processes and indirect experiments were interpreted with a single global reaction or with a few-step skeletal mechanism. The main task was the satisfactory parameterisation of such a skeletal mechanism which was often based on global rather than elemental reaction steps.

In the seventies and eighties, several researchers emphasized (see e.g. Westbrook and Dyer [1981, 1984](#)) that combustion mechanisms should be built up from elementary reactions only. Data collections were published (Warnatz [1984](#); Tsang and Hampson [1986](#)) that included rate parameters for many important elementary reactions of basic fuels. These rate parameters had been determined by direct measurements. In these measurements, the reaction conditions are selected in such a way that the measured signal depends mainly on the rate parameters of a single reaction step, thus a rate coefficient can be determined from it more directly. The extent to which the term “direct measurement” accurately describes such approaches depends on how well the experiment can be designed to isolate particular reaction steps. Nevertheless we go on to use this term in the discussion that follows.

Originally it was hoped that quantitatively accurate combustion mechanisms could be built solely on the basis of direct measurements. This expectation was fuelled by the fact that every year more and more new rate coefficients were measured over wide ranges of temperatures and pressures, and also rate coefficients were regularly re-measured using more and more accurate methods. Now it is clear that the parameterisation of combustion mechanisms cannot be based solely on direct measurements and theoretical calculations, partly because we are aiming to describe the oxidation of more and more complex fuels. The current trend is the increasing size of combustion mechanisms (Lu and Law [2009](#)) (see [Fig. 2.15](#)) due to the consideration of new fuels and aims to better describe pollutant formation from combustion processes. Many rate coefficients which are required to parameterise the detailed mechanisms described in the early chapters of the book have not yet been determined via direct measurements. Consequently, the ratio of rate coefficients based on direct measurements to those which require estimation is decreasing. An additional problem is that the accuracy of rate coefficients determined in even very accurate direct measurements is at best about 30 %, when considering both random and systematic errors. This accuracy may not be sufficient for some reactions, since a few percentage change of some important rate coefficient may result in a significant shift in the calculated ignition delay time or laminar flame velocity (Zsély et al. [2005](#); Zádor et al. [2005](#)). Theoretical methods have undergone significant improvements in accuracy in

recent years and can also contribute to the determination of important rate parameters. However, as discussed in detail at the end of the previous section, the accuracy of theoretical calculations is also limited. A typical uncertainty of a rate coefficient calculated using a high-level method is about a factor of two for simple abstraction reactions, while for a minor channel of a multichannel reaction it can be as high as a factor of 10 (Goldsmith et al. 2013; Prager et al. 2013).

When nominal values of rate parameters determined using direct measurements and theoretical calculations are used within a detailed reaction mechanism, the kinetic model often does not reproduce well the results of indirect measurements. In such cases, the authors of the detailed mechanism might identify the rate parameters having the highest local sensitivity coefficient with respect to the results of indirect measurements and tune some of these rate parameters within their range of uncertainty to get a better agreement (see e.g. Hughes et al. 2001). In almost all mechanisms suggested in the literature, some of the rate parameters have been tuned to reproduce target indirect experimental data. Problems arise when different authors tune different rate parameters and therefore a range of different mechanisms are available for the combustion of the same fuel.

To circumvent the problems caused by the limited availability of direct measurements and theoretical calculations, Frenklach (1984) suggested the systematic optimization of combustion mechanisms. The first articles on the topic of mechanism optimization were written by Frenklach and Miller (Frenklach and Miller 1983; Frenklach 1984) in the early eighties. A more developed approach was published by Frenklach et al. (1992). This approach was used during the creation of the GRI mechanisms, which describe the oxidation of methane and NO_x formation during methane combustion. The first versions of the GRI-mechanism [GRI-Mech 1.2 (Frenklach et al. 1995) and GRI-Mech 2.11 (Bowman et al. 2013)] were replaced in 1999 with GRI-Mech 3.0 (Smith et al. 1999). This is the last official version of the GRI-Mech. The details of the creation of the GRI-Mech are described on its home page (Smith et al. 1999) and in a later publication (You et al. 2011).

The “GRI methodology” included the following main steps. A new methane combustion mechanism was created and all rate parameters and enthalpies of formation were carefully revised, resulting in the “base mechanism”. Uncertainty parameters (see Eq. (16.5)) were assigned to each elementary reaction, usually taken from data evaluations. Typical uncertainty limits were factors of 2–4. Target values were selected that well characterized typical indirect experimental data at some conditions. These target values included shock tube ignition delay times, laminar flame velocities, maximum concentrations of some species in shock tubes or flames etc. In some cases the target values were identical to actual experimental data, while in other cases these were averages of several experiments carried out at similar conditions. For the creation of GRI-Mech 3.0, 77 target values were used. Using local sensitivity analysis, the highest sensitivity *A*-factors and enthalpies of formation of species with respect to the target values were identified. For the generation of GRI-Mech 3.0, trial fits were carried out with 108 parameters, but finally 32 parameters (31 *A*-factors and the enthalpy of formation of HCN) were

fitted to reproduce the 77 scalar “target values”. It was noticed that the optimization pushed the A -factors of several reactions to the edges of the allowed limits.

Fitting the model parameters required combustion simulations that had to be repeated several thousand times with different parameter sets, which is very computationally costly especially for flame simulations. To circumvent this difficulty, results of parameter changes were calculated with response surfaces. The response surface was in this case parameterised using a 2nd order polynomial. The parameters to be changed (called active parameters) were arranged within their uncertainty limits according to a central composite factorial design. Using the results of these factorial-design-directed calculations, the parameters of the polynomial functions were determined by regression analysis. The optimized methane combustion mechanism (with NO_x chemistry) provides a good to acceptable performance over a wide range of conditions, and accordingly it became a great success and is widely used even nowadays.

The GRI methodology has some features that are sometimes misinterpreted. Since only the A -factors are optimized, small errors in Arrhenius parameters n and E are compensated by changing the A -factors, and the latter is limited by the uncertainty factor f . The authors of the GRI-Mech warn (Smith et al. 1999) that the sets of the Arrhenius parameters of the optimized reaction steps are meaningful within the GRI-Mech only, these parameters should not be used in other mechanisms and these values should not be “updated” in the GRI-Mech. However, this warning is frequently not taken into account by other authors.

The GRI methodology subsequently evolved in several directions. GRI-Mech 3.0 served as an example of data collaboration studies in the papers of Frenklach et al. (2002, 2004, 2007); Feeley et al. (2004, 2006); Seiler et al. (2006); Frenklach (2007); Russi et al. (2008); You et al. (2011). The PrIME website was then created (Frenklach 2013) offering several important services. PrIME is an acronym of Process Informatics Model. The aims of the PrIME website are collecting and storing data, validating the data and quantifying uncertainties, and aiding the production of predictive combustion models with quantified uncertainties. PrIME includes collections of indirect measurements encoded in a special XML format (“PrIME format”), and a set of computer codes for simulation and model optimization. The application of the PrIME toolset for the optimization of a hydrogen combustion mechanism was recently demonstrated (You et al. 2012). Unfortunately the mechanism produced cannot be converted easily to a CHEMKIN format, and in the present form it can be used only within the PrIME framework. Nevertheless the basic strategy behind data collaboration has been demonstrated via these various examples.

Another branch of the evolution of the GRI methodology is linked to Wang and his co-workers. They optimized the combustion mechanisms of a series of other fuels, like propane (Qin et al. 2000), H₂/CO mixtures (Davis et al. 2005), ethylene (Sheen et al. 2009) and n-heptane (Sheen and Wang 2011). Also, a local sensitivity analysis based method was suggested for the calculation of response surfaces (Davis et al. 2004).

The most significant improvement was to merge model optimization and global uncertainty analysis (Sheen et al. 2009, 2013; Sheen and Wang 2011). This approach is called the method of uncertainty quantification and minimization using polynomial chaos expansions. Using this method, the response surface function is identical to a polynomial expansion (See Eq 16.20) and after the optimization the same polynomial can be used for the calculation of the uncertainty of the simulation results from the covariance matrix of the optimized A -factors. It is possible to show that the uncertainty of the determined parameters is low and therefore the uncertainty of the simulation results obtained from the optimized model is also low. This improvement was demonstrated in Fig. 16.7.

A drawback of the mechanism optimization approaches of Frenklach et al. and Wang et al. is that these methods use indirect measurements only and the knowledge from direct measurements and theoretical calculations is only taken into account in defining the uncertainty ranges of the A -factors. In the recent work of You et al. (2011) and Sheen and co-workers (Sheen et al. 2009; Sheen and Wang 2011) the objective function was extended so that deviations from the A -factors of the base mechanism were also penalized. This approach implicitly assumes that the A -factors used in the base mechanism e.g. based on direct measurements or theoretical calculations, are the best or most probable values. Using this approach, the optimized A -factors became closer to the evaluated ones which for well-studied reactions makes good sense. However, this approach cannot distinguish very well-known A -factors which are based on evaluations of several good measurements from those based on few and possibly conflicting direct measurements. For the former, a defined uncertainty based on a log normal distribution centred on the most likely value seems reasonable whereas for the latter case, a uniform distribution with no preferred value is perhaps more realistic.

The recent optimization methods described in (Turányi et al. 2012; Zsely et al. 2012; Prager et al. 2013; Burke et al. 2013) were developed based on experience gained from the previously described methods. These approaches attempt to utilise all kinetic information that is available for a chemical system during the parameter optimization. The results of indirect and direct measurements, and also those of theoretical calculations are used together. The optimization includes Arrhenius parameters A , n , E for each important reaction, 3rd body collision efficiencies and can also be extended to other types of parameters, like enthalpies of formation, Troe parameters etc. In the method of Turányi et al. all experimental data are stored in PrIME format XML files (Frenklach 2013). The local sensitivity analysis and optimization calculations utilise Matlab programs that call CHEMKIN-II (Kee et al. 1989) or Cantera (2013) combustion simulation codes.

In the approach of Turányi and co-workers, first, large amounts of experimental data of indirect measurements are collected and simulated using a complex reaction mechanism. Local sensitivity analysis is carried out with respect to the measured signals and the most sensitive rate parameters are selected for optimization. Results of direct measurements and theoretical calculations, which are usually available in the form of temperature—rate coefficient tables, belonging to the selected reactions are collected.

If an optimization includes A -factors only, the uncertainty parameters available in the databases (see Eq. (16.5)) can be used for the determination of the uncertainty ranges of the A -factors for each tuned reaction. Optimization of all Arrhenius parameters requires the knowledge of the domain of uncertainty of the Arrhenius parameters, and the optimized Arrhenius parameters can be accepted only within this domain. This domain of uncertainty can be obtained in such a way that the k^{\min} and k^{\max} values of the rate coefficients at several temperatures in the temperature range of interest are determined from the results of direct measurements and theoretical calculations. Then, using the method of Nagy and Turányi (2011), (2012) these values are transformed to a prior covariance matrix that defines the domain of uncertainty of the Arrhenius parameters.

The following objective function was used in these calculations:

$$E(\mathbf{p}) = \frac{1}{N} \sum_{j=1}^N \frac{1}{N_i} \sum_{j=1}^{N_i} \left(\frac{Y_{ij}^{\text{mod}}(\mathbf{p}) - Y_{ij}^{\text{exp}}}{\sigma(Y_{ij}^{\text{exp}})} \right)^2 \quad (16.24)$$

where

$$Y_{ij} = \begin{cases} y_{ij} & \text{if } \sigma(y_{ij}^{\text{exp}}) \approx \text{constant} \\ \ln y_{ij} & \text{if } \sigma(\ln y_{ij}^{\text{exp}}) \approx \text{constant} \end{cases}$$

Target values y_{ij}^{exp} may include rate coefficients k measured at given conditions (e.g. temperature, pressure, and bath gas) in direct experiments. y_{ij}^{exp} may also be a theoretically determined value and these are treated similarly to the results of the direct measurements. Target values y_{ij}^{exp} may also be the results of indirect measurements, like ignition delay times or laminar flame velocities. In this equation, N is the number of measurement series (direct and indirect datasets together) and N_i is the number of data points in the i th dataset. Data points published in the same article are usually treated as belonging to the same dataset, unless the article reports experimental data obtained on several different apparatuses or measured at very different conditions. Value y_{ij}^{exp} is the j th data point in the i th dataset. The corresponding modelled value $y_{ij}^{\text{mod}}(\mathbf{p})$ for parameter set \mathbf{p} can be obtained by calculating the rate coefficient at the given temperature (and pressure, bath gas etc.), or by carrying out a simulation at the conditions of the experiment with combustion kinetic codes using an appropriate detailed mechanism. The form of the objective function includes weighting according to the number of data points and the standard deviation of the data $\sigma(y_{ij}^{\text{exp}})$. If the simulation results perfectly agree with the experimental data and the source of deviation is only the scatter of the experiments, then E is expected to be equal to 1.

The objective function can be transformed into a simpler form by introducing a single index k which runs through all data points of all measurement series. A new

unified weight $\mu_k = 1/(N_k)$ is used for each data point, which further simplifies the objective function:

$$E(\mathbf{p}) = \sum_{k=1}^N \mu_k \left(\frac{Y_k^{\text{mod}}(\mathbf{p}) - Y_k^{\text{exp}}}{\sigma(Y_k^{\text{exp}})} \right)^2 \quad (16.25)$$

This equation can be condensed by introducing matrix–vector notation:

$$E(\mathbf{p}) = (\mathbf{Y}_{\text{mod}}(\mathbf{p}) - \mathbf{Y}_{\text{exp}})^T \mathbf{W} \Sigma_Y^{-1} (\mathbf{Y}_{\text{mod}}(\mathbf{p}) - \mathbf{Y}_{\text{exp}}) \quad (16.26)$$

Matrices \mathbf{W} and Σ_Y are the diagonal matrices of weights μ_k and variances $\sigma^2(Y_k^{\text{exp}})$. The covariance matrix of the fitted parameters $\Sigma_{\mathbf{p}}$ is estimated using the following equation:

$$\Sigma_{\mathbf{p}} = \left[(\mathbf{J}_0^T \mathbf{W} \Sigma_Y^{-1} \mathbf{J}_0)^{-1} \mathbf{J}_0^T \mathbf{W} \Sigma_Y^{-1} \right] (\Sigma_Y + \Sigma_{\Delta}) \left[(\mathbf{J}_0^T \mathbf{W} \Sigma_Y^{-1} \mathbf{J}_0)^{-1} \mathbf{J}_0^T \mathbf{W} \Sigma_Y^{-1} \right]^T \quad (16.27)$$

where $\Sigma_{\Delta} = \Delta \mathbf{Y} \Delta \mathbf{Y}^T$, $\mathbf{Y} = \bar{\mathbf{Y}}_{\text{mod}} - \mathbf{Y}_{\text{exp}}$. Here \mathbf{J}_0 is the derivative matrix of \mathbf{Y}_{mod} with respect to \mathbf{p} at the optimum.

The diagonal elements of matrix $\Sigma_{\mathbf{p}}$ are the variances of parameters $\sigma^2(p_i)$. The off-diagonal elements are covariances, $\text{cov}(p_i, p_j) = r_{p_i, p_j} \sigma_{p_i} \sigma_{p_j}$, therefore correlation coefficient r_{p_i, p_j} can be calculated from the off-diagonal element and the standard deviations:

$$r_{p_i, p_j} = \frac{(\Sigma_{\mathbf{p}})_{i,j}}{\sigma_{p_i} \sigma_{p_j}} \quad (16.28)$$

Covariances of the logarithm of the rate coefficients at temperature T can be calculated (Turanyi et al. 2012) in the following way:

$$\text{cov}(\ln k_i(T), \ln k_j(T)) = \Theta^T \Sigma_{\mathbf{p}, i, \mathbf{p}, j} \Theta \quad (16.29)$$

Here $\Theta := (1, \ln\{T\}, -T^{-1})^T$, $p_i := (\ln A_i, n_i, E_i/R)^T$ and $\Sigma_{\mathbf{p}, i, \mathbf{p}, j}$ denotes a block of matrix $\Sigma_{\mathbf{p}}$ that contains the covariances of the Arrhenius parameters of reactions i and j . Equation (16.29) provides variance $\sigma^2(\ln k_i(T))$, if $i = j$. The optimized values of the rate parameters of the selected elementary reactions within their domain of uncertainty are determined using a global nonlinear fitting procedure.

The procedure above can be used for two purposes. First, it can be used to determine rate parameters from several direct and indirect measurements. For example, a series of indirect measurements (e.g. H atom concentration profiles measured by ARAS (Atomic Resonance Absorption Spectroscopy) in a shock tube) can be interpreted (Zsely et al. 2012; Varga et al. 2012) in such a way that the related rate parameters are determined not only from the actual experimental data, but also by taking into account the results of direct measurements from other authors. In this way, the obtained mean values and the covariance matrix of the rate parameters reflect all available experimental information.

Burke et al. (2013) also demonstrated a similar approach in their study of the H_2O_2 decomposition mechanism. In this study they combined information from ab initio quantum chemistry calculations with data from previous shock tube studies within an optimization of 5 target reactions involving H_2O_2 , HO_2 and OH . The result is an optimized model that is consistent with ab initio calculations and experimental data for $\text{OH} + \text{HO}_2 = \text{H}_2\text{O} + \text{O}_2$ across wide temperature ranges and helps to resolve a previously apparent anomalous temperature dependence for this reaction. A similar approach was also adopted in a recent study by Prager et al. (2013) of parametric uncertainties for the hydrogen-atom-abstraction reaction $\text{CH}_3\text{CH}(\text{OH})\text{CH}_3 + \text{OH} \rightarrow \text{CH}_3\text{C}(\text{OH})\text{CH}_3 + \text{H}_2\text{O}$, of significant importance in low-temperature alcohol autoignition models. After identifying parameters causing significant uncertainty in the rate-coefficient calculations, a Bayesian statistical framework was employed in order to determine the joint *pdf* of the parameters for the reaction by combining data from ab initio calculations with previous high quality experimental OH-LIF data for isopropanol + OH.

Rather than studying single reactions or small subsets of mechanisms, another possibility is the optimization of a full reaction mechanism for the combustion of a selected fuel. For example, the optimization of a hydrogen combustion mechanism was reported (Zsély et al. 2012). Arrhenius parameters of eight selected elementary reactions and 3rd body collision efficiencies were fitted to ignition delay times measured in shock tubes (655 data points in 54 datasets) and rapid compression machines (166 data points in 9 datasets), all taken from literature sources, covering wide regions of temperature, pressure and equivalence ratio. Direct measurements (1823 data points in 47 datasets) for the selected rate coefficients were also taken into account. The optimized hydrogen combustion mechanism reproduced better not only the time to ignition data, but also the flame velocity measurements (631 data points in 71 datasets) when compared to other recently published hydrogen combustion mechanisms.

The features of this mechanism optimization method are illustrated here for the determination of rate parameters of reactions R1: $\text{H} + \text{O}_2 = \text{OH} + \text{O}$ and R2: $\text{H} + \text{O}_2 + \text{M} = \text{HO}_2 + \text{M}$ (low-pressure limit, $\text{M} = \text{N}_2$ or Ar). These two elementary reactions are among the most important reactions in hydrogen, wet CO, and hydrocarbon combustion systems for a wide range of conditions. Based on the uncertainty of the best direct measurements, Miller et al. (2005) estimated the uncertainty of the rate coefficients of these reactions to be about 30 and 50 %, respectively.

Large amounts of time to ignition data of hydrogen–oxygen mixtures (diluted with N_2 or Ar) measured in shock tubes were collected from the literature and simulated with the detailed hydrogen combustion mechanism of Ó Conaire et al. (2004). Local sensitivity analysis was carried out at each experimental condition and those data points were selected (79 data points from 11 experiments) where the simulated ignition time depended mainly on the rate parameters of reactions R1 and R2, and the relative sensitivity on the rate parameters of all other reactions was much smaller. The next step was the selection of direct measurements from the literature for the measurement of the rate coefficients of these two reactions.

For reactions R1 and R2, respectively, 745 rate coefficient values (from nine datasets) and 258 rate coefficient values (from 10 datasets) were selected. All these data were encoded in XML files in PrIME format (Frenklach 2013).

The next step was the determination of the temperature dependent uncertainty limits of the rate coefficients. All direct rate coefficient measurements were charted on an Arrhenius plot, which outlined the uncertainty limits of $\ln k$ (see Fig. 16.10). These uncertainty limits were converted to the domain of uncertainty of the Arrhenius parameters using the method described in articles (Nagy and Turányi 2011, 2012). The prior uncertainty limits determined in this way were slightly wider than those present in the data evaluations. For example, for reaction R1 it was $f = 0.2\text{--}0.3$ instead of $f = 0.1\text{--}0.2$ as recommended in Baulch et al. (2005). The reason for the difference is that the uncertainty estimation of Baulch et al. is based on some selected measurements, while for the creation of Fig. 16.10 all sensible experimental results were used. Considering a wider uncertainty region only slows down the calculations (the optimal rate parameters are looked for in a wider region), but does not distort the final results.

The optimal rate parameters were determined using a newly developed (Turanyi et al. 2012) global parameter estimation method. These included the third body collision efficiency factor of Ar relative to N_2 , which was $m = 0.494$ (standard deviation $\sigma = 0.010$). The Arrhenius parameters of reactions R1 and R2

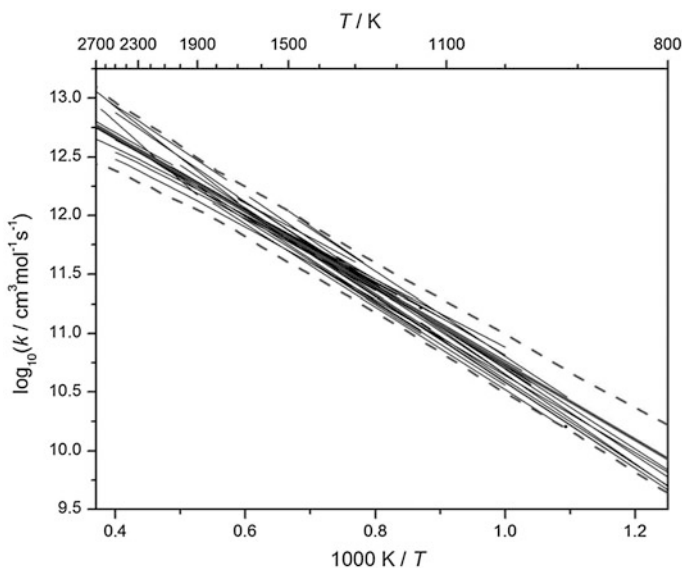


Fig. 16.10 Arrhenius plot of all direct measurements of reaction R1: $\text{H} + \text{O}_2 = \text{OH} + \text{O}$ (*thin lines*). The mean value (*thick black line*) is identical to the Baulch et al. evaluation (2005). The upper and lower limits ($k^{\text{min}}(T)$ and $k^{\text{max}}(T)$) determined from this figure are indicated by *dashed lines*. Adapted from (Turanyi et al. 2012) with permission from Wiley

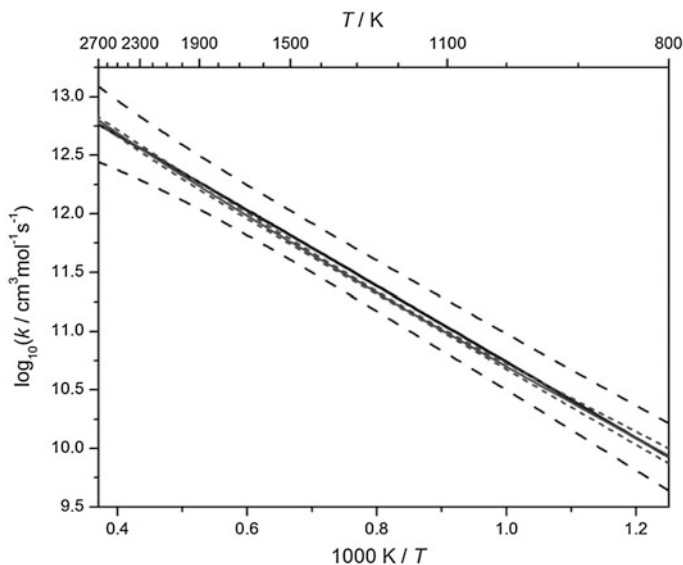


Fig. 16.11 Arrhenius plots of the initial and optimized main values and uncertainty limits for reaction R1: $\text{H} + \text{O}_2 = \text{OH} + \text{O}$. *Solid black line* initial value of optimization (identical to the Baulch recommendation). *Long dashed lines* prior uncertainty limits. *Solid grey line* optimized rate coefficient. *Short dashed lines* : posterior uncertainty limits. Adapted from (Turanyi et al. 2012) with permission from Wiley

were determined. The uncertainty parameter f as a function of temperature was also calculated for both reactions. The results are depicted in Figs. 16.11 and 16.12. It is clear from these figures that the optimized rate parameters are not very different from the recommendations in Baulch et al. (2005). However, since large amounts of direct and indirect measurements were used for the determination of the rate parameters, the average uncertainty parameter values are now $f = 0.025$ and $f = 0.049$ for reactions R1 and R2, respectively. These values correspond to 6 and 12 % uncertainty, respectively, which are much lower than those of the previous evaluations. However, there are also other differences. The previous uncertainty parameter values were estimations, while the uncertainty parameters derived here are results of statistical calculations. Previously, the uncertainty of parameters of reactions R1 and R2 were determined independently of each other. Since reactions R1 and R2 jointly determine the ignition delay time of hydrogen–oxygen mixtures at the selected conditions, the obtained optimized rate coefficients are highly correlated (the correlation coefficient between $\ln k_1$ and $\ln k_2$ is typically 0.8). In fact, the calculated covariance matrix is a much better characterization of the joint uncertainty of the rate parameters of reactions R1 and R2 than the traditionally used f parameters, provided independently for the rate coefficients.

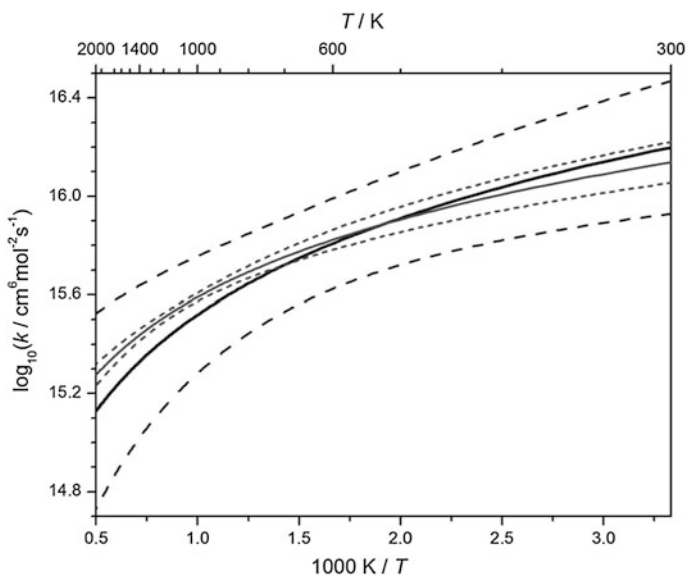


Fig. 16.12 Arrhenius plot for reaction R2: $\text{H} + \text{O}_2 + \text{N}_2 = \text{HO}_2 + \text{N}_2$ (low-pressure limit). *Solid black line* initial value of optimization (identical to the Baulch et al. recommendation). *Long dashed lines* prior uncertainty limits. *Solid grey line* optimized rate coefficient. *Short dashed lines* posterior uncertainty limits. Adapted from (Turányi et al. 2012) with permission from Wiley

16.7 Summary and Conclusions

Local linear sensitivity coefficients can be computed with reasonable efficiency using methods such as the decoupled direct method, automatic differentiation or even using the brute force method for systems with a low number of parameters. They usually form the starting point for the investigation of a mechanism and are useful for highlighting key reaction steps or thermodynamic parameters. However, if we wish to rank the importance of parameters in terms of their impact on the accuracy of predicted target outputs such methods require extension. They can be coupled with information on input parameter uncertainty in order to evaluate the contribution of each input to the overall predictive uncertainty. For systems with low input uncertainties (i.e. narrow input distributions), or which show mainly linear responses to changes in input parameters, the use of linear uncertainty analysis can be an efficient way to identify those parameters whose more accurate quantification could help to improve model robustness. However, many systems are highly nonlinear, and (for example in large hydrocarbon oxidation schemes) many parameters have to be estimated and therefore are highly uncertain. In such cases nonlinear methods for sensitivity and uncertainty analysis will give a more accurate picture of parameter importance, albeit at increased computational cost.

The sampling required by global methods can become a problem for such high dimensional systems if all parameters are included within a global analysis. Often therefore, screening methods such as linear sensitivity analysis are used in order to screen out unimportant parameters before a global analysis is carried out. Such an approach was demonstrated in Cord et al. (2012) where over 1300 reactions were present in the original mechanism. After screening using a linear brute force method, only 31 parameters were found to be significant and therefore were allowed to vary within the global analysis. Following screening, accurate results were obtained using a sample size of 4096 runs which is only about a factor of 3 larger than that required by the brute force method for the full scheme. The use of screening methods therefore makes global analysis tractable for even large reaction mechanisms.

The calculation of model error bars is still a difficult problem for large schemes however, since it relies on having reasonable estimates for the input parameter uncertainties. Ideally joint probability distributions for all significant parameters would be required. Whilst such distributions have been developed for small systems using optimization approaches (Nagy and Turányi 2011; Turanyi et al. 2012), they are not widely available and their development depends to a large degree on whether sufficient experimental and theoretical data are available to allow optimization. Since many parameters within complex hydrocarbon schemes are based on estimates or on a low number of theoretical calculations, uncertainties have not been detailed in the same way as those for well-studied parameters within data evaluations such as (Baulch et al. 2005) or from the use of optimization (Turanyi et al. 2012; Zsely et al. 2012). However, emerging methods for propagating uncertainties within theoretical calculations, coupled with those based on rigorous analysis of multiple data sets using optimization techniques, may assist progress in this area (Burke et al. 2013). If such methods are more widely applied then it may become possible to provide more accurate estimates of model predictive uncertainty, facilitating improvements in overall model robustness.

Acknowledgments TT acknowledges the financial support of OTKA grants K84054 and NN100523. AST acknowledges the financial support of EPSRC through grants GR/R76172/01(P) and GR/R39597/01.

References

- Balakrishnan S, Georgopoulos P, Banerjee I et al (2002) Uncertainty consideration for describing complex reaction systems. *AIChE J* 48:2875–2889
- Baulch DL, Cobos CJ, Cox RA et al (1992) Evaluated kinetic data for combustion modeling. *J Phys Chem Ref Data* 21:411
- Baulch DL, Cobos CJ, Cox RA et al (1994) Summary table of evaluated kinetic data for combustion modeling—supplement-1. *Combust Flame* 98:59–79
- Baulch DL, Bowman CT, Cobos CJ et al (2005) Evaluated kinetic data for combustion modeling: supplement II. *J Phys Chem Ref Data* 34(3):757–1397

- Bischof C, Carle A, Khademi P et al (1996) The ADIFOR 2.0 system for the automatic differentiation of FORTRAN 77 programmes. *IEEE J Comput Sci Eng* 3:18–32
- Bischof CH, Roh L, Mauer-oats AJ (1997) ADIC: an extensible automatic differentiation tool for ANSI-C. *Soft Pract Exp* 27:1427–1456
- Bischof CH, Bucker HM, Rasch A (2004) Sensitivity analysis of turbulence models using automatic differentiation. *SIAM J Sci Comput* 26(2):510–522
- Blatman G, Sudret B (2010) Efficient computation of global sensitivity indices using sparse polynomial chaos expansions. *Reliab Eng Syst Saf* 95(11):1216–1229
- Bowman C, Hanson R, Davidson D et al (2013) GRI-Mech 2.11. Available from http://www.me.berkeley.edu/gri_mech/. Accessed 15 March 2013
- Brown NJ, Revzan KL (2005) Comparative sensitivity analysis of transport properties and reaction rate coefficients. *Int J Chem Kinet* 37:538–553
- Brown MJ, Smith DB, Taylor SC (1999) Influence of uncertainties in rate constants on computed burning velocities. *Combust Flame* 117:652–656
- Burke MP, Klippenstein SJ, Harding LB (2013) A quantitative explanation for the apparent anomalous temperature dependence of $\text{OH} + \text{HO}_2 \rightarrow \text{H}_2\text{O} + \text{O}_2$ through multi-scale modeling. *Proc Combust Inst* 34:547–555
- Cantera An open-source, object-oriented software suite for combustion. <http://sourceforge.net/projects/cantera/>, <http://code.google.com/p/cantera/>. Accessed 15 March 2013
- Cheng HY, Sandu A (2009) Uncertainty quantification and apportionment in air quality models using the polynomial chaos method. *Environ Model Soft* 24(8):917–925
- Cord M, Sirjean B, Fournet R et al (2012) Improvement of the modeling of the low-temperature oxidation of n-butane: study of the primary reactions. *J Phys Chem A* 116(24):6142–6158
- Davis SG, Mhadeshwar AB, Vlachos DG et al (2004) A new approach to response surface development for detailed gas-phase and surface reaction kinetic model optimization. *Int J Chem Kinet* 36:94–106
- Davis S, Joshi A, Wang H et al (2005) An optimized kinetic model of H_2/CO combustion. *Proc Combust Inst* 30:1283–1292
- Davis MJ, Skodje RT, Tomlin AS (2011) Global sensitivity analysis of chemical-kinetic reaction mechanisms: construction and deconstruction of the probability density function. *J Phys Chem A* 115(9):1556–1578
- Dunker AM (1981) Efficient calculation of sensitivity coefficients for complex atmospheric models. *Atmos Environ* 15(7):1155–1161
- Dunker AM (1984) The decoupled direct method for calculating sensitivity coefficients in chemical kinetics. *J Chem Phys* 81(5):2385–2393
- Faure C (2005) An automatic differentiation platform: Odyssee. *Fut Gen Comput Sys* 21(8):1391–1400
- Feeley R, Seiler P, Packard A et al (2004) Consistency of a reaction dataset. *J Phys Chem A* 108:9573–9583
- Feeley R, Frenklach M, Onsum M et al (2006) Model discrimination using data collaboration. *J Phys Chem A* 110:6803–6813
- Feng X-J, Hooshangi S, Chen D et al (2004) Optimizing genetic circuits by global sensitivity analysis. *Biophys J* 87:2195–2202
- Frenklach M (1984) Systematic optimization of a detailed kinetic model using a methane ignition example. *Combust Flame* 58(1):69–72
- Frenklach M (2007) Transforming data into knowledge—process informatics for combustion chemistry. *Proc Combust Inst* 31:125–140
- Frenklach M PrIme Database. Available from <http://www.primekinetics.org/>. Available 15 March 2013
- Frenklach M, Wang H, Rabinowitz MJ (1992) Optimization and analysis of large chemical kinetic mechanisms using the solution mapping method—combustion of methane. *Prog Energy Combust Sci* 18:47–73
- Frenklach M, Wang H, Yu C et al (1995) GRI-Mech 1.2. Available from http://www.me.berkeley.edu/gri_mech/. Accessed 15 March 2013

- Frenklach M, Packard A, Seiler P (2002) Prediction uncertainty from models and data. In: Proceeding of the American control conference, Anchorage
- Frenklach M, Packard A, Seiler P et al (2004) Collaborative data processing in developing predictive models of complex reaction systems. *Int J Chem Kinet* 36:57–66
- Frenklach M, Packard A, Feeley R (2007) Optimization of reaction models with solution mapping. modeling of chemical reactions. R. Carr, Elsevier Science
- Goldsmith CF, Tomlin AS, Klippenstein SJ (2013) Uncertainty propagation in the derivation of phenomenological rate coefficients from theory: a case study of n-propyl radical oxidation. *Proc Combust Inst* 34:177–185
- Helton JC, Johnson JD, Sallaberry CJ et al (2006) Survey of sampling-based methods for uncertainty and sensitivity analysis. *Reliab Eng Syst Saf* 91(10–11):1175–1209
- Hughes KJ, Turányi T, Clague AR et al (2001) Development and testing of a comprehensive chemical mechanism for the oxidation of methane. *Int J Chem Kinet* 33:513–538
- Hughes KJ, Griffiths JF, Fairweather M et al (2006) Evaluation of models for the low temperature combustion of alkanes through interpretation of pressure-temperature ignition diagrams. *Phys Chem Chem Phys* 8(27):3197–3210
- Kee RJ, Rupley FM, Miller JA (1989) CHEMKIN-II: A FORTRAN chemical kinetics package for the analysis of gas-phase chemical kinetics. Sandia National Laboratories, Albuquerque
- Klippenstein SJ, Harding LB, Davis MJ et al (2011) Uncertainty driven theoretical kinetics studies for CH(3)OH ignition: HO(2) + CH(3)OH and O(2) + CH(3)OH. *Proc Combust Inst* 33:351–357
- Konnov AA (2008) Remaining uncertainties in the kinetic mechanism of hydrogen combustion. *Combust Flame* 152:507–528
- Li G, Rosenthal C, Rabitz H (2001) High dimensional model representations. *J Phys Chem A* 105:7765–7777
- Li G, Wang S-W, Rabitz H (2002a) Practical approaches to construct RS-HDMR component functions. *J Phys Chem A* 106:8721–8733
- Li G, Wang S-W, Rabitz H et al (2002b) Global uncertainty assessments by high dimensional model representations (HDMR). *Chem Eng Sci* 57:4445–4460
- Li J, Zhao ZW, Kazakov A et al (2007) A comprehensive kinetic mechanism for CO, CH₂O, and CH₃OH combustion. *Int J Chem Kinet* 39(3):109–136
- Lu T, Law C (2009) Toward accommodating realistic fuel chemistry in large-scale computations. *Prog Energy Combust Sci* 35:192–215
- Miller D, Frenklach M (1983) Sensitivity analysis and parameter estimation in dynamic modeling of chemical kinetics. *Int J Chem Kinet* 15:677–696
- Miller JA, Pilling MJ, Troe J (2005) Unravelling combustion mechanisms through a quantitative understanding of elementary reactions. *Proc Combust Inst* 30:43–88
- Nagy T, Turányi T (2011) Uncertainty of Arrhenius parameters. *Int J Chem Kinet* 43:359–378
- Nagy T, Turányi T (2012) Determination of the uncertainty domain of the Arrhenius parameters needed for the investigation of combustion kinetic models. *Reliab Eng Syst Saf* 107:29–34
- Najm H, Debusschere BJ, Marzouk YM et al (2009) Uncertainty quantification in chemical systems. *Int J Numer Meth Eng* 80:789–814
- Ó Conaire M, Curran HJ, Simmie JM et al (2004) A comprehensive modeling study of hydrogen oxidation. *Int J Chem Kinet* 36(11):603–622
- Oakley J, O'Hagan A (2002) Bayesian inference for the uncertainty distribution of computer model outputs. *Biometrika* 89(4):769–784
- Pilling MJ (2009) From elementary reactions to evaluated chemical mechanisms for combustion models. *Proc Combust Inst* 32:27–44
- Prager J, Najm HN, Zádor J (2013) Uncertainty quantification in the ab initio rate-coefficient calculation for the CH₃CH(OH)CH₃ + OH → CH₃C(OH)CH₃ + H₂O reaction. *Proc Combust Inst* 34(1):583–590
- Qin Z, Lissianski V, Yang H et al (2000) Combustion chemistry of propane: a case study of detailed reaction mechanism optimization. *Proc Combust Inst* 28:1663–1669

- Rabitz H, Alis OF (2000) Managing the tyranny of parameters in mathematical modelling of physical systems. In: Saltelli A, Chan K, Scott E (eds) *Sensitivity analysis*. Wiley, New York, pp 199–224
- Rabitz H, Aliu ÖF, Shorter J et al (1999) Efficient input-output model representations. *Comput Phys Commun* 117:11–20
- Reagan MT, Najm HN, Ghanem RG et al (2003) Uncertainty quantification in reacting-flow simulations through non-intrusive spectral projection. *Combust Flame* 132(3):545–555
- Reagan MT, Najm HN, Debusschere BJ et al (2004) Spectral stochastic uncertainty quantification in chemical systems. *Combust Theor Model* 8:607–632
- Ruscic B, Pinzon RE, Morton ML et al (2004) Introduction to active thermochemical tables: several key enthalpies of formation revisited. *J Phys Chem A* 108:9979–9997
- Russi T, Packard A, Feeley R et al (2008) Sensitivity analysis of uncertainty in model prediction. *J Phys Chem A* 112:2579–2588
- Saltelli A, Scott M, Chen K (eds) (2000) *Sensitivity analysis*. Wiley, Chichester
- Saltelli A, Tarantola S, Campolongo F et al (2004) *Sensitivity analysis in practice. A guide to assessing scientific models*. Wiley, Chichester
- Saltelli A, Ratto M, Tarantola S et al (2006) Sensitivity analysis practices: strategies for model-based inference. *Reliab Eng Syst Saf* 91(10–11):1109–1125
- Saltelli A, Ratto M, Andres T et al (2008) *Global sensitivity analysis: the Primer*. Wiley, New York
- Seiler P, Frenklach M, Packard A et al (2006) Numerical approaches for collaborative data processing. *Optim Eng* 7:459–478
- Sheen DA, Wang H (2011) The method of uncertainty quantification and minimization using polynomial chaos expansions. *Combust Flame* 158(12):2358–2374
- Sheen DA, You X, Wang H et al (2009) Spectral uncertainty quantification, propagation and optimization of a detailed kinetic model for ethylene combustion. *Proc Combust Inst* 32:535–542
- Sheen DA, Rosado-Reyes CM, Tsang W (2013) Kinetics of H atom attack on unsaturated hydrocarbons using spectral uncertainty propagation and minimization techniques. *Proc Combust Inst* 34:527–536
- Skodje RT, Tomlin AS, Klippenstein SJ et al (2010) Theoretical validation of chemical kinetic mechanisms: combustion of methanol. *J Phys Chem A* 114(32):8286–8301
- Smith G, Golden D, Frenklach M et al (1999) GRI-Mech 3.0. Available from http://www.me.berkeley.edu/gri_mech/. Accessed 15 March 2013
- Sobol IM (2001) Global sensitivity indices for nonlinear mathematical models and their Monte Carlo estimates. *Math Comput Sim* 55(1–3):271–280
- Sobol' IM (1967) On the distribution of points in a cube and the approximate evaluation of integrals. *USSR Comput Math Math Phys* 7(4):86–112
- Storlie CB, Helton JC (2008) Multiple predictor smoothing methods for sensitivity analysis: description of techniques. *Reliab Eng Syst Saf* 93(1):28–54
- Tomlin AS (2006) The use of global uncertainty methods for the evaluation of combustion mechanisms. *Reliab Eng Syst Saf* 91(10–11):1219–1231
- Tomlin AS (2013) The role of sensitivity and uncertainty analysis in combustion modelling. *Proc Combust Inst* 34:159–176
- Tomlin AS, Ziehn T (2011) The use of global sensitivity methods for the analysis, evaluation and improvement of complex modelling systems. In: Gorban AN, Roose D (eds) *Coping with complexity: model reduction and data analysis*, vol 75. Springer, Heidelberg, pp 9–36
- Tsang W (1992) Chemical kinetic data base for propellant combustion. II. Reactions involving CN, NCO, and HNC. *J Phys Chem Ref Data* 21:753–791
- Tsang W, Hampson RF (1986) Chemical kinetic database for combustion chemistry. I. Methane and related compounds. *J Phys Chem Ref Data* 15(3):1087–1279
- Turanyi T, Nagy T, Zsely IG et al (2012) Determination of rate parameters based on both direct and indirect measurements. *Int J Chem Kinet* 44(5):284–302

- Turányi T, Zalotai L, Dóbbé S et al (2002) Effect of the uncertainty of kinetic and thermodynamic data on methane flame simulation results. *Phys Chem Chem Phys* 4:2568–2578
- Varga T, Zsély IG, Turányi T et al (2012) Kinetic analysis of ethyl iodide pyrolysis based on shock tube measurements. COST action CM0901 3rd annual meeting. Sofia, Bulgaria
- Wang SW, Georgopoulos PG, Li G et al (2001) Computationally efficient atmospheric chemical kinetic modeling by means of high dimensional model representation (HDMR). *Lect Note Comput Sci* 2179:326–333
- Wang SW, Georgopoulos PG, Li GY et al (2003) Random sampling-high dimensional model representation (RS-HDMR) with nonuniformly distributed variables: application to an integrated multimedia/multipathway exposure and dose model for trichloroethylene. *J Phys Chem A* 107(23):4707–4716
- Wang H, You X, Joshi A et al (2007) USC Mech Version II. High-temperature combustion reaction model of H₂/CO/C₁-C₄ compounds. Available from http://ignis.usc.edu/USC_Mech_II.htm
- Warnatz J (1984) Rate coefficients in the C/H/O system. In: Gardiner WC (ed) *Combustion chemistry*. Springer, New York, pp 197–361
- Westbrook CK, Dryer FL (1981) Chemical kinetics and modeling of combustion processes. *Proc Combust Inst* 18:749–767
- Westbrook CK, Dryer FL (1984) Chemical kinetic modeling of hydrocarbon combustion. *Prog Energy Combust Sci* 10:1–57
- You XQ, Russi T, Packard A et al (2011) Optimization of combustion kinetic models on a feasible set. *Proc Combust Inst* 33:509–516
- You XQ, Packard A, Frenklach M (2012) Process informatics tools for predictive modeling: hydrogen combustion. *Int J Chem Kinet* 44(2):101–116
- Zádor J, Zsély IG, Turányi T et al (2005) Local and global uncertainty analyses of a methane flame model. *J Phys Chem A* 109:9795–9807
- Zádor J, Zsély IG, Turányi T (2006) Local and global uncertainty analysis of complex chemical kinetic systems. *Reliab Eng Syst Saf* 91(10–11):1232–1240
- Ziehn T (2008) Development and application of global sensitivity analysis methods in environmental and safety engineering. Ph.D., University of Leeds
- Ziehn T, Tomlin AS (2008) A global sensitivity study of sulphur chemistry in a premixed methane flame model using HDMR. *Int J Chem Kinet* 40:742–753
- Ziehn T, Tomlin AS (2009) GUI-HDMR—a software tool for global sensitivity analysis of complex models. *Environ Model Soft* 24(7):775–785
- Ziehn T, Hughes KJ, Griffiths JF et al (2009) A global sensitivity study of cyclohexane oxidation under low temperature fuel-rich conditions using HDMR methods. *Combust Theory Model* 13:589–605
- Zsely IG, Varga T, Nagy T et al (2012) Determination of rate parameters of cyclohexane and 1-hexene decomposition reactions. *Energy* 43(1):85–93
- Zsély IG, Zádor J, Turányi T (2005) Uncertainty analysis backed development of combustion mechanisms. *Proc Combust Inst* 30:1273–1281
- Zsély IG, Zádor J, Turányi T (2008) Uncertainty analysis of NO production during methane combustion. *Int J Chem Kinet* 40:754–768
- Zsély IG, Nagy T, Varga T et al (2012) Optimization of a hydrogen combustion mechanism. COST action CM0901 3rd annual meeting. Sofia, Bulgaria

Chapter 17

Mechanism Reduction to Skeletal Form and Species Lumping

Alison S. Tomlin and Tamás Turányi

Abstract The numerical simulation of practical combustion devices such as engines and gas turbines requires the coupling of descriptions of complex physical flows with complex chemistry in order to accurately predict phenomena such as ignition and flame propagation. For three-dimensional simulations, this becomes computationally challenging where interactions between large numbers of chemical species are involved. Historically therefore, such simulations used highly simplified descriptions of chemistry, which limited the applicability of the models. More recently, however, a range of techniques for reducing the size of chemical schemes have been developed, where the resulting reduced schemes can be shown to have accuracies which are almost as good as much larger comprehensive mechanisms. Such techniques will be described in this chapter. Skeletal reduction techniques are first introduced which aim to identify redundant species and reactions within a mechanism over wide ranges of conditions. Approaches based on sensitivity analysis, optimization and direct relation graphs are introduced. Lumping techniques are then discussed which exploit similarities between the structure and reactivity of species in describing lumped components, which can represent the sum of several isomers of a particular hydrocarbon species for example. Both approaches can lead to a substantial reduction in the size of chemical mechanisms (numbers of species and reactions) without having a significant impact on model accuracy. They are combined in the chemistry-guided reduction approach, which is shown to generate reduced chemical schemes which are small enough to be used within simulations of ignition behaviour in a homogeneous charge compression ignition (HCCI) engine.

A. S. Tomlin (✉)

Energy Research Institute, University of Leeds, Leeds, LS29JT, UK
e-mail: a.s.tomlin@leeds.ac.uk

T. Turányi

Institute of Chemistry, Eötvös University (ELTE), Budapest, Hungary
e-mail: turanyi@chem.elte.hu

17.1 Skeletal Model Reduction

The aim of chemical kinetic modelling is to accurately describe the concentration profiles of important species and/or the important features of the model predictions. Important species may include for example products of the reaction, pollutant concentrations, etc. and important features may include nonlocal outputs such as time-to-ignition, laminar flame velocities, etc. When using comprehensive mechanisms, the accurate simulation of these important species and features requires the simulation of changes in concentration of a large number of species including reactants, products and also coupled intermediates which may be important in determining the dynamic behaviour of the model. This unfortunately impacts on the computational cost of solving the chemical kinetics part of any combustion model, which may limit the use of comprehensive mechanisms within complex applications involving physical phenomena such as mixing and turbulence. It is crucial therefore to include only those species within a model whose presence is required for the accurate simulation of the important species and/or features as selected by the model user. These species are often termed necessary species (Turányi 1990b). The purpose of skeletal model reduction methods is the removal of any species, which are not important for the simulation of the desired targets, i.e. the redundant species. It may also be possible to remove redundant reaction steps which do not affect the prediction of important features. In skeletal model reduction therefore, the aim is to reduce the size of the chemical scheme but to retain its kinetic structure, i.e. the scheme is still described by elementary reactions. This is in contrast to the use of lumping methods, which often lead to changes in structure of the component reaction steps and are discussed in the second part of this chapter.

Skeletal reduction methods are often applied over specific sets of concentrations, pressures, temperatures and hence the accuracy of the reduced skeletal scheme when used in a more complex physical model is highly dependent on the reduction being applied over representative conditions compared to the intended final application. Local methods, therefore, tend to be applied over a range of conditions to give a reduced model of appropriate validity for the representation of selected model outputs. Typically, the reduced model will be developed using simulations of simplified experimental setups. For example, by using ignition simulations and perfectly stirred reactors (PSRs) to cover low temperature regions or 1-D flame simulations to represent high temperature regimes, a high degree of generality of the skeletal scheme can be obtained as long as a broad range of pressures is covered. The accuracy of the reduced model can be assessed by comparison with the full model for such setups with simple flow regimes since the computational times for the full model will be much lower than in a fully three-dimensional computational fluid dynamics (CFD) calculation. The selected reduced model can then be extrapolated to the CFD model as long as new temperatures/pressures, etc. are not encountered. The inclusion of high pressure conditions is particularly important if the reduced model is to be utilised in the simulation of practical devices such as internal combustion engines or gas turbines.

The reduction to a skeletal scheme usually consists of two stages. The first stage is the identification of redundant species and their reaction steps. The second stage involves the removal of redundant reactions that may involve important or necessary species but have only a minor influence on the overall dynamics of the model. The development of methods for skeletal model reduction has been ongoing for many years and includes the use of sensitivity-based approaches (e.g. (Turányi 1990a, b, c; Tomlin et al. 1992; Nagy and Turányi 2009), directed relation graph (DRG) based methods (e.g. Lu and Law 2005, 2006a, b) and optimization techniques (e.g. Edwards et al. 1998; Androulakis 2000; Banerjee and Ierapetritou 2003; Elliott et al. 2004, 2005).

17.1.1 Sensitivity-Based Methods

For a spatially homogeneous, dynamical system the change of the concentrations \mathbf{Y} in time can be calculated by solving the following initial value problem:

$$\frac{d\mathbf{Y}}{dt} = \mathbf{f}(\mathbf{Y}, \mathbf{x}), \quad \mathbf{Y}(t_0) = \mathbf{Y}_0 \quad (17.1)$$

where \mathbf{Y}_0 is the initial concentration and the parameter vector \mathbf{x} , having m elements, may include rate coefficients, Arrhenius parameters, thermodynamic data, etc. Even if we may be interested in the prediction of only a small number of species, large numbers of intermediates may need to be included within the equation system if they are strongly coupled to the species of interest. Not all species exhibit such strong couplings however, and the task of skeletal model reduction is usually to find groups of species whose removal does not impact on the overall accuracy of the chemical model.

The connectivity method was developed in Turányi (1990c) as a method of identifying redundant species via the investigation of the Jacobian of the system of Eq. (17.1). An element $(Y_i/f_i)(\partial f_i/\partial Y_i)$ of the normalised Jacobian shows the percentage change of the production rate of species j due to a small change in the concentration of species i . If the square of this effect is summed over all important species, then the resulting coefficient B_i shows the effect of a change in the concentration of each species on the concentrations of the group of important species:

$$B_i = \sum_j ((Y_i/f_i)(\partial f_i/\partial Y_i))^2 \quad (17.2)$$

Species characterised by large B_i values are closely connected to the group of important species, and therefore are necessary species. The method is iterative and during the next step, these necessary species are included in the summation and the B_i values are recalculated. The iteration is continued until all species that have a significant connection to the important species, either directly or indirectly are identified. All other species are considered redundant.

Since the Jacobian matrix is essentially local for nonlinear models, this procedure is repeated for a selection of representative concentration sets, e.g. at several points along a concentration trajectory and at different temperatures/pressures. Species that are redundant over all relevant simulation conditions can be removed from a general reduced mechanism, or different reduced mechanisms can be developed for different regions of the temperature/composition/pressure space. The consuming reactions of the redundant species can also be eliminated from the model at this stage (Turányi 1990c; Tomlin et al. 1992; Zsély and Turányi 2003). The method was first implemented in the program KINAL (Turányi 1990a) where at each iteration step the user had to select new species to be included in the summation on the basis of an ordered list of B_i values. It was later included in the option CONNECT of the code (KINALC 2013). In this code, the list of necessary species is increased by one during each iteration cycle, i.e. the species with the highest B_i value is added into the summation procedure.

A disadvantage of these previous connectivity methods is that the B_i values are not directly related to the final simulation error of important targets which can only be determined by comparing simulations using the reduced mechanism to those using the full scheme. It is therefore difficult to directly relate the size of the resulting reduced scheme, which in KINAL is determined by error thresholds set for the B_i values, to the final simulation error. The connectivity method was therefore further developed into the Simulation Error Minimization Connectivity Method (SEM-CM) (Nagy and Turányi 2009) where a number of trial reduced mechanisms are created, and the resulting simulation errors are used to guide the search for a nearly optimal reduced mechanism. The SEM-CM consequently requires more simulation time than the simple connectivity method, but with the advantage that the resulting reduced scheme may be much smaller. The main advantage of SEM-CM is that the required accuracy of the reduced mechanism can be defined a priori by the modeller.

Even within a mechanism composed of only necessary species there may still be redundant reactions that can be removed without affecting the accuracy of predictions of selected targets. Using a sensitivity-based approach these are usually identified through the investigation of the local rate sensitivity matrix $\mathbf{F} = \{\partial f_i / \partial k_j\}$ where f_i is the net rate of production of species i and k_j is the rate constant for the reaction under investigation. For large mechanisms, the analysis of \mathbf{F} may become complex and hence principal component analysis is often used to identify the relative importance of different reactions to the predictions of selected targets in the so-called PCAF approach (Turányi et al. 1989; Börger et al. 1992; Tomlin et al. 1992; Zsély and Turányi 2001, 2003). The objective function has the following form:

$$e' = \sum_{i=1}^{N_R} \left(\frac{\tilde{f}_i(t) - f_i(t)}{f_i(t)} \right)^2 \quad (17.3)$$

where f_i and \tilde{f}_i are the right-hand-side of kinetic system of ordinary differential equations (ODEs), calculated for the original values of parameter vector $\boldsymbol{\alpha} = \ln \mathbf{k}$

and at the modified values of parameters $\boldsymbol{\alpha} + \Delta\boldsymbol{\alpha}$, respectively. Turányi et al. (1989) showed that this objective function can be approximated by:

$$e'(\boldsymbol{\alpha}) \approx (\Delta\boldsymbol{\alpha})^T \tilde{\mathbf{F}}^T \tilde{\mathbf{F}} (\Delta\boldsymbol{\alpha}) \quad (17.4)$$

where $\tilde{\mathbf{F}} = \{(k_j/f_i)(\partial f_i/\partial k_j)\}$ is the normalised \mathbf{F} -matrix with rows corresponding to the variables present in the objective function (17.3). This means that elements of matrix $\tilde{\mathbf{F}}$ can be calculated algebraically from the concentration vector and therefore obtained in normalised form during the simulation of the kinetic ODE system from:

$$\tilde{F}_{ij} = \frac{\partial \ln f_i}{\partial \ln k_j} = \frac{k_j}{f_i} \frac{\partial f_i}{\partial k_j} = \left(\frac{v_{ij} r_j}{f_i} \right) \quad (17.5)$$

The eigenvalues of matrix $\tilde{\mathbf{F}}^T \tilde{\mathbf{F}}$ indicate the effectiveness of a simultaneous change of the values of a group of parameters on the production rate of species. Elements of the eigenvectors show the weight of the individual parameters in the corresponding parameter group. Therefore, important reactions may be identified as the largest elements of eigenvectors which relate to large eigenvalues. By defining suitable threshold values, reduced schemes of different sizes can be produced. Since this method is essentially local however, the analysis should be carried out at several suitable time points within a simulation and the resulting mechanism formed from the union of important reactions determined at each point. Whilst a simple model scenario can be used for the reduction process (e.g. zero-dimensional reactor simulations or a 1D flame simulation) it is important to ensure that the composition/temperature space covered in the chosen scenarios match those of the final intended model application. This topic was investigated in detail by Zsély and Turányi (2003).

This method was also coupled with simulation error minimization in the SEM-PCAF approach described by Nagy and Turányi (2009). Several reduced mechanisms are produced using various PCAF eigenvalue/eigenvector thresholds. The mechanism having the least CPU time requirement among the ones having almost the smallest error is selected. As with SEM-CM, the advantage for the user is that the required accuracy of the final model simulations can be defined as part of the reduction procedure. The combined application of both SEM methods was tested by Nagy and Turányi (2009) for a mechanism describing methane partial oxidation to high conversion. The initial scheme contained 6,874 irreversible reactions and 345 species (Gupta et al. 2006) and was reduced to 47 species in 246 reactions with the aim to accurately reproduce the concentration–time profiles of 12 major species with less than 5 % error for conditions relevant to an industrial application. The computational speed-up was found to be a factor of 116.

Zsély et al. (2011) used the SEM-CM and SEM-PCAF methods for the reduction of the NUIG Natural Gas Combustion Mechanism of 229 species and 1,359 reactions. Ignition of lean and stoichiometric mixtures containing 90 % methane and 10 % propane as fuels were investigated for 22 conditions relevant to

gas turbines, covering temperature and pressure ranges of 877–1,465 K and 7–40 atm, respectively. The smallest reduced mechanism developed contained 50 species and 186 reactions. It can reproduce ignition delays with 3.1 % maximum error and reproduces pressure rise precisely (with error $\approx 10^{-3}$ %). The reduced mechanism can be simulated 62 times faster than the full mechanism.

17.1.2 Graph-Based Methods

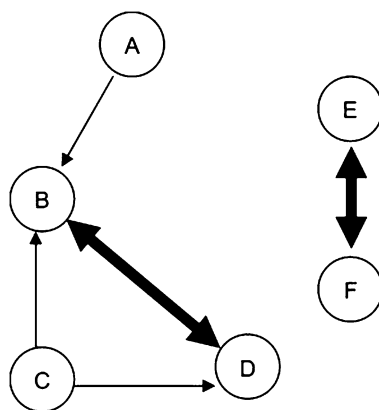
Reduction methods using directed relation graphs (DRGs) are based on identifying groups of species that may be internally coupled, but are not strongly coupled to selected important species within the mechanism and are not therefore necessary for the accurate simulation of important species profiles (Lu and Law 2005, 2006a, 2006b). In this sense, they have much in common with the connectivity method described above. In a DRG, each node represents a species and the edges between vertices represent the strength of coupling between the nodes. For example for the DRG shown in Fig. 17.1, an edge from A to B exists if and only if the removal of species B would directly induce significant error to the production rate of species A.

The direct influence of one species on another is represented by the width of the arrow in the figure and is quantified by the normalised contribution of species B to the production rate of species A:

$$r_{AB} = \frac{\sum_{i=1,J} |v_{A,i} R_i \delta_{Bi}|}{\sum_{i=1,J} |v_{A,i} R_i|} \quad (17.6)$$

$$\delta_{Bi} = \begin{cases} 1 & \text{if the } i^{\text{th}} \text{ elementary reaction involves species B,} \\ 0 & \text{otherwise,} \end{cases}$$

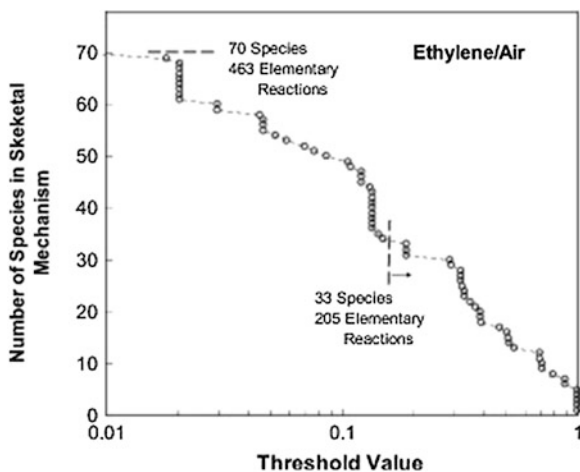
Fig. 17.1 A directed relation graph showing typical relationships between species. Reprinted from Lu and Law (2005) with permission from Elsevier



where R_i is the overall rate of reaction i and $\nu_{A,i}$ is the stoichiometric coefficient of species A in the i -th reaction. Hence, if r_{AB} is sufficiently large then removing species B from the mechanism will lead to errors in the production rate for species A. B is therefore coupled to A through the DRG and if A has to be kept in the mechanism then so does B. A threshold ε is then defined such that if $r_{AB} < \varepsilon$ then no edge is defined from A to B. Therefore for each set of important species there will exist a group of species that are reachable from this set and therefore should be retained as necessary species. In the example, reactions between species E and F shown in Fig. 17.1 represent a pair of fast reversible reactions and although they are strongly coupled to each other, they do not couple to any species in the dependant set of A and therefore could potentially be removed as a pair.

There are similarities between this method and the Jacobian-based connectivity method discussed above, since both are based on rates of production and are therefore essentially local methods. Hence to develop a generally applicable reduced scheme, the final model must represent the union of mechanisms derived for the selected conditions of each analysis. The success of the final reduced scheme will depend on the relevance of the local conditions chosen for analysis and the selected value of ε . Several thresholds can be applied and the accuracy of the resulting mechanisms tested in order to select an appropriate level of reduction. Lu et al. state that jumps in the number of required species may occur quite abruptly, signifying groups with strong internal coupling, but weak inter-group couplings moving in or out of the skeletal scheme (Lu and Law 2005). This is illustrated in Fig. 17.2 for the example of reduced models for ethylene-air combustion using different threshold values. The reduced models are based on PSR and auto-ignition simulations for pressures 0.1–30 atm, equivalence ratios 0.7–1.3, and initial temperatures of 300 K for PSR and 1,000–1,800 K for auto-ignition (Lu and Law 2005).

Fig. 17.2 Dependence of the species number of skeletal mechanisms for ethylene-air combustion based upon the chosen threshold value. Reprinted from Lu and Law (2005) with permission from Elsevier



It is worth stressing that in both the simple connectivity and DRG-based methods, controlling thresholds only controls the local accuracy of the rates of production of necessary species. This does not automatically control the potential growth of errors in a time or spatially dependant model and hence the connectivity methods were coupled with optimization approaches to aid the selection of appropriate threshold values as discussed above. Therefore, an extension to the DRG method has also been developed—DRG-aided sensitivity analysis (DRGASA) (Zheng et al. 2007; Niemeyer et al. 2010). The method does not include the calculation of sensitivities in the usual sense, but rather the error in the DRG-estimation for a group of redundant species based on several thresholds is checked using simulations. First, a group of redundant species is selected using a conservative threshold. Then a second group of species is identified using a tighter threshold, and these species are included into the reduced mechanism. A series of simulations are carried out where consequences of eliminating these species is investigated, one-by-one. The DRGASA method could be more effective than the basic DRG approach, since it investigates the simulation error directly. In this sense, it is more similar to the SEM methods described above.

The DRG method was first applied to ethylene combustion in a perfectly stirred reactor for simulated ignition delay times with a full scheme of 70 species (Lu and Law 2005) reducing it to 33 species. Later applications include n-heptane combustion with a full scheme of 561 species and iso-octane with a full scheme of 857 species (Lu and Law 2006a). Here, threshold values for ϵ of 0.19 and 0.17 resulted in schemes of 188 and 233 species for the n-heptane and iso-octane schemes, respectively. Lu and Law also suggested that for large hydrocarbon mechanisms, a two-stage reduction using DRG can lead to smaller skeletal mechanisms than a single stage reduction with a single value for ϵ . This is possible because the individual r values can change at the second stage due to the exclusion of redundant species resulting in a change to the graph structure. This potentially allows the removal of further species since larger values of ϵ can generally be accommodated at the second stage.

The DRG method was further extended by incorporating error propagation (DRGEP) (Pepiot and Pitsch 2005; Pepiot-Desjardins and Pitsch 2008). In this method, the assumption that all coupled species are equally important in the mechanism is lost, and errors are damped as they propagate along the graph from the initially selected important species. The DRGEP approach is combined with an integrity check which aims to avoid truncated chemical paths that may lead to mass accumulation in intermediate species whose consumption paths have been removed.

Extensions of the DRG and DRGEP approaches have also been applied adaptively in order to produce on-the-fly reduced mechanisms for n-heptane (Shi et al. 2010) and gasoline surrogate mixtures (Liang et al. 2009; Shi et al. 2010) in simulations of homogeneous charge compression ignition with significant computational speed-ups. The number of species required in the locally reduced models varies throughout the calculations but reaches a maximum of about 1/3 of the number of the initial species. Other applications include developing skeletal

models describing the oxidation of methyl decanoate, a large methyl ester used as a surrogate for biodiesel (Seshadri et al. 2009), methane oxidation (Jiang and Qiu 2009), nitrogen oxide emissions and their control (Lv et al. 2009; Luo et al. 2011), the combustion of surrogate jet fuels (Naik et al. 2010), surrogate biofuels (Luo et al. 2010, 2010) and the oxidation of iso-octane (Kelley et al. 2011).

17.1.3 The Use of Optimization in Model Reduction

The methods introduced so far are based on local error measures induced in the net rates of production of important and necessary species. Therefore, comparisons between simulations using the full and reduced schemes need to be performed in order to estimate the errors, which have propagated to the important species concentrations. Optimization-based reduction methods have also been suggested which are based on minimising an objective function (such as a measure related to the model error between the full and reduced models) subject to a set of constraints. The constraints for example may be based on the number of species or reactions required in the reduced mechanism. On the other hand, it would also be possible to search for the minimum number of reactions/species needed to satisfy specified error bounds (Edwards et al. 1998). If one is interested in the overall error during a simulation time then optimization becomes an integer nonlinear programming problem as discussed by Edwards et al. (2000) and also a combinatoric problem. For example, even for a small mechanism with five reactions there are $2^5 - 1$ possible reduced mechanisms to test. A possible solution to this problem is suggested by Androulakis (2000) where a pre-processing step is applied to identify a subset of important reactions with high ranking based on removing the reactions one at a time. This subset is then excluded from the constraints in the full optimization problem in order to improve computational efficiency. However, this type of approach does not take into account information on species interconnections in the same way as the connectivity and DRG methods, leading to the possible inclusion of fast reversible reactions which could perhaps be removed as a pair. Hence, the use of this pre-processing step will lead to an upper bound on the numbers of reactions within the final reduced scheme. The application of species removal prior to reaction removal may help to alleviate this problem.

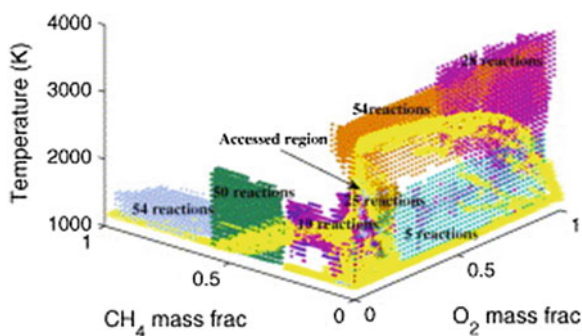
Binary encoded genetic algorithms (GAs) have also been applied to model reduction problems as discussed by Edwards et al. (1998); Banerjee and Ierapetritou (2003); Elliott et al. (2004, 2005). These are global search algorithms which in principle should be able to provide a reduced scheme with any prescribed error based on chosen constraints. The number of simulations required by these methods can however be very large. Approaches which combine information on species connectivity with error minimisation such as DRGASA or SEM-CM will perhaps be more effective. The choice of method is to a certain extent user driven. The user may wish to specify a tolerated error in the prediction of a target output. On the other hand, it may also be useful to use such methods to identify the

optimal scheme for a given number of variables. For example, in complex flow models such as three-dimensional turbulence problems, a limited number of scalars can usually be tolerated within the code due to computational costs. In such cases, it may be better to define the allowed number of variables and to use an optimization-based approach.

17.1.4 Adaptive and On-the-Fly Reduction

Within the course of a nonisothermal time dependent simulation of a combustion system the local species concentrations and temperatures may change substantially and therefore it may be more effective to exploit the existence of smaller reduced mechanisms for different local conditions, leading to the possibility of adaptive reduction. Two different types of approaches can be employed to achieve this. In the first, specific-reduced mechanisms are developed for different parts of the concentration temperature domain, which are called upon during the simulation of the final application. For example, optimization-based reduction methods have been extended in Bhattacharjee et al. (2003) based on earlier ideas developed by Schwer et al. (2003) to provide libraries of reduced models for combustion mechanisms, each with their own region of applicability. In Banerjee and Ierapetritou (2003), the feasible region is defined for a reduced model as the region of phase space over which a specified error constraint is satisfied. This could be determined by performing simulations of the full and reduced models over a grid in the major species concentrations and temperature. To reduce the sampling effort, Banerjee and Ierapetritou (2006) developed a genetic algorithm based sampling technique which exploits the typically small section of the entire space that is feasible within a simulation and hence reduces the sampling burden typical of grid-based procedures. A simplified flow model is generally adopted for the estimation of regions of validity of each reduced model, e.g. a pairwise mixed stirred reactor (PMSR) model (Banerjee and Ierapetritou 2006) as illustrated in Fig. 17.3.

Fig. 17.3 The range of temperatures and compositions addressed by different reduced methane oxidation models within an adaptive reduction approach. Reprinted from Banerjee and Ierapetritou (2006) with permission from Elsevier



The second approach uses an on-the-fly reduction where the reduced scheme is developed during a particular simulation. This requires a reduction technique which can be implemented quickly during a simulation and an approach based on element flux analysis is suggested by He et al. (2010a, b, c, d). This is integrated into the CFD calculations, and hence flux analysis is performed for each computational cell at each time step. Element fluxes are calculated for both forward and reverse steps for each reaction. A user selected cut-off value is then applied to a sorted list of source-sink pairs, so that species above the cut-off are included in the reduced mechanism, and others are considered redundant for the current local conditions. Therefore, ODEs are only solved for the chemical step for the necessary species although all species are included in the transport step and stored in the CFD calculation. This means that if a species becomes chemically active later in the simulation or in another grid cell its concentration can be readily retrieved. The approach is demonstrated for a numerical study of homogeneous charge compression ignition (HCCI) engine combustion using the CFD code KIVA-3 V employing a detailed n-heptane oxidation mechanism comprising 633 species and 2,827 reactions (He et al. 2011). The number of species required varied from below 50 to over 350 with an average of 94 compared to the original 653. Large mechanisms were found to be required during the period between cool flame ignition and the main ignition, i.e. during the build-up of the radical pool. The overall CPU time was found to be reduced by a factor of 18 compared to the full detailed mechanism with only 2.5 % of the simulation time devoted to the flux analysis and species source term evaluation. This level of reduction therefore greatly facilitates the description of complex chemistry within models of practical devices such as engines.

17.2 Lumping Methods

Whilst the skeletal model reduction methods described in the last section can lead to significant reductions in the CPU requirements for solving detailed chemistry in reactive flow problems, for very large and complex fuel mechanisms this may not be sufficient and other features of the starting mechanisms may have to be exploited in the context of reduction. Similarities between the structure and reactivity of species (e.g. chemical isomers) can for example be exploited within methods for species lumping, which at the simplest level may involve the use of lumped components representing the sum of several isomers of a particular hydrocarbon species. In this case, the different isomers are not distinguished if they have the same chemical formula and functional groups (Bounaceur et al. 1996; Battin-Leclerc et al. 2000) and therefore the resulting reactions are global rather than elementary. Species lumping can also be performed using strict mathematical principles (Huang et al. 2005), or using a chemical approach where parameters for the lumped scheme are derived from kinetic information from pre-calculated reactor experiments (Ranzi et al. 2001). Within mathematical approaches, the

relationship between the original species concentrations and the lumped variables may be based on either linear (Wei and Kuo 1969; Li and Rabitz 1989) or non-linear transformations (Li et al. 1993, 1994a, b; Tomlin et al. 1994). We restrict our discussion here to linear methods since these have been most commonly applied in combustion. Chemical lumping is usually based on a linear approach and therefore can be understood as a subset of linear lumping.

17.2.1 Mathematical Approaches to Lumping

The formal definition of lumping is the transformation of the original vector of variables \mathbf{Y} to a new variable vector $\hat{\mathbf{Y}}$ using a suitable transformation function \mathbf{h} :

$$\hat{\mathbf{Y}} = \mathbf{h}(\mathbf{Y}) \quad (17.7)$$

The dimension \hat{n} of the new variable vector $\hat{\mathbf{Y}}$ is smaller than that of the original concentration vector and hence a lower-dimensional kinetic system of ODEs is formed:

$$\frac{d\hat{\mathbf{Y}}}{dt} = \hat{\mathbf{f}}(\hat{\mathbf{Y}}, \hat{\mathbf{k}}), \quad \hat{\mathbf{Y}}(t_0) = \hat{\mathbf{Y}}_0 \quad (17.8)$$

It is often important to be able to recover the original vector of concentrations from the transformed variables $\hat{\mathbf{Y}}$ using an inverse transformation function $\bar{\mathbf{h}}$:

$$\mathbf{Y} = \bar{\mathbf{h}}(\hat{\mathbf{Y}}) \quad (17.9)$$

This inverse mapping is as important as the forward mapping not only because it provides the link between the lumped variables and the original species concentrations, but because its existence is a necessary condition of exact lumping. The function $\bar{\mathbf{h}}$ however, is not unique, since several different functions $\bar{\mathbf{h}}$ may belong to the same transformation function \mathbf{h} . Finding suitable inverse transformations is a key challenge of strict mathematical methods for exact lumping.

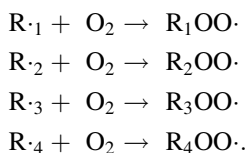
If the function \mathbf{h} is linear then in chemical kinetics this approach would be termed “linear species lumping” and is essentially a formalisation of the chemical lumping approach described in the next section and in Chaps. 2 and 3. In the linear case, the transformation is simply a matrix multiplication operation:

$$\hat{\mathbf{Y}} = \mathbf{M}\mathbf{Y} \quad (17.10)$$

where \mathbf{M} is a matrix of size $\hat{n} \times N_s$ and N_s the original number of variables. The new set of ODEs is therefore given by:

$$\frac{d\hat{\mathbf{Y}}}{dt} = \mathbf{M}\mathbf{f}(\mathbf{Y}) \quad (17.11)$$

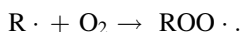
As a simple example, within the n-heptane scheme described in (Battin-Leclerc et al. 2000; Fournet et al. 2000) there are four alkyl radicals noted by $R_{\cdot 1}$, $R_{\cdot 2}$, $R_{\cdot 3}$, $R_{\cdot 4}$ giving rise to four reactions involving the addition of O_2 .



The lumped alkyl radical is then defined by:

$$[R\cdot] = [R_{\cdot 1}] + [R_{\cdot 2}] + [R_{\cdot 3}] + [R_{\cdot 4}],$$

with the corresponding lumped reaction given by:



The rate constant is calculated using the weighted mean of the elementary rate constants for the individual isomers:

$$k' = \frac{k_1 [R_{\cdot 1}] + k_2 [R_{\cdot 2}] + k_3 [R_{\cdot 3}] + k_4 [R_{\cdot 4}]}{[R\cdot]}.$$

A full description of the methodology is given by Fournet et al. (2000). It was shown by Battin-Leclerc et al. (2000) that using such techniques, the primary mechanism for n-heptane combustion could be reduced from 410 free radicals and 70 molecules in 1,654 reactions to a lumped scheme with only 25 free radicals and 189 reactions. The lumped mechanism was shown to give a good representation of the predictions n-heptane conversion compared to the full scheme in the negative temperature coefficient regime. The lumping process developed in Battin-Leclerc et al. (2000); Fournet et al. (2000) has been included as an integral part of the automatic reaction generation software EXGAS in order to allow the user to limit the size and improve the computational efficiency of the generated schemes where required. In this case however, the concentrations of the original isomers are not recovered, i.e. the inverse transformation is not defined. Therefore, the approach does not strictly satisfy the requirements of exact linear lumping but may be highly suitable in situations where the detailed concentrations of individual intermediates within a scheme are not required.

For exact linear lumping, $\mathbf{Mf}(\mathbf{Y})$ must be a function of $\hat{\mathbf{Y}}$ and therefore we require the inverse of \mathbf{M} since:

$$\mathbf{Y} = \overline{\mathbf{M}}\hat{\mathbf{Y}} \quad (17.12)$$

In order to determine the inverse transformation and satisfy the conditions of exact linear lumping, we need to find the invariant subspaces of the original equations, i.e. the invariant subspaces of the transpose of the Jacobian $\mathbf{J}^T(\mathbf{Y})$ so that the eigenvalues of $\mathbf{J}^T(\mathbf{Y})$ and $\mathbf{J}^T(\mathbf{M}^{-1}\mathbf{M}\mathbf{Y})$ are identical. This is relatively

straightforward for linear problems where the Jacobian is a constant matrix. However, this is a very difficult task for more general nonlinear ODEs where applying the restrictions imposed by exact lumping may limit the level of reduction possible for the reduced scheme.

More recent methods aim to be based on the formal mathematical principles described above but without leading to the stringent restrictions on the numbers of lumped species achievable caused by the application of exact linear lumping methods. Huang et al. defined a formal lumping procedure for intermediate species where the fraction of each component within the lump α_i (equivalent to the inverse lumping matrix $\bar{\mathbf{M}}$) is defined in terms of the fractional formation rate of the components of the lump (Huang et al. 2005). The intention of the procedure is to suggest suitable lumped groups, whilst maintaining the flexibility required in order to model the consequences of chemistry arising from reactions of the individual species within each lump. For example, for a lumped group containing three species A, B and C, α is calculated from:

$$\left\{ \begin{array}{l} \alpha_A = \frac{R_A}{R_A + m_1 R_B + m_2 R_C} \\ \alpha_B = \frac{m_1 R_B}{R_A + m_1 R_B + m_2 R_C} \\ \alpha_C = \frac{m_2 R_C}{R_A + m_1 R_B + m_2 R_C} \end{array} \right. \quad (17.13)$$

where R_i is the formation rate of species i , $m_1 = \gamma_{A,B}$, $m_2 = \gamma_{A,C}$ where for example $\gamma_{A,B}$ represents the ratio between the concentrations of species A and B, and $\alpha_A + \alpha_B + \alpha_C = 1$. The method was illustrated for the simulation of higher hydrocarbon generation during the isothermal oxidation of fuel-rich methane–oxygen mixtures, where 31 species were lumped into nine groups giving a reduction in the number of species of 22.

One advantage of using strictly mathematical approaches is that the parameters used in the lumped scheme can be completely derived from the original kinetic equations without any need for fitting. If the inverse transformation is also provided, then the original species concentrations can be retrieved. The disadvantage may be the complex algebra required to derive the relationships for highly non-linear applications.

17.2.2 Chemical Lumping

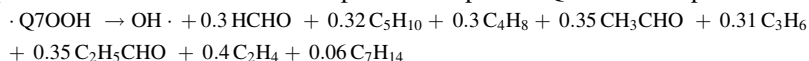
An alternative approach which is essentially a less formal method of linear lumping is that of chemical lumping and was briefly introduced for the n-heptane example above. Here, the approach used is based on the fact that for complex hydrocarbons with several isomers the main propagation reactions can be split into

relatively few reaction classes (see also [Chap. 3](#)). For example, for n-heptane the classes of propagation routes are defined by Ranzi et al. (1995) as:

1. Decomposition and isomerisation of alkyl radicals R·.
2. O₂ H-abstraction to form HO₂ and conjugate olefins.
3. Direct and reverse O₂ addition to R· to form peroxy radicals ROO·.
4. Internal isomerisation between ROO· and hydroperoxyalkyl radicals ·QOOH.
5. Decomposition of ·QOOH radicals to form olefins.
6. Decomposition of ·QOOH radicals to form HO₂ and conjugate olefins.
7. Decomposition of ·QOOH to form heterocomponents (cyclic ethers, aldehydes and ketones) and OH·.
8. Direct and reverse O₂ addition on ·QOOH to form hydroperoxyalkyl peroxy radicals ·OOQOOH.
9. Decomposition of ·OOQOOH radicals to form keto-hydroperoxides.

Reference rate parameters can be defined for each reaction class based on literature data or similarity rules (Ranzi et al. 1995). The pathways for each isomer and the resulting intermediate radicals can then be lumped to give a simplified scheme with only a single pathway representing degradation to the average products of all the isomers. The rate parameters for the lumped scheme can be obtained using fitting with respect to either experimental data, by calculating weighted averages for the different component isomers depending on the relative weights within the initial fuel, or based on the system of algebraic equations derived from the long-chain approximation, i.e. the QSSA approximation applied only to the propagation steps (Battin-Leclerc et al. 2000; Fournet et al. 2000).

A lumped n-heptane scheme was developed in Ranzi et al. (1995) containing only four lumped radicals. Here the rate constants for the lumped scheme were obtained by fitting against predictions from the full scheme. This high degree of lumping leads to reactions with noninteger stoichiometries which represent the relative weights of the different product channels. For example, in the lumped n-heptane scheme one of the decomposition steps for ·Q7OOH is represented by:



Other examples of reduced hydrocarbon mechanisms developed via chemical lumping include a primary oxidation mechanism for iso-octane containing only five intermediate lumped radicals (Ranzi et al. 1997), lumped schemes for higher *n*-alkanes up to *n*-hexadecane (Ranzi et al. 2005) and naphthenes (Granata et al. 2003). The approach has also recently been extended to oxygenated fuels such as methyl butanoate (Grana et al. 2012a) and methyl decanoate (Grana et al. 2012b). The combined lumped mechanism also allows the simulation of the combustion behaviour of intermediate methyl esters, by using the lever rule which allows the description of the intermediate methyl esters as a mixture of the reference components (Grana et al. 2012b).

17.3 Chemistry Guided Reduction

As pointed out by Ahmed et al. (2009) and in the previous section, low temperature mechanisms describing the oxidation of aliphatic hydrocarbons contain many parallel pathways and if no reduction is carried to reduce the number of these pathways prior to skeletal mechanism reduction then the resulting schemes may still be too large to apply in complex simulation scenarios. The chemistry guided reduction method discussed by Zeuch et al. (2008), Ahmed et al. (2009) therefore aims to combine chemical lumping approaches with species necessity analysis in order to produce a compact reduced mechanism that can be employed in, for example, detailed engine calculations. The aim is to develop compact mechanisms that can be generally applicable, i.e. for simulations of high- and low-temperature ignition and to shock tube, reactor and flame combustion (Zeuch et al. 2008). The chemical lumping approach adopted is based on a functional group method and hence the first stage of the reduction is to sort the isomeric species according to two rules: (i) the molecular positions at either primary (prefix p-) or secondary (prefix s-) carbon atoms (ii) the distance between functional groups and radical sites. For example, the low-temperature oxidation of *n*-heptane is initiated by O₂ addition to the *n*-heptyl radical, which subsequently isomerizes by internal H atom abstraction via five-, six-, seven-, or eight-membered rings to form QOOH species. The ring size of the transition state determines the distance between the functional groups that are subsequently formed in the oxidation process. Linear lumping of the low-temperature oxidation pathways with respect to the above criteria therefore creates a reorganization of the reaction pathways where the new order is based on the number of C atoms between the radical position and the OOH group after the first internal H-atom abstraction. As a result, the number of parallel isomerization pathways of the QOOH species can be reduced from 18 to 8 with little impact on the accuracy of simulated targets over a wide range of conditions. Zeuch et al. (2008) also state that for extension to larger linear alkanes such as *n*-decane, *n*-dodecane, or *n*-tetradecane, the number of parallel low-temperature isomerization pathways may not increase if the same lumping rules are applied. This gives the opportunity to dramatically simplify oxidation mechanisms for higher hydrocarbons or surrogate fuels and it is suggested that the lumping procedures could be incorporated directly into the mechanism development process. For the *n*-heptane, for example, the lumped mechanism consists of 196 species and 2,079 irreversible reactions compared to 246 species, 2,309 reactions within the detailed starting mechanism.

At the next stage of the CGR process, redundant species are identified based on the methods outlined by Soyhan et al. (2002) using combined concentration sensitivity analysis (for redundant species), reaction flow analysis (for redundant reactions) and the subsequent application of the QSSA (see Chap. 18 for a discussion of this). The selection of the QSSA species is based on local lifetime analysis. The final mechanism consists of 110 species and 1,170 irreversible reactions. Interestingly, the number of species in the reduced scheme by Zeuch

et al. (2008) is of a very similar size to the reduced n-heptane scheme produced by Hughes et al. (2009) which consisted of 110 species and 452 reactions. The method of Hughes et al., however, was based on a combined sensitivity analysis using KINAL (Turányi 1990a) and subsequent “vertical” reaction lumping based on the removal of QSSA species (see Chap. 18). Further reduction of the scheme of Hughes et al. may therefore be possible if “horizontal” species lumping was to be performed. In Ahmed et al. (2009), the skeletal heptane mechanism of Zeuch et al. (2008) was combined with a compact mechanism for toluene combustion and the resulting mechanism was validated using simulations of OH-concentration histories and ignition times from shock tube studies, HCCI engine experiments and flame speed measurements, again illustrating that complex kinetics can be incorporated into the simulation of practical combustion devices when appropriate reduction methods are employed.

17.4 Summary and Conclusions

A range of chemical mechanism reduction methods have been presented, which allow the representation of the important chemical features within a model using less species and reactions than the equivalent comprehensive scheme. The reduction to skeletal models usually involves the removal of redundant species and reactions over the range of conditions covered by the final intended application. Using the simplest approach, reduced schemes are developed for a wide range of temperatures, pressures and compositions, and the union of these schemes can be used in a general way. Adaptive reduction methods have also been discussed, where the reduced mechanism used may change through a simulation in order to optimally exploit any redundancies within the initial scheme. Skeletal mechanisms, in general, maintain the initial kinetic structure of the scheme and are composed of a smaller number of elementary reaction steps. Lumping procedures, which attempt to combine species, may lead to reactions with noninteger stoichiometric coefficients. However, such procedures may be necessary for reducing the number of variables in highly complex mechanisms which describe the oxidation of higher hydrocarbons or oxygenated fuels. The combined application of such techniques can lead to substantially smaller chemical schemes with associated savings in the computational time required to solve the resulting rate equations. However, for some applications, which may for example involve the coupling of complex turbulent flow models with detailed chemistry, the above reduction procedures may not go far enough. Other reduction methodologies have therefore been developed which attempt to exploit the time-scale separation between variables within the scheme. These will be discussed in the next chapter.

Acknowledgments TT acknowledges the financial support of OTKA grants K84054 and NN100523. AST acknowledges the financial support of EPSRC through grants GR/R76172/01(P) and GR/R39597/01.

References

- Ahmed SS, Mauss F, Zeuch T (2009) The generation of a compact n-heptane toluene reaction mechanism using the chemistry guided reduction (CGR) technique. *Zeitschrift Fur Physikalische Chemie-Int J Res Phys Chem Chem Phys* 223(4–5):551–563
- Androulakis IP (2000) Kinetic mechanism reduction based on an integer programming approach. *AIChE J* 46:361–371
- Banerjee I, Ierapetritou MG (2003) Development of an adaptive chemistry model considering micromixing effects. *Chem Eng Sci* 58(20):4537–4555
- Banerjee I, Ierapetritou MG (2006) An adaptive reduction scheme to model reactive flow. *Combust Flame* 144:619–633
- Battin-Leclerc F, Glaude PA, Warth V et al (2000) Computer tools for modelling the chemical phenomena related to combustion. *Chem Eng Sci* 55(15):2883–2893
- Bhattacharjee B, Schwer DA, Barton PI et al (2003) Optimally-reduced kinetic models: reaction elimination in large-scale kinetic mechanisms. *Combust Flame* 135:191–208
- Börger I, Merkel A, Lachmann J et al (1992) An extended kinetic model and its reduction by sensitivity analysis for the methanol/oxygen gas-phase thermolysis. *Acta Chim Hung* 129:855–864
- Bounaceur R, Warth V, Glaude PA et al (1996) Chemical lumping of mechanisms generated by computer—application to the modeling of normal-butane oxidation. *J Chim Phys Phys-Chim Biol* 93:1472–1491
- Edwards K, Edgar TF, Manousiouthakis VI (1998) Kinetic model reduction using genetic algorithms. *Comp Chem Eng* 22:239–246
- Edwards K, Edgar TF, Manousiouthakis VI (2000) Reaction mechanism simplification using mixed-integer nonlinear programming. *Comput Chem Eng* 24(1):67–79
- Elliott L, Ingham DB, Kyne AG et al (2004) Genetic algorithms for optimization of chemical kinetics reaction mechanisms. *Prog Energy Combust Sci* 30:297–328
- Elliott L, Ingham DB, Kyne AG et al (2005) Reaction mechanism reduction and optimization using genetic algorithms. *Ing Eng Chem Res* 44(4):658–667
- Fournet R, Warth V, Glaude PA et al (2000) Automatic reduction of detailed mechanisms of combustion of alkanes by chemical lumping. *Int J Chem Kinet* 32:36–51
- Grana R, Frassoldati A, Cuoci A et al (2012a) A wide range kinetic modeling study of pyrolysis and oxidation of methyl butanoate and methyl decanoate. Note I: Lumped kinetic model of methyl butanoate and small methyl esters. *Energy* 43(1):124–139
- Grana R, Frassoldati A, Saggese C et al (2012b) A wide range kinetic modeling study of pyrolysis and oxidation of methyl butanoate and methyl decanoate—note II: lumped kinetic model of decomposition and combustion of methyl esters up to methyl decanoate. *Combust Flame* 159(7):2280–2294
- Granata S, Faravelli T, Ranzi E (2003) A wide range kinetic modeling study of the pyrolysis and combustion of naphthenes. *Combust Flame* 132(3):533–544
- Gupta GK, Hecht ES, Zhu H et al (2006) Gas-phase reactions of methane and natural gas with air and steam in non-catalytic regions of a solid-oxide fuel cell. *J Pow Sources* 156:434–447
- He KY, Androulakis IP, Ierapetritou MG (2010a) Incorporation of detailed chemical mechanisms in reactive flow simulations using element-flux analysis. *Ing Eng Chem Res* 49:10471–10478
- He KY, Androulakis IP, Ierapetritou MG (2010b) Multi-element flux analysis for the incorporation of detailed kinetic mechanisms in reactive simulations. *Energy Fuels* 24:309–317
- He KY, Androulakis IP, Ierapetritou MG (2010c) On-the-fly reduction of kinetic mechanisms using element flux analysis. *Chem Eng Sci* 65(3):1173–1184
- He KY, Ierapetritou MG, Androulakis IP (2010d) Integration of on-the-fly kinetic reduction with multidimensional CFD. *AIChE J* 56(5):1305–1314

- He KY, Androulakis IP, Ierapetritou MG (2011) Numerical investigation of homogeneous charge compression ignition (HCCI) combustion with detailed chemical kinetics using on-the-fly reduction. *Energy Fuels* 25(8):3369–3376
- Huang H, Fairweather M, Griffiths JF et al (2005) A systematic lumping approach for the reduction of comprehensive kinetic models. *Proc Combust Inst* 30:1309–1316
- Hughes KJ, Fairweather M, Griffiths JF et al (2009) The application of the QSSA via reaction lumping for the reduction of complex hydrocarbon oxidation mechanisms. *Proc Combust Inst* 32:543–551
- Jiang Y, Qiu R (2009) Reduction of large kinetic mechanisms of hydrocarbon fuels with directed relation graph. *Acta Phys Chim Sin* 25(5):1019–1025
- Kelley AP, Liu W, Xin YX et al (2011) Laminar flame speeds, non-premixed stagnation ignition, and reduced mechanisms in the oxidation of iso-octane. *Proc Combust Inst* 33:501–508
- KINALC (2013) CHEMKIN based program for KInetic aNALysis. <http://garfield.chem.elte.hu/Combustion/kinalc.htm>
- Li G, Rabitz H (1989) A general analysis of exact lumping in chemical kinetics. *Chem Eng Sci* 44(6):1413–1430
- Li G, Tomlin AS, Rabitz H et al (1993) Determination of approximate lumping schemes by a singular perturbation method. *J Chem Phys* 99:3562–3574
- Li G, Tomlin AS, Rabitz H et al (1994a) A general analysis of approximate nonlinear lumping in chemical kinetics. I. Unconstrained lumping. *J Chem Phys* 101:1172–1187
- Li G, Tomlin AS, Rabitz H et al (1994b) A general analysis of approximate nonlinear lumping in chemical kinetics. II. Constrained lumping. *J Chem Phys* 101:1188–1201
- Liang L, Stevens JG, Raman S et al (2009) The use of dynamic adaptive chemistry in combustion simulation of gasoline surrogate fuels. *Combust Flame* 156:1493–1502
- Lu T, Law C (2006a) Linear time reduction of large kinetic mechanisms with directed relation graph: *n*-heptane and *iso*-octane. *Combust Flame* 144:24–36
- Lu T, Law CK (2006b) On the applicability of directed relation graphs to the reduction of reaction mechanisms. *Combust Flame* 146:472–483
- Lu T, Law CK (2005) A directed relation graph method for mechanism reduction. *Proc Combust Inst* 30:1333–1341
- Luo ZY, Lu TF, Liu JW (2011) A reduced mechanism for ethylene/methane mixtures with excessive NO enrichment. *Combust Flame* 158(7):1245–1254
- Luo ZY, Lu TF, Maciaszek MJ et al (2010a) A reduced mechanism for high-temperature oxidation of biodiesel surrogates. *Energy Fuels* 24:6283–6293
- Luo ZY, Lu TF, Som S et al (2010b) Numerical study on combustion characteristics of biodiesel using a new reduced mechanism for methyl decanoate as surrogate. *Proc Am Soc Mech Eng*, New York, pp 837–884
- Lv Y, Wang ZH, Zhou JH et al (2009) Reduced mechanism for hybrid NO_x control process. *Energy Fuels* 23:5920–5928
- Nagy T, Turányi T (2009) Reduction of very large reaction mechanisms using methods based on simulation error minimization. *Combust Flame* 156:417–428
- Naik CV, Puduppakkam KV, Modak A et al (2010) Validated F-T fuel surrogate model for simulation of jet-engine combustion. *Proc Am Soc Mech Eng*, New York, Paper No GT2010–23709
- Niemeyer KE, Sung CJ, Raju MP (2010) Skeletal mechanism generation for surrogate fuels using directed relation graph with error propagation and sensitivity analysis. *Combust Flame* 157(9):1760–1770
- Pepiot-Desjardins P, Pitsch H (2008) An efficient error-propagation-based reduction method for large chemical kinetic mechanisms. *Combust Flame* 154:67–81
- Pepiot P, Pitsch H (2005) Systematic reduction of large chemical mechanisms. In: 4th joint meeting of the U.S. Sections of the Combustion Institute, Philadelphia
- Ranzi E, Dente M, Goldaniga A et al (2001) Lumping procedures in detailed kinetic modeling of gasification, pyrolysis, partial oxidation and combustion of hydrocarbon mixtures. *Prog Energy Combust Sci* 27(1):99–139

- Ranzi E, Faravelli T, Gaffuri P et al (1995) Low-temperature combustion: automatic generation of primary oxidation reactions and lumping procedures. *Combust Flame* 102:179–192
- Ranzi E, Faravelli T, Gaffuri P et al (1997) A wide-range modeling study of iso-octane oxidation. *Combust Flame* 108(1–2):24–42
- Ranzi E, Frassoldati A, Granata S et al (2005) Wide-range kinetic modeling study of the pyrolysis, partial oxidation, and combustion of heavy n-alkanes. *Ing Eng Chem Res* 44(14):5170–5183
- Schwer DA, Lu P, Green WH (2003) An adaptive chemistry approach to modeling complex kinetics in reacting flows. *Combust Flame* 133:451–465
- Seshadri K, Lu TF, Herbinet O et al (2009) Experimental and kinetic modeling study of extinction and ignition of methyl decanoate in laminar non-premixed flows. *Proc Combust Inst* 32:1067–1074
- Shi Y, Ge HW, Brakora JL et al (2010a) Automatic chemistry mechanism reduction of hydrocarbon fuels for HCCI engines based on DRGEP and PCA methods with error control. *Energy Fuels* 24:1646–1654
- Shi Y, Liang L, Ge HW et al (2010b) Acceleration of the chemistry solver for modeling DI engine combustion using dynamic adaptive chemistry (DAC) schemes. *Combust Theor Modell* 14(1):69–89
- Soyhan H, Mauss F, Sorousbay C (2002) Chemical kinetic modeling of combustion in internal combustion engines using reduced chemistry. *Combust Sci Tech* 174:73–91
- Tomlin AS, Li GY, Rabitz H et al (1994) A general-analysis of approximate nonlinear lumping in chemical-kinetics. 2 constrained lumping. *J Chem Phys* 101(2):1188–1201
- Tomlin AS, Pilling MJ, Turányi T et al (1992) Mechanism reduction for the oscillatory oxidation of hydrogen: sensitivity and quasi-steady-state analyses. *Combust Flame* 91:107–130
- Turányi T (1990a) KINAL—A program package for kinetic analysis of reaction mechanisms. *Comput Chem* 14(3):253–254
- Turányi T (1990b) Reduction of large reaction mechanisms. *New J Chem* 14:795–803
- Turányi T (1990c) Sensitivity analysis of complex kinetic systems. Tools and applications. *J Math Chem* 5:203–248
- Turányi T, Bérces T, Vajda S (1989) Reaction rate analysis of complex kinetic systems. *Int J Chem Kinet* 21:83–99
- Wei J, Kuo JCW (1969) A lumping analysis in monomolecular reaction systems. *Ind Eng Chem Fundam* 8:114–123
- Zeuch T, Moréac G, Ahmed SS et al (2008) A comprehensive skeletal mechanism for the oxidation of n-heptane generated by chemistry-guided reduction. *Combust Flame* 155:651–674
- Zheng XL, Lu TF, Law CK (2007) Experimental counterflow ignition temperatures and reaction mechanisms of 1,3-butadiene. *Proc Combust Inst* 31:367–375
- Zsély IG, Nagy T, Simmie JM et al (2011) Reduction of a detailed kinetic model for the ignition of methane/propane mixtures at gas turbine conditions using simulation error minimization methods. *Combust Flame* 158:1469–1479
- Zsély IG, Turányi T (2001) Investigation and reduction of two methane combustion mechanisms. *Arch Combust* 21:173–177
- Zsély IG, Turányi T (2003) The influence of thermal coupling and diffusion on the importance of reactions: The case study of hydrogen-air combustion. *Phys Chem Chem Phys* 5:3622–3631

Chapter 18

Time-Scale Splitting-Based Mechanism Reduction

Ulrich Maas and Alison S. Tomlin

Abstract Chemical reaction systems, including those in combustion, often exhibit a large range of time-scales which can lead to stiffness in the resulting rate equations. This feature can however be exploited in the context of model reduction by recognising that certain fast species can relax to a quasi-equilibrium state or, in geometrical terms, that the evolution of the system of equations in composition space relaxes to lower and lower dimensional attractors. Time-scale separation therefore forms a basis for model reduction. This chapter introduces model reduction techniques based on time-scale splitting which may differ in their approach, but which all utilise the fact that chemical kinetic systems evolve with time-scales that often differ by orders of magnitude. The chapter will first discuss the mathematical basis on which time-scale separation is defined. It will then discuss approaches for model reduction based on algebraic approximations such as the quasi-steady state approximation or QSSA, trajectory-based approaches such as computational singular perturbation methods, geometrical approaches based on the presence of intrinsic low dimensional manifolds in composition space and methods based on thermodynamic principles such as the rate-controlled constrained-equilibrium method. Methods will be introduced for homogeneous reaction systems. The extension to reaction diffusion systems will then be discussed.

U. Maas (✉)

Institute of Engineering Thermodynamics, Karlsruhe Institute of Technology,
Engelbert-Arnold-Straße 4 76131 Karlsruhe, Germany
e-mail: Ulrich.Maas@kit.edu

A. S. Tomlin

Energy Research Institute, University of Leeds, Leeds LS29JT, UK
e-mail: A.S.Tomlin@leeds.ac.uk

18.1 Introduction

The use of detailed chemical kinetic models, which comprise more than a thousand species reacting in several thousand elementary reactions, is computationally prohibitive. Thus, methods are needed, which simplify the description of the physical and chemical processes without sacrificing accuracy, but nevertheless allow the mathematical models to be applied in realistic computations of three-dimensional reacting flows of practical interest. As early as one hundred years ago Bodenstein (1913) observed that some chemical reactions are so fast that certain chemical species in the reaction system are in a quasi-steady state. The reason for this behaviour is the great disparity of the chemical time-scales. In terms of the evolution of the system in composition space this means that the chemical kinetics relaxes the system to lower and lower dimensional attractors until the chemical equilibrium (zero-dimensional attractor) is reached. This can be seen from a plot of typical trajectories of hydrocarbon oxidation (Fig. 18.1; Blasenbrey and Maas 2000). This means that after a very fast relaxation process the chemical kinetics introduces correlations among the chemical species .

The consequence for the mathematical simulation of the system is that instead of solving differential equations for all the chemical species, rate equations have only to be solved for a small number of chemical species. Based on this behaviour different methods have been devised to obtain reduced models for the chemical kinetics. They differ in many aspects and each has its advantages and drawbacks. However, the feature that they have all in common is that they exploit the fact that the chemical kinetics evolves with time-scales that differ by orders of magnitude, and which can be shorter than microseconds (fast reactions leading to species in steady state) or as long as seconds (NO-formation).

18.2 Problem Formulation

Let us consider the evolution equation for the scalar field of a reacting flow, which can (for a low Mach number flow) be written as (see, e.g. Maas and Pope 1992a)

$$\begin{aligned} \frac{\partial \psi}{\partial t} &= F(\psi) - \vec{v} \cdot \text{grad} \psi + \frac{1}{\rho} \text{div} D \text{ grad} \psi \\ &= F(\psi) + \Xi_c(\text{grad} \psi) + \Xi_T(\psi, \text{grad} \psi, \text{div grad} \psi), \end{aligned} \quad (18.1)$$

where $\psi = (\psi_1, \psi_2, \dots, \psi_{S+2})^T$ is the thermokinetic state, which can, e.g. be expressed by the specific enthalpy h , the pressure p and the mass fractions w_i of the S chemical species: $\psi = (h, p, w_1, \dots, w_S)^T$, F denotes the chemical source term (which depends only on the thermokinetic state), \vec{v} the velocity, ρ the density and D the matrix of transport coefficients. The physical processes of convection and transport (which depend on the thermokinetic state as well as its spatial derivatives)

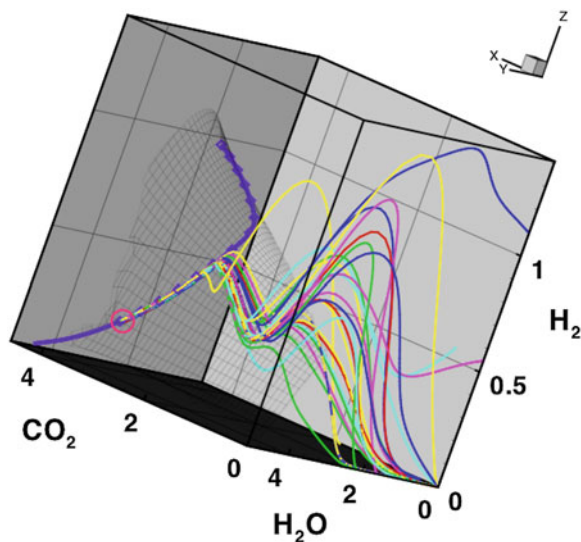


Fig. 18.1 The collapse of reaction trajectories onto an intrinsic low-dimensional manifold or ILDM (*black mesh*) for an iso-octane-air system plotted in a projection of the state space into CO_2 - H_2O - H_2 coordinates. 1D ILDM (*purple symbols*), 0D ILDM (equilibrium, *circle*). The *coloured lines* are homogeneous reactor calculations for different fuels using different reaction mechanisms. Species concentrations are in units of w_i/M_i , where w_i are mass fractions and M_i molar masses. See Blasenbrey and Maas (2000) for details. Reprinted from Blasenbrey and Maas (2000) with permission from Elsevier

shall be represented by Ξ_c and Ξ_T respectively. Because this equation does not invoke any modelling procedure, it is valid for laminar as well as for turbulent flows. The convective term $\Xi_c = -\vec{v} \cdot \text{grad}\psi$ can be eliminated by a transformation into Lagrangian coordinates, i.e. by a transformation into a reference frame moving with the flow, which simplifies the analysis considerably. The molecular transport term is characterised by the fact that the eigenvalues of the matrix D of transport coefficients have typically non-negative real parts, which causes the diffusion term to lead to a “contraction” of the accessed states ψ with time.

The source term F also has some important properties. The eigenvalues of the Jacobian matrix F_ψ , typically differ by several orders of magnitude. This introduces a large number n of different time-scales and n characteristic directions of the reaction progress (represented by the eigenvectors of the Jacobian). The strongly differing time-scales of the chemical kinetics cause the existence of attractors in the state space with the property that the chemical kinetics relaxes very fast to these attractors and that after a short initialization phase the chemical kinetics is governed by a movement along these attractors (Roussel and Fraser 1991; Maas and Pope 1992a, b). The reason is that the fast relaxation processes lead to species being in quasi-steady state or reactions in partial equilibrium, and thus introduce correlations among the various species.

18.3 Time-Scale Splitting of Pure Chemical Systems

In order to simplify the presentation, we first focus on simple homogeneous reaction systems (no spatial gradients), and return to the general equation system later. For homogeneous reaction systems Eq. (18.1) can be simplified to:

$$\frac{\partial\psi}{\partial t} = F(\psi) \quad (18.2)$$

In order to perform a splitting of the governing equation system based on the chemical time-scales, let us assume that we can find three invariant subspaces, which allow the separation of the governing equation system into three parts where the $n \times n_c$ -dimensional matrix Z_c spans the directions of the processes corresponding to variables conserved in chemical reactions, the $n \times n_s$ -dimensional matrix Z_s spans the directions of the slow chemical processes and the $n \times n_f$ -dimensional matrix Z_f spans the directions of the fast chemical processes. Note that this matrix is yet to be defined (this definition is in fact the major difference between the different reduction methods), and that these matrices may constitute only approximations for the different subspaces.

$$(Z_c Z_s Z_f) \cdot \begin{pmatrix} \tilde{Z}_c \\ \tilde{Z}_s \\ \tilde{Z}_f \end{pmatrix} = I \quad (18.3)$$

These invariant subspaces can be used to separate different processes with respect to the chemical time-scales.

$$\begin{aligned} \text{I:} \quad & \tilde{Z}_c \frac{\partial\psi}{\partial t} = \tilde{Z}_c F(\psi) \\ \text{II:} \quad & \tilde{Z}_s \frac{\partial\psi}{\partial t} = \tilde{Z}_s F(\psi) \\ \text{III:} \quad & \tilde{Z}_f \frac{\partial\psi}{\partial t} = \tilde{Z}_f F(\psi) \end{aligned} \quad (18.4)$$

If we assume that the time-scales associated with the fast invariant subspace are much larger than the time-scales associated with the physical processes, then (III) can be replaced by the so-called state equations:

$$\tilde{Z}_f F(\psi) = 0 \quad (18.5)$$

and (I and II) have to be projected according to the manifold defined by Eq. (18.5) yielding (Maas and Pope 1992a; Lam and Goussis 1994):

$$\frac{\partial\psi}{\partial t} = (I - \tilde{Z}_f Z_f) F(\psi) \quad (18.6)$$

Note that this equation system still describes the evolution in the whole composition space, although the fast modes have been eliminated. It can, however, be reformulated to describe the evolution on the manifold only (Bauer et al. 2006).

The main difference between the different reduction strategies is the definition of the fast subspace (i.e. the matrices Z_f and \tilde{Z}_f). These different methods are described in the following.

18.4 The Quasi-Steady State Approximation

This method, which dates back to the work of Bodenstein (1913), can be recast in the formulation of (18.5) by specifying \tilde{Z}_f as a matrix of the form:

$$\tilde{Z}_f = \begin{pmatrix} 0 & 0 & \delta_{1,i_1} & \delta_{2,i_1} & \cdots & \delta_{S,i_1} \\ 0 & 0 & \delta_{1,i_2} & \delta_{2,i_2} & \cdots & \delta_{S,i_2} \\ \vdots & \vdots & \vdots & \vdots & \ddots & \vdots \\ 0 & 0 & \delta_{1,i_q} & \delta_{2,i_q} & \cdots & \delta_{S,i_q} \end{pmatrix} \quad (18.7)$$

where i_k denotes the indices of the q species assumed to be in quasi-steady state. The problem is that the specification of the quasi-steady state assumptions has to be based on considerable knowledge of the underlying chemical kinetics. Several strategies have been devised to identify QSS species, such as methods based on CSP as discussed in the next section (Valorani et al. 2003; Lee et al. 2007; Valorani et al. 2007; Najm et al. 2010), instantaneous QSSA error (Turányi et al. 1993) or level of importance (Løvås et al. 2002a, b).

One of the earliest works which addressed the possible errors caused by the application of the QSSA was by Frank-Kamenetskii (1940), and was translated into English with detailed comments by Turányi and Tóth (1992). By assessing the errors induced by the application of the QSSA to each species within a mechanism over a wide range of temperatures and compositions, it is possible to select those with the lowest errors to be specified as QSS species. An approach for QSS species selection based on the early article of Frank-Kamenetskii was developed and further generalised in (Turányi et al. 1993). It involves the estimation of the instantaneous error in concentration of the QSS species caused by the application of the assumptions in Eqs. (18.5) and (18.7). For application to a single species (i.e. assuming no coupling between QSS species) this error can be estimated by the following expression:

$$\Delta Y_i = \left(-\frac{dY_i}{dt} \right) \left(-\frac{1}{J_{ii}} \right) \quad (18.8)$$

where Y_i is the concentration of species i , and J_{ii} is the diagonal element of the Jacobian matrix (Turányi et al. 1993). The term $(1/J_{ii})$ is equal to the chemical lifetime of species i , and therefore Eq. (18.8) implies that if the QSSA is applied for a single species, then the absolute value of the local QSSA error is equal to the

product of the species lifetime and its production rate. This is consistent with the local error being small if the species is consumed in fast reactions as discussed above. In such cases the production rate of the QSS species can be large and therefore the species may undergo significant concentration changes during the simulation. This is perhaps counter-intuitive since the term “steady state” usually implies low rates of change. However in this case, the term quasi-steady state means that the concentrations do not change significantly with respect to the slow species which may exhibit steep concentration gradients in time. Tomlin et al. (1992), for example, demonstrated the successful application of the QSSA for the simulation of oscillatory hydrogen ignitions.

For the application of the QSSA to groups of species the above equation needs to be modified in order to take account of couplings. In this case the error can be derived from the solution of the following system of algebraic equations:

$$\frac{d\mathbf{Y}^{(QSS)}}{dt} = \mathbf{J}^{(QSS)} \Delta \mathbf{Y}^{(QSS)} \quad (18.9)$$

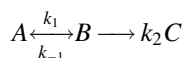
where $\frac{d\mathbf{y}^{(QSS)}}{dt}$ is the production rate of the QSS species at time t , and $\mathbf{J}^{(QSS)}$ is the submatrix of the Jacobian belonging to the QSS species (Turányi et al. 1993). Therefore, if the production rate of the QSS species and the matrix $\mathbf{J}^{(QSS)}$ are known, then the local error of a group of QSSA species at any local time t can be calculated. In reality, the local error induced by the application of the QSSA may grow over time and may spread through couplings to other species. The above equations therefore provide only an indication of potentially successful QSSA candidates. The selection of QSS species can be checked by comparing sample simulations for important species and features over selected conditions. DAE solvers such as DASSL can be used for this purpose (Maly and Petzold 1996).

The spread of errors partly relates to the sensitivity of simulations to the concentrations of the selected species and this was acknowledged in the Level of Importance (LOI) method developed in (Løvås et al. 2000, 2002a, b; Løvås 2009). The LOI index is defined as the product of the lifetime of a species and a local sensitivity term:

$$(\text{LOI})_{ij} = \frac{1}{J_{ii}} \sum_{l=1}^{N_R} \nu_{ij} \frac{\partial Y_i}{\partial \ln A_l} \quad (18.10)$$

The half-normalised local sensitivity coefficient $\partial Y_i / \partial \ln A_l$ shows the effect of perturbing the A-factor of reaction step l on concentration $\partial Y_i / \partial \ln A_l$, and ν_{ij} is the corresponding stoichiometric coefficient. The index $(\text{LOI})_{ij}$ estimates the error in the calculation of the concentration of species j due to the application of the QSSA to species i . Hence, species having short lifetimes are related to small local error of the QSSA, but this small error may cause large overall simulation errors if these species exhibit large sensitivities. In several combustion systems, the QSSA error of the H-atom has such a property. In this case the LOI-index is large and the QSSA is often not applicable for such a species as also suggested in Tomlin et al. (1992).

For simple systems it may be possible to describe the concentrations of QSS species via explicit algebraic expressions as functions of the slower species, i.e. to find analytical solutions of Eq. (18.5) coupled with Eq. (18.7). Historically, the QSSA has been applied in many by directly solving such algebraic expressions (e.g. Peters and Williams 1987). However, for complex schemes some simplification of the starting mechanism or truncation of the QSSA expressions was often required to facilitate analytical solutions. However, Hughes et al. (2009) demonstrated that such an approach based on algebraic equations could be applied to many QSSA species with low couplings within highly complex hydrocarbon oxidation schemes when algebraic manipulation packages such as MAPLE (Maplesoft 2012) are employed. The approach can be made equivalent to reaction lumping as shown here for the scheme:



If the QSSA is applied to B then:

$$\frac{d[B]}{dt} \approx 0 \quad (18.11)$$

so that

$$[B] = \frac{k_1}{k_{-1} + k_2} [A] \quad (18.12)$$

Hence:

$$\frac{d[C]}{dt} = k_2 [B] = \frac{k_1 k_2 [A]}{k_{-1} + k_2}, \quad (18.13)$$

where

$$k' = \frac{k_1 k_2}{k_{-1} + k_2}. \quad (18.14)$$

Therefore, the above set of reactions can be replaced by a single reaction of the form $A \rightarrow C$ with the effective rate coefficient k' , resulting in the removal of the intermediate B from the overall reaction mechanism. Hughes et al. (2009) demonstrated application of this approach for the reduction of a skeletal scheme describing the oxidation of n-heptane from 218 species to 110 species.

For highly coupled sets of QSSA species, solving the systems of resulting equations may not be possible analytically without truncations. Methods based on either inner or fixed point iteration methods (see for example Chap. 6 in Peters and Rogg (1993)) or matrix manipulations (Chen 1988) are therefore often used. Chen and Tham (2008) also proposed a hybrid method where matrix inversion was first used for strongly coupled QSS species and then fixed point iteration was used for the calculation of the concentrations of the other QSS species.

18.5 Computational Singular Perturbation

The CSP approach developed originally by Lam and Goussis (1988, 1991, 1994; Lam 1993) and then refined and implemented by several authors (Lam and Goussis 1991, 1994; Massias et al. 1999; Valorani and Goussis 2001; Valorani et al. 2005; Goussis and Valorani 2006; Lee et al. 2007) provides an iterative procedure for the calculation of the matrices Z_f and \tilde{Z}_f . It accounts for the fact that the vectors splitting the system into fast and slow processes change along a solution trajectory. A very efficient iterative procedure allows to account for this. The information obtained from the CSP analysis can be used to identify quasi-steady state species. Therefore, many applications use CSP to devise skeleton mechanisms and then further reduce them via quasi-steady state assumptions. An automatic procedure for skeletal mechanism production guided by CSP was described in (Valorani et al. 2006). The method has been applied to mechanisms describing the production of nitrogen oxides in premixed methane-air flames (Goussis and Skevis 2005), ignition processes (Treviño 1991; Treviño and Mendez 1991, 1992; Treviño and Solorio 1991; García-Ybarra and Treviño 1994; Treviño and Liñan 1994) and premixed flames (Prager et al. 2009). It has also been used to explore the interaction of a two-dimensional counter-rotating vortex-pair with a premixed methane-air flame showing that where intense chemical and transport activity takes place, the number of exhausted chemical time-scales can be quite small, i.e. the extent of reduction possible using time-scale-based methods is more limited in these regions (Valorani et al. 2003).

18.6 Intrinsic Low-Dimensional Manifolds

The ILDM concept (Maas and Pope 1992a, b) defines the matrices Z_f and \tilde{Z}_f via the invariant subspaces associated with the local Jacobian of the chemical source term according to:

$$F_\psi = (Z_c Z_s Z_f) \cdot \begin{pmatrix} N_c & & \\ & N_s & \\ & & N_f \end{pmatrix} \cdot \begin{pmatrix} \tilde{Z}_c \\ \tilde{Z}_s \\ \tilde{Z}_f \end{pmatrix}, \quad (18.15)$$

$$|\lambda_i(N_c)| < \tau_c, \quad \lambda_i^{\text{real}}(N_f) < \tau_s < \lambda_i^{\text{real}}(N_s)$$

where τ_c is an upper limit for the eigenvalues λ assumed to be associated with very slow processes (“almost conserved scalars”), and τ_s is an upper limit for eigenvalues assumed to be associated with fast relaxing (negative) time-scales. Since it has been developed, this method has been constantly improved, and many variants of the method are now available. Besides applications of the method in laminar and turbulent flame calculations most efforts concentrated on an efficient identification of the ILDM (Maas 1998), an analysis for domains with slow chemistry

(Bykov and Maas 2007a; König and Maas 2009), an extension to very large chemical systems (Blasenbrey and Maas 2000; Nafe and Maas 2003), coupling with laminar and turbulent transport processes (Bender et al. 2000), an adaptive dimension reduction (Deuffhard et al. 1996) and the decoupling of slow processes (Nafe and Maas 2002a, b). Furthermore, the method has also been applied to heterogeneous combustion processes (Yan and Maas 2000). Some nice theoretical investigations of the method have also been undertaken (Rhodes et al. 1999; Kaper and Kaper 2002). A variant of the method is based on an analysis of the eigenspaces of $F_\psi F_\psi^T$ (Bykov et al. 2006).

18.7 Global Quasi-Linearization

The GQL approach (Bykov and Maas 2007b; Bykov et al. 2008; Bykov and Maas 2009) allows a global analysis of the system hierarchy. The main mathematical framework behind the GQL is the so-called singular perturbed vector fields (SPVF) method (Bykov et al. 2005; Bykov and Gol'dshtein 2008). In order to find the relevant transformation we need to analyse the linear structure of the vector field defined in Eq. (18.1). The idea is that for n arbitrary representative points ψ_i , $i = 1, 2, \dots, n$ in the state space the vectors $F(\psi_i)$ are calculated. Then the vector $F(\psi)$ is for these n points represented exactly by:

$$(F(\psi_1)F(\psi_2) \cdots F(\psi_n)) = T(\psi_1\psi_2 \cdots \psi_n) \quad (18.16)$$

Now the invariant subspaces, which are used for the model reduction, are simply the invariant subspaces resulting from a decomposition of the matrix \mathbf{T} .

$$T = (Z_c Z_s Z_f) \cdot \begin{pmatrix} N_c & & \\ & N_s & \\ & & N_f \end{pmatrix} \cdot \begin{pmatrix} \tilde{Z}_c \\ \tilde{Z}_s \\ \tilde{Z}_f \end{pmatrix} \quad (18.17)$$

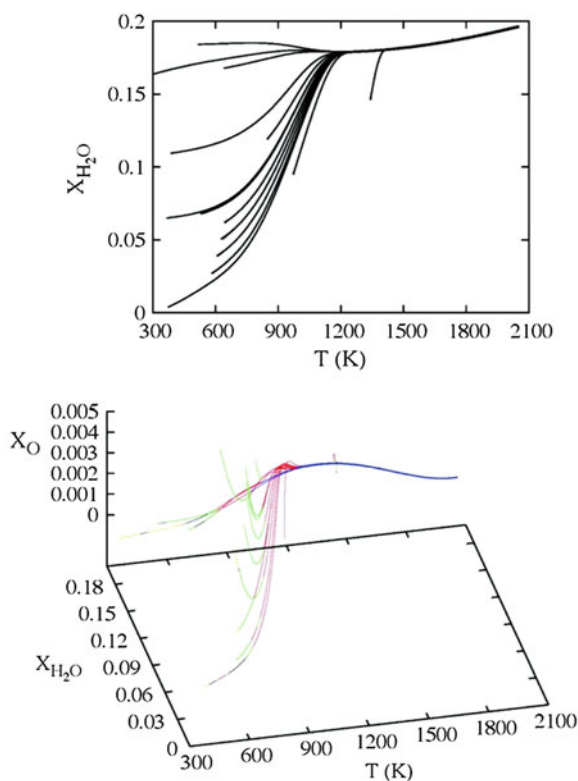
One of the major advantages of the constructed decomposition by the GQL is the fact that in order to decompose the system and find the slow/fast manifolds in the whole domain, we do not need to find the slow manifold (tabulate it), but the matrix \mathbf{T} or its invariant subspaces can be used. The matrix that defines the fast invariant subspace is constant and does not depend on the state variable ψ_i . The numerical effort for the evaluation of the manifold equation can be simplified considerably, because the computationally expensive procedure of decomposition into invariant subspaces has to be performed only once. Furthermore, the analysis of the slow invariant manifold's properties (stable, turning, repulsive, etc.) becomes possible (Bykov et al. 2008).

18.8 Slow Invariant Manifolds

According to Skodje and Davis, the exact slow invariant manifold (SIM) of a system is that to which propagated trajectories are attracted, whereas the ILDM is an approximation based on infinitesimally propagated trajectories (Skodje and Davis 2001). An example of such an attractive manifold is shown in Fig. 18.2 for steady one-dimensional premixed H_2/O_2 flames (Davis and Tomlin 2008a, b). The top panel shows a two-dimensional projection for 16 flames with varying boundary conditions but the same final equilibrium point. Above ~ 1200 K trajectories are seen to rapidly approach the 1D manifold. The bottom panel shows a three-dimensional projection and the trajectories are seen to collapse onto a cascade of manifolds of decreasing dimension, eventually reaching the 1D manifold and then the final 0D equilibrium point.

Once a trajectory has reached an invariant manifold it does not leave it (Gorban et al. 2004). The SIM is therefore a global attractor whereas the ILDM is a local attractor, although in many cases the ILDM provides a good approximation to the SIM. Roussel and Fraser (1991) proposed a methodology to identify slow invariant manifolds. The idea is to determine a low-dimensional manifold with the property

Fig. 18.2 The collapse of a range of trajectories to a 1D slow invariant manifold for steady one-dimensional premixed H_2/O_2 flames. The top panel shows a two-dimensional projection for 16 flames with varying boundary conditions. A three-dimensional projection is shown in the *bottom panel* including estimates of the local dimensionality (n) for each trajectory: $n = 1$ (blue), $n = 2$ (red), $n = 3$ (green), $n = 4$ (black), and $n = 5$ (yellow). The flames and calculation methods are fully described in Davis and Tomlin (2008a). Reprinted with permission from Davis and Tomlin (2008a). Copyright (2008) American Chemical Society



that it is an invariant manifold which governs the slow dynamics of chemical kinetics. Starting from an initial guess for the manifold, a functional iteration yields successive improvements and converges to the slow manifold. The method was applied mostly to simple test cases which can be treated analytically, although the method can also be applied for more complex systems. In order to improve convergence of the method, (Davis and Skodje 1999; Skodje and Davis 2001) used an ILDM as an initial guess. Based on this idea several numerical methods have been devised for the identification of the slow invariant manifold. It has been shown that the invariant manifolds can also be obtained by solving the partial differential equation system (Nafe and Maas 2002a):

$$\begin{aligned} \frac{\partial \psi(\theta, t)}{\partial t} &= (I - \psi_\theta(\theta)\psi_\theta^+(\theta))F(\psi(\theta)) & \psi(\theta, 0) &= \psi_0(\theta) \\ \frac{\partial \psi(\theta, t)}{\partial t} &= (I - \psi_\theta(\theta)\psi_\theta^+(\theta))F(\psi(\theta)) & \psi(\theta, 0) &= \psi_0(\theta), \end{aligned} \quad (18.18)$$

with $\psi_0(\theta)$ as an initial guess for the manifold (e.g. results of an ILDM). $(I - \psi_\theta\psi_\theta^+)$ is a projection operator, which eliminates all components of the evolution of ψ tangent to the manifold. Here ψ_θ is a matrix which spans the tangent space of the manifold, and ψ_θ^+ is a pseudo-inverse, with the condition that $\psi_\theta^+\psi_\theta = I$. In (Nafe and Maas 2002a, b), e.g., the Moore–Penrose- pseudo-inverse has been used. Related methods are the method of invariant manifolds (MIM) and the method of invariant grids (MIG), where the projection operator is a so-called “thermodynamic” projector (Gorban and Karlin 2003, 2005; Chiavazzo et al. 2007).

18.9 Related Methods

Several other methods have been developed, which are also based on time-scale splitting. One of these is the rate-controlled constrained-equilibrium method (RCCE), developed originally by Keck and Gillespie (1971), and used and improved by Jones and Rigopoulos (2005a, b, 2007) who applied it to several combustion systems including the simulation of methane laminar flames (Jones and Rigopoulos 2005a). It is based on the assumption that fast chemical processes lead to an equilibrium state, subject to the conditions that some major species have concentrations which evolve according to kinetics. The major species therefore evolve according to differential equations involving detailed chemical kinetics, whilst equilibrated species are determined by minimising the free energy of the mixture, subject to the additional constraints (i.e. in addition to the conservation of mass, energy and elements). The selection of constraints is a key aspect of the method and was achieved using an LOI index in Rigopoulos and Lovas (2009) and more recently in Lovas et al. (2011) where the constraints were selected adaptively in different regions of the composition space. Since the LOI index is related to the

species lifetime there is a cross over between QSSA and RCCE methods, since the constrained species become equivalent to non-QSS species.

Ren and Pope (2005) used the RCCE-concept to develop the ICE-PIC (invariant constrained equilibrium pre-image curve) concept. This is a trajectory-based method, where a very good approximation to the invariant manifold is determined by computing trajectories of the full system from appropriate initial conditions. The pre-image curve for a given composition of the reduced variables is generated by first finding the corresponding point on the constrained equilibrium manifold. A reaction trajectory from the boundary end of the pre-image curve is then calculated until it reaches the appropriate point (i.e. that with the given reduced variable composition) on the inertial manifold and the full thermochemical state is determined. The method is shown to achieve improved accuracy compared to RCCE and ILDM methods for the reconstructed species (i.e. fast species) for a methane ignition problem and a 1D laminar hydrogen oxygen flame, particularly at lower temperatures (Ren and Pope 2005). Further approaches include the minimum entropy production method (Lebiedz 2004) and the Zero Derivative Principle (Gear et al. 2005).

18.10 Time-Scale Splitting for Reaction–Diffusion Systems

In principle, all methods described above can also be used for model reduction for general reaction–diffusion systems. However, the coupling of the kinetics with the transport processes have to be accounted for in the analysis (see e.g. Maas and Pope 1992b; Goussis et al. 2005; Ren and Pope 2007) since the coupling of some chemical modes with relatively fast physical ones may disturb system trajectories from the low-dimensional manifold defined only by kinetics (Bykov and Maas 2007b). Davis also showed that the presence of diffusion can affect the attractiveness of the slow manifolds present in a reaction–diffusion model of ozone combustion (Davis 2006a, b). Again, we define the three invariant subspaces spanned by Z_c , Z_s , and Z_f , and use them to separate the different processes with respect to the chemical time-scales:

$$\begin{aligned}
 \text{I :} \quad & \tilde{Z}_c \frac{\partial \psi}{\partial t} = \tilde{Z}_c F(\psi) + \tilde{Z}_c \vec{v} \cdot \text{grad} \psi + \tilde{Z}_c \frac{1}{\rho} \text{div} D \text{ grad} \psi \\
 \text{II :} \quad & \tilde{Z}_s \frac{\partial \psi}{\partial t} = \tilde{Z}_s F(\psi) + \tilde{Z}_s \vec{v} \cdot \text{grad} \psi + \tilde{Z}_s \frac{1}{\rho} \text{div} D \text{ grad} \psi \\
 \text{III :} \quad & \tilde{Z}_f \frac{\partial \psi}{\partial t} = \tilde{Z}_f F(\psi) + \tilde{Z}_f \vec{v} \cdot \text{grad} \psi + \tilde{Z}_f \frac{1}{\rho} \text{div} D \text{ grad} \psi
 \end{aligned} \tag{18.19}$$

If we assume that the time-scales associated with the fast invariant subspace are much larger than the time-scales associated with the physical processes, then (III) can be replaced by the so-called state equations:

$$\tilde{Z}_f F(\psi) = 0 \quad (18.20)$$

and (I and II) have to be projected according onto the manifold defined by Eq. (18.4) yielding:

$$\frac{\partial \psi}{\partial t} = (I - \tilde{Z}_f Z_f)(F(\psi) + \vec{v} \cdot \text{grad} \psi + \frac{1}{\rho} \text{div} D \text{grad} \psi) \quad (18.21)$$

For a discussion of this approximation see, e.g. (Maas and Pope 1992b, 1994; Hadjinicolaou and Goussis 1998; Ren and Pope 2007). Note that this equation system still describes the evolution in the whole composition space, although the fast modes have been eliminated. It can, however be reformulated to describe the evolution on the manifold only (Bauer et al. 2006).

18.11 Reaction/Diffusion Manifolds

The concept of slow manifolds can be extended to general reaction–diffusion systems. The assumption that an invariant slow manifold of low dimension exists in the state space as an intrinsic property of the combustion system yields:

$$(I - \psi_\theta(\theta) \psi_\theta^+(\theta)) \cdot \left[F(\psi(\theta)) - \frac{1}{\rho} \text{div}(D \psi_\theta(\theta) \text{grad} \theta) \right] = 0, \quad (18.22)$$

which means that the vector field belongs to the tangent subspace of the manifold. In order to find the invariant manifold, it is advantageous to solve Eq. (18.22) by a time stepping method according to (Bykov et al. 2007; Bykov and Maas 2009; Konzen et al. 2011):

$$\begin{aligned} \frac{\partial \psi(\theta, t)}{\partial t} &= (I - \psi_\theta(\theta) \psi_\theta^+(\theta)) \cdot \left[F(\psi(\theta)) - \frac{1}{\rho} \text{div}(D \psi_\theta(\theta) \text{grad} \theta) \right] \\ \psi(\theta, 0) &= \psi_0(\theta) \end{aligned} \quad (18.23)$$

with initial and boundary conditions given, e.g. by an extended ILDM manifold (Bykov and Maas 2007b). However, in order to find the manifolds, estimates for the gradients of θ have to be supplied. It can be shown that the higher the dimension of the manifold, the smaller is its sensitivity with respect to the gradient estimate (Bykov and Maas 2007b, 2009).

Once the manifold has been identified, the governing equation for the scalar field of the reacting flow can be projected onto the manifold (Bykov and Maas 2007b, 2009; Maas and Bykov 2011):

$$\frac{\partial \theta}{\partial t} = \psi_\theta^+ F(\psi(\theta)) - \vec{v} \text{grad} \theta - \psi_\theta^+ \frac{1}{\rho} \text{div}(D \psi_\theta \text{grad} \theta) \quad (18.24)$$

The REDIM method can be applied to systems with complex transport models (Maas and Bykov 2011). Though different, the REDIM concepts have similarities to the strategies used in flamelet generated manifolds (Oijen and Goey 2000; Nguyen et al. 2010) or flamelet prolongation of ILDM (Gicquel et al. 2000). In the flamelet approach the edge of a turbulent flame is approximated by an ensemble of discrete, steady laminar flames, called flamelets (Libby and Bray 1980; Liew et al. 1981). The individual flamelets are assumed to have a similar structure to laminar flames for the same concentration and temperature conditions so that detailed calculations of the flamelet chemistry can be obtained either by experiment or from lower dimensional numerical calculations.

18.12 Summary and Conclusions

It was shown that the wide range of system time-scales within chemical models of combustion can be exploited in the context of model reduction both to reduce the number of active variables in the system and to reduce the system stiffness. Several approaches have been developed from the use of simple algebraic relations founded in the application of the QSSA to more sophisticated geometrical approaches based on approximating the behaviour of the system within low dimensional slow manifolds. The presence of such low dimensional manifolds can be further exploited using a range of tabulation and surrogate modelling techniques and these will be discussed in [Chap. 19](#) that follows.

Acknowledgments UM thanks DFG for financial support.

References

- Bauer J, Bykov V, Maas U (2006). Implementation of ILDMs based on a representation in generalised Flamelet coordinates. In: Wesseling P, Onate E, Periaux JLB (eds) European conference on computational fluid dynamics, ECCOMAS CFD, Egmond aan Zee, The Netherlands, 5–8 Sept 2006
- Bender R, Blasenbrey T, Maas U (2000) Coupling of detailed and ILDM-reduced chemistry with turbulent mixing. *Proc Combust Inst* 28:101–106
- Blasenbrey T, Maas U (2000) ILDMs of higher hydrocarbons and the hierarchy of chemical kinetics. *Proc Combust Inst* 28:1623–1630
- Bodenstein M (1913) Zur Kinetik des Chlorknallgases. *Z Phys Chem* 85:329
- Bykov V, Gol'dshtein V (2008) On a decomposition of motions and model reduction. *J Phys Conf Ser* 138(1):012003
- Bykov V, Gol'dshtein V, Bykov UML (2007). Global Quasi Linearization (GQL) for the automatic reduction of chemical kinetics. In: Proceedings of the European combustion meeting, Chania, Crete (Greece)
- Bykov V, Gol'dshtein V, Maas U (2008) Simple global reduction technique based on decomposition approach. *Combust Theor Model* 12(2):389–405

- Bykov V, Goldfarb I, Gol'dshtein I (2005) Novel numerical decomposition approaches for multiscale combustion and kinetic models. *J Phys Conf Ser* 22(1):1–29
- Bykov V, Goldfarb I, Gol'dshtein V et al (2006) On a modified version of ILDM approach: asymptotic analysis based on integral manifolds. *Ima J Appl Maths* 71:359–382
- Bykov V, Maas U (2007a) Extension of the ILDM method to the domain of slow chemistry. *Proc Combust Inst* 31:465–472
- Bykov V, Maas U (2007b) The extension of the ILDM concept to reaction-diffusion manifolds. *Combust Theor Model* 11(6):839–862
- Bykov V, Maas U (2009) Problem adapted reduced models based on Reaction-Diffusion Manifolds (REDIMs). *Proc Combust Inst* 32:561–568
- Chen JY (1988) A general procedure for constructing reduced reaction-mechanisms with given independent relations. *Combust Sci Technol* 57(1–3):89–94
- Chen JY, Tham YF (2008) Speedy solution of quasi-steady-state species by combination of fixed-point iteration and matrix inversion. *Combust Flame* 153:634–646
- Chiavazzo E, Gorban AN, Karlin IV (2007) Comparison of invariant manifolds for model reduction in chemical kinetics. *Commun Comput Phys* 2:964–992
- Davis J, Skodje RT (1999) Geometric investigation of low-dimensional manifolds in systems approaching equilibrium. *J Chem Phys* 111:859–874
- Davis MJ (2006a) Low-dimensional manifolds in reaction-diffusion equations. 1. Fundamental aspects. *J Phys Chem A* 110(16):5235–5256
- Davis MJ (2006b) Low-dimensional manifolds in reaction-diffusion equations. 2. Numerical analysis and method development. *J Phys Chem A* 110(16):5257–5272
- Davis MJ, Tomlin AS (2008a) Spatial dynamics of steady flames 1. Phase space structure and the dynamics of individual trajectories. *J Phys Chem A* 112:7768–7783
- Davis MJ, Tomlin AS (2008b) Spatial dynamics of steady flames 2. Low-dimensional manifolds and the role of transport processes. *J Phys Chem A* 112:7784–7805
- Deuffhard P, Heroth J, Maas U (1996) Towards dynamic dimension reduction in reactive flow problems. Modelling of chemical reaction systems. In: Warnatz J, Behrendt FLD (eds) Proceedings of an international workshop, Heidelberg, Germany, 24–26 July 1996
- Frank-Kamenetskii DA (1940) Условия применимости метода Боленштейна в химической кинетике. *Ж Физ Хим* 14:695–700
- García-Ybarra PL, Treviño C (1994) Asymptotic analysis of the boundary layer H_2 ignition by a hot flat plate with thermal diffusion. *Combust Flame* 96:293–303
- Gear CW, Kaper TJ, Kevrekidis IG et al (2005) Projecting to a slow manifold: singularly perturbed systems and legacy codes. *SIAM J Appl Dyn Syst* 4:711–732
- Gicquel O, Darabiha N, Thévenin D (2000) Laminar premixed hydrogen/air counterflow flame simulations using flame prolongation of ILDM with differential diffusion. *Proc Combust Inst* 28:1901–1908
- Gorban A, Karlin IV (2005) Invariant manifolds for physical and chemical kinetics. Springer, Berlin
- Gorban AN, Karlin IV (2003) Method of invariant manifold for chemical kinetics. *Chem Eng Sci* 58:4751–4768
- Gorban AN, Karlin IV, Zinovyev AY (2004) Constructive methods of invariant manifolds for kinetic problems. *Phys Rep* 396:197–403
- Goussis DA, Skevis G (2005) Nitrogen chemistry controlling steps in methane-air premixed flames. In: Bathe KJ (ed) Computational fluid and solid mechanics. Amsterdam: Elsevier, pp 650–653
- Goussis DA, Valorani M (2006) An efficient iterative algorithm for the approximation of the fast and slow dynamics of stiff systems. *J Comput Phys* 214:316–346
- Goussis DA, Valorani M, Creta F et al (2005) Reactive and reactive-diffusive time-scales in stiff reaction-diffusion systems. *Prog Comput Fluid Dyn* 5(6):316–326
- Hadjinicolaou M, Goussis DA (1998) Asymptotic solution of stiff PDEs with the CSP method: the reaction diffusion equation. *SIAM J Sci Comput* 20:781–810

- Hughes KJ, Fairweather M, Griffiths JF et al (2009) The application of the QSSA via reaction lumping for the reduction of complex hydrocarbon oxidation mechanisms. *Proc Combust Inst* 32:543–551
- Jones WP, Rigopoulos S (2005a) Rate-controlled constrained equilibrium: formulation and application to nonpremixed laminar flames. *Combust Flame* 142:223–234
- Jones WP, Rigopoulos S (2005b) Reduction of comprehensive chemistry via constraint potentials. *Proc Combust Inst* 30:1325–1331
- Jones WP, Rigopoulos S (2007) Reduced chemistry for hydrogen and methanol premixed flames via RCCE. *Combust Theor Model* 11(5):755–780
- Kaper HG, Kaper TJ (2002) Asymptotic analysis of two reduction methods for systems of chemical reactions. *Physica D* 165:66–93
- Keck JC, Gillespie D (1971) Rate-controlled partial-equilibrium method for treating reacting gas-mixtures. *Combust Flame* 17:237–248
- König K, Maas U (2009) On-demand generation of reduced mechanisms based on hierarchically extended intrinsic low-dimensional manifolds in generalized coordinates. *Proc Combust Inst* 32:553–560
- Konzen PHD, Richter T, Riedel U et al (2011) Implementation of REDIM reduced chemistry to model an axisymmetric laminar diffusion methane-air flame. *Combust Theor Model* 15(3):299–323
- Lam SH (1993) Using CSP to understand complex chemical kinetics. *Combust Sci Technol* 89:375–404
- Lam SH, Goussis DA (1988) Understanding complex chemical kinetics with computational singular perturbation. *Proc Combust Inst* 22:931–941
- Lam SH, Goussis DA (1991) Conventional asymptotics and computational singular perturbation for simplified kinetics modeling. In: Smooke MO (ed) *Reduced kinetic mechanisms and asymptotic approximations for methane-air flames*, vol 384. Springer, Berlin, pp 227–242
- Lam SH, Goussis DA (1994) The CSP method for simplifying kinetics. *Int J Chem Kinet* 26:461–486
- Lebiedz D (2004) Computing minimal entropy production trajectories: an approach to model reduction in chemical kinetics. *J Chem Phys* 120:6890–6897
- Lee JC, Najm HN, Lefantzi S et al (2007) A CSP and tabulation-based adaptive chemistry model. *Combust Theory Model* 11(1):73–102
- Libby PA, Bray KNC (1980) Implications of the laminar flamelet model in premixed turbulent combustion. *Combust Flame* 39(1):33–41
- Liew SK, Bray KNC, Moss JB (1981) A flamelet model of turbulent non-premixed combustion. *Combust Sci Technol* 27(1–2):69–73
- Løvås T (2009) Automatic generation of skeletal mechanisms for ignition combustion based on level of importance analysis. *Combust Flame* 156:1348–1358
- Løvås T, Amneus P, Mauss F et al (2002a) Comparison of automatic reduction procedures for ignition chemistry. *Proc Combust Inst* 29:1387–1393
- Løvås T, Hasse K, Mauss F et al (2002b) Development of adaptive kinetics for application in combustion systems. *Proc Combust Inst* 29:1403–1410
- Lovas T, Navarro-Martinez S, Rigopoulos S (2011) On adaptively reduced chemistry in large eddy simulations. *Proc Combust Inst* 33:1339–1346
- Løvås T, Nilsson D, Mauss F (2000) Automatic reduction procedure for chemical mechanisms applied to premixed methane/air flames. *Proc Combust Inst* 28:1809–1815
- Maas U (1998) Efficient calculation of intrinsic low-dimensional manifolds for the simplification of chemical kinetics. *Comput Vis Sci* 1:69–81
- Maas U, Bykov V (2011) The extension of the reaction/diffusion manifold concept to systems with detailed transport models. *Proc Combust Inst* 33:1253–1259
- Maas U, Pope SB (1992a) Simplifying chemical kinetics: intrinsic low-dimensional manifolds in composition space. *Combust Flame* 88:239–264
- Maas U, Pope SB (1992b) Implementation of simplified chemical kinetics based on intrinsic low-dimensional manifolds. *Proc Combust Inst* 24:103–112

- Maas U, Pope SB (1994) Laminar flame calculations using simplified chemical kinetics based on intrinsic low-dimensional manifolds. *Proc Combust Inst* 25:1349–1356
- Maly T, Petzold LR (1996) Numerical methods and software for sensitivity analysis of differential-algebraic systems. *Appl Num Maths* 20(1–2):57–79
- Maplesoft (2012) MAPLE, <http://www.maplesoft.com>
- Massias A, Diamantis D, Mastorakos E et al (1999) An algorithm for the construction of global reduced mechanisms with CSP data. *Combust Flame* 117:685–708
- Nafe J, Maas U (2002a) A general algorithm for improving ILDMs. *Combust Theor Model* 6:697–709
- Nafe J, Maas U (2002b) Modeling of NO formation based on ILDM reduced chemistry. *Proc Combust Inst* 29:1379–1385
- Nafe J, Maas U (2003) Hierarchical generation of ILDMs of higher hydrocarbons. *Combust Flame* 135:17–26
- Najm HN, Valorani M, Goussis DA et al (2010) Analysis of methane-air edge flame structure. *Combust Theor Model* 14:257–294
- Nguyen PD, Vervisch L, Subramanian V et al (2010) Multidimensional flamelet-generated manifolds for partially premixed combustion. *Combust Flame* 157:43–61
- Oijen JAV, Goey LPHD (2000) Modelling of premixed laminar flames using flamelet-generated manifolds. *Combust Sci Technol* 161:113
- Peters N, Rogg B (eds) (1993) *Reduced kinetic mechanisms for applications in combustion systems*. Springer, Berlin
- Peters N, Williams FA (1987) The asymptotic structure of stoichiometric methane air flames. *Combust Flame* 68(2):185–207
- Prager J, Najm HN, Valorani M et al (2009) Skeletal mechanism generation with CSP and validation for premixed n-heptane flames. *Proc Combust Inst* 32:509–517
- Ren Z, Pope SB (2005) Species reconstruction using pre-image curves. *Proc Combust Inst* 30:1293–1300
- Ren Z, Pope SB (2007) Transport-chemistry coupling in the reduced description of reactive flows. *Combust Theor Model* 11:715–739
- Rhodes C, Morari M, Wiggins S (1999) Identification of low order manifolds: validating the algorithm of Maas and Pope. *Chaos* 9(1):108–123
- Rigopoulos S, Lovas T (2009) A LOI-RCCE methodology for reducing chemical kinetics, with application to laminar premixed flames. *Proc Combust Inst* 32:569–576
- Roussel MR, Fraser SJ (1991) On the geometry of transient relaxation. *J Chem Phys* 94(11):7106–7113
- Skodje RT, Davis MJ (2001) Geometrical simplification of complex kinetic systems. *J Phys Chem A* 105:10356–10365
- Tomlin AS, Pilling MJ, Turányi T et al (1992) Mechanism reduction for the oscillatory oxidation of hydrogen: sensitivity and quasi-steady-state analyses. *Combust Flame* 91:107–130
- Treviño C (1991) Ignition phenomena in H₂/O₂ mixtures. *Prog Astronaut Aeronaut* 131:19–43
- Treviño C, Liñan A (1994) Numerical and asymptotic analysis of ignition processes. In: Buckmaster J, Jackson TL, Kumar A (eds) *Combustion in high-speed flows*. Kluwer Academic Publishers, Dordrecht, pp 477–490
- Treviño C, Mendez F (1991) Asymptotic analysis of the ignition of hydrogen by a hot plate in a boundary layer flow. *Combust Sci Technol* 78:197–216
- Treviño C, Mendez F (1992) Reduced kinetic mechanism for methane ignition. *Proc Combust Inst* 24:121–127
- Treviño C, Solorio F (1991) Asymptotic analysis of high temperature ignition of CO/H₂/O₂ mixtures. *Combust Flame* 86:285–295
- Turányi T, Tomlin AS, Pilling MJ (1993) On the error of the quasi-steady-state approximation. *J Phys Chem* 97:163–172
- Turányi T, Tóth J (1992) Comments to an article of Frank-Kamenetskii on the quasi-steady-state approximation. *Acta Chim Hung* 129(6):903–907 *Models in chemistry*

- Valorani M, Creta F, Donato F et al (2007) Skeletal mechanism generation and analysis for n-heptane with CSP. *Proc Combust Inst* 31:483–490
- Valorani M, Creta F, Goussis D et al (2006) An automatic procedure for the simplification of chemical kinetic mechanisms based on CSP. *Combust Flame* 146:29–51
- Valorani M, Goussis DA (2001) Explicit time-scale splitting algorithm for stiff problems: auto-ignition of gaseous mixtures behind a steady shock. *J Comput Phys* 169:44–79
- Valorani M, Goussis DA, Creta F et al (2005) Higher order corrections in the approximation of low dimensional manifolds and the construction of simplified problems with the CSP method. *JComput Phys* 209:754–786
- Valorani M, Najm HN, Goussis DA (2003) CSP analysis of a transient flame-vortex interaction: time-scales and manifolds. *Combust Flame* 134:35–53
- Yan X, Maas U (2000) Intrinsic low-dimensional manifolds of heterogeneous combustion processes. *Proc Combust Inst* 28:1615–1621

Chapter 19

Storage of Chemical Kinetic Information

Tamás Turányi and Alison S. Tomlin

Abstract This chapter describes various methods for storing chemical kinetic mechanistic information within combustion models. The most obvious way is the definition of the kinetic system of differential equations by a detailed reaction mechanism. Parameterisation of such reaction mechanisms is commented upon here. Another possible approach is to store the solution of the system of ordinary or partial differential equations that defines the model within look-up tables. Such data can then be “retrieved” during combustion simulations within complex reacting flow models instead of solving the kinetic system of differential equations, often at much lower computational cost. Several such methods for storage and retrieval are reviewed here. As an alternative approach, functional representations of the time dependant kinetic changes or the look-up table contents can be achieved, using for example polynomial functions or artificial neural networks and these are also discussed.

19.1 Definition of a Reaction Mechanism

The obvious method for the storage of chemical kinetic information within a combustion model is using a detailed reaction mechanism. [Chapter 2](#) of this book discusses the principles of the creation of detailed reaction mechanisms for the description of combustion chemical processes. In this section, we make some notes

T. Turányi (✉)

Institute of Chemistry, Eötvös University (ELTE), Budapest, Hungary
e-mail: turanyi@chem.elte.hu

A. S. Tomlin

Energy Research Institute, University of Leeds, Leeds LS29JT, UK
e-mail: A.S.Tomlin@leeds.ac.uk

on the flexibility and generality of the parameters that are used within such mechanisms.

The currently most widely used format was introduced within the CHEMKIN-II package (Kee et al. 1989). The CHEMKIN-II software was developed mainly for solving models based on detailed chemical reaction mechanisms and therefore its format specified that all reaction steps had to be balanced according to the number of atoms on each side of the reaction steps. This requirement hindered the application of many lumped reaction steps (see e.g. Chap. 17), and therefore in newer Chemkin versions unbalanced reaction steps are also permitted.

An important part of specifying a chemical reaction mechanism is providing accurate parameterisations of the rate coefficients. In combustion simulations, temperature may change by several hundred or even several thousand degrees during a simulation, and therefore instead of the original Arrhenius equation, the more versatile modified Arrhenius equation (also called extended Arrhenius equation) is used. This equation describes the temperature dependence of the rate coefficient by three parameters: $k = A T^n \exp(-E/RT)$. In the case of several elementary reactions, some of these parameters are set to zero, and forms $k = A T^n$ or $k = A \exp(-E/RT)$ are used for the characterisation of the temperature dependence of the rate coefficient. Although both the original and the extended Arrhenius equations are purely empirical (Pilling and Seakins 1995), in most cases, the uncertainty of either the experimental or the theoretical determination of the rate coefficient is much larger (Nagy and Turányi 2011) than the error introduced by the application of the empirical three-parameter modified Arrhenius equation. However, there are several reactions (such as reaction $\text{HO}_2 + \text{OH} = \text{H}_2\text{O} + \text{O}_2$), where the temperature dependence of the rate coefficient from room temperature to flame temperatures can be described (Burke et al. 2013) only by the sum of two extended Arrhenius expressions: $k = A_1 T^{n_1} \exp(-E_1/RT) + A_2 T^{n_2} \exp(-E_2/RT)$. In some mechanisms, the temperature dependence of certain rate coefficients is described by the sum of three extended Arrhenius expressions, but this is used very rarely and its application is probably not justified. The Arrhenius parameters used within detailed reaction mechanisms are stored within commonly accessed databases, such as that offered by NIST (2013) or are provided with individual reaction mechanisms.

The rate coefficients of unimolecular and complex forming bi-molecular reactions may also depend on pressure as well as temperature (Carstensen and Dean 2007). Consequently, the rate coefficients of most radical-radical reactions exhibit pressure dependence. Usually, separate high-pressure k_∞ and low-pressure k_0 rate coefficients are defined and their temperature dependence is given by separate extended Arrhenius expressions. Increasing the pressure, the decomposition rate of the excited species activated in collisions is decreasing, while the production rate of the species formed in the reactions of radicals (chemical activation) is increasing.

Based on the Lindemann approach, the pressure dependence of the rate coefficient of the unimolecular decomposition and the stabilization of a chemically activated species can be described by the following equation:

$$k = k_{\infty} \left(\frac{P_r}{1 + P_r} \right) F \quad (19.1)$$

Similarly, the decomposition rate coefficient of a chemically activated species can be calculated by equation

$$k = k_0 \left(\frac{1}{1 + P_r} \right) F \quad (19.2)$$

Here, P_r is the so-called reduced pressure:

$$P_r = \frac{k_0[M]}{k_{\infty}} \quad (19.3)$$

where M is the third body. When calculating the apparent concentration of the third body, the collision efficiencies m_{y_i} are also taken into account according to equation $[M] = \sum_i m_{y_i} [Y_i]$. Most mechanisms consider the collision efficiencies to be independent of temperature, while other authors use temperature dependent values. However, in most cases the latter can be questioned, since the uncertainty of these values is much larger than their variation with temperature in the relevant temperature interval.

There are several uncertainties in the representation of the pressure dependence. In the original Lindemann equation, $F = 1$ was assumed, but experimental results indicated that this was not optimal. Several mechanisms use temperature independent values (like $F = 0.5$) for the characterisation of the pressure dependence. The Chemkin mechanism format allows such a selection. Another possible approach is the application of the Troe formulation (Gilbert et al. 1983). Using the Troe parameterisation (see Eq. (2.6) in Chap. 2), the temperature dependence of F is parameterised by four parameters. The Troe equation and the similar SRI equation (Stewart et al. 1989) can represent properly the fall-off region only for single-well potential energy surfaces (Venkatech et al. 1997). For more complicated elementary reactions, the difference between the theoretically calculated rate coefficient and the best Troe fit can be as high as 40 %. A series of fitting formulas for the parameterization of the fall-off curves are discussed in (Zhang and Law 2009, 2011).

So far, the description of the pressure dependence of the rate coefficient was based on the parameterisation of the Lindemann approach. However, this pressure dependence can also be handled in a different way. In some mechanisms, the pressure dependence is given by the so-called “log p ” formalism (Zádor et al. 2011):

$$\ln k = \ln k_i + (\ln k_{i+1} - \ln k_i) \frac{\ln p - \ln p_i}{\ln p_{i+1} - \ln p_i} \quad (19.4)$$

Here, k is the rate coefficient belonging to pressure p , while the (p_i, k_i) pairs are a series of tabulated rate coefficients belonging to different pressures. The (p_i, k_i) pairs are obtained using high-level theoretical calculations. This approach is

perhaps not very elegant, but allows the utilisation of results from theoretical calculations without the loss of information. The “log p ” formalism above was not present in the original CHEMKIN-II format, but it is available in new Chemkin versions.

As discussed above, the currently used Chemkin parameterisation is flexible enough to store all chemical kinetic information within the uncertainty of the experimental and theoretical determinations. The information is then used within a kinetic system of differential equations and subsequent combustion simulations require the integration of these equations. As discussed in the previous chapters of Part IV of this book, for large mechanisms, the number of species that have to be solved for often makes the use of this approach computationally too expensive when the kinetic model is utilised within complex models such as three-dimensional simulations of turbulent reacting flows. Therefore, several methods have been proposed to store the integrated solutions of the differential equations, so that the stored information can be retrieved during more complex simulations. The stored solutions are usually obtained using less computationally demanding simulations, such as perfectly stirred reactor models, or 1D laminar flames. As long as a suitably wide range of compositions and temperatures are covered by these simulations, then the stored kinetic information will be relevant to more complex computational fluid dynamics (CFD) models. Other approaches develop databases of the kinetic information on the fly during a complex simulation. Time savings can be achieved using both these approaches since the same regions of thermochemical space may be accessed many times during a CFD calculation, and the stored information can be retrieved much more quickly than solving the often large systems of kinetic differential equations. For this reason, tabulation approaches are very often utilised within engineering simulations such as for example engine piston simulations (Mosbach et al. 2008).

19.2 Storing the Integrated Solution of a Kinetic Models

The solution of a combustion model based on a system of ordinary or partial system of differential equations can be defined in several ways. In one approach only a few, but interesting results of the model are handled. Such an important single simulation result could for example be the calculated laminar flame velocity for a given mixture composition, pressure and temperature. In other approaches, the system trajectory is described by a series of concentration/temperature–time points and information related to this trajectory can be stored in the form of a table or a recursive function. Most methods rely in an explicit or implicit way on the presence of time-scale separation in combustion systems as discussed in [Chap. 18](#).

19.2.1 Storing the Final Result of a Model

In many cases, the final result of a model simulation which is of interest to the user is a single number. In combustion modelling, examples could include the calculated time-to-ignition, laminar flame velocity, maximum concentration of a species, or even the concentration of a species at a given time point or location. Model simulations are performed, for example, to assess how these target outputs may vary according to the particular fuel used, the process conditions such as temperature, pressure, stoichiometry etc. Another frequently arising question is how a target output Q depends on the selection of the parameters in a model. This is important for the application of global uncertainty analysis studies, and also for parameter estimation and mechanism optimisation as discussed in Chap. 16. In this case, the task is to develop a surrogate model, which may consist of any mathematical function that provides value Q where the inputs are the values of the parameters within their joint domain of uncertainty. The length of the input vector can be very large and may consist of several hundred elements and therefore technical problems can arise in fitting such high-dimensional response surfaces. Suitable methods for fitting such surrogate models for application to global sensitivity analysis were discussed in Chap. 16 and included the use of High-Dimensional Model Representations (HDMR) and Polynomial Chaos Expansion based methods.

A special utilisation of the tabulation of the final result of a combustion model was incorporated into the NORA (NO Relaxation Approach) method in order to predict thermal NO in combustion chambers (Vervisch et al. 2011). In the NORA methodology, the NO reaction rate is written as a linear relaxation towards the equilibrium value Y_{NO}^{eq} with a characteristic time τ . Both parameters are tabulated as functions of equivalence ratio, pressure, temperature and dilution mass fraction. The table is generated on the basis of spatially homogeneous calculations but later used within turbulent combustion models designed to simulate piston engine applications. The approach has advantages for simulating NO emissions where global kinetic models or tabulations have been used to simulate the turbulent fuel combustion since sometimes radical concentrations may not be available for the post combustion NO_x simulations when using such approaches.

19.2.2 Storing Solution in Systems Without Time-Scale Separation

The characteristic time-scale of a system is the time period during which the events occur that are of interest to us. For the simulation of the same physical system, several different time-scales can be selected according to the purpose of the modelling. The requirement is that during this period all interesting changes should be completed. A mathematical model of a particular phenomenon should

represent the changes to its important features over the characteristic time-scale. In the case of combustion kinetics, this may include changes in concentrations or temperature. Usually, these changes are simulated by integrating the kinetic differential equations for the system but the changes can also be stored and re-accessed.

One possible approach for storing the solution of a kinetic model is according to the following general algorithm:

1. Time-step Δt is selected to achieve good resolution of the characteristic timescale of the system.
2. Several thousand spatially homogeneous simulations are carried out with a series of initial concentrations and/or temperatures, which are typical for the circumstances of applications of the final intended model.
3. The $\mathbf{c}(t)$, $\mathbf{c}(t + \Delta t)$ concentration vector pairs are stored in a database.
4. A function \mathbf{G} is fitted to the data and can then be used to predict the change in concentration after time step Δt : $\mathbf{c}(t + \Delta t) = \mathbf{G}(\mathbf{c}(t))$.

In spatially homogeneous simulations, the concentration–time curves (with resolution Δt) can be obtained via a recursive evaluation of function \mathbf{G} . If operator splitting is used in a reactive flow model (i.e. the solution of the flow and chemistry steps are separated), then this fitted function can be applied instead of typically using implicit integration methods to solve the chemical rate equations. Potentially large savings in computational effort can be achieved.

This method was called the repro-modelling approach in (Dunker 1986; Turányi 1994). The applicability of repro-modelling depends on the determination of function \mathbf{G} . This function converts m old to m new concentrations, thus this is a $\mathfrak{R}^m \rightarrow \mathfrak{R}^m$ function. However, it is equally good to fit separately m pieces of $\mathfrak{R}^m \rightarrow \mathfrak{R}$ functions. In order to be successful, the fitted function has to give an accurate approximation within the domain of applicability for the final intended model. The selection of the initial simulation conditions is therefore critical, since often, fitted functions may exhibit odd behaviour if utilised outside of the original fitting domain. The function should also be quick to evaluate and several possibilities exist for suitable functional representations of \mathbf{G} , as will be discussed in Sect. 19.3.

19.2.3 Storage of Information on Calculated Manifolds

We discussed in Chap. 18 that the presence of slow manifolds within chemical kinetic systems can help us to reduce the dimensionality of the system, while the reduced system is still able to reproduce the important system dynamics. This helps considerably when using storage and retrieval methods since the generation of the look-up table or fitted function can be restricted to the lower dimensional manifold. In fact, even when using trajectory methods, such a manifold would be rapidly approached during a simulation as the fast system time-scales collapsed.

Therefore, most storage and retrieval methods make use of the presence of such lower dimensional manifolds, either explicitly or implicitly.

Let us assume that we have identified a point in the space of variables that is on (or close to) an N_z -dimensional manifold. The manifold might be either a slow invariant manifold (SIM) or an Intrinsic Low-Dimensional Manifold (ILDM), as discussed in [Chap. 18](#). The state of the system can then be characterised by the following variable vector:

$$\alpha_1, \alpha_2, \dots, \alpha_{N_z}, g_1(\boldsymbol{\alpha}), g_2(\boldsymbol{\alpha}), \dots, g_{N_z}(\boldsymbol{\alpha}), Y_1, Y_2, \dots, Y_N \quad (19.5)$$

Here vector $\boldsymbol{\alpha}$ is the vector of the parameterizing variables of the manifold, vector $\mathbf{g}(\boldsymbol{\alpha})$ is its time derivative and the N -dimensional vector \mathbf{Y} defines the thermo-kinetic state of the system (see [Chap. 18](#)). For brevity, in the following we will refer to it as the vector of chemical concentrations although other variables such as temperature could be included. Knowing the N_z -dimensional manifold means that we possess a function $\mathbf{Y} = \mathbf{h}(\boldsymbol{\alpha})$ that projects the variables of the manifold onto the space of concentrations. The function $\boldsymbol{\alpha} = \mathbf{h}(\mathbf{Y})$ defines the relationship between the concentrations and the coordinates of the manifold.

If at least one point $\boldsymbol{\alpha}_0$ of the manifold is known, then we can calculate the progress of the kinetic system using the following system of differential equations with N_z variables:

$$\frac{d\boldsymbol{\alpha}}{dt} = \mathbf{g}(\boldsymbol{\alpha}), \quad \boldsymbol{\alpha}(t_0) = \boldsymbol{\alpha}_0 \quad (19.6)$$

This means that the number of equations which need to be solved have much fewer variables than the original kinetic system. The calculated $\boldsymbol{\alpha}$ values can be converted to the full concentration vector at any time point using function \mathbf{h} . Although initial value problem (19.6) contains only $N_z \ll N$ variables, the values of all concentrations can be obtained as though the original kinetic system of differential equations had been solved. Reduced models based on low-dimensional manifolds can usually be simulated faster than the full systems of differential equations, because the resulting dynamical system contains fewer variables and is usually not stiff. Explicit integration methods could therefore potentially be used.

In the derivation above there is an assumption that the manifold remains attractive as time progresses. This is not true for explosive systems, but it is valid for all other combustion systems. For explosive systems, the approach may still be valid but the dimensionality of the slow manifold chosen would have to be large enough to contain the explosive modes. This point was demonstrated in ([Brad et al. 2007](#)) where a low-dimensional repro-model describing the oscillatory ignition of CO-H₂ mixtures was developed using the ILDM concept. A manifold dimension of four was required in order to capture the complex dynamics associated with oscillatory ignition but the initial system dimensionality was 14 and hence substantial reductions and computational time savings were achieved. Further discussion of this example is given in the next section.

Reduced systems modelling based on initial value problem (19.6) requires the application of three functions. Function $\dot{\boldsymbol{\alpha}} = \mathbf{g}(\boldsymbol{\alpha})$ defines the time derivative of variables $\boldsymbol{\alpha}$, function $\mathbf{Y} = \mathbf{h}(\boldsymbol{\alpha})$ calculates the concentrations from the parameters of the manifold (mapping $\mathbb{R}^{N_z} \rightarrow \mathbb{R}^N$), while function $\boldsymbol{\alpha} = \bar{\mathbf{h}}(\mathbf{Y})$ (mapping $\mathbb{R}^N \rightarrow \mathbb{R}^{N_z}$) defines the relationship between the concentrations and the coordinates of the manifold.

Note that the classic mechanism simplification methods based on time-scale separation can also be interpreted in the same way as the above. For example, for the application of the quasi-steady state approximation (QSSA), variables $\boldsymbol{\alpha}$ is the concentrations of the non-QSSA species, function \mathbf{h} includes all algebraic equations that were obtained from the application of the QSSA (see Chap. 18) and function $\boldsymbol{\alpha} = \bar{\mathbf{h}}(\mathbf{Y})$ truncates the vector of all concentrations to the vector of non-QSSA species.

The approach above has several degrees of freedom:

- (1) *Method for the identification of the manifold.* As discussed in Chap. 18, there are many different mathematical approaches for the identification of the location of low-dimensional manifolds and thus for the definition of function \mathbf{h} .
- (2) *Selection of the parameterizing variables $\boldsymbol{\alpha}$.* This has implications for the final description of the function $\boldsymbol{\alpha} = \bar{\mathbf{h}}(\mathbf{Y})$. Usually, variables $\boldsymbol{\alpha}$ are selected to be identical to or functions of monotonically changing concentrations. For example, in several combustion systems the concentrations of H_2O and CO_2 are continuously increasing and therefore the concentrations of these two species are chosen as the parameters of a two-dimensional manifold. Mathematically, this means that function $\bar{\mathbf{h}}$ truncates the whole concentration vector to the concentrations of H_2O and CO_2 . This approach is not applicable when, e.g. CO_2 is a diluent in high temperature combustion systems because then the concentration of CO_2 may be a maximum function of the progress of the reaction. In this case, for example, H_2O and the sum of the concentrations of CO and CO_2 can be used as the two parameters of the manifold.

In principle, the function \mathbf{h} can be any linear or non-linear function. The requirement is that it should provide an unambiguous representation of the manifold. In a limited range, the concentration of any species may be a parameter of the manifold. A systematic method to define the parameterising variables was suggested in (Najafi-Yazdi et al. 2012). This method is based on a Principal Component Analysis (PCA) of species mass fractions in the composition space. The method yields the minimum number of linearly independent progress variables for a user-prescribed desirable accuracy.

- (3) *Representation of functions $\dot{\boldsymbol{\alpha}} = \mathbf{g}(\boldsymbol{\alpha})$ and $\mathbf{Y} = \mathbf{h}(\boldsymbol{\alpha})$.* If parameterizing variables $\boldsymbol{\alpha}$ of the manifold are identical to some of the concentrations, then the time derivative of them can be calculated from the right hand side of the kinetic system of differential equations. In general, function $\dot{\boldsymbol{\alpha}} = \mathbf{g}(\boldsymbol{\alpha})$ can be

obtained from the transformation function $\bar{\mathbf{h}}$ and the right hand side of the kinetic system of differential equations. During the simulations, \mathbf{g} can be calculated from \mathbf{h} and the kinetic system of ODEs or, alternatively, \mathbf{g} is also pre-calculated and stored as a fitted function. The requirement is that a mathematical function and its computational implementation is needed that calculates $\dot{\boldsymbol{\alpha}}$ and \mathbf{Y} from vector $\boldsymbol{\alpha}$ in a fast and accurate way. In the next section, several appropriate methods will be reviewed.

A special application of manifold based methods is when the location of the manifolds is identified directly from simulation results. This idea was introduced by several authors; one example is when the manifold-based simulation is connected with the repro-modelling approach (Turányi 1995; Büki et al. 2002; Brad et al. 2007). Here, a suitable dataset for fitting the low-dimensional repro-model is generated over a wide range of temperatures, pressures and mixture compositions, by integrating the system of differential equations from a variety of initial conditions chosen to include all behavioural properties of the system. Once the trajectories have settled onto the lower dimensional manifold, the concentrations are stored and can be fitted using the approach described above. The Flow-Controlled Chemistry Tabulation (FCCT) method was developed in (Enjalbert et al. 2012) where the stored chemistry is based on the simulation results of partially stirred reactors. For the simple reactor simulations the mixing, the conditions of the chemical reaction and the inflow/outflow were selected according to conditions expected within the turbulent flame to be modelled.

In situ adaptive tabulation (ISAT) also falls into the above category and was first introduced by Pope within a particle probability density function (*pdf*) model for turbulent combustion (Pope 1997). The basic idea underpinning ISAT is the in situ tabulation of accessed regions of composition space for a particular model application. In reality, these accessed regions of composition space are likely to be within a low-dimensional manifold. Further discussion of how tabulation is achieved within the ISAT method will be given in the next section.

An alternative methodology is to approximate the edge of a turbulent flame by an ensemble of discrete, steady laminar flames, called flamelets (Libby and Bray 1980; Liew et al. 1981). The individual flamelets are assumed to have a similar structure to laminar flames for the same concentration and temperature conditions; therefore, detailed calculations of the flamelet chemistry can be obtained from lower dimensional numerical calculations. This approach is adopted in the description of the chemical processes in flames through Flamelet Generated Manifolds (FGM) (van Oijen et al. 2001), also known as Flame Prolongated ILDMs (FPI) (Gicquel et al. 2000; Pera et al. 2009). In these methods, spatially one-dimensional, pre-mixed and non-premixed flames are first simulated using a detailed reaction mechanism. Counter-flow diffusion flame simulations are often used for this purpose (Verhoeven et al. 2012).

The flamelets are usually computationally cheap to produce, even using detailed mechanisms containing several hundred reaction steps since they are based on one-dimensional simulations. These simulations can therefore be performed over a

wide range of conditions, for example using a large number of boundary conditions, pressures and temperatures, so that the simulations cover the expected conditions within the three-dimensional turbulent flames of interest. The results of the calculations are stored in databases, and these empirical manifolds are used for the simulation of two- and three-dimensional flames, when direct simulation would require far more computational time. For the simulation of two- and three-dimensional flames, the values of only a few variables are usually calculated such as the local enthalpy and conversion. It is then assumed that the local structure of a flame having complex geometry is similar to those of a one-dimensional flame, and the concentrations of the calculated variables are obtained from the database. A number of applications of flamelet generated manifolds have been published and the accuracy of this approximation was investigated over various conditions for modelling the combustion of fuels such as hydrogen, methane (Bilger 1990; Gicquel et al. 2000; van Oijen and de Goey 2000, 2002; van Oijen et al. 2001; de Goey et al. 2003; Bongers et al. 2005; Fiorina et al. 2005; Gicquel et al. 2006; Godel et al. 2009; Verhoeven et al. 2012) and even Diesel oil (Bekdemir et al. 2011). In another approach (Michel et al. 2008, 2009, 2010), flamelet-like libraries were generated based on perfectly stirred reactor (PSR) calculations in terms of auto-ignition delays and steady state profiles of the progress variable.

19.3 Mathematical Approaches for the Storage of Information

In the previous section, several methods were reviewed that converted the solution of the kinetic system of differential equations to an algebraic function of either the parameters or the concentrations. The next step is an accurate and computationally efficient representation of these non-linear multi-variate functions within combustion simulation codes. The applied schemes are usually based on either tabulation and interpolation or on fitting methods and include the application of look-up tables, neural networks and various types of functions such as Taylor expansions, orthogonal polynomials, splines etc. A brief review of available methods was given in (Androulakis 2004). The success of the methods is judged by their ability to give accurate representations of the full kinetic system, the computational speed-up with respect to the full integration of the kinetic equations, and storage requirements. The time investment in generating the equivalent model is also important for some applications, although for models used in repeated design or operational control calculations this may not be such a high priority.

There will inevitably be some trade-off among model accuracy, storage requirements and time invested to generate the replacement model. In general, tabulation based methods use exact quantities at specified tabulation points and therefore will be highly accurate at these points. However, interpolation errors may occur at other points within the model domain and therefore there is a trade-off

between accuracy and the storage requirements of using a higher density of tabulation points. The storage and retrieval problem in high-dimensional domains may be addressed using binary tree type structures as employed within adaptive tabulation methods as describe below. For polynomial and neural network fitting methods, only the polynomial coefficients must be retrieved and therefore the storage requirements can be considerably lower than for standard tabulation methods. However, the overall accuracy of the operational model will depend on achieving a high accuracy of the fitted functional forms across the whole model domain of interest. A brief description of several of the most widely used methods will now be given.

19.3.1 Look-Up Tables

One possibility of achieving efficient access to chemical information during a simulation is to store the output information in tables. This approach (called look-up tables for the simulation of turbulent flames) means that the input and output vectors are stored within a potentially multi-dimensional table. When the handling software receives the input vector, it locates points within the table that are close to the input point within a high-dimensional space. The output vector is composed using linear interpolation between the output vector elements at the storage points.

During the creation of look-up tables, the following issues must be considered (Atanga 2012):

1. The information storage structure of the database must be optimised.
2. The procedure for information retrieval from the database must be optimised, that is the CPU time needed to retrieve a stored value must be minimal.
3. The accuracy of the retrieved value has to meet specific criteria.
4. The required memory needed to store all the desired data must be affordable.

However, the search and retrieval algorithms required to access the look-up tables can consume significant amounts of computer time. Special algorithms have been developed to speed up the search and retrieval process (Androulakis 2004).

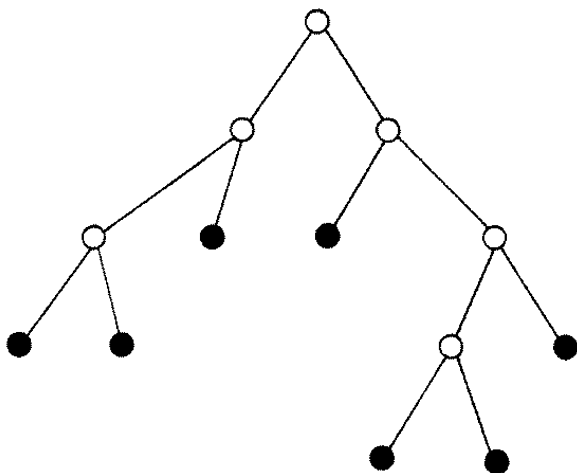
Early applications of tabulation methods in turbulent combustion simulations employed tabulations of large regions of the physically realisable composition or thermo-chemical phase space. As a result they tended to use highly reduced global mechanisms to generate the look-up tables, in order to avoid the dimensionality of the table becoming too large. In early implementations (Chen et al. 1995; Taing et al. 1993), a regular mesh was used to cover the realisable region of the composition space, with the reaction mapping determined by offline integration of a highly reduced model for storage within the look-up table. In such cases, the success of the tabulated model is limited by the accuracy of the reduced scheme employed to generate it. The interpolation error that is incurred for accessed regions between mesh points can be controlled by adaptive refinement of the mesh.

The need for mesh refinement is determined by establishing the region of accuracy for the tabulated points within the mesh. This is defined as the connected region containing initial conditions φ^0 consisting of perturbed points φ^q for which the local error in the reaction mapping terms ε does not exceed the specified tolerance ε_{tol} . The use of adaptive meshes may facilitate the use of more detailed chemical models for the table generation.

Tabulated chemistry was used in the simulation of cool flames (Colin et al. 2005), which was based on the representation of auto-ignition quantities such as cool flame ignition delay, fuel consumption and reaction rates. The values used in the tables were extracted from complex chemistry calculations for n-heptane. The approach was extended to the Variable Volume Tabulated Homogeneous Chemistry (VVTHC) approach in Jay and Colin (2011). This approach provides the evolution of major species and radicals from the onset of auto-ignition up to the end of the expansion stroke for compression ignition and spark ignition engine applications. It was first tested for homogeneous engine cases where it compared very well to complex chemistry simulations. It was implemented in a piston engine combustion model and used for the calculation of the burned gases volume variation behind a propagating flame at constant pressure and in reproducing the subsequent composition evolution.

The number of independent variables that can be included within a tabulation procedure is limited by the storage requirements of the tabulation. It is for this reason that early tabulation methods were based on calculations using highly reduced or global chemical mechanisms. This problem was addressed in later developments of tabulation methods based on *in situ* tabulation (Pope 1997). The method of *in situ* adaptive tabulation (ISAT) was first developed by Pope for turbulent combustion (Pope 1997) and is based on the *in situ* tabulation of accessed regions of composition space during a model simulation rather than the full realisable region. The tabulation is achieved by integrating the chemical source terms when a region is first accessed and storing the reaction mapping and sensitivity information in a binary tree data structure. The ISAT table therefore consists of a binary tree, a set of records, one for each leaf of the tree, and a set of cutting planes, one for each node of the tree (see Fig. 19.1 for a schematic of such a tree). Efficient search and retrieval algorithms can therefore be implemented. Subsequent estimations of the reaction mapping terms for points within a small distance of the previously tabulated ones are achieved using multi-linear interpolation. Any reaction mapping that cannot be interpolated with sufficient accuracy is generated by direct integration and added to the table. The tabulation is therefore performed *in situ* rather than using offline calculations that were employed within earlier tabulation approaches. It can be linked to the tabulation of low-dimensional manifolds, since in reality it is this manifold that will be accessed during the integration rather than the full composition space. The presence of low-dimensional manifolds within the chemical system ensures that the accessed region is usually much smaller than the full realisable region. The presence of such manifolds allows significant reduction of the tabulation effort and storage

Fig. 19.1 A sketch of a binary tree used within the ISAT approach. At each leaf ● there is a record; at each node ○ there is information about the cutting plane. Reprinted from Pope (1997) by permission of Taylor & Francis Ltd, www.tandfonline.com



requirements, allowing the use of detailed chemical mechanisms within the procedures.

The method was initially tested for methane—air combustion with 14 degrees of freedom in a pairwise mixing stirred reactor (Pope 1997). Cannon et al. compared the use of in situ methods to conventional tabulation techniques for NO_x predictions in CO combustion using a 5-step mechanism, showing that the storage requirements using in situ methods were up to three orders of magnitude lower than conventional techniques due to the much smaller size covered by the accessed region of composition space (Cannon et al. 1999). Further developments include the use of ISAT in a range of turbulent combustion simulations. Pope and coworkers (Saxena and Pope 1999; Tang et al. 2000; Xu and Pope 2000) have coupled the ISAT method with Monte Carlo joint *pdf* calculations of turbulent reacting flows using an operator splitting approach, allowing the representation of the finite rate kinetics necessary to capture important features such as local flame extinctions and pollutant formation with reported speed-ups of up to a factor of 60 compared to conventional chemistry calculations (Saxena and Pope 1999). Similar speed-ups were reported in (Wang and Fox 2003) for a *pdf* model predicting reactive precipitation in time-evolving flows and in (Xie et al. 2004) for a finite volume model of multi-phase fluidized beds. Higher speed-ups (up to 165) have been reported for pre-mixed combustors (James et al. 2001) indicating that the accessed regions of composition space are smaller for pre-mixed flames compared to diffusion flames. Masri et al. incorporated the ISAT technique into the commercial CFD code FLUENT using a hybrid Reynolds Averaged Navier–Stokes (RANS)-*pdf* approach with application to flame liftoff (Masri et al. 2004). Their work demonstrated the ability of ISAT to represent chemistry with sufficient detail to model auto-ignition phenomena within turbulent jets of H_2/N_2 mixtures into co-flows of hot gas mixtures. Engine simulations using ISAT were performed in (Contino et al. 2011). ISAT was also applied to simulations of the catalytic

combustion of methane on a platinum surface using an unstructured CFD approach (Kumar and Mazumder 2011).

The use of in situ flamelet-generated manifolds was suggested in Lodier et al. (2011). A procedure for building converged composition-space solutions for pre-mixed flamelets was proposed and tested. This method provides the framework for an efficient in situ calculation of complex chemistry with differential diffusion to be applied to three-dimensional unsteady flame simulations.

Despite the use of adaptive tabulation and efficient search and retrieval algorithms there is still a significant computational overhead in using tabulation methods. Various researchers have therefore attempted to develop functional fitting methods to overcome this problem and these will be discussed in the next sections.

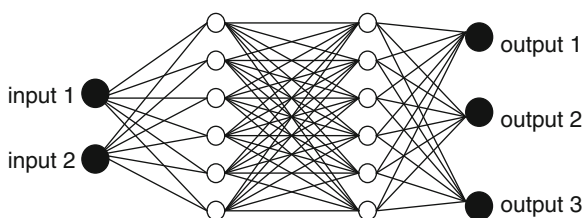
19.3.2 Artificial Neural Networks

Artificial Neural Networks (ANNs) are mathematical functions which are designed to resemble the interconnection of neurons within the nervous systems of the human brain. They can be fitted or “trained” to represent complex input–output relationships. Within an ANN, a network of neurons or nodes is constructed which are linked to each other by a series of ‘synapses’. Common functions used within the networks are non-linear weighted sums based on hyperbolic-tangent functions. This artificial model is then ‘trained’ by presenting it with examples of input–output relationships and adjusting the effect that the neurons have on each other until the system ‘recognises’ the examples. In principle, therefore ANNs should be capable of representing highly non-linear functions such as those which arise in chemical kinetic systems.

A schematic diagram of the architecture of an ANN with 2 input nodes, two hidden layers of 6 nodes and 3 output nodes is given in Fig. 19.2. The strengths of connections between the different neurons are stored as weights which are determined by an appropriate learning algorithm.

The approach can be summarised mathematically as:

Fig. 19.2 A schematic of an architecture of an ANN with 2 input nodes, two hidden layers of 6 neurons and 3 output nodes



$$y_i^l = f \left(\sum_{j=1}^{K_{l-1}} w_{ij}^l y_j^{l-1} + \phi_i^l \right)_{i=1, \dots, K_l, \dots, L} \quad (19.7)$$

where y_i^l is the output of the i -th neuron of the l -th layer, w_{ij}^l is the weight value of connection between the j -th node of the $(l-1)$ -th layer and the i -th neuron of the l -th layer and ϕ_i^l is the bias value of the i -th neuron of the l -th layer (Christo et al. 1995, 1996a, b; Blasco et al. 1999a, b, 2000; Chen et al. 2000; Flemming et al. 2000; Ihme et al. 2008). The non-linear transfer function $f(\cdot)$ is commonly represented using sigmoidal or hyperbolic-tangent functions. Through presenting input–output examples to the system and adjusting the synaptic weights w_{ij}^l in an appropriate manner, the system can be trained to recognise patterns or replicate complicated functions. The learning algorithm provides the means of adjusting the weights in order to reduce the fitting error of the ANN when compared to the training data. Commonly, a back-propagation algorithm is used as fully described in (Christo et al. 1996a) with a least squares error function.

ANNs are potentially flexible and can be used to represent a variety of data types. A possible disadvantage however, is the lack of general guidelines on how to optimise important features of the network such as the number of layers and neurons within each layer (Christo et al. 1996a). Optimising the network can therefore involve iterative trial and error procedures. For example, large numbers of weights are capable of providing a highly accurate fit to training data, but can lead to poor results for unseen data (over-fitting), in perhaps an analogous way to using polynomials of too high order (see later). The evaluation of ANNs may also require more computer time than using simpler polynomial fitting methods that are discussed in the next section.

Despite these potential drawbacks ANNs have successfully been used several times in combustion modelling (Christo et al. 1995). They were applied for the simulation of methane combustion by Blasco et al. in a zero-dimensional calculation using a four-step global scheme, where additional ANNs for density and temperature were included (Blasco et al. 1998). Here, a second-order scaled-conjugate-gradient method was used for the fitting procedure. The work was further developed in (Blasco et al. 1999b), where the accuracy of the ANN was improved by fitting separate networks to sub-domains of chemical composition space. Defining optimal sub-domains for which to develop the replacement models is a key component of balancing accuracy and storage and retrieval efficiency. In order to address this problem, Blasco et al. (2000) attempted to develop an automatic method for partitioning thermochemical space into optimal domains based on a self-organising map (SOM). The SOM performs a mapping between the high-dimensional thermo-chemical space and a two-dimensional (2D) map whilst attempting to preserve the topology of the original space. The idea is to ensure that points which are close to each other in the original space remain so in the corresponding 2D space. The SOM is then used in the retrieval stage to define which ANN to be used.

The use of ANNs has been coupled with several mechanism reduction methods. For example in (Chen et al. 2000), ANNs were used to fit an ISAT table, with an aim of reducing the storage requirements when compared to the multi-dimensional look-up tables used in ISAT. Here, there is a trade-off between the accuracy that ISAT provides through tabulating exact solution values at the tabulated points and potentially small interpolation errors, compared to potentially larger fitting errors but much smaller tabulation requirements of ANNs. The CPU requirements of both methods were found to be comparable for the partially stirred reactor simulations performed (Chen et al. 2000). In general, the choice of method could depend upon the intended application and required accuracy versus available storage memory.

Shenvi et al. (2004) applied neural networks based on a simple multi-variate polynomial architecture. The accuracy and efficiency of these ridge polynomial networks were demonstrated by modelling the kinetics of $\text{H}_2\text{-Br}_2$ reaction, formaldehyde oxidation and $\text{H}_2\text{-O}_2$ combustion. Choi and Chen (2005) also applied ANNs for the prediction of ignition delay times in homogeneously charged compression ignition (HCCI) engine combustion for a range of fuels including propane and iso-octane in a well-mixed reactor. Dyer and Korakianitis (2007) simulated propane—air detonation by representing heat-release and species information during the reaction via a mapping methodology. Multi-layer feed-forward neural networks were used as function approximators to reproduce the parameters extracted from the detailed integrations and to perform the non-linear interpolations required between reaction points. The mapping method results were accurate to within 1–3 % compared to the results of detailed integrations, and the computational effort was reduced by two orders of magnitude.

Ihme et al. (2009) carried out large-eddy simulations of a methane—hydrogen flame by employing two chemistry representation methods, the conventional structured tabulation technique and ANNs. The latter was based on the optimal artificial networks (OANNs) approach (Ihme et al. 2008). It was demonstrated that the ANN accuracies were comparable with the use of structured tables. Compared to the tabulation technique, data retrieval from the network was computationally slightly more expensive. In (Chatzopoulos and Rigopoulos 2013), the use of ANNs was combined with the Rate-Controlled Constrained Equilibrium (RCCE) approach (see Chap. 18) in models of two non-premixed and non-piloted, $\text{CH}_4/\text{H}_2/\text{N}_2$ turbulent flames. Large computational speed-ups were reported, with reasonable agreement in the simulation of major chemical species with respect to the full integration of the kinetic scheme. Some discrepancies were observed for the minor species, but the work indicates a potential of RCCE-ANN tabulation methodologies for future turbulent combustion computations.

19.3.3 Fitting Polynomials Using Factorial Design

Surrogate models are always created for a given domain of parameters. If these parameters are assumed to be independent from each other, then for each parameter a minimum x_i^{\min} and maximum x_i^{\max} value can be defined. The (x_i^{\min}, x_i^{\max}) sets for all parameters define a hyper-rectangle in the space of parameters, and this hyper-rectangle is identical to the accessible region of the parameters. The ensemble of the corner points of the hyper-rectangle is also called the full factorial design arrangement of the parameter values (Box et al. 1978). Frenklach et al. (1992) suggested the use of fitted second-order polynomials for the creation of surrogate models where the parameter vectors used as the independent variables of the fitting were arranged according to a full factorial design. This way all possible parameter value combinations were well represented. This method has been shown to provide reliable and accurate response surfaces. However, its application may become computationally expensive when the number of parameters is large. However, surrogate models based on factorial design have been and are routinely used in model optimisation studies (Feeley et al. 2004, 2006; Frenklach et al. 2004; You et al. 2011, 2012). For a discussion of optimisation methods see Chap. 16. In the field of model reduction, Marsden et al. (1987) suggested a similar method for the creation of a repro-model for ozone production in the troposphere using a 15-variate polynomial which was fitted to a series of simulations, arranged according to a factorial design.

19.3.4 Polynomial Approximation Using Taylor Expansions

As discussed in Chap. 16, the effect of changing the parameters within a model can be described by the following Taylor expansion:

$$Y_i(t, x + \Delta x) = Y_i(t, x) + \sum_{j=1}^m \frac{\partial Y_i}{\partial x_j} \Delta x_j + \frac{1}{2} \sum_{k=1}^m \sum_{j=1}^m \frac{\partial^2 Y_i}{\partial x_k \partial x_j} \Delta x_k \Delta x_j + \dots \quad (19.8)$$

where $\partial Y_i / \partial x_j$ is the first-order local *sensitivity coefficient* and $\partial^2 Y_i / \partial x_k \partial x_j$ is the second-order local sensitivity coefficient. It was also discussed in Chap. 16, that there are several efficient numerical methods for the calculation of the first-order local sensitivity coefficients. The second-order local sensitivity coefficients can be calculated from the first-order coefficients using a finite difference approximation.

Davis et al. (2004) proposed the application of a Taylor expansion (19.8) for constructing kinetic response surfaces used in the development and optimisation of reaction kinetic models. They termed it the sensitivity analysis based (SAB) method. Tests indicated that for gas-phase combustion models the response surface obtained with the SAB method was as accurate as the factorial design method previously used in reaction model optimisation, but using the sensitivity

coefficients calculated by the combustion simulation codes allowed significant computational savings. This method was used in all later mechanism optimisation works of Wang and co-workers and Sheen and co-workers (Davis et al. 2004; Sheen et al. 2009, 2013; Sheen and Wang 2011) (*c.f.* Chap. 16).

19.3.5 Orthogonal Polynomials

Polynomial fitting methods have also been commonly used within repro-modelling approaches for combustion applications. Fitting suitable polynomials involves choosing polynomials of a suitable order and estimating the coefficients which provide the best fit to the dataset. Since general high-order polynomials have a large number of coefficients, it follows that the approach becomes feasible, only if a large number of these can be set to zero. The method therefore has to be suitable for fitting a polynomial function to tens of thousands of data points and determining coefficients for only those terms which improve the quality of the fit within certain error bounds. Least squares methods are commonly employed. The application of orthonormal polynomials (Turányi 1994) can be advantageous for this task, since their coefficients can be determined independently from each other. A method for response surface fitting based on multi-variate orthonormal polynomials is therefore outlined below:

We first denote $\mathbf{x}^i = (x_1^i, x_2^i, \dots, x_m^i)$, $i = 1, \dots, n$ to be a dataset and φ_j , $j = 1, \dots, l$ to be a set of $\mathfrak{R}^m \rightarrow \mathfrak{R}$ functions with appropriate weights w_i , $i = 1, \dots, n$. The scalar product of functions φ_j and φ_k can be interpreted in the following way:

$$(\varphi_j, \varphi_k) = \sum_{i=1}^n w_i \varphi_j(\mathbf{x}^i) \varphi_k(\mathbf{x}^i) \quad (19.9)$$

This means that the scalar product is determined not only by functions φ_j and φ_k , but also the dataset and the values of weights w_i . Functions φ_j and φ_k are orthonormal with respect to scalar product (19.9), if

$$(\varphi_j, \varphi_k) = \begin{cases} 0 & \text{if } j \neq k \\ 1 & \text{if } j = k \end{cases} \quad (19.10)$$

Any function $F: \mathfrak{R}^m \rightarrow \mathfrak{R}$ can be approximated using the set of orthonormal functions φ_j , $j = 1, \dots, l$ by a Fourier expansion:

$$F \approx \sum_{j=1}^l (F, \varphi_j) \varphi_j \quad (19.11)$$

The deviation between function F obtained from the full model and its approximation can be characterised by the error r :

$$r = \left\| F - \sum_{j=1}^l (F, \varphi_j) \varphi_j \right\| \quad (19.12)$$

where $\| \cdot \|$ denotes the Euclidean norm. This error is also called the root mean square (*r.m.s.*) error.

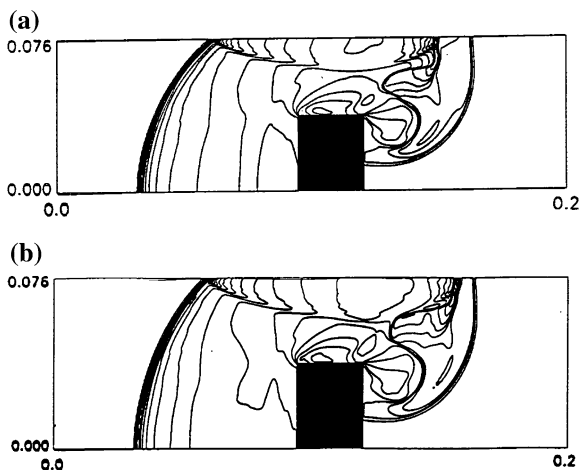
The application of Fourier expansion (19.11) requires orthonormal functions, which can be generated from independent functions using the Gram-Schmidt orthonormalization process. A possible set of linearly independent functions is the monomials of a polynomial. For example, the monomials of a trivariate, second-order polynomial are as follows: 1, x , y , z , x^2 , xy , xz , y^2 , zy and z^2 . Another possible option is to use linearly independent trigonometric functions.

The overall aim is to get a good fit using as few monomials as possible. Therefore, each polynomial is generated by initially fitting a constant to the data and calculating the *r.m.s.* error from Eq. (19.12). A new term is then added, an orthonormal polynomial is generated and the new *r.m.s.* error is calculated. If the change in *r.m.s.* error is greater than a pre-set tolerance, then this term is accepted and a new term is tested. In this way, the polynomial is built up with terms of progressively increasing order from first-order terms in each variable up to typically fourth- or fifth-order terms in combinations of variables. The fitting is stopped when the overall error becomes lower than a user-defined threshold. This means that the overall order of the final polynomial need not be selected before the fitting process, but rather the algorithm automatically finds the smallest order polynomial that fulfils the accuracy requirement. This should help to avoid problems related to “over-fitting” which sometimes occur when using high-order polynomials.

Repro-models based on polynomial fits have been applied in several combustion systems. Clifford et al. (1998) simulated the spread of a detonation wave at 2.5 Mach in hydrogen–oxygen–argon mixtures, its collision with an obstacle and reflection. The spatially 2D simulations were carried out using either a detailed reaction mechanism, or a repro-model based on fourth-order polynomials obtained using the above method for the variables pressure, temperature and conversion factor β . Within spatially homogeneous calculations, the application of the repro-model was 1,500 times faster than the simulation of the detailed model. The time dependent density maps obtained in 2D simulations were almost identical when calculated with a detailed mechanism (Fig. 19.3a) and the repro-model (Fig. 19.3b), but the repro-model based simulation was 100 times faster. Imbert et al. (2008) calculated the ignition times in detonation waves in a similar way using polynomial approximations over a wide range of conditions.

A similar method was also used for the generation of a repro-model describing the oscillatory ignition of CO–H₂ mixtures in a continuously stirred tank reactor (CSTR) at very low pressures (Brad et al. 2007). Using a 4-variable repro-model based on sixth-order polynomials, successful representation of the regions of steady state, cool flames and large temperature oscillations was achieved based on fits to a 14-variable full model. In this particular example, separate repro-models

Fig. 19.3 Time dependent density maps obtained in 2D simulations of the spread of a detonation wave at 2.5 Mach in hydrogen–oxygen–argon mixtures. Its collision with an obstacle (in black) and the reflection are shown. The density maps were calculated (Clifford et al. 1998) using **a** a detailed mechanism including nine species and **b** a repro-model. The latter calculation was 100 times faster. Reprinted from Clifford et al. (1998) with permission from Elsevier



were developed for different regions of the concentration/temperature space due to the need to control fitting errors to a very high degree of accuracy in some regions. For example, within low temperature regions at the start of the ignition period, smaller partitioned sets were required in order to achieve local fitting errors as low

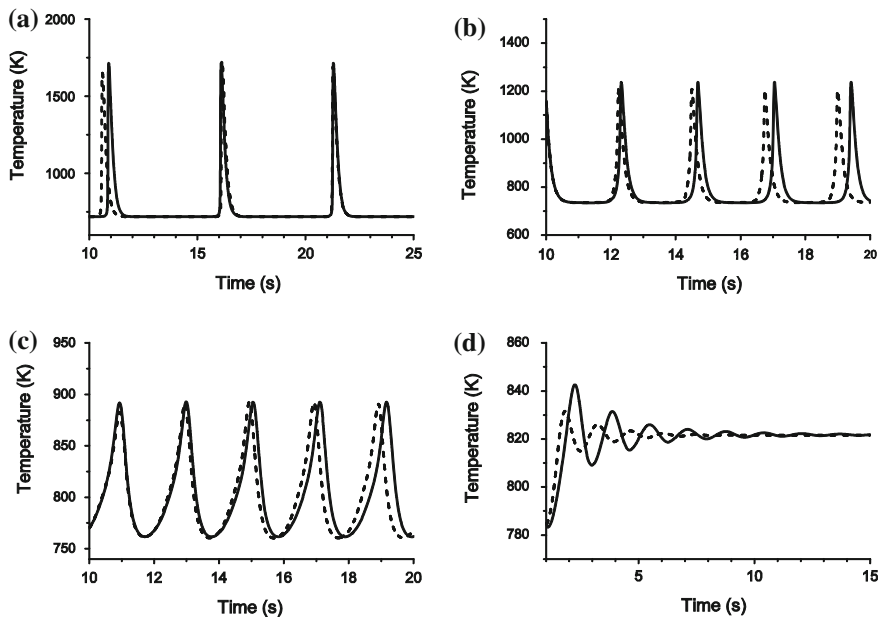


Fig. 19.4 Comparison between model simulations based on ordinary differential equations describing the reduced scheme (solid) and fitted polynomial repro-model (dashed) for oscillatory ignition of CO-H₂ mixtures at $P = 25$ Torr and 0.5 % H₂ and initial temperatures **a** 720 K, **b** 735 K, **c** 750 K, **d** 770 K. Reprinted from Brad et al. (2007) with permission from Elsevier

as 0.1 %. It was found that in such regions small differences in predicted concentrations could lead to large shifts in the ignition point. However, as a result of achieving low local fitting errors only small shifts in the phase of the oscillatory trajectories were found when using the repro-model as shown in Fig. 19.4. The application demonstrates however, that particular care may be required when applying repro-models to ignition applications.

19.3.6 Piecewise Reusable Implementation of Solution Mapping

In most cases, the functional mappings used to represent the solution of the chemical kinetic differential equations (i.e. the surrogate or repro-model) are prepared and fitted prior to the final intended combustion simulations within for example complex multi-dimensional reactive flow codes. However, within the ISAT approach described above, the tabulation is achieved during the simulation, with the advantage that only accessed regions of composition space have to be tabulated. A similar method, but using polynomial fits, was developed within the Piecewise Reusable Implementation of Solution Mapping (PRISM) approach (Tonse et al. 1999). In this approach, the fitted polynomial functions are developed during the calculation, and then reused when the fitted regions of composition space are revisited in subsequent time steps or in different spatial regions. PRISM uses second-order polynomials, so that multiple expressions are used in order to cover the whole realisable region, each of which is valid over a different portion of composition space (in common with (Brad et al. 2007)). In the PRISM approach, this is achieved by partitioning the chemical composition space into pre-determined non-overlapping adjacent hyper-cubes, spaced at regular intervals and thus allowing for the simple indexing required for efficient searching during reuse. Integration of the full kinetic equations provides the solution at selected points throughout a hyper-cube, in order to determine the polynomial coefficients of the repro-model. Factorial design methods are used to reduce the required number of computed points. An increase in accuracy is reported with reduced hyper-cube size, although there will be a trade-off between accuracy and the efficiency of polynomial generation as well as storage and retrieval. The largest hyper-cubes achievable for a given accuracy should be used in order to minimise the computational effort required. Improvements to efficiency were suggested in (Tonse et al. 2003; Brown and Tonse 2004) based on two alternative methods for the a priori identification of hyper-cubes that will have a high level of reuse. This allows for polynomial construction only for those hyper-cubes that are revisited enough times to make the construction worthwhile. The PRISM method has demonstrated successful application to hydrogen ignition, a 1D laminar hydrogen flame, a 2D axisymmetric turbulent jet (Tonse et al. 1999, 2003) and a turbulent pre-mixed hydrogen flame (Bell et al. 2000). The constructed polynomials could potentially

be stored for other calculations as long as the fitted regions of composition space are common and the basic parameterisation of the underlying chemical mechanism has not changed. Lee et al. (2005, 2007) approximated a reduced model based on a slow manifold derived using Computational Singular Perturbation (CSP, see Chap. 18) using large number of low-order polynomials based on a similar approach to the PRISM method. The approach was applied to the models describing the ignition of H₂-air and heptane-air mixtures.

19.3.7 High-Dimensional Model Representation

An additional group of methods relevant to reduced chemical model representations are based on rapidly convergent hierarchical correlated function expansions in the input variables. Such a High-Dimensional Model Representation (HDMR) can therefore essentially replace the integration of ODEs with a difference equation based on the HDMR functions in a similar way to tabulation or polynomial fitting methods. The functional form of the HDMR expansion and its use for global sensitivity analysis was already discussed in Chap. 16.

The purpose of creating such a hierarchical function expansion is to create a fast equivalent operational model (FEOM) giving sufficient accuracy with respect to the full chemical model, but with much lower computational expense. HDMR builds approximations recursively, based on the assumption that high-order correlated effects of the inputs are expected to have negligible input on the output. Applications have shown that the order of the correlations between the independent variables dies off rapidly and therefore only a few terms are usually required to represent even highly non-linear input-output relationships. The approach was applied in Li et al. (2008) to the simulation of ignition within homogeneous H₂/air mixtures over wide ranges of temperatures and pressures ($1000 < T_0 < 1500$ K, $0.1 < P < 100$ atm). The approach has also been tested on several atmospheric modelling systems including a stratospheric chemical model (Shorter et al. 1999) and a tropospheric alkane model (Wang et al. 2005). These test cases indicate that a low number of low-order terms are often sufficient to represent the model in equivalent form to good accuracy.

One potential advantage of such methods, is that only low-order expansion functions or coefficients must be stored, which drastically reduces storage requirements for high-dimensional systems when compared to standard tabulation methods and potentially even adaptive tabulation methods. In order to reduce computational effort, the terms in the expansion are usually represented by fitted orthogonal polynomial functions (Li et al. 2002) giving similarities with the polynomial approximation method discussed in the previous section. The main difference is that in case of HDMR it is the terms in the function expansions that are fitted rather than the direct input-output relationships. The methods could be coupled with ILDM based or other methods for the selection of key model variables in order to reduce the number of functional expansions required (Tomlin

et al. 2001). Additional information may also be obtained from the terms in the expansion which reveal cooperations between variables and highlight the extent of non-linearity of the input–output relationships. As with all operational model representations, the success of HDMR methods depends on using a large enough region of the input variable phase space so as to be relevant in the full model. None of these fitting methods should be expected to extrapolate well to new conditions outside of the fitted region.

19.4 Summary and Discussion

In most combustion simulations, chemical kinetic information is stored within a detailed reaction mechanism consisting of elementary reaction steps and a detailed parameterisation of the rate coefficients. This approach has the advantage that it is easy to update the mechanism, to add or delete reaction steps or to change the parameterisation of the rate coefficients when new information becomes available. The reaction mechanism is usually encoded in Chemkin format, which has limitations, but which is usually flexible enough for most modelling purposes. The detailed reaction mechanism can easily be converted to chemical source terms that are used on the right hand side of the differential equations that define the chemistry submodel of any larger combustion model.

For detailed modelling which attempts to investigate the kinetic processes which drive key combustion outputs such as ignition behaviour, flame characteristics, pollutant formation etc. it often suits the modeller to maintain this form of equations, even if some skeletal reduction of large comprehensive schemes is required (see Chap. 17). For engineering calculations however, descriptions of the chemical changes often have to be coupled with models of highly complex flows in two or three spatial dimensions. The number of variables within even skeletally reduced mechanisms is often therefore prohibitive from a computational point of view, and detailed chemistry in this form can often not be afforded within such models. For use within engineering design calculations however, the modeller may not require tracking large numbers of chemical species but may only require accurate reproduction of key model outputs. This is not to say that chemical kinetics does not help to determine these outputs, but for these types of calculations it may be more convenient to pre-process the chemical information and to use it in a condensed way. The approaches described in this chapter for this purpose are based on either tabulation/interpolation methods, or multi-variate fitting methods, or combinations of both. The use of look-up tables, ANNs and various polynomial based methods was discussed.

The advantage of such approaches is the reduced computational time required for the simulation of the chemical time step within a complex model. This could even have the advantage that detailed kinetics can be represented (albeit in a pre-processed way) and could help to avoid the usage of highly global models which may neglect key kinetic effects. The use of efficient adaptive tabulation or multi-

variate fitting methods can often be based on calculations using detailed chemical schemes. One possible disadvantage is that the generation of the surrogate model has to be performed again if the underlying model changes (e.g. a key rate parameter is updated or new reactions or species are added). However, where adaptive approaches are used, this issue does not appear to be prohibitive. The trade-offs between the different methods described within the chapter will relate to storage requirements, retrieval time and accuracy. Where storage is limited, then multi-variate fitting methods based on polynomials/HDMR could be advantageous. However, since tabulation methods store exact values at the chosen tabulation points they may offer higher accuracy for some applications. In all cases, the exploitation of low-dimensional manifolds present in combustion systems (see [Chap. 18](#)) significantly reduces the dimensionality of the surrogate model used and can often be utilised in an implicit way.

Acknowledgments TT acknowledges the financial support of OTKA grants K84054 and NN100523. AST acknowledges the financial support of EPSRC (GR/R39597/01).

References

- Androulakis IP (2004) Store and retrieve representations of dynamic systems motivated by studies in gas phase chemical kinetics. *Comput Chem Eng* 28:2141–2155
- Atanga GF (2012) Direct numerical simulation of turbulent flames on parallel computers, Ph.D. Thesis, Otto-von-Guericke-Universität
- Bekdemir C, Somers LMT, de Goey LPH (2011) Modeling Diesel engine combustion using pressure dependent flamelet generated manifolds. *Proc Combust Inst* 33:2887–2894
- Bell JB, Brown NJ, Day MS et al (2000) Scaling and efficiency of PRISM in adaptive simulations of turbulent premixed flames. *Proc Combust Inst* 28:107–113
- Bilger RW (1990) On reduced mechanisms for methane-air combustion in non-premixed flames. *Combust Flame* 80:135–149
- Blasco JA, Fueyo N, Dopazo C et al (2000) A self-organizing-map approach to chemistry representation in combustion applications. *Combust Theory Modell* 4:61–76
- Blasco JA, Fueyo N, Dopazo C et al (1998) Modelling the temporal evolution of a reduced combustion chemical system with an Artificial Neural Network. *Combust Flame* 113(1–2):38–52
- Blasco JA, Fueyo N, Dopazo C et al (1999a) Modelling the temporal evolution of a reduced combustion chemical system with an artificial neural network. *Combust Flame* 113:38–52
- Blasco JA, Fueyo N, Larroya JC et al (1999b) A single-step time-integrator of a methane-air chemical system using artificial neural networks. *Comput Chem Eng* 23:1127–1133
- Bongers H, van Oijen JA, de Goey LPH (2005) The flamelet generated manifold method applied to steady planar partially premixed counterflow flames. *Comb Sci Tech* 177(12):2373–2393
- Box GEP, Hunter WG, Hunter JS (1978) Statistics for experiments. An introduction to design, data analysis, and model building. Wiley, New York
- Brad RB, Tomlin AS, Fairweather M et al (2007) The application of chemical reduction methods to a combustion system exhibiting complex dynamics. *Proc Combust Inst* 31:455–463
- Brown NJ, Tonse SR (2004) PRISM piecewise reusable implementation of solution mapping to improve computational economy. *Abs Pap Am Chem Soc* 228:U308–U308
- Büki A, Perger T, Turányi T et al (2002) Repro-modelling based generation of intrinsic low-dimensional manifolds. *J Math Chem* 31:345–362

- Burke MP, Klippenstein SJ, Harding LB (2013) A quantitative explanation for the apparent anomalous temperature dependence of $OH + HO_2 \rightarrow H_2O + O_2$ through multi-scale modeling. *Proc Combust Inst* 34:547–555
- Cannon SM, Brewster BS, Smoot LD (1999) PDF modeling of lean premixed combustion using in situ tabulated chemistry. *Combust Flame* 119(3):233–252
- Carstensen HH, Dean AM (2007) The kinetics of pressure-dependent reactions. Modeling of chemical reactions. *Comprehensive Chemical Kinetics* 42:105–187
- Chatzopoulos AK, Rigopoulos S (2013) A chemistry tabulation approach via rate-controlled constrained equilibrium (RCCE) and artificial neural networks (ANNs), with application to turbulent non-premixed CH₄/H₂/N₂ flames. *Proc Combust Inst* 34:1465–1473
- Chen JY, Blasco JA, Fueyo N et al (2000) An economical strategy for storage of chemical kinetics: Fitting in situ adaptive tabulation with artificial neural networks. *Proc Combust Inst* 28:115–121
- Chen JY, Chang WC, Koszykowski M (1995) Numerical simulation and scaling of NO_x emissions from turbulent hydrogen jet flames with various amounts of helium dilution. *Combust Sci Technol* 111:505–529
- Choi Y, Chen JY (2005) Fast prediction of start-of-combustion in HCCI with combined artificial neural networks and ignition delay model. *Proc Combust Inst* 30:2711–2718
- Christo FC, Masri AR, Nebot EM (1996a) Artificial Neural Network implementation of chemistry with *pdf* Simulation of H₂/CO₂ flames. *Combust Flame* 106:406–427
- Christo FC, Masri AR, Nebot EM et al (1996b) An integrated PDF/neural network approach for simulating turbulent reacting systems. *Proc Combust Inst* 26:43–48
- Christo FC, Masri AR, Nebot EM, et al. (1995) Utilising artificial neural network and re-modelling in turbulent combustion. In: *Proceedings IEEE International Conference on Neural Networks*, vol 1. pp 911–916
- Clifford LJ, Milne AM, Turányi T et al (1998) An induction parameter model for shock-induced hydrogen combustion simulations. *Combust Flame* 113(1–2):106–118
- Colin O, Pires da Cruz A, Jay S (2005) Detailed chemistry-based auto-ignition model including low temperature phenomena applied to 3D engine calculations. *Proc Combust Inst* 30:2649–2656
- Contino F, Jeanmart H, Lucchini T et al (2011) Coupling of in situ adaptive tabulation and dynamic adaptive chemistry: An effective method for solving combustion in engine simulations. *Proc Combust Inst* 33:3057–3064
- Davis SG, Mhadeshwar AB, Vlachos DG et al (2004) A new approach to response surface development for detailed gas-phase and surface reaction kinetic model optimization. *Int J Chem Kinet* 36:94–106
- de Goey LPH, van Oijen JA, Bongers H et al (2003) New flamelet based reduction methods: the bridge between chemical reduction techniques and flamelet methods. In: *Proceedings of ECM*
- Dunker AM (1986) The reduction and parameterization of chemical mechanisms for inclusion in atmospheric reaction-transport models. *Atmos Environ* 20(3):479–486
- Dyer RS, Korakianitis T (2007) Pre-integrated response map for inviscid propane-air detonation. *Combust Sci Technol* 179:1327–1347
- Enjalbert N, Domingo P, Vervisch L (2012) Mixing time-history effects in large eddy simulation of non-premixed turbulent flames: Flow-controlled chemistry tabulation. *Combust Flame* 159:336–352
- Feeley R, Frenklach M, Onsum M et al (2006) Model discrimination using data collaboration. *J Phys Chem A* 110:6803–6813
- Feeley R, Seiler P, Packard A et al (2004) Consistency of a reaction dataset. *J Phys Chem A* 108:9573–9583
- Fiorina B, Gicquel O, Vervisch L et al (2005) Approximating the chemical structure of partially premixed and diffusion counterflow flames using FPI flamelet tabulation. *Combust Flame* 140:147–160
- Flemming F, Sadiki A, Janicka J (2000) LES using Artificial Neural Networks for chemistry representation. *Prog Comput Fluid Dynam* 5:375–385

- Frenklach M, Packard A, Seiler P et al (2004) Collaborative data processing in developing predictive models of complex reaction systems. *Int J Chem Kinet* 36:57–66
- Frenklach M, Wang H, Rabinowitz MJ (1992) Optimization and analysis of large chemical kinetic mechanisms using the solution mapping method—combustion of methane. *Prog Energy Combust Sci* 18:47–73
- Gicquel O, Darabiha N, Thevenin D (2000) Laminar premixed hydrogen/air counterflow flame simulations using Flame Prolongation of ILDM with differential diffusion. *Proc Comb Inst* 28:1901–1908
- Gicquel O, Ribert O, Darabiha N et al (2006) Tabulation of complex chemistry based on self-similar behavior of laminar premixed flames. *Combust Flame* 146:649–664
- Gilbert RG, Luther K, Troe J (1983) Theory of thermal unimolecular reactions in the fall-off range. II. Weak collision rate constants. *Berichte der Bunsengesellschaft für physikalische Chemie* 87(2):169–177
- Godel G, Domingo P, Vervisch L (2009) Tabulation of NO_x chemistry for large-eddy simulation of non-premixed turbulent flames. *Proc Combust Inst* 32:1555–1561
- Ilme M, Marsden AL, Pitsch H (2008) Generation of optimal Artificial Neural Networks using a pattern search algorithm: Application to approximation of chemical systems. *Neural Comput* 20:573–601
- Ilme M, Schmitt C, Pitsch H (2009) Optimal Artificial Neural Networks and tabulation methods for chemistry representation in LES of a bluff-body swirl-stabilized flame. *Proc Combust Inst* 32:1527
- Imbert B, Lafosse F, Catoire L et al (2008) Formulation reproducing the ignition delays simulated by a detailed mechanism: Application to n-heptane combustion. *Combust Flame* 155:380–408
- James S, Anand MS, Razdan MK et al (2001) In situ detailed chemistry calculations in combustor flow analyses. *J Eng Gas Turb Power* 123(4):747–756
- Jay S, Colin O (2011) A variable volume approach of tabulated detailed chemistry and its applications to multidimensional engine simulations. *Proc Combust Inst* 33:3065–3072
- Kee RJ, Rupley FM, Miller JA (1989) CHEMKIN-II: A FORTRAN chemical kinetics package for the analysis of gas-phase chemical kinetics. Sandia National Laboratories, USA
- Kumar A, Mazumder S (2011) Adaptation and application of the in situ adaptive tabulation (ISAT) procedure to reacting flow calculations with complex surface chemistry. *Comput Chem Eng* 35(7):1317–1327
- Lee JC, Najm HN, Lefantzi S, et al. (2005) On chain branching and its role in homogeneous ignition and premixed flame propagation. In: Bathe K (ed) *Computational fluid and solid mechanics* Elsevier Science, New York, pp 717–720
- Lee JC, Najm HN, Lefantzi S et al (2007) A CSP and tabulation-based adaptive chemistry model. *Combust Theor Model* 11(1):73–102
- Li G, Wang S-W, Rabitz H (2002) Practical approaches to construct RS-HDMR component functions. *J Phys Chem A* 106:8721–8733
- Li GY, Rabitz H, Hu JS et al (2008) Regularized random-sampling high dimensional model representation (RS-HDMR). *J Math Chem* 43(3):1207–1232
- Libby PA, Bray KNC (1980) Implications of the laminar flamelet model in premixed turbulent combustion. *Combust Flame* 39(1):33–41
- Liew SK, Bray KNC, Moss JB (1981) A flamelet model of turbulent non-premixed combustion. *Combust Sci Technol* 27(1–2):69–73
- Lodier G, Vervisch L, Moureau V et al (2011) Composition-space premixed flamelet solution with differential diffusion for in situ flamelet-generated manifolds. *Combust Flame* 158:2009–2016
- Marsden AR, Frenklach M, Reible DD (1987) Increasing the computational feasibility of urban air-quality models that employ complex chemical mechanisms. *JAPCA* 37(4):370–376
- Masri AR, Cao R, Pope SB et al (2004) PDF calculations of turbulent lifted flames of H₂/N₂ fuel issuing into a vitiated co-flow. *Combust Theor Model* 8(1):1–22

- Michel J-B, Colin O, Angelberger C (2010) On the formulation of species reaction rates in the context of multi-species CFD codes using complex chemistry tabulation techniques. *Combust Flame* 157:701–714
- Michel J-B, Colin O, Angelberger C et al (2009) Using the tabulated diffusion flamelet model ADF-PCM to simulate a lifted methane-air jet flame. *Combust Flame* 156:1318–1331
- Michel J-B, Colin O, Veynante D (2008) Modeling ignition and chemical structure of partially premixed turbulent flames using tabulated chemistry. *Combust Flame* 152:80–99
- Mosbach S, Aldawood AM, Kraft M (2008) Real-time evaluation of a detailed chemistry HCCI engine model using a tabulation technique. *Combust Sci Technol* 180(7):1263–1277
- Nagy T, Turányi T (2011) Uncertainty of Arrhenius parameters. *Int J Chem Kinet* 43:359–378
- Najafi-Yazdi A, Cuenot B, Mongeau L (2012) Systematic definition of progress variables and intrinsically low-dimensional, flamelet generated manifolds for chemistry tabulation. *Combust Flame* 159:1197–1204
- NIST (2013) Chemical kinetics database. <http://kinetics.nist.gov/kinetics/index.jsp>
- Pera C, Colin O, Jay S (2009) Development of a FPI detailed chemistry tabulation methodology for internal combustion engines. *Oil Gas Sci Technol Rev IFP* 64:243–258
- Pilling MJ, Seakins PW (1995) *Reaction kinetics*. Oxford University Press, Oxford
- Pope SB (1997) Computationally efficient implementation of combustion chemistry using in situ adaptive tabulation. *Combust Theor Model* 1(1):41–63
- Saxena V, Pope SB (1999) PDF simulations of turbulent combustion incorporating detailed chemistry. *Combust Flame* 117(1–2):340–350
- Sheen DA, Rosado-Reyes CM, Tsang W (2013) Kinetics of H atom attack on unsaturated hydrocarbons using spectral uncertainty propagation and minimization techniques. *Proc Combust Inst* 34:527–536
- Sheen DA, Wang H (2011) The method of uncertainty quantification and minimization using polynomial chaos expansions. *Combust Flame* 158(12):2358–2374
- Sheen DA, You X, Wang H et al (2009) Spectral uncertainty quantification, propagation and optimization of a detailed kinetic model for ethylene combustion. *Proc Combust Inst* 32:535–542
- Shenvi N, Geremia JM, Rabitz H (2004) Efficient chemical kinetic modeling through neural network maps. *J Chem Phys* 120:9942–9951
- Shorter JA, Ip PC, Rabitz HA (1999) An efficient chemical kinetics solver using high dimensional model representation. *J Phys Chem A* 103(36):7192–7198
- Stewart PH, Larson CW, Golden DM (1989) Pressure and temperature dependence of reactions proceeding via a bound complex. 2. Application to $2\text{CH}_3 \rightarrow \text{C}_2\text{H}_5 + \text{H}$. *Combust Flame* 75:25–31
- Taing S, Masri AR, Pope SB (1993) Pdf calculations of turbulent nonpremixed flames of H₂/CO₂ using reduced chemical mechanisms. *Combust Flame* 95(1–2):133–150
- Tang Q, Xu J, Pope SB (2000) Probability density function calculations of local extinction and no production in piloted-jet turbulent methane/air flames. *Proc Combust Inst* 28:133–139
- Tomlin AS, Whitehouse L, Lowe R et al (2001) Low-dimensional manifolds in tropospheric chemical systems. *Faraday Discuss* 120:125–146
- Tonse SR, Moriarty NW, Brown NJ et al (1999) PRISM: Piece-wise reusable implementation of solution mapping. An economical strategy for chemical kinetics. *Israel J Chem* 39:97–106
- Tonse SR, Moriarty NW, Frenklach M et al (2003) Computational economy improvements in PRISM. *Int J Chem Kinet* 35:438–452
- Turányi T (1994) Parametrization of reaction mechanisms using orthonormal polynomials. *Comput Chem* 18(1):45–54
- Turányi T (1995) Application of repro-modelling for the reduction of combustion mechanisms. *Proc Combust Inst* 25:948–955
- van Oijen JA, de Goeij LPH (2000) Modelling of premixed laminar flames using flamelet generated manifolds. *Comb Sci Tech* 161:113–137
- van Oijen JA, de Goeij LPH (2002) Modelling of premixed counterflow flames using the flamelet-generated manifold method. *Combust Theory Model* 6:463–478

- van Oijen JA, Lammers FA, de Goey LPH (2001) Modeling of complex premixed burner systems by using flamelet-generated manifolds. *Combust Flame* 127:2124–2134
- Venkatesh PK, Chang AY, Dean AM et al (1997) Parameterization of pressure- and temperature-dependent kinetics in multiple well reactions. *AIChE* 43:1331–1340
- Verhoeven LM, Ramaekers WJS, van Oijen JA et al (2012) Modeling non-premixed laminar co-flow flames using flamelet-generated manifolds. *Combust Flame* 159(1):230–241
- Vervisch PE, Colin O, Michel J-B et al (2011) NO relaxation approach (NORA) to predict thermal NO in combustion chambers. *Combust Flame* 158:1480–1490
- Wang LG, Fox RO (2003) Application of in situ adaptive tabulation to CFD simulation of nanoparticle formation by reactive precipitation. *Chem Eng Sci* 58(19):4387–4401
- Wang SW, Balakrishnan S, Georgopoulos P (2005) Fast equivalent operational model of tropospheric alkane photochemistry. *AIChE J* 51(4):1297–1303
- Xie N, Battaglia F, Fox RO (2004) Simulations of multiphase reactive flows in fluidized beds using in situ adaptive tabulation. *Combust Theor Model* 8(2):195–209
- Xu J, Pope SB (2000) PDF calculations of turbulent nonpremixed flames with local extinction. *Combust Flame* 123(3):281–307
- You XQ, Packard A, Frenklach M (2012) Process informatics tools for predictive modeling: Hydrogen combustion. *Int J Chem Kinet* 44(2):101–116
- You XQ, Russi T, Packard A et al (2011) Optimization of combustion kinetic models on a feasible set. *Proc Combust Inst* 33:509–516
- Zádor J, Taatjes CA, Fernandes RX (2011) Kinetics of elementary reactions in autoignition chemistry. *Prog Energy Combust Sci* 37(4):371
- Zhang P, Law CK (2009) A fitting formula for the falloff curves of unimolecular reactions. *Int J Chem Kinet* 41:727–734
- Zhang P, Law CK (2011) A fitting formula for the falloff curves of unimolecular reactions, II: Tunneling effects. *Int J Chem Kinet* 43:31–42

Part V
Thermodynamic and Kinetic Parameters
for Elementary Chemical Steps

Chapter 20

Calculation of Molecular Thermochemical Data and Their Availability in Databases

Elke Goos and György Lendvay

Abstract Thermodynamic properties of molecules can be obtained by experiment, by statistical mechanics in conjunction with electronic structure theory, and by empirical rules like group additivity. The latter two methods are briefly reviewed in this chapter. The overview of electronic structure methods is intended for readers less experienced in electronic structure theory and focuses on concepts without going into mathematical details. This is followed by a brief description of group additivity schemes; finally, an overview of databases listing reliable thermochemical data is given.

20.1 Introduction

Both our understanding and the reliability of predictions based on modeling complex reaction systems depend on the accuracy of the thermodynamic data of the molecules (stable molecules, radicals, individual atoms, and possibly ions) present in the system. Measurements of the most important thermodynamic properties like enthalpy, entropy and specific heat are not easy. Enthalpies of formation are derived from calorimetric experiments (Marsh 2001), which determine heats of reaction yielding unique products whose enthalpies of formation are known. To determine heats of formation of a compound, one can use Haber-Born type thermodynamic cycles (Atkins and De Paula 2005) involving reactions of the

E. Goos (✉)

Institute of Combustion Technology, Deutsches Zentrum für Luft- und Raumfahrt e.V.
(German Aerospace Center (DLR)), Pfaffenwaldring 38-40 70569 Stuttgart, Germany
e-mail: Elke.Goos@dlr.de

G. Lendvay (✉)

Institute of Materials and Environmental Chemistry, Research Center for Natural Sciences,
Hungarian Academy of Sciences, Pusztaszeri út 59-67, Budapest H-1025, Hungary
e-mail: lendvay.gyorgy@ttk.mta.hu

selected compound in which heats of formation of all other reactants and products are known. By measuring the reaction enthalpies in the cycle, one can get the heat of formation of the compound of interest. Such “ideal” reactions are complete combustion of hydrocarbons producing the stoichiometric amount of H₂O and CO₂. These methods are, unfortunately, not universally applicable because, for molecules above a certain complexity (more than about 20 atoms and/or several functional groups), design of appropriate thermodynamic cycles with well-defined stoichiometry is not simple. For example, there are species whose reactions (mostly those with multiple product channels) are very sensitive to the conditions, so that their stoichiometry is hard to control. For such reactions, the measurable “reaction enthalpy” actually refers to a set of simultaneous reactions whose relative importance is not well defined.

Even more complicated is the case of reactive species like free radicals whose heats of formation cannot be determined directly in calorimetric measurements. Instead, a completely different kind of experiments, the measurement of reaction rate coefficients needs to be performed, and heats of formation can be inferred indirectly from their data (Benson 1968).

A widely used method, the so-called Second Law analysis yields enthalpies and, in principle, entropies of reaction. The rate coefficients for the forward and reverse reaction are measured, from their ratio the equilibrium constant of the reaction and its temperature dependence is derived, and using the Van't Hoff equation enthalpies of reaction and of formation can be obtained.

The Third Law method requires the equilibrium constant at a single temperature, but the reaction entropy needs to be known from independent sources. The temperature dependence of the thermodynamic properties can be obtained from heat capacities, the measurement of which is not easier than that of enthalpies, so that the most useful is to derive them from the temperature dependence of enthalpies of formation, obtained in direct experiments.

Certain thermodynamic quantities such as dissociation and ionization energies of individual molecules can be determined by spectroscopic methods. These methods provide probably the most accurate experimental information on thermodynamic quantities. Their applicability, however, is limited: One needs to know several other data to get the desired quantity. For example, to derive the enthalpy of formation of a fragmentation product, one needs to measure the dissociation (or fragmentation) energy of the parent compound, know the enthalpy of formation of the latter and of the other fragmentation product. Spectroscopic measurements also provide molecular properties (vib-rotational energy levels etc.) from which entropies and heat capacities can be calculated.

The available thermodynamic data has been collected in databases. The earlier forms were simple printed tables (Cox and Pilcher 1970) while more recent versions are databases in electronic form with specified data formats (Gordon and McBride 1971; Kee et al. 1996) with the possibility of electronic data retrieval (Goos et al. 2013a; NIST-JANAF 2012). These tables are incomplete: The thermochemical properties are not available for all known chemical species. Even if there were experimental methods available for the determination of

thermodynamic properties of all kinds of compounds, the experiments would be hard to perform for all important species in a reactive system merely due to their enormous number: There are hundreds or thousands of species involved in a real chemical system like the combustion of fuels or even in that of a compound as simple as pure methane.

Theory can effectively help filling in the gaps in the thermochemical tables containing experimental data. Moreover, theoretical approaches can also allow correction of values that are not consistent with the rest of the data. There are two major approaches to determine thermodynamic properties of chemical species by applying computational methods. One direction is their calculation *ab initio* using up-to-date methods of electronic structure theory (quantum chemistry). The basis of these methods is that one considers the chemical system as an ensemble of atomic nuclei and electrons and solves the electronic Schrödinger equation numerically using sophisticated techniques and smart approximations. No chemical or other empirical information is used, and every molecule has to be calculated from scratch without any reference to the results obtained for related compounds. As a result, no generalization can be made except by handling the calculated data in the same way as experimental values and trying to observe tendencies and quantify them in “empirical” rules.

The other way of obtaining thermodynamic data without measurement is more empirical but very successful: It utilizes the fact that, especially in organic compounds, functional groups carry not only their chemical characteristics from one molecule to the other, but also numerical values of their physical properties. The values of the entire molecule’s physical quantities can be quite closely approximated by summing the contributions of the groups constituting the molecule. The additivity is not exact, i.e., a group’s contribution may depend on the environment, and a lot of empiricism is introduced for reliable predictions. As such, each additivity scheme is applicable only within the range of compounds it has been worked out for.

In the first part of this chapter the *ab initio* methods will be reviewed; the second will be devoted to an overview of group additivity techniques. In the third part, the available databases will be surveyed.

20.2 Calculation of Thermodynamic Properties Using Electronic Structure Theory

Electronic structure theory currently is at the level that for simple cases it can produce results that match, or even exceed the accuracy of measurements. For example, the experimental spectroscopic parameters of the H₂ molecule and its deuterium-substituted isotopomers have been reproduced by theory with almost 10⁻⁴ cm⁻¹ accuracy (Piszczatowski et al. 2009). A more complicated example is the vib-rotational spectrum of the water molecule whose spectral lines can be

assigned using the ab initio potential surface of the molecule calculated to be better than a cm^{-1} accuracy (Polyansky et al. 2003). Another example, directly connected to combustion chemistry is the standard heat of formation of the OH radical whose generally accepted value was 2 kJ mol^{-1} too low before a joint experimental and theoretical effort yielded the accurate value of $\Delta_f H_0(\text{OH}) = 8.85 \pm 0.07 \text{ kcal mol}^{-1}$ (Ruscic et al. 2002). For molecules that are more complicated, ab initio calculation of thermodynamic properties is less straightforward: The accessible accuracy decreases with the size of the molecule, expressed not only by the number of atomic nuclei, rather by the number of electrons.

The basic idea of electronic structure calculations is that the molecule (using the term in a wider sense to include radicals and ions) is taken to be a physical system consisting of atomic nuclei and electrons that interact via electrostatic forces. The description of the motion of electrons requires the use of quantum mechanics; the motion of the nuclei is at the borderline of the ranges of validity of quantum and classical mechanics. Accordingly, the accurate treatment of a system consisting of electrons and nuclei requires the solution of the corresponding Schrödinger equation.

Setting up the Schrödinger equation is trivial: The Hamiltonian operator, whose eigenvalues and eigenfunctions are searched for, consists of the kinetic energy operators of the electrons and of the nuclei and the ensemble of attractive potential energy terms describing the nucleus–electron interaction, and terms corresponding to the electron–electron as well as nucleus–nucleus repulsions (Fig. 20.1).

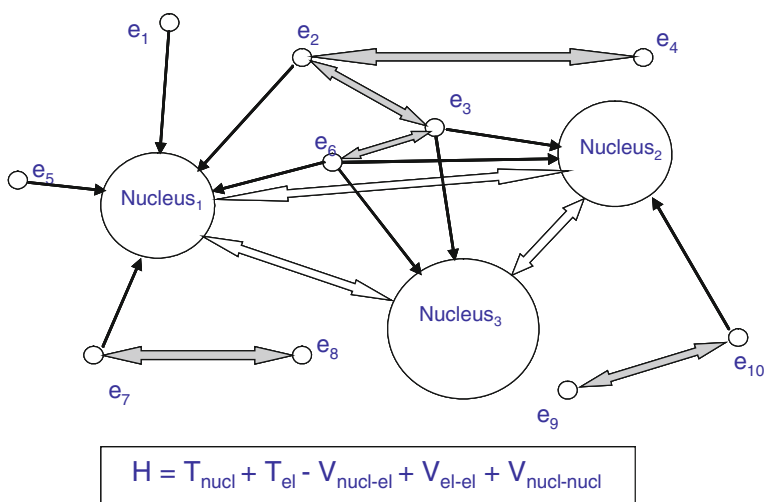


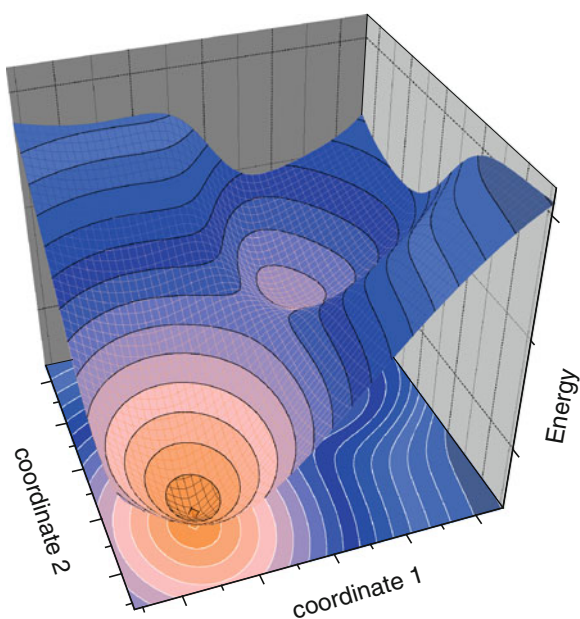
Fig. 20.1 The energy terms in the Hamilton operator for a polyatomic molecule (water in this example: Nucleus₁ = Nucleus₂ = H; Nucleus₃ = O). The *black arrows* denote attractive interactions, the *gray* and *white arrows* the electron–electron and nucleus–nucleus repulsions. Only a few examples of each kind of interaction are shown

The solution is much less trivial. No analytic solution can be written down even for the simplest systems, so that all methods of solving the molecular Schrödinger equation are based on approximate schemes. Some of the approximations are physical in nature, others are empirical in the sense that certain numerical contributions are neglected, or numerical tendencies are observed and based on them various approximate methods are constructed.

The most important approximation is the separation of nuclear and electronic motion (called *Born-Oppenheimer approximation*), based on the fact that the mass of electrons is much smaller than that of atomic nuclei (by a factor of about 2,000 for the lightest atom, protium). The reasoning is that as the heavy particles, the nuclei move, the electrons, moving much faster, can instantaneously adjust to the new Coulomb field of the nuclei. The detailed derivation shows that if certain conditions hold, the nuclear and electronic Schrödinger equations can be solved separately. Solving the electronic part at a fixed spatial arrangement (configuration) of nuclei, one obtains the energy eigenvalues corresponding to different electronic states. The eigenvalues, called electronic energies depend on the nuclear coordinates and, together with the nucleus–nucleus repulsion terms (that also depend on the nuclear arrangement), they constitute a potential energy function corresponding to each electronic state of the system. These scalar-vector functions are called potential energy surfaces (PES) and are the most important targets of electronic structure calculations (a schematic example is shown in Fig. 20.2).

A PES shows the relative energy of a chemical system (a given set of atoms) in different arrangements that may correspond to different compounds, with the

Fig. 20.2 Schematic view of the section of a potential energy surface along two coordinates. Two minima corresponding to two isomers as well as a saddle point separating them is visible



assumption that the nuclear motion is frozen. This is not what one can observe macroscopically: Thermodynamic properties refer to ensembles of vibrating–rotating molecules. Accordingly, calculation of thermodynamic observables requires further work: The knowledge of energy levels corresponding to nuclear motion is also needed. The vibrational and rotational energy levels can be obtained by solving the nuclear Schrödinger equation in which the forces acting on the atoms, represented by the nuclei are derived from the PES. Generally, approximate methods are used to estimate the energy levels of molecular vibrations and rotations.

The main purpose of electronic structure theory, often called *quantum chemistry*,¹ is then to provide a quantum mechanical description of electronic motion at fixed nuclear arrangements (referred to as nuclear or molecular geometry) and obtain the electronic energy. There are two paradigms applied for this purpose: The so-called wave-function-based methods and the density-functional-based methods (Table 20.1). The *wave-function-based methods* (wave function theory, WFT Truhlar 2008) are devoted to solve the Schrödinger equation, get the wave function and the energy eigenvalue corresponding to the given nuclear arrangement. The proper methods for the solution of the Schrödinger equation work “ab initio” (i.e., no empirical information is used) and are numerical (in contrast to being analytical).

They apply the principle of successive approximation and are often variational. If a method is variational, the best solution is the one that provides the lowest energy, so that finding the right wave function is equivalent to solving a general optimization problem. Various approximations can be introduced to make the problem tractable, but these are “controlled” in the sense that we know what we omit or simplify. As a result, in principle, the solution can be made to approach the exact value by omitting step by step the simplifications and approximations.

Density functional theory (DFT) applies a conceptually different approach, based on the Hohenberg–Kohn theorem. This theorem claims that there is a one-to-one correspondence between the energy and the total electron density at every molecular geometry (in mathematical terms, the energy is a *functional* of the electron *density*). The purpose is then to find the correct electron density, from which one can get the electronic energy at the selected molecular geometry. The problem is that the general mathematical form of the energy functional is not known and seems not to be feasible to obtain except for its qualitative behavior in limiting cases.

There are a number of approximate functional forms that contain numerical parameters. The latter are generally optimized, so that the energy calculated via the

¹ In fields where the needed molecular properties are calculated using electronic structure theory methods, one often finds the reference “quantum mechanical” to emphasize that the parameters are calculated using electronic structure theory instead of being estimated using empirical rules. This term is quite misleading as it makes the impression that the nuclear motion is also handled using the methods of quantum mechanics, which is generally done in a very approximate (rigid rotor—harmonic oscillator) way. “Quantum chemistry” is a much better term to describe the methodology in such applications.

Table 20.1 Some properties of ab initio and density functional theory-based quantum chemical methods

Property	Ab initio methods	Density functional theory methods
Object to find	Electron wave function	Electron density function
Way of improvement	Systematic	Empirical
Computational expense	Can be large	Small
Size of molecules routinely handled	Very accurate: 6 nonhydrogen average: 20–30 nonhydrogen atoms	Hundreds of atoms
Expertise needed	Very accurate: Significant, average: Medium	Little
Reliability	Very accurate: Large, average: Medium	Unpredictable
Systems not possible to handle	Large molecules, polyatomic transition metal complexes	Molecules where dispersion interactions are important

functional should match that obtained for selected systems from ab initio calculations considered to be exact. This is similar to introducing parameters that are taken from experiment, but here the external source of information is not experiment but accurate theory. Although DFT does not use empirical parameters, it can not be considered to be a truly ab initio method. This is why the term “first principles methods” (Truhlar 2008) for DFT has been introduced. A consequence of the way of selecting the numerical parameters is that the methods of DFT may work well for systems that are similar to those included in the parameter optimization set, but for those that differ significantly from the latter, the results provided by DFT may be far from good. There are numerous versions of DFT applying different functionals. Oddly enough, although DFT does not refer to the wave function directly, when the density is needed, in the majority of codes the machinery of the wave-function-based methods is applied, and the density is calculated from the wave function.

Finding the energy corresponding to the electronic motion is only one step on the way of getting thermodynamic properties of molecules. The absolute energy at a certain nuclear arrangement does not characterize a real molecule. Molecules are semi-rigid structures oscillating around some equilibrium geometry, rotating, and flying in space. The amplitude of vibrations, the speed of rotations, i.e., the internal energy corresponding to the given quantum state, as well as the velocity of flight is generally different for each molecule in the ensemble. The macroscopically observable properties are averages over ensembles of molecules in thermal equilibrium, characterized by the temperature. The population of various quantum states then follows the Boltzmann distribution. Accordingly, when thermodynamic properties are calculated, the effects of intra- and intermolecular nuclear motion, the *thermal contributions* need also be taken into account.

The accurate description of molecular vibrations and rotations also requires the application of quantum mechanics: One has to solve the Schrödinger equation for nuclear motion. The nature of motion is determined by the potential surface, more

precisely, by the shape of the PES near the equilibrium molecular structure. Any distortion of the molecule's geometry from this nuclear arrangement gives rise to forces preventing further distortion and directing the molecule back to the equilibrium. Taking into account that forces are the negative derivatives of the potential energy surface, this means that all derivatives are zero at the molecular geometry corresponding to the equilibrium and positive in its neighborhood, which means the energy is minimum at this structure.

The first step of electronic structure calculations is then finding the minimum on the potential energy surface, more precisely, the molecular geometry corresponding to it (the *equilibrium geometry*), which in numerical mathematical terms, is a multivariate optimization procedure. Once the minimum is found, one has to characterize the shape of the potential surface whose parameters go into the nuclear Schrödinger equation. Commercially available quantum chemistry packages are all equipped with programs handling the minimum search, often referred to as "geometry optimization".

Intramolecular motion is bound (in contrast to being free, like the motion of the center of mass of the molecule, which is free flight), and quantum mechanics tells that such systems have quantized energy levels. Molecules have a number of vib-rotational states having distinct energy levels and the population of these states varies depending on the temperature. These states and energy levels have to be determined in the next step on the way to thermodynamic quantities. Once the energy levels are known, the formulas of statistical mechanics can be applied to determine the values of the thermodynamic properties characterizing the molecule, the central quantity being the *partition function*. In a general case there is no analytical formula for the partition function, but various simplified models (for example, the normal mode approximation) allow one to derive such formulas. In critical cases, however, the magnitude of inaccuracy of these schemes is the same or larger than the actual effect to be calculated, so that it is necessary to apply corrections or obtain the energy levels from scratch and calculate the partition function numerically.

The molecular vib-rotational levels for relatively low-energy states are arranged systematically. The rules governing the spacing between them are generally interpreted using simplified models. These models are devoted to make possible the *assignment* of spectral transitions, so that one can tell which vibrational and rotational degree of freedom changes its quantum number from which value to which other. The most generally applicable approximate or zeroth-order model is the normal mode picture. This is based on the approximation that, if the amplitude of molecular motion is small, only that part of the PES is visited that is very close to the equilibrium geometry. Then, in the nuclear Schrödinger equation this part of the PES will determine the energy of the lowest vibrational states. Being close to a minimum, the potential surface can then be approximated as a set of quadratic terms. The kinetic energy is also a sum of quadratic terms, and for such systems with an appropriate coordinate transformation, the Hamiltonian can be decomposed into terms corresponding to separate harmonic oscillators that are called *vibrational modes*.

For an N -atomic molecule there are $3N-6$ such modes ($3N-5$ if the molecule is linear). For the normal-mode harmonic oscillators the energy levels are equally spaced, the spacing being h (Planck's constant) times the frequency ν that the oscillator had if it was classical, starting from a nonzero energy level $1/2 h\nu$.

At absolute zero temperature, all oscillators in a thermodynamic (canonical) ensemble occupy the lowest energy level (for this it is called the zero-point energy). For harmonic oscillators, there is a simple analytical formula for the partition function and other thermodynamic properties. It should be mentioned that the normal-mode picture is an approximation and in reality the normal vibrational modes are "coupled" to each other because of the failure of the quadratic approximation of the PES. This means that within the amplitude of vibration the PES deviates from the quadratic shape, higher order terms arise that first destroy the harmonicity of the vibration (levels are not equally spaced) then the separability of normal modes (meaning that the frequency of one vibration depends on the excitation of the other).

An additional complication is that molecules also rotate. At low excitation, rotation and vibrations can be considered separable (the rigid-rotor-harmonic oscillator, RRHO approximation). Then the partition function is also separable into terms corresponding to various degrees of freedom: Translational, vibrational, rotational, and electronic contributions that can be calculated from analytical formulas. It has to be kept in mind, however, that this picture is an approximation. The formulas can be found in many textbooks and reference works, they are not presented here.

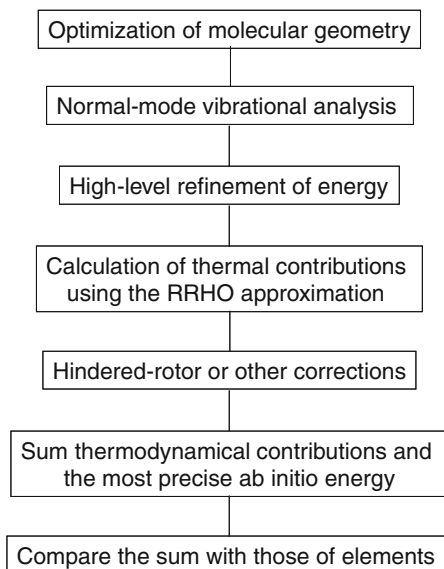
The most frequently occurring problem causing the failure of the RRHO approximation is that certain vibrational (most of the time torsional) modes have very low frequencies. It often happens that the torsional motion, a hindered internal rotation has a low barrier, so low that it is lower than the second (or sometimes even the first) harmonic vibrational energy level, causing the obvious failure of the approximation. There are several correction schemes for treating hindered rotors (Pitzer and Gwinn 1942; Ayala and Schlegel 1998; Ellingson et al. 2006; Vansteenkiste et al. 2006).

Most quantum chemistry codes are set up to perform the calculation of vibrational frequencies and the motion of atoms in the normal vibrational modes (the procedure is called *vibrational analysis*). From the equilibrium geometry of the molecule, the principal moments of inertia are calculated, from which the (rigid-rotor) rotational contribution to the partition function is obtained. The thermodynamic parameters are generally calculated using the RRHO approximation. The corrections that go beyond the RRHO approximations are generally handled with the user's own codes, although some quantum chemistry codes do contain ways for the automatic calculation of hindered-rotor partition functions.

The block diagram of the overall procedure is shown in Fig. 20.3. The need for the third block will become clear in the next section.

The theory described above is based on the Schrödinger equation written down for the electrons and nuclei of the molecule; no external interaction is taken into account. This is a good approximation for molecules in the gas phase. In

Fig. 20.3 The flow chart of the calculation of molecular thermodynamic parameters ab initio



condensed phase systems, the interaction with the neighboring molecules is much stronger than in the gas phase, but it generally does not completely destroy the picture working for the internal motion, yet the thermodynamic parameters generally differ significantly from the gas phase case. If the molecule in question is embedded in a liquid and forms a dilute solution, the solvent's electrostatic interaction with the electrons of the molecule can be included into the electronic structure part of the calculation. The precise calculation of the thermodynamic properties and the handling of solutions that are not diluted goes beyond the possibilities of ab initio quantum chemistry. Similar is the case of solids, whose quantum mechanical treatment requires completely different approaches and technologies. We do not detail these methods in this chapter.

20.3 Electronic Structure Methods

The ab initio methods available for routine calculations are all approximate. The mathematical details are often very complicated. The present description is intended to introduce the reader not familiar with electronic structure theory to the principles only, without any mathematical formulas, and as such, it is not absolutely precise in certain aspects. The emphasis is placed more on the hierarchy of approximations and the basic concepts and principles of electronic structure calculations. For interested users, a list of textbooks is provided at the end of the section.

Beyond the Born–Oppenheimer separation described in the previous section, the second approximation in most of the electronic structure methods currently in

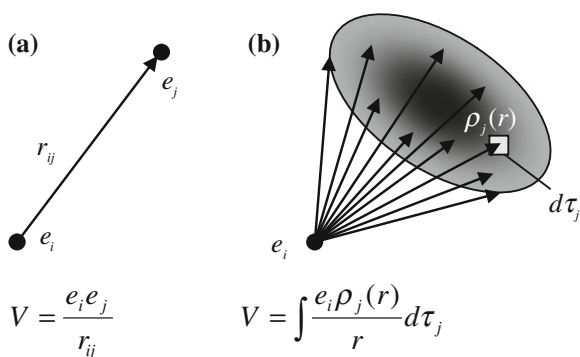
routine use is that electronic motion is described by the nonrelativistic electronic Schrödinger equation. Application of relativistic quantum mechanics is desirable, especially for compounds containing heavy atoms because of the high speed of the innermost electrons in the latter. There are various approximate methods to remedy the missed effects.

The third approximation is that most *ab initio* methods are based on the one-electron approximation or Hartree-Fock (HF) method, and various corrections are applied *a posteriori*. The HF method is based on a formal decomposition of the polyelectronic Hamiltonian into terms each depending on the coordinates of only one electron. The eigenfunctions of such Hamiltonians are the products of one-electron wave functions called *molecular orbitals* (MO). The equations are made a bit complicated by the fact that electrons are fermions, and the Pauli principle requires that the wave function be antisymmetric with respect to exchange of any two electrons. In particular, the simple product of MOs does not fulfill this requirement; the antisymmetry is achieved by summing all permutations of electrons among the MOs each with the proper sign (which is equivalent to forming a determinant, called Slater determinant).

The one-electron Hamiltonian of electron i contains its kinetic energy operator, the attraction exerted on it by the nuclei of all atoms in the molecule, and the sum of the average repulsion due to each of the rest of the electrons (the *mean* electron repulsion *field*). The average interaction between the selected electron i and another electron j depends on the location of electron i but not on that of electron j , because the potential energy is averaged over the spatial distribution of the latter. This is achieved by assuming that we know the wave function (the MO) of electron j ; then its square will give the probability that electron j is located at any selected point in space, which, multiplied by the charge of the electron is a charge density.

The overall interaction of the “cloud” of electron j with electron i (the latter being at a given point in space, Fig. 20.4) is the average of the interaction of the “parts” of electron j at each space element with electron i (an integral over the coordinates of electron j). This is an approximation that makes possible the decomposition of the polyelectronic Hamiltonian into one-electron terms. What we miss this way from the exact Hamiltonian is that, as electron i “feels” only the

Fig. 20.4 **a** The real interaction of two electrons: repulsion of two point charges. **b** The electron–electron interaction in the one-electron approximation: electron e_i is repelled by a diffuse charge distribution $\rho_j(r)$ corresponding to electron e_j



$$V = \frac{e_i e_j}{r_{ij}}$$

$$V = \int \frac{e_i \rho_j(r)}{r} d\tau_j$$

average repulsion of electron j , it can penetrate the cloud of the latter, instead of continuously “watching” where the other electron actually is and adjusting its own motion to avoid getting close to the other. In other words, in this model the motion of electrons is not *dynamically correlated*.

The wave function of electron i is the eigenfunction of the Hartree–Fock Hamiltonian or Fock operator. The latter contains the wave functions of all other electrons in the average repulsion terms. Those wave functions, however, are eigenfunctions of the respective Fock operators that can be written down and solved if we know the wave functions of the rest of electrons, including electron i . This problem is solved iteratively, by successive approximation: A set of trial wave functions is generated (often called initial guess), then the electron–electron repulsion (and some other) integrals are calculated, and each one-electron Schrödinger equation is solved, yielding a set of wave functions each of which changes from the initial guess, because they adjust themselves to match the mean field generated by the other electrons. This way a new repulsion field arises. These modified wave functions are fed again into the Fock operators, the eigenfunctions are found, and the procedure is repeated until the wave functions reproduce themselves, in other words, the Coulomb field is consistent with itself. This is called the *self-consistent field* (SCF) method, often meant to be synonymous to the HF method.

The question is how one can generate MOs that are flexible so that

1. they should be able to describe electron density where it is needed (near atoms, with the possibility of distortion towards other atoms) and
2. be easy to modify during the iteration.

It is hard to find simple analytical functions that fulfill these requirements. What helps is a theorem of quantum mechanics, which states that all wave functions can be expanded in terms of any set of functions that constitute a so-called *complete basis*. This means that the desired wave function can be constructed as a linear combination of the basis functions each having the appropriate coefficient. (It should be noted that a complete basis is always infinite-dimensional). Selecting a basis set, the MOs can be modified by changing the weights of the basis functions in the linear combination. The basis sets we can actually use are never complete in the mathematical sense (we can never use an infinite number of functions). The larger the number of basis functions, the more computationally intense is the solution of the Schrödinger equation. The good basis functions are those that look similar to what the desired orbitals look like, and only slight modifications need to be made. According to accurate numerical calculations, the one-electron wave functions of free atoms and, if they are in molecules, those of their inner shells resemble in shape those of the H atom (s, p, d etc. orbitals). This suggests that sets of wave functions, centered at nuclei and shaped like H-atom orbitals could be efficiently used as basis sets: From such atom-centered basis functions called *atomic orbitals* (AO) a relatively low number needs to be “mixed” to get a molecular wave function. Application of this principle constitutes the fourth approximation used in ab initio methods: The one-electron wave functions (the

MOs) are constructed from AOs by linear combination (LCAO-MO method). The variation of the MOs during the SCF iteration is possible by adjusting the linear combination parameters, the AO coefficients. Thus, the solution of the polyelectronic integro-differential Schrödinger equation is converted into a linear algebraic, matrix eigenvalue problem for which well-established and efficient numerical mathematical tools have been worked out.

The atomic orbital basis sets used in the expansion of MOs have to fulfill several criteria for making the solution of the Schrödinger equation efficient. There have been a number of basis sets worked out for LCAO-MO calculations and many of these are built into the commercial quantum chemistry codes or are available on the Internet (EMSL Basis Set Library webpage 2013; Schuchardt et al. 2007). The AO basis sets consist of hydrogen-type functions with varying parameters. This guarantees that the shape of the AOs is “almost good” at the atomic cores. A good set of atomic core wave functions is transferable from molecule to molecule. What is critical for the correct description of chemical bonds in molecules is the selection of valence orbitals. The application of several functions similar in shape, differing only in how far they extend from the nucleus enables one to describe the electron density farther from atomic nuclei, in regions between atoms (*split-valence basis sets*).

For technical reasons, the AOs generally are built from Gaussian functions of the distance from the atomic nucleus (Gauss-type orbitals, GTOs). This has a historical origin: In the 1950s, analytical formulas (series expansions) for integrals expressing the interaction of electrons were easier to derive than those for the (more appropriately shaped) exponential functions (Slater-type orbitals, STOs). Each hydrogen-type AO consists of a linear combination of GTOs with different width parameter and weight in the sum. Often a group of GTOs are *contracted*, so that their relative weights are kept constant and the group constitutes one AO.

Generally, the ensembles of sets of AOs for various atoms of the periodic table are referred to as basis set families. The GTO parameters for a family of AOs in a basis set are optimized to reproduce some target. In the early days of ab initio calculations, every researcher developed his own basis set for the molecule to be studied. Later “universal” basis set families were developed.

In the case of the so-called Pople-type basis sets (Hehre et al. 1971), the target is a set of experimental parameters like atomization energies for a group of molecules. A widely used example of Pople basis sets is that denoted as 6-31G(d) that has been worked out for all atoms of the periodic table. This basis set and its extensions (such as 6-311++G(3df,2p); generally the longer the notation, the better the basis set) work very well for the determination of equilibrium geometries of common organic molecules.

A different principle guides the selection of the optimization target for some other basis sets: They are intended to reproduce the results of very accurate ab initio calculations (mostly performed for atoms) or are derived from those. The correlation-consistent basis sets developed by Dunning and coworkers (Dunning Jr. 1989) (the basic example being the cc-pVDZ set) and the ANO (atomic natural orbital) basis sets first proposed by Almlöf and Taylor (1987) belong to this class.

Each basis set type has a number of extensions, the largest basis sets allowing the estimation of the HF energy in the infinite basis set limit, which is the accurate solution of the HF equations. This way the error caused by the fourth approximation in Table 20.2 can be recovered. If the number of orbitals in a basis set is K , the SCF procedure generates K MOs whose orbital energies are generally different. If there are N electrons in a molecule, then in the ground (lowest-energy) state of the molecule the *electron configuration* consists of the $N/2$ lowest-energy MOs filled with two opposite-spin electrons (if N is odd, $N = 2M + 1$, a single electron occupies the $M + 1$ -th MO). The MOs that are filled by electrons are called occupied MOs; the rest constitutes the ensemble of virtual MOs. In the calculation of the total electronic energy of the molecule, only the occupied MOs count.

Even if a *de facto* complete basis set is used, the exact solution of the HF equations is not the exact solution of the molecule's electronic Schrödinger equation, because the effects of electron correlation are not included in it. The exact energy eigenvalue is lower than that of the HF energy, by the amount that is called *correlation energy*. This is the error caused by the third (mean field) approximation in Table 20.2.

The computational (and intellectual) effort to correct the lack of electron correlation in the HF method is much larger than getting the HF energy and wave function. There are numerous methods for estimating the correlation energy, which are able to recover the correlation energy to various levels. The highest level methods can approach the accurate solution of the full nonrelativistic electronic Schrödinger equation very closely.

The principal fact that constitutes the foundation of these methods is that the set of all electron configurations (the assignment of electrons to different MOs, including now those that are unoccupied in the ground state) constitutes a basis set for the given molecule that allows the calculation of the correlation energy. The configurations are generally derived from the ground-state configuration as a reference, by “moving” one, two, three etc. electrons from an occupied to a virtual MO. Knowing the configurations, the molecule's wave function is expressed as the linear combination of configurations and the energy is calculated using the *exact nonrelativistic Hamilton operator*. The best wave function will be the one that

Table 20.2 The hierarchy of approximations of quantum chemistry

Approximation	Main feature not covered	Occurrence of failure
Born-Oppenheimer separation of electronic and nuclear motion	Nonadiabatic effects	Mostly away from equilibrium geometries
Nonrelativistic electronic Schrödinger equation	Inner shell relativistic effects; spin-orbit coupling	Mostly in compounds of atoms with large atomic number
One-electron (mean field) approximation	Dynamical and chemical electron correlation	Everywhere
Expansion of molecular orbitals in terms of atomic orbital basis sets	Accuracy because of incompleteness of basis set	Everywhere

provides the lowest energy, which is found by varying the linear combination coefficients. This method is called *configuration interaction* (CI). When *all possible* configurations arising from a HF calculation are used in the expansion, the method is the full configuration interaction (FCI) method (which is not necessarily the accurate solution, because the basis set for which such a calculation is possible is generally not close to complete). For large basis sets, the number of configurations can be huge (billions even for molecules with a few nonhydrogen atoms) and in practice is reduced according to different principles. The simplest principle is that only configurations coming from the HF ground-state configuration by single, double etc. *excitations* (in which at most one, two etc. electrons are simultaneously “moved” from occupied to virtual orbitals) are included in the expansion, constituting the CI-singles (CIS), CI-singles and doubles (CISD) etc. methods. Except for the CIS method, which provides the same energy as the HF method (but is good to estimate the energy of excited states), the CI methods are considered to produce very accurate energies, accounting for as much as 99 % of the correlation energy. The price, however, is high: With a reasonably large basis set, CISD calculations can be performed only for molecules containing not more than 10 or 20 nonhydrogen atoms.

Another approach to the calculation of the correlation energy is perturbation theory. The most commonly used version is *Møller-Plessett perturbation theory*, in which the “unperturbed” problem is the HF description of the system under consideration and the perturbation is the difference between the accurate and the HF Hamiltonian. Using perturbation theory, actually a number of selected excited configurations are introduced into the wave function. The “price”, the computational time and the memory and/or disk requirement increases quickly with the size of the system and the order of perturbation; in routine calculations higher than fourth-order perturbation theory is rarely applied. The goodness of the results rarely converges with the increase of the order of perturbation. The second-order version, MP2, theory accounts for approximately 60 % of the correlation energy. The third-order version, MP3, often yields worse results than MP2. MP4 generally produces very good results, but the computation time is comparable to the CI calculations. Care should be taken when applying MP theory: It is deemed to fail for systems where there are low-lying excited states (because the perturbational correction, which is expected to be small, contains the difference of the excitation energy in the denominator that is low in this case).

The other class of perturbational type theories is the *coupled cluster* (CC) approach, which is currently considered to be the most promising approach, producing benchmark results for other approximate methods. In the CC methods, a special principle is used to systematically increase the number of configurations to be included in the wave function. The state-of-the-art energy calculations are performed using the CC singles-doubles version supplemented by various approximate treatments of the triple excitations denoted as, for example, CCSD(T). The widely used QCISD(T) (Quadratic CI...) method, originally developed as a CI procedure, proved to be a truncated version of CCSD(T).

The HF method, by its nature, is not able to describe certain situations, where the problem is that the Slater determinant contains various arrangements of electrons among atoms with equal weight, this way producing a wave function that is physically incorrect. What is missed in such cases is the so-called *nondynamical* or *chemical correlation*. Textbook examples for such are the decomposition of the H₂ molecule (the HF wave function at large H–H distances yields an H⁺ and an H[−] ion instead of two atoms) and the ozone molecule. The right way of describing the electronic structure of this kind of molecules is inclusion of several configurations from the beginning. Selecting the most important electron configurations like in the valence bond method of early quantum chemistry requires care and is hard to automatize (in fact, the configurations should be selected by hand). There is, however, a version, the *complete active space (multiconfiguration) self-consistent field* (CAS [MC]-SCF) method, for which smart automatic algorithms have been worked out. The basic idea is that one selects the set of occupied and virtual orbitals explored preciously in a HF calculation as the ones between which electrons are allowed to “move” (generating new configurations). This is called the active space. The number of included occupied orbitals will determine the number of electrons (say m) that can be moved. In the CAS-SCF version of the MC-SCF method all possible configurations that can be generated within the active space are included in the expansion (which is nothing but a full CI calculation within the active space). Then, the coefficients and the atomic orbitals in the MOs *and* the coefficients in the CI expansion are simultaneously optimized. One often used notation for the method includes the number of orbitals in the active space (n) and the number of electrons (m) like CAS(m,n) or [n,m]-CASSCF. The number of configurations rises quickly with the size of the active space and the number of electrons; routine geometry optimizations are hard to do for larger than CAS(14,14) combinations. What is the key, however, is the kind of orbitals in the active space. It is desirable to include the antibonding pair of each included bonding MO (for example, a $\sigma(\text{C–C})$ MO together with the corresponding $\sigma^*(\text{C–C})$ type MO). The selection of MOs included in the active space is critical; with the wrong orbitals completely incorrect results can be obtained (they can correspond to some exotic excited state). An additional complication is that the method does not cover the correlation energy involving the electrons outside of the active space. This can be remedied by various perturbational schemes that in routine calculations rarely go beyond the second order. Even less routine are CI calculations starting from MC-SCF wave functions as references (MR-CI). Codes capable of doing such calculations should not be used as black boxes. The use of the CAS-SCF method and its extensions is recommended only for advanced users.

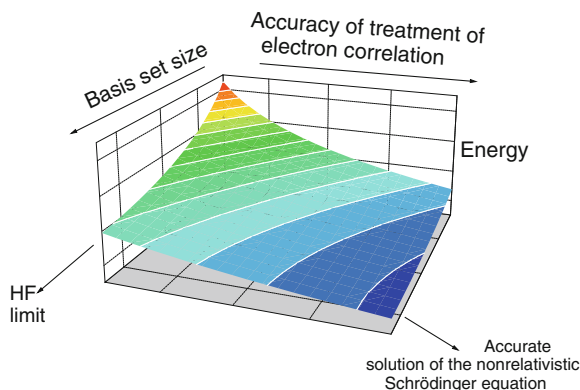
As mentioned in [Sect. 20.2](#), density functional theory is a conceptually different approach: It is intended to handle electron correlation from the beginning. The difficulty is that the way of doing so is not known and only approximate, more-or-less ad hoc formulas are used. However, these formulas and their parameterization have been worked out with amazing intuition, so that the resulting methods work very well, especially for the determination of molecular geometries—at dramatically lower computational cost than ab initio methods producing the same

accuracy. The relative energies are less accurate, especially for potential barriers of reactions. Most DFT methods also fail when the role of dispersion-type interactions are important in determining molecular geometries. There is an intense search for methods to cover dispersive interactions, mostly in empirical ways.

Even with various levels of sophistication, *ab initio* and first principles methods remain approximate. As was shown above, electronic structure theory is based on some fundamental approximations. The inaccuracies caused by the two lowest-level approximations, the expansion of MOs in AO basis sets and the mean field approximation can be corrected by using a large enough basis set and a high enough treatment of electron correlation. This allows one, in principle, to obtain the accurate solution. In real calculations, however, there are limitations: For large molecules, a high-level treatment of electron correlation cannot be performed with currently available computers. Calculations using the most accurate methods are out of reach already for moderate-sized molecules containing as few as 10 or 20 nonhydrogen atoms. In order to utilize the available computing power, one needs to select a method to be used. A so-called model chemistry (Hehre et al. 1986) is specified by the electronic structure method used (HF, a DFT parameterization or some *ab initio* level of treating electron correlation) and the basis set used for the MO expansion. The combination of the method and the basis set is also referred to as “level of theory”. There is a systematic change in the accuracy of various levels of theory.

The Pople diagram in Fig. 20.5 shows the basic principles. The two important properties that control the accuracy of a calculation are the basis set and the level of handling electron correlation. Basis sets of increasing size (or completeness) are placed on the *x* axis, and the methods of higher and higher level of electron correlation treatment are along the *y* axis (horizontal in the figure), with the HF method being at the origin. A point on the diagram corresponds to a level of theory. The qualitative change of energy is shown along the depth axis (vertical in the figure). The goal is to get the accurate solution of the nonrelativistic Schrödinger equation, the complete basis limit of the perfect treatment of electron correlation, which is far in the direction of the bottom right corner of the diagram.

Fig. 20.5 The change of the energy calculated for a system by solving the electronic Schrödinger equation with *ab initio* methods, with the increase of the basis set and of the level of treatment of electron correlation (a modified version of the original Pople diagram)



With the increase of the basis set along the x axis (without any treatment of electron correlation) the energy becomes lower and lower, sooner or later converging to the HF limit. If one uses a relatively low level of electron correlation treatment (e.g. MP2), the tendency is the same but the energies are consistently lower than the corresponding HF energies, etc.

When chemical properties of a series of molecules are needed, the level of theory (the model chemistry) should be selected, so that the smallest and largest molecule in the set could be treated with it. The results will not be consistent if for each molecule one uses the highest level of theory allowed by the available computational resources. Somewhat different attitude is more efficient when thermodynamic properties of a set of molecules are needed. In this case, the main issue is not that the qualitative and quantitative features be obtained with comparable accuracy; instead, we need accurate data.

In such a case, it is better to use a high-level theory for the small molecules in the set, and test less accurate methods against experimental data and/or the high-level theory as benchmarks. This enables one to select the method that proves to provide acceptably accurate results for the handling of the larger molecules in the set. Often one can observe some compensation of errors, so that a relatively low level of theory produces better agreement with the experiment than a somewhat higher level. Care should be taken in such cases, because it is hard to predict where the errors start not to compensate each other. It is important to note that when thermodynamic cycles are formed, only energies calculated with the same level of theory should be used for each compound in the cycle. If in a set the same molecule appears in different thermodynamic cycles described at different levels of theory, it has to be re-calculated at each level used for the other members in the respective cycle.

Acknowledging that electronic structure methods are approximate, but there are well-defined regularities in the details of the calculations, a number of composite electronic structure methods have been worked out. One can generate his/her own method that is optimized for the selected set of molecules. There are several "empirical" observations underlying the development of composite methods.

The first is that the goodness of the molecular geometry converges much faster than the goodness of energy. When a molecule's geometry is optimized, and one starts from scratch, an efficient strategy is that the first optimization is performed at a relatively low theoretical level. If one optimizes a guessed molecular structure for example successively with the HF, MP2, CCSD, and CCSD(T) methods, each optimization starting from the result of the previous lower level, the geometry change in the HF \rightarrow MP2 step will generally be relatively large, then much smaller in the MP2 \rightarrow CCSD step and generally negligible in the last. In addition, the error introduced by calculating the energy not at the optimum geometry corresponding to the given level of theory but at that from a lower level is relatively small.

The next observation is that the vibrational frequencies needed for statistical thermodynamics converge even faster. In addition, the frequencies with a given method differ systematically from the experimental ones (for example, the HF/6-

31G* method in average overestimates the frequencies by a factor of about 1.1). This enables one to obtain good frequency sets by using a relatively low-level theory and employing “empirical” scaling factors.

The third observation is that, once the basis set is large enough, the improvement of the energy when one step from one basis set to a higher one is approximately the same with a lower and a higher level of electron correlation treatment.

Applying such observations one can simulate a high-level calculation from the results of lower level calculations. A classical composite or multilevel scheme is the Gaussian-2 method of Pople and coworkers (Curtiss et al. 1991). In this method, the geometry is first optimized with the HF/6-31G(d) method, and vibrational frequencies are also calculated at this level. Then the geometry is re-optimized with the MP2/6-31G(d) method, and further calculations are performed at this geometry, treating the electron correlation at increasingly higher levels. The basis set is smaller and smaller as one goes from MP2 to MP4 and QCISD(T). (In the Pople diagram this corresponds to starting at a point relatively close to the origin on the correlation treatment axis but far from the origin along the basis set axis, at a large basis set, and stepping simultaneously one to the right and one toward smaller basis sets, always stretching the available computational power to approximately the same level.) Then the additive basis set corrections are stepwise collected and added to the QCISD(T)/6-311G(d,p) energy and with an empirical correction that depends on the number of electrons, a simulated QCISD(T)/6-311++G(3df,2p) energy can be obtained. Thermodynamic properties (originally, atomization energies) are calculated from these energies and the scaled HF/6-31G* frequencies of the compounds in the thermodynamic cycle.

Along these lines many composite methods have been developed. DFT has also been included, because it produces MP2 quality geometries at essentially HF price. It is important to note, however, that these methods are optimized for a set of molecules in a statistical sense, and for different members of the set the accuracy can be different. For example, halogen-containing molecules often form an island of large experiment–theory deviations. The more similar the molecules in a set to be studied are, the larger is the possibility to work out a project-oriented composite method. The condition for this is that the set should contain several members for which reference data are available for testing.

For the interested reader, here we list some textbooks of different levels that can be used to understand the physical, mathematical, and computational details used on electronic structure methods.

1. Introduction to Computational Chemistry (Jensen 2006): A comprehensive textbook on up-to-date methodology. It provides basic information not only on electronic structure methods, but also on statistical mechanics. Applications are also listed.
2. Molecular Electronic-Structure Theory (Helgaker et al. 2000, 2013): Another excellent comprehensive advanced textbook covering the foundations and mathematical details of electronic structure theory, including computational aspects.

3. *Quantum Chemistry: Fundamentals to Applications* (Veszprémi and Fehér 1999): A readable and didactic introduction to the basics of electronic structure theory; numerous applications are presented that help the reader to get hands-on experience.
4. *Ab Initio Molecular Orbital Theory* (Hehre et al. 1986): A textbook written for a chemist user, covering the foundations and a lot of applications at the level of the 1980s. The philosophy of the Pople school (work out methods that can provide accurate results approaching experiments, using empirical corrections if needed) can be well understood.
5. *Exploring Chemistry with Electronic Structure Methods* (Foresman and Frisch 1996): Intended to be a “manual” to the Gaussian suite of programs, this book contains a lot of applications that help the reader to learn how to do certain calculations. There are a number of practical tricks and caveats where a slightly incorrect calculation provides vastly incorrect results.
6. *Approximate Molecular Orbital Theory* (Pople and Beveridge 1970): Written at the time when ab initio quantum chemistry was not routinely used, the book is an excellent presentation of the foundations of theory and the philosophy of introducing approximations and the use of empirical parameters.
7. *Quantenchemie. Ein Lehrgang* (Zülicke 1973; Zülicke 1985): Another excellent textbook, written in German and also available in Russian, covering the quantum mechanical foundations and the mathematical details of quantum chemical methods.
8. *The Molecular Orbital Method and the Reactivity of Organic Molecules* (Basilevsky 1969; in Russian): The first part of this book provides an excellent brief introduction to Hartree–Fock theory. Although methods for accurate thermodynamic calculations are not included, the second part of the book covers a comprehensive overview and introduction to the application of the Hückel method to chemical problems that is instructive for a beginner.
9. *Theorems, proofs, and derivations in quantum chemistry* (Mayer 2003): A treatise written for advanced users, focusing on the physical and mathematical foundations and details many of which are just touched in regular textbooks. The book is self-contained: Proofs of all theorems are provided, satisfies even the “purist’s” expectations.
10. *Quantum Theory of Molecules and Solids* (Slater 1963–1974, 4 volumes): A comprehensive set of monographs covering all details of earlier quantum chemical methods.
11. *Essentials of Computational Chemistry, Theories and Models* (Cramer 2004): A textbook providing details extending from molecular mechanics, molecular orbital theory, and density functional theory to methods to calculate thermodynamic properties and some of its technical caveats, as well as spectroscopic properties of gaseous species. Additionally, it provides information about implicit and explicit models for calculation in condensed phases. Corrections for errors found in the book are reported on the Internet (Cramer 2013).

12. Quantum Chemistry (Levine 2007): This excellent textbook provides a solid basis for understanding physical and mathematical aspects of quantum mechanics and molecular electronic structure theory with clear explanation and hints about pitfalls. Examples with calculation results are used to explain the methods and limits of their applicability.

20.4 Additivity Schemes

A basic principle of chemistry is that the properties of functional groups are “almost” transferable from one compound to the other. While the transferability of chemical properties is hard to quantify, investigation of interrelationship of measured physical chemical properties of related compounds like heats of formation, yielded quantitative rules that allow the calculation of properties of unknown compounds from data on related ones. Transferability of properties means that the thermodynamic quantities of a compound can be obtained by summing the contributions from its constituent subunits. The crudest approximation, namely, that properties of atoms are transferable (which is not bad, for example, for paramagnetic susceptibilities) does not work in thermodynamics. At the next level, bonds, additivity of thermochemical properties works better (Pitzer 1940; Platt 1947; Platt 1952; Janz 1955; Greenshields and Rossini 1958; Janz 1958; Somayajulu and Zwolinski 1966), especially for well-defined classes of compounds, for example, hydrocarbons, but it is not accurate when used for a wide range of substances. It is the next level of complexity, that of properly selected groups of atoms (related, but not necessarily identical to functional groups in chemistry), for which thermochemical properties prove to be transferable. The scheme proposed by Benson and Buss (1958) became the most widely applicable (see also (Laidler 1956; Allen 1959) and (Cox and Pilcher 1970) about the equivalence of the three approaches). This method is widely referred to as “group additivity” scheme (maybe “group contribution additivity” would express more the idea beyond it).

In the terminology of Benson (Benson 1968), a group is “a polyvalent atom (ligancy ≥ 2) in a molecule together with all of its ligands”, denoted as $X-(A)_i(B)_j(C)_k(D)_l$, where X is the central atom attached to i atoms of the sort A , j atoms of sort B , and so on. The prototype groups in hydrocarbons are $C-(C)(H)_3$, $C-(C)_2(H)_2$, $C-(C)_3(H)$, and $C-(C)_4$, also denoted as P , S , T , Q , respectively, for primary, secondary etc. The heat of formation (or entropy, or heat capacity at a given temperature) of a molecule will be the sum of the contributions of these groups. For example, the heat of formation group values (GV), also referred to as group additivity value (GAV), for the $C-(C)(H)_3$ and $C-(C)_2(H)_2$ groups are $-41.8 \text{ kJ mol}^{-1}$ and $-20.9 \text{ kJ mol}^{-1}$, respectively (Cohen and Benson 1993). The estimated heat of formation of ethane (two P groups) then is

$$2 \times \text{GV}(\text{C}(\text{C})(\text{H})_3) = 2 \times (-41.8 \text{ kJ mol}^{-1}) = -83.6 \text{ kJ mol}^{-1}$$

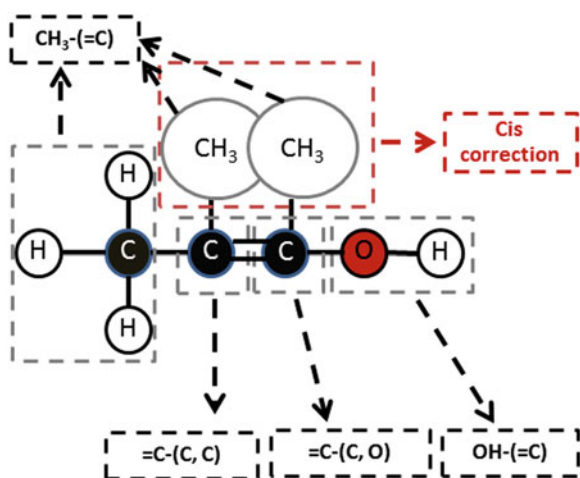
and propane (two P and a S group) one gets

$$2 \times \text{GV}(\text{C}(\text{C})(\text{H})_3) + \text{GV}(\text{C}(\text{C})_2(\text{H})_2) = 2 \times (-41.8 \text{ kJ mol}^{-1}) - 20.9 \text{ kJ mol}^{-1} \\ = 104.5 \text{ kJ mol}^{-1}.$$

Better estimates can be obtained if one takes into account the next neighbor atoms also. Such units are called components. The evaluation of component contributions requires a large, very accurate experimental database, and due to the lack of such, only a few component evaluations are available. As a result, component additivity values are not routinely used in additive estimates. Instead, the type of atoms are distinguished, for example for carbon the hybrids sp^3 (C), sp^2 (C_d), sp (C_t), aromatic sp^2 (C_b), and fused ring aromatic (C_{bf}) and allenic, $=\text{C}=\text{C}_a$ (Fig. 20.6). In addition, ring strain and nonbonded interactions are also taken into account, such as the repulsive 1,4 or *gauche* interaction of two methyl groups, and the *cis* and *ortho* interactions. Attempts were made to evaluate other noncovalent interactions, for example hydrogen-bonding interactions between two OH groups in vicinal diols and related compounds (Cohen 1996). However, not many went into common practice, partly due to the lack of accurate experimental data, and partly because of the intrinsic nonadditivity of the contributions of such extended groups. The same holds for the group values of heteroatoms such as sulfur, phosphorus, halogens or silicon, and corrections for their noncovalent interactions. It is important that care should be paid to the proper consideration of symmetry numbers when entropy contributions are calculated. GVs and interaction values are listed in several papers and books (Benson 1968; Cohen and Benson 1993; Poling et al. 2001).

The procedure of estimating the thermochemical properties of a compound is then:

Fig. 20.6 Representation of an unsaturated alcohol with a branched hydrocarbon chain by Benson-type groups



1. Write down the structural formula of the compound;
2. Analyze the structure, find the groups constituting it and count the occurrences of each type (an example is shown in Fig. 20.6);
3. Take into account the possible nonbonding interactions and count them by type;
4. Look up the group values in a compilation, multiply them by the number the group or interaction occurs in the compound, and sum them all.

This is an algorithm that is easy to program and several computer codes have been developed for the purpose (Stein et al. 1991 (NIST S&P); Ritter 1991; Ritter and Bozzelli 1991 (THERM); Muller et al. 1995 (THERGAS); CHETAH 1998; Blurock et al. 2012; RMG webpage 2012) (for the parameters used in CHETAH see Poling et al. (2001)). Some useful remarks on the applicability of the first three codes can be found in (Burcat 2009).

An interesting development is the evaluation of GVs for groups corresponding to transition structures (Cohen 1982; Cohen 1991; Sumathi et al. 2001a; Sumathi et al. 2001b; Sumathi et al. 2002) that can be used in the approximate calculation of reaction rate coefficients.

It should be noted that the accuracy of GVs depends not only on how accurately the additivity assumption is fulfilled but also on the reliability of the experimental database. Inconsistencies in the database yield ambiguous GVs. The most reasonable way of reducing the influence of data inconsistency is the use of active tables such as the Active Thermochemical Tables (see Sect. 20.5) developed at Argonne National Laboratory (Ruscic et al. 2005a, b; Goos et al. 2013a, b). When this approach is used, it is especially obvious that every time the thermochemical database or the set of groups or interactions is extended, the whole set of GVs has to be re-optimized, instead of keeping the previous values fixed and optimizing only the newly added ones.

A great help is provided by *ab initio* calculations of thermochemical properties. Theory can provide “replacements” for data unavailable experimentally, that can be used instead of measured ones. When possible, it is desirable to use very accurate high-quality *ab initio* data. When large molecules such as polyaromatic hydrocarbons are considered; however, the currently available strategy is that one selects the appropriate model chemistry. If there is a wide enough range of compounds calculated using electronic structure methods, and yet ambiguities arise in assigning GVs, one should also consider not only the possibility that the database is inconsistent but also that additivity may not be perfect.

Benson type GVs, for standard heats of formation, entropy and heat capacity contributions have been tabulated for groups from which one can build alkanes, alkenes, alkynes, aromatics, cycloalkanes and cycloalkenes, polycyclic aromatic hydrocarbons, as well as oxygenated, nitrogenous, halogenated, organosulfur, organophosphorus, organoboron, and organometallic compounds, and for free radicals. There are many papers in the literature listing GVs derived later with added values for groups not included in the earlier compilations. When starting a calculation using the additivity principle, it is important that data from a selected compilation not be mixed with those from other tables because of the danger of

reducing the accuracy of the estimation. A caveat: One should watch for errors within the same table (several inconsistent data have been detected).

Three remarks on the use of additivity schemes:

1. The additivity of properties beyond the atomic masses is actually not guaranteed by any law of Nature and is generally not strictly fulfilled. Bader and coworkers (Wiberg et al. 1987; Bader and Bayles 2000) using the topological definition of an atom in a molecule based on the analysis of the electron density (Bader 1990), showed that transferability of groups is generally only apparent, because changes of properties of one group are often compensated by the opposite changes of the neighboring group.
2. Use of additivity methods to estimate thermodynamic properties seems to be obsolete in light of obtainable *ab initio* data of equal or better quality. However, there are cases (for example, mechanism generation in combustion chemistry) when data on such a large number of compounds are needed that *ab initio* calculations would be too slow to get the desired data, especially for larger molecules, so that the speed of estimation offered by additivity-based techniques is a must.
3. The common philosophy used in deriving group values is that one starts with the simplest compounds containing the selected group, and expands the GV evaluation stepwise. Experimental or *ab initio* data for large molecules are rarely used when GVs are derived. As a result, “exporting” the GVs from small molecules to large ones does not necessarily yield accurate results. Application of the active table paradigm can help to get consistent GVs when extending the data set to include larger molecules, but that requires some solid data for the latter. Unfortunately, such numbers are not easily obtainable, because the accuracy of both the experimental and theoretical methods is reduced when the size of molecule increases.

20.5 Databases

Thermochemical data have been measured since the second half of the nineteenth century. Extensive work performed by Thomsen and by Berthelot yielded numerous enthalpies of reaction (especially of combustion). Probably, the first two databases on thermochemical data are their two monographs (Thomsen 1886; Berthelot 1879) in which the authors summarized their experimental data. The data were organized based on the principles and theorems they worked out. Notably, many of the data they listed are so accurate that their difference from the currently accepted values is less than a percent. Since then, numerous compilations have appeared that contain data on a few thousand compounds. A nonexhaustive overview of them up to 1988 was given by Gurvich (1988). Looking up data for a specific, not very trivial compound is quite cumbersome if the books are not to

hand. In the following, we list a few of these printed compilations and present a few electronic databases. It seems to be important to emphasize that Internet search for thermodynamic data, i.e., “the quick and easy method,” is not recommended. According to our experience, data obtained from such sources should be treated with caution as their quality and reliability is often dubious and difficult to verify due to inadequate referencing.

Thermodynamic data are available in various formats. Virtually, there has not yet been a widely accepted standard on how to archive thermodynamic data. In early sources, enthalpies of formation, heat capacities, and entropies were listed at a single or a few temperatures (mostly at 298.15 K). To represent the temperature dependence of thermodynamic data, polynomials are generally used. Widely used are the NASA polynomials (the earlier (McBride and Gordon 1967; Gordon and McBride 1971) 7- and the more recent (McBride et al. 2002) 9-parameter version). The basic formula determines the heat capacity C_p^0 as a fourth-order polynomial of the absolute temperature in the 7-parameter version, enhanced by first- and second-order terms of the inverse temperature in the 9-parameter version. Also popular are the Shomate polynomials (Shomate 1954), representing C_p^0 as a third-order polynomial in T plus a T^{-2} term. The polynomials allow the interpolation between measured or calculated data points. The validity of the polynomials is restricted to certain temperature ranges. In some cases, the polynomials produce a discontinuity when switching from one temperature range to another; it is advisable to check whether the data extracted from a database suffer from this error. Nowadays, the data are stored in machine-readable format. One standard is the NASA format (Gordon and McBride 1971) also adopted by the widely used CHEMKIN simulation code (Kee et al. 1996). More recently, two IUPAC projects were devoted to the development of a standard for storage and communication of thermodynamic data utilizing the Extensible Markup Language (XML) (ThermoML IUPAC Standard). This standard is recommended by many peer-reviewed journals, the data being made publicly available through the ThermoML Archive (ThermoML Web Archive 2013). Note that there is no reference to this database on the homepages of the journals.

The most reliable thermodynamic properties are those established by the Committee on Data for Science and Technology (CODATA) (Cox et al. 1989) for some key chemical substances. Use of these recommended, internally consistent values is encouraged in the analysis of thermodynamic measurements, data reduction, and preparation of other thermodynamic tables. As an extension, an IUPAC committee critically evaluated thermochemical properties of selected radicals (CH, CH₂(triplet), CH₂(singlet), CH₃, CH₂ OH, CH₃O, CH₃CO, C₂H₅O, C₆H₅CH₂, OH, and NH₂) (Ruscic et al. 2005a, b; extension is in progress).

Evaluated thermochemical data of thousands of substances can be found in different volumes of the Journal of Physical and Chemical Reference Data. Older reprints or monographs are available for free download (JPCRD and monographs Webpage, <http://www.nist.gov/srd/monogr.cfm>). Thermodynamic properties of a large number of hydrocarbons can be found in the book of Stull, Westrum, and

Sinke (Stull et al. 1969) and in the compilations published by the US National Bureau of Standards (Rossini et al. 1952, 1953; Domalski 1972).

Older, but excellent, thermochemical data tabulated for organic and inorganic substances and ions, are available in Gurvich's comprehensive thermochemical compendium (Gurvich et al. 1989, 1991, 1994, 1997). Note that the data for reactive species like radicals and biradicals in the Gurvich tables are outdated.

The compilation by Pedley (Pedley 1994; Pedley et al. 1986) contains critically evaluated enthalpies of formation for more than 3,000 organic compounds. Evaluated data on organic compounds are also listed in another publication of the Thermodynamic Research Center (Marsh et al. 1988). About 10 years ago TRC joined NIST, and the database (including much more than thermochemical data) is commercially available as the NIST-TRC Web Thermo Tables (WTT) (NIST TRC Web Thermo Tables, <http://www.grc.nasa.gov/WWW/CEAWeb/ceaThermoBuild.htm>). Another commercial database with thermochemical data is from Design Institute for Physical Properties (DIPPR 801 Database 2013).

The NIST-JANAF Thermochemical Tables (Chase et al. 1985; Chase 1998) have been great sources of data on inorganic molecules for a long time. It is wise to read the introduction of these volumes where it is explained how the data were evaluated, and what the uncertainties or problems with the different techniques are. Note that these older volumes contain numerous errors. Newer issues (e.g., Dorofeeva et al. 2001) include well-documented quantum chemical data, too. The NIST-JANAF database is available online (NIST Standard Reference Database 13, but the data is from 1985, [http:// kinetics.nist.gov/janaf/](http://kinetics.nist.gov/janaf/)).

The NIST Chemistry Webbook (NIST Chemistry <http://webbook.nist.gov/chemistry>) contains thermochemical data for more than 7,000 organic and small inorganic compounds, virtually independently from the JANAF tables. The listed data are obtained from the literature and are generally not subject to critical evaluation. It is advisable to check the cited literature source and check whether the values were taken correctly from the reference and whether corrections or updates are available (a relatively productive way is to look up papers that cite the original publication).

The NASA Glenn thermodynamic database (McBride et al. 2002) covers about 2,000 species. Carefully evaluated temperature-dependent data are provided in the form of 9-term NASA polynomials. They can be accessed online using the Thermo Build feature of the NASA Glenn chemical equilibrium computer program (NASA Thermo Build webpage 2012). The sources of data are referenced. Although it was intended to be continuously updated, the database seems to not contain data more recent than 2002.

Thermodynamic data on ions are listed in the JANAF (e.g., Chase 1998; Chase et al. 1985) and the Gurvich tables (Gurvich 1988; Gurvich et al. 1988, 1989, 1991, 1994, 1997) and the NASA Glenn database (NASA Thermo Build webpage 2012). A wealth of data on ions is listed in the more than 800-page long compendium of Lias et al. (Lias et al. 1988). Concerning thermodynamics of ions, there are two conventions, depending on how a gas-phase electron is handled. The *thermal electron convention* (TEC), mostly used by thermodynamicists, defines

the electron as a *standard chemical element* and treats its thermochemistry accordingly. In other words, at 298 K it has its own enthalpy, namely, the integrated heat capacity corresponding to an ideal Boltzmann gas, i.e. 6.197 kJ/mol. The *ion convention* (IC) is mostly used by the mass spectrometry community and defines the electron as a *sub-atomic particle*, having no thermodynamic properties. The heat of formation values obtained by the different conventions can be converted to each other: For positive ions (as well as for the formation of an electron), the IC heat of formation is 6.197 kJ/mol less than in the TEC scheme, while for negative ions the opposite holds. The ion convention is used for example in (McBride et al. 2002, NASA Thermo Build <http://www.grc.nasa.gov/WWW/CEAWeb/ceaThermoBuild.htm>) and (Lias et al. 1988); the thermal electron convention in the JANAF tables (e.g., Chase et al. 1985; Chase 1998) and (Gurvich's work (Gurvich 1988; Gurvich et al. 1989–1997)).

One database containing systematically measured and calculated thermochemical data is the NIST Computational Chemistry Comparison and Benchmark Database (NIST CCCBD 2013). It lists experimental and calculated data for species with well-established enthalpies of formation. Covered are mostly species containing C, H, O, and N with less than six nonhydrogen atoms, with more details than in the NIST Chemistry Webbook <http://webbook.nist.gov/chemistry>. Valuable are the comparisons of data from experiments and from quantum chemical calculations obtained with numerous semi-empirical (AM1, PM3), density functional and composite ab initio methods (G1, G2MP2, G2, G3, G3B3, CBS-Q).

The other extensive database that also focuses on quantum chemical data is the Extended Third Millennium Thermochemical Database (Goos et al. 2013a, b). It is a collection of evaluated thermochemical data of gaseous compounds, some liquids and solid, and contains data for pure elements, metals, inorganic and organic compounds, and reactive species like radicals and ions. In addition, it includes all inert gases and a limited number of compounds of 4th to 6th row elements such as Br, I, Cr, Mn, Fe, Co, Ni, Cu, Hg, Mo, Pb, Pd, Pt, Sb, Sn, W, Zn, Zr. For easy use in old and modern kinetic modeling and computational fluid dynamics software, temperature-dependent thermochemical data are provided in 7- or 9-term NASA polynomial format. The thermodynamic properties of about one half of the included species are also calculated with the G3B3 method (Baboul et al. 1999) (making this database the largest collection of data obtained with this method). G3B3 is a composite quantum chemical method producing molecular and thermochemical properties that compare very well with experimental results, the accuracy (with a 95 % confidence limit) being around ± 8 kJ/mol or better. The database is critically evaluated by the authors. They provide not only referenced literature values (calculated and measured ones) but also results of their own calculations. In the database the accuracy of the data is shown in detail, together with data used to calculate the partition functions. The deviations of the fitted temperature dependence of thermochemical properties in terms of NASA polynomials from the “accurate” data are also provided. The database is updated and enhanced on a regular basis, as well as on user requests.

This database contains more consistent thermochemical properties than other collections, because (for a part of the included species) a novel paradigm, the active table approach is used to check the congruency of data on different species. The active table approach (Ruscic et al. 2004; Ruscic et al. 2005a, b, Active Thermochemical Table Webpage 2013) addresses fitting a whole set of data simultaneously, in contrast to the usual “sequential” approach. In the latter, data for a few basic compounds are nailed down, and these serve as fixed values when new and new species are added. The danger here is that one can get different values for the same property when the calculation is based on different pathways. The active table approach, instead, considers the data for the whole set of species (*a thermochemical network*) simultaneously. The network (essentially a set of interlocking Haber-Born cycles) contains redundant information that makes it easy to pick data that are not consistent with the rest. Statistical analysis including simultaneous error propagation then produces thermochemical data usually with smaller error bars as compared to that derived for the same quantity from a set of measurements aimed at the determination of only the property in question. More importantly, the dataset obtained will be consistent, which is essential in, for example, combustion modeling when a multitude of compounds are involved in complex chemical mechanisms whose enthalpy production/consumption influences the kinetics itself. The approach has already provided valuable information by reducing the error bars on some key compounds (Ruscic et al. 2004). Even more impressive is that the approach helped to correct heats of formation of some radicals that were thought to be well established, such as OH (Ruscic et al. 2002), HO₂ (Ruscic et al. 2006), C₆H₅ (Stevens, Ruscic and Baer 2010), or NCN (Goos et al. 2013a, b). Future application of the active table approach will certainly have a major role in making our knowledge on thermochemical data more reliable and consistent.

20.6 Summary

Knowledge of accurate thermochemical data is essential to the modeling and design of reacting systems. Measurement of enthalpies of formation, the key quantity, is limited, not only because of experimental restrictions, but also because of the extraordinary number of compounds involved, for example, in combustion systems. The role of nonexperimental methods is essential in the collection of data. Electronic structure methods (quantum chemistry) offer various levels of precision, more accurate calculations being more expensive (in terms of computation time, memory and disk-space requirements). High-level calculations can match the accuracy of measurements but are limited to relatively small molecules. Larger molecules can be handled by relatively less expensive but at the same time less accurate methods. When using such levels of theory, calibration to experimental data on compounds related to those of interest is desirable. The multitude of species for which thermochemical data are needed is hard to handle even with such

lower level methods. The observation that thermochemical properties of functional groups and other molecular constituents are transferable from molecule to molecule allows inexpensive estimation of thermodynamic data. Various group additivity schemes have been developed with group values for different groups, often depending on the environment. The very high speed of these calculations allows quick derivation of thermochemical data, but for relatively large molecules, calibration against experimental or more easily available quantum chemical data is desirable.

The data available in the literature have been collected in databases, the more valuable being those involving expert evaluation. Especially useful is the active table approach that involves simultaneous fitting of data on several species using a thermochemical network connecting all species of interest including the relationships among their thermochemical data. Evaluated data are available for a few thousand species. For molecules not included in the tables, group additivity schemes can be used. If very high accuracy is needed or the goodness of the group additivity data is dubious, and the experimental determination of the thermochemical parameters is not possible, application of electronic structure methods can be a solution.

Acknowledgments This chapter has been written within the COST Action CM901 “Detailed Chemical Kinetic Models for Cleaner Combustion”. E. Goos and G. Lendvay thanks financial support from the Energy Program of Deutsches Zentrum für Luft- und Raumfahrt e.V. (DLR, German Aerospace Center) and from the Hungarian Scientific Research Fund, Grant No. K77938, respectively.

References

- Active Thermochemical Table Webpage <http://atct.anl.gov/>. Accessed 14 Jan 2013
- Allen TL (1959) Bond energies and the interactions between next-nearest neighbors. I. Saturated hydrocarbons, diamond, sulfanes, S₈, and organic sulfur compounds. *J Chem Phys* 31:1039–1049
- Almlöf J, Taylor PR (1987) General contraction of Gaussian basis sets. I Atomic natural orbitals for first- and second-row atoms. *J Chem Phys* 84:4070–4078
- Atkins P, De Paula J (2005) Elements of physical chemistry, Oxford University Press
- Ayala PA, Schlegel HB (1998) Identification and treatment of internal rotation in normal mode vibrational analysis. *J Chem Phys* 108:2314–2325
- Baboul AG, Curtiss LA, Redfern PC et al (1999) Gaussian-3 theory using density functional geometries and zero-point energies. *J Chem Phys* 110:7650–7657
- Bader RFW (1990) Atoms in molecules: a quantum theory. Oxford University Press, New York
- Bader RFW, Bayles D (2000) Properties of atoms in molecules: group additivity. *J Phys Chem A* 104:5579–5589
- Basilevsky MV (1969) The molecular orbital method and the reactivity of organic molecules. Khimia Publishers, Moscow (in Russian)
- Benson SW (1968) Thermochemical kinetics. Wiley, New York
- Benson SW, Buss JH (1958) Additivity rules for the estimation of molecular properties Thermodynamic properties. *J Chem Phys* 29:546–572
- Berthelot M (1879) Essai de mécanique chimique fondée sur la thermochimie. Dunod, Paris

- Blurock ES, Warth V, Grandmougin XF et al (2012) JThERGAS: Thermodynamic estimation from 2D graphical representations of molecules. *Energy* 43:161–171
- Burcat A (2009) Ab initio calculations of carbon-containing species and comparison with group additivity results. Part II. C4 species. *J Chem Eng Data* 54:1829–1835
- Burcat A, Ruscic B (2005) Third millennium ideal gas and condensed phase thermochemical database for combustion with updates from active chemical tables, technical report TAE 960 and ANL-05/20, Technion-IIT, Haifa, and Argonne National Laboratory, Argonne, Illinois, (Last print version outdated by now)
- Chase MW Jr (1998) NIST-JANAF thermochemical tables, Part I and II^{*} 4th ed. *J Phys Chem Ref Data*, Monograph 9:1–1951 <http://www.nist.gov/srd/monogr.cfm>, accessed 2 Jul 2013
- Chase MW Jr, Davies CA, Downey JR Jr et al (1985) JANAF thermochemical tables, 3rd ed. *J Phys Chem Ref Data* 14 (Suppl 1) :1–1856. Available from <http://www.nist.gov/srd/monogr.cfm>, accessed 2 Jul 2013
- CHETAH Version 7.2 The ASTM computer program for chemical thermodynamic and energy release evaluation (NIST Special Database 16), 4th edn. (1998) URL <http://www.astm.org>
- Cohen N (1982) The use of transition-state theory to extrapolate rate coefficients for reactions of OH with alkanes. *Int J Chem Kinet* 14:1339–1362
- Cohen N (1991) Are reaction rate coefficients additive? Revised transition state theory calculations for OH + alkane reactions. *Int J Chem Kin* 23:397–417
- Cohen N (1996) Revised group additivity values for enthalpies of formation (at 298 K) of carbon-hydrogen and carbon-hydrogen-oxygen compounds. *J Phys Chem Ref Data* 25:1411–1481
- Cohen N, Benson SW (1993) Estimation of heats of formation of organic-compounds by additivity methods. *Chem Rev* 93:2419–2438
- Cox JD, Pilcher G (1970) *Thermochemistry of organic and organometallic compounds*. Chapter. 7, Academic Press, New York
- Cox JD, Wagman DD, Medvedev VA (1989) CODATA key values for thermodynamics. Hemisphere Publishing Corporation. New York. Summary available at <http://www.codata.org/resources/databases/key1.html>. Accessed 27 Dec 2012
- Cramer CH (2013) *Essentials of computational chemistry: theories and models*. Errata on <http://pollux.chem.umn.edu/Book.html>. Accessed 3 Jan 2013
- Cramer CH (2004) *Essentials of computational chemistry: theories and models*, 2nd edn. Wiley, England
- Curtiss LA, Raghavachari K, Trucks GW et al (1991) Gaussian2 theory for molecular energies of first and second row compounds. *J Chem Phys* 94:7221–7230
- DIPPR 801 Database (2013) <http://www.aiche.org/dippr/events-products/801-database>
- Domalski ES (1972) Selected values of heats of combustion and heats of formation of organic compounds containing the elements C, H, N, O, P and S. *J Phys Chem Ref Data* 1:221–277
- Dorofeeva OV, Novikov VP, Neumann DB (2001) NIST-JANAF thermochemical tables. I. Ten organic molecules related to atmospheric chemistry. *J Phys Chem Ref Data* 30:475–514
- Dunning TH Jr (1989) Gaussian basis sets for use in correlated molecular calculations I the atoms boron through neon and hydrogen. *J Chem Phys* 90:1007–1023
- Ellingson BA, Lynch VA, Mielke SL et al (2006) Statistical thermodynamics of bond torsional modes: tests of separable, almost-separable, and improved Pitzer-Gwinn approximations. *J Chem Phys* 125:084305
- EMSL basis (2013). Set exchange library, based on Schuchardt et al (2007). *J Chem Inf Model* 47(3):1045–1052 <https://bse.pnl.gov/bse/portal>. Accessed 8 Jan 2013,
- Foresman JB, Frisch AE (1996) *Exploring chemistry with electronic structure methods*. 2nd edn. Gaussian Inc
- Goos E, Burcat A, Ruscic B (2013a) Ideal gas thermochemical database with updates from active thermochemical tables. Available via <ftp://ftp.technion.ac.il/pub/supported/aetdd/thermodynamics> mirrored at <http://garfield.chem.elte.hu/burcat/burcat.html> and also available from <http://www.dlr.de/vt/en/>
- Goos E, Sickfeld Ch, Mauß F et al (2013b) Prompt NO formation in flames: the influence of NCN thermochemistry. *Proc Comb Inst* 34:657–666

- Gordon S, McBride BJ (1971) Computer program for calculation of complex chemical equilibrium compositions, rocket performance, incident and reflected shocks and Chapman-Jouguet detonations, NASA Report SP-273
- Greenshields JB, Rossini FD (1958) Molecular structure and properties of hydrocarbons and related compounds. *J Phys Chem* 62:271–280
- Gurvich L (1988) Reference books and data banks on the thermodynamic properties of individual substances. *Pure Appl Chem* 61:1027–1031
- Gurvich LV, Veys IV, Alcock AB (1989) Thermodynamic properties of individual substances, 4th ed.vol 1, Hemisphere Publishing Co
- Gurvich LV, Veys IV, Alcock AB (1991) Thermodynamic properties of individual substances, 4th ed.vol 2, Hemisphere Publishing Co
- Gurvich LV, Veys IV, Alcock AB (1994) Thermodynamic properties of individual substances, 4th ed.vol 3, Hemisphere Publishing Co
- Gurvich LV, Veys IV, Alcock AB (1997) Thermodynamic properties of individual substances, 4th ed.vol 4–6, Hemisphere Publishing Co
- Hehre WJ, Ditchfield R, Pople JA (1971) Self-consistent molecular orbital methods XII further extensions of Gaussian-type basis sets for use in molecular orbital studies of organic molecules. *J Chem Phys* 56:2257–2261
- Hehre WJ, Radom L, Pvr Schleyer, Pople JA (1986) *Ab initio molecular orbital theory*. Wiley, New York
- Helgaker T, Jørgensen P, Olsen J (2000) *Molecular electronic-structure theory*, Wiley, 1st edn
- Helgaker T, Jørgensen P, Olsen J (2013) *Molecular electronic-structure theory*. In: Paperback reprint of 1st edn. Wiley, 2nd revised Edition Paperback expected
- Janz GJ (1955) The estimation of thermodynamic properties for organic compounds and chemical reactions. *Quart Rev Chem Soc* 9:229–254. doi:[10.1039/QR9550900229](https://doi.org/10.1039/QR9550900229)
- Janz GJ (1958) Estimation of thermodynamic properties of organic compounds. Academic Press, New York
- Jensen F (2006) *Introduction to computational chemistry*. 2nd edn, Wiley
- JPCRd and monographs reprints are available for free from <http://www.nist.gov/srd/reprints.cfm> or <http://www.nist.gov/srd/monogr.cfm>
- Kee RJ, Rupley FM, Meeks E, et al (1996) CHEMKIN-III: A FORTRAN chemical kinetics package for the analysis of gasphase chemical and plasma kinetics, Sandia Report UC-405, SAND96-8216
- Laidler KJ (1956) A System of molecular thermochemistry for organic gases and liquids. *Can J Chem* 34:626–648
- Levine IN (2007) *Quantum chemistry*. 6th International edition. Alpha Books, Pearson, California
- Lias SG, Bartmess JE, Liebman JF, et al (1988) Gas-phase ion and neutral thermochemistry. *J Phys Chem Ref Data* 17 (Supplement 1)
- Marsh KN (2001) Calorimetry, In: Moore JH, Spencer ND (2001) *Encyclopedia of chemical physics and physical chemistry*, vol 2. Institute of Physics Publishing, Bristol and Philadelphia
- Marsh KN, Das A, Frenkel M, et al (1988) TRC Thermodynamic Tables, Non-Hydrocarbons, Vols. I-VIII and Hydrocarbons, Vols. I-XII, Thermodynamics Research Center Texas A&M University, College Station, Texas; TRC (1997) Selected Values of Properties of Chemical Compounds, Thermodynamics Research Center, Texas A&M University, College Station, Texas
- Mayer I (2003) *Simple theorems, proofs, and derivations in quantum chemistry*. Kluwer Academic/Plenum Publishers, New York
- McBride BJ, Gordon S (1967) FORTRAN IV program for calculation of thermodynamic data, NASA TN-D 4097
- McBride BJ, Zehe MJ, and Gordon S (2002) NASA Glenn Coefficients for calculating thermodynamic properties of individual species. NASA report TP-2002-211556

- Muller C, Michel V, Scacchi G et al (1995) THERGAS—A computer program for the evaluation of thermochemical data of molecules and free-radicals in the gas phase. *Journal de Chimie Physique et de Physico-Chimie Biologiques* 92:1154–1178
- NASA Thermo Build <http://www.grc.nasa.gov/WWW/CEAWeb/ceaThermoBuild.htm> Accessed 29 Dec 2012
- NIST TRC Web Thermo Tables (WTT) <http://trc.nist.gov/tde.html>. Accessed 30 Dec 2012
- NIST JANAF thermochemical tables (1985). NIST Standard Reference Database 13 (Version 1.0) Data compiled and evaluated by Chase MW Jr, Davies CA, Downey JR Jr, Frurip DJ, McDonald RA, Syverud AN <http://kinetics.nist.gov/janaf/>. Accessed 28 Dec 2012
- NIST CCCBD, Computational Chemistry Comparison and Benchmark Database, NIST Standard Reference Database Number 101, Release 15b, August 2011, Russell D. Johnson III (ed), <http://cccbdb.nist.gov/>
- NIST Chemistry WebBook, NIST Standard Reference Database Number 69, <http://webbook.nist.gov/chemistry> Accessed 30 Dec 2012
- Pedley JB (1994) Thermochemical data and structures of organic compounds. vol. 1, (TRC Data Series) Thermodynamics Research Center, College Station, TX, USA
- Pedley JB, Naylor RD, Rylance SP (1986) Thermochemical Data of Organic Compounds, 2nd edn. Chapman and Hall, London
- Piszczatowski K, Lach G, Przybytek M et al (2009) Theoretical Determination of the Dissociation Energy of Molecular Hydrogen. *J Chem Theor Comp* 11:3039–3048
- Pitzer KS (1940) The vibration frequencies and thermodynamic functions of long chain hydrocarbons. *J Chem Phys* 8:711–720
- Pitzer KS, Gwinn WD (1942) Energy levels and thermodynamic functions for molecules with internal rotation: I Rigid frame with attached tops. *J Chem Phys* 10:428–440
- Platt JR (1947) Influence of neighbor bonds on additive bond properties in paraffins. *J Chem Phys* 15:419–420
- Platt JR (1952) Prediction of isomeric differences in paraffin properties. *J Phys Chem* 56:328–336
- Poling BE, Prausnitz JM, O'Connell JP (2001) The properties of gases and liquids, 5th edn. McGraw Hill, New York
- Polyansky OL, Császár AG, Shirin SV et al (2003) High-accuracy ab initio rotation-vibration transitions for water. *Science* 299:539–542
- Pople JA, Beveridge DL (1970) Approximate molecular orbital theory. McGraw Hill, New York
- Ritter ER (1991) THERM: a computer code for estimating thermodynamic properties for species important to combustion and reaction modeling. *J Chemical Information and Computer Sciences* 31:400–408
- Ritter ER, Bozzelli JW (1991) Therm: thermodynamic property estimation for gas phase radicals and molecules. *Int J Chem Kin* 23:767–778
- RMG—reaction mechanism generator, the link connects to the python version, but there is a Java version, too <http://greengroup.github.com/RMG-Py/>. Accessed 27 Dec 2012
- Rossini FD, Wagman DD, Evans WH et al (1952) Selected values of chemical thermodynamic properties, Circular of the National Bureau of Standards 500. National Bureau of Standards, US Department of Commerce
- Rossini FD, Pitzer KS, Arnett RL et al (1953) Selected values of physical and thermodynamic properties of hydrocarbons and related compounds. Carnegie Press, Pittsburgh, PA, American Petroleum Institute
- Ruscic B, Wagner AF, Harding LB et al (2002) On the enthalpy of formation of hydroxyl radical and gas-phase bond dissociation energies of water and hydroxyl. *J Phys Chem A* 106:2727–2747
- Ruscic B, Pinzon RE, Morton ML et al (2004) Introduction to active thermochemical tables: several “Key” enthalpies of formation revisited. *J Phys Chem A* 108:9979–9997
- Ruscic B, Boggs JE, Burcat A et al (2005a) IUPAC critical evaluation of thermochemical properties of selected radicals: Part I. *J Phys Chem Ref Data* 34:573–656
- Ruscic B, Pinzon RE, von Laszewski G et al (2005b) Active thermochemical tables: thermochemistry for the 21st century. *J Phys: Conf Ser* 16:561–570

- Ruscic B, Pinzon RE, Morton ML et al (2006) Active thermochemical tables: accurate enthalpy of formation of hydroperoxy radical, HO₂. *J Phys Chem A* 108:6592–6601
- Schuchardt KL, Didier BT, Elsethagen T et al (2007) Basis set exchange: a community database for computational sciences. *J Chem Inf Model* 47(3):1045–1052. doi:101021/ci600510j
- Shomate CH (1954) A method for evaluating and correlating thermodynamic data. *J Phys Chem* 58:368–372
- Slater JC (1963–1974) Quantum theory of molecules and solids, vols. 1–4: Electronic structure of molecules, McGraw-Hill, New York
- Somayajulu GR, Zwolinski BJ (1966) Generalized treatment of alkanes. *Trans Faraday Soc* 62:2327–2340
- Stein SE, Rukkers JM, Brown RL (1991) NIST standard reference database 25: NIST structures and properties database and estimation program; National Institute of Standards and Technology: Gaithersburg, MD, see also <http://webbook.nist.gov/chemistry/grp-add/S-and-P.html#ref5>. Accessed 29 Dec 2012
- Stevens WR, Ruscic B, Baer T (2010) The heats of formation of C₆H₅, C₆H₅⁺, and C₆H₅NO by TPEPICO and active thermochemical tables analysis. *J Phys Chem A* 114:13134–13145
- Stull DR, Westrum EF, Sinke GC (1969) The chemical thermodynamics of organic compounds. Wiley, New York
- Sumathi R, Carstensen HH, Green WH (2001a) Reaction Rate Prediction via Group Additivity Part 1: H abstraction from alkanes by H and CH₃. *J Phys Chem A* 105:6910–6925
- Sumathi R, Carstensen HH, Green WH Jr (2001b) Reaction rate prediction via group additivity. Part 2: H-abstraction from alkenes, alkynes, alcohols, aldehydes, and acids by H atoms. *J Phys Chem A* 105:8969–8984
- Sumathi R, Carstensen HH, GreenWH (2002) Reaction rate predictions via group additivity. Part 3: effect of substituents with CH₂ as the mediator. *J Phys Chem A* 106:5474–5489
- ThermoData Engine (TDE) (2012) NIST TDE 103a—pure compounds, NIST TDE 103b—pure compounds, binary mixtures, ternary mixtures and chemical reactions
- ThermoML IUPAC Standard is an XML based standard for thermodynamic data communication that was initially developed within IUPAC Project 2002-055-3-024, later extended within the IUPAC project 2007-039-1-024 (See also: Frenkel M et al. (2006) *Pure Appl Chem* 78:541–612, *Pure Appl Chem* (2011) 83:1937–1967) <http://www.iupac.org/namespaces/ThermoML/index.html>. Accessed 27 Dec 2012
- ThermoML web archive, <http://trc.nist.gov/ThermoML.html>. Accessed 14 Jan 2013
- Thomsen J (1886) Thermochemische Untersuchungen vol. IV, J. A. Barth, Leipzig in German
- Truhlar DG (2008) Molecular modeling of complex chemical systems. *J Am Chem Soc* 130, 16824–16827, Glossary, <http://pubs.acs.org/JACSbeta/JVI/issue3.html> and <http://pubs.acs.org/JACSbeta/jvi/glossary.html>
- Vansteenkiste P, Van Neck D, Van Speybroeck V et al (2006) An extended hindered-rotor model with incorporation of Coriolis and vibrational-rotational coupling for calculating partition functions and derived quantities. *J Chem Phys* 124:044314 additions and corrections (Publisher's Note) *J Chem Phys* 125: 049902
- Veszprémi T, Fehér M (1999) Quantum chemistry: fundamentals to applications. Kluwer Academic/Plenum Publishers, New York
- Wiberg KB, Bader RFW, Lau CDH (1987) Theoretical analysis of hydrocarbon properties. 2. Additivity of group properties and the origin of strain energy. *J Am Chem Soc* 109:1001–1012
- Zülicke L (1973) Quantenchemie. Ein Lehrgang. Band 1: Grundlagen und allgemeine Methoden. VEB Deutscher Verlag der Wissenschaften, Berlin (in German; a Russian edition is available)
- Zülicke L (1985) Quantenchemie. Ein Lehrgang. Band 2, Atombau, Chemische Bindung und molekulare Wechselwirkungen, Hüthig Verlag, Heidelberg (in German; a Russian edition is available)

Chapter 21

Statistical Rate Theory in Combustion: An Operational Approach

Matthias Olzmann

Abstract Statistical rate theory is a valuable tool to rationalize the microscopic mechanisms of elementary chemical steps in the gas phase, to analyze results of kinetic experiments, and to adequately parameterize the temperature and pressure dependence of rate coefficients. We briefly describe the essential elements of statistical rate theory that are relevant for the kinetic characterization of reactions under combustion conditions, emphasizing application aspects. The calculation of rate coefficients for reactions over potential energy barriers and potential energy wells is elucidated. In the former case conventional transition state theory is used, in the latter case the temperature and pressure dependence is described by means of master equations with specific rate coefficients from RRKM theory and the simplified statistical adiabatic channel model. Examples for the different types of reaction are given, and crucial quantities are discussed. The article primarily aims at readers on an intermediate level between graduate students and junior scientists, who are interested in performing practical calculations, and who are looking for a compact presentation of the topic as a guide to the extensive literature.

List of Important Symbols and Abbreviations

$\langle X \rangle$	Average of quantity X
\mathbf{A}	Vector/matrix containing elements $a(E_i)/a(E_i, E_j)$
B	Rotational constant
$B_{\text{cent}}(q)$	Rotational constant for centrifugal motion in SACM
D	Morse parameter
\mathbf{E}_i	i th eigenvector of the matrix \mathbf{J}
ΔE_{SL}	Energy transfer parameter of the stepladder model
$\langle \Delta E \rangle$	Average energy transferred per collision (all, up and down)
$\langle \Delta E \rangle_{\text{d}}$	Average energy transferred per down collision

M. Olzmann (✉)

Institut für Physikalische Chemie, Karlsruher Institut für Technologie (KIT), Kaiserstr. 12
76131 Karlsruhe, Germany
e-mail: matthias.olzmann@kit.edu

$\langle \Delta E \rangle_u$	Average energy transferred per up collision
ΔE_z	Zero-point energy correction in SACM
$E_{0(i)}$	Threshold energy of reaction i
$f(E)$	Initial distribution of the intermediate in a complex-forming bimolecular reaction
F_{AM}	Angular momentum coupling factor in SACM
F_E	Density of states correction factor
h	Planck's constant
HO	Harmonic oscillator
J	Total angular momentum quantum number
J	Matrix of the master equation, for definition see Eq. 21.3
k_i	Rate coefficient of reaction i
k_i^∞	High-pressure limiting value of the rate coefficient for reaction i
k_B	Boltzmann's constant
L_i	Reaction path degeneracy for reaction i
$n(E)$	Distribution of a reacting species
$n^s(E)$	Steady-state distribution of a reacting species
$\tilde{n}^s(E)$	Normalized steady-state distribution of a reacting species
P	Pressure
$P(E', E)$	Collisional transition probability (density) for a collision $E \rightarrow E'$
PST	Phase space theory
q	Reaction coordinate/interfragment distance
q_e	Equilibrium distance
q_{HIR}^*	Partition function for hindered internal rotor (local coordinate)
q_{HO}	Partition function for harmonic oscillator (normal coordinate)
q_{HO}^*	Partition function for harmonic oscillator (local coordinate)
Q	Partition function
R	Gas constant
R_1	Rate of reaction of a complex-forming bimolecular reaction
RRKM	Rice, Ramsperger, Kassel, Marcus
SACM	Statistical adiabatic channel model
T	Temperature
TST	Transition state theory
V	Volume
$V(q)$	Classical interfragment potential
W_i	Cumulative reaction probability/sum of states for reaction/transition state i
α	Interpolation parameter of simplified SACM or energy transfer parameter of the exponential down model
β	Morse parameter
γ_c	Collision efficiency in a chemically activated reaction
$\varepsilon(q)$	Vibrational or rotational quantum in SACM

λ_i	i th eigenvalue of the matrix \mathbf{J}
ρ	Density of states
σ	Symmetry number
ω	Collision frequency (unit: s^{-1})

21.1 Introduction

For the detailed chemical modeling of a combustion process, the underlying reaction mechanism and the rate coefficients of its elementary chemical steps have to be known. The evaluation of whether or not a proposed model is adequate has to rely on both the mechanism and the rate coefficients. The problem of setting up suitable mechanisms has been extensively discussed in Parts I and IV of this book. Here, we deal with the rate coefficients and their temperature and pressure dependence.

Clearly, the preferential way to obtain rate coefficients is a more or less direct measurement in appropriate kinetic experiments under well-defined conditions. Important experimental techniques for this purpose are reviewed in [Chaps. 22–24](#). In many cases, however, an experimental determination of rate coefficients under combustion conditions is difficult or even impossible. Often only partial information like relative rates or product branching ratios can be obtained, mostly restricted to rather narrow ranges of temperature and pressure. In these frequent cases, reliable microscopic models describing the elementary chemical step are needed to extract and evaluate absolute rate coefficients and to parameterize their temperature and pressure dependence for adequate inter- and extrapolation. Apart from this, also a purely theoretical calculation of rate coefficients from first principles becomes more and more important as a very useful supplement to experimental studies or even as a substitute in difficult cases.

In view of the size and complexity of most of the chemical species occurring in combustion mechanisms, the method of choice for the calculation of rate coefficients is statistical rate theory. The other theoretical access to rate coefficients, quantum and classical dynamics calculations, is still restricted to small molecules (currently up to six atoms, larger systems with reduced dimensionality, see [Clary 2008](#)) and are not routinely applied. Therefore, in a user-oriented approach, we will concentrate on statistical rate theory in this paper. Furthermore, we will keep the treatment strictly operational and mainly deal with application aspects under steady-state conditions. We touch more fundamental questions only in passing or insofar as they might present complications and pitfalls. The quantum chemical methods, which can provide the necessary input data, are elucidated in [Chap. 20](#).

21.2 Rate Coefficient and Potential Energy Surface

Every calculation of a rate coefficient starts with an exploration of the underlying potential energy surface. The practical approach differs depending on whether the reaction proceeds over a single potential energy barrier or over one or more potential energy wells along the reaction coordinate (see e.g. Steinfeld et al. 1989; Gilbert and Smith 1990).

21.2.1 Reactions over Potential Energy Barriers: Canonical Transition State Theory

For direct bimolecular reactions and unimolecular reactions in the high-pressure limit that proceed over single, well-pronounced potential energy barriers, conventional transition state theory (TST) (Glasstone et al. 1941) works surprisingly well, and for more details the reader is referred to standard textbooks on chemical kinetics (e.g. Steinfeld et al. 1989). The temperature-dependent rate coefficient, $k(T)$, which is independent of pressure in these cases, can be obtained from the familiar equation

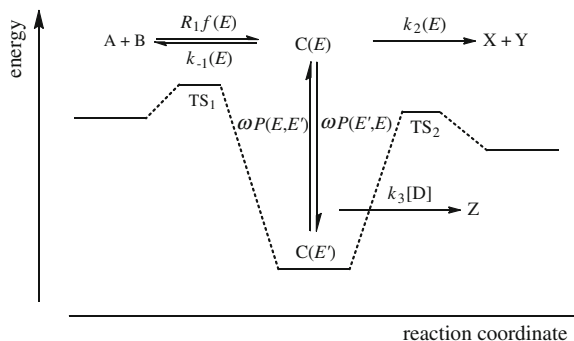
$$k(T) = \kappa L \frac{k_{\text{B}}T}{h} \frac{Q_{\text{TS}}(T)/V}{\prod_i [Q_i(T)/V]} \exp\left(-\frac{E_0}{RT}\right) \quad (21.1)$$

Here, $Q_n(T)$ denotes the partition functions of the transition state ($n = \text{TS}$) and reactants ($n = i$), V is the volume, and k_{B} and h are Boltzmann's and Planck's constant, respectively. The reader should note that the partition functions are calculated without symmetry numbers, which are incorporated in the reaction path degeneracy L instead (see below). The threshold energy E_0 is the energy difference between the rovibrational ground states of the TS and the reactants, and R denotes the gas constant. The dimensionless factor κ accounts for all non-classical effects, in particular tunneling. For a review on more recent aspects of canonical TST see e.g. Fernández-Ramos et al. (2006).

21.2.2 Reactions over Potential Energy Wells: The Master Equation

Much more complicated scenarios arise for unimolecular or complex-forming bimolecular reactions that proceed over one or more potential energy wells with separating barriers between them and multiple exit channels (Frankcombe et al. 2000; Klippenstein and Miller 2002; Miller and Klippenstein 2003; and Fernández-Ramos et al. 2006). In these cases the competition between the reactive

Fig. 21.1 Reaction system with one potential energy well, two unimolecular exit channels, and a bimolecular reaction $C + D \rightarrow Z$ with a rate coefficient k_3 (for explanations see text)



processes and collisional energy transfer is essential, and from this complex interplay, often nontrivial temperature and pressure dependences of the observable rate coefficients (if these exist at all, see below) arise. In the following, the general description of such reaction systems will be outlined for an example with one potential energy well. The most important quantities are displayed in Fig. 21.1. Details can be found in e.g. Gilbert and Smith (1990), Holbrook et al. (1996), and Forst (2003).

A crucial quantity to describe the kinetics of such reaction systems is the energy-dependent population, $n(E)$, of the species C. It is usually obtained by solving the so-called master equation, which is a balance of all gain and loss processes for a given energy level of C. Because at high energies the rovibrational energy levels of C are very close to each other and their number is enormous, they are lumped together in bins. In this way the master equation takes on a discrete form, and for the population of the i th bin, $E_i \dots E_i + dE$, one obtains

$$\frac{dn_i}{dt} = R_1 f_i - \omega n_i + \omega \sum_j P_{ij} n_j - (k_{-1i} + k_{2i} + k_3[D]) n_i \quad (21.2)$$

where the general notation $x_i = x(E_i)$ is used. Here, R_1 denotes the rate of reaction for $A + B \rightarrow C$, and f_i is the normalized nascent distribution of C as formed in the reaction $A + B$. The second and third terms describe the collisional depopulation and population, respectively, of the considered energy level E_i with the collision frequency ω and the transition probabilities $P_{ij} = P(E_i, E_j)$ for transitions $E_j \rightarrow E_i$. The next two terms represent the unimolecular decomposition steps $C \rightarrow A + B$ and $C \rightarrow X + Y$ with the specific rate coefficients k_{-1i} and k_{2i} , respectively, while the last term accounts for a possible consecutive bimolecular reaction $C + D \rightarrow Z$ with an energy-independent pseudo-first order rate coefficient $k_3[D]$.

Equation 21.2 can be cast into matrix form, and one obtains

$$(d/dt)\mathbf{N} = R_1 \mathbf{F} + [\omega(\mathbf{P} - \mathbf{I}) - \mathbf{K}_{-1} - \mathbf{K}_2 - k_3[D]\mathbf{I}]\mathbf{N} \equiv R_1 \mathbf{F} - \mathbf{JN} \quad (21.3)$$

with the vector \mathbf{F} , the matrix \mathbf{P} , the unit matrix \mathbf{I} , and the diagonal matrices \mathbf{K}_{-1} and \mathbf{K}_2 , where the lettering corresponds to that of Eq. (21.2). We note that the most common cases included in Eq. (21.3) are:

1. thermal unimolecular dissociation of C into the two product channels A + B and X + Y ($R_1 = 0$, $k_3[\text{D}] = 0$),
2. complex-forming bimolecular or chemically activated reaction $\text{A} + \text{B} \rightleftharpoons \text{C} \rightarrow \text{X} + \text{Y}$ ($R_1 \neq 0$, $k_3[\text{D}] = 0$).

For the solution of the master equation, we need to specify \mathbf{F} , \mathbf{P} , \mathbf{K}_{-1} , \mathbf{K}_2 , and, if applicable, $k_3[\text{D}]$. The rate of reaction $R_1 = k_1[\text{A}][\text{B}]$ is rarely explicitly needed, because most of the practically relevant quantities are expressed relative to R_1 (see Sect. 21.5.2).

Besides energy, also total angular momentum can play an important role in the kinetics of unimolecular reactions (e.g. Gilbert and Smith 1990; Baer and Hase 1996; and Forst 2003). This applies in particular to reactions via loose transition states that is, reactions without a barrier on the potential energy surface as e.g. simple bond fission reactions (see Sect. 21.3.3). In such cases an energy- and angular momentum-resolved, so-called two-dimensional master equation would provide the most detailed description (Gilbert and Smith 1990; Jeffrey et al. 1996; Forst 2003; and Miller and Klippenstein 2006). In practice, however, such calculations are rarely performed, because averaging over angular momenta is often adequate, and transition probabilities for rotational energy transfer are currently not well known. Often it is sufficient to account for angular momentum effects by calculating the quantities in Eq. (21.3) for thermally averaged angular momenta. Details are outlined below.

Note that in most practical calculations, cm^{-1} is used as energy unit, and the rovibrational ground state of C is taken as the energy zero.

21.3 Constituent Quantities of the Master Equation

21.3.1 Specific Rate Coefficients, $k_i(E)$

The diagonal matrices \mathbf{K}_{-1} and \mathbf{K}_2 in Eq. 21.3 contain as elements the specific rate coefficients $k_{-1i} = k_{-1}(E_i)$ and $k_{2i} = k_2(E_i)$. These rate coefficients are generally calculated from RRKM-like expressions, which are obtained from microcanonical TST (RRKM: Rice, Ramsperger, Kassel, Marcus) (Marcus 1952; Gilbert and Smith 1990; Baer and Hase 1996; Holbrook et al. 1996; Forst 2003; and Klippenstein 2003):

$$k_i(E) \equiv k_i(E, \langle J \rangle) = L_i \frac{W_i(E - E_{0(i)}(\langle J \rangle), \langle J \rangle)}{h\rho(E, \langle J \rangle)} \quad (21.4)$$

Here, L_i denotes the reaction path degeneracy, $W_i(E, J)$ is a cumulative reaction probability, and $E_{0(i)}(J)$ is the threshold energy of the unimolecular exit channel i ($i = -1, 2$), $\rho(E, J)$ is the density of states of the reactant/intermediate C. Note that ρ and W_i depend on the energy E and the total angular momentum quantum number

J of the reactant/intermediate C, and the threshold energies $E_{0(i)}$ also depend on J . As already mentioned above, it is often sufficient to calculate $\rho(E, J)$, $W_i(E, J)$, and also $E_{0(i)}(J)$ for thermally averaged angular momentum quantum numbers $J = \langle J \rangle$. For combustion temperatures, often simple estimates like $\langle J \rangle = (k_B T / B_{\text{av}})^{1/2}$ for linear molecules and $\langle J \rangle = [3k_B T / (2B_{\text{av}})]^{1/2}$ for nonlinear molecules with an arithmetically averaged rotational constant B_{av} work well. For the contribution of the orbital angular momentum to J in complex-forming reactions see Olzmann (1997). In the following sections, we will separately examine the computation of $\rho(E, J)$, $W_i(E, J)$, $E_{0(i)}(J)$, and L_i .

21.3.2 Densities of States, $\rho(E, J)$

The quantity $\rho(E, J)$, which appears in the denominator of Eq. (21.4) and also in the transition probability matrix \mathbf{P} in Eq. (21.3), is the density of rovibrational states of the reactant/intermediate C at an energy E for a total angular momentum quantum number J that is, the number of quantum states in an energy interval of unit width, usually 1 cm^{-1} . Because the total angular momentum is essentially associated with external rotation, a separation between internal, mainly vibrational degrees of freedom and external rotational degrees of freedom is customary. Accordingly, for the overall density of states, it follows (Troe 1983b)

$$\rho(E, J) = \sum_{K=-J}^{J*} \rho_{\text{int}}[E - E_{\text{rot}}(J, K)] \quad (21.5)$$

with the density of states for the internal degrees of freedom $\rho_{\text{int}}(E)$ and the rotational energy of a symmetric top $E_{\text{rot}}(J, K)$ with the quantum numbers J and K . From the overall energy E , the amount $E - E_{\text{rot}}(J, K)$ is allotted to the internal degrees of freedom, and the overall density of states is obtained by summation over all allowed values of K in the range $-J \leq K \leq J$ with the additional condition $E - E_{\text{rot}}(J, K) \geq 0$, denoted by the symbol $*$ in Eq. (21.5). We note that the $(2J + 1)$ -fold M degeneracy (see e.g. Atkins 1983) is usually neglected here, because it would also appear in W_i and cancel in Eq. (21.4). Furthermore, symmetry numbers are not included but are combined in the reaction path degeneracy L_i (see below).

If the sum in Eq. (21.5) is substituted by an integral, useful analytical approximations of the form

$$\rho(E, J) \sim \rho_{\text{int}}(E^*) F_\rho(E^*, J) \quad (21.6)$$

can be obtained (Troe 1983b). Here, F_ρ is a correction factor, which depends on the type of the symmetric top, and $E^* = E - BJ(J + 1)$ for spherical and prolate symmetric top molecules and $E^* = E - BJ(J + 1) - (B - C)J^2$ for oblate symmetric top molecules (Olzmann and Troe 1994).

Densities of states for internal degrees of freedom, $\rho_{\text{int}}(E)$, are nowadays almost exclusively calculated by exact counting methods. In this context it is useful to recall that the density of states of a system, which is combined from two separable subsystems I and II is obtained by convolution:

$$\rho_{\text{I+II}}(E) = \int_0^E \rho_{\text{I}}(\varepsilon)\rho_{\text{II}}(E - \varepsilon)d\varepsilon = \rho_{\text{I}} * \rho_{\text{II}} \quad (21.7)$$

From this fact, it follows that for instance the combined density of states of s harmonic oscillators can be obtained from the densities of states of the single oscillators by an $(s - 1)$ -fold integration/summation. The famous Beyer-Swinehart counting routine is a very efficient implementation of this multiple convolution integral/sum (Beyer and Swinehart 1973). It was extended to degrees of freedom with unequally spaced energy levels by Stein and Rabinovitch (1973), and Astholz et al. (1979) proposed a particularly effective way to include free internal rotors. For more details see e.g. Gilbert and Smith (1990), Baer and Hase (1996), Holbrook et al. (1996), and Forst (2003).

A subtle point is the proper incorporation of hindered internal rotors. Here, correction factors relying on classical approximations for the density and sum of states were derived by Troe (1977b). Later on, coupling effects were examined by using inverse Laplace transformation of partition functions (Gang et al. 1996; Knyazev 1998). A readily applicable approximation, which works well for canonical rate coefficients, was proposed by Vansteenkiste et al. (2006). We applied this method to the ring-closure reaction of the 6-oxo-1-hexyl radical and obtained a very good agreement with experimentally determined rate coefficients (Welz et al. 2008). This is outlined in Sect. 21.4. An extension of this method to microcanonical rate coefficients can be achieved by applying inverse Laplace transformation to the corrected partition functions. An application of this approach to the ring-closure reactions of chemically activated oxo-alkyl radicals is described in Hoyermann et al. (2010).

21.3.3 Cumulative Reaction Probabilities, $W_i(E, J)$

For the calculation of the cumulative reaction probabilities $W_i(E, J)$, it is important to distinguish between reactions proceeding via tight or loose transition states. In the former case, which is typical for isomerization and complex elimination reactions, a well pronounced potential energy maximum along the reaction coordinate and hence a well localized transition state exist. In the latter case, which is typical for simple bond fission reactions (and the reverse radical combination reactions), the potential energy curve for $J = 0$ monotonously increases with increasing interfragment distance and asymptotically approaches the value for the separated fragments. For $J > 0$ centrifugal maxima arise, which move to smaller

interfragment distances for increasing J . That is, the transition state configuration in this case depends on E and in particular on J .

Tight Transition States For these reactions the cumulative reaction probability $W_i(E, J)$ is just the number of states with an energy less than or equal to E at a given J of the transition state TS_i (Marcus 1952). This is normally called the sum of states of the transition state. Because in general $\rho(E, J) = \partial W(E, J)/\partial E$, sums and densities of states can be calculated principally by the same methods. These were already outlined in Sect. 21.3.2.

Loose Transition States The situation is more complicated in absence of a well-defined transition state. Here, the cumulative reaction probability can be determined either by variational methods or identified with the number of open rovibrationally adiabatic reaction channels for given E and J .

The variational methods utilize the fact that classical TST always provides an upper limit of the actual rate coefficient (Wigner 1937; Horiuti 1938; Keck 1967; Bunker and Pattengill 1968; Truhlar and Garrett 1980). This is essentially due to the fact that the transition state is considered as a “point of no return”, and that recrossing of trajectories from the product part of the phase space to the reactant part of the phase space are neglected. However, recrossing does occur, and TST counts such trajectories as reactive, overestimating the rate. Therefore, the smallest rate coefficient is the best approximation. Accordingly, the molecular configuration with the minimum sum or density of states along the reaction coordinate is the optimum choice for the transition state.

Within the statistical adiabatic channel model (Hirschfelder and Wigner 1939; Eliason and Hirschfelder 1959; Quack and Troe 1974), one constructs reaction channels correlating reactant and product rovibrational eigenstates along the reaction coordinate under observation of total angular momentum conservation. Here, the cumulative reaction probability is set equal to the number of *open* reaction channels, which are the channels that have a maximum energy below or equal to E for a given J .

The currently most common formulations of the microcanonical variational TST for unimolecular reactions, viz. flexible RRKM theory (Wardlaw and Marcus 1988) and variable reaction coordinate RRKM theory (Klippenstein 1991) were recently reviewed by Klippenstein (2003) and Fernández-Ramos et al. (2006). Accordingly, we will focus our discussion in the following on the statistical adiabatic channel model (SACM) (Quack and Troe 1974). In particular in its simplified version (Troe 1981; Troe 1983b), it represents a compact and sufficiently adequate approach to obtain $k(E, J)$ for master equation calculations of bond fission reactions under typical combustion conditions. For an illustration of an exact SACM calculation and the complicated channel pattern, which arises even for a very simple product pair like two identical linear dipoles, see Maergoiz et al. (1991). In the following we briefly describe the characterization of reaction channels along the reaction coordinate as used in the simplified SACM and outline the determination of the number of open channels, $W_{\text{SACM}}(E, J)$.

In the simplified version of SACM, the isotropic part of the interfragment potential as a function of the reaction coordinate q (e.g. the distance between the

centers of mass of the separating fragments), is expressed as the sum of the classical potential, $V(q)$, the contribution from the zero-point vibrational energies, $\Delta E_z(q)$, and the centrifugal potential, $V_{\text{cent}}(q, J) = B_{\text{cent}}(q)J(J + 1)$:

$$V_a(q, J) = V(q) + \Delta E_z(q) + B_{\text{cent}}(q)J(J + 1) \quad (21.8)$$

The classical potential, $V(q)$, is usually approximated by a Morse function

$$V(q) = D\{1 - \exp[-\beta(q - q_e)]\}^2 \quad (21.9)$$

with the Morse parameters, D and β , and the reactant equilibrium value of the reaction coordinate, q_e . The q dependence of ΔE_z is examined below. For the effective rotational constant of the orbital motion of the separating fragments, $B_{\text{cent}}(q)$, useful approximations for quasi-diatomic and quasi-triatomic systems exist (Troë 1981), which are sufficient for most practically relevant cases.

For the calculation of the number of open reaction channels, it is important to distinguish between conserved degrees of freedom, which retain their character in going from reactant to products (vib \rightarrow vib, rot \rightarrow rot), and disappearing oscillators, which become external rotors of the products (vib \rightarrow rot).

The q dependence of the energy eigenvalues of the conserved degrees of freedom is approximated by an exponential switch function (Quack and Troë 1974):

$$\varepsilon(q) = \varepsilon(q_e) \exp[-\alpha(q - q_e)] + \varepsilon(\infty)\{1 - \exp[-\alpha(q - q_e)]\} \quad (21.10)$$

with the interpolation parameter, α , the corresponding eigenvalue of the reactant, $\varepsilon(q_e)$, and the correlated eigenvalue of the product, $\varepsilon(\infty)$. As examples, consider for $\text{CH}_4 \rightarrow \text{CH}_3 + \text{H}$ the correlation of a C–H stretch vibration in CH_4 (e.g. $\varepsilon(q_e) = \nu_3(\text{CH}_4) = 3019 \text{ cm}^{-1}$) with the corresponding C–H stretch vibration in CH_3 ($\varepsilon(\infty) = \nu_1(\text{CH}_3) = 3044 \text{ cm}^{-1}$) and a one-dimensional external rotation of CH_3 ($\varepsilon(q_e) = B_{\text{CH}_4} = 5.24 \text{ cm}^{-1}$) becoming a one-dimensional external rotation of CH_3 ($\varepsilon(\infty) = B_{\text{CH}_3} = 9.58 \text{ cm}^{-1}$) (Quack and Troë 1974; Troë 1981; Brouwer et al. 1987). The sum or density of states for these conserved degrees of freedom, $W_{\text{cons}}(E)$ and $\rho_{\text{cons}}(E)$, respectively, can be easily determined by using the above mentioned Beyer-Swinehart/Stein-Rabinovitch counting procedure with the interpolated wavenumbers and rotational constants as input. The zero-point energy correction in Eq. (21.8), $\Delta E_z(q)$, is obtained by the analogous interpolation (Troë 1981).

A somewhat different approach has to be employed for the disappearing oscillators. As an example, consider the H–C–H bending vibration in CH_4 ($\varepsilon(q_e) = \nu_2(\text{CH}_4) = 1534 \text{ cm}^{-1}$) that becomes a free rotation of CH_3 ($\varepsilon(\infty) = C_{\text{CH}_3} = 4.79 \text{ cm}^{-1}$). Here, vibrational eigenstates have to be correlated with rotational eigenstates. The energy dependence and spacing of the eigenvalues for these two limiting cases are different. Therefore, the interpolated channel eigenvalues sensitively depend on the parameter α . In general the energy dependence of the sum of states for the disappearing oscillators can be classically expressed in the form

$W_{\text{disapp}}(E) \propto E^x$, where $x = 1$ and $x = 0.5$ represent the limiting cases of a harmonic oscillator and a one-dimensional free rotor, respectively (Troë 1981). The actual sum of states, $W_{\text{disapp}}(E)$, is calculated classically (Eq. 3.3 in Brouwer et al. 1987 with $r = 0$, because conserved internal rotors were already included in ρ_{cons} above) with values for x obtained from a switch function similar to Eq. (21.10) (Eq. 3.18 in Troë 1981). The overall number of open reaction channels is then obtained by the convolution $W_{\text{SACM}}(E) = \rho_{\text{cons}} * W_{\text{disapp}}$, where again the Beyer-Swinehart/Stein-Rabinovitch counting routine can be used. $W_{\text{SACM}}(E)$ calculated in this way accounts for all degrees of freedom but neglects total angular momentum.

In the simplified version of SACM, this is corrected for by introducing an angular momentum coupling factor, $F_{\text{AM}}(E, J)$, with which $W_{\text{SACM}}(E, J) = W_{\text{SACM}}(E) \times F_{\text{AM}}(E, J)$ (Troë 1983b). In general the influence of angular momentum can be most accurately treated for the reactant and the completely separated fragments. The general principle in simplified SACM is again to interpolate between these two limiting cases (Eq. 3.10 in Troë 1983b). The angular momentum coupling factor for the reactant, $F_{\text{AMe}}(E, J)$, depends on the type of symmetric top, and expressions for the different cases are available (Troë 1983b); a compact formula for prolate symmetric top molecules is derived in Olzmann and Troë (1994). Angular momentum coupling factors, $F_{\text{AM}\infty}(E, J)$, for the separated, non-interacting fragments are related to the so-called phase space limit of the sum of states, W_{PST} . One defines $F_{\text{AM}\infty}(E, J) = W_{\text{PST}}(E, J)/W_{\text{PST}}(E)$, where $W_{\text{PST}}(E, J)$ and $W_{\text{PST}}(E)$ are counted with and without observation of angular momentum conservation, respectively (Troë 1983b; Olzmann and Troë 1992). Here, the index PST stands for phase space theory, which is a limiting case of TST, where the cumulative reaction probability is calculated by using the molecular properties of the completely separated fragments (Nikitin 1965; Pechukas and Light 1965; Chesnavich and Bowers 1977; see also Baer and Hase 1996 and Forst 2003).

In order to apply Eq. (21.10), the interpolation parameter α has to be specified. It turned out in extensive case studies (Cobos and Troë 1985) that in simplified SACM the calculated rate coefficients are by far more sensitive to the dimensionless ratio α/β (with Morse parameter β) than to α itself. Moreover, it was found that many experimental rate coefficients could be reproduced with $0.3 < \alpha/\beta < 0.6$ (Cobos and Troë 1985). Accordingly, in practical calculations the ratio α/β is either fitted to experimental rate coefficients for a given bond dissociation energy or set equal to 0.5 as a standard value (Cobos and Troë 1985). Note that an increase of α/β causes an increase of the rate coefficient, because the number of open reaction channels approaches its phase space limit.

Since there is a simplified SACM available for both microcanonical (Troë 1983b) and the high-pressure limit of canonical (Troë 1981) rate coefficients, the ratio α/β can be fitted to either one, allowing a reasonably consistent calculation of the other one. For fitting, also rate coefficients of combination reactions can be employed by making use of detailed balancing (Cobos and Troë 1985). However, in contrast to the negative temperature dependence, which is often observed for high-pressure limiting rate coefficients of combination reactions, simplified SACM

mostly predicts a slightly positive temperature dependence. This is mainly due to the use of the Morse function for the radial potential, which is somewhat too flat at larger distances, causing too a fast increase of the centrifugal barriers with increasing J . If both α/β and D are treated as adjustable quantities, the simplified SACM can be considered as one of several two-parameter formulations of TST with an entropic and an energetic parameter.

Under practical aspects we finally note that in simplified SACM, harmonic oscillator wavenumbers and rotational constants of reactants and products have to be correlated simply in the order of descending magnitude (Troe 1981).

21.3.4 Threshold Energies, $E_{0(i)}(J)$

In the case of a tight transition state, the threshold energy $E_{0(i)}(J)$ is obtained from the energy difference between the rovibrational ground states of the transition state TS_i and the reactant, $E_{0(i)} = E_{0(i)}(J = 0)$, plus the minimum rotational energy of the transition state (rotational constant $B_{\text{TS}(i)}$) for a given J . For transition states, that are linear, spherical tops, or prolate symmetric tops, it follows $E_{0(i)}(J) = E_{0(i)} + B_{\text{TS}(i)}J(J + 1)$. For oblate symmetric tops the situation is a bit more complicated, because the K -dependent energy levels below $B_{\text{TS}(i)}J(J + 1)$ have to be accounted for (see e.g. Atkins 1983), if applicable also for the reactant. In the case of loose transition states the threshold energy $E_{0(i)}(J)$ is obtained as the maximum of $V_a(q, J)$ along q according to Eq. (21.8).

We note that, here, the rovibrational ground state of the reactant is taken as energy zero. Sometimes it is more useful to take the rovibrational ground state of the reactant plus $BJ(J + 1)$ as energy zero. Then, of course, the energy scale has to be adapted properly.

21.3.5 Reaction Path Degeneracies, L_i

Symmetry effects in chemical reactions can sometimes be puzzling. Under practical aspects we, therefore, recommend to calculate partition functions as well as sums and densities of states without symmetry numbers and to multiply the rate coefficients by a reaction path degeneracy or statistical factor $L_i = n_{\text{TS}(i)}\sigma/(n\sigma_{\text{TS}(i)})$ instead (Gilbert and Smith 1990). Here, σ and $\sigma_{\text{TS}(i)}$ denote the overall symmetry numbers of the reactant and transition state TS_i , respectively, and n and $n_{\text{TS}(i)}$ are the corresponding numbers of optical isomers (2 for chiral species, 1 otherwise). A detailed review of the problem is given by Pollak and Pechukas (1978), and a thorough but accessible summary is presented in Gilbert and Smith (1990). For symmetry considerations in simplified SACM see Quack and Troe (1977) and Troe (1983b).

If hindered internal rotors are present, the simplifying concept of symmetry numbers may break down. In these complicated cases, it is always useful to recall that it is after all a correlation between rovibrational states of the reactant and the transition state, which has to be established. An example is outlined in Hack et al. (2001).

21.3.6 Nascent Distributions, $f(E)$

The normalized nascent energy distribution $f(E)$ of a chemically activated intermediate C produced in an exothermic reaction $A + B \rightarrow C$ (see Fig. 21.1) can be obtained from the cumulative reaction probability $W_1(E) = W_{-1}(E)$, again calculated for averaged $J = \langle J \rangle$:

$$f(E) = N \times W_{-1}(E - E_{0(-1)}) \exp[-(E - E_{0(-1)})/k_B T] \quad (21.11)$$

with N being the normalization factor (Gilbert and Smith 1990; Holbrook et al. 1996; Forst 2003). If W_{-1} is not available, it can be very well approximated by the sum of states of C itself, W_C (Forst 1973).

21.3.7 Collisional Energy Transfer Probabilities, $P(E', E)$

The rate coefficient of collisional energy transfer from $E_j \rightarrow E_i$ in Eq. 21.2 is expressed as a product $\omega P(E_i, E_j) = \omega P_{ij}$ of the collision frequency, ω , and the energy transfer probability, P_{ij} . The collision frequency $\omega = Z_{LJ}[M]$ is calculated from the Lennard-Jones collision number, Z_{LJ} , and the bath gas concentration, $[M]$ (Hippler et al. 1983; Gilbert and Smith 1990; Forst 2003). Note that $P(E_i, E_j)$ is the discrete representation of $P(E', E)$ in the continuum picture, cf. Fig. 21.1.

For the energy transfer probabilities, two different models are commonly used: the exponential down model or the stepladder model (Gilbert and Smith 1990, Holbrook et al. 1996, Forst 2003). In the exponential down model, a transition probability for downward collisions ($E' < E$) of the form $P_d(E', E) = c(E) \exp[-(E - E')/\alpha]$ is used, in the stepladder model $P_d(E', E) = c'(E) \delta(E - E' - \Delta E_{SL})$. Here, $c(E)$ and $c'(E)$ are normalization factors, the quantities $\alpha > 0$ and $\Delta E_{SL} > 0$ are parameters, and δ denotes the Dirac delta function. In the exponential down model, the transfer of small amounts of energy is more likely than the transfer of larger amounts, whereas in the stepladder model only fixed amounts $E - E' = \Delta E_{SL}$ are transferred.

The transition probabilities have to satisfy two constraints, detailed balancing and normalization. Detailed balancing ensures that the equilibrium distribution, once reached, is not interfered by collisions. The condition is that the transition rates between reciprocal energy levels for a Boltzmann distribution are equal, that is $P_d(E', E) \rho(E) \exp(-E/k_B T) = P_u(E, E') \rho(E') \exp(-E'/k_B T)$. The normalization

condition reads as $\int_0^E P_d(E', E)dE' + \int_E^\infty P_u(E', E)dE' = 1$. From these two constraints, the transition probability for upward collisions $P_u(E', E)$ can be calculated for any given $P_d(E', E)$, and normalization factors can be obtained by a recursive algorithm (Gilbert and King 1980; Gilbert et al. 1983; Gilbert and Smith 1990). For the exponential down model, analytical expressions are also available (Troe 1977a). Furthermore, it can be shown that the parameters α and ΔE_{SL} represent the average energy transferred per down collision, $\langle \Delta E \rangle_d$, in the respective model, that is $\langle \Delta E \rangle_d = \alpha$ and $\langle \Delta E \rangle_d = \Delta E_{SL}$ (Holbrook et al. 1996). For the average energy transferred per collision (up and down), $\langle \Delta E \rangle$, the approximate relation

$$\langle \Delta E \rangle = -\langle \Delta E \rangle_d \tanh\left(\frac{\langle \Delta E \rangle_d}{2F_E k_B T}\right) \quad (21.12)$$

holds (Snider 1986; Troe 1987). Here, F_E characterizes the energy dependence of the density of states above E_0 (Troe 1977b). For more complex models of collisional transition probabilities, which may be necessary to describe experiments with high energy resolution, see Hold et al. (1997).

For the calculation of temperature- and pressure-dependent rate coefficients, the choice of the transition probability model is not critical, because the details are averaged out (Troe 1977a; Snider 1986; Troe 1987). There is also little theoretical guidance as to the absolute magnitudes of $\langle \Delta E \rangle_d$ or its energy dependence $\langle \Delta E \rangle_d(E)$ (Gilbert and Smith 1990; Oref and Tardy 1990). Experiments with laser excitation (Hippler et al. 1983; Rossi et al. 1983; Hold et al. 1997) have shown, however, that the average energies transferred per collision depend more on the bath gas than on the excited molecule. Typical values are collected in Table 21.1. Note that for highly excited molecules $\langle \Delta E \rangle < 0$, because deactivating collisions prevail, while by definition $\langle \Delta E \rangle_d > 0$. For an extensive

Table 21.1 Typical values of energy transfer parameters from laser excitation experiments (adapted from Gilbert and Smith 1990)

Excited molecule (excitation energy/cm ⁻¹)	Collider gas	$-\langle \Delta E \rangle$ /cm ⁻¹	$\langle \Delta E \rangle_d$ /cm ^{-1a}
Azulene (17500)	Ar	145	260
Toluene (52000)		130	245
Ethyl acetate (17000)		130	245
CH ₃ CH ₂ NC (13500)		140	255
CF ₃ I (15000)		70	175
Toluene (52000)	He	75	180
	N ₂	130	245
	O ₂	160	275
	CH ₄	260	365
	CF ₄	320	420
	Toluene	770	800
	C ₁₁ H ₂₄	1340	1345

^a Calculated from $\langle \Delta E \rangle$ with Eq. (21.12) for $T = 298$ K with $F_E = 1$

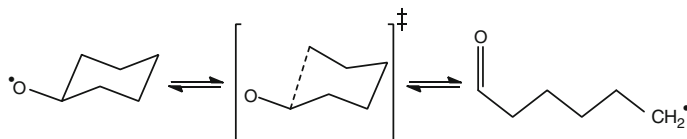
review on collisional energy transfer and a useful compilation of numerical data see Oref and Tardy (1990).

In practical calculations of rate coefficients, mostly the exponential down or the stepladder model are used with an energy-independent $\langle \Delta E \rangle_d$ treated as a fitting parameter. In many cases the values obtained in this way for $\langle \Delta E \rangle_d$ and $|\langle \Delta E \rangle|$ are somewhat higher than those from laser excitation experiments.

21.4 Rate Coefficients from Canonical Transition State Theory

As was already outlined in Sect. 21.2.1, conventional canonical TST works well for reactions proceeding over potential energy barriers. Here, it is most important to use reliable values for the threshold energy E_0 , which are now in many cases available from quantum chemical calculations with reasonable accuracy (see Chap. 20).

In the following we give an example, which demonstrates the adequacy of the method, but emphasizes at the same time a remaining critical issue, namely, the proper incorporation of anharmonicity effects in the partition functions. In this respect, hindered internal rotors can be particularly important. We illustrate the problem in terms of the reversible ring-opening/ring-closure reaction of the cyclohexoxy radical (Welz et al. 2008):



Here the effect is most pronounced in the ring-closure reaction, because five hindered internal rotors become torsional vibrations in going from the open-chain radical to the cyclic transition state with a corresponding decrease in entropy.

We experimentally determined first-order rate coefficients for the ring-opening and ring-closure reaction in the temperature range 293–341 K at pressures between 5 and 55 bar (Welz et al. 2008). The *c*-C₆H₁₁ONO radicals were produced by laser photolysis of *c*-C₆H₁₁ONO and detected by time-resolved laser-induced fluorescence. Rate coefficients were obtained from biexponential fits of the intensity-time profiles. Their temperature dependence is shown in Fig. 21.2; no pressure dependence was observed.

Rate coefficients were also calculated from canonical TST, Eq. (21.1), on the basis of molecular and transition state properties from quantum chemical calculations on G3MP2B3 level of theory (for details see Welz et al. 2008). It turned out that the results for ring-opening can be very well reproduced within the harmonic oscillator (HO) approximation as can be realized from Fig. 21.2.

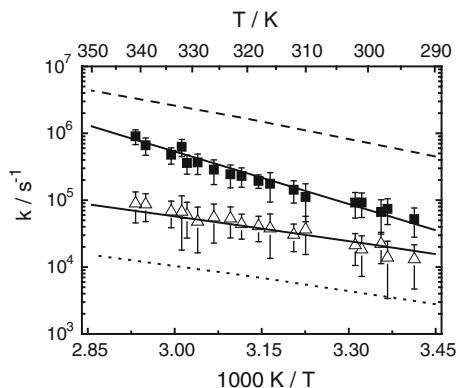


Fig. 21.2 Experimentally determined rate coefficients for the ring-opening (■) and ring-closure (Δ) reaction of $c\text{-C}_6\text{H}_{11}\text{ONO}$ and results from TST calculations (lines); *upper solid line*: ring-opening with HO approximation, *dashed line*: ring-closure with HO approximation ($q_{\text{HO},i}$), *dotted line*: ring-closure with $q_{\text{HIR},i}^*$, *lower solid line*: ring-closure with $q_{\text{HO},i} f_i^*$; for explanations see text (Reproduced from Welz et al. 2008—Reproduced by permission of the PCCP Owner Societies)

The rate coefficient for ring-closure, however, is overpredicted in the HO approximation (vibrational partition functions $q_{\text{HO},i}$) by almost two orders of magnitude. Since the slopes in the Arrhenius plots, that is the energies of activation, for the measured and calculated rate coefficients are very similar (see Fig. 21.2), it is obviously the entropy of activation that is overestimated. This, in turn, is rather the result of an underestimation of the entropy for the open-chain radical than an overestimation for the transition state, because the latter predicts the rate coefficient of the ring-opening reaction very well.

Accordingly, the agreement is likely to be improved by treating the five torsional vibrations in the open-chain radical as hindered internal rotors, which have higher entropy. To this end we calculated for these degrees of freedom the potential energy as a function of the corresponding dihedral angle, allowing all other degrees of freedom to relax. We then numerically solved the one-dimensional Schrödinger equations and calculated the five partition functions (hindered internal rotor partition functions: $q_{\text{HIR},i}^*$) by exact summation of the energy levels obtained (Welz et al. 2008).

A naïve substitution of $q_{\text{HO},i}$ by $q_{\text{HIR},i}^*$ in Eq. (21.1), however, lead to too a strong decrease of the rate coefficients as can be realized from Fig. 21.2. A reason for the discrepancy is that the $q_{\text{HO},i}$ refer to normal modes, that is to linear combinations of internal coordinates, whereas the $q_{\text{HIR},i}^*$ refer to dihedral angles that is to internal coordinates itself (Vansteenkiste et al. 2006). Accordingly, the $q_{\text{HO},i}$ do not represent the limiting cases of the respective $q_{\text{HIR},i}^*$ for vanishing anharmonicities, because the force constants and reduced masses/moments of inertia are different.

An obviously much better approximation was proposed in Vansteenkiste et al. (2006). These authors emphasized that any corrected partition function must refer

to the same coordinate as the original one. Accordingly, harmonic oscillator partition functions, $q_{\text{HO},i}^*$ are calculated for the same dihedral angles as the $q_{\text{HIR},i}^*$. This can be accomplished by using harmonic potentials with force constants that correspond to the minima of the dihedral angle scans. Then ratios $f_i^* = q_{\text{HIR},i}^*/q_{\text{HO},i}^*$ are formed, and the denominator in Eq. 21.1 is multiplied by the product $\prod f_i^*$ that is the $q_{\text{HO},i}$ are formally substituted by $q_{\text{HO},i} f_i^*$. In this way the agreement with the experiment becomes much better as can be realized from Fig. 21.2. Despite its simplicity, this approximation seems to work astonishingly well. For a recent review and comparison of several other hindered internal rotor approximations, the reader is referred to Ellingson et al. (2006).

It is instructive also to compare our results with thermochemical estimates. For the ring-closure we obtained from the above calculations a relatively low preexponential factor of $3.02 \times 10^8 \text{ s}^{-1}$. In Benson (1976) an entropy decrement of $(19.7 \pm 1.3) \text{ J K}^{-1} \text{ mol}^{-1}$ per disappearing internal rotor is estimated for the formation of C_6 and C_7 rings from the corresponding open-chain species. If, in a zero-order approximation, the contributions from all other degrees of freedom are neglected, an entropy of activation $\Delta S^\ddagger = -5 \times 19.7 \text{ J K}^{-1} \text{ mol}^{-1} = -98.5 \text{ J K}^{-1} \text{ mol}^{-1}$ is obtained in our case. With a reaction path degeneracy of 2, this value corresponds to a preexponential factor of $2.6 \times 10^8 \text{ s}^{-1}$ for $T = 320 \text{ K}$ in striking agreement with the result of our detailed calculations above (Welz et al. 2008). This gives additional evidence for the quality of the approximation proposed by Vansantenkiste et al. (2006).

21.5 Rate Coefficients from Solutions of the Master Equation

A necessary condition for the validity of canonical TST is that the equilibrium energy-distribution of the reactant(s) is not depleted by the reaction step itself or, in other words, that the rate of collisional energy transfer is much higher than the rate of reaction. The most important cases from combustion chemistry, where this condition is usually *not* fulfilled, are unimolecular reactions, complex-forming bimolecular reactions, and recombination reactions, each away from its high-pressure limit (Troe 1988; Miller et al. 2005). All those reaction systems have in common the participation of one or more unimolecular steps.

In general, the macroscopic rate coefficient, $k_i(T, P)$, of a unimolecular reaction step i under steady-state conditions can be obtained by averaging its specific rate coefficient, $k_i(E)$, over the normalized energy distribution, $\sim \tilde{n}^s(E)$, of the reactant (Gilbert and Smith 1990; Holbrook et al. 1996; Forst 2003):

$$k_i(T, P) = \int_0^\infty k_i(E) \tilde{n}^s(E; T, P) dE \quad (21.13)$$

Here, the tilde denotes normalization, and the superscript s stands for steady-state. The specific rate coefficients can be calculated, for averaged J , as outlined in Sects. 21.3.1–21.3.5. The steady-state distribution, which parametrically depends on T and P , follows from the solution of an appropriate master equation. In the following two sections, we outline the general approach for thermal unimolecular and complex-forming bimolecular reactions.

21.5.1 Thermal Unimolecular Reactions

The master equation for a thermal unimolecular reaction follows from Eq. (21.3) with $R_1 = 0$ and $k_3[\text{D}] = 0$. The general solution is (Gilbert and Smith 1990; Holbrook et al. 1996; Forst 2003)

$$\mathbf{N}(t) = \sum_{k=1}^m \exp(-\lambda_k t) a_k \mathbf{E}_k \quad (21.14)$$

with λ_k and \mathbf{E}_k being the eigenvalues and eigenvectors, respectively, of the matrix \mathbf{J} , and a_k denoting expansion coefficients. The upper limit of the summation, m , is equal to the dimension of \mathbf{J} . For typical upper energy limits in the range of 10^4 – 10^5 cm^{-1} and grain sizes of 10 cm^{-1} , values of m between 10^3 and 10^4 result. Note that according to the definition of \mathbf{J} in Eq. (21.3), all eigenvalues are positive. At not too high temperatures, that is for $k_B T < E_{0(i)}$ (Pritchard 1984, Pilling and Robertson 2003), one has $\lambda_1 \ll \lambda_2, \lambda_3, \lambda_4, \dots, \lambda_m$, where the eigenvalues are ordered by increasing magnitude. From this sequence it is obvious that monoexponential decay only occurs at $t > \lambda_2^{-1}$, when all higher terms, $k > 1$, in Eq. (21.14) have vanished. This is the steady-state regime, where the populations of all energy levels decay with the same rate, and the shape of the energy distribution does not longer change with time. We emphasize that only under these conditions it is meaningful to define a rate coefficient $k(T, P)$; it is identical to the lowest eigenvalue λ_1 .

The corresponding steady-state distribution can be normalized, $\tilde{\mathbf{N}}^s = \mathbf{E}_1/|\mathbf{E}_1|$, and the rate coefficient of reaction channel i is obtained from Eq. (21.13). Obviously, the relations

$$\lambda_1 = k(T, P) = \sum_i k_i(T, P) \quad (21.15)$$

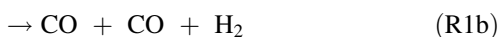
hold and can be used to check the numerical consistency of the lowest eigenvalue and eigenvector. We note in passing that the higher eigenvalues are governed by the rate of collisional energy transfer (Pritchard 1984; Gilbert and Smith 1990).

Depending on the character of the matrix \mathbf{J} (tridiagonal for the stepladder model, band-diagonal for the exponential down model), the eigenvalues and eigenvectors can be determined by standard methods like QL decomposition. A very useful compilation of numerical methods and computer routines can be found

in Press et al. (1992). In our master equation with the stepladder model, we use the EISPACK routine tq12 (Smith et al. 1974) after symmetrization of the matrix \mathbf{J} (Gilbert and Smith 1990; Forst 2003). To enable an energy resolution of 10 cm^{-1} , we permit for ΔE_{SL} only integer multiples of 10 cm^{-1} and solve $n = \Delta E_{\text{SL}}/10 \text{ cm}^{-1}$ independent master equations, which are shifted with respect to each other by 10 cm^{-1} . The rate coefficient is then obtained by averaging the lowest eigenvalues of these n master equations, which are always found to be in very close agreement (within 5 %). Analogously, the normalized eigenvector is obtained. The restriction of ΔE_{SL} to integer multiples of 10 cm^{-1} allows in each case a sufficiently fine adjustment of the calculated rate coefficients to the experimental results.

For practical calculations, we generally recommend to smooth the density of states, $\rho(E)$, at low energies, where it can be discontinuous. Sometimes, also at low energies, the conditions for detailed balancing and normalization of the $P(E', E)$ may appear conflicting (Oref and Tardy 1990). In this case priority must be given to normalization, because otherwise unwanted sinks are introduced into the master equation, which can lead to serious errors. In contrast, a (slight) violation of detailed balancing, in particular at low energies, has virtually no influence on the rate coefficients and can be tolerated. Numerical problems due to stiffness (Press et al. 1992) can be avoided by using compiler options that enable 128 bit word length.

We illustrate some general aspects of such calculations with an example from our own work, the thermal unimolecular decomposition of glyoxal, $(\text{CHO})_2$ (Friedrichs et al. 2008). The reaction was studied in two different shock tubes at temperatures ranging from 1106 to 2320 K at total densities between 1.7×10^{-6} and $1.9 \times 10^{-5} \text{ mol cm}^{-3}$ corresponding to pressures between 0.15 and 3.6 bar with argon as the bath gas. Concentration-time profiles of $(\text{CHO})_2$, HCO, and H were monitored. The overall decomposition reaction consists of four parallel steps:



Reactions (R1a–R1c) have well pronounced transition states, and specific rate coefficients were calculated from RRKM theory. For the bond fission reaction (R1d), the simplified SACM was used. All specific rate coefficients were calculated for $\langle J \rangle_{T=1400\text{K}} = 70$. Test calculations with $\langle J \rangle_{T=800\text{K}} = 54$ and $\langle J \rangle_{T=2500\text{K}} = 96$ were also performed, but the rate coefficients do not deviate more than $\pm 6 \%$ from the results for $\langle J \rangle = 70$. The master equation with the stepladder model was solved, and the experimental rate coefficients could be best reproduced with $\Delta E_{\text{SL}} = 1200 \text{ cm}^{-1}$. The quality of the fit is demonstrated for reaction (R1d) in Fig. 21.3. Specific rate coefficients and normalized molecular energy distributions are displayed in Fig. 21.4.

Fig. 21.3 Arrhenius plot for reaction (R1d), *filled symbols*: from experimental [HCO] profiles, *open symbols*: from experimental [H] profiles (H from $\text{HCO} \rightarrow \text{H} + \text{CO}$), *solid lines*: master equation modeling (Modified from Friedrichs et al. 2008—Reproduced by permission of the PCCP Owner Societies)

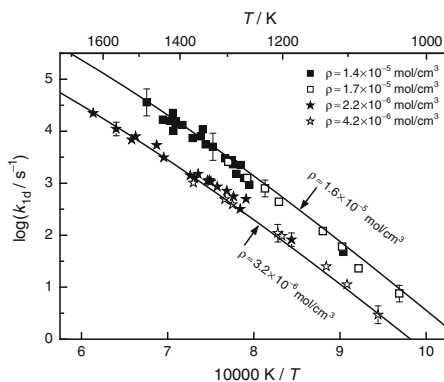
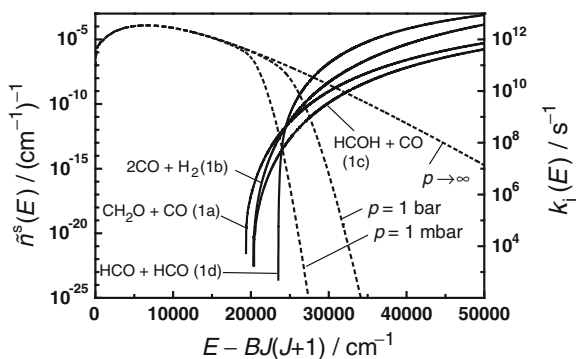


Fig. 21.4 Specific rate coefficients, $k_i(E)$ (*solid curves, right axis*), for the decomposition reactions of $(\text{CHO})_2$ and normalized steady-state distributions, $\tilde{n}^s(E)$ for $T = 1500 \text{ K}$ and different pressures (*dashed curves, left axis*) (Modified from Friedrichs et al. 2008—Reproduced by permission of the PCCP Owner Societies)



From Fig. 21.4 it is obvious that the energy dependence of the rate coefficient k_{1d} for the loose reaction channel is much more pronounced than the energy dependence of k_{1a} , k_{1b} , and k_{1c} with tight transition states. Accordingly, the curve for k_{1d} crosses the curves of the other three rate coefficients, and at high energies, that is at high temperatures and high pressures, the $\text{HCO} + \text{HCO}$ channel (R1d) becomes predominant.

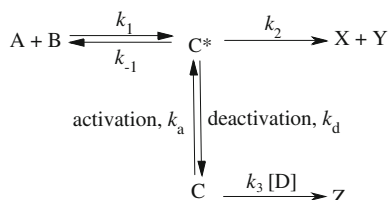
Normalized steady-state distributions of the reactant, glyoxal, are displayed in Fig. 21.4 for two different pressures and the high-pressure limiting case, which corresponds to the Boltzmann equilibrium distribution. It is interesting to note that at pressures near 1 bar, the population at high energies, where the $\text{HCO} + \text{HCO}$ channel predominates, is strongly depleted. That is, this channel is strongly pressure-dependent under these conditions, which is experimentally confirmed as can be realized from Fig. 21.3. The agreement of the temperature and pressure dependence between the measured and calculated rate coefficients is very good. In contrast, the reactant population at lower energies, where the tight channels prevail, is still close to the high-pressure limit at pressures near 1 bar. That is, these channels exhibit under the same experimental conditions a weaker pressure dependence, which is also experimentally confirmed (Friedrichs et al. 2008).

This is an example of how the temperature and pressure dependence of a thermal unimolecular multichannel reaction can be rationalized in terms of $k_i(E)$ and $\tilde{n}^s(E; T, P)$. For a more detailed discussion see Friedrichs et al. (2008).

21.5.2 Complex-Forming Bimolecular Reactions

Equation (21.3) with $k_3[D] = 0$ represents the familiar master equation for a complex-forming bimolecular reaction or, in other words, a chemically activated unimolecular reaction. The general time-dependent solution for a one-well system is presented in Schranz and Nordholm (1984), Smith et al. (1989), and Gilbert and Smith (1990). For extensions to multi-well systems, the reader is referred to Klippenstein and Miller (2002), Miller and Klippenstein (2006), and Fernández-Ramos et al. (2006). In particular, the kinetics of these multiwell systems can become very complex. In the following, we focus on steady-state solutions of the one-well problem, Eq. (21.3), which are helpful for a general understanding and often also provide a sufficiently accurate description.

Two different steady-state regimes have to be considered (Snider 1984; Schranz and Nordholm 1984). These can be rationalized with the following simplified kinetic scheme, where the meaning of the symbols can be inferred from a comparison with Fig. 21.1:



First we consider the case $k_3[D] = 0$. If we set $[\text{C}^*] = [\text{C}] = 0$ and switch on the $\text{A} + \text{B}$ reaction at $t = 0$, a first steady-state, $d[\text{C}^*]/dt = 0$, appears after a certain induction period. This is denoted the *intermediate* (Schranz and Nordholm 1984) or *pseudo* (Snider 1984) steady-state, and it governs the product branching ratio $[\text{X}]/[\text{C}]$, which is identical to the ratio of the rates of decomposition/stabilization (D/S), which is often used in the analysis of chemical activation systems at low temperatures (Forst 1973; Forst 2003). After the stabilization reservoir, C, is filled up, a second steady-state, $d([\text{C}^*] + [\text{C}])/dt = 0$ occurs, which is called the *asymptotic* or *final* steady-state (Schranz and Nordholm 1984), and one has $-d[\text{A}]/dt = d[\text{X}]/dt$. For the chemical activation master equation, Eq. (21.3), the general steady-state condition is

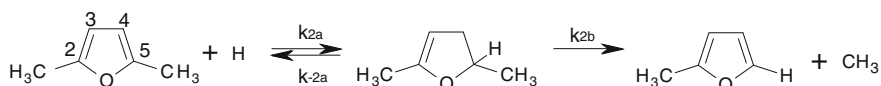
$$R_1 \mathbf{F} - \mathbf{JN}^s = 0 \quad (21.16)$$

This corresponds to the final steady-state if all collisional transition probabilities are correctly normalized. The intermediate steady-state can be invoked by setting the transition probabilities for upward collisions $P_u(E', E) = 0$ for energies E below a certain limit, E_{abs} . In this way a sink or absorbing barrier is introduced at $E = E_{\text{abs}}$, and molecules C once stabilized below E_{abs} cannot be reactivated to energies $E > E_{\text{abs}}$ (Holbrook et al. 1996; Forst 2003). Note that the exact location of E_{abs} is not critical; it should merely be located somewhat below the lowest threshold energy in the system.

The transition from the intermediate to the final steady state occurs at $t \sim \lambda_1^{-1} = [k(T, P)]^{-1}$ with λ_1 being the smallest eigenvalue of \mathbf{J} that is, $k(T, P)$ is the *thermal* rate coefficient for the unimolecular decomposition of C (Schranz and Nordholm 1984). For combustion modeling, it is usually the *final* steady-state that is relevant.

The normalized vector of the molecular distribution function, $\tilde{\mathbf{N}}^s$, can then be obtained by solving Eq. (21.16) for \mathbf{N}^s and subsequent normalization. Note that normalization eliminates R_1 . For the stepladder model, the matrix \mathbf{J} is tridiagonal, and, for instance, the routines `banbks` and `bandec` from Press et al. (1992) can be used. The rate coefficients are then obtained from Eq. (21.13).

We illustrate this approach with an addition–elimination reaction that is important in the pyrolysis of 2,5-dimethylfuran (25DMF), a potential biofuel. The reaction $25\text{DMF} + \text{H} \rightarrow \text{products}$ was studied in a shock tube with time resolved detection of H atoms by atom resonance absorption spectrometry (Frieze et al. 2013). Several product channels are accessible. The most important one is hydrogen addition to C atom 2 or 5 followed by $\beta\text{-CH}_3$ elimination from the intermediate radical:



Also important are the H addition to C atom 3 or 4 and the direct H abstraction reaction from the CH_3 group. The temperature dependences of these rate coefficients are shown in Fig. 21.5.

The H addition/ CH_3 elimination reaction can be modeled with a chemical activation master equation. The corresponding quantities are displayed in Fig. 21.6. The nascent distribution, $f(E)$, starts at the threshold energy of the reverse reaction of the formation reaction, $E_{0(-2a)}$, and the effect of collisional stabilization is evident in the steady-state distribution, $\tilde{n}^s(E)$. It is noteworthy that for this reaction system, $\tilde{n}^s(E)$ at pressures near 1 bar is hardly pressure-dependent and already close to the high-pressure limit.

The rate coefficient $k(T, P)$ of the overall reaction $25\text{DMF} + \text{H} \rightarrow 2\text{MF} + \text{CH}_3$ can be expressed as the product of the rate coefficient of the formation of the intermediate adduct radical and a yield factor quantifying the relative branching

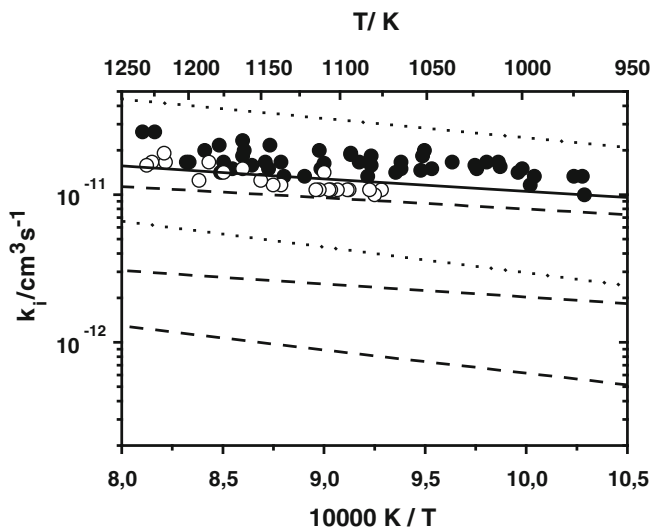


Fig. 21.5 Arrhenius plot for different product channels of the 25DMF + H reaction, *symbols*: overall rate coefficients from experiment (*full symbols*: $P \sim 1.6$ bar, *open symbols*: $P \sim 4.8$ bar), *dashed lines*: calculations, from *bottom to top*: H abstraction from CH_3 (canonical TST), H addition to C3/4 (high-pressure limit, canonical TST), H addition to C2/5 followed by CH_3 elimination (master equation and Eq. (21.17), see text), *full line*: sum of all channels, *dotted lines*: estimations from Lifshitz et al. (1998) (Reproduced from Friese et al. 2013; Copyright Elsevier)

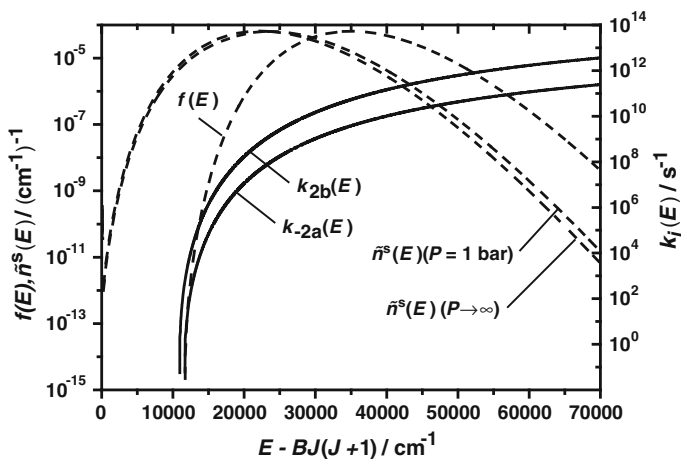


Fig. 21.6 Specific rate coefficients, $k_i(E)$ (*solid curves*, *right axis*), nascent distribution, $f(E)$, and normalized steady-state distributions, $\tilde{n}^s(E)$, for the decomposition reactions of the 25DMF + H adduct radical at $T = 1500$ K and two different pressures (*dashed curves*, *left axis*), calculated with $\Delta E_{\text{SL}} = 250 \text{ cm}^{-1}$, the numbering of the rate coefficients corresponds to the reaction scheme given in the text

fraction of the forward reaction (Troë 1994). The intermediate is formed with the high-pressure limiting (or capture) rate coefficient, k_{2a}^∞ , and one has:

$$k(T, P) = k_{2a}^\infty(T) \frac{k_{2b}(T, P)}{k_{2b}(T, P) + k_{-2a}(T, P)} \quad (21.17)$$

Under the conditions of the final steady-state, the rate coefficients k_{-2a} and k_{2b} are always larger or equal to their thermal high-pressure limit, because the intermediates are formed with a minimum energy of $E_{0(-2a)}$, and a pressure-dependent depletion above $E_{0(2b)}$, which would be responsible for the falloff effect in a thermal reaction, cannot occur, because these high levels are continuously populated by reaction 2a. This applies in particular to reaction systems with $E_{0(-2a)} \geq E_{0(2b)}$ and at high temperatures, where $f(E)$ is broad. This effect is discussed in more detail in González-García and Olzmann (2010). In many cases, the pressure dependencies in the yield factor of Eq. (21.17) tend to cancel, which explains the weak pressure dependence of the overall rate coefficients for complex-forming bimolecular reactions at high temperatures. Even approximations of the yield factor with thermal rate coefficients can be adequate as is illustrated in Bentz et al. (2007) and Friese et al. (2013).

Additional complications can arise, when the condition $k_3[D] = 0$ is dropped that is, when a bimolecular reaction of the intermediate species occurs (Olzmann 2002). If the pseudo-first order rate coefficient of this reaction, $k_3[D]$, is distinctly smaller than the rate coefficient of the thermal decomposition of the intermediate, $k_{-2a}^{\text{therm}}(T, P) + k_{2b}^{\text{therm}}(T, P)$, the final steady-state distribution is hardly influenced, and the above approach remains valid. If $[k_{-2a}^{\text{therm}}(T, P) + k_{2b}^{\text{therm}}(T, P)] < k_3[D] < \gamma_c \omega$, where $\gamma_c \omega$ is an effective collision frequency (unit: s^{-1}) for stabilization, with the dimensionless collision efficiency γ_c (Troë 1983a) often in the range $0.01 < \gamma_c < 0.1$, the *intermediate* steady-state is maintained. And finally, if $\gamma_c \omega < k_3[D]$, which is rarely the case under realistic conditions, mainly chemically activated intermediates would undergo the bimolecular reaction, before being collisionally stabilized, and the product yield of the unimolecular forward reaction would decrease below its value for the intermediate steady state. This is quantified in Olzmann (2002).

21.6 Summary, Software and Further Reading

In this chapter we have elucidated the essential elements of statistical rate theory that are relevant for practical calculations of rate coefficients for gas-phase reactions. We have aimed at readers on an intermediate level between graduate students and junior scientists, emphasizing fundamental aspects and touching only in passing most recent developments such as eigenvector-eigenvalue expansions. The general treatment is, of course, not restricted to reactions under combustion

conditions, and the chapter hopefully can be read with benefit by anybody who is interested in calculating rate coefficients for gas phase reactions.

Several master equation codes are available in the scientific community. The currently most common are, in alphabetical order: CHEMRATE (Knyazev and Tsang 2000), MESMER (Glowacki et al. 2012), MULTIWELL (Barker 2001, Barker and Ortiz 2001), and UNIMOL (Gilbert and Smith 1990). We refrain here from giving current URL addresses and refer the reader to search engines instead. All codes can be easily found and are currently free of charge. A compilation with some comments is given in Carstensen and Dean (2007).

For further studies, apart from the most recent standard monographs (Gilbert and Smith 1990, Baer and Hase 1996, Holbrook et al. 1996, Forst 2003) and the review articles already given in the text, useful presentations of several basic and application aspects, including empirical parameterizations for $k(T, P)$, can be found in: Allen et al. (2012), Carstensen and Dean (2007), Glowacki et al. (2012), Golden and Barker (2011), Pilling (2008), and Pilling and Robertson (2003).

Acknowledgments Financial support by the Deutsche Forschungsgemeinschaft (SFB 606 “Non-Stationary Combustion: Transport Phenomena, Chemical Reactions, Technical Systems”) and by the European Cooperation in Science and Technology (COST, Action CM0901 “Detailed Chemical Kinetic Models for Cleaner Combustion”) is gratefully acknowledged.

References

- Allen JW, Goldsmith CF, Green WH (2012) Automatic estimation of pressure-dependent rate coefficients. *Phys Chem Chem Phys* 14:1131–1155
- Astholtz DC, Troe J, Wieters W (1979) Unimolecular processes in vibrationally highly excited cycloheptatrienes. I. Thermal isomerization in shock waves. *J Chem Phys* 70:5107–5116
- Atkins PW (1983) *Molecular Quantum Mechanics*, 2nd edn. Oxford University Press, Oxford
- Barker JR (2001) Multiple-well, multiple-path unimolecular reaction systems. I. MultiWell computer program suite. *Int J Chem Kinet* 33:232–245
- Barker JR, Ortiz NF (2001) Multiple-well, multiple-path unimolecular reaction systems. I. MultiWell computer program suite. *Int J Chem Kinet* 33:246–261
- Baer T, Hase WL (1996) *Unimolecular reaction dynamics: theory and experiments*. Oxford University Press, Oxford
- Benson SW (1976) *Thermochemical Kinetics*, 2nd edn. Wiley, New York
- Bentz T, Giri BR, Hippler H et al (2007) Reaction of hydrogen atoms with propyne at high temperatures: an experimental and theoretical study. *J Phys Chem* 111:3812–3818
- Beyer T, Swinehart TF (1973) Algorithm 448: Number of multiply-restricted partitions. *Comm Assoz Comput Mach* 16:379–379
- Brouwer L, Cobos CJ, Troe J et al (1987) Specific rate constants $k(E, J)$ and product state distributions in simple bond fission reactions. II. Application to $\text{HOOH} \rightarrow \text{OH} + \text{OH}$. *J Chem Phys* 86:6171–6182
- Bunker DL, Pattengill M (1968) Monte carlo calculations. VI. A re-evaluation of the RRKM theory of unimolecular reaction rates. *J Chem Phys* 48:772–776
- Carstensen H-H, Dean AM (2007) The kinetics of pressure-dependent reactions. In: Carr RW (ed) *Modeling of chemical reactions*. Comprehensive chemical kinetics, vol 42. Elsevier, Amsterdam, pp 101–184

- Chesnavich WJ, Bowers MT (1977) Statistical phase space theory of polyatomic systems: Rigorous energy and angular momentum conservation in reactions involving symmetric polyatomic species. *J Chem Phys* 66:2306–2315
- Clary DC (2008) Theoretical studies on bimolecular reaction dynamics. *Proc Natl Acad Sci USA* 105:12649–12653
- Cobos CJ, Troe J (1985) Theory of thermal unimolecular reactions at high pressures II. Analysis of experimental results. *J Chem Phys* 83:1010–1015
- Eliason MA, Hirschfelder JO (1959) General collision theory treatment for the rate of bimolecular, gas phase reactions. *J Chem Phys* 30:1426–1436
- Ellingson BA, Lynch VA, Mielke SL et al (2006) Statistical thermodynamics of bond torsional modes: Tests of separable, almost-separable, and improved Pitzer–Gwinn approximations. *J Chem Phys* 125:084305/1–084305/17
- Fernández-Ramos A, Miller JA, Klippenstein SJ et al (2006) Modeling the kinetics of bimolecular reactions. *Chem Rev* 106:4518–4584
- Forst W (1973) *Theory of Unimolecular Reactions*. Academic Press, New York
- Forst W (2003) *Unimolecular Reactions: A Concise Introduction*. Cambridge University Press, Cambridge
- Frankcombe TJ, Smith SC, Gates KE et al (2000) A master equation model for bimolecular reactions via multi-well isomerizing intermediates. *Phys Chem Chem Phys* 2:793–803
- Friedrichs G, Colberg M, Dammeier J et al (2008) HCO formation in the thermal unimolecular decomposition of glyoxal: Rotational and weak collision effects. *Phys Chem Chem Phys* 10:6520–6533
- Friese P, Simmie JM, Olzmann M (2013) The reaction of 2,5-dimethylfuran with hydrogen atoms—an experimental and theoretical study. *Proc Combust Inst* 34:233–239
- Gang J, Pilling MJ, Robertson SH (1996) Partition functions and densities of states for butane and pentane. *J Chem Soc Faraday Trans* 92:3509–3518
- Gilbert RG, King KD (1980) Gas/gas and gas/wall average energy transfer from very low-pressure pyrolysis. *Chem Phys* 49:367–375
- Gilbert RG, Luther K, Troe J (1983) Theory of thermal unimolecular reactions in the fall-off range. II. Weak collision rate constant. *Ber Bunsenges Phys Chem* 87:169–177
- Gilbert RG, Smith SC (1990) *Theory of unimolecular and recombination reactions*. Blackwell, Oxford
- Glasstone S, Laidler KJ, Eyring H (1941) *The theory of rate processes*. McGraw-Hill, New York
- Glowacki DR, Liang C-H, Morley C et al (2012) MESMER: an open-source master equation solver for multi-energy well reactions. *J Phys Chem A* 116:9545–9560
- Golden DM, Barker JR (2011) Pressure- and temperature-dependent combustion reactions. *Combust Flame* 158:602–617
- González-García N, Olzmann M (2010) Kinetics of the chemically activated HSO₅ radical under atmospheric conditions—a master-equation study. *Phys Chem Chem Phys* 12:12290–12298
- Hack W, Hoyermann K, Kersten C et al (2001) Mechanism of the 1-C₄H₉ + O reaction and the kinetics of the intermediate 1-C₄H₉O radical. *Phys Chem Chem Phys* 3:2365–2371
- Hippler H, Troe J, Wendelken HJ (1983) Collisional deactivation of vibrationally highly excited polyatomic molecules. II. Direct observations for excited toluene. *J Chem Phys* 78:6709–6717
- Hirschfelder JO, Wigner E (1939) Some quantum-mechanical considerations in the theory of reactions involving an activation energy. *J Chem Phys* 7:616–628
- Holbrook KA, Pilling MJ, Robertson SH (1996) *Unimolecular reactions*, 2nd edn. Wiley, Chichester
- Hold U, Lenzer T, Luther K et al (1997) Collisional energy transfer probabilities in the deactivation of highly vibrationally excited aromatics. *Ber Bunsenges Phys Chem* 101:552–565
- Horiuti J (1938) On the statistical mechanical treatment of the absolute rate of chemical reaction. *Bull Chem Soc Japan* 13:210–216

- Hoyermann K, Maarfeld S, Nacke F et al (2010) Rate coefficients for cycloalkyl + O reactions and product branching in the decomposition of chemically activated cycloalkoxy radicals: an experimental and theoretical study. *Phys Chem Chem Phys* 12:8953–8967
- Jeffrey SJ, Gates KE, Smith SC (1996) Full iterative solution of the two-dimensional master equation for thermal unimolecular reactions. *J Phys Chem* 100:7090–7096
- Keck JC (1967) Variational theory of reaction rates. *Adv Chem Phys* 13:85–121
- Klippenstein SJ (1991) Variational optimizations in the Rice–Ramsperger–Kassel–Marcus theory calculations for unimolecular dissociations with no reverse barrier. *J Chem Phys* 96:367–371
- Klippenstein SJ (2003) RRKM theory and its implementation. In: Green NJB (ed) *Unimolecular kinetics Part 1. The reaction step*. *Comprehensive chemical kinetics*, vol 39. Elsevier, Amsterdam, pp 55–103
- Klippenstein SJ, Miller JA (2002) From the time-dependent, multiple-well master equation to phenomenological rate coefficients. *J Phys Chem A* 106:9267–9277
- Knyazev VD (1998) Density of States of one-dimensional hindered internal rotors and separability of rotational degrees of freedom. *J Phys Chem A* 102:3916–3922
- Knyazev VD, Tsang W (2000) Chemically and thermally activated decomposition of secondary butyl radical. *J Phys Chem A* 104:10747–10765
- Lifshitz A, Tamburu C, Shashua R (1998) Thermal decomposition of 2,5-dimethylfuran. Experimental results and computer modeling. *J Phys Chem A* 102:10655–10670
- Maergoiz AI, Nikitin EE, Troe J (1991) Adiabatic channel potential curves for two linear dipole rotors: II. Analytical representation of channel potentials and rate expressions for identical rotors. *Z Phys Chem* 172:129–156
- Marcus RA (1952) Unimolecular dissociations and free radical recombination reactions. *J Chem Phys* 20:359–364
- Miller JA, Klippenstein SJ (2003) From the multiple-well master equation to phenomenological rate coefficients: Reactions on a C₃H₄ potential energy surface. *J Phys Chem A* 107:2680–2692
- Miller JA, Klippenstein SJ (2006) Master equation methods in gas phase chemical kinetics. *J Phys Chem A* 110:10528–10544
- Miller JA, Pilling MJ, Troe J (2005) Unravelling combustion mechanisms through a quantitative understanding of elementary reactions. *Proc Combust Inst* 30:43–88
- Nikitin EE (1965) Statistical theory of endothermic reactions, Part 2. Monomolecular reactions. *Theor Exp Chem* 1:90–94
- Olzmann M (1997) On nascent angular-momentum distributions in complex-forming bimolecular reactions. *Ber Bunsenges Phys Chem* 101:533–537
- Olzmann M (2002) On the role of bimolecular reactions in chemical activation systems. *Phys Chem Chem Phys* 4:3614–3618
- Olzmann M, Troe J (1992) Rapid approximate calculation of numbers of quantum states $W(E, J)$ in the phase space theory of unimolecular bond fission reactions. *Ber Bunsenges Phys Chem* 96:1327–1332
- Olzmann M, Troe J (1994) Approximate determination of rovibrational densities of states $\rho(E, J)$ and number of states $W(E, J)$. *Ber Bunsenges Phys Chem* 98:1563–1574
- Oref I, Tardy DC (1990) Energy transfer in highly excited large polyatomic molecules. *Chem Rev* 90:1407–1445
- Pechukas P, Light JC (1965) On detailed balancing and statistical theories of chemical kinetics. *J Chem Phys* 42:3281–3291
- Pilling MJ (2008) Interaction between theory and experiment in the investigation of elementary reactions of importance in combustion. *Chem Soc Rev* 37:676–685
- Pilling MJ, Robertson SH (2003) Master equation models for chemical reactions of importance in combustion. *Annu Rev Phys Chem* 54:245–275
- Pollak E, Pechukas P (1978) Symmetry numbers, not statistical factors, should be used in absolute rate theory and in Broensted relations. *J Am Chem Soc* 100:2984–2991
- Press WH, Teukolski SA, Vetterling WT et al (1992) *Numerical recipes in fortran: the art of scientific computing*, 2nd edn. Cambridge University Press, Cambridge

- Pritchard HO (1984) The quantum theory of unimolecular reactions. Cambridge University Press, Cambridge
- Quack M, Troe J (1974) Specific rate constants of unimolecular processes II. Adiabatic channel model. *Ber Bunsenges Phys Chem* 78:240–252
- Quack M, Troe J (1977) Unimolecular processes V: Maximum free energy criterion for the high pressure limit of dissociation reactions. *Ber Bunsenges Phys Chem* 81:329–337
- Rossi MJ, Pladziewicz JR, Barker JR (1983) Energy-dependent energy transfer: Deactivation of azulene (S_0 , E_{vib}) by 17 collider gases. *J Chem Phys* 78:6695–6708
- Schranz HW, Nordholm S (1984) Theory of chemically activated unimolecular reactions. Weak collisions and steady states. *Chem Phys* 87:163–177
- Smith BT, Boyle JM, Garbow BS et al (1974) Matrix eigensystem routines—EISPACK guide. In: Goos G, Hartmanis J (eds) *Lecture Notes in Computer Science*, vol 6. Springer, Berlin
- Smith SC, McEwan MJ, Gilbert RG (1989) The relationship between recombination, chemical activation and unimolecular dissociation rate coefficients. *J Chem Phys* 90:4265–4273
- Snider N (1984) Deductions from the master equation for chemical activation. *J Chem Phys* 80:1885–1893
- Snider N (1986) Model dependence of collision efficiencies for thermal unimolecular reactions. *J Phys Chem* 90:4366–4372
- Stein SE, Rabinovitch BS (1973) Accurate evaluation of internal energy level sums and densities including anharmonic oscillators and hindered rotors. *J Chem Phys* 588:2438–2445
- Steinfeld JI, Francisco JS, Hase WL (1989) *Chemical kinetics and dynamics*. Prentice Hall, Englewood Cliffs
- Troe J (1977a) Theory of thermal unimolecular reactions at low pressures. I. Solution of the master equation. *J Chem Phys* 66:4745–4757
- Troe J (1977b) Theory of thermal unimolecular reactions at low pressures. II. Strong collision rate constants. *J Chem Phys* 66:4758–4775
- Troe J (1981) Theory of thermal unimolecular reactions at high pressures. *J Chem Phys* 75:226–237
- Troe J (1983a) Approximate expressions for the yields of unimolecular reactions with chemical and photochemical activation. *J Phys Chem* 87:1800–1804
- Troe J (1983b) Specific rate constants $k(E, J)$ for unimolecular bond fissions. *J Chem Phys* 79:6017–6029
- Troe J (1987) On the role of collisional processes in thermal unimolecular reactions. *Z Phys Chem Neue Folge* 154:73–90
- Troe J (1988) Towards a quantitative understanding of elementary combustion reactions. *Proc Combust Inst* 22:843–862
- Troe J (1994) The colourful world of complex-forming bimolecular reactions. *J Chem Soc Faraday Trans* 90:2303–2317
- Truhlar DG, Garrett BC (1980) Variational transition-state theory. *Acc Chem Res* 13:440–448
- Vansteenkiste P, Van Neck D, Van Speybroeck V et al (2006) An extended hindered-rotor model with incorporation of Coriolis and vibrational-rotational coupling for calculating partition functions and derived quantities. *J Chem Phys* 124:044314/1–044314/14
- Wardlaw DM, Marcus RA (1988) On the statistical theory of unimolecular processes. *Adv Chem Phys* 70:231–263
- Welz O, Striebel F, Olzmann M (2008) On the thermal unimolecular decomposition of the cyclohexoxy radical—an experimental and theoretical study. *Phys Chem Chem Phys* 10:320–329
- Wigner E (1937) Calculation of the rate of elementary association reactions. *J Chem Phys* 5:720–725

Chapter 22

Primary Products and Branching Ratios for Combustion Multi-Channel Bimolecular Reactions from Crossed Molecular Beam Studies

Nadia Balucani, Francesca Leonori and Piergiorgio Casavecchia

Abstract The identification of the primary products and the determination of their branching ratios as a function of translational energy for multi-channel elementary reactions of importance in combustion chemistry still represent a challenge for traditional kinetics experiments. However, this kind of information is central for the detailed modeling of combustion systems. In this chapter, the significant contribution provided by the crossed molecular beam (CMB) method with “universal” mass spectrometric detection and time-of-flight analysis is illustrated. In particular, we describe the basics of the CMB method empowered with “soft” electron impact ionization as recently implemented in our laboratory and report on its application to the study of the multi-channel elementary reactions of atomic oxygen with unsaturated hydrocarbons (acetylene, ethylene, and allene) and hydrocarbon radicals (methyl and allyl), which are of paramount interest in the combustion of hydrocarbons. The complementarity to kinetics studies and implications of the dynamics results for the modeling of combustion chemistry will be noted.

Introduction

A complete understanding of combustion processes requires the construction of realistic global chemical mechanisms, especially if one is interested in the emission of pollutants which are formed in trace amounts (Gardiner 2000; Warnatz et al. 2001). Combustion chemistry is governed by chain reactions where a complex coupling between elementary steps (unimolecular, bimolecular, and

N. Balucani · F. Leonori · P. Casavecchia (✉)
Dipartimento di Chimica, Università degli Studi di Perugia, Perugia, Italy
e-mail: piero@dyn.unipg.it

N. Balucani
e-mail: nadia.balucani@unipg.it

termolecular) accounts for the overall transformation from reactants to products. Because of this complexity, computer models that include all the possible elementary reactions and the appropriate boundary conditions are necessary. Obviously, to construct a realistic model, knowledge of the chemical transformation at the molecular level for all the important steps is required (Carl et al. 2007; Leonori et al. 2012b). Only in this way can a complete characterization and possibly a control of the combustion system be achieved. The focus of this chapter is on bimolecular reactions. Those of relevance in combustion processes involve at least one open-shell species, because the reactions involving two closed-shell species are too slow to make an important contribution. The rate coefficients for many bimolecular reactions involving abundant radicals in combustion systems have been determined in kinetics experiments at room temperature or, in numerous cases, at the temperatures of relevance in combustion (Baulch et al. 2005). In contrast, much less is known on the chemical identity of the primary products and their branching ratios (BRs). This piece of information is, however, very relevant, since the products of an elementary reaction are the reactants of a subsequent one that may be chain propagating or chain terminating and may lead to the formation of different pollutants with different efficiencies. In the case of multichannel reactions, the primary products are not easy to predict. Quite often, in the absence of any information, the most exothermic channels are assumed to be the dominant ones. This criterion, however, is oversimplified and in many real cases the most exothermic channels are not the dominant ones, as it is the underlying potential energy surface that determines which channels are open and to what extent they contribute to the overall reaction. Therefore, versatile experimental techniques able to identify the primary products and their branching ratios are of fundamental importance.

The crossed molecular beams (CMB) technique coupled to mass spectrometric (MS) detection is an efficient experimental method for the investigation of polyatomic multichannel elementary reactions under single collision conditions (Lee 1987a, b; Casavecchia 2000; Casavecchia et al. 2009). This technique is especially suitable to identify the nature of the primary products. First of all, its application is rather general because any species (including transient radicals) can be detected as mass spectrometry is a “universal” detection method. Therefore, each possible product can be observed even when its formula and structure is unknown, which is a common situation for polyatomic multichannel reactions. In this respect, the use of universal MS detection is decisive, because it allows determining the mass (and, in favorable cases, the gross molecular formula) of all possible products, while the application of spectroscopic detection techniques would require the knowledge of their optical properties.

Two beneficial factors make CMB-MS experiments more advantageous with respect to common MS flow reactors. First of all, the two reactants are not simply mixed together, but are confined into distinct supersonic molecular beams (well defined in angle and velocity) which cross each other at a specific angle. The atomic/molecular species of each beam collide only with those of the other beam at the collision center where the reaction products are formed. Once formed, the

products fly toward the detector without undergoing secondary or wall collisions, since the pressure of the collision chamber is maintained very low (10^{-7} hPa) and the mean free path of the products is much larger than the dimensions of the vacuum chamber (see Fig. 22.1). In this way, the outcome of many identical well-defined molecular encounters under single collision conditions is observed. This is particularly important in establishing the nature of the primary products, because they are normally transient species which, in bulk experiments, could undergo secondary collisions capable of altering their nature.

Another advantage of the CMB-MS technique is that it makes possible the measurement of the angular and velocity distributions (see below) of each reaction product. From the analysis of those functions, it is possible to shed light on the reaction mechanism and to infer the energetics of the various reaction channels, thus distinguishing isomeric products with different enthalpy of formation (Casavecchia et al. 2001; Balucani et al. 2006). Finally, since the electron ionization cross sections are known or can be reliably estimated for many species (Fitch and Sauter 1983), it is possible to derive the branching ratios from the observed product number densities (Schmoltnner et al. 1989a, b).

In conclusion, the CMB-MS technique permits (a) determining the nature of the primary reaction products, (b) deriving the branching ratios of competing reaction

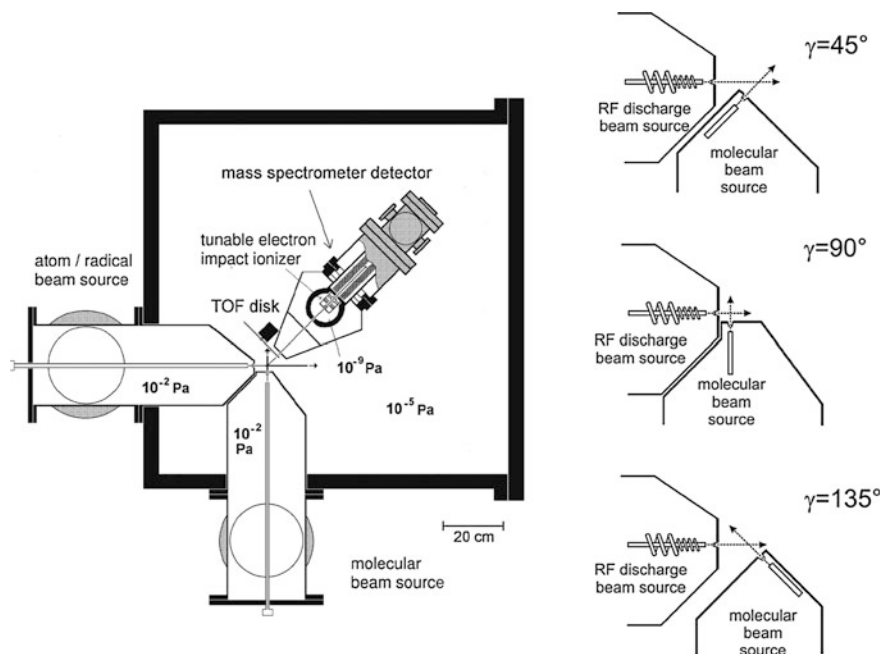


Fig. 22.1 Schematic view of the crossed molecular beams apparatus with rotating TOF mass spectrometer detector and 90° beam crossing angle geometry (left-hand-side). On the right-hand-side the geometries for 45° and 135° beam crossing angle are also depicted (Adapted with permission from Casavecchia et al. 2009. Copyright (2009), Royal Society of Chemistry)

channels, (c) elucidating the microscopic reaction mechanisms, and (d) measuring the product energy partitioning. The characterization of the reaction mechanism and of the product energy release can also improve the modeling of the dense environments of combustion, because if the reaction goes through long-lived intermediate complexes, those can be collisionally stabilized, inducing a change in the product branching ratios. In addition, vibrationally hot radicals produced by very exothermic reactions can be much more reactive than implied by the average flame temperature. The benefits of the CMB-MS technique have motivated its extension to the study of reactions of interest in combustion chemistry. The CMB-MS method has been employed to study bimolecular reactions of relevance in combustion processes in numerous laboratories and has become a valuable complementary approach to kinetics experiments. Bimolecular reactions of atomic species—such as $O(^3P)$ (Capozza et al. 2004; Leonori et al. 2007; Casavecchia et al. 2005, 2009; Balucani et al. 2011; Leonori et al. 2012b; Fu et al. 2012a, b) and $C(^3P)$ atoms (Kaiser and Mebel 2002; Gu et al. 2007a; Leonori et al. 2008a), simple radicals—such as $OH(X^2\Pi)$ (Alagia et al. 1993a, b), $CN(X^2\Sigma^+)$ (Kaiser and Balucani 2001, Leonori et al. 2010, 2012a), $C_2H(X^2\Sigma^+)$ (Stahl et al. 2001), $C_6H_5(X^2A_1)$ (Gu and Kaiser 2009, Albert and Davis 2010) and $CH(X^2\Pi)$ (Maksyutenko et al. 2011)—and other transient species as $C_2(X^1\Sigma_g^+, a^3\Pi_u)$ and $C_3(X^1\Sigma_g^+)$ have been characterized (Gu et al. 2007b, Leonori et al. 2008b) in recent years. Central for the successful study of multichannel reactions (of $O(^3P)$ in particular) has been the implementation in CMB-MS instruments of the “soft” ionization by tunable low-energy electrons (Capozza et al. 2004; Casavecchia et al. 2009) or VUV synchrotron radiation (Lee et al. 2009). Another innovation in the CMB apparatus of Perugia has been a variable beam crossing angle configuration (see Fig. 22.1), which allows varying the experimental collision energy (E_c) across a much wider range with respect to the fixed crossing angle set-up (Balucani et al. 2006; Casavecchia et al. 2009).

In this chapter, after a brief description of the CMB-MS technique, a survey of recent results on the reactions $O(^3P)+C_2H_2$, $O(^3P)+C_2H_4$, $O(^3P)+CH_2CCH_2$ (allene) and also on the radical–radical reactions $O(^3P)+C_3H_5$ (allyl) and $O(^3P)+CH_3$ (methyl) is given. The attention will be focused on the identification of primary products and the determination of their branching ratios. Finally, possible implications in the combustion modeling will be commented on.

22.1 Experimental

The basic principles of CMB experiments with MS detection and time-of-flight (TOF) analysis have been widely illustrated in several reviews and book chapters (Lee 1987b; Alagia et al. 1995; Casavecchia 2000; Casavecchia et al. 2010). In our CMB apparatus (see Fig. 22.1), two beams of atomic or molecular species are produced with narrow angular and velocity spread and are crossed at a specific collision angle (45° , 90° or 135°) in a high-vacuum (10^{-7} hPa) chamber. A

chopper wheel is placed in front of the detector when measuring TOF spectra. The detector is composed of a tunable electron-impact ionizer followed by a quadrupole mass filter. The ionizer is in the innermost chamber of a triply differentially pumped ultra-high-vacuum (10^{-11} hPa) chamber. The detector chamber can be rotated in the collision plane around the axis passing through the collision center.

The improvements brought recently to our CMB instrument have opened new perspectives on reactive scattering studies of polyatomic reactions of relevance in combustion chemistry. In particular, the capability of generating intense continuous beams of a variety of transient species, the possibility of increasing the collision energy by changing the collision angle, and the increased sensitivity of the detection system, mainly due to the introduction of the *soft* electron ionization (EI) detection by electrons with tunable, low energy, have been crucial to facing the study of the reactions between atomic oxygen and unsaturated hydrocarbons (Capozza et al. 2004; Casavecchia et al. 2005, 2009; Leonori et al. 2012b; Fu et al. 2012a, b) as well as with hydrocarbon radicals (Leonori et al. 2007; Balucani et al. 2011). The main features of our CMB apparatus and recent improvements have been recently detailed (Casavecchia et al. 2009) and will not be further commented on here. We only wish to emphasize that the *soft* EI approach, although not affording the same degree of selectivity as VUV synchrotron radiation, offers similar advantages with respect to the dissociative ionization problem, which had represented the main limitation of the method; in addition, *soft* EI gives us the bonus of determining branching ratios, since absolute EI cross sections are often known or can be reliably estimated (Fitch and Sauter 1983). Furthermore, the implementation of a variable beam crossing set-up with the two reactant beams crossing at 45° , or 90° , or 135° (see Fig. 22.1) allows us to vary the collision energy in a much wider range than previously possible. The reason is that the relative collision energy in a CMB experiment is given by $E_c = \frac{1}{2}\mu v_r^2$, where μ is the reduced mass of the system and v_r is the relative velocity. In general, $v_r^2 = v_1^2 + v_2^2 - 2v_1v_2 \cos \gamma$, where v_1 and v_2 are the two reactant beam velocities in the LAB frame and γ the crossing angle of the two beams (see Fig. 22.1-*rhs*).

22.2.1 *Laboratory Product Angular and Velocity Distributions and Center-of-Mass Product Angular and Translational Energy Distributions*

The quantities which are measured in a CMB experiment with MS/TOF detection are the product intensity as a function of the scattering angle, what we call the laboratory angular distribution, $N(\Theta)$, and the product intensity as a function of the scattering angle Θ and arrival time t , what we call the time-of-flight spectrum, $N(\Theta, t)$. The measurements are carried out in the laboratory (LAB) system of coordinates, but for the physical interpretation of the scattering data it is necessary to perform a coordinate transformation and move to the center-of-mass (CM)

reference frame (Lee 1987b). It can be easily demonstrated that for each reaction channel the relation between LAB and CM product flux is given by $I_{LAB}(\Theta, v) = I_{CM}(\theta, u)v^2/u^2$, where Θ and v are the LAB scattering angle and velocity, respectively, while θ and u are the corresponding CM quantities. Since the EI mass-spectrometric detector measures the number density of products, $N(\Theta)$, rather than the flux, the actual relation between the LAB density and the CM flux is given by $N_{LAB}(\Theta, v) = I_{CM}(\theta, u)v/u^2$. Because of the finite resolution of experimental conditions (angular and velocity spread of the reactant beams and angular resolution of the detector), the LAB to CM transformation is not single valued, and therefore analysis of the laboratory data is usually performed by forward convoluting tentative CM distributions over the experimental conditions. The *differential cross-section* $I_{CM}(\theta, u)$ is commonly factorized into the product of the velocity (or translational energy) distribution, $P(u)$ (or $P(E'_T)$), and the angular distribution, $T(\theta)$: $I_{CM}(\theta, E) = T(\theta) \times P(E'_T)$. In some cases, the coupling between the $T(\theta)$ and $P(E'_T)$ functions needs to be accounted for. The $T(\theta)$ and $P(E'_T)$ functions contain all the information about the dynamics. When multiple reaction channels contribute to the signal at a given m/z ratio, as in the combustion systems discussed here, a more complex situation arises. In these cases, a weighted total CM differential cross section reflecting the possible contributions to a specific m/z is used in the data analysis of the LAB distributions, that is, $I_{CM}(\theta, E'_T) = \sum_i w_i \times [T(\theta) \times P(E'_T)]_i$, with the parameter w_i representing the relative contribution of the integral cross-section of the i th channel (Balucani et al. 2006). The $T(\theta)$ and $P(E'_T)$ functions and the relative weight w_i for each channel are iteratively adjusted until calculated LAB angular distributions and TOF spectra match those from experiment.

22.2.2 Branching Ratios

One of the most useful information desirable on multichannel reactions is the branching ratio of the various channels. In CMB experiments, it is difficult to determine the absolute concentrations of reactants and products; however, it is possible to determine the ratios between the yields of the various product channels starting from their apparent cross-sections (i.e., the relative weights w_i discussed in the previous section and used in the best-fit analysis) (Schmoltner et al. 1989a, b). We can determine the ratio between the relative reactive cross-sections of the formation channels of two generic products A and B , $\sigma(A)$ and $\sigma(B)$, from the relation:

$$\frac{\sigma(A)}{\sigma(B)} = \left(\frac{\sigma^0(A)}{\sigma^0(B)} \right) \times \left(\frac{\sigma_{ion}(B)}{\sigma_{ion}(A)} \right) \times \left(\frac{f(B \rightarrow m/z)}{f(A \rightarrow m/z)} \right) \quad (22.1)$$

where $\sigma^0(A)$ and $\sigma^0(B)$ are the apparent cross-sections of A and B (whose ratio is equal to the ratio of the w_A and w_B weights), $\sigma_{ion}(A)$ and $\sigma_{ion}(B)$ are the values of

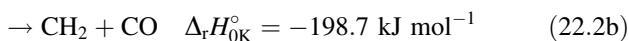
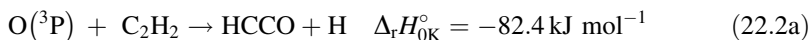
the ionization cross-section of A and B , and $f(A \rightarrow m/z)$ and $f(B \rightarrow m/z)$ are the fractions of A and B giving ions at that m/z ratio (the mass-dependent quadrupole transmission is taken into account). It should be noted that because of the soft ionization method, the fragmentation of the parent ions is, in general, significantly reduced with respect to when using the typical hard ionization conditions (employing 70–100 eV electrons) (see Casavecchia et al. 2009; Lee et al. 2009).

22.2 The Reactions Between Atomic Oxygen and Simple Unsaturated Hydrocarbons

The reaction of atomic oxygen, $O(^3P)$, with small unsaturated hydrocarbons are among the most important elementary steps in fuel rich hydrocarbon flames (Williams and Smith (1970); Gardiner (2000); Battin-Leclerc (2002); Alzueta et al. (2008)). These reactions play a key role in the combustion mechanism of many hydrocarbons, because small unsaturated hydrocarbons are easily formed during the combustion of methane, larger aliphatic hydrocarbons, and aromatics. Therefore, the characterization of these reactions is essential for the accurate description of the chain propagation steps in the combustion of hydrocarbons. In our laboratory, we have investigated the reactions of atomic oxygen with acetylene (ethyne), ethylene (ethene), and allene (propadiene), which are also the simplest members of the alkynes, alkenes and dienes families, respectively. For this reason, the investigation of these reactions can provide useful insights into the general oxidation mechanism of these three important chemical classes. In our studies, we have been able to determine the product BRs at high collision energies corresponding to high temperatures (between 2,000 and 4,000 K) for all three reactions. Here, we summarize the main experimental findings for each of the above systems and discuss the derived product BRs.

22.3.1 $O(^3P) + \text{Acetylene}$

The reaction $O(^3P) + C_2H_2$ is characterized by two competing channels:



Because of its importance, reaction (22.2a) has been extensively investigated in kinetics experiments starting from the 1960s (see Nguyen et al. 2006b, and references therein). The overall rate coefficient has been determined over a wide temperature range (from 200 to 2,500 K) and the recommended value of $k(T)$ is $1.95 \times 10^{-15} T^{1.40} \exp(-1110/T) \text{ cm}^3 \text{ molec}^{-1} \text{ s}^{-1}$ (Baulch et al. 2005). As for the

identity of the primary reaction products and their BR, there has been considerable debate over the years (for a critical survey until 2005, see Baulch et al. 2005; see also Capozza et al. 2004), but it is now accepted that the channel leading to $\text{HCCO} + \text{H}$ is dominant, with a yield of $\sim 80\%$ in the range 250–2500 K (Baulch et al. 2005). The most recent independent determinations at room temperature has furnished $k(22.2a)/[k(22.2a) + k(22.2b)] = 0.80 \pm 0.15$ (Michael and Wagner 1990) and $k(22.2b)/[k(22.2a) + k(22.2b)] = 0.17 \pm 0.08$ (Peeters et al. 1994). Reaction (22.2a) has also been investigated from a theoretical point of view. According to recent work (Nguyen et al. 2006b) in which the two lowest lying triplet ($^3A''$ and $^3A'$) potential energy surfaces (PES) were computed by high-level ab initio electronic structure calculations, the first excited triplet $^3A'$ surface can play a role in the reaction since it leads adiabatically to the HCCO radical in its low lying, energetically accessible A^2A' electronically excited state ($\sim 13 \text{ kJ mol}^{-1}$ above the X^2A'' ground state). RRKM calculations on the PESs assign a dominant role to channel (22.2a), with a practically energy-independent yield of $\sim 80\%$. Quite interestingly, the role of the excited PES leading to $\text{HCCO}(A^2A')$ is found theoretically to become important at high temperatures and this compensates a slightly decreasing yield of HCCO in the ground state. In a very recent theoretical study (Rajak and Maiti 2010), the effect of intersystem crossing (ISC) to the singlet OC_2H_2 PES has been examined and found to make a significant contribution to the CH_2 channel (up to 7% of the total reaction yield at $E_c = 39.7 \text{ kJ mol}^{-1}$) through the production of CH_2 in the excited singlet state \tilde{a}^1A_1 . However, the experimental search for CH_2 in its X^3B_1 ground state has failed so far (Huang et al. 1994).

Reaction (22.2a, 22.2b) was investigated in CMB-MS experiments in the early 1980s (Schmoltner et al. 1989a, b), but the only channel identified in those experiments was (22.2a). The detection of the heavy HCCO (ketenyl) product is, in fact, very favorable in CMB experiments, since it is scattered by the light H co-product and is therefore confined in a narrow angular range around the CM angle (see below). On the contrary, the detection of any of the two co-products from channel (22.2b) is problematic as, besides an unfavorable kinematics that brings the two co-products having comparable mass scattered over a wide angular range, the detection of CO is affected by the high inherent detector background at $m/z = 28$ due to residual CO in UHV chambers, while the detection of the co-product CH_2 at $m/z = 14$ is affected by the inherent background at this mass due to dissociative ionization of residual CH_4 to CH_2^+ and N_2 to N^+ . In addition, a potential source of interference comes from the dissociative ionization to $^{13}\text{CH}^+$ of the main HCCO product and of the elastically scattered, intense C_2H_2 beam. Although ^{13}C represents only a very small fraction ($\approx 2\%$) of the total carbon in HCCO and C_2H_2 , the $^{13}\text{CH}^+$ signal originating from these species is comparable to the CH_2 reactive scattering signal. To surmount this problem, Schmoltner et al. (1989a, b) used a beam of isotopically labeled ^{18}O and detected the CO product as C^{18}O^+ at $m/z = 30$, but a spurious contribution still originating from the dissociative ionization of the molecular product HCC^{18}O from channel (22.2a) could

not be avoided. This caused considerable uncertainty in the estimate of the branching ratio between channels (22.2a) and (22.2b). A relative cross-section $\sigma(22.2a)/[\sigma(22.2a) + \sigma(22.2b)]$ of 0.58 ± 0.21 was derived at $E_c = 25 \text{ kJ mol}^{-1}$, which is at variance with the best determination from kinetics studies.

Because of its importance, we have recently re-investigated the dynamics and branching ratio of this system using our improved CMB apparatus, first at $E_c = 39.7 \text{ kJ mol}^{-1}$ (Capozza et al. 2004) and, more recently, in order to characterize the trend of BRs with E_c , also at 34.3 and 52.7 kJ mol^{-1} (Leonori et al. 2013). We have exploited the capability of detecting the CH_2 radical by soft EI at 17 eV to suppress interfering dissociative ionization processes (see Fig. 22.2). In this way, we have been able to detect CH_2 cleanly from interferences, to measure its angular and TOF distributions and to determine $\sigma(22.2a)/[\sigma(22.2a) + \sigma(22.2b)]$ without ambiguity at the three different E_c s. Figure 22.3 shows the LAB angular distributions and typical TOF spectra of HCCO and CH_2 products. The Newton diagram in Fig. 22.3 shows how the HCCO product scattered from the very light H atom co-product is confined within a very small Newton circle, i.e., within a narrow angular range in the LAB frame, and hence its detection sensitivity is very much enhanced with respect to the CH_2 product which is, in contrast, scattered from the heavy CO co-product within a much larger Newton circle.

In the cases of the three experiments, we have determined the same $\sigma(\text{CH}_2)/\sigma(\text{HCCO})$ which is 0.26 ± 0.05 , corresponding to $\sigma(22.2a)/[\sigma(22.2a) + \sigma(22.2b)] = 0.79 \pm 0.05$. The derived product BRs are presented and compared with the recommended values from kinetics and statistical studies (Baulch et al. 2005) and with values from dynamical calculations on ab initio PESs in

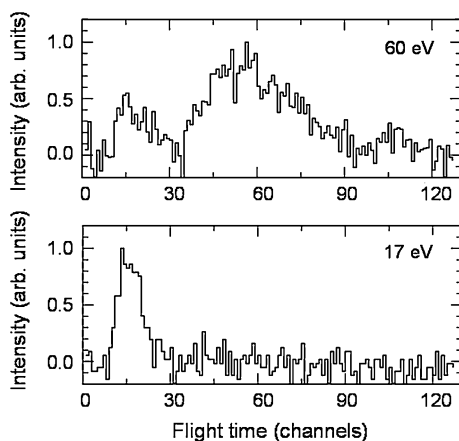


Fig. 22.2 TOF spectra (5 $\mu\text{s}/\text{channel}$) at the LAB angle of 30° for the reaction $\text{O}(^3\text{P}) + \text{C}_2\text{H}_2$ ($E_c = 39.7 \text{ kJ mol}^{-1}$) at $m/z = 14$ using an electron energy of 60 eV (top), and 17 eV (bottom). Note, when moving from 60 to 17 eV, the suppression of the dissociative ionization to $^{13}\text{CH}^+$ of the HCCO product and the elastically scattered C_2H_2 reagent (Adapted with permission from Capozza et al. 2004. Copyright (2004), American Institute of Physics)

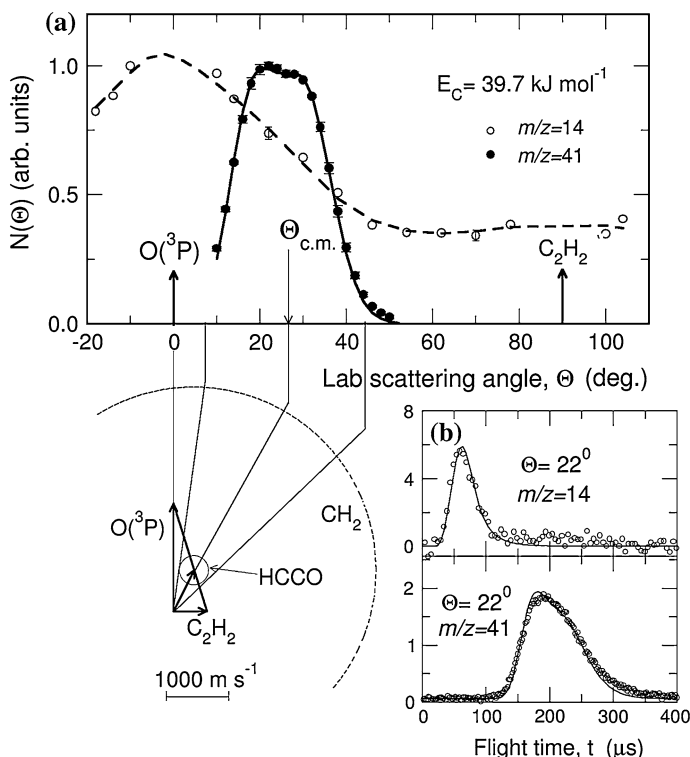


Fig. 22.3 **a** HCCO and CH₂ product LAB angular distributions from the O(³P) + C₂H₂ reaction at $E_C = 39.7 \text{ kJ mol}^{-1}$. Solid and dashed lines are best-fit curves obtained from the best-fit CM product angular and translational energy distributions. The Newton diagram of the experiment is also shown; there the circles delimit the maximum velocity that the indicated products can attain assuming that all the available energy is channeled into translation. **b** Exemplary TOF spectra (intensity (arb. units) as a function of flight-time) of $m/z = 41$ and $m/z = 14$ products at the LAB angle of 22° . The HCCO and CH₂ spectra are recorded at 2 and 5 $\mu\text{s}/\text{channel}$, respectively, using the single-shot TOF method. Solid lines are best-fit curves obtained from the best-fit CM functions (Adapted with permission: from Capozza et al. 2004, Copyright (2004), American Institute of Physics; and from Casavecchia et al. 2009, Copyright (2009), Royal Society of Chemistry)

Table 22.1. For details on how the BRs are estimated from signal intensities, ionization cross-sections, and dissociative ionization fractions, see Casavecchia et al. 2004 (for O + C₂H₂) and also Fu et al. 2012b (for O + C₂H₄).

It should be noted that the average E_c associated to a Maxwell–Boltzmann distribution at room temperature can be obtained via the equation $E_c = 3/2RT$; hence, the BRs derived from kinetics studies at room temperature can be associated to $E_c = 3.7 \text{ kJ mol}^{-1}$. The reverse conversion of CMB E_c values into temperatures is not straightforward. The simplest (but too simplistic) way of doing it would be to consider again the relation $E_c = 3/2RT$, which is, however, only valid

Table 22.1 Product branching ratios for the reaction $O(^3P) + C_2H_2$

Reaction channels	Kinetics and theoretical studies ^a Recommended over the range 200–2500 K	CMB studies E_c (kJ mol ⁻¹)			QCT-SO calculations ^c $E_c = 39.7$ kJ mol ⁻¹
		34.3 ^b	39.7 ^{c,d}	52.7 ^b	
HCCO + H	0.8	0.79 ± 0.05	0.79 ± 0.05	0.79 ± 0.05	0.786 ± 0.097
CH ₂ + CO	0.2	0.21 ± 0.05	0.21 ± 0.05	0.21 ± 0.05	0.214 ± 0.046

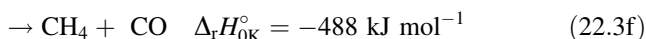
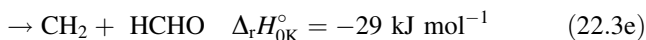
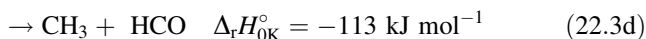
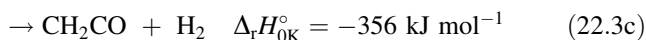
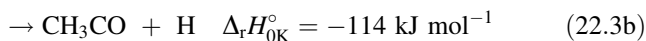
^a Baulch et al. 2005^b Leonori et al. 2013^c Capozza et al. 2004^d Casavecchia et al. 2004^e Rajak and Maiti 2010

when considering the average collision energy of a gaseous sample described by a Maxwell–Boltzmann distribution at a certain T . In CMB experiments this is not the case, because the reactant beams are obtained by supersonic expansion, so that the collision energy spread is small and not described by a Maxwell–Boltzmann distribution. If we use the $E_c = 3/2RT$ equation to derive the temperatures of our experiments on $O(^3P) + C_2H_2$, those would be ~ 2700 , 3200 and 4200 K. These values are largely overestimated, because at those temperatures there would also be a significant contribution of the internal energy of the reactants, which is, instead, negligible in CMB experiments. Nguyen et al. (2006b) treated this problem in the following way. Since the reaction proceeds through the formation of a bound intermediate, they assumed that E_c is completely converted into additional internal vibrational energy of the initially formed triplet adduct. They verified that a similar average thermal energy of the reactants would be acquired at a temperature of about 750 K in the case of the experiment at $E_c = 39.7$ kJ mol⁻¹, that is a value much smaller than $3,200$ K. In conclusion, as there is not an unambiguous relation between CMB E_c s and bulk temperatures, the comparison between CMB BRs as a function of E_c and kinetics BRs as a function of temperature should be done with caution.

Interestingly, the value obtained at a collision energy formally corresponding to ~ 4200 K is still very similar to the room temperature recommended value. The substantial invariance of the product yield in such a wide energy/temperature range confirms what was anticipated by the calculations of Michael and Wagner (1990) and of Nguyen et al. (2006b). In the light of the latter theoretical results, however, this apparent invariance is actually the result of a compensation of varying factors, such as the contribution of the excited triplet PES and of the ISC to the singlet PES. More theoretical work is needed to address this point and experimental evidence of HCCO and CH₂ formation in their excited states is desirable. Unfortunately, in our CMB experiments we could not distinguish the formation of excited radicals because of the small difference in their energetics compared to the total energy available. Clearly, a significant presence of electronically excited radicals in combustion environments can affect the final outcome and should be considered in combustion models.

22.3.2 $O(^3P) + Ethylene$

Another reaction of great importance in the combustion of most hydrocarbons is $O(^3P) + C_2H_4$, which has the following thermodynamically allowed product channels:



Also for this system numerous kinetics experiments have been performed (starting from the 1950s), by using a variety of techniques under different conditions of pressure and temperature. The overall rate constant has been established to be (from 220 to 2000 K) $2.25 \times 10^{-17} T^{1.88} \exp(-92/T) \text{ cm}^3 \text{ molec}^{-1} \text{ s}^{-1}$ (Baulch et al. 2005), but the question of the identity of the primary products and their relative importance has been a subject of considerable controversy over the years (see Fu et al. 2012b, and references therein). The kinetics studies at room temperature of Endo et al. (1986) and Bley et al. (1988) reported accurate branching fractions for the three most important channels (22.3a), (22.3d), and (22.3e). The recommended BRs at room temperature from a recent review (Baulch et al. 2005) are $k(22.3a)/k_{\text{tot}} = 0.35$, $k(22.3d)/k_{\text{tot}} = 0.6$; $k(22.3e)/k_{\text{tot}} = 0.05$. More recently, Miyoshi et al. (2009) have determined accurate branching fractions for channel (22.3d) ($k(22.3d)/k_{\text{tot}} = 0.53 \pm 0.04$) and, for the first time, channel (22.3c) ($k(22.3c)/k_{\text{tot}} = 0.0019 \pm 0.001$). The acetyl channel (22.3b) has never been observed in kinetics studies. It should be noted that most kinetics characterizations of the channel yields have been conducted at room temperature, which is far from the typical conditions of combustion. Measurements of BRs at high temperature, of interest in combustion, are needed for an accurate modeling of hydrocarbon combustion. As mentioned in the Introduction, these quantities can be more readily provided by CMB dynamics experiments as a function of relative translational (collision) energy.

Early CMB experiments (Schmoltner et al. 1989b) at $E_c \sim 25 \text{ kJ mol}^{-1}$ were able to characterize the dynamics of channel (22.3a), the easiest to detect for kinematics reasons. Channels (22.3c), (22.3d), and (22.3e) are, instead, characterized by an unfavorable kinematics and the masses of their products suffer either from strong background peaks and/or from interfering signals coming from the dissociative ionization of the CH_2CHO product and of the elastically scattered

C₂H₄ reactant. The problem with HCO detection from channel (22.3d) was partly overcome in the CMB study of Schmoltner et al. (1989b) by using a beam of isotopically labeled ¹⁸O, that affords detection of HCO at $m/z = 31$ (HC¹⁸O⁺) and 30 (C¹⁸O⁺). A relative branching ratio of 0.71 ± 0.26 for channel (3d) was obtained from the ratio $\sigma(\text{HCO})/\sigma(\text{CH}_2\text{CHO})$. It should be noted that this value was somewhat larger than any previous kinetics estimate, which gave values ranging from 0.44 to 0.55. A revised value of 0.38 ± 0.05 was later on reported (Morton et al. 2001).

Due to the incompleteness of the previous CMB studies, we have undertaken in our laboratory a detailed investigation of reaction (22.3a–22.3f) and by exploiting soft EI ionization, we have been able to unambiguously detect products from the first five reaction pathways (22.3a), (22.3b), (22.3c), (22.3d), and (22.3e), while the products of (22.3f) could not be identified. Figure 22.4 shows typical experimental data; in particular, the LAB angular distribution and a TOF spectrum at $m/z = 15$, together with a velocity vector diagram of the experiment. The signal at this mass originates from the parent ion of the CH₃ product (channel (22.3d)) and the daughter ion of the CH₂CHO (vinoxy) product (channel (22.3a)); as can be seen the two contributions are well disentangled in the TOF measurements (for details, see Fu et al. 2012a, b). We have determined the reaction mechanism for each channel and their BRs, first at E_c of 57.3 kJ/mol (Casavecchia et al. 2005), and, very recently (Fu et al. 2012a, b), at 35.1 kJ/mol (the latter paper contains also a revision of the earlier BRs at the higher E_c). The resulting BRs (affected by an uncertainty of roughly $\pm 20\%$) are reported in Table 22.2.

Notably, while channels (22.3a) and (22.3e) are expected to occur on the triplet PES, all other channels involve nonadiabatic pathways, i.e., intersystem crossing from the triplet to the singlet PES. Indeed, theoretical work (see references in Fu et al. 2012b) carried out on this reaction clearly indicates that channels (22.3b), (22.3c), (22.3d), and (22.3f) can only be accessed after ISC to the singlet PES. As matter of fact, from a fundamental point of view reaction (22.3a–22.3f) can be considered as a prototypical polyatomic nonadiabatic multichannel reaction, which involves multiple PESs of different spin multiplicity, and as such, it is of great interest to both experimental and theoretical dynamicists. A very comprehensive theoretical study of both triplet and singlet PESs, including statistical calculations of the branching ratios, has been published (Nguyen et al. 2005). However, in this study the contributions from the two PESs have been obtained adiabatically and the BRs have been estimated by assuming a varying extent of the ISC. The extent of ISC that better reproduces the most accurate kinetics BR determinations of Endo et al. (1986); Smalley et al. (1986) and Miyoshi et al. (2009), as well as our previous CMB results at $E_c = 57.3$ kJ mol⁻¹ (Casavecchia et al. 2005), is $\sim 55\%$ of the total reaction.

A more refined way of accounting for ISC consists in the calculation of the coupling term between the singlet and triplet PES, which has been recently done (Hu et al. 2008), and to perform QCT surface-hopping calculations. However, these calculations, which were based on a limited number of trajectories on PESs generated on the fly at the unrestricted B3LYP/6-31G(d, p) fairly low level of

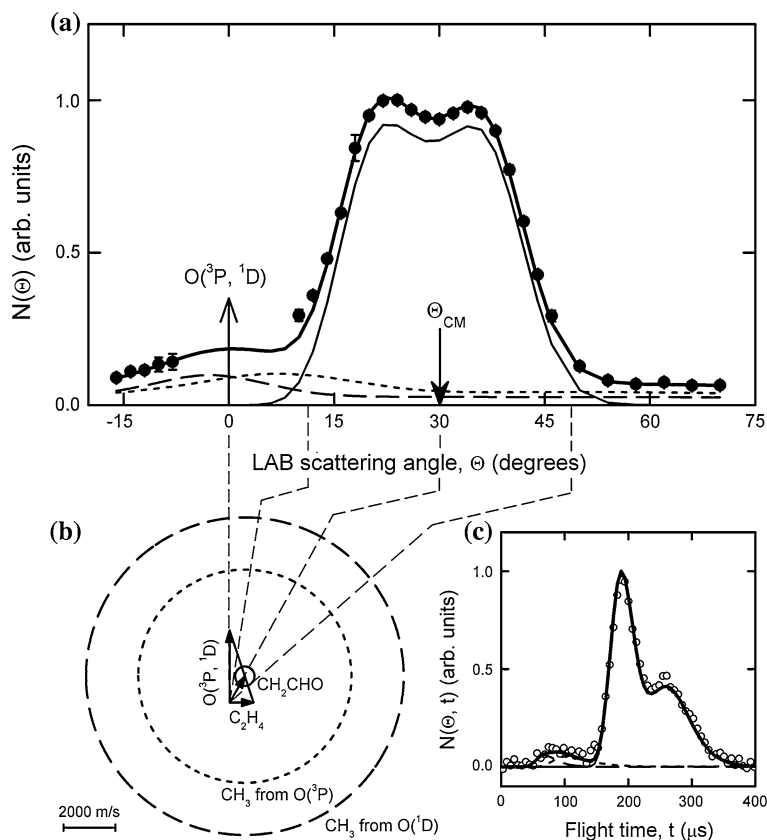


Fig. 22.4 **a** Dots LAB angular distributions at $m/z = 15$. The solid black curve represents the calculated distribution when using for the various contributions the weighted best-fit CM functions (see Fu et al. 2012a). The separate contributions to the calculated global LAB angular distributions from the CH_3 and CH_2CHO channels are also shown: Light black line CH_2CHO from $\text{O}(^3\text{P})$. Dotted line CH_3 from $\text{O}(^3\text{P})$. Dashed line CH_3 from $\text{O}(^1\text{D})$. **b** Newton diagram showing the circles that delimit the angular range and CM speed for the products CH_2CHO (light black line) and CH_3 (dotted line) from the reaction $\text{O}(^3\text{P}) + \text{C}_2\text{H}_4$ at $E_c = 35.1 \text{ kJ mol}^{-1}$. The circle of the CH_3 product from the reaction $\text{O}(^1\text{D}) + \text{C}_2\text{H}_4$ is indicated with dashed line. **(c)** TOF distribution at $m/z = 15$ recorded at 30° (Reprinted with permission from Fu et al. 2012a. Copyright (2012), National Academy of Sciences)

theory, were found to overestimate the role of ISC. Nevertheless, the results were in qualitative agreement with CMB experimental data in showing the significance of the intersystem crossing. This motivated, very recently, a theoretical investigation of these complex dynamics in far more detail, in synergy with detailed comparisons with previous and recent CMB results from our laboratory. In this combined experimental/theoretical work (Fu et al. 2012a, b), the group of Bowman has generated new global, high-level ab initio-based PES by fitting about 200,000 and 54,000 ab initio energies computed with the RCCSD(T) method and

Table 22.2 Product branching ratios for the reaction $O(^3P) + C_2H_4$ at three different collision energies, as from kinetics and CMB experiments, and theoretical BRs at one E_c (for references see Fu et al. 2012b)

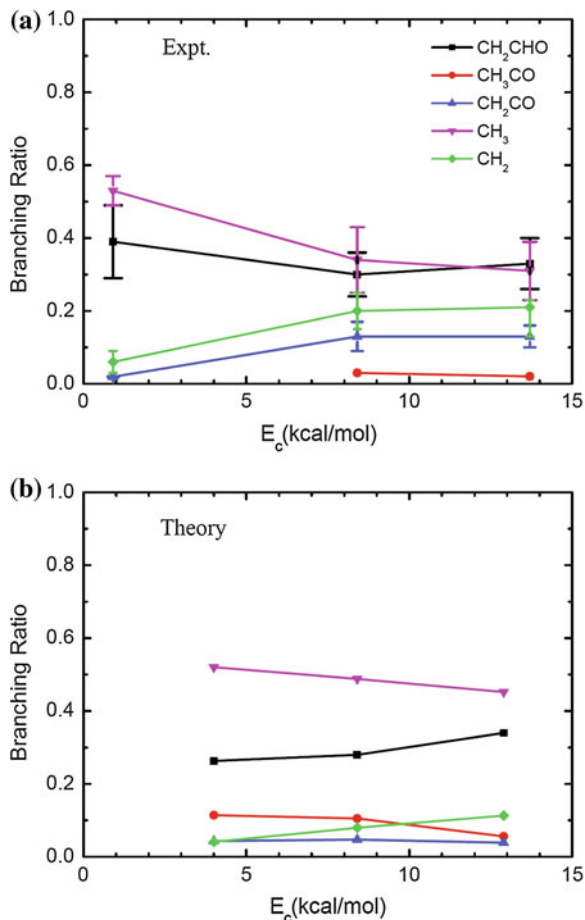
<i>Product</i> → <i>Reference</i>	CH ₂ CHO Vinoxy	CH ₂ Methylene	CH ₃ CO Acetyl	CH ₂ CO Ketene	CH ₃ Methyl
Kinetics experiment's (~300 K) $E_c \sim 3.8 \text{ kJ mol}^{-1}$	0.39 ±0.10	0.06 ±0.03	–	0.019 ±0.001	0.53 ±0.04
CMB experiment's $E_c = 35.1 \text{ kJ mol}^{-1}$	0.30 ±0.06	0.20 ±0.05	0.03 ±0.01	0.13 ±0.04	0.34 ±0.09
CMB experiment's $E_c = 57.3 \text{ kJ mol}^{-1}$	0.33 ±0.07	0.22 +0.02 –0.08	0.02 ±0.01	0.13 ±0.03	0.31 ±0.08
Theory (QCT-SO) $E_c = 35.1 \text{ kJ mol}^{-1}$	0.28	0.08	0.10	0.05	0.49

the aug-cc-pVTZ basis for the singlet and triplet PES, respectively. About a total of a million trajectories were then run on these PESs using the surface-hopping (SO) method to treat the ISC (Fu et al. 2012a, b). At the crossing points between the two PESs, Landau-Zener transition probabilities were computed assuming a fixed calculated spin-orbit coupling parameter of 35 cm^{-1} . BRs were calculated at $E_c = 57.3 \text{ kJ mol}^{-1}$ and 35.1 kJ mol^{-1} to compare with the CMB results and at $E_c = 16.7 \text{ kJ mol}^{-1}$ to mimic the kinetics results at 300 K (Fu et al. 2012a, b). The theoretical BRs at $E_c = 35.1 \text{ kJ mol}^{-1}$ are also shown in Table 22.2 along with the experimental results.

It is interesting to examine the trend (both experimental and theoretical) of the BRs with collision energy. This is depicted in Fig. 22.5. As can be seen the yield of one of the channels occurring along the triplet PES, (22.3a), decreases, but it is compensated by the increase of the other triplet channel, (22.3e). At the same time, the yield of one of the channels that requires ISC to the singlet PES decreases, but that of the other ISC channel increases. In other words, the contribution of ISC to the total reaction is roughly 50 % and remains substantially constant with E_c within the error bars (see Fig. 22.6). As can be seen theory appears to somewhat overestimate the extent of ISC, but the trend with E_c is well predicted.

Detailed comparisons were made for the translational energy and angular distributions of three most significant channels, $CH_2CHO + H$, $CH_3 + HCO$ and $CH_2 + H_2CO$ between theory and experiment at $E_c = 35.1 \text{ kJ mol}^{-1}$. The agreement between experimental and theoretical functions is excellent (Fu et al. 2012a, b), indicating that theory has reached the capability of describing relatively complex multichannel nonadiabatic reactions. In particular, the observed good agreement between detailed theoretical and experimental results for the $O(^3P) + C_2H_4$ reaction leads to the conclusion that QCT surface-hopping calculations, using reliable coupled multidimensional PESs, can yield reliable dynamical information for polyatomic multichannel reactions in which ISC plays an important role. Theoretical modeling of combustion systems (Lopez et al. 2009) could benefit greatly of these advances.

Fig. 22.5 Branching ratios of five (*indicated*) product channels as a function of E_c (experiment (a) and theory (b)) for the $O(^3P) + C_2H_4$ reaction ($1 \text{ kcal mol}^{-1} = 4.184 \text{ kJ mol}^{-1}$) (Reprinted with permission from Fu et al. 2012b. Copyright (2012), American Institute of Physics)

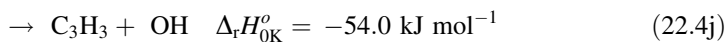
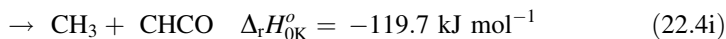
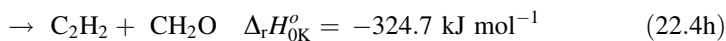
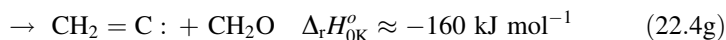
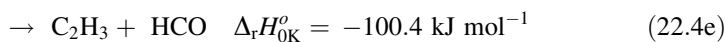
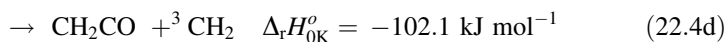
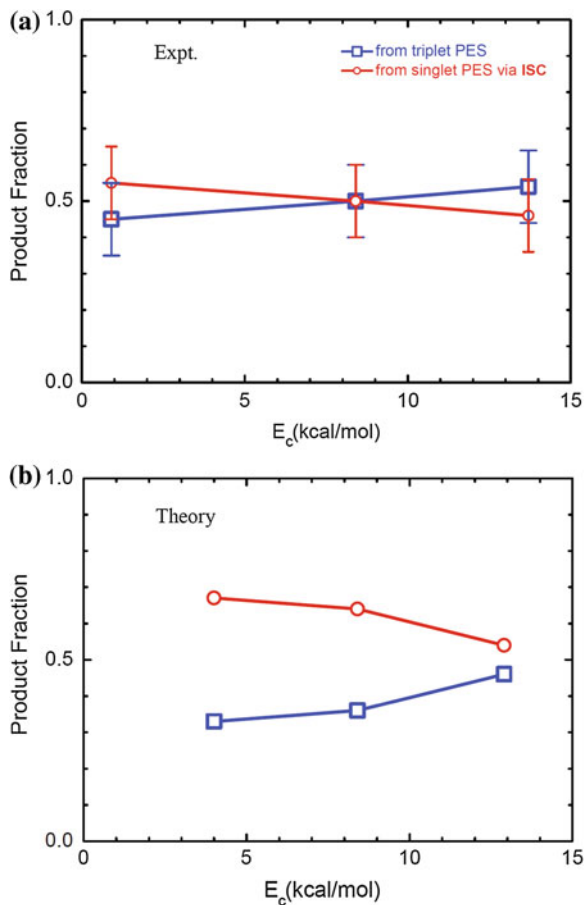


22.3.3 $O(^3P) + \text{Allene}$

The reaction of $O(^3P)$ with allene is the prototype of the $O + \text{diene}$ reactions which are not well characterized. While the room temperature rate constant for $O + \text{allene}$ has been reported to be $1.3 \times 10^{-12} \text{ cm}^3 \text{ molec}^{-1} \text{ s}^{-1}$ (Atkinson and Pitts 1977), little is known about the products. This reaction exhibits 10 energetically allowed competing pathways:



Fig. 22.6 Extent of ISC (product fraction from *triplet* PES and *singlet* PES) as a function of E_c (experiment (a) and theory (b)) for the $O(^3P) + C_2H_4$ reaction ($1 \text{ kcal mol}^{-1} = 4.184 \text{ kJ mol}^{-1}$) (Reprinted with permission from Fu et al. (2012b). Copyright (2012), American Institute of Physics)



For the values of the reaction enthalpies see Leonori et al. (2012b). In a previous CMB study at $E_c \sim 30 \text{ kJ mol}^{-1}$, Schmoltner et al. (1993), by exploiting an ^{18}O beam, identified as products $\text{CH}_2 = \text{C-CHO}$, CO and HCO , without providing BRs. In a recent, detailed theoretical study of this reaction, quantum mechanical statistical calculations of product BRs on adiabatic triplet and singlet PESs have been carried out, but without accounting for ISC (Nguyen et al. 2006a). According to the theoretical predictions, on the triplet PES the dominant channel which follows O attack on the central carbon is channel (22.4d), while channel (22.4a) follows the attack on the terminal carbon. On the singlet PES, channel (22.4f) (leading to $\text{C}_2\text{H}_4 + \text{CO}$) is predicted to be dominant, with channels (22.4e) and (22.4h) being minor.

With the aim of identifying the primary products and their BRs, we have studied reaction (22.4a–22.4j) at $E_c = 39.3 \text{ kJ mol}^{-1}$ in CMB-MS experiments by exploiting soft EI detection to interrogate all energetically allowed channels. The use of soft EI has permitted us to operate with essentially zero background; in these conditions no signal was detected at mass-to-charge ratios (m/z) of 15 and 17, which rules out (within our sensitivity, i.e., $\text{BR} < 0.3 \%$), channels (22.4i) and (22.4j). From measurements at $m/z = 55, 54, 53$, and 52 (using 60 eV electrons) also the occurrence of channel (22.4c) was ruled out, as the measured distributions were superimposable and hence attributable to the H-displacement channels (22.4a) or (22.4b) (that is, the $m/z = 54, 53$, and 52 are daughter ions produced by dissociative ionization of the mass 55 product). Reactive signal has been observed also for all the other competing channels. Because of linear momentum conservation, the heavy co-product $\text{C}_3\text{H}_3\text{O}$ of the H-displacement channel is confined into a much narrower angular range compared to those associated to the C–C bond breaking channels, where two co-fragments of comparable masses are produced. Because of this the signal recorded for the H-displacement channel appears to be dominant in the LAB reference frame (see Fig. 22.7 (*lhs*) where the LAB angular distributions measured at $m/z = 53, 29, 27, 26$, and 14 are reported). The TOF distributions recorded at the center-of-mass angle, θ_{CM} , for the five masses are reported in Fig. 22.7 (*rhs*). While the distributions recorded at $m/z = 55$ –52 were obtained by using an ionizing electron energy of 60 eV, as no significant improvement in the signal-to-noise ratio (S/N) was obtained by reducing it (note that because of best S/N, the final measurements were carried out at $m/z = 53$), to measure product angular and TOF distributions at m/z of 29, 27, 26, and 14, we took full advantage of the soft EI technique (at 17 eV), as the distributions at these masses could be measured only by reducing the background signal and interferences from dissociative ionization processes. As can be seen in Fig. 22.7, even at 17 eV in the angular and TOF distributions at $m/z = 29, 27$, and 26 there is a significant contribution arising from dissociative ionization of the $\text{CH}_2 = \text{C-CHO}$ product (from the channel which appears the dominant one in the LAB frame—see Fig. 22.7 (*lhs*)). Product intensity is clearly visible at LAB angles which are outside the angular range amenable to channels (22.4a/22.4b). The shapes of the additional contributions at the $m/z = 29, 27, 26$, and 14 distributions are quite different, thus implying different signal sources. Additional information on the

various contributions to the observed signal is given by the TOF spectra. While the $m/z = 53$ TOF spectrum is unimodal, the other spectra exhibit a pronounced structure with two or three peaks. Quantitative information is obtained by moving from the LAB coordinate system to the center-of-mass (CM) one and analyzing the product angular, $T(\theta)$, and translational energy, $P(E'_T)$, distributions into which the CM product flux can be factorized. The solid lines superimposed on the experimental results in Fig. 22.7 are calculated curves when using the best-fit CM functions. According to our analysis at $m/z = 29$, we have a contribution from H_2CO (which is known to strongly dissociate to daughter ion HCO^+) from channel (22.4g) and from the formyl radical produced in channel (22.4e). The analysis at $m/z = 27$, instead, leads to the attribution of two products, that is C_2H_4 (via dissociative ionization to C_2H_3^+) and C_2H_3 radical (parent ion) produced in the channels (22.4f) and (22.4e), respectively. Both products C_2H_4 and C_2H_3 give a contribution also at $m/z = 26$, where the additional contribution from acetylene (channel 22.4h) is also visible. Finally, at $m/z = 14$ (CH_2^+) we have measured together the CH_2 parent ion and the CH_2CO daughter ion originating from the same channel (the appearance energy of CH_2^+ from CH_2CO is only 13.8 eV and, amongst the various molecular products formed in the reactions, only ketene can produce CH_2^+ at 17 eV). The TOF peak of the contribution associated to CH_2 is much faster than that associated to CH_2CO , because the lighter co-product is produced with a much higher speed.

The best-fit CM functions associated to the various channels (see Leonori et al. 2012b) show intensity distributed in the entire angular range and this is consistent with the formation of one or more long-lived complexes (i.e., living several rotational periods), as predicted by Nguyen et al. (2006a). The product translational energy distributions, $P(E'_T)$ s, exhibit a quite different shape for each channel, so implying that they experience different parts of the PES. While the H-displacement channel has an average fraction of available energy released as product translational energy of 0.42, the C–C bond breaking channels are all characterized by much smaller fractions. This clearly indicates that when two molecular fragments are produced, the fraction of energy channeled into their internal degrees of freedom is much larger.

The CMB experimental results are in line with the description of the reaction mechanism obtained by the ab initio and RRKM calculations of Nguyen et al. (2006a). According to them, the O-addition to the π system of allene can occur in two ways, that is, O can add to one of the terminal carbon atoms or to the central one. The addition to the central C atom (characterized by a barrier height of 3.8 kJ/mol) leads to the formation of CH_2COCH_2 diradical (oxyallyl) that, according to RRKM calculations, preferentially dissociates into $\text{CH}_2 + \text{CH}_2\text{CO}$, if the system remains in the triplet PES. Triplet oxyallyl can undergo ISC to the singlet PES and singlet oxyallyl easily isomerizes to cyclopropanone. Because of the high internal energy content with which cyclopropanone is formed, in collision free conditions it undergoes fragmentation, preferentially to the products $\text{CO} + \text{C}_2\text{H}_4$. Once passed to the singlet PES, other products such as $\text{H}_2\text{CO} + \text{C}_2\text{H}_2$ can be formed. The O-atom addition to one of the terminal carbon atoms, instead, leads to the

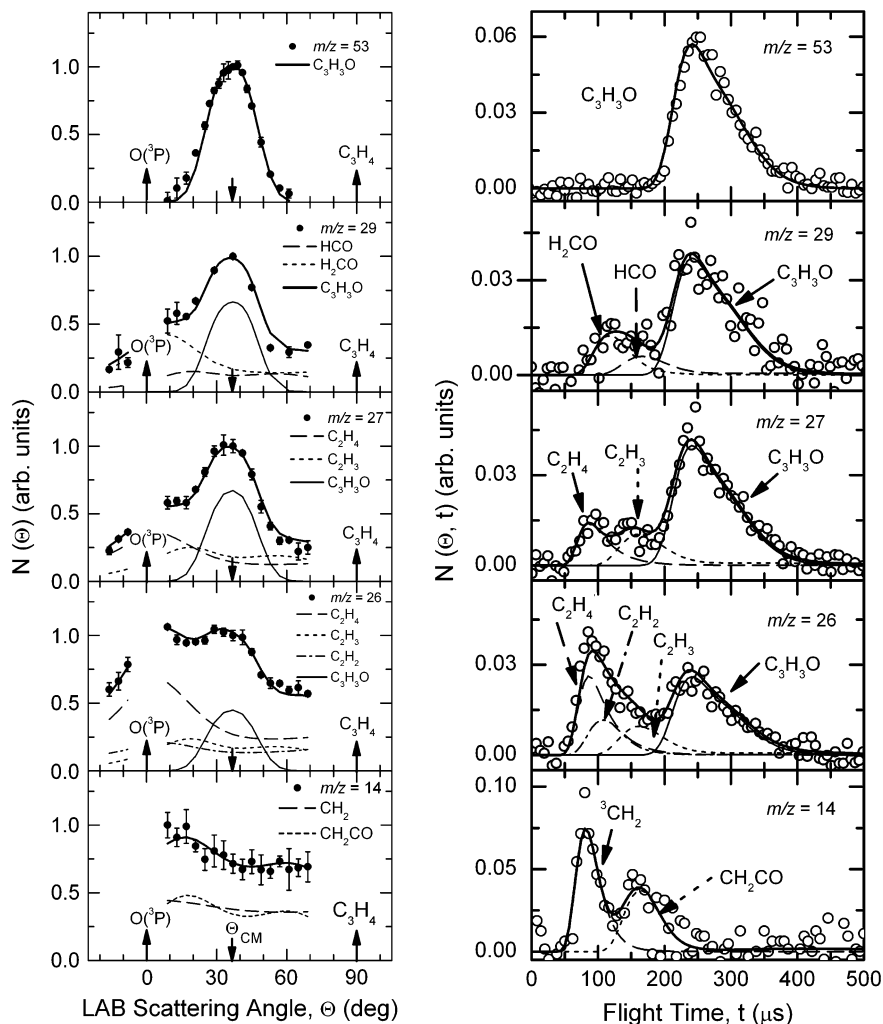


Fig. 22.7 LAB angular distributions (*l.h.s.* panel) and TOF distributions (recorded at $\Theta_{CM} = 37^\circ$) (*r.h.s.* panel) at $m/z = 53, 29, 27, 26, 14$. The *solid black curves* represent the calculated distributions when using the best-fit CM functions (see Leonori et al. 2012b). The separate contributions to the calculated global LAB angular and TOF distributions are also shown. *Light black line* H-displacement channel leading to $\text{CH}_2 = \text{C}-\text{CHO}$. *Dashed line* CH_2 ; *dotted line* CH_2CO , both produced in channel (d). *Dotted line* C_2H_3 ; *dashed line* HCO , both produced in channel (e). *Dotted line* H_2CO ; *dashed-dotted line* C_2H_2 , both produced in channel (h). *Dashed line* C_2H_4 , produced in channel (f) (Reprinted with permission from Leonori et al. (2012b). Copyright (2012), American Chemical Society)

formation of a much less stable intermediate, $\text{O}-\text{CH}_2-\text{C}-\text{CH}_2$ (barrier height 5.6 kJ/mol) which can easily fragment into $\text{CH}_2-\text{C}-\text{CHO} + \text{H}$ or, after some rearrangements, into $\text{C}_2\text{H}_3 + \text{HCO}$. The two initial addition intermediates can

isomerize to each other and the complete scheme of the PES is quite complex (Nguyen et al. 2006a).

From the CMB data, once the origin of the various ion signals was sorted out, the relative yield of each product was derived from the estimated ionization cross-section and the measured total ion yield for a specific product. The following BRs were obtained (Leonori et al. 2012b): 1.6 % channel (a); 0.3 % channel (d); 81.5 % channel (f); 7.0 % channel (e); and 9.6 % channel (h). The estimated yield uncertainty is about ± 20 % for each channel. While channels (a) and (d) take place on the triplet PES, channels (e), (f), and (h) can only be rationalized by invoking ISC from the triplet to the singlet PES. Therefore, our study indicates that the $O(^3P) + CH_2 = C=CH_2$ reaction is largely dominated (>90 %) by ISC. Quite interestingly, the main channel is a C–C bond breaking channel and that means that the 3-carbon chain of allene is not maintained when attacked by atomic oxygen.

No previous experimental estimates of the BRs were available. Since the statistical BRs can only be estimated by rate theory computations on the adiabatic PES, there is a need for dynamical calculations which take into account nonadiabatic effects (and, in particular, ISC), similar to those recently reported for the related reactions $O(^3P) + C_2H_2$ (Rajak and Maiti 2010) and $O(^3P) + C_2H_4$ (Fu et al. 2012a, b). It is also desirable to have an estimate of the BRs from kinetics experiments at room temperature, by using for instance the discharge flow technique with MS product monitoring, exploiting photoionization detection by tunable VUV synchrotron radiation. Information on the BR at room temperature ($E_c \sim 3.7$ kJ mol⁻¹) from kinetics experiments and at higher E_c from CMB experiment would provide useful information on the extent of ISC as a function of translational energy (temperature) also for this other important combustion reaction.

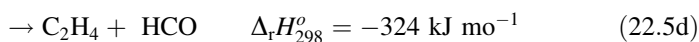
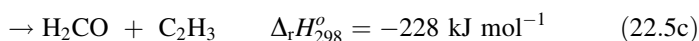
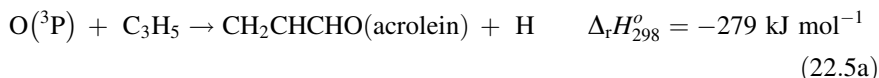
22.3 The Reactions Between Atomic Oxygen and Simple Hydrocarbon Radicals

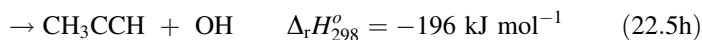
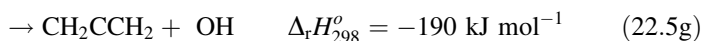
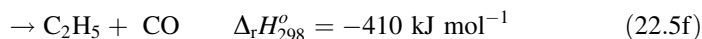
In combustion processes, an important role is also played by bimolecular reactions involving two radicals, in particular atomic oxygen or OH radical and hydrocarbon radicals. Analogously to the reactions of $O(^3P)$ with unsaturated hydrocarbons, also for these radical–radical reactions several channels are usually open and knowledge of their branching ratios is important to understand the details of combustion chemistry. Numerous kinetics studies have been performed on radical–radical reactions (Baulch et al. 2005), while dynamical studies of reactions involving two open-shell species are sparse (Patel-Misra et al. 1991; Choi 2006; Kaiser et al. 1997), the main reason being that there exist considerable experimental difficulties in generating two transient species with a density high enough to perform reactive scattering experiments. The signal recorded in CMB experiments at a specific laboratory angle is proportional to the product of the number density of the two reactants. Typically, the number density of transient atomic or radical species in CMB experiments is about 10^9 – 10^{10} particles/cm³, which is about two orders of

magnitude smaller than for stable molecules. As a consequence, there is a loss of 2–3 orders of magnitude in the signal in radical–radical reactions with respect to reactions involving one radical and a stable molecule. Until recently, the only CMB-MS study on a radical–radical reaction was carried out by Kaiser et al. (1997). After that pioneering CMB-MS study, there have been no other attempts to measure differential cross-sections of radical–radical reactions in CMB-MS experiments until our recent work on $O(^3P) + C_3H_5$ (allyl) (Leonori et al. 2007). In that study we showed that by using our improved CMB instrument equipped with soft ionization detection and exploiting the capability of producing intense continuous supersonic beams of hydrocarbon radicals by flash-pyrolysis, it has become possible to investigate bimolecular collisions involving atomic oxygen and small hydrocarbon radicals. As presented in the next section, for these radical–radical systems we did not achieve the same level of accuracy in the determination of the product BRs as for the reactions between atomic oxygen and unsaturated hydrocarbons. Nevertheless, we have been able to identify and characterize the reaction mechanism of the main products for the reaction $O(^3P) + CH_3$ (methyl) (Balucani et al. 2011), while for the reaction $O(^3P) +$ allyl we have been able to identify also the products originating from the C–C bond breaking channels (Leonori et al. 2007; Casavecchia et al. 2009). The H-elimination channel in several $O(^3P) +$ hydrocarbon radical reactions has been investigated in a series of pulsed crossed beam experiments with VUV LIF detection of the H atom at the interaction region (Choi 2006, and references therein); in these experiments also the minor H abstraction channel leading to OH formation was studied in detail using LIF detection of the OH radical.

22.4.1 The Reaction $O(^3P) + C_3H_5$ (Allyl)

Allyl is a relatively stable radical that can be formed during the pyrolysis and oxidation of hydrocarbons. Because of its stability it does not undergo decomposition or high temperature oxidation by molecular oxygen. Its main consumption mechanisms are therefore reactions with atoms and free radicals, such as atomic oxygen. The $O(^3P) + C_3H_5$ reaction is very fast ($k = 3 \pm 1 \times 10^{-10} \text{ cm}^3 \text{ molec}^{-1} \text{ s}^{-1}$) in the 300–600 K range (Slagle et al. 1990) and has the following numerous open chan





Only acrolein produced in channel (22.5a) was identified in kinetics studies (Slagle et al. 1990) as the main reaction product, while attempts to identify other molecular or radical products (such as H_2CO , HCO , C_2H_4 and C_2H_3) failed, leading to the conclusion that other possible channels contribute less than 10 %. Ab initio electronic structure calculations of the stationary points of the relevant PES and RRKM estimates (Park et al. 2003), however, pointed out that the above nine reaction channels are open, as they are connected to the reactants by one or more adiabatic pathways. By using the CMB-MS technique with soft EI, we have characterized the dynamics of channel (22.5a) and explored some C–C bond breaking channels, namely, channels (22.5c) and (22.5d). It should be noted that formation of C_2H_4 and HCO (channel 22.5d) is predicted by RRKM calculations (Park et al. 2003) to be by far the dominant pathway originating from one of the three addition intermediates formed following the electrophilic attack of $\text{O}(^3\text{P})$ to the allyl radical. With the aim of verifying whether one or both of these channels (22.5c and 22.5d) are open, we have explored the relevant range of masses to examine the possible formation of these products. We have observed reactive signals at $m/z = 27$ and 29, and measured LAB angular distributions for both masses and TOF spectra for the fragment at $m/z = 27$ (see Fig. 22.8). Measurements at these masses were only possible by reducing the background signal coming from the dissociative ionization of species contained in the allyl beam by employing a 17 eV electron energy (see Casavecchia et al. 2009).

As can be seen from Fig. 22.8, the $m/z = 27$ spectrum shows, in addition to a main, slow peak coming from dissociative ionization of acrolein (and therefore it is similar to that recorded at $m/z = 55$), a fast shoulder which is expected to originate mainly from C_2H_3 (vinyl) from the $\text{H}_2\text{CO} + \text{C}_2\text{H}_3$ channel (22.5c) and, to a lower extent at this relatively low electron energy, from dissociative ionization of C_2H_4 product from the $\text{C}_2\text{H}_4 + \text{HCO}$ channel (22.5d). From the observed differences in the $m/z = 27$ and 29 angular distributions, we have inferred that the two signals are originating from two dynamically different channels (22.5c and 22.5d). However, the experimental results were not sensitive enough to allow us to extract the relevant CM functions and to establish in detail the reaction mechanisms; further experiments are planned to address this point. Although not conclusive, the scattering results provide evidence that at the collision energy of the experiment, at least two C–C bond breaking channels are also open, those leading to $\text{C}_2\text{H}_4 + \text{HCO}$ and $\text{H}_2\text{CO} + \text{C}_2\text{H}_3$, and from the extent of the reactive intensities

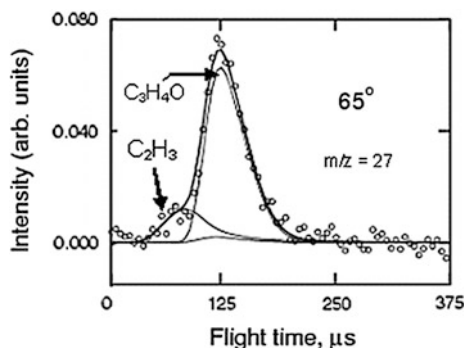


Fig. 22.8 TOF distribution of the $m/z = 27$ product from the reactions $O(^3P) + C_3H_5$ at $E_c = 73.0 \text{ kJ mol}^{-1}$ measured at a LAB angle of 65° using 17 eV electron energy. The main peak and the faster shoulder are attributed to dissociative ionization of the acrolein product and to the parent ion of the vinyl radical product (channel 22.5c), respectively (Reprinted with permission from Casavecchia et al. (2009). Copyright (2009), Royal Society of Chemistry)

we anticipate that the cross-sections for the latter processes are comparable (likely larger) with respect to that of the H-elimination channel, at least at the E_c of the experiment. We recall that the abstraction channel leading to OH formation has also been observed by LIF studies, but it is concluded to be a minor channel (Park et al. 2003).

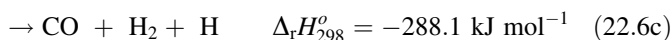
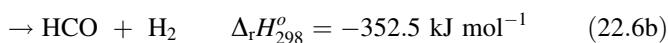
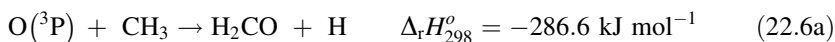
More recently, FitzPatrick et al. (2008) used photodissociation (at 193 nm) of epichlorohydrin to produce the cyclic- OCH_2CHCH_2 radicals with an internal energy content ranging from 71 to 293 kJ mol^{-1} with a maximum at 159 kJ mol^{-1} . This radical has enough internal energy to undergo a facile ring opening and isomerize to the straight chain OCH_2CHCH_2 radical intermediate, which can dissociate to one or more product channels of the O + allyl bimolecular reaction. Photo-ionization by VUV synchrotron light in a crossed laser-beam experiment is then used to detect the velocity distribution of the possible products. The data (TOF spectra at $m/z = 56, 30, 29, 28,$ and 27) identify three dominant product channels as C_3H_4O (acrolein) + H, $C_2H_4 + HCO$ and H_2CO (formaldehyde) + C_2H_3 (vinyl). The branching ratio of the acrolein channel was estimated to be 0.18 while those of the C–C bond breaking channels were not derived. Notably, the most exoergic $C_2H_5 + CO$ channel was not observed to contribute significantly, while a small signal from CH_2CO (ketene) was also detected. Unfortunately, a direct comparison between these results and our CMB results is not possible because the internal energy content of the OCH_2CHCH_2 radical intermediate in our CMB experiment is above the O + allyl reactant asymptote, while in the case of the study of FitzPatrick et al. (2008) is significantly below.

The importance of the C–C bond-breaking channels has been recently confirmed by kinetics experiments where the BRs have been derived (Hoyermann et al. 2009). In the same work, the effects of the new reaction pathways on benzene and allyl concentration profiles in fuel-rich propene flames, on the propene flame speed, and on propene ignition delay times were also established.

In conclusion, it appears that also in polyatomic radical–radical reactions all (or nearly all) the energetically allowed channels actually occur, as was observed for the O + alkene reactions. In the case of the O + allyl reaction it is now clear that H elimination, H abstraction, and C–C bond breaking are all occurring at some extent.

22.4.2 The Reaction $O(^3P) + CH_3$ (Methyl)

The reaction $O(^3P) + CH_3$ is of great importance in combustion chemistry, because it represents an important CH_3 removal route under lean or moderately rich fuel conditions. Its reaction kinetics has been studied extensively. The rate coefficient of the overall reaction recommended by a recent critical data evaluation (Baulch et al. 2005) is $k = 1.4 \times 10^{-10} \text{ cm}^3 \text{ mol}^{-1} \text{ s}^{-1}$ over the temperature range 294–2500 K. On the other hand, however, quite some uncertainty still exists also for this reaction concerning the product branching ratios. The possible competitive reaction channels are:



According to the first study, only channel (22.6a) leading to formaldehyde was believed to be open (Slagle et al. 1987), but more recent experiments pointed out that CO is also formed as a primary product with a relative yield ranging from 0.17 to 0.45 (Seakins and Leone 1992; Fockenberg et al. 1999; Preses et al. 2000; Fockenberg and Preses 2002; Hack et al. 2005). The CO product has been suggested to originate from the fast dissociation of HCO formed in channel (22.6b) (Marcy et al. 2001), because HCO is produced in a very exothermic channel and the bond energy of H–C in HCO is very weak ($D_0 = 55 \text{ kJ mol}^{-1}$). As a matter of fact, every attempt to observe directly HCO has failed (Slagle et al. 1987; Fockenberg et al. 1999). Therefore, the formyl radical has to undergo fast dissociation to a very large extent and in a very short time scale.

In our CMB experiments, we have characterized channel (22.6a) leading to formaldehyde, but we failed to observe HCO formation from channel (22.6b). From the analysis of the measured distributions at $m/z = 29$ and 31 (HCO^+ and $HC^{18}O^+$), we concluded that the possible contribution of the HCO product is less than 10 %, while measurements at the mass of CO were inconclusive because of some interferences (Balucani et al. 2011). In conclusion, our experimental results appear to confirm that if HCO is formed in channel (22.6b), it undergoes extensive dissociation within the timescale of our experiments.

22.4 Conclusions and Outlook

The characterization of multi-channel reactions of importance in combustion chemistry is a challenging task and requires a multidisciplinary approach. Since kinetics experiments are not always able to characterize all the primary products and their yields at the temperature of relevance in combustion, the CMB technique with MS detection, especially when resorting to soft electron ionization (or soft VUV photo-ionization), is a valuable complementary technique, able to provide BRs in well-defined conditions.

Theoretical calculations can provide information on the reaction potential energy surfaces and adiabatic branching ratios via statistical (RRKM) calculations or, better, dynamical calculations. The latter are based on the QCT method and require reliable multidimensional PESs. An important issue is that in most reactions of $O(^3P)$ with hydrocarbons, intersystem crossing to singlet PESs plays a major role. An accurate treatment of nonadiabatic effects in polyatomic reactive systems is still a challenge for theory. The detailed information achievable in CMB experiments provides a useful benchmark to test theoretical predictions which take into account ISC. This has become feasible only very recently, as exemplified in a recent, combined experimental and theoretical study of the $O(^3P) + C_2H_4$ reaction (Fu et al. 2012a, b). Once the employed theoretical method is proved to be reliable, it can be extended to the prediction of any quantity that characterizes an elementary reaction. The success achieved in the $O(^3P) + C_2H_4$ case offers good promises for the future.

In our laboratory, we are planning to extend further the CMB investigations to other combustion relevant reactions such as those of atomic oxygen with the isomer of allene, methylacetylene, and larger dienes (i.e., butadienes), and other radical–radical reactions, such as those of $O(^3P)$ with ethyl and isopropyl radicals. The aim is to characterize combustion elementary reactions, but also to provide benchmark results for dynamical calculations (at the QCT surface-hopping level) taking into account nonadiabatic effects. These studies should possibly be complemented by theoretical studies of the relevant PESs as well as by studies on the dissociation of radical intermediates and by kinetics studies.

Such a systematic study is highly desirable, because we have had indication that the extent of ISC is specific for every system since it is related to the details of the relative PESs. For instance, preliminary data (work in progress) have indicated that ISC channels are less important in the case of the $O + CH_3CCH$ reaction with respect to $O + CH_2CCH_2$ (CH_3CCH and CH_2CCH_2 are structural isomers and their reactions experience different regions of the same PES). However, ISC is important for the reaction $O + CH_3CCH$, while it is minor for $O + C_2H_2$: the substitution of one acetylenic H with a methyl group implies a dramatic change. Any kind of extrapolation along the series $O +$ acetylene, methylacetylene, ethylacetylene, and so on cannot be done. Only detailed studies of the same kind as those reported here will permit to characterize the extent of ISC and the branching ratios for the reactions involving atomic oxygen and small hydrocarbons.

Combustion models might benefit considerably from the additional, detailed information that can be obtained from studies such as those described here, and new insights into the global chemical scheme of combustion will be ultimately achieved.

Acknowledgments Support over the years from the Italian MIUR (PRIN projects, including the present PRIN 2010–2011) and from current EC COST Action CM0901 “Detailed Chemical Models for Cleaner Combustion” is gratefully acknowledged.

References

- Alagia M, Balucani N, Casavecchia P, Stranges D, Volpi GG (1993a) Crossed beam studies of four-atom reactions: the dynamics of OH + D₂. *J Chem Phys* 98:2459–2462
- Alagia M, Balucani N, Casavecchia P, Stranges D, Volpi GG (1993b) Crossed beam studies of four-atom reactions: the dynamics of OH + CO. *J Chem Phys* 98:8341–8344
- Alagia M, Balucani N, Casavecchia P, Stranges D, Volpi GG (1995) Reactive scattering of atoms and radicals. *J Chem Soc Faraday Trans* 91:575–596
- Albert DR, Davis HF (2010) Collision complex lifetimes in the reaction C₆H₅ + O₂ → C₆H₅O + O. *J Phys Chem Lett* 1:1107–1111
- Alzueta MU, Borruey M, Callejas A, Millera A, Bilbao R (2008) An experimental and modelling study of the oxidation of acetylene in a flow reactor. *Combust Flame* 152:377–386
- Atkinson R, Pitts JN Jr (1977) Absolute rate constants for the reaction of O(3P) atoms with allene, 1,3-butadiene, and vinyl methyl ether over the temperature range 297–439 K. *J Chem Phys* 67:2492–2495
- Balucani N, Capozza G, Leonori F, Segoloni E, Casavecchia P (2006) Crossed molecular beam reactive scattering: From simple triatomic to multichannel polyatomic reactions. *Int Rev Phys Chem* 25:109–163
- Balucani N, Leonori F, Bergeat A, Petrucci R, Casavecchia P (2011) Crossed-beam dynamics studies of the radical–radical combustion reaction O(³P) + CH₃ (methyl). *Phys Chem Chem Phys* 13:8322–8330
- Battin-Leclerc F (2002) Development of kinetic models for the formation and degradation of unsaturated hydrocarbons at high temperature. *Phys Chem Chem Phys* 4:2072–2078
- Baulch DL, Bowman CT, Cobos CJ, Cox RA, Just Th, Kerr JA et al (2005) Evaluated kinetic data for combustion modeling: Supplement II. *J Phys Chem Ref Data* 34:757–1397
- Bley U, Dransfeld P, Himme B, Koch M, Temps F, Wagner HG (1988) Primary products of the reaction between O(³P)-atoms and C₂H₄ studied with ESR- and LMR-detection. 22nd Symposium (International) on Combustion (The Combustion Institute, Pittsburgh), pp. 997–1006
- Capozza G, Segoloni E, Leonori F, Volpi GG, Casavecchia P (2004) Soft electron impact ionization in crossed molecular beam reactive scattering: The dynamics of the O(³P) + C₂H₂ reaction. *J Chem Phys* 120:4557–4560
- Carl SA, Vereecken L, Peeters J (2007) Kinetic parameters for gas-phase reactions: Experimental and theoretical challenges. *Phys Chem Chem Phys* 9:4071–4084
- Casavecchia P (2000) Chemical reaction dynamics with molecular beams. *Rep Prog Phys* 63:355–414
- Casavecchia P, Balucani N, Cartechini L, Capozza G, Bergeat A, Volpi GG (2001) Crossed beam studies of elementary reactions of N and C atoms and CN radicals of importance in combustion. *Faraday Discuss* 119:27–49
- Casavecchia P, Capozza G, Segoloni E (2004) Crossed molecular beam reactive scattering: towards universal product detection by soft electron-impact ionization. In: Yang X, Liu K

- (eds) Modern trends in chemical reaction dynamics, part II: experiment and theory, advanced series in physical chemistry, Vol 14. World Scientific, Singapore, Ch. 7, pp 329–381
- Casavecchia P, Capozza G, Segoloni E, Leonori F, Balucani N, Volpi GG (2005) Dynamics of the $O(^3P) + C_2H_4$ Reaction: identification of five primary product channels (vinoxy, acetyl, methyl, methylene, and ketene) and branching ratios by the crossed molecular beam technique with soft electron ionization. *J Phys Chem A* 109:3527–3530
- Casavecchia P, Leonori F, Balucani N, Petrucci R, Capozza G, Segoloni E (2009) Probing the dynamics of polyatomic multichannel elementary reactions by crossed molecular beam experiments with soft electron-ionization mass spectrometric detection. *Phys Chem Chem Phys* 11:46–65
- Casavecchia P, Liu K, Yang X (2010) Reactive scattering: reactions in three dimensions. In: Brouard M, Wallance C (eds) *Tutorials in molecular reaction dynamics*. Royal Society of Chemistry Publishing, Cambridge, UK Ch VI:167–213
- Choi JH (2006) Radical–radical reaction dynamics: a combined crossed-beam and theoretical study. *Int Rev Phys Chem* 25:613–653
- Endo Y, Tsuchiya S, Yamada C, Hirota E, Koda S (1986) Microwave kinetic spectroscopy of reaction intermediates: O + ethylene reaction at low pressure. *J Chem Phys* 85:4446–4452
- Fitch WL, Sauter AD (1983) Calculation of relative electron impact total ionization cross sections for organic molecules. *Anal Chem* 55:832–835
- FitzPatrick BL, Lau K-C, Butler LJ, Lee S-H, Lin J Jr-M (2008) Investigation of the O + allyl addition/elimination reaction pathways from the OCH_2CHCH_2 radical intermediate. *J Chem Phys* 129:084301–084312
- Fockenberg C, Hall GE, Preses JM, Sears TJ, Muckerman JT (1999) Kinetics and product study of the reaction of CH_3 radicals with $O(^3P)$ atoms using time resolved time-of-flight spectrometry. *J Phys Chem A* 103:5722–5731
- Fockenberg C, Preses JM (2002) Temperature dependence of the rate constant and product distribution of the reaction of CH_3 radicals with $O(^3P)$ atoms. *J Phys Chem A* 106:2924–2930
- Fu B, Han Y-C, Bowman JM, Leonori F, Occhiogrosso A, Angelucci L, Petrucci R, Balucani N, Casavecchia P (2012a) Intersystem crossing and dynamics in $O(^3P) + C_2H_4$ multichannel reaction: experiment validates theory. *PNAS (Proc Natl Acad Sci USA)* 109: 9733–9738
- Fu B, Han Y-C, Bowman JM, Leonori F, Balucani N, Angelucci L, Occhiogrosso A, Petrucci R, Casavecchia P (2012b) Experimental and theoretical studies of the $O(^3P) + C_2H_4$ reaction dynamics: collision energy dependence of branching ratios and extent of intersystem crossing. *J Chem Phys* 137:22A532-1–22A532-22
- Gardiner WC Jr (2000) *Gas-phase combustion chemistry*. Springer-Verlag, New York
- Gu X, Guo Y, Zhang F, Kaiser RI (2007a) Investigating the chemical dynamics of the reaction of ground state carbon atoms with acetylene and its isotopomers. *J Phys Chem A* 111:2980–2992
- Gu XB, Guo Y, Mebel AM, Kaiser RI (2007b) A crossed beam investigation of the reactions of tricarbon molecules, $C_3(X^1\Sigma_g^+)$, with acetylene, $C_2H_2(X^1\Sigma_g^+)$, ethylene, $C_2H_4(X^1A_g)$, and benzene, $C_6H_6(X^1A_{1g})$. *Chem Phys Lett* 449:44–52
- Gu XB, Kaiser RI (2009) Reaction dynamics of phenyl radicals in extreme environments: a crossed molecular beam study. *Acc Chem Res* 42:290–302
- Hack W, Hold M, Hoyermann K, Wehmeyer J, Zeuch T (2005) Mechanism and rate of the reaction $CH_3 + O$ —revisited. *Phys Chem Chem Phys* 7:1977–1984
- Hoyermann K, Nacke F, Nothdurft J, Olzmann M, Wehmeyer J, Zeuch T (2009) The reaction of allyl radicals with oxygen atoms: rate coefficient and product branching. *Proc Combust Inst* 32:157–164
- Hu W, Lendvay G, Maiti B, Schatz GC (2008) Trajectory surface hopping study of the $O(^3P) + Ethylene$ reaction dynamics. *J Phys Chem A* 112:2093–2103
- Huang X, Xing G, Bersohn J (1994) Dynamics of the reaction of $O(^3P)$ atoms with acetylene. *J Chem Phys* 101:5818–5823
- Kaiser RI, Balucani N (2001) The formation of nitriles in hydrocarbon-rich atmospheres of planets and their satellites: laboratory investigations by the crossed molecular beam technique. *Acc Chem Res* 34:699–706

- Kaiser RI, Mebel AM (2002) The reactivity of ground-state carbon atoms with unsaturated hydrocarbons in combustion flames and in the interstellar medium. *Int Rev Phys Chem* 21:307–356
- Kaiser RI, Sun W, Suits AG, Lee YT (1997) Crossed beam reaction of atomic carbon, $C(^3P_j)$, with the propargyl radical, $C_3H_3(X^2B_2)$: observation of diacetylene, $C_4H_2(X^1\Sigma_g^+)$. *J Chem Phys* 107:8713–8716
- Lee SH, Chen WK, Huang WJ (2009) Exploring the dynamics of reactions of oxygen atoms in states 3P and 1D with ethene at collision energy 3 kcal mol^{-1} . *J Chem Phys* 130:054301–054313
- Lee YT (1987a) Molecular-beam studies of elementary chemical processes. *Science* 236:793–798
- Lee YT (1987b) Reactive scattering I: non-optical methods. In: Scoles G (ed) *Atomic and molecular beam methods*. Oxford University Press, New York, pp 553–568
- Leonori F, Balucani N, Camozza G, Segoloni E, Stranges D, Casavecchia P (2007) Crossed molecular beam studies of radical–radical reactions: $O(^3P) + C_3H_5$ (allyl). *Phys Chem Chem Phys* 9:1307–1311
- Leonori F, Petrucci R, Segoloni E, Bergeat A, Hickson KM, Balucani N, Casavecchia P (2008a) Unraveling the dynamics of the $C(^3P, ^1D) + C_2H_2$ reactions by the crossed molecular beam scattering technique. *J Phys Chem A* 112:1363–1379
- Leonori F, Petrucci R, Hickson KM, Segoloni E, Balucani N, Le Picard SD, Foggi P, Casavecchia P (2008b) Crossed molecular beam study of gas phase reactions relevant to the chemistry of planetary atmospheres: the case of $C_2 + C_2H_2$. *Planet Space Sci* 56:1658–1673
- Leonori F, Hickson KM, Le Picard SD, Wang XG, Petrucci R, Foggi P, Balucani N, Casavecchia P (2010) Crossed-beam universal-detection reactive scattering of radical beams characterized by laser-induced fluorescence: the case of C_2 and CN. *Mol Phys* 108:1097–1113
- Leonori F, Petrucci R, Wang X, Casavecchia P, Balucani N (2012a) A crossed beam study of the reaction $CN + C_2H_4$ at a high collision energy: the opening of a new reaction channel. *Chem Phys Lett* 553:1–5
- Leonori F, Occhiogrosso A, Balucani N, Bucci A, Petrucci R, Casavecchia P (2012b) Crossed molecular beam dynamics studies of the $O(^3P) +$ allene reaction: primary products, branching ratios and dominant role of intersystem crossing. *J Phys Chem Lett* 3:75–80
- Leonori F, Balucani N, Casavecchia P (2013) Crossed molecular beam studies of the $O(^3P) +$ acetylene reaction: primary products and branching ratios as a function of collision energy. *Phys Chem Chem Phys* (In preparation)
- Lopez JG, Rasmussen CL, Alzueta MU, Gao Y, Marshall P, Glarborg P (2009) Experimental and kinetic modeling study of C_2H_4 oxidation at high pressure. *Proc Combust Inst* 32:367–375
- Maksyutenko P, Zhang F, Gu X, Kaiser RI (2011) A crossed molecular beam study on the reaction of methylidyne radicals $[CH(X^2\Pi)]$ with acetylene $[C_2H_2(X^1\Sigma_g^+)]$ —competing $C_3H_2 + H$ and $C_3H + H_2$ channels. *Phys Chem Chem Phys* 13:240–252
- Marcy TP, Diaz RR, Heard D, Leone SR, Harding LB, Klippenstein SJ (2001) Theoretical and experimental investigation of the dynamics of the production of CO from the $CH_3 + O$ and $CD_3 + O$ reactions. *J Phys Chem A* 105:8361–8369
- Michael JW, Wagner AF (1990) Rate constants for the reactions $O + C_2H_2$ and $O + C_2D_2 \rightarrow$ products, over the temperature range ~ 850 – 1950 K , by flash photolysis-shock tube technique. Determination of the branching ratio and a further theoretical analysis. *J Phys Chem* 94:2453–2464
- Miyoshi A, Yoshida J, Shiki N, Koshi M, Matsui H (2009) Product branching fractions for the reaction of $O(^3P)$ with ethane. *Phys Chem Chem Phys* 11:7318–7323
- Morton ML, Szpunar DE, Butler LJ (2001) Photodissociating methyl vinyl ether to calibrate $O +$ ethylene product branching and to test propensity rules for product channel electronic accessibility. *J Chem Phys* 115:204–216
- Nguyen TL, Vereecken L, Hou XJ, Nguyen MT, Peeters J (2005) Potential energy surfaces, product distributions and thermal rate coefficients of the reaction of $O(^3P)$ with $C_2H_4(X^1A_g)$: a comprehensive theoretical study. *J Phys Chem A* 109:7489–7499

- Nguyen TL, Peeters J, Vereecken L (2006a) Quantum chemical and statistical rate study of the reaction of $O(^3P)$ with allene: O-addition and H-abstraction channels. *J Phys Chem A* 110:12166–12176
- Nguyen TL, Vereecken L, Peeters J (2006b) Quantum chemical and theoretical kinetics study of the $O(^3P) + C_2H_2$ reaction: a multistate process. *J Phys Chem A* 110:6696–6706
- Park JH, Lee H, Choi JH (2003) A theoretical study of the reaction of $O(^3P)$ with allyl radical C_3H_5 . *J Chem Phys* 119:8966–8978
- Patel-Misra D, Sauter DG, Dagdigian PJ (1991) Internal state distribution of OD produced from the $O(^3P) + ND_2$ reaction. *J Chem Phys* 95:955–962
- Peeters J, Boullart W, Langhans I (1994) Branching ratio of the $C_2H_2 + O$ reaction at 290 K: from kinetic modelling of relative methylene concentration versus time profiles in $C_2H_2/O/H$ systems. *Int J Chem Kinet* 26:869–886
- Preses JM, Fockenberg C, Flynn GW (2000) A measurement of the yield of carbon monoxide from the reaction of methyl radicals and oxygen atoms. *J Phys Chem A* 104:6758–6763
- Rajak K, Maiti B (2010) Direct dynamics study of the $O(^3P) + C_2H_2$ reaction: contribution from spin nonconserving route. *J Chem Phys* 133:011101-1–011101-4
- Schmoltner AM, Chu PM, Lee YT (1989a) Crossed molecular beam study of the reaction $O(^3P) + C_2H_2$. *J Chem Phys* 91:5365–5373
- Schmoltner AM, Chu PM, Brudzynski RJ, Lee YT (1989b) Crossed molecular beam study of the reaction $O(^3P) + C_2H_4$. *J Chem Phys* 91:6926–6936
- Schmoltner AM, Huang SY, Brudzynski RJ, Chu PM, Lee YT (1993) Crossed molecular beam study of the reaction $O(^3P) +$ allene. *J Chem Phys* 99:1644–1653
- Seakins PW, Leone SR (1992) Laser flash photolysis/time-resolved FTIR emission study of a new channel in the reaction of $CH_3 + O$: production of $CO(v)$. *J Phys Chem* 96:4478–4485
- Slagle IR, Kaczynski D, Gutman D (1987) Kinetics of the reaction between methyl radicals and oxygen atoms between 294 and 900 K. *J Phys Chem* 91:4375–4379
- Slagle IR, Bernhardt JR, Gutman D, Hanning-Lee MA, Pilling MJ (1990) Kinetics of the reaction between oxygen atoms and allyl radicals. *J Phys Chem* 94:3652–3656
- Smalley JF, Nesbitt FL, Klemm RB (1986) Branching ratio for the hydrogen atom product channel in the reaction of ground-state atomic oxygen with ethylene. *J Phys Chem* 90:491–497
- Stahl F, Schleyer PV, Bettinger HF, Kaiser RI, Lee YT, Schaefer HF (2001) Reaction of the ethynyl radical, C_2H , with methylacetylene, CH_3CCH , under single collision conditions: implications for astrochemistry. *J Chem Phys* 114:3476–3487
- Warnatz J, Maas U, Dibble RW (2001) Combustion: physical and chemical fundamentals, modeling and simulation, experiments, pollutant formation. Springer-Verlag, Berlin
- Williams A, Smith DB (1970) The combustion and oxidation of acetylene. *Chem Rev* 70:267–293

Chapter 23

Kinetic Studies of Elementary Chemical Steps with Relevance in Combustion and Environmental Chemistry

Christa Fittschen

Abstract Elementary chemical reaction steps, relevant to combustion and environmental chemistry, involve in many cases the reaction between a radical species and a closed-shell molecule. Rate constants and product branching ratios of such elementary reactions are important input parameter in complex models, describing combustion processes or the chemistry of the atmosphere. Different experimental setups, widely used to study such reactions, are described in this chapter. The main difference consists in the way radicals are generated (either pulsed or continuous) and the way the time resolution is obtained. The coupling of these different experimental setups with commonly used detection methods is also described.

23.1 Introduction

Combustion in a gas turbine or in a motor represents a complex chemical reaction system involving generally hundreds of species, either stable molecules or reactive intermediates such as radicals, reacting together in just as many reactions. Atmospheric chemistry, i.e., the degradation of trace gases of either anthropogenic or biogenic origin, is comparable to a combustion system: hundreds, if not thousands of species react together in countless reactions. Understanding these complex systems in detail is important for optimizing combustion processes and thus increasing fuel efficiency and decreasing pollutant emission, the detailed understanding of atmospheric chemistry helps to improve the forecast of future evolutions of phenomena such as pollution events or climate change. A very general approach to increase the understanding of such complex systems is

C. Fittschen (✉)

PhysicoChimie des Processus de Combustion et de l'Atmosphère, PC2A, UMR CNRS 8522, Université Lille 1 Sciences et Technologies, Cité Scientifique, Bâtiment C11, 59655 Villeneuve d'Ascq, France
e-mail: christa.fittschen@univ-lille1.fr

identical for both research areas: the evolution of numerous species is followed under different conditions (e.g., different concentrations and pressures in combustion systems or summer/winter or urban/remote environments in atmospheric chemistry) and the evolution of these species is then reproduced by chemical models. Important input parameters in these models are the rate constants for elementary reactions as well as the branching ratios between different possible reaction products.

The most important reactions driving the reactivity of both combustion and atmospheric chemistry, involve radicals. Radicals can be, for example, the reactant in unimolecular reactions such as the decomposition of alkoxy radicals (Caralp et al. 1999) or a reaction partner in bi- or termolecular reactions, for example in the reaction of alkoxy radicals with NO or O₂ (Fittschen et al. 1999) or in the reaction of alkyl radicals with O₂ (Taatjes 2006). Peroxy radicals are important species not only in atmospheric chemistry, but also in low temperature combustion processes (Orlando and Tyndall 2012). Rate constants have been reviewed and summarized in several databases such as NIST database (<http://kinetics.nist.gov/kinetics/>), the evaluated kinetic data of the IUPAC subcommittee for Gas Kinetic Data Evaluation (<http://www.iupac-kinetic.ch.cam.ac.uk/>) as well as their review concerning reactions under combustion conditions (Baulch et al. 1992, 1994, 2005), the NASA Evaluation (Sander et al. 2011) or the data base on the gas phase reactions of oxygenated VOCs (<http://www.era-orleans.org/eradb/>).

This chapter describes the basic principles about methods used to measure rate constants and branching ratios of reactions involving radicals. The chapter is organized into three sections treating each a different aspect of such experiments. In the first section, different ways of generating radicals are described. In the second section, different and commonly used spectroscopic techniques for the detection of reactants or products are described. And in the last section, the principles of two different ways of assembling radical generation and detection methods such as laser photolysis and fast flow reactors, largely used for the measurement of rate coefficients, are briefly described. Shock tubes, a widely used instrument for the study of elementary reactions at high temperatures, is treated in [Chap. 24](#) of this book and is therefore not discussed here.

23.2 Radical Generation

Radicals are the driving species in combustion and atmospheric chemistry and are involved in most of the reactions. Radicals are highly reactive species and can therefore not be prepared in advance, but must be generated in situ. Two different modes are generally used such as direct photolysis of an appropriate precursor and chemical generation. Both the methods have their advantages and disadvantages and can sometimes be complementary.

23.2.1 Photolytic Radical Generation

The photolytic generation of radicals can be carried out in two different modes, both of them widely used: either by *pulsed* photolysis or by *continuous* photolysis.

23.2.1.1 Pulsed Versus Continuous Photolysis

The choice of the method depends on the experimental setup (see below). The principle is the same in both cases: a suitable precursor is excited above its dissociation threshold by absorption of a photon of a suitable wavelength, i.e., these photons need to have

- high enough energy to initiate the dissociation of the precursor, in general ultraviolet (UV) light is used in the wavelength range from ≈ 190 to 360 nm
- a wavelength is needed where the precursor has an absorption cross section large enough to enable the generation of sufficiently high radical concentrations

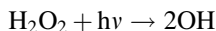
The choice of the precursor is important in order to minimize secondary reactions. Such unwanted reactions can have different origins, they can arise from reactions of the co-products of the precursor photolysis, but also from a possible simultaneous (and unwanted) photolysis or photoexcitation of the reaction partner itself: this can occur, if the reaction partner is absorbing at the same wavelength.

Very common light sources used for pulsed photolysis are excimer lasers emitting at 193, 248, 308, or 351 nm, depending on the gas mixture used. Other frequently used sources for a pulsed photolysis are frequency quadrupled YAG lasers emitting at 266 nm, but pulsed flashlamps are also being used (Zhang et al. 2012). The employment of lasers as light sources has the advantage to provide very intense (up to several 100 mJ cm^{-2}) and also very short (on the order of 10 ns) light pulses. This has the advantage that fast reactions can be studied, because the generation of radicals should occur on a time scale much shorter than the subsequent reactions. However, if the photon flux is high, multiphoton absorption processes might occur (Jain et al. 2012) and care should be taken by carrying out experiments at different photolysis energies in order to unravel a possible influence of the photolysis pulse on the chemistry.

For the continuous photolysis, fluorescence tubes or bulbs are often used: mercury, Hg, is excited in a discharge and emits light predominantly at 254 nm. These photons are either used directly if the lamp cover is made of quartz, or these photons are absorbed by a suitable coating of the quartz tube: this coating then subsequently emits photons at wavelengths anywhere above 254 nm, depending on the material chosen. Using appropriate materials and filters, these tubes can also be used to simulate the sunlight in laboratory experiments in order to imitate atmospheric conditions.

23.2.1.2 Photolytic Generation of OH Radicals

The OH radical is the most important oxidant in both atmospheric and combustion chemistry, and its reactivity is therefore often studied. A common photolytic precursor for OH radicals is the UV-photolysis of H₂O₂:



This precursor has the advantage of being a clean source for OH-radicals, i.e. no other products are directly formed during the photolysis (Thiebaud et al. 2007; Vaghjiani and Ravishankara 1990). However, one drawback of this precursor is that the reaction between OH-radicals and the precursor H₂O₂, leading to formation of HO₂ radicals, is rather fast ($k = 1.7 \times 10^{-12} \text{ cm}^3 \text{ molecules}^{-1} \text{ s}^{-1}$) (Atkinson et al. 2004). Therefore, high concentrations of the reaction partners X have to be used in order to make the reaction of OH radicals with X the predominant reaction path for OH radicals rather than the reaction with H₂O₂. Furthermore, the absorption cross sections of H₂O₂ become small at longer wavelengths (Nicovich and Wine 1988), and therefore this precursor is mainly photolysed at $\lambda \leq 266 \text{ nm}$ in order to generate sufficiently high concentrations of OH radicals with relatively low H₂O₂ precursor concentration. However, H₂O₂ has also been employed to generate OH radicals in atmospheric simulation chambers by using photolysis wavelengths above 300 nm (Picquet et al. 1998). Other common OH precursors in the same wavelength range are the photolysis of HNO₃, leading to NO₂ as co-product or the photolysis of ozone, O₃, leading to O(¹D) which in the presence of H₂O lead rapidly to formation of two OH radicals. Unwanted reactions in this system can occur from O(³P) atoms, that are easily formed by quenching of O(¹D) atoms. For example, the reaction

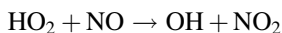


is relatively fast ($k = 3.5 \times 10^{-11} \text{ cm}^3 \text{ molecules}^{-1} \text{ s}^{-1}$ (Atkinson et al. 2004)) and can induce unwanted reactions.

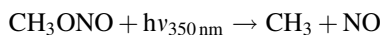
Precursors at longer wavelengths are rather sparse, and one of the most widely used direct precursors at wavelengths above 300 nm is the photolysis of HONO

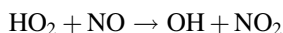
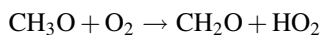


While this precursor has the advantage of long-wavelength photolysis, NO is formed as a co-product and might subsequently become involved in the reaction mechanism, for example by the rapid conversion of HO₂ radicals to OH radicals



Another more indirect precursor, widely used for the continuous generation of OH radicals in atmospheric simulation chambers at wavelength above 300 nm, is the photolysis of methylnitrite, CH₃ONO, in the presence of O₂ and NO:

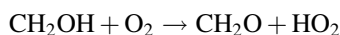
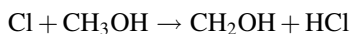
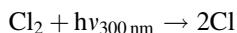




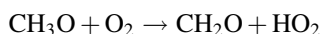
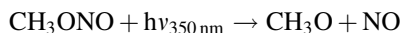
It can be seen from the above paragraph, that the choice of the radical precursor is delicate and depends very much on the available experimental setup, the reaction conditions and restrictions.

23.2.1.3 Photolytic Generation of HO₂ Radicals

The HO₂ radical is another very important species in atmospheric chemistry and also during low-temperature combustion chemistry. There is unfortunately no direct photolytic source for this radical, and therefore it needs to be generated in a short reaction sequence. A commonly used reaction pattern is the reaction of Cl-atoms with CH₃OH in the presence of O₂:

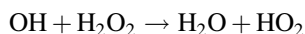


Cl atoms can be generated by photolysis of Cl₂ at wavelengths above 300 nm, but the 248 nm photolysis of phosgene, COCl₂, can also serve as a clean photolytic source of Cl atoms. Another commonly used precursor for HO₂ radicals is the photolysis of methylnitrite, CH₃ONO



It has been shown above, that this precursor, photolysed in the presence of excess NO, is also a widely used precursor for OH radicals in atmospheric simulation chambers. However, the inevitable presence of NO in the reaction mixture makes this precursor of limited use in kinetic experiments.

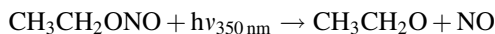
Another photolytic HO₂ source can be the above-mentioned photolysis of H₂O₂, leading finally to HO₂ radicals by the subsequent reaction (Thiebaud et al. 2007):



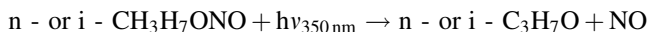
By using high concentrations of H₂O₂, this reaction can be made relatively fast on the time scale of the experiment and can therefore be a clean source of HO₂ radicals. In all cases, the formation of HO₂ is not instantaneous; therefore, one has to evaluate carefully all possible parallel reactions of the different intermediates with other reaction partners.

23.2.1.4 Photolytic Generation of Alkoxy Radicals

Alkoxy radicals, RO, are another important class of reactive intermediates in atmospheric and also combustion chemistry and their reactivity has been extensively studied in laboratory experiments. They can be photolytically generated in a very selective way from the appropriate nitrite, i.e., ethoxy radicals (Caralp et al. 1999):



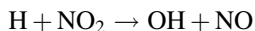
or propoxy radicals (Fittschen et al. 1999)



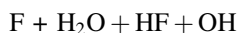
The choice between pulsed or continuous photolysis depends on the experimental setup to be used (see below). Pulsed photolysis is a very direct way for kinetic measurement: radicals with a certain initial concentration are generated on a short-time scale (compared to the total reaction time) and the evolution of the radical concentration can then be observed by time-resolved measurements. Continuous photolysis is commonly employed in atmospheric simulation chambers, widely used for mechanistic studies under atmospheric conditions, but kinetic information can only be obtained by relative methods.

23.2.2 Chemical Radical Generation

This method is very commonly used in connection with fast flow reactors; radicals are generated in a continuous manner by a short sequence of chemical reactions. The reaction chain is generally initiated by radicals or atoms that have been created beforehand in a microwave discharge or more rarely by photolysis (Kovacs and Brune 2001). OH radicals can be generated through reaction of H atoms, obtained by microwave discharge of H₂ in helium, with NO₂

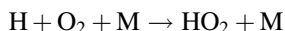


Another possibility is the generation of F atoms by microwave discharge of F₂ in helium, followed by a fast reaction with H₂O.



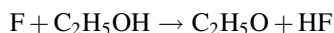
HO₂ radicals can be generated by microwave discharge of Cl₂ in helium and subsequent reaction of the Cl atoms with methanol, CH₃OH, and O₂, very similar to the photolytic HO₂ formation. The possible generation through a reaction of H atoms (from a microwave discharge in H₂/He) with O₂ is not a very efficient method of HO₂ generation because of the pressure dependence of the rate constant of the reaction between H atoms and O₂: microwave discharges are commonly used in connection with flow-tube experiments, which in turn are generally

operated at low pressures (up to 10 mbar). Also, microwave discharges are easier to handle at low pressures. Under these conditions, the reaction



is still in its low pressure limit and therefore rather slow (Fernandes et al. 2008).

Alkoxy radicals can be generated from a reaction of F atoms, generated in a microwave discharge of F₂, with the appropriate alcohol, e.g., (Caralp et al. 1999)

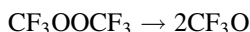


The formation of alkyl radicals through abstraction of an H atom from the carbon chain is only a minor pathway (Khatoun et al. 1989).

Continuous radical generation by thermal decomposition can also be a good choice, if an appropriate precursor can be found. NO₃ is an important species in the night time chemistry of the troposphere, and many laboratory studies have been devoted to this radical. It can be obtained in a continuous way by the thermal decomposition of N₂O₅ (Olariu et al. 2004)



Also, CF₃O radicals, an intermediate in the degradation of some hydrofluorocarbons, have been generated by the thermal decomposition of its dimer, CF₃OOCF₃ (Caralp et al. 1997)



23.3 Spectroscopic Methods

In the above paragraphs, a brief and certainly not comprehensive overview over different ways to generate different radicals has been given. The accent has been set on radicals that are important in atmospheric chemistry as well as in low temperature combustion processes, i.e., at temperatures where peroxy radicals still play a role ($T < 800$ K). In the following section, the basic principles of some spectroscopic methods, widely used in kinetic measurements, will be presented.

23.3.1 Emission Spectroscopy

23.3.1.1 Laser-Induced Fluorescence LIF

Laser-induced Fluorescence, LIF, is a highly sensitive detection method for OH radicals (Heard 2006) but has also been applied for many other radicals (alkoxy radicals for example (Caralp et al. 1999)) or stable species (CH₂O for example

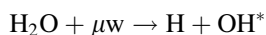
(Hottle et al. 2009)). For small species having sharp and individual absorption lines, like OH radicals, it is also a highly selective method. Due to vibrational relaxation within the excited electronic state, the emitted fluorescence light is usually less energetic than the initially absorbed photons, i.e., the fluorescence is red-shifted with respect to the excitation light. At constant fluorescence excitation energy, the intensity of the emitted fluorescence is in principle proportional to the concentration of the target species. However, fluorescence is generally used as a relative technique, because it is very difficult to deduce absolute concentrations from fluorescence intensities. Different processes other than fluorescence can lead to a depopulation of the excited state and thus to a decrease in fluorescence intensity:

- The excited species can undergo intersystem crossing (ISC) into a state with different spin multiplicity, from where it can radiatively decay to the ground state (phosphorescence).
- Internal conversion (IC) can happen, when the electronically excited state overlaps with high vibrational levels of a lower lying electronic state with the same spin multiplicity.
- Energy can be removed in collisions with the surrounding bath gas. This process called quenching depends strongly on the nature and concentration of the collision partners.

It is difficult to take quantitatively into account these loss processes, which make it difficult to determine the proportional factor between concentration and fluorescence intensity. This detection technique is most widely being used in a pulsed way, but some experiments have also been performed using CW lasers for fluorescence excitation (DeSain et al. 2005).

23.3.1.2 Resonance Fluorescence

This technique uses the same physical phenomena, i.e., the detection of fluorescence, described in the above paragraph. However, the excitation is carried out in a slightly different way; the photons necessary for the excitation of the species are not emitted by a laser, but by a so-called resonance lamp. In this lamp (generally a quartz tube closed with a quartz window and surrounded by a microwave discharge), the species to be detected is generated in an excited state by microwave discharge, i.e., if OH radicals are to be detected, this species is generated in a microwave discharge of H₂O:



In this process, OH radicals are formed in an electronically excited state, which will subsequently, amongst other possible pathways such as quenching, relax to the ground state by emitting a photon. These photons are then used to excite fluorescence of OH radicals in the reaction cell for (a very selective) detection.

Another advantage of this technique compared to LIF is the reduced cost, the lamp is much cheaper than the laser needed for LIF. However, the number of detectable species is limited and only small species, that can be generated selectively in a microwave discharge (e.g., OH, OD, all kinds of atoms such as H (Bergeat et al. 2009), I (Vipond et al. 2002), O (Fernandez and Fontijn 2001) or Cl (Hickson et al. 2010)), are possible candidates. Please note that this type of lamp can also be used for absorption spectroscopy, leading to very selective and highly sensitive absorption spectrometers, widely used for the detection of atoms. Resonance fluorescence is always used in a continuous way.

23.3.2 Absorption Spectroscopy

Absorption spectroscopy is a widely used method in kinetic measurements. It is an absolute technique based on the measurement of the decrease of light intensity due to absorption by the species to be detected. The Beer–Lambert’s law connects the attenuation of light intensity to the concentration of the species and the path length that the light has passed:

$$\ln(I/I_0) = -\varepsilon c d$$

where I_0 and I designate the light intensity before and after passing through the absorbing media, respectively, c is the concentration of the absorbing species, d is the path length, and the proportionality factor ε is the absorption cross section of the absorbing species at a given wavelength.

Absorption spectroscopy is applied in a large range of wavelengths, extending from ultraviolet to microwave. For kinetic applications, the most widely used wavelength ranges are UV and infrared (IR). In the following paragraphs, the peculiarities for these two wavelength ranges are briefly described.

23.3.2.1 UV Absorption Spectroscopy

Many species have large absorption cross sections in the UV (sometimes extending even for small species into the visible range, for example for NO_2 or I_2), resulting from transitions between the ground state and an electronically excited state. A good database summarizing the absorption spectra of many stable molecules, but also some radicals, has been established by Keller-Rudeck and Moortgat (<http://www.atmosphere.mpg.de/enid/2295>).

While UV absorption spectroscopy can be very selective for small species having a structured absorption spectrum like OH radicals, the absorption features of many other species are often very broad, originating from a transition into a non-binding excited state. The possible result is overlapping absorption bands of different species present simultaneously in the reaction mixture, which might

result in a low selectivity. Nowadays, fast CCD cameras enable the time-resolved acquisition of absorption spectra over a large wavelength range with a high time resolution, sometimes allowing a deconvolution of overlapping spectra of educts and products (Rowley et al. 1996).

The advantage of UV absorption spectroscopy is, that this technique can be applied for many species: nearly all species do absorb at some wavelength in the UV range with reasonably high absorption cross sections. This is in contrast to LIF, which can, of course, only be applied to fluorescing species. UV absorption has therefore been for many years one of the main techniques used in kinetic measurements. Most often, broadband emitting lamps are used in connection with a monochromator for wavelength dispersion and either a photomultiplier or a CCD camera for detection (Brand et al. 1990; Raoult et al. 2004). However, laser absorption can be used as well for the detection of small species such as OH radicals (Bohn and Zetzsch 1999). A major advantage of using laser absorption spectroscopy for OH radicals instead of LIF is that this technique keeps its sensitivity even at higher pressure, where LIF suffers from quenching, especially in the presence of high O₂ concentrations.

23.3.2.2 Tunable Diode Laser Absorption Spectroscopy TDLAS

While electronic transitions are excited with the energetic photons in the UV and visible (Vis) range, photons in the IR range lead to a vibrational excitation. Line positions and absorption cross sections have been tabulated for many species in two databases (Jacquinet-Husson et al. 2011; Rothman et al. 2009). Diode lasers, tuneable over a small wavelength range, are sometimes employed for the detection of small species, having narrow absorption features with high absorption cross sections in the IR wavelength region (Dusanter et al. 2005; Estupinan et al. 2007; Tang et al. 2010). Unfortunately, this advantage diminishes rapidly with increasing pressure due to pressure broadening of the absorption lines (Kanno et al. 2005). Therefore, this technique is mostly limited to low-pressure experiments and is of limited use for kinetic studies.

23.3.2.3 FTIR Spectroscopy

In contrast to TDLAS, which uses in general a single absorption line in a very narrow wavelength range, FTIR allows acquiring spectra in a large wavelength range and therefore simultaneous identification and quantification of different species. The drawback of this technique is its low temporal resolution: obtaining a good quality spectrum can take several minutes. This technique is therefore mainly used in connection with atmospheric simulation chambers where the reaction time can take several hours and a wide variety of reaction products are formed (Meunier et al. 2003; Tyndall et al. 2002).

23.3.3 Cavity-Enhanced Absorption Spectroscopy

A subcategory of direct absorption spectroscopy uses cavities consisting of highly reflective mirrors: the goal of using such cavities is to increase the absorption path length and with this the sensitivity. The development of a wide variety of techniques, all using cavities to improve the sensitivity, was triggered by the development of pulsed Cavity Ring Down Spectroscopy (CRDS) in 1988 (O’Keefe and Deacon 1988). The principle is very appealing and simple: photons are trapped in an optical cavity consisting of highly reflective mirrors (reflectivity close to 1, i.e., 0.9999). At each round-trip, few photons are transmitted through the mirrors and a cavity-ring-down signal consists in the time-resolved measurement of these photons. The escape decay time τ_0 of the photons from this cavity is exponential and is governed by the reflectivity of the mirrors: the higher reflective the mirrors, the longer the decay time. Additional loss through the presence of absorbing species within the cavity leads to a shorter decay time τ . By measuring both τ_0 and τ , the absorbance α due to the presence of the absorbing species, given by the product of the absorption cross section σ and the concentration $[A]$, can be calculated:

$$\alpha = [A] \times \sigma = \frac{L}{c} \left(\frac{1}{\tau} - \frac{1}{\tau_0} \right)$$

with L being the ratio of absorption path length over the length of the cavity and c being the speed of light. The advantage of this method is a much higher sensitivity compared to “classical” absorption methods, and this for two reasons: (a) the use of a cavity extends the absorption path, and depending on the reflectivity of the mirrors, path lengths on the order of several km can be achieved in a reactor with a geometrical length of less than a meter and (b) compared to the “classical” absorption techniques, where the small difference between two large signals (I_0 and I) needs to be measured, CRDS measures rather an exponential decay rate.

A more recent variant of CRDS has been developed in 1997 (Romanini et al. 1997) and uses CW lasers: the advantage of CW lasers versus pulsed lasers is a generally smaller bandwidth of CW lasers compared to pulsed lasers. There are two major consequences of this: (a) high-resolution spectroscopy can be achieved and (b) ring-down events present generally an improved signal-to-noise ratio (due to higher intracavity energies obtained by the excitation of a single longitudinal mode), leading in turn to a higher sensitivity. These improvements come at the expense of a somewhat more complex experimental setup of CW-CRDS compared to pulsed CRDS. This is especially important with respect to time-resolved measurements because the timing schemes are directly concerned: pulsed CRDS is easier to set up, as the occurrence of a ring-down event can be easily controlled by controlling the pulsed laser, whereas a synchronization of CW-CRDS is more difficult to realize, as the occurrence of a ring-down event is not precisely controllable. Therefore, many experiments have been set up combining pulsed CRDS for kinetic measurements (Atkinson and Hudgens 1997; Romanzin et al. 2008;

Zhu and Johnston 1995), while the use of CW-CRDS in kinetic experiments is rather sparse (Atkinson and Spillman 2002; Parker et al. 2011a, b; Thiebaud and Fittschen 2006).

23.3.4 Mass Spectroscopy

Mass spectroscopy is a rather selective detection technique: molecules or radicals are ionized using different methods (electron impact, multiphoton or VUV absorption, and chemical ionization). The resulting ions are then mass-selective detected whereby kinetic experiments use mostly either a time-of-flight (TOF) or a quadrupole detector. The use of mass spectroscopy in time-resolved experiments has been pioneered by Gutman and coworkers (Slagle et al. 1981). A drawback of mass spectroscopy is the possible fragmentation of the species during ionization due to high energies used in the ionization. A major improvement on this drawback has recently been realized (Osborn et al. 2008; Taatjes et al. 2008): they use tuneable VUV radiation from a synchrotron as ionization source in a TOF mass spectrometer. Doing so, they are able to precisely adjust the ionization energy just above the ionization threshold of the species by fine-tuning the wavelength of the VUV-photon, thus avoiding fragmentation. Another major advantage of this method compared to other conventional ionization methods is that isomers, having the same mass and which can thus not be differentiated in common mass spectrometers, can be differentiated due to their different ionization potentials.

23.4 Reactors and Timing Schemes

In the above paragraphs, different methods of generating radicals have been described as well as different detection methods, commonly used in kinetic experiments. Before presenting in the last section of this chapter the most commonly employed methods for the measurement of kinetic data, a brief reminder of the basics in chemical kinetics is given (Steinfeld et al. 1998). An elementary reaction can be classified as uni-, bi-, or termolecular reaction, depending on how many reaction partners are involved in the elementary reaction step and the experimental approach for measuring the rate constant depends on the reaction type.

Let us first consider the simplest reaction type, a unimolecular reaction



The change in the concentration of A in such a reaction can be expressed as

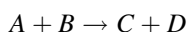
$$\frac{d[A]}{dt} = -k \times [A]$$

with k being the rate constant of the reaction. Integration of the differential equation leads to the following expression

$$[A]_t = [A]_0 \times e^{-kt}$$

i.e., the concentration of $[A]$ is decaying exponentially. In order to determine the rate constant k it is therefore not necessary to know the absolute concentration of $[A]$: measuring the decay of $[A]$ using a relative method is sufficient. This is particularly interesting when $[A]$ consists of a radical because it is often delicate to reliably determine the absolute concentration of radicals.

The situation gets more complicated when considering a bi-(or ter-)molecular reaction:



The rate constant k of this reaction is then defined as

$$\frac{d[A]}{dt} = \frac{d[B]}{dt} = -k \times [A] \times [B]$$

and integration leads to:

$$\ln \left\{ \frac{[A]_t}{[B]_t} \right\} = \ln \left\{ \frac{[A]_0}{[B]_0} \right\} + \{[A]_0 - [B]_0\} \times kt.$$

A common approach to simplify the experimental determination of rate constants for bi- (and also ter-)molecular reactions is to work with one (or two) species in large excess. By considering that $[B]_0 \gg [A]_0$, it can be approximated that the concentration of $[B]$ does not change during reaction, i.e., $[B]_0 = [B]_t$, and the above equation simplifies to an exponential decay

$$[A]_t = [A]_0 \times e^{-k't}$$

with k' being the pseudo-first order rate constant

$$k' = k \times [B]_0$$

Under these conditions, the so-called pseudo-first order conditions, we are again in the favorable situation where the absolute concentration of one of the reactants does not need to be known. Figure 23.1 shows a typical example: the rate constant for the reaction of OH radicals with CH_4 has been measured by following OH decays in the presence of different CH_4 concentrations (left panel): the rate constant is then obtained by plotting the observed pseudo-first order rate constants as a function of the CH_4 concentration (right panel) (Parker et al. 2011a, b).

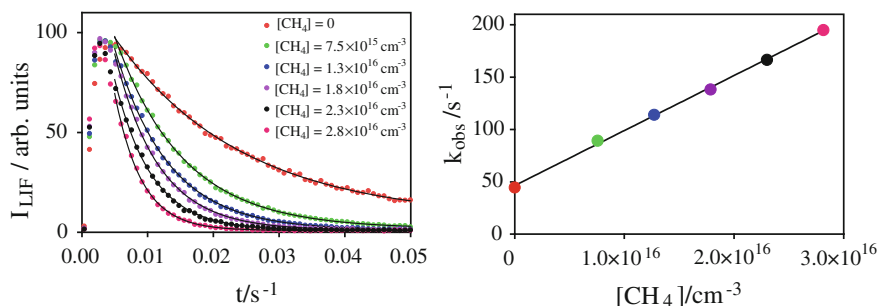


Fig. 23.1 Typical example for the measurement of a rate constant. *Left panel* shows exponential decays of OH radicals in the presence of excess CH_4 . *Right panel* shows plot of pseudo-first order decay rate as a function of the CH_4 -concentration, the slope leads to the rate constant of the bimolecular reaction, the intercept corresponds to the decay of OH radicals in the absence of reactant

23.4.1 Flash Photolysis

This type of setup uses a pulsed initiation of the reaction, i.e., the initial concentration of radicals is generated on a short time scale. This can be on the nano- or picosecond time scale in the case of laser flash photolysis, but also on the millisecond timescale in the case of UV-lamp flash photolysis. It is however important that the generation of the radicals occurs on a time scale much shorter than the subsequent reactions. The evolution of the concentration of selected species following the photolysis pulse is then observed in a time-resolved manner. The most direct way for obtaining a rate constant is to follow the decay of the initially produced radical, but following the rate of formation of a stable reaction product can also be carried out.

In case of a unimolecular decomposition, the rate constant depends on the pressure, and thus the exponential decay is often studied as a function of pressure. In this way, information about the fall-off behavior of the reaction can be deduced (Caralp et al. 1999; Devolder et al. 1999).

In the case of bi- or termolecular reactions, rate constants are generally obtained by working under pseudo-first order conditions: the exponential decays ($k' = k \times [B]_0$, see above), at a given pressure, are measured as a function of the initial concentration $[B]_0$: the slope of the plot of k' as a function of $[B]_0$ leads directly to the rate constant k . The intercept of such plot represent the loss of radicals in the absence of reactant. This can have different reasons: radicals can react with impurities present in the bath gas, they can react with themselves or on the reactor wall. Their concentration can also decrease due to diffusion out of the detection volume. In this type of experiments, the decay time of the species, and with this the necessary time resolution of the detection, can be influenced by the experimentalist through controlling the concentration of $[B]_0$: the higher $[B]_0$, the faster the decay of $[A]$. In this way the reaction time can be adapted to the time

resolution of the experimental setup. However, care has to be taken that the pseudo-first order condition is always fulfilled (a good rule of thumb is $[B]_0 > 10 \times [A]$).

Laser photolysis is widely used and can be coupled to a variety of detection methods, as long as the time resolution of the method is appropriate. In-situ optical techniques, that have been coupled to laser photolysis, include CW-detection methods such as UV-absorption spectroscopy (Brand et al. 1990; Villenave and Lesclaux 1996), TDLAS (Devolder et al. 2006; Tang et al. 2010), resonance fluorescence (Zhang et al. 2012); CW-LIF (DeSain et al. 2005) or infrared frequency modulation spectroscopy (DeSain et al. 2001). Using these techniques, the evolution of the species can be monitored continuously following the photolysis pulse and only the start of the acquisition period needs to be synchronized with the pulsed initiation of the reaction. Pulsed detection methods describe the concentration–time profiles from a series of data-points, obtained at different delays between the photolysis pulse and the detection pulse. This can be achieved using photolysis and detection at the same repetition rate, i.e., by acquiring the signal level at a given delay after the photolysis pulse and then change the delay at the next photolysis pulse. This is the very common case for laser photolysis/LIF experiments (Delbos et al. 2006; Dillon and Crowley 2008; Fulle et al. 1999), where both lasers work generally at, e.g., 10 Hz. Recent developments in laser technology have brought high repetition rate dye lasers (10 kHz or higher) allowing to obtain the full concentration–time profile with a time resolution of 100 μ s (in the case of a 10 kHz laser) after each photolysis shot (Mollner et al. 2010; Parker et al. 2009). Coupling of pulsed CRDS to laser photolysis is mostly used the same way as pulsed LIF, i.e., both lasers firing at 10 Hz with the delay being varied systematically (Sakamoto et al. 2009; Zhu and Johnston 1995). Another interesting variant of CRDS coupled to laser photolysis is the so-called simultaneous kinetic and ring-down technique (Brown et al. 2000; Guo et al. 2003): here, the experimental conditions are arranged in a way that the kinetic decay occurs on a timescale faster than the optical cavity decay. The result is a double exponential decay, giving access to the rate constant. A more sophisticated timing scheme is needed for the coupling of CW-CRDS to laser photolysis, because the timing of CW-CRD is not easily controllable (Atkinson and Spillman 2002; Parker et al. 2011a, b; Thiebaud and Fittschen 2006).

Figure 23.2 illustrates the application of such a setup to the study of an equilibrium reaction: HO₂ radicals react with formaldehyde in a rapidly equilibrating reaction where the adduct, HO₂CH₂O, undergoes rapid intramolecular isomerisation to form a hydroxylperoxy radical, O₂CH₂OH. This equilibrium was first studied in 1979 by (Su et al. 1979) and in 1980 by (Niki et al. 1980). They investigated the Cl atom initiated oxidation of CH₂O in a large photoreactor, coupled to a detection of reaction products by FTIR. The reaction of CH₂O with HO₂ was later again investigated by (Veyret et al. 1982) by flash photolysing a mixture of CH₂O, O₂ and NO and monitoring the rate and the yield of NO₂ appearance. They fitted the NO₂ formation yield and rate to a complex model, from which the rate constants for the equilibrium reaction of HO₂ radicals with

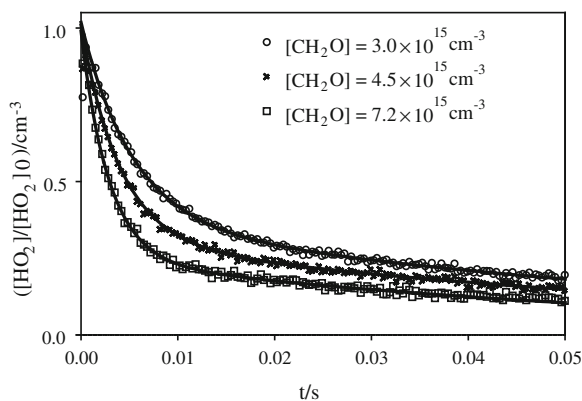


Fig. 23.2 Example of time-resolved, normalized HO_2 profiles, obtained by laser photolysis coupled to CW-CRDS (Morajkar et al. 2013): HO_2 radicals have been generated in the presence of different concentrations of CH_2O , always in large excess. The rapid decay represents the loss of HO_2 through establishment of the equilibrium; the slow decay on longer timescales is due to the loss of radicals through diffusion out of the observation volume or through secondary chemistry

CH_2O was obtained in a rather indirect way. In 1985, Barnes et al. (1985) studied the reaction in a large photoreactor at 273 K in the presence of NO_2 . They monitored the reactants and their products by FTIR absorption spectroscopy. A selective and time-resolved detection of HO_2 radicals, generated through laser photolysis in the presence of excess CH_2O , allowed to directly determine the equilibrium constant and also the rate constants for both forward and backward reaction. Later, Veyret et al. (1989) reinvestigated the reaction of HO_2 with CH_2O using flash photolysis coupled to time-resolved UV absorption spectroscopy, HO_2 radicals were generated by flash-photolysing a $\text{Cl}_2/\text{CH}_2\text{O}/\text{O}_2$ mixture. However, UV absorption spectroscopy is not very selective because both HO_2 and HOCH_2O_2 radicals have large and unstructured bands in the same wavelength region, a common problem with UV-absorption spectroscopy. Experiments such as shown in Fig. 23.2 have therefore allowed to measure for the first time directly this equilibrium reaction: while the equilibrium constant was found to be in good agreement with the only other temperature-dependent determination of this equilibrium constant Veyret et al. (1989), the rate constants for the forward and back reaction were found to be two times slower.

Sampling of the photolysed volume into the detection device has been initially pioneered by Gutman and co-worker (Slagle et al. 1981) by using time-resolved mass spectroscopy. The principle of this idea is used by several groups (Baeza-Romero et al. 2012; Ludwig et al. 2006) and a sophisticated variant has recently been set up by Osborn et al. (2008), where they use tuneable VUV-synchrotron radiation as ionization source, which allows the selective detection of isomers (Greenwald et al. 2009). The impact of the velocity distribution due to the sampling on the rate constant has been analyzed by Taatjes (2007). Recent developments

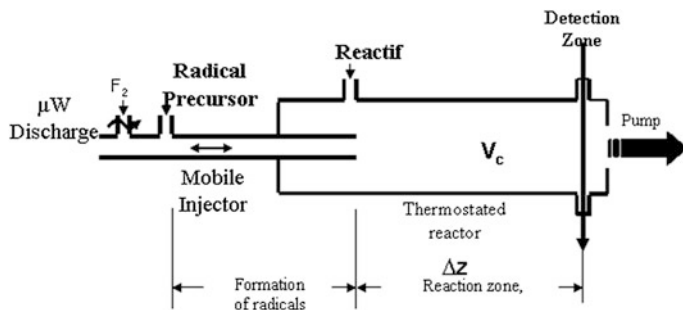


Fig. 23.3 Schematic view of a fast flow reactor. In this example, radicals are formed within the injector from a reaction of F-atoms with a suitable precursor. The injector can be moved and thus varying the length of the reaction zone

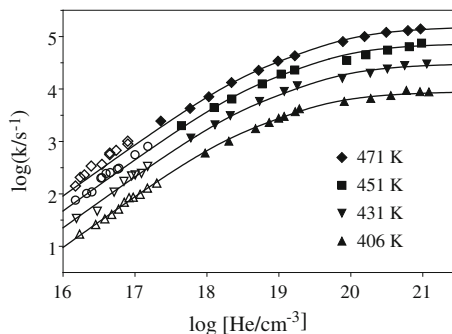
have also coupled separated photolysis volumes and LIF detection units (Sadanaga et al. 2004): such a combination might enable the measurement of reactions of OH or HO₂ at high temperatures and high pressures, which is difficult to realize with in situ detection.

23.4.2 Fast Flow Tube

Fast flow tubes generally require a continuous generation of radicals, for example by a microwave discharge. These radicals, highly diluted in the bath gas, are pumped at high speed (in the order of m/s) through the reactor. Their concentration is then detected at the end of the flow tube by either continuous or pulsed detection methods. The reaction partner is added to this fast flowing mixture at various distances, and the reaction time can be calculated from the distance Δz , i.e., the distance between the mixing point of the reaction partners to the detection point, divided by the flow velocity. Shifting the mixing point of the reaction partners with a movable injector (see Fig. 23.3) allows varying the reaction time and information on the kinetic of the reaction can be obtained.

Several schemes are possible: the radicals can be generated in the movable injector and the stable reaction partner is added at a fixed point in the reactor, such as shown in Fig. 23.3, or vice versa. Both configuration lead to a different behavior if the radical loss is measured in the absence of any reaction partner: in the first configuration, the radical concentration decreases with increasing Δz due to an increased heterogeneous loss of radicals on the reactor wall. In the second configuration the radical concentration increases with increasing Δz due to a decreased heterogeneous loss on the decreasing surface of the injector wall. Many different detection techniques have been adapted for this experimental technique, for example LIF (Caralp et al. 1997), mass spectroscopy (Loison et al. 2005) or cavity enhanced absorption spectroscopy (Kasyutich et al. 2003).

Fig. 23.4 Falloff curves of the first-order rate constants k for the decomposition of ethoxy radicals at different temperatures over a very large pressure range, spanning from 0.001 to 50 bar (Caralp et al. 1999); *symbols*: experimental results; *solid lines*: best fit to a falloff expression developed by Troe (1983)



The flow tube technique can be complementary to laser photolysis setups, because lower pressures can be attained (generally, flow tubes are used below 10 Torr in order to maintain laminar flow conditions, while laser photolysis can be problematic towards low pressures, if the photolytically generated, highly excited radical is not thermalized fast enough). Also, the study of radical–radical reactions might be easier in flow tubes, because both radicals can be prepared separately, while it can be difficult to selectively generate two radicals simultaneously by photolysing suitable precursors.

Figure 23.4 illustrates the complementarity of both techniques. The rate constant for the unimolecular decomposition of the ethoxy radical, an important intermediate in the oxidation of hydrocarbons, is pressure- and temperature-dependent. For a reliable parameterization of the rate constant, it is indispensable to measure it over a large pressure and temperature range, thus allowing for a reliable extrapolation to various experimental conditions. In Fig. 23.4, the first order rate constants for this reaction are shown in a pressure range spanning over five orders of magnitude (Caralp et al. 1999): experiments below 10 mbar ($\log[\text{He}/\text{cm}^{-3}] < 17.5$, open symbols) were carried out in a flow tube, while the high-pressure experiments ($\log[\text{He}/\text{cm}^{-3}] > 18$, filled symbols) were carried out by laser photolysis.

23.5 Summary

In this chapter, the basic principles of experimental techniques commonly used for the determination of rate constants and branching ratios of elementary reactions have been reviewed. In most reaction system, including combustion chemistry, radicals are the driving force. Therefore, different possibilities of their in-situ generation have been presented in the first part. In the following section, frequently used detection methods have been presented, and finally different experimental setups, combining radical generation and detection, were presented in the last section. Major progress has been made in the last decades by the development of more sensitive and more selective detection method. These new methods will, in

close association with theoretical methods such as presented in Chaps. 20 and 21, unravel in upcoming years more and more details from the very complex chemical mechanism taking place in the atmosphere or in combustion systems.

References

- Atkinson DB, Hudgens JW (1997) Chemical kinetic studies using ultraviolet cavity ring-down spectroscopic detection: self-reaction of ethyl and ethylperoxy radicals and the reaction $O_2 + C_2H_5 \rightarrow C_2H_5O_2$. *J Phys Chem A* 101:3901–3909
- Atkinson DB, Spillman JL (2002) Alkyl peroxy radical kinetics measured using near-infrared CW-cavity ring-down spectroscopy. *J Phys Chem A* 106:8891–8902
- Atkinson R, Baulch DL, Cox RA et al (2004) Evaluated kinetic and photochemical data for atmospheric chemistry: volume 1—gas phase reactions of O_x , HO_x , NO_x , and SO_x , species. *Atmos Chem Phys* 4:1461–1738
- Baeza-Romero MT, Blitz MA, Goddard A et al (2012) Time-of-flight mass spectrometry for time-resolved measurements: some developments and applications. *Int J Chem Kinet* 44:532–545
- Barnes I, Becker KH, Fink EH et al (1985) FTIR spectroscopic study of the gas-phase reaction of HO_2 with H_2CO . *Chem Phys Lett* 115:1–8
- Baulch DL, Cobos CJ, Cox RA et al (1992) Evaluated kinetic data for combustion modelling. *J Phys Chem Ref Data* 21:411–429
- Baulch DL, Cobos CJ, Cox RA et al (1994) Evaluated kinetic data for combustion modelling. Supplement I. *J Phys Chem Ref Data* 23:847–1033
- Baulch DL, Bowman CT, Cobos CJ et al (2005) Evaluated kinetic data for combustion modeling: supplement II. *J Phys Chem Ref Data* 34:757–1397
- Bergeat A, Moisan S, Mereau R et al (2009) Kinetics and mechanisms of the reaction of CH with H_2O . *Chem Phys Lett* 480:21–25
- Bohn B, Zetzsch C (1999) Gas-phase reaction of the OH-benzene adduct with O_2 : reversibility and secondary formation of HO_2 . *Phys Chem Chem Phys* 1:5097–5107
- Brand U, Hippler H, Lindemann L et al (1990) C–C and C–H bond splits of laser-excited aromatic-molecules. 1. Specific and thermally averaged rate constants. *J Phys Chem* 94:6305–6316
- Brown SS, Ravishankara AR, Stark H (2000) Simultaneous kinetics and ring-down: rate coefficients from single cavity loss temporal profiles. *J Phys Chem A* 104:7044–7052
- Caralp F, Rayez MT, Forst W et al (1997) Kinetic study of the pressure dependence of the reaction $CF_3O + NO_2$ at 298 K—rate constant measurements ($P = 0.5$ –9 Torr) and competition between association (CF_3ONO_2) and disproportionation ($CF_2O + FNO_2$) channels. *J Chem Soc, Faraday Trans* 93:3751–3756
- Caralp F, Devolder P, Fittschen C et al (1999) The thermal unimolecular decomposition rate constants of ethoxy radicals. *Phys Chem Chem Phys* 1:2935–2944
- Delbos E, Fittschen C, Hippler H et al (2006) Rate coefficients and equilibrium constant for the $CH_2CHO + O_2$ reaction system. *J Phys Chem A* 110:3238–3245
- DeSain JD, Clifford EP, Taatjes CA (2001) Infrared frequency-modulation probing of product formation in Alkyl + O_2 reactions: II. The reaction of C_3H_7 with O_2 between 296 and 683 K. *J Phys Chem A* 105:3205–3213
- DeSain JD, Jusinski LE, Taatjes CA (2005) Temperature dependence and deuterium kinetic isotope effects in the HCO plus NO reaction. *J Photochem Photobiol A* 176:149–154
- Devolder P, Fittschen C, Frenzel A et al (1999) Complete falloff curves for the unimolecular decomposition of i-propoxy radicals between 330 and 408 K. *Phys Chem Chem Phys* 1:675–681

- Devolder P, Dusanter S, Lemoine B et al (2006) About the co-product of the OH radical in the reaction of acetyl with O₂ below atmospheric pressure. *Chem Phys Lett* 417:154–158
- Dillon TJ, Crowley JN (2008) Direct detection of OH formation in the reactions of HO₂ with CH₃C(O)O₂ and other substituted peroxy radicals. *Atmos Chem Phys* 8:4877–4889
- Dusanter S, ElMaimouni L, Fittschen C et al (2005) Fall-off curves for the unimolecular decomposition of two acyl radicals: RCO (+M)→R + CO (+M) by pulsed laser photolysis coupled to time resolved infrared diode laser absorption. *Int J Chem Kinet* 37:611–624
- Estupinan EG, Smith JD, Tezaki A et al (2007) Measurements and modeling of DO₂ formation in the reactions of C₂D₅ and C₃D₇ radicals with O₂. *J Phys Chem A* 111(19):4015–4030
- Fernandes RX, Luther K, Troe J et al (2008) Experimental and modelling study of the recombination reaction H + O₂ (+M)→HO₂ (+M) between 300 and 900 K, 1.5 and 950 bar, and in the bath gases M = He, Ar, and N₂. *Phys Chem Chem Phys* 10:4313–4321
- Fernandez A, Fontina A (2001) Wide temperature range kinetics of the O + CHF₃ reaction. *J Phys Chem A* 105:8196–8199
- Fittschen C, Frenzel A, Imrik K et al (1999) Rate constants for the reactions of C₂H₅O, i-C₃H₇O, and n-C₃H₇O with NO and O₂ as a function of temperature. *Int J Chem Kinet* 31:860–866
- Fulle D, Hamann HF, Hippler H (1999) The pressure and temperature dependence of the recombination reaction HO + SO₂ + M→HOSO₂ + M. *Phys Chem Chem Phys* 1:2695–2702
- Greenwald EE, Ghosh B, Anderson KC et al (2009) Isomer-selective study of the OH initiated oxidation of isoprene in the presence of O₂ and NO. I. The minor inner OH-addition channel. *J Phys Chem A* 114:904–912
- Guo Y, Fikri M, Friedrichs G et al (2003) An extended simultaneous kinetics and ringdown model: determination of the rate constant for the reaction SiH₂ + O₂. *Phys Chem Chem Phys* 5:4622–4630
- Heard DE (2006) Atmospheric field measurements of the hydroxylradical using laser-induced fluorescence spectroscopy. *Annu Rev Phys Chem* 57:191–216
- Hickson KM, Bergeat A, Costes M (2010) A low temperature study of the reactions of atomic chlorine with simple alkanes. *J Phys Chem A* 114:3038–3044
- Hottle JR, Huisman AJ, DiGangi JP et al (2009) A laser induced fluorescence-based instrument for in-situ measurements of atmospheric formaldehyde. *Environ Sci Technol* 43:790–795
- Jacquinet-Husson N, Crepeau L, Armante R et al (2011) The 2009 edition of the GEISA spectroscopic database. *J Quant Spectrosc Radiat Transfer* 109:1043–1059
- Jain C, Morajkar P, Schoemaeker C et al (2012) Formation of HO₂ radicals from the 248 nm two-photon excitation of different aromatic hydrocarbons in the presence of O₂. *J Phys Chem A* 116:6231–6239
- Kanno N, Tonokura K, Tezaki A et al (2005) Nitrogen- and water-broadening coefficient measurements in the 000-000 band of HO₂ using high-resolution diode laser two-tone frequency modulation spectroscopy. *J Mol Spectrosc* 229:193–197
- Kasyutich VL, Bale CSE, Canosa-Mas CE et al (2003) Cavity-enhanced absorption: detection of nitrogen dioxide and iodine monoxide using a violet laser diode. *Appl Phys B: Lasers Optics* 76:691–697
- Khatoun T, Edelbüttel-Einhaus J, Hoyermann K et al (1989) Rates and mechanisms of the reactions of ethanol and propanol with fluorine and chlorine atoms. *Ber Bunsenges Phys Chem* 93:626–632
- Kovacs TA, Brune WH (2001) Total OH loss rate measurement. *J Atm Chem* 39:105–122
- Loison J-C, Sanglar S, Villenave E (2005) Discharge flow tube coupled to time-of-flight mass spectrometry detection for kinetic measurements of interstellar and atmospheric interests. *Rev Sci Instrum* 76:053105–053106
- Ludwig W, Brandt B, Friedrichs G et al (2006) Kinetics of the Reaction C₂H₅ + HO₂ by time-resolved mass spectrometry. *J Phys Chem A* 110:3330–3337
- Meaner N, Dousing JF, Chevalier E et al (2003) Atmospheric fate of alkoxy radicals: branching ratio of evolution pathways for 1-propoxy, 2-propoxy, 2-butoxy and 3-pentoxy radicals. *Phys Chem Chem Phys* 5:4834–4839

- Milner AK, Valluvadasan S, Fang L et al (2010) Rate of gas phase association of hydroxyl radical and nitrogen dioxide. *Science* 330:646–649
- Morajkar P, Schoemaeker C, Okumura M et al (2013) Direct measurement of the equilibrium constants of the reaction of formaldehyde and acetaldehyde with HO₂ radicals. *Int J Chem Kin*, submitted
- Nicovich JM, Wine PH (1988) Temperature-dependent absorption cross-sections for hydrogen-peroxide vapor. *J Geophys Res-Atmos* 93:2417–2421
- Niki H, Maker PD, Savage CM et al (1980) FTIR studies of the Cl-atom initiated oxidation of formaldehyde: detection of a new metastable species in the presence of NO₂. *Chem Phys Lett* 72:71–73
- O’Keefe A, Deacon DAG (1988) Cavity ring-down optical spectrometer for absorption measurements using pulsed laser sources. *Rev Sci Instrum* 59:2544–2551
- Olariu RI, Bejan I, Barnes I et al (2004) Rate coefficients for the gas-phase reaction of NO₃ radicals with selected dihydroxybenzenes. *Int J Chem Kinet* 36:577–583
- Orlando JJ, Tyndall GS (2012) Laboratory studies of organic peroxy radical chemistry: an overview with emphasis on recent issues of atmospheric significance. *Chem Soc Rev* 41:6294–6317
- Osborn DL, Zou P, Johnsen H et al (2008) The multiplexed chemical kinetic photoionization mass spectrometer: a new approach to isomer-resolved chemical kinetics. *Rev Sci Instrum* 79:104103
- Parker A, Jain C, Schoemaeker C et al (2009) Kinetics of the reaction of OH radicals with CH₃OH and CD₃OD studied by laser photolysis coupled to high repetition rate laser induced fluorescence. *React Kinet Catal Lett* 96:291–297
- Parker A, Amedro D, Schoemaeker C et al (2011a) OH reactivity measurements by FAGE. *JEEM* 10:107–114
- Parker A, Jain C, Schoemaeker C et al (2011b) Simultaneous, time-resolved measurements of OH and HO₂ radicals by coupling of high repetition rate LIF and CW-CRDS techniques to a laser photolysis reactor and its application to the photolysis of H₂O₂. *Appl Phys B: Lasers Optics* 103:725–733
- Picquet B, Heroux S, Chebbi A et al (1998) Kinetics of the reactions of OH radicals with some oxygenated volatile organic compounds under simulated atmospheric conditions. *Int J Chem Kinet* 30:839–847
- Raoult S, Rayez M-T, Rayez J-C et al (2004) Gas phase oxidation of benzene: kinetics, thermochemistry and mechanism of initial steps. *Phys Chem Chem Phys* 6:2245–2253
- Romanini D, Kachanov AA, Sadeghi N et al (1997) CW cavity ring down spectroscopy. *Chem Phys Lett* 264:316–322
- Romanzin C, Gans B, Douin S et al (2008) 193 nm photolysis of CHCl₃: probe of the CH product by CRDS. *Chem Phys* 351:77–82
- Rothman LS, Gordon IE, Barbe A et al (2009) The HITRAN 2008 molecular spectroscopic database. *J Quant Spectrosc Radiat Transf* 110:533–572
- Rowley DM, Harwood MH, Freshwater RA et al (1996) A novel flash photolysis/UV absorption system employing charge-coupled device (CCD) detection: a study of the BrO + BrO reaction at 298 K. *J Phys Chem* 100:3020–3029
- Sadanaga Y, Yoshino A, Watanabe K et al (2004) Development of a measurement system of OH reactivity in the atmosphere by using a laser-induced pump and probe technique. *Rev Sci Instrum* 75:2648–2655
- Sakamoto Y, Yamano D, Nakayama T et al (2009) Atmospheric chemistry of BrO radicals: kinetics of the reaction with C₂H₅O₂ radicals at 233–333 K. *J Phys Chem A* 113:10231–10237
- Sander SP, Abbatt J, Barker JR et al (2011) Chemical kinetics and photochemical data for use in atmospheric studies, evaluation no. 17. JPL Publication 10–6, Jet Propulsion Laboratory, Pasadena

- Slagle IR, Yamada F, Gutman D (1981) Kinetics of free radicals produced by infrared multiphoton-induced decompositions. 1. Reactions of allyl radicals with nitrogen dioxide and bromine. *J Am Chem Soc* 103:149–153
- Steinfeld JJ, Francisco JS, Hase WL (1998) Chemical kinetics and dynamics. Prentice Hall, Upper Saddle River
- Su F, Calvert JG, Shaw JH (1979) Mechanism of the photooxidation of gaseous formaldehyde. *J Phys Chem* 83:3185–3191
- Taatjes CA (2006) Uncovering the fundamental chemistry of Alkyl + O₂ reactions via measurements of product formation. *J Phys Chem A* 110:4299–4312
- Taatjes CA (2007) How does the molecular velocity distribution affect kinetics measurements by time-resolved mass spectrometry? *Int J Chem Kinet* 39:565–570
- Taatjes CA, Hansen N, Osborn DL et al (2008) “Imaging” combustion chemistry via multiplexed synchrotron-photoionization mass spectrometry. *Phys Chem Chem Phys* 10:20–34
- Tang Y, Tyndall GS, Orlando JJ (2010) Spectroscopic and kinetic properties of HO₂ radicals and the enhancement of the HO₂ self reaction by CH₃OH and H₂O. *J Phys Chem A* 114:369–378
- Thiebaud J, Fittschen C (2006) Near infrared CW-CRDS coupled to laser photolysis: spectroscopy and kinetics of the HO₂ radical. *Appl Phys B: Lasers Optics* 85:383–389
- Thiebaud J, Aluculesei A, Fittschen C (2007) Formation of HO₂ radicals from the photodissociation of H₂O₂ at 248 nm. *J Chem Phys* 126:186101
- Troe J (1983) Theory of thermal unimolecular reactions in the fall-off range. I. Strong collision rate constants. *Ber Bunsen-Ges Phys Chem* 87:161–169
- Tyndall GS, Orlando JJ, Wallington TJ et al (2002) Mechanism of the reaction of OH radicals with acetone and acetaldehyde at 251 and 296 K. *Phys Chem Chem Phys* 4:2189–2193
- Vaghjiani GL, Ravishankara AR (1990) Photodissociation of H₂O₂ and CH₃OOH at 248 nm and 298 K: quantum yields for OH, O(³P) and H(²S). *J Chem Phys* 92:996–1003
- Veyret B, Rayez JC, Lesclaux R (1982) Mechanism of the photo-oxidation of formaldehyde studied by flash-photolysis of CH₂O–O₂–NO mixtures. *J Phys Chem* 86:3424–3430
- Veyret B, Lesclaux R, Rayez MT et al (1989) Kinetics and mechanism of the photo-oxidation of formaldehyde. 1. Flash photolysis study. *J Phys Chem* 93:2368–2374
- Villenave E, Lesclaux R (1996) Kinetics of the cross reactions of CH₃O₂ and C₂H₅O₂ radicals with selected peroxy radicals. *J Phys Chem* 100:14372–14382
- Vipond A, Canosa-Mas CE, Flugge ML et al (2002) A discharge-flow study of the self-reaction of IO. *Phys Chem Chem Phys* 4:3648–3658
- Zhang SL, Strekowski RS, Monod A et al (2012) Temperature-dependent kinetics study of the reactions of OH with C₂H₅I, n-C₃H₇I, and iso-C₃H₇I. *J Phys Chem A* 116:9497–9506
- Zhu L, Johnston G (1995) Kinetics and products of the reaction of the vinoxy radical with O₂. *J Phys Chem* 99:15114–15119

Chapter 24

Shock Tube Studies of Combustion Relevant Elementary Chemical Reactions and Submechanisms

Robert S. Tranter and Kenneth Brezinsky

Abstract Shock tubes are vital experimental tools that are used to study high temperature gas-phase kinetics and shock tube research accounts for most of the high temperature experimental data relevant to combustion. Several shock tube techniques are briefly discussed and references to prior more detailed reviews supplied. The use of shock tube techniques to elucidate reaction rates and mechanisms for elementary unimolecular and bimolecular reactions is discussed. Particular attention is given to studies that provide fundamental data that can be extrapolated to systems that cannot be studied in isolated experiments. In this context, experiments on the dissociation and isomerization of fuel radicals, pyrolysis of saturated cyclic and heterocyclic molecules of importance in surrogate fuels and nontraditional fuels, and the role of resonantly stabilized radicals in formation of polycyclic aromatic hydrocarbons are discussed.

24.1 Introduction

In the chemical kineticist's toolkit, there are many experimental techniques for studying elementary reactions. A quick browse of the literature reveals studies performed with various permutations of static and flow reactors coupled to a large variety of detectors. However, many of these devices operate best at relatively low reaction temperatures, <1,000 K. For temperatures >800 K shock tubes are often the instrument of choice, particularly for studies of elementary reactions.

R. S. Tranter (✉)
Chemical Sciences and Engineering Division, Argonne National Laboratory,
9700 S. Cass Avenue, Argonne, IL 60439, USA
e-mail: Tranter@anl.gov

K. Brezinsky
Mechanical and Industrial Engineering Department, University of Illinois at Chicago,
842 W. Taylor St, Chicago, IL 60607, USA

Shock tubes are extremely versatile and in combustion related studies they have been applied to topics ranging from vibrational relaxation and energy transfer (Kiefer et al. 2000, 2005) through heterogeneous chemistry related to corrosion of rocket nozzle liners induced by flame radicals (Culbertson et al. 2008). This brief review focuses on elementary reaction chemistry relevant to homogenous combustion, i.e., the basic reactions that underpin gas-phase reaction mechanisms upon which simulations of practical devices are based and a period covering the last 15 years, at the time of writing. For a broader perspective of shock tube research, the reader is referred to the review article by Bhaskaran and Roth (2002) which gives an excellent overview of many shock tube techniques and references a number of earlier review articles that collectively detail the development of shock tubes as important research tools. Volume 3 of the 'Handbook of Shock Waves' (Ben-Dor et al. 2001) presents more detailed discussions of the basis and application of the main shock tube techniques used to investigate combustion chemistry and elementary reactions. In 'Shock Waves in Chemistry', Gardiner presents methods for modeling chemical reactions in shock waves (Gardiner et al. 1981). Additional information regarding the study of hydrocarbon oxidation and elementary kinetics can be found in the remainder of the book. In this short review, references to the literature are not comprehensive but are selected to highlight key aspects of shock tube research.

Currently, shock tube practitioners are experiencing an exciting period where very difficult chemical problems can be tackled with greater precision and accuracy than previously possible. These advances are partly due to new designs of shock tubes and in part to improvements in diagnostic equipment, data acquisition hardware and computing power. Increased precision and accuracy in experimental results has been mirrored by advances in theoretical chemistry and in modern shock tube research experiment and theory are complementary. Kern, in his closing statements on 'Chemical and Combustion Kinetics' (Kern et al. 2001) gives a very good description, with reference to cyclopentadiene dissociation, of the interplay between different shock tube techniques and theoretical methods that are necessary to obtain a comprehensive description of an elementary reaction from the structures and thermochemical properties of the species through the reaction path and rates.

24.2 Shock Tubes

Shock tubes have been accepted as chemical kinetic research tools since about the mid 1960s. They can simplistically be thought of as temperature and pressure jump reactors where the reagents, normally dilute in inert gas, are instantaneously, on the timescale of the experiment, taken from their initial temperature and pressure to the reaction conditions. It is the near instantaneous change and the extreme, well-defined conditions that can be generated with relative ease that make shock tubes such useful tools. For instance, post shock pressures from <10 Torr

(Santhanam et al. 2003; Srinivasan et al. 2003) to as high as 1,000 bar (Tranter et al. 2005) are routinely obtained and post shock temperatures from a few hundred to several thousand Kelvin can be generated in a single apparatus (Srinivasan et al. 2003; Saxena et al. 2007). Of course, the shock tube itself is just one part of a complete experimental apparatus and without suitable detectors one would learn nothing regarding chemistry in shock waves. A large variety of analytical methods and detectors are used in shock tube research including atomic resonance absorption spectroscopy (ARAS), ultraviolet/visible/infrared (UV/Vis/IR) spectroscopy, frequency modulation spectroscopy, laser schlieren densitometry (LS), gas chromatography (GC), and mass spectrometry (MS).

ARAS techniques are especially sensitive. In well-designed apparatuses, they allow work at extremely low dilutions which suppress secondary reactions allowing the reaction of interest to be isolated. Michael et al. exploited a very sensitive implementation of H-ARAS to study roaming radical reactions (Sivaramakrishnan et al. 2010, 2011a, b), a class of reaction that has only recently been discovered in dissociation of neutral molecules (Townsend et al. 2004; Suits 2008). UV absorption has been used to study reactions of organic radicals and molecules (Horn et al. 1998; Fernandes et al. 2005; Yasunaga et al. 2008). However, at shock tube temperatures, UV absorption spectra of organic species are broad, limiting sensitivity, and selectivity. Laser UV absorption has, however, been especially valuable in the study of reactions involving OH radicals (Srinivasan et al. 2007a, b; Vasu et al. 2010b) where very sensitive detection is possible. In recent years, considerable advances have been made in the application of infrared spectroscopy by Hanson et al. to the determination of molecular concentrations in shock waves (Hong et al. 2011; Pyun et al. 2011). This has been possible due to new highly tunable lasers emitting at previously unobtainable wavelengths and the relative ease with which precise spectroscopic parameters can be calculated from high level theory allowing unique absorption lines to be identified in complex spectra.

Rather than targeting individual species, a different approach is taken with LS (Kiefer 1981). Here density gradients, a mixture property, are measured in reacting gases and kinetic and mechanistic data are extracted through simulation of density gradient/time signals. The technique has provided considerable data on very fast unimolecular reactions, often in the high temperature falloff regime, as well as vibrational relaxation and incubation times (Srinivasan et al. 2003; Kiefer et al. 2005; Yang et al. 2009). Recently, LS has also been extended to the determination of bimolecular rates (Tranter et al. 2010, 2011). However, LS experiments provide no direct information regarding specific species and apart from simple systems additional data may be needed to accurately simulate a complete LS profile. Furthermore, LS experiments require much higher reagent concentrations than many other optical methods and secondary reactions are often significant. However, these generally yield additional information especially on radical recombination reactions which are discussed later and radical dissociation reactions, for instance the rate of dissociation of cyclopentadienyl radicals (Kern et al. 1998).

It is rare that a single experiment yields as much information as necessary to fully understand an elementary reaction due to limitations of the detection schemes and temperature/pressure ranges accessible in a particular shock tube. Consequently, as mentioned by Kern et al. 2001, reactions are often studied independently by several groups providing a broad range of data and a number of groups have either built multiple shock tubes or equipped a single tube with multiple detectors to expand their experimental range.

The use of multiple shock tubes is exemplified by the groups of Frank (Horn et al. 1998) and Hidaka (Yasunaga et al. 2010). While this approach provides considerable flexibility, it has the disadvantage that each measurement is made under somewhat different reaction conditions and possibly with different concentrations of reagent depending on the techniques employed. Recently, Davidson et al. have made significant advances by monitoring several species simultaneously in reflected shock experiments with a variety of tunable UV/Vis/IR lasers (Davidson et al. 2011). This work suggests a possible route by which shock tube research may develop particularly as the lasers and detectors become more affordable. However, the accurate measurement of multiple species, especially large molecules which tend to have overlapping spectral features at shock tube temperatures, is currently best done by nonoptical, techniques including offline GC with a variety of detectors (Rajakumar et al. 2003; Awan et al. 2011a; Gudiyella et al. 2011) and direct coupling of a shock tube to a time-of-flight mass spectrometer (TOF-MS) (Kern et al. 2001; Tranter et al. 2007; Duerrstein et al. 2011a, b).

Offline techniques continue to yield a wealth of information as exemplified by very recent work on the formation of large polycyclic aromatic hydrocarbons (PAH) in aromatic rich pyrolysis systems (Comandini and Brezinsky 2011; Comandini 2011; Comandini et al. 2012). In these studies, quantitative analyses were obtained for around 50 species from acetylene (C₂) to pyrene (C₁₆) and the structures of each molecule, including many isomers, were determined from mass spectrometry. This level of detail is not currently obtainable by any real-time shock tube method. However, the offline techniques suffer from yielding no direct information about reactive or unstable intermediate species or how the concentrations of species vary with respect to reaction time. Directly coupling a shock tube to a time-of-flight mass spectrometer, TOF-MS, potentially addresses this problem because time dependent, species selected concentration data can be obtained. A mass spectrometer is a near universal detector for organic molecules and modern data acquisition systems and TOF-MSs allow complete mass spectra (up to about 300 amu) to be obtained every 6.5 μ s which permits rate coefficients up to about 10^5 s⁻¹ to be measured. However, all current shock tube/TOF-MS apparatuses use electron impact ionization and with the ionization energies needed to generate sufficient signal (>28 eV) most organic species fragment in the ion source severely complicating interpretation of the mass spectra. Nevertheless, even from complex mass spectra detailed mechanistic information can be obtained by carefully accounting for fragmentation (Kern et al. 2001; Yang et al. 2011).

In addition to species concentrations, it is equally important to determine the reaction temperature and pressure accurately and precisely. In shock tube experiments, the pressure is either measured with a piezoelectric pressure transducer or calculated from the initial conditions using methods similar to those in Gaydon and Hurlé's book (Gaydon and Hurlé 1963). Determining the reaction temperature is more challenging as the response of thermocouples is generally too slow to accurately track the fast temperature changes that occur in shock tubes. Some spectroscopic methods have been used to determine temperatures in shock tubes (Li et al. 2007; Farooq et al. 2009) and show good accuracy when compared with calibration experiments. However, the techniques rely on the presence of a dopant such as CO₂ or H₂O and this may limit general applicability. For conditions where ideal gas behavior can be assumed the shock temperature can be calculated, assuming frozen conditions, from the initial conditions and the incident shock wave velocity (Gaydon and Hurlé 1963). The velocity is obtained from the time taken for the shock wave to traverse known distances between pressure transducers mounted on the side of the shock tube close to the observation point. Typically, estimated errors in temperature are 0.5–1 %. At very high pressures, ideal gas behavior cannot be assumed and calculating shock conditions in the normal way leads to very large errors (Davidson and Hanson 1996). To account for real gas effects and other gas dynamic effects in a very high pressure single pulse shock tube, Brezinsky et al. (Tranter et al. 2001) use an adaptation of the chemical thermometer and comparative rate techniques developed by Tsang for single pulse shock tube studies (Tsang 1981).

Chemical thermometers are simply molecules that dissociate in a well-known manner, preferably to stable products in a single step, and for which the rate coefficients over the desired range of temperature and pressure are available with sufficient precision. Two common chemical thermometers are 1,1,1-trifluoroethane ($\text{H}_3\text{CCF}_3 \rightarrow \text{H}_2\text{CCF}_2 + \text{HF}$) and cyclohexene ($\text{C}_6\text{H}_{10} \rightarrow \text{C}_2\text{H}_4 + \text{C}_4\text{H}_6$). The shock temperature is obtained from the residence time and the first-order rate law, assuming the chemical thermometer decays by a first-order process (Tranter et al. 2001). In the comparative rate method, the chemical thermometer is co-decomposed with the molecule of interest (Tsang 1981; Awan et al. 2011b). Care has to be taken to avoid cross-reaction and ideally the reagent and chemical thermometer have similar reaction barriers and rates of reaction. However, it is advantageous that both molecules experience identical reaction conditions. Brezinsky et al. perform separate experiments to obtain correlations between incident shock velocity and the temperature behind the reflected shock wave. This has the advantage of avoiding cross-reaction and allows shock wave temperatures to be obtained for strongly exothermic reactions such as oxidation. However, it requires that the reagent mixtures are sufficiently dilute in the inert shock tube bath gas to ensure that the reagents do not significantly affect the shock wave properties and that the reaction zone remains nearly isothermal during an experiment (Tranter et al. 2001). There are a large number of species that are suitable for chemical thermometers particularly in the 700–1,200 K range and a number of these are summarized in references (Tranter et al. 2001; Awan et al. 2011b; Burgess and

Manion 2011). However, there is a lack of suitable species for higher temperatures, primarily due to secondary reactions between the parent molecule and its dissociation products. Recently, the dissociation of CS_2 has been successfully used for $T > 1,600$ K by Culbertson (2009) and while secondary reactions are important when they are sufficiently well understood to allow reasonable accuracy to be obtained.

24.3 Elementary Reactions and Sub-Mechanisms

As mentioned earlier, shock tubes have been used to study a large variety of elementary reactions and elucidate details of small groups of interlinked reactions that form subsets of larger reaction mechanisms. As is apparent from other sections of this book, combustion models can contain thousands of reactions and hundreds of species and it would be impractical to try and measure all of these. Consequently, a large part of shock tube kinetics research is aimed at obtaining accurate rate coefficients and mechanisms for the most fundamental elementary steps upon which combustion mechanisms are built and to elucidate information that can be used to form tools to accurately predict rates and mechanisms for species that cannot be measured experimentally. Examples are given in the remainder of this chapter that illustrate the role of shock tube research in the study of fundamental reactions, pyrolysis of fuel radicals, elucidation of rates and mechanisms for the decomposition of saturated cyclic species, and finally the formation of polycyclic aromatic species from small resonantly stabilized and aromatic radicals. The focus here is on experimental work, but it should be kept in mind that many of the experiments were complemented by theoretical studies to elucidate details not accessible through experiment, extrapolate rate coefficients to broad ranges of temperature and pressure, and compare pure theoretical predictions of rate and mechanism with experimental observations.

In the last 15 years, there have been around 100 investigations targeting unimolecular and bimolecular reactions of radicals. These radicals have to be generated in situ and currently all chemical shock tubes use thermal sources of radicals by pyrolyzing a precursor, although photolytic sources have also been employed previously (Michael 1992) and may well be in the future especially for low temperature radical/molecule reactions. At low temperatures where the dissociation may be relatively slow on the time scale of the experimental observations, or high concentrations or high pressure, reaction between the radical and any undissociated precursor may be unavoidable and reaction mechanisms accounting for secondary reactions are necessary.

In the remainder of this chapter, three areas of shock tube research are discussed that highlight the use of different shock tube techniques to study elementary reactions and submechanisms that are important in combustion. The topics span decomposition of fuels, attack by H atoms and OH radicals, which are typically

produced in large amounts in pyrolysis and oxidation systems, through molecular growth and formation of PAHs from resonantly stabilized radicals.

24.3.1 Dissociation and Isomerization of Fuel Radicals and Molecules

Traditional transportation fuels consist of mixtures of many linear, branched and cyclic alkanes, and aromatic molecules. At combustion temperatures, the rates of pyrolysis of these species are often much greater than their reaction rates with oxygen. Understanding their pyrolysis is critical to understanding the oxidation of fuels. Figure 24.1 shows a schematic of the main reaction paths involved in the dissociation of the 5-methyl-1-hexyl radical (Awan et al. 2010). The complexity is typical of even modestly sized alkanes where multiple isomerization reactions lead to a large number of products. Identifying all the stable species to elucidate mechanistic details with optical methods or online TOF-MS would be near impossible. In the former case, due to overlapping spectral features and in the later fragmentation in the ion source would make it challenging to assign peaks to individual species. However, with the comparative rate single pulse shock tube technique, Tsang et al. were able to identify the stable products by GC and assign species to unique reaction paths. From the relative concentrations of the products, it was possible to assess the importance of the various isomerization and decomposition pathways. The initially formed alkyl radicals either dissociated by β -scission of a C-C bond, relative to the radical site, or participated in a sequence of reversible, intra-molecular hydrogen transfer isomerization reactions prior to dissociation. From the range of alkyl radicals studied, Tsang et al. determined the relative importance of 1,4-, 1,5- and 1,6-transfers as well as the effect of methyl substituents on 1,4- and 1,5-transfers. These results allow predictions of isomerization and decomposition reactions in alkanes that cannot be easily studied experimentally but are found in real fuels. Consequently, they constructed a database of isomerization and decomposition reactions for linear (Tsang et al. 1998, 2007, 2009; Babushok et al. 2001), cyclic (Awan et al. 2011a) and branched alkyl radicals (McGovern et al. 2008; Awan et al. 2010) representative of those found in fuels.

The comparative rate experiments were performed with very dilute reagent mixtures to suppress bimolecular reactions and, H-atoms and methyl radicals produced were scavenged to minimize reaction with the parent molecule. Radicals were generated from iodides by cleavage of the weak C-I bond. The experiments were performed at relatively low temperatures, 850–1,150 K, and pressures of 1–2 bar and the results were extrapolated to a much wider range of temperature and pressure by fitting time-dependent Rice-Ramsperger-Kassel-Marcus/master equation, RRKM/ME, simulations to the experimental results.

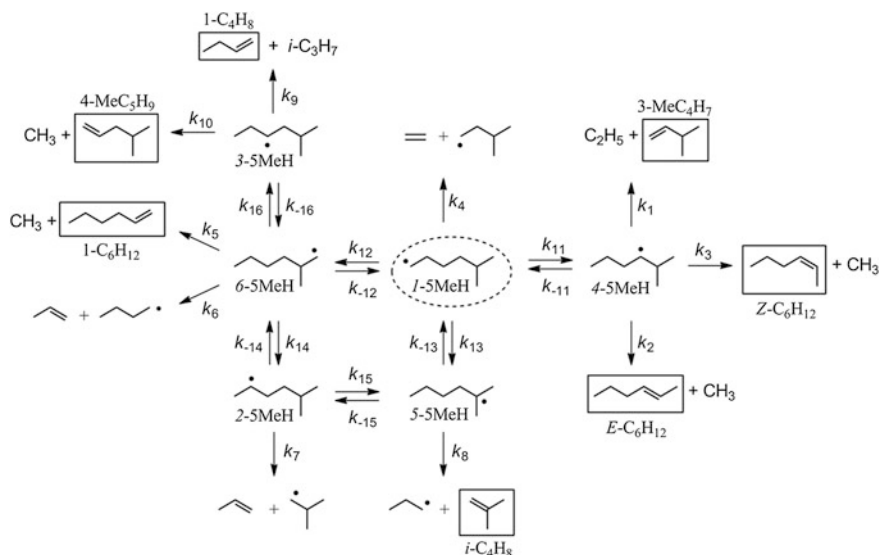


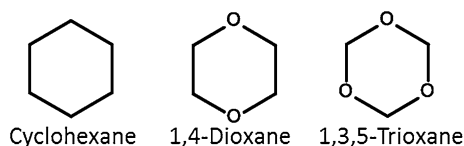
Fig. 24.1 Principle pathways in the dissociation of 5-methyl-1-hexyl radical. Nomenclature is that of reference (Awan et al. 2010). Reprinted with permission from Awan I.A et al. (2010) *J. Phys. Chem. A*. 114:7832-7846. Copyright 2010 American Chemical Society

Linear and branched molecules are only part of the rich soup that composes a real fuel. Aromatic and nonaromatic cyclic species are also present in concentrations of up to 12–40 % each. Cyclohexane and methylcyclohexane are frequently used to represent the saturated cyclic component in surrogate fuel mixtures (Manley et al. 2008) and toluene, the main aromatic component of fuels, often also represents the aromatic fraction in surrogate fuels. Consequently, the pyrolysis and oxidation mechanisms of these molecules have received considerable attention and shock tube experiments have been conducted to investigate the initial dissociation mechanisms. Heterocyclic molecules are found in many fuels and are formed as intermediates in combustion of fossil fuels. Thus, the effect of heteroatoms on the dissociation of cyclic and bicyclic species has also been studied.

Pyrolysis and oxidation of heterocyclic molecules leads to formation of complex gaseous mixtures and detailed species information are best obtained by single pulse shock tube techniques. Lifshitz et al. have applied this method with gas chromatography to a number of heterocyclics including methylated furans (Lifshitz et al. 1997, 1998) which have recently received renewed attention as direct replacements for gasoline (Simmie and Curran 2009; Zhong et al. 2010, Wu et al. 2011). The product distributions obtained from the shock tube experiments are important targets for developing a reaction mechanism. The increasing interest in methylated furans as fuels has promoted a much higher level ab initio investigation of their dissociation than would have been possible when the single pulse shock tube experiments were performed (Simmie and Metcalfe 2011). These calculations

complement the shock tube data by providing details of the initial dissociation that cannot be elucidated in high temperature experiments. Lifshitz also studied dissociation of a number of bicyclic heterocyclics with both O and N substituents (Lifshitz et al. 2000, 2001, 2006a, b, c) and obtained results that allowed the effect of the relative locations of the heteroatoms on the dissociation mechanism to be determined.

Single pulse shock tube experiments yield considerable detail about decomposition mechanisms. However, isolating elementary steps to directly measure rate coefficients remains challenging, although in situ experiments complemented by theoretical studies can yield kinetic and mechanistic data. Cyclic molecules can be particularly challenging as dissociation may involve several simultaneous reaction steps. Some of the challenges posed in obtaining accurate mechanistic and rate information experimentally for cyclics are illustrated by the series of six membered saturated molecules: Cyclohexane, 1,4-dioxane and 1,3,5-trioxane with zero, two and three O-atoms respectively.



Cyclohexane and 1,4-dioxane are structurally similar and exist in chair and boat forms. They both dissociate to linear molecules and it is the dissociation of these species and their products that generate strong chain reactions as clearly seen in LS experiments (Kiefer et al. 2009; Yang et al. 2011). From experiment and theory, it has been established that cyclohexane first breaks a C–C bond to form a diradical (Tsang 1978; Kiefer et al. 2009) and then undergoes a 1,5-intramolecular H-atom transfer to 1-hexene. In 1,4-dioxane the C–O and C–C bonds are of similar strengths. Scission of the C–O bond is accompanied by a simultaneous 2,6-H-atom transfer to either the terminal O or C atom yielding ethylene glycol vinyl ether or 2-ethoxyacetaldehyde, respectively. LS and TOF–MS shock tube experiments indicate that the former dominates (Yang et al. 2011). Whereas if the C–C bond breaks a high energy diradical is formed with a radical site on each terminal C-atom and a 1,6-H-atom shift localizes the lone pair onto one of the terminal C-atoms. Further, reaction is inhibited by very high energy barriers and back reaction to 1,4-dioxane is preferred. Figure 24.2 (Yang et al. 2011) shows a potential energy surface for the initial steps of 1,4-dioxane pyrolysis. Finally, 1,3,5-trioxane dissociates via a concerted mechanism breaking three C–O bonds simultaneously to give three formaldehyde molecules and is a clean high temperature source of formaldehyde (Irdam and Kiefer 1990; Vasudevan et al. 2007). Thus, introduction of oxygen atoms into the ring causes distinct changes in mechanism with dissociation occurring preferentially at the C–O bonds.

The rates of dissociation cyclohexane, 1,4-dioxane and 1,3,5-trioxane have also been obtained in shock tube studies. For 1,3,5-trioxane, there is good agreement

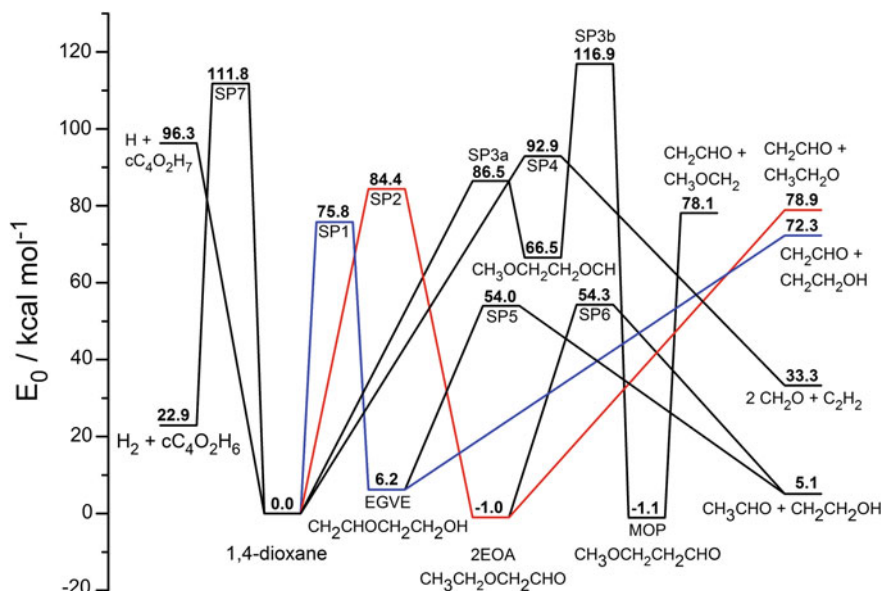


Fig. 24.2 Composite potential energy surface for the dissociation of 1,4-dioxane. Zero point inclusive energies (kcal/mol) were calculated with multireference CASPT2/CBS//CASPT2/aug-cc-pVDZ for SP1, SP2, SP3b. All other energies were obtained from single reference QCISD(T)/CBS//B3LYP/6-311 ++G(d,p) calculations. Structures of saddle points (SPx) and stationary points are given in the original article. (Yang et al. 2011). Reproduced (adapted) by permission of the PCCP owner societies

between shock tube LS (Irdam and Kiefer 1990) and laser absorption experiments (Vasudevan et al. 2007) and lower temperature studies (Aldridge et al. 1991; Hochgreb and Dryer 1992). The LS technique was also applied to dissociation of 1,4-dioxane and was able to resolve pressure dependencies due to the high temperatures accessible in LS experiments (Yang et al. (2011), a consequence of the very short observation times, $<10 \mu\text{s}$. Cyclohexane pyrolysis has been studied in LS, single pulse and H-ARAS shock tube experiments and these demonstrate the difficulties of obtaining precise and accurate rate coefficients for complex systems even with well-established experimental techniques. The LS work of (Kiefer et al. 2009) (1,300–2,000 K, 25–200 Torr) yielded rate coefficients that showed pressure dependence and they used RRKM simulations to fit the experimental results and extrapolate to k_{∞} . The calculated k_{∞} were in very good agreement with theoretical predictions of Sirjean et al. (2006) and very low pressure pyrolysis experiments of Brown et al. (1986), but 3–4 times greater than the single pulse shock tube results of Tsang (1978). Peukert et al. (2011) (1,320–1,550 K, 1.8–2.2 bar) simulated H-ARAS profiles to determine rates of dissociation of cyclohexane. However, the measurement was somewhat indirect as cyclohexane itself does not yield H-atoms, but rather they are produced by dissociation of allyl radicals from 1-hexene the only product of cyclohexane. All three shock tube groups also studied dissociation

of 1-hexene, the sole product of cyclohexane, and the k_{∞} for dissociation of 1-hexene are in good agreement. However, when simulating the H-atom concentrations obtained from cyclohexane experiments, Peukert et al. found the values of Tsang gave good agreement while the higher values of Kiefer et al. resulted in over prediction of H-atom concentrations. LS experiments typically give accurate rate coefficients for strongly endothermic dissociations such as conversion of cyclohexane to 1-hexene. At this time, the reason for the difference between the LS results and the single pulse and H-ARAS results is not clear. However, it does highlight the difficulty of obtaining precise and accurate rate coefficients from complex reaction systems and the need to employ multiple techniques.

24.3.2 Bimolecular Reactions

A very fruitful area of shock tube research has been investigation of bimolecular reactions. In particular, considerable effort has been devoted to reactions between H-atoms and molecules, and OH radicals and molecules. The hydrogen atom studies encompass some of the most fundamental combustion reactions such as $\text{H} + \text{O}_2 + \text{M} = \text{HO}_2 + \text{M}$ ($\text{M} = \text{Ar}, \text{O}_2, \text{N}_2, \text{H}_2\text{O}, \text{CO}_2$), one of the most important termination reactions (Michael et al. 2002; Mertens et al. 2009; Hong et al. 2011; Vasu et al. 2011a), to H attack on aromatics (Oehlschlaeger et al. 2006; Giri et al. 2009).

Of particular note, Michael and co-workers (Mielke et al. 2003; Michael et al. 2004) used a very sensitive implementation of H-ARAS (Michael and Lifshitz 2001) to reinvestigate the most elementary set of reactions $\text{H} + \text{H}_2 = \text{H}_2 + \text{H}$; $\text{H} + \text{D}_2 = \text{HD} + \text{D}$; $\text{D} + \text{H}_2 = \text{HD} + \text{H}$ (Michael et al. 2004) and in combination with state-of-the-art theory obtained complete agreement between experiment and theory bringing to closure a problem of fundamental importance to kinetics that had existed for around 75 years. As they state ‘This is the first completely solved problem in chemical kinetics’ a view that has recently received support (Fleming et al. 2011). That this reaction system is the only one considered completely solved, and despite the simple nature of the reactants and products has taken a long time to bring to closure, is indicative of the inherent difficulties of obtaining precise and accurate results in kinetics research.

Hong et al. recently applied a new diagnostic technique to examine $\text{H} + \text{O}_2 = \text{OH} + \text{O}$ (Hong et al. 2011), a key branching step in H_2/O_2 combustion by monitoring H_2O production with narrow line laser absorption in the I.R. at $\sim 2.5 \mu\text{m}$. While H_2O is not a direct product of the reaction of interest but rather the end product of a number of reactions Hong et al. demonstrated by sensitivity analysis that the predicted H_2O concentrations are only sensitive to the rate of the target reaction. Thus, modeling of the H_2O profiles allowed the desired rate coefficient to be determined. The rate coefficients obtained showed extremely low scatter suggesting that the measurement technique is precise. Combination of the results with higher temperature data from the same group gave an Arrhenius

expression with estimated errors of just a few percent over a wide range of reaction conditions and demonstrates the precision attainable with modern optical diagnostics, at least for simple systems.

Hydrogen atoms are prevalent in oxidation and pyrolytic systems and in reactions with aromatic molecules can lead to formation of resonantly stabilized radicals that participate in molecular growth. Consequently, H-ARAS has been used to study the reactions between H-atoms and a number of aromatic species. The technique is very sensitive and only low concentrations of reagents are required effectively suppressing secondary reactions. Additionally, the study of species with quite low vapor pressures such as phenol is facilitated by the requirement of dilute reagent mixtures. Frank et al. studied H + phenol by H-ARAS (Horn et al. 1998) and found that both addition ($C_6H_6 + OH$ products) and abstraction channels ($C_6H_5O + H_2$) suggested by (He et al. 1988) were necessary to simulate the observed H-atom profiles. The channel forming the phenoxy radical, C_6H_5O , is important because it readily dissociates to form cyclopentadienyl, C_5H_5 , (Brezinsky 1986) a key radical for soot production. In a different shock tube, Giri et al. studied $H + C_6H_6 = C_6H_5 + H_2$ and $H + C_6H_5 = C_6H_6$ by H-ARAS (Giri et al. 2009) both of which are important in pyrolytic systems producing soot.

H-ARAS is only one method of studying H atom reactions and Oehlschlaeger et al. used UV absorption behind reflected shock waves to study the formation of benzyl radicals from H + toluene, (Oehlschlaeger et al. 2006) an important step in toluene pyrolysis and oxidation. Similar to the H-ARAS work, this study was facilitated by a sensitive diagnostic which allowed secondary reactions to be suppressed and a narrow line light source that was tuned to a unique absorption feature of the product, something that is often not possible due to the fact that UV spectra are broad at high temperatures and in more concentrated mixtures overlapping spectra from products other than benzyl would interfere.

Similar to reactions involving H-atoms, OH attack on a wide variety of combustion species has also been an active area, because OH radicals are one of the most important species in combustion. In recent years, most of the emphasis has moved from reactions with small radicals and molecules to studies of large alkanes (Sivaramakrishnan and Michael 2009a; Sivaramakrishnan et al. 2009; Vasu et al. 2011b), cyclic species (Sivaramakrishnan and Michael 2009b), and n-butanol, (Vasu et al. 2010a) a potential biofuel. Of course, there have also been studies on OH with small radicals and molecules including CH_4 (Srinivasan et al. 2005), CH_3 (Krasnoperov and Michael 2004; Srinivasan et al. 2007a; Vasudevan et al. 2008), and CH_2 (Krasnoperov and Michael 2004). For application to combustion modeling, a particularly significant investigation is that of Sivaramakrishnan et al. where they investigated OH abstraction of an H-atom from a carefully selected series of alkanes under pseudo first-order conditions (Sivaramakrishnan and Michael 2009a; Sivaramakrishnan et al. 2009). OH radicals were generated by thermal decomposition of *tert*-butylhydroperoxide and detection was through absorption at 308 nm with White cell optics with ~ 40 – 80 passes to increase path length. Thereby resulting in high sensitivity and permitting the use of very dilute mixtures to minimize secondary reaction. The alkanes studied spanned propane to

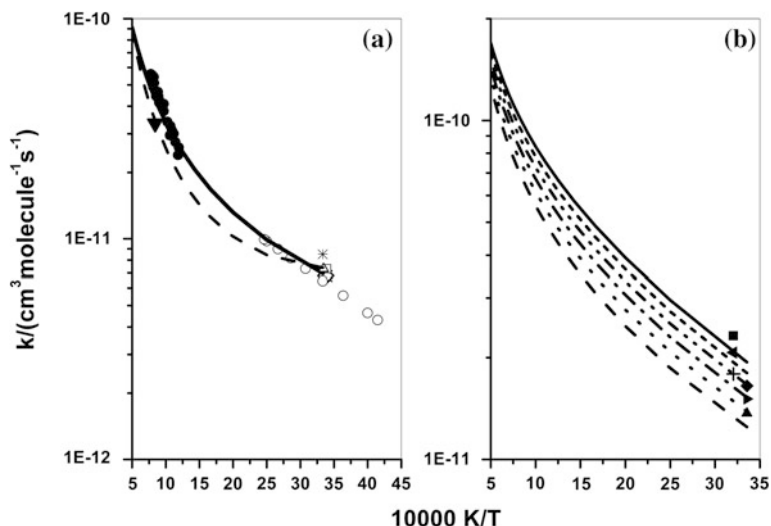


Fig. 24.3 Predictions of rate coefficients for OH + alkanes using the group scheme of Sivaramakrishnan et al. (Sivaramakrishnan and Michael 2009a). **a** OH + n-heptane. Experiment: ● (Sivaramakrishnan and Michael 2009a); ▼ (Koffend and Cohen 1996); Δ (Atkinson et al. 1982); ◇ (Anderson et al. (2004b); * (Klopffer et al. 1986); ○ (Wilson et al. 2006). Predictions: solid line (Sivaramakrishnan and Michael 2009a); Dash line (Cohen 1991). **b** Experimental data at 298 K (Atkinson 2003) : ▲ $n\text{-C}_{11}\text{H}_{24}$; ► $n\text{-C}_{12}\text{H}_{26}$; ◆ $n\text{-C}_{13}\text{H}_{28}$; + $n\text{-C}_{14}\text{H}_{30}$; ◄ $n\text{-C}_{15}\text{H}_{32}$ and ■ $n\text{-C}_{16}\text{H}_{34}$. Lines represent predictions (Sivaramakrishnan and Michael 2009a). Reprinted (adapted) with permission from Sivaramakrishnan R, Michael JV (2009) J Phys Chem A 113:5047-5060. Copyright 2009 American Chemical Society

octane and included branched as well as linear members. From the results, a set of group parameters were developed which included corrections for axial and equatorially oriented secondary hydrogens and resulted in accurate prediction of the measured rate coefficients and more importantly accurate prediction of OH abstraction of a H-atom from any site in alkanes too large to study experimentally, e.g., those found in biofuels. Rate coefficients predicted from the group parameters of Sivaramakrishnan et al. (Sivaramakrishnan and Michael 2009; Sivaramakrishnan et al. 2009) accurately reproduce experimental data from low to high temperatures and improve on those of earlier schemes, Fig. 24.3.

24.3.3 Reactions Involving Resonantly Stabilized Radicals and Aromatics

Resonantly stabilized and aromatic radicals such as propargyl, allyl, cyclopentadienyl, and phenyl can reach quite high concentrations in flames and are generally not easily oxidized. Thus, they often participate in addition reactions leading to formation of PAH. Recombination of propargyl radicals (C_3H_3) was first proposed

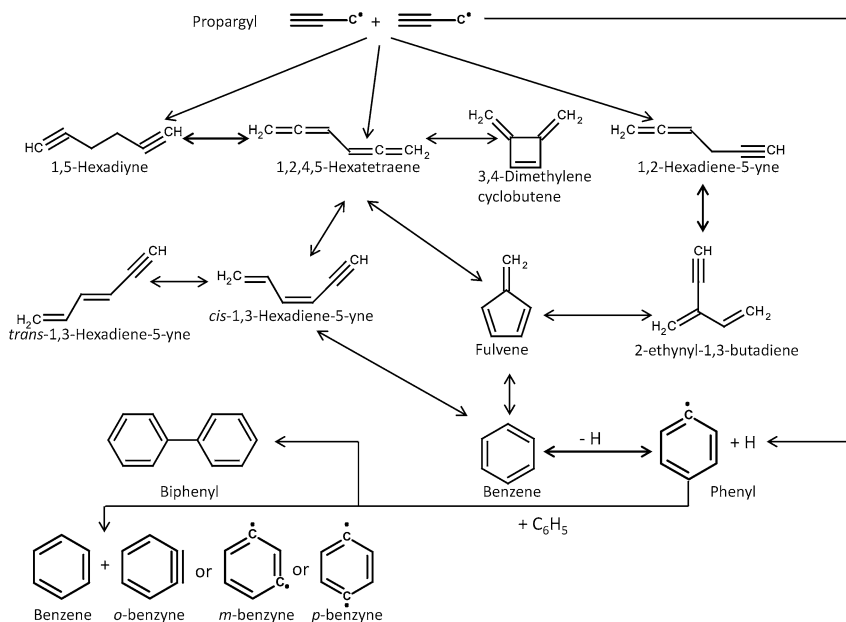


Fig. 24.4 Schematic reaction paths outlining the conversion of two propargyl radicals to benzene and subsequent recombination of phenyl radicals

by Kern to explain the observation of benzene in shock tube/TOF-MS experiments on the dissociation of acetylene (Wu et al. 1987). It is now accepted as one of the main routes forming benzene in combustion systems, although it is by no means the only path for molecular growth. Since the reaction was first proposed by Kern, it has received considerable attention both by experimentalists and theoreticians.

Increasingly refined and extensive theoretical studies were conducted by Miller et al. on propargyl recombination (see Georgievskii et al. 2007 and references therein). These resulted in a detailed, complex potential energy surface which showed benzene formation was the end result of a complex series of isomerization reactions involving eight stable isomers with the formula C_6H_6 , Fig. 24.4. Miller and Klippenstein (2003) also performed master equation calculations to obtain rate coefficients for some of the reactions.

During the same period, a number of experimental studies of propargyl recombination were performed at relatively low temperatures, $T < 1,000$ K (Alkemade and Homann 1989; Fahr and Nayak 2000; Giri et al. 2003; Shafir et al. 2003). Miller and Klippenstein (2003) resolved a discrepancy between theory and experiment regarding whether fulvene and benzene were formed simultaneously or consecutively by discovery of a route to benzene through *cis*-1,3-hexadiene-5-yne, Fig. 24.4. At higher temperatures, the mechanism and kinetics of propargyl recombination have been probed with a variety of shock tube studies which combined cover a very broad experimental range.

The rate of recombination of propargyl radicals at high temperatures has been measured in three shock tube studies (Scherer et al. 2000; Fernandes et al. 2005; Tranter et al. 2011) and two others examined the isomerization reactions of the initial adducts (Scherer et al. 2000; Tang et al. 2005). All of the studies used thermal dissociation of propargyl iodide which dissociates rapidly and cleanly by C–I scission for $T > 1,000$ K (Tranter et al. 2011) as the source of propargyl radicals. However, detailed speciation of the post shock mixtures in single pulse shock tube experiments by Tang et al. (2005) showed that for $T < 750$ K isomerization to iodoallene is competitive with dissociation.

Fernandes et al. monitored C_3H_3 concentrations by UV absorption behind reflected shock waves (Fernandes et al. 2005) and obtained $k_{(C_3H_3+C_3H_3)}$ by fitting a second-order rate expression to the data. An important point raised by Fernandez et al. is that the location of t_0 , the start of reaction, has some uncertainty due to the thickness of the shock front and they considered this to be the major source of error, $\pm 30\%$, in their measurements. Scherer et al. employed a less direct method using non-resonant absorption at 121.53 nm which they attributed to a combination of absorption by C_3H_3 radicals and C_6H_6 species (Scherer et al. 2000). Rate coefficients were extracted by simulation of the absorption signal with a two reaction model. Tranter et al. (2011) studied C_3H_3 recombination by LS. These experiments are sensitive to enthalpies of reaction and rates of reaction and they extracted recombination rates from the LS profiles with a model using thermochemical properties and isomer distributions provided by Miller. The

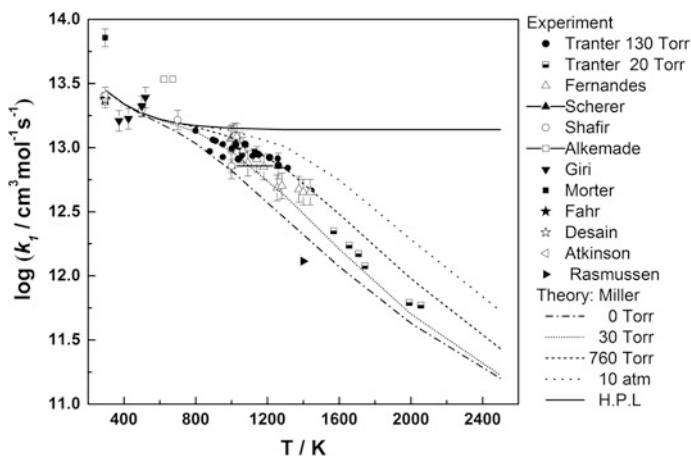


Fig. 24.5 Rate coefficients for $C_3H_3 + C_3H_3 \rightarrow$ products. Tranter (Tranter et al. 2011), Fernandes (Fernandes et al. 2005), Scherer (Scherer et al. 2000), Shafir (Shafir et al. 2003), Alkemade (Alkemade and Homann 1989), Giri (Giri et al. 2003), Morter (Mortier et al. 1994), Fahr (Fahr and Nayak 2000), Desain (Desain and Taatjes 2003), Atkinson (Atkinson and Hudgens 1999), Rasmussen (Rasmussen et al. 2005), Miller (Gieorgievskii et al. 2007). Reproduced with permission by Elsevier. Originally published in Tranter RS et al. (2011) Proc. Combust. Inst. 33:259–265

recombination rate coefficients from these studies are shown in Fig. 24.5 along with the results of calculations by Miller et al. (Georgievskii et al. 2007). Considering the challenges of the experimental work, there is actually rather good agreement with the theoretical values. The data in Fig. 24.5 represent an enormous range of experimental techniques spanning 3 mbar–140 bar and 295–2,000 K with successive refinements to the theoretical models. While the low temperature experiments are important, it is only the shock tube methods that could access high temperatures such as found in soot forming regions of flames and isolate the target reaction.

While the optical techniques measured the recombination rate coefficients over a wide range of reaction conditions, they provided no information regarding the intermediates that are formed on the way to benzene. However, the propargyl recombination system is somewhat unusual in that following the initial addition step only stable molecules are formed in the conversion to benzene. Consequently, single pulse shock tube methods are very well suited to probing the product distributions and elucidating mechanistic details of propargyl recombination.

Scherer et al. withdrew gaseous samples from a shock tube and analyzed them by GC/MS (Scherer et al. 2000). They observed eight distinct C_6H_6 isomers of which they were able to identify only 1,5-hexadiyne and benzene. Their shock tube was not configured as a single pulse tube and as they noted the temperature history of the sampled gases could not be determined and the product analyses were purely qualitative. Brezinsky et al., however, used high pressure single pulse shock tube experiments to examine the products of propargyl recombination (Tang et al. 2005) and the isomerization reactions of the adducts (Anderson et al. 2004a; Tranter et al. 2004; Miller et al. 2006). Similar to Scherer et al., they found eight C_6H_6 products by GC/MS analyses. However, with a novel GC-MS/mi-FTIR (Anderson et al. 2004a) (GC-mass spectrometry/matrix isolation Fourier transform infrared spectroscopy) they were able to positively identify all the C_6H_6 isomers from the IR spectra and authentic standards for some species. In addition, from GC/MS analyses they obtained quantitative measurements of species concentrations. The only species not observed from Fig. 24.4 was 1,2,4,5-hexatetraene which Miller et al. (2006) later showed, in single pulse shock tube experiments, quickly isomerized for $T > 600$ K to 3,4-dimethylcyclobutene. Considering 3,4-dimethylenecyclobutene as a surrogate for 1,2,4,5-hexatetraene, Tang et al. found constant fractions of the three initial adducts of propargyl recombination, Fig. 24.2, for $T < 750$ K, the only products observed. The relative concentrations of these adducts were in good agreement with Miller and Klippenstein's prediction of the initial branching ratio. At higher temperatures, all the stable C_6H_6 isomers predicted by Miller et al. were found and simulation of the experimental data allowed several rate coefficients to be recovered that were in good agreement with the master equation predictions of Miller and Klippenstein. In addition to studying propargyl recombination, Brezinsky et al. also studied isomerization of 1,5-hexadiyne (Tranter et al. 2004), 1,2,4,5-hexatetraene (Miller et al. 2006) and 1,2-hexadiene-5-yne (Miller et al. 2006), the initial adducts and rate coefficients for a

number of key reactions at high temperatures and pressures were obtained that are in good agreement with theoretical predictions.

Once benzene has been formed then subsequent reactions will generate phenyl radicals and these also participate in recombination reactions. Unlike propargyl recombination which initially forms three linear C_6H_6 molecules, recombination of phenyl radicals has recently been found to be extremely complex. LS and TOF-MS shock tube experiments (Tranter et al. 2010) showed that reaction of two phenyl radicals is not simply addition to form biphenyl as previously thought but that at shock tube temperatures roughly half of the radicals participate in a disproportionation reaction yielding *o/m/p*-benzynes and benzene. These experimental results were fully supported by high level theoretical calculations (Tranter et al. 2010) which revealed an extremely complex potential energy surface involving: sigma bond addition, abstraction on both singlet and triplet surfaces, and attack by a phenyl radical on the π -bonds of another C_6H_5 . In separate shock tube TOF-MS experiments the same products were found by Duerrstein et al. (2011b), as by Tranter et al. (2010).

The addition of acetylene to phenyl radicals has been studied in a high pressure single pulse shock tube with phenyl iodide as the precursor (Comandini and Brezinsky 2011). Rate coefficients for the self-reaction of phenyl radicals were not obtained but species were observed consistent with the LS and TOF-MS investigations. However, Comandini also observed a variety of fused cyclic species, many with concentrations <1 ppm, up to four fused aromatic rings. The shock tube studies of phenyl self-reaction are significant, because they indicate that benzyne radicals will be formed in much larger amounts than previously thought and therefore play a much larger role in PAH formation than would have been expected. Comandini and Brezinsky (2011, 2012) have also conducted theoretical studies examining the role *o*-benzyne and cyclopentadienyl radicals in addition reactions, based on their high pressure single pulse shock tube results and demonstrate that many of the species observed can only be explained by these reactions.

Reactions of benzene and toluene with radicals will result in formation of single ring aromatic radicals phenyl, benzyl, and cyclopentadienyl with the latter coming primarily from dissociation of the phenoxy, (C_6H_5O) radical (Brezinsky 1986). The aromatic radicals and corresponding molecules have been studied by a number of shock tube techniques. Dissociation of cyclopentadiene to $C_5H_5 + H$ has been studied in shock tubes by Roy et al. (1998) with H-ARAS. Kern et al. (1998) used a combined set of experiments, LS and TOF-MS, to also study dissociation of cyclopentadiene and from simulation of the LS profiles obtained pressure-dependent rates of dissociation for cyclopentadienyl dissociation. Similar to many other shock tube studies, complementary theoretical studies were performed to determine mechanisms by which C_5H_6 and C_5H_5 dissociate (Kern et al. 1998). These revealed that cyclopentadienyl dissociates by a 1,2-H atom shift prior to ring opening rather than simple breaking of a C-C bond. The 1,2 shift effectively reduces the activation energy for dissociation and with a reaction path degeneracy

of 10 has a net effect of making the dissociation of cyclopentadienyl easier than would be expected from the C–C bond strength.

The Benzyl radical is by far the major product of toluene pyrolysis and a recent study of partially deuterated toluene with a very sensitive H/D-atom ARAS detection scheme (Michael and Lifshitz 2001) by Sivaramakrishnan and Michael (2011) resulted in precise measurements for branching between formation of benzyl+H and phenyl+CH₃ from toluene. The experimental values are in excellent agreement with very high level theoretical predictions. Sivaramakrishnan et al. (2011c) also examined pyrolysis of Benzyl radicals and partially deuterated benzylns and obtained rate coefficients for loss of H-atoms from the ring and the side chain and they also suggest a small fraction of the benzyl radicals undergo ring contraction to form cyclopentadiene and ethyne.

24.4 Conclusions

The above discussion gives an overview of the many uses of shock tubes in the investigation of elementary reactions at combustion temperatures. The wide variety of techniques available allow broad classes of reactions to be accessed and new diagnostic techniques are permitting very accurate measurements of rate to be made. However, it should also be noted that older techniques such as LS, ARAS, and single pulse are still cornerstones of shock tube research and also provide very accurate results. Combinations of experimental and theoretical methods have allowed considerable detail to be uncovered about complex reactions. In the future, it is likely that these collaborations will become even more beneficial as accurate, affordable theoretical methods advance, and more precision is obtained in experiments.

Acknowledgments RST gratefully acknowledges support from Office of Basic Energy Sciences, Division of Chemical Sciences, Geosciences, and Biosciences, U.S. Department of Energy, under contract number DE-AC02-06CH11357.

We are grateful to J. A. Manion for providing Fig. 24.1 and R. Sivaramakrishnan and J. V. Michael for Fig. 24.3.

References

- Aldridge HK, Liu X, Lin MC, Melius CF (1991) Thermal unimolecular decomposition of 1,3,5-trioxane—Comparison of theory and experiment. *Int J Chem Kinet* 23:947–956
- Alkemade U, Homann KH (1989) Formation of C₆H₆ isomers by recombination of propynyl in the system sodium vapor propynylhalide. *Z Phys Chem Neue Folge* 161:19–34
- Anderson KB, Tranter RS, Tang W et al (2004a) Speciation of C₆H₆ isomers by gas chromatography-matrix isolation Fourier transform infrared spectroscopy-mass spectrometry. *J Phys Chem A* 108:3403–3405
- Anderson RS, Huang L, Iannone R et al (2004b) Carbon kinetic isotope effects in the gas phase reactions of light alkanes and ethene with the OH radical at 296 ± 4 K. *J Phys Chem A* 108:11537–11544

- Atkinson DB, Hudgens JW (1999) Rate coefficients for the propargyl radical self-reaction and oxygen addition reaction measured using ultraviolet cavity ring-down spectroscopy. *J Phys Chem A* 103:4242–4252
- Atkinson R (2003) Kinetics of the gas-phase reactions of OH radicals with alkanes and cycloalkanes. *Atmos Chem Phys* 3:2233–2307
- Atkinson R, Aschmann SM, Carter WPL et al (1982) Kinetics of the reactions of OH radicals with normal-alkanes at 299 ± 2 K. *Int J Chem Kinet* 14:781–788
- Awan IA, McGivern WS, Tsang W et al (2010) Decomposition and isomerization of 5-methylhex-1-yl radical. *J Phys Chem A* 114:7832–7846
- Awan IA, Burgess DR Jr, Tsang W et al (2011a) Shock tube study of the decomposition of cyclopentyl radicals. *Proc Combust Inst* 33:341–349
- Awan IA, Burgess J, Tsang W et al (2011b) Standard reactions for comparative rate studies: experiments on the dehydrochlorination reactions of 2-chloropropane, chlorocyclopentane, and chlorocyclohexane. *Int J Chem Kinet*. doi:10.1002/kin.20566
- Babushok V, Tsang W, Awan I et al (2001) Initial stages of heptane decomposition. *Chem Phys Process Combust* 198–201
- Ben-Dor G, Igra O, Elperin T et al (2001) Handbook of shock waves, vol 3. Academic Press, Burlington
- Bhaskaran KA, Roth P (2002) The shock tube as wave reactor for kinetic studies and material systems. *Prog Energy Combust Sci* 28:151–192
- Brezinsky K (1986) The high-temperature oxidation of aromatic hydrocarbons. *Prog Energy Combust Sci* 12:1–24
- Brown TC, King KD, Nguyen TT (1986) Kinetics of primary processes in the pyrolysis of cyclopentanes and cyclohexanes. *J Phys Chem* 90:419–424
- Burgess J, Manion JA (2011) Ab initio calculations and RRKM/master equation modeling of chloroalkanes \rightarrow alkenes + HCl reactions for use in comparative rate studies. *Int J Chem Kinet*. doi:10.1002/kin.20565
- Cohen N (1991) Are reaction rate coefficients additive? revised transition state theory calculations for OH + alkane reactions. *Int J Chem Kinet* 23:397–417
- Comandini A (2011) Thesis: high pressure chemistry of phenyl radical reactions with acetylene. University of Illinois, Chicago
- Comandini A, Brezinsky K (2011) Theoretical study of the formation of naphthalene from the radical/pi-bond addition between single-ring aromatic hydrocarbons. *J Phys Chem A* 115:5547–5559
- Comandini A, Brezinsky K (2012) Radical/pi-bond addition between o-benzyne and cyclic C(5) hydrocarbons. *J Phys Chem A* 116:1183–1190
- Comandini A, Malewicki T, Brezinsky K (2012) Chemistry of polycyclic aromatic hydrocarbons formation from phenyl radical pyrolysis and reaction of phenyl and acetylene. *J Phys Chem A* 116:2409–2434
- Culberston B (2009) Thesis: homogeneous and heterogeneous reaction rates for the reactions of carbon with carbon dioxide and water. University of Illinois, Chicago
- Culbertson B, Sivaramakrishnan R, Brezinsky K (2008) Elevated pressure thermal experiments and modeling studies on the water-gas shift reaction. *J Propul Power* 24:1085–1092
- Davidson DF, Hanson RK (1996) Real gas corrections in shock tube studies at high pressures. *Isr J Chem* 36:321–326
- Davidson DF, Hong Z, Pilla GL et al (2011) Multi-species time-history measurements during n-dodecane oxidation behind reflected shock waves. *Proc Combust Inst* 33:151–157
- Desain JD, Taatjes CA (2003) Infrared laser absorption measurements of the kinetics of propargyl radical self-reaction and the 193 nm photolysis of propyne. *J Phys Chem A* 107:4843–4850
- Duerstein SH, Aghsaee M, Jerig L et al (2011a) A shock tube with a high-repetition-rate time-of-flight mass spectrometer for investigations of complex reaction systems. *Rev Sci Instrum* 82:084103-1-084103/7
- Duerstein SH, Olzmann M, Aguilera-Iparraguirre J et al (2011b) The phenyl + phenyl reaction as pathway to benzynes: an experimental and theoretical study. *Chem Phys Lett* 513:20–26

- Fahr A, Nayak A (2000) Kinetics and products of propargyl (C₃H₃) radical self-reactions and propargyl-methyl cross-combination reactions. *Int J Chem Kinet* 32:118–124
- Farooq A, Jeffries JB, Hanson RK (2009) Measurements of CO₂ concentration and temperature at high pressures using 1f-normalized wavelength modulation spectroscopy with second harmonic detection near 2.7 μ m. *Appl Opt* 48:6740–6753
- Fernandes RX, Hippler H, Olzmann M (2005) Determination of the rate coefficient for the C₃H₃ + C₃H₃ reaction at high temperatures by shock-tube investigations. *Proc Combust Inst* 30:1033–1038
- Fleming DG, Arseneau DJ, Sukhorukov O et al (2011) Kinetics of the reaction of the heaviest hydrogen atom with H(2), the (4)He μ + H(2) \rightarrow (4)He μ H + H reaction: experiments, accurate quantal calculations, and variational transition state theory, including kinetic isotope effects for a factor of 36.1 in isotopic mass. *J Chem Phys* 135:184310
- Gardiner WC, Walker BF, Wakefield CB (1981) Mathematical methods for modeling chemical reactions. In: Lifshitz A (ed) *Shock waves in chemistry* Marcel Dekker inc, Dekker, New York, pp 319–374
- Gaydon AG, Hurlle IR (1963) *The shock tube in high temperature chemical physics*. Chapman and Hall Ltd, London
- Georgievskii Y, Miller JA, Klippenstein SJ (2007) Association rate constants for reactions between resonance-stabilized radicals: C₃H₃ + C₃H₃, C₃H₃ + C₃H₅, and C₃H₅ + C₃H₅. *Phys Chem Chem Phys* 9:4259–4268
- Giri BR, Hippler H, Olzmann M et al (2003) The rate coefficient of the C₃H₃ + C₃H₃ reaction from UV absorption measurements after photolysis of dipropargyl oxalate. *Phys Chem Chem Phys* 5:4641–4646
- Giri BR, Bentz T, Hippler H et al (2009) Shock-tube study of the reactions of hydrogen atoms with benzene and phenyl radicals. *Z Phys Chem Int J Res Phys Chem Chem Phys* 223:539–549
- Gudiyella S, Malewicki T, Comandini A et al (2011) High pressure study of m-xylene oxidation. *Combust Flame* 158:687–704
- He YZ, Mallard WG, Tsang W (1988) Kinetics of hydrogen and hydroxyl radical attack on phenol at high-temperatures. *J Phys Chem* 92:2196–2201
- Hochgreb S, Dryer FL (1992) Decomposition of 1,3,5-trioxane at 700–800-K. *J Phys Chem* 96:295–297
- Hong Z, Davidson DF, Barbour EA et al (2011) A new shock tube study of the H + O₂ \rightarrow OH + O reaction rate using tunable diode laser absorption of H₂O near 2.5 μ m. *Proc Combust Inst* 33:309–316
- Horn C, Roy K, Frank P et al (1998) Shock-tube study on the high-temperature pyrolysis of phenol. *Symp (Int) Combust Proc* 27:321–328
- Irdam EA, Kiefer JH (1990) The decomposition of 1,3,5-trioxane at very high-temperatures. *Chem Phys Lett* 166:491–494
- Kern RD, Zhang Q, Yao J et al (1998) Pyrolysis of cyclopentadiene: rates for initial C-H bond fission and the decomposition of c-C₅H₅. *Symp (Int) Combust Proc* 27:143–150
- Kern RD, Singh HJ, Jhang Q (2001) Mass spectrometric methods for chemical kinetics in shock tubes. In: Ben-Dor G, Igra O, and Lifshitz A (eds.). *Handbook of shock waves*, vol 3, Academic Press, New York, pp 77–105
- Kiefer JH (1981) The laser schlieren technique in shock tube kinetics. In: Lifshitz A (ed). *Shock waves in chemistry*, Marcel Dekker, New York, pp 219–277
- Kiefer JH, Buzyna LL, Dib A et al (2000) Observation and analysis of nonlinear vibrational relaxation of large molecules in shock waves. *J Chem Phys* 113:48–58
- Kiefer JH, Santhanam S, Srinivasan NK et al (2005) Dissociation, relaxation and incubation in the high-temperature pyrolysis RRKM of ethane, and a successful modeling. *Proc Combust Inst* 30:1129–1135
- Kiefer J, Gupte K, Harding L et al (2009) Shock tube and theory investigation of cyclohexane and 1-hexene decomposition. *J Phys Chem A* 113:13570–13583

- Klopffer W, Frank R, Kohl EG et al (1986) Quantitative presentation of photochemical transformation processes in the troposphere. *Chem Ztg* 110:57–61
- Koffend JB, Cohen N (1996) Shock tube study of OH reactions with linear hydrocarbons near 1100 K. *Int J Chem Kinet* 28:79–87
- Krasnoperov LN, Michael JV (2004) High-temperature shock tube studies using multipass absorption: rate constant results for OH + CH₃, OH + CH₂, and the dissociation of CH₃OH. *J Phys Chem A* 108:8317–8323
- Li H, Farooq A, Jeffries JB et al (2007) Near-infrared diode laser absorption sensor for rapid measurements of temperature and water vapor in a shock tube. *Appl Phys B: Lasers Opt* 89:407–416
- Lifshitz A, Tamburu C, Shashua R (1997) Decomposition of 2-methylfuran. experimental and modeling study. *J Phys Chem A* 101:1018–1029
- Lifshitz A, Tamburu C, Shashua R (1998) Thermal decomposition of 2,5-dimethylfuran. experimental results and computer modeling. *J Phys Chem A* 102:10655–10670
- Lifshitz A, Suslensky A, Tamburu C (2000) Thermal reactions of 2,3-dihydrobenzofuran: experimental results and computer modeling. *Proc Combust Inst* 28:1733–1739
- Lifshitz A, Suslensky A, Tamburu C (2001) Thermal reactions of isodihydrobenzofuran: experimental results and computer modeling. *J Phys Chem A* 105:3148–3157
- Lifshitz A, Tamburu C, Suslensky A et al (2006a) Decomposition and isomerization of 1,2-benzisoxazole: single-pulse shock-tube experiments, quantum chemical and transition-state theory calculations. *J Phys Chem A* 110:11677–11683
- Lifshitz A, Tamburu C, Suslensky A et al (2006b) Decomposition of anthranil. single pulse shock-tube experiments, potential energy surfaces and multiwell transition-state calculations. the role of intersystem crossing. *J Phys Chem A* 110:8248–8258
- Lifshitz A, Tamburu C, Suslensky A et al (2006c) Thermal reactions of benzoxazole. single pulse shock tube experiments and quantum chemical calculations. *J Phys Chem A* 110:4607–4613
- Manley DK, McIlroy A, Taatjes CA (2008) Research needs for future internal combustion engines. *Phys Today* 61:47–52
- McGivern WS, Awan IA, Tsang W et al (2008) Isomerization and decomposition reactions in the pyrolysis of branched hydrocarbons: 4-Methyl-1-pentyl radical. *J Phys Chem A* 112:6908–6917
- Mertens JD, Kalitan DM, Barrett AB et al (2009) Determination of the rate of $H + O_2 + M \rightarrow HO_2 + M$ ($M = N_2, Ar, H_2O$) from ignition of syngas at practical conditions. *Proc Combust Inst* 32:295–303
- Michael JV (1992) Measurement of thermal rate constants by flash or laser photolysis in shock tubes: oxidations of hydrogen and deuterium. *Prog Energy Combust Sci* 18:327–347
- Michael JV, Lifshitz A (2001) Atomic resonance absorption spectroscopy with flash or laser photolysis in shock wave experiments. In: Ben-Dor G, Igra O, Elperin T et al (eds) *Handbook of shock waves*. Academic Press, New York
- Michael JV, Su MC, Sutherland JW et al (2002) Rate constants For $H + O_2 + M \rightarrow HO_2 + M$ in seven bath gases. *J Phys Chem A* 106:5297–5313
- Michael JV, Su MC, Sutherland JW (2004) New rate constants for $D + H_2$ and $H + D_2$ between 1150 and 2100 K. *J Phys Chem A* 108:432–437
- Mielke SL, Peterson KA, Schwenke DW et al (2003) $H + H_2$ thermal reaction: a convergence of theory and experiment. *Phys Rev Lett* 91:063201-1-063201/4
- Miller CH, Tang W, Tranter RS et al (2006) Shock tube pyrolysis of 1,2,4,5-hexatetraene. *J Phys Chem A* 110:3605–3613
- Miller JA, Klippenstein SJ (2003) The recombination of propargyl radicals and other reactions on a C₆H₆ potential. *J Phys Chem A* 107:7783–7799
- Morter CL, Farhat SK, Adamson JD et al (1994) Rate-constant measurement of the recombination reaction $C_3H_3 + C_3H_3$. *J Phys Chem* 98:7029–7035
- Oehlschlaeger MA, Davidson DF, Hanson RK (2006) Experimental investigation of toluene + H → benzyl + H₂ at high temperatures. *J Phys Chem A* 110:9867–9873

- Peukert S, Naumann C, Braun-Unkhoff M et al (2011) Formation of H-atoms in the pyrolysis of cyclohexane and 1-hexene: a shock tube and modeling study. *Int J Chem Kinet* 43:107–119
- Pyun SH, Cho J, Davidson DF et al (2011) Interference-free mid-IR laser absorption detection of methane. *Meas Sci Technol* 22:025303-1-025303/9
- Rajakumar B, Reddy KPJ, Arunan E (2003) Thermal decomposition of 2-fluoroethanol: single pulse shock tube and ab initio studies. *J Phys Chem A* 107:9782–9793
- Rasmussen CL, Skjoth-Rasmussen MS, Jensen AD et al (2005) Propargyl recombination: estimation of the high temperature, low pressure rate constant from flame measurements. *Proc Combust Inst* 30:1023–1031
- Roy K, Horn C, Frank P et al (1998) High-temperature investigations on the pyrolysis of cyclopentadiene. *Symp (Int) Combust Proc* 27:329–336
- Santhanam S, Kiefer JH, Tranter RS et al (2003) A shock tube, laser-schlieren study of the pyrolysis of isobutene: relaxation, incubation, and dissociation rates. *Int J Chem Kinet* 35:381–390
- Saxena S, Kiefer JH, Tranter RS (2007) Relaxation, incubation, and dissociation in CO₂. *J Phys Chem A* 111:3884–3890
- Scherer S, Just T, Frank P (2000) High-temperature investigations on pyrolytic reactions of propargyl radicals. *Proc Combust Inst* 28:1511–1518
- Shafir EV, Slagle IR, Knyazev VA (2003) Kinetics and products of the self-reaction of propargyl radicals. *J Phys Chem A* 107:8893–8903
- Simmie JM, Curran HJ (2009) Formation enthalpies and bond dissociation energies of alkylfurans. The strongest C-X bonds known? *J Phys Chem A* 113:5128–5137
- Simmie JM, Metcalfe WK (2011) Ab initio study of the decomposition of 2,5-dimethylfuran. *J Phys Chem A* 115:8877–8888
- Sirjean B, Glaude PA, Ruiz-Lopez MF et al (2006) Detailed kinetic study of the ring opening of cycloalkanes by CBS-QB3 calculations. *J Phys Chem A* 110:12693–12704
- Sivaramakrishnan R, Michael JV (2009a) Rate constants for OH with selected large alkanes: shock-tube measurements and an improved group scheme. *J Phys Chem A* 113:5047–5060
- Sivaramakrishnan R, Michael JV (2009b) Shock tube measurements of high temperature rate constants for OH with cycloalkanes and methylcycloalkanes. *Combust Flame* 156:1126–1134
- Sivaramakrishnan R, Michael JV (2011) Pyrolysis of C₆D₅CH₃: rate constants and branching ratios in the high-temperature thermal decomposition of toluene. *Proc Combust Inst* 33:225–232
- Sivaramakrishnan R, Srinivasan NK, Su MC et al (2009) High temperature rate constants for OH + alkanes. *Proc Combust Inst* 32:107–114
- Sivaramakrishnan R, Michael JV, Klippenstein SJ (2010) Direct observation of roaming radicals in the thermal decomposition of acetaldehyde. *J Phys Chem A* 114:755–764
- Sivaramakrishnan R, Michael JV, Wagner AF et al (2011a) Roaming radicals in the thermal decomposition of dimethyl ether: experiment and theory. *Combust Flame* 158:618–632
- Sivaramakrishnan R, Su MC, Michael JV et al (2011b) Shock tube and theoretical studies on the thermal decomposition of propane: evidence for a roaming radical channel. *J Phys Chem A* 115:3366–3379
- Sivaramakrishnan R, Su MC, Michael JV (2011c) H- and D-atom formation from the pyrolysis of C₆H₅CH₂Br and C₆H₅CD₂Br: implications for high-temperature benzyl decomposition. *Proc Combust Inst* 33:243–250
- Srinivasan NK, Kiefer JH, Tranter RS (2003) Dissociation, relaxation, and incubation in the pyrolysis of neopentane: heat of formation for tert-butyl radical. *J Phys Chem A* 107:1532–1539
- Srinivasan NK, Su MC, Sutherland JW et al (2005) Reflected shock tube studies of high-temperature rate constants for OH + CH₄ → CH₃ + H₂O and CH₃ + NO₂ → CH₃O + NO. *J Phys Chem A* 109:1857–1863
- Srinivasan NK, Su MC, Michael JV (2007a) High-temperature rate constants for CH₃OH + Kr → products, OH + CH₃OH → products, OH + (CH₃)₂CO → CH₂-COCH₃ + H₂O, and OH + CH₃ → CH₂ + H₂O. *J Phys Chem A* 111:3951–3958

- Srinivasan NK, Su MC, Michael JV (2007b) Reflected shock tube studies of high-temperature rate constants for $\text{OH} + \text{C}_2\text{H}_2$ and $\text{OH} + \text{C}_2\text{H}_4$. *Phys Chem Chem Phys* 9:4155–4163
- Suits AG (2008) Roaming atoms and radicals: a new mechanism in molecular dissociation. *Acc Chem Res* 41:873–881
- Tang W, Tranter RS, Brezinsky K (2005) Isomeric product distributions from the self-reaction of propargyl radicals. *J Phys Chem A* 109:6056–6065
- Townsend D, Lahankar SA, Lee SK et al (2004) The roaming atom: straying from the reaction path in formaldehyde decomposition. *Science* 306:1158–1161
- Tranter RS, Sivaramakrishnan R, Srinivasan N et al (2001) Calibration of reaction temperatures in a very high pressure shock tube using chemical thermometers. *Int J Chem Kinet* 33:722–731
- Tranter RS, Tang W, Anderson KB et al (2004) Shock tube study of thermal rearrangement of 1,5-hexadiyne over wide temperature and pressure regime. *J Phys Chem A* 108:3406–3415
- Tranter RS, Raman A, Sivaramakrishnan R et al (2005) Ethane oxidation and pyrolysis from 5 bar to 1000 bar: experiments and simulation. *Int J Chem Kinet* 37:306–331
- Tranter RS, Giri BR, Kiefer JH (2007) Shock tube/time-of-flight mass spectrometer for high temperature kinetic studies. *Rev Sci Instrum* 78:034101
- Tranter RS, Klippenstein SJ, Harding LB et al (2010) Experimental and theoretical investigation of the self-reaction of phenyl radicals. *J Phys Chem A* 114:8240–8261
- Tranter RS, Yang X, Kiefer JH (2011) Dissociation of $\text{C}_3\text{H}_3\text{I}$ and rates for C_3H_3 combination at high temperatures. *Proc Combust Inst* 33:259–265
- Tsang W (1978) Thermal-stability of cyclohexane and 1-hexene. *Int J Chem Kinet* 10:1119–1138
- Tsang W (1981) Comparative-rate single-pulse shock tube studies on the thermal stability of polyatomic molecules. In: Lifshitz A (ed) *Shock waves in chemistry*. Marcel Dekker Inc., New York
- Tsang W, Walker JA, Manion JA (1998) Single-pulse shock-tube study on the decomposition of 1-pentyl radicals. *Symp (Int) Combust Proc* 27:135–142
- Tsang W, Walker JA, Manion JA (2007) The decomposition of normal hexyl radicals. *Proc Combust Inst* 31:141–148
- Tsang W, McGivern WS, Manion JA (2009) Multichannel decomposition and isomerization of octyl radicals. *Proc Combust Inst* 32:131–138
- Vasu SS, Davidson DF, Hanson RK et al (2010a) Measurements of the reaction of OH with n-butanol at high-temperatures. *Chem Phys Lett* 497:26–29
- Vasu SS, Hong ZK, Davidson DF et al (2010b) Shock tube/laser absorption measurements of the reaction rates of OH with ethylene and propene. *J Phys Chem A* 114:11529–11537
- Vasu SS, Davidson DF, Hanson RK (2011a) Shock tube study of syngas ignition in rich CO_2 mixtures and determination of the rate of $\text{H} + \text{O}_2 + \text{CO}_2 \rightarrow \text{HO}_2 + \text{CO}_2$. *Energy Fuels* 25:990–997
- Vasu SS, Huynh LK, Davidson DF et al (2011b) Reactions of OH with butene isomers: measurements of the overall rates and a theoretical study. *J Phys Chem A* 115:2549–2556
- Vasudevan V, Davidson DF, Hanson RK et al (2007) High-temperature measurements of the rates of the reactions $\text{CH}_2\text{O} + \text{Ar} \rightarrow \text{products}$ and $\text{CH}_2\text{O} + \text{O}_2 \rightarrow \text{products}$. *Proc Combust Inst* 31:175–183
- Vasudevan V, Cook RD, Hanson RK et al (2008) High-temperature shock tube study of the reactions $\text{CH}_3 + \text{OH} \rightarrow \text{products}$ and $\text{CH}_3\text{OH} + \text{Ar} \rightarrow \text{products}$. *Int J Chem Kinet* 40:488–495
- Wilson EW, Hamilton WA, Kennington HR et al (2006) Measurement and estimation of rate constants for the reactions of hydroxyl radical with several alkanes and cycloalkanes. *J Phys Chem A* 110:3593–3604
- Wu CH, Singh HJ, Kern RD (1987) Pyrolysis of acetylene behind reflected shock-waves. *Int J Chem Kinet* 19:975–996
- Wu XS, Daniel R, Tian GH et al (2011) Dual-injection: the flexible, bi-fuel concept for spark-ignition engines fuelled with various gasoline and biofuel blends. *Appl Energy* 88:2305–2314

- Yang X, Goldsmith CF, Tranter RS (2009) Decomposition and vibrational relaxation in CH₃I and self-reaction of CH₃ radicals. *J Phys Chem A* 113:8307–8317
- Yang X, Jasper AW, Giri BR et al (2011) A shock tube and theoretical study on the pyrolysis of 1,4-dioxane. *Phys Chem Chem Phys* 13:3686–3700
- Yasunaga K, Kubo S, Hoshikawa H et al (2008) Shock-tube and modeling study of acetaldehyde pyrolysis and oxidation. *Int J Chem Kinet* 40:73–102
- Yasunaga K, Gillespie F, Simmie JM et al (2010) A multiple shock tube and chemical kinetic modeling study of diethyl ether pyrolysis and oxidation. *J Phys Chem A* 114:9098–9109
- Zhong S, Daniel R, Xu H et al (2010) Combustion and emissions of 2,5-dimethylfuran in a direct-injection spark-ignition engine. *Energy Fuels* 24:2891–2899

Index

A

Ab-initio method or calculation, 517, 524, 525
Absorption, 304, 306, 310–317, 321, 325
Absorption spectroscopy, 615, 616, 621, 622
Accelerated solvent extraction
 microwaves, 291
Activation energy, 22, 25, 39, 40, 97, 99, 102
Active thermochemical table, 416, 537, 542
Adaptive reduction, 456
Addition to oxygen, 28
Airborne PAH, 288
Alcohol, 94–96, 98, 99, 101–103, 220, 226, 243
Aldehyde, 251
Alkane, 26, 31, 39, 41, 75
Alkoxy radical, 608, 612, 613
Angular momentum, 554, 555, 557, 559
Approximations in quantum chemical
 methods, 517, 522, 523
Arrhenius parameters, 34, 412, 433, 434, 436–438, 449, 486
Arrhenius parameters, 34, 433–438
Atomic natural orbital, 527
Atomic orbital, 527, 530
Atomic orbitals (AO), 526
Atomic oxygen, 581, 583, 597, 598, 602
Autoignition, 20, 24, 26, 27
Automatic differentiation (AD), 413, 440
Automatic generation, 63, 64, 66, 69, 88
Average energy transferred per collision, 562

B

β -scission decompositions, 27, 78, 96
Base mechanism, 42, 43
Basin-hopping optimisation, 395
Benzynes, 156, 157
Bimolecular reaction, 552, 553, 565, 578
 benzyl radical, 646
 H atom, 635, 640

OH radicals, 640
 phenyl radical, 645
 propargyl radical, 641, 643
Biodiesel, 259
Biomass, 112–116, 118, 125, 129, 131, 136
Bio-oil, 115, 125, 128, 133, 136
Bond dissociation energy, 95
Born-Oppenheimer approximation, 519, 524
Branching agents, 43
Branching ratio, 578–582, 589, 597, 602, 607, 608, 624
Branching step, 23, 26, 28, 83
Brute force method, 414, 441
Bunsen flame, 234
Butanol, 220, 225

C

Canonical form or canonicity, 64, 66
Carboxylic acid, 254, 255
Cavity enhanced absorption spectroscopy, 617, 623
Cavity ring-down spectroscopy, 200
Cellulose, 112, 116, 119, 120., 125
Cellulose acetate, 289
Certified reference materials, 294
 Printex-U, 296, 333
 SRM 1650b, 165, 294
Char, 111, 113, 119
Characterization, 115–117, 136
Chemical activation, 569, 570
Chemical thermometer, 633
 atomic resonance absorption spectroscopy, 436, 631
 infra-red absorption, 196, 197
 laser schlieren densitometry, 231
 ultra-violet absorption, 350, 351, 354, 609
Chemical correlation, 530
Chemisorbed species, 119
Chemistry guided reduction, 447

Coagulation, 364, 365, 372–374
 Coalescence, 364, 373, 374
 Collision efficiency, 402
 Collisional energy transfer, 553, 561, 563, 565, 566
 Commercial burner, 286
 Mckenna burner, 286
 Complete active space self-consistent field (CAS-SCF) method, 530
 Complete basis, 526, 528, 531
 Complex-forming bimolecular reaction, 552, 566, 569
 Composite quantum chemical method, 541
 Computational singular perturbation, 505
 Configuration interaction (CI), 529
 Connectivity method, 449, 450, 452, 453
 Continuous stirred-tank reactor, 185
 Cool flame, 28, 46
 Cooling rate, 138, 147, 322, 325
 Correlation energy, 528–530
 Counter-flow flames, 245, 263, 493
 Coupled cluster, 529
 Crossed molecular beam (CMB), 577
 Cross section, 311, 314, 317, 318, 321
 Cross sectional area, 311
 Computational singular perturbation (CSP), 505
 Cumulative reaction probability, 554, 557, 559, 561
 Cyclic ether, 26, 38, 41, 103, 267

D

Decomposition reaction, 635
 cyclohexane, 636–639
 1,4-dioxane, 637, 638
 furan, 636
 Decoupled direct method, 413, 440
 Dehydration, 95, 96
 Dehydrogenation, 95–97
 Density functional theory (DFT), 520
 Density of states, 554–557, 562, 567
 Detailed combustion mechanism, 20
 Detailed kinetic model, 18, 27, 75, 97, 202
 Detection, 608, 613, 614, 624
 Diesel fuel or engine, 4, 6, 19, 52, 94, 211, 219, 220, 265
 Diffusion flame, 261, 266, 286, 382, 497
 Dimethoxymethane, 220, 226, 227
 Dimethylether, 220, 226
 Directed relation graph (DRG), 449, 452–455
 Dynamics correlation, 526

E

Eigenvalue, 558, 566, 570, 572
 Eigenvector, 566, 572
 Electron configuration, 528, 530
 Electronic structure theory, 517, 520, 524, 531, 535
 Elemental analysis, 333, 335, 349
 Elementary reaction or step, 22–24, 607, 618
 EMSL basis set library, 527
 Enthalpy of formation, 516
 Entropy, 515, 516, 535–537
 Equilibrium geometry, 521–523
 Equilibrium reaction, 621, 622
 Ester, 94, 95, 97, 99, 100, 102, 104, 259
 Ethanol, 220–223
 Ether, 220, 225, 226
 Exact nonrelativistic hamilton operator, 255, 528
 EXGAS software, 22, 36, 59, 69, 75, 77, 79, 98, 100, 104, 459
 Exhaust gases, 286
 Exponential down model, 561, 562, 566

F

Factorial design, 505
 Fast flow tube, 623
 Final steady-state, 569, 570, 572
 First principles method, 521, 531
 Flamelet, 493, 498
 Flame structure, 232, 238, 240–242, 244, 253, 254, 257, 271
 Flash photolysis, 620, 622
 Flat-flame burner, 238, 245, 246, 259, 286
 Fluorescence spectroscopy, 355, 357
 Fourier transform infrared (FTIR) spectroscopy, 347, 616, 621
 Fractal structure, 320, 321
 Free radical, 23, 26
 Functional group, 29, 31, 34, 61, 67, 87

G

G3//B3LYP (G3B3) method, 541
 Gas chromatography, 196, 213, 241, 250, 319, 636
 coupled to mass spectrometry (GC-MS), 292
 Gasoline, 19, 49
 Gas-phase reaction, 119, 129, 133
 Gaussian-2 method, 533
 Gauss-type orbitals, 527

Glass fibre filter, 289
Global reaction, 35, 36, 47
Global sensitivity analysis, 416, 418, 419, 423,
425–427, 489, 506
GRI-mechanism, 432, 433
Group additivity method, 543
Group additivity values, 515, 535

H

HACA route, 284
Hartree-Fock (HF) method, 525, 528–530
Heat capacity, 535, 537, 539, 541
Heat of formation, 516, 535, 541
Hemicellulose, 112
Hetero-homogeneous reaction, 194
Hierarchical structure, 42
High dimensional model representation
(HDMR), 419, 489, 506
High dimensional model representations, 419,
489
High performance liquid chromatograph, 293
Hindered internal rotor, 556, 561, 563–565
HO₂ elimination, 38, 41
HO₂ radical, 523, 610–612, 621, 622
Homogeneous charge compression ignition
(HCCI) engine, 447, 454, 457, 463,
500
Hydrocarbon, 26, 31, 36, 37, 39, 42, 43, 49,
63, 70, 72, 77
Hydrogen atom abstraction or H-abstraction,
26, 39, 40, 67, 70, 72, 77, 86, 97
Hydroperoxide, 26, 27

I

Ignition delay time, 164, 165, 170, 172, 173,
175
Important species, 448, 449, 453, 455
Inception, 363, 365, 366, 378, 382
Inner-shell relativistic effects, 528
In situ adaptive tabulation (INSAT), 493–499
Intermediate steady-state, 570, 572
Internal standards, 292
Intramolecular isomerization, 100
Intermolecular potential, 394
Intrinsic low dimensional manifold (ILDM),
491, 493
Ion convention, 541

J

Jacobian, 413, 414, 449, 453

Jet-cooled laser induced fluorescence (JCLIF),
303, 304
Jet fuel, 50
Jet Fuels, 17, 19, 50, 455
Jet-stirred reactor, 100, 183–189, 191

K

Kernels, 393
Ketone, 250
Kinetic mechanism, 113, 116, 118
Kinetic Monte-Carlo model, 392, 396–398

L

Laminar burning velocity, 234
Laminar flame, 414, 423, 431, 432, 435, 448,
488, 489, 493
Laser desorption, 304, 316, 318, 319
Laser-induced fluorescence (LIF), 177, 304,
307, 310, 311, 325, 613
Laser-ion-induced incandescence (LII), 304, 320,
322, 326
Lennard-Jones potential, 394
Levoglucosan, 120, 133
Lewis structure, 29–31
Lignin, 112
LII, 320, 322, 326
Linear notation, 64, 65, 75
Local molecular environment, 34
Local sensitivity analysis, 412, 432–434
Local uncertainty analysis, 423
Lone pair, 32
Look-up table, 485, 490, 494, 495, 507
Loose transition state, 554, 556, 557, 560
Low-temperature oxidation, 26, 72, 101, 104
Lumping, 36, 43, 47, 70, 73, 78, 447, 448

M

MAMOX system, 70, 72
Mass spectrometry, 618, 622, 623, 634
 electron impact ionization, 152
 fragmentation, 362, 374–376, 392, 499,
 516, 618
 time-of-flight (TOF-MS), 198, 304, 316,
 581, 618
Master equation, 549, 552, 554, 565–567, 569,
570, 573
MC-SCF method, 530
Mean field approximation, 531
Methanol, 220, 221, 226, 228
Microprobe, 307, 311, 312, 317

- Modeling, 202
Molecular cooling, 304
Molecular dynamics, 401
Molecular growth, 363, 366, 368, 372
Molecular orbital, 525, 534
Møller-Plessett perturbation theory, 529
Multichannel reactions, 578, 580, 582, 591
Multiconfiguration self-consistent field (MC-SCF) method, 530
Multi-sectional method, 363, 366, 377
- N**
Naphthalene, 309, 311–313
NASA polynomial, 22, 539–541
Nascent distribution, 553, 561, 570
Necessary species, 448–450, 453–455
Negative temperature coefficient, 27, 42
Nonadiabatic effects, 597, 602
Nondynamical correlation, 530
Nonrelativistic electronic Schrödinger equation, 525, 528
- O**
O₂ addition, 26, 461
OH radical, 610, 611, 613–616
One-electron approximation, 525
On-the-fly reduction, 456
Open diffusion flame, 286
Optical diagnostics, 176
 See Fluorescence spectroscopy
 See Laser-induced fluorescence (LIF)
 See Laser-induced incandescence (LII)
 See UV-Visible spectroscopy
Optimization, 411, 412, 428–430, 432–434, 449, 454–456, 501
Orthogonal polynomial, 494, 502, 506
Oxidation, 191, 204
Oxidation-induced fragmentation, 374, 383, 384, 386
Oxygenated compound or oxygenate, 213, 219, 220, 231, 232
Oxygenated fuel, 94, 96, 98
Oxygen atom reaction, 581, 583, 597, 598, 602
- P**
Partition function, 522, 523, 541, 552, 560, 563, 564
Pathway, 34, 40, 42, 43, 69, 80, 83, 85–87
Perfectly stirred reactor, 185
Peroxy radical, 31, 40
Phenyl radical, 156
 perfluorinated, 157
 precursor, 156
 recombination/disproportionation, 157
Photoionisation, 304, 313, 318, 319, 326
Physical adsorption, 333, 335
Piecewise reusable implementation of solution mapping, 505
Planar flame, 238
Plank's law, 304
Plug flow reactor, 214–218, 294
Polycyclic aromatic hydrocarbons (PAH), 155, 334
 Collection techniques, 287
 Cooling, 307
 Primary particles model (PAH-PP), 390
Polynomial chaos expansion, 418, 421, 427, 434
Polytetrafluoroethylene, 289
Polyurethane foam, 288
Pople diagram, 533
Potential energy surface (PES), 519, 552, 554
Potentials, 394
Premixed flame, 286
 concentration, 363, 366
 flat-flame burner, 286
 H/C ratio, 363, 366
Pressure-dependent reaction network, 69
Primary atom of carbon, 33
Primary mechanism or reaction, 26, 39, 42, 43, 70, 73, 77, 78, 95
Principal component analysis, 450, 492
Probe sampling, 241
Propagation, 23, 77
Propanol, 220, 221, 224–226
Pseudo-first order, 619, 620
Pyrene, 313
Pyrolysis, 69, 70, 112–114, 119, 120, 125, 127, 135, 204
Pyrolysis condition, 286
- Q**
Quantum chemistry, 24, 399
Quartz fibre filter, 289
Quasi-steady state approximation (QSSA), 492
- R**
Radical detection, 608, 613, 614, 624
Radical generation, 608, 609, 612, 613
Radical precursor, 611
Radical–radical reaction, 580
Radical reaction, 13
 alkyl radical, 635

- intra-molecular H transfer, 635
- Raman spectroscopy, 333, 335, 344
- Rapid compression machine (RCM), 163, 164, 171, 175
- Rate constant, 21–25, 33, 40, 41, 69, 72, 83, 86, 96–102, 104, 612, 618–621, 624
- Rate-controlled constrained equilibrium (RCCE), 500
- Rayleigh, 321
- Reaction class, 34, 37, 41, 42, 60–63, 67, 68, 77, 85–87, 95, 104
- Reaction Dynamics, 577, 582
- Reaction path degeneracy, 552, 554, 555, 560, 565
- REACTION system, 62, 85, 87
- Reduced mechanism, 48, 50
- Redundant species, 447, 449, 450, 454
- Reference component, 116, 117, 129
- Refractive index, 321
- Repro-modelling, 490, 493, 502
- Residence time, 185, 213–215, 217, 219
- Residence time distribution, 185, 213, 216
- Resonance enhanced multiphoton ionisation (REMPI), 314, 315
- Resonance fluorescence, 614, 621
- Response surface, 418, 421, 426, 433, 501
- Reynolds number, 189, 217
- Rigid rotor-harmonic oscillator, RRHO approximation, 523
- RMG software, 80
- RRKM theory, 549, 557, 567

- S**
- Scanning electron microscopy, 338
- Scattering, 320, 321, 325
- Schrödinger equation, 517–523, 527
- Secondary mechanism or reaction, 42, 43, 78, 95
- Self consistent field (SCF) method, 526, 528
- Self-organising map, 499
- Semi-empirical methods, 541
- Sensitivity analysis, 411, 417, 418, 423, 447, 501
- Sensitivity coefficient, 412–415, 417, 424, 432, 440, 501
- Sensitivity matrix, 413, 450
- Shock tube, 143
 - effective reaction time, 46
 - gas sampling, 144, 159
 - molecular beam sampling, 153
 - pressure trace, 146
 - sample port, 145, 146
 - shock tube/TOF-MS, 154
 - single-pulse technique, 7, 145
 - supersonic jet cooling, 151, 307
 - thermal boundary layer, 153
- Simulation error, 450, 451
- Simulation error minimization connectivity method, 450
- Single stage ignition, 165, 175
- Size exclusion chromatography, 333, 335
- Skeletal mechanism, 44, 47, 431, 454
- Slater-type orbital, 527
- Slow Invariant manifold, 491
- SMILES notation, 64, 67
- Solvent extraction technique, 286
 - ultrasonic extraction, 291
 - microwaves, 291, 296
 - accelerated solvent extraction, 291
 - supercritical fluid extraction, 291
 - soxhlet extraction, 291
- Soot characterization, 333, 334
- Soot reactivity, 333, 335
- Soot volume fraction, 303, 304, 320, 327, 360, 366, 383
- Species pool, 60–62, 77, 80, 86
- Specific heat, 515
- Specific rate coefficient, 549, 553, 554, 565, 567
- Specific surface area, 333–337, 341, 349
- Spectroscopic method, 613
- Spherically expanding flame, 235
- Spin-orbit coupling, 591
- Split-valence basis set, 527
- Spray burner, 286
- Standard heat of formation, 518
- State space, 397, 398, 469, 475, 479
- Statistical adiabatic channel model, 12, 549, 557
- Statistical mechanics, 522
- Statistical rate theory, 551, 572
- Stepladder model, 561, 563, 566, 567, 570
- Submechanism, 41
- Sum of states, 556–558, 561
- Supercritical fluid extraction, 291, 296
- Supersonic expansion, 307, 326
- Surface response method, 418
- Surrogate, 49, 488, 489, 493–496, 498, 500, 505–507

- T**
- Tabulation, 494
- Taylor expansion, 412, 494, 501
- TDLAS, 616, 621
- Temperature gradient, 191, 213, 217
- Temperature measurement, 242

- Termination criteria, 61, 62, 80
Theory of the free jet, 187
Thermal electron convention (TEC), 540
Thermochemical data, 22, 29, 76, 537, 538, 540–542
Thermogravimetry (TGA) analysis, 333, 346
Threshold energy, 552, 554, 560, 563, 570
Tight transition state, 557, 560, 568
Transition state theory, 25, 26, 33, 34, 549, 552
Transmission electron microscopy (TEM), 338, 339
Tubular flow reactor, 212, 213
Tubular reactor, 286, 431
Two-stage ignition, 165, 175
- U**
Ultrasonic extraction, 291
Uncertainty analysis, 411, 412, 415, 417, 423, 434, 440, 489
- Unimolecular reaction, 552, 554, 557, 565, 566, 569, 608, 618
Unsaturated hydrocarbon, 598, 581, 583
UV-Visible spectroscopy, 351
- V**
Vibrational analysis, 523
Vibrational mode, 522, 523
- W**
Wall reaction, 201, 202
Water, 286
Wave function theory, 520
- X**
XAD resin, 288
X-ray diffraction, 333, 335, 342
Xylose, 122